

CONF-760503-P1

# PROCEEDINGS



## INTERNATIONAL CONFERENCE ON LIQUID METAL TECHNOLOGY IN ENERGY PRODUCTION

MAY 3-6, 1976  
CHAMPION, PENNSYLVANIA

## NOTICE

This report was prepared as an account of work sponsored by the United States Government. Neither the United States nor the United States Energy Research and Development Administration, nor any of their employees, nor any of their contractors, subcontractors, or their employees, makes any warranty, express or implied, or assumes any legal liability or responsibility for the accuracy, completeness or usefulness of any information, apparatus, product or process disclosed, or represents that its use would not infringe privately owned rights.

This report has been reproduced directly from the best available copy.

Available from the National Technical Information Service, U. S. Department of Commerce, Springfield, Virginia 22161

Price: Paper Copy \$12.00 (domestic)  
                  \$14.50 (foreign)  
      Microfiche \$3.00 (domestic)  
                  \$4.50 (foreign)



**Proceedings**  
**of the**  
**International Conference on Liquid Metal Technology in Energy Production**

**Seven Springs Mountain Resort May 3—6, 1976**

**Champion, Pennsylvania**

**Editor: M. H. Cooper**

**November 1976**

**Sponsored by: American Nuclear Society, Material Sciences Division;  
AIME, Institute of Metals Division;  
United States Energy Research & Development Administration;  
Pittsburgh Section, American Nuclear Society**

# INTERNATIONAL CONFERENCE ON LIQUID METAL TECHNOLOGY IN ENERGY PRODUCTION

## PREFACE

The development of sodium-cooled fast breeder reactors to produce electric power is truly a technological undertaking of international proportions. Extensive development is underway in many countries and notable progress is being made. Liquid metal technology is a central effort in this activity, and it is, therefore, necessary that the community of individuals working in this area meet periodically to exchange views, discuss recent developments, sharpen understanding for future work, and re-kindle the spirit for the tasks that remain.

success of this meeting. We look forward to a continuing association with you and to the next meeting when we can meet as colleagues again.

Edgar Berkey  
General Chairman

Martin H. Cooper  
Technical Program Chairman

This conference took place in a beautiful rustic setting in the Laurel Mountains of Southwestern Pennsylvania in early May 1976. This environment blended together with the enthusiastic participation of the attendees to produce a meeting that we will all remember. On behalf of the Organizing Committee for the International Conference on Liquid Metal Technology in Energy Production, we would like to express our deep appreciation to all of those who made this conference a significant milestone in our mutual contributions to this international activity.

Many persons, too numerous to mention individually in this brief note, representing industry, the American Nuclear Society, the AIME, and the U.S. Government assisted in the many efforts necessary to create this conference. The success of their efforts are amply chronicled in these proceedings.

Our invited speakers, Congressman Mike McCormack, Mr. George Hardigg, and Dr. G. W. Cunningham gave timely and informative talks, and their contributions have also been included herein.

Special conference events were sponsored by Atomic International, General Electric Co., and Westinghouse Electric Corp., and refreshments were provided by Mine Safety Appliances Research, Basic Technology, and O'Donnell Associates. The cooperation of Westinghouse Electric Corp. in providing substantial support for committee members and for secretarial and graphics assistance is gratefully acknowledged.

Finally, we would like to thank each of the authors and attendees, many of whom travelled large distances to join us, for contributing, each in their way, to the

# MEETING OFFICIALS

**General Chairman:** E. Berkey (WRL)

**Honorary Chairman:** P. Murray (WARD)

**Program Committee:**

M. H. Cooper (WARD), Chairman  
J. L. Ballif (WHC)  
F. A. Cafasso (ANL)  
G. D. Collins (GE)  
C. C. Conners (LMEC)  
J. H. DeVan (ORNL)  
E. E. Hoffman (ERDA)  
J. R. Weeks (BNL)

**Finance:**

W. S. Brown (WPWR Systems)  
D. G. Lorentz (WPWR Systems)

**Arrangement:**

R. E. Witkowski (WRL)  
R. M. Lowy (WRL)

**Publicity:**

G. A. Whitlow (WARD)

**Tour:**

J. H. Saling (WARD)

**Transportation:**

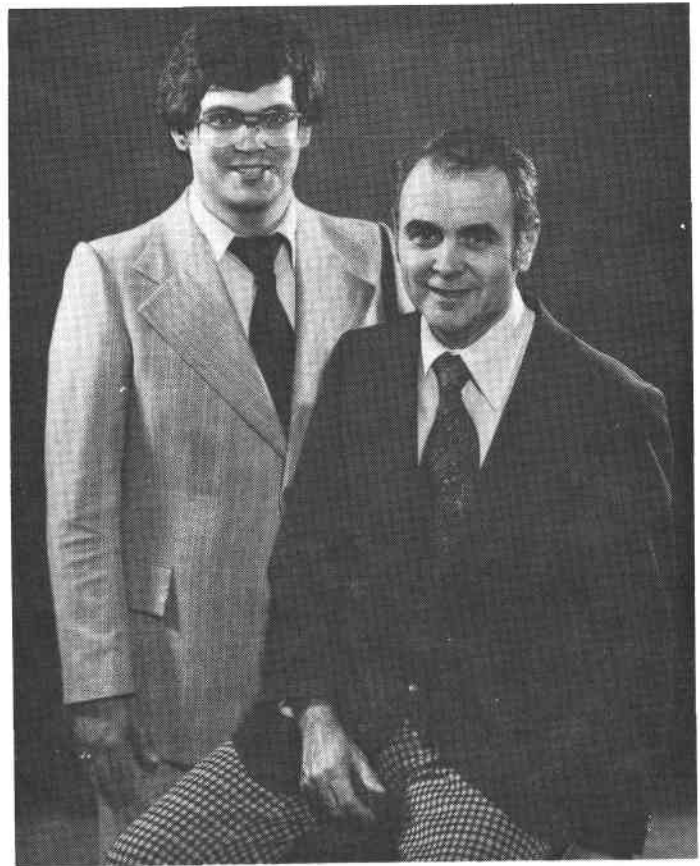
S. A. Shiels (WARD)  
W. H. Reed (WRL)

**ANS Liaison:**

D. E. Thomas (WRL)

**Publications:**

M. H. Cooper (WARD), Editor  
E. A. Weaver (WARD), Editorial Assistant  
C. Ornot, K. Perry (WARD),  
S. Rittinger (WRL), Typists



Donald G. Lorentz (standing) and  
William S. Brown (seated)



Edgar Berkey (seated)  
Donald E. Thomas (standing) } WRL



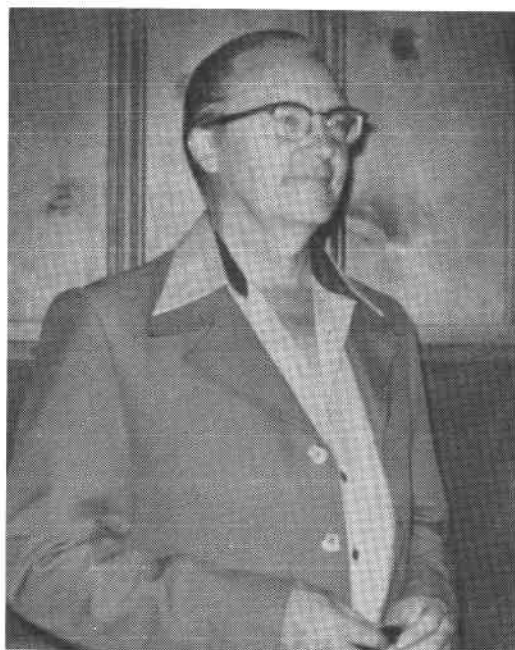
From left to right:Graham A. Whitlow, Stuart A. Shiels, Peter Murray, James H. Saling and Martin H. Cooper.



From left to right:J.R. Weeks,E.E. Hoffman, J.L. Ballif, C.C. Connors and M.H. Cooper.



From left to right  
 Robert M. Lowy  
 William H. Reed  
 Robert E. Witkowski } WRL



G.D. Collins

CONTENTS

Part 1

KEYNOTE

ADDRESS: G. W. Cunningham (ERDA)

Session I - Operating Reactors

Chairman: L. Minnick (EPRI)

I-1	"Some Aspects of Sodium Technology Issued from the Operating Lacroix (CEA-Marcoule).	1
I-2	"Sodium Technology at EBR-II," J. T. Holmes, C. R. F. Smith, W. H. Olson (ANL-Idaho).	12
I-3	"Impurity Deposition in PFR Plugging Meters and Cold Traps," C. G. Allan (UKAEA-DERE).	22
I-4	"Radioactive Product Behavior During the Operation of Sodium-Cooled Reactors of the U.S.S.R.," V. I. Polyakov, N. V. Krasnoyarov, Yu. V. Chechetkin (Lenin Atomic Reactor Research Institute).	30
I-5	"Activity Deposition in DFR Primary Cold Traps," C. G. Allan and T. A. H. Taylor (UKAEA-DERE).	35
I-6	"Tube Tightness Survey During PHENIX Steam Generator Operation," E. Cambillard (CEN-Sacaly).	44
I-7	"Evolution of Sodium Purification, Rapsodie, Phenix," Super Phenix, R. Abramson, X. Elie (CEA-Cadarache) J. M. Saur, M. Thevenin, F. Velin (CIRNA)	51
	Discussion	120

Session II A - Loop Operations

Chairman: C. C. Conners (LMEC)

II A-1	"Metallurgical Problems Associated with Large Sodium Loop Operations," N. J. Hoffman (LMEC).	60
II A-2	"Materials Experience with Large Sodium Loops and Components," H. Mausbeck (Interatom).	67
II A-3	"Experience with Sodium Purification on Large-Scale Operational Test Loops in France," E. Benoist, M. Cambillard (CEA-Cadarache) and J. L. Quinet (EDF).	75
II A-4	"Identification of Impurities in Sodium and Its Purification," B. I. Subbotin, L. G. Voltchkov, F. A. Kozlov, Ju. I. Zagorulko, E. K. Kuznetsov (Institute of Physics and Power Engineering).	83
II A-5	"Sodium and Cover Gas Chemistry in the High Temperature Sodium Facility," J. J. McCown and H. C. Duncan (WHC).	94

II A-6	"Sodium Characterization During the Starting Period of a Sodium Loop," F. Lievens, C. Parmentier, M. Soenen (CEN/SCK-Mol).	105
II A-7	"Characterization of Particulate Material Extracted from a Large Sodium Loop," T. R. Padden, S. A. Meacham, H. W. Brandt (WARD).	112
II A-8	"Operational Techniques Employed for the Liquid Sodium Source Term Control Loops," L. E. Chulosa (WHC).	116
	Discussion	120

Session II B - Friction, Wear, and Self-Welding

Chairman: K. Horton (ERDA)

II B-1	"Development of Low Friction Materials for LMFBR Components," R. N. Johnson, R. C. Aungst (WHC), N. J. Hoffman (LMEC), M. G. Cowgill, G. A. Whitlow, W. L. Wilson (WARD).	122
II B-2	"Friction and Wear in Liquid-Metal Systems: Comparability Problems of Test Results Obtained from Different Test Facilities," E. Wild and K. J. Mack (Karlsruhe).	131
II B-3	"Corrosion and Tribological Investigations of Chromium Carbide Coatings for Sodium Cooled Reactor Applications," G. A. Whitlow, W. L. Wilson, T. A. Galioto, R. L. Miller, S. L. Schrock (WARD), N. J. Hoffman, J. J. Droher (LMEC), R. N. Johnson (WHC).	138
II B-4	"Experimental Investigations of the Frictional and Wear Behavior of Tungsten Carbide Cermet Ball Bearings Under Axial Load in Liquid Sodium," K. W. Kleeefeldt (Karlsruhe).	145
II B-5	"Friction and Wear Behavior of Colmonoy and Stellite Alloys in Sodium Environment," S. Kanoh, S. Mizobuchi, H. Atsumo (PRNFDC).	153
II B-6	"Wear of Rolling Element Bearings in Sodium," C. S. Campbell (UKAEA-REML).	160
II B-7	"Evaluation of Cobalt and Nickel Base Materials for Sliding and Static Contact Applications in a Liquid Metal Fast Breeder Reactor," N. J. Hoffman, J. J. Droher (LMEC), W. L. Wilson, T. A. Galioto, G. A. Whitlow, R. L. Miller, J. Y. Chang, S. L. Schrock (WARD), R. N. Johnson (WHC).	167
II B-8	"Investigations into the Self-Welding Behavior of Metallic Materials Exposed to Sodium," F. Huber and K. Mattes (Karlsruhe).	177
	Discussion	184

# INTERNATIONAL CONFERENCE ON LIQUID METAL TECHNOLOGY IN ENERGY PRODUCTION

## Session III A - Free Electron Notes I

Chairman: M. H. Cooper (WARD)

III A-1	"Bagged Maintenance Techniques for Sodium Systems," A. Stewart (AI).	187
III A-2	"Development and Testing of High-Performance Fuel Pin Simulators for Boiling Experiments in Liquid Metal Flow," V. Casal (Karlsruhe).	187
III A-3	"LMFBR, Sodium/Steam Generator with an Inert Liquid Metal Interface," J. H. McLoughlin (James Henry Consultants).	188
III A-4	"Dynamic Response of EBR-II Secondary Sodium System to Postulated Leaks of Steam and Water into Sodium," S. Srinivas, P. S. Chopra, C. C. Stone (ANL).	188
III A-5	"Events Following Postulated Failures in EBR-II Steam Generator System," G. C. Wolz, C. Gukeisen, P. S. Chopra (ANL).	189
III A-6	"Primary Steam Generators for the LMFBR," J. D. Mangus (WARD).	189

## Session III B - Free Electron Notes II

Chairman: F. Arcella (WRL)

III B-1	"Investigation of Embrittlement by Liquid-Metals," M. Nicholas (UKAEA-AERE).	191
III B-2	"Some Observations on the Sodium-Sodium Hydroxide System," F. A. Cafasso, K. M. Myles, A. K. Fischer (ANL).	191
III B-3	"Corrosion Model for Iron-Base Alloys in Sodium," G. Scibona (CNEN).	191
III B-4	"Plasma and Detonation Gun Applied Coatings-Design Alternatives to Reduce Friction and Wear," T. A. Wolfla, and R. K. Dagley (UCC).	191
III B-5	"Small Sodium Leak Characteristics in Low Moisture, Low Oxygen, Nitrogen Atmospheres," W. L. Matheys, G. R. Taylor (WARD).	192

## Session IV A - Steam Generator

Chairman: G. W. Meyers (AI)

IV A-1	"Materials Engineering Issues, LMFBR Steam Generators," C. N. Spalaris, K. D. Challenger, R. A. Day, D. Dutina, P. J. Ring (GE).	193
IV A-2	"Studies on Some Problems of Leaks in Sodium-Water Steam Generator," F. A. Kozlov, G. P. Sergeev, A. R. Sednev, V. M. Makarov (Institute of Physics and Power Engineering).	202
IV A-3	"Qualification of Alloy 800 for Sodium Heated Steam Generators," J. M. Duke, C. E. Sessions, (W-Tampa), W. E. Ray, (WARD).	211
IV A-4	"Calculation of Wastage by Small Water Leaks in Sodium Heated Steam Generators," K. Tregonning (UKAEA-DERE).	218
IV A-5	"Small Leak Shutdown, Location and Behavior in LMFBR Steam Generators," D. W. Sandusky (GE).	226
IV A-6	"Small Leak Damage and Protection Systems in Steam Generators," D. Greene (GE).	233
IV A-7	"Large Scale Sodium-Water Reaction Tests for Monju Steam Generators," M. Sato, H. Hiroi, M. Hori (PRNFDC).	242
IV A-8	"Fail-Safety of the EBR-II Steam-Generator System," P. S. Chopra, C. C. Stone, E. Hutter, W. K. Barney, and R. G. Staker (ANL).	248
IV A-9	"Sodium and Steam Leak Simulation Studies for Fluidized Bed Steam Generators," A. R. Keeton, W. G. Vaux, P. K. Lee, R. E. Witkowski (WRL).	256
	Discussion	262

## Session IV B

### Radioactive Corrosion and Fission Product Transport

Chairman: J. Ballif (WHC)

IV B-1	"Radioactive Corrosion Product Transport and Control," W. F. Brehm (WHC).	263
IV B-2	"Sorption of Radionuclides on Sodium Sampling Vessels," H. H. Stamm (Karlsruhe).	271
IV B-3	"The On-Line Separation of Radioiodine in Highly Radioactive EBR-II Sodium," R. Villarreal and C. C. Miles (ANL-Idaho).	278
IV B-4	"A Computational Technique for Estimating Corrosion Product Release in an LMFBR," W. L. Kuhn (WHC).	280
IV B-5	"Fission Product Measurements in the Inpile Fission Product Loop," N. Mitsutsuka, Y. Gohshi, H. Shimojima (Toshiba), H. Feuerstein (Karlsruhe).	284

# INTERNATIONAL CONFERENCE ON LIQUID METAL TECHNOLOGY IN ENERGY PRODUCTION

## Session V B - Corrosion I

**Chairman:** J. Weeks (BNL)

<b>IV B-6</b>	"Fission Product Deposition in a Stainless Steel Sodium System," N. Mitsutsuka, Y. Gohshi, H. Shimojima (Toshiba), H. Feuerstein (Karlsruhe).	291	<b>V B-1</b>	"Corrosion, Transport and Deposition of Stainless Steel in Liquid Sodium," B. H. Kolster, L. Bos (TNO).	368
<b>IV B-7</b>	"Control of Tritium in LMRBR Sodium by Cold Trapping," C. C. McPheeters and D. Raue (ANL).	298	<b>V B-2</b>	"In-Reactor Corrosion Behavior of Stainless Steel in High Temperature Sodium," J. W. Weber (WHC).	378
<b>IV B-8</b>	"Radiochemical Measurement of Mass Transport in Sodium," M. H. Cooper (WARD) and S. H. Chiang (U. of Pittsburgh).	304	<b>V B-3</b>	"The Influence of LMFBR Fuel Pin Temperature Profiles on Corrosion Rate," S. A. Shiels, C. Bagnall, S. J. Orbon, S. L. Schrock (WARD).	386
	Discussion	310	<b>V B-4</b>	"The Corrosion of Steels in Liquid Sodium," C. F. Clement and P. Hawtin (UKAEA-AERE).	393
			<b>V B-5</b>	"Thermodynamic and Diffusion Studies on Corrosion of Austenitic Stainless Steel in Liquid Sodium," H. R. Konvicka, K. L. Komarek, (Univ. of Vienna), I. E. Schreinlechner (OSA).	400
			<b>V B-6</b>	"Solubility of Oxygen in Liquid Sodium: Effect on Interpretation of Corrosion Data," K. T. Claxton (UKAEA-AERE).	407
				Discussion	415

## Session V A

### Effects of Sodium on Mechanical Properties

**Chairman:** C. Brinkman (ORNL)

<b>V A-1</b>	"Material Effects in LMFBR Sodium Systems," W. Dietz, E. D. Grosser, H. Lorenz (Interatom).	313
<b>V A-2</b>	"The Effect of Liquid Sodium Thermochemical Reactions with Stainless Steels on Mechanical Response," G. Subbaraman and K. L. Reifsnider (VPI).	324
<b>V A-3</b>	"The Influence of Sodium Corrosion on the Mechanical Properties of Fuel Element Cladding," H. U. Borgstedt and G. Frees (Karlsruhe).	331
<b>V A-4</b>	"Effect of Sodium on the Creep-Rupture Behavior of Type 304 Stainless Steel," K. Natesan, O. K. Chopra, T. F. Kassner (ANL).	338
<b>V A-5</b>	"Influence of Dynamic Sodium on the Creep Properties of Stabilized Austenitic Steels," H. Tas, F. Casteels (CEN/SCK-Mol), M. Schirra (Karlsruhe).	346
<b>V A-6</b>	"Low Cycle Fatigue Testing in Flowing Sodium at Elevated Temperatures," J. R. Kahrs, P. N. Flagella (WARD).	353
<b>V A-7</b>	"Influence of Sodium on the Low-Cycle Fatigue Behavior of Types 304 and 316 Stainless Steel," D. L. Smith, G. J. Zeman, K. Natesan, T. F. Kassner (ANL).	359
	Discussion	365

## Session VI A - Advanced Applications

**Chairman:** J. DeVan (ORNL)

<b>VI A-1</b>	"Compatibility of Structural Materials with Boiling Potassium," J. H. DeVan (ORNL).	418
<b>VI A-2</b>	"Application of Boiling Liquid Metals in Industrial Processes," H. M. Kottowski, C. Savatteri, P. Fiebelmann, M. Mol (ISPARA).	427
<b>VI A-3</b>	"The Role of Alkali Metals in Energy Conservation," G. E. Rajakovics (VEW) and N. Schwarz (OSA).	431
<b>VI A-4</b>	"Solution Behavior of Hydrogen Isotopes and Other Non-Metallic Elements in Liquid Lithium," V. A. Maroni, W. F. Calaway, E. Veleckis, R. M. Yonco (ANL).	437
<b>VI A-5</b>	"The Corrosion of Ferrous Alloys in Nitrogen Contaminated Liquid Lithium," D. L. Olson and W. L. Bradley (Col. Sch. of Mines).	446

## Part 2

<b>VI A-6</b>	"Corrosion of Iron-Based Alloys by Lithium," J. E. Selle (ORNL).	453
<b>VI A-7</b>	"Compatibility of Bismuth and Bismuth-Lithium Solutions with Refractory Metals and Graphite," J. R. DiStefano (ORNL).	462
<b>VI A-8</b>	"Liquid Metal Current Collectors for High-Speed Rotating Machinery," S. L. Carr (D. W. Taylor Naval Ship R&D Center)	470

**Session VI C  
Sodium Removal and Requalification**

**Chairman:** G. R. Taylor (WARD)

<b>VI A-9</b>	"Technology Developments for a 3000-hp Homopolar Generator with Liquid Metal Current Collectors." F. G. Arcella, A. R. Keeton, R. E. Witkowski, E. Berkey (WRL) and C. J. Mole (SC Electric Machinery Systems).	477	<b>VI C-1</b>	"Sodium Removal Technology—The Alcohol Process." F. H. Welch, O. P. Steele III, J. G. Asquith (AI).	548
<b>VI A-10</b>	"Liquid Metal Electrodes in Secondary Batteries." R. K. Steunenberg (ANL).	485	<b>VI C-2</b>	"Review of Sodium Removal Processes Using Water." C. W. Funk, M. C. Crippen, G. B. Barton (WHC).	554
	Discussion	492	<b>VI C-3</b>	"Experience from Purification of Sodium-Wetted Components at the KNK-Facility." H. Richard, K. Ch. Stade, H. Breitlander (KBG), H. Zschetke (Interatom).	561

**Session VI B - Instrumentation I**

**Chairman:** L. PohI (GE)

<b>VI B-1</b>	"Water-to-Sodium Leak Detectors: Development and Testing." J. M. McKee (ANL).	494
<b>VI B-2</b>	"Performance of PFR Hydrogen Leak Detection System Based on Water and Hydrogen Injection into the Steam Generator Units." R. A. Davies, J. L. Drummond, D. W. Adaway, D. M. Wallace (UKAEA-DERE).	502
<b>VI B-3</b>	"EBR-II Water-to-Sodium Leak Detection System." M. M. Wrightson, K. McKinley, W. E. Ruther, J. T. Holmes (ANL-Idaho).	508
<b>VI B-4</b>	"Small Sodium-to-Gas Leak Behavior in Relation to LMFBR Leak Detection System Design." J. Hopenfeld (ERDA), G. R. Taylor (WARD), L. A. James (WHC).	515
<b>VI B-5</b>	"An Ultrasonic Method for the Measurement of Oxygen in Sodium." G. M. Glover (CEGB-Leatherhead).	523
<b>VI B-6</b>	"Multicomponent Impurity Detection with a Sodium Plugging Indicator." J. C. Biery and D. A. Montevideo (U. of Florida).	529
<b>VI B-7</b>	"Electrochemical Measurement of Carbon Potential in Sodium-Steel Systems." M. R. Hobdell, J. R. Gwyther, A. J. Hooper, S. P. Tyfield (CEGB-BNL).	533
<b>VI B-8</b>	"Measurement of Oxygen and Carbon Activities in Liquid Sodium by Electro-Chemical Techniques." P. Roy (GE).	541
	Discussion	546

<b>VI C-4</b>	"Decontamination of Materials After Exposure in LMFBR Primary Circuit." A. Lafon, D. Msika, E. Sermet, J. C. Broutin (CEN-Cadarache).	567
<b>VI C-5</b>	"An Analysis of Methods Available for the Removal of Sodium from Corrosion Test Samples." M. G. Barker, M. E. Down, T. K. Leung (U. of Nottingham).	571
	Discussion	575

**Session VI D - Component Development**

**Chairman:** E. C. Bishop (WARD)

<b>VI D-1</b>	"Post-Corrosion Analyses of a Sodium-Sodium Heat Exchanger After 60,000 Hours Sodium Exposure." F. Casteels, H. Tas, J. Dresselaers, A. Cools, L. Knaepen (CEN/SCK-Mol).	577
<b>VI D-2</b>	"Post-Test Examination of a 30-MW Sodium-to-Sodium Intermediate Heat Exchanger." G. M. Goodwin, B. C. Leslie, B. E. Foster, G. M. Slaughter, J. H. DeVan (ORNL).	584
<b>VI D-3</b>	"The Effect of Argon Desorption on the Heat Transfer Performance of a Fast Reactor Intermediate Heat Exchanger." J. T. Klaschka, R. A. Huber (UKAEA-AERE).	591
<b>VI D-4</b>	"Development Program and Major Test Results for Thermal Insulation Used in Presence of Sodium Vapors and Aerosols." G. Lemerrier, M. Sauvage (CEN-Cadarache).	599
<b>VI D-5</b>	"Transport of Sodium Through the Cover Gas of a Sodium Cooled Fast Reactor." C. F. Clement, P. Hawtin (UKAEA-AERE).	603
<b>VI D-6</b>	"Development Tests in Sodium on Two Types of Gripper Drive." P. H. Delves and G. D. Hill (UKAEA-REML).	610
	Discussion	617



# INTERNATIONAL CONFERENCE ON LIQUID METAL TECHNOLOGY IN ENERGY PRODUCTION

## Session VII A - Physical Chemistry

**Chairman:** F. Cafasso (ANL)

<b>VII A-1</b>	"The Solubilities of the Noble Gases in Liquid Sodium," F. A. Cafasso, E. Veleckis, H. M. Feder, H. C. Schnyders (ANL).	619	<b>VII B-6</b>	"The Corrosion of Stainless Steels by High Temperature, Low Oxygen Alkali Metals," N. F. Schwarz (OSA) and G. E. Rajakovics (VEW).	623
<b>VII A-2</b>	"Studies on the Sodium-Vanadium-Oxygen System at Low Oxygen Potential," A. J. Hooper, E. A. Trevillion (CEGB-BNL).	623	<b>VII B-7</b>	"Compatibility of Ferritic Steels in a Sodium Environment," O. K. Chopra, K. Natesan, T. F. Kassner (ANL).	730
<b>VII A-3</b>	"Monitoring and Measurement of Oxygen Concentrations in Liquid Sodium," D. L. Smith (ANL).	631	<b>VII B-8</b>	"Corrosion Considerations in Alloy Development," W. F. Brehm and R. P. Anantamula (WHC).	738
<b>VII A-4</b>	"The Preparation and Characterization of Sodium and Transition Metal Double Oxides," P. C. S. Wu (WARD), P. Chiotti, J. T. Mason (Ames).	638		Discussion	743
<b>VII A-5</b>	"Impurity Crystallization in Liquid Sodium Systems," D. J. Hebditch and B. J. Gliddon (CEGB-Marchwood).	643			
<b>VII A-6</b>	"Experimental Characterization of Sodium Cold Traps and Modeling of Their Behavior," B. R. Grundy (WARD).	650	<b>Session VIII A - Instrumentation II</b>		
<b>VII A-7</b>	"The Experimental Vapor Pressure and Critical Point of Sodium," V. S. Bhise and C. F. Bonilla (Columbia University).	657	<b>Chairman:</b> G. Collins (GE)		
<b>VII A-8</b>	"Fundamental Studies on the Mechanism of Sodium Combustion," R. N. Newman and J. F. B. Payne (BNL-CEGB).	667	<b>VIII A-1</b>	"Development and Testing of Instrumentation Sensors for Sodium Coolant Systems," K. A. Davis, B. E. Fischer, G. E. Turner, F. L. Fletcher, G. J. Twa (LMEC).	746
<b>VII A-9</b>	"The Reaction of Potassium Superoxide in Excess Potassium," S. A. Sloan (CEGB-Leatherhead).	675	<b>VIII A-2</b>	"Utilisation and Performance of Sodium Instrumentation During Start-up and Initial Operation of PHENIX," N. Lions, H. Buis, J. Baron, C. Fournier, J. Gourdon (CEN-Cadarache), A. Jeannot (CEN-Saclay), A. LaCroix (CEA-Marcoule).	755
	Discussion	681	<b>VIII A-3</b>	"Test Results and Still Existing Problems of the Sodium Instrumentation for LMFBR's," K. Schmidt, R. Hans (Interatom).	762
<b>Session VII B - Corrosion II</b>			<b>VIII A-4</b>	"On-Line Sodium and Cover Gas Purity Monitors as Operating Tools at EBR-II," C. R. F. Smith, W. J. Richardson, J. T. Holmes (ANL-Idaho).	770
<b>Chairman:</b> E. E. Hoffman (ERDA)			<b>VIII A-5</b>	"On-Line Radiometric Analysis of FFTF's Cover Gas—Basic Analytical Features," F. E. Holt (WHC).	777
<b>VII B-1</b>	"Some Aspects of the Mass Transfer Behaviour in Sodium of Steels of Interest in UK Fast Reactor Programme," A. W. Thorley, C. Tyzack, B. Longson, A. C. Raine (UKAEA-REML).	685	<b>VIII A-6</b>	"A Dynamic Sparger for Measuring Low Helium Concentrations in Liquid Sodium," B. R. Grundy, G. R. Taylor (WARD).	782
<b>VII B-2</b>	"Formation and Hydraulic Effects of Deposits in High Temperature Sodium Coolant Systems," W. Yunker (WHC).	698	<b>VIII A-7</b>	"Development of a Sodium Ionization Detector for Sodium-to-Gas Leaks," W. H. Reed, J. E. Bauerle, E. Berkey (WRL), S. A. Lane (WNICD).	789
<b>VII B-3</b>	"Mass Transfer Related Pressure Drop Fluctuations in Flowing Sodium Systems," A. A. Bishop (U. of Pitt), J. Hopfenfeld (ERDA), S. J. Orbon, S. L. Schrock, G. A. Whitlow (WARD).	702	<b>VIII A-8</b>	"Development of an In-Core Flow Meter for the LMFBR," A. Dohi, M. Oda, S. Iida (Mitsubishi).	796
<b>VII B-4</b>	"An Experimental Investigation of Cavitation Inception and Damage in a Flowing Sodium Environment," Y. S. Cha (ANL), T. J. Costello (WARD), J. Hopfenfeld (ERDA), R. L. Miller (WARD).	709	<b>VIII A-9</b>	"Flow Measurement by Ultrasonic Method," H. Araki, Y. Matsunaga, M. Oda, S. Iida (Mitsubishi).	802
<b>VII B-5</b>	"Investigations of Changes in the Surface Layer Composition of Materials Exposed to Sodium by Glow Discharge Optical and Auger Electron Spectroscopy," H. Schneider (Karlsruhe).	716		Discussion	808

# INTERNATIONAL CONFERENCE ON LIQUID METAL TECHNOLOGY IN ENERGY PRODUCTION

## Session VIII B - Corrosion

**Chairman:** T. Kassner (ANL)

<b>VIII B-1</b>	"Carbon and Nitrogen Transport in Sodium Systems," S. L. Schrock, S. A. Shiels, C. Bagnall (WARD).	809
<b>VIII B-2</b>	"Carbon Transport and Material Property Degradation in a Model of the Clinch River Breeder Reactor Secondary Sodium System," J. L. Krankota and K. D. Challenger (GE).	819
<b>VIII B-3</b>	"An Analysis of Carbon Transport in the EBR-II and FFTF Primary Sodium Systems," R. B. Snyder, K. Natesan, T. F. Kassner (ANL).	826
<b>VIII B-4</b>	"Carbon Transfer Between 2-1/4 Cr-1 Mo Alloy and Austenitic Steels (Experiments in Anisothermal Loops)," M. Besson, P. Baque, L. Champeix (CEN-Cadarache), J. R. Donati, C. Oberlin, P. Saint-Paul (EDF).	834
<b>VIII B-5</b>	"The Corrosion of Steels in Molten Sodium Hydroxide," R. N. Newman, C. A. Smith, R. J. Smith (CEGB-BNL).	841
<b>VIII B-6</b>	"Sodium Compatibility and Corrosion Tests for Component Materials," S. Yuhara, N. Aoki, A. Maruyama, S. Kanoh, K. Mochizuki, H. Atsumo (PRNFDC).	849
<b>VIII B-7</b>	"A Preliminary Chemical Investigation of Sodium-Concrete Reactions by Differential Thermal Analysis" R. E. Witkowski and R. G. Charles (WRL).	860
<b>VIII B-8</b>	"Direct Measurements of Oxygen Activity Thresholds for Liquid Alkali Metal-Oxide Fuel Reactions," M. G. Adamson, E. A. Aitken, D. W. Jeter (GE).	866
<b>VIII B-9</b>	"The Compatibility of Refractory Materials with Boiling Sodium," S. A. Meacham (WARD).	875
Luncheon Address, G. W. Hardigg		883
Banquet Address, Representative Mike McCormack		886
Official Registration List		892
Organizations		897

\*Signifies invited paper

# INTERNATIONAL CONFERENCE ON LIQUID METAL TECHNOLOGY IN ENERGY PRODUCTION

## KEY NOTE ADDRESS

May 3, 1976

Dr. G. W. Cunningham  
Deputy Director  
Reactor Development & Demonstration Division  
U.S. Energy Research & Development Administration

First of all, I am pleased to be here and see many old friends in the liquid metal field from all over the world. RDD was very pleased to have the opportunity to co-sponsor this meeting for several reasons. First of all, because the LMFBR is now the priority advanced reactor system for development in all the major nations of the world. Second, because this is an appropriate time for further technology exchanges since many aspects of the total program are now reaching significant stages. Third, in addition to the importance of the exchange of technology, such meetings are invaluable in increasing communications on up-to-date developments and positions, and improving international cooperation towards our common goal of establishing the LMFBR as the prime energy source between now and the end of the century, and realizing the goal of energy independence regardless of national boundaries.

Now the complexity and depth of the energy problems of all nations have been brought into very clear and dramatic focus in the last two years, and as a reaction, a sense of urgency has been directed, particularly in this country, towards developing a new source that will assure future supplies of energy. The LMFBR is this prime source and time and again during the last few years my conclusion has been reinforced that the breeder is a virtually inexhaustible energy system that can begin to provide significant supplies of energy by the turn of the century. No technology however, including the breeder, becomes a fact without a strong national commitment and hard work on the part of all involved. There are no short cuts to developing any complex electrical power generation technology, no matter what the proponents of other technologies such as solar, fusion, or geothermal tell us. The experience in this country and elsewhere has demonstrated that it takes decades between the laboratory phase and the establishment of a reliable, high technology option for commercialization. Underlying this national commitment is the fundamental management philosophy of developing a firm technology base by obtaining a comprehensive understanding of the key scientific and engineering elements. In this way, problems are anticipated, identified, and resolved before the breeder reactors are built commercially. In a very real sense, it is the adequacy of this technology base that will assure the success of the LMFBR program; but there are two stages of development of a different kind which are important to all of us. When a technology is in its embryonic stages of development, it is surrounded by an optimism that comes from seeing only the promise. I do not need to remind you of this tendency in respect of technologies other than the LMFBR, but in this phase, the problems are not yet evident and the questions that arise appear to have the engineering solutions just around the corner. As the technology develops, the romance dims, and while the promise is still evident, the realistic problems of component development begin to appear. This occurs when large, first-of-a-kind pieces of hardware and components are actually being fabricated and complex facilities are being built to proof-test

them. Here unforeseen problems show up that demand immediate hard and fast engineering solutions, and it is not until this stage is reached that the full effects on cost and schedule of bringing a budding technology to maturity are recognized.

All these aspects have played a part in the emerging of our national plan for the LMFBR summarized in the LMFBR environmental impact statement. The overall program objective is to develop a broad technological and engineering base for the LMFBR, with extensive utility and industrial involvement, so that upon this base a capability can be established for a competitive commercial breeder industry as a means for meeting national energy needs in the 1990s and beyond.

The planned program is structured to maintain continuity of plant design effort by scheduling the start of each successive plant shortly after completion of design of the previous plant. Each plant will thus reflect experience gained in the design, procurement, licensing, and component fabrication and testing of the preceding plant. In addition, operating experience gained in plants earlier than the immediately preceding plant will be available to the designer. On this basis, the design of the first commercial plant could begin 1982-83, with commitment to construction occurring around 1986. In more detail, the "LMFBR Program Approach" is:

- Completion and operation of FFTF on the present schedule.
- Completing and bringing CRBR into operation by the end of 1983.
- Proceeding with the joint design study between ERDA and EPRI on the Prototype Large Breeder Reactor leading to a specific commitment to proceed with the PLBR project in 1978-79.
- Starting the design of the first commercial LMFBR in 1983.
- Having the technical base completed for a decision for widespread deployment of the LMFBR by 1986.

Now, of course, we are not alone in our commitment to the LMFBR. France, Great Britain, and the Soviet Union have operating demonstration size LMFBR's, and Germany and Japan have breeders under construction. All these major LMFBR programs have goals similar to ours, and it was a pleasure to see recently that the commitment had been made to go ahead with Super Phenix. In determining the rate of progress, it is also appropriate to compare the position now with that when we held the last major liquid metal technology meeting in the United States in 1968 at Argonne National Lab. At that time:

- In the U.S., EBR-II was operational, FFTF was in the conceptual design stage.

## INTERNATIONAL CONFERENCE ON LIQUID METAL TECHNOLOGY IN ENERGY PRODUCTION

- In the U.K., DFR was operating and PFR was under design and construction.
- In France, Rapsodie was operating; Phenix was under design and construction.
- In Germany, KNK was being converted. SNR-300 was in detail design stage.
- In the USSR, BR-5 was operating, BN-350 was under design and construction, and BN-600 was in the conceptual design stage.
- In Japan, a test reactor Joyo was in the design stage.

Today,

- In the U.S., the FFTF is 70% completed, the CRBR preliminary design is completed and ground breaking is scheduled for late this year, and the prototype large breeder program has been initiated.
- In the U.K., PFR has operated at partial power, and design studies are in progress on CFR.
- In France, Phenix has operated very successfully for the past two years, and the commitment has been made to go ahead with Super Phenix.
- In Germany, KNK is operating and SNR is under construction.
- In the USSR, BN-350 is operational, BN-600 is expected to be operational in 1977-78.
- In Japan, Joyo test reactor is very near completion and design is proceeding on the Monjo demonstration plant.

So, it is clear that considerable progress has been made. Progress is also very evident when we consider the detailed structure of the sessions in this meeting. For example, it is now becoming possible from the operational experience being developed on sodium cooled reactors to feed back to sodium technology, and a large part of the meeting will be devoted to this aspect and also to the testing of models and prototype components in large test loops. In addition, since 1968, attention has become more focused on components, particularly the steam generator, and you will see not only from the sessions in this conference, but also from the national plans, that components development and testing to establish reliability and availability objectives is now becoming a major feature in all programs. While other aspects such as validation of high temperature design and closure of the fuel cycle are also important, development of reliable components is a vital issue. The steam generator can be singled out to delineate the complex factors involved in the development of this component and to point out the general approach being taken to assure the reliability of all components.

In the steam generator, sodium and water/steam are necessarily in close proximity, with the water/steam pressure very much higher than that of the sodium. Sodium reacts with water to form sodium hydroxide and free hydrogen and releases some 3,500 Btu of heat per pound of water reacting with sodium. In addition, there is also a potential for caustic stress corrosion from the introduction of the sodium hydroxide reaction products into the plant system.

The philosophy of design of the steam generator system involves three levels of reliability. First, fully proven material fabrication techniques (e.g., methods of making tube-to-tubesheet joints) and reliable quality assurance techniques must be used in the manufacture of steam generators in order to ensure to the greatest extent practical that leaks will not occur. Second, on the assumption that some leaks will nevertheless occur, the characteristics of small leaks must be established, the steps necessary to prevent their propagation to adjacent tubes must be determined and implemented, and rapid leak detection methods must be developed to assure that even if a massive failure takes place, the products of reaction can be safely vented without damage to the steam generator enclosure or other parts of the coolant system. Achievement of these three levels of reliability requires the conduct of a development program involving failure modes, investigations of the hydrodynamics of handling the hydrogen and steam from a large leak, thermodynamics, structural analysis, and proof-testing of large-scale models of candidate designs. The behavior of components such as the steam generator in sodium is a key requirement in our commercialization plan.

Now, in preparing this key note address, it also afforded me an opportunity to "stand back and stare" and several points became evident from this wider perspective. First of all, the primary thrust of this conference is on sodium technology and engineering, because this is the heart of the matter. Secondly, the need for the breeder and its worldwide recognition has been reinforced during the past few years because of the recognition that the oil and gas resources of this planet are limited. In addition, the continuing analyses that have been made, such as in the ERDA program plans, show clearly that known uranium reserves will be committed in a few years from now for consumption in plants, which essentially are now on order. By 1991, all of these reserves will have been consumed, so in the 1990's we will begin to approach a crunch point on uranium availability. Thirdly, the designs of the LMFBR worldwide are converging and similar basic materials, temperature ranges, and components' designs are being developed. Although there are differences in the equipment arrangements, loop versus pool, the greater part by far of all the technology being developed is applicable to both types.

We are very happy, therefore, to have this meeting at this time. The Program Committee are to be congratulated on doing an outstanding job of organizing the contributions in the critical areas. My quick evaluation of the summaries of the papers leads me to believe that we will have a very successful conference. As I have indicated, there is now a major emphasis on components development and testing in sodium, the program is most comprehensive, and all of us can learn from it. With the thoughts that I have presented, it is appropriate in this bicentennial year to close with a quotation from Oliver Wendell Holmes:

"I find the great thing in life is not so much where we stand as in what direction we are moving. To reach the port of heaven, we must sail sometimes with the wind and sometimes against it, but we must sail and not drift, or lie at anchor".

I might add that much of the time we seem to sail against the wind, but with a good ship, pointing into the wind is no problem.

# INTERNATIONAL CONFERENCE ON LIQUID METAL TECHNOLOGY IN ENERGY PRODUCTION

## SOME ASPECTS OF SODIUM TECHNOLOGY ISSUED FROM THE OPERATING EXPERIENCE OF RAPSODIE AND PHENIX

J. Kremser

Département des Réacteurs  
à Neutrons Rapides  
C.E.A. Cadarache

A. Lacroix

Centrale PHENIX  
C.E.A. Marcoule

### ABSTRACT

This paper deals with the experience on sodium technology gained from RAPSODIE and PHENIX operation. Problems encountered with sodium circuits, main components, handling equipment and instrumentation are discussed. Some information related to the contamination by radioactive products of sodium and sodium circuits is given.

#### 1 - INTRODUCTION

Current French successes with sodium-cooled reactors, as demonstrated by 9 years of continuous operation for the RAPSODIE experimental reactor and nearly 2 years of full-power operation for the PHENIX power station, are the outcome of a coherent twenty-year research and development program.

After satisfactory results were obtained on RAPSODIE from the initial start-up in January, 1967, the green-light was given for the construction of PHENIX beginning in 1969.

Meanwhile, RAPSODIE assumed a dual role:

- . as a fast-flux irradiation facility for the materials and fuels used in LMFBRs,
- . as a means of testing components and instrumentation related to sodium technology. Thermal power was increased from 20 to 24 MW late in the first operating year, and in 1970 major alterations were carried out to reach a power level of approximately 40 MWth (RAPSODIE - FORTISSIMO).

PHENIX was completed on schedule, and since mid-1974 it has demonstrated the effectiveness of the French sodium reactor system

for the production of electrical energy, having generated nearly 3 billions KWh to date.

#### 2 - OPERATING EXPERIENCE WITH RAPSODIE

Reactor operation consists of irradiation runs separated by shut-downs for modifying the core composition. Run duration has gradually been increased in order to optimize the load factor : from an initial mean duration of 40 days, the current figure is 60 days and should reach 80 days within less than a year.

During the first 3 operating years, a few major incidents occurred, although fortunately the consequences were not serious :

- . sodium overflow in the small rotating plug during testing prior to criticality
- . overflow of small rotating-plug fusible seal in the reactor vessel
- . core sub-assemblies damaged during handling.

These incidents were described in detail in a published article <sup>(1)</sup> and will not be taken up again here.

Since operation began in the FORTISSIMO configuration, the mean load factor has been approximately 65 %, the availability factor being better than 85 %, which is quite satisfying for an experimental reactor.

#### 2.1. - Main Sodium Circuits

Since reactor start-up, a primary and a secondary sodium pumps have thus far accumulated about 70 000 and 50 000 operating hours respectively.

## INTERNATIONAL CONFERENCE ON LIQUID METAL TECHNOLOGY IN ENERGY PRODUCTION

During preliminary sodium tests, all four pumps were disassembled and cleaned-up for modifications. In 1968 a primary pump having 13 000 operating hours was disassembled for visual inspection. It was cleaned of sodium and decontaminated. Each time, the pumps were reassembled and put back into service without any problem.

More recently, during the FORTISSIMO work, their characteristics were modified as the higher power output required an increase of about 30 % in cooling flow. Consequently the hydraulic units were replaced on all four pumps.

The intermediate heat-exchangers tube bundles were also replaced. As the increased sodium flow rate was a potential source of unacceptable vibrations, new bundles with additional vibration-damping jackets were installed.

Equipment modifications for RAPSODIE - FORTISSIMO were described in detail at a previous conference (2).

The decontamination measures taken at the same time, and the results obtained, were presented at another conference (3). It is sufficient here to note that after heating to 180°C to induce sodium melting and draining, the components were steam-heated at 150°C and rinsed with water.

After modification, the pumps were visually checked, reinstalled and put back into service without any special testing. Since this time, they have operated in a perfectly satisfactory manner, except for the seizure of a secondary circuit pump caused by the thermal shock after the corresponding primary circuit pump cut out in July, 1972. Subsequent analysis showed that a sudden variation in the sodium inflow temperature (a drop of 80°C in less than 1 minute) could reduce sodium bearing clearance to one-tenth of its nominal value (i.e. 0.4 mm). When the pump was disassembled

- without difficulty - traces of seizure were apparent. Rather than to increase the clearance significantly, however, it was judged preferable to install a safety system which cuts out the secondary pump when the primary pump shuts down, in order to minimize the thermal shock.

### 2.2. - Sodium Purification

Sodium purification causes no particular difficulty in RAPSODIE. In the primary circuit two identical nitrogen-cooled traps are fed from the expansion tank by an electromagnetic pump. Only one of these traps is in operation at any given time :

. one is used if significant pollution occurs after a technical intervention or in case of an incident such as overflow of the small rotating-plug fusible seal : this occurred in 1969, when about 50 kg of Sn-Bi eutectic spilled into the reactor vessel.

. the other is in continuous service, whether the reactor is operating or shut-down.

Sodium flow is about 2 cubic meters per hour, and the lower plugging temperature is easily kept below 110°C. Tests make clear that the cold trap might be stopped without any increase of this temperature. It tends to rise only when the sodium is reheated after handling operations. In this case, sodium purification is resumed and a few hours later the normal plugging temperature is obtained.

On the secondary side, there is no need for sodium purification except after a technical intervention on the circuits and the cold traps are put into service only when necessary.

In RAPSODIE, sub-assemblies are handled through a channel in the small rotating plug and, in spite of all the precautions taken, accidental air intake may occur. However, submerged metal surfaces no doubt account for the largest proportion of sodium pollution.

Nevertheless, the amount of oxygen introduced remains slight : estimates based on plugging temperature evolution with the cold trap inoperative indicate an upper limit value of 1 mg of oxygen per unit of surface area ( $1 \text{ m}^2$ ) according to Eichelberger's solubility curve - which corresponds to values previously published. It should be noted that when these measurements were made, handling was carried out in argon atmosphere rather than in helium as it is now. Although a number of problems were encountered during the changeover from argon to helium, no effect was noted on overall sodium purity.

2.3. - Sodium aerosols

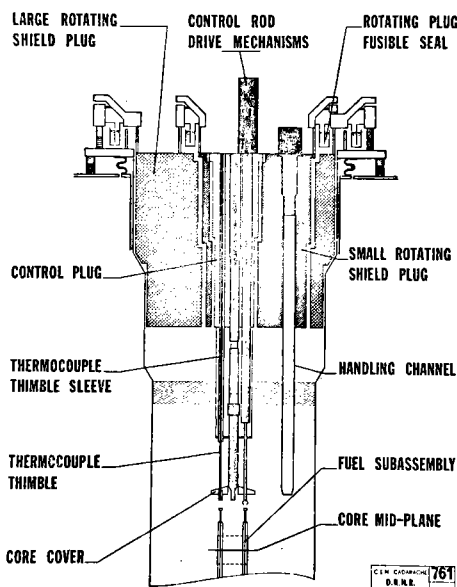
Sticking of the large rotating plug, caused by the condensation of sodium aerosols in the annular gap (16 mm thick x 2,5 m high) between the plug and the reactor vessel, occurred several times during the initial operating years. In each case makeshift methods were used to free the system until the final solution was tested and perfected after the FORTISSIMO work : it consists in injecting helium into the top portion of the annular gaps in order to obtain uniform wall temperatures.

(Circumferential temperature gradients had previously been observed around the plugs because of structural asymmetry, and were thought to contribute to the formation of aerosols-carrying argon convection currents).

This solution proved successful. Injection rates were determined empirically so as to reduce the temperature spread ; making allowance for gas analysis and pressure regulation sampling flows, the gas-blanket composition finally obtained was 70-80 % He and 30-20 % Ar. This technique was used for several years without incident.

It was recently proposed that a low-temperature absorbent carbon purifying unit for fission gases be installed in the gas sampling circuit. As this process proved more efficient with helium as the vector gas, it was decided that argon would no longer be used in the reactor vessel. A supplementary advantage is the elimination of  $^{41}\text{Ar}$  which was quite disturbing for the cover gas radioactive analysis in case of fission gases release. Following a development period to work out a few difficulties which arose during handling operations (see below), RAPSODIE has been under "all-helium" operation since mid 1975.

FIG.1 RAPSODIE : UPPER SHIELD STRUCTURES



2.4. - Fuel handling

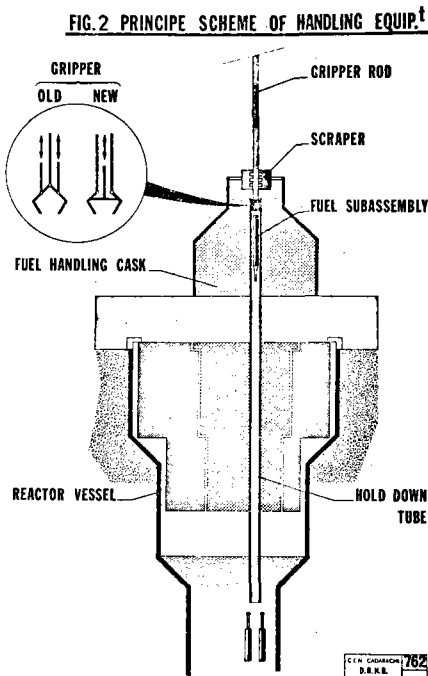
Initially, only a single handling cask was available for fresh and irradiated sub-assemblies. It was complicated, slow-moving machine which created a number of problems - particularly for control.

It was replaced in 1970 by three simplified casks which can be set up more quickly for their specialized functions :

- . a discharge cask for irradiated sub-assemblies
- . a charging cask for fresh sub-assemblies
- . a cask for transferring sub-assemblies between the core and the peripheral storage zone.

All three were built to the same model with a cask body (lead-lined on the discharge cask), a gripper-shaft guide superstructure and a system for coupling it to the handling channel.

The inner chamber is fed with inert gas (formerly argon and now helium), and the gripper sleeve which drives the claws, passes into the open air through a scraper-rings box to remove superficial sodium deposits. A considerable portion of the sleeve (approx 1.5m) immersed in the sodium when the gripper is in its lowered position thus transmits the scraper unit with each movement.



Formerly, when handling was carried out in argon atmosphere with sodium temperature lowered to 180°C, frequent disassemblies were required to clean from sodium the scraper unit in order to prevent seizure of the gripper. The charging cask was heated to ease this problem, but no similar solution was possible for the discharge cask.

It was then decided to design and manufacture a new type of gripper with reversed action, including a bellows unit between the

sleeve and the internal control shaft to prevent sodium from rising inside the sleeve.

During this time, all efforts to substitute helium for argon during handling operations were unsuccessful because of the discharge cask. Thermal exchange conditions were improved the sodium froze even more quickly on the gripper sleeve and seizures occurred more frequently.

Handling under helium atmosphere became possible only after the sodium temperature was raised from 180°C to 250°C for an altogether different reason : to reduce thermal cycle amplitude in the reactor vessel.

Another problem arose during testing of the new gripper : bellows heating - which was calculated for argon - is inadequate in helium atmosphere, and sodium freezing again causes gripper seizure after a few operations.

This series of minor incidents illustrates the difficulties involved in designing mechanisms for simultaneous operation in sodium and gas. It is only fair to note that they become troublesome only during handling operations long enough to include numerous repetitions of the same sequence.

## 2.5. - Instrumentation

Sodium outflow temperatures from the core sub-assemblies are measured by a set of 85 thermocouples located in a structural element immersed in sodium, known as the core-cover. Temperature data are processed by digital computer and incorporated in the reactor safety system.

The detectors are conventional chromel - alumel junctions clad with low-carbon stainless steel (1 mm dia.). They are guided from the top shield upper-side to the top of the sub-assembly heads by stainless steel thimbles (I.D. = 2 mm x O.D. = 3 mm) which run through the control plug, the blanket gas and the sodium. These tubes, kept in argon atmosphere,

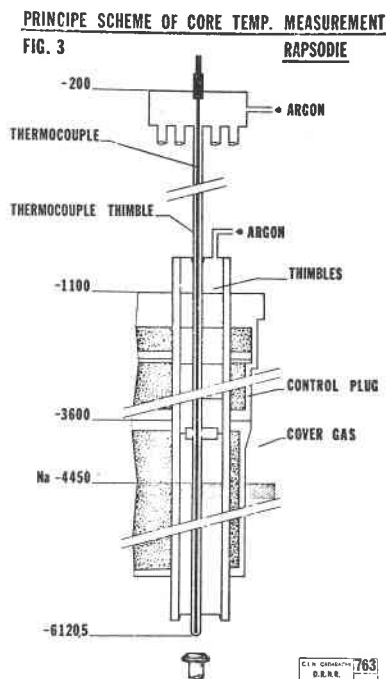


## INTERNATIONAL CONFERENCE ON LIQUID METAL TECHNOLOGY IN ENERGY PRODUCTION

are arranged in bundles of 14 ; there are thus 6 tube bundles around the perimeter of the control plug, which is secured to the small rotating plus and also carries the 6 control-rod mechanisms.

Theoretically, the thermocouples are replaceable. Although the operation itself is rather delicate - because of their length-to-diameter ratio (they are approximately 6m long) - it has been performed about twenty times thus far, either after a connector failure or because of poor signal quality.

On three occasions the thermocouple has broken with no possibility of recovering the tip from the thimble. These three thermocouples are in the same bundle, and the breaks occurred at about the level of a thimble junction box in the bundle.



A corrosion phenomenon with traces of sodium was detected on examination of the fragments that were recovered. Pressure testing of the tubes also revealed a leak below the free sodium level.

It seems likely that, after a leak

occurred with one tube for undetermined reasons, sodium rose in the tube by attraction up to the bundle junction box (located just below the underside of the plug) and from there penetrated into the other tubes.

This possibility had been feared since the first thermocouple failed in 1968. Both for reactor safety considerations and to maintain experimental irradiation facilities, a replacement control plug was manufactured. It is currently available and is scheduled to be installed in the coming months, as the phenomenon seems to be accelerating : the second thermocouple failed in mid 1974, and the third in late 1975.

A shut-down of about 4 months will be required for this exceptional operation, which will certainly be most instructive.

In the new plug, the temperature sensors which are paired in each thimble, are mounted on stringers as for PHENIX. There is no interconnection between the thimbles to avoid any consequential effect of a single defect with one of them to the others.

### 3 - OPERATING EXPERIENCE WITH PHENIX

Start-up testing continued into the first half of 1974, as was discussed in a number of papers at the BNES Conference in March of that year <sup>(4)</sup>. The power station was put into industrial service on July 14, 1974, with a six-weeks interruption for scheduled maintenance in August - September, 1975. Overall performance has been thoroughly satisfactory: the mean load factor at the end of 1975 was 68 %, and cumulative gross energy production totaled 2.433 billion kWh.

On three occasions in 1975, however, power was reduced to 2/3 of the nominal level after slight sodium leakage, in a secondary circuit (March and July) and because of leakage in a steam generator water-feed pipe in December. The plant operated perfectly with only two secondary circuits in service.

The reactor program provides for irradiation cycles of about 2 months each separated by shut-downs for fuel replacement. The 7<sup>th</sup> such cycle was completed in January, 1976.

### 3.1. - Main Sodium Circuits

The main primary components (pumps and heat exchangers) had accumulated 17 000 operating hours in sodium as of January 1, 1976. During start-up testing, all three primary pumps were disassembled once as a non-return valve malfunction became obvious. After cleaning of sodium, the outline of the non-return valves holders has been modified. On this occasion, thermocouples locations for measuring the sodium inlet temperature have been changed. These operations followed by the pumps reassembly brought a worthwhile experience.

At the same time, the three main secondary circuits had been in operation for 20 000 hours in sodium. The only incidents to be noted are 3 small sodium leaks which appeared in secondary circuit N° 2 at the weld seam on the reheater sodium flow-control valve : the valve body is made of 304 austenitic steel, while the sodium pipe is made of 321 austenitic steel.

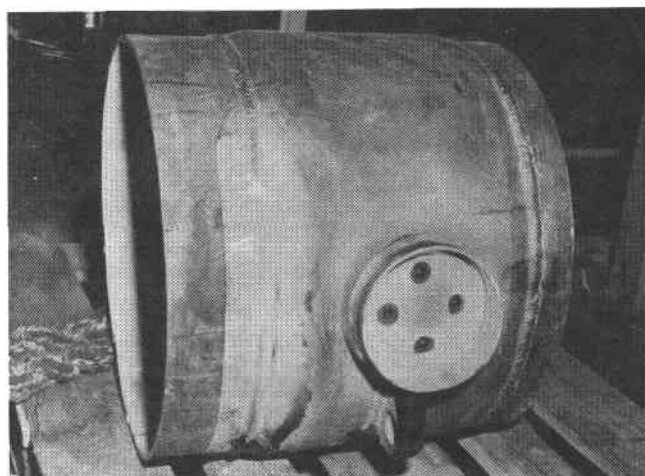
The first of these leaks was revealed by the leak detector cord in September, 1974, after about 2500 operating hours at 540°C. The valve in this case was replaced by an identical new valve.

In March, 1975, another identical leak appeared under similar conditions in the same circuit after 2900 hours at 540°C. The valve was not dismantled, but was repaired in place: the crack was precisely located and stopped by drilling out each end, then the defect zone was capped with a welded tube.

Figure 4 (next column)

High : sodium valve with the insulating material removed after the first leak occurred.

Low : part of the dismantled valve showing the repair with the welded tube uncapped.



The third sodium leak was detected on July 17, 1975, near the zone repaired in March. When the insulating material had been removed, about 300g of sodium leakage was found at the top of the cap welded on four months earlier.

A decision was then made to replace the sodium flow-control valves on the reheaters of the 3 secondary circuits by diaphragms made of 321 steel previously tested on a water circuit at the Cadarache Research Center.

When the valve was dismantled from circuit N° 2 and the cap removed, it was observed that the initial crack had increased in size. Studies currently in progress on cracking phenomena have shown that this is undoubtedly

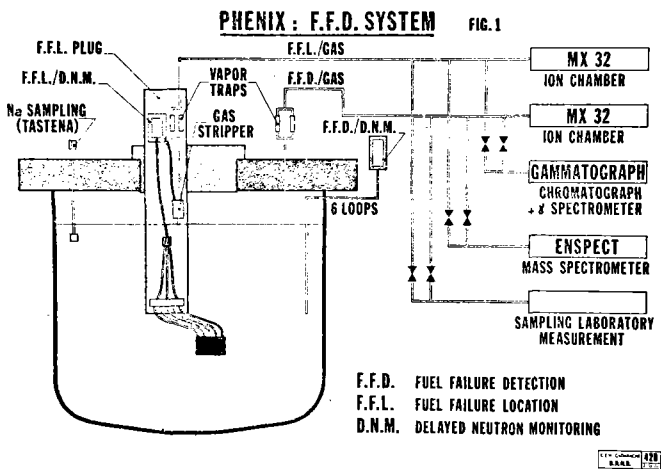
a case of tensile creep rupture due to significant residual stresses, and aggravated by machining near the weld seam.

The experience acquired with these sodium leaks demonstrates one of the advantages associated with the reactor type for which PHENIX is the prototype : leak detection in all three cases was immediate. The absence of pressure in the circuit was no cause for alarm ; in each case the repair work was quickly and reliably carried out and the reactor started up again without difficulty. Finally, the design concept of 3 independent secondary circuits was substantiated : no special operating problems arose with only 2 steam generators running, aside from a production output drop of one-third during the repair work.

3.2. - Auxiliary Sodium Circuits

3.2.1. Fuel failure detection and location

(FFD & FFL)



With the FFL plug, a part of the outlet flow of each subassembly is sampled in succession through a set of tubes leading to a mechanical selector valve, an immersed EM pump, a delayed neutron monitor (DNM) and a gas stripper. Gaseous fission products are then carried in a vector gas current to various equipment : ionization chamber, gamma or mass spectrometers. By means of 2 mechanical selectors, the sample may be alternately representative of :

- . all sub-assemblies throughout the core
- . a group of 3 sub-assemblies
- . a single sub-assembly.

The FFL plug has given rise to a number of mechanical and hydraulic problems since it was installed. The sodium flow sampled by the electromagnetic pump dropped regularly until the fifth cycle when it stabilized at about 75% of the nominal flow rate ; it is assumed that this is the result of pump "aging". The small mechanical selector for sodium sampling from individual sub-assemblies has been jammed since the third cycle. Finally, after the fifth cycle, the gas stripper filters and purifiers were fully clogged and now prevent FFL gas sampling. Fully satisfactory results, however, have been obtained with the FFD/DNM system (primary sodium sampled at the IHXs inlet). DNM measurements have always been consistent with core contamination levels and confirm FFL/DNM measurements by overall or triple sub-assembly monitoring.

Proper computer processing of these measured values permits sub-assembly monitoring under different reactor operating conditions (power transients, low-power operation, etc).

Finally, successful FFD/Gas system operation revealed a fuel element leak during the 5th cycle. Gas releases are small and did not vary significantly with irradiation. So far no delayed neutron signal has been recorded.

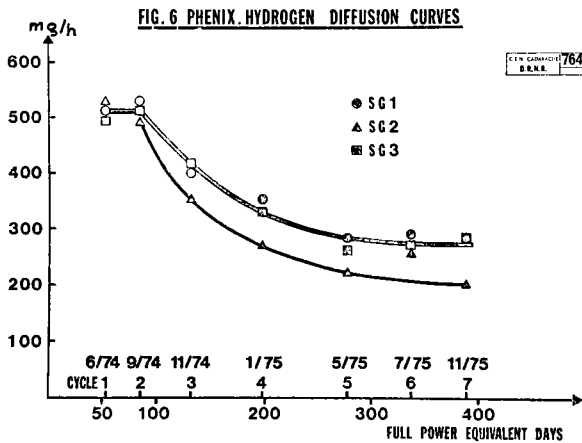
3.2.2. Purification Circuits

The primary purification circuit has operated without incident since the beginning. A single cold trap has been used since the reactor went operational in sodium and, irrespective of the operating conditions - full power, shut-down for handling or for any other reason -, the plugging temperature has always remained below 110°C. Each secondary circuit has its own purification circuit ; again, there is nothing unusual to report. Cold traps absorb the hydrides - formed by the hydrogen released from steel corrosion - which diffuse through the steam-generator water tubes.

If allowance is made for the hydrogen injected during calibration testing of the hydrogen detector system, and for contamination subsequent to inspection or work on the main sodium circuits, each secondary cold trap has absorbed approximately 4 kg of hydrogen, or about 100 kg of hydrides. These units are monitored in operation by thermal and hydraulic measurements, and are thought to be capable of absorbing about 350 kg of hydrides each.

3.3. - Hydrogen Detection

This system has functioned perfectly since it became operational in October, 1973. The hydrogen diffusion rate through the water tubes remained stable at about 500mg/h per steam generator during the first two cycles and has regularly declined since then to its current stable value of approximately 250mg/h.



The resulting residual hydrogen concentration in the sodium is on the order of 0.080 ppm when the cold trap is operating at 110°C. It is possible to detect concentration variations of 0.005 ppm. It is estimated that the minimum detectable leakage rate which will allow localization of the defective module is 0.03 g/sec.

4 - RADIOACTIVE CONTAMINATION OF CIRCUITS AND SODIUM

Although a number of data sources are available, the most important are :

- sodium sampling analysis findings. The sampling and analysis techniques developed on RAPSODIF have been applied to PHENIX ; sampling, which requires only simple operations, is carried out as necessary.

- direct measurements on the system lines and components. Such measurements are possible - after draining off the sodium - on the main circuits in RAPSODIE, and on the auxiliary circuits only at PHENIX.

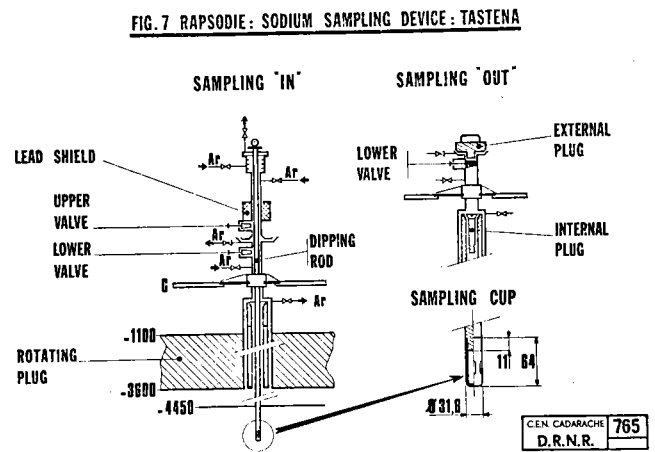
The principal objectives of these studies are :

- to define the kinetics of emission phenomena : with reference to FFD observations, for example, in the case of failed fuel elements.
- to broaden our understanding of trapping and deposit build-up phenomena in order to predict their consequences and, if possible, to control them.

4.1. - Sodium technology and analysis techniques

Two kinds of sampling methods are used jointly on both PHENIX and RAPSODIE :

- samples may be taken directly in the reactor vessel using a nickel sampling cup with a sodium capacity of about 10g, screwed onto the end of a stainless steel rod. This method is known as the TASTENA system.



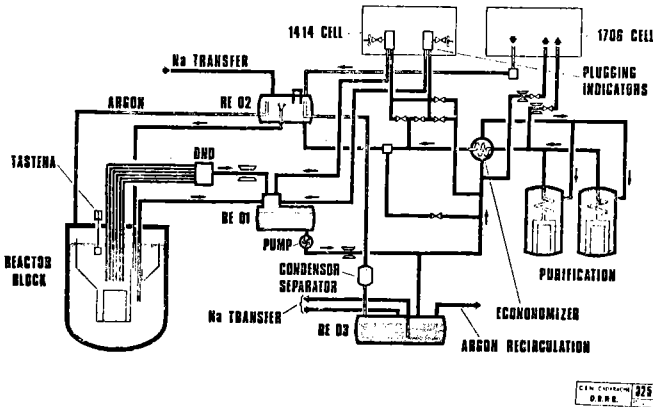
Under normal sampling conditions, the minimum sodium temperature is 400°C, and the sampling cup is in contact with the sodium for no more than 30 seconds.

- sampling is also possible using removable test sample tubes on branches in the auxiliary circuits. The sampling point in RAPSODIE is on a purification circuit by-pass line, while in PHENIX sodium may be sampled before or after the cold traps. Nickel sampling tubes are used, and sodium flow is initiated only for very short periods under carefully controlled conditions prior to each sampling, after placing the relevant cell under nitrogen atmosphere.

Sodium sample analysis always includes spectrometry, with or without prior chemical separation,

generally 8 or 9 days after sampling to allow for 24 Na decay. For determination of short-lived radioactive substances, TASTENA samples may be analyzed within 24 hours after sampling ; in this case hot-cell chemical separation is indispensable.

PHENIX : PRIMARY AUXILIARY CIRCUIT, SIMPLIFIED SCHEME Fig 1



4.2. - Sodium Analysis Findings

As far as fission products are concerned, the spotlight is focused primarily on the elements of the Te-I-Xe-Cs chain. Experience has proved that no sampling problems arise, at least for iodine and cesium isotopes which are dissolved in the sodium. Analysis findings for these elements are in agreement, whether the samples are taken directly from the reactor vessel (TASTENA) or by removable sampling tubes.

Sodium sample analysis of activation products - Mn and Co - has provided no significant contributions, as sampling is complicated by their weak concentration and their tendency to form a deposit.

The following table lists the specific activity values for the major elements determined in the primary sodium at RAPSODIE and PHENIX. Among the fission products in RAPSODIE sodium, the activity measured for the short half-life elements 131 I (8 days) and 136 Cs (13.6 days) is highly dependent on the status of the core (presence or absence of fuel failures). To date about 20 fuel failures have been recorded in RAPSODIE, and only one leaky fuel element in PHENIX. The specific activities quoted for PHENIX were measured at the end of 7th cycle, with the leaky fuel element still in the core.

PRINCIPAL ELEMENTS DETERMINED IN THE PRIMARY SODIUM AT RAPSODIE AND PHENIX

ELEMENT	RAPSODIE	PHENIX
24 Na (mCi/g)	20 *	6 *
22 Na (µCi/g)	6 x 10 <sup>-1</sup>	1.8 x 10 <sup>-1</sup>
113 Sn (µCi/g)	2 **	-
131 I (µCi/g)	10 <sup>-4</sup> to 10 <sup>-1</sup>	3 x 10 <sup>-5</sup>
134 Cs ( " )	4 to 5 x 10 <sup>-2</sup>	1 x 10 <sup>-4</sup>
136 Cs ( " )	2x10 <sup>-3</sup> to 2x10 <sup>-2</sup>	3 x 10 <sup>-4</sup>
137 Cs ( " )	6 x 10 <sup>-1</sup>	1.3 x 10 <sup>-3</sup>

\* Equilibrium values at P<sub>N</sub>.  
 \*\* Caused by overflow of Sn-Bi seal into vessel.

NOTE : 24 Na activity in PHENIX secondary circuits :  
 2.8 x 10<sup>-4</sup> µCi/g.

Application : Sodium leak detection in double envelope of RAPSODIE vessel and primary circuits :

Research has been done on sodium leak detection by measuring the radioactivity of the nitrogen circulating in the double envelope. Testing was carried out with artificially induced leaks in the sodium sampling cell, while a continuous nitrogen tap from the cell was channeled through filter paper set up in front of a gamma probe.

Sensitivity, expressed in grams of sodium aerosols per liter of nitrogen for a two-fold increase in probe background noise over a reasonable time (10 to 20 mn), was found to be :  
 10<sup>-10</sup> g/l with 24 Na present  
 10<sup>-8</sup> g/l without 24 Na

for RAPSODIE sodium at temperatures between 180°C and 400°C.

It should be noted that detection is possible in the absence of 24 Na, largely because of the volatility of cesium isotopes. A concentration factor of 1000 was recorded between the 180°C sodium flowing out from the leak and the collected aerosols.

4.3. - Contamination of the main RAPSODIE circuits

An initial measurement campaign was undertaken while the reactor was shut down in 1970 for the FORTISSIMO work. A preliminary inventory was drawn up for the various radionuclides (fission and activation products) deposited on surfaces in contact with the sodium. Shut-downs during 1972 and 1974 for maintenance works were used to carry out measurements similar to those made in 1970. As the main circuits were drained, it was possible to enter the cells after allowing for adequate 24 Na decay time. All measurements were made through structural walls and insula-

tion, so that only activity from gamma-emitters could be recorded. However, as the irradiation dose rates reached high levels - up to 200-300 mrem/h at some points - it was necessary to ensure maximum instrument protection using lead shields, and to limit the measuring teams to the shortest possible exposure in view of prevailing radiation protection standards.

The accessible portions of system pipes, pumps and heat exchangers were inspected using two complementary techniques :

- . discrete gamma-flux measurements using ionization chamber provide an overall activity profile ;
- . gamma-spectrum recordings made with GeLi probes at a number of points revealed by the ionization chamber indicate the activity of the nuclides present in the deposits.

The instruments are calibrated using sources covering the entire gamma-spectrum with geometrical distributions approaching the actual layout. In general, most of the primary circuit activity is deposited in the heat exchangers and in the "cold" pipes (heat exchanger-to-pump and pump-to-reactor vessel lines) with 400°C sodium flow. The hot pipes, between vessel and heat exchanger, and the pumps themselves are the least active zones in the circuit.

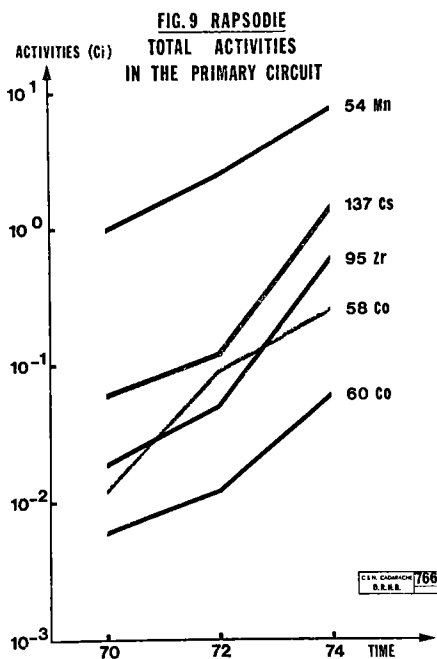
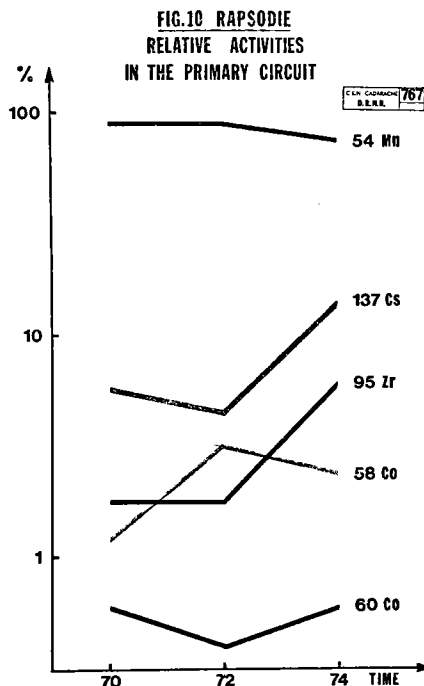


Figure 9 shows the evolution over the 3 measuring campaigns of the total activity (cold traps not included) for the principal nuclides : 54 Mn, 58 Co,

60 Co, 95 Zr and 137 Cs. As may be observed, 54 Mn is the most heavily deposited element, but it increases more slowly than the two fission products 95 Zr and 137 Cs. This trend is revealed by the graphs showing the evolution in the relative proportion of each nuclide in the circuit.



This evolution is very closely related to the reactor operating conditions. The activity of 54 Mn, with a 300-day half-life, could reasonably have been expected to stabilize (RAPSODIE had been in operation for 500 days when the first measurements were made). The increase noted between the first two measurements results from the increase in reactor operating power from 24 to 40 MWth, while the rise between 1972 and 1974 levels comes from the lengthened in-core time for experimental and driver sub-assemblies. A noteworthy point is the relatively low activity level for 58 Co and 60 Co - only a few per cent of the manganese activity - which seems to be explained by the fact that deposits are likely to form on hot areas near the emission point. The sharp increase in the fission products 95 Zr and 137 Cs is directly related to the fuel failures which occurred in the reactor.

These measurements were used to refine the CORONA code, which involves a model describing the emission and transfer of corrosion products in sodium-cooled fast reactors. From a practical point of view the access to the cells with medium irradiation dose

rates was not a serious problem in the past, but difficulties might arise in the future with respect to the experimental program trends towards high burn-up levels and by the way an increasing number of fuel failures. Next measurements in the coming months during the shut-down above mentioned will give very interesting information on this matter.

#### 4.4. - Contamination studies in PHENIX

During the scheduled shut-down in August 1975, after one year of industrial operation without a single fuel failure, contamination profiles were established in the primary auxiliary sodium circuit lines, and the principal radionuclides trapped by the operating cold trap were measured. The dose rates measured in contact with the insulation one month after reactor shut-down were low and constant (a few millirems per hour) except in the cold portions of the circuit (economizer at the entry to the cold trap) where the rate was approximately 1 rem/h. Results obtained at pipe elbows were generally not markedly different from other points in the circuit. These dose rates are essentially accounted for by the following radiocontaminants:  $^{22}\text{Na}$ ,  $^{54}\text{Mn}$ ,  $^{58}\text{Co}$ ,  $^{60}\text{Co}$  and  $^{65}\text{Zn}$ , among which  $^{54}\text{Mn}$  is generally predominant, while  $^{65}\text{Zn}$  appears only in zones where sodium aerosols are found - which is not at all surprising. However, the presence of  $^{54}\text{Mn}$  in the argon lines and in the condenser separator, although beyond any doubt, is both surprising and unexplained.

The radiocontaminants found in the cold trap are  $^{22}\text{Na}$ ,  $^{54}\text{Mn}$ ,  $^{58}\text{Co}$ ,  $^{60}\text{Co}$ ,  $^{65}\text{Zn}$ ,  $^{124}\text{Sb}$ ,  $^{134}\text{Cs}$ ,  $^{136}\text{Cs}$  and  $^{137}\text{Cs}$ . Quantitative analysis of the gamma spectrometry findings is a risky undertaking and it is difficult at the present time to obtain valid data on cold trap activity levels and on the internal distribution of the accumulated impurities.

Concurrently with the measurement operations described above, a test sample tube was withdrawn from an intermediate heat exchanger (on the primary sodium side) in order to determine the contamination profile of these components.

At the time it was extracted, irradiation dose rates did not exceed a few mrems per hour: gamma-spectrometry showed that the dominant radiocontaminant was  $^{54}\text{Mn}$ , and that it settles out increasingly as the temperature drops. The presence of  $^{51}\text{Cr}$ ,  $^{58}\text{Co}$ ,  $^{60}\text{Co}$  and  $^{59}\text{Fe}$  was also noted.

The operating experience of RAPSODIE and PHENIX is undoubtedly the most valuable source of information in the field of sodium technology. In this paper, the authors wish simply to point out some aspects of it and do not intend to be complete. Moreover a few points are discussed with more details in companion papers to this conference. RAPSODIE and PHENIX will continue to provide an irreplaceable contribution to our day-to-day experience. RAPSODIE has at least two major advantages over PHENIX:

- . it has been in service for a longer period, and provides preliminary data on the degree or absence of equipment aging;
- . its status as a research reactor and its loop design better suit it to certain tests and observations in highly specialized areas such as the behavior of radioactive products in the sodium flow.

Clearly, however, PHENIX is in the spotlight where the technology of large-scale reactors is concerned. Interestingly enough, most of the early run defects affected the water/steam circuits rather than the sodium circuits themselves. Of course, a number of problems arose with sodium in both RAPSODIE and PHENIX. The significant point is that, up to now, they have always been overcome. This is the reason why we are reasonably confident in the LMFBR's future.

Acknowledgments: The authors express their appreciation for the contribution given to this paper by Mrs BERLIN and M'SIKA (DRNR - Cadarache) concerning contamination problems.

#### REFERENCES

- (1) J.P. ARGOUS, H. CHANTOT, J. PETIT, S.J. STACHURA  
Safety experience gained from Rapsodie operation.  
Nuclear safety vol.14 N°1 - January February 1973.
- (2) J.M. CHAUMONT et al.  
Upgrading of fast flux test reactor: Rapsodie Fortissimo.  
Conference on fast reactors (March 7-10, 1971).  
PALO-ALTO, California (U.S.A.).
- (3) R. de FREMONT, J.M. GIRAULT, C. LEVILLAIN.  
Sodium removal and decontamination experience on Rapsodie - A.I.E.A. Specialists' meeting on decontamination of plant components from sodium and radioactivity - DOUNREAY (G.B.) - April 1973.
- (4) "FAST REACTOR POWER STATIONS"  
Proceedings of the international conference organized by the B.N.E.S.  
LONDON - 11-14 March, 1974.

# INTERNATIONAL CONFERENCE ON LIQUID METAL TECHNOLOGY IN ENERGY PRODUCTION

## SODIUM TECHNOLOGY AT EBR-II

J. T. Holmes, C. R. F. Smith, W. H. Olson

Argonne National Laboratory  
Idaho Falls, Idaho 83401

### ABSTRACT

Since the installation of purity monitoring systems in 1967, the control of the purity of the primary and secondary sodium and cover gas systems at the Experimental Breeder Reactor II (EBR-II) has been excellent.

A rigorous monitoring program is being used to assure that operating limits for more than 25 chemical and radioactive impurities are not exceeded. The program involves the use of sophisticated sampling and analysis techniques and on-line monitors for both sodium and cover gas systems.

Sodium purity control is accomplished by essentially continuous cold trapping of a small side stream of the total circulating sodium. The cold traps have been found to be very effective for the removal of the major chemical impurities (oxygen and hydrogen) and tritium but are almost ineffective for  $^{131}\text{I}$  and  $^{137}\text{Cs}$  that enter the sodium from fuel cladding breaks. Purging with pure argon maintains the cover gas purity.

### INTRODUCTION

The ability to maintain low levels of impurities in the EBR-II sodium and cover gas systems has been a major positive factor in the almost 12 years of safe and reliable plant operation. In 1975 the plant capacity factor was over 65%. EBR-II, initially a demonstration fast breeder reactor power plant with integral fuel reprocessing and refabrication, is currently being used as an experimental irradiation test facility for fuels, materials, and nuclear instrumentation. The important design and current operating parameters for the EBR-II's primary and secondary sodium systems are given in Table I.

For the first three years of power operation (1964-1967) sodium purity was monitored with plugging temperature indicators and infrequent sodium samples. Cover gas purity was monitored by grab samples and on-line gas chromatographs. After discovery of high copper concentrations in the primary sodium in early 1967<sup>(1)</sup>, a rigorous routine of sodium and cover gas

Table I. EBR-II Design and Operating Parameters

	<u>Primary System</u>	<u>Secondary System</u>
Power	62.5 MWt	19.5 MWe*
Volume of Sodium	341,000ℓ (90,000 gal)	37,900ℓ (10,000 gal)
Pumping Rate	34,100ℓpm (9,000 gpm)	22,000ℓpm (5,800 gpm)
Hot Leg Temperature	480°C (900°F)	470°C (880°F)
Cold Leg Temperature	370°C (700°F)	290°C (520°F)
Cold Trap Flow Rate	95ℓpm (25 gpm)	45ℓpm (12 gpm)

\*Electricity is produced in a conventional steam power plant.

purity monitoring was implemented.<sup>(2,3)</sup> Sodium purification by cold trapping has been changed from the original as-needed basis to the currently used, nearly continuous, cold-trap operation. Sodium sampling capabilities have been improved from the early flow-through tube samplers to the current use of overflow cup-type samplers and specimen equilibrium techniques.<sup>(4)</sup> The use of in-sodium meters for continuous hydrogen and oxygen monitoring was initiated in 1972.<sup>(5,6)</sup> Other than the copper impurity increase prior to 1967, EBR-II has operated with only minor upsets in sodium and cover gas purity.

The sodium and cover gas monitoring activities at EBR-II have proved useful in detecting and diagnosing abnormal conditions. For example, measurements of  $^{131}\text{I}$  and  $^{137}\text{Cs}$  in primary sodium are routinely used as an aid in diagnosing fuel cladding ruptures; increases of Sn in primary sodium have indicated losses of the tin-bismuth alloy from the seal trough of the rotating plug; increases of hydrogen and oxygen in sodium during cold-trap outages have been used to estimate source rates and to identify sources of these impurities. The presence of helium in the primary cover gas has signaled leakage from experimental subassemblies. Erratic increases of methane in the primary cover gas have been correlated with hydrocarbon contamination from the fuel handling activities.



# INTERNATIONAL CONFERENCE ON LIQUID METAL TECHNOLOGY IN ENERGY PRODUCTION

## SODIUM AND COVER GAS PURITY MONITORING

### Monitoring Program

The basic purpose of our purity monitoring program is to assure uninterrupted plant availability, and long component life. Sodium and cover gas purity is assured by holding to specified impurity limits through the use of a vigorous monitoring program. The program requires periodic sampling and analysis and in some cases, continuous monitoring of sodium and cover gas for the radioactive and nonradioactive impurities. In the primary sodium 13 nonradioactive species and 12 radioisotopes are analyzed monthly. In the secondary sodium only one radioisotope ( $^{24}\text{Na}$ ) and three nonradioactive species are monitored monthly using flow-through sampling techniques. In the near future, additional nonradioactive species and  $^3\text{H}$  will be monitored in secondary sodium using a new overflow cup sampler and specimen equilibration device. The primary cover gas is monitored continuously for He,  $\text{H}_2$ ,  $\text{O}_2$ , and  $\text{N}_2$  by a gas chromatograph. The secondary chromatograph monitors  $\text{H}_2$ ,  $\text{O}_2$ , and  $\text{N}_2$ .<sup>(6)</sup>

### Sodium Samplers

Two techniques are used for taking samples of EBR-II sodium for impurity analysis. These are termed the "flow-through" and "overflow" techniques.<sup>(2)</sup>

In flow-through sampling, a length of tubing or other vessel is installed directly in-line in the sampling system. Sodium flow is initiated through the sampler and continued for a period of time to clean up or "condition" the sample tube or vessel. The sample is then isolated and frozen. The sample vessel is removed from the system and transported to the laboratory for analysis.

The principal disadvantage of analysis on flow-through samples is that either the total sample is not analyzed, or the sample must include a segment of tubing. The first case is subject to errors caused by impurity segregation. The second case is subject to errors inherent in a tubing "blank". Flow-through samples have been used mostly for oxygen, hydrogen, and carbon analysis by mercury amalgamation, amalgam reflux, and oxyacidic flux methods respectively.<sup>(4)</sup> With the development of equilibration methods for the analyses of these impurities, the flow-through technique now receives little use.

The preferred sampling method for most other impurities is now the overflow technique. In overflow sampling, one or more cups of 3 to 60 g capacity are placed on a rack in a vessel inerted with argon. Sodium flows from spigots into the sample cups until they overflow. Sodium level in the vessel is maintained below the sample cups by adjusting the argon cover gas pressure. Following the desired flushing period, the sampler is isolated and the samples are allowed to freeze. Samples are removed from the vessel and transported to the laboratory for analysis. The total sample contained in the cup is used in the analysis to avoid potential errors due to impurity segregation.

### Equilibration Devices

Since 1972 the EBR-II primary sodium system has been equipped with a device for equilibrating O, H and C impurities with appropriate metal specimens.<sup>(8)</sup> The equilibration device exposes specimens (wires or foils) to a flowing stream of  $750^\circ\text{C}$  sodium. An equilibration device has recently been put into service in the secondary sodium system. Combined exposures of vanadium (for oxygen), low-carbon 18-Cr, 8-Ni steel (for carbon), and nickel-foil wrapped scandium (for hydrogen) are performed at  $750^\circ\text{C}$  for 24 hours. These specimens are equilibrated with the impurity content in the sodium; after cooling, they are removed, cleaned in alcohol and analyzed by standard chemical methods. The impurity content of the sodium is related to the impurity content in the specimens from known chemical activity distribution relationships.<sup>(4)</sup> The advantages of the equilibration method are that (1) it measures chemical activity rather than total impurity content, (2) the exposed specimens are not contaminated by exposure to air, (3) the specimens are specific for the impurity of interest, (4) the method is not subject to errors caused by impurity segregation, and (5) the analytical sensitivity of the method is enhanced because the concentration of the impurity in the equilibrated specimen is as much as 1000 times greater than in the sodium.

### Cover Gas Samplers

Carbonaceous gases (hydrocarbons) in both the primary and secondary cover gas are periodically sampled in a small diameter copper tube about 100 ml in volume. Analysis is by a laboratory chromatograph that uses a flame ionization-type detector.<sup>(4)</sup> Sensitivities of <1 ppm by volume are achieved.

## INTERNATIONAL CONFERENCE ON LIQUID METAL TECHNOLOGY IN ENERGY PRODUCTION

Xenon fission product gases ( $^{133}\text{Xe}$  and  $^{135}\text{Xe}$ ) and  $^{41}\text{Ar}$ , an activation product of the cover gas, are measured six times daily by direct gamma spectrometry on samples taken from the primary cover gas in 10 ml glass bulbs. These Xe analyses provide a method of monitoring for fuel cladding breaks. The normal background, due to tramp fissionable material in the sodium, is about  $1.2 \times 10^3$  nCi/l and  $2.3 \times 10^3$  nCi/l for  $^{133}\text{Xe}$  and  $^{135}\text{Xe}$  respectively and about 3.2 nCi/l for  $^{41}\text{Ar}$ .

Tritium is measured periodically in both primary and secondary cover gases using 2l glass sample flasks. The tritium is counted by scintillation techniques after being converted to water. <sup>(4)</sup>

### On-line Monitors

The primary sodium (since 1972) and secondary sodium (since 1975) have been equipped with on-line oxygen and hydrogen meters which are used to continuously monitor those systems. <sup>(6)</sup>

The oxygen meters are electrochemical cells with thoria-yttria ceramic electrolytes and air reference electrodes. <sup>(9)</sup> Calibration is provided monthly by analysis of the oxygen in sodium by the equilibration of vanadium specimens.

The hydrogen meter uses a 0.25-mm thick nickel membrane to allow diffusion of hydrogen into an ion-pumped vacuum system. <sup>(7)</sup> The hydrogen equilibrium pressure is periodically measured using a vacuum gauge. The equilibrium pressure is related to the hydrogen content in sodium via Sievert's Law. An alternative (and continuous) method for measuring hydrogen is to measure the ion pump current which can be related to hydrogen-in-sodium by calibration via the equilibrium pressure method.

The continuous signals from the oxygen and hydrogen meters are monitored and are used to detect trends so that corrective action can be taken prior to reaching the limits for the reactor operating impurity concentrations.

The primary cover gas is monitored continuously for He, H<sub>2</sub>, O<sub>2</sub>, and N<sub>2</sub> by an on-line gas chromatograph. The secondary chromatograph monitors all but helium since there is no potential source of helium to the secondary cover gas. <sup>(6)</sup>

## SODIUM AND COVER GAS PURITY CONTROL

### Operating Limits

The operation of EBR-II requires the maintenance of sodium and cover gas purity to below set operating limits for the various impurities. Table II gives the normal impurity concentrations and the plant operating limits. Exceeding the limits uncontrollably for plugging temperature, oxygen, or hydrogen requires plant shutdown until the source is identified and minimized and the purity is returned to less than the limiting values.

Exceeding the limits for other impurities in sodium or cover gas requires an investigation into the cause of the high concentration, its impact on continued reactor operation and the minimization of the source of contamination. These limits do not automatically call for a reactor shutdown.

### Sodium Purity Control

Impurities considered important and routinely analyzed in EBR-II sodium and cover gas are given in Table II. Many of these (e.g., O, H, Bi, Mn,  $^3\text{H}$ ) are controlled by cold trapping of a small side stream from the primary and secondary sodium inventories. Other impurities, evidently not controlled by cold trapping, are simply monitored for unexpected changes in concentration. Observed changes are investigated to identify the cause and to eliminate the source, if possible.

### Cold Trap Description

EBR-II cold traps are essentially the same design as those developed in U. S. reactor programs in the early 1950's. The crystallizer tank is a chamber fitted with stainless steel mesh. The chamber is divided into two nearly equal volumes by a cylindrical flow divider. The in-flowing sodium is cooled as it passes downward through the outer, mesh-filled annulus. The sodium returns upward through the center, mesh-filled section. The primary cold trap crystallizer tank has about a 1100 liter volume and is about 0.95 meters in diameter. The crystallizer for the secondary trap has a 550 liter volume and is about 0.7 meters in diameter. Heat is regenerated between inlet and outlet streams by a toroidal-shaped, tube-and-shell economizer located immediately above the crystallizer tank.

**INTERNATIONAL CONFERENCE ON LIQUID METAL TECHNOLOGY IN ENERGY PRODUCTION**

Table II. Impurity Concentrations for EBR-II Sodium and Cover Gas Systems

Parameter†	SODIUM SYSTEMS (By weight)			
	PRIMARY SYSTEMS		SECONDARY SYSTEMS	
	1975 Normal Value	Limit	1975 Normal Value	Limit
Plugging Temperature	<115°C	150°C	<115°C	160°C
Oxygen	1.1 ppm	2.0 ppm	0.8 ppm	3.5 ppm
Hydrogen	100.0 ppb	200.0 ppb	120.0 ppb	300.0 ppb
Carbon	0.2 ppm	0.7 ppm	0.3 ppm (1976)	0.7 ppm
Boron	<0.05 ppm	10.0 ppm		**
Bismuth	2.9 ppm	5.0 ppm		**
Chromium	<0.02 ppm	10.0 ppm		**
Iron	0.07 ppm	10.0 ppm		**
Lithium	<0.0005 ppm	10.0 ppm		**
Manganese	<0.005 ppm	10.0 ppm		**
Nickel	<0.04 ppm	10.0 ppm		**
Silicon	0.2 ppm	10.0 ppm	0.5 ppm	10.0 ppm
Tin	37.0 ppm	50.0 ppm		**
Uranium	<2.0 ppb	10.0 ppb		**
Tritium	85.0 nCi/g	300.0 nCi/g		**
<sup>22</sup> Na	90.0 nCi/g	200.0 nCi/g		**
<sup>24</sup> Na	2.6 mCi/g	5.0 mCi/g	20.0 nCi/g	**
<sup>54</sup> Mn	0.2 nCi/g	1.0 nCi/g		**
<sup>110m</sup> Ag	2.0 nCi/g	5.0 nCi/g		**
<sup>113m</sup> In	22.0 nCi/g	50.0 nCi/g		**
<sup>117m</sup> Sn	11.0 nCi/g	50.0 nCi/g		**
<sup>125</sup> Sb	3.6 nCi/g	10.0 nCi/g		**
<sup>131</sup> I	60.0 pCi/g	2 X normal†		**
<sup>137</sup> Cs	64.0 nCi/g	2 X normal†		**
<sup>210</sup> Po	160.0 pCi/g	250.0 pCi/g		**
<sup>239</sup> Pu	<0.3 pCi/g	10.0 ppb		**

COVER GAS SYSTEMS (By volume)

Nitrogen	3000.0 to 6000.0 ppm	7000.0 ppm	100.0 to 500.0 ppm	*
Oxygen	0 ppm	1400.0 ppm	0 ppm	*
Hydrogen	0-200 ppm	280.0 ppm	<10.0 ppm	100.0 ppm
Helium	<10.0 ppm	280.0 ppm	--	--
Carbon Compounds				
Methane	1-10 ppm	*	1-5 ppm	*

\* No limit established at this time.

\*\* Not sampled and analyzed since 1972 when the overflow cup sampler became inoperable due to a sodium leak. <sup>131</sup>I and <sup>137</sup>Cs may increase dramatically following a fuel cladding breach.

† Other impurities analyzed routinely are: Ag, Al, Ca, Co, Cu, K, Mg, Mo, Pb, N, F, Cr

The primary sodium cold trap is cooled by a circulating-NaK to silicon-oil, to water, heat transfer system. The secondary sodium cold trap is cooled by a static-NaK to Dowtherm, to water, heat-transfer system.

The thermal performance of both EBR-II cold traps is less than design specification. As a result, both traps must be operated at one-quarter to one-half their

design flowrates. The design deficiency appears to be in the heat transfer that can be achieved in the economizer.

Cold Trap Performance History

The initial cleanup of primary sodium was accomplished with a temporary cold trap similar in design to the permanent trap. The first permanent trap was used

## INTERNATIONAL CONFERENCE ON LIQUID METAL TECHNOLOGY IN ENERGY PRODUCTION

from March 1963 to June 1968. It processed approximately 87 million liters (23 million gallons) of sodium. From 1963 through 1966 it was operated approximately 15% of the time. From 1966 until it was removed in 1968, it operated 75% of the time. A more rigorous operation of the cold traps followed the discovery of copper in primary sodium in early 1967.

The second primary trap began operating in November, 1968, and still remains in service. At the end of January, 1976, it had processed 216 million liters (57 million gallons) of sodium and has been operated 66% of the time.

The first cold trap used for the secondary sodium plugged during initial system cleanup. The temporary cold trap used to purify primary sodium was installed in the secondary system to complete the initial cleanup.

The second permanent secondary cold trap operated from 1963 to April, 1972. It is estimated that this trap was on-line less than 50% of the time.

The third, and current, secondary cold trap began operation in June, 1972. At the end of January, 1976, it had processed 72 million liters (19 million gallons) and operated 86% of the time.

### Oxygen and Hydrogen Purification

Oxygen and hydrogen purity control is of major concern to plant operations because of potential detrimental effect of the oxygen on materials and because both form low solubility sodium compounds that can cause blockages in coolant channels. EBR-II cold traps are effective in controlling oxygen to less than 1 ppm in the primary and secondary sodium. Hydrogen is controlled to less than 100 ppb and less than 140 ppb in the primary and secondary sodium respectively.

The primary and secondary cold traps have been purposely taken out of service on occasion to measure the oxygen and hydrogen source rates. The results are given on Table III.

The source rates for hydrogen and oxygen to the primary sodium essentially correspond stoichiometrically to water. The maximum source rates are observed only during periods of fuel insertion and removal from the primary sodium. At other times these source rates are negligible. It is believed that water is being introduced from residual moisture on the fuel or the fuel handling equipment that is water-washed and dry-

Table III. Oxygen and Hydrogen Source Rates to EBR-II Sodium Systems

	Source Rates	Time Plant Can Operate Without Na Purification	Probable Nature of Source
PRIMARY SODIUM	Oxygen 0-10 g/day	5 to 6 weeks with normal fuel handling, longer without fuel handling	Source is moisture from intermittent fuel insertion & removal operations
	Hydrogen 0-1 g/day		
SECONDARY SODIUM	Hydrogen 0-0.5 g/day	10 days if reactor is operating at power, longer if reactor is shut down	Hydrogen is produced from steam-side corrosion that diffuses into the sodium

argon dried as part of normal operating procedures. Reactor operating limits for oxygen, hydrogen and plugging temperature will be reached in 5 to 6 weeks if the primary cold trap is inoperable during fuel handling activities.

During periods when the reactor is operated at full power, hydrogen is produced in the steam generators by water-side corrosion at a fairly rapid rate. The hydrogen diffuses through the tube walls into the sodium at a rate of about 0.5 g/day. This source rate causes the hydrogen concentration to change from its normal 80 ppb when the plant is shut down to 120-130 ppb when the reactor is at power and the cold trap is operating. Without the cold trap operating, the concentration would continue to rise and reach its operating limit in about ten days. The plugging temperature limit would be reached at the same time. There appears to be no significant source of oxygen to the secondary sodium.

Although EBR-II has not experienced water-to-sodium leaks, such leaks are a potential source of both oxygen and hydrogen contamination. The normal hydrogen source rate would be equal to a water leak rate of about 20 $\mu$ g H<sub>2</sub>O/sec. A system of ten hydrogen meters that are capable of alarming water leak rates of <2 mg H<sub>2</sub>O/sec (a rate that is well below those that cause rapid damage) is described in a companion paper. (10)

The normal source rate of hydrogen is too small to interfere with the water-to-sodium leak detection capabilities.

# INTERNATIONAL CONFERENCE ON LIQUID METAL TECHNOLOGY IN ENERGY PRODUCTION

## Impurity Removal by Cold Trapping

The effectiveness of EBR-II cold traps for removing various impurities has been measured using data during periods when the source rate of the impurity is essentially zero or after the cold trap has been put into operation.

The general mathematical equation that describes the bulk concentration of any species is:

$$\frac{dC}{dt} = \frac{I}{M} - \left( \frac{FE}{M} (C - C_e) + \lambda C \right) \quad (1)$$

Production Rate                      Removal Rate

I is the total source rate by in-leakage, diffusion, fission, neutron capture, decay or other mechanism. M is the total mass of sodium (assumed to be well-mixed), F is the crystallizer flow rate, E is the fraction of the impurity removed per pass through the crystallizer, C is concentration of impurity, and  $\lambda$  is the decay constant for the isotope of interest. The solution of equation (1), normalized to  $C_o - C_e$  (initial concentration minus the solubility concentration at the cold trap temperature), is:

$$\frac{C - C_e}{C_o - C_e} = e^{-\left(\frac{FE}{M} + \lambda\right)t} + \frac{I}{FE(C_o - C_e)} \left(1 - e^{-\frac{FE}{M}t}\right) \quad (2)$$

Evaluating equation (2) for hydrogen, oxygen,  $^{131}\text{I}$ ,  $^{137}\text{Cs}$ ,  $^{54}\text{Mn}$  and  $^3\text{H}$  led to the following conclusions:

1. Hydrogen is trapped effectively and rapidly. The fraction removed per pass is about 3/4 for the primary cold trap and about 1/2 for the secondary trap.
2. Oxygen is trapped rapidly but the fraction removed per pass appears to be less than 1/2. Cleanup from an oxygen excursion takes longer than from a hydrogen excursion.
3.  $^{131}\text{I}$  is not removed effectively by the primary cold trap. The fraction removed per pass is less than 1/20. The major removal mechanism for  $^{131}\text{I}$  is radioactive decay (8.0 day half-life).
4.  $^{137}\text{Cs}$  shows anomalous behavior. During the first year of its operation (1968-1969) the present cold trap removed about 30% of the  $^{137}\text{Cs}$  from the primary sodium. Subsequently,  $^{137}\text{Cs}$  was not effectively removed following the stepwise increase caused by certain fuel cladding failures. A single measurement of the  $^{137}\text{Cs}/^{22}\text{Na}$  concentration factor (made in June

1972) showed that the ratio of the  $^{137}\text{Cs}/^{22}\text{Na}$  activities in the cold trap were a factor of 50 greater than the same ratio in the  $371^\circ\text{C}$  bulk sodium. This is approximately the enhancement of activity that would be caused by the initial (30%) removal of  $^{137}\text{Cs}$ .

5.  $^{54}\text{Mn}$  appears to be effectively removed by the primary cold trap. About 3/5 is removed per pass. The normal bulk sodium concentration is maintained at <1 nCi/g.

6. The primary cold trap controls the tritium concentration in the primary sodium to less than 100 nCi/g. The effectiveness of the primary cold trap varies from about 1/10 to over 1/2 fractional removal per pass.

7. Although quantitative data for fractional removal estimates is not available the following general conclusions have been reached:

a. Impurities that appear to be effectively controlled by cold trapping include:

Bismuth	< 2 ppm
Copper	<20 ppb
Manganese	< 5 ppb

b. Impurities that do not appear to be well controlled by cold trapping include all other impurities listed on Table II and not previously discussed.

## Cover Gas Purity Control

The EBR-II primary and secondary cover gas is argon. Its purity is maintained within the limits given on Table II by replacing argon lost due to leakage and occasionally purposely adding and venting fresh argon. Within the next year a cryogenic gas-purification system will be installed for the removal of fission product gases (mainly Xe and Kr). The new system will permit continuous reactor operation with defected fuel cladding.

The sources and behavior of various impurities in the EBR-II cover gas systems are as follows:

1. Oxygen is introduced to the cover gas by air which enters during fuel handling and certain maintenance operations. It is normally not detected by the gas chromatograph since it rapidly reacts with the sodium.
2. Nitrogen is also introduced by air. A residual of 1000-3000 ppm is normal in the primary cover gas but can exceed 6000 ppm during times when fuel

## INTERNATIONAL CONFERENCE ON LIQUID METAL TECHNOLOGY IN ENERGY PRODUCTION

handling activities are intensified. A residual of 100-300 ppm nitrogen in the secondary cover gas is normal.

3. Hydrogen is introduced from moisture in air or the fuel handling operation. Hydrogen in the primary cover gas can reach 200 ppm during fuel handling but it reacts with the sodium and is normally <10 ppm. Moisture introduction is the likely cause of the hydrogen excursions in the primary cover gas. Hydrogen is normally less than 4 ppm in the secondary cover gas. Higher levels in the secondary cover gas might indicate the presence of a water-to-sodium leak. No water-to-sodium leaks have occurred.

4. Methane in the primary and secondary cover gas is normally less than 5 ppm and is traceable to impurities in the argon supply. At times, concentrations up to 100 ppm have been observed in the primary cover gas. These appear to be correlated with fuel handling operations. The source is thought to be lubricants from the argon blowers associated with the fuel handling equipment. Another potential source is lubricants from the primary pumps. The methane is removed by the natural cover gas leakage and, possibly, by its slow reaction with sodium.

5. Helium is normally not detectable in the primary cover gas but can exceed 50 ppm if certain helium blanketed fuel elements or experiments leak or are purposely vented.

6. Radioisotopes including those of Xe, Kr and Ne are always present in the primary cover gas. The Xe and Kr are produced from background concentrations of fissionable material in the sodium or on the fuel cladding or structural materials. Ne is a short-lived activation product of sodium that is detected only by the Germanium Lithium Argon Scanning System. When a fuel cladding ruptures the Xe and Kr activities can exceed safe limits in the reactor building and the reactor is shut down. Removal of the excess activity is achieved by purging with fresh argon.

7. Activities of tritium in the primary and secondary cover gases are variable. They are dependent on a large number of parameters, not all of which can be measured accurately. In general, the activity of tritium in the primary cover gas is 4-20 times greater than its activity in the secondary cover gas. A typical example is given by the samples of primary and secondary cover gas taken on Aug. 3, 1975. These samples showed tritium activities of 75 and 12 nCi/l,

respectively. In this instance, the reactor had been at full power and the cold traps had been operating without interruption for at least 11 days.

### RADIOACTIVITY BEHAVIOR IN SODIUM SYSTEMS

The concentration of radionuclides in the EBR-II sodium systems has in general increased over the operating life of the plant.<sup>(3)</sup> The reasons are:

1. Long-lived radionuclides are still approaching saturation activities.

2. Increased neutron activation, as the maximum reactor power was raised from 30 MWt in 1964 through a number of steps to 62.5 MWt in 1970.

3. Softening of the neutron spectra by replacing the depleted uranium blanket with a stainless steel reflector in 1972.

4. Release of fission products from ruptured fuel elements.

5. Loss of tin-bismuth alloy to the sodium providing for an increase in certain activation products.

6. Progressive, slow corrosion of the stainless steel components, adding activated corrosion products to the sodium.

### In-Sodium Results

Some specific examples of radioisotope behavior are as follows:

1. Sodium-22 and  $^{24}\text{Na}$  are the predominant activities in the EBR-II primary sodium system.  $^{22}\text{Na}$ , with its 2.6 year half life has increased steadily over the life of the plant. Its current activity is near 100 nCi/g. It is the principal source of radioactivity after the decay of 15 hr  $^{24}\text{Na}$ .  $^{24}\text{Na}$  has shown a number of step increases in activity related to reactor power changes and the use of a stainless steel reflector. It now reaches saturation at about 3 mCi/g at full power operation. This activity is over 10,000 times greater than any other radioactivity in the sodium. Sodium sample handling or direct maintenance on the primary system requires about five days of decay of the  $^{24}\text{Na}$  activity.

2. Cesium-137 is a dominant fission product in EBR-II sodium. It is introduced by fuel cladding breaks and was first noted in 1967. Measurable step increases have been noted and related to specific sub-assembly ruptures. Its activity is now near 70 nCi/g.

## INTERNATIONAL CONFERENCE ON LIQUID METAL TECHNOLOGY IN ENERGY PRODUCTION

$^{137}\text{Cs}$  tends to concentrate in the cover gas regions and in the cold trap but in spite of this the  $^{137}\text{Cs}$  activity continues to increase as additional fuel cladding ruptures take place.

3. Iodine-131 is analyzed frequently as an indicator of the seriousness of a fuel cladding rupture. The iodine measured is possibly related to the size or nature of the cladding breach.  $^{131}\text{I}$  reaches a saturation activity of 20-100 pCi/g during reactor operation and is produced by background fissionable materials. Activities close to 10,000 pCi/g have been measured following fuel cladding breaks.

4. Tin-113 and  $^{113}\text{In}$  are produced by neutron capture or electron capture in material from the tin-bismuth rotating plug seal alloy. A step increase in the activity of these isotopes was noted in 1972 and a steady increase has been noted since that time to their present activity of about 20 nCi/g. The increases are due to the ingress of the seal alloy which has been confirmed by a fourfold increase in the nonradioactive tin concentration over a ten-year period.

5. Polonium-210 is another activity that results from the tin-bismuth seal alloy getting into the sodium. It is an activation and decay product of  $^{209}\text{Bi}$ . The  $^{210}\text{Po}$  is an alpha emitter with a 138-day half life. Its activity has steadily increased since it was first detected in 1971 to its current level of about 200 pCi/g.

6. Uranium and plutonium are both below their analytical detection limits (<1 ppb and <0.5 pCi/g, respectively). This is not surprising since subassemblies with ruptured fuel cladding are removed immediately after the break is detected and essentially all cladding breaks to date have been rather innocuous.

### RESULTS OF COMPONENT EXAMINATIONS

The principal radionuclides found, more or less generally, on components in the EBR-II primary sodium system are  $^{22}\text{Na}$ ,  $^{54}\text{Mn}$ ,  $^{137}\text{Cs}$  and  $^{60}\text{Co}$ . Somewhat less pervasive is  $^{182}\text{Ta}$ . Other radionuclides found in minor amounts or in localized concentrations are  $^{210}\text{Po}$  (in deposits on the primary-pump impeller) and  $^{58}\text{Co}$  (in stainless steel from the SURV-3 subassembly and on cap-screws from primary pump No. 1). Not listed here are relatively short-lived (<3 days) radionuclides, or radionuclides on in-core materials.

Results from examinations of specific components are summarized below: (11)

1. The irradiated-fuel monitor thimble had been exposed to sodium in the primary tank for almost two years. Axial gamma scans with a GeLi detector measured relative activities of  $^{54}\text{Mn}$ ,  $^{137}\text{Cs}$ , and  $^{60}\text{Co}$ . Steam cleaning of the thimble removed 23% of the  $^{54}\text{Mn}$  activity, 93% of the  $^{137}\text{Cs}$  activity, and 0.3% of the  $^{60}\text{Co}$  activity.

2. Primary pump No. 1 was removed in 1971 after 32,000 hrs of service and almost seven years in the primary tank. Radiation levels, measured on the uncleaned pump generally ranged from 15 mR/hr at 0.3 m (near the shield plug) to 130 mR/hr at 0.3 m (near the discharge). These radiation levels posed no serious problem during the repair of the pump.

The  $^{137}\text{Cs}/^{22}\text{Na}$  ratios found on  $\text{Na}/\text{Na}_2\text{O}$  deposits on pump surfaces that resided in the cover-gas region were as high at 100-400X the ratios of  $^{137}\text{Cs}/^{22}\text{Na}$  in the bulk sodium before shutdown. This finding indicates that  $^{137}\text{Cs}$  is volatile and tends to condense in the cover gas regions of the primary tank.

Axial scans of the pump assembly and of the pump components were made with a GeLi detector. Besides  $^{22}\text{Na}$ , the major activities found on uncleaned pump surfaces were  $^{54}\text{Mn}$ ,  $^{60}\text{Co}$ ,  $^{137}\text{Cs}$ , and  $^{182}\text{Ta}$ . Decontamination of the pump components by scrubbing in hot baths of organic acids removed 44-67% of the  $^{54}\text{Mn}$  activity, 42-92% of the  $^{60}\text{Co}$  activity, and about 65% of the  $^{137}\text{Cs}$  activity (only one case studied). The  $^{182}\text{Ta}$  activity was essentially not removed, but appeared to be redistributed.

Decontamination of the pump and successive acid treatments of the baffle-subassembly capscrews show that  $^{54}\text{Mn}$  and  $^{137}\text{Cs}$  are strongly attached to the stainless steel. Roughly half the activity from these radionuclides was removed by nondestructive decontaminating solutions; the remainder yielded only to vigorous attack by hot mineral acids.

3. The intermediate heat exchanger (IHX) is the original IHX installed in 1962. Since wet criticality, an estimated  $60 \times 10^6 \text{ m}^3$  of primary sodium have passed through it.

In 1971, several radiation scans were made along the axis of the IHX by lowering probes into the secondary inlet pipe after the sodium was pumped out.

## INTERNATIONAL CONFERENCE ON LIQUID METAL TECHNOLOGY IN ENERGY PRODUCTION

Essentially all the observed radiation originated on the primary side of the IHX. Maximum dose rates measured near the lower end of the IHX were 230 mR/hr. Dose rates measured below the level of the primary sodium were generally greater than 140 mR/hr. The contribution of  $^{22}\text{Na}$  to these measurements is estimated to be less than 77 mR/hr. Thus, 50% or more of the measured dose rate must have originated from deposits of fission products and activated corrosion products.

4. The pump duct of the fuel-element-rupture-detector (FERD) loop continuously samples a 380  $\mu\text{m}$  stream of primary-sodium effluent from the IHX. This stream of sodium is monitored for delayed-neutron activity and then returned to the primary tank. The pump duct was replaced in April, 1970. A radiometric scan of the drained, but uncleaned, duct with a GeLi detector revealed only  $^{54}\text{Mn}$  and  $^{60}\text{Co}$  activities. An alcohol-water rinse removed 28% of the  $^{54}\text{Mn}$  and 52% of the  $^{60}\text{Co}$  activities. Cesium-137 was not detected. Presumably the  $^{137}\text{Cs}$  diffused from the pump surfaces into the sodium when the pump duct was heated before the sodium was drained.

5. The SURV subassemblies are a set of 10 materials-irradiation subassemblies that were loaded into the EBR-II on March 1, 1965. On Feb. 24, 1971, subassembly SURV-3 was removed from the reactor core for examination. Wash water from its cleaning showed a high  $^{182}\text{Ta}$  activity. Tantalum is one of the test materials exposed to sodium. Specimens were cut from the Type 304 stainless steel shroud that guided the flow of primary sodium past the test materials. One of these specimens was examined by electropolishing successive  $1.3 \times 10^{-2}$  mm layers from the surface until  $13 \times 10^{-2}$  mm of material had been removed. Measurements of the activities of the principal radionuclides in the electropolishing solutions showed that  $^{182}\text{Ta}$  was totally removed with the first  $1.3 \times 10^{-2}$  mm of steel. The concentrations of  $^{54}\text{Mn}$ ,  $^{58}\text{Co}$  and  $^{60}\text{Co}$  were distributed fairly uniformly throughout the top  $13 \times 10^{-2}$  mm of surface, although  $^{58}\text{Co}$  and  $^{54}\text{Mn}$  activities were slightly higher in the outer  $1.3 \times 10^{-2}$  mm layer.

### Results of External Cold Trap Gamma Scans

Beginning in 1971 and at intervals thereafter, radiation levels around the perimeter of the primary cold trap were measured using survey meters. The radiation level of the trap has increased roughly in

proportion to the cumulative energy produced by the reactor. Isodosic maps of the radiation show two persistent "hot spots". One, near the bottom of the tank at the NaK-coolant inlet, was to be expected because this area is where precipitating impurities should collect. The other "hot spot" was 3.14 radians around the tank from the first and near the top of the tank. This locus of radioactivity was not expected and, at the moment, remains unexplained. The most recent survey, made in April 1975, showed radiation levels of  $<1$  R/hr at both of these "hot spots" 31 days after the trap had been isolated from flowing primary sodium ( $^{24}\text{Na}$  was essentially completely decayed).

One gamma-energy scan of the cold trap, made in June, 1972, using a GeLi detector, 81 days after shutdown, identified  $^{22}\text{Na}$ ,  $^{54}\text{Mn}$ ,  $^{60}\text{Co}$ ,  $^{65}\text{Zn}$ ,  $^{124}\text{Sb}$ ,  $^{134}\text{Cs}$  and  $^{137}\text{Cs}$ . The concentration factor for  $^{137}\text{Cs}/^{22}\text{Na}$  in the cold trap vs the  $370^{\circ}\text{C}$  ( $700^{\circ}\text{F}$ ) bulk sodium was 50. This shows that the cold trap has removed some ( $\sim 30\%$ ) of the  $^{137}\text{Cs}$  arising from fission-product releases to the sodium. The principal radioisotopes found in this scan, listed in descending order of activity, were:  $^{137}\text{Cs}$ ,  $^{54}\text{Mn}$ ,  $^{125}\text{Sb}$ ,  $^{134}\text{Cs}$  and  $^{22}\text{Na}$ .

### SUMMARY

EBR-II has operated in a safe and reliable manner for almost 12 years. Excellent sodium purity control supported by a rigorous purity monitoring program has been instrumental in achieving this history. Sodium technology efforts at EBR-II will continue to contribute to the high availability and operability of the reactor and coolant systems.

### REFERENCES

1. Olson, W. H., Miles, C. C., and Cissel, D. W., "Impurities in EBR-II Sodium and Cover Gas," ANL-7520 Part I, pp. 222-226 (1968).
2. Olson, W. H., "Sampling and Analysis of EBR-II Sodium," ANL-7844 (1971).
3. Smith, C.R.F. and Holmes, J. T., "Purity of EBR-II Sodium: 1967-1974," ANL 75-26 (1975).
4. "Methods for the Analysis of Sodium and Cover Gas," RDT Standard F3-40T, (January 1976).
5. Holmes, J. T. and Haroldsen, G. O., "The Utilization of On-line Monitors at EBR-II for Sodium



## INTERNATIONAL CONFERENCE ON LIQUID METAL TECHNOLOGY IN ENERGY PRODUCTION

- Purity," Nuclear Technology 21, pp 228-234  
(March 1974).
6. Smith, C.R.F., Richardson, W. J. and Holmes, J.T.,  
"On-line Sodium and Cover Gas Purity Monitors as  
Operating Tools at EBR-II," International Confer-  
ence on Liquid Metal Technology in Energy Pro-  
duction, Session VIII A, Champion, Pa. (May 3-6,  
1976).
  7. Vissers, D. R., Holmes, J. T., Bartholme, L. G.,  
and Nelson, P.A., "A Hydrogen Activity Meter for  
Liquid Sodium and Its Application to Hydrogen  
Solubility Measurements," Nuclear Technology 21,  
pp. 235-244 (March 1974).
  8. Kolba, V. M., Slawewski, M. A., Filewicz, E. C.,  
McKee, J. M., Holmes, J. T., and Nelson, P. A.,  
"Carbon Meter - Equilibration Module for LMFBR's:  
Design and Operation," ANL-7941 (May 1972).
  9. McKee, J. M., Vissers, D. R., Nelson, P. A.,  
Grundy, B. R., Berkey, E., and Taylor, G.R.,  
"Calibration Stability of Oxygen Meters for LMFBR  
Sodium," Nuclear Technology 21, pp 217-227 (March  
1974).
  10. Wrightson, M. M., McKinley, K., Ruther, W. E.,  
and Holmes, J. T., "EBR-II Water-to-Sodium Leak  
Detection System," International Conference on  
Liquid Metal Technology in Energy Production,  
Session VI B, Champion, Pa. (May 3-6, 1976).
  11. Smith, C.R.F., "Radioactivity of EBR-II Compon-  
ents: I. Examinations in FY 1971," ANL-7873,  
(1972).

# INTERNATIONAL CONFERENCE ON LIQUID METAL TECHNOLOGY IN ENERGY PRODUCTION

## IMPURITY DEPOSITION IN PFR PLUGGING METERS AND COLD TRAPS

C G Allan

United Kingdom Atomic Energy Authority  
Dounreay Experimental Reactor Establishment  
Thurso, Caithness, Scotland, U.K.

### ABSTRACT

Plugging meter and cold trap performance were examined during the initial clean up of the PFR primary circuit. The kinetics of impurity deposition in the plugging meters were analysed, and showed second order dependence on concentration driving force or supersaturation. The analysis suggested that oxide was the fast plugging species when multiple plugging breaks were present, and this was consistent with the results of an extensive analysis of the composition and distribution of the deposits in the exhausted PFR cold trap. Oxide was the major impurity present in the trap, with approximately equal quantities of hydride and hydroxide. Most of the impurities (70% by weight) had deposited in the first 40 - 110 mm of mesh depth, with deposit build-up to a depth 45 - 70 mm upstream of the mesh. The oxide, hydride and hydroxide contents of the local deposits were highest near the trap inlet, in the sludge deposit in the bottom of the vessel, and in the mesh, respectively.

### INTRODUCTION

Impurity monitoring and control are probably the most important operations on fast reactor sodium circuits. Plugging meters and cold traps are the most proven and reliable equipment available for sodium purity monitoring and control. Fast reactors still rely heavily on them, and it is therefore essential that the maximum information on impurity levels and impurity behaviour in sodium be obtained from plugging meters. The main cold trap requirements are a high trap efficiency for all important impurities in the sodium, a good trap capacity for these impurities and several years of effective trap life. This is especially important for primary circuit cold traps, which will become intensely radioactive due to the collection of fission products and activated corrosion products, creating considerable incentive for reducing

the frequency of basket change.

Forced circulation mesh-packed cold traps were installed in the PFR Primary and Secondary Cold Trap Loops (PCTL and SCTL), with 6 automatic plugging meters (APM's) as the main impurity monitoring instruments on the sodium circuits. This paper analyses the records from the two APM's on the PCTL during the initial clean-up of the PFR primary circuit, and the kinetics of deposition in the plugging meter orifices. The performance of the primary cold trap during this period is also examined, and the distribution and composition of the deposits in the exhausted cold trap are investigated.

### THE PFR PRIMARY COLD TRAP LOOP

The Primary Cold Trap Loop (PCTL) is an auxiliary circuit on the PFR primary vessel, and is situated in its own shielded vault, adjacent to the reactor vault. In addition to the cold trap, it consists of two 6.5 kg/sec (23 te/hour) centrifugal impeller pumps, a 2 kg/sec DC electromagnetic pump, a regenerative heat exchanger (RHX), an inlet plugging meter (IPM), an outlet plugging meter (OPM) and an in-line sodium sampler - distillation unit (SDU). A diagram of the PCTL sodium circuit is shown in Figure 1, with the PCTL cold trap in Figure 2. The sodium enters the PCTL at main pool temperature (400 - 450°C typical), and passes through the shell side of the RHX. The cold trap inlet temperature is maintained at approximately 10°C above the plugging temperature measured on the IPM. Temperature control is achieved by diverting up to 1/3 of the cold trap outflow through a RHX bypass line. The 2 kg/second EM pump on this bypass is used to regulate the bypass flow, a high flow giving a high cold trap inlet (RHX shell-side outlet) temperature. The sodium is cooled 30 - 70°C in the outer annulus of the trap, by air cooling the outside of the cold trap vessel, and a practical minimum cold trap temperature is approximately 120°C.

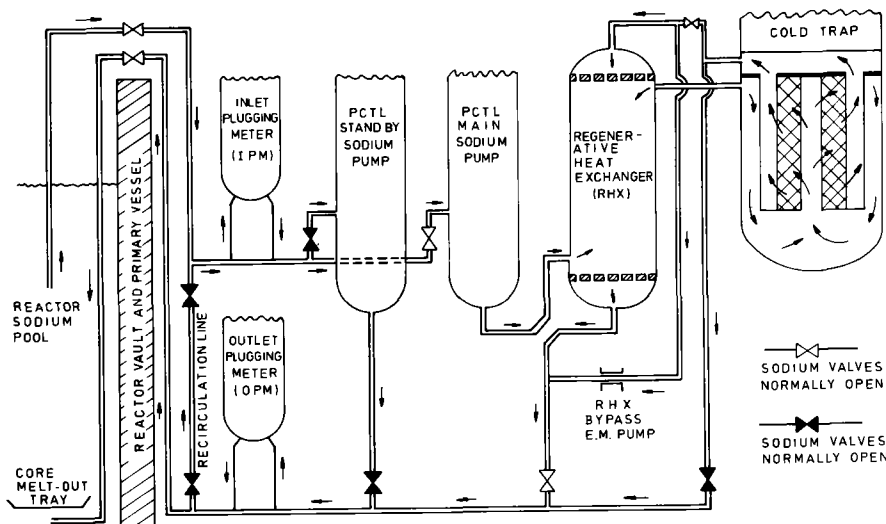


FIG. 1. P.F.R. PRIMARY COLD TRAP LOOP - SODIUM CIRCUIT.

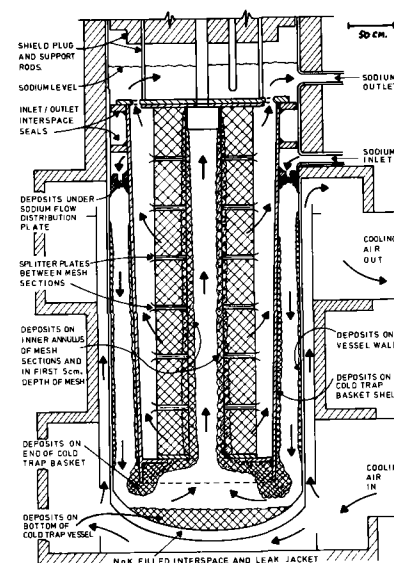


FIG. 2. DEPOSIT DISTRIBUTION IN PFR PRIMARY COLD TRAP

## INTERNATIONAL CONFERENCE ON LIQUID METAL TECHNOLOGY IN ENERGY PRODUCTION

The PFR automatic plugging meters have been described elsewhere<sup>(1)</sup>. They are designed to operate automatically in the equilibrium mode, in which the orifice is cooled until a significant reduction in orifice flow occurs (10% say), and the orifice cooling is controlled to maintain this flow. They can also be operated manually in the temperature ramp scan mode, in which the orifice is cooled at a constant rate and the orifice flow record is examined for significant flow changes. Slow dissolution of impurity deposits from plugging meter orifices does not appear to be subject to an unsaturation bias, similar to the supersaturation bias shown by the deposition process.<sup>(2)</sup> Of the three common modes of plugging meter operation, the equilibrium mode should therefore give the least biased estimate of the impurity saturation temperature.

### PCTL PLUGGING METER PERFORMANCE

Most of the information on plugging meter performance was derived from PCTL plugging meter records produced during two coolant clean-up runs, the Low Temperature and High Temperature Dynamic Runs. These records were in the form of orifice temperature and flow traces on recorder charts, from the operation of the two PCTL plugging meters in the automatic and manual scan (cooling ramp) modes.

In the two weeks between primary circuit filling and the start of the Low Temperature Dynamic Run, automatic mode plugging temperatures oscillated in the range 155 - 185°C with periods in the range 5-10 hours. These oscillations generally had a characteristic form. A step increase in orifice flow (typically 5-15%) was quickly followed by a rapid fall in orifice temperature. The orifice flow then remained relatively stable while the rate of orifice cooling fell to zero. After a short period of stable orifice temperature the orifice flow began to fall and the orifice temperature began to rise. The original orifice flow and temperature were approached slowly and maintained until a further flow step occurred, restarting the oscillation cycle.

Adjusting the control settings (integral term) of the plugging meters gave smoother traces. Examination of the records over several days showed that the oscillation amplitude was unchanged while the oscillation period had approximately doubled. The interpretation of the oscillations was not clear, and the oscillation range created unacceptable uncertainty in the plugging temperatures, especially when the impurity levels in the main pool increased. Continuous operation of the two PCTL plugging meters in the automatic mode was therefore terminated, and manual temperature scans (cooling ramps) were used instead, during much of the clean-up runs.

When operated in the automatic mode at high impurity levels, the plugging temperature oscillation amplitudes increased. The maximum amplitude observed was 65°C, but amplitudes of 10-35°C were more normal. The range of oscillation periods also increased to 5-36 hours, the longer periods being much more variable than the shorter ones which remained constant (± 20% approximately) over several days, but more than 75% of period measurements lay in the range 5-15 hours.

The three most probable explanations for the oscillation behaviour in the automatic mode are oscillations between the saturation temperatures of two different impurities, oscillations between the plugging and unplugging temperatures of one impurity, or response lag in the control of the plugging meter. Two breaks in the manual scans appeared when the main pool temperature exceeded 200°C, the higher temperature

break having a much slower rate of orifice blockage than the lower temperature break. The temperatures of both plugging breaks increased rapidly as the main pool temperature increased. High orifice cooling rates gave lower plugging temperatures than low cooling rates. Cooling rates less than 1°C/minute gave an undercooling bias less than 15°C for plugging temperatures greater than 160°C.

The primary circuit clean-up records in Figures 3 and 4 show that the upper and lower oscillation limits in the automatic mode were in good agreement with the slow and fast plugging breaks, respectively, in the manual mode when the orifice cooling rate was less than 1°C/minute. Oscillations greater than 15°C were therefore due to multiple impurities in the sodium, unless the instrument control lag was as high as 1 hour. A periodic perturbation of the system was required to start the oscillation cycle, for instance: breakage of a fragile plug, possibly initiated by system vibration dislodging part of the plug, or flow changes caused by sodium level fluctuations in the plugging meter vessel. Different flow impedances in the orifice and coaxial bypass circuits, or their inlets or outlets at different levels, could account for this.

The perturbation created a control imbalance in the plugging meter, which treated it as a step change in the impurity level in the sodium. Rapid orifice cooling was applied, the cooling rate being defined by the reset rate of the control unit integral term. The rapid fall in orifice temperature continued until impurity deposition in the orifice caused a significant reduction in orifice flow. The perturbation therefore made the automatic plugging meter seek the fastest plugging species and control was initially re-established on it.

Since the sodium contained multiple impurities, some of which had fast plugging rates, and others with higher saturation temperatures had slower plugging rates, the orifice was not in equilibrium with these slower plugging species. Their deposition in the orifice continued, causing a slow fall in orifice flow accompanied by a slow rise in orifice temperature under servo control. The composition of the plug changed slowly due to the dissolution of the fast plugging species from the orifice, and its gradual replacement by the slow plugging species. The orifice temperature settled at the highest saturation temperature of the major impurities present in the sodium.

### DEPOSITION KINETICS IN PLUGGING METERS

The PFR primary circuit clean-up records indicated that considerable difference existed between Na<sub>2</sub>O and NaH in the plugging meters, but the identification of NaOH was less clear. The plugging meter is basically a kinetic instrument, and it was not unexpected that the most pronounced differences between impurities would be in their deposition kinetics. Any understanding of plugging meter specificity using deposition kinetics, therefore requires an analysis of these kinetics.

Solute deposition from supersaturated solution fits the general kinetic equation:<sup>(3,4)</sup>

$$\dot{m} = kA_d(C_B - C_S)^n \quad (1)$$

where  $\dot{m}$  is the rate of mass deposition in the orifice, ( $\mu\text{g sec}^{-1}$ )

$k$  is the deposition rate constant, ( $\mu\text{g sec}^{-1} \text{cm}^{-2} (\text{ppm})^{-n}$ )

# INTERNATIONAL CONFERENCE ON LIQUID METAL TECHNOLOGY IN ENERGY PRODUCTION

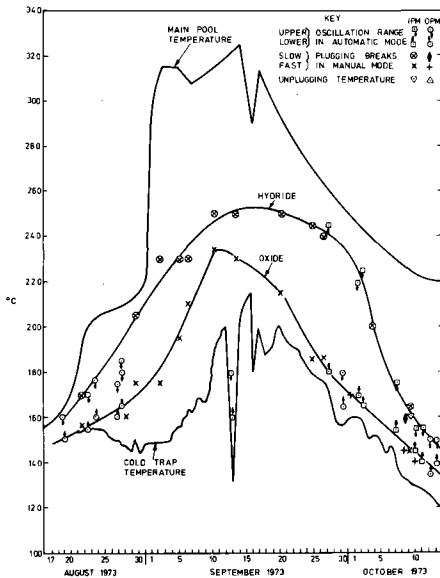


FIG. 3 FIRST LOW TEMPERATURE DYNAMIC RUN

$A_d$  is the deposition surface area, ( $\text{cm}^2$ )

$C_B$  is the impurity level in the bulk Na entering the orifice (ppm)

$C_S$  is the saturation solubility of the impurity in sodium at the orifice temperature  $T_s$  (ppm)

and  $n$  is an exponent, which depends on the rate controlling step in the deposition process.  $n$  values as high as 3 have been observed in crystallisation and deposition processes, but a value  $n=1$  is often assumed.

Orifice temperature and flow are the parameters which are directly measurable in the operation of a plugging meter, and the more useful kinetic equations will involve them. For uniform deposition in a square orifice of side  $d$  and length  $l$  cm,

$$\dot{m} = - \frac{f_v \rho d^2 l}{F_i} \dot{F} \quad \mu\text{g sec}^{-1}$$

where  $F_i$  is the initial sodium flow through the orifice ( $\text{cm}^3 \text{sec}^{-1}$ )

$F_t$  is the orifice flow at time  $t$  ( $\text{cm}^3 \text{sec}^{-1}$ )

$f_v$  is the volume fraction of the impurity in the plug

and  $\rho$  is the density of the pure solid impurity ( $\text{gm cm}^{-3}$ )

Also, the deposition surface area at time  $t$  is

$$A_d = 4ld \sqrt{\frac{F_t}{F_i}} \quad \text{cm}^2$$

therefore

$$\sqrt{\dot{F}} = \frac{2kF_i}{f_v \rho d} (C_B - C_S)^n \quad (2)$$

The deposition rate constant  $k$ , and possibly the exponent  $n$ , may be characteristic of the impurity and may enable it to be identified. When the bulk impurity level  $C_B$  is known, the values of  $k/f_v$  and  $n$  can be derived by graphical or least squares analysis. When  $C_B$  is not known (the current position on the PFR primary circuit) the data can be analysed with trial values of  $n$ , using:

$$C_S = C_B - \sqrt{\frac{f_v \rho d}{4kF_i F_t}} (-\dot{F}) = C_B - \sqrt{\frac{f_v}{k}} Y \quad (3)$$

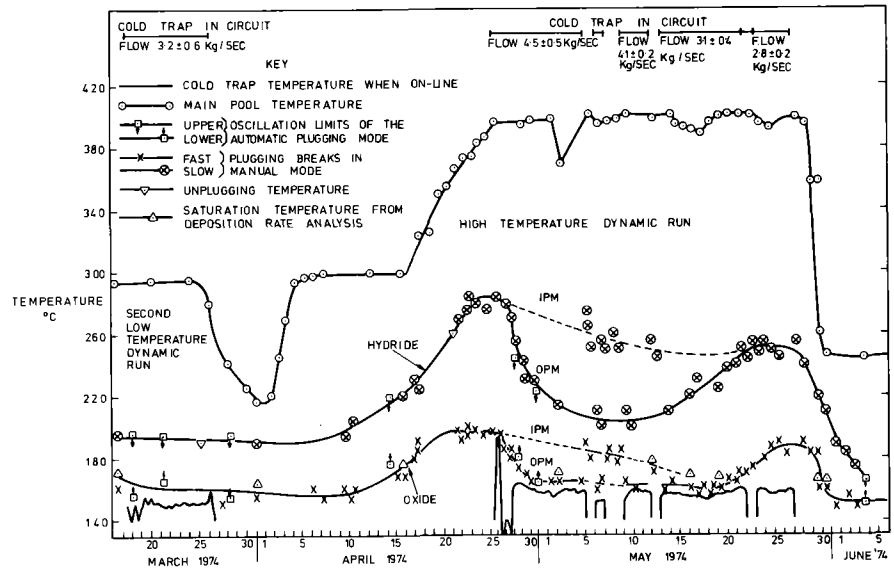


FIG. 4. PFR PRIMARY CIRCUIT CLEAN-UP MARCH-JUNE 1974

The bulk impurity level  $C_B$  is obtained as an intercept, when the plugging rate  $-\dot{F}$  is identically zero. Impurity deposition or crystallisation does not generally occur until the supersaturation:

$$C = 1 - \frac{C}{C_B}$$

exceeds some critical value. Equation (1) only applies after this value is exceeded, ie, for  $C_S < C$ . Analysis of plugging kinetics in this way should therefore give impurity levels  $C_B$  free of undercooling error. Equation (3) was applied to the PFR plugging records by taking time intervals  $\Delta t$  sufficiently short that

$$\frac{\Delta F}{\Delta t} \approx \dot{F} \quad \text{or} \quad \frac{\Delta \sqrt{F}}{\Delta t} \approx \frac{1}{2} \frac{\dot{F}}{\sqrt{F}}$$

Intervals  $\Delta t$  between 1 and 5 minutes were found to be satisfactory in analysing the fast plugging break on the PFR primary plugging meters. Intervals as long as 15 minutes will probably be satisfactory for the slow plugging species.

A good linear fit to equation (3) was obtained for the fast plugging break with  $n = 2$ , over a wide range of plugging rates. The plots showed considerable curvature with  $n$  values less than 1.5 and greater than 2.5. The value  $n = 2$  suggests that firmation of the deposit in the orifices was the rate determining step of the plugging process in the PFR instruments. Mass transport of impurity from the sodium to the surface is generally assumed to be the rate determining step, in similar work in plugging meters and cold traps. If this latter step is diffusion controlled in the liquid metal phase,  $k$  is directly related to the mass transfer coefficient of the impurity in the orifice, and  $n = 1$ .

As expected, plugging rate plots using data recorded over several months were approximately parallel, giving a mean value of  $k/f_v = 8.6 \pm 2.6 \mu\text{g Na}_2\text{O cm}^{-2} \text{sec}^{-1} (\text{ppm})^{-2}$  or  $11.2 \pm 4.8 \text{mg NaH cm}^{-2} \text{sec}^{-1} (\text{ppm})^{-2}$  for the fast plugging species. The hydride value is impossibly large, indicating that  $\text{Na}_2\text{O}$  was the fast plugging species. This was confirmed by the interpretation of the PFR primary circuit clean-up records and the analysis of the cold trap deposits.

# INTERNATIONAL CONFERENCE ON LIQUID METAL TECHNOLOGY IN ENERGY PRODUCTION

The  $C_B$  values derived for oxide by extrapolating the plugging rate to zero, are included in Figure 4. They are consistent with the other data recorded during the Hot Dynamic Run, and confirm that orifice cooling rates less than 1°C/minute gave undercooling errors less than 15°C at plugging temperatures greater than 160°C. The rate analysis method gave  $C_B$  values with coefficients of variation less than 20% comparing favourably with most other methods of impurity estimation in sodium at this level. The method is applicable at oxygen levels as low as 3 ppm in the sodium, indicating a saturation temperature (unplugging temperature) of 150°C, or a plugging temperature of approximately 130°C for 1°C/minute cooling rate. The method will be applicable to the slow plugging species as well, but will require records of higher quality than those obtained during the PFR clean up runs. A value  $k/fv = 30 \mu\text{g NaH cm}^{-2} \text{ sec}^{-1} (\text{ppm})^{-2}$  was estimated from the existing records, as an upper limit for the slow plugging species.

Solution of the differential equation (2) gives an expression relating orifice flow to time throughout the plugging process. However,  $F_t$  is a function of time and  $C_S$  is a function of orifice temperature  $T_S$ ; which is itself a function of time. A constant cooling rate  $\chi$  is obtained when the PCTL plugging meters are operated in the manual mode. Therefore:

$$\frac{dF}{dt} = \frac{2k\sqrt{F_i}}{f_v d \chi e} (C_B - C_S)^n$$

now  $(C_B - C_S)^n = C_B^n \left[ 1 - \exp(-\psi) \right]^n = C_B^n e^{-n\psi}$

where  $\psi = \frac{\Delta H}{R} \left( \frac{1}{T_S} - \frac{1}{T_B} \right) = \frac{\Delta H}{R} \left( \frac{\Delta T}{T_B T_S} \right)$

$\Delta H$  is the partial molar heat of solution of the impurity (k.cal.mole<sup>-1</sup>),  
 $R = 1.987 \text{ k cal mole}^{-1} \text{ }^\circ\text{K}^{-1}$  is the Thermodynamic Constant,  
 $T_S$  is the absolute temperature of the orifice, and  
 $T_B$  is the saturation temperature for the bulk sodium entering the orifice.

Using the binomial expansion for  $\left[ 1 - \exp(-\psi) \right]^n$  and a series expansion of  $\exp(-b\psi)$  gives a linear expression suitable for term-by-term integration to give:

$$1 - \sqrt{\frac{F_t}{F_i}} = \frac{2k\Delta T}{f_v e d \chi} (C_B - C_S)^n = \frac{2kt}{f_v e d} (C_B - C_S)^n$$

where

$\Delta T = T_B - T_S = \chi t$ . For oxide as the fast plugging species, with  $t$  in minutes,  $C_B$  in ppm (weight) of oxygen,  $e = 2.27 \text{ gm cm}^{-3}$  for solid  $\text{Na}_2\text{O}$ , and  $n = 2$ ,

$$1 - \sqrt{\frac{F_t}{F_i}} = 4.5 \pm 1.4 \times 10^{-3} t (C_B - C_S)^2$$

This is the  $F$ - $t$  equation of the PCTL plugging meter orifice flow in the manual operating mode (cooling ramp).

## CIRCUIT CLEAN-UP PERFORMANCE

### The Low Temperature Dynamic Run

The PCTL was sodium filled in mid-July 1973, a month before the PFR primary circuit. The cold trap basket analysed in this project was used intermittently between the end of August 1973 and early June 1974. The cumulative operating time during this period was approximately 2000 hours. Primary circuit clean-up began on 1 September 1973, when the main pool sodium temperature was raised to approximately 300°C. Main

pool, cold trap and plugging temperatures are summarised in Figure 3.

Early difficulties were experienced with the cold trap flow, which tended to fall slowly over 12 - 24 hours, then rise suddenly<sup>(5)</sup>. Blocking and unblocking of the 19 mm holes in the flow distribution plate between the cold trap inlet header and the cooling annulus (Figure 2) was suspected, although redistribution of deposit in the mesh could also have been responsible. Since the inlet plugging temperature approached the PCTL sodium inlet temperature, the RHX control limited on maximum by-pass EM pump current. This gave insufficient bypass flow capacity to achieve a high enough cold trap inlet temperature with a trap minimum temperature of 150°C. The PCTL flow therefore had to be reduced to  $2.7 \pm 0.8 \text{ kg/sec}$ , and this eliminated the erratic flow problem. Cold trap temperatures up to 220°C were required, and the cold trapping rate was therefore low. Figure 3 shows evidence of oxide removal by the cold trap during the short period above 300°C, but no evidence of removal of the slow plugging species. Analysis of deposition kinetics suggested that oxide was the fast plugging species, in which case the oxide level in the PFR primary sodium increased by 90 kg  $\text{Na}_2\text{O}$  in the period 18 August - 11 September 1973 and was reduced by 80 kg in the period 11-30 September. If the slow plugging species was hydride, the NaH level in the sodium rose and fell by 80 and 30 kg respectively, in the same periods.

Oxide and hydride trapping efficiencies are required before trapping rates can be calculated. The cold trap efficiency is defined by

$$E = \frac{C_t - C_l}{C_t - C_s}$$

where  $C_t = C_i$  is the impurity level at the PCTL inlet after the clean-up period  $t$ ,  
 $C_l$  is the impurity level in the sodium leaving the PCTL outlet,  
 and  $C_s$  is the impurity level in sodium at the cold trap minimum temperature, derived from the solubility equation.

Relatively few outlet plugging temperatures were obtained, with only one during the important period in the middle of the Run when inlet plugging temperatures were highest. This gave a value  $E = 0.9$  for oxide, and this high efficiency was confirmed by the good agreement between the cold trap temperature and the other oxide outlet plugging temperatures in Figure 3. Similar oxide cold trap efficiencies were obtained in the Hot Dynamic Run. The outlet plugging temperatures of the slow plugging species were very similar to the corresponding inlet plugging temperatures, indicating a low trap efficiency for this species.

Circuit contamination rates were calculated using oxide and hydride trapping efficiencies of 0.90 and 0.75, respectively, from the Hot Dynamic Run. A cold trap flow  $F = 2.7 \text{ kg/second}$  was used in the mass balance equations

$$(\dot{C}_+)_O = 0.335 F E_O (C_t - C_s)_O - 3.51 (\dot{C}_+)_O \text{ kg Na}_2\text{O/day} \quad (4)$$

$$(\dot{C}_+)_H = 2.07 F E_H (C_t - C_s)_H - 21.7 (\dot{C}_+)_H \text{ kg NaH/day} \quad (5)$$

where  $C_t$  and  $C_s$  are in weight ppm,  $\dot{C}_+$  is the rate of fall of the impurity level in the PFR main pool sodium (ppm/day), and the subscripts O and H denote oxide and hydride respectively.

The oxide results show a definite dependence on circuit temperature, rising to a maximum of 10 kg  $\text{Na}_2\text{O}/$

# INTERNATIONAL CONFERENCE ON LIQUID METAL TECHNOLOGY IN ENERGY PRODUCTION

day when the circuit temperature reached its maximum of 325°C. The hydride contamination rates followed changes in circuit temperature much less closely, and showed a slower response to temperature changes than oxide. The contamination rate equations probably over-estimated the  $\dot{C}_+$  values, especially during the period at the start of the Low Temperature Dynamic Run when the trap flow (and probably trap efficiencies) were erratic.

The plugging temperatures of both species fell rapidly at main pool sodium temperatures below 250°C. The reason for this marked fall in both inlet plugging temperatures so far below the main pool sodium temperature is not clear, but a reversible impurity deposition mechanism appeared to operate in the PFR primary circuit for both the fast and slow plugging species. Negative contamination rates of up to 4 kg Na<sub>2</sub>O/day were calculated for the period 22-30 September 1973, but positive ( $\dot{C}_+$ )<sub>H</sub> values were maintained till 3 October.

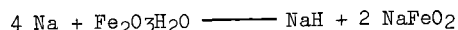
Impurities introduced into the circuit during maintenance operations and in the live core loading operation in January - February 1974, raised the plugging temperatures of the fast and slow plugging species to maxima of 175 and 200°C respectively. A second Low Temperature Dynamic Run was carried out between 18 and 28 March 1974, at a main pool sodium temperature of 290±5°C. The cold trap temperature was maintained at 150±10°C with a sodium flow in the PCTL of 3.2±0.6 kg/sec. Negligible clean-up of the slow plugging species was achieved, but the plugging temperature of the fast plugging species was reduced to 150-155°C.

### Hot Dynamic Run

This run began on 13 April 1974, when the main pool temperature was raised from 280°C to 400°C. Main pool, cold trap and plugging temperatures are summarised in Figure 4. The oxide maximum plugging temperature was 40°C below its maximum in the previous run, confirming that considerable oxide clean-up had been achieved. The oxide plugging temperature reached its maximum very quickly, on 20 April when the main pool sodium temperature had reached 340°C but the hydride plugging temperature continued to rise towards 280°C until the cold trap was brought on-line. Outlet plugging temperatures for oxide fell rapidly to 165±5°C, giving a trap efficiency of 0.85 - 0.90 except during the first 3 days of operation. Hydride clean up was much slower, the maximum trap efficiency being 0.75. Cold trap flow began to fall after 4 May 1974, requiring PCTL pump operation at maximum from that time. The flow fell to 2.7 kg/second before the trap was isolated on 27 May. The cold trap efficiency for oxide fell in a very similar manner at the same time reaching zero on 20 May, suggesting that trap blockage and oxide deposition were related.

Negligible hydride clean up occurred after 10 May, although hydride trapping efficiencies remained at over 50% for a further 6 days. Oxide clean-up continued until the trap efficiency for oxide was approximately zero. The minimum oxide and hydride levels (on 20 May) were approximately 20% and 50% of their initial values, respectively. The fall in PCTL inlet plugging temperatures for oxide and hydride over this period (Figure 4) indicates that the impurity level of the PFR primary sodium was reduced by 19 kg Na<sub>2</sub>O and 74 kg NaH in 24 days during the Hot Dynamic Run. After 20 May, the impurity levels began to rise slowly while the primary circuit remained at 400°C. The rise in oxide level was greater than the rise in hydride, and an inlet plugging temperature approaching its value at

the start of clean-up was achieved before the circuit temperature fell. The source of the additional oxide may have been the slow decomposition of NaOH. Circuit contamination rates  $\dot{C}_+$  were therefore important, as the trapping rates  $\dot{C}_-$  were effectively zero.  $\dot{C}_+$  values for oxide and hydride were derived using equations 4 and 5. The oxide values were slightly lower than those calculated for the previous run, but the hydride values were considerably greater. The formation of NaFeO<sub>2</sub> or a similar mixed oxide would explain the large difference between the oxide and hydride contamination rates observed during the Hot Dynamic Run:



the rust being derived from ferritic surfaces, such as the neutron shield rods in the PFR primary circuit.

The oxide plugging temperature fell rapidly to 150±5°C, and the hydride plugging temperature more slowly to 170±10°C, after the main pool temperature was reduced to 250±5°C at the beginning of June 1974. Therefore, the reversible deposition process still operated for both impurities at the end of the Hot Dynamic Run. The circuit contamination rates for oxide and hydride showed a dependence on clean-up time *t* and circuit heating or cooling rate  $\dot{T}_c$ , in addition to the dependence on circuit temperature *T<sub>c</sub>* established during the Low Temperature Dynamic Run.

$$\text{Therefore } \dot{C}_+ = f(t, T_c, \dot{T}_c, (A/V)_c, \dots)$$

where  $(A/V)_c$  is the surface area - volume ratio of the sodium circuit (12.9 m<sup>-1</sup> for the PFR primary circuit).

### COLD TRAP BASKET DISCHARGE AND DEPOSIT SAMPLING

The basket assembly was raised from the PCTL vessel, with the sodium at 150°C. After a period of drip-drainage, the basket was transferred in an argon inflated bagging system to the PCTL mortuary, which was argon purged before loading the basket into it, and kept at approximately +5kN/m<sup>2</sup> argon pressure. A transparent viewing section of the transfer bag was used to examine and photograph the deposits, by raising the basket assembly from the mortuary into the bag. Gloves fitted to the viewing section enabled deposit samples to be taken for analysis. The uppermost mesh ring (Ring 1 in the knit mesh column) came away with the shield plug and top plate when these were removed for steam cleaning. The ring was exposed to air for 24 - 36 hours before being transferred to a large argon filled glove box for sectioning, after detailed examination of the deposits in the ring. The second mesh ring was recovered from the PCTL mortuary by grappling. It was kept under argon at all times during its transfer to the glove box. The remaining five mesh rings separated after removal from the PCTL mortuary. They were exposed to air for 10-12 hours during this operation, before being stored in an argon purged tank until they could be weighed and examined.

Hacksaws and wire shears were used to give large sample blocks (typically 10 cm x 10 cm x 36 cm) for analysis. This method of sampling was used in preference to the coring methods used in the Enrico Fermi cold trap analysis<sup>(6)</sup>, as much less physical damage to the samples resulted. Coarse toothed hacksaws were very efficient in cutting the solid packed deposits in the mesh rings (fine toothed saws clogged with metallic sodium), but were very inefficient in cutting the unblocked mesh. The fine mild steel mesh in these rings was easily cut by hand shears. The large samples, and the elimination of severe physical damage during sampling, minimised the effects of surface contamination during basket transfer to the PCTL mortuary and the transfer of the mesh rings to the

# INTERNATIONAL CONFERENCE ON LIQUID METAL TECHNOLOGY IN ENERGY PRODUCTION

glove box.

The sample blocks were transferred in argon to a purged glove box, and the outer 1-2 cm of each block discarded as being potentially contaminated. Multiple samples were taken from various parts of each block for analysis. The main analysis methods were thermo-volumetric analysis for NaH and NaOH<sup>(7)</sup> with mass-spectrometric gas analysis, X-ray diffraction analysis of minor phases by the Debye-Scherrer powder method using Lindemann glass capillaries as sample containment, and atomic absorption spectrophotometry of trace metallic impurities.

While the basket breakdown proceeded, the sodium in the PCTL vessel was lowered to a level approximately equal to the bottom of the basket skirt in Figure 2, using a variable height discharge device to transfer the sodium back to the reactor. The level restriction was designed to avoid the transfer of any debris from the bottom of the vessel to the reactor. A sample of sludge was obtained by trawling a weighted mesh bucket on a swivel arm around the bottom of the vessel, and the sludge was discharged to a portable bowser using a heated dip leg, for transfer back to the PFR Tank Farm through a filter.

## IMPURITY DISTRIBUTION IN THE TRAP

Very little deposition had occurred in the trap inlet header, but some deposit had collected under the inlet flow baffle. A thin friable deposit was present on the basket skirt, while a much heavier and denser deposit had collected around the bottom rim of the basket skirt, and on the basket underside (Figure 2). Light deposits, resembling those left by scums, were present on the vessel walls near the piston-ring seals which permitted removal of the basket assembly from the vessel. The deposits on the cooled wall of the vessel were similar to those on the basket skirt, and a heavier deposit was present near the bottom of the vessel wall, above the wall, above the sodium level in the vessel after drainage.

Deposition in the mesh rings was localised in the first 40 - 110 mm of mesh measured downstream from the mesh inlet surface. The rest of the mesh was relatively clean with a sharp transition between the blocked mesh and clean mesh zones. A heavy build-up of deposit occurred on the inner surface of the mesh rings, reducing the radius of the central passage of the trap by 45 - 70 mm. Considerable deposition also occurred on the 8 mm diameter cross-rods for lifting the splitter plates between the mesh rings. The localised deposits in the mesh rings were very dense, and no sodium flow route through them could be seen. Radial penetration into the mesh was relatively uniform round the central passage, and increased towards the bottom of the basket, with a maximum penetration of 110 mm in rings 5 and 6.

The results of the analyses of the major phases in the deposits are summarised in Table 1, and are combined with the estimated amounts of deposits in the different regions of the trap, to give the impurity inventories in the trap. Na<sub>2</sub>O was the major impurity present, with approximately equal amounts of NaH and NaOH. The inventories of these three impurity sodium compounds were 140<sup>+50</sup>, 62<sup>+30</sup>, and 70<sup>+30</sup> kg respectively. The PFR cold trap can be divided into four zones of different hydrodynamic, thermal and supersaturation conditions (Table 2):

- a. a cooling zone (outer annulus of trap)
- b. a precipitation zone (the dished end of the vessel)

- c. an isothermal zone (the central passage of the mesh rings)
- and
- d. a deposition and filtration zone (the mesh packing)

Other zones, such as the outflow annulus and the inlet and outlet headers, are neglected as deposition would not be expected there except under abnormal operation conditions, and did not occur in the PFR trap.

The lowest sodium contents were found in deposits from the cooled walls of the vessel. The highest values were found in the small amount of deposit under the inlet flow baffle, and not unexpectedly, in the sludge deposit at the bottom of the vessel. Deposits having low sodium contents were found in regions where high deposition rates were expected, such as regions of high heat rejection rate (the vessel wall) or regions of turbulence and high Reynolds number (central passage in mesh rings). The results in Table 1 are also expressed as weight % of the total impurity compounds in each deposit. This eliminated the effect of the sodium content of the deposits, and showed preferential deposition of oxide near the trap inlet, demonstrating its fast deposition kinetics. The hydride deposition pattern was very different, with the lowest levels near the trap inlet and the highest levels in the sludge at the bottom of the cold trap vessel. This confirmed that hydride was a slower depositing species than oxide. The deposition of hydroxide further along the trap than the other major phases was probably due to its solubility in sodium being greater than that of oxide or hydride.

Sodium entering the cooling zone is unsaturated with impurities, if the trap inlet temperature is correctly controlled. Since only a small fraction of the total impurities were found in the cooling zone, the sodium leaving this zone was highly supersaturated, or carried crystallised impurities in suspension. Outwards growth of deposit is expected on cooled surfaces such as the cold trap vessel wall. Deposit slumping, due to loss of buoyancy as the sodium level in the cold trap vessel was lowered, could have removed deposit from the wall to the sludge at the bottom of the vessel. The impurity contents of the sludge and the residual deposit on the vessel walls were significantly different. This indicates that heavy deposition on the vessel wall did not occur, and that the sludge at the bottom of the vessel was deposited there, probably by particle sedimentation at low sodium velocities.

The filtration efficiency of the mesh was expected to be low, but heterogeneous crystal growth on the mesh from supersaturated solution would cause local deposition at the mesh entry plane. The high surface area - volume ratio of the mesh packing provided an ideal site for impurity crystallisation from saturated solution, and acted as a retention medium for the deposits. It is possible that the deposits found in the mesh were laid down in the central passage of the mesh rings and injected into the first layer of mesh under the sodium flow pressure in the trap. The low cold trap efficiencies observed at the start of the Hot Dynamic Run were probably due to crystallised impurities passing through the trap without being retained by the mesh. Enhanced deposition probably resulted from an increase in Reynolds number (based on diameter of wire plus deposit) and filtration as deposit built up on the mesh. An increase in trap efficiency is often observed when the trap is partially loaded with impurities. The heavy deposition in the central passage of the mesh rings could not be explained by simple deposition kinetics or by particulate processes such as Brownian motion or agglomeration.

# INTERNATIONAL CONFERENCE ON LIQUID METAL TECHNOLOGY IN ENERGY PRODUCTION

TABLE 1 RESULTS OF COLD TRAP DEPOSIT ANALYSES

Deposit Location	Composition of Deposit Samples (weight % as Na compounds)				Impurity Content (wt % Na Compounds)			Estimated amount kg	Impurity Inventory		
	Na <sub>2</sub> O	NaH	NaOH	Na	Na <sub>2</sub> O	NaH	NaOH		Na <sub>2</sub> O	NaH	NaOH
Under inlet flow baffle	25-30	0.04-0.08	0.27-0.38	68-72	90-93	0.1-0.2	0.8-1.1	10	2.8	0.1	0.1
On vessel walls	55-64	2.1-4.0	6.2-7.5	26-35	84-86	3.0-6.4	8.9-1.1	10	6.0	0.4	0.7
On basket skirt	49-56	2.9-5.2	6.7-8.3	32-39	82-84	4.6-7.9	11-13	1	0.5	0.1	0.1
Around skirt bottom	38-47	7.2-9.5	3.7-6.2	40-49	74-77	13-17	6.7-11	20	8.5	1.7	1.0
Thick deposit on skirt bottom rim	24-30	10-14	6.6-9.8	50-56	54-60	22-28	14-20	15	4.0	1.8	1.2
Basket underside	25-31	9.8-15	7.5-9.2	48-54	54-60	21-29	16-19	25	6.9	3.2	2.1
Sludge at bottom of vessel	13-19	10-17	1.2-2.7	66-74	44-54	35-48	3.8-7.9	120	22	20	2.7
Mesh ring 7 (bottom)	21-26	13-19	17-23	37-43	37-42	23-30	30-37	50	12	8	10
Mesh ring 6	20-24	14-18	18-25	37-43	35-39	24-29	32-39	55	12	9	12
Mesh ring 5	20-26	10-15	14-20	45-51	41-47	20-27	29-36	55	13	7	9
Mesh ring 4	22-28	7.3-11	12-19	47-54	47-53	15-21	26-36	50	12	5	7.7
Mesh ring 3	25-31	4.0-6.8	10-17	49-57	57-62	8.8-14	23-34	40	11	2.2	5.2
Mesh ring 2	30-38	1.7-4.8	14-21	40-48	59-64	3.2-8.5	27-36	30	14	1.3	7.5
Mesh ring 1 (top)	24-31	3.7-5.9	12-18	49-56	56-61	8.0-12	27-36	40	13	2.5	7.5
TOTALS								520 ± 80	140 (±50)	62 (±30)	70 (±30)

TABLE 2

ZONAL DISTRIBUTION OF DEPOSITS IN THE COLD TRAP

Trap Zone	Cooling Annulus	Dished end of vessel	Isothermal Zone (Central passage)	Mesh packed zone
Weight Na kg	23	115	64	96
Weight Na <sub>2</sub> O -	20	31	35	52
Weight NaH	3.1	24	14	21
Weight NaOH	2.6	5.4	24	35
Zone utilisation (vol % incl Na)	2.4	19	40	15
Mean Na residence time (seconds)	310	170	54	200
Mean Na velocity (mm sec <sup>-1</sup> )	7	5	22	1
Mean Reynolds No	4400	5000	14000	0.8
Surface area - Vol ratio (m <sup>-1</sup> )	6.6 (cooled surface)	6.4	3.2	380
Heat rejection kW m <sup>-2</sup>	50	5	0	0

Momentum transfer to the particules in turbulent flow (high Reynolds' number) may be the cause.

The distribution of the deposits in the trap, the nature of the deposits and the capacity utilisation of the trap were similar to the results of other cold trap investigations<sup>(6,8,11)</sup>. Localised deposition of impurities at the entry to the mesh packing was a frequent phenomenon, probably caused by trap operation at high supersaturation, ie high ΔT between inlet plugging and basket minimum temperatures. The heavy

deposition on surfaces immediately upstream of the mesh also occurred under similar conditions. Flow difficulties were experienced, especially during the initial period of trap operation and premature blockage of the trap occurred at mesh loadings of 8-25 volume % (compare 15 volume % in the PFR trap). Sudden changes in trap flow also occurred, probably due to deposit redistribution in the trap before further deposition increased the mechanical strength of the deposits. Sludge deposits were also observed in traps having geometries suitable for sludge collection. Some deposition occurred in the cooling zone of the trap, but this only had significant effect on trap life if the cooled zone was mesh packed, in which case the trap blocked at very low loadings.

### SUMMARY AND CONCLUSIONS

When operated in the automatic equilibrium mode, the PFR primary circuit plugging meters oscillated due to the presence of multiple impurities in the sodium. The oscillation limits were in good agreement with the two flow breaks obtained when the plugging meters were operated manually with cooling rates less than 1°C/minute. The oscillations appeared to be triggered off by step increases in orifice flow, probably caused by vibration induced breakage of brittle plugs. The more aperiodic oscillations were probably due to sodium level fluctuations in the plugging meter vessel, causing sudden flow changes in the plugging meter orifices.

Application of kinetic equations to the plugging meter records showed that the deposition rate was second order in concentration driving force. Therefore, the formation of the deposit on the orifice surface was the rate determining step, not the mass transfer of impurity to the surface from the sodium. The fast plugging species was identified as Na<sub>2</sub>O with a deposition rate constant of 8.6 ± 2.6 μg Na<sub>2</sub>O cm<sup>-2</sup> sec<sup>-1</sup> (ppm)<sup>-2</sup>. NaH could not be this species as an



# INTERNATIONAL CONFERENCE ON LIQUID METAL TECHNOLOGY IN ENERGY PRODUCTION

improbably large rate constant would be required. Extrapolation of the deposition process against orifice saturation concentration to zero deposition rate gave a precise, and probably unbiased, estimate of the impurity level in the sodium for the fast plugging species. Coefficients of variation less than 20% were obtained at saturation temperatures as low as 160°C. The method is applicable at impurity levels as low as 3 ppm oxygen in sodium. This corresponds to a saturation temperature of 150°C or a plugging temperature of approximately 130°C at an orifice cooling rate less than 1°C/minute.

The cold trap basket used during the initial clean-up of the PFR primary sodium circuit blocked with impurities during the Hot Dynamic Run, after approximately 2000 hours usage. Oxide was the major impurity phase present in the exhausted trap with approximately equal amounts of hydride and hydroxide. The inventories of these three impurity compounds in the trap were 140 ± 50, 62 ± 30 and 70 ± 30 kg respectively. Extensive deposition did not occur in the outer cooling annulus of the trap, probably due to preferential deposition of impurities from supersaturated solution onto large numbers of small crystal particles nucleated in the solution. Sedimentation of the larger particles formed a sludge at the bottom of the vessel. Heavy deposition occurred on the bottom rim of the basket skirt, on the basket underside and in the central flow passage of the mesh rings, probably due to momentum transfer to the particles in turbulent flow. Deposition in the mesh packing was localised in the first 40-110 mm depth measured downstream from the sodium inlet plane of the mesh. The localised deposition in the central flow passage and in the mesh was the main reason for the trap blockage, with only 15 volume % utilisation of the mesh. This pattern of deposition, and the premature blockage at low mesh loading appears to be characteristic of externally cooled, mesh packed traps.

The oxide levels in the deposits were highest near the trap inlet, indicating fast deposition kinetics, while hydride levels were highest in the sludge. This suggests faster growth of homogeneously nucleated hydride crystals in supersaturated sodium, probably due to hydride supersaturation in the cooling annulus being greater than that of oxide as its solubility in sodium is lower. Hydroxide deposited preferentially in the central flow passage and in the mesh, but this probably reflects its greater solubility in sodium and lower supersaturation.

The PFR plugging meters enabled the clean up of the primary sodium circuit to be followed in detail, and gave considerable information on the cold trapping behaviour of impurities in sodium. Cold trap efficiencies up to 90% and 75% were observed for oxide and hydride respectively. Low efficiencies were observed at the start of the Hot Dynamic Run, probably due to the reduction of supersaturation by impurity nucleation and deposition in trap regions other than the mesh packing, and the passage of the fine particle fraction through the mesh. Low efficiencies were also observed as the trap blocked up, due to a reduced fines retention by the mesh as the sodium velocity and Reynolds number fell. Hydride clean-up was considerably slower than oxide clean-up, mainly due to a circuit contamination rate for hydride approaching its clean-up rate.

## ACKNOWLEDGEMENT

Considerable assistance was afforded by Mrs C Prentice, Dr W R Watson and Mr N R Sinclair during this work. The discharge and breakdown of the cold trap basket was performed by PFR Operations personnel.

## REFERENCES

1. P F Roach, D F Davidson; "Sodium Impurity Monitoring by Automatic Plugging Meters." Nuclear Engineering International Vol 16 No 179 334-337 (1971).
2. B R Grundy, R Swinhoe; "Plugging Meter Behaviour in Liquid Sodium." UKAEA TRG Report 1934(R), (1968).
3. J W Mullin; "Crystallisation"; 2nd Edition; Butterworths, London. 1972. pp 160-168, 185-193.
4. A R Konak; "New Model for Surface Reaction Controlled Growth of Crystals from Solution." Chemical Engineering Science; Vol 29, No. 7 pp 1537-1543 (1974).
5. R A Davies, C M Robertson. "Impurity Monitoring and Analysis in PFR." Proceedings of the International Conference on Fast Reactor Power Stations; British Nuclear Energy Society, London; pp 481-6 (1974).
6. J Herb et al; "Examination of the Enrico Fermi Sodium Cold Trap," USAEC Report WCAP-4321, (1965).
7. S A Meacham, E F Hill; "The Determination of Hydrogen in Sodium Metal." USAEC Report APDA-183, (1966)
8. V I Subbotin, F A Kozlov; "Precipitation of Oxides from a Sodium Stream." Proceedings of Int. Symp. on Alkali Metal Coolants. Paper SM35/48 pp 535-551. IAEA Vienna (1967). Translated as ORNL Tr 1611 (1967).
9. A D Gadeken, M C Plummer. "SEFOR Cold Trap Experience." USAEC Report GEAP 10548 (1972).
10. V I Subbotin, P L Kirillov, F A Kozlov. "The Purification of Sodium from Oxygen, and Monitoring of the Oxygen Content of Sodium." USSR Report 701. Translated as UKAEA PG Information Series 10(R), (1965)
11. R B Hinze. "Cold Trap Performance Limitations, a State-of-the-Art Review, in Research and Development Studies in Environmental Pollution and in Reactor Cooling Systems. Nuclear Engineering Part 21; A I Chem. E; Chemical Engineering Progress, Symposium Series 104: Vol 66, pp 94-106, (1970).

# INTERNATIONAL CONFERENCE ON LIQUID METAL TECHNOLOGY IN ENERGY PRODUCTION

RADIOACTIVE PRODUCT BEHAVIOR DURING THE OPERATION OF SODIUM-COOLED REACTORS OF THE USSR

N. V. Krasnoyarov

V. I. Polyakov

Yu. V. Chechetkin

V. I. Lenin Atomic Reactor Research Institute

## ABSTRACT

Results concerning fission and corrosion product behavior at BR-5 and BOR-60 are discussed in this report. A conclusion about the limited feasibility of sodium-cooled reactor operation with failed fuel pins has been drawn. The permissible number of failed pins is defined by both the capability for coolant decontamination from fission products and the radioactivity level during maintenance.

### 1.0 INTRODUCTION

Atomic power engineering plays an increasingly important role in the energy production industry; and breeders occupy a special place in that role.

At present, sodium breeder reactors have been operating as demonstration power plants: BN-350 in the USSR, "PHENIX" in France, PFR in Great Britain. New designs for large 1,200-, 1,500- and 2,000 MWe plants are being developed. When operating the plant whose conditions are defined by an energy user, there exists the possibility for failure of the fuel pin clads. The reactor may be shut down in this case or its operation may be possible up to a convenient time when those failed pins can be removed and changed. And if such operation is possible, then for how long may it last and what number of defective pins is permissible? Subsequent operation provides a high burn-up, which is an advantage from the point of view of economics, but at the same time it results in the contamination of the circuit by fission products.

In an effort to answer these questions, a number of fuel pin tests were carried out in the USSR at BR-5 and BOR-60 until the initiation of the failure of the fuel pin clads; and their operation was prolonged beyond failure to study the release of fission products, their behavior in the primary circuit and the possibility of decontamination of the system from these products.

Conditions during these tests approached those of future atomic power plants. BR-5 has been operating with PuO<sub>2</sub>, UO<sub>2</sub> and UC; at BOR-60, UO<sub>2</sub> has been used as fuel. Sodium temperature at the core outlet exceeds 600°C (up to 700°C with superheating), the core heat density amounts to 1,100 KW/l and specific power of fuel pins is 550 W/cm<sup>2</sup>. BOR-60 fuel burn-up reaches 10 to 13% before reloading.

Results of these investigations and the fission product behavior pattern are the points of this report.

### 2.0 RELEASE AND BEHAVIOR OF FISSION GAS PRODUCTS

When a fuel pin clad fails, fission gases are under high pressure and, naturally, a major fraction is released in the form of bubbles into the reactor cover gas. Radioactivity of the cover gas increases rapidly to the level that corresponds to the release of active gases from the fuel inside the clad; and then, as a result of the decay, it decreases to the level that corresponds to the slower gas release. Further increases may be due to the failure of the other fuel pin clads or to the release of gases from the same pin. Figure 1 illustrates this assumption.

Analysis of gas releases showed that they are multiples of a minimum value that is assumed for a single fuel pin. The <sup>133</sup>Xe activity release from one fuel pin amounts, therewith, to 5.3±1% of the total <sup>133</sup>Xe activity built up in the fuel pin.

The release of shorter-lived isotopes is relatively less and is given in Figure 2.

Some fraction of the gas is not, however, released from sodium and is entrained in the sodium in the form of bubbles. This process was studied when the fission gases originated from the pin surface contaminated by fuel. The relation of <sup>133</sup>Xe and <sup>135</sup>Xe is given in Figure 3.

The characteristic was obtained and called the period for gas "half-release" from sodium that amounted to 5.5 hours at BOR-60 and 7 to 15 hours at BN-350.

The period of "half-release" is not the only characteristic in this process. It would be if the gases being released from the sodium to cover gas and back would not penetrate sodium. But there is a possibility of gas trapping by sodium. In this case we define the period of exchange although it is not indicative of gas fraction in sodium. The experiments on cover gas decontamination from radioactive <sup>133</sup>Xe and its subsequent build-up in sodium proved to be very useful. Figure 4 illustrates the data.

Based on the results of these experiments, the relation between the <sup>133</sup>Xe fraction in cover gas and in sodium can be derived. The <sup>133</sup>Xe fraction in sodium at BOR-60 corresponds to the relation between the half-life and half-release periods; i.e., there is no inverse trapping. As for BR-5, the xenon fraction in sodium was found to be very high (up to 70 percent), which testifies to the extensive gas exchange between cover gas and sodium. Such an exchange was eliminated in BOR-60 and BN-350 since it is not desirable.

Experience gained in operating the reactor with failed fuel pins shows that with an adequate tightness of circuits the radioactivity in cover gas does not present unusual problems and does not to a large extent limit the number of failed pins. The number of such pins at BOR-60 reached 1 percent of the total load. During reloading and maintenance the gas cavity can be easily decontaminated by circulating the gas through activated carbon.

### 3.0 VOLATILE FISSION PRODUCTS

Among the volatile fission products, <sup>131</sup>I holds a special place, being a sufficiently long-lived and radiotoxic element. Despite the fact that the <sup>131</sup>I release from the failed fuel pins is about 10 times less than that of <sup>137</sup>Cs, its activity in sodium may be decisive after <sup>24</sup>Na decay because of the shorter half-life. During the last years of operation, <sup>131</sup>I was constantly observed in coolant at BR-5 and BOR-60 and occasionally were trace amounts found when measuring radioactivity of the cover gas. Hazard from this isotope is associated with sodium leaks and removal of the components.

## INTERNATIONAL CONFERENCE ON LIQUID METAL TECHNOLOGY IN ENERGY PRODUCTION

Iodine does not present any difficulty in normal operation of the reactor since practically all is removed from sodium by the circuit cold trap and disintegrates in it. During operation  $^{131}\text{I}$  fraction in the circuit is controlled by the relation of the sodium exchange period through the trap to  $^{131}\text{I}$  half-life,  $^{131}\text{I}$  concentrations in sodium can be easily maintained at a low level.

Among the fission products, cesium is another important volatile nuclide that governs sodium radioactivity after reactor shutdown. The contribution of cesium isotopes to the coolant activity is illustrated in Table 1. Averaging the amount of  $^{137}\text{Cs}$  released to the coolant according to the number of failed pins (November 1973-February 1974, 30±10 fuel pins), an average  $^{137}\text{Cs}$  release fraction was obtained, 40±15 percent. At the same time, the released  $^{137}\text{Cs}$  fraction depends on the lifetime of such a defected fuel pin. Gamma-spectrometric analysis of both tight-sealed and damaged fuel pins in a hot cell shows that a considerable migration of cesium within the fuel pin occurs; and the loss in  $^{137}\text{Cs}$  from the failed fuel pin ranges from 20 to 50 percent. The release of  $^{134}\text{Cs}$  from failed fuel pins is comparable to that of  $^{137}\text{Cs}$ , and its activity in the coolant is one order of magnitude less than that of  $^{137}\text{Cs}$ .

A very long lifetime of  $^{137}\text{Cs}$  and its considerable contribution to the total activity require investigation of the methods for its removing from coolant. Under BR-5 conditions, it was found that about 90 percent of cesium can be concentrated in a cold trap. Similar measurements at BOR-60 showed that only one-third of  $^{137}\text{Cs}$  was concentrated in the cold trap and, subsequently, this fraction proved to be even less. Special experiments performed both on an independent spectrometric BOR-60 loop with primary sodium circulation and under the laboratory conditions showed that cesium removal was performed independently of oxygen; the removal efficiency remained low. No dependence of the amount of cesium release on the trap metallic area was observed, despite the fact that cesium deposits on the walls while draining, particularly in the "cold" points. Therefore, to operate the reactor with failed fuel pins, special cesium decontamination techniques are required.

A result of  $^{137}\text{Cs}$  decay with gamma-irradiation of 662 KeV is the formation of  $^{137\text{m}}\text{Ba}$  which subsequently transforms to a stable nuclide,  $^{137}\text{Ba}$  during its 2.5-minute half-life. Therefore, when analyzing the radiation from primary sodium and components, the difference in behavior between cesium and barium should be taken into account. In stationary sodium the activities of  $^{137}\text{Cs}$  and  $^{137\text{m}}\text{Ba}$  are equal, but with circulating sodium, the equilibrium is disturbed since barium tends to deposit on metallic surfaces. The primary core surface is much more extended and its vertical pipe sections may have lower radiation at the energy of 662 KeV (for BOR-60 it was lower by a factor of two with a sodium flow rate of 200 m<sup>3</sup>/h). Unfortunately, this phenomenon can be used only in particular cases. In primary system cells, the decrease in dose rate amounts to only 40 percent.

#### 4.0 NON-VOLATILE FISSION PRODUCTS

Among the non-volatile fission products,  $^{140}\text{Ba}$ - $^{140}\text{La}$  and  $^{95}\text{Zr}$ - $^{95}\text{Nb}$  are the most important. Their release from the failed fuel pins at BOR-60 ranged from 0.1 to 0.5 percent. The importance of non-volatile fission products can be proven by the activity of the primary pipe surface deposits (Table 2). The major fraction of these fission products occurs on the "cold"

sections of the pipes and heat exchanger. The contribution of these products to the coolant activity is not significant. The cold trap concentrates these products similarly, but it is not an effective tool for their removal.

#### 5.0 CORROSION AND ACTIVATION PRODUCTS

Among the corrosion products, the most important are  $^{60}\text{Co}$  and  $^{54}\text{Mn}$ . Their behavior is similar in some respects to the non-volatile fission products. They tend to deposit on pipe and component surfaces, and manganese primarily on "cold" surfaces.

As for activation products, one should pay attention to  $^{110\text{m}}\text{Ag}$ . The activity of this nuclide, however, ranges between 1/3 and 1/2 of that of  $^{22}\text{Na}$ .

#### 6.0 RADIATION CONDITIONS IN PRIMARY SYSTEM CELLS

The contribution of different radioactive products to the exposure dose rate in the vicinity of primary pipes is illustrated in Table 3 for different BOR-60 operating periods.

At the first stage, the activities from  $^{22}\text{Na}$ ,  $^{110\text{m}}\text{Ag}$  and corrosion products prevailed. Because the radiation contribution from Cs can be reduced by sodium draining, the contribution from corrosion products is of importance.

During the reactor operation with failed fuel pins, a major fraction comes from the fission products, particularly from  $^{137}\text{Cs}$  and  $^{134}\text{Cs}$ . While removing the pump, the surface activity must be decontaminated to achieve levels ensuring safe work.

#### 7.0 FISSION PRODUCT RELEASE FROM CARBIDE FUEL

BR-5 operating experience showed that in the event of fuel pin clad failure, the release of many fission products did not depend on the half-life. It indicates that the main factors were the recoil phenomenon on the fuel surface and very likely the entrainment of fuel with its fission products. Under these conditions, the total radioactivity contamination of the primary circuit was found to be essentially lower with carbide fuel than that of oxide fuel.

#### 8.0 CONCLUSIONS

Throughout loss of integrity of the pin clad with oxide and carbide fuels and reaction of the sodium fuel, disastrous effects would occur. In principle, operation is permissible with some portion of such failed fuel pins in the core, but some fission product build-up does occur concurrently. Cover gas radioactivity can be reduced by the argon purification system with an activated carbon; the iodine activity is concentrated by the oxide cold trap where iodine undergoes radioactive decay. A system is required for cesium removal.

To solve the problems concerning both the permissible number of the failed fuel pins and the possible period for power plant operation under such conditions, analyses of radiation conditions during operation, maintenance and emergency conditions are required.

INTERNATIONAL CONFERENCE ON LIQUID METAL TECHNOLOGY IN ENERGY PRODUCTION

Table I  
BOR-60 Coolant Radioactivity

Operational period	Measurement period	Radioactivity, Ci/kg							
		<sup>22</sup> Na	<sup>110m</sup> Ag	<sup>65</sup> Zn	<sup>86</sup> Rb	<sup>131</sup> I	<sup>137</sup> Cs	<sup>136</sup> Cs	<sup>134</sup> Cs
Leak-tight zone	November 1970	49	16	10	38	-	≤ 0,1	-	0,2
	February 1971	73	24	12	100	-	≤ 0,1	-	0,2
	September 1971	190	90	14	110	≤ 0,4	≤ 0,1	-	0,3
Damaged fuel zone	March 1972	250	110	16	72	11	210	15	13
	August 1972	330	140	20	-	15	1800	-	160
	March 1973	350	160	-	-	46	3600	400	330
	October 1973	420	190	-	-	2800	8500	620	720
	March 1974	480	220	-	-	-	19000	-	1700
	August 1974	580	230	-	-	-	21000	-	1740
	February 1975	590	200	-	-	-	20000	-	1800

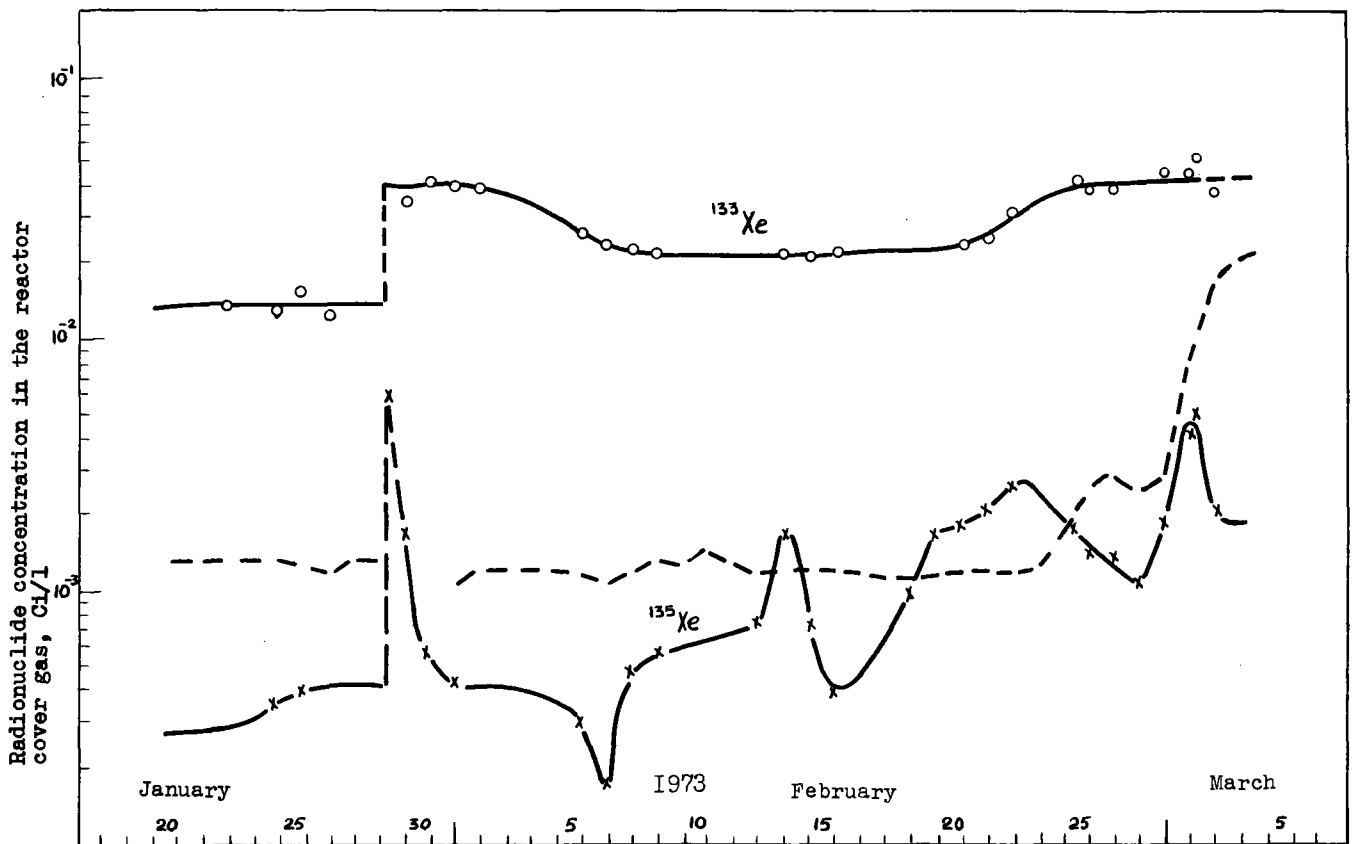


Figure 1. <sup>133</sup>Xe and <sup>135</sup>Xe concentration changes in BOR-60 cover gas in the case of fuel pin clad failure

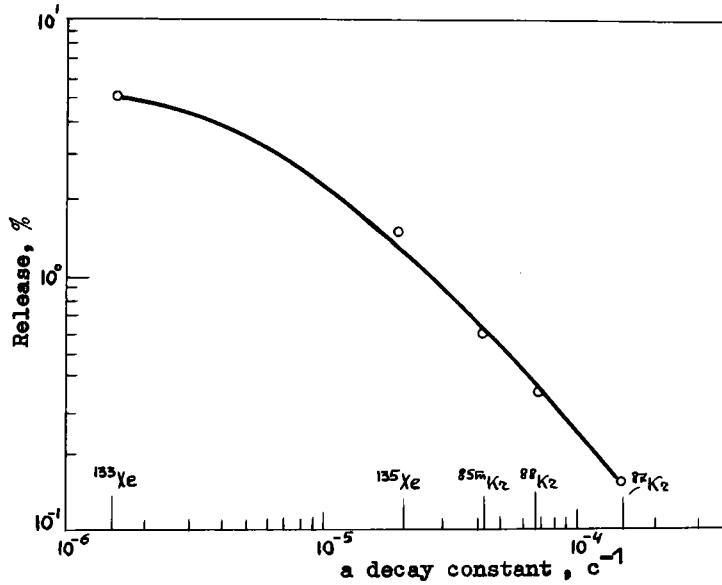


Figure 2. Dependence of the radioactive fission gas release from failed fuel subassemblies into the BOR-60 gas system on a decay constant

Table 2  
Primary Pipe Surface Radioactivity\*

Nuclides	Period	Pipe from the reactor to heat exchanger	Heat exchanger	Pipe down the heat exchanger
<sup>60</sup> Co	1971	0,2	no change	no change
	1972	1,1	3-7	5,4
	1973	2,1	14-60	7,0
	1974	1,8	5-IIID	3,5
	1975	0,6	no change	1,9
<sup>54</sup> Mn	1971	1,0	no change	no change
	1972	2,9	3-4	7,1
	1973	4,9	8-34	16
	1974	1,9	5-32	27
	1975	0,9	no change	19
<sup>95</sup> Nb	1972	25	4	48
	1973	23	36-190	68
	1974	3	-	15
	1975	2	no change	1,6
<sup>140</sup> Ba	1972	4,3	0,1-12	87
	1973	5,4	15-130	78
<sup>140</sup> La	1974	13	0,5-1,3	110
	1975	1,3	no change	14

\*Values given in mCi/m<sup>2</sup>

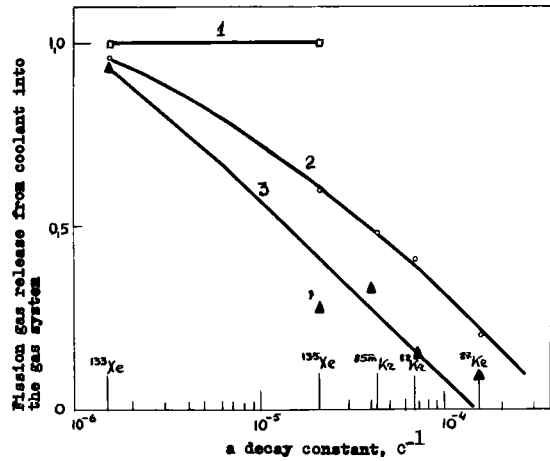


Figure 3. Fission gas release into the reactor gas systems when contaminating the fuel clad surface by the fuel

1. Data obtained at BR-5
2. Data obtained at BOR-60
3. Data obtained at BN-350

Table 3

Exposure Dose Contribution from both "Cold" Sodium Pipe and Some Nuclides Gamma-Irradiation

D a t a	Total dose rate $\mu$ /sec	Some nuclide gamma-irradiation contribution, %							
		Coolant				Deposits			
		$^{22}\text{Na}$	$^{110\text{m}}\text{Ag}$	$^{137}\text{Cs}$ - $^{137\text{m}}\text{Ba}$	$^{134}\text{Cs}$	$^{60}\text{Co}$	$^{54}\text{Mn}$	$^{140}\text{Ba}$ - $^{140}\text{La}$	$^{95}\text{Zr}$ - $^{95}\text{Nb}$
March 1972	20	38	19	6,7	1,6	16	12	2,4	4,8
August 1972	100	8,5	4,5	9,2	3	6,2	2,1	54	12,5
March 1973	130	8,5	4,9	25	7,6	4,9	2,4	31	15,7
October 1973	140	8,9	5,5	47	13	4,5	5,2	6,4	9,5
February 1974	280	5,2	2,7	55	12	1,6	1,4	20	2,1
August 1974	240	6,8	3,2	64	15	1,7	3	3,7	2,6

Note: Results were recorded 15 days after reactor shutdown.

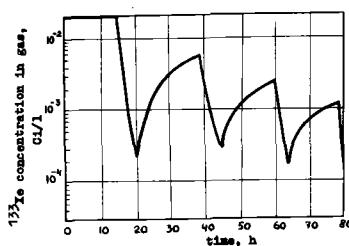
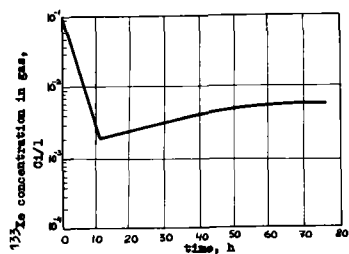


Figure 4. Decontamination of the BOR-60 and BR-5 gas systems from  $^{133}\text{Xe}$  and  $^{135}\text{Xe}$  extraction from coolant

- a. Results obtained at BOR-60
- b. Results obtained at BR-5

# INTERNATIONAL CONFERENCE ON LIQUID METAL TECHNOLOGY IN ENERGY PRODUCTION

## ACTIVITY DEPOSITION IN DFR PRIMARY COLD TRAPS

C G Allan

T A H Taylor

United Kingdom Atomic Energy Authority  
Dounreay Experimental Reactor Estab.  
Thurso, Caithness, Scotland, UK.

### ABSTRACT

The deposition of fission products and other impurities in 5 DFR primary circuit cold traps has been measured. Steam cleaning and acid pickling was used to remove the activity, and the decontamination liquors were analysed by high resolution gamma spectrometry. Direct gamma spectrometry of two of the baskets at different stages of the decontamination considerably increased the value of the results. It enabled the distribution of the individual nuclides to be measured in the traps, and gave decontamination efficiencies for each decontamination stage.  $^{131}\text{I}$  collected in the traps by filtration cold trapping, but was easily removed by steam cleaning.  $^{137}\text{Cs}$  collected by adsorption on the steel surfaces of the trap, and deep surface penetration made its removal extremely difficult.  $^{137}\text{Cs}$  will therefore cause difficulties in the maintenance of fast reactor components.  $^{129}\text{m}\text{Te}$  also collected in the trap and required an acid pickle for its removal.  $^{125}\text{Sb}$  appeared to be associated with small amounts of particulate fuel collected by the trap. Surface penetration by  $^{129}\text{m}\text{Te}$ ,  $^{125}\text{Sb}$  and other fission products did not occur.

### INTRODUCTION

The behaviour of fission products, activated corrosion products and fissile material in liquid alkali metals are important factors in the economics of fast reactors. Local deposition of activity is a major problem in the maintenance of primary circuit components. The design of these components and their maintenance procedures requires considerable knowledge of the extent and nature of activity deposition in the circuit.

The use of vented uranium-molybdenum alloy fuel<sup>(1)</sup>

as the driver charge in the Dounreay Fast Reactor (DFR) has caused considerable contamination of the NaK coolant. DFR therefore, is in many ways representative of a reactor with some years of cumulative operation using failed fuel cladding, and is an important source of information on fission product and fissile material behaviour in LMFBR's. Core, coolant and cladding temperatures in DFR are generally lower than is usual in more modern fast reactors, and activated corrosion product behaviour in DFR will not be typical.

The primary circuit cold trap is one of the most important deposition zones for activity released to the coolant in the reactor core. This paper describes the analysis of the activity deposited in a number of DFR primary circuit cold trap baskets. The activity deposition profiles in some of the baskets were measured by direct high resolution gamma spectrometry, and a total activity decontamination was attempted.

### COLD TRAP BASKET HISTORY

The primary circuit cold traps involved in the decontaminations were of a full flow design (Figure 1), packed with stainless steel knit-mesh. They were installed in the original by-pass circuit cold trap positions in 1963, in place of the original cold trap baskets which had blocked during the initial clean-up of the reactor circuit in July 1959. The new baskets were intended to provide cold trapping capacity additional to that of the Permanent Cold Trap Loop (PCTL), and were raised when they became exhausted in 1967. The baskets were believed to be clear of the NaK, and therefore the only decay activities were expected to be from long-lived radionuclides, such as  $^{137}\text{Cs}$ , when the baskets were discharged recently.

The PCTL is a sub-loop on two breeder circuits of the DFR. It was installed in early 1962, as an

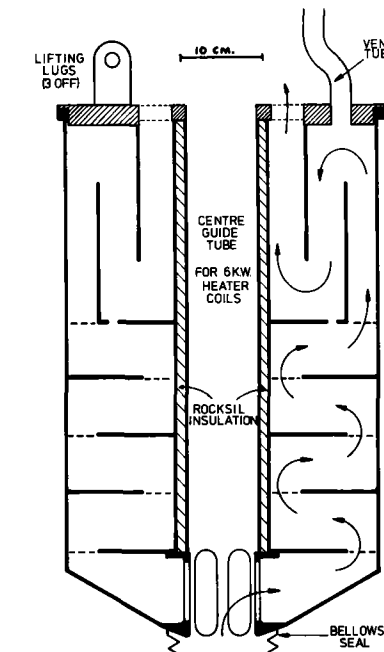


FIG. 1

8B COLD TRAP BASKET

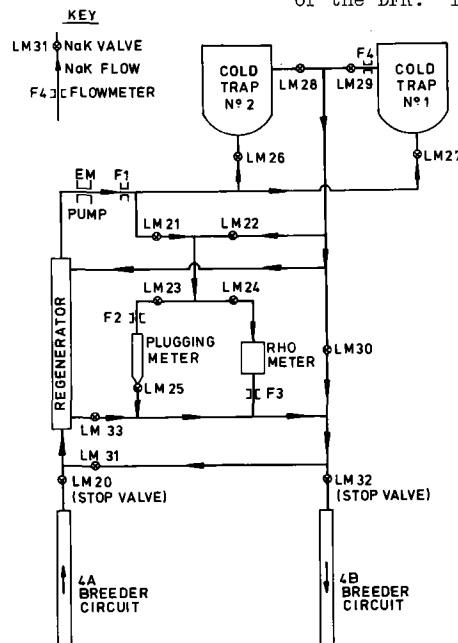


FIG. 2. P.C.T.L. CIRCUIT

35

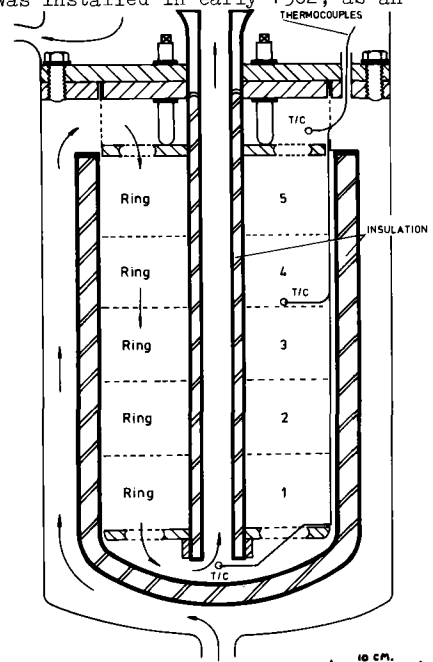


FIG. 3 PERMANENT COLD TRAP LOOP BASKET

## INTERNATIONAL CONFERENCE ON LIQUID METAL TECHNOLOGY IN ENERGY PRODUCTION

additional purification and purity monitoring facility for the DFR primary NaK. The PCTL has two cold traps in parallel, and a rhometer and plugging meter for purity monitoring. A simplified circuit diagram is shown in Figure 2, and a diagram of the PCTL cold trap basket is shown in Figure 3. The PCTL is operated for 10 to 14 days at the start of each reactor run, until the plugging temperature is 105°C (approximately 1 ppm weight of oxide). It is filled using the 240 kNm<sup>-2</sup> differential between the loop and the DFR gas blanket to force the NaK up into the loop. The trapping procedure used attempts to transfer to Trap 1 any debris collected in Trap 2.

The cold trap baskets were discharged from the breeder circuits in the sequence 8B, 7B, 9B and 9A, to eliminate any possibility of their contaminating the coolant. The PCTL basket was also discharged as it was approaching exhaustion.

### EXPERIMENTAL

The cold trap baskets were discharged from their vessels in the primary circuit into an inert gas filled flask. The  $\gamma$  radiation levels were measured through the flask at a distance of 20 cm from the basket shell, as the baskets were raised into the flask. A Ge (Li) high resolution gamma detector and multi-channel analyser were used to record the gamma spectra from four of the five baskets before steam cleaning. The radiation level from the PCTL basket, at contact with the flask, was too high to permit pre-decontamination gamma scanning without unacceptably high personnel doses.

The baskets were decontaminated with steam-nitrogen in a stainless steel lined pit in the DFR Element Storage Building (ESB). The discharge flask was positioned over the pit, which was thoroughly purged with nitrogen before lowering the basket from the flask. The steam-nitrogen jets entered the pit from perforated steam rings on the pit walls. The ESB pit was cleaned out, before and after each use, by a 48 hour hot soak with 0.04 M HNO<sub>3</sub> - 0.1M citric acid - 0.2M oxalic acid, followed by two water washes. The effectiveness of this treatment was checked by gamma spectrometric analysis of samples of the acid and wash solutions.

The alkaline decontamination liquors collected at the bottom of the pit vessel, and were agitated by nitrogen injection before sampling for analysis. The steam cleaned baskets were wrapped in 0.8 mm thick polythene sheet, and the  $\gamma$  and  $\beta\text{-}\delta$  radiation levels were measured at contact with each basket along its length. The 9B basket was also soaked in approximately 1% phosphoric acid for 5 hours and monitored again. The 7B and 9B baskets were then gamma scanned using the Ge (Li) detector through a 3.75 cm diameter collimator hole in a 10 cm thick lead wall. The detector-to-basket shell distance was 15 cm, and the gamma radiation level at this distance was 150-180mR/hr from both baskets. The 8B basket was not scanned in this way, as it was immediately disposed to waste to allow further basket decontaminations in the ESB.

The last two baskets analysed, the 9A and PCTL baskets, were axially gamma scanned more thoroughly than the others, using a Ge (Li) detector in a shielded assembly. The gamma spectra were recorded from both baskets at a number of points along their lengths. The point count rates ( $\gamma$ pm per point) were calculated from these spectra for each radionuclide at each point. The 9A and PCTL baskets were pickled for 60 hours in 4M HNO<sub>3</sub> - 0.7M HF, initially hot, in PVC lined mild

steel drums. The pickle liquors were sampled for analysis, and the baskets were monitored and axially gamma scanned as before, to estimate the decontamination efficiencies for each radionuclide.

The total alkali content of the decontamination liquors was determined by acid titration and Na:K ratios were measured by flame photometry against standards of approximately the same composition. Radionuclidic impurities were identified and quantitatively analysed by high-resolution gamma spectrometry. Chemical and spectrographic methods gave total analyses for the main non-radioactive impurities. Caesium and uranium were determined by mass spectrometry after ion exchange and chromatographic separation, and the plutonium content was measured by alpha counting. Particulate and suspended matter in the decontamination liquors was removed by filtration for separate analyses.

### RESULTS

The  $\gamma$  and  $\beta\text{-}\delta$  radiation levels from the baskets before and after steam cleaning, and after acid pickling where applicable, are summarised in Table 1. The gamma spectra, obtained by direct measurement of the baskets, are compared in Table 2 for the different stages of decontamination, and the results of alkalinity and other chemical analyses of the decontamination liquors are summarised in Table 3. Tables 4 and 5 give high resolution gamma spectrometry results for these liquors, decay corrected to the reactor shut-downs prior to the discharge of each basket. The results of gamma spectrometric analysis of the DFR primary NaK are given in Table 6 for comparison. Only 137-Cs was observed in the 7B and 9B baskets before steam cleaning, therefore no detailed analyses of their decontamination liquors were carried out. Fissile material inventories, where measured, are summarised in Table 7.

Figures 4 and 5 show the results of the detailed gamma scanning of the 9A and PCTL baskets, respectively, before and after acid pickling. The decontamination efficiency is conveniently expressed by the decontamination factor  $f$ , defined as the ratio of the initial activity  $I$  associated with the cold trap basket, to the activity  $L$  left after decontamination.  $f$  values of 100 and 10 represent 99% and 90% decontamination respectively. For the pickling exercise (denoted by subscript  $p$ )  $f_p$  was related to the point count rate, averaged over the length of the basket:

$$f_p = \frac{I_p}{L_p} = \frac{(\overline{C_p})}{(\overline{C_p})} \quad (1)$$

This gave averaged gamma decontamination factors for each radionuclide.

$$\text{Therefore } I_p = \frac{A_p f_p}{f_p - 1} \quad (2)$$

$$\text{and } L_p = \frac{A_p}{f_p - 1} \quad (3)$$

where  $A_p$  is the activity of the radionuclide in the pickle liquor.

Values of  $I_p$  and  $L_p$  calculated for each nuclide in the 9A and PCTL baskets, using equations (2) and (3), are included in Table 5 along the pickle decontamination factors  $f_p$  calculated using equation (1).

The 9A basket was also gamma scanned before and after steam cleaning. Equation (1) was used to calculate steam-clean decontamination factors  $f_s$  for each nuclide detected in these gamma scans and the results are included in Table 4. The activity  $I_p$  of a given



INTERNATIONAL CONFERENCE ON LIQUID METAL TECHNOLOGY IN ENERGY PRODUCTION

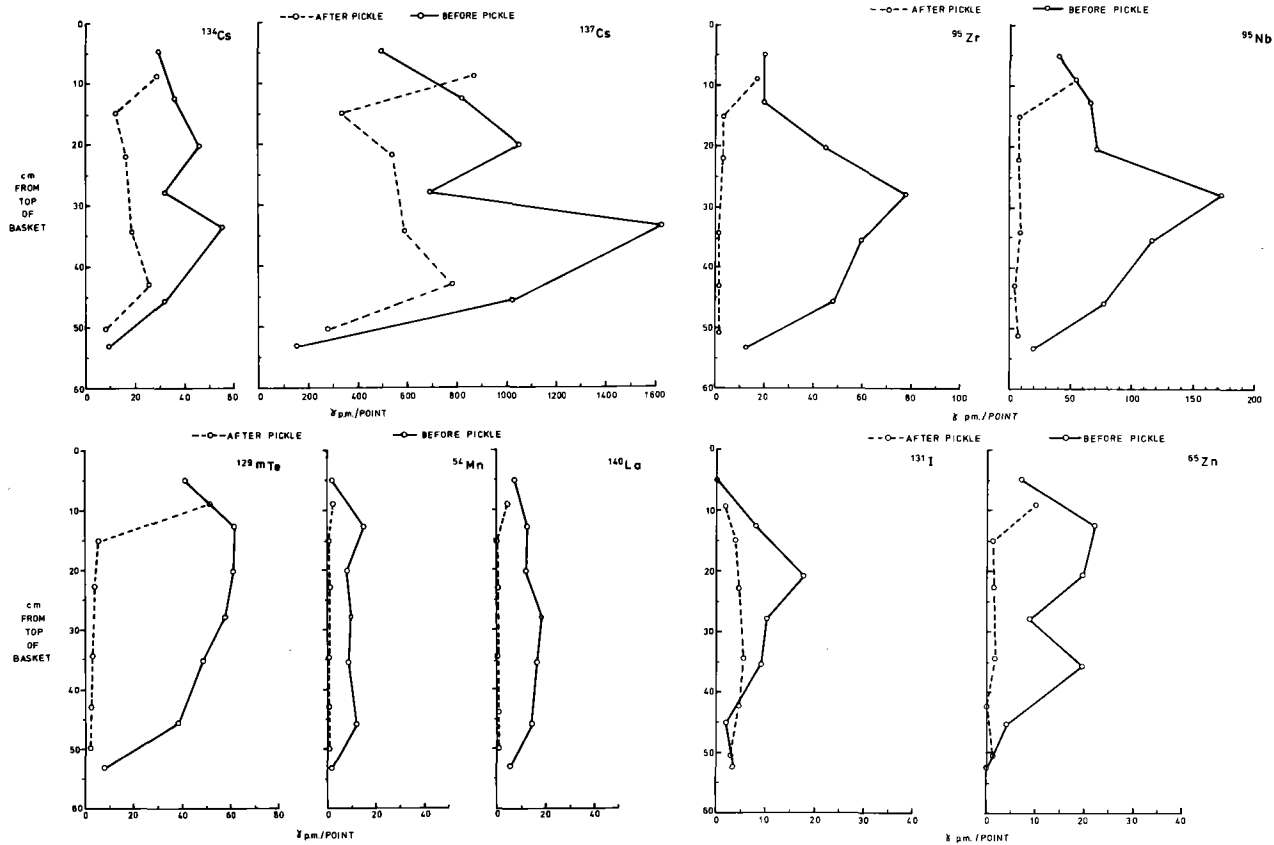


FIGURE 4 GAMMA COUNT-RATE PROFILES FROM 9A BASKET

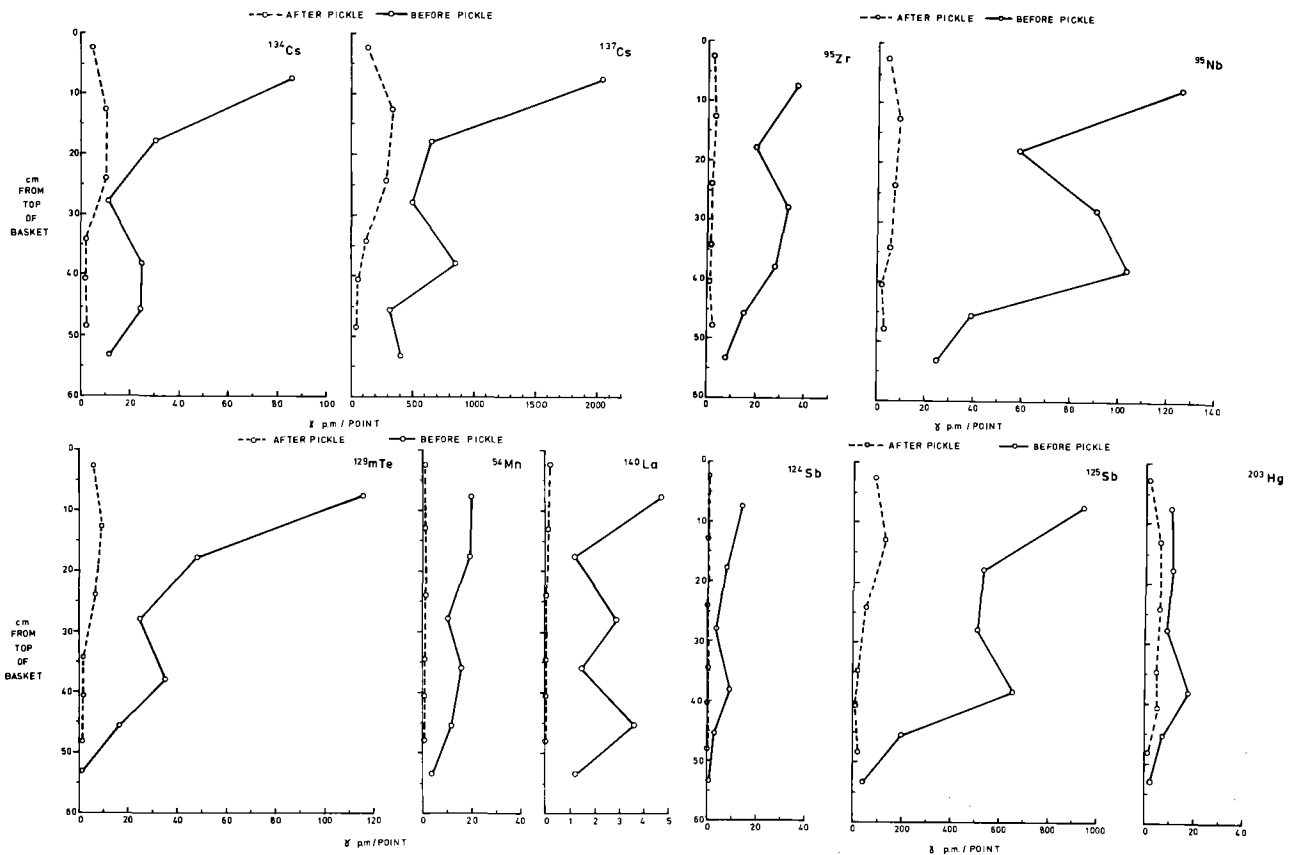


FIGURE 5 GAMMA COUNT RATE PROFILES FROM PCTL BASKET

## INTERNATIONAL CONFERENCE ON LIQUID METAL TECHNOLOGY IN ENERGY PRODUCTION

nuclide in the 9A basket before pickling was the same as the activity  $I_s$  of the nuclide left in the basket after steam cleaning. Therefore

$$I_s = \frac{A_p f_p}{f_p - 1}$$

and the activity  $I_s$  of the nuclide in the 9A basket before steam cleaning was

$$I_s = I_s f_s = \frac{A_p f_p f_s}{f_p - 1} \quad (4)$$

Values of  $I_s$  calculated using equation (4) are included in Table 4.

The high radiation levels from the 9A and PCTL baskets prevented the disconnection of the baskets from their gas space shield plugs before steam cleaning. Part of the nuclide activities in the 9A and PCTL alkaline liquors therefore came from the shield plugs. The activity  $I_s$  on the basket and shield plug together before steam cleaning was calculated from the expression

$$I_s = \frac{A_s f_s}{f_s - 1} \quad (5)$$

This assumed that the steam-clean decontamination factors  $f_s$  for the basket were the same as those for the shield plug. The  $I_s$  value calculated for the 9A basket is included in Table 4.

### DISCUSSION

#### Liquid Metal and Oxide Content

The bulk of the DFR NaK is  $74.4 \pm 1.4\%$  sodium by weight<sup>(2)</sup>. This is significantly less than the sodium contents of the cold trap basket decontamination liquors, as shown in Table 3, and was due to oxide collection in the baskets before raising from the NaK or low temperature drainage of the residual NaK in the cold trap baskets.

On cooling below  $50^\circ\text{C}$ , the NaK separates into solid sodium and potassium enriched NaK. Low temperature drainage of the cold trap baskets therefore gives a high sodium content in the residual NaK. The minimum temperature in the DFR primary circuit is  $240^\circ\text{C}$  and the gas space temperature immediately above the NaK is approximately  $200^\circ\text{C}$ . Sodium separation from the NaK film on the cold trap basket surfaces was therefore unlikely. The 4 primary circuit cold trap baskets were of a fully drainable design, and the immersed surface area was estimated to be  $8.3 \text{ m}^2$ . The NaK contents of the alkaline liquors shown in Table 3 were equivalent to surface loadings of  $31\text{--}114 \text{ gm NaK/m}^2$ . These values are somewhat greater than the sodium or NaK loadings on drained steel surfaces<sup>(3)</sup>, which lie in the range  $7\text{--}35 \text{ gm/m}^2$  for components with good drainage characteristics. It is therefore unlikely that the high sodium content of the baskets was due to long-term drainage.

Potassium monoxide is thermodynamically unstable in sodium or NaK. Cold trapping of sodium monoxide would explain the high sodium content of the decontamination liquors in Table 3, and the  $\text{Na}_2\text{O}$  and NaK data were calculated on this basis. The 8B and PCTL baskets contained considerably more NaK than the others. This was expected of the PCTL basket, as the PCTL had been operated during the run before the basket discharge. The high NaK content of the 8B basket was therefore due to its recent partial immersion in the NaK, and this was confirmed by a "tide-mark" on the basket shell, 23 cm below the basket top plate. The 8B and 9A

baskets contained considerable amounts of  $^{131}\text{I}$ . The half life of this nuclide is 8 days, indicating that the 9A basket was also partially immersed in the NaK during the run before its discharge.

#### Halide behaviour in the cold traps

Tracer experiments in steel capsules and a recirculating sodium loop enabled the low temperature solubilities of NaBr and NaI in sodium to be measured, and showed that halide partitions between steel surfaces and sodium<sup>(4,5)</sup>. The halides were found to collect efficiently and reversibly in the loop cold trap, and the collection mechanism was not dependent on the presence of oxide in the trap. Iodine was present in the NaK as NaI, and the volatility of this compound relative to that of sodium or NaK is very low at  $200\text{--}250^\circ\text{C}$ <sup>(5)</sup>. The  $^{131}\text{I}$  activity on the 9A basket shield plug was therefore small, as shown in Table 4.

The 8B and 9A baskets contained 97 and 44 curies of  $^{131}\text{I}$  respectively, equivalent to 120 and 96 mCi  $^{131}\text{I/kg}$  of NaK remaining in the baskets. The  $^{131}\text{I}$  enrichments relative to the DFR primary NaK were therefore 810 and 660 respectively. Interpretation of the NaK sample results in Table 6 gave an area deposition factor of  $178 \text{ mCi }^{131}\text{I/m}^2$  and a deposition corrected contamination level in the DFR NaK of  $146 \text{ mCi }^{131}\text{I/kg}$  NaK. Therefore,  $1.48$  curie  $^{131}\text{I}$  was deposited on the 8B and 9A trap surfaces and  $0.05\text{--}0.12$  curie was dissolved in the NaK. 98% of the  $^{131}\text{I}$  in the 8B trap basket was collected by filtration cold trapping or adsorption on the oxide in the trap. 96% of the  $^{131}\text{I}$  in the 9A basket collected in the same way. Stable iodine ( $^{127}\text{I}$ ) and  $^{129}\text{I}$  ( $t_{1/2} = 1.7 \times 10^7$  years,  $E_\beta = 0.038 \text{ MeV}$ ) are significant fission products, and the specific activity of  $^{131}\text{I}$  in the trap was expected to be low. Total iodine analysis of the basket decontamination liquors showed this to be so.

The NaK flowmeters on the PCTL indicated that the loop basket was also immersed in fresh NaK at the start of the reactor run prior to its discharge and the PCTL basket also contained  $^{131}\text{I}$ . This was not detected as it had decayed by a factor of  $10^4$  in the 3.5 months which elapsed before the contents of the basket were analysed.

#### Caesium behaviour in the cold traps

The only nuclide present in all the cold trap baskets at the curie level was  $^{137}\text{Cs}$ . The baskets contained  $3.9\text{--}6.5 \text{ Ci}$  of  $^{137}\text{Cs}$ , with enrichment factors in the NaK in the baskets ranging from 34 to 104, relative to the  $^{137}\text{Cs}$  content of the DFR primary NaK. Deposition experiments in DFR<sup>(2)</sup> gave small but reproducible area deposition factors for  $^{137}\text{Cs}$  on stainless steel, and showed that the deposition-corrected  $^{137}\text{Cs}$  activity level in the DFR coolant was reasonably stable. An area deposition factor of  $8.2 \text{ mCi }^{137}\text{Cs/m}^2$  of steel surface gave  $0.068 \text{ Ci }^{137}\text{Cs}$  on the surface of the primary circuit cold trap baskets. A deposition-corrected activity level of  $193 \text{ mCi }^{137}\text{Cs/kg}$  of DFR NaK accounted for a further  $0.02\text{--}0.16 \text{ Ci }^{137}\text{Cs}$ . Therefore, only  $1.4\text{--}4.2\%$  of the  $^{137}\text{Cs}$  found in the cold trap baskets could be accounted for by surface deposition and the NaK content of the baskets.

Caesium isotope ratios in DFR NaK samples have been determined<sup>(2)</sup> by mass spectrometry, after separation from  $\text{Na}^+$  and  $\text{K}^+$  on ammonium molybdatophosphate (AMP) ion exchange columns. The ratios have changed little in the past 6 years, and a sample taken in December 1970 gave a composition:—

$39.33\% \text{ }^{133}\text{Cs}$ ;  $31.43\% \text{ }^{135}\text{Cs}$  and  $28.65 \pm 0.58\% \text{ }^{137}\text{Cs}$ .

## INTERNATIONAL CONFERENCE ON LIQUID METAL TECHNOLOGY IN ENERGY PRODUCTION

The total caesium content of the trap basket is  $(40.1 \pm 0.8)S$  mg, where S is the total  $^{137}\text{Cs}$  content of the basket in curies. The cold trap baskets therefore contained 0.16 to 0.26 grams of caesium, with a specific activity of 24 curies  $^{137}\text{Cs}$  per gram of caesium. The  $^{137}\text{Cs}$  inventory in the DFR primary coolant is approximately  $10^4$  curies and the collection efficiency of the cold traps for caesium was therefore extremely low, considering the long half life of  $^{137}\text{Cs}$ . This suggests a collection mechanism other than filtration cold trapping, consistent with the thermodynamic instability of  $\text{Cs}_2\text{O}$  in sodium or NaK, and the miscibility of Cs with the other alkali metals.

There is evidence for Cs deposition on  $\text{Na}_2\text{O}$ <sup>(7,8)</sup> or oxidised steel surfaces<sup>(8-10)</sup>, and the formation of sodium ferrites and chromites is possible in oxide contaminated traps. Cs deposition on these mixed oxides, or its inclusion to form the analogous mixed alkali compounds are further mechanisms of  $^{137}\text{Cs}$  collection in cold traps. These mechanisms are variations of an adsorption process, and all of them may contribute without a clear distinction.

The efficiency of steam cleaning for  $^{137}\text{Cs}$  removal was lower than its efficiency for  $^{131}\text{I}$  removal. 80-90% of the residual gamma activity on the baskets after steam cleaning was due to  $^{137}\text{Cs}$ . This high residual  $^{137}\text{Cs}$  gamma activity has been observed before<sup>(7,11-14)</sup> on decontaminated components from sodium or NaK cooled reactors, and is probably due to diffusion of Cs into the steel surface or Cs penetration up the grain boundaries. The diffusion process may occur at high temperatures, on fuel cladding in the core, for instance. It is unlikely to be important at the low temperatures found in cold traps.

Grain boundary penetration probably proceeds by a wedging mechanism, involving the formation of caesium or mixed alkali ferrites or chromites in the grain boundaries.  $^{137}\text{Cs}$  penetration depths of up to 4 microns have been reported,<sup>(11,14)</sup> with surface etching<sup>(11)</sup> giving higher results than lapping techniques when expressed as  $^{137}\text{Cs}$  activity per micron of steel removed. This suggests non-uniform penetration. Steam decomposition of the sodium ferrite would produce the fine  $\text{Fe}(\text{OH})_3$  suspension observed in the decontamination liquors. These ferric suspensions settled out of the alkaline liquors over 2-3 days, and were filtered off for analysis. The residues from the 8B alkaline liquor gave the gamma spectrum:-

47.3%  $^{137}\text{Cs}$ , 39.3%  $^{131}\text{I}$ , 8.5%  $^{140}\text{BaLa}$ , 3.7%  $^{95}\text{Zr}$ , 0.9%  $^{134}\text{Cs}$ , 0.3%  $^{95}\text{Nb}$ .

### Tellurium Behaviour

Both the 9A and the PCTL baskets after steam cleaning contained significant amounts of  $^{129m}\text{Te}$ , an important fission product with a 34.5 day half-life. The solubility of tellurium in sodium is reported to be 900 ppm (weight) at  $200^\circ\text{C}$ <sup>(15)</sup>, which is very high when compared with the solubilities of similar solutes (Bi, Sb, I, Br) in sodium<sup>(4,5,16,17)</sup>. Re-determination of the solubility of Te in sodium showed it to be 15-20 ppm (weight) at  $200^\circ\text{C}$ <sup>(2)</sup>. Therefore tellurium is also likely to collect in a cold trap by precipitation. Tellurium is probably present in sodium or NaK as the telluride  $\text{Na}_2\text{Te}$ , which is soluble in water or in alkaline solutions.

Like the  $^{131}\text{I}$  collected in the baskets, the  $^{129m}\text{Te}$  activity should be readily removed by steam cleaning. Its resistance to decontamination suggests that the tellurium had reacted with the steel. Acid pickling was efficient in removing  $^{129m}\text{Te}$  activity,

indicating that the tellurium did not penetrate the steel as deeply as caesium. A similar surface reaction was observed in tellurium solubility and deposition experiments<sup>(2)</sup>.

The fission product deposition experiments performed in the DFR NaK sampling facility also showed that tellurium deposited strongly on stainless steel surfaces<sup>(2)</sup>. Deposition specimens were immersed in the NaK for 5 hours at  $250^\circ\text{C}$ , and the deposited activity was found to be difficult to remove. Area deposition factors of 11-42  $\text{mCi}/\text{m}^2$  were obtained in these experiments, approximately 20% of the values calculated from the cold trap activities. If the cold trap results (66 and 190  $\text{mCi }^{129m}\text{Te}/\text{m}^2$  for the 9A and PCTL baskets respectively) approached surface saturation, the achievement of 20% saturation in 5 hours suggested that tellurium deposition was fast.

### Behaviour of other fission products

$^{140}\text{Ba,La}$  was also observed in the 8B, 9A and PCTL baskets, with enrichments up to 7.2 in the trap NaK, relative to the primary NaK.  $^{140}\text{Ba,La}$  has a short half-life (12.8 days) and this confirms the recent immersion of these traps in the DFR NaK. Barium and lanthanum form stable oxides in sodium or NaK, and were probably present as fine particles suspended in the NaK. The deposition of particles on surfaces is probably not a simple adsorption process, and will be effectively irreversible in the initial stage<sup>(2)</sup>. High decontamination factors were obtained in acid pickling as surface penetration was negligible.

The area deposition factor for  $^{140}\text{Ba,La}$  was 40  $\text{mCi}/\text{m}^2$  for immersion of the sampling crucibles in the DFR NaK, and was expected to increase with time. Assuming uniform distribution in the 8B trap, the 0.33 curie  $^{140}\text{Ba,La}$  was equivalent to a terminal area deposition factor of 40  $\text{mCi}/\text{m}^2$ . This was similar to the value obtained after 5 hours, and indicated that the deposition process was fast and the surface saturated quickly, or that the trap baskets were only partly immersed in the NaK during the run prior to its discharge. The second explanation is more likely.  $^{95}\text{Zr,Nb}$ ,  $^{141}\text{Ce}$  and  $^{144}\text{Ce}$  also form stable oxides in sodium or NaK, and collected in the cold traps by deposition of oxide particles in the same way.

The PCTL basket contained a significant quantity of  $^{125}\text{Sb}$ , whereas the other baskets did not. Antimony is present in sodium or NaK as  $\text{Na}_3\text{Sb}$ , and shows a low solubility (2 ppm at  $200^\circ\text{C}$ ) in sodium<sup>(16,17)</sup>. Although antimony might be expected to deposit in cold traps in a similar manner to tellurium or iodine, the cold trap analyses confirm the unpredictable behaviour of  $^{125}\text{Sb}$  observed in the DFR fission product deposition experiments, some of which gave a deposition factor of 0.34  $\text{mCi }^{125}\text{Sb}/\text{m}^2$  while identical experiments gave negligibly small factors. This unpredictable behaviour is characteristic of particulate material in suspension in the coolant. Fissile material shows similar behaviour in sodium and NaK circuits<sup>(2)</sup>. The PCTL basket contained 10 times as much uranium as the other baskets, and it is possible that the higher antimony activities were associated with fissile material particles collected by the trap.

### Fissile Material Behaviour

The uranium contents of the 8B and 9A liquors were very similar, but the uranium content of the PCTL liquors was considerably greater (Table 7). This probably reflects the longer cumulative operation of the PCTL with NaK flow through the basket. The plutonium contents of the liquors the same. Plutonium tends to

## INTERNATIONAL CONFERENCE ON LIQUID METAL TECHNOLOGY IN ENERGY PRODUCTION

form colloids in aqueous solutions of low acidity, and precipitates with uranium in basic solution. Indeterminate amounts of uranium and plutonium may have remained in the baskets after decontamination, and the uranium and plutonium results are therefore lower contamination limits.

Since the true solubility of uranium or  $UO_2$  is extremely low in sodium or NaK containing dissolved oxygen,<sup>(2)</sup> the uranium in the trap baskets was present as particulate matter.  $UO_2$  and  $Na_2UO_4$  are stable in sodium and the particles were collected by deposition on the trap surfaces,<sup>(2)</sup> or by aggregation, sedimentation and filtration processes. Assuming uniform deposition in the cold trap baskets, the area deposition factors were 25-490 mg "U"/m<sup>2</sup>. This is up to approximately 500 times higher than values found in loop experiments,<sup>(2)</sup> but can be explained by the much longer immersion time of the traps in the NaK. The corresponding area deposition factors for plutonium were 0.17 - 0.27 mg Pu/m<sup>2</sup>.

The 235-U enrichment of the uranium found in the PCTL pickle liquor was considerably greater than the enrichment of the uranium in the alkaline liquor. This was probably due to the presence of two kinds of fissile material particles in the coolant, large particles of high enrichment from the driver charge and small particles of low enrichment from the breeder. Oxygen in the NaK causes spalling of large  $UO_2$  particles from the driver fuel. Smaller particles from the  $UO_2$  breeder have a longer residence time in the NaK and will be converted to  $Na_2UO_4$  in the core. Steam cleaning degrades large  $UO_2$  particles much less than small  $Na_2UO_4$  particles, and the 235-U enrichment in the baskets may have been greater than 8.7%.

### Behaviour of other impurities

The 9A and PCTL baskets, especially that from the PCTL, contained significant quantities of 65-Zn. In addition, the PCTL basket contained a small quantity (less than 1m Ci) of 203-Hg. The 65-Zn and 203-Hg were produced by fast neutron activation of zinc and mercury impurities in the NaK, respectively. The mercury came from the gas seals on the rotating shield, but the source of the zinc is much less certain. Although the DFR fuel is not normally analysed for zinc, the billet fabrication route will eliminate zinc by volatilisation. The DFR fuel is therefore unlikely to be a significant source of zinc. Brass and bronze metal contain 30-35% Zn, and exposure of these alloys to the NaK will cause zinc contamination of the NaK.

Zinc will distribute evenly around the reactor circuit, as its solubility in sodium<sup>(17)</sup> and NaK is high (100 ppm at 200°C). Zinc oxide is not stable in liquid alkali metals, and no alkali-zinc oxides are likely to be formed. Zinc forms intermetallic compounds with iron and steel and its collection in cold traps was probably due to chemisorption on steel surfaces in the traps. Since this is a uniform process rather than local penetration of the steel, the acid pickle was effective in removing 65-Zn activity.

Fast neutron irradiation of zinc (48.8% 64-Zn) in DFR gives an estimated specific activity of 90 Ci 65-Zn per gram of zinc. This is readily detectable in a 1 gram sample of NaK containing more than 0.1 ppm zinc. The absence of significant 65-Zn activity in the DFR deposition experiments<sup>(2)</sup>, and in the previously decontaminated 7B, 8B and 9B baskets, suggested that the normal zinc level in the DFR primary NaK was less than 0.1 ppm by weight. The DFR NaK was therefore slightly contaminated with zinc, probably by the recent exposure

of brass or bronze metal to the NaK.

The behaviour of mercury in sodium and NaK is very similar to that of zinc. The 203-Hg content of the DFR primary NaK was found to be reasonably stable at 2-7m Ci/kg NaK in the fission product deposition experiments<sup>(2)</sup>. A significant rise to 24 mCi/kg NaK on one occasion was found to correspond to a rise in the total mercury content of the NaK from less than 30 ppm to 140 ppm.

Significant amounts of aluminium and calcium were also found in the trap decontamination liquor. These are important impurities in sodium and NaK, and form stable oxides in liquid alkali metals. They were probably collected in the cold trap as oxide or mixed particles, which were converted to hydroxides or hydrated oxides by steam decontamination. The only activated corrosion products detected in the cold traps were 51-Cr and 54-Mn. These were present in negligible amounts, due to the low core temperature in DFR. They were associated with the cold trap surfaces, and were readily removed by the acid pickle.

### Gamma scan profiles and radiation levels of the 9A and PCTL baskets

The gamma scan profiles of the 9A and PCTL baskets before pickling were quite different. This was partly due to differences in NaK flow path, which was upwards in the 9A basket and downwards in the PCTL basket. The stainless steel mesh packing density rose from 158kg/m<sup>3</sup> at the basket inlet, to 316kg/m<sup>3</sup> at the outlet (the coldest point), in both baskets. The high point count rates at the top of the PCTL basket showed that the heaviest deposition of adherent fission products (not removed by steam cleaning) occurred at the basket inlet. The smaller maximum 40 cms from the top of the basket corresponded to the dense packing region of the basket mesh.

The partial immersion of the 9A basket complicated its gamma scan profiles, especially since the NaK level probably fluctuated during the reactor runs. The effects of this were superimposed on the trap inlet deposition effect, and the effect of the increased surface area-to-volume ratio in the more densely packed region of the trap. Volatile impurities (134-Cs, 137-Cs and possibly 65-Zn) transferred through the gas space to the exposed upper part of the basket. Impurities showing strong surface activity (129m-Te, 131-I) concentrated at the fluctuating NaK - argon interface, while particulate impurities (95-Zr, Nb and 140-Ba, La) deposited in the immersed part of the trap. The gamma scan profiles of the 9A basket suggested that the NaK level fluctuated mainly between 10 cms and 25 cms from the top of the basket, during the reactor run prior to the basket discharge.

The gamma scan profiles after pickling were flat for most nuclides in both baskets. 134-Cs and 137-Cs showed considerable resistance to decontamination due to ferrite formation, especially in the 9A basket. The acid pickle solutions were made up hot in the PVC lined bins, with the cold trap baskets in the bins, and allowed to cool overnight. The solution levels fell as the solutions cooled, and in the case of the 9A basket the cold solution level was approximately 12 cms below the top of the basket. The first gamma scan points on the 9A basket after pickle were high for this reason. The very small or negligible decontamination effected during this cooling period indicated that the decontamination rates were slow for most of the nuclides, especially 129m - Te.

# INTERNATIONAL CONFERENCE ON LIQUID METAL TECHNOLOGY IN ENERGY PRODUCTION

The gamma radiation levels from the 9A and PCTL baskets before steam cleaning were 8R/hr and 35R/hr respectively, at contact with the 5cm thick transfer flask. The very high radiation level from the PCTL basket was probably due to the higher NaK content of this basket shown in Table 3, and reflected its poorer drainage characteristics. After steam cleaning, the radiation levels were reduced to 1.3-2.4R/hr  $\beta\delta$  and 0.3-0.6R/hr  $\gamma$  at contact with the baskets, through 0.8 mm thick polythene. Pickling in 4M HNO<sub>3</sub> - 0.7M HF further reduced these radiation levels to less than 0.6R/hr  $\beta\delta$ , 0.2R/hr  $\gamma$ .

## CONCLUSIONS

Five DFR primary cold trap baskets have been analysed. Steam cleaning and acid pickling in 4M HNO<sub>3</sub> - 0.7M HF was used to remove the activity from the baskets, and the decontamination liquors were analysed by high resolution gamma spectrometry. Direct gamma spectrometry of two of the baskets before and after the different stages of decontamination considerably increased the value of the results, enabling the distribution of individual nuclides in the baskets to be measured, and decontamination factors to be calculated for each nuclide detected.

Steam cleaning is not the ideal decontamination technique if analysis of residues and impurities is intended. The chemical form of many of the important species will be changed during decontamination, and many of the more powerful analytical techniques can not be applied to the reaction products. When analysis is not required, steam cleaning is an efficient first step in the decontamination process. Significant amounts of 137-Cs and beta activity will remain after steam cleaning and dilute acid rinsing.

131-I, 137-Cs, 125-Sb and 129m - Te were the major fission products in the cold trap baskets, with significant amounts of 144-Ce, 141-Ce, 95-Zr, Nb and 65-Zn. Iodine collected as NaI by filtration cold trapping while caesium collected by an adsorption mechanism on the trap surfaces, probably involving the formation of caesium or mixed-alkali ferrites. Grain boundary penetration by these compounds explained the difficulty in removing the 137-Cs activity by acid pickling.

The collection of 125Sb appeared to be associated with the particulate fuel collected by the traps. The amounts of 129m - Te and 65-Zn were unexpected. The tellurium required an acid pickle for effective removal and appeared to have reacted with the steel surfaces of the trap. The zinc was probably a minor impurity in the NaK, recently introduced by the exposure of some zinc alloy to the coolant. Impurity collection was most extensive at the mesh inlet plane with a less important collection zone in the region of densest packing, which was also the coldest point in the trap. The cold trap baskets probably contained less than 10 grams total uranium and less than 10 mg of plutonium.

Gamma radiation levels up to 35R/hr were measured, through the transfer flask, from the cold trap baskets before steam cleaning. After steam cleaning, the radiation levels were reduced to 1.3 - 2.4R/hr  $\beta\delta$  and 0.3 - 0.6R/hr  $\gamma$  at contact through polythene sheet, and pickling reduced these levels to less than 0.6R/hr  $\beta\delta$ , 0.2R/hr  $\gamma$ . The acid pickle was much more severe than could ever be used on components intended for re-installation in a reactor, although it is unlikely that exhausted primary cold trap baskets would be intended for re-use. The difficulty in removing 137-Cs will cause serious problems in the maintenance of components from the primary circuits of fast reactors.

## REFERENCES

1. Proceedings of the Symposium on the Dounreay Fast Reactor; London (1960). Institute of Mechanical Engineers, London (1961).
2. C G Allan. Unpublished work, DERE (1970-5).
3. J van Dievoet, A Michel, R Lanckman. "Sodium Evaporation in an Argon Flow". Proceedings of the International Conference on Sodium Technology and Large Fast Reactor Design, Argonne (1968). USAEC Report ANL 7520, Part 1; pp 418-425 (1968).
4. C G Allan. "Solubility of Sodium Bromide and Sodium Iodide in Sodium". UKAEA - TRG Report 2458(D), (1973).
5. C G Allan. "The Solubilities and Deposition Behaviour of Sodium Bromide and Sodium Iodide in Sodium - Stainless Steel Systems". Proceedings of the International Conference on Liquid Alkali Metals. Nottingham, (1973). British Nuclear Energy Society, London (1973).
6. A W Castleman. "LMFBR Safety, Part 1, Fission product behaviour in Sodium". Nuclear Safety; Vol 11, No. 5; pp 379-390 (1970).
7. A I Hansen. "Effects of Long Term Operation on SRE Sodium System Components". USAEC Report NAA-SR-11396 (1965).
8. J Guon. "Deposition of Caesium and Barium in a Sodium-stainless Steel System". USAEC Report AI-AEC-12952 (1970).
9. H E Evans, W R Watson. "The Behaviour of Radioactive Isotopes in Liquid Metal Cooled Fast Reactors; Part 2, an investigation of adsorption of Cs and Ba isotopes from solution in liquid sodium". CEBG Report RD-B-N 1513 (1970).
10. R P Colburn. "Nature of Cs and I Deposits in Sodium Systems". Transactions of the American Nuclear Society; Vol 14, No. 2; pp 626-7 (1971).
11. H E Johnson. "Corrosion and Activity Transfer in the SRE Primary Sodium System". USAEC Report NAA-SR-5363 (1960).
12. A I Leipunskii et al. "5 Years Operating Experience of the BR5 reactor". Third International Conference on the Peaceful Uses of Atomic Energy; Geneva (1964); Paper 312, Vol 6, pp 51-61. United Nations, New York (1965).
13. R A Davies, J L Drummond. "The Behaviour of Radioactive Impurities in the DFR Primary Liquid Metal Coolant". UKAEA-TRG Report 2362(D) (1973).
14. J Saroul. "Investigation of the Behaviour of Fission Products in Sodium and Argon - PIRANA Experiments". Proceedings of the International Conference on the Safety of Fast Reactors; Aix en Provence, (1967). Paper 5B-1, Documentation Francaise, Paris (1968).
15. R A Walker, J N Pratt. "The solubility of Bismuth and Tellurium in Liquid Sodium". Journal of Nuclear Materials; Vol 34, No. 2; pp 165-173 (1970).
16. H E Evans, W R Watson. "A Novel Method for the Determination of the Solubility of Solutes in Liquid Metals; The Solubility of Antimony in Sodium from 190-550°C". Journal of Nuclear Materials; Vol 40, No. 2; pp 195-204 (1971).
17. T D Claar. "Solubilities of Metallic Elements in Liquid Sodium". Reactor Technology: Vol 13, No. 2; pp 124-146 (1970).

# INTERNATIONAL CONFERENCE ON LIQUID METAL TECHNOLOGY IN ENERGY PRODUCTION

TABLE 1 RADIATION LEVELS FROM DFR COLD TRAP BASKETS (R/hr)

	Radiation	7B	8B	9A	9B	PCTL	Notes
Before steam cleaning		3	35	8	5	35	(a)
After steam cleaning		8	8	1.3-1.8	12	1.3-2.4	(b)
		0.5	2	0.4-0.6	2.5	0.25-0.55	(b)
After acid washing or pickling		-	-	0.15-0.65	9	0.1-0.4	(b)
		-	-	0.10-0.15 (c)	0.5 (d)	0.10-0.12 (c)	(b)

**Notes**

- a. Through 5cm thick mild steel wall of inert gas flask. Probe - basket shell distance 20cm.  
 b. Through 0.8cm polythene sheet. At contact.  
 c. Pickled in 4M HNO<sub>3</sub> - 0.7M HF for 60 hours.  
 d. Acid washed for 5 hours in 1% phosphoric acid.

TABLE 2 COMPARATIVE GAMMA SPECTRA

Basket decontam. stage	Nuclides (% of total gammas)						
	131-I	125-Sb	137-Cs	129mTe	95Zr	65Zn	140BaLa
7B 1	ND	ND	100	ND	ND	ND	ND
	ND	ND	100	ND	ND	ND	ND
8B 1	53	ND	45	ND	0.1	ND	1.6
	Basket was not gamma scanned.						
9A 1	77	ND	21	1.2	0.1	ND	0.5
	ND	ND	58	38	3.7	0.6	ND
	ND	ND	79	20	0.8	0.2	ND
9B 1	ND	ND	100	ND	ND	ND	ND
	ND	ND	100	ND	ND	ND	ND
PCTL 1	Basket was not scanned.						
	ND	17	12	64	2	5	ND
	ND	20	28	46	2	4	ND

- Stage 1 Before steam cleaning.  
 2 After steam cleaning.  
 3 After acid pickling.  
 ND = Nuclide not detected.

TABLE 3 ANALYSIS OF BASKET DECONTAMINATION LIQUORS

	8B	9A	9B	PCTL
Na: K ratio	3.50	10.5	7.85	3.25
% Na	77.8	91.3	88.7	76.3
% K	22.2	8.7	11.3	23.7
gm "NaK" of observed Na: K ratio	945	260	350	390
NaK loading on surfaces mg NaK cm <sup>-2</sup>	11.3	3.1	4.2	4.6
gm NaK at 74.4% Na	802	90	190	360
gm Na <sub>2</sub> O	170	230	210	40
Al content (grams)	2.2	1.1	3.1	3.9
Ca content (grams)	0.4	0.2	0.9	0.9
Li content (grams)	0.08	0.05	0.2	0.2
NaI content (grams)	0.075	0.029	0.022	0.039
Cs content (grams) (from 137-Cs specific activity)	0.23	0.26	0.16	0.27

TABLE 4 ACTIVITY REMOVAL BY STEAM CLEANING OF COLD TRAP BASKETS

Nuclide	Activity in 8B alkaline liquor A <sub>S</sub> curies	9A Cold Trap Basket				Nuclide activity in PCTL alkaline liquor (b) A <sub>S</sub> curies
		Activity A <sub>S</sub> in alkaline liquor (b) A <sub>S</sub> curies	Decontamination factor f <sub>S</sub> (c)	Curies on basket before steam cleaning I <sub>S</sub> (d)	Curies on basket and plug before steam cleaning I <sub>S</sub> ' (e)	
		131-I	97	34.5	5	
125-Sb	(a)	(a)	(a)	(a)	(a)	0.81
137-Cs	5.4	5.0	4	0.81	6.5	6.3
134-Cs	0.15	0.20	2	0.02	0.37	0.22
95-Zr,Nb	0.001	(a)	(a)	(a)	(a)	(a)
140-Ba,La	0.33	(a)	(a)	(a)	(a)	(a)

**Notes**

- a Nuclides such as 24-Na which had decayed, and those which were not detected, are not included.  
 b The activity A<sub>S</sub> in the alkaline liquor contains a contribution from the gas space shield plug, which was steam cleaned along with the baskets.  
 c Calculated using equation (1), from the results of gamma scanning the 9A basket before and after steam cleaning.  
 d Calculated from A<sub>S</sub> and f<sub>S</sub> using equation (4).  
 e Calculated using equation (5) on the assumption that the steam clean decontamination factor for the shield plug was the same as that for the basket.  
 f The volatility of NaI in sodium or NaK at 200 to 250°C is very low, therefore I<sub>S</sub> = I<sub>S</sub>' for 131-I.

**INTERNATIONAL CONFERENCE ON LIQUID METAL TECHNOLOGY IN ENERGY PRODUCTION**

TABLE 5

ACTIVITY REMOVAL IN 9A AND PCTL BASKET PICKLES

Nuclide	Activity in 9A basket before and after pickling (milli-curies)		Activity in 9A Pickle liquor Ap (m Ci)	9A Pickle Decontam Factor fp (c)	Activity in PCTL basket before and after pickling (m Ci)		Activity in PCTL Pickle liquor Ap (mCi)	PCTL Pickle Decontam Factor fp (c)
	Ip=L <sub>S</sub> (a)	Lp (b)			Ip=L <sub>S</sub> (a)	Lp (b)		
144-Ce	(d)	(d)	13	(d)	(d)	(d)	9.6	(d)
141-Ce	(d)	(d)	14	(d)	(d)	(d)	(d)	(d)
51-Cr	(d)	(d)	(d)	(d)	(d)	(d)	64	(d)
125-Sb	(d)	(d)	4	(d)	190	20	170	9.5
137-Cs	190	130	60	1.5	40	8	32	5
129m-Te	550	140	410	4	650	70	580	9
95-Zr	11	1	10	11	7.0	0.7	6.3	10
134-Cs	4	2	2	2	0.8	0.1	0.7	8
54-Mn	0.4	0.03	0.4	13	0.64	0.04	0.60	16
65-Zn	1.2	0.3	0.9	4	11.2	0.8	10.4	14
140-La	(e)	(e)	(e)	20	(e)	(e)	(e)	50
124-Sb	(d)	(d)	(d)	(d)	(d)	(d)	(d)	20

Notes

- a Calculated from Ap and fp using equation (2).
- b Calculated using equation (3).
- c Calculated using equation (1) from results of gamma scanning the baskets before and after pickling.
- d Not detected by direct Gamma scanning, but detected in the pickle liquor due to the higher sensitivity of the detector used.
- e Decayed in the pickle liquors before analysis.

TABLE 6 FISSIION PRODUCTS IN DFR NaK SAMPLES

Nuclide	mCi/kg NaK (not corrected for deposition)	Area deposition factor mCi/m <sup>2</sup>	mCi/kg NaK (deposition corrected)
144-Ce	6.44	1.2	4.36
141-Ce	11.0	1.6	8.23
132-Te	46.8	15.9	19.2
203-Hg	1.95	ND	1.95
131-I	455	17.8	146
125-Sb	ND	0.34	ND
137-Cs	207	8.2	193
95-Zr	9.80	1.3	7.55
95-Nb	31.4	6.4	20.2
134-Cs	4.02	0.16	3.74
136-Cs	2.53	0.10	2.36
86-Rb	5.14	ND	5.14
22-Na	4.49	ND	4.49
24-Na	1.67 x 10 <sup>4</sup>	ND	1.67 x 10 <sup>4</sup>
140-BaLa	128	39.6	39.3

TABLE 7 FISSILE MATERIAL CONTENT OF LIQUORS

Basket and Liquor Identification	Total U (gms)	235-U Enrich %	Total Pu (mg)
8B Alkaline Liquor	0.21	3.9	1.7
9A Alkaline Liquor	0.284	5.4	1.5
Pickle Liquor	0.122	8.7	0.8
Total	0.406	6.4	2.3
9B Alkaline Liquor	0.27	4.6	2.1
PCTL Alkaline Liquor	3.86	0.6	ND
Pickle Liquor	0.21	2.6	1.4
Total in PCTL	4.07	0.7	1.4
ND Not detected			

ABSTRACT

Phenix steam generators are once-through vessels with single-wall heat-exchange tubes. This design means that any leakage of water into the sodium must be detected as quickly as possible so that the installation can be shut down before extensive damage occurs.

The detection of water leaks in Phenix steam generators is based on measurement of the concentration in the sodium, of hydrogen produced by the sodium-water reaction. Since the various modules - evaporators, superheaters, and reheaters - have no free sodium surfaces, detection of hydrogen in argon is not used in Phenix steam generators. The measurement systems employ a probe made of nickel tubes 0.3 mm thick. Hydrogen in the sodium diffuses into a chamber kept under vacuum by an ion pump. The hydrogen pressure in the chamber is measured by a quadrupole mass spectrometer. The nine measurement systems (three per steam generator) are calibrated by injecting hydrogen into the sodium of the secondary circuits. The data-processing computer calculates the hydrogen concentration in the sodium from the spectrometer signals and the probe temperatures, which are not regulated in Phenix; it generates instructions that enable the operator to act if a leak appears. So far, no leaks have been detected. These systems also make it possible to determine rates of hydrogen diffusion caused by corrosion of the steel walls on the water side.

DESCRIPTION OF THE HYDROGEN SYSTEMS

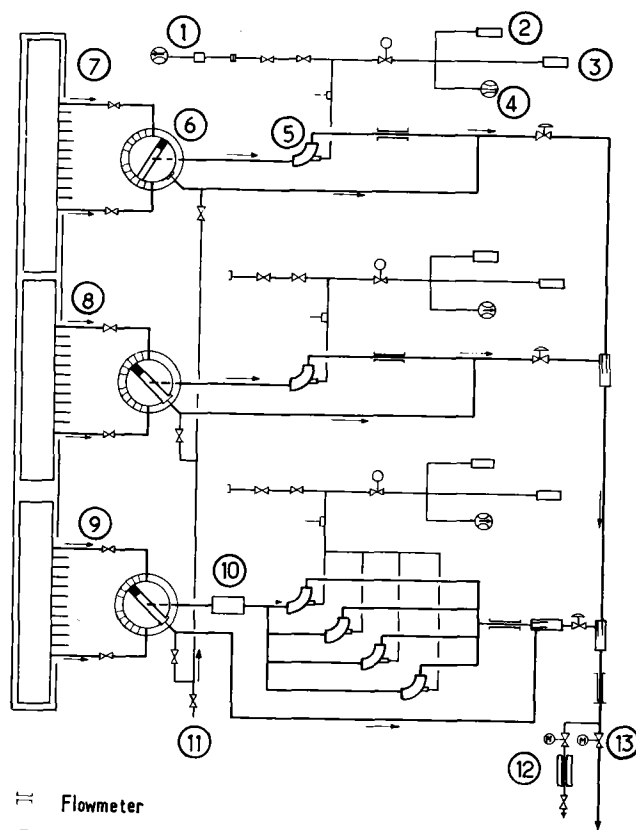
Each generator has a system measuring the hydrogen concentration in the sodium, shown schematically in figure 1.

Sodium circuit

The steam generator of a Phenix secondary circuit consists of 12 evaporator modules, 12 superheater modules, and 12 reheater modules; steam reheat is by sodium. The characteristics of each module are given in Table 1.

Sodium is sampled through a tap at the outlet of each module. The sample extraction piping of the evaporator, superheater and reheater modules forms three groups of 12 tubes each; each group leads to a selector that feeds either a fraction of the mixture of the 12 sodium samples (for leak detection) or each sodium sample in turn (for leak location) to the nickel-tube probe. By-pass piping on the probe gives a total sampling flow rate that remains essentially constant in all selector settings. A selector has a rotary nozzle whose shaft is driven by a pneumatic cylinder; the shaft is sealed by a gasket of frozen sodium plus a conventional packing gland and O-rings. The normal setting of a selector is the detection mode. When a leak has been detected, the nozzle is turned to locate the

defective module.



- ∩ Flowmeter
- ⊕ Control valve
- ⊗ Air actuated valve
- ⊙ Motor actuated valve
- ⊘ Hand actuated valve

- 1 Auxiliary vacuum pump
- 2 Calibrated hydrogen leak
- 3 Quadrupole mass spectrometer
- 4 Ion pump
- 5 Hydrogen detector
- 6 Sodium selector
- 7 Reheater
- 8 Superheater
- 9 Evaporator
- 10 Electric heater
- 11 Argon supply
- 12 E. m. pump
- 13 Line to dump tank

Fig. 1 - Diagram of hydrogen detection system

The evaporator measurement system has four separate nickel probes, while the remaining two systems have only one each; the extra diffusion area is needed to compensate for the decrease in the permea-



bility of the nickel caused by operation at 350° rather than 475°C as in the superheaters and reheaters.

In Phenix, the temperature of the sodium reaching the nickel tubes may vary; a correction for the temperature effect is made by the data-processing computer that calculates the concentration of hydrogen in the sodium. An electric heater keeps the temperature of the sodium reaching the evaporator measurement-system probes over 300°C so that flow rate of diffused hydrogen remains adequate.

The various samples of sodium are collected before being sent to the secondary circuit by an electromagnetic pump. If this pump is shut off, the sodium flow may be fed to the storage tank by working two motor-actuated valves. In addition, the sodium of the hydrogen detection circuit may be drained into the storage tank independently of the main circuit by using the cut-off valves of each sampling tap and the argon couplings leading to each selector.

Calculations have shown that it is necessary to place flow-restrictive orifices at various points to obtain the desired flow values; three hand adjustment valves are used to control flow rates in the three measurement systems.

#### Hydrogen measurement device

The first component is the probe; a single probe consists of a bundle of four nickel tubes with an outside diameter of 7.2 mm, 0.3 mm thick, in a stainless-steel housing. The assembly is in the shape of a 90° elbow to eliminate strains caused by differential expansion of the tubes and housing. The diffusion area is approximately 226 sq. cm.

The sodium circulates inside the nickel tubes so that the whole diffusion surface is in contact with the liquid metal, the velocity of which is accurately known. The thickness of 0.3 mm was chosen following experimental measurements of the response times of probes with nickel tubes from 0.2 to 0.8 mm thick. With a thickness of 0.3 mm, changes in the hydrogen concentration in the sodium are detected with a lag of approximately 45 seconds when the temperature of the nickel tubes is 350°C.

The hydrogen that diffuses across the nickel tubes enters a circuit kept under vacuum by an ion pump with a flow rate of 200 l/sec. This flow rate was chosen so that transition times for the partial pressure of the hydrogen would be short when the flow of diffused hydrogen varies rapidly.

The partial pressure of the hydrogen is measured by a quadrupole mass spectrometer. This instrument has two filaments, one in operation and the other on standby. Residual-gas spectra made on the vacuum circuits, after installations had been started up, showed that there remained practically nothing but hydrogen; the total pressure is therefore essentially equal to the partial pressure of hydrogen. The current through the ion pumps is proportional to the total pres-

sure, but this is not used as the measurement signal; the pumps are sometimes affected by instabilities, and the reading may be affected by the existence of leakage currents.

A calibrated hydrogen leak is connected to the vacuum circuit; this consists of a small nickel membrane 0.2 mm thick and 1 sq. cm in area at an operating temperature of 400°C; the known flux of diffused hydrogen may be used for periodic checks of the spectrometer (operation and drift).

A pneumatically-actuated valve makes it possible to cut off the ion pump and the spectrometer if a sodium leak develops in a nickel tube. The closing is activated by a signal from a leak-detection electrode or from the ion pump current, if it exceeds a preset threshold.

#### SET-UP OF HYDROGEN MEASUREMENT SYSTEMS

The set-up of the hydrogen measurement systems included degassing of the vacuum circuits, calibrating the spectrometers using calibrated leaks, and adjusting sodium sampling flow rates<sup>2</sup>; injections of hydrogen into the sodium of the secondary circuits was one of the major set-up operations.

#### Purpose of injections of hydrogen

Since the temperature of the sodium reaching the detectors in Phenix is not regulated, that of the nickel tubes may vary widely. Since the permeability of nickel to hydrogen varies considerably with temperature, the relationship between the spectrometer signal and the probe temperature must be known so that the hydrogen concentration of the sodium can be determined at any moment.

The theoretical relationship among the various parameters is as follows :

$$s - s_o = K (\text{CH}_2)^n e^{-b/T} \quad (1)$$

in which :

- s is the spectrometer signal;
- s<sub>o</sub> is the residual signal measured with the cut-off valve closed;
- CH<sub>2</sub> is the concentration of hydrogen in the sodium;
- k, n, b are constants.

Injections of known quantities of gaseous hydrogen into the sodium of the secondary circuits are used to calibrate the measurement systems.

These calibrations consist of determining constants K, n and b of the relation (1). With the spectrometer signal and probe temperature known, concentration CH<sub>2</sub> can then be determined. The data-processing computer receives these two parameters for each measurement channel and calculates the concentration using relation (1).

The test injections also made it possible to

determine how the measurement systems reacted to the introduction of hydrogen into a secondary circuit at various temperatures and sodium flow rates.

#### Calibration results

Measurements were made at constant secondary-circuit temperatures of 350, 400, and 450 °C, with the hydrogen concentration increased by successive injections. The maximum concentrations reached during the various tests ranged from 0.42 to 0.79 ppm. Other measurements were made at constant hydrogen concentrations (from 0.16 to 0.18 ppm, depending on the secondary circuit), with the sodium temperature decreasing from 410 to 250 °C.

During these tests, the steam generator tubes were filled with nitrogen at 7 bars. The gaseous hydrogen was introduced from a pressurized tank into the circuits upstream of the steam generators. The temperature and pressure of hydrogen in this tank were measured before and after injection. These measurements were used to determine the mass of gas injected, since the volume of the injection tank was known.

The injections were preceded by a sodium purification sequence using cold traps working at cold-point temperatures close to 110 °C. The cold traps were stopped several hours before the start of the tests, to check the stability of the residual hydrogen concentration in the sodium.

The value of  $n$  was found to lie between 1.13 and 1.49, with an average value of 1.29. Constant  $b$  is equal of the ratio of diffusion-process activation energy to the perfect gas constant; the mean value of activation energy was found to be 11,400 cal/mole.

Figure 2 shows a typical calibration curve giving the relationship between signal ( $s - s_0$ ) and hydrogen concentration at a given sodium temperature. The residual concentration of hydrogen resulting from operation of the cold trap before the injections was determined by extrapolating the calibration curve to  $s - s_0 = 0$ . With trap cold-point temperatures in the neighborhood of 110 °C, the residual hydrogen concentration was approximately 0.05 ppm.

The smallest measurable variation in hydrogen concentration is 0.005 ppm.

#### Response of hydrogen-measurement installations

When the sodium temperature is above 300 °C, the response of the installation is practically immediate except for the time of transit of the sodium in the steam generator and sample extraction piping and the response time of the measurement device. Figure 3 shows a typical response of the measurement installation, recorded at 414 °C with gaseous hydrogen injected upstream of the steam generator. For several hours following the end of the injections, the spectrometer signal remained practically stable, with the sodium temperature constant to within  $\pm 0.5$  °C.

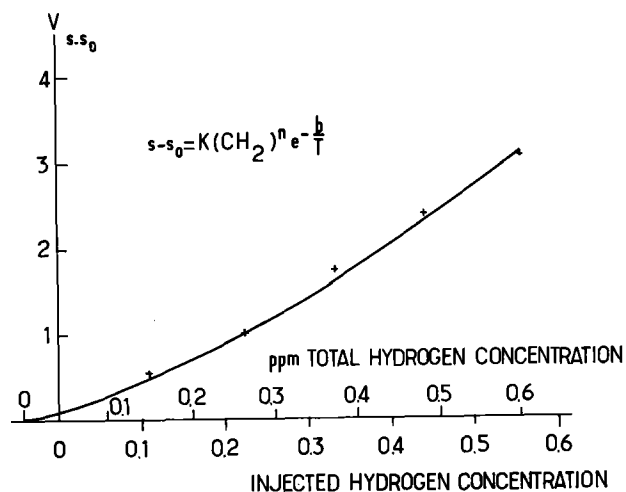


Fig. 2 - Spectrometer signal as a function of hydrogen concentration. Sodium temperature : 350 °C - Measurement at the evaporator outlet - Circuit 2.

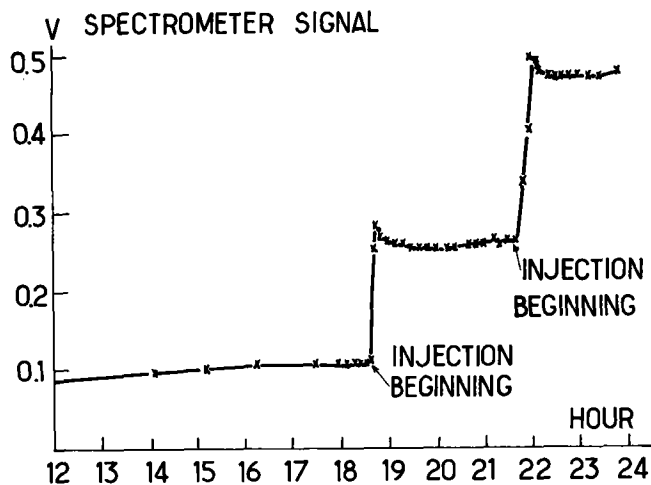


Fig. 3 - Spectrometer signal as a function of time during hydrogen injections - Sodium temperature : 414 °C - Measurement at the reheater outlet - Circuit 2.

When the sodium temperature is below 300 °C, the hydrogen concentration as measured by the evaporator-module measurement systems may take several hours to reach its equilibrium value. The measured value is also lower than that calculated from the known quantity of hydrogen injected. The effectiveness of the measurement installations (ratio of measured increase in concentration to calculated increase in concentration) is less than 60%. In addition to temperature, the sodium flow rate and the existence or absence of an interconnection between the storage tank and the expansion tank may affect the results.

Eleven injections of hydrogen were made during

isothermal operation at temperatures ranging from 150 to 250 °C; the pump speed ranged from 100 to 800 rpm and the storage and expansion tanks were interconnected in some cases and not in others. These injections were made into the same secondary circuit, either upstream of the steam generator or downstream of the superheater modules, after the residual hydrogen concentration had been reduced to its minimum value. The effectiveness of the measurement installations seems to be on the order of 40% between 150 and 160 °C, falls to approximately 15% between 160 and 190 °C, and recovers to 60% between 190 and 250 °C. The time taken to reach a stable concentration is on the order of one hour when effectiveness is low and several hours when effectiveness reaches 40%.

Temperature is the most important parameter, but the presence of argon spaces and the flow rate of the sodium also play a part, which could not be determined quantitatively, in explaining these results. Figure 4 shows a response curve with a sodium temperature of 150 °C.

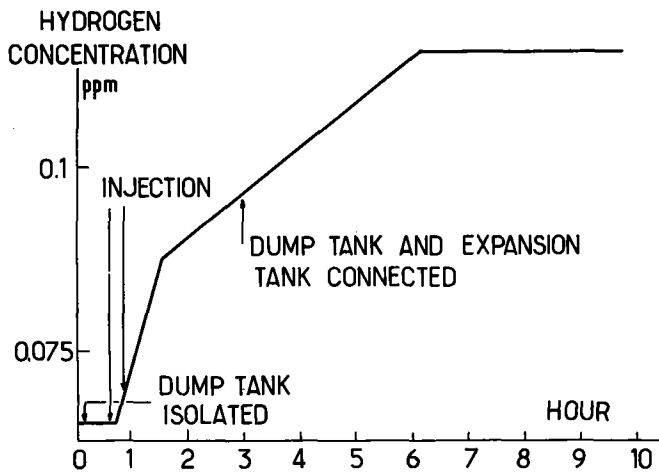


Fig. 4 - Hydrogen concentration as a function of time during a hydrogen injection - Sodium temperature : 150 °C - Pump speed : 200 rpm - Circuit 3.

MONITORING THE HYDROGEN CONTENT OF THE SODIUM

A leak is indicated when the hydrogen concentration in sodium as calculated by the computer reaches a threshold, S, which by experience we place at 0.02 ppm over the residual concentration.

The detection time includes : the time taken for the concentration to increase by 0.02 ppm,  $t_1$ ; the time taken by the sodium to traverse the steam generator and the sample extraction piping,  $t_2$ ; and the response time of the measurement system,  $t_3$ .

Let us consider the case of a leak in an evaporator module operating at rated power. To calculate

$t_1$ , we assume that the leak occurs instantaneously and that its flow rate is constant in time; we further suppose that the cold trap is operated at a flow rate of 20 m<sup>3</sup>/h with a cold-point temperature of 110 °C.

The value of  $t_1$  determined by assuming zero diffusion of the hydrogen produced by the sodium-water reaction give a step-wise curve in which each step corresponds to the time of transit of the sodium in the secondary circuit. Supposing instantaneous diffusion throughout the mass of the secondary sodium, we obtain a curve passing through the discontinuities of the foregoing curve. Since this second assumption gives pessimistic detection times, the corresponding curve will be used for theoretical estimates. At rated secondary flow rate (2657 t/h), the maximum time of transit of the sodium in an evaporator module is 19 s and the time of transit of sodium in sample extraction piping, independent of the secondary sodium flow rate, is approximately 26 s; this gives a maximum value of 45 s for  $t_2$ .

With 0.3 mm thick nickel tubes, changes in hydrogen concentration in sodium at 350 °C are detected with a lag of approximately 45 s; this is the essential component of measurement-system response time  $t_3$ .

Curve 1 of figure 5 shows detection time  $t_1 + 90$  s as a function of the rate of leakage.

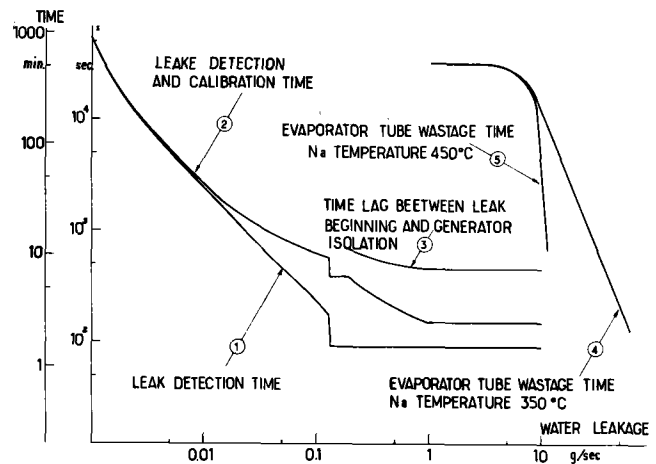


Fig. 5 - Time available for shutting down the reactor, in the event of water leak in an evaporator module.

When the hydrogen concentration of the sodium reaches threshold S, the computer calculates the slope of the concentration curve and compares it to linear functions representing leakage flow rates of 0.05 and 0.18 g/s. The limiting value of 0.18 g/s was chosen on the basis of experimental wastage results showing that damage to neighboring tubes was slight at this rate of leakage. The comparisons made are translated by the computer into signals displayed at the main control panel, and the operator must act as follows :

- if the estimated leakage flow rate is greater than 0.18 g/s, the display reports "serious leak" and the

steam generator must be shut down,

- if the estimated leakage flow rate is between 0.05 and 0.18 g/s, the display reports "moderate leak" and the operator has, in theory, enough time to operate the selector and determine which module is defective before cutting off the steam generator,

- if the estimated leakage flow rate is below 0.05 g/s, the operator monitors changes in concentration.

The time taken to deliver these signals is 300 s if the rate of leakage is less than 0.18 g/s; at higher values, it decreases to a minimum of one minute.

Curve 2 of figure 5 shows the sum of the theoretical times required to detect a leak and to estimate its flow rate.

To avoid unjustified steam generator shut-downs, the operator should wait for confirmation of a serious leak before acting. This confirmation comes within 5 minutes. In consequence, the total time to steam generator shut-down includes a leakage evaluation term which ranges from 6 to 10 minutes (curve 3).

This last curve should be compared to experimental wastage results giving the time taken for perforation of an evaporator target tube as a function of leakage flow rate (curves 4 and 5). The hydrogen detection system is effective in this case for leak having flow rates up to 10 g/s.

The cold traps of the secondary circuits are always in service to keep the hydrogen concentration in the sodium at a minimum.

The smallest detectable leak causes an increase of 0.02 ppm in the concentration at the end of a theoretically infinite time interval, with a flow rate of approximately 1 mg/s.

If a water leak is detected, the faulty module can be located by using the selector, provided that the difference between the hydrogen concentration in sodium, at the outlet of a sound module and the faulty module is at least 0.02 ppm. At rated secondary flow rate, the smallest rate of leakage, which allows to locate a faulty module, is 0.011 g/s.

So far, no leaks have been detected by the installations measuring the hydrogen concentration in the sodium.

DIFFUSION OF HYDROGEN ACROSS THE STEAM GENERATOR WATER TUBE WALLS

When the steam generators are in service, the reaction between the water and the iron of the tubes produces hydrogen that diffuses across the tube walls. This flow of hydrogen that diffuses across the thermal level, which must be higher than the diffusion threshold.

Before the reactor is started up, the residual concentration of hydrogen in the sodium of the secondary circuits depends on the operating temperatures

of the cold traps. After start-up, it increases because of the diffusion of hydrogen; the level it reaches depends on the cold-trap flow rate.

When the steam generators are operated at full power, it takes approximately 3 to 4 days for the residual concentration of hydrogen in the sodium to reach its equilibrium value. Figure 6 shows a typical curve, recorded on circuit no. 2 during a start-up. (The differences between the hydrogen concentration at the outlets of the evaporator, superheater and reheater are caused by calibration uncertainties, but remain practically constant with changes in concentration). Figure 7 shows changes in the hydrogen concentration during a 40% variation in reactor power starting from rated power; the mean temperature of the sodium fell approximately 30 °C between full rated power and 60%.

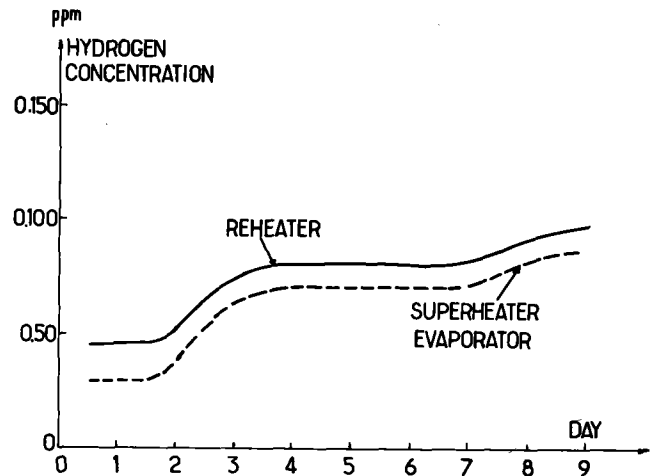


Fig. 6 - Hydrogen concentration level during steam generator start-up and full power operation. Circuit 2.

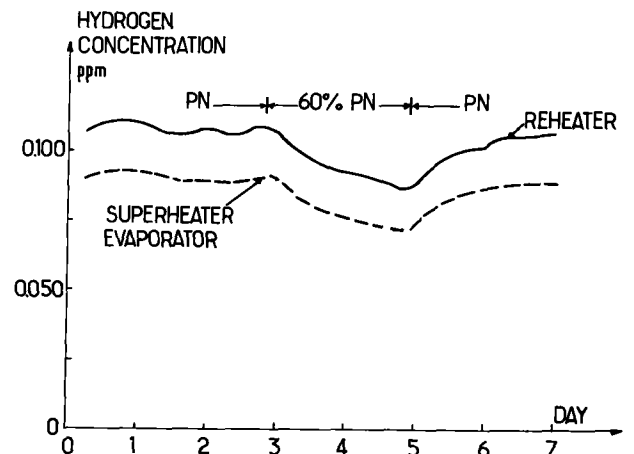


Fig. 7 - Hydrogen concentration level during power changes - Circuit 2 - Cold-trap : 10 m<sup>3</sup>/h flow rate, 107 °C temperature.

Rates of diffusion across steam generator tube walls are measured periodically by isolating the cold traps and measuring the increase in hydrogen concentrations for approximately 24 hours. These measurements suppose that the concentration was at equilibrium at the beginning of the 24 hour test. So far, they have been made at rated reactor power. Figure 8 shows typical changes in concentration as a function of time. With the purification system off, the curves showing the hydrogen concentration at the evaporator, superheater and reheater outlets are linear and parallel, differences between them being explained by calibration uncertainties. As soon as the cold trap is turned on, an immediate drop in the hydrogen concentration in the sodium can be observed.

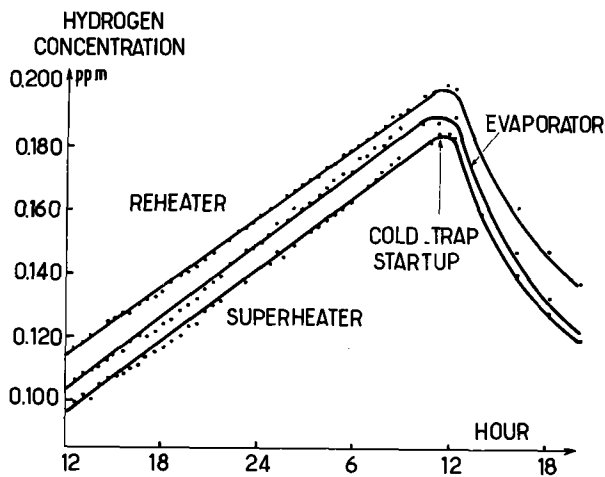


Fig. 8 - Hydrogen diffusion rate evaluation. Circuit 2.

The diffusion rates derived from these measurements are given in figure 9 as a function of full-power equivalent days. The mean rate per steam generator was 505 mg/h ( $0.7 \text{ mg/h/m}^2$ ) up to 80 days, then decreased to 250 mg/h ( $0.35 \text{ mg/h/m}^2$ ), a value at which there seems to be a plateau.

The evaporator modules are of ferritic steel containing 0.07% C, 2.25% Cr, and 1% Mo in the case of circuits 1 and 3 and ferritic steel containing 0.1% C, 2.25% Cr, 1% Mo, and 1% Nb in the case of circuit 2. The superheater and reheater modules are made of TP 321 steel. The diffusion rates obtained are for the total area of each steam generator. The diffusion rate of steam generator 2 is slightly lower than the two others, but no significance can currently be assigned to this difference.

CONSEQUENCES OF HYDROGEN DIFFUSION IN STEAM GENERATORS

After reactor start-up, hydrogen diffusion across steam generator tube walls causes an increase in hydrogen concentration just as if there was an equivalent leak. In Phenix, for example, when the cold trap functions at  $10 \text{ m}^3/\text{h}$ , the total increase in hydrogen concentration is approximately 0.058 ppm at the greatest

diffusion rate. The threshold of 0.020 ppm is thus passed; this means that the operator must periodically reset the thresholds of the various measurement channels, keeping differences always less than or equal to 0.020 ppm. Under these conditions, the hydrogen detection system retains its leakage detection capability unaltered. Moreover, the operator may check that changes in hydrogen concentration match the curves recorded during earlier start-ups.

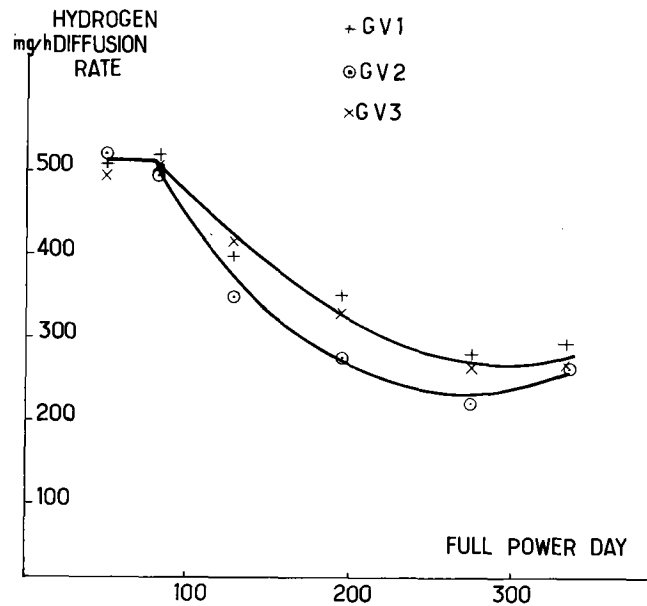


Fig. 9 - Hydrogen diffusion rates as a function of time in full power days.

The diffusion hydrogen forms a hydride that is stopped by the cold trap. The quantities of hydride so formed are large, requiring adequate purification equipment. During the first 334 full-power equivalent days, the weight of hydride collected by the cold trap in circuit number three, which had the highest measured diffusion rate, was approximately 73 kg.

From the quantity of diffused hydrogen given off by the reaction between water and iron, we can attempt to determine the wall thickness corroded inside the water tubes. In the case of Phenix, there is no way of measuring the respective diffusion levels in the evaporators (ferritic steel) and in the superheaters and reheaters (austenitic steel) separately. In addition, the measurements made provide no way of determining the amount of corrosion-produced hydrogen remaining in the water. The results of our calculations may therefore be below the actual values. Moreover, we calculate a mean value, but certain zones may be more corroded than others. Under these conditions, during the first 334 full-power equivalent days, mean corrosion thickness was  $26 \mu\text{m}$  if only evaporator area is taken into account, and  $12 \mu\text{m}$  if the total steam generator area is used ( $1 \mu\text{m} = 10^{-6} \text{ m}$ ).

# INTERNATIONAL CONFERENCE ON LIQUID METAL TECHNOLOGY IN ENERGY PRODUCTION

## CONCLUSION

The installations for measuring the hydrogen concentration of the sodium in the secondary circuits of Phenix operate with the anticipated characteristics. The data-processing computer derives concentrations from the spectrometer signals and hydrogen probe temperatures, and transmits to the operator signals enabling him to implement shut-down procedures if the hydrogen concentration in the sodium increases. In Phenix, there is no automatic control by concentration measurements. The flow rate of the smallest leak detectable is 1 mg/s. The smallest measurable variation in hydrogen concentration is 0.005 ppm. If, in an evaporator module operating at rated power, a leak with a flow rate of less than 10 g/s occurred, the sodium hydrogen measurement system should make it possible to shut down the steam generator before wastage resulting from the leak causes the perforation of nearby tubes. So far, no leak have been detected.

The corrosion of steam generator tube walls on the water side gives off hydrogen that diffuses across the tube walls into the secondary sodium. The diffusion rate is measured periodically at full reactor power by isolating the secondary cold traps. It fell from a initial value of 0.7 mg/h/m<sup>2</sup> (total steam generator area) to 0.35 mg/h/m<sup>2</sup> at the end of 334 full-power equivalent days. Hydrogen diffusion entails special procedures for monitoring steam generator tube water-tightness during reactor start-ups. The secondary cold traps of Phenix absorbed approximately 73 kg of sodium hydride during the first 334 full-power equivalent days.

## ACKNOWLEDGMENTS

The author would like to thank M. A. Lacroix and M. J. Viala of Phenix power station and M. G. Langlois of Technicatome for their contributions to the set-up of hydrogen detection systems and the hydrogen concentration measurements.

## REFERENCES

- 1 - L. DUCHATELLE, L. de NUCHEZE, and M.G. ROBIN - "Theoretical and experimental study of Phenix steam generator prototype modules" Nuclear Technology, Vol.24, pp.123-136 (November 1974)
- 2 - E. CABBILLARD, A. LACROIX, G. LANGLOIS, and J. VIALA - "Générateur de vapeur de Phénix. Mesure de la concentration d'hydrogène du sodium pour la surveillance de l'étanchéité des tubes d'eau-vapeur" I.A.E.A., I.W.G.F.R./1, Study Group Meeting on Steam Generators for LMFBR'S, Bensberg, October 14-17, 1974.

TABLE 1

PHENIX STEAM GENERATORS

	Module characteristics		
	Evaporator	Superheater	Reheater
Water or steam tube Tube o.d.x wall thickness mm	28 x 4	31.8 x 3.6	42.4 x 2
Vessel shell Shell o.d.x wall thickness mm	197.7 x 6.3	193.7 x 5.4	193.7 x 5.4
Heat transfer length m	60.78	26.88	21.85
Heat transfer area computed from tube i. d. m <sup>2</sup>	26.73	14.54	18.45
Material	2.25 Cr - 1 Mo <sup>o</sup>	TP 321	TP 321

<sup>o</sup> 2.25 Cr, 1 Mo and 1 Nb for the modules of steam generator no. 2.

# INTERNATIONAL CONFERENCE ON LIQUID METAL TECHNOLOGY IN ENERGY PRODUCTION

## EVOLUTION OF SODIUM PURIFICATION RAPSODIE PHENIX SUPER PHENIX

R. ABRAMSON, X. ELIE : CEA - CADARACHE J.M. SAUR, M. THEVENIN, F. VELIN : CIRNA - SACLAY - FRANCE

### SUMMARY

Fast reactors require large quantities of sodium. In order to reduce the initial purification period, special precautions are taken during fabrication, assembly, and the filling of storage facilities and tanks.

The operating experience acquired with RAPSODIE and PHENIX has enabled a good definition to be obtained of permanent purification features for future reactors.

### I INTRODUCTION

- 1 - A very high level of purity must be maintained for the liquid sodium. This applies to both the fluid in production factories and the fluid circulating in small experimental loops. In this way, the plugging of small tubes can be avoided, and the high temperature corrosion of steels used in the structures reduced.
- 2 - A series of precautions and rules have been established for RAPSODIE and PHENIX to maintain the cleanliness of sodium in tanks, storage facilities and circuits.  
Prior to this, special procedures were respected during the various construction stages, and start up tests (surface treatments, assembly of components under clean conditions, filling with sodium, transfer between different tanks and storages, purification and start-ups).
- 3 - The experience acquired enables the evolution and design of purification installations for large sodium cooled reactors to be predicted.

### II SUPPLY AND STORAGE OF SODIUM

- 1 - Industrial sodium contains about 450 ppm of calcium in metallic form : because of its reducing power, lime is formed at 500 °C leading to plugging risks at various places in the circuits.

The correct cooling of fuel pins can be prejudiced by packets of impurities in the assembly subchannels. The elimination of calcium and other impurities is carried out by the supplier, METAUX SPECIAUX, (P.U.K.) : oxidation of the calcium with sodium peroxide followed by several filtrations at low temperature results in a nuclear quality sodium ; an analysis of its composition has been performed ; this composition is compared to that of commercial sodium (figure 1).

SODIUM QUALITY		
Impurity analysis	Commercial ppm	Nuclear ppm
Calcium	450	5
Barium	15	< 5
Chlorine + Bromium	30	15
Carbon		24
Sulfur		20
Boron		< 5
Lithium		< 5
Silver		< 5

Figure 1.

Small quantities of oxygen and hydrogen are present ; Precise information is not given as oxygen and hydrogen form compounds with sodium, which are easily eliminated from the installations.

- 2 - Transport : 20 t fluid carrying trucks are used. In the case of PHENIX, 40 t of sodium were produced each week ; it was necessary to spread out delivery over 10 months, and to begin filling storage facilities, 18 months before putting sodium into the reactor.

## INTERNATIONAL CONFERENCE ON LIQUID METAL TECHNOLOGY IN ENERGY PRODUCTION

It is always necessary to envisage planning for the construction and installation of storage reservoirs before the rest of the plant.

As the size of the reactor is increased, increasingly larger storage facilities must be envisaged (see figure 2).

SODIUM QUANTITIES				
		Rapsodie	Phenix	Super Phenix
Thermal power	MW	20-40	600	3000
Reactor Vessel diameter	m	2,35	11,8	21
Weight of primary sodium	t	30	820	3250
Total useful storage	t	100	1200	5000
Total sodium supply	t	100	1520	5460

Figure 2.

3 - The partial or total draining of active tanks and storage facilities : reactor, active circuits, and storage drum will only take place very occasionally. In the case of PHENIX, draining can be carried out at low temperature (180 °C), vertical carbon steel tank having useful volumes of 88 m<sup>3</sup> being used for the purpose.

For economy measures, the associated measurements are minimized (single level measurement, three temperature measurements), and steam is preferred for the preheating.

The oxide traces and various impurities in suspension are eliminated by three consecutive filtrations.

4 - For cleanliness reasons, installation storage facilities are filled at 110 °C. In this way, the amount of dissolved impurity is minimized ; the transferred sodium contains less than 1 ppm of

dissolved oxygen (according to EICHELBERGER solubility curve).

5 - The PHENIX secondary circuits each have sodium storage facilities in the form of horizontal austenitic stainless steel tanks having useful volumes of 137 m<sup>3</sup>.

If an incident occurs, the sodium at 450 °C can be drained out in 16 minutes.

### III PRECAUTIONS DURING FABRICATION AND ASSEMBLY

1 - All tanks, storage facilities and stainless steel parts in contact with sodium are treated in order to minimize pollution effects during the temperature rise of the sodium.

The surface treatments of stainless steels consist of : degreasing, descaling, passivation, rinsing ; the pieces are dried and leaktight packed.

2 - The assembly of equipment and circuits is carried out under nuclear cleanliness conditions, i.e. precautions are taken in order to ensure that the insides of tanks and storage facilities are free from dust and filings...

For example, tubes are welded in a closed workshop provided with an airlock entrance. No other operations are carried out in this workshop. The elements and parts are not unpacked until the last moment. Stainless steel tools are used. Operations are performed by white coated personnel with clean gloves.

3 - Pressure and leaktightness tests are carried out. These tests are followed by flushing out with dry and cold nitrogen ; this flushing out is then performed under hot conditions during the circuit preheating tests. This process for eliminating oxygen and humidity is the only one possible for large volumes which cannot be put under vacuum. The nitrogen employed comes from a liquid nitrogen tank whose oxygen and humidity contents are less than 5 ppm.

The PHENIX vessel was flushed out with nitrogen in order to eliminate oxygen and humidity ; the vessel was, at first cold ; it was then preheated.

The fuel element storage drum was flushed out with



an amount of nitrogen equivalent to 10 times its volume ( $200 \text{ m}^3$ ). When the drum was filled with sodium, the following oxygen and humidity contents were obtained : 150 ppm and 320 ppm respectively. It is interesting to note that the humidity dropped to 50 ppm a few minutes after the drum was filled with sodium.

- 4 - The nitrogen was not replaced by argon until the storage facilities and tanks were filled with sodium.

The argon impurity contents currently observed in the roof of PHENIX are as follows :

O <sub>2</sub>	<	30	ppm
He	~	40	ppm
N <sub>2</sub>	~	700	ppm

IV INITIAL PURIFICATION OF PRIMARY SODIUM

- 1 - In spite of all the precautions taken some impurities remain (principally oxygen and hydrogen occluded in material surfaces).

When the temperature of the sodium in the vessel and secondary circuit is raised, during precriticality tests, these impurities are transformed into sodium compounds, oxides, and hydrides.

- 2 - The initial purification of sodium in the PHENIX reactor was performed at  $20 \text{ m}^3/\text{h}$  using a cold trap with a nominal  $30 \text{ m}^3/\text{h}$  flow. The inlet temperature of the cold trap was fixed at  $190 \text{ }^\circ\text{C}$  using an exchanger-economizer ; the cold point of the trap was successively lowered to  $110 \text{ }^\circ\text{C}$ . Control of purification was carried out with the aid of plugging meters :

- . a discontinuous cyclic type giving a lower plugging temperature constantly less than  $140 \text{ }^\circ\text{C}$ .
- . a continuous type giving an upper plugging temperature constantly less than  $240 \text{ }^\circ\text{C}$ .

Plugging temperature measurements made at the cold trap outlet during maximum flow operation yielded a lower plugging temperature similar to the temperature of the trap cold point. This demonstrates the very high efficiency of this equipment for the elimination of impurities at the lower plugging temperature. Unfortunately, its performance is

only mediocre for impurities at the higher plugging temperature. Nevertheless, these impurities form deposits less easily and behave differently to the other impurities. The rapid increase in plugging temperatures observed when the temperature of the sodium exceeds  $250 \text{ }^\circ\text{C}$ , and above all  $300 \text{ }^\circ\text{C}$ , confirms a known phenomenon.

From  $350 \text{ }^\circ\text{C}$  onwards, most of solubilization of impurities has terminated as plugging temperatures exhibit stabilization tendencies.

- 3 - In the PHENIX primary circuit, an area of  $12\,000 \text{ m}^2$  of stainless steel is in contact with sodium ; it is estimated that the impurities to be removed consist, essentially, of oxygen and a little hydrogen released from air and water vapor occluded in material surfaces.

If the hypothesis that oxygen is the main cause of initial sodium pollution is accepted, then the plugging meter results indicate that approximately  $2 \text{ g/m}^2$  of oxygen are eliminated by the initial purification (see EICHELBERGER oxygen solubility curve).

This value is currently used as a reference for studies concerning the design of initial purification installations for this type of reactor. Figure 3 shows that the active purification phase associated with sodium temperature rise tests (PHENIX) lasts 45 days.

PHENIX FIRST PRIMARY SODIUM PURIFICATION

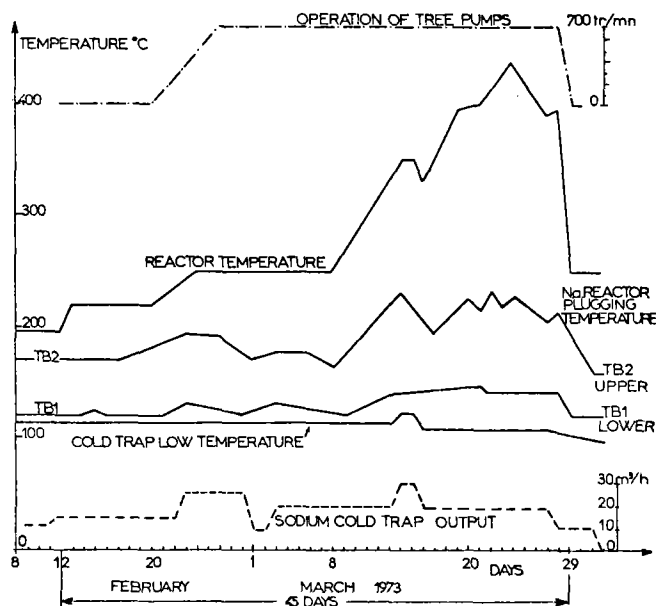


Figure 3.

V

PERMANENT PURIFICATION OF  
PRIMARY SODIUM

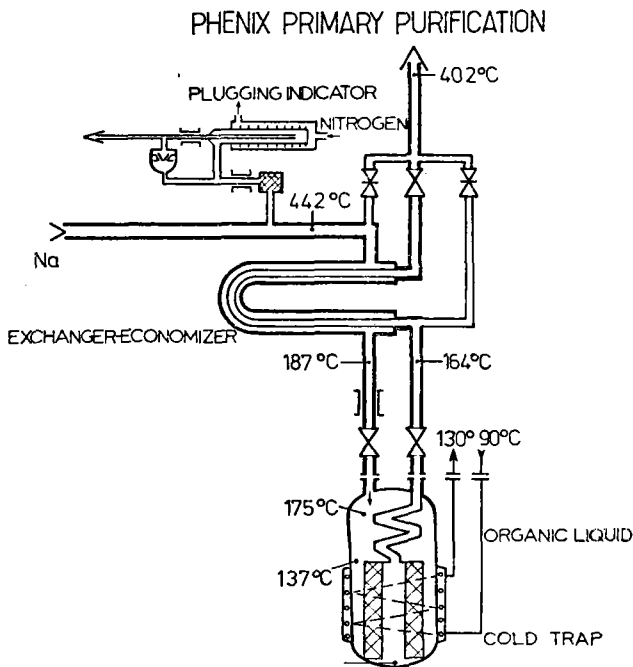
1 - During permanent operation, the likely causes of primary sodium pollution in the reactors : RAPSODIE and PHENIX are reduced to a minimum :

- . the cover gas is maintained at a pressure of 20 mb in excess of the surrounding atmospheric pressure.
- . the argon or helium (RAPSODIE) in the roof of the reactor is passed through NaK bubblers in order to remove oxygen and humidity traces.

The sodium purification flow rate for RAPSODIE and PHENIX during operation was reduced to half that initially envisaged i.e.  $2 \text{ m}^3/\text{h}$  (RAPSODIE) and  $18 \text{ m}^3/\text{h}$  (PHENIX).

The temperature of the cold point in the PHENIX trap is maintained in the region of  $109 \text{ }^\circ\text{C}$ .

The nominal operational point for the trap is defined in Figure 4 (currently accepted value).



NOMINAL OPERATING POINT March 1976

Figure 4.

The lower plugging temperature is less than  $110 \text{ }^\circ\text{C}$ . The upper plugging temperature is maintained at  $190 \text{ }^\circ\text{C}$ .

2 - During shut-down, pollution results from periodic fuel handling operations, and from special component handling operations.

In the case of RAPSODIE, experiments were performed during 1972 and 1973 in order to evaluate the sources of primary sodium pollution. The following conclusions can be drawn :

- . the pollution brought about by impurities in the argon used to flush out the handling flasks is negligible (Gas analysis yields the following results :  $5 \text{ ppm O}_2$  and  $5 \text{ ppm H}_2\text{O}$ ).
- . the main source of pollution (oxygen and water vapor) is probably due to air leaks of the order of 10 l/day resulting from the coupling and uncoupling of flasks and connecting parts and the introduction of surfaces cleaned after each handling campaign, but exposed to air during immersions and withdrawals from the sodium (case of gripping device sheath which passes alternatively from sodium into argon and then air during its passage across the scraping device).
- . the pollution introduced by newly immersed parts (fuel assemblies) obviously varies with the state of their surfaces, but is small (of the order of  $1 \text{ gr/m}^2$ ).
- . this pollution of the primary sodium does not manifest itself until a temperature of  $350 \text{ }^\circ\text{C}$  is reached during the temperature rise phase ( $180$  to  $400 \text{ }^\circ\text{C}$ ) preceding criticality.

In the case of PHENIX, improvements to the fuel handling system have greatly reduced the causes of pollution ; these causes arise, essentially, from argon in the lock and to a lesser extent from the introduction of fresh fuel.

Purification is discontinued during periodic handling in order to allow the visus to function correctly ; in this way a plugging temperature lower than that which can be measured is obtained during the rise in temperature phase of the primary circuit.

3 - Dismantlable traps have been provided for RAPSODIE and PHENIX. No trap handling equipment has yet

been constructed for PHENIX as the lifetime envisaged for its components is greater than 10 years. One of RAPSODIE's cold traps is employed for purification during start-up, and the other, for trapping active impurities.

A single cold trap has been operating in PHENIX over the past 2 years.

During the operation of PHENIX, the purification was stopped. It was observed that the lower plugging temperature remained less than 110 °C, while the upper plugging temperature rose from 190 °C to 240 °C in 15 days. It seems that the primary sodium is permanently polluted.

VI EVOLUTION IN THE DESIGN OF PRIMARY PURIFICATION CIRCUITS

1 - The mass of sodium contained in pool type reactor vessels increases with reactor power (PHENIX : 820 t, SUPER PHENIX : 3250 t). The problems associated with the supply and storage of sodium are becoming increasingly complex. Nevertheless, in relation to volume, sodium/atmosphere interfaces and wet steel surfaces are smaller. Purification requirements should thus be less constraining.

2 - In the case of SUPER-PHENIX, the experience already acquired has led to the decomposing of purification operations into two stages :

. initial purification,

In SUPER-PHENIX, an area of 45000 m<sup>2</sup> is in contact with sodium. In PHENIX, an area of 12000 m<sup>2</sup> is in contact with sodium.

The results acquired with PHENIX indicate that in the initial purification circuit, a flow rate of 60 m<sup>3</sup>/h is sufficient.

This start-up purification circuit will then be used to purify sodium in the fuel element storage drum.

. permanent purification,

Because of the large mass of sodium in SUPER PHENIX, the plugging temperature following special handling of large components will constantly be less than 150 °C. This temperature is not considered to be a constraint for the operation of the pumps. It is possible to carry out permanent purification with relatively small flow rates ; a flow rate of 10 m<sup>3</sup>/h is envisaged

for SUPER-PHENIX.

As the diameter of pool type reactor vessels increases (PHENIX : 11.8 m and SUPER PHENIX : 21 m), it becomes increasingly possible to locate purification assemblies on residual surfaces between large components fixed to the slab (for SUPER PHENIX two 1500 millimeter overall diameter assemblies are envisaged).

This purification is performed by a circuit integrated into the reactor and slab which consists of :

- a cold trap (useful volume : 1.2 m<sup>3</sup>), which can be dismantled independently, provided with a nitrogen blower (15 bars).
- a d.c. electromagnetic pump (flow 10 m<sup>3</sup>/h) for the sodium,
- a valve operated exchanger-economizer.

Both these assemblies can be dismantled using special hoods constructed before the start-up of the reactor.

Two integrated 50 l/h plugging meters are used to measure the degree of purity.

3 - The design adopted for SUPER-PHENIX will certainly be retained for future large reactors. Efforts will be made to reduce the cost of initial purification.

VII SPECIAL SECONDARY CIRCUITS PROBLEMS

1 - Initial purification for PHENIX

The secondary circuits were assembled under nuclear cleanliness conditions.

Nuclear quality sodium was supplied. It was filtered on arrival at the plant.

Purification during storage at 190 °C enabled the purification circuits to be tested.

Two plugging temperatures (110 °C and 180 °C) were observed for the first temperature increase stage (200 °C to 450 °C).

The initial purification time was approximately 1 day.

It was not possible to determine the nature and the quantities of the trapped impurities.

The steam generators led to a permanent contamination as soon as they were put into service.

## 2 - Normal operation of PHENIX

The purification of each of PHENIX's secondary loops is absolutely necessary because of the hydrogen diffusion across the walls of the steam generator.

This hydrogen is released during the formation of magnetite by the action of water on iron inside the tubes carrying water.

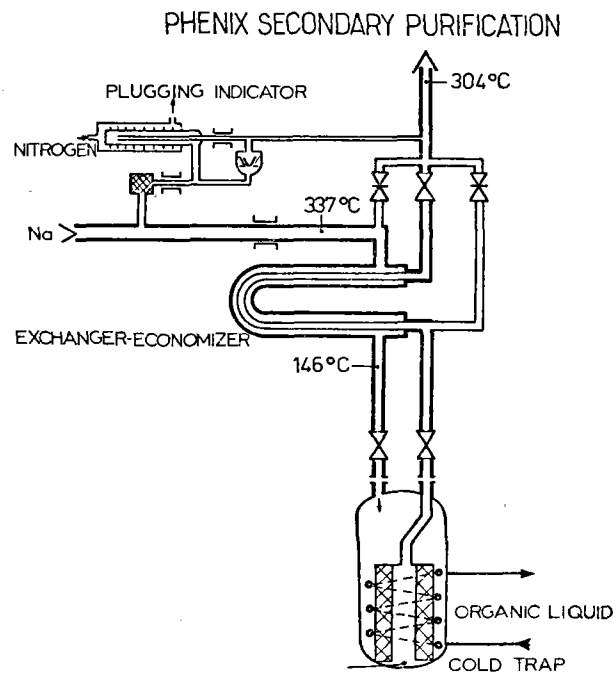
The equilibrium diffusion of hydrogen is in the 220 mg/h to 250 mg/h range.

This level of hydrogen is sufficient to be detected by the detectors at the basic threshold level.

The purification flow is  $10 \text{ m}^3/\text{h}$  and the cold point of the trap is  $106^\circ\text{C}$ . The lower plugging temperature is less than  $110^\circ\text{C}$  and the upper plugging temperature greater than  $190^\circ\text{C}$ ; it appears that fluctuations in the lower plugging temperature are directly dependent on hydrogen diffusing across the steam generator.

Thus, it is concluded that the lifetimes of secondary cold traps are less than those of primary cold traps.

In consequence, it is considered desirable for economic reasons to place the exchanger-economizers outside the cold trap. However special operating conditions require that a certain minimum area of the exchanger - economizer be inside the trap. This is not the case for PHENIX (see figure 5).



NOMINAL OPERATING POINT March 1976

## 3 - Special purification

- a) In the case of a sodium-water reaction, the hypothesis of secondary sodium pollution leading to a plugging temperature of  $380^\circ\text{C}$  (SUPER-PHENIX) is put forward. The same cold trap should also be capable of operating with a high flow rate at high temperatures, if it is to rapidly eliminate sodium-water reaction products from the circuit, while at the same time reducing plugging risks due to the precipitation of dissolved products.
- b) During the servicing of one of PHENIX's loops, a large amount of air was accidentally admitted through two openings, one situated at the bottom and the other at the top. When the reactor was restarted, the sodium was subjected to purification; the sodium remained saturated for 5 days at a temperature of between  $150$  and  $180^\circ\text{C}$ ; the temperature of the sodium was then brought up to  $340^\circ\text{C}$  in two days, the corresponding plugging temperature being in the region of  $110^\circ\text{C}$ . This servicing incident nevertheless necessitated 7 days purification.

- 4 - Large purification equipment will be required for the secondary circuits of future large reactors, because maintenance operations put large surfaces in contact with air, and because considerable pollution could result from a sodium-water reaction.

VIII

CONCLUSION

There is no need to emphasize the importance of sodium purity in ensuring the high performance of nuclear installations and fuels in fast sodium cooled reactors.

Extensive precautions will have to be taken in the construction and design of primary and secondary sodium purification equipment.

Satisfactory results have already been obtained by the operating teams of RAPSODIE and PHENIX. The results of studies and tests currently being carried out in the framework of the SUPER-PHENIX project will be helpful in designing future fast reactors.

# INTERNATIONAL CONFERENCE ON LIQUID METAL TECHNOLOGY IN ENERGY PRODUCTION

## DISCUSSION

Paper I-1: "Some Aspects of Sodium Technology Issued from the Operating Experience of Rapsodie and Phenix"

J. McCown: Did the gradual buildup of  $^{137}\text{Cs}$  occur in Phenix and, if so, did it begin before or after fuel failure?

J. Kremser: Although  $^{137}\text{Cs}$  activity increases slightly with time, we have neither established any connection with the gas leak nor the time of initial increase. It should be noted that a gas leak, not a fuel failure, occurred and that  $^{137}\text{Cs}$  activity was very low, near the detection limit, at the time the leak appeared.

J. McCown: Have the holes on the FFL plug stripper become clogged; and what is the clogging substance?

J. Kremser: While clogging did occur, the location and substance have not been determined.

K. Stade: Do you have experience with cleaning and re-qualifying loaded primary cold traps?

J. Kremser: No, to date only one cold trap is in operation at each site and neither has required a change. Presently we have no procedure for a blocked cold trap that has been replaced.

C. Allan: Was the  $110^\circ\text{C}$  plugging temperature you report at Phenix recorded by the plugging meter in the automatic or the manual cooling scan mode? In our experience, the manual mode yields slightly lower results.

J. Kremser: The  $110^\circ\text{C}$  plugging temperature was recorded by both modes and no difference in results has been observed.

K. Phillip: Did failure of 304/321 valve weld result from use of sodium; or would material with the given metallurgical state and heat treatment have failed in any environment?

J. Kremser: We believe that sodium had no effect and that failure would occur in any environment.

Paper I-2: "Sodium Technology at EBR-II"

C. Allan: Could the cold trap efficiencies of 50 percent for oxide and 5 percent for  $^{131}\text{I}$  be due to low levels in the circuit, i.e., 1 to 5 ppm oxygen and less than 1 ppm total iodine?

W. Olson: For  $^{131}\text{I}$ , oxygen and hydrogen, low effectiveness may be attributable to low concentrations. From source-rate studies we can only conclude that hydrogen is trapped more effectively than oxygen and that the primary cold trap, which operates at higher velocities, is more effective than the secondary trap. Both are consistent with the theory that trapping efficiency is diffusion limited.

Paper I-3: "Impurity Deposition in PFR Plugging Meters and Cold Traps"

B. Grundy: In discussion of your mass transfer equation, you mentioned that the exponent  $n$  was equal to 2, although you noted that in similar work it is usually assumed that  $n = 1$ . In connection with cold trap precipitation work I think that data can be accounted for with  $n = 1$ . It is implied with  $n = 1$  that deposition rate is mass transfer or diffusion rate controlled, and  $n$  approaches 2 when a reaction rate is controlling. Is there any implication in your work that chemical interactions might be taking place in the plugging meter orifice?

C. Allan: I agree with the interpretation that  $n = 1$  implies mass transfer control in the sodium phase and  $n = 2$  probably indicates that surface deposition is the rate controlling step. Use of  $n = 1$  has had only variable success in application to cold traps, but it is definitely possible that the rate controlling steps might be different in plugging meters and cold traps. For instance, impurity nucleation into suspended particles followed by momentum transfer induced deposition might explain the heavy deposition in the inner annulus of the mesh in the PFR trap.

PFR plugging meter data suggest that no interactions occur in the orifice unless the reduction of undercooling bias in the manual mode is due to such an effect.

H. Borgstedt: Have you detected sodium carbonate while analyzing the contents of your cold traps?

C. Allan: No, we did not analyze for carbonate, but only for Na,  $\text{Na}_2\text{O}$ , NaH NaOH and trace metals.

W. Olson: Have you detected plugging temperatures attributable to impurities other than oxide and hydride?

C. Allan: No, these would be evident only in the manual mode of operation, and interpretation of data is rather subjective. Although deposits of three or more impurity species have been reported in the plugging meter orifices, I have seen no definite evidence in the PFR plugging meter records of more than two breaks in the flow curves.

C. McPheeters: How did you determine the mass of the impurity deposits in the plugging orifice to determine the mass transfer coefficients? In my experience, this calculation involves some difficult assumptions regarding the density and geometry of the deposit.

C. Allan: The geometry problem did not arise since only a small percent of the impurity entering the plugging meter orifice was deposited. To eliminate the deposit density problem, the mass transfer coefficient  $k$  was replaced by  $k/fv$ , where  $fv$  is a constant void fraction in the rate analysis.

Paper I-4: "Radioactive Product Behavior in Sodium-Cooled Reactors of the U.S.S.R"

## INTERNATIONAL CONFERENCE ON LIQUID METAL TECHNOLOGY IN ENERGY PRODUCTION

H. Stamm: Were BR-5 and BOR-60 run at the same temperature during your degassing experiment or are the different degassing rates the result of different sodium temperatures?

N. Krasnoyarov: Although temperature dependence is a possibility, temperature in this case remained in a range from 200 to 300°C, and the change in degassing rates resulted from different conditions in the sodium-argon boundary.

H. Stamm: While you ran BOR-60 with tight fuel elements, you found some  $^{134}\text{Cs}$  in the primary coolant. Was the origin of this radionuclide a Cs contamination of your sodium?

N. Krasnoyarov: Yes.

J. Kremser: Have you experienced fuel failures with BN-350 and, if so, how did you manage them?

N. Krasnoyarov: There has been no fuel failure in BN-350; the results I presented were obtained with fuel contamination on the cladding surfaces.

J. Kremser: What are your plans in the event of fuel failure? How long do you expect to restrict it to the core and thus avoid sodium and sodium circuit contamination problems?

N. Krasnoyarov: If fuel failure occurred, the sub-assembly would not be reloaded immediately, and contamination would increase. Because it is necessary to limit contamination, we are developing an instrument to measure the level during operation.

G. Subbaraman: Can you estimate the magnitude of fission-gas pressure within the fuel element?

N. Krasnoyarov: The pressure can reach up to 40 atmospheres.

Paper I-5: "Activity Deposition in DFR Cold Traps"

W. Kuhn: You mentioned that  $^{54}\text{Mn}$  activity in the cold trap was minor. Can you estimate what fraction of the released  $^{54}\text{Mn}$  transports to the cold trap?

C. Allan: We have not been successful in estimating inventories, largely because of the masking effect of the fission products.

M. Adamson: You mentioned that fissile material collected in the cold traps was in particulate form. What evidence do you have and what size are the fuel particles?

C. Allan: Sampling of DFR coolant for fissile material and deposition experiments with fissile material in DFR and in a 30-kg sodium loop show that blank values are always of similar magnitude to the total fissile material content of the samples and depend on sodium immersion time. This result can be interpreted with simple first order time dependence, especially in the initial period of deposition. Particle deposition statistics that use

sticking-leaving probabilities are helpful, and our loop work suggested particle sizes on the order of 1-10  $\mu\text{m}$ , with up to 50  $\mu\text{m}$  suggested in some DFR sampling. Particles tend to rapidly degrade in sodium or NaK.

R. Villarreal: How many grams of NaI did you find in the cold trap you analyzed, and why do you attribute your findings to solubility?

C. Allan: By using the Sandell-Kolthoff method of chemical analysis, from 22 to 75 mg NaI were found. Less than 2% of the activity found could be attributed to a partition mechanism using our partition coefficient K values, although co-precipitation may have assisted collection.

INTERNATIONAL CONFERENCE ON LIQUID METAL TECHNOLOGY IN ENERGY PRODUCTION  
METALLURGICAL PROBLEMS ASSOCIATED WITH LARGE SODIUM LOOP OPERATIONS

N. J. Hoffman  
Liquid Metal Engineering Center  
Canoga Park, CA 91304

ABSTRACT

Sodium loops have had many years of successful operation throughout the world. There are certain phenomena occurring during operation of these loops that are of interest to the metallurgist. In this paper, a number of these phenomena are discussed in terms of problems and their solutions. The problems are discussed in the areas of cleaning and refilling of a loop, friction, mass transfer, aging effects, energy transfer, and metallurgical aspects in loop design, construction, and maintenance.

INTRODUCTION

Six aspects of large sodium-loop operation of particular interest to metallurgists are discussed:

- 1) Cleaning loops and refilling them with sodium.
- 2) Rubbing surfaces in contact under sodium.
- 3) Mass transfer of atoms through sodium.
- 4) Aging of structural alloy after long times at temperature.
- 5) Energy transfer through sodium associated with structural metal failure.
- 6) Metallurgical aspects in loop design, construction, and maintenance.

These areas of interest are considered in detail in the following sections.

CLEANING AND REFILLING LOOPS WITH SODIUM

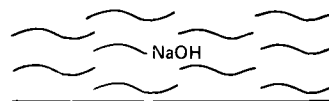
Caustic Stress Corrosion Cracking

When a sodium loop is drained, a film of sodium is retained on the walls of a system that has been wetted. In unwetted loops, the walls retain droplets of sodium. This remnant sodium can be removed by distillation, steam cleaning; solvent flushes, or combinations of the above. If no cleaning action is taken, air-exposed sodium reacts with the moisture and CO<sub>2</sub> in the air to form sodium hydroxide, hydrated sodium hydroxide, aqueous solution of sodium hydroxide (caustic solution), caustic solution crusted over with a sodium carbonate hydrate, and eventually a dry powder mixture of various sodium carbonate hydrates.

During the time that an aqueous solution of sodium hydroxide is in contact with the structural alloy of the loop, one of the conditions required for caustic stress corrosion cracking (SCC) is satisfied. Other pre-

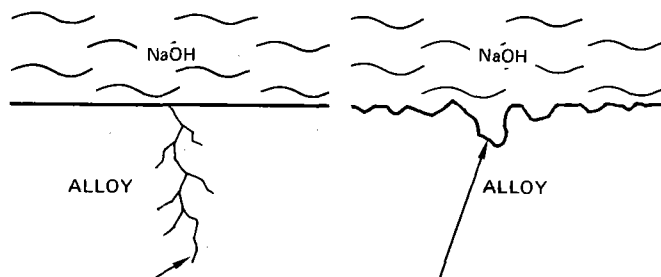
requisites for caustic cracking include very high stress, apparently near  $\sigma_y$ , and a specific temperature range for the alloy under consideration. A weld that is not stress-relieved provides a site for sufficient residual stress.

Caustic cracking appears to be associated with a plastically-flowed volume of metal at the tip of a very sharp crack. This volume of metal presents a relatively very small, highly anodic area within a large cathodic area. If general corrosion is significant, the crack tip blunts and caustic SCC is alleviated. If the caustic solution is at high temperatures and high concentrations of caustic, the crack tip can be blunted by crack wall corrosion (Figure 1). Thus, welds of each alloy that are not stress-relieved may have a unique temperature - caustic concentration range that is dangerous. For austenitic stainless steels, the dangerous temperature range for a system under about 1 atm of total pressure is 120 to 177°C (250 to 350°F). For



ALLOY

a. REGIME OF LOW-TEMPERATURE,  
LOW-NaOH CONCENTRATION



CRACK VERY THIN WITH  
VOLUME OF YIELDING  
ALLOY AT TIP OF CRACK  
ANODIC TO CRACK WALL

CRACK WALL CORROSION  
RESULTING IN WIDE, FINGER-  
LIKE DISSOLUTION PATHS  
RATHER THAN THIN CRACK

b. REGIME OF TEMPERATURE  
AND NaOH CONCENTRATION  
THAT ALLOWS SCC

c. REGIME OF HIGH-TEMPERATURE,  
HIGH-NaOH CONCENTRATION  
THAT ALLOWS PITTING BUT  
NOT SCC

Figure 1. Crack wall corrosion.

Session II A - Loop Operations  
Chairman: C. C. Conners (LMCC)



INTERNATIONAL CONFERENCE ON LIQUID METAL TECHNOLOGY IN ENERGY PRODUCTION

ferritic steels, the temperature range is 80 to 107°C (175 to 225°F). At higher total system pressure, the upper temperature limit is higher. The temperature range is associated with an NaOH concentration range in aqueous solution. This is illustrated in Figure 2, which includes the boiling point curve for aqueous NaOH at 1 atm total pressure.

The curve shown in Figure 2 does not show a time axis. If a contaminated loop is heated slowly enough, evaporation can concentrate an aqueous pool of NaOH to high concentrations without entering the caustic SCC regime. If heated fast enough, it can pass through the SCC regime rapidly enough to avoid any damage other than almost negligible intergranular attack (Figure 3). For austenitic stainless steel, ~25°C/h appears to be a fast enough heatup rate for loop piping. For 2-1/4 Cr - 1 Mo with a ferrite-plus-pearlite structure and for 1008 carbon steel, a rate greater than ~1°C/h appears to be sufficiently fast to avoid problems.

For each alloy, a hold in the critical temperature ranges should be avoided in contaminated systems. The ability of a loop operator to avoid such holds depends on the number and distribution of controllers on the trace heaters of the loop piping. Pipes full of sodium are quite easy to keep at the correct temperature, but drained piping requires careful electrical design. When refilling a contaminated system with sodium, heaters must not only have enough controllers but must also be capable of heating piping fast enough through critical temperature regimes. The above

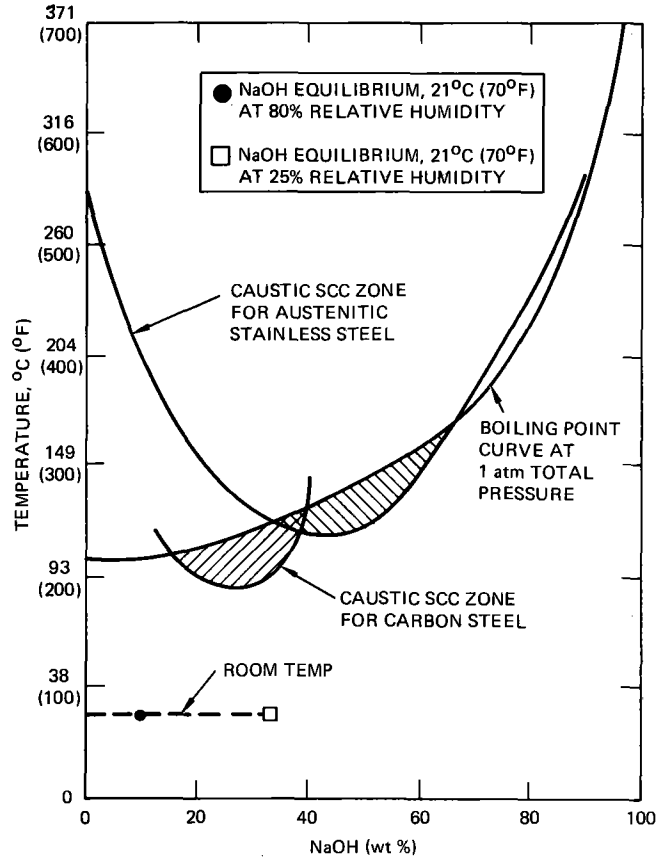


Figure 2. Boiling point curve for NaOH.

considerations are important only when a sodium-contaminated loop is to be refilled with sodium.

Theoretically, caustic SCC may also occur during cooling of a loop that has suffered a water leak into

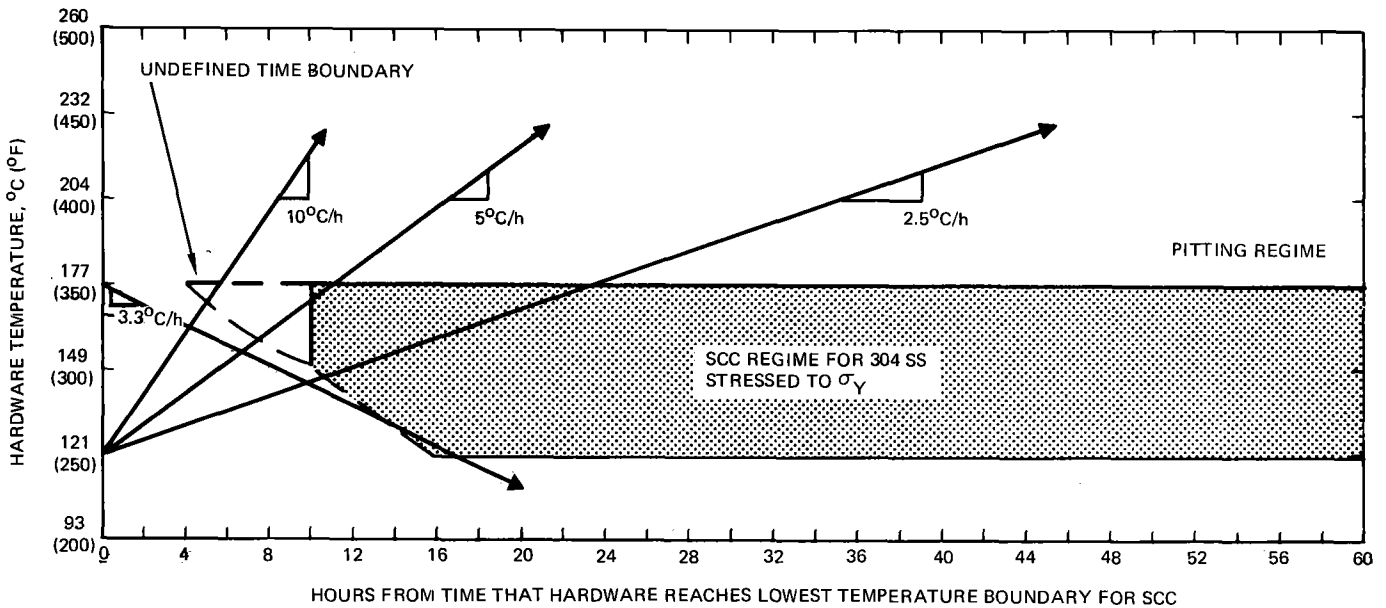


Figure 3. Heatup through critical range.

the sodium. Cooling of piping made from 300 series stainless steel may well be slow enough through the critical 120 to 177°C (250 to 350°F) range (Figure 2), but enough water vapor must be present to assure that a sufficiently dilute solution of sodium hydroxide is present adjacent to a weld.

#### Chloride Stress Corrosion Cracking from Pipe OD

Austenitic stainless steels are susceptible to halide, particularly chloride, stress corrosion cracking. Unlike the case for caustic SCC, ferritic steels are immune to halide SCC. Sodium loops often operate in temperature regimes which cause chromium carbide to precipitate out in grain boundaries of austenitic stainless steel. The resultant chromium depletion adjacent to the grain boundary causes the austenitic stainless steel to become more sensitive to both intergranular corrosion and chloride SCC. Austenitic stainless steel that has been sensitized may suffer chloride SCC even at room temperature.

For unsensitized stainless steel, temperatures from 80°C (170°F) to the boiling point of water appear to be required. Stress is again a prerequisite, but at levels far below that required for caustic SCC. Water droplets evaporating from the outside of piping as a system is heating up for a sodium fill are usually the main sources of the chloride SCC.

#### System Cleanup

When water in the form of steam or fog is used to clean up a system, the time at temperature is critical. Again, 120 to 177°C (250 to 350°F) is the critical range for austenitic stainless steel and a few hours of accumulated time in this range is the maximum permissible.

Dowanol or alcohol cleaning is often used, occasionally with acetic acid and water additions. A water rinse somewhere in the cleaning cycle is usually required to completely eliminate sodium from surfaces.

Sodium flushes can also be used to clean up an air-contaminated sodium loop. If the loop has been opened to air at some period weeks prior to the cleanup, the sodium film or droplets have probably been converted to some form of sodium carbonate. Such species dissolve too slowly in sodium at temperatures under 600°C (1115°F) to utilize straight dissolution as the cleanup method. Fortunately, when the sodium wets the walls, the sodium carbonates will wash off the walls and be transported in the sodium as undissolved powder. Cold traps that are partially filled with sodium oxide and sodium hydride will easily filter out this powder.

When the contaminant on the loop walls is sodium oxide or sodium hydride, straight dissolution into the sodium and subsequent cold trapping will clean up the system.

#### Refilling with Sodium

When sodium is flowed into a contaminated system, either as a cleaning step or as a refill, the sodium at loop temperature can be saturated with hydrogen, oxygen, or both. Solid Na<sub>2</sub>O or NaH or a mixture of the two may precipitate out at any part of the loop that is slightly cooler than another part. When a system is supersaturated, unwanted precipitation can occur where the boundary layer is thin, such as in a high-velocity part of the loop or at a bend in the piping.

Heat exchanger tubing in a loop is particularly susceptible to problems of saturated or supersaturated flowing sodium. Suspended carbonate particles can coat the upstream face of an oxide or hydride precipitate, making subsequent dissolution very difficult once complete blockage of a passageway is encountered. If the loop temperature is raised to bring the sodium temperature above saturation, the saturated sodium must pass through a temperature range where a few degrees drop in temperature causes a large amount of sodium oxide and/or sodium hydride to precipitate out. The best technique is to clean up the sodium before circulating through a heat exchanger. If a loop must be operated with saturated sodium, steady cold-trapping with a minimum flow of the bulk sodium may be used.

#### RUBBING SURFACES IN CONTACT UNDER SODIUM

Rubbing parts may produce high friction in sodium. Under certain circumstances of oxygen content and temperature, the equilibrium surface of an alloy may be bare metal rather than metal oxide or sodium metalates (Figure 4).

Bare metal rubbing against bare metal may produce high friction; however, NaCrO<sub>2</sub> may be used as a lubricant. Ductile, face-centered-cubic (FCC) alloys tend to suffer adhesive wear and exhibit high dynamic friction. Carbides and aluminides tend to have low dynamic friction. Hardfacing alloys are used when low wear is required, but these may have high friction. Diffusion bonding or self-welding can also be a severe problem. FCC alloys seem to be particularly susceptible to this phenomenon. Grains of alloy may be leached or pulled out of a metal surface (Figure 5) and lodge between two rubbing surfaces.<sup>(1)</sup>

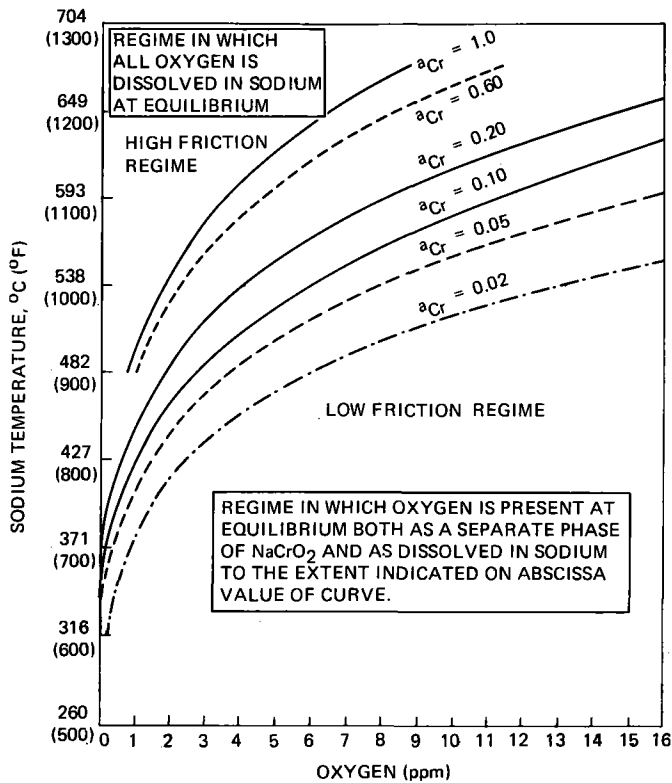


Figure 4. Temperature vs oxygen content, showing regimes of bare metal.

These grains can either be plastically deformed or serve as plows that scratch the rubbing surfaces. In either case, forces are generated that oppose motion, combining with the dynamic friction force. If all the forces together are great enough to stop the motion, seizing has occurred. Since dissolution of grain boundaries into sodium is a real phenomenon for many alloys and dynamic friction in sodium is often high, seizing can be a real problem for sliding surfaces immersed under sodium.

MASS TRANSFER OF ATOMS THROUGH SODIUM

Substitutional Atoms

Dissolution of a structural alloy into sodium and consequent deposition of the atoms of that alloy at other sites in the loop can be a problem. The equation shown below is a great help in evaluating the parameters that affect this mass transfer when the bulk sodium is being thoroughly mixed by convection. (2)

$$t \text{ to reach } c = -\frac{\Delta}{D} \frac{V_{\text{liquid}}}{A_{\text{solid liquid}}} \ln \frac{1 - c/c_{\text{sat}}}{1 - c_0/c_{\text{sat}}}$$

where

$c$  = concentration at time,  $t$ , where  $c = c_0$  when  $t = 0$  (any units)

$t$  = time in seconds

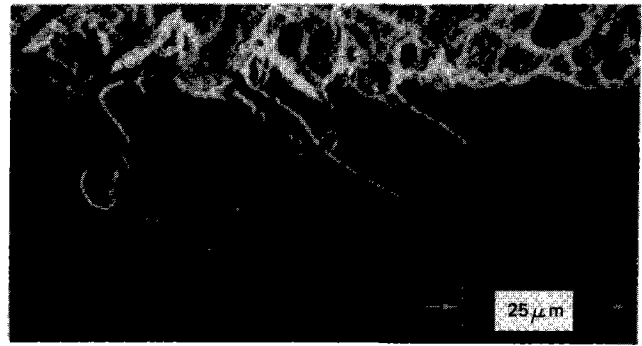


Figure 5. Inconel 718 grain fallout.

$c_{\text{sat}}$  = concentration for saturation at bulk sodium temperature

$\Delta$  = boundary layer thickness in cm

$D$  = diffusion coefficient in  $\text{cm}^2/\text{s}$

$V$  = volume of sodium in  $\text{cm}^3$

$A$  = area of liquid/solid interface in  $\text{cm}^2$

By using this equation, we have assumed that the rate-controlling factor is diffusion across a thin boundary layer adjacent to the dissolving surface. The thickness,  $\Delta$ , of this layer controls the diffusion rate, and this thickness is controlled by the hydrodynamics of the sodium flow. High velocity, or an abrupt turn in flow, increases the rate of both dissolution into an unsaturated solution and deposition from a supersaturated solution. Flow patterns through a partially closed valve may produce thin boundary layers, causing deposition site problems.

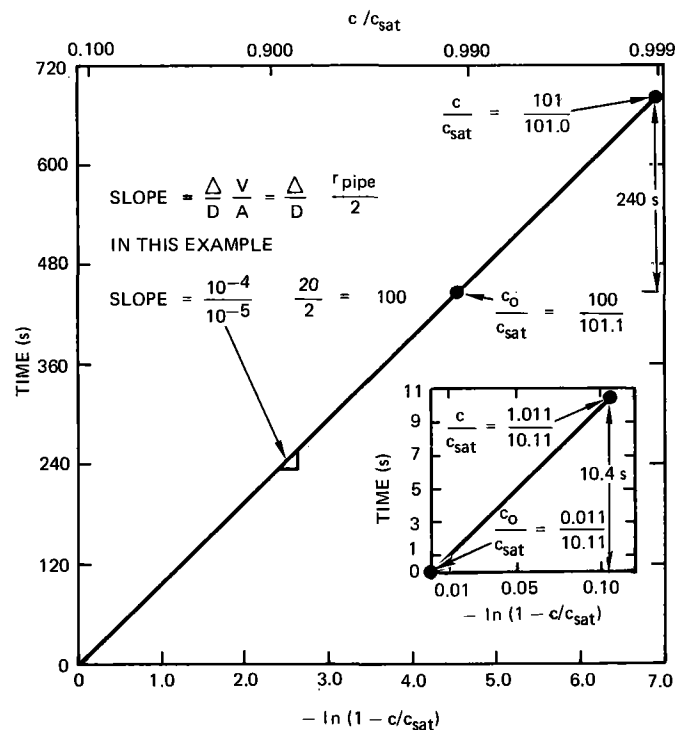


Figure 6. Time vs  $\ln(1 - c/c_{\text{sat}})$

The  $\ln(1 - c/c_{sat})/(1 - c_o/c_{sat})$  term rather than the  $c_{sat}$  value determines how long a time is required to build up solute concentration of sodium to a concentration,  $c$ , particularly when  $c_o = 0$ . In sodium loops, however,  $c_o$  is rarely zero. The  $c_o$  value for the hot dissolution site is usually the  $c_{sat}$  value at the cold deposition site. We can easily show that the  $c_{sat}$  value at that hot dissolution site does not determine how fast the structure dissolves into hot sodium. Here are two examples to illustrate this point.

**Example 1:**  $c_{sat}$  at cold spot = 0.011 ppm solute,  $i$   
 $c_{sat}$  at dissolution site = 10.11 ppm solute,  $i$

Solve for the time it takes the solute,  $i$ , to dissolve away into the coolant to the extent that it will build up an additional 1 ppm in the sodium.

$$c_o = 0.011 \quad t_i = -(\text{constant}) \times \ln \frac{1 - (1.011/10.11)}{1 - (0.011/10.11)}$$

$$c = 1.011 \quad t_i = -(\text{constant}) \times \ln 0.901$$

$$c_{sat} = 10.11 \quad t_i = (\text{constant}) \times 0.104$$

**Example 2:**  $c_{sat}$  at cold spot = 100.0 ppm solute,  $j$   
 $c_{sat}$  at dissolution site = 101.1 ppm solute,  $j$

Solve for the time it takes for the solute,  $j$ , to dissolve away into the coolant to the extent that it will build up an additional 1 ppm in the sodium.

$$c_o = 100.0 \quad t_j = -(\text{constant}) \times \ln \frac{1 - (101.0/101.1)}{1 - (100.0/101.1)}$$

$$c = 101.0 \quad t_j = -(\text{constant}) \times \ln 0.09$$

$$c_{sat} = 101.1 \quad t_j = (\text{constant}) \times 2.40$$

Using the relationship that  $\ln a/b = \ln a - \ln b$ , these examples can be plotted (Figure 6).

Thus, for the same amount of structure to be dissolved away, the example with the lower overall solubility, Example 1, turns out to be the more severe case by a rate factor of >20 for the elements considered. The reason, of course, is that the slope of the log solubility vs reciprocal temperature curve is the important consideration, not the  $c_{sat}$  value.

A specific example of the above is a comparison of nickel and copper in sodium. At temperatures under 260°C (500°F), the solubility of copper is less than that of nickel in sodium, though the increase in solubility with temperature is a steeper curve for copper than for nickel. Unalloyed copper at these temperatures will dissolve and plate out to an alarming extent in a sodium loop, while nickel alloys appear to take more time to dissolve (Figure 7).

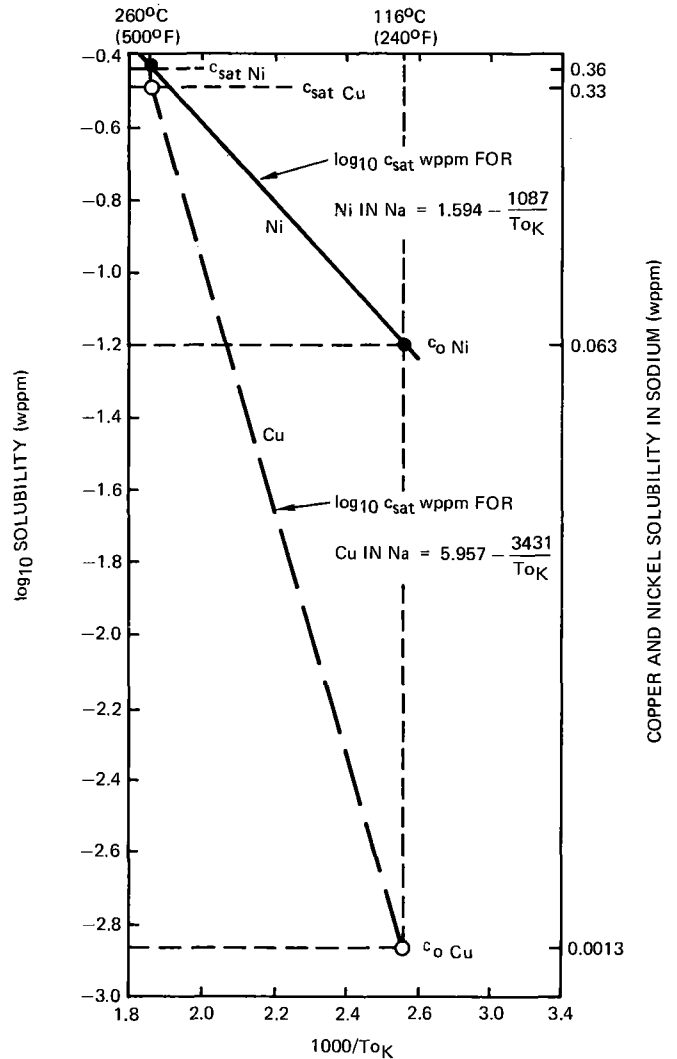


Figure 7. Slope of solubility vs  $1/T$  for Cu and Ni in Na<sup>(3,4)</sup>

Going through the same calculations as before, this time using actual elements, assume a system where precipitation is occurring at 115.5°C (240°F) and dissolution at 260°C (500°F), the elements dissolving into sodium being nickel and copper. The nickel has a high solubility under 260°C (500°F) but the copper has a steeper solubility slope. Determination of the time it takes to build up the solute content of the sodium by, for example, 0.25 ppm as the flow passes from the precipitation sites past the initial dissolution site is made as follows.

For copper:  $c_{sat} = 0.33$   
 $c_o = 0.0013$   
 $c = c_o + 0.25 = 0.2513$

$$t = -(\text{constant}) \times \ln \frac{1 - (0.2513/0.33)}{1 - (0.0013/0.33)}$$

$$= -(\text{constant}) \times \ln (0.2384/0.9961)$$

$$t = -(\text{constant}) \times \ln 0.2394$$

$$t = (\text{constant}) \times 1.4295$$

For nickel:  $c_{\text{sat}} = 0.36$

$$c_o = 0.063$$

$$c = c_o + 0.25 = 0.313$$

$$t = -(\text{constant}) \times \ln \frac{1 - (0.313/0.36)}{1 - (0.063/0.36)}$$

$$= -(\text{constant}) \times \ln (0.13056/0.825)$$

$$t = -(\text{constant}) \times \ln 0.15824$$

$$t = (\text{constant}) \times 1.843$$

Ratio of time to dissolve enough metal to raise the sodium content by 0.25 ppm =  $t_{\text{Ni}}/t_{\text{Cu}} = 1.28$ . If  $(\Delta/D)$   $(V/A) \approx 100$ , the dissolution time for a 0.25 ppm increase is 184 s for nickel and 143 s for copper.

The downstream effect where dissolution is less severe down the length of an isothermal hot pipe, can be seen to be the  $c_o$  term for any point on the pipe. When diffusion through the boundary layer is the rate-controlling mechanism boundary layer thickness, the term,  $\Delta$ , not only covers the velocity effect but also swirling effects. Oxygen content effects are probably seen as changes in the  $c_{\text{sat}}$  term and in the steepness of the solubility versus temperature curve for the solute element in the sodium solvent.

Temperature effects are expressed in absolute values of both the  $D$  and  $c_{\text{sat}}$  terms but, as shown above, the slope of the temperature-solubility curve overrides the importance of these absolute values. Thus, for iron, nickel, and chromium, temperatures above 500°C (930°F) are needed before dissolution is important, yet for copper, one must be very wary of dissolution at any temperature above the melting point of sodium.

#### Interstitial Atoms

Carburization and decarburization may be a problem in sodium loops where ferritic and stainless steels are used and loop temperatures are over 550°C (1050°F). Hot trapping a sodium system with a carbon getter, such as zirconium, can also bring about decarburization problems. Decarburization of 300 series stainless steels can weaken the stainless steels both in stress rupture and fatigue. When ferritic steels are in the loop with austenitic stainless steels in non-hot-trapped sodium above 550°C (1020°F), the austenitic stainless steel will carburize while the ferritic steel decarburizes with consequent loss in strength.

After many thousands of hours at temperature, certain alloys can undergo precipitation and phase changes that are not observed after exposures of 1000 hours more. Such precipitation may include Laves phases, sigma phase, carbides, and other intermetallics. Inconel 718, for example, has a time-temperature-transformation (TTT) plot that indicates potential problems of this nature during very long exposures in the 500 to 650°C (930 to 1200°F) range. Cobalt base alloys with an FCC structure that contains chromium in the same temperature range can convert to the hexagonal close-packed (HCP) crystal structure (Figure 8). Materials that contain carbides can change their stoichiometry. In the 300 to 500°C (570 to 930°F) range, embrittling phases can precipitate out along crystallographic directions in highly strained FCC cobalt alloys. The solution to this problem has been careful long-term testing of potential candidate alloys for structural applications to make sure that the metallurgical phase changes which will occur over long periods of time would not be detrimental to loop operation.

#### ENERGY TRANSFER THROUGH SODIUM

Sodium-hammer problems have been blamed for several cases of rupture disk failures in experimental systems. The pressure transmitted through a liquid by a fast-closing valve is dependent on the speed of sound in the liquid. A small amount of entrained gas in the liquid will drastically cut the speed of sound (Figure 9). A system that contains a liquid free of entrained gas is often protected against overpressure

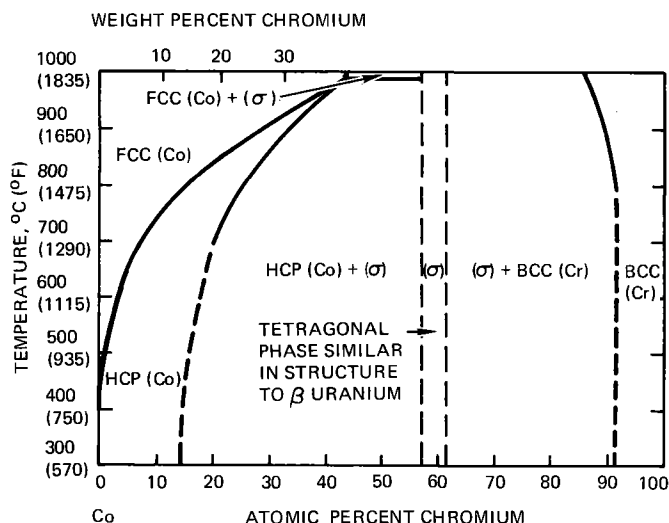


Figure 8. Cobalt-chromium phase diagram (adapted from reference 5).

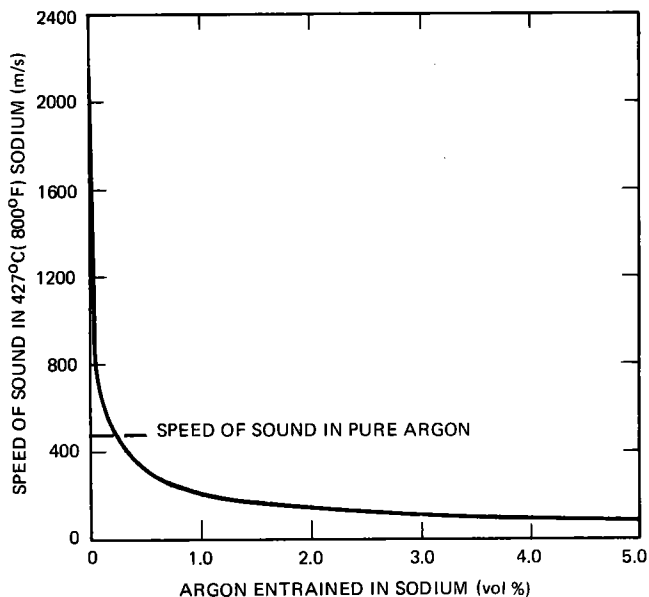


Figure 9. Speed of sound vs percent entrained gas.

by pressure relief valves. When a system filled with any liquid is protected by rupture disks, care must be taken in the design of the rupture disk assembly and in the speed at which valves close in order to prevent unexpected rupture disk failures.

Thermal transients must be considered in sodium systems because of the ability of liquid sodium to change the temperature of adjacent structural metal so rapidly.

#### METALLURGICAL ASPECTS IN LOOP DESIGN

In this section, only a few of the most common areas of metallurgical concern are listed.

Experience has shown that a sodium loop should be designed with adequate attention paid to heaters and controllers on piping and components to assure nearly uniform temperatures during preheat and holding. A loop should be designed to avoid flowing through heat exchangers during sodium cleanup phases. Construction practices of metallurgical interest include such diverse

items as marking inks used, pipe storage methods, tank storage methods, welding, methods of constructing bladders and dams to direct the gas purge flow to the space behind the joint to be welded, insulation materials, and many other items.

Maintenance practices of metallurgical interest include methods of maintaining argon purge purity and pressure during repair, weld joint preparation to avoid sodium contamination, identification of artifacts from nondestructive testing of structures and welds, corrosion considerations from the ambient environment or from leaching of insulation, and many other aspects.

#### SUMMARY

This paper has described many interesting phenomena discovered by a metallurgist involved with large sodium loop operations. The technology involved has not encountered any insoluble problems.

#### REFERENCES

1. N. J. Hoffman, et al., "Evaluation of Cobalt and Nickel-Base Materials for Sliding and Static Contact Applications in a Liquid Metal Fast Breeder Reactor," International Conference on Liquid Metal Technology in Energy Production, held May 3 to 6, 1976.
2. N. J. Hoffman and I. Minkoff, "Dissolution of a 2-Phase Alloy in a Pure Liquid Component," *Journal of Crystal Growth*, Vol 6 (1969).
3. R. L. Eichelberger and R. L. McKisson, "Solubility of Copper in Sodium," AI-AEC-12671 (May 1968).
4. R. L. Eichelberger and R. L. McKisson, "Solubility Studies of Cr, Co, Mn, Mo, Ni, Nb, Ti, V, and Zr in Sodium," AI-AEC-12955 (May 1970).
5. M. Hansen and P. Anderka, Binary Alloy System, McGraw-Hill, New York (1958).

The work reported herein was done at the Liquid Metal Engineering Center, operated by Atomic International Division of Rockwell International under Contract E(04-3)-700 with the U. S. Energy Research and Development Administration.

# INTERNATIONAL CONFERENCE ON LIQUID METAL TECHNOLOGY IN ENERGY PRODUCTION

## MATERIALS EXPERIENCE WITH LARGE SODIUM LOOPS AND COMPONENTS

H. Mausbeck  
INTERATOM, FRG

The properties of sodium as a heat transfer fluid for fast reactors influence the design of the system components. Examples of the properties to be discussed are the affinity of sodium for oxygen and water, and the physical characteristics which lead to the sodium frost phenomena and impurity solubility.

### 1. Tightness Criteria

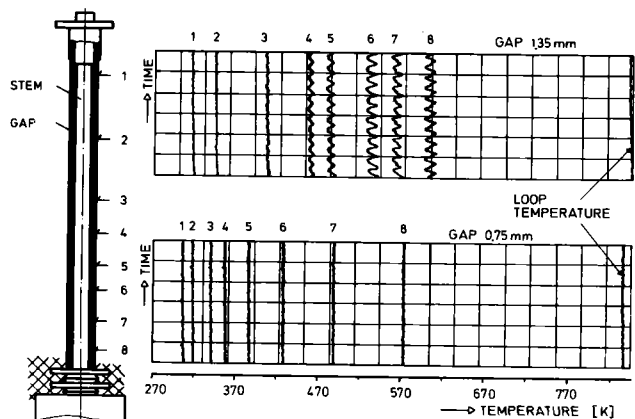
The affinity of sodium for oxygen requires that the entire system has to be extremely tight. Outer walls in contact with liquid sodium are normally welded or brazed. The necessity for penetrations in pumps, valves and shield plugs creates additional problems.

#### 1.1 Freeze Seal

The freeze seal is a typical solution for penetrating valve stems under liquid sodium. Gate valves pose the greatest problem with respect to length and shape of the freeze seal and the transport of air into the frozen sodium. Sodium from the system enters the annulus at the prologed stem. Its temperature decreases along the stem below the freezing point. This arrangement represents the primary seal of the system. The main problem of this frozen sodium plug is the thermal lay-out with

- movement of the freezing point as a result of different operating temperatures of the system and time sequence of operation of the valve stem itself,
- sodium transport through the secondary safety packing to the outside,
- level and variation of the valve operating forces.

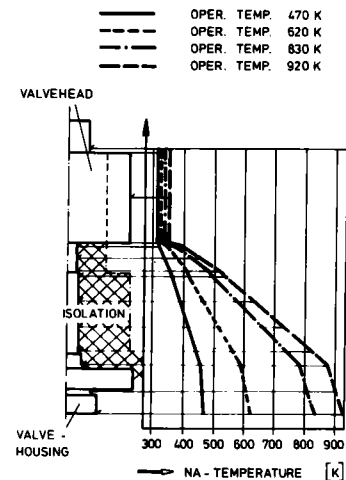
These problems will mainly be solved by geometry and material selection of the shaft. For fabrication tolerances it is advisable to enlarge the annulus as far as possible. This is limited by the heat capacity and the possibility of free convection of the sodium in the gap and would make the temperature distribution unstable and reduce the efficiency of the seal.



TEMPERATURE DISTRIBUTION ALONG A FREEZE SEAL FOR DIFFERENT GAPS

Fig. 1.

Figure 1 shows the temperature distribution of a freeze seal without cooling fins for two different size annuli. The curves give the temperature versus time for the different measuring points, the location of which along the freeze seal is shown on the left-hand side. Temperature increase and temperature variation of larger gaps are caused by low heat resistance or sodium convection respectively.



TEMPERATURE PROFILE OF AN OPTIMIZED FREEZE SEAL

Fig. 2.

Figure 2 shows the optimized geometry of a freeze seal with measured temperature profiles at different operation temperatures of the loop. In this case optimization means that the freezing point of the sodium stays within a narrow area at all tolerable operation temperatures. To obtain this behavior we concentrated a large amount of metal and a large heat transfer surface at the upper end of the freeze seal. With this arrangement, even with a repeated operation of the valve, the temperature profile remains stable. Below the head area of the freeze seal the shaft is insulated to assure a steady temperature decrease and to prevent the sodium freezing along the shafts, since this would increase the forces required for valve operation.

#### 1.2 Rotating Shield System

The largest sealing area of a sodium cooled fast breeder system against the outer atmosphere is normally the top side of the reactor tank. This is especially true for the design being used by INTERATOM which is a rotating shield plug system. The requirements for this system are

- sealing
- shielding
- thermal insulation to the top side

## INTERNATIONAL CONFERENCE ON LIQUID METAL TECHNOLOGY IN ENERGY PRODUCTION

- positioning of the fuel handling equipment during fuel exchange
- accessibility for the core, instrumentation and the control rod systems.

The complexity of the system led to the remarkable amount of development in this respect. The steps were:

- an experimental single rotating shield plug (diameter 1 m, height 3 m, weight 5 t),
- a double rotating shield plug at the KNK reactor (diameter 2.8 m, height 3 m, weight 40 t),
- a rotating shield plug system with three shield plugs located eccentrically within one another (diameter 5.5 m, height 3 m, weight 200 t), which is approximately the SNR 300 reference size.

It is one of the fundamental problems of the rotating shield system to seal the argon cover gas above the free sodium surface from the operating floor of the reactor building during reactor operation and fuel handling. According to the safety rules for SNR 300, the maximum tolerable loss of argon gas from the reactor vessel amounts to 0.66 volume % per day equivalent to a leakage rate of 5.4 mbar l/s. The required small leakage rates which have to be matched even under rotation are influenced by the fabrication tolerances of large diameter plugs, the potential presence of sodium and sodium aerosols, the location of bearings and sealings, temperature and radiation.

The problems will be described at the prototype SNR 300 rotating shield plug shown in figure 3. The three independent rotating shields have the same vertical arrangement of the layers. From top to bottom they are composed of the mounting plate, the case which contains the basalt granules serving for radiation shielding, and the heat reflecting plates. The sealing and bearing regions are located above the mounting plate where temperature and radiation are greatly reduced to save the sealing material. The sealing of the cover gas atmosphere is done by two changeable inflatable seals in series with buffer gas between them. These inflatable seals can be changed during reactor shut-down.

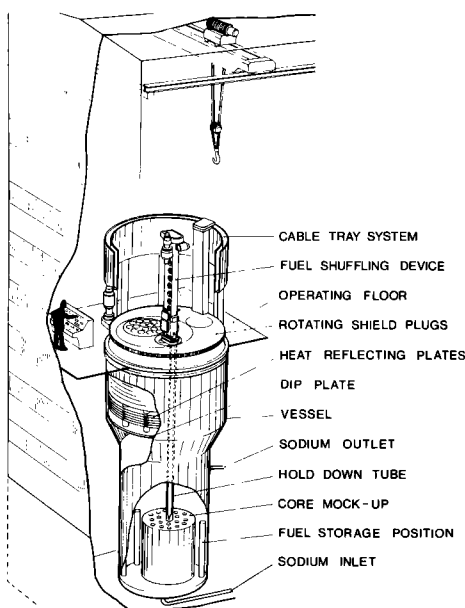


Fig. 3.: RSB test facility

As a result of an extensive development we decided to use for these sealing purposes the so-called "membramatic rolling seals" (Fig. 4). Every seal only requires a simple square groove for mounting. Depressurized, the seal does not touch the sliding surface. The seal makes contact under inflated conditions with the sliding surface without any self-expansion of the seal material.

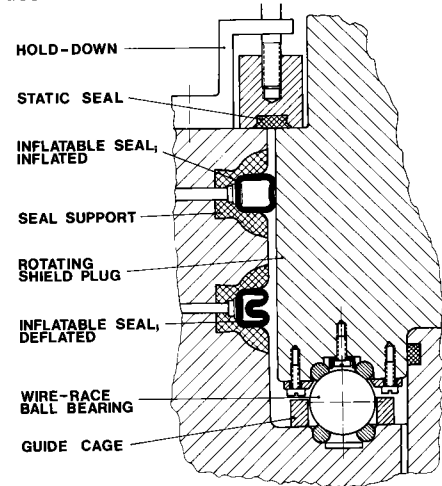


Fig. 4. DETAIL OF ROTATING SHIELD PLUG

Low mass accumulation and constant low cross-section of the sealing assure a high leak tightness even at variations of the gap size and large tolerances of the sealing surface.

Silicon rubber, best suited because of its materials behavior with respect to friction, wear, and temperature resistance, has a fairly high permeability rate for the gases in comparison to other materials. This disadvantage could be overcome by an inner layer of a different material. The good sliding behavior of the silicon material could be improved by a special treatment of the sliding surface.

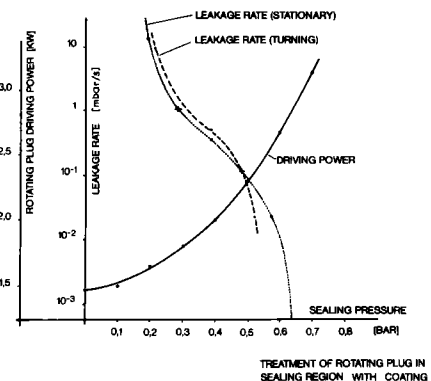


Fig. 5.

Figure 5 shows a leakage rate of one of the inflatable seal systems as a function of the sealing pressure. The leakage rate is measured by the pressure drop in the buffer gas region between the two seals. The leakage rate is given for the stationary and the operating conditions. In addition, the driving power



## INTERNATIONAL CONFERENCE ON LIQUID METAL TECHNOLOGY IN ENERGY PRODUCTION

is shown as a function of the sealing pressure. At a sealing pressure of about 1.7 bar the driving power is doubled as compared to the non-sealed condition. This pressure was chosen as normal condition for all handling operations since according to our test results it is a good compromise between tightness of the system and wear of the sealing itself.

Under these conditions we measured a leakage rate of  $10^{-3}$  mbar l/s under rotation. Under stationary conditions, which does mean normal reactor operation, the measured leakage rate is  $10^{-4}$  mbar l/s. During rotation of the system three parameters are controlled:

- driving power,
- pressure of the inflatable seals,
- pressure of the buffer gas region.

The shield system contains, as already mentioned, a large number of penetrations which are sealed by static seals. During the first tests with the rotating shield system in our test rig we found the total leakage rate to be  $4 \times 10^5$  higher than the leakage rate of the inflatable seals themselves. By special measures, this value could be improved, but the remaining leakage rate is still too high. For this reason we put more emphasis on the design of static seals for the SNR 300. This comprises the selection of sealing materials, size and shape of the gaps for O-rings and the corrosion protection of all sealing areas. Furthermore, sealwelds are introduced where ever possible and the other static seals are double seals with buffer gas between them. With these measures we expect a remarkable reduction of the leakage rate. The inflatable seals guarantee already an excellent sealing effect.

### 2. Sodium Frost Phenomena

Gas spaces above sodium with high temperature create the problems of sodium aerosol transport and sodium deposit. Natural convection of the cover-gas (argon) leads to a supersaturation in the cover gas atmosphere. This phenomenon is important for the rotating shield plug system. At walls below the freezing temperature of sodium solid deposits must be expected. This is extremely important for the gap clearances of the rotating shield plug. In general, sodium aerosols enter the gaps by natural convection. An unequal temperature distribution across the shield plug which supports the convection can normally not be avoided in such a large non-uniform system.

The first operating period of the KNK reactor gave a good example for forming sodium deposits in the gap clearances of the rotating shield plugs. Particularly, the outer gap was loaded with sodium deposits, so that a proper rotation of the large shield plug was no longer possible. Sodium deposits were even found in the wire-race ball bearing area of the shield plugs. Figure 6 shows the wire-race ball bearing region without and with sodium deposits.

The counter-measures at KNK were:

- an additional inflatable seal which is deflated during plug rotation in front of the bearing,
- improvement of the temperature distribution of the shield plug by re-design of the nitrogen cooling system,

- development of an operating procedure to melt down the deposits,
- drilling of holes to make the gap-clearances accessible for inspection and removal of deposits.

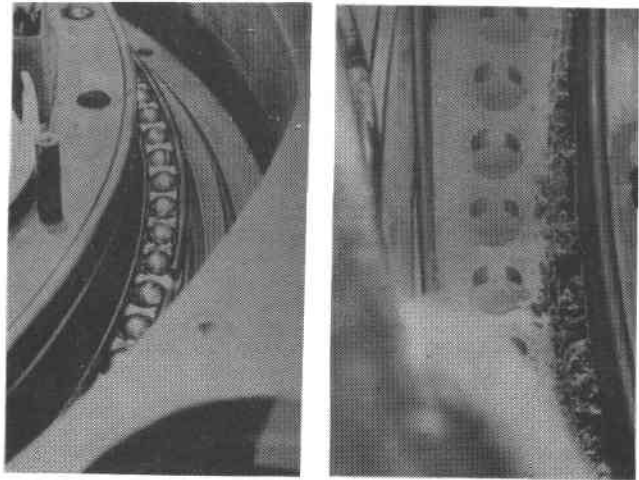


Fig. 6.: KNK ball bearing region

The melting operation used prior to every rotation cycle of the shield plugs turned out to be extremely satisfactory. The inspection holes were used to make measurements on the deposition rate of aerosols in the gap system. The measured deposition was in good correlation with the theoretical prediction of about  $10^{-2}$  (kg/m<sup>2</sup>/h) at a temperature of 800 ° K in the sodium system and the geometrical conditions of KNK. This result is also supported by the more integral observation that the gap was filled with sodium within one to some hundred hours.

According to these results the design for the SNR 300 will include the KNK experience and allow the shield plugs to obtain an equal temperature distribution. Melting off the sodium deposits is possible too. In addition, the SNR shield plug system will be equipped with so-called convection barriers in the lower part of the shield plugs (Fig. 7). For reactor operating conditions each shield plug rests on its convection barrier. The efficiency of the convection barrier will be supported by a scavenging circuit. This system shall prevent the sodium aerosols from entering the annuli and thus avoid sodium deposits in the gaps.

The scavenging circuit draws the cover gas out of the tank via a vapor trap, pressurizes it and feeds it into the gap between bearing and convection barrier. The flow rate of the gas will be controlled to assure a gas velocity of more than 2 cm/s in the residual gaps of the convection barrier. After 12 months of operation of the test rig and sodium temperature higher than 820 ° K no sodium aerosol was found in the annuli with an operating system composed of convection barrier and scavenging circuit.

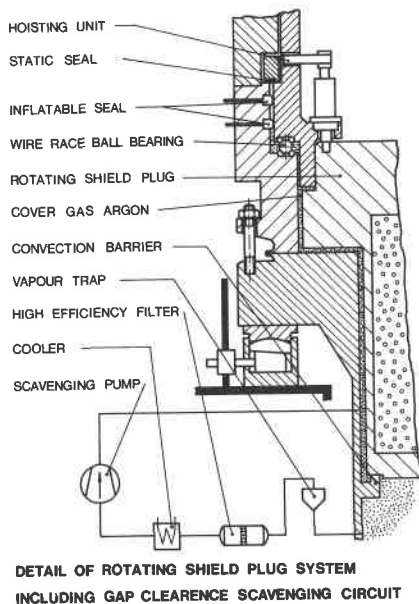


Fig. 7.

To get more information on the effectiveness of the influencing parameters two special test runs were performed:

For a test period of 1.5 months the argon down stream in the gap was stopped, but still no deposition of sodium was detected. To enlarge the convection rate the forced cooling was used to artificially create a temperature difference of 50 °K across the shield plug diameter. Even these extreme conditions did not lead to sodium deposits during a test run of 1.5 months.

This satisfactory result is interconnected with an accurate fabrication process of convection barrier and opposite surface. The fabrication tolerances define the size of the argon scavenging circuit.

### 3. Vapor Traps

Vapor traps have been developed to eliminate the need for trace heating of the whole argon system which is in contact with sodium and to prevent distribution of the aforementioned sodium frost phenomena over large parts of the argon system. Sintered stainless steel filters for vapor traps have been used for the KNK reactor. For the SNR 300 we have chosen the same principal, however, the filters were enlarged to allow a much higher gas flow rate. The temperature of the filter is the main parameter to achieve an undistributed long-time operation.

The vapor traps consist of a pressure vessel which contains 60 filter discs with an outer diameter of 300 mm. The discs are mounted on a bracing tube with distance rings in between which are hermetically sealed at the end. The discs are fabricated of a highly porous material with a porosity of 15 - 65  $\mu\text{m}$ . The filter-surface was selected at a specific gas flow rate of 2.5  $\text{Nm}^3/\text{m}^2\text{h}$ .

The design flow rate amounts to 20  $\text{Nm}^3/\text{h}$ . Near the entrance nozzle the sodium-loaded gas flow will be distributed by a baffle plate which has the function of loading the discs nearly uniformly.

At the sintered metallic surface small sodium droplets are formed which enlarge during operating until they flow away by gravity forces. This process including the flow patterns can be seen at figure 8.

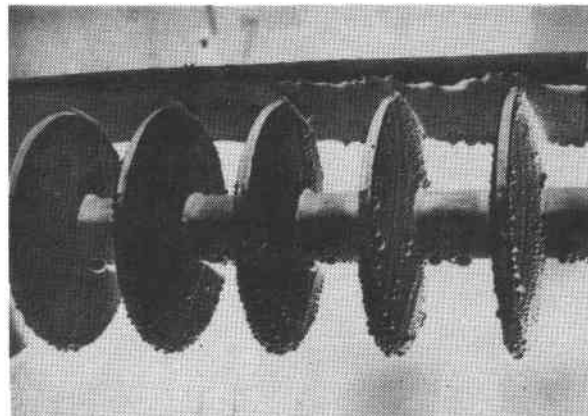


Fig. 8.: SNR 300 vapor trap with sintered stainless steel filters.

As mentioned before, the filter temperature determined by the temperature of the incoming gas is of great importance for the function of the vapor trap. To stabilize the gas temperature at the entrance of the vapor trap a heater/cooler is connected in series to the vapor trap. The precipitated sodium flows back into the sodium system through the gasline itself.

The operation of this type of vapor trap is influenced by the purity of the sodium transported by the argon gas. This is best characterized by citing the tolerable gas impurities of the argon cover gas. The tolerated impurity levels are:  $\text{H}_2 \approx 50$  vpm,  $\text{N}_2 \approx 1000$  vpm. In experimental loops this type of vapor trap was operated for more than 3000 h with a total argon flow up to 40.000  $\text{Nm}^3$  at a sodium system temperature of 830°K. The argon gas was loaded with sodium aerosols of a concentration of 21 - 23 g sodium/ $\text{Nm}^3$ . During this long endurance test the total precipitation rate of the system including tubes, heater, cooler and vapor trap was determined to be better than 99.999%. The operation of the vapor trap was also assured for abnormal operating conditions like stepwise change of flow rate between 0 and 100% of flow. The SNR 300 will be provided with 37 of these sodium filters. A total of 14 filters have been in operation in the KNK plant for more than 30.000 hours, 8 of them with a flow rate of 0.25  $\text{Nm}^3/\text{h}$  and 6 of them with 1.0  $\text{Nm}^3/\text{h}$ .

### 4. Sodium Purity

#### 4.1 Impurity Survey

Measurement and survey of impurities in sodium and cover gas are indispensable for the operational safety of loops and reactor plants, since the measured deviation of "normal" impurity levels allows the indication of abnormal operation conditions and gives the chance for counter measures in adequate time.

# INTERNATIONAL CONFERENCE ON LIQUID METAL TECHNOLOGY IN ENERGY PRODUCTION

During operation impurities of the sodium can be induced by the following sources:

- delivery condition,
- air-, water-, and oil leakages,
- cover gas impurities,
- impurity intake by handling and repair.

For a reactor system

- corrosion of activated cladding and structural material,
- cladding failures,
- neutron activation

have to be added.

The concentration of the inactive sources is generally in the range of 1 to 100 ppm and that of the activated products in the range of  $10^{-10}$  to  $10^{-3}$  ppm.

The most reliable instrument for plant operation is still the plugging meter in spite of its well-known limitations. More precise information can be obtained by sampling of sodium and chemical analysis, and continuous analytical instruments, specific for a certain impurity. Sampling systems allow the analysis of all important impurities and the calibration of the analytical instrumentation.

The main tool for impurity control in all of our test rigs is, beside the plugging meter, the outline distillation method. It consists of a sampling vessel which contains the crucibles and is sealed against outside influences by two "siphon" plugs (Fig. 9). Dependent on the system temperature the sodium will be circulated for 1 to 4 hours across the sampling unit to clean it before the sample will be drawn. The excess sodium flows back to the loop, the two siphons will be plugged after having cooled down the unit. The residue in the crucible, after distillation of sodium, can be used for a complete analysis of all interesting impurities in sodium. Table I shows the limiting sensitivity for the different materials and a brief note on the method used.

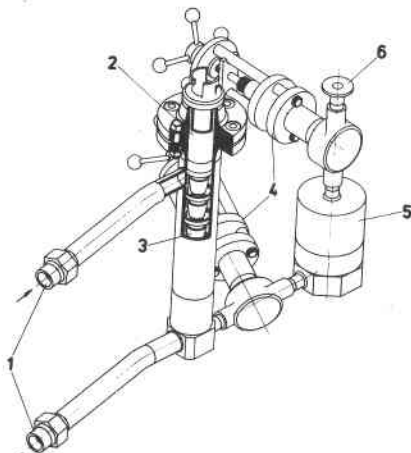


Fig. 9.: Out-line sampling system

- 1 sodium inlet and outlet
- 2 sample crucible inset
- 3 sample crucible
- 4 valves
- 5 sodium sample
- 6 vacuum connection

Element	Limiting Sensitivity (ppm)			Method
Al	1,5	+	0,5	AAS
B	1,0	+	0,5	photometry
C	0,5	+	0,1	oxidation
Ca	0,05	+	0,01	AAS
Cd	0,05	+	0,005	AAS
Co	0,02	+	0,005	AAS
Cr	0,01	+	0,002	AAS
Cu	0,05	+	0,004	AAS
Fe	0,05	+	0,002	AAS
K	0,5	+	0,03	AAS
Li	0,05	+	0,004	AAS
Mg	0,001	+	0,0001	AAS
Mn	0,02	+	0,005	AAS
Ni	0,005	+	0,005	AAS
O	2,0	+	1,0	titration
Pb	0,5	+	0,001	AAS
Sn	1,0	+	0,3	AAS
Zu	0,005	+	0,001	AAS

Table I: Limiting sensitivity of impurities in sodium (weight of sample 4 g)

The large number of samples which we analysed last year showed a systematic difficulty at low  $O_2$  values. Even under extremely clean conditions the analysed values were higher than the plugging values drawn from solubility curves like Eichelberger.

We hope to overcome this discrepancy by use of the inline distillation method, the development of which we considered necessary to allow also an easier handling of the radioactive primary system samples of the nuclear plant. The already distilled sample will be transferred to an inert gas lock through the manipulator box (Fig. 10). First results with a prototype show a good reproducibility of filling and distillation process.

For the continuous measurement of  $O_2$  an electrolytical cell with the well-known principle of the  $ThO_2 - 7.5\% Y_2O_3$  electrolyte is used where the main emphasis was put on the development of a sodium resistant connection of a small crucible to the assembly (Fig. 11.). We tested these instruments successfully up to 6.000 h in different loops.

The continuous carbon-meter with a molten salt electrolyt looks physically similar to the oxygen meter. It has now only passed the laboratory stage of development.

## 4.2 Cold Trap

The sodium impurities will be precipitated in the cold traps. The soluble sodium impurities such as oxygen, carbon, hydrogen, sodium hydroxide, sodium hydride and several metals have a temperature-dependent solubility. Their precipitation will occur when the sodium temperature is lowered. Suspended solid particles settle down as a result of lower sodium velocity.

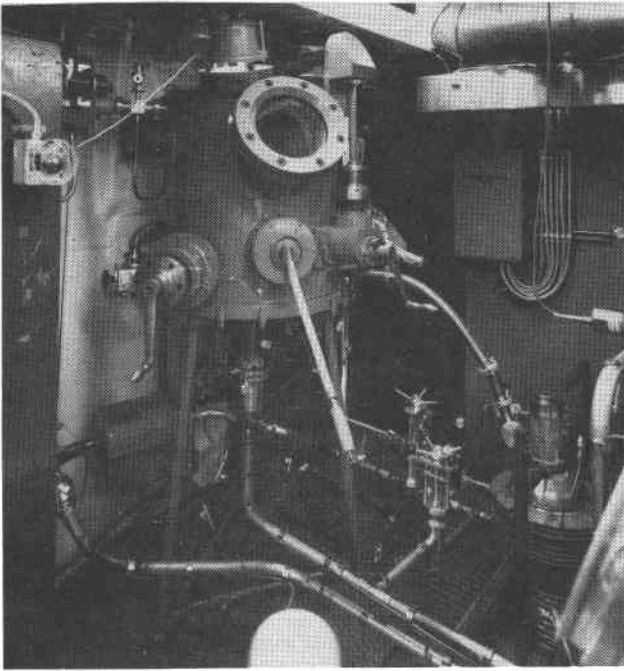


Fig. 10.: In-line sampling system in the chemistry loop.

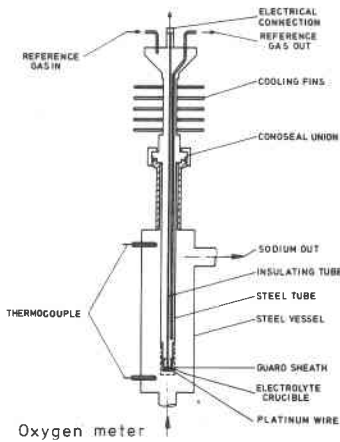
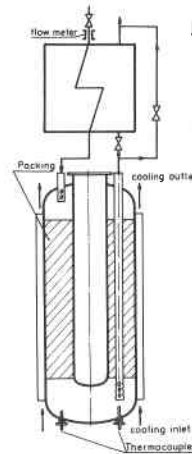


Fig. 11.

The cold traps, designed for the sodium purification in the SNR 300 with a nominal flow rate of  $10 \text{ m}^3/\text{h}$ , were tested in an extensive operational and developmental program. Figure 12 presents a cross section of the SNR prototype cold trap with design data and the most important test results.

The sodium is cooled by passing through a recuperative heat exchanger and enters the cold trap at the top. The vessel will be cooled by air or nitrogen. During the decrease of the sodium temperature in the cold trap the impurities are

suspended and settled in the packing. The cleaned metal leaves the vessel by a bayonet tube and cooles the counter-flowing sodium in the heat exchanger.



**Design data of SNR 300 cold trap**

Volume	1,95m <sup>3</sup>
Precipitation surface	:220m <sup>2</sup>
Sodium flow rate	:10m <sup>3</sup> /h
Material of cold trap	:15Mo3 $\approx$ AISI 4017
Packing	:Pallings

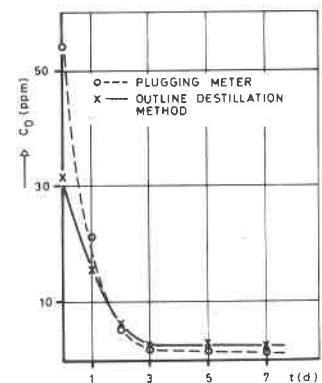
**Results of SNR 300 cold trap tests**

Trapping rate increased from	:5g O <sub>2</sub> /h to 16g O <sub>2</sub> /h
Efficiency	>80%
Capacity for impurities	>20%
Purification of sodium from	
nonmetallic impurities	:O <sub>2</sub> , H <sub>2</sub> , C, NaOH, NaH
metallic impurities	:Fe, Ni, Cr, Ca, Sn etc.
radioactive impurities	: <sup>54</sup> Mn, <sup>60</sup> Co, <sup>182</sup> Ta, <sup>65</sup> Zn etc.
solid particles	:globule, dust etc.

Fig. 12.

Two SNR prototype cold traps were successfully operated as start-up cold traps in the KNK reactor primary and secondary system, which consisted of carbon steel structural material ( $\approx 2 \frac{1}{4} \text{ Cr } 1 \text{ Mo Nb}$  stabilized). The system had a total inventory of about 100 tons of sodium. The installed SNR prototype cold trap of the KNK primary system was dismantled after start-up operation. The SNR prototype cold trap of the KNK secondary system remained in service for about 20.000 h until shutdown for KNK modifications.

A third SNR prototype cold trap was tested in an extensive test program for about 4 years in the pump test facility APB. The test facility is constructed with SNR specified material (X6 Cr Ni 1811  $\approx$  AISI 304 H). The facility contains 140 metric tons of sodium. Full utilization of the capacity for impurities could not be detected during the tests. A plugging meter and sodium sampling system were installed to monitor the sodium purification in the test facility. The oxygen measurement during the first cleaning process of the test facility is shown in figure 13.



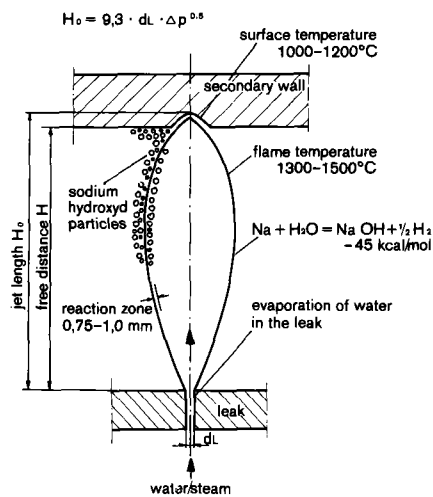
FIRST CLEANING PROCESS OF THE PUMP TEST FACILITY

Fig. 13.

Four cold traps are provided in the SNR primary system and three cold traps in secondary system for purification. The purification time required prior to the start-up of the reactor or following a high level impurity eruption during plant perturbations is expected to be short.

5. Sodium Water Reactions

A small water/steam leakage is the most likely incident in a sodium heated steam generator. Such leaks in the order of some tenth of a millimeter in diameter resulting in leak rates of 0,05 to some 10 g/s are characterized by the formation of a flame-shaped reaction zone. By evaluation of pertinent literature and the performance of additional experiments an empirical prediction of such flame-type reaction zones is possible (Fig. 14.). The flame, depending on its size, may reach the wall of an adjacent water/steam tube. In that case a more or less intensive material wastage takes place. This wastage mechanism can be explained as follows:

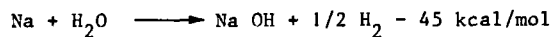


MODELL OF REACTION FLAME

Fig. 14.

A steam jet enters the sodium forming a flame-type reaction zone. The reaction mainly occurs in a boundary mixing zone of approximately 1 mm thickness. The maximum temperature of this flame amounts to 1500 - 1800 K. The wall temperature in the affected region reaches values of up to 1250 - 1450 K. These values were also observed by direct temperature measurement as well as by metallurgical re-investigations of test specimens.

By the reaction

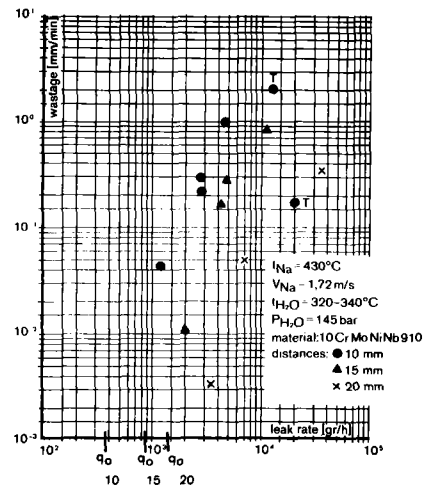


particles of sodium hydroxide are formed. The vaporisation temperature of NaOH is about 1600 °K, a temperature which is consistent with our measured temperatures. These particles impinge on the surface of the adjacent tube wall at velocities of about 100 m/s. The process of wastage can be divided into different mechanisms:

- the adjacent wall is heated up by the reaction products impinging upon it
- at high temperature and high concentrations of Na OH corrosion takes place
- the corroded surface immediately becomes eroded by the impinging Na OH droplets, whereby the corrosion process is maintained continuously on a clean and unprotected surface.

Some results of wastage tests performed by INTERATOM are shown in figure 15. The niobium stabilized version of 2 1/4 Cr 1 Mo steel has been used as the structural material. Besides the influence of leak size, distance, sodium temperature and velocity on wastage rates, the material plays a dominant role as demonstrated by the test results. If one defines a relative wastage resistivity factor and normalizes it to 1 for the 2 1/4 Cr/Mo steel, the following values have been found:

- 2 1/4 Cr 1 Mo ferritic = 1
- 9 - 12% Cr ferritic = 1,2 - 1,5
- AISI 304, 316, 437 austenitic = 2,5 - 3
- Incoloy 800 = 5 - 6



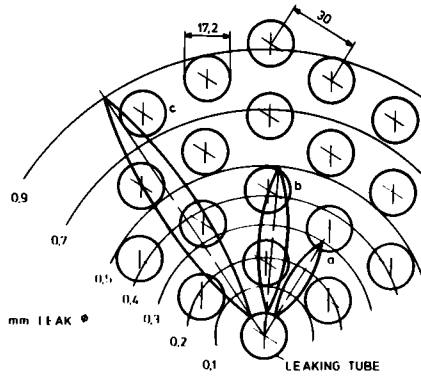
WASTAGE TESTS ON PRESSURIZED TUBES

Fig. 15.

The reaction and the resulting wastage zone are small, nearly point type concentrated. Accordingly, approx. 85% to 90% of the tube wall can be removed by the concentrated wastage, and due to the internal pressure the affected tube fails by forming a secondary leak. These secondary leaks tend to have a diameter of about 5 times the size of the initial leak size.

The applicability of wastage results and reaction flame sizes shall be demonstrated at the SNR 300 straight tube steam generator. Figure 16 shows the ideal flame shape in the tube arrangement of this steam generator. Wastage on the first adjacent tube starts with leak sizes of about 0.1 mm in diameter. A leak of 0.3 mm even leads to wastage in a second row of tubes. The maximum intensity values of wastage rates are shown in figure 17. The indicated values are maximum values because the maximum sodium temperature has been combined with the minimum sodium flow velocity.

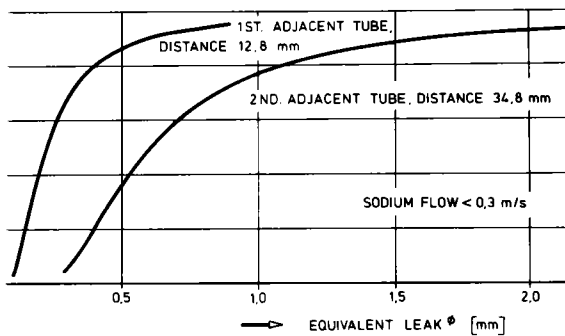
FLAME LENGTH :  $H_0 = 9,3 \cdot d_L \cdot p_0^{0,5}$   
 STEAM PRESSURE : 170 bar



a = FLAME at 0,3 mm LEAK  $\phi$   
 b = FLAME at 0,5 mm LEAK  $\phi$   
 c = FLAME at 0,9 mm LEAK  $\phi$

STRAIGHT TUBE STEAM GENERATOR  
 AND IDEAL REACTION ZONES

Fig. 16.



STRAIGHT TUBE STEAM GENERATOR  
 WASTAGE RATES VS. LEAK SIZE AND DISTANCE

Fig. 17.

It is obvious that such leaks must be detected as early as possible to avoid a failure propagation. The detection of hydrogen which is formed by the chemical reaction is considered to be state-of-the-art.

Measurements of different groups have indicated that a small leak itself will enlarge suddenly after a period of time. The mechanism for this event is not yet known. In the meantime, INTERATOM has started an intensive test program on this phenomenon. First test results will be available in summer 1977. In parallel to these tests the development of an acoustic leak detection system is planned. If it will prove to be applicable to the steam generator problems, its advantage should be its independence from the transport time of the reaction products.

# INTERNATIONAL CONFERENCE ON LIQUID METAL TECHNOLOGY IN ENERGY PRODUCTION

EXPERIENCE WITH SODIUM PURIFICATION ON LARGE-SCALE OPERATIONAL TEST LOOPS IN FRANCE

E. BENOIST

Département des Réacteurs  
à Neutrons Rapides  
C.E.A. CADARACHE

M. CABBILLARD

Département des Réacteurs  
à Neutrons Rapides  
C.E.A. CADARACHE

J.L. QUINET

E.D.F. Etudes et Recherches  
C H A T O U

## ABSTRACT :

After a discussion of the major characteristics of four large test loops operational in France, this paper reviews the sodium purification equipment used in conjunction with these test facilities, the purification monitoring devices and operational procedures.

Operating experience is also described with particular attention to three types of impurities : calcium from " industrial grade " sodium, oil from the mechanical pumps and hydrogen from the steam generators.

## INTRODUCTION

The operation of sodium test loops provides valuable data beyond the scope of the major initial objectives which determined their construction. Such complementary findings include information on both the equipment and materials used in the loops. For the purposes of this paper, we have decided to discuss the data provided by test loop operation in France as it applies to the field of sodium purification. In this context, we have selected four large test loops : two of them are used for testing reactor primary circuit components ( mechanisms in static sodium, and sub-assembly mock-ups), while the remaining two loops concern the secondary circuit and are used for steam generator testing.

After a brief survey of the major characteristics of these four loops, we shall first describe the equipment used to purify and monitor the sodium, and the procedures involved in these operations.

We shall then discuss the problems encountered and the solutions developed from our operating experience with these loops in the presence of three types of normal or incidental impurities : calcium from industrial-grade, oil from pumps and hydrogen from the generators.

## 1 - DESCRIPTION OF THE 4 TEST LOOPS

The 4 test loops were built in preparation for the PHENIX program. " OBELIX " consists of 7 pots supplied in parallel, and is used for static sodium testing of reactor components (fuel control and handling mechanisms, for example). " CAPHE " was built for endurance testing of core sub-assembly mock-ups (fuel, fertile and control sub-assemblies, etc.) exposed to thermal shocks or in isothermal sodium environment. The 5 MW circuit at " GRAND QUEVILLY " was designed for basic research on steam generator behavior ; its principal feature is a NaK secondary loop with a primary sodium loop. The 50 MWT " CGVS " loop has been used to test full-scale PHENIX steam generator modules and reduced size SUPER PHENIX modules.

Table 1 summarizes the major characteristics of these loops. It must be emphasized that the load factor for each of the four test rigs is quite satisfactory, and that incidents arising during sodium operation have had only minor repercussions on their serviceability.

## 2 - DESIGN & OPERATION OF PURIFICATION SYSTEMS

Sodium test loop operation poses a problem which does not arise during reactor operation : the loop must be opened at regular intervals between different test campaigns.

Whatever precautions may be taken, the sodium is invariably contaminated at the outset of each new series of test and must be purified as quickly as possible.

This requirement assumes a thorough grasp of purification problems, which may be broken down as follows :

- Purification equipment
- Purification control systems
- Operational procedures coherent with the means employed.

INTERNATIONAL CONFERENCE ON LIQUID METAL TECHNOLOGY IN ENERGY PRODUCTION

TABLE 1

TABLE 1	OBELIX	CAPHE	5 MW	50 MW/CGVS
Site	Cadarache	Cadarache	Grand Quevilly near ROUEN	Les Renardières near FON-TAINEBLEAU
Agency	CEA	CEA	CEA	EDF
Type of testing	Reactor components in static sodium	Core Sub-assembly mock-ups	Steam Generators	Steam Generators
Date of initial operation	1969	1968	1964	1970
Number of hours of operation in sodium	18,600* 53,400*	34,000	37,000	21,000
Sodium mass (metric tons)	55	1,7	P : 2.6** S : 2.7	104
Max. sodium temperature (°C)	600	600	P : 600** S : 585	650
Max. sodium flow rate m <sup>3</sup> /hour	30	150	P : 65** S : 100	1.000

Notes : \* 18600 hours is the cumulative sodium operating time for pot n°1 ; 53,400 hours is the total time during which at least one pot was in service.

\*\* " P " refers to the primary sodium loop.  
" S " refers to the secondary sodium-potassium loop.

2.1. Purification equipment

2.1.1. Cold traps

The basic means of purifying sodium is the cold trap. At least one of which is installed in every loop. On some loops (CAPHE), two cold traps are connected in parallel with only one of them in operation so that testing need not be interrupted in case of plugging.

TABLE 2

COLD TRAP DATA	OBELIX	CAPHE	5 MW		50MW/CGVS
Sodium volume ( m <sup>3</sup> )	1.5	0.2	0.4	0.4	4
Flow rate through trap (m <sup>3</sup> /h) with circuit temperature of ... °C	10 400	1 400	1 560	1.3 550	16 350
Time required for passage of the total sodium volume in the loop (hours)	6	3	3	2.5	8
Cooling system	organic liquid + water	air	air	air	organic liquid + water
Internal (I) or external (E) economizer	I + E	I	I	I	I + E

Table 2 shows the major characteristics of the different cold traps. It should be noted that, although the cold traps may be used irrespective of the temperature in the loop, the maximum flow rate through the trap decreases as the loop temperature rises. The time required for all the sodium to transit the cold trap ranges from 3 to 8 hours in the different test loops. This characteristic is essential for specifying trap dimensions ; on the four loops in question it means that sodium purification can be achieved within 2 to 4 days (provided that the trap is not clogged).

Figure 1 is a schematic view of the trap used on the OBELIX loop which is similar to the CGVS cold trap. Noteworthy features include the built-in economizer which reduces the likelihood of premature clogging, the peripheral organic liquid flow cooling system with a NaK thermal seal, and the centripetal sodium circulation throughout the lower portion of the trap. The smaller traps are of similar conception, but are air-cooled.

The service life of a cold trap is difficult to determine in advance. The original trap is still in use on OBELIX : based on temperature measurements inside the filter it is currently estimated that the trap is clogged up to about two-thirds of the height



of the filter. The cold trap has been replaced on an average of every 18 months in CAPHE ; the total surface area of a fuel sub-assembly is very extensive, and hence the total quantity of impurities introduced by absorption. Hydrogen is the dominant impurity found in the steam generator test loops, and the quantity to be trapped can be predicted with greater accuracy, as will be discussed later.

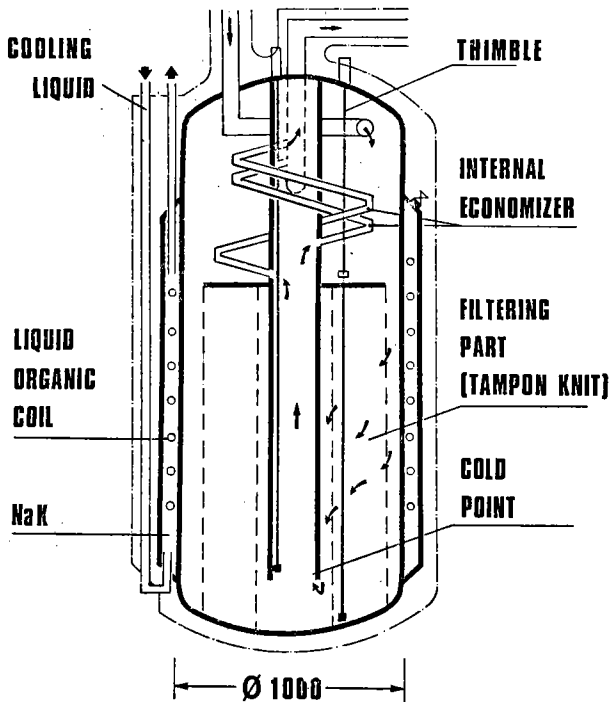


Figure 1 : Cold trap in the OBELIX loop

2.1.2. Filters

No filter is provided on the OBELIX test loop, while the other loops include a fill-in filter with porosity ranging from 10 to 50  $\mu$ m. This difference is explained by the use of purified sodium storage for OBELIX (refer to paragraph 2.3.1.) and the absence of mechanical pumps requiring protection from swept metal particles.

The CGVS loop includes an additional 100  $\mu$ m filter on the mechanical pump in flow line to provide full protection against metal particles.

The filters used are made from sintered stainless steel or from wire gauze.

2.2. Purification control

2.2.1. Plugging indicator

The plugging indicator is the basic instrument used to monitor sodium purification operations. Although it does not provide precise identification of the impurities themselves, it indicates immediately whether or not the sodium is contaminated. This very useful device also makes it possible to ensure a certain degree of sodium purity during testing. Figure 2 is a cut-away view of a plugging indicator widely used on test loops.

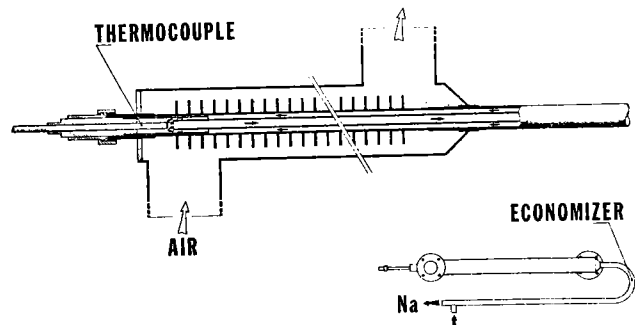


Figure 2 : Plugging indicator

Current practice involves sequential, automatic plugging indicator operation which provides temperature slope or step plots. The major advantage of automated operation is to ensure that the measurements are reproducible.

2.2.2. Hydrogen detection

In addition to the plugging indicator, the steam generator test loops are equipped with a nickel-membrane hydrogen detector, described in detail by Mr. CABBILLARD in another paper presented at this conference.

2.2.3. Sodium sampling

All the test loops include some means of taking sodium samples for laboratory analysis ; several techniques are used. The essential quality of any method is to obtain a perfectly representative sample, i.e. the sodium must not be contaminated during the sampling operation itself nor during transfer to the inert-atmosphere glove box.

Figure 3 shows a typical sampling unit : the one in service on the CGVS test loop at LES RENARDIERES.

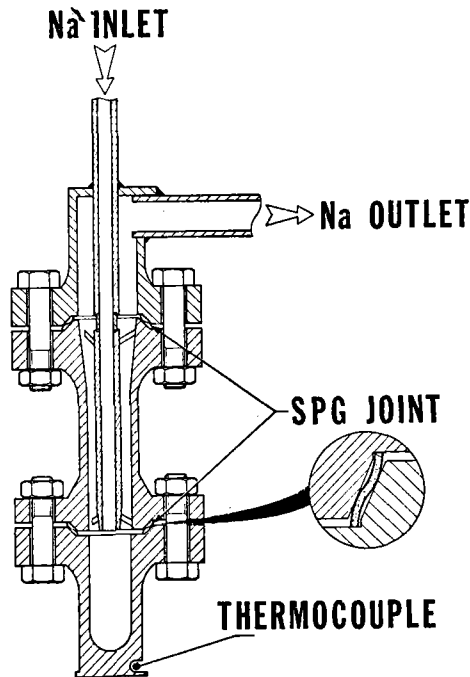


Figure 3: ACTINA sampling unit

It consists essentially of :

- . an upper section (1) connected to the sodium inflow and outflow lines, and which is not disassembled from the loop.
- . the intermediate (2) and lower (3) sections, which are removed from the loop as a unit and are only separated under helium atmosphere in the glove box. The intermediate section (2) protects the lower portion (3) during transport and handling.

Depending on the circumstances, the impurities determined in the sodium include oxygen, carburized compounds, and metals (Fe, Ni, Cr, Ca). Such determinations are generally useful in qualifying the sodium during testing, and are indispensable when unusual impurities are encountered.

### 2.3. Loop purification procedures

#### 2.3.1. Purification of stored sodium

The first loop built in FRANCE all included low-temperature storage with no provision for connection to the cold trap. It was assumed that the impurities

would be deposited on the walls of the storage tank and that purification would thus occur "automatically".

Current practice has reversed this configuration. Sodium is now stored at higher temperatures (400°C) and may be channeled through the cold traps. This arrangement has been adopted on OBELIX and on other more recent loops.

The reasons behind this technique are simple :

- The storage temperature of 400°C was selected to minimize the effects of thermal shocks in case of rapid draining of 600°C sodium.
- Impurities previously deposited on the walls will almost certainly be dissolved at 400°C, and this temperature is high enough to ensure satisfactory purification by cycling the sodium through a cold trap.
- It is always advantageous to fill a loop with clean sodium, thereby simplifying the entire purification process.

#### 2.3.2. Purification sequence

Each new test in a loop begins with a purification operation; the procedure is fairly well defined :

- The loop is filled with sodium at a temperature of 150 - 180°C.
- The cold trap and plugging indicator are put into operation immediately (cold point temperature : 130 - 150°C).
- The temperature in the circuit is raised in 20°C steps. Each temperature use is permitted only when the plugging temperature is near the cold point in the trap.
- When the loop temperature reaches 400°C the cold point temperature of the trap is lowered to 110°C.
- As soon as the plugging temperature drops below 120°C the purification process is considered to be complete, and the loop temperature may be raised to 600°C without further purification measures.

On completion of the process, the cold trap is generally kept in operation. Plugging temperatures

are recorded at regular intervals, and should remain stable at about 110° C.

Sodium purification procedures are similar on steam generator test loops, with the hydrogen detector operative from the beginning of the process. The power rise is only initiated after purification is completed. During operation under power, the major impurity in this type of loop is hydrogen ; this problem is discussed in paragraph 3.3. below.

3 - OPERATING EXPERIENCE WITH CERTAIN IMPURITIES

Sodium purification is a routine procedure which raises few problems in well equipped and well run loops. This is not true, however, when impurities other than those from circuit walls are introduced accidentally or intentionally into the sodium. Three such impurities have been of particular significance:

- Calcium : voluntarily introduced, since new loops at CADARACHE are generally filled from the outset with industrial grade sodium.
- Oil from pumps : an accidental impurity found in the three loops equipped with mechanical pumps (CAPHE, 5 MWT, 50 MWT).
- Hydrogen : unavoidable in steam generators.

3.1. Calcium

"Industrial grade " sodium (Ca content less than 500 ppm) costs only half the price of " nuclear grade " sodium (Ca content below 10 ppm). For this reason new loops at CADARACHE are filled with industrial grade sodium in spite of a few drawbacks arising during start-up operations.

Two types of difficulties may be noted :

- Plugging measurements are difficult to interpret with fresh sodium, as demonstrated by the values recorded during the start-up of the OBELIX Loop (refer to Figure 4). This loop included two storage tanks ; one contained older sodium without calcium, for which the plugging indicator gave perfectly normal results. The other tank was filled with fresh industrial grade sodium which gave this rather unusual readout - notably between points 10 and 20

where the flow rate falls off sharply while the temperature rises.

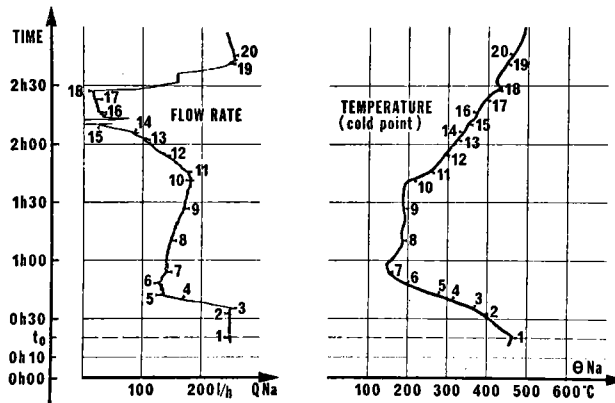


Figure 4 : Plugging measurements with calcium-charged sodium

- On one occasion the flat channel of an electromagnetic pump was plugged. Analysis showed that the obstruction contained significant amounts of calcium and carbon, although the chemical form of these elements could not be accurately determined.

Such incidents clear up as soon as the calcium content drops below 50 ppm. Fortunately this occurs after only a short time : calcium, a strong reducing agent, combines with other impurities in the sodium to form insoluble compounds which are quickly deposited in the storage tanks, the filters or the cold traps.

The procedure that has been adopted consists first in filling the loop and heating the sodium above 300° C, then draining it off into the storage tanks where it is allowed to cool. The loop is next refilled with cold sodium ( 150° C) which is cycled through a filter. The cold trap and plugging indicator are then put into service and, finally, sodium samples are analyzed for a calcium content.

In this way the calcium content falls off rather quickly, and the few days which may be lost during this process are more than offset by the saving involved in buying a less expensive grade of sodium.

### 3.2. Oil from mechanical pumps

Although the mechanical pumps are designed to prevent oil spillage from the upper bearing into the sodium, such incidents may occur because of operating errors. On CAPHE and on the 5 MWT loop, the oil recovery tank overflowed after improper draining or after a bad pipe connection. More recently, in October 1975 on the CGVS loop, oil leakage was caused by accidentally induced vacuum conditions prior to sodium filling. Such oil leakage is a serious incident in the loop : the oil decomposes in sodium to form a number of gases - hydrogen in particular - and solid, carbon-based compounds which are virtually insoluble in sodium and often adhere to loop walls.

It is worth discussing how the oil was detected in these three sodium loops, how it was subsequently eliminated, and what were the consequences on the loop components.

#### 3.2.1. Initial signs of oil leakage

On CAPHE, gradual oil leakage was observed during endurance testing at 600° C. The first signs appeared on the plugging indicator and cold trap, but the most significant indication was plugging in the argon lines - no doubt caused when the oil reacted with sodium aerosols in the argon. These plugs were insoluble in the sodium even at 500 °C.

On the 5 MWT loop, leakage occurred on the primary circuit pump. The first anomaly noted was the sudden rise in the plugging temperature from 120° C to nearly 300° C, followed by complete plugging of the system. After replacement of the indicator and the cold trap, a second distinctive sign appeared : the hydrogen content increased in the secondary circuit. A hydrogen influx of 52 mg/h measured in the sodium/potassium of the secondary circuit could only have come from the primary sodium by diffusion through the intermediate heat exchanger.

This hypothesis was confirmed when a 315° C diffusion threshold was revealed, and by studying hydrogen content variations according to the relation  $e^{-\frac{K}{T}}$  which characterizes the diffusion process.

On CGVS the initial sign was clear : the mecha-

nical pumps could not be started because of seizure of the lower bearings by carbonaceous compounds.

#### 3.2.2. Carbon elimination from the loops

The carbon was eliminated from CAPHE by completely replenishing the sodium and cleaning out the storage tank. The plugs in the argon lines were destroyed by disconnecting them from the rest of the loop, injecting water-bearing nitrogen and finally rinsing them liberally with water.

In spite of these measures, the carbon content was still 170 ppm when the loop was started up again ; three months later this value had dropped to 20 ppm and has remained practically stable since then.

The sodium in the 5 MWT loop was purified by using the cold trap - first singly and then in conjunction with filters : six filters were used in turn with porosity decreasing from 90 to 6  $\mu\text{m}$ . After several months of filtration and purification, the carbon content was still 130 ppm and solid particles continued to be trapped by the filters. More than one year of operation was required to return to normal operating conditions.

The same technique is currently applied on the CGVS loop.

#### 3.2.3. Carburization of metal surfaces

Samples were taken of pipe sections on CAPHE and the 5 MWT loop for metallurgical analysis. In both cases, superficial carburization was observed, 150  $\mu\text{m}$  deep on the 5 MWT and 500  $\mu\text{m}$  deep on CAPHE.

Similar phenomena were observed on the sub-assembly mock-up in the CAPHE loop when the oil leak occurred. The metal fuel pins were carburized, causing extensive corrosion when the same mock-up was subsequently tested in a water circuit.

These carburization phenomena require even more stringent sodium purification to ensure that whenever the temperature exceeds 400° C only very pure sodium is present in the loop. Such precautions then could induce gradual decarburization of the metal surfaces. This process must be closely monitored by sampling at regular intervals.

It goes without saying that all due care should be taken to prevent further oil leakage.

3.3. Hydrogen from steam generators

Hydrogen is inevitably present in any circuit because of the humidity remaining from the initial assembly, and introduced during each subsequent dismantling operation. Metal components in the loop also contain hydrogen which diffuses into the circuit as the temperature rises.

The major source of hydrogen in steam generator test loops is diffusion through heat exchanger walls. The rate of this diffusion depends on the nature of the tube materials and on the steam generator operating temperature and thermal power level.

Hydrogen is eliminated by means of a cold trap in which the cold point temperature is maintained at approximately 110 °C. Experience has shown that the hydrogen is trapped in this way without difficulty.

Quantitative data on cold trap behavior with hydrogen has been provided by two types of test :

- A plugging temperature vs. hydrogen content curve was plotted from measurements made after introducing known quantities of hydrogen into the sodium of several circuits (see Figure 5). It was observed that the

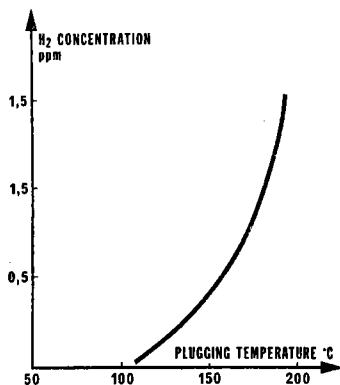


Figure 5 : Hydrogen content variations versus plugging temperature

plugging temperature for cold-trap outflow sodium could be related specifically to its hydrogen content, and that its value approximated the cold point tempe-

perature in the trap.

- The following operations were carried out during stable operation of the steam generators (refer to Figure 6) :

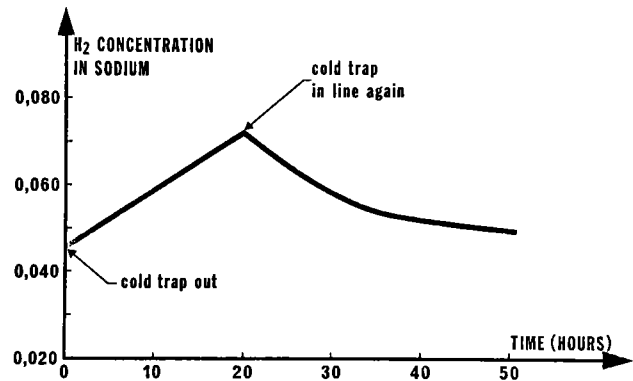


Figure 6 : Typical plot of hydrogen concentration in the sodium versus time

. When the cold trap was isolated from the loop, the hydrogen concentration increased at a linear rate with respect to time; the mean hydrogen diffusion rate could be calculated from the total sodium mass and the thermal exchange surface area on the water side of the steam generator.

. The hydrogen concentration in the sodium dropped immediately when the loop sodium was again cycled through the cold trap. The curve tends to level off at a value which depends on the hydrogen diffusion rate, on the cold point temperature and on the sodium flow rate through the cold trap. Actual experimental values were in close agreement with the calculated hydrogen concentration curves.

It should also be pointed out that hydrogen may be reintroduced into the loop by a cold trap as easily as it is eliminated. This phenomenon was revealed by incidental rises in cold trap regulation temperature. This regulation should be checked whenever the hydrogen concentration increases in the sodium to ensure that the cold trap itself is not responsible.

Measurements of hydrogen diffusion rates on various test facilities have shown that this phenomenon is not at all negligible. It must be considered with

## INTERNATIONAL CONFERENCE ON LIQUID METAL TECHNOLOGY IN ENERGY PRODUCTION

respect to the sensitivity of the hydrogen detection system used to monitor steam generator leakage ; but it also constitutes a major source of sodium pollution which may reduce cold trapping efficiency and require replacement or regeneration of the cold trap.

### 4 - CONCLUSIONS

Experience in operating sodium loops has been invaluable in designing purification equipment, monitoring facilities and operational procedure.

It is currently possible to obtain clean sodium permitting representative testing of reactor sodium.

This experience has also confirmed that correctly purified sodium does not induce significant corrosion on loop components : none of the sodium leaks observed in these loops could be attributed to corrosion phenomena. Continuous operation with clean sodium is unquestionably one of the major factors in reactor service life.

The experience acquired thus far has provided valuable data for mastering the detrimental effects of certain impurities. Many aspects of calcium behavior are still undetermined, but its effects are not generally serious. Oil leakage from the mechanical pumps is, however, a major problem : it is very difficult to eliminate from the loop and its effects on loop soundness are not at all negligible. Hydrogen impurities are readily measurable (with plugging indicators and hydrogen meters), easy to eliminate in the cold trap, and predictably formed during steam generator tests as well as in reactor secondary circuits.

### ACKNOWLEDGMENTS

The authors would like to thank the following persons, whose work provided much of the data in this paper :

Messrs J.C. COCHET	C.E.A. CADARACHE
J. GIRARD	C.E.A. CADARACHE
L. IANNOU	E.D.F. CHATOU
J.C. MASSON	E.D.F. LES RENARDIERES
C. OBERLIN	E.D.F. LES RENARDIERES
A. TIBI	C.E.A. CADARACHE

### REFERENCES

- (1) MILLIAT (J.P.), BEAUFRERE (J.), LECOQ (P.), CHAUVIN (M.) - Circuit d'essais à grande puissance de générateurs de vapeur chauffés au sodium (CGVS). Symposium on progress in sodium-cooled fast reactor engineering. IAEA, MONACO, 23 - 27 Mars 1970.
- (2) BEAUFRERE (J.), DE MONTARDY (A.), LECOQ (P.), LLORY (M.) - Essais sur le C.G.V.S. d'une maquette de 45 MW du générateur de vapeur de PHENIX. Entropie n° 53, Septembre - Octobre 1973.
- (3) FONTAINE (J.P.), IANNOU (L.), LLORY (M.), MASSE (J.), MASSON (J.C.), QUINET (J.L.) - Synthèse d'essais de maquettes d'un générateur de vapeur proposé pour la Centrale SUPER PHENIX. Conférence Nucléaire Européenne - PARIS, Avril 1975.
- (4) LECOQ (P.), IANNOU (L.), MASSON (J.C.) - Surveillance de l'étanchéité sodium-eau des générateurs de vapeur chauffés au sodium par dosage de l'hydrogène. Application industrielle au C.G.V.S. I.A.E.A. - S.M. - 168/E.7 VIENNE 1973.
- (5) BERGE (Ph.), OBERLIN (C.), SAINT-PAUL (P.) - Journal of Nuclear Materials 57, p. 283-286, 1975.
- (6) ROBIN (M.G.), Station d'essais thermiques de GRAND QUEVILLY. Circuit de sodium de 5 MW avec générateur de vapeur surchauffée à 545°C. Rapport CEA R. 2520 - CEN/SACLAY Juillet 1964.

# INTERNATIONAL CONFERENCE ON LIQUID METAL TECHNOLOGY IN ENERGY PRODUCTION

## IDENTIFICATION OF IMPURITIES IN SODIUM AND ITS PURIFICATION

B.I. Subbotin

F.A. Kozlov

Ju.I. Zagorulko

E.K. Kuznetsov

L.G. Voltchkov

The Institute of Physics &  
Power Engineering  
Obninsk, USSR

### ABSTRACT

The paper presents some investigation results on sodium technology. In particular, a description is given of a calculation method for evaluation of sodium-cover gas-impurities equilibrium compositions as well as experimental results on development of methods for sodium sampling, equipment for non-metallic impurities (oxygen, hydrogen, carbon) constant control in sodium. The investigation results on sodium purification with cold traps are presented.

### INTRODUCTION

The use of sodium as a coolant in fast reactor power plants motivated development of a special field of scientific and technical investigations-sodium technology. To its main problems should be related, in the first turn, provision of necessary purity of sodium coolant under the conditions of power plant operation and control of impurities content.

It is evident that technical and economic possibilities of solving sodium technology problems are inextricably connected with definition of extensive studies of fundamental problems of sodium chemistry, physical-chemical characteristics of sodium-impurities-structural materials-cover gas systems, kinetic and hydrodynamic aspects of impurity behaviour in sodium coolant. Many of the above mentioned problems have been discussed in works published in the USSR and other countries.

In paper a survey of main works is given as well as recent data on purification of sodium from impurities and their indication obtained in the USSR with the participation of the authors of this paper.

### Impurities in Sodium Coolant, Thermodynamic Methods for Analysis of Sodium-Shielding Gas-Impurities Systems

For solving the problems of impurities identification in sodium and its purification important is the information on impurities state, solubility, chemical reactions taking place in the system impurity-coolant-structural material-cover gas. Unfortunately, the information on these problems at present is insufficient.

A comparison of chemical analysis results for commercially produced sodium (see Table I) and of data on impurity solubility in sodium is indicative of the fact that both in sodium charged in the plants and in sodium in the circuits that main part of impurities is in the state of suspensions.

Table I

Concentration of Main Impurities in Sodium Charged in the Plants [I]

Impurities	In sodium supplied by manufacturer, ppm	In sodium prepared for filling reactor circuits, ppm		
		BR-5	BOR-60	BN-350
Potassium	200	200	200	50
Calcium	60	<10	60	25
Carbon	60÷70	40	40	20
Nitrogen	10÷15	10	12	4
Chlorine	20÷40	15	12	25
Oxygen	~100	<10	~5	~7
Hydrogen	~40	6	6	5

This obstacle considerably influences the solution of problems of representative sampling and identification of impurities in sodium and may cause complications at operation of commercial plants. Preliminary information on impurity state in the system sodium-cover gas and on their effect on structural and technological materials may be obtained using thermodynamic calculation methods of equilibrium states.

In a general case the system sodium-cover gas-impurities, consisting of  $i$ -components formed by chemical elements in the state of chemical equilibrium (at  $P, T = \text{const}$ ), is a polyvariant system containing  $\alpha$  phases, the general number of which being determined by the Gibbs phase rule.

The chemical potential of the  $i$ -th substance in phase  $\alpha$  has the form of:

$$\mu_i^\alpha = \bar{\mu}_i^\alpha + \Delta \mu_i^\alpha, \quad (1)$$

where  $\Delta \mu_i^\alpha$  - is the excessive chemical potential,  $\bar{\mu}_i^\alpha$  - corresponds to an ideal system.

In its turn,

$$\bar{\mu}_i^\alpha(N_i^\alpha, T, P) = \bar{\mu}_i^\alpha(T, P) + RT \ln \left( \frac{N_i^\alpha}{N^\alpha} \right) \quad (2)$$

Taking into account (1) and (2) the equation of chemical equilibrium for formation reactions for each  $i$ -component of  $k$  chemical elements ( $j=1 \dots k$ ) may given (omitting phase indexes) as:

$$\frac{N_i/N}{\prod_{k=1}^K (N_k/N)^{a_{kj}}} = K_i \Delta K_i, \quad (3)$$

where  $a_{kj}$  - is the stoichiometric matrix for the formation reaction of the system components by chemical elements,  $\Delta K_i$  - is the equilibrium constant corresponding to the excessive chemical potential. When adding the material balance equations for chemical elements to (3):

$$\sum_{\alpha=1}^P \sum_{j=1}^K a_{ij} N_i^\alpha - N_i^0 = 0 \quad (4)$$

a closed equation system is obtained. This system completely describes chemical equilibrium of an arbitrary thermodynamic system. Taking into consideration the given system in the ideal approximation, i.e. assuming  $\Delta K_j = 1$  and postulating the presence of two phases only (of gas and condensated ones) where all the substances may be mixed in arbitrary ratios, we come to a system formed by  $i = i^g + i^c$  components consisting of  $k$  series of chemical elements ( $k = 1 + m$ ). The system composition is arithmetized relative to some basis that can be most suitably chosen from the formation reaction of the system components of chemical elements involved. In this case two stoichiometric matrices  $g_{ie}$  and  $c_{im}$  are obtained for gas and condensated phases correspondingly. The complete equation system of chemical equilibrium with account for arithmetization



carried out has the form of:

$$N_i^g = K_{ig} P^{\sum q_{ie} - 1} (N^g)^{-\sum q_{ie}} (N^c)^{-\sum c_{im}} \prod N_c^{q_{ie}} \prod N_m^{c_{im}}, \quad (5)$$

$$N_i^c = K_{ic} P^{\sum q_{ie}} (N^g)^{-\sum q_{ie}} (N^c)^{-\sum c_{im}} \prod N_c^{q_{ie}} \prod N_m^{c_{im}}, \quad (6)$$

$$\sum N_i^g - N^g = 0, \quad (7)$$

$$\sum N_i^c - N^c = 0, \quad (8)$$

$$\sum q_{ij} N_i^c + \sum c_{ij} N_i^g - \sum q_{ij} (N_i^{0,g} + N_i^{0,c}) = 0 \quad (9)$$

Difficulties of numerical solution of non-linear equation system (5)-(9) can be eliminated by preliminary linearization of the system according to Newton-Rafson with using the computational algorithm that consists of successive solution of the system (5)-(9) for some set of subsystems each of which relates to substances formed by sodium and correspondingly by two and so on chemical elements. In this case the solution of the preceding step is used as initial approximations for the next one.

In Fig. 1 a graphical example is given of a calculation for equilibrium composition of the system Na-Ar-O-C-H in the temperature range of 700-1000°K. Fig. 2 presents temperature dependences of equilibrium constants for the reaction of forming the components included into the system.

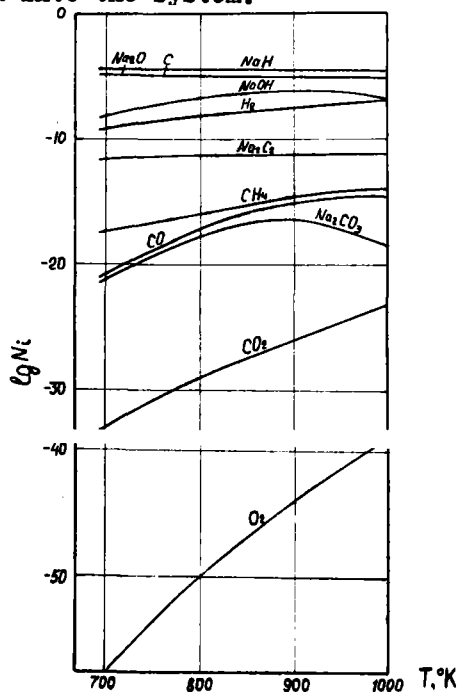


Fig. 1. An example of

equilibrium state calculation for Na-Ar-O-C-H system.

Initial composition of the system:

Na - 1 mole  
 O<sub>2</sub> - 2,5 ppm  
 P<sub>Ar</sub> = const = 1 n/m<sup>2</sup>  
 C - 5 ppm  
 H<sub>2</sub> - 1 ppm

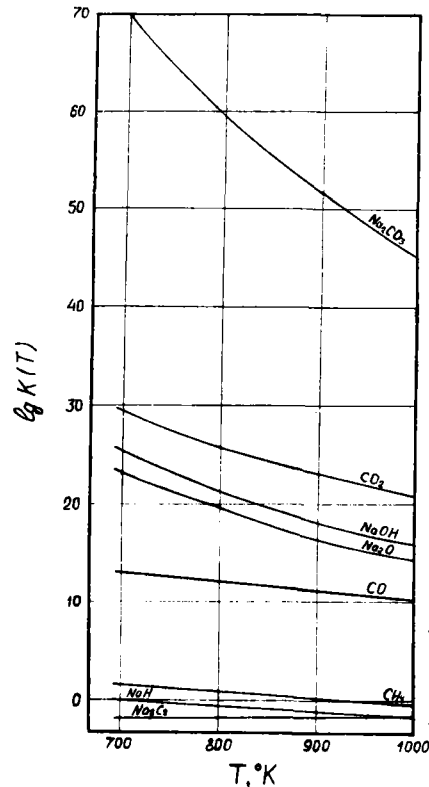


Fig. 2. Equilibrium state constants for formation reactions of some matters included in the system Na-C-O-H of simple matters.

### III. Problems of Sampling and Identification of Impurities in Sodium

Universal sampler-distillator is widely used for sodium sampling in experimental rigs [2]. Its design is shown in Fig. 3. The sampler can be used for work with alkali metals and their alloys, it makes it possible take out 5-6 samples for further analysis on metal and non-metal impurities. The sampler design and distillation regimes adjusted

(chosen) allow to withdraw sodium from the sampling chamber before its contact with ambient atmosphere for removal of crucibles with sample residues after distillation. At analysis of sodium samples for oxygen nickel and molybdenum crucibles are used. Sample volume is 100 cm<sup>3</sup>. When analyzing sodium for carbonaceous impurities quartz cylinders of 15 cm<sup>3</sup> volume are used.

The following distillation regimes were found (chosen) experimentally:

- analyses for oxygen-temperature within the distillator - 450°C, distillation time - 5 hours, vacuum -  $\sim 10^{-2}$  mm Hg, mean value of dummy correction at identification of oxygen content in sodium was  $1.6 \pm 0.2$  ppm;
- analyses for carbon forms (total solid (non-volatile) carbon and carbonate carbon) - temperature within the distillator - 360°C, distillation time - 6-8 hours, vacuum -  $\sim 10^2$  mm Hg, mean value of dummy correction for carbon identification (solid forms) in sodium was  $4 \pm 0.5$  ppm.

Additional experiments were carried out for studying behaviour of carbonaceous impurities in the process of distillation.

Peculiarities of acetylide behaviour during distillation were discovered when comparing the results of sodium samples analysis. The samples were taken from the experimental rig sodium containing acetylide with constant concentration with preliminary distillation and without it.

At distillation temperature of 360°C for 7-8 hours (vacuum of  $10^{-3}$ - $10^{-2}$  mm Hg) practically a complete loss (within the analysis precision limits) occurred of acetylide from sodium samples quartz crucibles ( $V = 15$ - $20$  ml). The analysis results of simultaneously taken samples without distillation gave acetylide concentration of 8-9 ppm.

Direct experiments with distillation of weighed amount (27 g) of sodium and collection of condensate showed that sodium condensate contained  $\approx 50\%$  of acetylide as compared to the initial amount.

The experiments on choice of distillation regimes at sodium sampling for carbonate analysis showed that a noticeable loss

of carbonate was already observed at distillation temperature of 350-400°C. Carbonate weighed amount (50 mg) was introduced into quartz crucibles. This portion was prepared by concentration by evaporation of carbonate aqueous solution. The crucibles were inserted into the sampler-distillator and were then filled with sodium. After distillation at 400°C only 77% of the carbonate introduced were found. Studies of gas evolution at carbonate exposure in sodium at temperatures of 350-400°C in the atmosphere of purified helium and at periodical gas blowing through the freezing trap did not show any noticeable accumulation of CO<sub>2</sub> in the trap in comparison with the dummy experiment. From these experiments it followed that carbonate did not dissociate noticeably under the temperatures mentioned. Its losses in the process of distillation are likely to be caused acetylide formation (under the temperatures  $> 360^\circ\text{C}$ ) with its further transport into sodium.

Impurity plugging meters are widely used in plants and experimental rigs with sodium coolant to control the general level of contamination.

The designs of plugging meters operating in periodical and continuous automatic regimes are described in literature [3-7]. Detailed studies of plugging meter operation of periodical action are given in [8]. Later in [9] a possibility of plugging meter use is mentioned for identification of impurity type causing plugging of orifices. It should be said that in principle this possibility follows from the theoretical analysis of processes in the plugging meter. But verification of this phenomena on sodium has shown that experimental data obtained are ambiguous, especially when impurities are present simultaneously. It has been noticed that the plugging meter well registrates the products of carbonate reaction with sodium. Fig. 4 gives the results of one of the experiments after introduction of 40 g of sodium carbonate into the circuit.

A noticeable interaction of carbonate with sodium occurred at temperatures of

350-360°C.

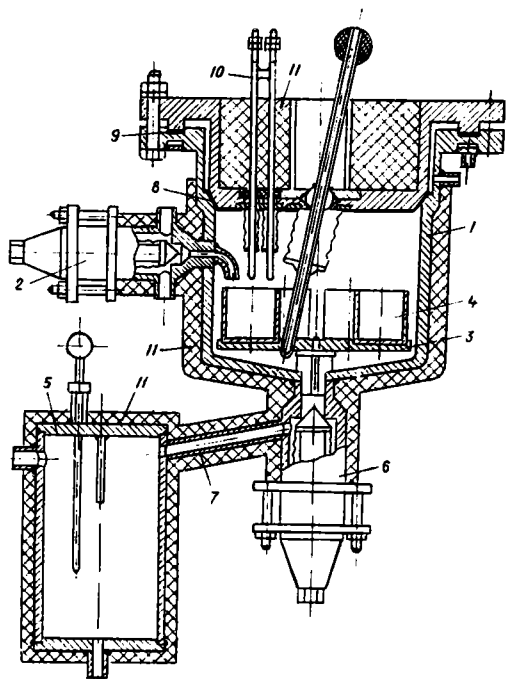


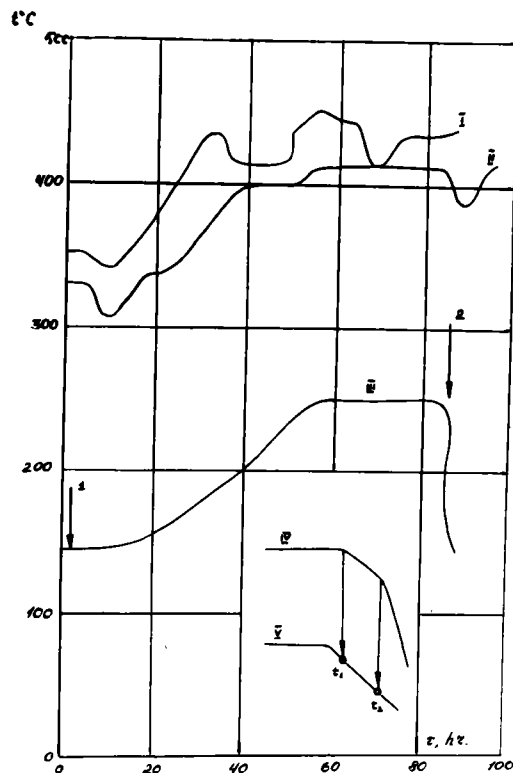
Fig. 3. Sampler-distillator.

1 - distillator body; 2 - valve for samples drainage; 3 - rotating platform; 4 - crucible for a sample; 5 - condenser; 6 - valve; 7 - piping between distillator and condenser; 8 - conical bolt with metallic gasket; 9 - rubber sealing; 10 - level meter; 11 - heating and insulation.

Peculiar is the presence of initial sloping section on sodium flow rate curve through the plugging meter and of two angularities corresponding to two plugging temperatures ( $t_1$  and  $t_2$ ).

The beginning of the second plugging temperature increase corresponds to the moment of the first sloping section appearance. The experiments with the plugging meter make it possible to investigate temperature stability of carbonate in sodium. The final value of  $t_2 = 250^\circ\text{C}$  in the experiment described corresponded to completion of carbonate with sodium reaction. Oxygen concentration calculated with account for Noden's equation [10] for  $255^\circ\text{C}$  was 36 ppm,

that (within the accuracy limits the plugging meter) was in good agreement with oxygen concentration obtained at complete decomposition of all the carbonate (38 ppm). Double angularities were similarly noticed on flow rate curves through the plugging meter at simultaneous presence of oxygen and hydrogen in sodium.

Fig. 4. Variation of plugging meter readings at exposure of  $\text{Na}_2\text{CO}_3$  in a circulation sodium rig.

- I - sodium temperature at main heater outlet;
- II - sodium temperature of the rig inspiratory capacity;
- III - plugging temperature  $t_2$ ;
- IV - curve of sodium flow rate through the plugging meter;
- V - curve of temperature variation on the plug indicator orificies;
- $t_1$  - first plugging temperature;
- $t_2$  - second plugging temperature;
- 1 - introduction of  $\text{Na}_2\text{CO}_3$  into the circulation rig inspiratory capacity;
- 2 - cold trap insertion.

Plugging meters were calibrated at sodium contamination with oxygen, hydrogen, water. The experiments for definition of oxygen saturation curve carried out recently without its additional contamination with hydrogen gave the results close to Noden's generalization [10].

$$\lg C_{O_2} = 6,26 - \frac{2444,5}{T} \quad (10)$$

(110-550°C)

The saturation curve at contamination of sodium with hydrogen obtained with the plugging meter has the form of:

$$\lg C_{H_2} = 6,98 - \frac{3209}{T} \quad (11)$$

(200-350°C)

At sodium contamination with water the following equation of solubility curve (calculated for hydrogen) was obtained:

$$\lg C_{H_2} = 5,93 - \frac{2650}{T} \quad (12)$$

(200-450°C)

The tests of the automatic plugging meter (APM) performed by us confirm its efficiency. The interval of automatically regulated (controlled) temperatures was 145-260°C. Measurement accuracy is compared with the accuracy of the plugging meter of periodical action. Automatically regulated saturation temperature corresponded to an impurity with high rate of mass transfer. In our tests that was a low-temperature impurity in equilibrium with the cold trap temperature.

Variation of hydraulic characteristics due to impurity settling in the throttle on the test element by-pass of the plugging meter as well as inadequacy of sodium heating system after the cooler and behind the orifices are the main disadvantages complicating the APM operation.

These difficulties restricted the time of the plug indicator stable operation.

#### IV. Methods of Continuous Impurity

##### Control in Sodium

Hydrogen indicator in sodium comprises a unit maintaining constant temperature of sodium, nickel membrane, magnetic-discharge pump and high-voltage power pack of the pump and current measurement equipment.

The indicator has undergone laboratory tests on sodium circulation rig during 1500 hours. Its separate units were tested, and calibration characteristics were obtained. In this case calibration was done by dosing of known water quantities into the sodium circuit. Main technological parameters and characteristics of the hydrogen indicator obtained during the tests are given in table 2.

Table 2

Main Parameters of Hydrogen Indicator in Sodium

Sodium flow rate, m <sup>3</sup> /hr	:	0.5 - 1
Sodium inlet temperature, °C	:	250 - 500
Membrane temperature, °C	:	500 ± 1°C
Membrane dimensions	:	∅ 6 x 0.25 mm; : F = 20 cm <sup>2</sup>
Membrane time constant, sec	:	< 14
Pressure operation range,	:	1.10 <sup>-5</sup> ± 1.10 <sup>-7</sup> mm Hg :
Pumping-out rate, l/sec	:	~ 10
Pump supply voltage, kv	:	7
Calibration characteristic	:	ΔC <sub>H<sub>2</sub></sub> · wt% = : = 5.2 x 10 <sup>-7</sup> ΔJ, : mka
Maximum permissible sensitivity, wt% H <sub>2</sub>	:	~ 5 · 10 <sup>-6</sup>
Range of hydrogen concentrations measured in sodium, wt %	:	~ 1.10 <sup>-5</sup> - 1.10 <sup>-3</sup>

Galvanic cells for oxygen activity control in sodium have been developed in the Central Institute for Nuclear Research in GDR. Studies of their characteristics are carried out on sodium rigs in the USSR [11]. Ceramics on the base of thorium oxide with different additions is used as a material for solid electrolyte.

During cell testing it has been stated that during the first 40-60 hours of cell operation at nominal temperature growth of e.m.f. occurs, that is likely to be caused by the processes in the solid electrolyte and on the interface of solid electrolyte-sodium. Later the e.m.f. drift considerably

decreases nevertheless it exists. This fact and individual difference of the e.m.f. from its theoretical value necessitate periodical calibration of the cells that complicates their use with analytical purpose. For the whole time of testing not a single case of cell untightness was fixed.

Temperature coefficients of the cells during the initial period of their operation were close to the theoretical ones. Concentration coefficients of cell various cells were from 0.5 to 1 of the theoretical value.

In the process of operation with the galvanic cells experimentally was found the influence of hydrogen on oxygen in sodium (with hydrogen concentration increasing oxygen activity in sodium decreased).

For final conclusions on prospects of application indicators being developed for commercial plants it is supposed to continue testing on experimental rigs, to accumulate statistics, to improve stability factors.

Carbon meter. Realization of continuous control of carbon thermodynamic activity in sodium is more complicated as compared with possibilities to control such impurities as oxygen and hydrogen. The principle of diffusion membrane of carbon-penetrable materials (iron-armco) used requires increasing sodium temperature in the meter zone location up to 700-750°C [12]. For these reasons the diffusion cell is adjusted at a special heated by-pass of the main circuit with a part of sodium from the main circuit to follow through this by-pass.

Due to the fact that in the main circuit carbonaceous impurities are present in two conditions (solution and suspensions) there arise difficulties in interpretation of meter readings.

The experiments were performed on measurements of carbon activity in sodium on the experimental rig with introduction of acetylene into the sodium circuit. Before the experiments sodium was purified in a cold trap to the plugging temperature  $t_{\text{plug}} < 120^{\circ}\text{C}$ .

Sodium chemical analyses after purifica-

showed 1-2 ppm of carbon nonvolatile forms. Sodium acetylde was not found.

Two diffusion carbon meters were placed in different points of sodium circuit.

Before acetylene supply into the expansion tank of the rig the first meter signal was 0, on the second meter it was  $(1.82 - 2.13) \cdot 10^{-7}\%$  wt  $\text{CH}_4/\text{cm}^2$ .

After dozing acetylene into the circuit where the temperature was kept equal to 180°C, at subsequent heating of sodium up to 400°C chemical analyses have shown (according to the results of 6 samplings) 0.9 ppm of acetylde in sodium.

Depending on sodium flow rates through the meters from 62 l/hr to 107.5 l/hr on the first and from 78 l/hr to 132 l/hr on the second meter, their signals varied correspondingly from 0 to  $1.38 \cdot 10^{-5}\%$  wt  $\text{CH}_4/\text{cm}^2$  for the first meter and from  $2.13 \cdot 10^{-7}$  to  $1 \cdot 10^{-5}$  wt%  $\text{CH}_4/\text{cm}^2$  for the second meter.

The character of the signals was irregular reducing to some constant value at flow rate stabilization.

Sharp drops of sodium flow rate through the rig expansion tank, where the products of sodium with acetylene interaction were located, caused signal oscillations in the detectors in the ranges mentioned above.

The data presented are indicative of the complex mechanism of carbonaceous impurities behaviour in sodium, present as suspensions, and of determining value of hydrodynamic regimes in sodium circuit in the processes of carbon transport and of possible variations of its activity. From the other hand, due to this fact uncertain are the problems of detector readings interpretation as the characteristic of sodium carburizing potential.

#### V. Sodium Purification from Impurities with Cold Traps

Cold traps are at present the main means for sodium coolant purification from impurities.

In the USSR [13-15] on the basis of considerable experimental data the trap

design given in Fig. 5 is taken as fundamental one.

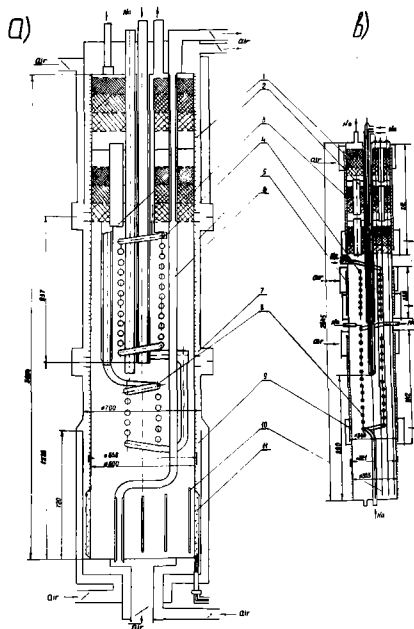


Fig. 5. Cold trap design

a) 800-liter trap

b) 180-liter trap

- 1,- channel for filter cooling;
- 2 - overflow pipes;
- 3 - filter packing;
- 4, 8 - tube coil-recuperator;
- 5 - air channel of final cooling-zone;
- 6 - air pipe;
- 7 - air mixer;
- 9 - cooling channel of settler;
- 10 - pockets for removable thermocouples;
- 11 - heater of settler bottom.

Its three peculiarities are: settler nonisothermicity, presence of oncoming mixed convection (OMC) in the final cooling zone, filter isothermicity.

OMC developing in the final cooling zone results in appearance of descending flow of cold sodium at the cooled wall. This flow descending into the settler thoroughly mixes with coming hot flow causing its cooling and dilution on impurity concentration. OMC is the cause of appearance of sodium circulation in the zone of final cooling, the flow rate in

which can sometimes exceed the main sodium flow rate through the trap. This leads to formation of a temperature field in the trap characterized by insignificant radial and axial gradients, the temperature in the zone of final cooling being practically equal to the temperature of sodium at the trap outlet.

Sodium downward flow at the cooled wall causes additional braking of incoming jet and formation of stagnation zone at the trap bottom. As mass exchange processes in the stagnation zone are strongly reduced, it is necessary to choose correctly the velocity of the incoming jet to use the trap volume more efficiently.

Mixing of cold and hot flows at the cut of the trap central tube leads to nucleation of impurity crystals in sodium flow. This impurity flow on mass exchange surface has two components: molecular one and in the form of particles. The nature of transfer processes in units Fig. 5, determine mass exchange characteristics obtaining of maximum accumulation quantities in the range of thorough mixing in the settler and at the filter inlet, Fig. 6 a.

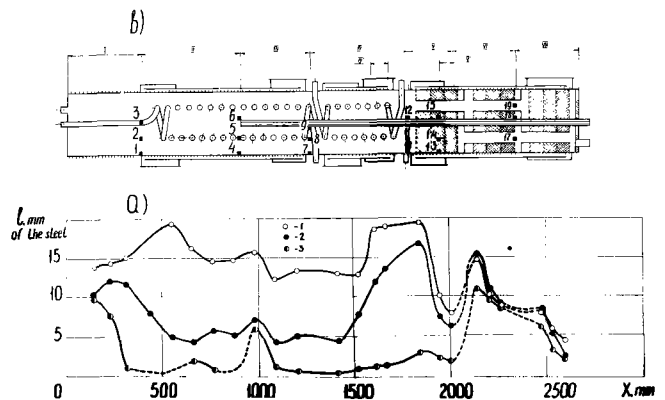


Fig. 6. a) Sodium oxide distribution over the height of 180-liter trap

- -  $G_{Na_2O} = 14$  kg, ● -  $G_{Na_2O} = 63$  kg,
- -  $G_{Na_2O} = 111$  kg.

b) Sectional cut of 180-liter trap and positions of local sampling:

INTERNATIONAL CONFERENCE ON LIQUID METAL TECHNOLOGY IN ENERGY PRODUCTION

1. ... 19. -positions of local sampling

The distribution shown in this figure of Na<sub>2</sub>O was obtained by the 180-liter trap examination with γ-rays.

The coefficient of oxygen retention in the trap, Fig. 5b, increased from ~0.7 in a clean trap to 1 after accumulation of ~68 kg of Na<sub>2</sub>O in it. The retention coefficient of sodium with water and hydrogen reaction products in the 180-liter trap increased from ~0.6 to 1 after accumulation of 24.9 wt % of impurities. The capacity of the 180-l trap on Na<sub>2</sub>O (concentration) was ~47 wt %. The distribution of Na<sub>2</sub>O and Na H over this trap height is shown in table 3. The capacity of the 800-l trap on sodium-water reaction products (concentration) was equal to ~ 24.9 wt %. It is considerably lower

than in case of the 180-l trap, that is determined by specific features of precipitation in the trap of a hydrogen-bearing impurity. The fact of capacity pointed out was mentioned in earlier works.

The main operation regimes of the trap-mechanical filter, purification at nominal conditions, redistributions - are described in [15] .

The mechanism of sodium purification from carbonaceous impurities by cold traps is still not clear up to now. Carbon retention in a cold trap is likely to be governed by simultaneous processes of dissolved carbonaceous impurities crystallization, of carbon coprecipitation with other impurities, for example, with oxygen or hydrogen, of precipitation of rather large particles due to small sodium rates within the cold trap suspensions retention in the filtration zone. At present all the data necessary for evaluation of each of this processes contribution into the mechanism of purification are not available.

Table 3

Concentration (content) of Na<sub>2</sub>O and NaH in the 180-l trap

	Na <sub>2</sub> O		NaH	
	: Gas-distillation-weight method		: NaH detected, g	
	: Na <sub>2</sub> O detected, kg		: C = $\frac{G_{NaH}}{G_{Na} + G_{NaH} + G_{Na_2O}} \times 100$ , wt %	
	: C = $\frac{G_{Na_2O}}{G_{Na_2O} + G_{Na}} \cdot 100$ , wt %			
I	14.4	36.8	8.2	0.021
II	34.7	69	12	0.0239
III	13.0	41	-	-
IV	29.1	61	171.5	0.387
V	9.2	51	65.8	0.477
VI	4.5	19	41.3	0.174
VII	3.8	17.5	7.3	0.0338
-----				
All the trap,				
kg			0.306	
-----				
Mean for all				
the trap,		46.6		0.132
wt %				

The ratio of impurity total concentration in sodium flow and of their concentration in dissolved state may be presented as:

$$\frac{\sum C_i}{\sum Si(T)} = \frac{1}{P_{Na} \sum_{i=1}^n Si(T)} [m_{tr.s.} + P_{Na} \sum_{i=1}^n Si(T)] \quad (13)$$

At sodium temperatures of 300°C this correlation, for instance, for  $\sum Si = 10$  ppm, can accept values from 100 to 500 depending on composition of impurities in sodium.

If it is assumed that sodium purification with a cold trap from carbon-bearing impurities is carried out only at the expense of impurity particles dissolving at the circuit temperature, corresponding to sodium temperature at the trap inlet, and subsequent crystallization processes and their complete retention in the cold trap, then the purification time ( $\tau$ ) from some initial level of the i-th impurity type C to some concentration  $C_{i,\tau} > Si(T_c)$  may be written in the form of:

$$\tau = \frac{P_{Na} (C_i - C_{i,\tau})}{G_t (Si(T_c) - Si(T_{c.t. outlet}))} \quad (14)$$

Calculations of  $\tau$  with the equation for some carbon impurities from the concentration  $C_i = 10$  ppm to  $C_{i,\tau} = 5$  ppm with the value of  $P_{Na}/G_t = 10$  and temperatures of  $T_c = 300^\circ C$ ,  $T_{c.t.} = 150^\circ C$  are given in table 4.

Table 4  
Calculation results for sodium purification from acetylide, cyanide and graphite (according to (14))

Impurity type	Si at $T_c = 300^\circ C$ , ppm	$\tau$ hr
Sodium acetylide	$7.2 \cdot 10^{-2}$	695
Sodium cyanide	$7.1 \cdot 10^{-3}$	7040
Graphite	$4.5 \cdot 10^{-3}$	11100

The values of  $\tau$  obtained considerably exceed the data found experimentally.

Table 5 shows the purification of commercially produced sodium obtained on the experimental rig with the total amount of the metal 288g at  $T_c = 300^\circ C$  and  $T_{c.t.} =$

$= 120-130^\circ C$ . The cold trap was a prototype of commercial traps used in the BN-350 plant.

At dosage into the circuit of considerable amounts of carbon-bearing impurities, such as graphite (particles of 2-5 mkm dispersion) with carbon concentration (150ppm), carbonate (40 ppm), acetylide (110 ppm) during 7-10 hours of purification with the same cold trap concentrations of 3 ppm were attained (carbon nonvolatile forms) at graphite dosage, 2 ppm at carbonate dosage and 2 ppm in case of acetylide.

After introduction of paraffin into sodium in the amount equivalent to 170 ppm of carbon, in 260 hours of sodium purification with the cold trap, carbon concentration in sodium was 41 ppm. Paraffin was introduced at the circuit temperature of 400-450°C, i.e. at temperatures when practically its complete pyrolysis took place. The products formed were characterized by relatively high transport characteristics, their retention by the cold trap required much time.

Table 5

Results of commercially produced sodium purification from carbon-bearing impurities with the cold trap.  $P_{Na}/G_t \approx 1$

Purification: time, hr	Impurity concentration in sodium during purification, ppm			
	Carbon solid forms	Acetylide	Carbonate	Carbon volatile forms
0		5	8	3 15
4		was not detected	6	was not detected not detected
8	- " -		4	- " - - " -
12	- " -		4	- " - - " -
16	- " -		6	- " - - " -
20	- " -		5	- " - - " -
23	- " -		2	- " - - " -
27	- " -		2	- " - - " -
31	- " -		3	- " - - " -
35		1	2	1 8



The experimental data presented indicate that the mechanism of sodium purification with the cold trap from carbon-bearing impurities cannot be explained by the crystallization processes and that determining are the processes of suspensions mass transfer between sodium and surfaces within the cold trap.

#### NOMENCLATURE

$\tau$	- time, hr;
T	- temperature, $^{\circ}\text{K}$ ;
P	- pressure, $\text{n/m}^2$ ;
R	- gas constant, $\text{j/moll. deg.}$ ;
$N_i^{\alpha}$	- number of i-component moles in $\alpha$ -phase;
$N^{\alpha}$	- total number of moles in $\alpha$ -phase;
$N_i^{0,\alpha}$	- initial number of moles of i-th component in $\alpha$ -phase;
$\alpha_{i,j}, \epsilon_{i1}, C_{im}$	- stoichiometric matrices of formation reactions for the system components of corresponding chemical elements;
g, C	- phase indices for gas and condensation phases, respectively;
$K_{ig}, K_{ic}$	- equilibrium constants for the system component formation reactions correspondingly in gas and condensation phases;
$C_i$	- concentration of i-th component, ppm;
$P_{Na}$	- sodium weight, kg;
Si	- concentration of i-th component corresponding to solubility limit, ppm;
$G_t$	- sodium flow rate through the trap, kg/hr;

#### REFERENCES

1. Karpov A.V., Arkhipov V.M., Matveev V.P., Baklushin P.N. Problems of Coolant Preparation for Fast Reactors. Paper to the Soviet-American Seminar on Fast Reactors. Obninsk, June 2-5, 1975.
2. Kozlov F.A., etc. A Device for Liquid Metal and Alloys Sampling. Author's certificate 355334, M., cl. G 01 1/10, 1972.
3. Bruggeman W.H., A.J.Ch.E. Journal, 2, 153 (1956).
4. Liquid Metals, Collection of articles, under the editorship of Kirillov P.V., M., Atomizdat, 1967.
5. Davidson D.F. and Rooch P.F. An Experimental Continuous-Indication Plugging Meter for Impurity Monitoring in Liquid Alkali Metals, UKAEA TRG Report 1640(K) (1968).
6. Rooch P.F., Davidson D.F. Sodium Impurity Monitoring by Automatic Plugging Meters. UKAEA, Nuclear Engineering International Technical Survey No 4, April (1971), vol. 16, No 179, p.p. 334-337.
7. Delesle J.P. In Alkali Metal Coolants, JAEA, Vienna (1967) (SM-85/4).
8. Subbotin B.I. et al. IAEA, Vienna (1967) (SM - 85/49).
9. Arnoldov M.N. et al. Atomnaya Energiya, v. 33, ed. 5, November 1972.
10. Noden J.D. J. Brit. Nucl. Eng. Soc., 12, No 3, 329, 1973.
11. Kozlov F.A. et al. Oxygen and Hydrogen Control in Sodium Circulation Circuit by Electrochemical Measurement Methods. Proceedings of the Second COMECON Symposium, Obninsk, September 1-5, 1973, v. 11, Obninsk, 1975.
12. Natesan K., Kassner T.F. et al. Reactor Technology, vol. 15, 4, 1972.
13. Voltchkov L.G. et al. Atomnaya energiya, v. 35, ed. 6 (December, 1973), p. 396.
14. Voltchkov L.G. et al. Development of Cold Traps for Sodium Impurities for Commercial Power Plants. Paper at the Soviet-American Seminar "Experience and Problems of Fast Neutron Sodium Cooled Reactor Construction and Operation", Obninsk, June 2-5, 1975.
15. Bagdasarov Ju.E. et al. Technical Problems of Fast Neutron Reactors. Under the editorship of Bagdasarov Ju.E., M., Atomizdat, 1962.

# INTERNATIONAL CONFERENCE ON LIQUID METAL TECHNOLOGY IN ENERGY PRODUCTION

## SODIUM AND COVER GAS CHEMISTRY IN THE HIGH TEMPERATURE SODIUM FACILITY

J.J. McCown

H.C. Duncan

Hanford Engineering Development Laboratory  
Richland, WA.

### ABSTRACT

The equipment and procedures used in following sodium and cover gas chemistry changes in the High Temperature Sodium Facility are presented. The methods of analysis and results obtained are given. Impurity trends which have been measured during the facility operations are discussed.

### INTRODUCTION

The High Temperature Sodium Facility (HTSF) is one of the major U.S. test facilities used in support of the Fast Flux Test Facility (FFTF) and the overall Liquid Metal Fast Breeder Reactor program. The HTSF is operated for the U.S. Energy Research and Development Administration by the Westinghouse Hanford Company at the Hanford Engineering Development Laboratory located a few miles north of Richland, Washington.

The HTSF consists of several major systems: the ex-vessel piping, pumps and storage tank; the main test vessel; several small side loops connecting the purification and characterization equipment and the argon cover gas system.

The primary purpose of the HTSF is to checkout FFTF reactor and fuel handling equipment in a non-radioactive sodium environment at temperatures up to 593°C (1100°F). It also provides operating experience with a large system, for the training of FFTF operators, and for the testing of maintenance techniques. The ex-vessel loop and auxiliary systems have been in operation since March 1974. The main test vessel was filled some 6 months later and the testing of full size FFTF in-vessel hardware, primarily the Instrument Tree and In-Vessel Handling Machine (IVHM), has been in progress for the past 18 months.<sup>(1)</sup>

During the facility startup, a major goal was to determine the operational parameters associated with sodium and cover gas purification and characterization in order to provide the basis for similar FFTF operations. The impurities in the cover gas

and sodium were measured periodically using state-of-the-art samplers,<sup>(2)</sup> plugging temperature indicators,<sup>(3)</sup> and on-line meters.<sup>(4)</sup> During the fill and first temperature ascension tests with the main test vessel, the chemistry changes occurring in the sodium and cover gas were followed in order to measure the pick-up of impurities from a system fabricated and installed under rigid cleanliness control.

### FACILITY DESCRIPTION

The HTSF is illustrated in Figures 1, 2 and 3. The high bay area is 53.3 m (175 ft) long, 22.9 m (75 ft) wide, and 27.4 m (90 ft) high and provides space for the movement of the Closed Loop Ex-Vessel Machine (CLEM); and for the handling of the In-Vessel Handling Machine (IVHM) and Instrument Tree as they are moved in and out of the Composite Reactor Component Test Activity (CRCTA) vessel and into the Alkali Metal Cleaning Facility (AMCF) located nearby. The CRCTA [4.6 m (15 ft) by 9.5 m (31 ft) deep] contains about 148 m<sup>3</sup> (39,000 gallons) of sodium and is capable of testing full-size FFTF and LMFBR components at temperatures to 593°C (1100°F). The ex-vessel sodium system contains heating, cooling, purification, and characterization equipment and maintains the sodium at



Figure 1. Exterior View of HTSF building

HIGH TEMPERATURE SODIUM FACILITY

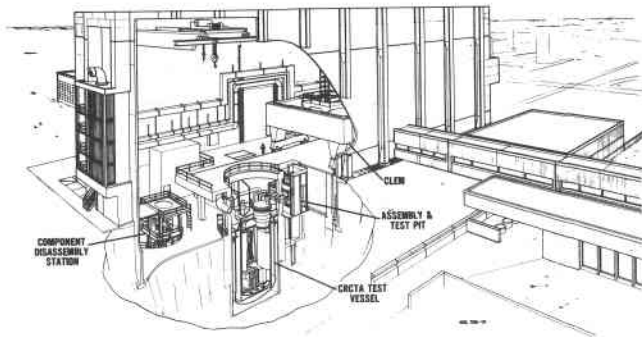


Figure 2. Cutaway of HTSF High Bay Area

CRCTA

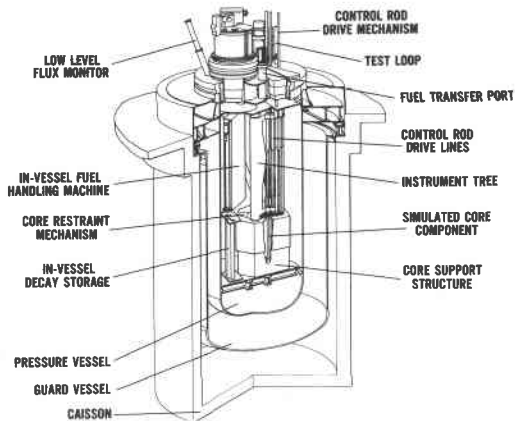


Figure 3. CRCTA Vessel and Components temperatures of 149-593°C (300-1100°F) with flow rates of up to 31.5 dm<sup>3</sup>/sec (500 gpm) in the vessel. A diagram of the overall system is shown in Figure 4. An argon cover gas is maintained above the sodium in the test vessel which is a full-scale mockup of a 2.1 radian (120°) sector of the FFTF vessel and includes a dummy core, core storage module, fuel transfer port, and space for one instrument tree and the IVHM.

Some parameters of the main loop and test vessel are presented in Table I.

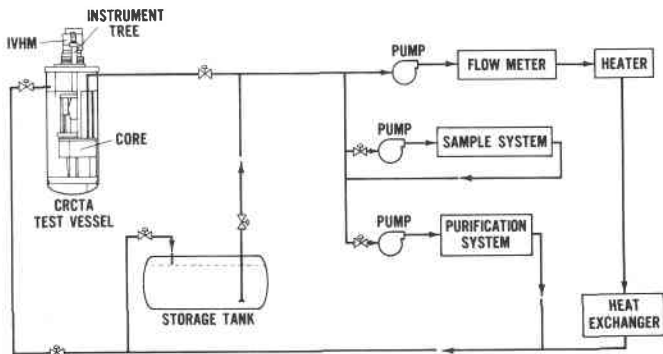


Figure 4. HTSF/CRCTA Sodium System Diagram

Table I. HTSF/CRCTA Parameters

Pipe Size	- Outside diameter 66.80 mm and 133.6 mm (nominal 2" and 4")
Sodium Volume	- 148 m <sup>3</sup> (39,000 gallons)
Sodium Weight	- 132.9 mg (293,000 lbs)
Sodium Flow In-Vessel	- 12.6-31.5 dm <sup>3</sup> /sec (200-500 gpm)
Cover Gas Volume	- 14.2 m <sup>3</sup> (500 ft <sup>3</sup> )
Cover Gas Flow	- 0.47 dm <sup>3</sup> /sec (1 scfm)
Design Temperature	- 593°C (1100°F)

SODIUM PURIFICATION AND CHARACTERIZATION SYSTEM (SPACS)

The auxiliary piping and equipment used for sodium purification and characterization are identical in most respects with that used on the Prototype Applications Loop (PAL) at HEDL.<sup>(5,6,7)</sup> One exception is the HTSF cold trap which is a full scale prototype of an FFTF plant unit. Some parameters of the SPACS are presented in Table II.

Table II. HTSF/SPACS Parameters

Pipe Size	- Outside diameter 16.7 mm and 66.80 mm (nominal 1/2" to 2")
Sodium Flow in Cold Trap	- 3.79 to 5.05 dm <sup>3</sup> /sec
Cold Trap Crystallizer Tank	- 1.5 m <sup>3</sup> (400 gallons)
Cold Trap Capacity	- 304 kg (670 lbs) Na <sub>2</sub> O - 127 kg (280 lbs) NaH
Sampling Loop Flow	- 0.63 dm <sup>3</sup> /sec (10 gpm)
Characterization Equipment	- Plugging Temp. Indicator - Flow-Through Tube Sampling - Multipurpose Sampler - Oxygen Meter - Hydrogen Meter

The characterization equipment includes a distribution loop containing an FFTF plugging meter, multipurpose sampler, flow-through tube sampler, and on-line hydrogen and oxygen meters as shown in Figures 5, 6, 7, 8, 9, and 10. A detailed description of these devices and data on their performance have been presented previously.<sup>(8,9)</sup>

HEDL 7604-34.1\*

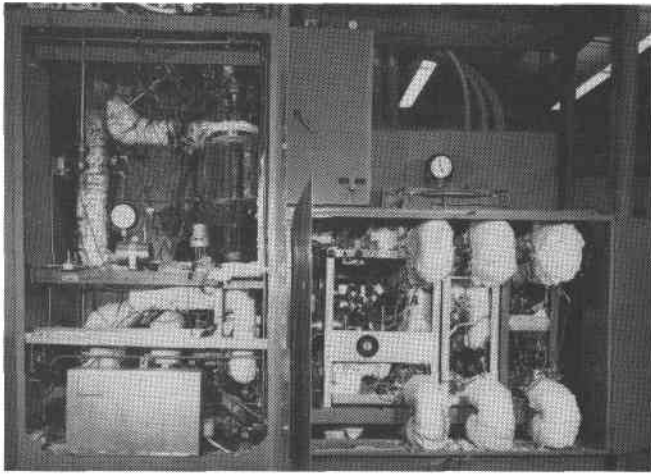


Figure 5. Sodium Characterization System

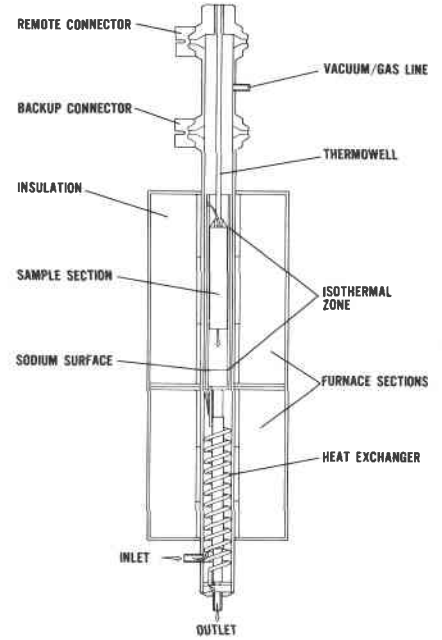


Figure 7. Multipurpose Sampler

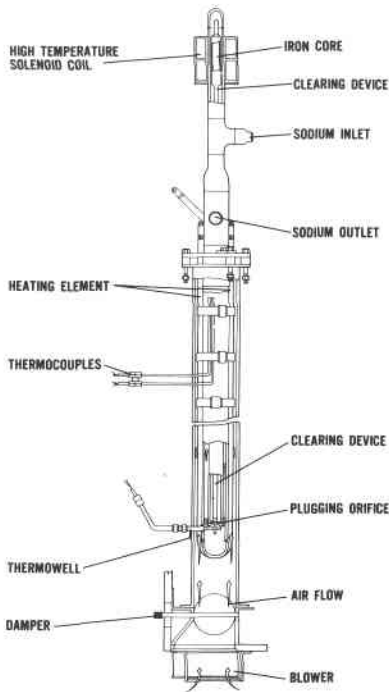


Figure 6. Plugging Temperature Indicator

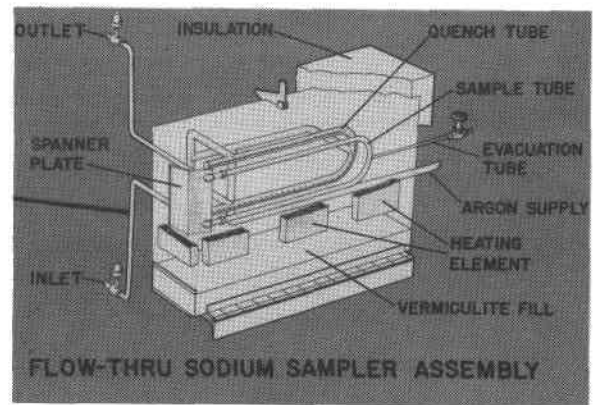


Figure 8. Flow Through Tubing Sampler

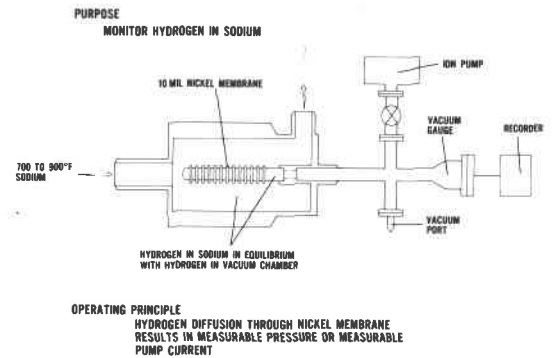


Figure 9. Hydrogen Meter

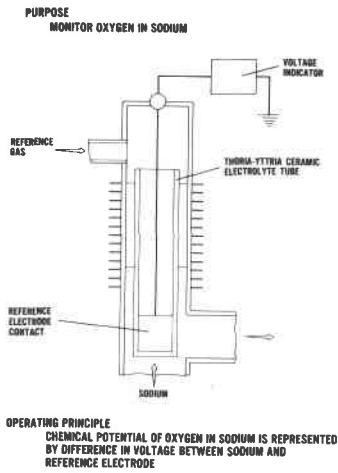


Figure 10. Oxygen Meter

COVER GAS SYSTEM

Argon cover gas is maintained above the sodium in the CRCTA vessel and in the HTSF storage tank. The exit gas passes through a controlled temperature profile vapor trap<sup>(10)</sup> and filter arrangement. The trap is shown in Figure 11. The system is monitored periodically by valving a sample into a gas chromatograph<sup>(11)</sup> in a system such as the one shown in Figure 12.

CHEMICAL ANALYSIS METHODS

Sodium samples taken from the HTSF are analyzed by the methods shown in Table III. The methods used<sup>(12)</sup> were prooftested on PAL prior to HTSF startup and are included in a methods manual in use throughout the U.S. LMFBR program.

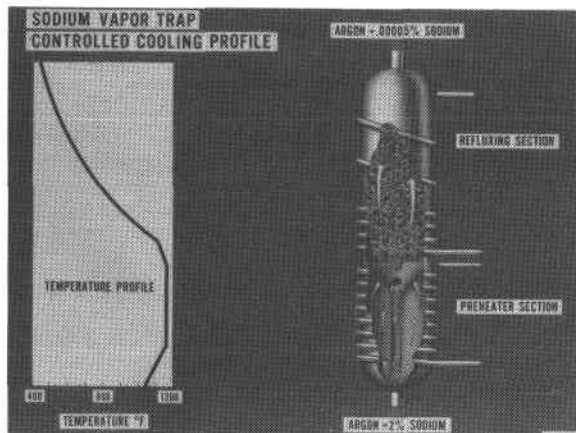


Figure 11. Vapor Trap

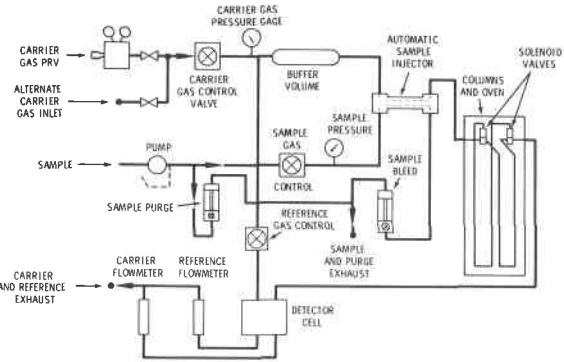


Figure 12. Gas Flow Diagram for Gas Chromatograph

Table III. Analytical Methods Used on HTSF Samples

Impurity	Method	Impurity	Method	Impurity	Method
Al	AA	H	M/E	Rb	FE
Ba	AA	In	AA	Si	C
Bi	AA	Fe	AA	Ag	AA
		Pb	AA		
C	E	Li	FE		
Cd	AA			Sn	AA
Ca	AA	Mg	AA		
Cs	FE	Mn	AA		
		Mo	AA	V	AA
Cl	SIE	Ni	AA		
Cr	AA	O	M/E	Zn	AA
Co	AA				
Au	AA	K	FE		

AA - Atomic Absorption  
 C - Colorimetric  
 E - Equilibration  
 FE - Flame Emission  
 M - In-Line Meter  
 SIE - Specific Ion Electrode

EXPERIMENTAL

Sodium Impurity Control and Measurement during Ex-Vessel System Fill and Startup

Reactor grade sodium was used to fill the HTSF.<sup>(13)</sup> The sodium was transferred from tank cars into the HTSF storage tank. Sintered metal filters (20 micron absolute) were used in the fill lines to prevent any large particles being transferred. Overflow cup samples were taken twice: during the filling of the tank cars and during the transfer into the storage tank. Three

**INTERNATIONAL CONFERENCE ON LIQUID METAL TECHNOLOGY IN ENERGY PRODUCTION**

samples were used for each batch due to the different requirements for performing the various analyses. The results obtained on the samples obtained by the manufacturer are presented in Table IV. The samples taken during the transfer operation were analyzed for a number of trace metals with the results shown in Table V. In all cases the values were well within the limits set

in the U.S. specifications for reactor grade sodium. The sodium was stored frozen under nitrogen for almost a year before it was transferred to the storage tank. It was then kept molten in the carbon steel storage tank for three months before the ex-vessel piping systems were activated. Prior to the start of the fill operation the storage tank was evacuated and backfilled with argon

Table IV. Vendor Supplied Analysis of HTSF Sodium

BATCH No.	72-4	72-5	72-6	72-7	72-8	73-1	73-2	73-3	AVERAGE	M13-1I
TOTAL SODIUM PURITY (%)	99.95	99.98	99.90	99.96	99.93	99.94	99.92	99.91	99.94	≥99.9
CA (PPM)	0.4	8.5	10.2	3.3	3.4	<1	8.6	4.0, 0.14	≤4.4	10
C (PPM)	4.5	24	6.2	1.6	5.5	1.4	5.4	2.7	6.4	30
CL (PPM)	1.7	0.7	0.7	≤20	30.6	0.3	6.5	<0.5	≤7.6	50
K (PPM)	370	350	410	406	370	326	350	330	364	1000
B (PPM)	0.025			≤0.3	≤0.2	≤0.01		0.30	≤0.17	
LI (PPM)	<0.1			≤0.3	0.4	≤0.2		<0.01	≤0.20	

Table V. HEDL Analysis of HTSF Fill Sodium

Impurity	ppm					Average
	#1	#2	#3	#4	#5	
Ag	0.02	0.35	0.05	0.25	0.17	0.17
Al	<0.02	0.04	<0.02	<0.02	<0.01	<0.022
Au	<0.004	<0.004	<0.004	0.015	<0.002	<0.006
B	All less than 0.5					<0.5
Bi	All less than 0.01					<0.01
Ca	0.03	0.04	0.03	0.06	0.01	0.03
Cd	All less than 0.01					<0.01
Co	<0.004	<0.004	<0.004	0.005	<0.002	<0.004
Cr	0.02	0.13	0.06	0.17	0.12	0.10
Cs	All less than 0.01					<0.01
Cu	0.05	0.11	0.13	1.15	0.04	0.3
Fe	0.15	0.53	0.41	0.95	0.43	0.5
K	350.	340.	390.	385.	370.	370.
Li	All less than 0.001					<0.001
Mg	<0.003	0.013	0.04	0.011	0.007	<0.015
Mn	0.002	0.008	0.004	0.015	0.025	0.011
Mo	<0.04	<0.04	<0.04	<0.03	<0.02	<0.034
Ni	0.11	0.06	0.11	0.12	0.05	0.09
Pb	<0.005	0.05	<0.007	0.03	0.007	<0.020
Rb	0.02	0.03	0.03	0.03	0.02	0.026
Sc	All less than 0.03					<0.03
Sr	All less than 0.003					<0.003
U	Composite less than 0.001					<0.001
V	All less than 0.02					<0.02
Zn	<0.01	<0.01	<0.01	0.03	<0.01	<0.014

## INTERNATIONAL CONFERENCE ON LIQUID METAL TECHNOLOGY IN ENERGY PRODUCTION

several times and the purity limits of the argon in the system prior to sodium fill were maintained at less than 100 ppm of oxygen and water vapor and less than 10 ppm hydrocarbons. The ex-vessel piping systems were sodium filled after having been inerted, preheated to 149°C (300°F), and evacuated.

The first measurements of the sodium purity following fill and startup of the ex-vessel systems were performed with the plugging temperature indicator. Runs were made with the PTI cooled to 113°C (235°F) with no indication of plug formation. Four days later saturation temperatures of 129°C (265°F) were measured by the one break method and an average of 144°C (292°F) was measured using the oscillating mode. The system was heated to 177°C (350°F) and cold trap operations commenced at 149°C (300°F). Results obtained on the first on-line sample taken at 177°C (350°F) are presented in Table VI.

Table VI. First On-Line Sample Results

<u>Impurity</u>	<u>ppm</u>	<u>Impurity</u>	<u>ppm</u>
H	0.37	In	<0.2
C	<1	Fe	1.7
Al	<0.01	Pb	<0.01
Ba	<1	Mg	0.001
Bi	<0.01	Mn	0.06
Cd	<0.01	Mo	<0.02
Ca	0.5	Ni	0.14
Cs	<0.2	K	380
Cl	2.	Rb	0.4
Cr	0.19	Ag	0.001
Co	0.004	Sn	<5
Cu	0.006	V	<0.02
Au	<0.002	Zn	0.02

Following the startup of the cold trap the system was taken from 204° to 299°C (400 to 570°F) in two steps with the saturation temperature remaining below 138°C (280°F). Several vanadium wire equilibration samples were analyzed with results of 1.2 ppm oxygen at 177°C (350°F), 1.0 ppm oxygen at 204°C (400°F), and 0.5 ppm oxygen at 299°C (570°F). The HTSF was then operated for several months at temperatures of 204-299°C

(400-570°F) with the cold trap on-line intermittently. Oxygen and hydrogen levels were maintained by the cold trap as expected and no changes were noted in the trace metal levels. (Although no major differences were found from the results obtained on the fill samples, some slight pickup of a few of the common elements was indicated.)

### Sodium Impurity Trends during the CRCTA Fill and Temperature Ascension to 1100°F

Following sodium fill and initial operation of the ex-vessel systems, the next major goal was to fill the CRCTA vessel and perform a temperature ascension to 593°C (1100°F). The CRCTA vessel was preconditioned simply by purging with argon, since the system was not designed to withstand a vacuum. In September, 1974, approximately 148 m<sup>3</sup> (39,000 gallons) of sodium were transferred into the CRCTA vessel with the system at 163°C (325°F). The system was then brought to 204°C (400°F) and held to perform characterization measurements. All operations were done with the cold trap off-line in order to determine the type and level of impurity pickup resulting from filling and operating a large system which had been fabricated and installed to rigid cleanliness specifications.

During the 204°C (400°F) hold the characterization capabilities were expanded by the addition of an on-line meter module equipped with oxygen and hydrogen meters. Prior to the start of the temperature ascension the sodium purity was analyzed using metal wires and tabs to determine oxygen, hydrogen, and carbon plus a bulk sample for trace metals. The oxygen data were also used to calibrate the on-line meter. The saturation temperature as measured with the PTI continued to hold at <135°C (275°F). A viewport on the vessel head was used to monitor the sodium surface appearance during fill and the surface could be seen to contain some thin film areas on a predominantly mirror-like surface. All surface films disappeared after heatup was started. The equilibrium analyses indicated 1 ppm O<sub>2</sub>, 0.1 ppm H<sub>2</sub> and 0.17 ppm C at the 204°C (400°F) hold point.

Temperature ascension tests were performed in 66°C (150°F) increments over a period of several

## INTERNATIONAL CONFERENCE ON LIQUID METAL TECHNOLOGY IN ENERGY PRODUCTION

weeks. At each hold, equipment performance was verified and chemistry data were obtained. The changes in some impurity levels over the range of 205-427°C (400-800°F) are shown in Table VII.

During the 5-6 day period covering the 204-427°C (400-800°F) rise, the O<sub>2</sub> meter output followed the changes indicated in the above table and held steady at 399-427°C (750-800 F) and beyond. The hydrogen meter ion gauge readout was malfunctioning which prevented the direct calculation of hydrogen concentrations from the on-line meter; however, several foil measurements and cover gas analyses indicated increasing amounts with the largest increase occurring shortly after reaching the 800°F hold point. The bulk sample showed no pickup of trace metals but did show some variations from sample to sample, indicating the presence of particles (non-homogeneous samples).

Following the 427°C (800°F) hold the temperature ascension was continued. During other HEDL loop startups high plugging temperatures had been experienced at system temperatures above 566°C (1050°F). In order to minimize the amount of high temperature plugging material in the system and in order to evaluate cold trap performance over this temperature range, the HTSF cold trap was placed in operation for the 427 to 593°C (800 to 1100°F) heatup. A plugging temperature of <138°C (280°F) was maintained with the cold trap on line.

Shortly after reaching the 593°C (1100°F) hold it was noted that the cold trap economizer performance was not adequate. This created a possible stress problem at a mixing tee so the decision was made to by-pass the cold trap.

Within a matter of a few hours after the cold trap was shut down, the presence of a relatively insoluble compound was indicated by steady flow decreases in small valves in the SPACS system (valve temperature 524°C (975°F) and by slow flow decreases in the PTI at orifice temperatures of up to 371°C (700°F). Based on other loop experience, the plugging was attributed to a very insoluble carbon species (possibly carbide) which is thought to form from the decomposition of sodium carbonate. Sodium carbonate has been produced in loops by the reaction of sodium with steel surfaces at temperatures above 566°C (1050°F) and by the reaction of sodium with CO<sub>2</sub>, from air introduced during maintenance. When the HTSF cold trap was again placed on-line the material was gradually removed from the system and the flows returned to normal. Several flow through tube samples were obtained during this time and analyzed for carbon species. Concentrations of carbon as carbonate were 5 to 10X the background level of 0.1 ppm normally found in well purified older sodium systems. No increases in oxygen or hydrogen were indicated by either meter data or by metal equilibration analyses during the same period. The same behavior has been noted during subsequent operations in the 566-593°C (1050-1100°F) regime on HTSF and other sodium loops at HEDL.

### Sodium Impurity Trends during Reactor Hardware Testing

During the past 18 months the HTSF/CRCTA has been used in testing large FFTF components, primarily the Instrument Tree and the In-Vessel Handling Machine. The IVHM was introduced into the vessel after the vessel was filled with sodium. It has since been removed from CRCTA for sodium

Table VII. Changes in Non-Metallic Impurities during First Temperature Ascension Tests

System Temperature °C (°F)	ppm (±10%)			Saturation Temperature (PTI)	
	Oxygen	Hydrogen	Carbon	°C	(°F)
204 (400)	0.8	0.09	0.17	129	(260-270)
288 (550)	1.3	--	--	129	(260-270)
316 (600)	1.5	--	0.14	132	(270)
399 (750)	1.7	--	--	141	(285)
427 (800)	1.9	0.4	0.13	166	(330)



## INTERNATIONAL CONFERENCE ON LIQUID METAL TECHNOLOGY IN ENERGY PRODUCTION

removal and inspection.<sup>(14)</sup> Oxygen and hydrogen levels remained low during the placement, testing and removal operations.

The cold trap has been taken off-line for several months at a time resulting in measurable increases of 1-2 ppm oxygen and 0.10 to 0.15 ppm hydrogen per month. Each time the system is heated to 593°C (1100°F) without cold trapping, high carbonate levels are found and some plugging problems are experienced in small valves and orifices.

Recently some changes in several steel constituents were noted as shown in Table VIII. The variations cannot be correlated with any obvious operational parameters. They appear to be due to non-homogeneous samples, i.e. particulates. A program is underway to study particulates during future HTSF operations.

### Cover Gas Impurity Levels

As mentioned previously the HTSF storage tank and ex-vessel piping were inerted with argon prior to filling with sodium. The plant argon contains <20 ppm each of oxygen, water vapor and hydrocarbons as measured with the plant gas chromatograph. The chromatograph contains dual molecular

sieve columns with ionization detectors. The detection limit is ~5 ppm H<sub>2</sub> and 20 ppm for the other impurities measured. The cover gas system operates on a feed-and-bleed arrangement with a normal flow of 1 scfm through the CRCTA vessel. The levels of hydrogen and nitrogen present in the CRCTA vessel prior to sodium fill are shown in Figure 13. Increases in nitrogen represent those times when the system was opened for operational reasons. Hydrogen level variations during this period were due to three causes, namely: changes in purge rates; introduction from the steel either from adsorbed water vapor or by bakeout of hydrogen gas; and by decomposition of organic residues on the internal surfaces.

During the 427-593°C (800-1100°F) temperature ascension tests the gas analyses indicated that hydrogen, methane, and some high molecular weight organic compounds were present in both the tank and guard vessel. Changes in sampling line and vent line arrangements demonstrated that most of the contaminants were not in the cover gas areas but were being introduced through a gas balance line connection coming from the dummy plug for the IVHM. This plug evidently contained oil which was undergoing thermal decomposition as the vessel temperature was raised.

Table VIII. Recent Trace Metal Variations

Date	Temperature °C (°F)	IVHM	CT	ppm			
				Fe	Cr	Ni	Si
8/75	218 (425)	In	Off	0.6	0.03	0.08	2.5
9/75	218 (425)	In	Off	0.9	0.2	0.1	0.2
11/75	218 (425)	In	Off	80	1.8	4.5	0.8
12/75 <sup>(1)</sup>	218 (425)	Out	Off	6.2	0.8	0.65	-
12/75 <sup>(2)</sup>	218 (425)	Out	Off	0.4	0.1	<0.1	-
1/4/76	218 (425)		Off	9.0	0.4	0.2	0.2
1/6/76	427 (800)		On	4.0	0.6	0.3	-
1/7/76	538 (1000)		On	1.0	0.2	0.1	-
1/9/76 <sup>(3)</sup>	577 (1070)		On	40	4	6	3.7
1/12/76	577 (1070)		On	0.2	0.03	<0.1	0.06
1/16/76 <sup>(4)</sup>	577 (1070)		On	9.0	3.4	2.4	0.18

(1) Distillation residue contained particulates.

(2) No particles found on 15 micron filter.

(3) Eight mg particles found on 7 micron filter (v100 gallons).

(4) One mg particles found on 7 micron filter.

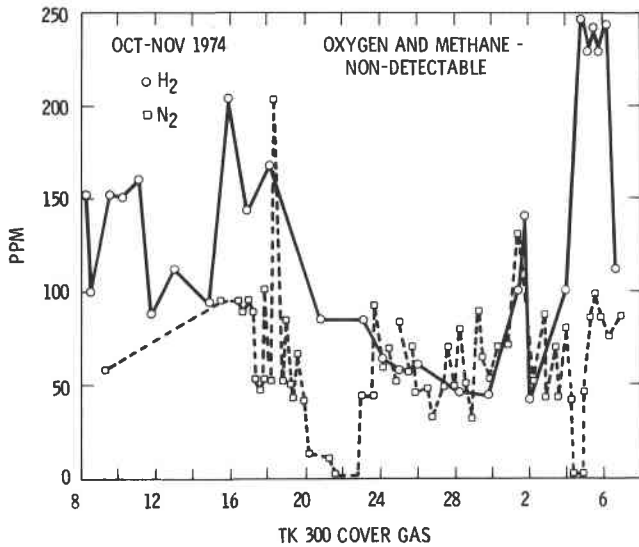


Figure 13. Cover Gas Impurity Levels Prior to Na Fill

After the gas sampling system was modified to obtain a more representative sample, the levels of impurities dropped to the values shown in Table IX. These values represent the normal day to day range seen with the system tightly sealed and testing in progress. During the introduction or removal of hardware, such as the IVHM, nitrogen spikes are seen which represent air contamination. The oxygen reacts with sodium vapor above the pool and is not detected in cover gas samples.

Table IX. Cover Gas Impurity Levels during Routine Operations

	ppm	
H <sub>2</sub>	10 - 20	
N <sub>2</sub>	40 - 80	
CH <sub>4</sub>	ND	ND*
O <sub>2</sub>	ND	ND*

\* Not Detectable.

Sodium Frost

Some work has been performed at HTSF to investigate sodium frost buildup. This was done by studying Control Rod Drive Plugs and the IVHM Penetration Plug and has been reported in detail.<sup>(14)</sup> Figures 14 and 15 illustrate some frost formed during 20 days exposure of the plugs above the 593°C (1100°F) sodium pool. Gas convection restrictor rings were used to close the annulus to

30 mils radial clearance (from 1/8") on two plugs and were successful in inhibiting frost buildup above the ring area.

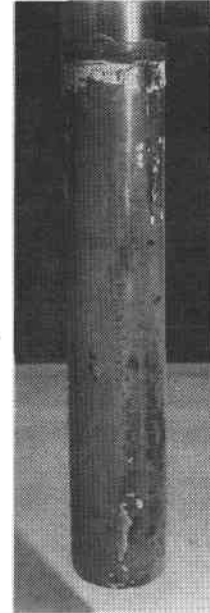


Figure 14. Sodium Deposition with Restrictor

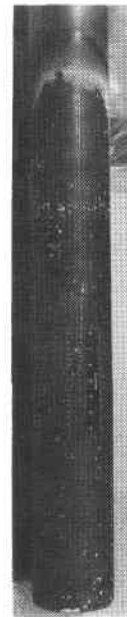


Figure 15. Sodium Deposition without Restrictor

# INTERNATIONAL CONFERENCE ON LIQUID METAL TECHNOLOGY IN ENERGY PRODUCTION

## CONCLUSIONS

### Sodium Chemistry

From the impurity data obtained during the HTSF startup and temperature ascension tests the following conclusions were made:

- 1) The oxygen concentration in the sodium remained at <2 ppm.
- 2) Hydrogen was the major impurity introduced on a percentage basis.
- 3) The total impurities added to the cold trap during fill and initial cleanup represent less than 1% of trap capacity.
- 4) Saturation temperature measurements (PTI) cannot be interpreted in terms of sodium oxide present.
- 5) At high temperatures, >566°C (1050°F), chemical species form which may cause plugging problems. Carbon is involved in the formation of such compounds.
- 6) Cold trapping with the system at high temperature removes the carbon species.

In addition to the above, the HTSF tests have demonstrated that reactor hardware can be inserted, operated, and removed from a large sodium vessel without the significant addition of impurities to the sodium. FFTF components, seals, and operational techniques were demonstrated to be successful in maintaining a high quality environment.

### Cover Gas Chemistry

Several interesting points were learned from the study of the impurity trends in the HTSF cover gas. These include:

- a) Nitrogen in the cover gas of a large sodium system can be maintained at <50 ppm.
- b) The reaction of organic materials with sodium produced detectable amounts of hydrogen and methane.
- c) No oxygen is detectable in the cover gas during normal equipment handling operations. The introduction of air is indicated by nitrogen increases.

- d) The reactor sized [2.35 dm<sup>3</sup>/sec(5 scfm)] Controlled Temperature Profile (CTP) vapor trap performed as predicted.

One final observation is that analytical methods plus sampling and monitoring hardware now developed and tested for sodium systems represents a substantial improvement in the state-of-the-art from that described in previous liquid metal technology meetings. Such equipment and techniques are presently in use on EBR-II and will be utilized on future LMFBR systems.

## REFERENCES

1. H. C. Duncan and J. B. Waldo, "Startup and initial operation of the high temperature sodium facility," Trans. Am. Nuclear Society, Winter Meeting, (November 1975).
2. V. Kolba, J. Holmes, S. Skaladzien, M. Slawewski, E. Filewicz, and P. Nelson, "Multipurpose sodium sampler for LMFBR's: Design and operation," ANL 8031 (February 1974).
3. G. E. Meadows, "A comparison of the fluted valve and orifice plate plugging meters," HEDL-TEM 71-63 (May 1971).
4. V. Kolba, M. Slawewski, E. Filewicz, D. Vissers, D. Rowe, J. Holmes, and P. Nelson, "Oxygen-hydrogen meter module for LMFBR's: Design and operation," ANL 7940 (May 1972).
5. J. J. McCown, "Prototype Applications Loop (PAL) - one year of operations . . . Interim Report," HEDL-TME 73-41 (March 1973).
6. J. J. McCown, "Prototype Applications Loop - two years of operation," HEDL-TME 74-24 (March 1974).
7. G. W. Mettler and J. J. McCown, "Prototype Applications Loop: status of development and test results," HEDL-TME 75-84 (August 1975).
8. J. J. McCown and J. L. Ballif, "A review of methods for measuring stainless steel interstitial elements in sodium - application to LMFBR's," NACE Corrosion/74 Meeting (March 1974).
9. J. J. McCown, "The prototype applications loop characterization system, a comparison of methods for oxygen in sodium," Trans. Am. Nuclear Society, Winter Meeting, Vol. 17 (November 1973).
10. G. B. Barton, "Development of sodium vapor traps for FFTF cover gas sampling lines," HEDL-TME 73-18 (February 1973).
11. G. B. Barton, "Performance of a process gas chromatograph analyzing sodium cover gas," HEDL-TME 73-73 (September 1973).

## INTERNATIONAL CONFERENCE ON LIQUID METAL TECHNOLOGY IN ENERGY PRODUCTION

12. R. F. Keough and J. J. McCown, "Recent developments in the analysis of coolant sodium for fast breeder reactors," Trans. ACS National Meeting (August 1975).
13. W. Yunker, "Sampling, analysis, and handling of sodium for the HTSF," HEDL-TME 74-14 (March 1974).
14. C. W. Funk, M. Crippen, and G. B. Barton, "Review of sodium removal processes using water," Trans. International Conference on Liquid Metal Technology in Energy Production (May 1976).
15. W. J. Donker, "Sodium frost observations on CRCTA control rod dummy plugs," HEDL-TME 75-27 (March 1975).

# INTERNATIONAL CONFERENCE ON LIQUID METAL TECHNOLOGY IN ENERGY PRODUCTION

## SODIUM CHARACTERIZATION DURING THE STARTING PERIOD OF A SODIUM LOOP.

F. Lievens

C. Parmentier

M. Soenen

S.C.K./C.E.N.  
Mol - Belgium

### ABSTRACT

A sodium loop, for analytical chemistry studies has been built by S.C.K./C.E.N. at Mol Belgium. Its first working period was used to test analytical methods, to characterize the sodium and to define the operating parameters of the loop. This reports covers the working parameters of the loop, the characterization of the filling sodium and its purity evolution during the first working period of the loop.

### INTRODUCTION

In May 1975, The Analytical Sodium Loop "ASL" was started. The main purpose of this loop is to provide characterized sodium for analytical methods development and calibration, to test sodium sampling methods, and to evaluate on-line monitors in order to examine their relative merits and reliability.

The design of the loop provides the possibility to use the test sections as well for installing on-line meters, as for collecting sodium samples. During the start-up this versatility was used to characterize as completely as possible the sodium and to study impurity pick-up and deposition during the initial stage of operation of the loop.

The operation of the loop during the first months was performed such as to allow the best quantitative interpretation of the analytical results. Most of the time the cold trap was left out of operation, in order to obtain constant levels of contamination for the sodium, on which representative samples can be taken.

During the chemical characterization of the sodium, special attention was given to the carbon impurity in order to obtain information about the mechanism of carbon transfer in the loop, leading to carburization and decarburization of the structural materials.

Since carbon transfer is expected to involve very low concentration levels, the analytical methods have been adapted to reach the p.p.m. or sub p.p.m. level. The analytical method for carbon and oxygen are specific for sodium, and will be described with more detail than the determination methods of the other impurities which are carried out by conventional methods applied to the samples after conversion to a sodium salt, or after separation by the distillation procedure.

### DESIGN AND CONSTRUCTION OF THE LOOP

#### General Description

A general flow sheet of the loop is shown in Fig. 5. The main circuit, following the direction of sodium flow includes, an electromagnetic pump, a Na-Na recuperator (tube side), an electrical heater of 50 kW automatically regulated over a phase angle fired thyristor unit, 4 hot test sections to be branched either in series or in parallel, a static expansion tank, a Na-Na recuperator (shell side), a Na-air cooler, 3 cold test sections to be branched either in series or in parallel and an electromagnetic flow meter. The purification and oxygen detection system consists of a cold trap with a discontinuous plugging circuit using

a plugging valve to disturb the plug mechanically by opening the valve if heat alone is insufficient to dissolve the plug.

#### Main Characteristics

The main characteristics of the loop are as follows :

Flow	: variable up to $2 \text{ m}^3 \cdot \text{h}^{-1}$
Pressure head-pump	: up to $1.5 \text{ kg/cm}^2$
temperature	: up to $700^\circ\text{C}$
Heat load	: up to 50 kW
Design pressure	: $6 \text{ kg.cm}^{-2}$ at $700^\circ\text{C}$
Sodium volume	: of the order of 75 $\ell$

The construction material of the loop is stainless steel AISI 316. The main circuit consists of a 3/4" pipe. The purification, the test sections and the dump line of the main circuit are made of 1/2" pipe. The plugging circuit and the dump lines of the test sections are made of 1/4" pipe.

The pump is a single-phase conduction pump. The power is adjusted manually with a variable voltage autotransformer.

The heat exchanger is U-shaped with a total length of 2.40 m. and consists of two concentric tubes.

The purification circuit is connected to the main circuit by a heat exchanger and a heater of 12 kW. The cold trap is a cylinder of 168 mm diameter and 528 mm height. It contains 11.7  $\ell$ . The sodium flows down in the external ring, and returns up in the inner part which is filled with wire-mesh. Cold air is circulated through the jacket, and cools the vessel walls while coldtrapping is in progress. The plugging meter is located in the purification circuit, but can be operated independently from the cold-trap. The plugging valve contains 6 holes of 0.88 mm<sup>2</sup> section.

The sampler is given in Fig. 6. The construction allows all seven test sections to be used for sampling. A dump line is connected to the test section and is used to evacuate the excess sodium from the samplers.

#### Filling and Dumping of the loop

The loop is evacuated with a primary vacuum pump and is heated to a temperature above  $125^\circ\text{C}$ . The sodium in the dump tank is heated to  $125^\circ\text{C}$  and allowed to rise in the loop, through a filter heated at  $125^\circ\text{C}$ , by applying an argon pressure of  $400 \text{ g/cm}^2$  to the dump tank. When the desired level is obtained in the expansion tank, the dump tank valve is closed and a pressure of  $2 \text{ kg/cm}^2$  of argon is applied to the expansion tank. The sodium is then circulated with the pump and the auxiliary heatings are switched off.

To dump the sodium of the loop, the dump line is heated, pump and mean heater are switched off, the argon pressure is released, and the sodium is drained to the dump tank under vacuum.

ANALYTICAL PROCEDURES

Chemical analyses were used to measure oxygen, carbon, and metallic impurities in sodium. Occasionally chloride was measured because this element results from the manufacturing procedure used for metallic sodium. (1) Since no contamination is expected, its concentration pattern should show its elimination by the cold trap. Hydrogen was not included in the available analytical procedures and as will be explained later was necessary by the start up of the loop. An equilibration method with nickel at 400°C was tried but was unsuited for levels below 3 p.p.m.. Elements like uranium, originating from contact of the sodium with fuel elements were not investigated, because these elements are unlikely to be present in A.S.L.

The analytical procedure, used for the impurity determinations in sodium, have been adapted from existing procedures in the Analytical Chemistry Section with an appropriate step in the sample preparation. Methods specific for sodium, like oxygen and carbon determinations have been developed using information from literature (2) (3) and from other laboratories active in this field in the Netherlands(4) and in Germany(5).

Sampling Procedure

The sampling technique used on A.S.L. is similar for all determinations. In order to obtain representative samples of the bulk of the sodium in the loop the following precautions were taken in the design of the sampler :

- sodium is sampled at the highest temperature used in the experiment
- sodium is collected in crucibles, in which the sodium is isolated from the bulk of the sodium in the loop, during cooling
- the crucibles with sodium are isolated from the atmosphere by a sodium plug, until the sampler is opened in a glove-box for analysis.

The samplers are made from AISI 316 stainless steel and located in the test sections of A.S.L.. The sodium flows from above and streams down along the crucibles. Normally 5 crucibles containing 3 to 4 g of sodium are used in the samplers but the internal structure can be interchanged to accommodate other volumes, and to hold vanadium wires, together with two normal size crucibles.

Determination of oxygen

A distillation procedure was used, because it has a lower blank than amalgamation techniques, and is less time consuming. Equilibration with vanadium wires was not used during the start up period of A.S.L., because the temperature needed for equilibrations is higher than the temperatures at which the loop was operated.

The apparatus used for distillation is given in figure 1. It is made from borosilicate glass, and uses a two-stage vacuum pump with a cold trap at -196°C. A vacuum of 10<sup>-3</sup> torr is obtained before the distillation is started. In order to protect the sample from the residual gases from the walls and from the residual pressure in the distillation chamber, a getter film of sodium is evaporated using a dummy sample before the actual sample is loaded. Heating is obtained from a 1 KVA R.F. induction generator. All operations on sodium are carried out under pure argon atmosphere in a glove-box coupled with a purification unit He 193-2 from V.A.C.

The distillation temperature is measured directly on the wall of the crucible, by short-circuiting the thermocouple branches on the nickel crucible as shown in figure 2. The distillation of sodium is carried out in half an hour at 360°C. At this temperature the partial pressure of the sodium above the crucible is 10<sup>-1</sup> torr (6). At the end of the distillation the temperature increases and the heating is switched off at 450°C

The sodium oxide remaining in the crucible is collected with 0.1 N HNO<sub>3</sub> and analysed by atomic absorption spectrometry. The oxygen is calculated from the sodium content of the crucible residue assuming that all the oxygen is present as Na<sub>2</sub>O.

Determination of carbon

Two procedures are used for the determination of carbon in sodium. A wet chemical method determines the carbides, cyanide, carbonyl, carbonate and free carbon chemical states. A combustion method determines the total carbon.

Wet chemical procedure : determines the chemical forms of carbon in a stepwise sequence. In the first step the sodium sample is hydrolysed with water, which liberates hydrogen for metallic sodium and decomposes the carbides of sodium by establishing hydrogen-carbon bindings for sodium carbon bonds. The hydrocarbons are carried by a helium stream to a cold trap at liquid nitrogen temperature, measured manometrically for the total carbide content, and transferred to a gas chromatograph. The hydrocarbons are separated on a molecular sieve column and measured with a flame ionization detector. Carbonyl, methane and hydrogen are not retained in this step. The helium carrier passes them over copper oxide at 400°C where carbonyl is converted to carbon dioxide. This carbon dioxide is collected in a cold trap at liquid nitrogen temperature, and measured manometrically. Water from the hydrogen is separated before the cold trap, and methane, if present is practically not oxidized on the copper oxide, and is not accounted for.

From the residue of hydrolysis, cyanide is separated by acidification with sulphuric acid and distillation. An ion selective electrode is used to measure the cyanide in the distillate.

Carbonate is separated from another hydrolysis residue by acidification and is carried with helium to a cold trap at liquid nitrogen temperature, and measured manometrically.

On the acidified residue from the previous steps, the residual carbon forms are sometimes measured, by wet oxidation with van Slycke reagent, collection of the carbon dioxide formed, and manometric determination.

The limits of detection reached are :

0.01	p.p.m. for individual carbide forms,
0.01	p.p.m. for cyanide,
1	p.p.m. for carbonyl,
1	p.p.m. for carbonate,

The residual carbon determination is hampered by a high blank, resulting from the carbon traces in all previous reagents. In favourable circumstances the blank could be reduced to 6.5 µg of carbon on a 4 g sample, or 1.6 p.p.m.

# INTERNATIONAL CONFERENCE ON LIQUID METAL TECHNOLOGY IN ENERGY PRODUCTION

A flow sheet of the wet chemical procedure is given in figure (3).

- Combustion procedure : This procedure is useful for several reasons :
- detailed knowledge of the chemical states of carbon is not always needed, and a method for total carbon is less time-consuming than the wet chemical method.
  - Since the wet chemical method analyses each carbon compound separately, the total carbon obtained by summing-up all components, will present a cumulative blank. A much lower blank may be expected for a one-step method.
  - A total carbon determination may be used to confirm that no important chemical state for carbon has been overlooked in the wet chemical procedure.

To obtain a low blank in total carbon determination the combustion in an oxygen stream is preferred because the oxygen reagent is very easy to purify, or can be purchased in a sufficiently pure state.

By direct oxidation of sodium with oxygen, sodium oxide and sodium carbonate are obtained. The sodium carbonate is decomposed by heat and the liberated carbon dioxide is collected in a conductometric cell and measured.

- Two difficulties are dealt with, when using direct oxidation :
- during oxidation the temperature should be as low as possible, not to volatilize the metallic sodium or the oxide to the colder zones of the apparatus, where it will retain some carbon dioxide.
  - at the temperature needed for the decomposition of the sodium carbonate, the oxide will be corrosive and incompatible with most containment materials.

In order to reduce these difficulties the sodium is evaporated under reduced pressure at 360°C, and the residue together with the distillation crucible are introduced in a quartz combustion tube and heated to 950°C under oxygen carrier stream. The carbon dioxide evolved is measured by conductimetry in alkaline solution. The sampling and combustion are based on the work of CTI-TNO (7) (8).

## Determination of metals

Three techniques have been used :

- atomic absorption spectrophotometry for potassium, calcium, cadmium and zinc.
- X-ray fluorescence spectrometry for iron, chromium, nickel, manganese, cobalt, copper, lead, cadmium, zinc, bismuth and tin.
- emission spectrography for aluminium, cobalt, chromium, copper, iron, manganese, molybdenum, lead, tin, titanium, and vanadium.

Emission spectrometry is carried out on the residue after sodium distillation. The other two methods are used after dissolution of the sample in alcohol and carrier precipitations (9).

## RESULTS

The operating parameters of the ASL were selected with the objective to obtain the maximum chemical information on the sodium and on its behaviour during the start-up period. To make the data more quantitative and their interpretation easier, it was decided :

- to leave the cold trap out of function,
- to operate the complete loop as close as possible to

- the isothermal condition,
- to reach equilibrium and representative conditions for sodium sampling, before affecting the integrity of the loop by taking samples for off-line chemical analysis ;
- to purify the sodium of the loop stepwise,
- to eliminate the impurities, as much as possible out of the loop, instead of precipitating them in the cold trap,
- to increase the temperature of the loop stepwise.

All these conditions could not be perfectly realized, but the loop was operated in such a way that quantitative interpretation was not impaired.

Three separate series of experiments were performed namely : (A) purification by dumping, (B) purification with the cold trap, and (C) runs at temperatures above 400°C

## Purification by dumping (A)

- These experiments involve the following actions :
- 1- the dump tank is heated to 125°C
  - 2- the sodium is raised from the dump tank to the loop at 125°C
  - 3- the sodium is circulated, at a temperature of 400°C
  - 4- plugging temperatures are recorded and samples are taken
  - 5- the sodium of the loop is dumped at 400°C and cooled in the dump tank.

This complete procedure was repeated 5 times, in order to evaluate its interest for sodium purification purposes. It combines also a good quantitative measurement of the impurities present in the loop during the start-up, with their elimination out of the loop to the dump tank, keeping the cold trap clean for further experiments.

The information concerning these first 5 experiments with the loop are summarized in Table I. The results of the analysis are given in Tables II and III. The purity of the sodium used in the loop is given in Table III.

After the fifth experiment it became clear that no further decrease in oxygen content could be obtained by this dumping procedure. The oxygen value of 3.8 p.p.m. comes from contamination by air during the sampling procedure.

## Purification with the cold trap (B)

After this first period, the loop was purified by lowering the temperature of the cold trap. To avoid an abrupt precipitation of impurities, the temperature of the cold trap was lowered progressively. It was possible to detect a plug down to 145°C. The evolution of the loop parameters are given in figure (4). A second plug was detected at 260°C, and could be traced down to 230°C. This second plug was also present during experiment (A). The purity of the sodium at the end of experiment (B) is given in the tables II and III.

## Operation of the loop above 400°C : Experiments (C)

Below 400°C, the diffusion of carbon in stainless steel is very low. With a temperature increase from 400°C to 700°C it was expected that diffusion will become measurable, and that a chemical analysis of the

## INTERNATIONAL CONFERENCE ON LIQUID METAL TECHNOLOGY IN ENERGY PRODUCTION

sodium will allow detection of the chemical elements and carbon forms liberated in the sodium stream by the walls of the containment.

To avoid chemical contamination by the sampling procedure and to increase the sensitivity, the following set of steps was carried out.

- 1- the samplers are connected, and the loop is operated isothermally at 400°C for 48 hours, with the cold trap in use at 120°C.
- 2- the cold trap is shut off from the loop, and the temperature of the hot leg is increased to 550°C for 24 hours.
- 3- the samples are taken in the hot section at 550°C. This procedure was repeated at 500°C, 600°C and 675°C. A test at 400°C was run in identical conditions for comparison purposes. The results of the chemical analyses are given in tables II, III and IV.

### DISCUSSION

#### Oxygen impurity

When the new clean loop was filled with sodium the contamination level of the sodium with oxygen is about 13.8 p.p.m. or  $\sim 1$  g of oxygen for the total loop. This level is not dangerous, and lower levels may be expected for larger loops.

The plugging meter indication is not related to the oxygen impurity. In table V are given the plugging temperatures, the oxygen levels measured by chemical analysis and those calculated with the relation given by Noden (10), which is very close to the recommended relation of Eichelberger (11).

It is obvious that the plug in the first experiments is related to another impurity present in the sodium and which precipitates in the plugging meter.

Hydrogen has been assumed to be the plugging impurity for the following reasons :

- the impurity responsible for the plug at 310°C comes from the stainless steel, since the loop was filled at 125°C, through a filter,
- hydrogen is an impurity which diffuses at an appreciable rate through stainless steel at 400°C,
- samples of the steel used for the construction of the loop were analysed for hydrogen. The amount found is of the right order of magnitude to justify the presence of 13.4 ppm hydrogen in the sodium of the loop.

It was investigated if hydrogen could be measured by equilibrating with nickel, but a blank value was observed equivalent to a hydrogen concentration ranging from 2 to 3 ppm. This blank does not allow the determination of the concentrations expected in cycles A3 to A5, and no direct chemical evidence is available for the presence of hydrogen in the start-up period of ASL.

Except for the first cycles A1 and A2 and the first rise to 550°C (see table IV) the agreement between oxygen concentration and the plugging temperature is acceptable. Below 145°C or 2.5 ppm O<sub>2</sub>, no plug was detected.

#### Carbon impurity

During the start-up of the loop the carbon is present at levels from 5 to 17 ppm, and no carbide or carbonate was detected. The purification by cold

trapping proceeds very slowly. Five dumping cycles are insufficient to lower the level significantly, and half a month with the cold trap at 120°C is insufficient to lower the carbon level by more than a factor two.

The solubility of carbon (12) is not in agreement with the cold trap or plugging temperature as shown in table VI.

Since in all experiments the cold leg of ASL was at 400°C, the maximum carbon concentration allowed by the solubility data from Ainsley et al. (12) is 0.06 ppm.

The behaviour of carbon may be explained if it is assumed that carbon below 400°C was in an inert state, which is carried through the loop, but does not react. When the temperature is increased above 550°C the carbon is transformed to an active form, and from then on, either reacts to carburize the walls, or precipitates in the colder parts of the loop.

About the active and inactive forms insufficient information is available, but the low levels of Na<sub>2</sub>C<sub>2</sub> measured may support the conclusion of Ainsley (13) that the decarburizing and carburizing form is the diatomic species.

#### Chloride impurity

The chloride present in the sodium used for filling ASL remained at the same level, and was not eliminated by the cold trap, or by the dumping cycles. The amount of chloride is in excess of the solubility calculated by extrapolating the data of Bredig et al. (14)

#### Metallic impurities

It was observed that cold trapping eliminates calcium very rapidly, but does not affect the potassium at the 40 ppm level. Iron was observed to increase slightly above 1 ppm at 400°C, but disappeared when the temperature of the hot leg of the loop was increased above 400°C.

Most of the other metallic elements were below the W.p.p.m level, and were very close to or below the detection limit. A first group below the background of the analytical method contains Bi, Cd, Co, Mo, Pb, Sn, Ti and V. The second group, which showed a slight increase above background as a function of time and temperature contains Al, Cr, Cu, Mn and Ni.

### CONCLUSIONS

The chemical characterization of the sodium during the start-up of A.S.L., yielded the following information :

- Oxygen during the first loading of the loop reached 13.8 W.p.p.m., which is not dangerous, and does not constitute the main impurity indicated by the plugging meter.
- Hydrogen is suspected to be the main impurity at a level of 13.4 W.p.p.m.
- Carbon is present at levels ranging from 5 to 17 W.p.p.m., which are far above the solubility. This is assumed to be in an inactive form, which is transformed into an active form above 550°C and is eliminated very quickly once transformed.
- Chloride and potassium are not eliminated by cold trapping while calcium is reduced to  $\sim 5$  W.p.p.m.
- Other metallic elements are below 1 p.p.m., but Fe, Ni, Al, Cr, Cu and Mn show slight increase with time and temperature.



REFERENCES

- (1) MARSHALL SITTIG, "Sodium, its manufacture, properties and uses", Reinhold publishing Corporation, New York, 1956, pp 10-46
- (2) BORIS L., CAFASSO F.A., MEYER R.J., BARSKY M.H., EDWARDS H.S. ; ANL-ST6, Jan. 1971
- (3) BERGSTRESSER K.S., WATERBURY G.R., METZ C.F. ; LA-3343 - UC4 Chemistry - TID-4500 (43 ed), Aug. 1965
- (4) CTI-TNO Report 70-0860 File 3963A-3013 "Analysis instruction : Determining the oxygen content of sodium", March 1970.
- (5) BORGSTEDT H.U., SCHNEIDER H., SCHUMANN H., WITTIG; IMF-Arbeitsbericht N° 66/70, July 1970
- (6) NESMEYANOV A.N., "Vapor pressure of the chemical elements", Elsevier publishing company, Amsterdam, London, New York, 1963, p 444
- (7) ROHDE J.F.M., HISSINK M. and BOS L. ; Journal of Nuclear Energy, Vol. 24 pp 503-508
- (8) ROHDE J.F.M. CTI-TNO Report SR-TN/7009-32 Sept. 1970
- (9) SCHNEIDER H., BORGSTEDT H.U., Proceedings of the International Conference of BNES, Nottingham April 4-6, 1973 pp 77-80
- (10) NODEN J.D., RD/B/N 2500, Dec. 1972
- (11) EICHELBERGER R.L., AI-AEC-12685, 1968
- (12) AINSLEY R., Mrs HARTLIB L.P., HOLROYD P.M. LONG G.; AERE-R 6731
- (13) idem p.18
- (14) BREDIG M.A., JOHNSON J.W., SMITH W.T. jr ; J. Am. Chem. Soc., 77, pp 307-312, 1955

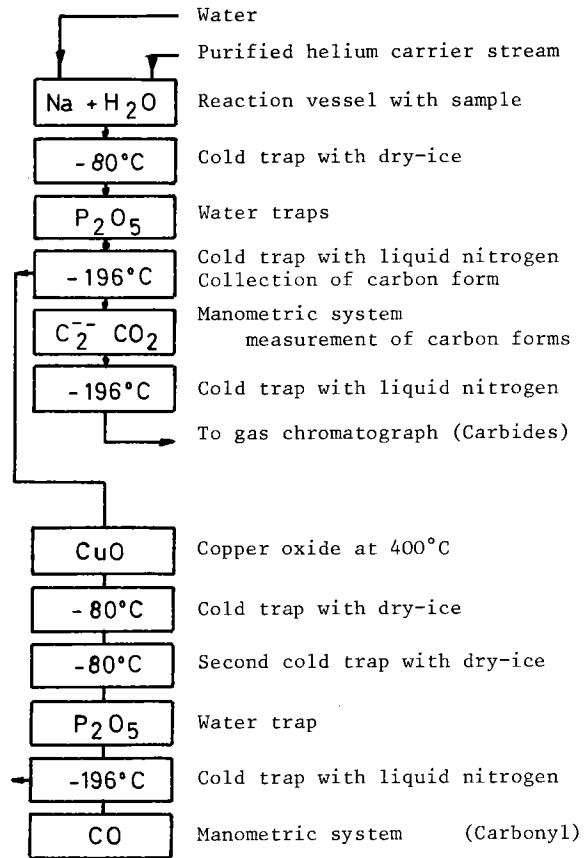


FIG. 3 CARBON DETERMINATION BY THE WET CHEMICAL PROCEDURE

FIG. 1 DISTILLATION SET UP

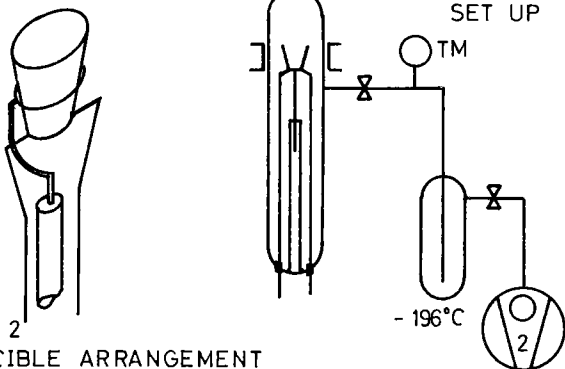


FIG. 2 CRUCIBLE ARRANGEMENT FOR DISTILLATION OF SODIUM

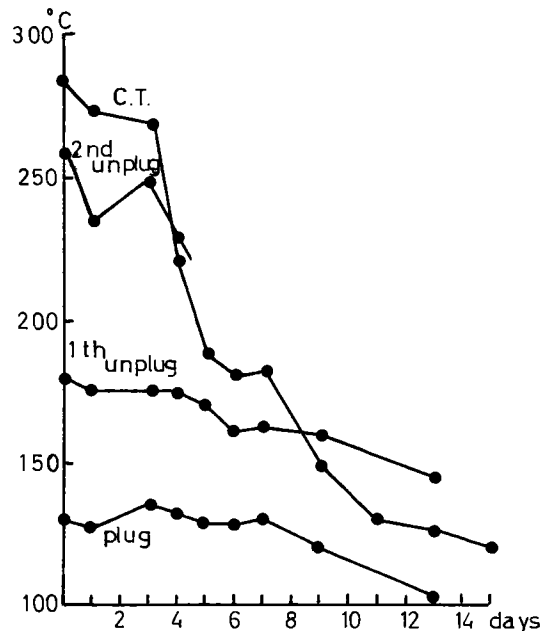





FIG. 4 PURIFICATION WITH THE COLD TRAP plugging temperature related to the cold trap temperature

- C : AIR COOLER
- CS orcs: COLD SECTION
- CT COLD TRAP
- E EXPANSION TANK
- D DUMPTANK
- F FLOWMETER
- FL FILTER
- HS orhs HOT SECTION
- P PUMP
- R RECUPERATOR
- VP VAPOR TRAP
- MAIN CIRCUIT (subscript m)
- PURIFICATION CIRCUIT (subscript p)
- - - PLUGGING CIRCUIT (subscript pl)
- - - - - FILL DUMP CIRCUIT

-  Motor - blower - valve
-  Regulating valve
-  Normal valve

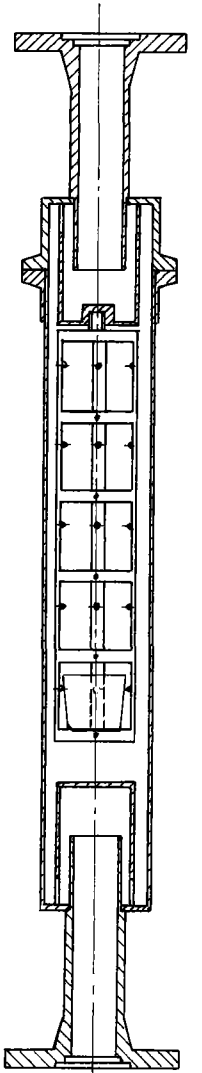
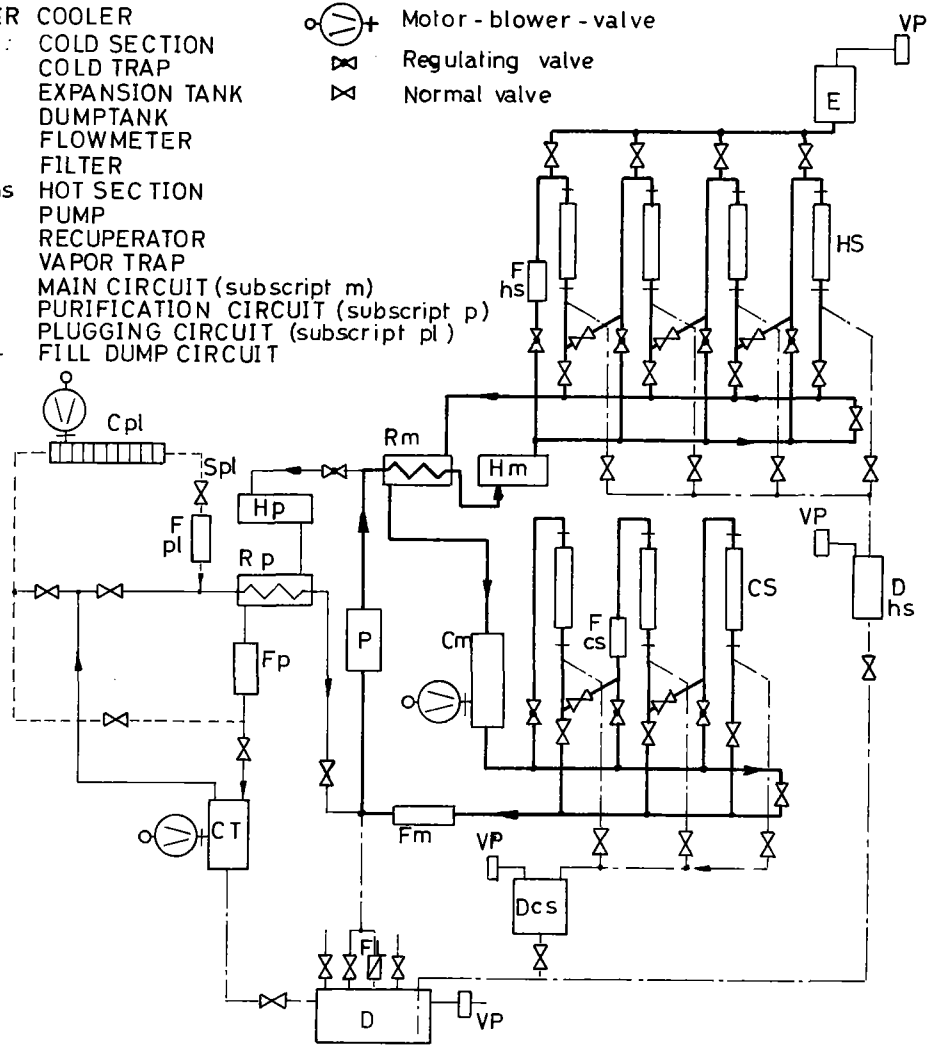


FIG. 5 FLOW SHEET OF THE LOOP ASL - 1

FIG. 6 SAMPLE TAKER OF ASL-1

Table I Operating parameters and results during purification by dumping

Experiment Period	A1 6/5-7/5	A2 13/5-29/5	A3 16/6-23/6	A4 24/6-4/7	A5 7/7-10/7
Sodium flow m <sup>3</sup> /h					
- main circuit	1.86	1.96	1.33	1.26	1.38
- purification	0.77	0.49	0.86	0.65	0.74
Temperature °C					
- of filling	125	125	140	125	125
- at HS1	398	397	401	400	400
- at HS4	381	387	388	385	392
- at CS1	383	357	363	357	363
- at CS3	377	29	360	354	360
- at cold trap	381	392	367	355	345
- of 1st plug	310	280	190	180	175
- of 2nd plug	-	-	270	260	255
ppm oxygen	13.8	8.6	12.3	6.7	3.8
ppm carbon	15.1	7.1	5.2	6.0	17.3
ppm carbide C.	<0.19	<0.31	<0.32	<1.8	<0.52
ppm carbonate C.	<0.16	<0.04	<0.37	<0.19	1.73
ppm residual C.	9.0	8.1	11.3	7.5	11.3

**INTERNATIONAL CONFERENCE ON LIQUID METAL TECHNOLOGY IN ENERGY PRODUCTION**

Table II Analysis of carbon forms in sodium of ASL (p.p.m.)

Experiment	A1	A2	B end	C 400°C 21-10-75	C 550°C 28-10-75	C 675°C 11-12-75
Total carbon p.p.m.	15.1	7.1	7.7	11.0	1.69	0.91
Carbonate carbon	<0.16	<0.05	2.1	20.2	10.4	1.83
Cyanide carbon	-	-	-	<0.01	<0.1	0.44
Carbonyl carbon	-	-	0.3	1.16	0.7	0.46
Residual carbon	9.0	8.1	2.7	-	-	-
Carbides yielding						
C <sub>2</sub> H <sub>2</sub>	0.012	0.013	0.21	0.040	0.054	
C <sub>2</sub> H <sub>4</sub>	0.022	0.023	0.039	0.020	0.015	
C <sub>2</sub> H <sub>6</sub>	0.047	0.038	0.037	0.018	0.017	
C <sub>3</sub> H <sub>8</sub>	0.022	0.019	<0.01	<0.01	<0.01	
C <sub>3</sub> H <sub>6</sub>	0.018	0.028	0.028	0.018	0.010	
C <sub>4</sub> H <sub>8</sub>	<0.010	<0.010	<0.01	0.029	0.042	
Total carbide carbon	<0.16	<0.3	0.5	3.5	4.5	0.48
ppm Oxygen	13.8	8.6	0.65	1.42	3.44	2.06
Plugging temperatur.	310°C	280°C	<145°C	<145°C	<145°C	<145°C

Table III Analysis of metals and chloride in sodium of ASL (p.p.m.)

Experiment	Filling sodium	A1	A5	B end	C400°C	C550°C	C675°C
A1	<0.2	-	0.34	<0.2	0.21	0.3	0.5
Au	<0.01	-	0.04	<0.01	<0.01	0.01	0.03
Bi	<0.7	-	-	-	-	-	<0.7
Ca	447	9	-	4.6	-	-	-
Cd	0.8	<2	-	<2	-	-	<0.4
Cl <sup>-</sup>	13	16.9	-	16.1	-	-	-
Co	0.3	-	<0.6	<0.6	<0.6	<0.6	<0.2
Cr	<0.3	-	0.2	<0.2	<0.2	<0.2	0.8
Cu	<0.1	-	0.2	<0.08	<0.08	0.08	0.2
Fe	<0.2	1.5	1.25	1.63	0.6	<0.6	<0.2
K	38.5	42.9	-	43.5	-	-	-
Mn	<0.5	2.37	0.36	<0.3	<0.3	<0.3	0.45
Mo	<0.003	-	0.02	0.16	0.003	0.003	<0.003
Ni	<0.1	-	-	-	-	-	1.4
Pb	0.4	-	<0.7	<0.7	<0.7	<0.7	0.7
Sn	<0.03	-	<0.02	<0.02	<0.02	<0.02	0.04
Ti	0.3	-	<0.2	<0.2	<0.2	0.15	0.15
V	0.02	-	0.005	<0.005	<0.005	0.15	1
Zn	0.3	<2	-	<2	-	-	0.7

Table V Plugging temperature and oxygen concentration

Experiment	A1	A2	A3	A4	A5
Plugging temp. °C	310	280	190	180	175
Calculated oxygen ppm	116	69	9.5	7.3	6.3
Measured oxygen ppm	13.8	8.6	12.3	6.7	3.8
Hydrogen calculated ppm	13.4	7.2	-	-	-

Table VI Carbon solubility calculated and measured

Temperature	400°C	500°C	550°C	600°C	675°C
C ppm solubility	0.06	0.84	2.5	6.4	22.3
C ppm measured	{ 5.2 17.3	5.8	3.3	4.0	{ 0.91 2.6

Table IV Oxygen and carbon impurity during experiment C

	21.10.75	29.10.75	2.12.75	5.12.75	11.12.75	30.12.75
Temperature Hot leg	400°C	550	500	600	675	675
Plugging temperature	<145°C	275	<145	<145	<145	<145
Oxygen ppm	1.42	7.49	1.65	4.9	2.06	0.79
Total carbon ppm	11.	3.3	5.8	4.0	0.91	2.6
Carbide carbon ppm	3.5	5.0	2.69	2.3	0.48	0.4
Carbonate Carbon	20.2	5.15	0.71	2.72	1.83	9.9
Carbonyl Carbon	1.16	1.25	2.64	1.3	0.46	0.42
Cyanide Carbon	<0.01	<0.01	0.045	0.05	0.44	0.09

T. R. Padden, S. A. Meacham, H. W. Brandt

Westinghouse Electric Corporation  
Advanced Reactors Division  
Madison, Pennsylvania  
U.S.A.

## ABSTRACT

The particulate material entrained in the sodium of the Westinghouse ARD's General Purpose Sodium Loop No. 2 (GPL-2) was evaluated as part of the Liquid Metal Fast Breeder Reactor (LMFBR) Pump Bearing Test. The test plan specified a weight fraction concentration of solid particulates in the sodium to be less than 1 part per million (ppm) and an upper size limit on the particle unit of  $50 \mu\text{m}$  (2 mils). The particulate matter was evaluated because of the potential enhancement of wear on the pump bearing surface and because of the possibility of entrapment of the particles in the small clearance areas of the hydrostatic bearing. This paper discusses the results of the evaluation and concludes that a low concentration of particulate material can be maintained. However, due to the friability of the material, the effective "particle size" should be defined in terms of the application in setting loop specifications, in order to make those specifications meaningful.

## INTRODUCTION

The particulate material entrained in the sodium of the Westinghouse ARD's General Purpose Sodium Loop No. 2 was evaluated as part of the LMFBR Pump Bearing Test. For this test, the facility was operated at a flow rate of 500 gallons/minute minimum and at temperatures between  $204^\circ\text{C}$  ( $400^\circ\text{F}$ ) and  $582^\circ\text{C}$  ( $1080^\circ\text{F}$ ). The particulate material was evaluated because of the potential enhancement of wear on the pump bearing surfaces and because of the possibility of entrapment of the particles in the small clearance areas of the hydrostatic bearing. In preparation for the test, the facility was flushed repeatedly with filtered sodium to remove particulate material introduced during assembly of the test article and the test chamber.

Figure 1 is a general view of the GPL-2 Test Facility. The structure on the left is the test chamber for the LMFBR pump bearing assembly. It is pertinent to the general subject of entrained particulates to consider that this is a large test loop, which is breached frequently to change test articles and to add or remove monitoring instrumentation.

For the pump bearing test, the test plan specified a weight fraction concentration of solid particulates in the sodium to be less than 1 ppm and an upper size limit on the particle unit of  $50 \mu\text{m}$  (2 mils). Accepted methods used in the United States specify methods for sampling the sodium using stainless steel filters in bypass lines to determine the weight fraction of entrained solids. This standard does not cover evaluations of the size of the particle units in the collected solids. There was no method specified in the test plan and at the present time, there is no standard method for performing this evaluation. As will be shown in this paper, simply measuring the longest dimension of the as deposited particle units is misleading and may overestimate the effective particle size relative to the application of the sodium loop system.

## WEIGHT FRACTION OF SOLIDS

The procedure for sampling the GPL-2 sodium during the pump bearing test was consistent with accepted standards used in the United States. Figure 2 is a schematic showing the filter housing and the filter used to collect the particulates. The filter unit was cleaned, assembled, helium leak checked, and installed in the by-pass sample line of the loop. After the particulates from the appropriate volume of sodium were collected, the filter unit was cooled, allowing the sodium to freeze, and then removed from the by-pass line.

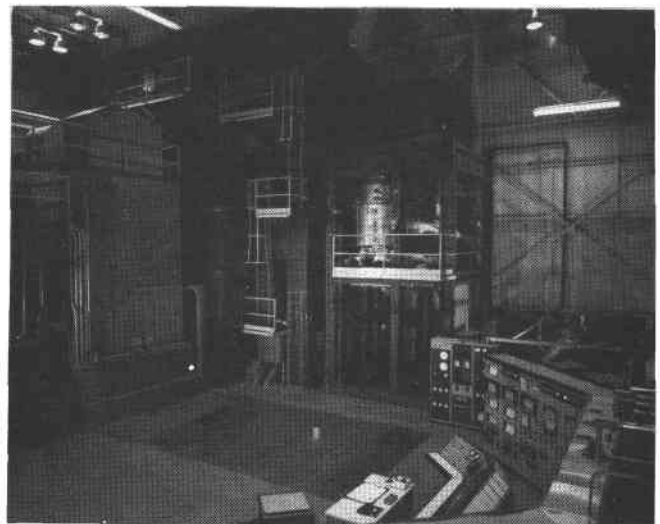


Fig. 1: General View of GPL-2 Facility

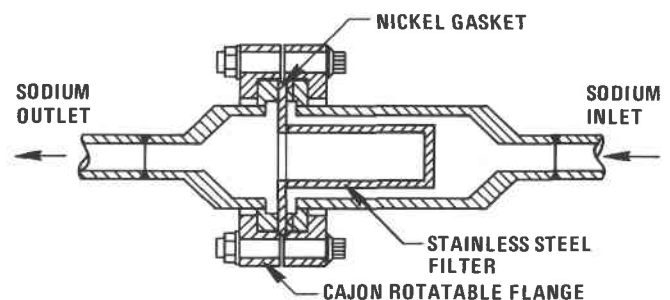


Fig. 2: Schematic of Filter Unit

The particulates were collected by flowing approximately 150 gallons of sodium at 315°C (600°F) through the sintered stainless filter which had a 10 μm nominal porosity and was located in the bypass sampling line. The flowrate through the filter in the bypass line corresponded to approximately 1% of the GPL-2 loop. This type filter is certified to collect 95% of all particulates greater than 10 μm in size, assuming spherical shape. The residual sodium was removed by vacuum distillation and the particulates were separated from the stainless steel filter by ultrasonic cleaning in pre-filtered ACS certified xylene and then in pre-filtered demineralized water, and subsequently collected on a pre-tarred membrane filter. The membrane filter was dried, weighed, and the weight fraction of the collected particles determined.

Throughout the pump bearing test, the measured weight fraction of solids from the various samples was consistently below the limit specified in the test plan. The range in concentration for the eight samples taken at various times during the test was 1.2 to 6.4 parts per billion (ppb) as shown in Table I. These levels were in all cases less than 1% of the specified limit, one part per million.

MICROSCOPIC CHARACTERIZATION

Of the samples listed in Table I, Number 2-43 was given the most thorough characterization. Particle units greater than 50 μm were of particular interest because of the hydrostatic bearing being tested. Figure 3 illustrates the appearance on the filter of the 0.59 mg of solids collected from the 150 gallon sodium sample. Figure 4, which is a higher magnification of area 1 of Figure 3, illustrates the general morphologies of the as-deposited particle units. The circled particles in Figure 4 are units which are the threshold size for concern; 50 μm.

The as-deposited units on the filter were characterized by microscopic examination at higher magnification using various types of illumination. The filter deposit consisted primarily of black, irregular flakes or film shaped particles which were smaller in the depth direction than in the length or width. The minor constituents in the sample were thin black rods or slivers, small transparent particles having the appearance of glass or sand and a white translucent material existing either as individual small particles or translucent particles containing black flakes. These particle morphologies are illustrated by Figure 5. The very minor constituents were small particles of various colors; of these, salmon colored units were the most frequent. The deposit also contained transparent to translucent fibers and films which had the appearance of cellulose or plastic.

TABLE I  
PARTICULATE CONCENTRATION IN SODIUM

Sample No.	Sodium wt, kg	Particulate wt, mg	Concentration, ppb
2-34	396	2.06	5.2
2-36	1939	3.82	2.0
2-39	201	0.74	3.7
2-40	442	1.13	2.6
2-43	498	0.59	1.2
2-45	564	3.61	6.4
2-48	507	1.58	3.1
2-50	507	1.38	2.7

These were presumed to have been introduced during processing of the filtered material. Within the scope of this examination no particles were observed which could be identified as solid metallic chips or turnings based on color or shape.

For the purposes of this investigation, it was the larger particle units which were of particular interest. The frequencies of units with one dimension of 50 μ or greater were tabulated for the areas designated 1, 5, and 6 of Figure 3. From these measurements and the area fraction sampled, (5.5%) it was estimated that the total filter contained approximately 2000 particles which were 50 μm or larger in the greatest dimension.

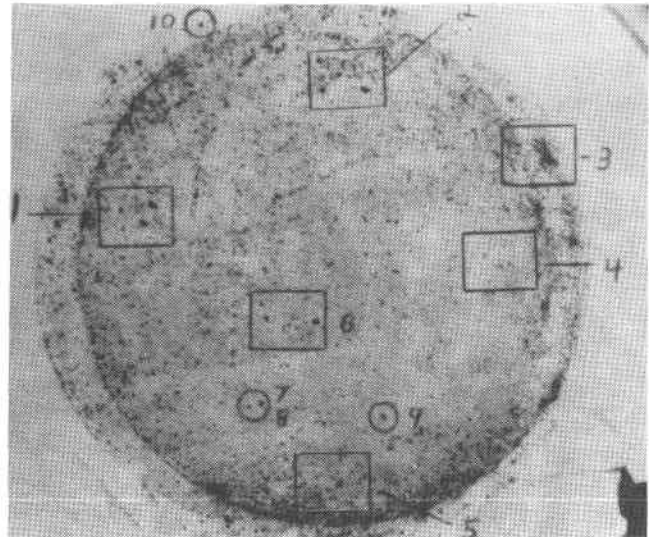


Fig. 3: Sample 2-43 at 3X

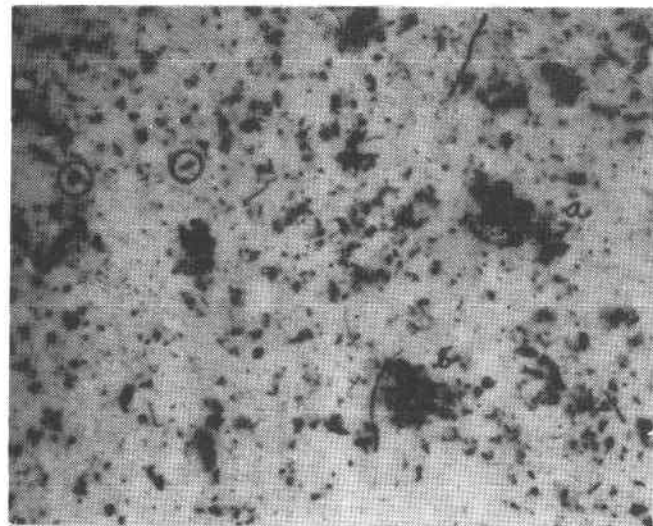


Fig. 4: Area 1 of Fig. 3 at 30X

Twelve of the largest particles selected from the whole filter area were measured in the depth direction as well as the maximum length and width. Seven intermediate size particles were similarly measured. On the 12 largest particles, which range in length up to  $356\ \mu\text{m}$ , only 5 were greater than  $50\ \mu\text{m}$  in the depth direction. The thickest of these was  $64\ \mu\text{m}$  in depth. None of the intermediate size particles which ranged in length up to  $115\ \mu\text{m}$  were greater than  $50\ \mu\text{m}$  thick. Although there were about 2000 estimated units, from the 150 gallons of sodium, which exceeded  $50\ \mu\text{m}$  in the largest dimension, only a few exceeded this size in the smallest dimension.

Five of the largest and two of the intermediate size particles were then used for a friability test. The particles were transferred under a microscope from the Millipore membrane filter to a clean glass slide containing a drop of xylene. Another slide was placed on top and slid with reciprocating motion relative to the bottom slide, with or without additional force applied perpendicular to the top slide. From this test the friability was subjectively assessed.

Four of the large particles plus the two intermediate size particles broke down into smaller units with little or no perpendicular force required. The sub-units were translucent in strong light. On the basis of this test these six particles were judged to be friable and nonmetallic and probably would readily fracture if caught in the bearing.

The seventh particle compressed to  $1/5$  its thickness rather than breaking under considerable finger pressure. When the slides were parted, it separated into two pieces which were also partially translucent. This particle was judged to be non-friable but plastic in nature. It was not a solid piece of metal. It too would probably cause no problem with the bearing.

None of the particulates were analyzed chemically. That was outside the scope of the investigation. In general, however, the particle units appeared to be films and flakes of partially continuous sub-units such as pieces of deposit layers which flaked off the walls of the sodium facility.

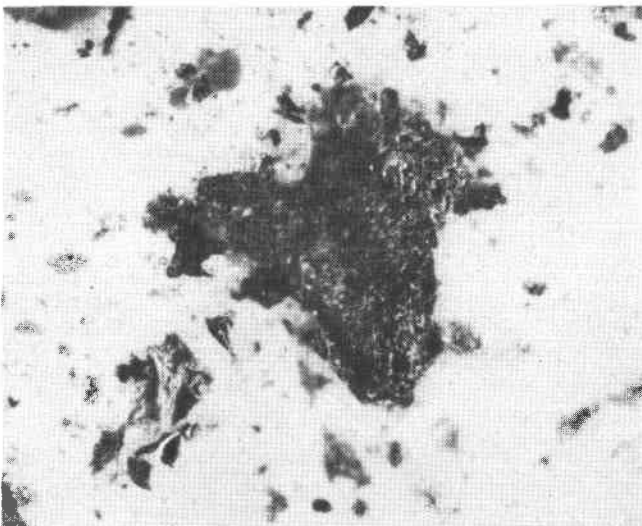


Fig. 5: Flake and Rod Shaped Friable Particles at 200X

Three additional samples of particulates were also characterized using Sample 2-43 as the basis of comparison. Taking into account the friability of the particle units and the objective of the investigation, an additional preparation step was added to the procedure and applied to the later samples. After the weight fraction of solids in a sample was determined, the particulates were resuspended in xylene and given a standard "Wiggle Bug" treatment to break down the aggregates and the friable units. This treatment involved vigorous agitation of the material contained within a  $5\ \text{cm}^3$  plastic vial. Normally, an internal plastic ball is used to break up small amounts of material by this treatment. In this case, no ball was used and the particulates suspended in the xylene simply agitated for 60 seconds to determine ease of reducing the aggregates to smaller units.

For all three samples there was a marked reduction in the frequency of particle units in the  $50\ \mu\text{m}$  or greater size class. Those remaining were generally flakes and films similar to those observed in Sample 2-43. There were some differences between the samples, however. In addition to the flakes and films, Sample 2-45 also contained some chunky particles consisting of a white translucent phase with black flakes, and fine metallic turnings. Thirteen of the flake and film particles, the largest being a chunky particle  $152 \times 147 \times 81\ \mu\text{m}$  were all shown to be friable. The fine metallic turnings could have been introduced during the installation and/or removal of the filter assembly.

Sample 2-48 was similar to Sample 2-53 except that it contained a few chunky particles which were not readily friable. The largest was  $356 \times 203 \times 61\ \mu\text{m}$ . Considerable pressure was required to fracture these particles. They broke into blocky-like pieces which were not transparent. Several of the pieces were mounted and polished in cross section. They all had a metallic luster and similar microstructure which is shown in Figure 6. It appears to be a two phase cast structure. From the brittleness and the structure, the most likely identification is some type of hardfacing, perhaps from a valve tip.

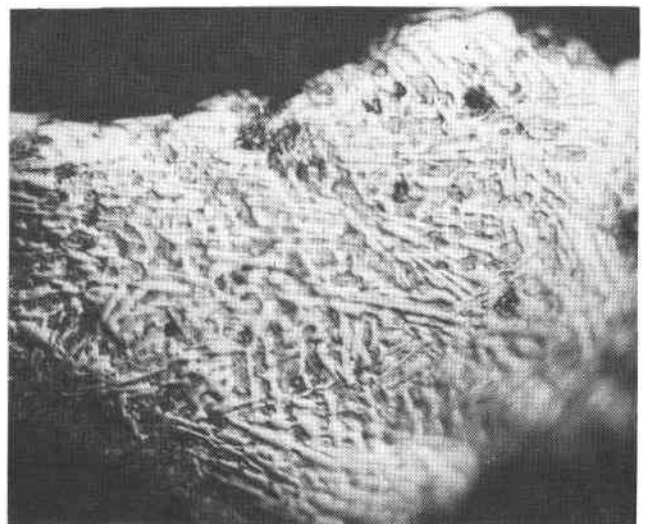


Fig. 6: Sample 2-48 at 500X - Non-Friable Particle

## INTERNATIONAL CONFERENCE ON LIQUID METAL TECHNOLOGY IN ENERGY PRODUCTION

The presence of chunky, non-friable particles greater than 50  $\mu\text{m}$  in the smallest dimension indicated a potential danger of damage to the test bearing at the time this sample was taken. The subsequent sample, Number 2-50, contained no chunky particles, no metallic slivers and, in general, was similar to Sample 2-43 except it contained fewer units in the 50  $\mu\text{m}$  size class. Twelve of the largest particles were tested for friability. All broke readily.

A post test evaluation of the bearing after 10,000 rotations indicated there were no detrimental effects to the bearing surfaces due to particulates entrained in the flowing sodium.

### CONCLUSIONS

1. Low concentration of particulates in the sodium were achieved, 1.2 to 6.4 parts per billion (ppb). These levels were less than 1% of the maximum concentration permitted by the test specification (1 ppm).
2. Most of the filtered particulates larger than 50  $\mu\text{m}$  consisted of friable flakes, films and aggregates of smaller particle units.
3. A low frequency of non-friable particles which were greater than 50  $\mu\text{m}$ , was also observed. The presence of this very minor constituent in the sodium caused no enhanced wear on the pump test bearing.
4. Because of the friability of the solids collected from sodium, the effective "particle size" should be defined in terms of the application in setting loop specifications, in order to make those specifications meaningful.

Work performed on ARD Contract AT(11-1)-3045 Task 14

OPERATIONAL TECHNIQUES EMPLOYED FOR THE  
LIQUID SODIUM SOURCE TERM CONTROL LOOPS

By

L. E. Chulos

ABSTRACT

Four Source Term Control Loops (STCL's) have been designed, constructed, and placed into operation at the Hanford Engineering Development Laboratory (HEDL) as part of the Radioactivity Control Technology program. The data obtained are used to determine the corrosion and deposition of LMFBR materials, including corrosion product radionuclides, in a non-isothermal flowing sodium system. This paper discusses operation of the STCL Facilities and, in particular, the methods used for controlling the oxygen content of the liquid sodium. These methods include cold trapping techniques, hot trapping, seeding the cold traps with sodium oxide, and precipitating the oxygen in the cold trap in a controlled manner. Operational problems encountered with the STCL Facilities and the techniques for correcting these problems are also discussed.

INTRODUCTION

The four Source Term Control Loops (STCL) at HEDL were constructed and placed into operation as a means for determining the corrosion and deposition of LMFBR materials, including corrosion product radionuclides, in a non-isothermal flowing sodium system. The loops are capable of sustained operation with a hot leg temperature up to 700°C and a system  $\Delta T$  of 180°C at a main system flow of 0.45 m<sup>3</sup>/hr (2 gallons/min). A shielded specimen chamber is provided for irradiated corrosion specimens. Two additional specimen chambers are provided for non-irradiated specimens, one in the hot leg and one in the cold leg. The sodium characterization portion of the STCL's is composed of a cold trap, a hot trap (STCL-1 only), an oxygen meter, and a vanadium wire equilibration device (VWED) or a multipurpose sampler (MPS). The new series of STCL's (Loop 2, 3, and 4) shown in Figure 1 are operated by an on-line digital

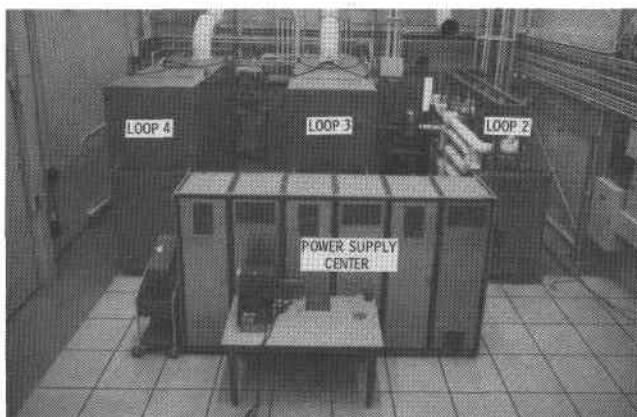


FIGURE 1. Loop Room.

control system with an 8K memory unit computer. One computer is used to control the three loops on an independent basis (Figure 2).



FIGURE 2. Control Room.

SODIUM CHARACTERIZATION AND CONTROL

Cold Trapping

One method for controlling the oxygen concentration in the STCL Facilities is the cold trapping system. Using this method the cold trap temperature (see Figure 3) is set according to the level of oxygen concentration desired.

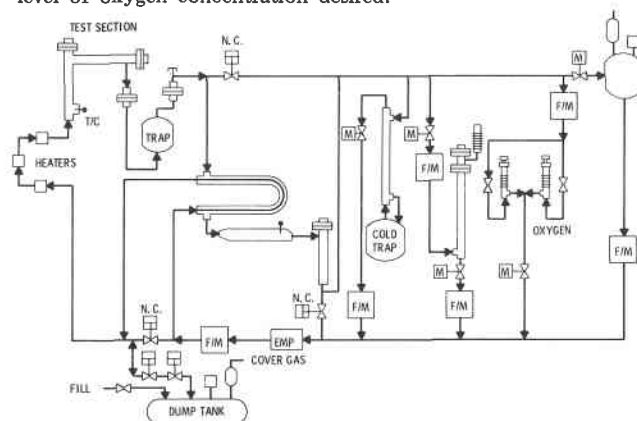


FIGURE 3. Engineering Flow Diagram STCL No. 2, No. 3, and No. 4.



The relationship of temperature and oxygen concentration is determined by the oxygen solubility curve<sup>(1)</sup> as shown in Figure 4.

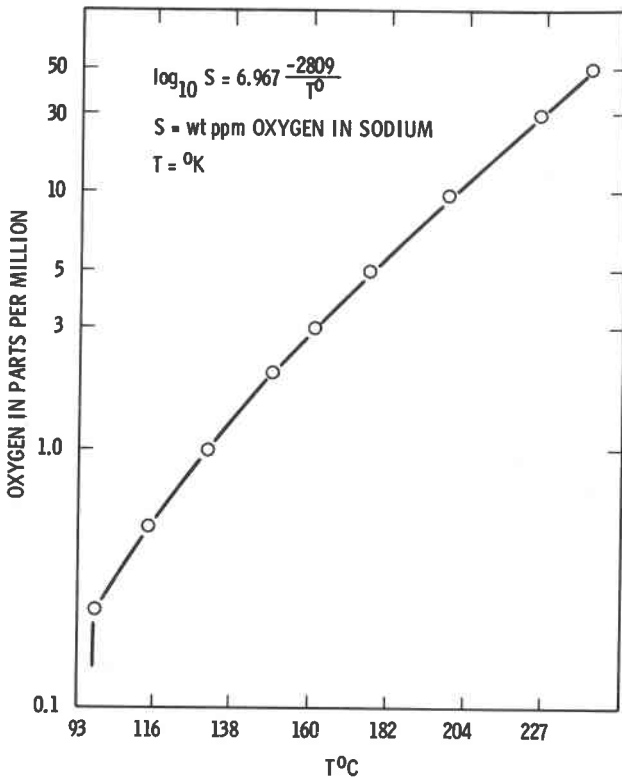


FIGURE 4. Oxygen Solubility Curve.

The concentration of oxygen in the loops is determined by the vanadium wire equilibration technique<sup>(1)</sup>; this technique also furnishes a calibration for the on-line oxygen meter which continuously monitors the oxygen activity in the flowing sodium. Equilibrations of vanadium wires are done in the VWED on STCL-1 (Figure 5) or in the MPS in STCL-2, 3, and 4 (Figure 6).

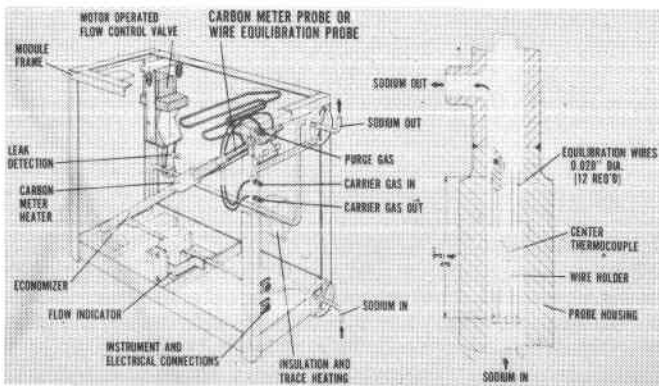


FIGURE 5. Wire Equilibration Probe.

Theoretically, it is possible to remove virtually all of the oxygen in solution by lowering the temperature to near the freezing point of sodium and trapping the oxides on the wire mesh in the cold trap crystallizer. There are various methods for controlling the cold trap temperature; however, most are not reliable for tight temperature control and there is the danger that the temperature may fall below the freezing point causing

MULTIPURPOSE SAMPLER  
FOR APPLICATIONS ON FFTF SYSTEM 85  
SODIUM CHARACTERIZATION

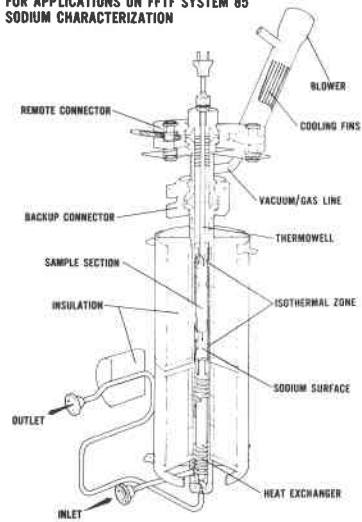


FIGURE 6. Multipurpose Sampler.

the cold trap flow to stop. The cold trap will then have to be re-heated until the oxides go back into solution and flow is re-established; this will result in a flushing of the trap and a subsequent increase in the oxygen concentration of the sodium.

The original method for temperature control of the cold trap on STCL-1 was achieved by a continuously operating fan forcing air through a louver and onto the external wall of the cold trap crystallizer (Figure 7). The correct temperature of the

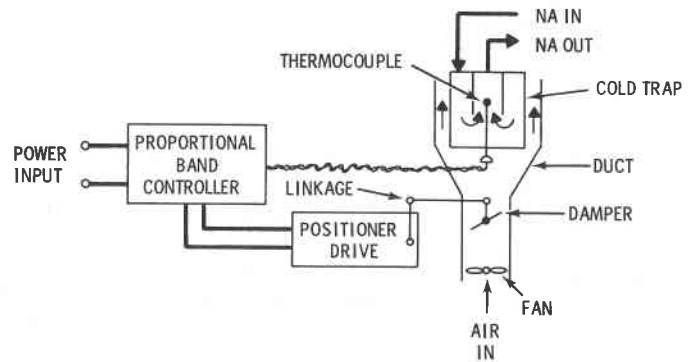


Figure 7. Old Control Method for STCL Cold Parts.

sodium was maintained by an internal thermocouple monitoring the sodium temperature and by a controller which opened or closed the louver to keep the temperature at the control set point. This method was found to be inadequate due to the slow operation of the mechanical linkage and subsequent slow temperature response of the cold trap system. Even with proportional band control, the temperature tended to overshoot and oscillate about the set point.

A more precise method for controlling the temperature was conceived in which the mechanical linkage and louvers were eliminated and a resistance heater was used instead (Figure 8).

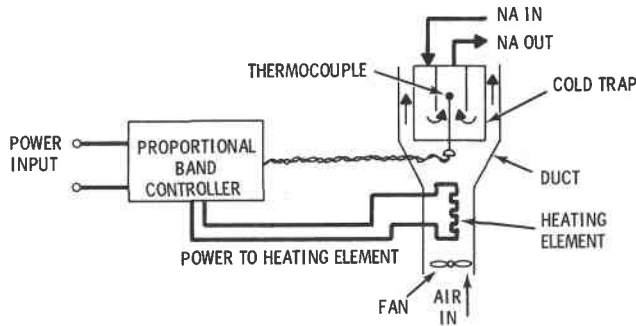


Figure 8. Improved Control Method for STCL Cold Traps.

In this system, the controller keeps the internal temperature constant by increasing or decreasing the current to a resistance heater with a blower continuously forcing air across the heating coil. The lag time tends to be minimal with temperature control constant within plus or minus 1°C or less. Ambient room temperature changes and/or changes in main loop temperatures were found to have no appreciable effect; thus there is no reason why the above described device could not be successfully used on larger cold trapping systems of either single or multiple heat exchange designs.

Hot Trapping

For small inventory systems of less than 50 liters, the hot trapping technique appears to be very efficient. Hot trapping is accomplished very rapidly for oxygen levels down to about 0.01 ppm. A hot trap operates with sodium flowing across zirconium foil at about 700°C with the foil acting as an oxygen getter. Although the hot trapping technique has been known for many years, no accurate measurement of oxygen levels under these conditions had been possible until recently. With development of the oxygen meters and the vanadium wire equilibration technique, the hot trap has proved to be able to remove oxygen from sodium down to as low as  $1 \times 10^{-3}$  ppm.

Source Term Control Loop 1 is equipped with a hot trap which contains 1.7 m<sup>2</sup> of 0.5mm thick zirconium foil. The hot trap module has an economizer which allows sodium up to greater than 700°C to flow across the foil for optimum getting of the oxygen. The sodium volume of STCL-1 is about 23 liters with a flow of about 0.045 m<sup>3</sup>/hr of sodium through the trap (see Figure 9).

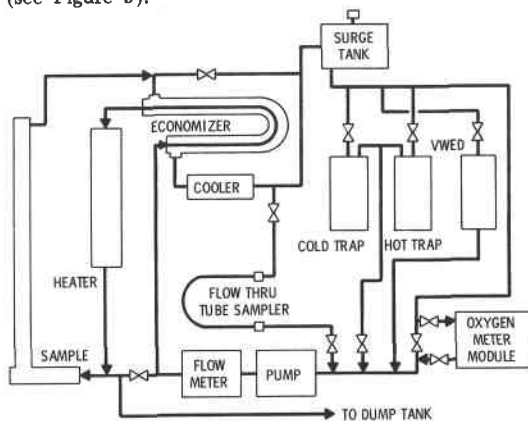


Figure 9. Source Term Control Loop.

The oxygen meter on STCL-1 was calibrated at the extremely low oxygen level produced during hot trapping by the vanadium wire technique as described below.

After introducing sodium into STCL-1 from the dump tank, the loop was raised to operating temperatures of 427°C cold leg and 604°C hot leg. The cold trap was then preheated and valved in. The oxygen level was established at 0.5 ppm by setting the cold trap temperature at 115°C and operating for about one day to assure steady-state operation. The cold trap was then valved out and the hot trap preheated, with the inlet and outlet valves being opened as they reached 150°C. The observed oxygen meter voltage began to rise almost immediately thus indicating that oxygen was being removed even at fairly low hot trap temperatures. The hot trap temperature was raised to 700°C, and after a period of about five days, the oxygen meter had attained a voltage of 1.894 volts which remained steady.

A vanadium wire equilibration run was performed several days later. A small amount of air is normally trapped in the vanadium wire bypass line, so when flow was introduced, the oxygen level of the sodium increased, as indicated by a sharp decrease in the meter voltage. The temperature of the vanadium wire module was raised to 750°C after the voltage had increased to 1.880 volts. The analysis of the vanadium after the exposure extrapolated to an oxygen content in sodium of  $0.007 \pm 0.003$  parts per million ( $7 \pm 3$  ppb) at a voltage of 1.880 volts. This compares very favorably with 3 ppb obtained by extrapolating the previous meter calibration downward over three orders of magnitude. After several thousand hours of STCL-1 operation the voltage on the meter eventually reached 1.905 volts, which corresponds to an oxygen level of 1 to 3 parts per billion, as seen on Figure 10. In order to have sufficient material to perform the vacuum-fusion analysis for oxygen

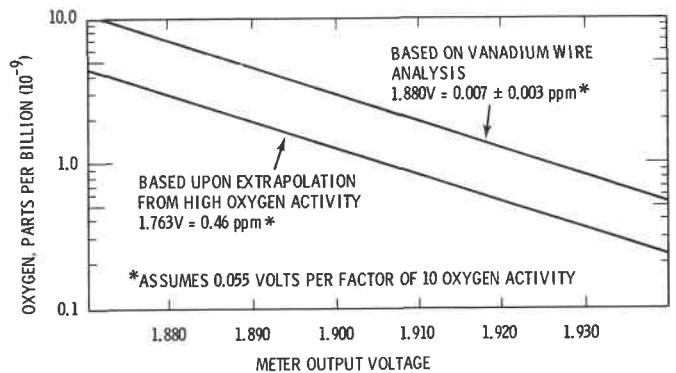


FIGURE 10. Oxygen Meter Calibration Curve STCL-1.

in the vanadium it was necessary to use a larger than normal sample of vanadium. A second vanadium wire equilibration performed after 4000 hours of STCL-1 operation gave identical results.

This is the first time that a vanadium wire equilibration run has ever been attempted at this oxygen level (less than 0.01 ppm), and the comparison of the vanadium wire analysis and extrapolated oxygen meter voltage curve appears to be very close.

## INTERNATIONAL CONFERENCE ON LIQUID METAL TECHNOLOGY IN ENERGY PRODUCTION

### Oxygen Replenishment

It has been necessary to periodically replenish the supply of oxygen in the cold trap to maintain the desired oxygen level. The need to do this underscores the role of oxygen in the corrosion process. The oxygen is apparently converted to a species other than sodium oxide which reaches an equilibrium corresponding to very low oxygen activity in sodium. In a small, tight test system such as STCL run for long periods, the oxygen is consumed by this process and the cold trap acts as a source, not a sink, for oxygen. In a larger system there may be leakage that will supply oxygen for the corrosion reaction, hence the need for the cold trap which in that case would be a sink for oxygen.

Six grams of sodium oxide, equivalent to 20 ppm oxygen in sodium in STCL-1, are added to the loop via the sampling ports (the flow-through tube sampler in STCL-1 and the multi-purpose sampler cup in STCL-2 and -3). This step can be done while the test is in progress, provided that the loop temperature is reduced to less than 400°C.

The cold trap temperature was raised to 280°C to allow all of the oxygen to remain in solution in the sodium. With the sampler and cold trap valved in, the cold trap temperature was lowered in 28° increments. After each increment, the oxygen meter was monitored and when the meter no longer showed a voltage rise, the cold trap temperature was lowered another 28° until the cold trap was at 115°C and the meter voltage remained constant. The temperature of the test loop was then raised to the 604°C test condition. A vanadium wire equilibration was then conducted to verify that the oxygen level was 0.5 ppm.

### Relief of Pressure Buildup

Upon blowing down the multipurpose sampler (MPS) after completion of a vanadium wire equilibration run, sometimes an unequal pressure between the MPS and surge tank will cause an excess of argon gas to be trapped in the MPS when the valves are shut. When the MPS is reheated for another run and flow commences, the gas will be released to the main loop causing main EM pump shutdown. The situation is corrected by attempting to sweep the gas to the surge tank by starting the EM pump and increasing voltage to about 75% of the previous set point and repeating. If this procedure is unsuccessful, then all valves in the main loop are opened and flow is established. The valves are shut one at a time as the gas is swept out of the main loop to the surge tank. It may be necessary to repeat this sequence several times. NOTE: Pump must be started with a low voltage and power gradually increased, due to the risk of breaking the ceramic oxygen meter tube because of a pressure surge.

When preheating the two dump valves, there is the danger of rupturing the bellows due to a temperature induced pressure buildup. The loop is normally filled at 312°C from the dump tank, and the dump valves are maintained at 312°C; however, when the main loop is heated to a higher temperature, the piston operated valve (POV) next to the main loop starts receiving heat from the main loop. In fact, the hot leg passes within a few inches of the POV, and the temperature rises to nearly 540°C. To keep from rupturing a bellows due to sodium ex-

pansion with the two dump valves shut, the POV next to the dump tank should be cycled with every 50°C temperature rise.

### Protection of Oxygen Meter Tubes Against Breakage

The ceramic oxygen meter tubes are extremely sensitive to pressure and temperature transients. The meter piping does not drain when the loop is drained so when preheating extreme precautions must be taken to always heat away from a free sodium surface in sequence. As soon as the outlet motor operated valve reaches 150°C, the valve can be opened to allow for thermal expansion. The heater set points are set to loop cold leg temperature. As soon as the inlet hand operated valve reaches 150°C, it is opened slightly until flow barely registers on the oxygen meter flowmeter. The internal meter temperature is observed and flow adjusted to obtain a temperature rise of 35°/minute. When the meter reaches operating temperature (400-500°C) flow is increased to the normal rate of 0.023 to 0.045 m<sup>3</sup>/hr (0.1 to 0.2 gallons/min).

Using these procedures, ceramic tube lifetimes in excess of one year are being achieved even with several intermittent system shutdowns.

### REFERENCES

1. D.L. Smith and R.H. Lee, "Characterization of the Vanadium-Wire Equilibration Method for Measurement of Oxygen Activity in Liquid Sodium", USERDA Report ANL-7891 (January 1972).

# INTERNATIONAL CONFERENCE ON LIQUID METAL TECHNOLOGY IN ENERGY PRODUCTION

## DISCUSSION

Paper IIA-3: "Metallurgical Problems Associated with Large Sodium Loop Operations"

N. Krasnoyarov: Under what conditions did you note carburization to a depth of approximately 500  $\mu\text{m}$ ?

E. Benoist: Carburization to a depth of 500  $\mu\text{m}$  was observed in the CAPHE loop after an oil leak from the mechanical pump. During a 2-week period, a small leak of 2 or 3 liters of oil entered sodium, which was at 600°C in the loop. Oil reacted with sodium in the argon section of the pump, and several plugs were observed in the argon line. While saturation with carburized products was high, we believe that high temperature has a greater effect on carburization.

D. Greene: Have significant differences in the hydrogen (produced by water-side corrosion) permeation rates been measured in steam generating systems, e.g., 5-MW, 50-MW and Phenix systems?

E. Benoist: Results obtained on the loop and on Phenix are very similar in hydrogen permeation. Of course, we must compare only the result that can be compared. For example, results obtained at equilibrium disregarding the cold trap are the same.

C. Allan: Did you examine the distribution of deposited impurities in your exhausted cold traps and did you find local blockage of the packing? Did operation of the cold trap at temperatures approaching the plugging temperature improve uniformity of distribution in the packing?

E. Benoist: We have opened cold traps on the CAPHE loop after use, but generally have not found local blockage of the packing. Blockage is dependent on operating conditions in the cold trap, primarily temperature. To avoid blockage, temperature of sodium at the economizer, which is the same as that at the inlet of the cold trap, should be maintained at a higher level than plugging temperature. If sodium in the loop is very dirty, temperature of the loop must be maintained at a sufficiently low level until the plugging temperature decreases.

Paper IIA-4: "Identification of Impurities in Sodium and Coolant Purification"

K. Stade: Of what materials and sizes are the crucibles used in your sodium sampling in-line distillation unit?

F. Kozlov: When analyzing sodium for oxygen, nickel and molybdenum crucibles with a 100-cm<sup>3</sup> volume are used; and, when analyzing for carbonaceous impurities, quartz crucibles with a 15-cm<sup>3</sup> volume are used.

K. Stade: Do you use the in-line distillation unit in reactor systems such as BOR-60 or BN-350?

F. Kozlov: The in-line distillation unit was used in experimental rigs and in BN-350 during commissioning.

K. Stade: Do you have experience with the electrochemical oxygen meter under reactor conditions?

F. Kozlov: The electrochemical oxygen meter was studied on sodium rigs; we are now installing it on BOR-60.

C. Allan: You note capacities for your two traps as 25 wt% and 47 wt%. How are these values affected by the settling zones in the lower part of the trap and the mesh packed zone?

F. Kozlov: In the settler, the lower part of the trap, the Na<sub>2</sub>O concentration was 37 to 60 wt%; in the first part of the filter, it was 57 wt%.

J. McCown: What carbon compound was added to the system in evaluating the response of the carbon meter?

F. Kozlov: Acetylene was introduced into the expansion tank of the circuit.

Paper IIA-5: "Sodium and Cover Gas Chemistry in the High Temperature Sodium Facility"

D. Greene: Do you notice any significant absorption of hydrogen by the controlled temperature vapor trap? In your opinion, would its use in monitoring cover gases for H<sub>2</sub>O leak detection be affected?

J. McCown: When we change the hydrogen level by adding NaOH to the Na or H<sub>2</sub> to the cover gas, the hydrogen concentration changes in both the sodium and cover gas and is evidenced on the in-line H<sub>2</sub> meter and the gas chromatograph on the gas stream. An equilibrium between the hydrogen in the two phases is established. While we are aware of some absorption in the vapor trap, it does not prevent subsequent changes. Dr. Barton of HEDL has made some calculations on this and can provide further detail.

Paper IIA-6: "Sodium Characterization During the Starting Period of a Sodium Loop"

Y. Gohshi: Is there any correspondence between the spectra of hydrocarbons and the kind of carbides?

F. Lievens: During hydrolysis of the carbides, a hydrogen atom is substituted for each sodium atom. Therefore, a correspondence is expected between the hydrocarbon as observed by gas chromatography after hydrolysis and the kind of sodium carbides in the liquid sodium sample. But the large amount of hydrogen produced during the reaction of the sample with water and the local heating may promote the formation of some saturated hydrocarbons and longer carbon chains. To date we have not determined whether secondary reactions spoil the correspondence since some local heating could not be avoided during the reaction. However, no quantitative relationship was observed between the amount of acetylenide and the higher hydrocarbons.

W. Brehm: What was the construction material of the loop?

## INTERNATIONAL CONFERENCE ON LIQUID METAL TECHNOLOGY IN ENERGY PRODUCTION

F. Lievens: All of the structural material of the loop is AISI 316.

F. Kozlov: Did you use a distillation method for analysis of sodium carbides in sodium?

F. Lievens: Sodium carbides in sodium are determined by hydrolysis of the sodium sample without distillation.

C. Miles: How many determinations did you perform to obtain each carbon concentration?

F. Lievens: Each carbon concentration given in the paper is the result of a single determination.

C. Miles: Is not the method you used inherently imprecise?

F. Lievens: The method is reproducible to  $\pm 10\%$ . When used on other materials, like stainless steels and other metals, or when calibrated with sodium carbonate or graphite. Nevertheless, for duplicate sodium samples taken with the same sampler, deviations of up to a factor of 2 were observed. Therefore, some doubts are cast on the sampling procedure, which is not suitable for the carbon species present in the loop.

Paper IIA-7: "Characterization of Particulate Material Extracted from a Large Sodium Loop"

W. Brehm: In your opinion, did the filters act as nucleation sites for small particles to develop?

S. Meacham: Since neither flow velocities, temperature nor porosity was a parameter, it is difficult to identify the mechanism of deposition. In my opinion, the aggregate formation observed occurred either during filtering of the sodium or distillation of the sodium metal. Particles less than  $10 \mu\text{m}$  were observed on the membrane filter but may be attributable to the ultrasonic process causing particulate "break up".

W. Kuhn: Was the loop operated isothermally with respect to the filter?

S. Meacham: The filter was operated at  $315^\circ\text{C}$  regardless of the primary sodium loop temperature that ranged from  $250^\circ$  to  $550^\circ\text{C}$ .

W. Kuhn: Can you distinguish between particles collected from the circulating sodium and those which may have grown on the filter?

S. Meacham: No attempt was made to characterize the particulates on the stainless steel filter; only after their removal by ultrasonic means were the particulates photo-micrographed. Particulates collected were primarily in aggregate form, suggesting formation at the filter site rather than existence of the aggregate in the flowing sodium system.

Paper IIA-8: "Operational Techniques Employed for the Liquid Sodium Source Term Control Loops"

G. Grassi: How long is the vanadium test section?

L. Chulos: The vanadium test section isothermal zone was about 10 cm long.

G. Grassi: What temperature distribution did you obtain along the vanadium wire?

L. Chulos: Wires were restricted to the isothermal zone and were comprised of 6 to 10 wires, each 5 to 10 cm long. Therefore, there was no temperature gradient along the wire.

# INTERNATIONAL CONFERENCE ON LIQUID METAL TECHNOLOGY IN ENERGY PRODUCTION

## DEVELOPMENT OF LOW FRICTION MATERIALS FOR LMFBR COMPONENTS

R. N. Johnson, R. C. Aungst

Hanford Engineering Development  
Laboratory  
Westinghouse-Hanford Company  
Richland, Washington

N. J. Hoffman

Liquid Metal Engineering  
Center  
Canoga Park, California

M. G. Cowgill, G. A. Whitlow, W. L. Wilson

Westinghouse Advanced Reactors Division  
Westinghouse Electric Corporation  
Madison, Pennsylvania

### ABSTRACT

The number of materials capable of providing low friction, low wear, and good corrosion resistance in low-oxygen (< 1 ppm) sodium at temperatures up to 650°C are extremely limited. This paper describes the development, evaluation, and qualification of low-friction materials for this environment with emphasis on chromium carbide base coatings and nickel aluminide diffusion coatings. Design criteria and typical applications in liquid-metal-cooled reactors are described and recommendations offered for conditions under which these materials should and, perhaps more importantly, should not be used. Design parameters required to achieve optimum performance of these materials are discussed.

### INTRODUCTION

Development of low-friction and wear-resistant materials for liquid sodium environments has long been recognized as one key to the successful design and operation of LMFBR (liquid metal fast breeder reactor) components. Low friction surfaces provide reliable operation of mechanical components, ease of assembly of complex and close tolerance parts, reduced operating forces and power requirements, lower stresses in components, and reduced surface damage and wear. Some nuclear applications impose a maximum allowable friction coefficient that makes a low-friction material or coating virtually mandatory. A variety of industrial bearings, lubricants, and materials are available to provide low friction or low wear, but when the special environments and temperatures of LMFBR's are considered, the list of candidate materials for low-friction applications becomes severely restricted. Besides being a poor lubricant, sodium is a highly reactive coolant, which precludes the use of nearly all known liquid or solid lubricants. High-temperature sodium is also exceptionally effective in stripping oxide layers from most material surfaces. The resulting highly-cleaned surfaces can exhibit much higher friction and self-welding tendencies than the same surfaces would show in most other environments.

The United States Energy Research and Develop-

ment Administration's National Friction, Wear, and Self-Welding Program\* has been developing, evaluating, and qualifying low friction and wear resistant materials for advanced energy systems, with most efforts so far directed toward liquid metal environments. Materials include structural materials and alloys, weld-deposited hardfacings, coatings and platings, cast bearing materials, and lubricants. LMFBR applications for such wear-resistant materials include fuel assembly interfaces, control rod drive mechanisms, fuel handling machines, heat exchangers, valve seats and bearings, coolant pump bearings, test loop components, and many others. The scope of this paper will be confined to describing the development and applications of coatings specifically required for low friction applications in the Fast Flux Test Facility (FFTF) and the Clinch River Breeder Reactor (CRBR), and to design recommendations for their use in liquid metal systems. More detailed information on test methods and test results for some of these and other materials will be given in later papers.<sup>(1,2)</sup>

### FRICTION AND SODIUM PURITY LEVELS

In the last few years significant advances have been made in the measurement and control of sodium purity. This development has resulted in improved environmental controls for wear and friction testing. Wear testing of materials in liquid sodium has been conducted from at least as early as the 1950's.<sup>(3-6)</sup> Freede, et al,<sup>(7)</sup> and Hoffman, et al,<sup>(8)</sup> later performed much of the work our present efforts are based on. Developments in sodium purity technology, however, force us to re-evaluate much of the early friction and wear data, since oxygen content of the sodium has a major influence on the wear behavior of many materials. Tests are now routinely conducted in sodium of 0.5 to 1 ppm oxygen content as measured by VWE (vanadium wire equilibration), whereas in much of

\*USERDA's National Friction, Wear, and Self-Welding Program is a cooperative program under the technical direction of the Hanford Engineering Development Laboratory (HEDL), operated by Westinghouse Hanford Company and involves the efforts of HEDL, the Westinghouse Advanced Reactors Division, the Liquid Metal Engineering Center, and Atomics International.

the earlier testing oxygen contents were frequently specified as < 10 ppm or < 20 ppm or even higher. Sodium purity levels maintained in our present test programs are the levels to which US liquid metal fast breeder reactors will be controlled.

The low oxygen levels chosen for the LMFBR's have two major effects. First, the corrosion rate of many materials in sodium is directly related to the oxygen content of the sodium. Lower oxygen contents lead to lower corrosion losses, lower mass transport effects, and lower radioactivity in ex-vessel piping. The second major effect is on the wear behavior of materials. Lower oxygen contents restrict temperature regimes where lubricative sodium-oxygen-metal complexes (principally sodium chromite) are stable, and may also impede the kinetics of such film formations. The importance of these film formations in friction behavior is shown in tests on a chromium carbide + NiCr coating, where friction coefficients have varied from as high as 0.9 when no film was present to less than 0.5 on the same surface at the same temperature after the film had been allowed to form. Similar behavior has been noted on a wide variety of materials including Inconel 718, 316 stainless steel, and Stellite 6. The presence of the sodium chromite film on a given surface depends upon the temperature, oxygen content of the sodium, chromium activity of the surface, and the time allowed (kinetics). The effectiveness of the lubricant film in reducing friction is dependent upon the film thickness, the rate of removal of the film by rubbing versus the rate of formation of the film, and the ratio of film thickness to surface roughness. A thin film, for example, can provide much more effective lubrication on a smooth surface than on a rough one.

Figure 1 shows the general relationship for film stability as a function of oxygen content and temperature for a chromium-containing alloy.<sup>(9)</sup> Particular values associated with the curves will be dependent upon chromium activity in the surface of the alloy. Note also that while we know these high and low friction regimes exist, the precise position of the boundaries remains to be determined.

One of the objectives of the National Friction, Wear, and Self-Welding Program is to develop, evaluate, and qualify materials that will provide low friction, good wear resistance, and good corrosion behavior in sodium of low oxygen contents over the

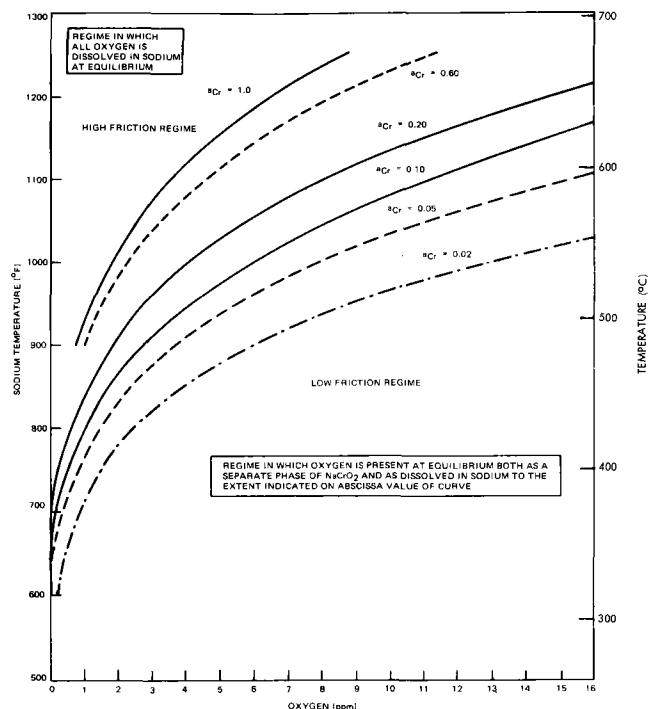


Fig. 1. High and low friction regimes as influenced by presence or absence of  $\text{NaCrO}_2$  (Ref. 9).

range of temperatures from 200°C ( $\sim$  400°F) to 650°C ( $\sim$  1200°F).

#### LOW FRICTION COATINGS FOR CORE APPLICATIONS

One of the challenging problems in developing low friction materials for LMFBR applications has been the qualification of an adequate material for core component wear pads. Figure 2 shows a fuel duct assembly for the Fast Flux Test Facility (FFTF). Low friction coatings are required on rubbing interfaces between ducts to assure optimum core compaction and to minimize forces required during refueling operations.

#### Design Criteria

The criteria for acceptance of a low friction coating are given below:

- The material shall have a coefficient of friction of 0.4 or less in sodium at 230°C and no more than 0.9 at 625°C. The maximum allowable friction coefficient at any temperature where core compaction must take place is 0.57.
- The coating shall not wear or corrode more than 1/2 the coating thickness over its service life.

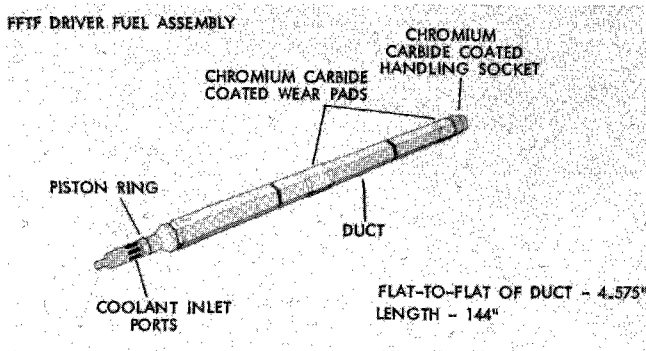


Fig. 2. FFTF Driver Fuel Assembly.

- The material shall sustain the equivalent of 120 reactor scram cycles (cool from 625°C to 425°C in sodium in less than 1 minute) without cracking, spalling or flaking.
- The material shall be capable of withstanding fast neutron exposures of  $8 \times 10^{22} \text{ n/cm}^2$  without spalling or flaking or failing to perform its function as a low friction surface.
- The material shall not transmute to undesirable radioactive products (e.g.,  $^{60}\text{Co}$ ) that can contaminate downstream components and piping.
- The material shall be attachable to core components in such a way that dimensional tolerances are maintained and cold-worked levels of substrate materials are unchanged. (20% cold work is required in the 316 stainless steel fuel ducts for irradiation swelling resistance.)

#### Coating Development

Over 65 materials combinations including metals, ceramics, and cermets were subjected to friction screening tests in sodium. Test results showed that bonded carbides, especially chromium carbide base materials, provided the lowest, most consistent friction coefficients. Further investigation of a variety of processes for applying chromium carbide-base materials revealed that only one, the detonation-gun process, was able to provide a coating that could pass the friction, wear, sodium corrosion, thermal cycling, mechanical integrity, and irradiation tests required to meet acceptance criteria.<sup>(10)</sup> Diffusion coatings required temperatures that would anneal-out the cold work and reduce irradiation swelling resistance of the substrate. The spark transfer process provided a

versatile capability but did not give sufficiently uniform coating; it might have with considerable development. Sputtered coatings cracked and spalled, as did all normal plasma-sprayed coatings when subjected to thermal cycling tests in sodium and when irradiated to total neutron fluences of  $1 \times 10^{22} \text{ n/cm}^2$  or more.<sup>(11)</sup> Figures 3 and 4, for example, show chromium carbide + 15 vol-% NiCr \* coatings deposited by plasma spray and by detonation gun, respectively, after irradiation. The voids shown in the interfaces between coating and substrate were caused by alumina particles retained in the surface after grit-blasting the substrate prior to coating. Modifying the grit-blasting procedure virtually eliminated interface contamination.<sup>(12)</sup>

The first detonation-gun coating composition evaluated was  $\text{Cr}_3\text{C}_2 + 12 \text{ vol-}\% \text{ NiCr}$ . Modifications in particle size and coating parameters resulted in a coating of  $\text{Cr}_3\text{C}_2 + 15 \text{ vol-}\% \text{ NiCr}$ , which had a more uniform distribution of the binder phase. Both coatings showed similar friction and wear behavior in sodium, and the latter composition, after successful

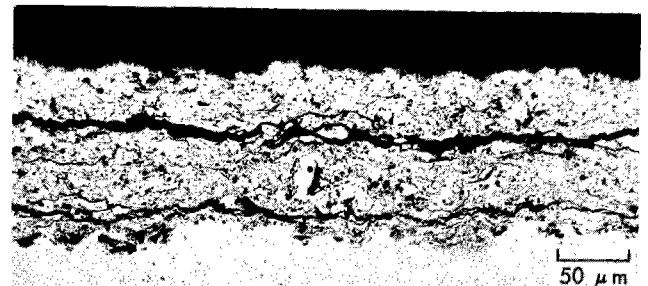


Fig. 3. Plasma-sprayed chromium-carbide coating (CN-1P) on 316 stainless steel after irradiation test.

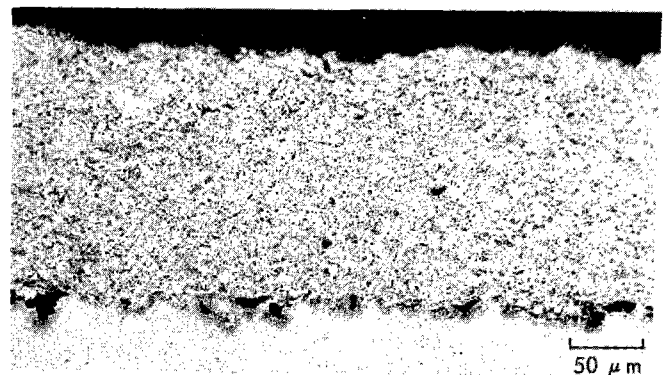


Fig. 4. Detonation-gun-applied chromium carbide coating (LC-1H) on 316 stainless steel after irradiation test.

\*80% Ni-20% Cr alloy.



# INTERNATIONAL CONFERENCE ON LIQUID METAL TECHNOLOGY IN ENERGY PRODUCTION

completion of all qualification tests, was chosen as the reference coating. Figure 5 shows the friction behavior of the reference coating.

Note that although the starting chromium carbide composition is  $Cr_3C_2$ , X-ray diffraction studies show that the actual as-deposited carbide is a mixture of  $Cr_3C_2$ ,  $Cr_7C_3$  and  $Cr_{23}C_6$ . With increasing exposure times in high-temperature sodium, the composition gradually shifts to  $Cr_{23}C_6$  as the most stable phase, due to carbon removal by the sodium and to reaction with the chromium in the nickel-chromium alloy binder.

### Improved Coating Development

An early objective of the coating development effort was to provide a back-up coating or process, in case the reference coating should show unacceptable long-term behavior. (Irradiation test durations, for example, are frequently measured in years.) Later, wear test results showed that the reference coating (with the NiCr binder) exhibited higher than desirable breakaway friction coefficients (self-welding tendencies) after dwell periods at temperatures of 600 to 625°C.

Efforts are still in progress to develop alternate and improved coatings. The objectives of these efforts are: 1) To provide a qualified back-up coating and process, 2) To develop a coating with improved resistance to self-welding, and improved high-temperature friction behavior, and 3) To qualify a process capable of applying a coating to the inside diameter of a tubular components. (The detonation-gun process is limited to external surfaces and to internal surfaces approximately one hole-diameter deep.) Table 1 lists the coatings that have been and are being evaluated, and the status of each coating.

Many alternate coating selections were based on evidence that the NiCr binder was responsible for self-welding tendencies at higher temperatures. However, only a small improvement was found when Inconel 718 was substituted for NiCr. The duplex coating CN-1C, where the binder was completely removed from the surface layer, showed slightly improved high-temperature friction and self-welding characteristics, but did not provide the improvement expected. Coatings of 100% Tribaloy 700 (50 Ni, 32 Mo, 15 Cr, 3 Si, a laves phase hardened DuPont alloy) markedly improved high temperature friction performance, but still showed high breakaway friction coefficients. Nevertheless, this material shows attractive properties, and

TABLE 1 - CANDIDATE COATING COMPOSITIONS<sup>(a)</sup>

COATING DESIGNATION	COMPOSITION (VOL. %)	APPLICATION METHOD	REMARKS
<i>Coatings which have passed qualification tests</i>			
LC-1H	$Cr_3C_2$ -15% NiCr <sup>(b)</sup>	D-Gun <sup>(g)</sup>	Reference coating
LC-1C	$Cr_3C_2$ -12% NiCr	D-Gun	Back-up coating
CI-D	$Cr_3C_2$ -15% In 718 <sup>(c)</sup>	D-Gun	Back-up coating
<i>Coatings which have failed qualification tests</i>			
CN-1P	$Cr_3C_2$ -15% NiCr	Plasma	Failed irradiation
CI	$Cr_3C_2$ -15% In 718	Plasma	Failed irradiation
CM	$Cr_3C_2$ -15% Mo	Plasma	Failed irradiation and thermal cycling
TM	TiC-15% Mo	Plasma	Failed corrosion
TN	TiC-15% NiCr	D-Gun	Failed corrosion
CT-7M	$Cr_3C_2$ -15% Tr 700 <sup>(d)</sup>	Mach II <sup>(h)</sup> plasma	Failed thermal cycling
TR-7P	Tribaloy 700 <sup>(d)</sup>	Plasma	Failed thermal cycling
TR-7M	Tribaloy 700	Mach II plasma	Failed thermal cycling
CN-1C	$Cr_3C_2$ on LC-1H	D-Gun	Failed thermal cycling
CN-100	$Cr_{23}C_6$ -65% on LC-1H <sup>(e)</sup>	D-Gun	Failed thermal cycling
<i>Coatings which are in qualification testing</i>			
CT-7D	$Cr_3C_2$ -15% Tr 700 <sup>(d)</sup>	D-Gun	Nearing qualification status
CT-7G	Graded $Cr_3C_2$ -15% TR 700 <sup>(f)</sup>	Plasma	In test
TR-7D	Tribaloy 700	D-Gun	In test
TR-7G	Graded Tr 700 <sup>(f)</sup>	Plasma	In test
CN-200	$Cr_{23}C_6$ -35% Cr <sup>(e)</sup> on LC-1H	D-Gun	In test
CN-450	$Cr_{23}C_6$ -35% $Cr_7C_3$ on LC-1H <sup>(e)</sup>		

**Notes:**

- (a) All coatings on 20% cold-worked 316 stainless steel
- (b) NiCr, alloy of 80% Ni-20% Cr
- (c) Inconel 718, trademark of International Nickel Co.
- (d) Tribaloy 700, trademark of DuPont de Nemours Co.
- (e) Duplex coating with LC-1H as intermediate layer
- (f) Duplex coating with intermediate layer of coating composition mixed with 50% 316 stainless steel
- (g) Trademark of Union-Carbide Corp.
- (h) High velocity plasma process, trademark of Plasmadyne, Inc.

is continuing in the test and qualification program. The most significant improvement so far was found when Tribaloy 700 was mixed with chromium carbide for the CT-7D coating. Both high temperature friction behavior and self-welding tendencies appear to be significantly better than those of the reference coating. Irradiation test results on this material are not yet available, however, and qualification tests are continuing.

The duplex coatings are designed to minimize thermal expansion stresses in the coating when a surface layer is desired that has a significantly different thermal expansion coefficient than the substrate. In addition, those coatings containing high chromium concentrations in the surface (CN-100, CN-200) were formulated to attain a high chromium activity and thus maximize the range of temperatures and oxygen contents where lubricative sodium chromite film would be stable. Friction results are not yet available on these materials.

Recommendations for Carbide Coating Applications

The following recommendations are provided as a designer's guide, based on experience obtained in FFTF applications and upon data generated in the National Friction, Wear, and Self-Welding Program.

Substrates - Detonation-gun coatings on austenitic stainless steels and nickel-base alloys have been successful when the surfaces were properly prepared by grit-blasting prior to coating. Alloys with lower thermal expansion coefficients may allow other coating compositions or plasma-deposited coatings to be used for less severe service conditions. Substrate material will not be protected from sodium corrosion by these coatings due to the porosity inherent to the process. Therefore, substrate materials should be chosen with corrosion resistance equal or superior to the coating material.

Mating materials - Chromium carbide coatings provide optimum friction and wear behavior when used in self-rubbing (carbide-to-carbide) applications or when mated against another very hard, wear-resistant surface, such as a nickel aluminide coating formed by the diffusion coating of a nickel-base alloy. When the carbide coating is rubbed in sodium against softer material such as 316 stainless steel, Inconel 718, or similar nickel-base alloys, the result is frequently higher friction and higher wear than would have been the case had no coating been present. This occurs because carbide rapidly removes surface material from the softer metal, which then adheres to the carbide coating and soon exhibits the friction behavior of two rough or galled surfaces of the softer material.

Coating Thickness - Chromium carbide coatings can be applied by detonation-gun process in thicknesses of up to 250  $\mu\text{m}$  (0.010 in), or even thicker depending upon substrate compatibility. However, stress in the coating is usually proportional to its thickness, and thinner coatings are much more resistant to cracking, spalling, or other damage. FFTF components have coatings specified as 100  $\mu\text{m} \pm 25 \mu\text{m}$  (0.004  $\pm$  0.001 in) thick. With longer term corrosion data available,<sup>(2)</sup> however, it appears that a 50  $\mu\text{m}$  (0.002 in) coating may be adequate for corrosion losses, and may provide a greater margin of safety in resistance to cracking or spalling. Future testing will be aimed at qualifying the thinner 50  $\mu\text{m}$  coatings.

Surface Finish - The best friction results have been

obtained on coatings that were brush-finished with a fine silicon carbide-impregnated nylon brush to a finish of about 2 to 3  $\mu\text{m}$  (80-120  $\mu\text{in}$ ) Arithmetic Average (AA). The resulting surface texture is best described as a smooth-feeling, pebbly finish. Rougher surfaces tend to higher friction due to increased asperity interlocking and interference. Smoother surfaces, such as those obtained by grinding and lapping, show higher friction in unlubricated wear in sodium due to the increased real area of contact of the surfaces. Note, however, that if a lubricant is present, the finer finishes should give a lower friction.

Loads and Geometries - Carbide coatings perform best in flat-on-flat sliding applications under pressures of up to at least 7MPa (1000 psi)(with 316 stainless steel substrates). The upper limit of load carrying capability has not been determined, but the limit will depend on properties of the substrate and the thickness of the coating. A thin coating well-bonded to a hard strong substrate would be expected to sustain heavier loads without damage than either a thicker coating or one on a softer substrate. Carbide coatings are not recommended for applications involving high hertzian stresses, such as can be obtained with high point-contact or line-contact loads, nor should these coatings be used in rolling contact bearings.

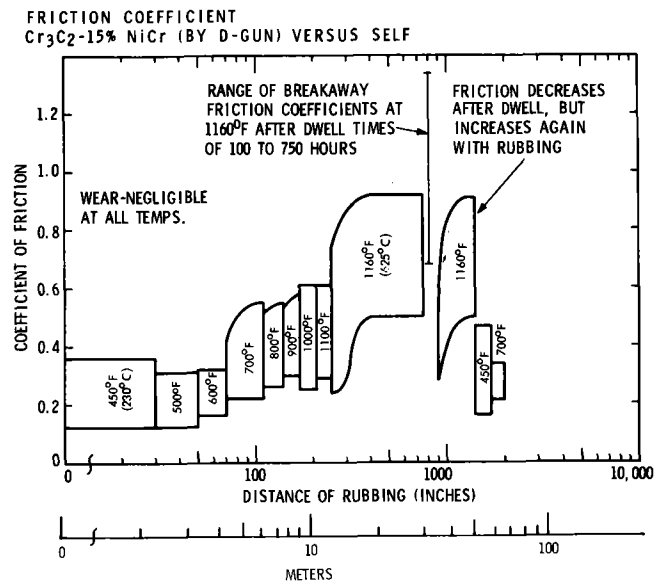


Fig. 5. Chromium carbide friction in sodium (Ref. 13).

Temperatures - Carbide coatings have been tested at temperatures from 200°C to 650°C in sodium and have performed well over this range. As shown in Figure 5, at temperatures of about 600°C and above, friction coefficients increase with rubbing distance for chromium carbide-NiCr coatings with maximums observed in the 0.9 range. At temperatures below 600°C, friction coefficients range from 0.2 to 0.6, with averages usually less than 0.4.<sup>(13)</sup> Wear rates have been negligible over all temperatures and loads tested (up to 625°C and 7 MPa or 1000 psi).

DIFFUSION COATINGS

Although much work remains in development and qualification of diffusion coatings for LMFBR applications, it is already apparent that the potential for these materials is great. Diffusion coatings have been used in jet engine manufacture for years, but until recently have not been recognized by most materials engineers in the liquid metals field.

Diffusion coatings are typically formed by the pack-cementation process, where the part to be coated is packed in a retort with a powdered compound containing the coating substance. The retort is heated in the presence of a gas capable of reacting with and transporting the coating substance as a vapor to the part surface. The coating substance is deposited on the part surface and may react with the surface or diffuse into the surface. It usually does both. More detailed discussion of diffusion coating principles is provided by Wachtell.<sup>(14)</sup>

Most effort thus far has been in evaluating aluminide coatings on nickel-base alloys, in particular on Inconel 718 and on Inconel 600. The process

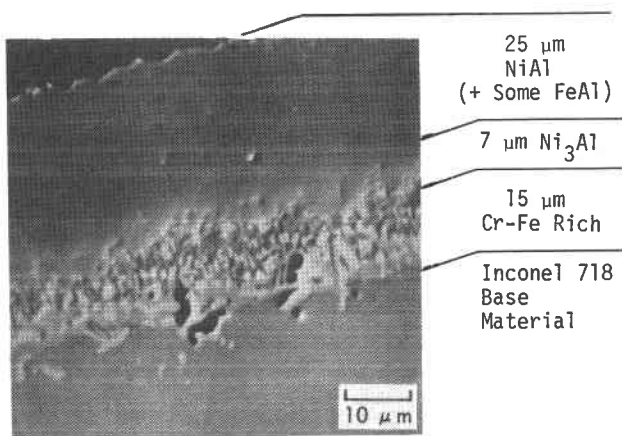


Fig. 6. Diffusion zones in aluminized Inconel 718.

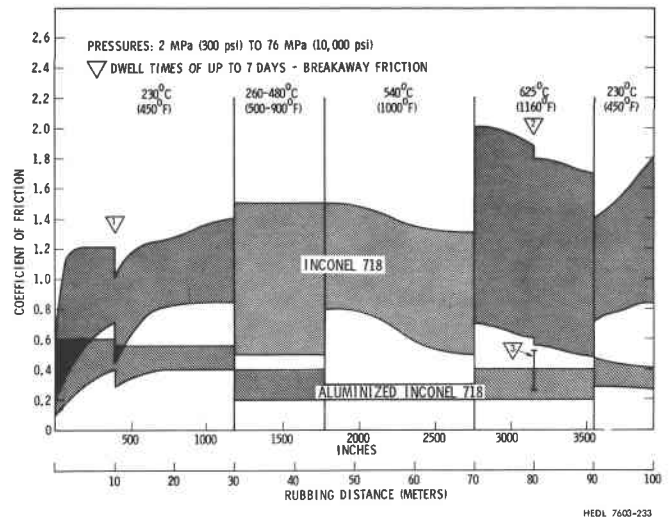


Fig. 7. Effect of aluminide coating on friction of Inconel 718.

involves vapor phase transport of aluminum to nickel alloy surfaces at temperatures of about 1000°C. The aluminum diffuses into the surface and reacts with the nickel in the alloy to form a surface layer of NiAl. Figure 6 shows the structure of an aluminide coating on Inconel 718.

Characteristics of Nickel-Aluminide Coating

Depending on the particular coating process parameters used, nickel-aluminide coatings can be provided in a range of compositions, hardnesses, ductilities, and thicknesses on nickel-base and some high-nickel iron-base alloys. Only one variety has been investigated so far in the present program. The coating typified in Figure 6 is a hard, low-ductility coating providing low friction and low wear in sodium, as well as excellent corrosion resistance.

The wear behavior of the aluminide coating is best described by comparing the behavior of coated and un-coated Inconel 718. Inconel 718 exhibits adhesive wear and surface damage when rubbed against itself or most other materials in sodium at temperatures up to 625°C.<sup>(1)</sup> When aluminized, however, coated Inconel 718 shows negligible wear, a resistance to adhesion with most materials, and a friction coefficient frequently 50% or more below that of uncoated Inconel 718 under the same conditions. Figure 7 shows a comparison of friction coefficients of Inconel 718 and an aluminide coating on Inconel 718 in a series of tests in sodium at loads from 2 to 70 MPa (300 to 10,000 psi).

Unlike plasma or detonation-gun coatings, nickel aluminide diffusion coatings are non-porous and can be used for corrosion protection. As Table 2 shows, both corrosion rate and wear of Inconel 718 are markedly reduced when the diffusion coating is applied.

TABLE 2 - EFFECT OF ALUMINIDE DIFFUSION COATING ON CORROSION AND WEAR BEHAVIOR OF INCONEL 718 IN SODIUM<sup>(15)</sup>

	INCONEL 718	ALUMINIDE COATING ON INCONEL 718
Corrosion rate*	6 $\mu\text{m}/\text{yr}$	0.75 $\mu\text{m}/\text{yr}$
Maximum wear depth**	53 $\mu\text{m}$	no measurable wear

\* Avg. rate in 2000 hrs in 625°C flowing Na.  
 \*\*70 MPa (10,000 psi) rubbing for  $\sim 200$  m ( $\sim 8000$  inches) at 540°C.

Aluminide diffusion coatings appear to be resistant to damage by neutron irradiation. A number of specimens of nickel aluminide coatings on Inconel 718 were irradiated in sodium-filled capsules at temperatures from 450 to 600°C to total fluences of up to  $4 \times 10^{22}$  n/cm<sup>2</sup>. No visible evidence of coating deterioration was found. Further irradiation experiments are in progress.

#### Applications of Aluminide Coatings in FFTF

The closed loop test assemblies in the FFTF consist of a series of concentric tubes over 12 meters in length extending through the reactor core to provide a coolant environment independent of the reactor sodium supply. Fuels and materials can be irradiated in these test loops in flowing sodium at temperatures up to 760°C. At a number of close tolerance interfaces in these tubes, there is significant thermal expansion movement; at these locations friction and galling must be minimized to prevent excessive stress concentrations in the assemblies. Nickel aluminide coatings on Inconel 718 or on Inconel 600 are used at several of these locations. At one location a chromium carbide coating (LC-1H) is applied by detonation gun to the outside diameter of a 316 stainless steel component, and a nickel aluminide layer is applied by diffusion coating to the inside diameter of the mating Inconel 600 surface. This combination shows lower friction coefficients in screening tests than either the chromium carbide against itself or aluminized Inconel 718 against itself.

At other locations in the assembly, piston ring

seals are used to separate inlet sodium at 425°C (800°F) from outlet sodium at 650°C (1200°F). Control of leakage past the piston ring seals is critical to proper operation of the loop. A number of piston ring/liner materials combinations were tested for wear to find a combination capable of maintaining a smooth, damage-free surface on both ring and liner in order to meet leakage restrictions. Materials tested included various combinations of Inconel 718, 17-4 PH, Haynes 25, 316 stainless steel, Haynes 90, Hastelloy C, chromium plating, a chromium diffusion coating, and the nickel aluminide diffusion coating. Materials combinations exhibiting sufficient freedom from surface damage at 650°C all involved rubbing against the nickel aluminide diffusion coating, with the least damage shown by nickel aluminide rubbing against itself. Prototypic wear and leakage testing of piston rings and liners confirmed the results of the wear screening tests. Wear was so slight on the aluminide/aluminide combination that the ring could not be made to "seat" or wear-in against the liner within a reasonable rubbing time. Lowest leakage was obtained, therefore, with a piston ring of Inconel 718 rubbing against the aluminized Inconel 718 liner, which is now the reference material combination.

#### Recommendations for Use of Aluminide Coatings

While nickel aluminide coatings exhibit attractive friction, wear, and corrosion properties in sodium, the following factors must be considered in selecting these materials.

Processing and Fabrication - The biggest deterrent to the use of aluminide coatings is the high temperatures ( $\sim 1000^\circ\text{C}$  or above) required for processing. First, if the substrate material requires heat treatment, it must be done after coating since the times and temperatures of coating will anneal most materials. Cold-worked materials, of course, will also be left in the annealed condition. Slow cooling is normal in most diffusion coating processes, which can sometimes be used, with proper controls, to age substrate materials after coating/annealing; but if a quench is required from annealing temperatures, the part must be re-annealed after coating. Second, the high temperatures used and the possible need for re-heat treatments demand careful selection of part geometry and processing parameters if thermal distortions are to be within acceptable limits, particularly for close-tolerance parts. The coating thickness (25 to 75  $\mu\text{m}$  usually)

## INTERNATIONAL CONFERENCE ON LIQUID METAL TECHNOLOGY IN ENERGY PRODUCTION

allows very limited resizing after coating, so parts must be coated and heat treated after final machining. In spite of these limitations, closed loop components were machined, coated, and welded into position while maintaining concentricity and ovality tolerances within  $50\ \mu\text{m}$  (0.002 in) for parts  $\sim 8$  to 12 cm ( $\sim 3$  to 5 in) in diameter.

Masking - Masking a part (to coat only limited areas) can be done with some difficulty, but it is recommended that whenever possible the processor be given the freedom to coat the entire part. The coating can be removed by grinding if necessary for a weld preparation, for example.

Finishing - In tests thus far, as-coated surface roughness of a part has been about the same or slightly rougher than pre-coating roughness, except that as-coated roughnesses of less than  $\sim 0.25\ \mu\text{m}$  (10  $\mu\text{in}$ ) AA are difficult to achieve. Normal grinding, lapping, or polishing techniques, however, can be used to improve the finish if care is used to avoid excessive material removal. In most applications an as-coated finish of about  $0.8\ \mu\text{m}$  (32  $\mu\text{in}$ ) AA has been adequate for good friction behavior.

Machining, Grinding - If the coating must be removed from an unwanted area, the best practice yet found has been to remove the coating by grinding, or to use a diamond wheel. An alternative is to cut through the coating with a diamond or other grinding wheel along one boundary and to finish the coating removal by normal machining, using a heavy enough cut that the tool is under the coating. The coatings tested have been of the hard, low-ductility variety where cracking and chipping adjacent to the area of the cut could be avoided only with careful grinding practice.

Substrates - Diffusion coatings of one variety or another can be applied to nearly all iron, nickel, and cobalt-base materials used in the LMFBR program. Our experience with aluminide coatings, however, has been limited to nickel-base alloy substrates and to austenitic stainless steel substrates, the latter still in the early stages of testing. Low-friction, wear-resistant diffusion coatings on austenitic stainless steels may also be candidates for liquid metal applications.

Loads - The nickel aluminide diffusion coating on Inconel 718 has been wear tested at loads from 0.7 to 70 MPa (100 to 10,000 psi) at temperatures up to  $625^\circ\text{C}$  in sodium without degradation of the coating. In two

tests conducted at 172 MPa (25,000 psi), however, at  $600^\circ\text{C}$ , one specimen performed well, but the other showed localized cracking and spalling. The recommended load limit for the aluminide coating on Inconel 718 is, therefore, 70 MPa, with the actual limit probably in the range from 100 to 170 MPa. Load limits for other substrates should be dependent on the substrate mechanical properties. Aluminide coatings are not recommended for rolling contact bearing surfaces. Flat-on-flat sliding configurations are best.

Mating Materials - As with carbide coatings, aluminide diffusion coatings perform best when rubbed against themselves or against other hard surfaces, such as chromium carbide. Unlike the LC-1H chromium carbide coating, however, nickel aluminide coatings also exhibit low wear and low friction in combination with many softer materials, due to the aluminide's resistance to adhesive wear behavior in sodium. The aluminide coating, for example is the only material found against which Inconel 718 can be rubbed in sodium at  $600^\circ\text{C}$  without adhesive surface damage to the Inconel 718.

### SUMMARY

The number of materials capable of providing low friction, low wear, and good corrosion resistance in low oxygen ( $< 1\ \text{ppm}$ ) sodium at temperatures up to  $650^\circ\text{C}$  are extremely limited. In addition, each application imposes its own combination of requirements of temperature, thermal cycles, loads, rubbing distance, allowable friction coefficients and wear rates, irradiation stability, and service life, which further restrict the number of candidate materials. Three classes of coatings have been identified that can provide low friction in high temperature sodium.

- Chromium carbide coatings applied by a process such as the detonation-gun are used in a variety of locations, but primary use has been for rubbing interfaces of core components and fuel assemblies. A chromium carbide-15 Vol-% NiCr coating has been qualified for high neutron fluence applications, and improved coatings are being tested. Successful application of the carbide coatings demands care in selecting coating process and parameters used, substrate and its preparation, mating interface material, loads and geometries of interfaces, and coating thickness and surface finish.

## INTERNATIONAL CONFERENCE ON LIQUID METAL TECHNOLOGY IN ENERGY PRODUCTION

- A metal hardfacing alloy coating, Tribaloy 700, shows low-friction properties in sodium and appears to have a future in liquid metal systems, but qualification testing is still in progress. A combination of the Tribaloy 700 and chromium carbide applied as a detonation-gun coating is also nearing completion of tests and appears to offer better friction, corrosion and self-welding characteristics than either the reference chromium carbide-NiCr coating or the pure Tribaloy 700.
- Diffusion coatings of nickel aluminide on nickel-base alloys provide low friction, good wear, and excellent corrosion resistance. Wear behavior is characterized by resistance to adhesive and galling interactions with many other materials. Primary use has so far been for sliding surfaces and piston ring sealing surfaces in reactor test loop assemblies and on the fuel handling machine test model. Successful use requires attention to the same design considerations as for the carbide coatings and also to particular restrictions imposed by high processing temperatures.

### REFERENCES

1. N. J. Hoffman, et al., "Evaluation of cobalt and nickel-base materials for sliding contact applications in a liquid metal fast breeder reactor", to be published in Proc. Int. Conf. on Liquid Metal Tech. in Energy Production, ANS-AIME Meeting, Champion, Pa. (1976).
2. G. A. Whitlow, et al., "Corrosion and tribological investigations of chromium carbide coatings for sodium cooled reactor applications", to be published in Proc. Int. Conf. on Liquid Metal Tech. in Energy Production, ANS-AIME Meeting, Champion, Pa. (1976).
3. L. F. Coffin, Jr., "Theory and application of sliding contact of metals in sodium", KAPL-828 (1952).
4. D. B. Vail, "Summary of journal bearing tests with copper bearings and tungsten-carbide journals operating in sodium-potassium alloy", KAPL-877 (1953).
5. J. W. Kissel, et al., "Frictional behavior of sodium-lubricated materials in a controlled high-temperature environment", Wear, 5, p. 446, (1962).
6. W. H. Roberts, "Friction and wear behavior of possible bearing materials in high-purity liquid sodium at temperatures up to 500°C", Proceedings of IME Conference on Non-Conventional Lubricants, p. 25 (1962).
7. W. J. Freede, et al., "Static and sliding contact behavior of materials in sodium environments at elevated temperatures", NAA-SR-12446 (1967).
8. N. J. Hoffman, et al., "Friction and wear screening tests of materials in sodium", LMEC-70-10, (1970).
9. Liquid Metal Engineering Center (LMEC), Annual Technical Progress Report, January-December 1973, LMEC-74-1, p. 1-157, (1974).
10. R. N. Johnson, S. L. Schrock, and G. A. Whitlow, "Wear-resistant coatings for reactor components in liquid sodium environments", J. Vac. Sci. Technol., Vol. 11, No. 4 (July/Aug. 1974).
11. A. L. Ward, R. N. Johnson, G. L. Guthrie, and R. C. Aungst, "Irradiation effects on low-friction coatings for LMFBR applications", HEDL-TME 75-108, (1975).
12. T. A. Wolfla and R. N. Johnson, "Refractory metal carbide coatings for LMFBR applications - a systems approach", J. Vac. Sci. Technol., Vol. 12, No. 4, (July/Aug. 1975).
13. Nuclear Systems Materials Handbook, Vol. 1, Part II, Group 1, Section 1, Property Code 5101, p. 1.0, TID-26666.
14. R. L. Wachtell, "The basic principles of diffusion coating", in Science and Technology of Surface Coating, ed. by B. N. Chapman and J. C. Anderson, Academic Press, N. Y., p. 105 (1974).
15. G. A. Whitlow, et al., "Observations on the in-sodium corrosion and tribology of aluminide coatings on Inconel 718", Microstructural Science, Volume 3, ed. by P. M. French, et al., American Elsevier Publishing Co., p. 775 (1975).

# INTERNATIONAL CONFERENCE ON LIQUID METAL TECHNOLOGY IN ENERGY PRODUCTION

## FRICION AND WEAR IN LIQUID-METAL SYSTEMS:

### COMPARABILITY PROBLEMS OF TEST RESULTS OBTAINED FROM DIFFERENT TEST FACILITIES

E. Wild

K.J. Mack

Kernforschungszentrum Karlsruhe  
Institut für Reaktorbauelemente  
Federal Republic of Germany

#### ABSTRACT

Operational induced relative movements take place between contacting components in the core region of sodium cooled reactors. To ensure reliable long term functioning of such friction loaded components, materials are needed with good sliding properties and high wear resistance. Therefore, tribological properties of material combinations in liquid metal have been investigated experimentally for many years at various research establishments. However, despite identical boundary conditions, the comparison of results published does not yield a satisfactory agreement. The cause must be seen in the individual design and concept of the test sections used.

This discrepancy was investigated. The results show that the elasticity, mass movement, and relative motion characteristic to the system prove to be the most important criteria influencing the test results.

#### INTRODUCTION

To allow an optimum design of friction loaded components in the core region of sodium cooled reactors, tribological investigations have been made for about 20 years in several countries. Initially wear resistance of materials had been the subject of principal interest. When core clamping problems gained in priority the friction behaviour (dynamic and static friction coefficient) strongly increased in significance.

The comparison of results derived from such experiments often entailed difficulties because they had been obtained with a different target in mind, with different parameters and above all in various test section systems. The target of tribological experiments in

sodium mainly determines the design features of the test sections to be used. On the one hand, the material specimens are placed in sodium heated up to 1200<sup>0</sup>F. On the other hand, shaft penetrations and bearings as well as connections of measuring devices can only be installed in areas subjected to substantially lower temperatures. This requires that specimen supports, guides and drive elements must be withdrawn from the zone of hot liquid metal via the cover gas, and flanges. For reasons of rigidity these mostly long vertical components have been designed with appropriate cross sections and consequently large masses to be moved. Their oscillation behaviour may influence unfavorably both the friction behaviour and the transfer of measuring signals in the respective test section. In specific areas in the reactor core relative movements are cyclic at very different time dependent relative rates. The simulation of such movements in test facilities is generally performed by means of excentrics or crank-shafts. The experimental results obtained are assigned in general to "mean" velocities. This poses particular problems at high temperatures and low driving rates. At such conditions the friction movement is no longer continuous but intermittent (stick-slip).

The design and selection of materials for the fuel element duct load pads in fast reactors are presently of high interest. Static friction to be classified between static welding and dynamic friction plays a particular role in this context.

Static friction is a variable with short-term occurrence at the beginning of each friction

movement and it is not insignificant whether this friction movement takes place after extended dwell times or after only short-term interruption of the rubbing process in case of stick-slip.

Consequently, work discussed here and performed at GfK concentrated on the friction behaviour of materials, taking especially into account the equipment criteria characteristic of the friction systems. At the beginning, the experimental results showed relatively great scattering band widths whose causes were unknown. In later experiments tendencies became already recognizable and finally different results could be unequivocally assigned to the certain test sections used.

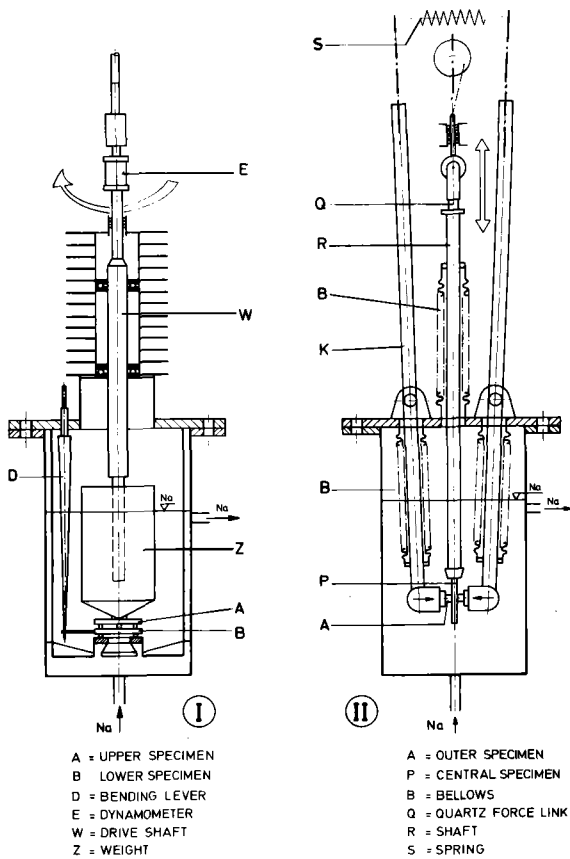


Fig.1 Friction Test Sections

Actually, three different movement characteristics are involved, to which different driving rates must be assigned. These important aspects for the design of tribological test sections and for comparison of results were investigated in numerous spe-

cific experiments.

TEST FACILITY

Experiments were carried out with different test sections. They were connected to the sodium purification and supply loop NVP II. This arrangement allows individual setting of the operation data required. To monitor and control the sodium chemistry a pluggingmeter, an oxygen meter, and a sodium sampling device have been installed /1,2/. Operational conditions are shown in Tab.1. In Fig.1 test section I represents a "pin-disk"-system, test section II a "plate-plate" system. They are comparable by their function and design with the test sections used for liquid metal operation at other research establishments /3,4,5/. In these test sections different system elasticities and mass distributions have been investigated to study their influence on friction behaviour. Additionally a new system with a tilting plane was recently developed and put into operation with liquid sodium (Fig.2). According to information available this system has been used so far only with other media /6,7/. From this new design considerably reduced equipment influence is expected on the friction process as well as on the signal transfer.

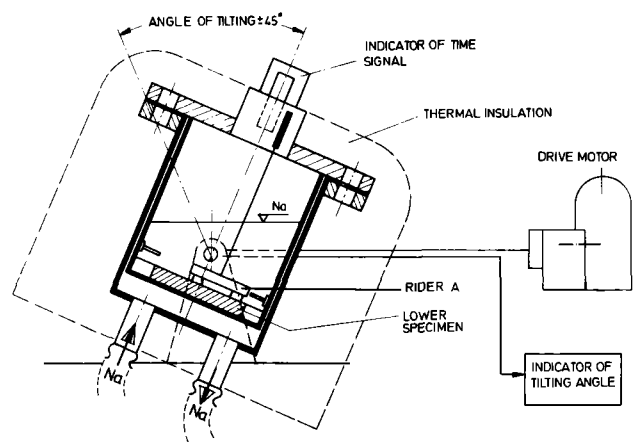


Fig.2 Tilting Plane Friction Apparatus



RELATIVE MOTION	RECIPROCATING
STROKE LENGTH	± 5mm
SURFACE PRESSURE	0.8 kp/mm <sup>2</sup>
SODIUM TEMPERATURE	600 °C
O <sub>2</sub> -CONTENT IN NA	<10ppm (≈ 2ppm)
SURF. ROUGHNESS	0.8 - 2 μm
Tab. 1	TEST CONDITIONS

In test sections I and II (Fig.3) has been varied the system elasticity using different specimen supports and different measuring principles. In test section II the mass of the system has been changed by applying the load either through a prestressed spring or through weights:

**Test section Ia**

The upper material specimen A loaded by the dead-weight Z (Fig.1) is driven by the shaft W. The support B with the lower specimen has been fixed by an axial bearing C so that it will pivot freely. It is prevented from simultaneous rotation by the bending lever D. The latter will be bent by the friction

force applied and its deflection is measured by strain gauges. In addition a torsion cell E measuring the torque of the driving shaft has been installed.

**Test section Ib**

The lower specimen support has been attached to the bottom of the test section. The friction force is recorded only by the torsion cell E in the driving shaft.

**Test section Ic**

The lower specimen support has been fixed so that it too is allowed to pivot freely. The friction force is measured by the bending rod D.

**Test section Id**

Again the specimen support B has been locked in position. The bending rod and the torsion cell are removed. A quartz force link has been installed into the driving system above the test section.

**Test section IIa**

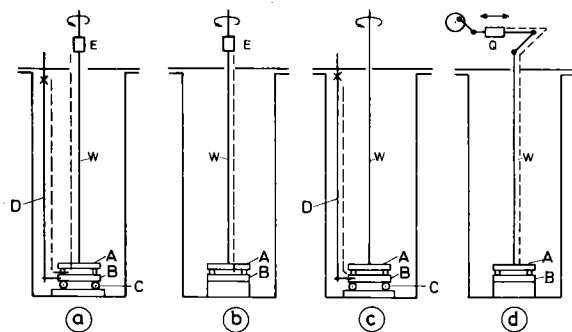
Two specimens A are contacted to the intermediate plate P by the lever arms K with the load applied either by the spring S or weights. P is moved up and down by the pull rod R. The friction force is recorded by the quartz force link installed in R. As before the specimen support has been fixed to the lever arms and it too will pivot freely.

**Test section IIb**

In comparison to IIa the support and guide of the outer specimens have been arranged in a more compact construction.

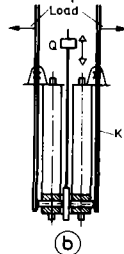
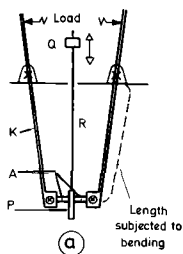
With these different test section arrangements the elasticities in Tab.2 could be achieved.

In the tilting plane system the relative movement between the material specimens is effected by tilting the whole test section and hence the slipping plane. Beginning of sliding of the rider A is recorded. This signal is assigned to the slope of the sliding plane.



**Testsection I**

- A = Upper Specimen
- B = Lower Specimen
- Elastic Length
- E = Dynamometer
- K = Power Rod
- C = Axial Ball Bearing
- D = Bending Lever
- Q = Quartz Force Link
- W = Drive Shaft
- P = Central Specimen



**Testsection II**

Fig.3 Rubbing Systems of Different Rigidity

PERFORMANCE OF TESTS

Since the influence of equipment variables on friction processes is to be investigated, all disturbing factors (even if part of them were relatively low) known from previous experiments were first studied separately. Among others there are:

- friction on the shaft packing
- friction in the axial bearing
- weight of the central pull rod
- elastic force of the bellows.

The results of these preexaminations were taken into account evaluating the test results.

To reduce the influence from mass acceleration forces in the pin-disk- and the plate-plate-test section, or from the fluid motion in the tilting plane version, very low driving velocities (0,25 and 2,5 mm/min) were selected for the initial runs. They were subsequently increased to 25 and 150 mm/min. Afterwards the elasticities and masses of the test section systems were subjected to variation (Tab.2). All other parameters were kept constant. The materials used exclusively were Stellite 6 and Inconel 718. These are the reference pad materials currently of main interest for the German Sodium Cooled Fast Breeder Reactor SNR 300. To exclude uncertainties the surface roughness of the probes was kept constant.

TESTSECTION	C OF TORQUE AND FORCE LINKS ( $\mu\text{m}/\text{kp}$ )	C OF COMPONENTS OF STRUCTURE ( $\mu\text{m}/\text{kp}$ )	C OF TOTAL SYSTEM ( $\mu\text{m}/\text{kp}$ )
I a	814	20	834
I b	380	12	392
I c	434	8	442
I d	0,015	72,985	73
II a	0,015	68,785	68,8
II b	0,015	28,485	28,5

Tab. 2 ELASTICITY  $C \approx df/dP$  OF TESTSECTION I AND II

TEST RESULTS

Commonly experimental data can be obtained either by computerized acquisition systems or by analog recorders. The latter method has been chosen in this case, since a recorder diagram instantly shows the characteristic of the rubbing process.

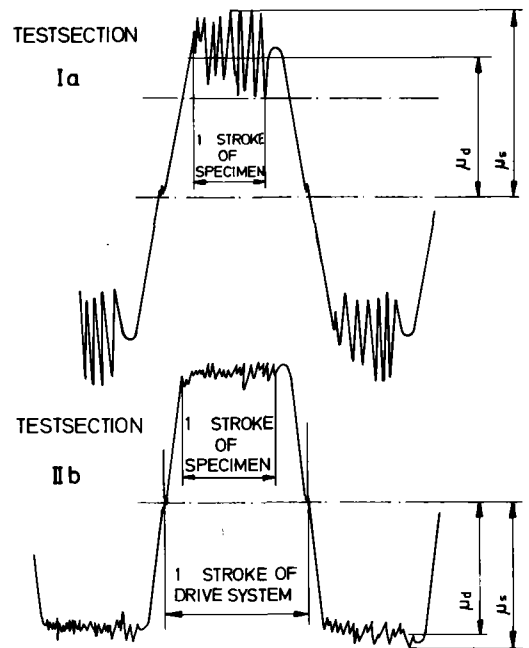


Fig.4 Friction Diagrams (Different Rigidity of Test Sections)

Two typical friction force curves are shown in Fig.4 from experiments carried out to investigate the influence of variable elasticity on test section systems. The dynamic friction coefficient  $\mu_d$  is calculated from the average value between the minimum and the maximum friction force, the static friction coefficient  $\mu_s$  from the maximum peak of the friction curve. Easy recognizable is the difference between the upper curve, taken from the most elastic system (Ia) and the lower curve, taken in the most rigid system (Iib). The amplitude of the system oscillation is greater and the maximum friction force (static) higher in test section Ia. This difference is also evident in Fig.5. Here, the static and dynamic friction coefficients of Stellite 6 and Inconel 718 are plotted as a function of system elasticity. The cumulative rubbing distance of each run has been 10 m. For high system elasticity (Ia) the friction values of both materials are greater than for low elasticity (Iib). In the more elastic system the static friction coefficients are higher up to 20% than the dynamic values while this difference is substantially reduced with decreasing elasticity (increasing

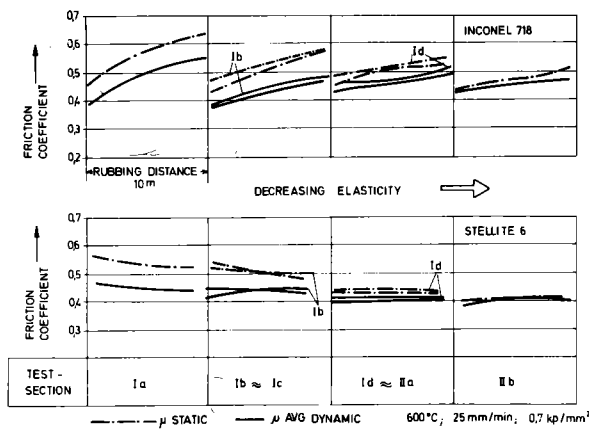


Fig. 5 Friction Coefficient of Materials in Na as a Function of Testsection Elasticity

rigidity). Friction values of approximately identical magnitude were obtained from different test sections when their oscillation behaviour as a function of geometry, mass, and elasticity were similar. (Tab. 2:  $I_b \approx I_c$ ,  $I_d \approx II_a$ ). These results are shown for a mean drive velocity of 25 mm/min. Similar results are obtained with rubbing velocities in the range of 0,25 to 150 mm/min.

The influence of the average drive velocity  $V_a$  on static and dynamic friction coefficients of Stellite 6 and Inconel 718 shows Fig. 6 for the most elastic system (Ia).

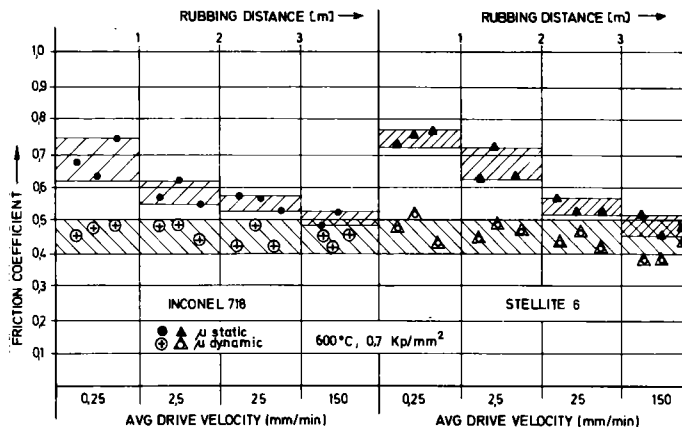


Fig. 6 Friction Coefficient as a Function of Avg Drive Velocity ( Ia )

The static friction factors are again higher than the dynamic ones and the differences between them are reduced with increasing drive velocities. Most interesting are these results in the lower range of drive velocity

$V_d \approx 2,5$  mm/min where the static friction coefficient is essentially higher (50 ÷ 60%) than the dynamic value.

These results seem to contradict most of the literature references stating that the influence of the rubbing velocity on friction factors is extremely low. This discrepancy can be explained from Fig. 7. A friction force plot has been traced. It is characteristic in case of stick-slip and shows the course of friction movement for one stroke. The movement carried out by the specimen in a number of individual steps is of intermittent characteristic. Between these steps, the materials remain under static contact. Different velocities could be assigned to this friction diagram: An average drive velocity  $V_a$  or the instantaneous velocity  $V_d$  of the drive system. Both don't describe exactly the prevailing motion. During each individual friction step occur relative movements between the material pairs. Then one can assign the real rubbing velocity  $V_t$  which is in general higher than the drive velocity.

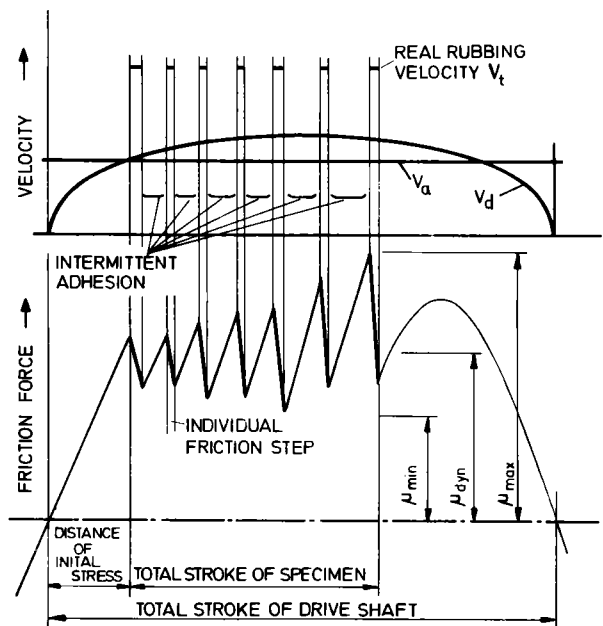


Fig. 7 Friction Force and According Real Rubbing and Drive Velocity

Whilst Fig. 7 represents a more schematic description Fig. 8 shows the quantitative situation. The real rubbing velocity is plotted as a

function of different average drive velocities  $V_a$ . The increasing average drive velocity is associated with a rise in the real rubbing velocity but between both is no proportionality. At very low driving rates (0,25 mm/min) one gets  $V_t \approx 25 \times V_a$  and at the highest we obtained  $V_t \approx 4 \times V_a$ . There is also no proportionality between the static friction coefficients and the real rubbing velocity. So far, the static friction coefficient is rather a function of the rest time of the specimens in static contact between the friction steps. Results of experiments from other test sections seem to sustain these results and showed a good agreement.

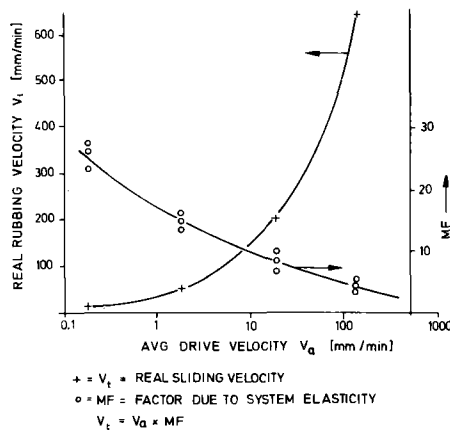


Fig.8 Ratio of Avg Drive Velocity and Real Rubbing Velocity in Test Section Ia

The influence of mass acceleration gets visible in all cases of stick-slip friction, and especially the dynamic friction coefficient might become falsified. In Fig.9 the

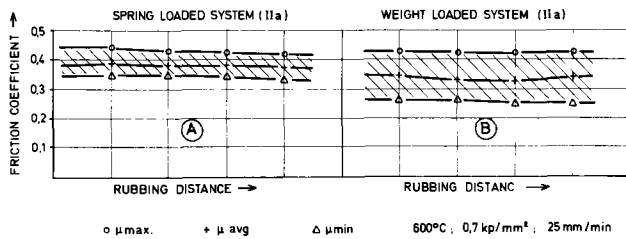


Fig.9 Friction Coefficient of Stellite 6 as a Function of Different Masses

friction coefficients of Stellite 6 are shown in (A), obtained from a test section with the load applied by a spring and in (B) from one with the load applied by weights. As can be seen, the width of the scattering band is

obviously increased in the weight loaded system. This result could not be expected, since commonly a greater mass acts as a damping element. Nevertheless, the different oscillation of the system can be explained by the traces shown in Fig.10. In the spring

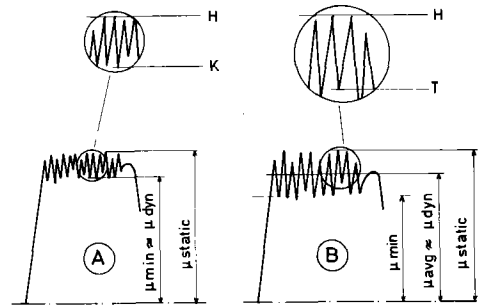


Fig.10 Friction Force Curves, (A) from a Spring Loaded, (B) from a Weight Loaded System

loaded system (A), the sliding was realized in many more, but smaller steps than in the system with the greater mass. If mechanical relaxation occurs causing individual components of the system to move, the system with the greater mass will oscillate with higher amplitude and a lower frequency.

Considering one individual oscillation cycle of the spring loaded test section it is evident that the system, having overcome static friction H, moves only as long as the value K is reached which is identical with the dynamic friction force. In the weight loaded test section the system with the greater mass moves in a longer cycle, exceeding the dynamic friction value, down to T. From here on the prestressing phase of the system begins for the following friction step. However T is not consequently identical with the value K in the spring loaded system. In this case the dynamic friction coefficient rather approximates to the average between maximum and minimum of the curve.

To avoid the influence of system elasticity and in addition to maintain as much as possible the surface structure of the material specimens, tests were performed in a tilting plane test section at low surface pressure (0,2 Kp/mm<sup>2</sup>) and with short sliding paths (1,5 to 10 m). The friction coefficients

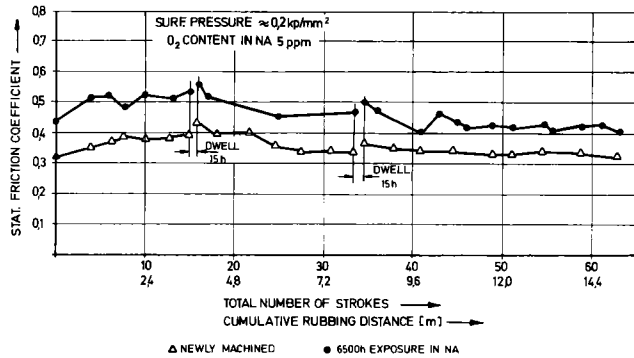


Fig.11 Static Friction Coefficient of Stellite 6 Testsection 5 Ti

recorded show a very narrow scattering band. Higher adhesive forces (breakway) after intermediate corrosion periods (dwell) are clearly recognized because there is no overlapping by other (equipment) influences as shown in Fig. 11.

CONCLUSION

With respect to the comparability of test results from different facilities it is evident that, in addition to quite a number of operational parameters, the test section design contributes to the magnitude of friction coefficients between material pairs. Most important is the elasticity and the mass distribution of the respective system. They are responsible for the occurrence and intensity of relaxation oscillations and essentially characterize the friction behaviour of the specimens and influence above all the friction coefficient.

The total elasticity of such a friction system is composed of the elasticity of

- the constructional elements (pull rod, shaft)
- the measuring cells (dynamometer, quartz force links)
- the friction materials employed.

It appeared that in relatively elastic systems dynamic friction coefficients and in relatively rigid system static friction coefficients can be recorded only with insufficient accuracies.

However, tests performed in different test section systems with the boundary conditions remaining unchanged yielded similar friction coefficients if the elasticity and mass dis-

tribution of the test sections were similar. This means for the comparison of test results obtained from different facilities that the most important equipment criteria must be known and taken into account. Therefore, for a tribological test design the criteria of the original components in the reactor core should be known and simulated.

LITERATURE

- /1/ E.Wild, K.J.Mack, G.Drechsler  
Das Verschleißverhalten von Werkstoffkombinationen in flüssigem Natrium; Versuchseinrichtungen und experimentelle Ergebnisse  
KFK-Bericht 1659/1972
- /2/ H.U.Borgstedt, G.Drechsler, G.Frees, G.Wittig,  
Erfahrungen mit elektrochemischen Sauerstoffsonden in Natrium-Kreisläufen  
ATW, July (1974)
- /3/ P.Barrau, J.P.Fontaine, B.Morin,  
Friction and Wear in Liquid Metals  
ANL-7520 Part I, 1968
- /4/ N.J.Hoffmann, J.J.Droher,  
Friction and Wear in Sodium  
Internat.Corrosion Forum Chicago 1974
- /5/ W.H.Roberts,  
Friction and Wear Behaviour of Sliding Bearing Materials (in Sodium Environments at Temperature up to 600°C)  
TRG Report 1269/1968
- /6/ M.A.Shaw, E.W.Leavey,  
Friction of Dry Solids in Vacuo. Phil. Mag. Vol.10 Nr. 66; Nov.1930
- /7/ E.Rabinowicz,  
The Determination of the Compatibility of Metals through Static Friction Tests.  
ASME/ASLE Lubrication Conference Cincinnati Oct. 1970

# INTERNATIONAL CONFERENCE ON LIQUID METAL TECHNOLOGY IN ENERGY PRODUCTION

## CORROSION AND TRIBOLOGICAL INVESTIGATIONS OF CHROMIUM CARBIDE COATINGS FOR SODIUM COOLED REACTOR APPLICATIONS

G. A. Whitlow, W. L. Wilson, T. A. Galoto,  
R. L. Miller, S. L. Schrock  
Westinghouse Advanced Reactors Division  
Madison, PA 15663, USA

N. J. Hoffman, J. J. Droher  
Liquid Metal Engineering Center  
Canoga Park, California 91304, USA

R. N. Johnson  
Hanford Engineering Development Lab  
Westinghouse Hanford Company  
Richland, Washington 99352, USA

### ABSTRACT

The dynamic and static friction behavior of chromium carbide coatings containing Nichrome, Inconel 718, or Tribaloy 700 as binder materials, has been investigated in sodium environments at temperatures ranging from 232 - 627°C (450 - 1160°F). In general, dynamic friction coefficients of these materials at 232°C were found to be  $\leq 0.4$ , but increased with temperature and cumulative rubbing, with values as high as 0.9 observed at 627°C following extensive rubbing. The detonation gun applied chromium carbide/Nichrome coated 316 stainless steel, exhibited a definite self-bonding tendency in high purity sodium, but little wear was observed. Static or breakaway friction coefficients were influenced by temperature, dwell time, contact pressure, and the presence of tangential forces at the contacting interfaces. Friction coefficients at 627°C were significantly lower for irradiated material than for similar unirradiated coatings.

A general equation describing the weight loss-time dependence of chromium carbide/Nichrome coatings in sodium of the form,  $\Delta W = 0.67 + 1.71 \times 10^{-4}t$  was developed, valid between 17 and 15,000 hours at 627°C, 0.3 m/s (1 fps) sodium velocity and 0.5-1.0 ppm oxygen concentration in the sodium. The chromium carbide/Nichrome coating has satisfied test requirements of 8000 hours in 627°C (1160°F) sodium and 120 thermal cycles: 627  $\rightleftharpoons$  427°C (1160  $\rightleftharpoons$  800°F). Irradiation screening data on this coating did not reveal any degradation in tests in static 482 and 584°C (900 and 1083°F) sodium at total neutron fluences ranging from  $1 \times 10^{22}$  to  $4 \times 10^{22}$  n/cm<sup>2</sup>.

### INTRODUCTION

The success of many design features and components of sodium cooled fast breeder reactors requires movement of adjacent surfaces with minimum friction coefficients in sodium. Major material requirements for in-core applications such as load pads on fuel and control rod ducts are low friction coefficients ( $\leq 0.4$  during refueling and  $\leq 0.9$  during operation), low corrosion, thermal and irradiation stability, and the absence of galling, fretting, and self welding at temperatures up to 627°C (1160°F). A current, cooperative, U.S. development program has as its objective therefore, the evaluation of low friction coatings for use in these applications, where the performance of uncoated austenitic materials like the 300 series stainless steels is unsatisfactory. Since its inception in 1970, many materials combinations, coating processes, and vendors have been evaluated with chromium carbide coatings offering the most promise<sup>(1-5)</sup>. Similar studies in Germany have appeared to place emphasis on uncoated materials for these applications<sup>(6,7)</sup>.

The United States Energy Research and Development Agency (USERDA) sponsored program is being conducted at the Westinghouse Advanced Reactors Division (W ARD),

the Liquid Metal Engineering Center (LMEC) and Atomic International (AI) under the overall coordination of Hanford Engineering Development Laboratory (HEDL). Screening studies conducted at AI were reported in a previous publication<sup>(8)</sup>. In this paper, results from the joint US program at W ARD, LMEC, and HEDL on friction and wear, sodium corrosion, and irradiation testing of chromium carbide coated Type 316 stainless steel are described.

### MATERIALS AND EXPERIMENTAL PROCEDURES

The chromium carbide based coatings, processes and vendors evaluated in this program are described in Table I. Test samples typically consisted of 76-126  $\mu\text{m}$  (0.003-0.005 in.) thick coatings on a stainless steel substrate pre-machined into the final form of plates and flat faced pins. Full details of the coating selection philosophy, design requirements and coating mechanics may be found in the papers by Johnson et al<sup>(2,9)</sup>.

The friction and wear test machines permit testing in sodium at temperatures up to 649°C (1200°F) under controlled impurity contents (0.5 - 1.0 ppm oxygen) and flow rates of 0.3 m/s ( $\sim 1$  fps). The basic experimental approach at W ARD was to press two diametrically opposed horizontal specimens (pins) against mating specimen surfaces (plates) which were mounted on a vertically reciprocating rod<sup>(10)</sup>. At LMEC, tests were performed using a plate rotating back and forth over three flat-faced pins<sup>(11)</sup>. Stroke amplitudes were generally one pin diameter (d) at temperatures  $\leq 371^\circ\text{C}$  (700°F) and d/4 at higher temperatures. Friction and wear test conditions employed in this program were prototypical of certain reactor component operations. Flat-faced rubbing surfaces were in full planar contact under normal loading while immersed in sodium, and during all changes in test temperature. Standard operating procedures required that the sodium be initially brought to  $> 371^\circ\text{C}$  ( $> 700^\circ\text{F}$ ) to achieve wetting before testing began. Testing usually was started at 232°C (450°F), a typical LMFBFR\* refueling temperature, with the bulk of the testing at 627°C (1160°F), the maximum bulk temperature in the vicinity of the duct load pads. The contact loads (normal static loads), the force necessary to move the plates (frictional load), and the displacement were continuously measured and recorded. Friction coefficients were calculated as the ratio of the frictional and the normal static loads on the pin-plate specimens. Wear data were obtained from weight changes and measured height changes of the pin and from quantitative analysis of wear scars on the plate specimens using a surface profile instrument. The irradiated materials tests utilized a disk-on-disk specimen configuration with reciprocating motion.

\*LMFBFR: Liquid Metal Cooled Fast Breeder Reactor

INTERNATIONAL CONFERENCE ON LIQUID METAL TECHNOLOGY IN ENERGY PRODUCTION

TABLE I  
COATING COMBINATIONS EVALUATED\*

Coating Designation	Binder** Material	Coating	
		Process	Vendor†
CN-1b	Nichrome	D-Gun	UC
CN-1b-2 <sup>ξ</sup>	Nichrome	D-Gun	UC
CN-1P	Nichrome	Plasma	UC
CI-D	Inconel 718	D-Gun	UC
CI	Inconel 718	Plasma	UC
CM	Molybdenum	Plasma	UC
CT-7D	Tribaloy 700	D-Gun	UC
CT-7M	Tribaloy 700	Plasma	Q
CT-7G***	Tribaloy 700/ 316 SS	Plasma	Q
CN-1C††	---	D-Gun	UC

\*All coatings are chromium carbide (-5 μm Cr<sub>3</sub>C<sub>2</sub> starting powder) containing ~15 v/o binder (typically - 20 μm starting powder), on a 20 percent cold worked, Type 316 stainless steel substrate. Samples surface finished after coating to 75-100 μ ins. AA.

\*\*Nichrome: nominally 80 Ni, 20 Cr; Inconel 718: International Nickel Co. (53 Ni, 19 Cr, 19 Fe, 5 Nb, 3 Mo); Tribaloy 700: Dupont Co. (50 Ni, 32 Mo, 15 Cr, 3 Si).

†UC: Union Carbide Corporation; Q: Quantum Corporation.

††Overlay of Cr<sub>23</sub>C<sub>6</sub> on CN-1b coating.

<sup>ξ</sup>CN-1b-2 is same coating as CN-1b, but was deposited on a substrate surface processed by a different grit blasting technique. These coatings are the same as the LC-1H coating described in references (2) and (9).

\*\*\*Graded coating of Cr<sub>3</sub>C<sub>2</sub> plus 15 v/o Tribaloy 700 on top of layer of 50 v/o of above composition plus 50 v/o of Type 316 stainless steel.

The test specimens consisted of a 12.7 mm (0.5 in.) diameter spot of chromium carbide/Nichrome applied by the Detonation Gun process (D-Gun) to a 15.87 mm (0.625 in.) diameter 316 stainless steel substrate disk. Irradiation was performed in a sodium-filled subcapsule in the EBR-II reactor to a fluence of 1 x 10<sup>22</sup> n/cm<sup>2</sup> (E > 0.1 Mev) at 584°C (1083°F). The unirradiated control specimens were of similar geometry and were thermally aged in a sodium-filled capsule to the same conditions experienced by the irradiated specimens.

The sodium compatibility testing was performed in a pumped sodium loop system constructed of stainless steel and designed for the exposure of 19.05 x 19.05 x 4.57 mm (3/4 x 3/4 x 0.180 in.) coated plate samples to high temperature sodium. This loop system, which is of a type described in detail elsewhere,<sup>(12)</sup> was operated non-iso-

thermally at a test section temperature of 627°C (1160°F), and at a sodium flow velocity of 0.3 m/s (1 fps), and an oxygen impurity level in the sodium in the range 0.5 to 1.0 ppm. Average corrosion rates for the various time periods were calculated from the change in weight of the test samples resulting from the sodium exposure. Coating stability under in-sodium thermal shock conditions, using the following test cycle was studied using a thermal cycling facility described previously<sup>(4)</sup>.

- Hold at 627°C (1160°F) for from 8 h to 4 days
- Quench in < 1 minute to 427°C (800°F) in sodium
- Raise temperature of sodium at rate of 18°C/h (50°F/h) to 627°C
- Repeat cycle

Samples of the different coatings were screened for their resistance to fast neutron damage in sodium filled capsules inserted in the EBR-II reactor at temperatures of 482 and 584°C (900 and 1083°F). The fluence accumulated was nominally 3 x 10<sup>22</sup> n/cm<sup>(13)</sup>.

TRIBOLOGICAL RESULTS

Dynamic friction results for D-Gun applied chromium carbide coatings having Nichrome, Inconel 718, and Tribaloy 700 binders, are summarized in Figure 1. Also included are the range of dynamic friction coefficients for uncoated Type 316 stainless steel under similar test conditions. Friction testing was performed at intermediate temperatures of 371, 538, and 593°C, (700, 1000 and 1100°F)<sup>(10)</sup>, but in this paper only data from the upper and lower test temperatures are presented in detail.

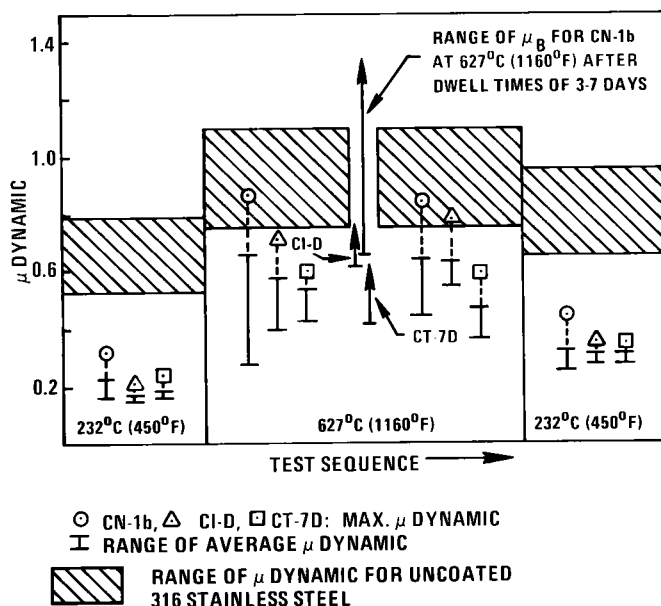


Figure 1. Comparison of dynamic friction results for various chromium carbide coatings in 232°C (450°F) and 627°C (1160°F) sodium.

At all temperatures investigated, the chromium carbide coatings displayed dynamic friction coefficients considerably lower than those for uncoated 316 stainless steel. Friction coefficients were found to increase with cumulative rubbing distance, the most dramatic increase occurring at 627°C (1160°F). Following a 3-7 day soak period under load at 627°C, initial dynamic friction coefficients were significantly lower than those immediately prior to the soaking period or dwell. Binder composition was found to influence the dynamic and breakaway friction (static friction measured in shear following a dwell) behavior primarily at the higher temperatures. Coatings having a Tribaloy 700 binder displayed the lowest dynamic and breakaway friction coefficients of the three materials tested.

Results of short time dwell-breakaway studies were essentially in agreement with dynamic friction results in that the chromium carbide coatings showed considerably lower self-bonding tendencies in high purity sodium than uncoated 316 stainless steel. The range of self-adhesion coefficients, expressed as  $\Delta\mu$  (breakaway friction minus average dynamic friction coefficients), for chromium carbide/Nichrome and 316 stainless steel are presented in Figure 2. Breakaway friction coefficients ( $\mu_B$ ) were measured in 427 - 649°C (800 - 1200°F) sodium following increasing dwell times from 1 - 100 minutes at the temperatures indicated. The magnitude of  $\mu_B$  was found to increase with dwell time and test temperature and to decrease with increasing contact pressure 2.07 - 20.7 MPa (300 - 3000 psi).

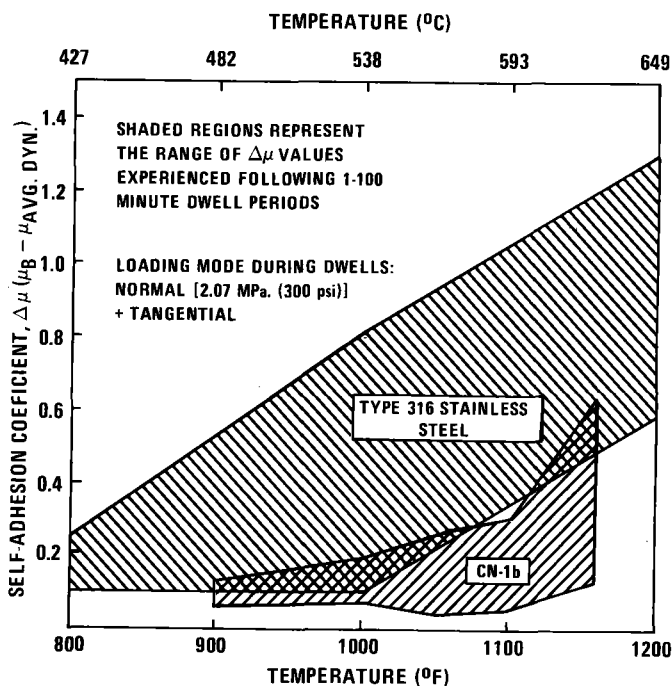


Figure 2. Influence of chromium carbide/Nichrome coating on the self-bonding tendency of Type 316 stainless steel in high temperature sodium.

The technique of loading during a dwell was found to have a significant influence on resultant adhesion coefficients. If both tangential and normal forces were applied to the contacting interfaces during a dwell, the force subsequently required to break the junction and initiate motion was markedly greater than the force following a dwell with normal loading only. This phenomenon has been reported by other investigators<sup>(14)</sup> and is thought to result from an increase in the real area of contact by plastic flow under the influence of combined normal and tangential stresses. Accordingly, the breakaway data summarized in Figure 2 were obtained following static dwells with both normal and tangential loading.

Dynamic friction studies on irradiated chromium carbide/Nichrome coatings showed friction coefficients in 627°C (1160°F) sodium to be significantly lower for the irradiated material than for similar unirradiated coatings. Friction coefficients for the irradiated material couple remained relatively constant with cumulative travel over the entire 12.7 m (500 in.) of rubbing at 627°C. In contrast, the unirradiated couple displayed the continuously increasing friction coefficients throughout both the pre and post dwell rubbing periods illustrated in Figure 3.

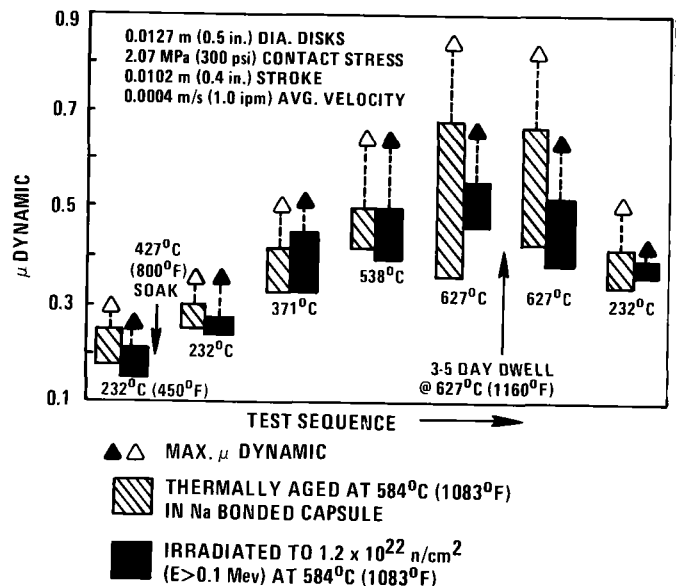


Figure 3. The effect of irradiation on the dynamic friction behavior of chromium carbide/Nichrome coating in sodium (0.5 - 2.0 ppm oxygen).

None of the chromium carbide coatings tested showed significant wear following an average of 28 m (1100 in.) of cumulative travel at nominal contact pressures up to 6.86 MPa. (1000 psi) in 627°C (1160) sodium. Surface profilometry and scanning microscopy examinations revealed that, other than a polishing and smoothing of initially high surface asperities, no significant wear or material removal had occurred. The typical wear incurred by a chromium carbide/Nichrome coating is shown in Figure 4. Minimum wear rates were also verified by specimen weight change data.



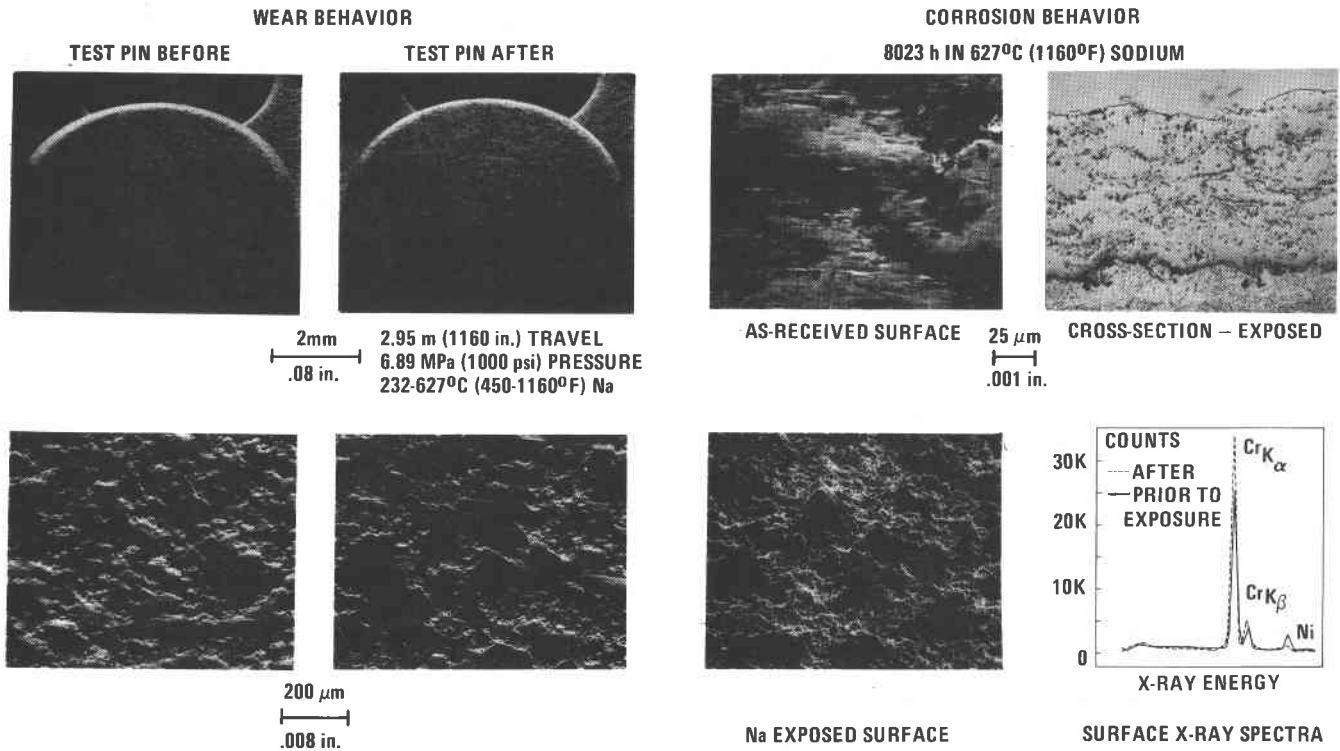


Figure 4. Wear and corrosion behavior of chromium carbide/Nichrome coated Type 316 stainless steel in sodium (0.5 - 1.0 ppm Oxygen).

SODIUM COMPATIBILITY EVALUATION

In the compatibility part of this program, a vital complement to the identification of materials with acceptable friction and wear properties, chromium carbide coated samples have been sodium exposed for times up to 15,000 hours. The results of these exposures are presented together with thermal cycling and bend testing observations in this section.

The first sodium compatibility testing series included specimens of chromium carbide coatings with such binders as Nichrome, molybdenum and Inconel 718. These were produced by Union Carbide Corporation using both detonation-gun (D-Gun) and plasma spray techniques. Short term exposure to sodium showed that the D-Gun produced coatings were very stable and exhibited low corrosion rates<sup>(4)</sup>. Longer term testing of these and the other coating combinations detailed in Table I, in 627°C (1160°F), 0.3 m/s (1 fps) sodium containing 0.5 - 1.0 ppm O<sub>2</sub> has enabled the corrosion data shown in Table II to be generated. All coatings listed have demonstrated acceptably low corrosion rates of ~0.1 mpy (25 μm/year). A total of 54 data points for the chromium carbide/Nichrome coated 316 stainless steel (CN-1b and CN-1b-2) have been obtained<sup>(15)</sup>, and fitted to the linear equation:

$$\Delta W = A + Bt$$

where, ΔW is the measured weight change, (mg/cm<sup>2</sup>); t is the exposure time (h) in 627°C (1160°F) sodium, and A and B are constants with values of (0.67) and (1.71 x 10<sup>-4</sup>)

TABLE II  
CORROSION RATE DATA FOR CHROMIUM CARBIDE COATINGS IN 627°C (1160°F) SODIUM<sup>†</sup>

Coating Type	Maximum Exposure Time, (h)	Weight Loss at Time, t (mg/cm <sup>2</sup> )	Average Corrosion Rate From 0-t, h (mpy)*	Instantaneous Corrosion Rate** (mpy)*
CN-1b-2	8467	1.54	0.10	0.08
CN-1b	15527	3.10	0.11	0.09
CN-1C	7969	1.97	0.12	0.07
CI-D	10061	2.27	0.12	0.08
CT-7D	7969	1.51	0.10	0.08

<sup>†</sup>average corrosion rate for 316 stainless steel after 8000 h in 627°C sodium (0.3 m/s, 0.5 - 1.0 ppm O<sub>2</sub>) is ~0.02 mpy.

\*mpy: mils (10<sup>-3</sup> in. ≡ 25 μm) of thickness loss per year.

\*\*based on slope of weight change vs. time plot.

respectively. Similar analyses performed on the data for the chromium carbide coatings containing Inconel 718 and Tribaloy 700 binders have enabled the relationships shown in Figure 5 to be established.

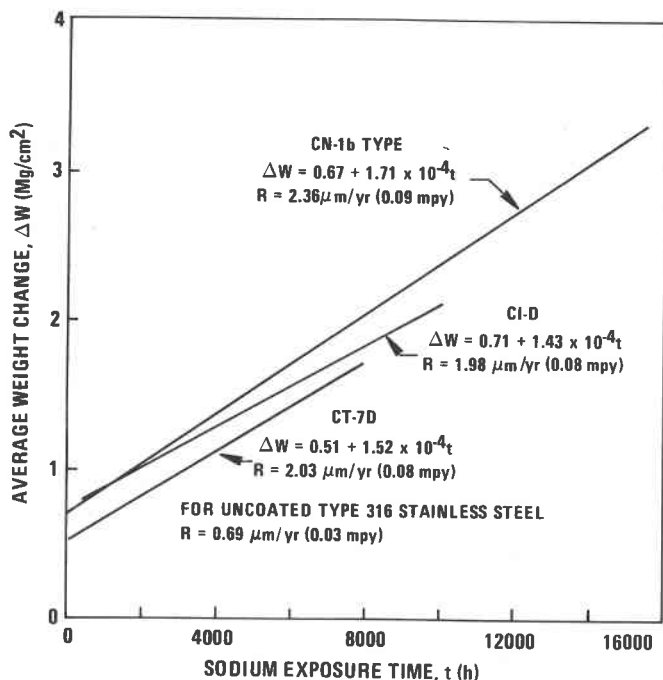


Figure 5. Weight change - time relationships for several chromium carbide based coatings on Type 316 stainless steel in 627°C (1160°F), 0.3 m/sec (1 fps), 0.5 - 1.0 ppm O<sub>2</sub> sodium ( $R$  value represents corrosion rate calculated from slope of  $\Delta W$  vs.  $t$  line).

Optical and scanning electron microscopical examination of the long-term (8000 h) exposed samples of the duct load pad coatings CN-1b and CN-1b-2 and some alternate coatings CI-D and CT-7D has not revealed any deterioration in the form of cracking or coating spalling. The only changes noted were the anticipated near-surface loss of nickel and the consequent micropitting surface attack<sup>(4)</sup>. Figure 4 illustrates some typical results of these examinations of the chromium carbide/Nichrome (CN-1b-2) coating. Metallographic and surface chemistry studies yielded similar results for the very promising Tribaloy 700 containing coating, CT-7D. Characterization of alternate coating combinations revealed that the duplex chromium carbide coating (CN-1C) had separated between the half mil thick surface layer of pure chromium carbide and the three mil thick under-coat layer of CN-1b during sodium exposure.

During the course of this experimental program a number of the coating combinations examined have failed to satisfy the designer-specified qualification requirements of 8000 h in 627°C (1160°F) sodium and 120 in-sodium thermal cycles 627  $\rightleftharpoons$  427°C (1160  $\rightleftharpoons$  800°F). In a previous paper by Whitlow et al<sup>(4)</sup>, plasma sprayed chromium carbide coatings with various binders on Type 316 stainless steel substrates did not look promising for these applications. Coating deterioration took the form of separation very close to, or at the coating/substrate interface. Additional testing to longer exposure times has confirmed these results, such that the plasma sprayed coatings CN-1P, CM and the Inconel 718 containing coating, CI have been eliminated from consideration. Two more recent additions to this test program, CT-7M and CT-7G, have been exposed to 627°C (1160°F) sodium for ~1000 h. These are both plasma sprayed chromium carbide coatings

with Tribaloy 700 binders from an alternate vendor. Coating instability demonstrated by samples of CT-7M resulted in the material being eliminated, but CT-7G (a graded duplex coating, See Table I) demonstrated adequate short term compatibility.

Thermal cycling results have in general complemented the sodium corrosion data. Coating failure occurred in almost all plasma sprayed samples when thermally cycled, with failure being observed at or near the interface. The D-Gun coatings, CN-1b, CN-1b-2, and CI-D have all withstood 120 such cycles without any detectable deterioration. Samples of the chromium carbide/Tribaloy 700 coating CT-7D have successfully withstood 60 such cycles in a continuing test.

An attempt was made at evaluating the mechanical integrity of some of these chromium carbide coatings. Acoustic emission techniques were used to detect coating cracking in a monotonically loaded four point bend test specimen with the coating loaded in tension or compression<sup>(16)</sup>. The Nichrome and Tribaloy 700 containing coatings (CN-1b and CT-7D) in 627°C tension tests were found to exhibit both an increase in brittleness and a decrease in strength after prior aging in sodium. Both materials showed considerably higher failure resistance when tested in compression than in tension.

#### IRRADIATION DAMAGE STUDIES

A variety of wear resistant, low-friction materials were irradiated in the EBR-II reactor in order to assess their response to LMFBR environments<sup>(13)</sup>. Pre- and post-irradiation testing and examination efforts emphasized candidate materials such as chromium carbide coatings for application to the duct wear pads. Chromium carbide coatings applied by the D-Gun process showed essentially no irradiation damage (cracking, spalling, unbonding) and the reference chromium carbide/Nichrome coating (CN-1b-2) was qualified for service relative to the effects of irradiation. Plasma-sprayed chromium carbide coatings of all compositions showed spalling or cracking of the coating at all fluence levels.

#### DISCUSSION

The dynamic friction and self-adhesion tendencies of Type 316 stainless steel in high purity sodium have been shown to be significantly improved by the application of a chromium carbide coating (Figures 1 and 2). This improved behavior, under sliding and static contact situations, results primarily from certain superior physical characteristics of these carbide coatings. Both penetration hardness and creep rate may influence the real area of contact and, hence, subsequent frictional forces. In general, under identical loading conditions, the real area of contact is considerably less for harder materials, resulting in reduced friction. The high surface waviness of the D-Gun applied coatings (see Figure 4) could also be an important factor in determining the number of real contact points and associated frictional characteristics.

With the exception of the irradiated chromium carbide/Nichrome coating, all coatings displayed increasing coefficients of friction with cumulative rubbing, particularly at the higher temperatures. The magnitude of the average friction coefficient range (bars in Figure 1) indicates the extent to

which friction coefficients varied over the entire rubbing period. The low initial friction values and the increase in friction with cumulative rubbing displayed by these coatings at 627°C (1160°F) suggests the presence of a lubricative surface film (possibly a sodium-metal-oxygen complex) which forms and is stable at temperatures >537°C (1000°F). Film formation could be such in the 627°C (1160°F) tests (a continuous 25.4 mm/s (1.0 in/min) velocity), that, the film is worn away at a slightly greater rate than it can form. Thus, friction increases with continuous rubbing. During a 3-7 day soak period (no rubbing) there may be sufficient time for the film to reform, resulting in low initial friction coefficients following this dwell period.

The above observations have significant design implications. If relative motion of adjacent fuel ducts is such that time is available between periods of rubbing to permit the reformation of stable surface films, friction coefficients at operating temperature could be significantly less than values obtained from continuous rubbing experiments.

The reason for the relatively constant friction coefficient displayed by the irradiated chromium carbide/Nichrome couple at 627°C (1160°F) is not known. This behavior could possibly have resulted from an irradiation hardening effect or possibly from complex surface chemistry changes which occurred under the combined influence of neutron and sodium exposure.

From the sodium compatibility viewpoint, the measured corrosion rates for these chromium carbide base coatings are no cause for concern. For the load pad application, where an in-core residence time of less than two years is projected, a rate of 2.5  $\mu\text{m}/\text{yr}$  (0.1 mpy) is very low and well within the requirement that no more than half the coating thickness be lost to corrosion. Since the instantaneous corrosion rate decreased with increasing exposure time, conservative estimates of long term corrosion may be made utilizing the rate equation. Exposure to sodium does not, however result in a uniform thickness loss, but takes the form of a selective leaching out of nickel from the binder material with some consequential "falling out" of carbide particles. The thermal cycling in sodium performed in this work, established on the basis of "worst case conditions" for sodium reactor service, has demonstrated the high resistance to thermal shock possessed by the D-Gun applied chromium carbide based coated stainless steel materials. Limitation of expansion coefficient mismatch between coating, binder and substrate has resulted in associated lattice strains, which can be accommodated by the material during such thermal shocks. The good irradiation damage resistance is probably attributable in part to similar "neutronic" compatibility between the coating, binder and substrate.

#### CONCLUSIONS

Chromium carbide base coatings with Nichrome, Inconel 718 or Tribaloy 700 binders have been shown to possess superior friction and wear properties to uncoated Type 316 stainless steel in a prototypic sodium environment. These coatings in the form of a 75  $\mu\text{m}$  (0.003 in) thick layer on 20% cold worked 316 stainless steel substrates have demonstrated low corrosion rates in 627°C sodium, good thermal shock resistance and resistance to irradiation damage. A D-Gun applied chromium carbide/Nichrome coating has been qualified for reactor service as the duct load pad bearing surface. No plasma sprayed coating has

yet been qualified and the search must be continued for an alternative or back-up coating process/coating vendor.

#### REFERENCES

1. Liquid Metal Engineering Center (LMEC), Annual Technical Progress Report, January-December 1973, LMEC-74-1, 1-107, 1974.
2. R. N. Johnson, S. L. Schrock, G. A. Whitlow, "Wear resistant coatings for reactor components in liquid sodium environments," *J. Vac. Sci. Technol.*, 11, 759-764, 1974.
3. N. J. Hoffman, and J. J. Droher, "A review of wear in sodium presented at NACE Meeting," *Corrosion* 74, Chicago, March 1974, Paper No. 15, 1974.
4. G. A. Whitlow, R. L. Miller, S. L. Schrock, P. C. S. Wu, "Sodium compatibility studies of low friction carbide coatings for reactor application," *Corrosion*, 30, 12, 420-426, 1974.
5. G. A. Whitlow, R. L. Miller, W. L. Wilson, T. A. Galieto, "Observations on the in-sodium corrosion and tribology of aluminide coatings on Inconel 718," *Microstructural Science*, 3, 775-788, American Elsevier Publishing Co., New York, 1975.
6. E. Wild, K. J. Mack, H. Hoffman, "The wear behavior of steels and alloys in liquid sodium," *EURFNR-696*, (KFK-973), 1969.
7. E. Wild, K. J. Mack, "Tribology in the Core of a Sodium-Cooled Fast Breeder Reactor," *Wear*, 34, 331-340, 1975.
8. W. J. Kurzeka, R. M. Oliva, and F. W. Poucher, in *Atomics International Rockwell International Annual Technical Progress Report, Sodium Technology and Cover Gas Seal Development Programs Government Fiscal Year 1972*, AI-AEC-13037, 59-87, 1972.
9. T. A. Wolfla, and R. N. Johnson, "Refractory metal carbide coatings for LMFBR applications - a systems approach," *J. Vac. Sci. Technol.* 12, 777-783, 1975.
10. W. L. Wilson, B. Minushkin, and E. J. Chelen, "Friction and wear testing in support of FFTF components - Interim summary report," Westinghouse Electric Corporation Report WARD-NA-3045-13, 1974.
11. Liquid Metal Engineering Center (LMEC) Semi-Annual Technical Progress Report, LMEC-71-7, 43-45, 1972.
12. G. A. Whitlow, J. C. Cwynar, R. L. Miller, and S. L. Schrock, "Sodium corrosion of alloys for fast reactor applications," *Proc. Symp. Chemical Aspects of Corrosion and Mass Transfer in Liquid Sodium*, 1971 Meeting of AIME, Detroit, 1-63, 1973.
13. A. L. Ward, R. N. Johnson, G. L. Guthrie, and R. C. Aungst, "Irradiation effects on low friction coatings for LMFBR applications," Hanford Engineering Development Laboratory Report HEDL-TME-75-108, 1975.

## INTERNATIONAL CONFERENCE ON LIQUID METAL TECHNOLOGY IN ENERGY PRODUCTION

14. F. P. Bowden, and G. W. Rowe, "The Adhesion of Clean Metals," Proc. Roy. Soc., 233, 429-442, 1956.
15. Westinghouse Advanced Reactors Division, Sodium Technology Program Friction, Wear and Self Welding Quarterly Progress Report for Period Ending July 31, 1975, WARD-NA-3045-28, 1975.
16. Westinghouse Advanced Reactors Division, Sodium Technology Program Quarterly Progress Report for Period Ending October 31, 1972, WARD-NA-3045T1-7, 520-523, 1972.

# INTERNATIONAL CONFERENCE ON LIQUID METAL TECHNOLOGY IN ENERGY PRODUCTION

## EXPERIMENTAL INVESTIGATIONS OF THE FRICTIONAL AND WEAR BEHAVIOR OF TUNGSTEN CARBIDE CERMET BALL BEARINGS UNDER AXIAL LOAD IN LIQUID SODIUM

K.W.Kleefeldt

Kernforschungszentrum Karlsruhe  
Institut für Reaktorentwicklung  
7500 Karlsruhe, Postfach 3640  
Federal Republic of Germany

### ABSTRACT

This paper describes part of the R & D work performed on ball bearings operated in a liquid sodium environment and tested under conditions which are felt to be representative for high precision mechanisms in LMFBR's. After a short introduction, mainly dealing with the experimental results of other authors, a description will be given of the test facility, the test procedure, the ball bearings and the basis for the selection of the materials. The paper covers the experimental phase, which has been carried out in two steps. In the first phase material screening tests demonstrated the tungsten-carbide-cobalt cermet to be superior to the other materials tested with respect to friction and wear. This material, therefore, was selected for a more detailed parameter test programme during phase 2. Up to now a series of tests have been performed with bearing load and speed as parameters, indicating that fatigue is the life limiting factor. It shows that a life-load relationship, similar to that known for conventional ball bearing technology, also seems appropriate for the test conditions and environment investigated here.

### INTRODUCTION

Since the adoption of liquid sodium as heat exchange fluid in reactor technology during the fifties some effort has been made to take advantage of the more attractive features of rolling contact friction as compared to those of sliding motion friction for application in precision mechanisms, operating in sodium or sodium vapor environment at elevated temperatures. In LMFBR's roller and ball bearings are basically used in fuel handling devices (8), that means under low speed, intermittent and alternating motion conditions.

The earliest studies of Greenert and Rawlings (1) and of Markert and Ferguson (2) in 1956 and 1957 respectively, using SAE 52100 steel ball bearings in sodium-potassium alloy, revealed fundamental differences with respect to load capacity and failure modes, when operated in liquid metal as compared to conventional lubricated conditions, even at moderate temperatures of only 120 °C. A number of subsequent tests using different materials (including wear resistant alloys such as Cobalt-base alloys), different test conditions and design modifications also demonstrated, that excessive wear and cage binding were the predominant life limiting factors for ball bearing operation under LMFBR conditions (3,4,5,6,7). From all test material available in the open literature it can be concluded that the effective roller bearing life is reduced by at least 2 or 3 orders of magnitude as compared to the life times predicted by the conventional dynamic capacity calculation method. Due to the large scattering of the test results no alternative rating method is known for high temperature sodium application. Nevertheless it has been demonstrated that the bearing performance can be improved to a degree, attractive for the above mentioned intermittently operating systems by using

adequate material and/or adequate design measures. For example, Takea Uga found out, that the wear rate could be reduced by approx. two orders of magnitude by increasing hardness, using stainless steel, nickel base alloy and cobalt base alloy (5). Jamison and Mc Veigh obtained quite satisfactory wear resistance, especially at moderate temperatures (316 °C), by means of incorporation of relief grooves in the races and use of Molybdenum alloy cages (7).

The work reported herein was designed to demonstrate the potential of refractory material for use in ball bearings to be operated in sodium under a variety of test conditions. The tests are being performed in the framework of the SNR-related sodium technology program.

### TEST BEARINGS

The test bearings correspond in the boundary dimensions to ISO-standard 6207 type ball bearings with 35 mm bore diameter (Fig.1). In contrast to the usual design a cageless bearing with 16 balls was chosen in order to avoid cage binding problems, thus omitting cage related parameters like material and cage/ball clearance. This design requires, that one ring (in this case the inner ring) has only one ring land for assembling purposes. It also means, that the axial load has

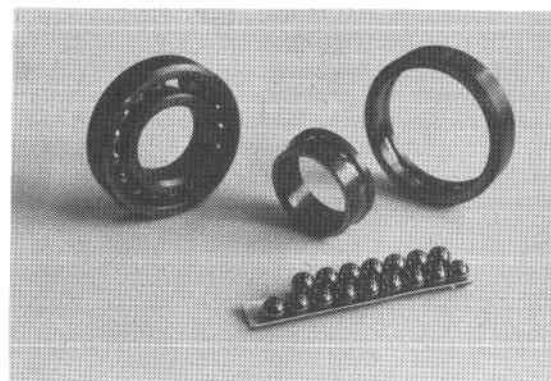
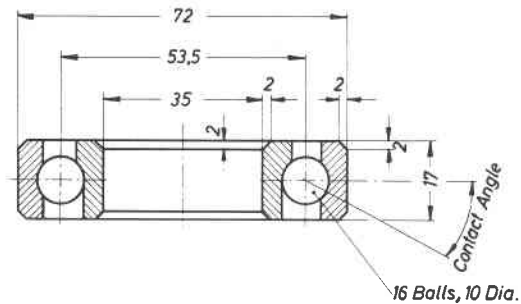


Fig. 1 - Cageless Test Bearing, Dimensions in Millimeters

INTERNATIONAL CONFERENCE ON LIQUID METAL TECHNOLOGY IN ENERGY PRODUCTION

to dominate the radial load sufficiently in order to avoid radial dislocation, which in these tests is guaranteed by applying pure axial load, thus the test bearing works as an angular contact thrust bearing with a nominal contact angle of approx. 15°. Bearing size has been selected arbitrarily with the aim of being typical for a medium size LMFBR application.

Since the test results obtained in different laboratories are hardly convertible due to inconsistent test conditions, the studies have been carried out in two steps. In the first phase ball bearings out of five different materials, e.g. tool steel (DMo5 equivalent to S-6-5-2), stainless high speed steel (BG42), stellite (Virium 11 and 12), ferrotitanit (WF13.5) and tungsten carbide/cobalt cermet (WC-Co), have been compared with respect to friction and wear. The chemical composition and hardness numbers are given in Tab.I. The selection of these materials was based on the following considerations: first of all it was aimed to have representatives out of three material categories, i.e. conventional tool steel for easy fabrication, low friction and wear resistant alloy for improving sodium operation and refractory alloys with their outstanding hardness at elevated temperatures. After that within each category the general properties required for sodium application were considered, as for instance corrosion resistance, dimensional stability and self-welding behavior, although in most cases only a qualitative judgement has been possible because of scarce sources. In the cases of WC-Co alloy and stellite slightly different alloys for rings and balls have been chosen for availability reasons, as noted in Tab.I. In the second phase the most promising material from phase I is being subjected to a more detailed parametric test programme, keeping the material unchanged, which is the WC-Co alloy.

In order to minimize tolerance effects on test results, an excessive quality control was performed. Quality requirements with respect to dimensional tolerances and clearances were in accordance with DIN 620 specification, class 0. Tab.II shows the main specified data as well as the lower, mean and upper deviations measured in the as-fabricated bearings.

Material	Composition (Weight Percent)	Hardness RC measured at 20 °C
DMo5 (Tool Steel)	0.9C, 0.3Si, 0.3Mn, 4.3Cr, 5.0Mo, 6.5W, 1.9V, Bal. Fe	64.5 - 65.2
BG42 (Stainless High Speed Steel)	1.5C, 0.5Mn, 0.35Si, 0.01S, 0.01P, 15Cr, 4.2Mo, 1.2V, 0.2Ni, Bal. Fe	60.4 - 63.2
WF13.5 (Ferro Titanit)	0.6C, 34.5TiC, 13.5Cr, 3.0Mo, 1.0Cu, 0.02B, Bal. Fe	61.0 - 66 (Balls 68)
GT20 <sup>**</sup> (Tungsten Carbide-Cobalt Cermet)	85WC, 3TiC + TaC, 12Co	HV=1,34-1,39 (10 <sup>10</sup> N/m <sup>2</sup> ) (Balls 68)
GT10 <sup>**</sup> (Tungsten Carbide-Cobalt Cermet)	94WC, 6Co	HV=1,5 (10 <sup>10</sup> N/m <sup>2</sup> )
Virium 11 <sup>**</sup> (Stellite)	30Cr, 12W, < 2Fe, 4Si, Mo, Ni, C, Bal. Co	56
Virium 12 <sup>**</sup> (Stellite)	28Cr, 8W, < 2Fe, 4Si, Mo, Ni, C, Bal. Co	44 - 49

\* For Rings only      \*\* For Balls only

Table II - SPECIFICATION AND QUALITY CONTROL DATA FOR LIQUID SODIUM TEST BEARINGS

	Reference Dimension (mm)	Tolerance (µm)	Deviation from Ref.
			Min./Avg./Max (µm)
Bearing Envelope Dimensions	6207	Class 0	Gageless, 1 Land
OR Outside Diameter	72	0/-13	-1/-5.5/-12
OR Land Diameter	60	x	
OR Groove Diameter	63.5	15/55	-14/+14/+96
OR Groove Meridian Radius	5.175	0/100	**
IR Bore Diameter	35	0/-12	-1.5/-5.8/+2
IR Land Diameter	47	x	
IR Groove Diameter	43.5	+20/-20	-62/-20/+78
IR Groove Meridian Radius	5.175	0/100	**
Size of Balls	10		**
Number of Balls	16		**
Diametral Clearance		34/47	**
Contact Angle (zero Load)	15	x	
Pitch Diameter	53.5		

x Not specified      \*\* See Fig. 2

Fig.2 summarizes additional quality control results for the contact surfaces of all test bearings, subdivided for the five materials used and compared with the specified tolerances. It can be stated, that in most cases the specification is met, except for the ring groove diameter, which exceeds the tolerance limits at a few rings made out of WC-Co alloy and WF13.5. This discrepancy has been compensated by matching the rings in a way, that the diametral clearance meets the specification, thus it is irrelevant for the test procedure. Furthermore the surface roughness of the WC-Co and WF13.5 ring grooves was beyond the specified limits due to the fact, that these surfaces have just been ground instead of being honed as in the other cases. In general it should be mentioned, that the fabrication of the WC-Co-bearings, which was conducted by SKF Schweinfurt, West Germany, required special techniques, particularly for the grinding procedure.

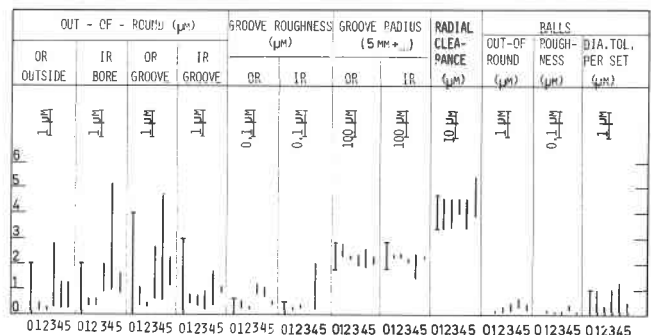


Fig. 2 - Summary Quality Control Data for Test Bearings out of five Materials. Material Identification: 1=DMo5, 2=BG42, 3=WF13.5, 4=GT10/20, 5=Virium 11/12, 0=as specified

## BALL BEARING TEST FACILITY

The test facility used in this investigation consists of a liquid sodium tank facility and a bearing test fixture, which is inserted into the liquid sodium vessel. The tank facility supplies the required sodium environment along with the necessary provisions as temperature control, purification and cover gas. The test vessel contains approx.  $0.17 \text{ m}^3$  of stagnant sodium during bearing testing. Prior to the test, the sodium is cleaned by circulation through an auxiliary cold trap loop to an oxygen concentration level of less than 10 ppm.

The test fixture, schematically shown in Fig. 3, is designed to support two test bearings in a duplex arrangement fully immersed in sodium and axially loaded by a pneumatic actuated central tie rod, the inner rings being rotated. The outer rings are fixed in a common housing, which is linked to a torque measuring bending beam, thus the sum of the friction torque generated within the bearing couple is transmitted continuously via the bending beam, strain gages, carrier frequency amplifier to the friction torque recorder. A sodium hydraulic damper attached to the bending beam had to be incorporated to suppress measuring system vibration generated by friction variations. The shaft drive mechanism outside the sodium vessel is of conventional design and consists of a variable speed DC-motor, an overload clutch and a belt drive, capable for shaft speeds between 20 and 1000 rpm. For disassembly of the test bearings the sodium has to be drained, the facility cooled down to less than  $50^\circ \text{C}$  and the test fixture removed.

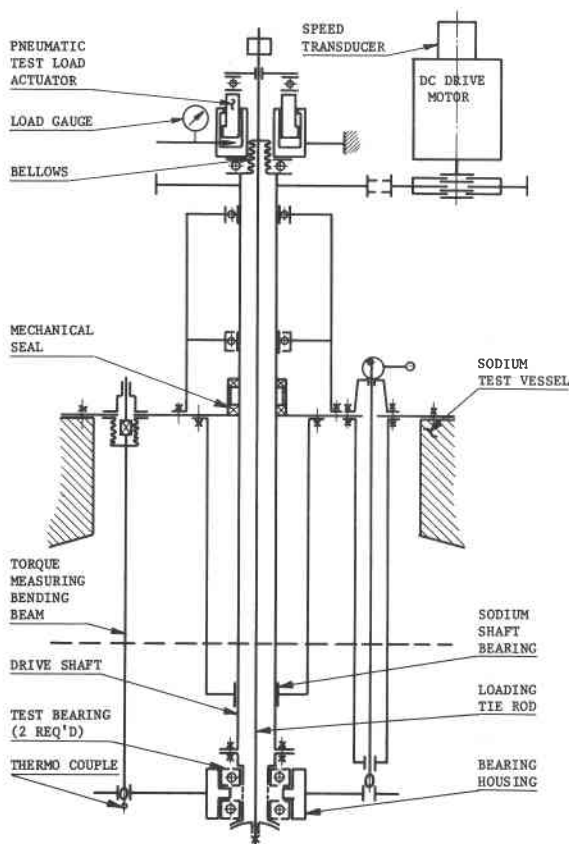


Fig. 3 - Ball Bearing Test Facility (Scheme)

## BALL BEARING TEST PROCEDURE

A total of 18 tests, the summary data of which are listed in Tab.III, have been performed so far, using throughout a couple of ISO-size 6207 ball bearings in duplex arrangement. The tests can be divided into two series: the phase 1 tests no.1 through 13, constituting material screening tests with ball bearings out of five different materials exposed to nominally uniform operating conditions, the so-called standard conditions, for a preset test duration of  $0.2 \cdot 10^6$  revolutions (3000 N axial load, 200 rpm speed,  $400^\circ \text{C}$  sodium temperature,  $< 10 - 20$  ppm oxygen concentration). In the phase 2 tests no. 14 through 19 and following, ball bearings out of the most promising materials from phase 1, which proved to be the tungsten carbide/cobalt cermet, are tested under various conditions (i.e. 1800-5000N axial load, 200 -500 rpm speed, temperature variation  $300 - 500^\circ \text{C}$  being planned) till the end of life. Several interruptions for intermediate inspections were made.

In the course of one test run, i.e. between two bearing examinations, the following procedure steps can be distinguished with respect to chemical, mechanical and thermal bearing conditions: (1) preparation and installation of the unlubricated bearing assembly, (2) attachment of the fixture to the argon-flushed test vessel at room temperature, (3) preheating of the apparatus to approx.  $200^\circ \text{C}$  within one hour, (4) fill with sodium and obtain test temperature within approx. one hour under sodium circulation, (5) purification at test temperature for at least 4 hours and stop sodium circulation, (6) apply speed and load and run test, (7) drain sodium to storage tank after electrical heater shut-off, (8) cool down system to below  $50^\circ \text{C}$  within approx. 40 hours and disassemble test bearings, (9) clean bearings with water.

During the test period, step 6, the continuous friction torque recording in combination with noise observation proved to be a useful means for a qualitative judgement of the bearing performance. In addition, the axial approach of both inner rings as a result of wear was recorded in those experiments, where abrasion was substantial, i.e. basically in the phase 1 tests. The post test and intermediate examination respectively consisted of the microscopic investigation of the balls and races, the determination of the weight losses of all individual bearing parts and the repetition of the most important dimension control at selected samples by the vendor.

## BALL BEARING SCREENING TEST RESULTS

From the total of 12 screening tests with 5 different materials, performed in phase 1 under standard operating bearing conditions (Tab.III, tests No. 1-13) the following comparative test results with respect to wear, friction and surface damage can be summarized after a preset test duration of  $0.2 \cdot 10^6$  revs. More detailed results are reported in ref.9.

INTERNATIONAL CONFERENCE ON LIQUID METAL TECHNOLOGY IN ENERGY PRODUCTION

Table III - SUMMARY TEST DATA

Test No.	Bearing Material	Axial Load (N)	Speed (rpm)	Temp. (°C)	Test Duration		Total Weight Loss (10 <sup>-3</sup> g)	Torque <sup>x</sup>		Intermediate Inspections at (10 <sup>6</sup> revs)	Test Ended by
					(Hrs)	(10 <sup>6</sup> revs)		Avg. (N-m)	Peak (N-m)		
1	DMo5	4700	210	410	18.3	0.23	394/1850	6	7	non	excessive noise
2	BG42	2800	208	410	16	0.2	1050/863	3	4.5	non	target
3	DMo5	2750	210	410	16	0.2	273/21	4	6	non	target
4	BG42	2800	210	403	16	0.2	673/85	2.5	6	non	target
5	DMo5	2700	210	409	16.3	0.205	23/95	4	5.5	non	target
6	GT10/20	2750	215	409	15.5	0.2	3.2/2.4	1.2	1.2	non	target
7	GT10/20	2850	206	405	16.2	0.2	0.3/2.3	1.2	1.2	non	target
8	Virium11/12	2770	211	402	7.7	0.097	xx	3	10	non	Ball rupture
10	Virium11/12	2930	210	412	10.3	0.130	22/75	2	5	non	excessive noise
11	WF13.5	2900	218	410	15.2	0.2	24/17	1.5	2.5	non	target
12	WF13.5	2870	218	405	15.2	0.2	26/11	1.5	2.5	non	target
13	Virium11/12	2930	227	408	14.6	0.2	283/493	xx	xx	non	target
14	GT10/20	3080	216	405	308.4	4.0	7.4/7.0	1.0	1.2	0.2,0.4,0.8,1.6,3.2	noise, spalling
15	GT10/20	3140	504†	400	69.5	1.83	5.0/1.8‡	0.5	1.1	0.2,0.4,0.8,1.6	rupture
16	GT10/20	5030	203	400	96.6	1.174	6.1/6.6‡	1.5	2.0	0.2,0.4,0.8	rupture
17	GT10/20	5030	503†	400	56.1	1.11	12.6/14.0	1.5	2.0	0.2,0.4,0.8	noise, spalling
18	GT10/20	1930	500	395	44.7	1.34	19.5/507	1.2	1.5	non	noise, wear
19	BG42/GT10	3200	206	398	17	0.21	26.2/0.3	1.8	2	non	noise, wear

<sup>x</sup> Torque is measured for a bearing couple  
<sup>xx</sup> No measurement  
 † 200 rpm during the first 0.2 · 10<sup>6</sup> revs.  
 ‡ 200 rpm during the first 0.4 · 10<sup>6</sup> revs.  
 § Value from the last intermediate inspection

Weight Loss and Wear Rate

A comparison of the weight losses for each of the four cageless 6207 ball bearings tested in the five material groups is shown in Fig.4. Looking at the average weight loss within one material group the following results are obtained:

- The slightest weight loss, i.e. approx. 2 mg per bearing, is evidenced by the tungsten-carbide-cobalt bearings (GT 10/20).
- The weight loss of the ferro-titanit bearings (WF13.5) is also relatively small, but exceeds the former one by about one order of magnitude.
- The most severe damage is exhibited by the BG 42 and DMo5 steel bearings as well as by the stellite bearings amounting to 668, 98 and 218 mg weight loss respectively.

If the weight loss per bearing is related to the total distance traveled by each ball against the inner and the outer race and to the normal contact load between balls and races, as proposed by T.Uga et al. (5), a specific wear rate is defined, analogue to the definition often used in sliding wear studies.

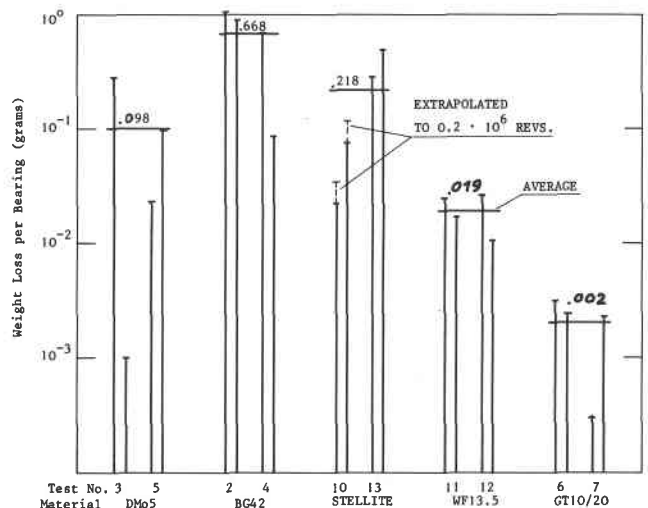


Fig. 4 - Total Weight Loss per Bearing after Material Screening Tests in Sodium for the five Materials tested (400 °C, 200 rpm, 3000 N axial Load, 0.2 · 10<sup>6</sup> Revolutions)



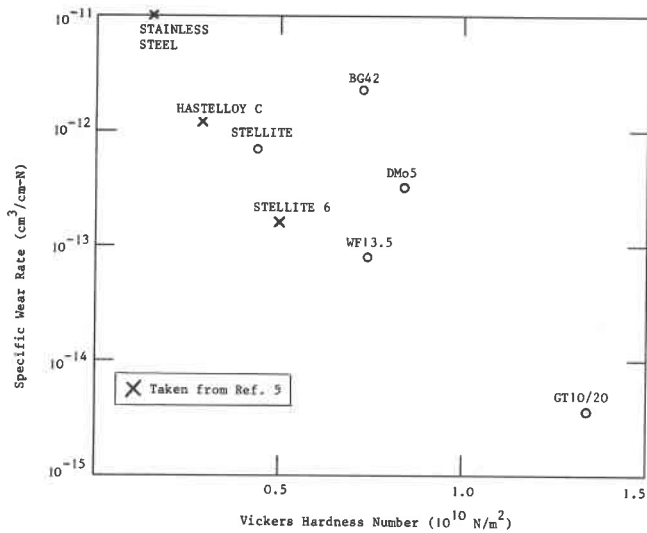


Fig. 5 - Specific Wear Rate vs. Hardness Number for Ball Bearings out of different Materials tested in Sodium

Plotting these specific wear rates versus the pertaining material hardness numbers one finds a very strong decrease of wear rate with increasing hardness as shown in Fig.5. For comparison, the results published in ref.5 for Stainless Steel, Hastelloy C and Stellite are added and fit fairly well with the data reported herein.

Frictional Behavior

A qualitatively similar material relation as was noted for the wear was also found for the friction torque. In general, the friction torque revealed to be of irregular alternating nature, with the fluctuations and vibrations becoming intensified with increasing roughness of the mating surfaces. This is due to the fact, that the friction torque for one bearing is generated by the rolling motion of 16 balls with 32 contact spots, where a permanent load redistribution and a temporal and local roughness change occurs. Thus, a combination of random vibrations with high frequencies (> 10 Hz), periodic oscillations with frequencies of the order of shaft speed and long term fluctuations

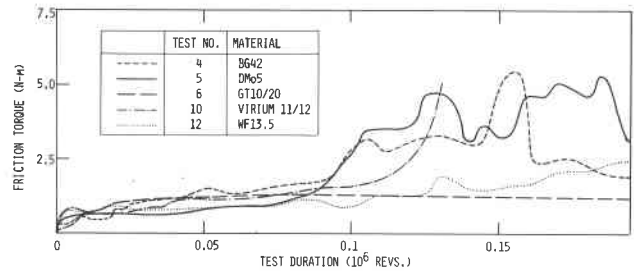


Fig. 6 - Friction Torque for Bearing Couples out of five different Materials vs. Test Duration in Sodium (400 °C, 200 rpm, 3000 N axial Load)

are observed. In general, the friction torque is poorly reproducible and no quantitative correlation between friction and surface roughness was found, however a qualitative judgement of the bearing condition is possible, as will be shown in Fig.6.

For each material investigated an initial breaking-in period is observed, in which the friction torque rises from a low, unmeasurable value to a quasi stationary value of about 0.4 to 0.6 N-m per bearing. In the case of the tungsten/cobalt alloy this value is preserved for the rest of the test period, whereas for the remaining four materials more or less severe friction torque fluctuations develop at about 10<sup>5</sup> revs., indicating growing surface damage. The above mentioned stationary friction torque of 0.4 to 0.6 N-m corresponds to a friction number  $\mu \approx 0.008$  to 0.012, which is by a factor of approx. 10 higher than the friction number for ball bearings under well lubricated conditions. The maximum friction number obtained for steel and stellite bearings in advanced roughened conditions as described below amounts up to  $\mu \approx 0.06$ .

Surface Damage Phenomena

Examples for typical wear tracks on the ball surfaces are shown in Fig.7 for the five materials investigated in the screening tests. Except for the tungsten/cobalt alloy, there are two different types of damages visible at a twentyfold microscopic magnification: (1) equatorial wear tracks within a limited belt zone generated by ball-to-ball friction and (2) overall surface roughness created partly by the ball-to-ring micro slippage and, to an unknown

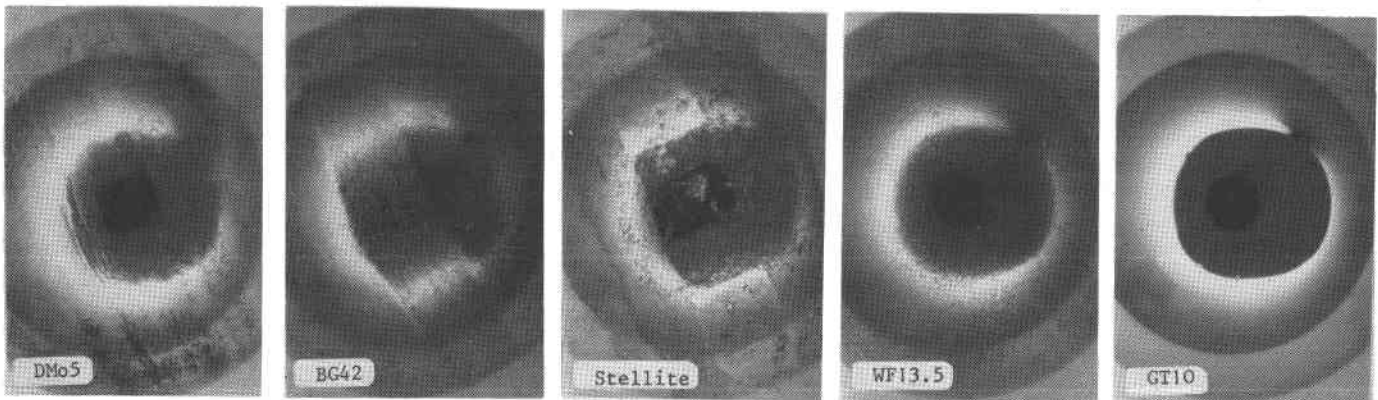


Fig. 7 - Typical Wear Tracks on Balls after Material Screening Tests in Sodium, showing the good condition of the WC-Co Balls (GT10). Test Conditions: 400 °C, 200 rpm, 3000 N axial Load, 0.2 · 10<sup>6</sup> Revolutions.

extent, by corrosion effects. The first type of wear tracks indicates, that most of the balls (about 60 %) maintain a fixed rotation axis during an extended period of test duration. In some instances also two or three crossing belts are observed.

The roughness pattern of the ring races generally show a zone of excessive wear in the region of maximum Hertzian stress with a gradual roughness decrease towards the outer race zones. The degree of wear is alternating even for rings out of the same material, the affected width of the races ranging from 2.5 mm to the entire ring groove width. Again, the tungsten/cobalt alloy rings demonstrate an exceptional appearance, i.e. basically a polished surface, which will be discussed later. According to the degree of surface damage and the development of the friction torque during  $2 \cdot 10^5$  revs. the following life times in  $10^6$  revs. can be assigned to the bearings under standard test conditions (3000 N, 400 °C, 200 rpm): for steel (DMo5 and BG42) and stellite 0.1; for ferrotitanit 0.2 and for WC-Co  $\gg 0.2$  (see next paragraph).

From the ball bearing screening test results it can be concluded, that the tests run with bearings out of tool steel, stainless high speed steel and stellite underline the results obtained by other authors with similar materials<sup>(3,5,7)</sup>. The wear resistance of the WC-Co bearings exceeds that of all the other bearings tested here by far. WC-Co was, therefore, selected for parametric studies reported below.

PARAMETRIC TESTS WITH WC-Co BALL BEARINGS

The parametric studies with 6207 type ball bearings are focused on the variation of the main operating conditions, e.g. axial load, speed and sodium temperature. So far five test series have been performed, using various axial loads and speeds at a constant sodium temperature of 400 °C (see Tab.III, tests No. 14 through 18). All tests were run until a discernable bearing failure was obtained and one important result is that the terminating failure mode is given by fatigue of the superhard alloy in contrast to excessive

wear or binding which was found with less hard materials in the screening tests and by other authors.

Surface Damage Phenomena and Bearing Life

One problem is to assess life terminating criteria, which is complicated by the fact that fatigue usually occurs with large scattering and no statistical results from sodium tests are available. For determination of the life time numbers reported below a combination of torque measurement, failure mapping during intermediate inspections and noise judgement has been applied. In order to illustrate this method the sequence of incipient failure modes along with the accompanying phenomena, typical for these tests, will be described by means of test No. 14.

After only  $0.2 \cdot 10^6$  revolutions polished tracks of the balls had developed on the ring grooves, contrasting from the original ground surface. These polished tracks have a width of approx. 2 to 2.5 mm depending on conformity and load and remain essentially unchanged in shape during the life time. Close to the middle of the polished zones several roughened lines or narrow bands were found, which partially disappeared with increasing test duration. Fig.8 shows a sequence of the outer ring groove surface indicating the smoothing effect (dark area) and the extinction of incipient binding marks (light horizontal lines). These marks are not considered to be of fatigue nature, they rather represent minor abrasion, which does not affect the bearing performance with respect to friction torque, noise or clearance in a measurable way. Thus they are inefficient as terminating criteria. At  $4 \cdot 10^6$  revs. another type of failure was observed for the first time in test No. 14: Each of the four rings showed single spalls of approx. 0.1 to 0.4 mm diameter scattered over the entire polished track, indicating material fatigue. A similar behavior was exhibited by the balls. A few local galls with less than 0.2 mm diameter, which had been observed at some individual balls in an early test stage, did not propagate significantly up to  $3.2 \cdot 10^6$  revs. They are considered to be material defects and can be subdivided into three

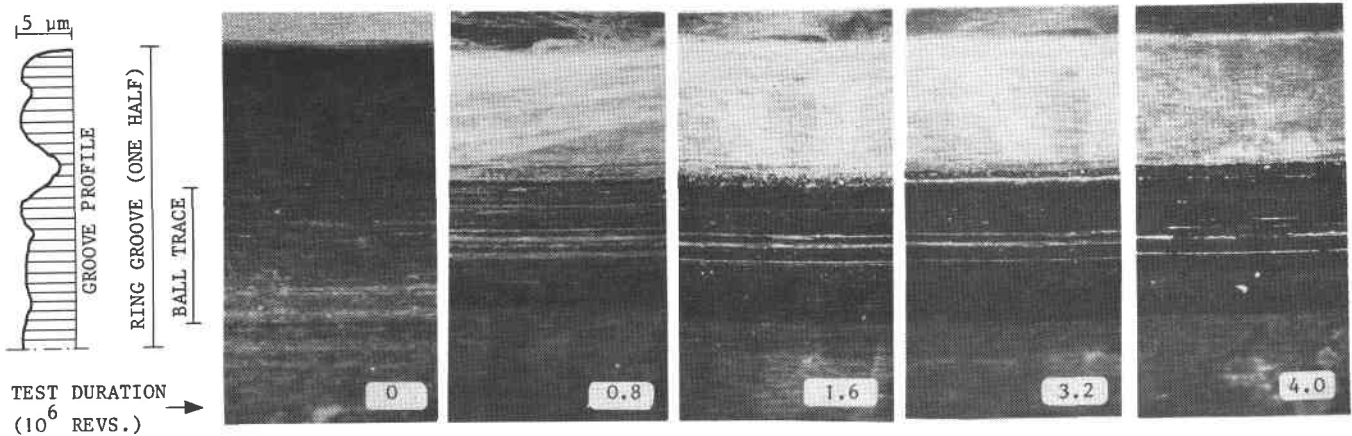


Fig. 8 - Typical pattern on an outer Ring Groove of a 6207 Type WC-Co Ball Bearing after different Test Durations in Sodium, showing increasing Polishing (dark Area) of the ground Surface. Note incipient Spalls after  $4 \cdot 10^6$  Revolutions (400 °C, 200 rpm, 3000 N axial Load).

INTERNATIONAL CONFERENCE ON LIQUID METAL TECHNOLOGY IN ENERGY PRODUCTION

categories: (1) single surface sores (rough spots) caused by local porous zones, (2) more or less numerous tiny pittings (<0.1 mm), which in some instances also were observed in the as fabricated condition and (3) single craters or collapsed pores (Fig.9a), which obviously are caused by material voids in the surface region (up to approx. 0.2 mm size). Some characteristic defects of these have been recognized at every intermediate inspection and were found not to act as nuclei for failure propagation. With advanced test duration a fourth category of defects emerged and grew in frequency and size: scale type pittings of up to 0.5 mm diameter and approx. 0.05 mm depth, typical for fatigue damage (Fig.9b). The rate of this type of pittings versus test duration is illustrated in Fig.10, where the relative number of balls, having one or several pittings, from a total of 32 balls per test run is plotted for the tests No. 14, 15, 16 and 17. As can be seen from tests 14, 16 and 17 the number of damaged balls and also the pitting frequency at a particular ball (not shown) increases dramatically towards the end of the test. This is accompanied by aggravated bearing noise and irregular fluctuations in friction torque. It is expected, that an operation beyond this state will lead to a rapid complete damage either by excessive wear or rupture. Thus, increasing noise and fluctuating friction torque signal the end of life, complemented by failure mapping after disassembly.

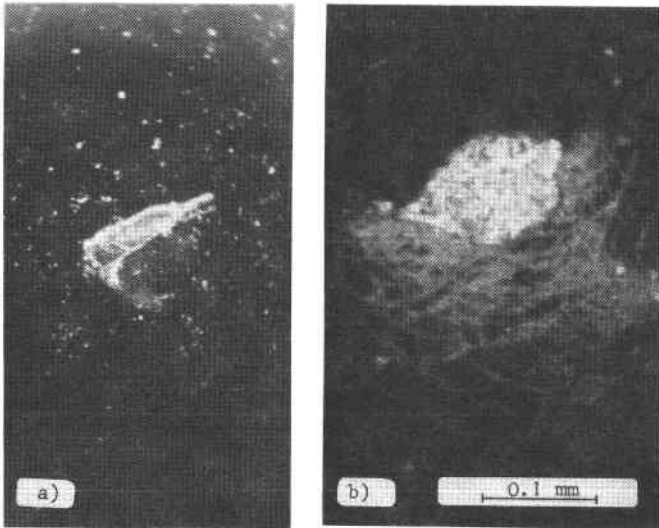


Fig. 9 - Examples for Surface Defects on WC-Co Balls after Sodium Testing (Test No. 14): a) Collapsed Pore, b) Scale type Pitting due to Fatigue

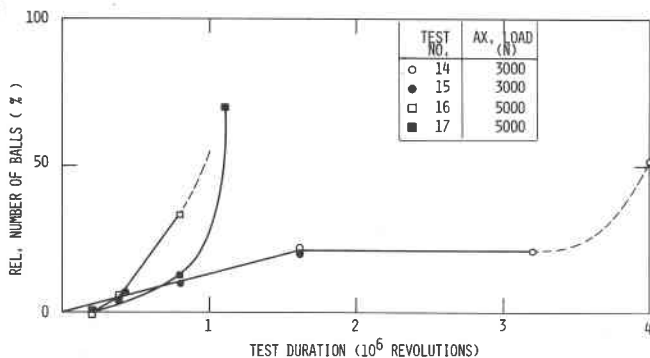


Fig. 10 - Relative Number of balls occupied with medium size Pittings (up to 0.3 mm dia.) vs. Test Duration

Table IV - NOMINAL TEST CONDITIONS AND BEARING LIFE FOR WC-CO BALL BEARINGS IN SODIUM

Test No.	Nominal Test Conditions			Life (10 <sup>6</sup> revs)
	Axial Load (N)	Speed (min <sup>-1</sup> )	Temperature (°C)	
14	3000	200	400	4.0-4.2
15	3000	500	400	1.8- ?
16	5000	200	400	1.1
17	5000	500	400	1.1-1.2
18	2000	500	400	1.2-1.3
19*	3000	200	400	0.15-0.2

\* Different Material Combination: Rings BG42, Balls WC-Co

On the basis of these findings the bearing life listed in Tab.IV can be assigned in the parametric tests performed so far. It should be noted, that the degree of damage of both bearings tested at a time was somewhat different. This shall be indicated by the estimated range given in Tab.IV. Due to the different conformity of the individual ball-to-groove contact areas the Hertzian stress varies considerably for a given axial load. The maximum stress level for each particular ring, calculated by the aid of Hertzian theory using the actual new condition groove radii is listed in Tab.V. In a life-stress-plane the uncertainty ranges for the life (Tab.IV) and for the Hertzian stress in each test form rectangles, which are plotted in Fig.11 for the parameter tests no. 14 to 18 in a double logarithmic scale. These rectangles, with one exception, fit very well a straight line with a slope of -9.2, which is in good agreement with the conventional load rating system. This gives a life(L)-load(F) relationship of the form  $L \sim F^{-p}$ , with  $p = 3$  for ball bearings. Substitution of the load by the Hertzian stress (H) for a given bearing leads to  $L \sim H^{-9}$ , which is very close to the test results.

Table V - WIDTH OF BALL TRACKS, CONTACT ANGLE, HERTZIAN STRESS FOR WC-CO BALL BEARINGS TESTED IN SODIUM

Test No.	Bearing No.	Width of Ball Track		Contact Angle (°)	max. Hertzian Stress IR/OR (10 <sup>9</sup> N/m <sup>2</sup> )
		Measured IR/OR (mm)	Calculated IR/OR (mm)		
14	2/2C	2.5/2.0	1.88/1.59	18	3.6/3.2
	5/5C	2.5/2.0	1.99/1.55	19.5	3.4/3.2
15	1/1C	2.15/1.5	1.89/1.54	18	3.6/3.3
	4/4C	2.2/1.6	1.96/1.76	16	3.8/3.3
16	6/6C	2.2/2.15	1.89/1.72	21	4.3/4.2
	7/7C	2.1/2.5	1.97/1.99	21.5	4.1/3.8
17	8/8C	2.2/2.2	1.88/1.76	22	4.1/3.6
	9/9C	2.0/2.7	1.88/1.97	22	4.1/3.5
18	10/10C	2.7/2.5	1.44/1.76	~ 21	3.0/2.6
	11/11C	4.5/3.8	1.34/1.21	~ 26	2.8/2.5

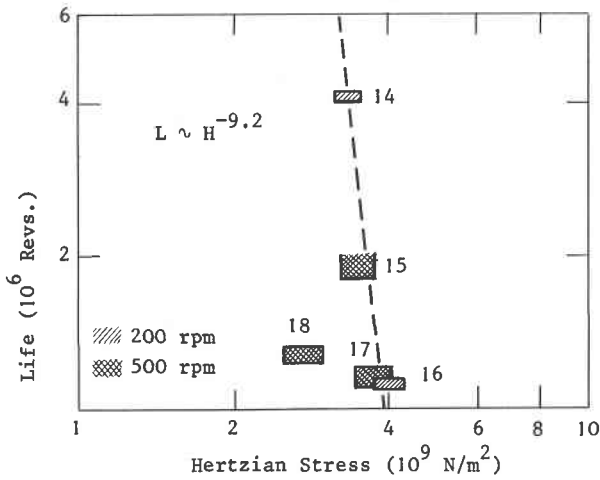


Fig. 11 - Life Time vs. Hertzian Stress for WC-Co Ball Bearings tested in Sodium at 400°C (Numbers refer to Test-No.)

Friction and Wear

The weight loss per bearing as evaluated at the intermediate inspections is shown in Fig.12 for the tests with 3000 and 5000 N axial load. A linear relationship between weight loss and test duration is demonstrated by the low load runs within a fairly narrow band, resulting in an average rate of  $1.3 \cdot 10^{-9}$  g/rev. In the high load runs a considerable scattering of the measurements is found, leading to a weight loss per bearing rate of approx.  $(20 \pm 6) \cdot 10^{-9}$  g/rev. during an initial break-in phase and then leveling off to a value comparable to the former one. This behavior is in agreement with the width of the visible ball tracks in the ring grooves, which basically also increase during the first  $0.4 \cdot 10^6$  revs. and then remain nearly unchanged. These quasi steady state widths of the ball tracks identified by the polished zones (Fig.8) are listed in Tab.V along with the corresponding calculated values applying the Hertzian theory. It is shown that the measured data are on an average of approx. 16 % for the inner rings and 20 % for the outer rings higher than the calculated values. Taking into account the uncertainties in measurements and possibly minor lateral shift of the tracks during the life time towards increasing con-

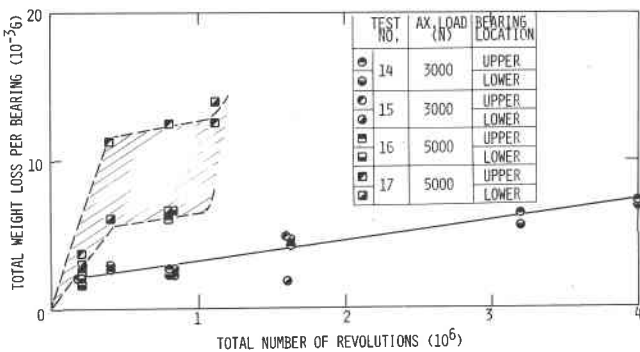


Fig. 12 - Total Weight Loss per Bearing vs. Test Duration for 6207 Ball Bearings tested in 400°C Sodium under various axial Loads

tact angles, the test results confirm the effectiveness of the Hertzian theory in this case.

The friction recorder essentially revealed the phenomena described for the screening test, i.e. an initial rise during a few thousand revolutions to an almost stationary value, which lasts for the major part of the bearing life. Towards the end of life increasing scattering and fluctuations develop, amounting up to approx.  $\pm 50\%$  of the average friction torque. During the stationary period the friction torque is proportional to the axial load, resulting in a friction number  $\mu \approx 0.01 \pm 0.005$ .

CONCLUSIONS

The life time of the WC-Co ball bearings tested at medium speed in sodium is terminated by fatigue due to the high hardness of this superalloy, in contrast to the other less hard bearing materials chosen for screening tests, where wear was found to be dominant. There seems to exist a similar life-load relationship as it is known from the conventional ball bearing technology, but more tests are necessary in order to establish general rules. Even though the load capacity amounts to only a few percent of the values listed for normal operating conditions, it seems to be attractive for intermittently operated equipment in sodium. An axial load of 5000 N which is equivalent to a max. Hertzian stress of approx.  $4 \cdot 10^9$  N/m<sup>2</sup>, seems to be the upper limit. There is no positive evidence of an influence of speed in the range between 200 and 500 rpm on life time, but the relatively short life in test no. 18 with low load and high speed requires additional research in this respect. The cageless design proved to be serviceable, omitting cage material and binding problems.

REFERENCES

[1] W.J. Greenert, H.M. Rawlings: "Basic Information on the Bearing Properties of Various Materials in Oil and Sodium-Potassium Alloy", United States Naval Engineering Experimental Station, Annapolis, Md. Report No. 090014D, (April 1956)

[2] W. Markert jr., K. Ferguson: "Use of Rolling Contact Bearings in Low Viscosity Liquid Metal Lubricants", *Journal of Am. Soc. of Lubrication Eng.*, (May 1957)

[3] S. Jwai et.al.: "Testing of Feasibility of Ball Bearings in Liquid Sodium Environments", ANL-7520, (1968)

[4] P.H. Delves, W. Rodwell: "Mechanism in Sodium", IAEA-SM-130/14, p. 757, (1970)

[5] Takea Uga et.al.: "Friction and Wear of Ball Bearings in Liquid Sodium", *Journal of Nucl. Science and Technology*, 8 (1971)

[6] W.E. Jamison et.al.: "Development of High Temperature Rolling Bearings for Operation in Liquid Sodium", Interim Final Report No. 1, NYO-4117-9, (1972)

[7] W.E. Jamison, J.J. Mc Veigh: "Ball Bearings for High Temperature Liquid sodium", *ASLE Transactions*, Volume 18, No. 1, p. 5-14

[8] K. Kleefeldt: "Über die Verwendung von Wälzlagern in der Natriumtechnik", *KFK-Nachrichten*, 7. Jahrgang Nr. 2/75, p. 5-13, (1975)

[9] K. Kleefeldt, G. Gering: "Reibung und Verschleiß von Kugellagern in flüssigem Natrium, 1. Teil: Vergleichsversuche zur Werkstoffauswahl", *KFK-Bericht Nr. 2157* (Juli 1975)

# INTERNATIONAL CONFERENCE ON LIQUID METAL TECHNOLOGY IN ENERGY PRODUCTION

## FRICITION AND WEAR BEHAVIOR OF COLMONOY AND STELLITE ALLOYS IN SODIUM ENVIRONMENT

S. Kanoh

S. Mizobuchi

H. Atsumo

Power Reactor and Nuclear Fuel Development Corporation (PRNFDC)

Oarai, Ibaraki, Japan

### ABSTRACT

We are carrying out a series of experiments in sodium environment for the research and development of friction and wear resistant material used for the sliding components of sodium cooled fast breeder reactor. The present study relates to the friction and wear characteristics of nickel-base alloy "Colmonoy" and cobalt-base alloy "Stellite" with respect to temperature, load, sliding velocity, sliding mode and sodium flushing. Also we compare the friction behavior of these alloys in sodium with that in argon.

### INTRODUCTION

Ordinary lubricant prevents the metal surfaces from mutual direct contact to improve their friction and wear resistant characteristics by producing adsorption layer or chemical reaction film (oxidation film, etc.) on metal surfaces. On the other hand, liquid sodium, i.e. coolant for the fast breeder reactor, provides thin lubricating layer because of lower viscosity and damages or reduces the reaction film on metal surfaces because it is used in high temperature and has active chemistry, resulting in the direct contact of metal surfaces. To prevent components from the deterioration of performance and the shortening of life, the friction and wear resistant materials should be used for the sliding components of the fast breeder reactor. PRNFDC is carrying out the friction and wear tests in sodium environment to obtain design information for these components. The present report describes Colmonoy and Stellite alloys which are generally used as the friction and wear resistant materials. The friction coefficients and wear rates of these alloys were determined with respect to sodium temperature, load (contact pressure), sliding mode, sliding velocity, time and sodium flushing. Also the tests in argon environment were carried out since some sliding components existed in cover gas argon of the fast breeder reactor and these results were compared with those in sodium.

### MATERIALS INVESTIGATED

Table 1 shows the chemical composition of materials investigated. All of Colmonoy and Stellite alloys were overlaid on Type 304SS or Type 316SS by the oxy-acetylene gas weld using the welding rod of 5 mm dia. and finished mechanically to the overlayer thickness of final 2 mm and the surface roughness of  $0.4 \sim 1 \mu\text{m}$ .

### EXPERIMENTAL METHODS

Fig. 1 shows the Self-Welding & Wearing Test Loop made of Type 316SS. During the test, a fixed amount of sodium controlled the purity by cold trap was supplied to the test section. Fig. 2 shows two test sections (SW-1 and SW-2). Three units of one-directional continuous slide equipment are installed in SW-1 and 2 units of 120 degrees oscillating slide one in SW-2. A pair of test pieces of ring and disc configuration is mounted in each equipment. The size of the sliding surface is 33 mm inside diameter and 37 mm outside diameter.

In SW-1, the friction test and wear test were carried out. In the friction test, the static friction coefficient  $\mu_s$  under each load

was calculated from the initial torque obtained through torque meter by manually rotating the test piece at the rotational side while increasing stepwise dead weight. In the wear test the kinetic friction coefficient  $\mu_k$  under each load was calculated from the average sliding torque for 15 minutes by increasing the load stepwise every 15 minutes while rotating the test piece at the rotational side continuously in one direction by a drive motor. At the same time the wear depth  $W_D$  during the test was obtained from the displacement of differential transformer. Some combinations of materials were slid for 10 hours under the contact pressure of  $1 \text{ kg/mm}^2$  at the sliding velocity of  $3.6 \text{ cm/sec}$ .

In SW-2, on the other hand,  $\mu_k$  was calculated from the sliding torque at the angular position of 60 degrees by oscillating the test piece at the rotational side by 120 degrees with rotary actuator while increasing the load stepwise by oil pressure. Table 2 shows the test conditions.

### RESULTS AND DISCUSSIONS

Fig. 3 shows the relation between  $\mu_s$  and sodium temperature obtained by SW-1. The higher the temperature became, the larger  $\mu_s$  of Stellite alloy became, but the smaller  $\mu_s$  of Colmonoy alloy became. But  $\mu_s$  of Colmonoy alloy remained constant or became larger as the temperature was raised when the mating material was Type 304SS. This shows that the condition of sliding surface was varied according to the temperature. The asterisk in the figure is  $\mu_s$  obtained after the measurement of  $\mu_k$ , its value having been higher than that of  $\mu_s$  obtained prior to the measurement of  $\mu_k$  because the metal surface was made rough by the continuous sliding.

Fig. 4 shows the relation between  $\mu_k$  and load obtained by SW-1. Each  $\mu_k$  in  $450^\circ\text{C}$  sodium was below 0.5 and approximately constant under the load of  $100 \sim 400 \text{ kg}$ . On the other hand,  $\mu_k$  in room temperature argon varied remarkably with load, being higher than that in sodium.

The roughness of sliding surface after the measurement of  $\mu_k$  was  $1 \sim 2 \mu\text{m}$  in  $450^\circ\text{C}$  sodium, whereas the surface was made remarkably rough in room temperature argon, indicating the value of  $10 \sim 20 \mu\text{m}$ .

Also in observation of the cross-sectional microstructure of sliding regions, they were hardly subject to the plastic deformation in  $450^\circ\text{C}$  sodium, while in room temperature argon were subject to the plastic deformation up to the depth of  $30 \sim 40 \mu\text{m}$ .

Since the friction test, different from the wear test, generated little friction heat, and the oxidation film produced in air was not damaged in argon,  $\mu_s$  in argon was below 0.3, remaining constant with load. The  $\mu_s$  in  $450^\circ\text{C}$  sodium was also below 0.3, not showing the dependence upon load.

Continuous sliding tests were carried out for 10 hours under the contact pressure of  $1 \text{ kg/mm}^2$  at the sliding velocity of  $3.6 \text{ cm/sec}$  in  $450^\circ\text{C}$  and  $540^\circ\text{C}$  sodium. The  $\mu_k$  value did not show so large variation with respect to time. The  $\mu_k$  values of Colmonoy

alloys were reduced by flushing in 540°C sodium on the way of the continuous sliding. Stellite alloys and Type 304SS did not clearly show this effect.

Fig. 5 shows  $\mu_s$  and  $\mu_k$  obtained by SW-1 with various material combinations in room temperature argon and 450°C sodium environments. The  $\mu_s$  in sodium was higher than that in argon since sodium temperature was high and the oxidation film produced in air was damaged in sodium. On the other hand,  $\mu_k$  in argon was apt to be higher than that in sodium. This is due to the following reasons. The argon has much lower thermal conductivity than the sodium so that only little amount of friction heat can be removed and the temperature of sliding surface becomes higher, thereby the oxidation film produced in air is damaged. Next the sodium shows more excellent lubricating effect than the argon.

Also  $\mu_k$  was apt to be larger compared with  $\mu_s$ . In particular, when the mating material was Type 304SS,  $\mu_k$  became still larger. This is because sliding surfaces were roughened by continuous sliding. This effect is particularly remarkable in Type 304SS which has lower high temperature strength than Colmonoy and Stellite alloys.

The values of  $\mu_s$  and  $\mu_k$  of Colmonoy No.5 among the material combinations tested by SW-1 showed the lowest values in both argon and sodium environments.

To investigate the effect of the sliding velocity on  $\mu_k$ , the test in 450°C sodium was carried out at the sliding velocity of 0.18 ~ 72 cm/sec under the contact pressure of 1 kg/mm<sup>2</sup> with respect to the various combinations of Colmonoy No.4, Stellite No.6 and Type 304SS. The  $\mu_k$  varied greatly at the sliding velocity less than 0.5 cm/sec, but it showed approximately constant value at the sliding velocity of 0.5 ~ 7.2 cm/sec. As the sliding velocity becomes higher, the sliding surface is roughened so that the variation of  $\mu_k$  is thought to become larger until the seizure of contact surface may take place.

Fig. 6 shows the relation between load and wear rate. The ordinate represents the integral value of wear depth till each load that was increased stepwise at the interval of 15 minutes. Even the combinations of hard facing alloys showed high wear rates in argon. The wear rates in 540°C sodium were less than those in argon. The wear depth of Colmonoy No.5 could not be detected at all in 540°C sodium. The wear rates in 450°C sodium were further less and other hard facing alloys except for Colmonoy No.6 did not wear at all. When the mating material was Type 304SS, it showed higher wear rate than the combination of hard facing alloys each other.

Fig. 7 shows an example of the relation between friction torque and rotational angle obtained by SW-2. The value of torque shows reverse sign as the reciprocation of test piece. In Fig. 7, is shown the results of the test piece which was reciprocated 3 times. the gradual increase of torque together with reciprocation is thought due to the roughening of sliding surface.

The  $\mu_k$  of Colmonoy alloy was reduced by flushing in 540°C sodium for 24 hours, while that of Stellite alloy was increased. Similar phenomenon was also observed by SW-1.

Fig. 8 shows the relation between load and  $\mu_k$  of Colmonoy and Stellite alloys obtained by SW-2 in different environments. A remarkable difference was observed between the friction behavior of Colmonoy and Stellite alloys. The  $\mu_k$  of Colmonoy alloy in so-

dium was lower than those in argon and air. Also so much differences were not found between  $\mu_k$  in 280°C sodium and that in 540°C sodium, these values remaining constant with load. On the other hand,  $\mu_k$  of Stellite alloy in sodium remarkably varied according to temperature. The  $\mu_k$  of Stellite alloy in 540°C sodium (~ 1.0) was higher than those in argon and air, and varied together with load. The  $\mu_k$  of Stellite alloy in argon was apt to be lower than that of Colmonoy in argon.

Next the results of SW-1 and SW-2 having different sliding modes will be compared as follows. SW-2 showed higher values than SW-1 with respect to  $\mu_k$  under the contact pressure of 1 kg/mm<sup>2</sup> in both sodium and argon environments as shown in Fig. 5 and 8. Since the sliding surface plastically flows to the sliding direction, its asperity has directional property so that friction torque is increased by the interlocking effect of asperity when the sliding direction is reversed. For this reason  $\mu_k$  obtained by SW-2 with oscillating sliding is mainly thought to have been higher than that obtained by SW-1 with one-directional continuous sliding. Also the sliding surface obtained by SW-2 was more roughened in spite of lower sliding velocity and sliding path.

Finally the difference between the friction behavior of Colmonoy and Stellite alloys in sodium will be mentioned. As shown in Fig. 3 and 8, as the temperature was raised, the friction coefficients of Colmonoy alloys remained constant or were lower, and those of Stellite alloys were higher. Also the reduction of  $\mu_k$  by 540°C sodium flushing was more significant in Colmonoy alloys than Stellite alloys. When exposed to sodium, metallic material is generally subject to sodium corrosion. The higher the sodium temperature is, the more remarkable the effect of corrosion is. Hence, the lubricating effect of corrosion products on the surface of Colmonoy alloy is considered more significant than that of Stellite alloy.

## SUMMARY

- (1) As the sodium temperature is raised,  $\mu_k$  of Stellite alloy becomes higher, but  $\mu_k$  of Colmonoy alloy remains constant or is rather lower. In argon environment  $\mu_k$  of both alloys becomes higher as the argon temperature is raised.
- (2) The  $\mu_k$  of Colmonoy alloy becomes lower by 540°C sodium flushing. The  $\mu_k$  of Stellite alloy remains constant or is rather higher.
- (3) The dependence of  $\mu_s$  and  $\mu_k$  upon the load is low in sodium environment. In argon the dependence of  $\mu_s$  upon the load is not found, but  $\mu_k$  varies according to the load.
- (4) The dependence of  $\mu_k$  upon the sliding velocity is not found in sodium environment except for that in low velocity area.
- (5) The friction behavior is influenced by sliding mode. The  $\mu_k$  in oscillating sliding is higher than that in one-directional continuous sliding. Also in oscillating sliding the sliding surface is more roughened and the dependence of  $\mu_k$  upon the load is higher.
- (6) In sodium the values of  $\mu_s$  and  $\mu_k$  of Colmonoy alloy are apt to be lower than those of Stellite. Also these values of Colmonoy and Stellite alloy become higher when the mating material is Type 304SS.
- (7) The  $\mu_s$  is lower in argon than in sodium, while  $\mu_k$  is apt to be lower in sodium. The  $\mu_k$  of Stellite alloy in 540°C sodium, how-

**INTERNATIONAL CONFERENCE ON LIQUID METAL TECHNOLOGY IN ENERGY PRODUCTION**

ever, is higher than that in argon. Also the plastic deformation of sliding surface is more remarkable in argon than in sodium.

- (8) The wear rate is much higher in argon than that in sodium. Also the wear rate in 540°C sodium is higher than that in 450°C sodium. When the mating material is Type 304SS, the wear rate of Stellite or Colmonoy is higher than that in combination of Stellite and/or Colmonoy each other.

ACKNOWLEDGMENT

We express our thanks for the advice of Mr. R. Saito, manager of Sodium Engineering Division, Dr. K. Mochizuki, assistant manager of Fast Breeder Reactor Development Project and Mr. K. Yamamoto, senior engineer of the same Project in this study.

REFERENCES

- (1) Glaeser, W.A., "Wear and friction characteristics of structural materials in liquid sodium," Reactor Technol., vol.15, pp.1-10 (1972).
- (2) Johnson, R.N., et al., "Wear resistant coatings for reactor components in liquid sodium environments", J. Vac. Sci. Technol., vol.11, pp.759-764 (1974).
- (3) Wild, E. and Mack, K.J., "Tribology in the core of a sodium-cooled fast breeder reactor," Wear, vol.34, pp.331-340 (1975).

*Table - 1 Chemical Composition*

Material	Symbol	Chemical Composition (w/o)									
		C	Si	B	Fe	Cr	Ni	Co	W	Mo	Mn
Type 304 SS	304	0.06	0.59		Ba1	18.64	8.63				1.54
Type 316 SS	316	0.06	0.47		Ba1	16.58	10.76			2.15	1.00
Colmonoy No.2	C2	0.20	3.00	1.00	3.20	5.00	Ba1				
Colmonoy No.4	C4	0.40	3.00	2.00	3.20	10.00	Ba1				
Colmonoy No.5	C5	0.54	3.47	2.05	3.47	11.50	Ba1				
Colmonoy No.6	C6	0.75	4.25	3.00	4.75	13.50	Ba1				
Stellite No.1	S1	2.58	1.16		0.28	31.33		Ba1	12.49		
Stellite No.6	S6	1.04	1.17		0.27	28.65		Ba1	4.20		
Stellite No.12	S12	1.30	1.20		2.50	29.00		Ba1	8.00		

*Table - 2 Test Conditions*

Environment	Test Factor	SW-1	SW-2
Sodium	Sodium Temperature, (°C)	280, 450, 540	280, 540
	Cold Trap Temp. (°C)	200	200
	Sodium Flow Rate (ℓ/min)	4	4
	Load (kg)	max. 440 (Dead Weight)	max. 500 (Oil Pressure)
	Sliding Velocity(cm/sec)	max. 7.2	0.25
	Apparent Contact Area of Test Piece (cm <sup>2</sup> )	2.2	2.2
	Flushing Time (hrs)	24~72	24
Argon	Argon Temperature (°C)	Room Temperature	280, 540
	Argon Flow Rate (ℓ/min)	0	0.5
	Argon Purity (%)	>99.995	>99.999
	Load (kg)	max. 440 (Dead Weight)	max. 500 (Oil Pressure)
	Sliding Velocity(cm/sec)	3.6	0.25
Apparent Contact Area of Test Piece (cm <sup>2</sup> )	2.2	2.2	

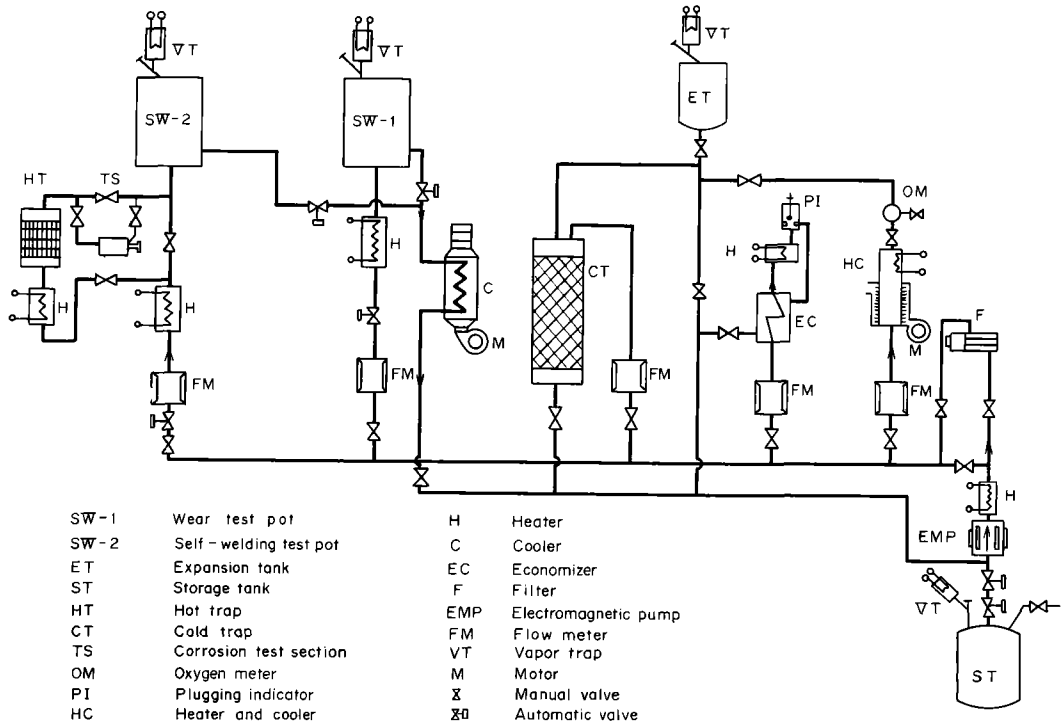


Fig. 1 Flow sheet of Self-Welding and Wearing Test Loop.

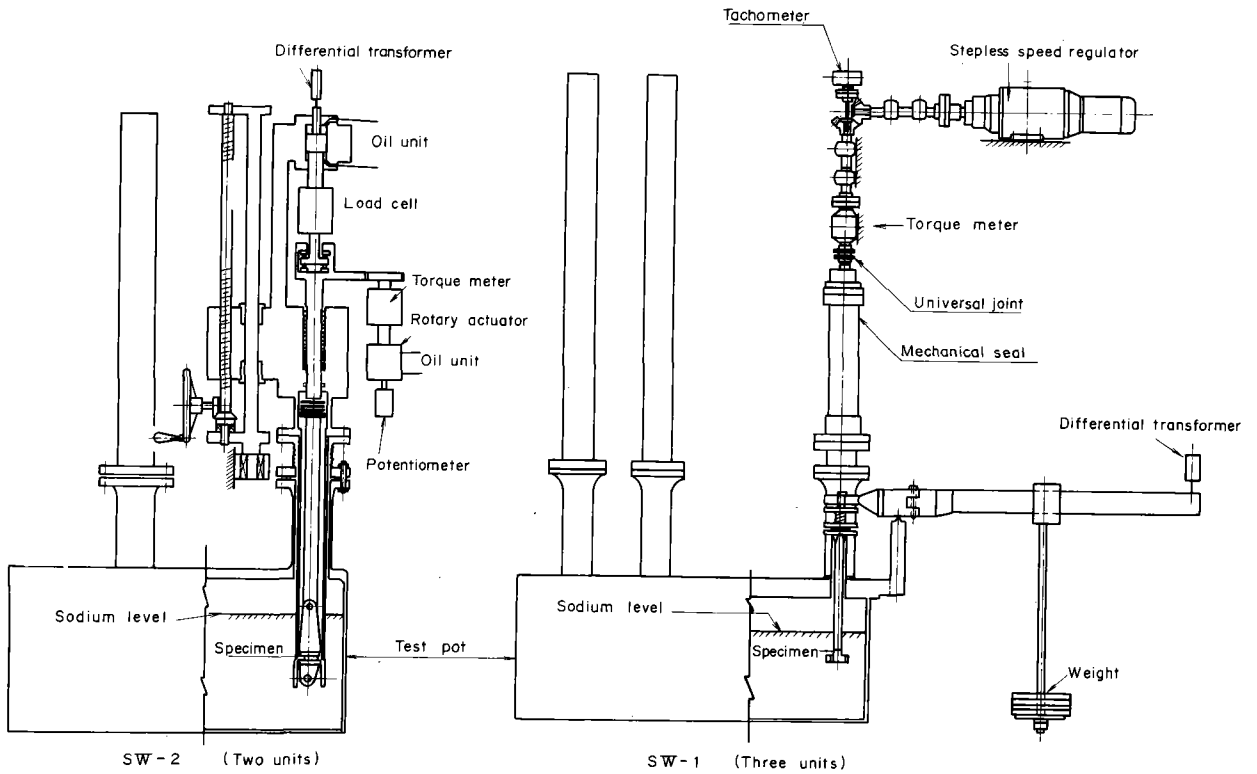


Fig. 2 Test section



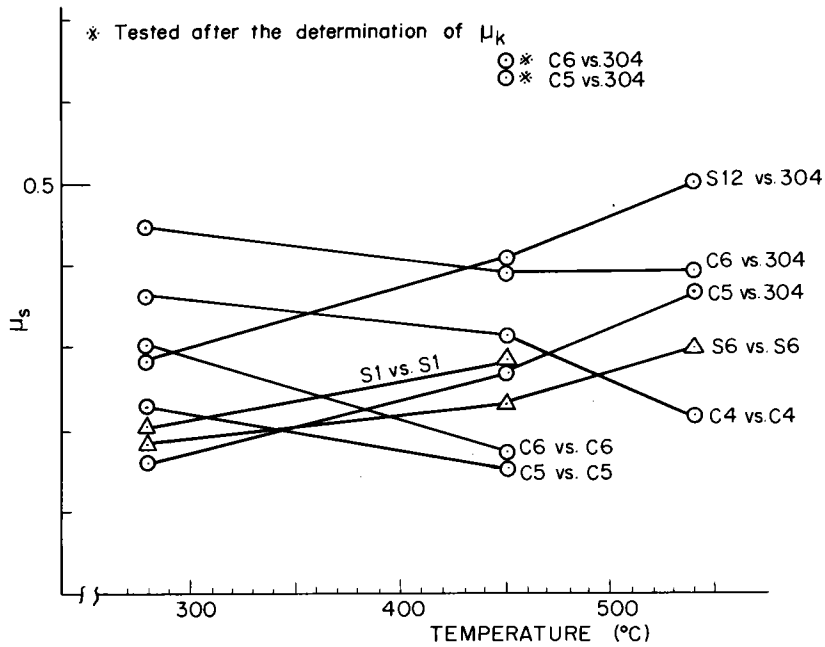


Fig. 3 Relation between  $\mu_s$  and sodium temperature under the contact pressure of 1 kg/mm<sup>2</sup> (SW-1).

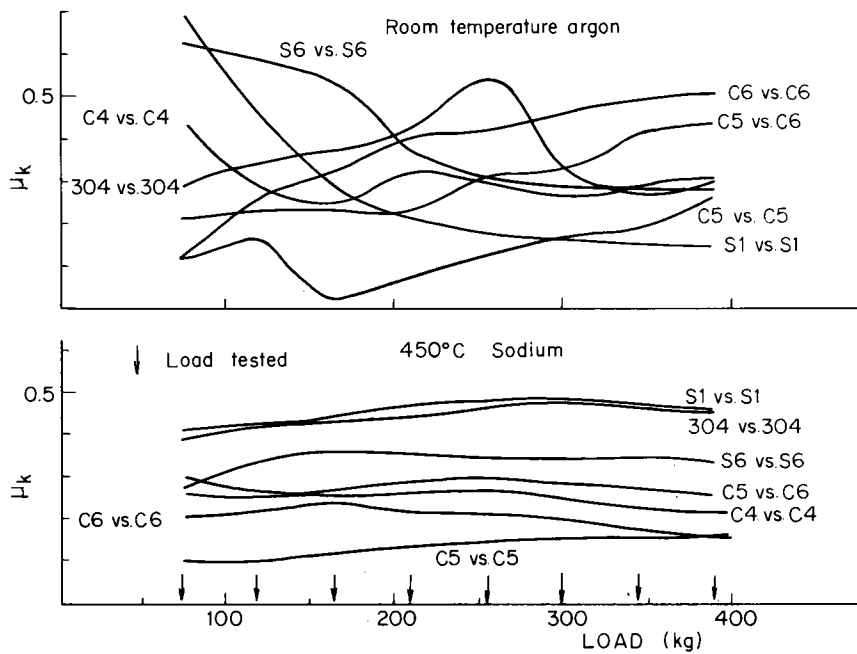


Fig. 4 Relation between  $\mu_k$  and load at the sliding velocity of 3.6 cm/sec in different environments. (SW-1).

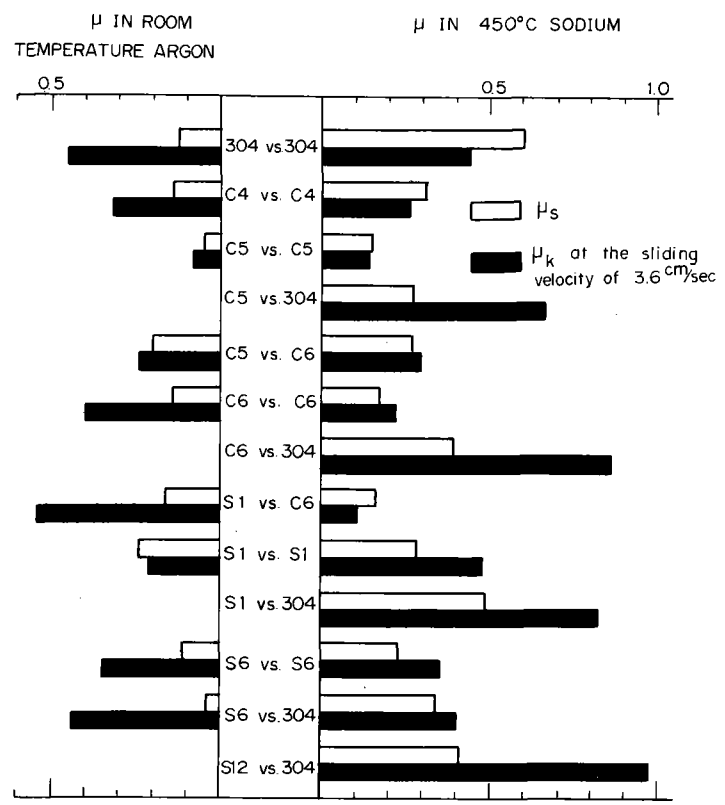


Fig. 5  $\mu_s$  and  $\mu_k$  under the contact pressure of  $1 \text{ kg/mm}^2$  in different environments (SW-1).

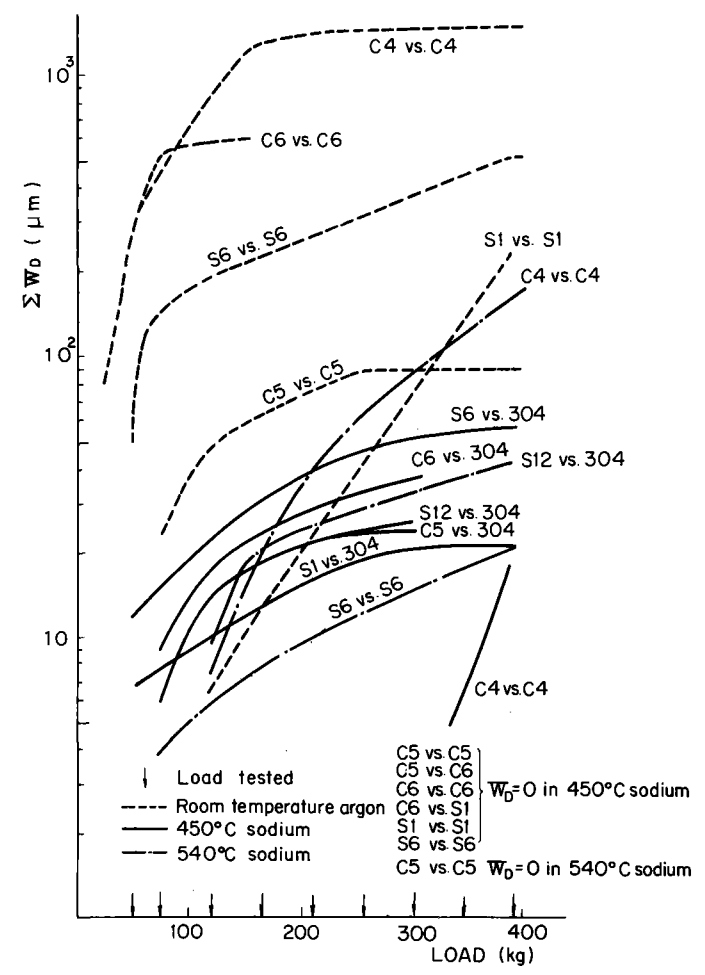


Fig. 6 Relation between  $\Sigma W_D$  and load at the sliding velocity of  $3.6 \text{ cm/sec}$  in different environments (SW-1).

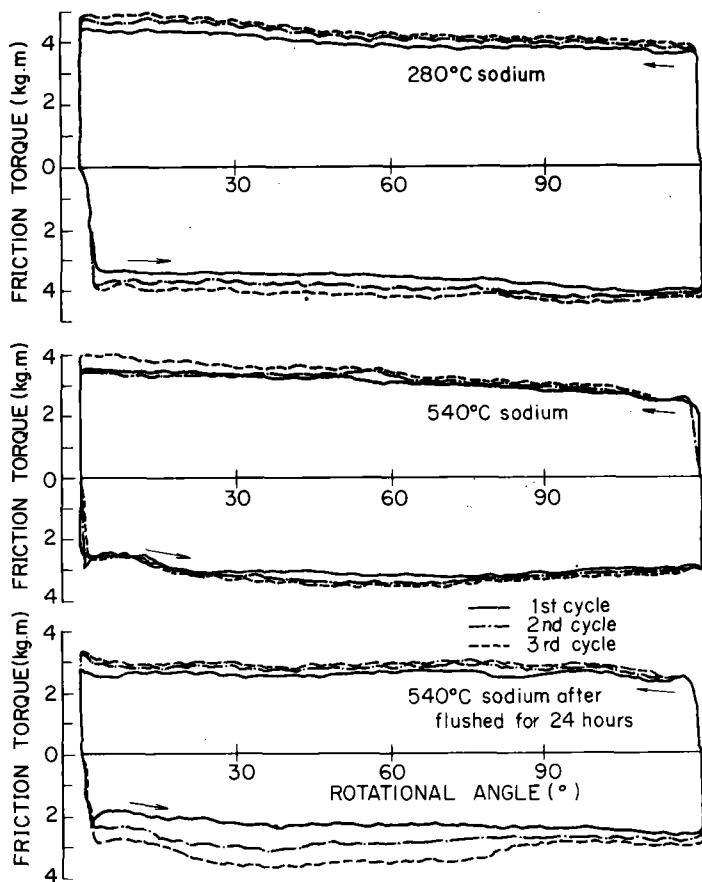


Fig. 7 Result of oscillating friction test on Colmonoy No.6 under the nominal load of 500 kg in different environments (SW-2).

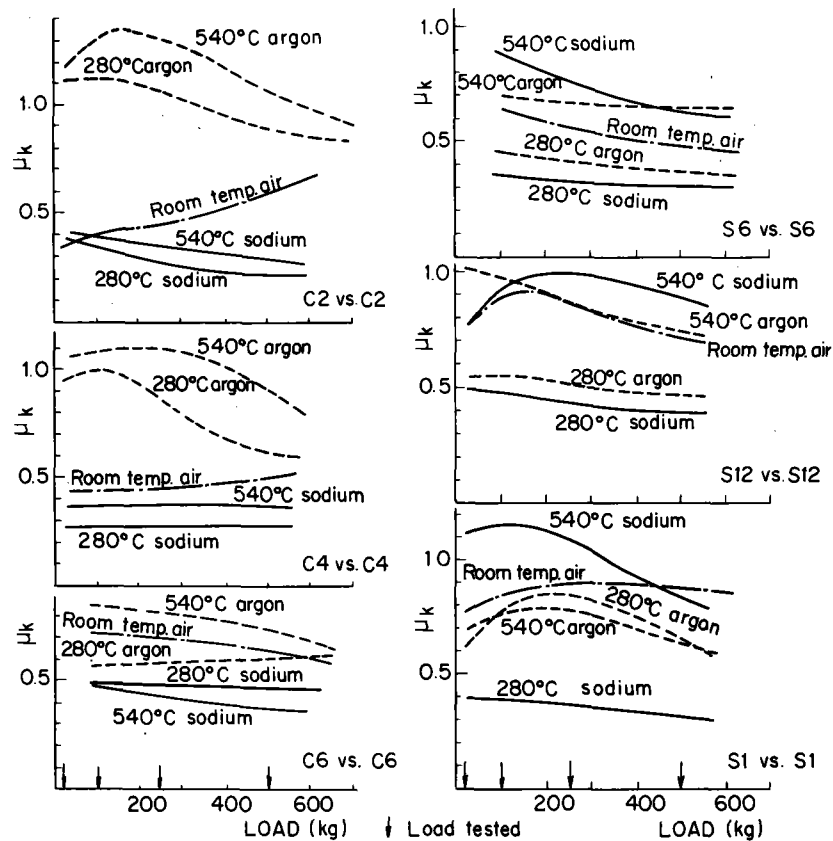


Fig. 8 Relation between  $\mu_k$  and load in different environments (SW-2).

# INTERNATIONAL CONFERENCE ON LIQUID METAL TECHNOLOGY IN ENERGY PRODUCTION

## WEAR OF ROLLING ELEMENT BEARINGS IN SODIUM

C S Campbell

UKAEA-REML  
Risley, Warrington, Cheshire, England

### ABSTRACT

Rolling element bearings and related mechanisms are attractive for service in liquid sodium but it is not clear what minimum wear rate can be anticipated. For axially loaded angular contact bearings rotation is incompatible with pure rolling on both races and wear arises from the resulting ball spin. The initial pressure distributions and sizes of the contact eclipses can be calculated but will change with bearing wear. However, the most effective distribution for producing wear would be for the full loads to be borne on the tips of the contact areas, whose maximum length is given by examination of the race wear tracks. A calculation on such a basis should set a lower limit for the wear coefficient.

Both the torque and instantaneous wear rate of a bearing will be similar functions of the integral over the contact areas of the product of contact pressure and radius from the ball spin axis. A better estimate of wear coefficient should be obtained by relating the average torque, the average wear, the initial torque and the initial wear where the conditions are known. Analysis of tests in sodium at 400°C of high speed steel and Stellite bearings by these methods indicates specific wear rates of the order of  $10^{-15} \text{ m}^3/\text{N-m}$ , not unduly out of line with the range of values found in conventional sliding tests.

### INTRODUCTION

The operation and servicing of a sodium cooled reactor inevitably presents requirements for mechanisms which are capable of functioning, if only on an intermittent basis, immersed in or wetted on the rubbing surfaces by films of liquid sodium. In some cases, as with sodium pump bearings, it may be possible to employ hydrostatic bearings where the centralising forces come from sodium pumped through the bearings. In general however the low viscosity of liquid sodium, comparable to that of gasoline, effectively rules out the possibility of self generated fluid film lubrication such as is commonly employed in simple journal bearings. Conventional lubrication is clearly not possible and while complex oxide films formed on the metal surfaces may give a situation not as fundamentally unfavourable as might be feared, the

designer is faced nevertheless with a situation where, at the least, bearings may have a friction even greater than found with only boundary lubrication and where wear rates cannot be entirely forgotten. Under these circumstances there has been a continuing interest in rolling element bearings of all types. In conventional service such bearings have low torques even at low rotational speeds and if their use were feasible in liquid sodium could have a number of additional advantages. Thus a ball nut and screw not only requires substantially lower torque than a simple nut and screw but is more compact and positive than other alternatives. Tests have therefore been carried out over the years by a number of investigators in various organisations to examine the feasibility of the rolling element concept in liquid sodium<sup>(1-5)</sup>.

Clearly materials can only be seriously considered if at the temperatures of interest they have sufficient strength to withstand adequately the contact stresses involved and are also resistant to liquid sodium in respect to dissolution, decarburisation or similar changes. Accordingly, while at temperatures of the order of 400°C higher alloy steels such as H.S. steels and non-ferrous alloys such as Stellites can be included, conventional bearings in the usual 1% Cr 1% C steel must be excluded. Difficulties can also arise with cage interactions and it has generally been found better to dispense with a cage and employ a full, or nearly full, complement of balls.

Under the very high contact pressures found even at light loads in rolling element bearings the viscosity of conventional lubricants is transiently increased locally by orders of magnitude. Despite the high contact pressures, therefore, surfaces normally remain separated by a thin fluid film of, effectively, very high viscosity lubricant. No such effect is to be expected with liquid sodium and it is perhaps therefore not surprising that the torques measured in rolling element bearing tests in sodium are higher than would be expected with conventional lubrication. These torques though increasing with time apparently as a result of wear are still however considerably less than for plain bearings of a similar size operating in liquid sodium and low enough to satisfy the generality of possible uses envisaged for such bearings.

## INTERNATIONAL CONFERENCE ON LIQUID METAL TECHNOLOGY IN ENERGY PRODUCTION

After what under conventional conditions would be considered a very limited life such bearings can begin to show considerable play and a loss of locational precision. This may still be acceptable but clearly such behaviour falls short of what could normally be expected for lubricated bearings of this type. If grit and corrosive conditions are excluded, wear of balls and races is not normally a problem with well-lubricated conventional rolling element bearings. Failure of these, ignoring failures involving the cages is usually due to pitting or spalling as a result of the repeated application of the high contact loads. Design of rolling element bearings is therefore normally based on bringing the contact stresses down to levels where the fatigue failure rate is acceptable. Shear stresses in a lubricated contact are at a maximum a little distance below the surface, but with the much higher coefficients of friction with sodium "lubrication", maximum shear stresses will come much closer to the surface and the pattern of fatigue failure might be considerably modified. If fatigue of any type lies at the root of the observed wear a further reduction in stress levels would be helpful whereas a reduction in simple wear might require a reduction in conformity with a consequent increase in stress levels.

It is not immediately clear whether the rates of wear found in rolling element bearing tests in sodium are compatible with what might be anticipated from conventional rubbing friction and wear tests or whether some alternative mechanism or mechanisms involving, say, fatigue under transverse load are required to account for the observed rates. In uncaged bearings balls may in some circumstances rub against each other up to the point of jamming, difficulties with alignment may result in unexpectedly high loads, or there may be special factors such as, for example, heavier wear occurring in the transfer passage of a ball screw nut. These, or other possibilities, may be giving some additional contributions to the overall wear and might, hopefully, be minimised by redesign, but it would be useful, both in optimising design and in assessing the true potential of rolling element bearings in such environments to have some indication of the minimum wear rate which might be expected.

In rubbing tests in the presence of sodium vapour but under conditions where water vapour could probably

not be entirely excluded, wear rates have been at least as good as in cold-trapped liquid sodium, but wear coefficients in nominally pure argon or helium, probably more typical of the gettered conditions which may be expected for most reactor situations involving cover gas, are in general rather higher and wear behaviour is less satisfactory. As even operation in liquid sodium may involve operation of some parts of any mechanism all or part of the time in the cover gas, it is perhaps therefore all the more important to understand the mechanisms for the deterioration of rolling element bearings in sodium if their limitations in these environments are to be recognised and designs improved.

### ESTIMATION OF WEAR COEFFICIENTS

No matter how well the geometry of unworn rolling element bearing is known, it is clear that in most cases the loss of comparatively small amounts of material by wear could drastically change the known initial conditions. Thus in an axially loaded ball bearing the degree of conformity between the ball and the inner and outer races will change, altering the size and shape of the contact ellipses, their pressure distribution and the contact angle of the balls with the races. A roller bearing should preserve the initial geometry rather better and therefore be more susceptible to analysis. Unfortunately the total sliding distance will be somewhat indeterminable, the axial sliding of the rollers depending on their angle of slew which is not easily found and the microslip on the tractive force which will also be a function of the angle of slew. On the other hand the major sliding in the case of an axially loaded ball bearing arises from ball spin which is less uncertain. Rotation of such a bearing is not compatible with pure rolling of the balls at both their contacts, the necessary ball spin to preserve pure rolling at one contact being in the opposite sense to that required to preserve pure rolling at the other.

Such mathematical treatments of ball motion as have been put forward are highly complex and, at best, difficult to grasp<sup>(6-11)</sup>. In a high speed well-lubricated bearing the gyroscopic and centrifugal forces acting on the rotating balls are not negligible while the frictional forces available are limited. This would not be the case for the conditions under which rolling element bearings have been tested in sodium and a very much simplified approach would be

fully justified particularly in view of the uncertainties in other areas and the inherent scatter in friction and wear results.

Consideration of ball spin is more convenient if the balls are taken as stationary in space but rotating, as they roll on the inner and outer races. In a pure thrust bearing pure rolling at the ball contacts would require the balls also to spin at the same angular velocity as the races; this is not simultaneously possible at the two contact areas to each ball as the races are counter rotating. In the context of overall wear it is immaterial whether spinning occurs at one contact or the other or whether there is some degree of spin at both; the combined angular velocity in a pure thrust bearing will equal the angular velocity of the bearing. In a pure radial bearing there is no conflict for pure rolling at both contacts, ie there is zero ball spin; with angular contact and axially loaded deep groove bearings the combined ball spin velocity is equal to the resolved angular velocity of the bearing, ie directly related to the sine of the contact angle. While the contact geometry conditions at the inner and outer races of the unworn bearing will not be identical, in practice they will be comparable and particularly as wear will tend to equalise what differences exist, this need not be pursued further.

As the contact loads resulting from any given axial load are inversely proportional to the sine of the contact angle and the ball spin velocities are proportional to the sine of the contact angle, it is clear that the product of ball load and ball spin velocity should be substantially unaffected by wear. The wear produced by the spin will, however, depend on the size of the contact areas and the pressure distribution within them. Initially these are given by the Hertzian theory but both will change as the bearing wears. Pressure rises to a maximum at the centre of the contact ellipses but the sliding velocity decreases as the spin axis of the ball is approached. The balls may preserve their spherical form as a result of the wear being averaged out over their entire surface but the races could depart significantly from their original geometry, altering not only the degree of conformity but the pressure distribution. This affects the further wear so that it becomes difficult either to predict the course of wear or to ascribe a value to the wear coefficient from an

observed wear, though it would seem that as the contact patches will lengthen with wear, the wear rate must correspondingly increase.

Despite the uncertainty as to the pressure distribution within the contact areas as a result of wear it is clear that the most effective distribution for producing wear would be for the full load to be borne on the tips of the contact areas. A wear coefficient calculated on this basis must therefore necessarily set a lower limit above which the true value must lie. An upper bound to the average width of the contact areas will be given by the observed final widths of the wear tracks on the races particularly as these must also include the shift in contact angle from wear during the test. Such a value, albeit a lower limit rather than an estimate, could nevertheless give a useful guide on wear mechanisms.

As illustration of this approach we may take results obtained by Hill at REML, Risley on cageless tungsten high speed steel (Type T1) angular contact bearings tested in sodium at 400°C<sup>(12)</sup>. In one test a bearing was run under axial loads equivalent to 4448N (1000 lbf) for  $6.2 \times 10^6$  revolutions and had then lost  $0.13 \times 10^{-6} \text{ m}^3$  from the balls with tracks on the races worn to about 12mm wide. The lower limit for the wear coefficient for the balls would then be simply  $0.13 \times 10^{-6} / (4448 \times 2\pi \times 6 \times 10^{-3} \times 6.2 \times 10^6) \text{ m}^3/\text{N-m}$  or  $0.12 \times 10^{-15} \text{ m}^3/\text{N-m}$ . In another essentially similar test under the same loading conditions ball wear only amounted to about  $3 \times 10^{-9} \text{ m}^3$  after  $4.2 \times 10^6$  revolutions with a track wear scar only about 3.2mm wide, which would give a lower limit in the wear coefficient in this run of  $0.016 \times 10^{-15} \text{ m}^3/\text{N-m}$ .

If we can assume that the wear rate would never be lower than initially we could also estimate a coefficient on the basis of the original Hertzian conditions which would plausibly give an upper limit to the wear coefficient. Treating wear as being proportional to load and sliding distance, the wear rate at any moment of time is related to the product of load-sliding distance integrated over the entire area of the contact ellipses. If it is assumed that the balls are spinning at either or both ends over the whole of the contact ellipses, the integral of load-sliding distance is equal to  $2\pi \times$  (integral of load-radial distance from the spin axis). For the unworn condition numerical integration assuming a Hertzian elliptical pressure distribution gives for a range of typical conformities

## INTERNATIONAL CONFERENCE ON LIQUID METAL TECHNOLOGY IN ENERGY PRODUCTION

(major/minor axis ratios  $\approx 8$ ) values very close to a limiting ratio of 0.375 of that corresponding to the load concentrated at the tips of the contact ellipses. The bearings tested by Hill used 13 or 14 balls 7.54mm radius rolling on races of radius 7.78 and 7.87mm at a nominal unloaded contact angle of  $30^\circ$ . Calculation gives the lengths of the semi-major axes as about 1.4mm, giving suggested upper limits for the wear coefficients for the balls in these two runs of  $1.3 \times 10^{-15}$  and  $0.045 \times 10^{-15} \text{ m}^3/\text{N-m}$  respectively.

It is possible however in some circumstances to go somewhat further than this in estimating a wear coefficient. On the same basis as for the wear rate the frictional torque about the spin axes of the balls will also be proportional to the integral of load-radial distance from the spin axis and the torque for the unworn condition will similarly approach a limiting ratio of 0.375. As the resolved torque about the bearing axis will be proportional to the sine of the contact angle while the contact loads will be inversely proportional to the sine of the contact angle, this mathematical equivalence will extend to the torque of the bearing as a whole. The equations for instantaneous wear rate and bearing torque at that time will therefore be of a closely similar form, both responding similarly to changes in pressure distribution at the contact areas, contact area geometry and contact angle. Hence if the torque of a bearing has been measured through a test and if the coefficient of friction can be taken as reasonably constant, the time-averaged torque should be related to the overall wear in the same way as the initial torque to the initial wear rate and where the pressure distribution and the size of the contact ellipses are known from the Hertzian equations. As the contact pressures and linear dimensions of the contact ellipses both increase as the cube root of the contact load, we might expect the bearing torque to be proportional to the two thirds power of the axial load. Results obtained by Hill confirm such a relationship and lead to values for the coefficient of friction in reasonable agreement with those found in conventional friction and wear experiments<sup>(12)</sup>.

These particular experiments do not permit further analysis but in tests reported by Kleefeldt and Gering the wear of axially loaded deep groove ball bearings of specified geometry has been measured after runs where the torque has been followed throughout<sup>(5)</sup>.

The combinations examined included bearings in high speed steel and Stellite. The runs were carried out at  $400^\circ\text{C}$  in liquid sodium with an axial load of about 2750N using uncaged bearings with 16 balls 5mm radius rolling on races of radii 5.23mm with an unloaded nominal contact angle of  $15^\circ$ . Calculation gives the half lengths of the major axes of the initial contact ellipses as just over 1mm for both cases. For high speed steel (M2 type) the initial torque for a pair of bearings each under a load of 2650N was about 0.61N-m which would lead to a not unreasonable coefficient of friction of 0.29. For a pair of Stellite bearings (a combination of Stellite 3 balls and Stellite 12 races) each under a load of 2890N the initial torque was about 0.75N-m and gives a coefficient of friction of about 0.34 which, again, would not be unreasonable.

The average torque for the high speed steel bearing pair over 205,000 revolutions was about 2.41N-m; if the initial load distribution gives a wear rate of 0.375 of that corresponding to the load being applied at the tips of the original contact ellipses, the average wear rate should correspond to 4 times this or an overall factor of 1.5. On this basis a weight loss from balls and races of 118mg from both bearings would lead to a wear coefficient of about  $1.3 \times 10^{-15} \text{ m}^3/\text{N-m}$  for the wear from both balls and races or about  $0.1 \times 10^{-15} \text{ m}^3/\text{N-m}$  for the balls alone. Such wear coefficients would be broadly comparable with the limits calculated for the bearing tests of Hill.

A similar calculation for the Stellite bearing where the average torque over 130,000 cycles was about 1.39N-m and the total wear about 97mg gives a total wear coefficient of about  $3.2 \times 10^{-15} \text{ m}^3/\text{N-m}$ . Ball wear rates if averaged over the two bearings would be zero but taking the bearing with a positive weight loss for an upper limit, ball wear coefficients can be said to be  $1 \times 10^{-15} \text{ m}^3/\text{N-m}$  or less.

Ideally the comparison with wear coefficients obtained in simple sliding wear tests should be for identical materials rubbed under closely similar conditions. A number of tool steels and Stellites have been examined at NCT/REML in crossed cylinder geometry in liquid sodium in unidirectional rubbing over a temperature range including  $400^\circ\text{C}$ . A semi-cylindrically ended square pin about 7.9mm x 7.9mm in section has been pressed against a rotating cylindrical sleeve about 51mm in diameter. Typically the load has been in the range 20-50N, the sliding speed 30mm/sec

and the sliding distance  $10^3$  m. Contact pressures could be considered comparable to those in bearing tests. Pin wear rates have been calculated from the size of the pin wear scar; sleeve wear rates from profile measurements of the sleeve wear scar. The materials combinations examined have not included an M2 type high speed steel but have covered a tungsten high speed steel of the type used by Hill and have not included a Stellite 3/Stellite 12 combination. However the scatter in wear rates found with both these classes of materials is such that compositional differences have not been found to have a marked effect.

Lumping high speed tool steels together as a class, pin wear coefficients at  $400^\circ\text{C}$  have been of the order of  $0.1 \times 10^{-15} \text{ m}^3/\text{N-m}$  and nett coefficients for sleeve wear, corresponding to net weight losses, of the order of  $0.3 \times 10^{-15} \text{ m}^3/\text{N-m}$ . Stellite pin wear rates at  $400^\circ\text{C}$  cover the range  $0.01 \times 10^{-15}$  to  $1 \times 10^{-15} \text{ m}^3/\text{N-m}$ , clustering about  $0.1 \times 10^{-15} \text{ m}^3/\text{N-m}$  with corresponding nett sleeve wear coefficients about an order of magnitude higher. Similar differences between flat-ended "pin" and "disc" wear rates have been observed by Wild<sup>(13)</sup>. As an additional comparison, flat-ended pin wear coefficients of about  $0.5 \times 10^{-15} \text{ m}^3/\text{N-m}$  at  $427^\circ\text{C}$  have been reported for a number of high speed tool steels by Hoffman, Goggin and Droher but the corresponding disc wear rates have not been measured in this work<sup>(14)</sup>.

Wear coefficients calculated from the bearing tests are therefore possibly slightly higher than the average of what has been found in conventional friction wear tests but within a factor as little as the order of three. Bearing in mind the scatter found in the friction and wear data, the limited indications from the bearing tests where a comparable variability probably also exists and the uncertainties as to the possible effects of the variables, any difference cannot be said to lie outside what might reasonably be expected and thereby point to the existence of unsuspected additional factors.

Metallographic and EPMA examination of bearings tested in sodium by Hill has not brought to light any relevant features such as surface decarburisation which might account for higher wear rates or white etching sheared zones which can be indicative of unduly high stress levels in conventional bearings. Hardness measurements have shown an increase rather than a decrease in surface hardness and no loss of

hardness such as might follow temperature rises from ball skidding.

Higher wear rates could also result if balls crowd together and begin to rub directly against one another. This should show up by corresponding increases in bearing torque but would not give higher wear coefficients where the estimation of this has involved averaged torque measurements.

The general conclusion would therefore be that the observed rates of deterioration of axially loaded high speed steel and Stellite ball bearings in liquid sodium are reasonably consistent with the wear rates to be expected from conventional rubbing tests and that no evidence has emerged pointing to other mechanisms. A similar situation presumably exists with other types of rolling element bearing in liquid sodium. If the model is also applicable to unlubricated ball bearings in inert atmospheres such as the cover gas of a LMFBR, materials showing poorer rubbing behaviour under such conditions than in oxygen-containing liquid sodium might be expected, by extension, to behave correspondingly less well in such environments.

#### REFERENCES

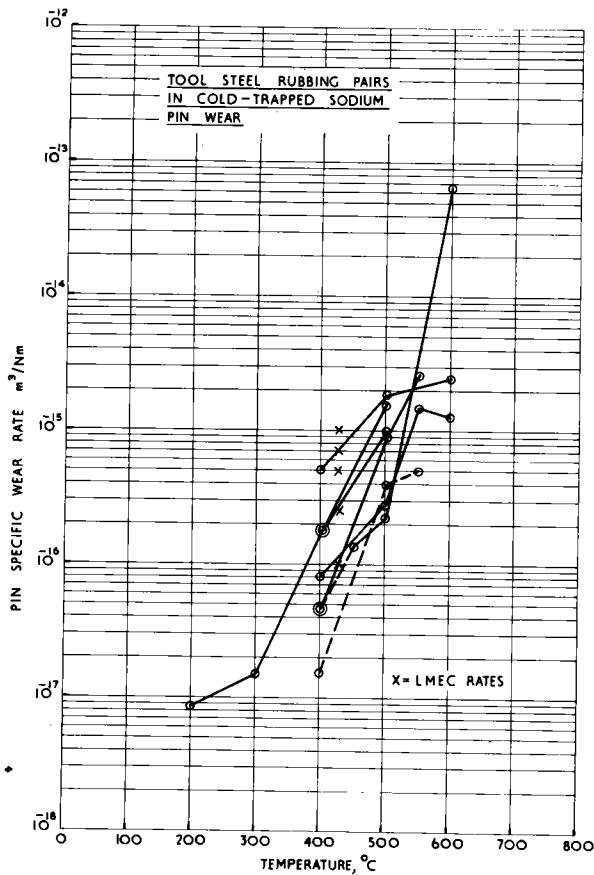
1. Iwai S, et al., "Testing of feasibility of ball bearings in liquid sodium environments", Proceedings International Conference on Sodium Technology and Large Fast Reactor Design, ANL-7520 (Part II), pp 121-129, (1968).
2. Delves P H and Rodwell W., "Mechanisms in sodium", Symposium on Progress in Sodium-cooled Fast Reactor Engineering, Monaco, pp 757-770, (1970).
3. Uga T, Ikushima T, Nozawa M and Sugiyama H. "Friction and wear of ball bearings in liquid sodium", J. Nucl. Sci. & Tech. (Tokyo), 8, pp 16-22, (1971).
4. Jamison W E. "Development of high temperature rolling bearings for operation in liquid sodium", NYO-4117-9, (1972).
5. Kleefeldt K and Gering G. "Reibung und Verschleiss von Kugellagern in flüssigem Natrium I. Teil: Vergleichversuche zur Werkstoffauswahl", KFK 2157, (1975).
6. Jones A B. "Ball motion and sliding friction in ball bearings", J. Basic Eng, 31, 1, pp 1-12, (1959).

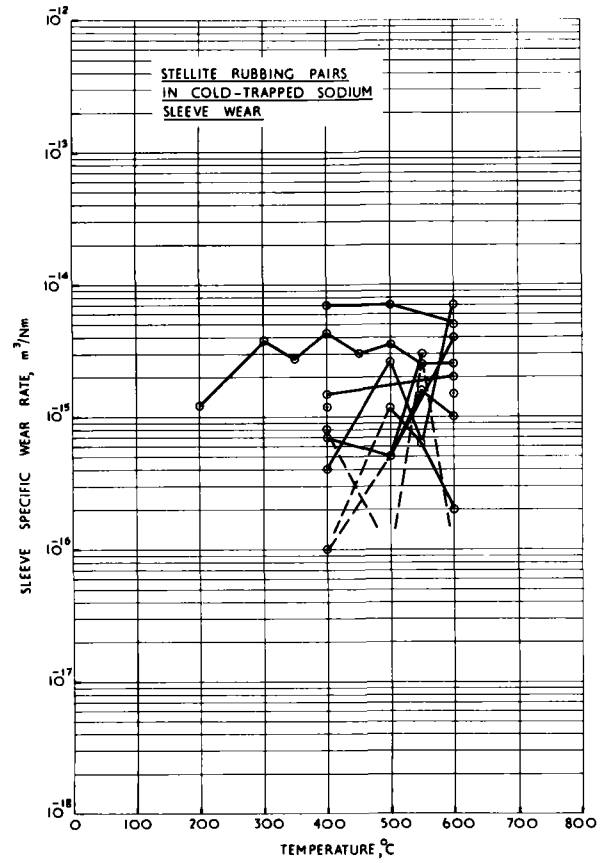
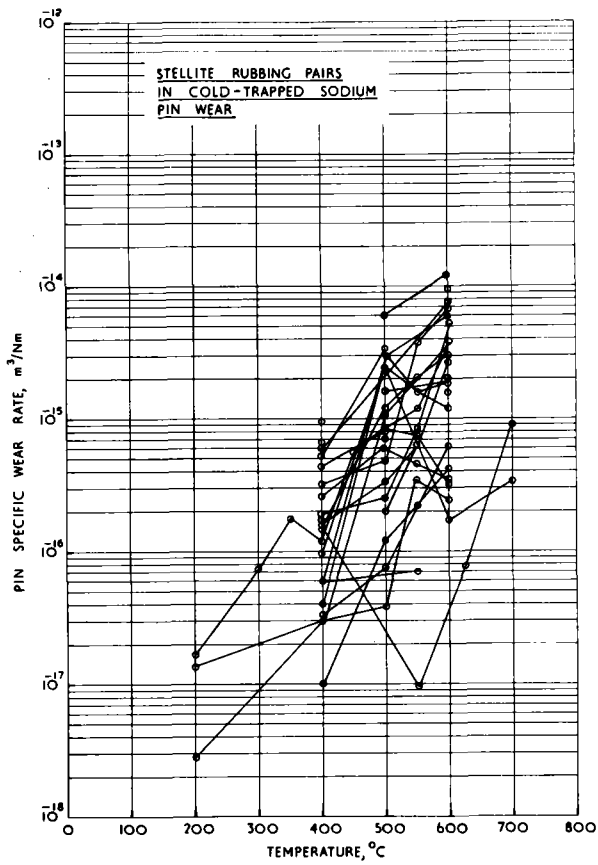


INTERNATIONAL CONFERENCE ON LIQUID METAL TECHNOLOGY IN ENERGY PRODUCTION

7. Halling J, "Analysis of spin/roll conditions and the frictional energy dissipation in angular-contact thrust ball bearings", Proc. Instn. Mech. Engrs., 181, pt 1, 16, pp 349-362, (1966-67).
8. Poplawski J V and Mauriello A, "Skidding in lightly loaded, high speed ball thrust bearings", ASLE Paper 69 - LUB S-20, (1969).
9. Harris T A, "Ball motion in thrust-loaded, angular contact bearings with Coulomb friction", J. Lub. Tech., 93, 1, pp 32-38, (1971).
10. Walters C T, "The dynamics of ball bearings", J. Lub. Tech., 93, 1, pp 1-10, (1971).

11. Boness R J and Gentle C R, "Ball motion in thrust loaded ball bearings", Wear, 35, pp 131-148, (1975).
12. Nicod A R E and Hill G D, Unpublished work - REML, UKAEA, (1975).
13. Wild E, Mack K J and Drechsler G, "Das verschleissverhalten von Werkstoffkombinationen in flussigem natrium", KFK 1659, (1972).
14. Hoffman N J, Groggin D E and Droher J J, "Friction and wear screening tests of materials in sodium", LMEC-70-10, p 112, (1970).





# INTERNATIONAL CONFERENCE ON LIQUID METAL TECHNOLOGY IN ENERGY PRODUCTION

## EVALUATION OF COBALT AND NICKEL BASE MATERIALS FOR SLIDING AND STATIC CONTACT APPLICATIONS IN A LIQUID METAL FAST BREEDER REACTOR\*

N. J. Hoffman, J. J. Droher  
Liquid Metal Engineering Center  
Canoga Park, CA 91304

J. Y. Chang, T. A. Galioto  
R. L. Miller, S. L. Schrock,  
G. A. Whitlow, W. L. Wilson  
Westinghouse - Advanced Reactors Division  
Madison, PA 15663

R. N. Johnson  
Westinghouse - Hanford Engineering  
Development Laboratory  
Richland, WA 99352

### ABSTRACT

This paper covers pertinent metallurgical and tribological aspects of three alloys that are being considered for surfaces that must rub while immersed in liquid sodium coolant within a fast breeder reactor system. The alloys are cobalt-base hardfacing alloy type 6, Tribaloy 700, and Inconel 718. Topics discussed include chemistry and microstructure, hardness, and behavior in high-temperature sodium with respect to dynamic friction, diffusion bonding, and corrosion.

### INTRODUCTION

Workers investigating the tribological properties of a wear surface have long been aware of the importance of lubricative films on the rubbing surfaces. Since these films are dependent on the chemistry of both the sodium and the rubbing surfaces, the chemistry of the interacting surface layers has been of interest to the metallurgist involved in performing friction and wear tests in sodium. In order to understand the tribological properties of an alloy, the metallurgist must also be aware of the microstructure and hardness of the material surface and how these aspects can change. These changes can be due to variations in the unexposed material prior to sodium exposure or due to service in high-temperature sodium for long periods of time.

In this presentation, we will discuss the above considerations for three of the most important alloys for rubbing applications in sodium-cooled reactors. The first alloy to be discussed dates from the discovery by Elwood Haynes in 1895 that the cobalt-chromium alloys had interesting hardness properties and this property could be enhanced by the addition of ~5% tungsten. The specific alloy discussed here is the RCrCo-A type alloy called Stellite 6 or Stody 6. The second alloy to be discussed here will be one of the duPont Triballoys, a type of alloy that uses Laves phase precipitation to obtain desired levels of hardness. The particular alloy of this type analyzed here is Tribaloy 700, a non-cobalt-base variety. The third alloy is one of the nickel-base alloys that hardens by  $\gamma'$  precipitation, specifically Inconel 718.

\*This work was performed by LMEC, WARD, and HEDL under contracts with the U.S. Energy Research and Development Administration.

### COBALT-BASE HARDFACING ALLOY TYPE 6

#### Chemistry and Microstructure

A typical chemical analysis of the cobalt-base, chromium-tungsten hardfacing alloy corresponding to the AWS A5.13-70 RCoCr-A specification is shown in Table 1. This composition of undiluted hardfacing is often called Stellite 6 or Stody 6. A wrought alloy of almost identical composition is called Stellite 6B; but Stody 6N is an entirely different material. Nomenclature and specifications are further clarified in Table 1.

The carbon content is important in these alloys and 1.1 wt % is the desired content. When an oxy-acetylene torch is used to apply this alloy as a hardfacing, a 3X flame (i.e., a flame with an excess acetylene feather three times the length of the inner cone) is used, and this can add carbon to the deposited hardfacing alloy. If an inert gas welding process is used, carbon can be lost during deposition of the hardfacing alloy; thus a carbon content of at least 1.1 wt % should be present in the hardfacing alloy prior to application by the latter process, or extreme care should be taken to avoid overheating and carbon loss.

The microstructure of the Stellite or Stody 6 alloy when applied in the form of hardfacing consists of dendrites of matrix with very small surrounding volumes of carbide (see Figure 1).

The dendrites of matrix are a metastable face-centered cubic (FCC) structure with ~72 wt % cobalt, ~23 wt % chromium, and ~4 wt % tungsten. The majority of the carbide is initially  $M_7C_3$ . The microstructure of Stellite 6B consists mainly of the metastable FCC matrix with carbide islands of  $M_7C_3$  with a grain boundary of  $M_{23}C_6$  (see Figure 2).

In one important study,<sup>(1)</sup> the Stellite 6 transformation from a metastable FCC structure to a hexagonal close-packed (HCP) structure with an accompanying linear contraction of 0.092% was observed when this alloy was heated in the 370 to 650°C (700 to 1250°F) range for 1000 h. The above study postulated that three independent metallurgical reactions occur in Stellite 6B when heated in the 475 to 785°C (885 to 1450°F) range:

INTERNATIONAL CONFERENCE ON LIQUID METAL TECHNOLOGY IN ENERGY PRODUCTION

Table 1. Nomenclature and Composition of Cobalt-Base Chromium-Tungsten Alloy Type 6\*

Alloy Designation	Composition in Weight Percent									Total Other Elements
	Co	Cr	W	C	Mn	Ni	Mo	Fe	Si	
AWS A5.13-70, RCoCr-A (bare, cast rods)	Balance	26.0-32.0	3.0-6.0	0.9-1.4	1.00	3.0	1.0	3.0	2.0	0.50
Stellite 6** (cast shapes)	Balance	27.0-31.0	3.5-5.0	0.9-1.4	1.00	3.0	1.5	3.0	1.5	NR
Stellite 5 nuclear grade, Mil-R-17131A, Class RCoCr-Al (bare, cast rods)	Balance	28.5 nom	4.0 nom	1.1 nom	NR†	NR	NR	1.5	NR	NR
Stellite 6H (bare, cast rods for gas-tungsten arc only)	Balance	30.0 nom	5.5 nom	1.3 nom	NR	NR	NR	NR	NR	NR
Stellite 6B (wrought products)	Balance	28.0-32.0	3.5-5.5	0.9-1.4	2.00	3.0	1.5	3.0	2.0	NR
Stellite 6 (powder form)	Balance	28 nom	4.0 nom	1.0 nom	NR	NR	NR	3.0	1.0 nom	1.5 nom

\*Single values represent maximum wt % unless otherwise specified. For bare rods the analysis given is for the as-manufactured rod and for coated electrodes the analysis given is for deposited weld metal.

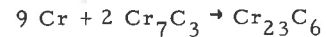
\*\*Another manufacturer of this alloy uses the trade name "Stoody."

†NR indicates not reported.

- 1) Minor hardening of the matrix by precipitation of one phase.
- 2) Gross hardening of the matrix by precipitation of another phase.
- 3) Transformation of the matrix from FCC to HCP structure.

The net result of this is that Stellite 6B could exist with a metastable FCC structure with a hardness in the  $R_c$  37 to 40 range,<sup>(1,2)</sup> or as an HCP structure hardened with fine precipitate in the  $R_c$  48 to 56 range,<sup>(1,3)</sup> or as an HCP structure with a different precipitate giving a hardness in the  $R_c$  41 to 42 range. The friction and wear properties could well be different for each of the above structures. X-ray diffraction can be used to establish the presence of a significant amount of matrix

transformation. In both the wrought and cast forms<sup>(4)</sup> of this alloy, the reaction



may be important, resulting in a very fine dispersed volume of  $\text{Cr}_{23}\text{C}_6$  surrounding particles of  $\text{Cr}_7\text{C}_3$  in the matrix.

Exposure to 720°C (1325°F) sodium appears to leach chromium from the matrix at the surface and reduce hardness.<sup>(5)</sup> This loss of chromium at the surface may inhibit the breakdown of massive  $\text{Cr}_7\text{C}_3$  particles to a fine spray of  $\text{Cr}_{23}\text{C}_6$  in the matrix and, independently, may stabilize the FCC form of the matrix when the alloy is subsequently exposed in the 425 to 625°C (800 to 1250°F) range.

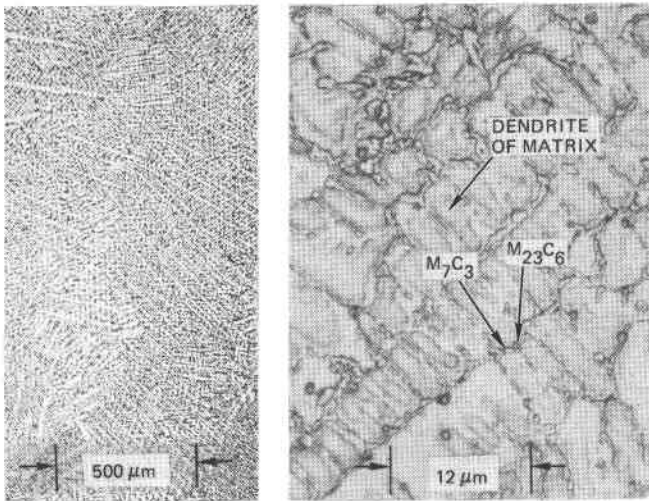


Figure 1. Stellite 6, showing typical structure at external surface, polished and etched with acidified  $\text{FeCl}_3$ .

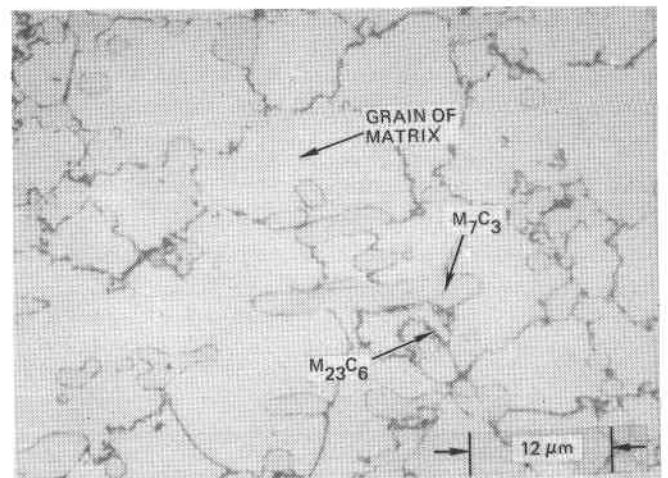


Figure 2. Stellite 6B, showing typical microstructure perpendicular to rubbing surface.

Hot Hardness Characteristics

The hot hardness characteristics of this type of alloy are shown as a function of temperature in Figure 3. Due to aging, the actual values may be considerably higher than the values shown, as discussed above. When applied by hardfacing, dilution of the alloy with molten-base alloy can cause lower hardnesses. Loss of carbon from the hardfacing alloy can also lower the hardness.

Dynamic Friction

The dynamic friction properties of the RCoCr-A type hardfacing rubbing against itself is summarized in Figure 4.

Note that a friction minimum occurs in the 482 to 538°C (900 to 1000°F) range. One must keep in mind that the microstructure is changing with time at high temperature. Dendrites of matrix with an FCC structure plus particles of  $M_7C_3$  are converting to a matrix with an HCP structure plus  $M_7C_3$  particles surrounded by a shell of  $M_{23}C_6$ . These microstructural changes

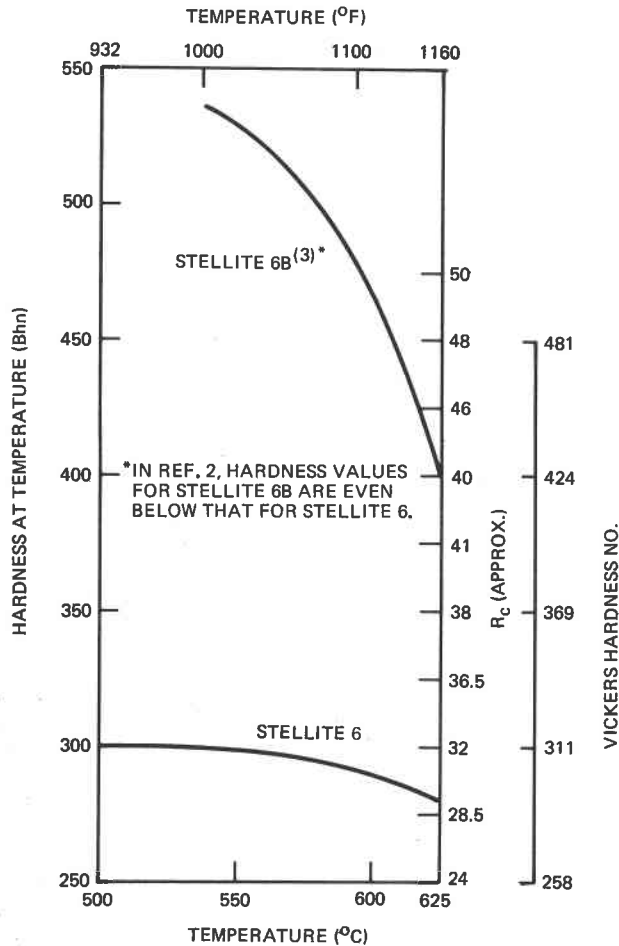


Figure 3. Hot hardness characteristics of type 6 alloy.

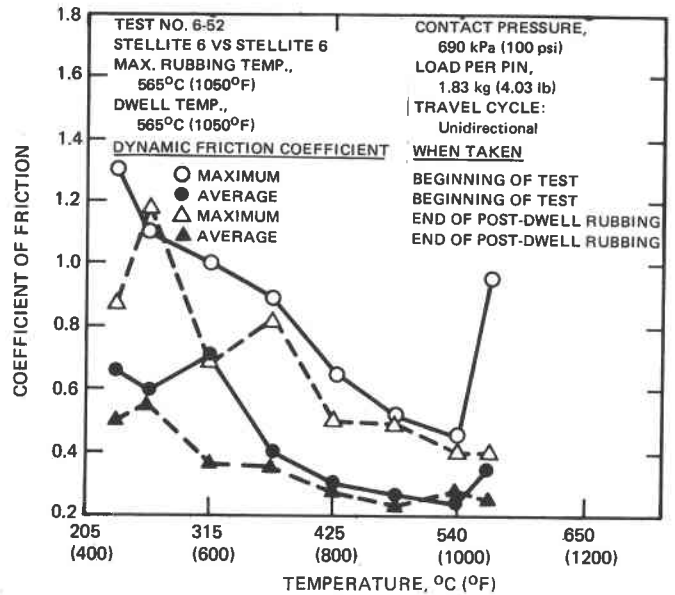


Figure 4. Dynamic friction of Stellite 6 hardfacing.

alone could affect the friction properties of this alloy with time during a period of >1000 h at temperatures greater than 480°C (900°F).

Diffusion Bonding

Tests are being performed at Westinghouse ARD on the diffusion bonding or self-welding phenomena. Preliminary data on Stellite 6 self-welding are listed along with those of Inconel 718 in Table 2. Note that for Stellite 6 these very early data indicate that self-welding is increased by load cycling (i.e., prior break-aways) when the previous breakaway had a measurable tensile separation force. Thus the possibility exists that the long-established practice of "breaking" a normally closed valve every few months may not be beneficial to the self-welding problem on Stellite 6.

TRIBALLOY 700

Chemistry and Microstructure

A family of proprietary intermetallic alloys based on either cobalt or nickel appears to offer a unique combination of low friction and wear, good corrosion resistance in many service environments, and relatively easy application techniques. At present, Triballoy 700 is one of four distinct alloys sold by E. I. duPont de Nemours & Co. under the Triballoy trade name. The chemical composition of Triballoy 700 is as follows: 50 wt % Ni, 32 wt % Mo, 15 wt % Cr, and 3 wt % Si. The volume percent Laves phase is 60%. We note that carbon is not a significant alloying element and, perhaps more importantly, that Triballoy 700 is based upon nickel rather than cobalt.

**INTERNATIONAL CONFERENCE ON LIQUID METAL TECHNOLOGY IN ENERGY PRODUCTION**

Table 2. Self-Weld Test Results and Test Conditions for Stellite 6 vs Itself and Inconel 718 vs Itself<sup>(6)</sup>

Material, Surface Finish, Geometry, and Hertzian Stress (kPa)	Test No.	Test Temp (°C)	Tensile Separation Force in Parenthese (kPa)													
			Exposure Time in Months													
			0	1	2	3	4	5	6	7	8	9	10			
Stellite 6/Stellite 6 <1 μm (<40 μin.) Curved surface on curved surface (82 740)	1	455	(0)	(0)	(0)	(0)										
		555					(0)									
		602							(0)							(6690)
	2	455				(0)	(0)									
		555						(0)								
		602								(4210)						(9930)
	3	455					(0)									
		555						(0)								
		602														(8410)
	4	593			(0)											
	5	602				(0)										
	6	563								(4410)						
	Inconel 718/Inconel 718 <0.65 μm (<25 μin.) Curved surface on flat surface (1 020 500)	7-86	455	(0)	(0)	(0)	(0)									
			555						(0)							
			602								(2970)					(29 810)
		7-87	455				(0)	(0)								
			555							(0)						
			602									(1100)				(3210)
7-88		455					(0)									
		555								(0)						
		602													(2280)	
7-32		568		(0)												
7-53		562				(0)										
7-54		563								(0)						

The Laves phase in Tribaloy 700 is an HCP compound of the A<sub>2</sub>B type where A atoms may be either nickel or silicon, and B atoms may be either molybdenum or chromium. Therefore, this Laves phase may be represented as (Ni,Si)<sub>2</sub>(Mo,Cr). The matrix phase of Tribaloy 700 has an FCC structure (Figures 5 and 6). Long-time aging characteristics of this alloy are unknown.

Methods of Applying

Tribaloy 700 may be applied as weld-deposited hard-facing by detonation-gun (D-gun) and plasma-spray. The D-gun method has produced a coating with very good adhesion when applied to a substrate such as austenitic stainless steel or Inconel 718. These D-gun-

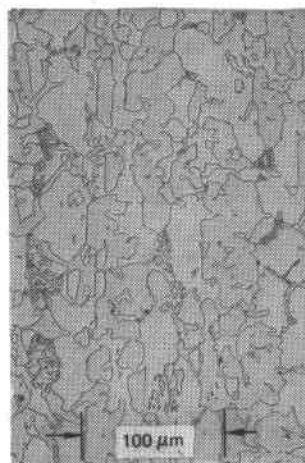


Figure 5. As-cast microstructure of Tribaloy 700.

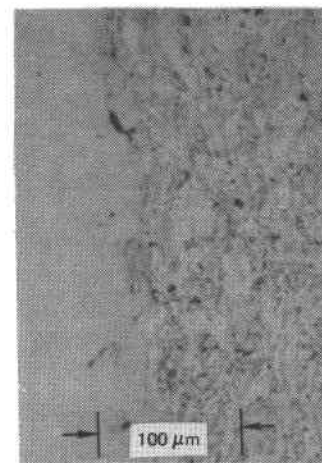


Figure 6. Plasma-sprayed version of Tribaloy 700.

applied coatings even resist thermal shock, if applied to a substrate with thermal expansion characteristics reasonably near that of Tribaloy. Plasma-spray coatings to date have exhibited a distinct tendency to spall or flake when exposed to sodium at elevated temperatures.

The desirable coating thickness is generally a function of the allowable wear tolerance permitted on the part. There is little advantage in applying more coating than necessary. In general, thinner coatings have more impact and shock resistance and are less costly to apply. Most coatings are 0.05 to 0.4 mm (0.002 to 0.015 in.) thick; an additional 0.1 mm (0.004 in.) allowance should be made if the coating will be subsequently thinned by grinding.

Hardness Characteristics

Depending on composition, the Vickers hardness number (VHN) of the Laves phase is 1 000 to 2 200 and the matrix is 200 to 800. Overall bulk hardness varies with phase size, which is a function of the method of manufacture. In general, Tribaloy 700 is somewhat softer than the other Tribaloy compositions.

Dynamic Friction

Dynamic friction coefficients of Tribaloy 700 in liquid sodium were obtained as a function of temperature while heating from 230 to 625°C (450 to 1160°F). At 625°C (1160°F) the specimens were rubbed in oscillatory short-stroke motion (0.5d) for a total of 1270 cm (500 in.) of cumulative distance, permitted to dwell ~1 week at this temperature, and then rubbed for another 1270 cm (500 in.). Data were then obtained while cooling down to 230°C (450°F). Maximum and average dynamic coefficients for like combinations of D-gun-applied Tribaloy 700 under a contact pressure of 2070 kPa (300 psi) are plotted in Figure 7. Also included are pre-test friction measurements in ambient air and in argon at room temperature.

Diffusion Bonding

Self-welding tests in sodium involving tensile separation are in progress at ARD but data are not yet available. However, a body of information on shear breakaway has been produced at ARD and AI. The dependence of breakaway on time and temperature is

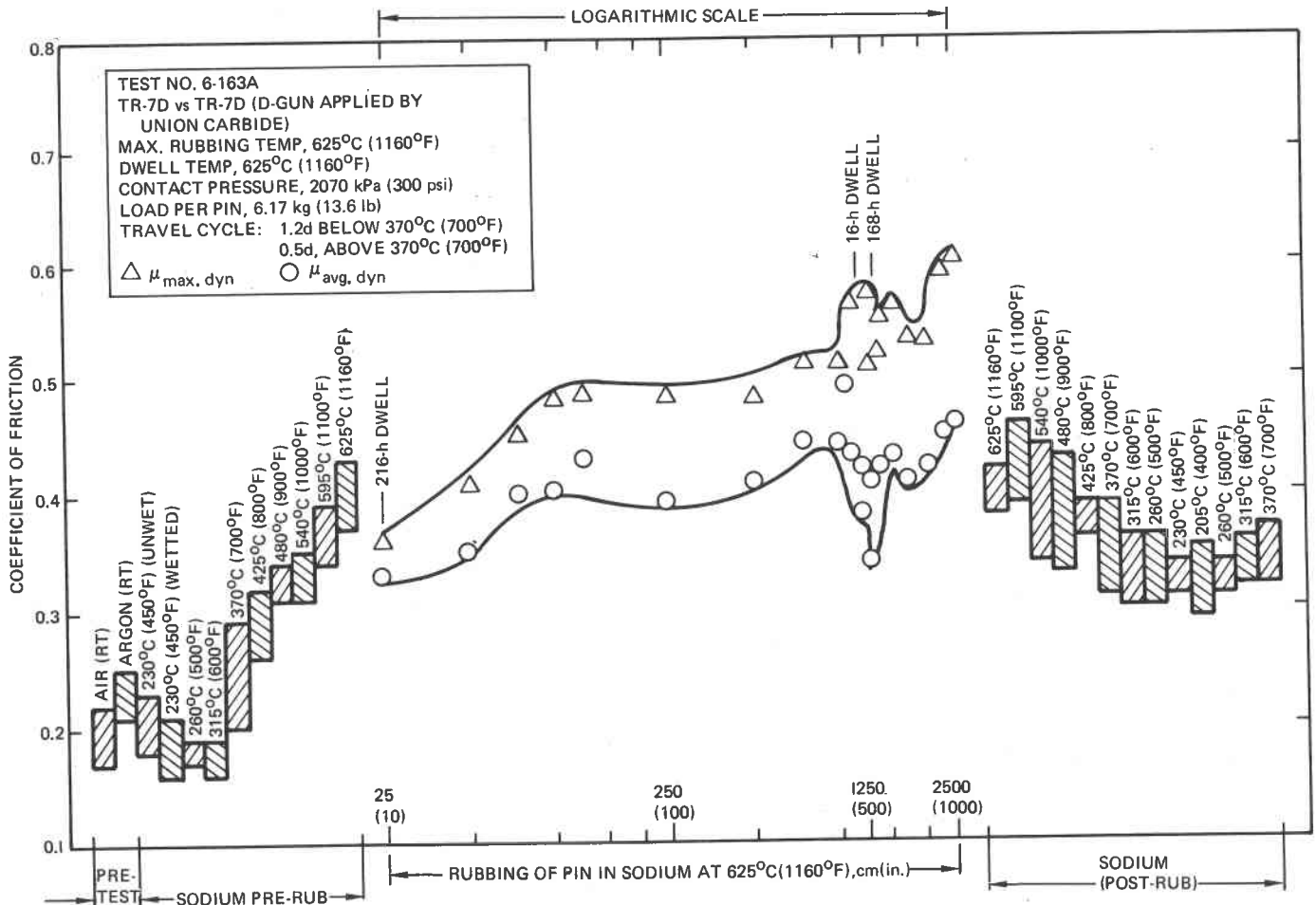


Figure 7. Dynamic friction of Tribaloy 700.

shown in Figure 8 for Tribaloy 700 material applied by D-gun to a type 316 stainless steel substrate.

INCONEL 718

Chemistry and Microstructure

The chemistry and microstructure of Inconel 718 are indicated in Table 3. The microstructure of this alloy (7,8,9,10,11,12,13) is an FCC matrix, called  $\gamma$ , with age-hardening coming from a coherent precipitate of FCC  $\text{Ni}_3(\text{Cb,Ti,Al})$  called  $\gamma'$ . With time in the 540 to 760°C (1000 to 1400°F) range, the FCC  $\gamma'$  very slowly becomes an incoherent precipitate of tetragonal structure with  $c/a = 2.05$ .<sup>(4)</sup> Large particles called carbonitrides (Cb,Ti)(C,N) are also present.

If the carbon content is near the high end of its limits in Inconel 718, carbonitrides are formed at the expense of the  $\gamma'$ . Slow cooling from above 760°C (1400°F) or improper aging can create an acicular Widmannstatten morphology of orthorhombic  $\text{Ni}_3\text{Cb}$  needles and a grain boundary precipitate of a chromium-rich, body-centered-cubic (BCC) phase, perhaps with  $\sigma$ . Laves compound can also be present as an interdendritic phase formed during initial solidification, though in wrought Inconel 718 there probably is no Laves phase. Grain boundary carbides are also possible. CbC may be present as a grain boundary film. Boron segregates to grain boundaries and Inconel 718 with high but acceptable boron can possibly form a thin liquid layer of borate in the grain boundary of the Inconel 718 at high temperature in the presence of oxygen. Differing amounts of these phases on the rubbing surfaces could conceivably cause heats of Inconel 718 to behave in a different tribological manner with

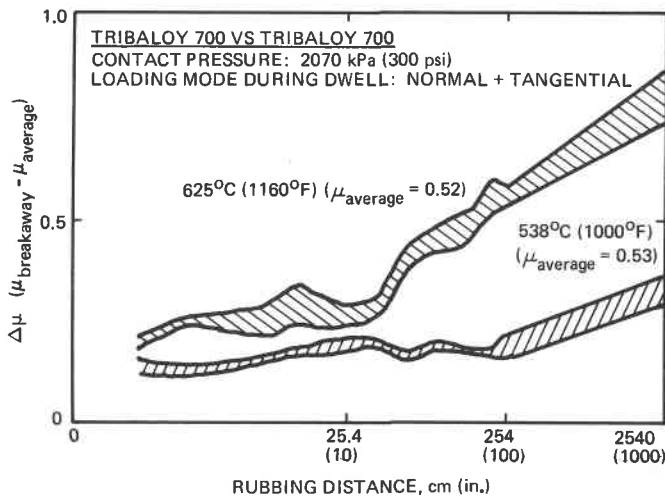


Figure 8. Breakaway phenomena for Tribaloy 700, D-gun applied.

Table 3. Chemistry and Microstructure of Inconel 718 Limiting Chemistry in Weight Percent Except as Noted

B	60 ppm	Co	1.00 max
C	800 ppm	Mn	0.35 max
Ni	50.0-55.0	Si	0.35 max
Fe	Balance	Cu	0.30 max
Cr	17.0-21.0	P	0.015 max
Cb+Ta	4.75-5.50	S	0.015 max
Mo	2.80-3.30		
Ti	0.65-1.15		
Al	0.20-0.80		

Inconel 718 after Usual Double Age (AMS 5596)

Description	Structure	Comments
Phases:		
Matrix $\gamma$	FCC	Stable
Coherent $\gamma'$ ( $\text{Ni}_3\text{Cb}$ )	FCC, coherent with matrix	Metastable
Incoherent $\gamma''$	Tetragonal	Metastable
Incoherent $\delta$	Orthorhombic	Stable(?)
Grain Boundary $\text{Ni}_3\text{Cb}$	Orthorhombic	May form after 1000 h above 600°C (1115°F)
$\alpha'$ possibly with $\sigma$ phase	BCC	Occasionally observed in grain boundary
Carbides	-	If carbon is near 800-ppm limit, carbide can form at expense of $\gamma'$ during aging; may form after 1000 h above 600°C (1115°C)
Boron compounds	-	May be present in grain boundaries

respect to friction. Grain boundary films are a particularly important consideration.

Hardness

The hardnesses of Inconel 718 in the temperature range of interest are shown in Figure 9, superimposed on the time-temperature-transformation (TTT) diagram<sup>(7)</sup> for a typical composition of this alloy solution treated for one hour at 1150°C (2100°F) and water-quenched.

Inconel 718 overages very slowly; i.e., the coherent  $\gamma'$  takes a long time to go to the incoherent tetragonal  $\text{Ni}_3(\text{Cb,Ti,Al})$ , and then to the orthorhombic  $\text{Ni}_3\text{Cb}$ , so softening that may occur after many years is not indicated by exposures on the order of 1000 h.

Dynamic Friction and Wear

The dynamic friction of Inconel 718 is indicated in Figure 10. As was the case in the self-welding data (Table 2), the dynamic friction is highly variable from test to test and within the same test.<sup>(14)</sup> The time, temperature, and rubbing history of the Inconel 718 are extremely important parameters in determining the friction. A good initial wear-in period appears to be critical to achieving subsequent low friction.



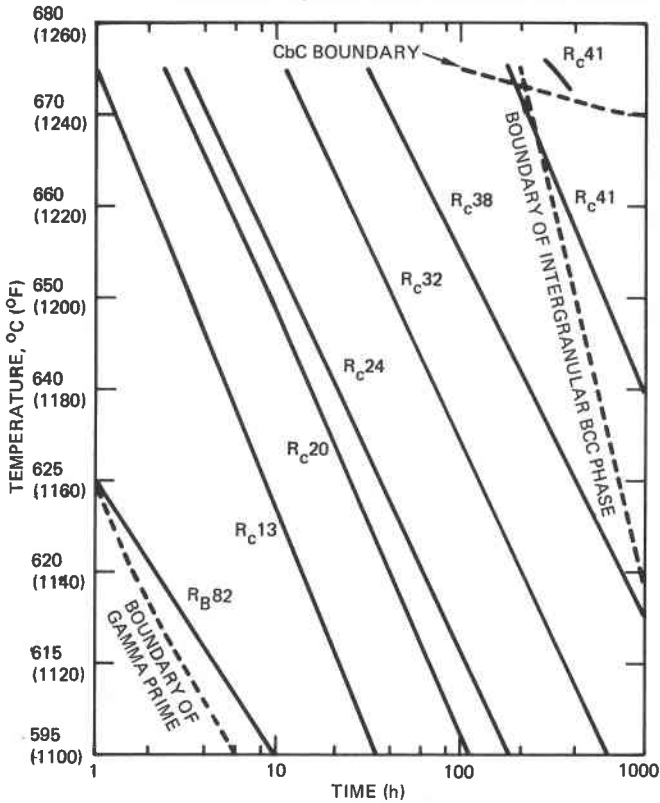


Figure 9. Room-temperature hardness of Inconel 718.

In using the experimental data summarized here, the designer should assume the worst friction properties shown for this alloy, since good friction properties cannot be assumed from heat to heat or from one application to subsequent applications.

The wear of Inconel 718 is adhesive in nature. Pieces of Inconel 718 transfer back and forth. Wear coefficients can show weight gain as well as weight loss in a somewhat random manner. Scanning electron micrographs indicate that rubbed surfaces of Inconel 718 often resemble smeared butter (Figure 11) though optical micrographs of the rubbed surface cross section indicate that the majority of surface grains are not deformed (Figure 12). Grain boundary cracking may be a critical consideration (see Figure 13).

Initial rubbing conditions appear to be quite important in establishing further wear characteristics. Inconel 718 rubbing against a hardfacing such as Stellite 6 leaves a coating of Inconel 718 on the hardfacing after ~127 cm (~50 in.) of rubbing, with subsequent tribological properties of the couple resembling Inconel 718 rubbing against itself.

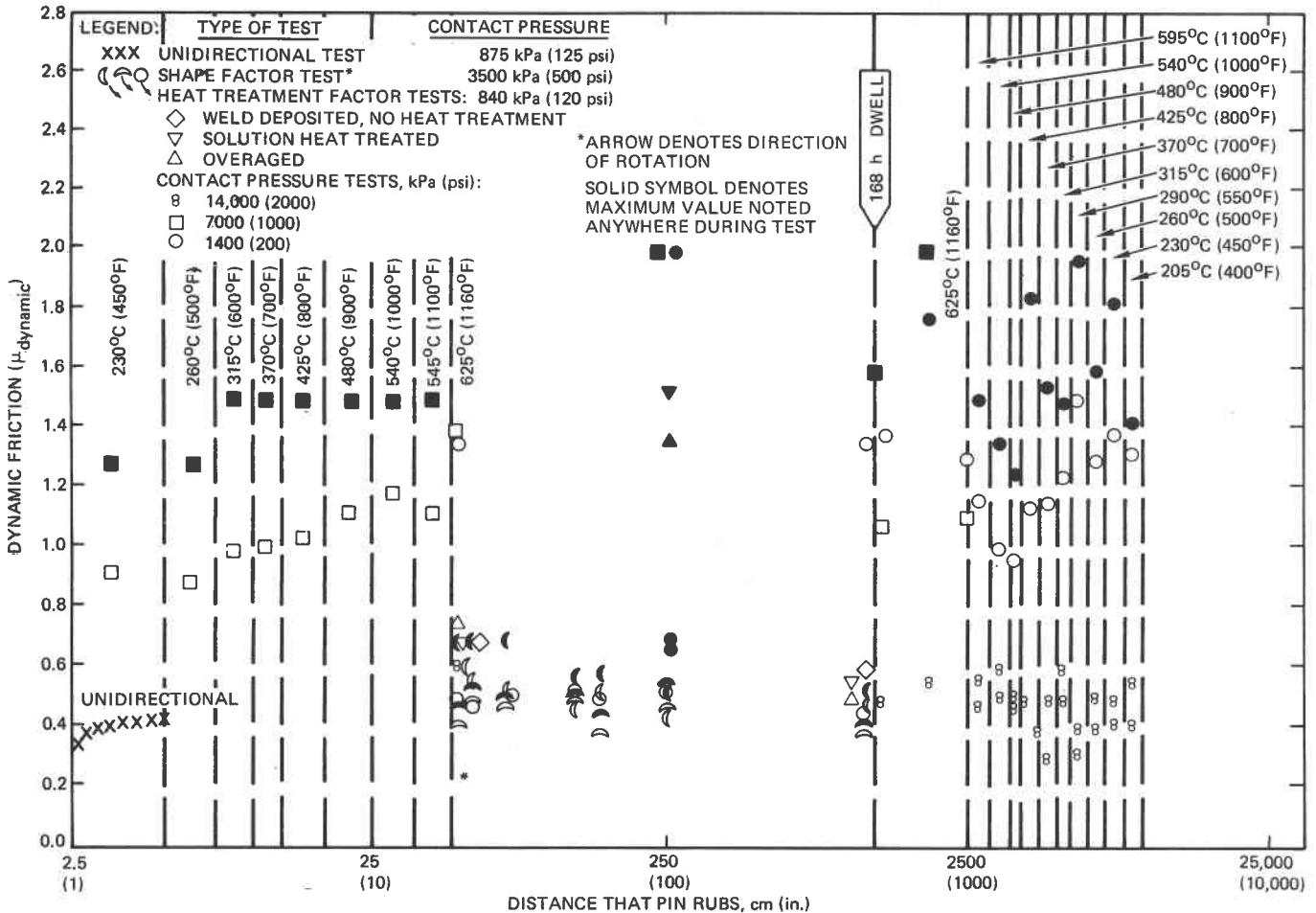


Figure 10. Dynamic friction of Inconel 718.

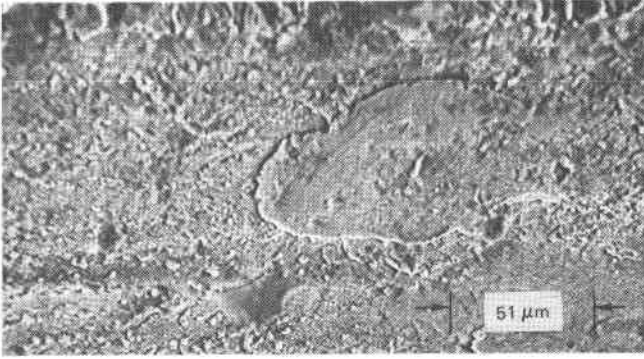


Figure 11. Smeared appearance of rubbed Inconel 718.

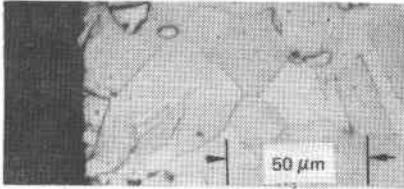


Figure 12. Cross section of rubbed surface of Inconel 718.

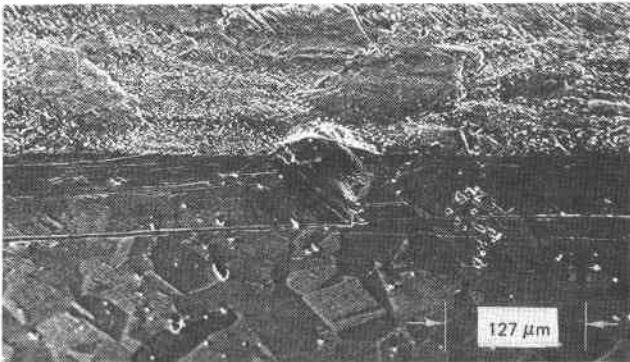
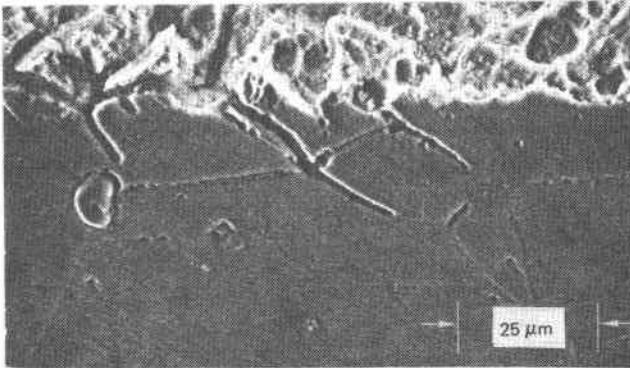


Figure 13. Grain boundary separation in Inconel 718.

Theory to Explain the Variation in Dynamic Friction

The measured dynamic friction of Inconel 718 in liquid sodium has shown very wide variation from test to test and even within the same test. One of the main reasons for the wide variation appears to be related to the occasional loss of individual Inconel 718 grains from the bulk alloy and consequent deformation of the grain between the rubbing surfaces. The relatively

large force needed to smear the grain would be measured as an additional friction force. The loss of individual grains from the rubbing surfaces appears to be associated with intergranular dissolution of Inconel 718 and with mechanical forces.

Other factors that contribute to this variation in frictional behavior may include the metallurgical structure of the alloy, and the time, temperature, and rubbing history of the surfaces in sliding contact, as discussed above. In addition, the imposed load and the oxygen content of the sodium may be a main contributor to the variation, as discussed below.

The equations for dynamic friction of Inconel 718 rubbing against itself in liquid sodium are as follows:

$$F_{\text{measured}} = K + \mu_{\text{true dyn}} F_{\text{imposed}}$$

$$F_{\text{measured}}/F_{\text{imposed}} = \mu_{\text{measured dyn}} =$$

$$K(1/F_{\text{imposed}}) + \mu_{\text{true dyn}}$$

which is the form  $y = mx + b$ , where

$F_{\text{measured}}$  = force required to slide Inconel 718 over itself.

$F_{\text{imposed}}$  = normal force pushing the Inconel 718 surfaces together.

$K$  = bonding force not linearly dependent upon  $F_{\text{imposed}}$

$\mu_{\text{true dyn}}$  = true load-independent dynamic coefficient of friction.

$\mu_{\text{meas dyn}}$  = the apparent dynamic coefficient of friction.

A plot of  $\mu_{\text{measured}}$  versus  $1/F_{\text{imposed}}$  has the form shown in Figure 14. As this plot indicates, very low imposed forces can give very high apparent coefficients of friction. When the load is on the order of a kilogram or less, the friction data shown here may be too low.

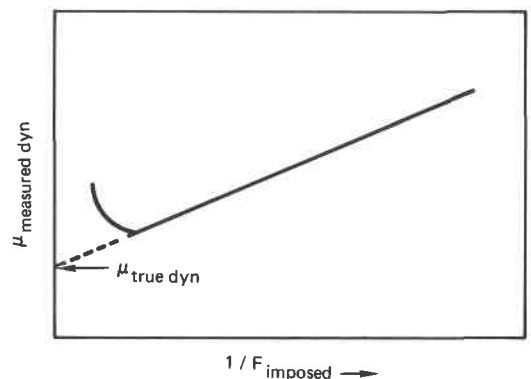


Figure 14. Method of obtaining  $\mu_{\text{true dyn}}$

The oxygen content of the sodium determines the equilibrium surface film on the Inconel 718 at a particular temperature. At sodium temperatures over 540°C (1000°F), reaction rates are such that a lubricative film of sodium metalate can form, the thickness of which depends upon the time between rubbing. At somewhat higher temperatures, bare metal is the equilibrium phase, and high frictions can be expected. Tests in the 480 to 625°C (900 to 1160°F) range have shown that oxygen levels from 0.2 to 5.0 ppm do not affect the friction in sodium.

Plowing forces related to the projected frontal area of a rubbing surface were at one time postulated to be one of the prime reasons for wide variation in Inconel 718 friction tests. Extensive tests have eliminated this parameter as the source of friction variation. On the other hand, adhesion of wear debris in the form of flash at the edges of a rubbing surface appears to be an important factor in giving spurious high friction values. The thin plate of flash can buckle against the side of a wear scar, causing additional forces to be recorded as friction. Buckling of flash and deformation of individual grains lost from the bulk alloy surface are now considered the two main reasons for the anomalous friction properties of bare Inconel 718.

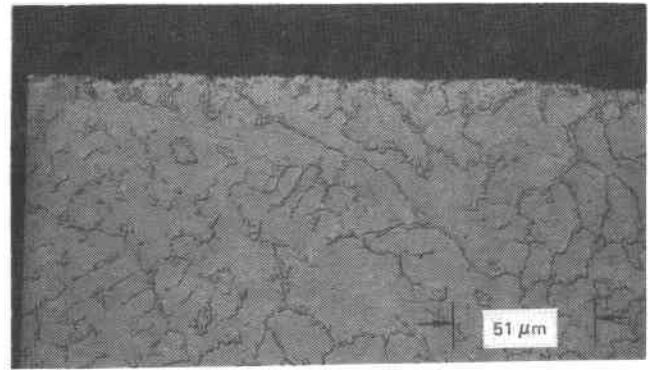


Figure 16. Stellite 6 surface after sodium exposure.

CORROSION OF THESE THREE ALLOYS IN SODIUM

Westinghouse ARD performed corrosion tests on these alloys in a ΔT loop. The results of this work are shown in Figure 15. These data are based on weight change and each experimental point represents the slope of a line drawn from the zero/zero point to the weight-loss/exposure-time point of a particular experiment. In the case of Inconel 718, the attack is intergranular, so that mils-per-year data based on the assumption of uniform surface regression do not indicate the true extent of attack.

For example: After 8000 h exposure to sodium at 627°C (1150°F), 30 cm/s (1 ft/sec), and 0.5 to 1.0 ppm oxygen, Inconel 718 exhibited an average corrosion rate expressed as a uniform reduction in thickness of 3.75 μm/year (0.15 mil/year).<sup>(15,16)</sup> However, examination of the samples revealed that intergranular attack had occurred, resulting in an affected depth of ~0.0025 cm (~0.001 in.). This type of attack results from removal of nickel from the surface by the sodium leaving a surface consisting of holes (where grains have been removed) and peaks of an Fe,Mo-rich phase. Consideration is being given to the effects of such surface and near-surface chemistry and microstructural changes on friction and wear behavior and fatigue properties.<sup>(15)</sup>

The grain boundary separation, so dramatically shown for a rubbed Inconel 718 surface in Figure 13, may be due substantially to corrosion or dissolution of a grain boundary phase. Aluminizing Inconel 718 will eliminate this problem.<sup>(14,17)</sup> The practically negligible corrosion of Stellite 6 in 595°C (1100°F) sodium is shown in Figure 16.

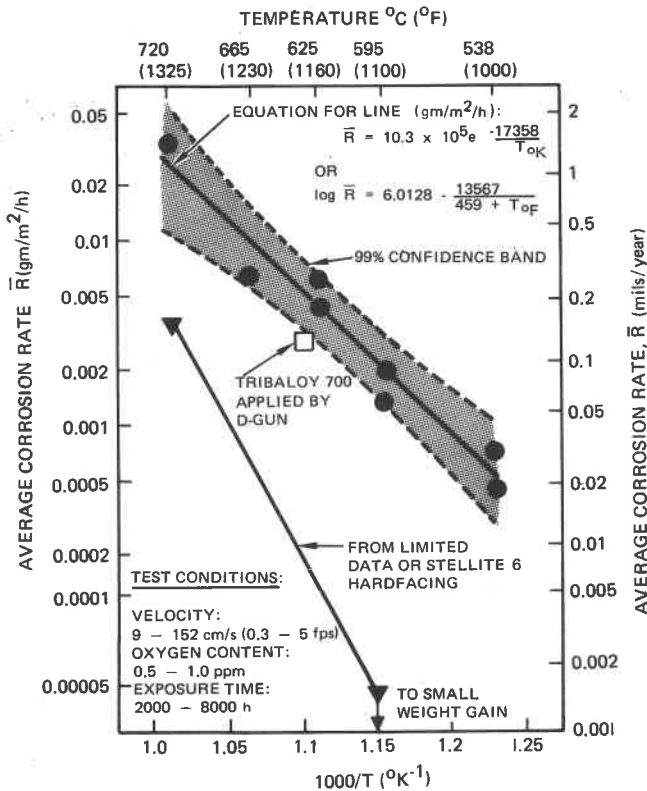


Figure 15. Corrosion of Stellite 6, Triballoy 700, and Inconel 718 in sodium.

## INTERNATIONAL CONFERENCE ON LIQUID METAL TECHNOLOGY IN ENERGY PRODUCTION

The sodium corrosion behavior of Tribaloy 700 is similar to many nickel-base alloys in that weight losses are exhibited due to leaching of nickel from the exposed surface. This alloy has exhibited an average corrosion rate of  $2.5 \mu\text{m}/\text{year}$  (0.1 mil/year) after 8000 h exposure at  $627^\circ\text{C}$  ( $1160^\circ\text{F}$ ). The somewhat lower rate than that for Inconel 718 may be related to the presence of molybdenum, a generally corrosion-resistant element, in the Tribaloy 700.

### ACKNOWLEDGMENT

The authors would like to thank Dr. Mel Cowgill of Westinghouse Advanced Reactors Division for his consultation and advice on the experimental requirements and for his insights into the problem of presenting our data usefully to the LMFBR designer and engineer.

### REFERENCES

1. H. Derow and H. E. Bleil, "Elevated Temperature Instability of Stellite 6B," NASA CR 1590 (May 1970).
2. Manufacturers Data Sheet F 30542, Stellite Division, Cabot Corp (1974).
3. G. A. Fritzlen and J. K. Elbaum, "Cobalt-Chromium-Tungsten-Molybdenum Alloys," Metals Handbook, Vol 1, p 670 (1961).
4. J. L. deBrouwer and D. Coutsouradis, "Influence of Tungsten and Carbon Contents on the Microstructure and Properties of a Cobalt-Base Hardfacing Alloy," Cobalt 32 (Sep 1966).
5. G. A. Whitlow et al., "Sodium Corrosion of Alloys for Fast Reactor Applications," Proceedings of Symposium on Chemical Aspects of Corrosion and Mass Transfer in Liquid Sodium, 1971 Meeting of AIME, Detroit, pp 1-63 (1973).
6. J. V. Chang et al., "Self-Welding Evaluation of Reactor Materials in Flowing Sodium," TANSO 22, pp 200-202 (1975).
7. H. L. Eiselstein, "Metallurgy of a Columbium-Hardened Nickel-Chromium-Iron Alloy," Advances in the Technology of Stainless Steels and Related Alloys, Special Technology Bulletin No. 369, ASTM (1965).
8. A. Kaufman et al., "Intensity Anomalies in the X-ray Diffraction Pattern of  $\text{Ni}_3\text{Nb}$  and Their Relationship to Those for Martensite," Scripta Metallurgica 3, pp 715-720 (1969).
9. B. G. Koepke et al., "Mechanism and Kinetics of Aging in Inconel 718," Rocketdyne Research Report 64-13 (1964).
10. M. Kaufman and A. E. Palty, "The Phase Structure of Inconel 718 and 702 Alloys," Trans. AIME 221 (Dec 1961).
11. J. F. Muller and M. J. Donachie Jr., "The Effects of Solution and Intermediate Heat Treatments on the Notch-Rupture Behavior of Inconel 718," Met. Trans. V6A (Dec 1975).
12. J. F. Barker et al., "Long Time Stability of Inconel 718," J. of Metals (Jan 1970).
13. R. F. Decker, "Strengthening Mechanisms in Nickel-Base Superalloys," presented at Steel Strengthening Mechanisms Symposium, Zurich, Switzerland, May 5, 1960.
14. R. N. Johnson et al., "Development of Low Friction Materials for LMFBR Components," to be published in Proceedings of International Conference on Liquid Metal Technology in Energy Production, ANS - AIME - ERDA Meeting, Champion, PA (1976).
15. G. A. Whitlow et al., "Observations on the In-Sodium Corrosion and Tribology of Aluminide Coatings on Inconel 718," Microstructural Science, pp 775-778 (1975).
16. G. A. Whitlow and R. L. Miller, "Sodium Technology Program: Friction, Wear, and Self-Welding," Quarterly Report for Period Ending July 31, 1976, WARD-NA-3045-32, Westinghouse Electric Corp (1976).
17. N. J. Hoffman and J. J. Droher, "Friction and Wear in Sodium," Section 4, Annual Technical Progress Report, LMEC-76-1, Liquid Metal Engineering Center (1976).

# INTERNATIONAL CONFERENCE ON LIQUID METAL TECHNOLOGY IN ENERGY PRODUCTION

## INVESTIGATIONS INTO THE SELF-WELDING BEHAVIOR OF METALLIC MATERIALS EXPOSED TO SODIUM

F. Huber

K. Mattes

Kernforschungszentrum Karlsruhe  
 Institut für Reaktorentwicklung  
 7500 Karlsruhe, Postfach 3640  
 Federal Republic of Germany

### ABSTRACT

To determine the parameters responsible for self-welding, experimental investigations were carried out at the Karlsruhe Nuclear Research Center. These activities are related to the SNR 300 prototype sodium-cooled fast breeder reactor. The experimental equipment, test materials and conditions as well as the results obtained are described and an attempt is made to present a general applicable explanation of the self-welding phenomena.

### INTRODUCTION

Under specific conditions self-welding may occur in liquid sodium on components of sodium cooled reactors and must therefore be taken into account according to its consequences on operating reliability. To determine the parameters responsible for the mechanisms of self-welding, experimental investigations were performed at the Institute for Reactor Development of the Gesellschaft für Kernforschung, Karlsruhe (1-3). The test-materials and conditions were largely selected with a view to the SNR 300 prototype sodium-cooled fast breeder reactor. It was first attempted in quite a number of basic tests to find the influence of the respective parameter by variation of the sodium temperature, the contact pressure, the contact area and the surface finish. At a later date specific tests were performed above all to evaluate more accurately the self-welding behavior of the materials Inconel 718 (nickel base alloy) and Stellite 6 (cobalt base alloy). These materials are to be used for the SNR 300 fuel element spacer pads.

### EXPERIMENTAL EQUIPMENT

The investigations were made in the sodium tank test facility (NABEA) of the Institute for Reactor Development (4). Two types of devices represented schematically in Fig. 1 were used to carry out the tests.

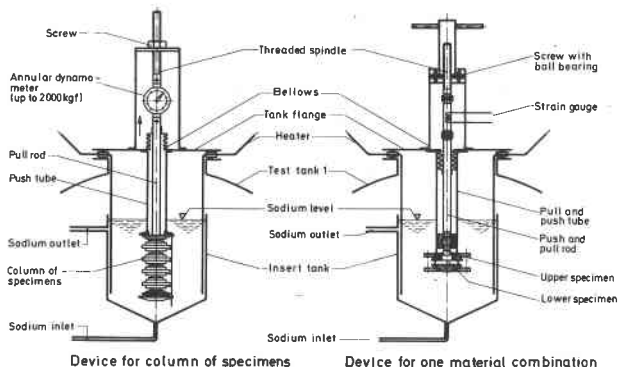


Fig. 1: Scheme of the two types of test devices

In the first type annular disks with a defined contact area were used as material specimens. About 35 of these specimens can be assembled into a column and pressed against each other by use of a central pull rod. The maximum load is 2000 kgf. This test device allows the combination of different specimens, so that the test parameters: material, contact area (contact) pressure, respectively) and surface finish can be varied in one test. An annular dynamometer has been installed in the pull rod to measure the contact force. After the test the specimens which had undergone self-welding were separated in a tensile test machine at ambient temperature. The disadvantage of this device is that for pairs of materials having different thermal expansion coefficients shear forces occur during the cooling process, which might entail falsification of the breakaway force to be measured. This disadvantage is eliminated by the second type of device which both allows the contact and separation of a specimen pair under sodium. The forces so produced are determined by means of strain gauges and recorded with a light chart strip recorder during separation. With this device forces up to 2000 kgf can be applied. The geometries of specimens adapted to the respective types of devices are represented in Fig. 2.

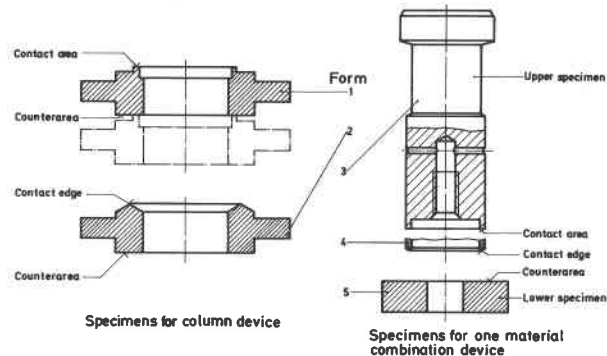


Fig. 2: Forms of specimens

Form 1 was the specimen geometry most frequently used. Shapes 2 and 4 have been provided with an edge instead of the contact area. If a pair containing such a specimen is contacted, the contacting edge gets deformed under the influence of the contact pressure according to the hot yield point. After separation of this pair a circular stamp of the contact area is left which can be measured by optical methods. This surface is identical with the surface  $A_{tp}$  formed by plastic deformation (Eq. 4) and significant for the breakaway force. The contact area of specimens of form 1 had been lathed or lapped; the contact areas of the other forms had only been lathed.

### TEST MATERIALS

Table 1 contains a selection of materials tested including their alloying constituents. The selection was essentially governed by the SNR 300. Since the Inconel 718 and Stellite 6 materials are intended for use as fuel element spacer pads, these materials were especially important. In search of pairs resistant to self-welding, which are equally suitable for this pur-

# INTERNATIONAL CONFERENCE ON LIQUID METAL TECHNOLOGY IN ENERGY PRODUCTION

TEST-MATERIAL	STELLITE 6	INCONEL 718	COUMONDY 4	PAT. No. 1,4981	PAT. No. 1,4301	PAT. No. 1,6770	TZn	Zr
C	1.0	0.06	0.45	0.06	0.06	0.047	-	-
Si	0.8	0.03	2.25	0.48	0.9	0.06	-	-
Mn	-	0.02	-	1.31	1.25	0.55	-	-
P	-	<0.005	-	0.027	0.022	0.01	-	-
S	-	0.002	-	0.008	0.03	-	-	-
Fe	13.2	18.73	2.5	63.4	71.0	95.5	-	-
Cr	23.6	18.46	10.0	16.61	17.95	2.4	-	-
Mo	-	2.96	-	1.75	<0.2	0.81	98.7	-
Ni	3.3	53.45	82.8	15.56	8.42	0.07	-	-
Nb	-	5.27	-	0.84	0.2	0.53	-	-
Ti	-	0.99	-	-	-	-	0.46	-
Al	-	0.52	-	-	-	-	-	-
B	-	0.003	2	-	-	-	-	-
W	4.2	-	-	-	-	-	-	-
Zr	-	-	-	-	-	-	0.7	100
Co	51.5	-	-	-	-	-	-	-
O	-	-	-	-	-	-	0.15	-

1) MATERIAL NO. DUE TO DIN 17007  
 2) IMP = INSTITUT FÜR MATERIAL- UND FESTKÖRPERFORSCHUNG  
 3) DEN = DEUTSCHE EDELSTAHLWERKE

Tab. 1: Test materials and alloying constituents

pose, specimens were tested which had been coated by carbide materials.

### EXPERIMENTAL CONDITIONS

Table 2 presents a survey of the test conditions selected.

FLUSHING TEMPERATURE	$T_s$	$^{\circ}\text{C}$	550; 600; 700
FLUSHING TIME	$t_s$	$\text{h}$	24
CONTACT TEMPERATURE	$T_A$	$^{\circ}\text{C}$	380; 550; 600; 700
CONTACT TIME	$t_A$	$\text{h}$	4; 24; 72; 168; 336; 1008
CONTACT PRESSURE	$F_A$	$\text{kgf}$	275; 500; 550; 825; 1000; 1100
CONTACT AREA	$A$	$\text{mm}^2$	$A_{TP}^1$ ; 150; 220; 300; 440; 600; 880
BREAKAWAY TEMPERATURE	$T_Z$	$^{\circ}\text{C}$	$T_R^2$ ; $T_A$
PEAK-TO-VALLEY-HEIGHT	$\lambda_{\mu\text{m}}$	$\mu\text{m}$	$>4$ (LATHED); $<1$ (LAPPED)
PLUGGING TEMPERATURE	$T_p$	$^{\circ}\text{C}$	$<150$

1)  $A_{TP}$  SUPPORTING AREA, FORMED BY PLASTIC DEFORMATION  
 2)  $T_R$  AMBIENT TEMPERATURE

Tab. 2: Test conditions

These conditions complied with two requirements. First, the test should serve the purpose of analyzing the process of self-welding and of assessing the influence of the respective test parameters (fundamental studies). Secondly, given pairs should be tested under defined conditions. In the first case the test conditions were so selected that self-welding was to be expected. In the second case the question was asked whether a pair will undergo self-welding or not under the given conditions. Except for a few cases, the tests were conducted with a flushing phase included. In this phase the specimens are kept apart to allow the sodium to act upon both surfaces. The duration of this phase was 24 hours. With few exceptions the temperature during the flushing phase corresponded to that of the contact phase. The plugging temperature at the time of specimen contacting was  $130 \leq T_p \leq 140$  °C. During the contact phase the specimens were in stagnant sodium.

### EXPERIMENTAL PROCEDURE

After installation of the devices into the tank

and preheating, the devices were flooded with sodium at 150 °C from the storage tank. Subsequently the sodium was heated to the flushing temperature and cleaned at the same time. During cleaning the plugging temperature decreased to  $T_p < 150$  °C. After the flushing and cleaning period the circulation was stopped and the test load applied. The test conditions remained unchanged during the preset rest duration. Depending on the type of device, the specimens were separated under sodium at the test temperature or in the other case in a tensile machine after cooling, removal, disassembly and cleaning. In each case the breakaway force was measured with which the specimens were attached to each other. Together with the other test parameters this force serves as a measure of the extent of self-welding.

### TEST RESULTS AND DISCUSSION

The majority of tests were performed with the device equipped with the specimen column. Thus the following results are derived from these tests only.

#### Influence of the Contact Area

Fig. 3 shows the breakaway forces obtained with the 1.4981 austenitic steel as a function of the contact area and with the peak-to-valley height as a parameter. It appears from this figure that under constant test conditions the breakaway force is influenced by the peak-to-valley height. With lathed specimens the breakaway forces are more independent of the contact area. Contrary to the results of the lathed specimens, those of the lapped specimens are characterized by the tendency that the breakaway forces increase with increasing contact areas. As a whole, the breakaway forces of lapped specimens are higher than those of the lathed specimens. This is also applicable to the other materials tested.

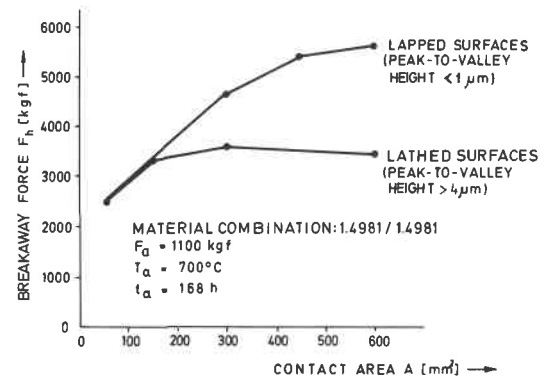


Fig. 3: Influence of the contact area and the surface finish on the breakaway force for material 1.4981

#### Influence of Test Material

In Fig. 4 the breakaway forces obtained with the lapped specimens are represented as a function of the contact area with the pairing materials as parameters.

Maximum breakaway forces were measured with the 1.6770 ferritic steel; lower breakaway forces were obtained with austenitic steels, and the lowest breakaway force was measured for Inconel 718. If the breakaway forces obtained are compared with the high-tem-

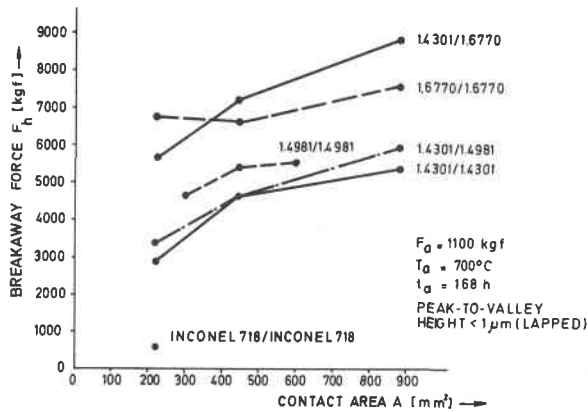


Fig. 4: Influence of the test material on the breakaway force

perature strength of the respective materials, it can be seen that the breakaway force decreases with increasing high-temperature strength. The example of the pairs made of the 1.4301 austenitic steel and the 1.6770 ferritic steel also shows that the welding behavior is determined by the material with the lower high-temperature strength.

Influence of the Contact Pressure

Fig. 5 is a plot of the breakaway forces obtained for lathed specimens of material 1.4981, versus the contact pressure with the contact area as a parameter.

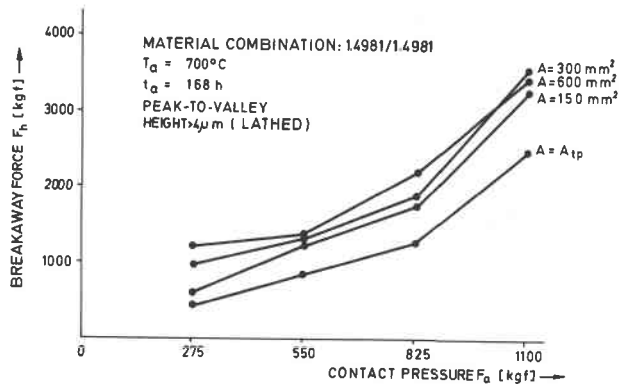


Fig. 5: Influence of the contact pressure on the breakaway force

This figure shows that for specimens with a contact edge, i.e. with a contact area  $A=A_{tp}$ , the breakaway force is nearly proportional to the contact pressure. Taking into account the influence exerted by the area, this behavior is truly analogous with respect to larger and lapped contact areas. The deviating values for the contact pressure  $F_a = 1100$  kgf can be explained by better surface reduction during the flushing phase in this experiment.

Influence of the Contact Time

In Fig. 6 the influence exerted by the contact time is represented for identical materials. It appears

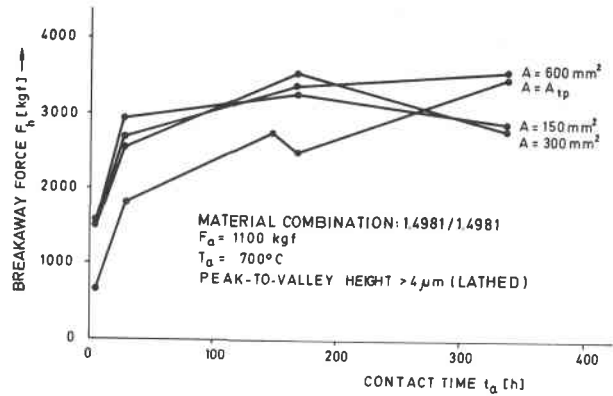


Fig. 6: Influence of the contact time on the breakaway force

that apart from relatively short periods the contact time does not exert a noticeable influence on the breakaway force.

If, as represented in Fig. 7, the breakaway forces obtained for specimens with a contact edge are plotted versus the supporting area generated, with the time as a parameter, a good proportionality is found to exist between the supporting area and the breakaway force. One can conclude from this behavior that the influence of time is exerted in an indirect way via the creep properties of the respective pairing materials.

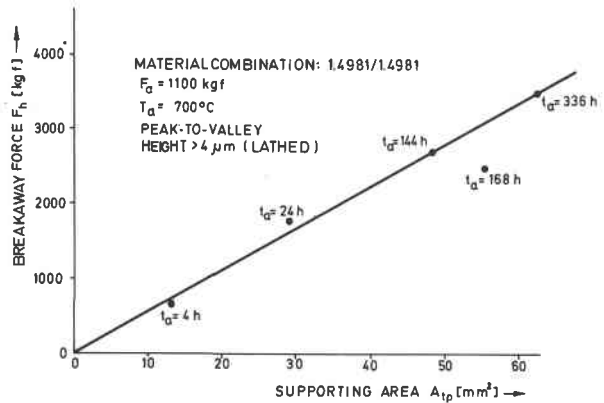


Fig. 7: Influence of the supporting area on the breakaway force

Influence of the Contact Temperature

As already stated, the breakaway forces are influenced by the high-temperature strength of the pairing materials. Investigations carried out in this field yielded an average breakaway force of about 2.500 kgf for specimens of material 1.4981 with a contact edge at a temperature and pressure of  $700^\circ\text{C}$  and 1100 kgf, respectively. At  $550^\circ\text{C}$  the average force was about 600 kgf under the same contact pressure. The ratio of the breakaway forces obtained was 4:1. According to the material sheet issued by Deutsche Edelstahlwerke the creep rupture strength  $B/10000$  for material 1.4981 is 8.5 kgf/mm<sup>2</sup> at  $700^\circ\text{C}$  and 33 kgf/mm<sup>2</sup> at  $550^\circ\text{C}$ . Consequently, the ratio of the creep rupture strengths indicated is 1:4; so it can be stated in this case that the breakaway forces obtained are inversely proportion-



al to the creep rupture strengths indicated. Generalizing, it may be concluded that the influence of temperature on the breakaway force is exerted indirectly via the temperature-dependent strength properties of the pairing materials. However, to obtain a general survey of the influence exerted by the temperature, the numbers were stated in Table 3 for a substantial amount of material pairs used at the respective temperatures and the percentages stated in which self-welding was observed. The contact time did not last longer than 336 hours. The results obtained with the Stellite 6 and Inconel 718 materials within the temperature range between 550 and 600°C (cf. Table 3) can be transferred only with considerable reservations to the long service times encountered in the reactor. Similar investigations conducted by Westinghouse, Madison, USA, at 565 °C and at the National Tribology Center, Risley, UK at 600°C show that these materials might well undergo self-welding during service periods > 1000 h. Similar results were confirmed by a long-term test of 1008 hours performed at GfK.

COMBINATION	MATERIAL-COMBINATION	TEST TEMPERATURE (°C)							
		380		550		600		700	
		N	N <sub>w</sub> /N	N	N <sub>w</sub> /N	N	N <sub>w</sub> /N	N	N <sub>w</sub> /N
COMBINATION XX	STELLITE 6/STELLITE 6	7	0	18	0	-	-	25	0,6
	INC. 718/INC. 718	-	-	32	0	31	0	64	0,77
	COLMONOY 4/COLMONOY 4	18	0	129	0,37	2	(0)	327	0,98
	1.4981/1.4981	-	-	50	0,72	-	-	113	0,97
	1.4301/1.4301	-	-	19	0,58	-	-	43	0,97
	1.6770/1.6770	10	0	10	0	-	-	14	0,86
TZM/TZM	-	-	-	-	-	-	-	5	0
COMBINATION XY	STELLITE 6/INC. 718	2	0	6	0	-	-	9	0,67
	STELLITE 6/1.4981	-	-	-	-	-	-	4	0,75
	STELLITE 6/1.6770	-	-	-	-	-	-	4	1
	INC. 718/COL. 4	-	-	4	0	-	-	6	1
	TZM/STELLITE 6	-	-	-	-	-	-	1	(0)
	TZM/INC. 718	-	-	-	-	-	-	2	(0)
	TZM/1.4981	-	-	-	-	-	-	1	(0)

( ) STATISTICALLY INSUFFICIENT  
 N NUMBER OF TESTED MATERIAL COMBINATIONS  
 N<sub>w</sub> NUMBER OF SELF-WELDED MATERIAL COMBINATIONS

Tab. 3: Influence of test temperature

Influence of Flushing

The influence of flushing was investigated using columns which consisted of identical specimens at a contact temperature of 550°C. One column was flushed for 24 h at 550°C, the other one for the same time at 700°C but with a zirconium getter placed in the sodium to reduce the oxygen concentration. After termination of the flushing phase the columns were pressed together. In the first case none of the 35 pairs were welded together. In the second case all 35 pairs were welded together. Disassembly yielded a marked difference in appearance of the two columns of specimens. The specimens flushed at 550°C had undergone strong oxidation, while the specimens flushed at 700°C were metallic. These results show clearly that the welding behavior is influenced by oxide layers on the contact area. This surface condition depends on the redox processes which are mainly determined by the oxygen concentration and the sodium temperature existing during the flushing phase. Therefore, self-welding

must always be anticipated under conditions leading to oxide-free metallic surfaces.

Micro-structure

Fig. 8 shows the micrograph of a self-welded contact point of a specimen with a contact edge, tested for 336 hours at a contact pressure of 550 kgf in sodium at 700°C. A clear separating line between the two specimens is no longer recognizable. In the boundary zone of the contact points of the purely plastically deformed contact edge the material has undergone recrystallization.

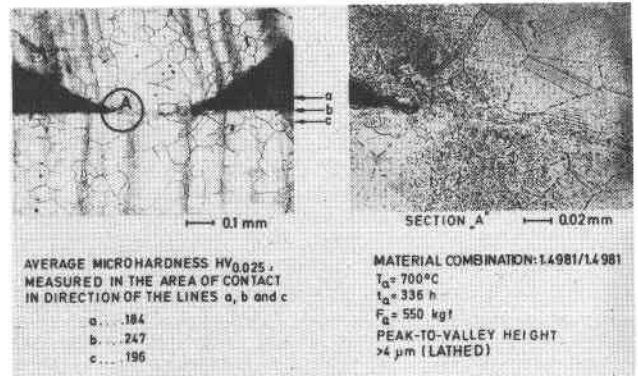


Fig. 8: Metallograph of a self-welded pair (contact edge/counter area)

Behavior of TZM and of Zr Vapor Deposited Specimens

For pairs consisting of specimens of the Zr containing molybdenum base alloy TZM self-welding was not detected even at a contact temperature of 700°C. The decisive factor for this behavior seems to be the Zr content, which forms an oxide layer preventing self-welding. Influenced by this effect we have subjected specimens made of the 1.4981 material to Zr vapor deposition exposed to a temperature of 700°C in a test. In this case self-welding was not observed contrary to the specimens not exposed to vapor deposition.

ATTEMPT ON AN EXPLANATION OF SELF-WELDING

The dependencies achieved allow the description of self-welding by three separate phenomena:

- a) Reduction of a material surface by sodium.
- b) Deformation of the points of contact and formation of a supporting area due to the effect of contact pressure.
- c) Self-welding of the supporting area as a result of recrystallization.

The phenomenon a) involves the influence of the redox processes of the material surfaces dependent on the temperature and oxygen concentration; phenomenon b) the influence of temperature-dependent mechanical properties and of temperature as well as of time-dependent creep properties of the paired materials, their surface profile and contact pressure; and phenomenon c) the influence of temperature and strain-dependent recrystallization properties of the paired materials.



In a parameter study the relation Eq. 1 was derived (2):

$$F_h = \alpha \cdot \sigma_R \left[ \frac{k \cdot F_a}{c' \cdot \sigma_{0.2}(T_a; t_a)} + \frac{A^{1/3}}{1.9} \left( \frac{(1-k) F_a \cdot L}{R \cdot E} \right)^{2/3} \right]$$

where

- $F_h$  /kgf/ breakaway force
- $\alpha$  self-welding factor
- $\sigma_R$  /kgf/mm<sup>2</sup>/ real ultimate strength of the material
- $k$  fraction of the contact pressure causing plastic deformation
- $F_a$  /kgf/ contact pressure
- $c'$  proportionality factor
- $\sigma_{0.2}(T_a; t_a)$  /kp/mm<sup>2</sup>/ yield point depending on temperature and time
- $A$  /mm<sup>2</sup>/ contact area
- $L$  /μm/ distance from one support point to the other
- $R$  /μm/ roughness depth of the surface
- $E$  /kgf/mm<sup>2</sup>/ elasticity modulus

The following considerations led to this relation:

- The breakaway force  $F_h$  is calculated from the real ultimate strength  $\sigma_R$  of the material and the self-welded surface  $A_v$

$$F_h = \sigma_R \cdot A_v \quad \text{Eq. 2}$$

- The self-welded surface is part of the supporting area  $A_t$  formed by deformation

$$A_v = \alpha \cdot A_t \quad \text{Eq. 3}$$

- The supporting area is composed of two parts, one part caused by plastic ( $A_{tp}$ ) and the other by elastic ( $A_{te}$ ) deformation

$$A_t = A_{tp} + A_{te} \quad \text{Eq. 4}$$

- The contact pressure is subdivided into one component giving rise to plastic deformation ( $F_{ap}$ ) and one component resulting in elastic deformation ( $F_{ae}$ ).

$$F_a = F_{ap} + F_{ae} = k \cdot F_a + (1-k) F_a \quad \text{Eq. 5}$$

- According to (5) the supporting area formed by plastic deformation is calculated with Eq. 6

$$A_{tp} = \frac{k \cdot F_a}{c' \cdot \sigma_{0.2}(T_a; t_a)} \quad \text{Eq. 6}$$

- Assuming a sinusoidal waveform on the surface the supporting area formed by elastic deformation can

be derived according to /15/ with Eq. 7

$$A_{te} = \frac{A^{1/3}}{1.9} \left( \frac{(1-k) F_a \cdot L}{R \cdot E} \right)^{2/3} \quad \text{Eq. 7}$$

According to the definition (5) the factor  $k$  equals 1 for purely plastic deformation as observed in specimens provided with a contact edge, which means that the corresponding breakaway force  $F_{hp}$  can be calculated from Eq. 8

$$F_{hp} = \frac{a}{c'} \cdot F_a \frac{\sigma_R}{\sigma_{0.2}(T_a; t_a)} \quad \text{Eq. 8}$$

The relation Eq. 8 says that for pairs with a contact edge the breakaway force is proportional to the contact force and proportional to the ratio of the actual ultimate strength to the yield point depending on time and temperature. This relation agrees with the experimental results.

For contact areas satisfying the condition  $A > A_{tp}$  the fraction of breakaway force  $\Delta F_{he}$  resulting from elastic deformation would be calculated from Eq. 7 according to Eq. 9.

$$\Delta F_{he} = \alpha \cdot \sigma_R \frac{A^{1/3}}{1.9} \left( \frac{(1-k) \cdot F_a \cdot L}{R \cdot E} \right)^{2/3} \quad \text{Eq. 9}$$

Assuming at first that the fraction of contact pressure  $(1-k) F_a$  causing elastic deformation has a constant value, relation Eq. 9 confirms the influence found experimentally of the contact area as well as that of the surface finish expressed here by  $L$  and  $R$ . Also the assumption is confirmed that for contact areas  $A > A_{tp}$  the supporting area is formed partly by plastic and partly by elastic deformations. The factor  $(1-k)$  expressing the amount of contact force causing elastic deformation depends on the number and shape of the individual supporting points and on the force acting on the respective supporting points. It is thus a function of the parameters  $A$ ;  $F_a$ ;  $L$  and  $R$  given in Eq. 9. Starting from the above considerations one can say that with increasing  $F_a$  and  $R$  the  $(1-k)$  value decreases and increases with increasing  $A$ ,  $L$  and  $E$ . The result is that for constant values of  $F_a$ ,  $R$  and  $E$  the influence of the area must be greater than proportional to  $L \exp. 2/3$ . Since the profile of a real surface cannot be expressed by  $L$  and  $R$  and the function for  $(1-k)$  is not known, an empiric approach Eq. 10 for the estimation of the breakaway force was made.

$$F_h = \alpha \cdot \sigma_R \cdot A_{tp} \left( \frac{A}{A_{tp}} \right)^m \quad \text{Eq. 10}$$

The function  $F_h(A)$  for lathed and lapped specimens was derived from the experimental results for the 1.4981/1.4981 material combination (Fig. 9), leading to the following exponents  $m$

- for lathed surfaces  $m = 0.2$
- for lapped surfaces  $m = 0.32$ .

The exponent  $m$  is basically influenced by the specific surface finish. Accordingly, the values found can be regarded as representative also for other material pairs. The self-welding factor  $\alpha$  cannot be transferred

to other materials on account of the material specific redox and recrystallization processes; however, under favorable conditions, i.e., low oxygen concentration, high test temperature and perfect recrystallization, it can take the value  $\alpha = 1$ .

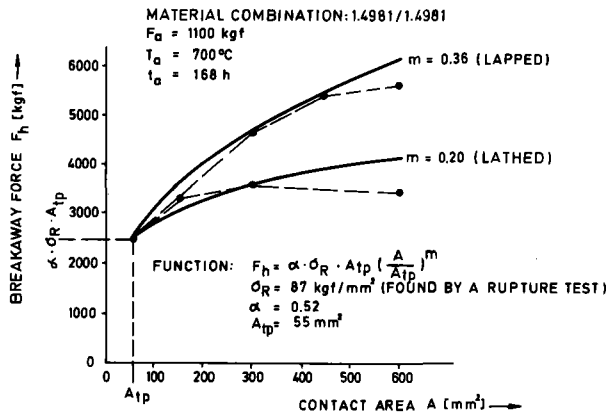


Fig. 9: Breakaway force as a function of the contact area; experimental results and best fit using Eq. 10.

The previous considerations essentially applied to pairs made of similar materials. If two different materials are pressed against each other, the strength values of the less rigid material must be introduced into the respective relations for the breakaway force.

#### SUMMARY AND CONCLUSIONS

About 1500 specimen pairs were tested in stagnant sodium at temperatures up to 700°C. The results can be summarized as follows:

- At 700°C all materials tested with the exception of TZM showed a tendency of self-welding.
- Self-welding can be avoided even at 700°C by the application of a thin layer of a reduction material to sodium, e.g. vapor deposition of zirconium.
- Under constant test conditions the breakaway force exhibited a dependence on the strength properties of the respective pair materials.
- The self-welding behavior was determined essentially by the material having the lowest strength values.
- For lapped contact areas (low peak-to-valley height) the breakaway force was influenced by the size of the area at constant contact force. It increased with the contact area becoming larger.
- For lathed contact areas (great peak-to-valley height) the breakaway force showed little dependence on the size of the area at constant contact pressure.
- The breakaway force revealed to be nearly proportional to the contact pressure for a given contact area.
- The redox processes initiated by the flushing phase influenced the self-welding behavior to a large extent.

Specimens oxidized at the time of contacting exhibited little or no self-welding.

- The time and temperature did not directly influence the breakaway force. The influence of time was exerted by the time-dependent creep effects at the contact points and the influence of temperature was due to the temperature-dependent redox processes and the high-temperature strengths of paired materials. Recrystallization is influenced both by the time and by the temperature.

Regarding temperature the results obtained can be supplemented by the following statements:

- Self-welding can be excluded at temperatures up to 380°C.
- At temperatures between 550 and 600°C self-welding of pairs made of ferritic or austenitic steels must be expected. Pairs made of the nickel and cobalt base alloys tested by GfK did not undergo self-welding at these temperatures and for contact times < 168 hours. For contact times > 1000 hours self-welding cannot be excluded.
- At 700°C self-welding must be anticipated. The Zr coated specimens or pairs containing TZM make an exception.

As a conclusion from the results listed above the following design recommendations can be given so as to keep low the breakaway forces expected from self-welding.

- Use of materials having good high-temperature strength properties.
- Shaping the contact points in such a way that point or line contact occurs (Hertzian stress, i.e., no large contact areas).
- Selection of a fabrication technique (coarse lathing, planing) which yields high roughness values.
- Coating of surfaces with compounds resistant to self-welding (carbides, zirconium).

#### OUTLOOK

Investigations of self-welding have been terminated for the time being. However, it is intended to perform in the future some tests with carbide coated specimens and with specimens made of special materials.

#### ACKNOWLEDGEMENTS

The authors wish to express their gratitude to H. Schneider for chemical analysis of test materials and sodium samples, to U. Schlenker for preparations and photographs of metallographic specimens, and to H.U. Borgstedt and E. Wild for their helpful assistance in the interpretation of the self-welding phenomena.

#### References

- (1) K. Benndorf:  
Experimental Investigations of Self-welding of Structural Materials under Sodium  
Nucl.Eng.Des. 14/1, 1970

## INTERNATIONAL CONFERENCE ON LIQUID METAL TECHNOLOGY IN ENERGY PRODUCTION

- (2) F. Huber, K. Mattes, W. Weinhold:  
Selbstverschweißen von Strukturwerkstoffen in  
flüssigem Natrium  
KFK 1903, 1974
- (3) H.U. Borgstedt, K. Mattes, E. Wild:  
Selbstverschweiß-, Reib- und Verschleißver-  
halten spezieller Werkstoffe in Natrium unter  
korrodierenden Bedingungen.
- (4) F. Huber, R.A. Müller:  
The Karlsruhe Sodium Tank Test Facility  
KFK 1203, 1970
- (5) F.B. Bowden, D. Tabor:  
The Friction and Lubrication of Solids,  
2nd Edition, Oxford, 1954
- (6) H. Hertz:  
Journal für reine und angewandte Mathematik  
1886

## DISCUSSION

Paper IIB-1: "Development of Low-Friction Materials for LMFBR Components"

W. Apblett: How was the maximum friction coefficient of 0.57 established?

R. Johnson: It is the maximum theoretical friction coefficient allowing movement of interfaces in a hexagonal array when radial clamping forces are applied. Since the force applied to a face of a hexagonal assembly is at 60° to the face, the maximum allowable friction coefficient may be expressed as  $\mu_{\max} < \frac{\cos 60^\circ}{\sin 60^\circ} = 0.57$ .

Thus, if the friction coefficient equals or exceeds 0.57, no amount of radial clamping force will be successful in achieving further compaction of a "bridged" hexagonal array.

G. D. Hill: Since deposited coatings (e.g., D-gun raise potential quality assurance problems does this imply an increasing preference for diffusion coatings?

B. Johnson: To date, our quality control experience with the D-gun coatings has been much better than our experience with diffusion coatings. However, we have devoted much more attention to the D-gun coatings since diffusion coatings cannot be used on our fuel ducts without annealing the cold work levels required for irradiation swelling resistance.

K. Phillips: In high temperature gases and other environments, we have found that the surface finish of a metal can have a considerable effect on both the friction and wear. Does your work in sodium consider the effect of different surface finishes and methods of obtaining those finishes on friction?

R. Johnson: Our studies have shown that the lowest friction coefficients are formed when the surfaces are neither very smooth ( $< \sim 0.3 \mu\text{m AA}$ ) nor very rough ( $> \sim 5 \mu\text{m AA}$ ). The shape of asperities on the surface can also have an important effect. Minimum friction on the carbide coatings was obtained by brush-finishing with a silicon-carbide impregnated nylon flap-brush to a finish of about 2 to 3  $\mu\text{m}$  (80-120  $\mu\text{m AA}$ ).

K. Phillips: What is the maximum temperature at which Aluminide coatings on Inconel 718 can be used over long periods?

R. Johnson: We have not identified the maximum temperature for aluminide coatings over long periods in sodium since no coating has failed. Tests to date have been conducted for  $\sim 8000$  hrs in 625°C sodium without serious effect on the coating. In oxidizing environments, such as jet engine applications, service times of 30,000 hrs at temperature greater than 850°C have been reported.

D. Ferriss: What is the basis for selecting 15% by volume binder phase (NiCr, Triboloy 700, etc) with  $\text{Cr}_3\text{C}_2$ ?

R. Johnson: Screening tests on a  $\text{Cr}_3\text{C}_2$ -12% NiCr coating were conducted by recommendation of the coating vendor

when modifications in the particle size tended to make the coating more brittle and less impact resistant, NiCr was increased to 15% as compensation. Further coating developments were standardized at the 15% binder level for comparison of materials. Higher binder contents tend to increase the coating ductility, and lower binder contents are expected to reduce friction and decrease the self-welding tendencies. The 15% level was selected in an attempt to achieve optimum ductility and friction properties. Additional tests were planned to further optimize the carbide/binder ratio, but have not yet been conducted because of the success of the present compositions.

Paper IIB-3: "Corrosion and Tribological Investigations of Chromium Carbide Coatings for Sodium-Cooled Reactor Applications"

K. Phillips: Adhesion can occur by pressure welding or by diffusion which can have considerable effect on friction. What is the mechanism of adhesion in your tests and, if diffusion, do you expect increased friction with longer times or increases in surface area?

G. Whitlow: Adhesion or self-welding during a dwell period is due to diffusion. Activation energies indicate that diffusion is rate-controlling at the beginning of exposure, changing to creep processes after long-term exposures. The breakaway friction coefficient increases with dwell time.

D. Sandusky: If the radiation exposure significantly exceeds  $8 \times 10^{22}$  n/cm<sup>2</sup>, the cold-worked 316 substrate may be expected to swell significantly. Do you expect cracking and spalling of the  $\text{Cr}_3\text{C}_2$  coating? Also, has  $\text{Cr}_3\text{C}_2$  swelling tendency been observed?

G. Whitlow: Irradiation tests in static sodium (482-584°C have shown that D-gun applied chromium carbide/michrome coated 316 stainless steel did not spall at total neutron fluences of 1 to  $4 \times 10^{22}$  n/cm<sup>2</sup>. Although no data are available, the coating may spall at the level you suggest, if excessive swelling of the substrate occurs.

Paper IIB-4: "Experimental Investigations of the Frictional and Wear Behavior of Tungsten Carbide Cermet Ball Bearings Under Axial Load in Liquid Sodium"

E. Klimek: Did you notice any leaching of the Co binder and could this have initiated the fatigue failures? Have you worked with other grades of WC+Co to determine effects of Co content and carbide particle size?

K. Mattes: To my knowledge, no leaching of the Co binder was observed. Normally the WC-Co-ball-bearings failed by fatigue, i.e., by arising of pittings. Because of brittleness, the ball bearings are completely destroyed in time. No other grades of WC and Co were evaluated.

Paper IIB-5: "Friction and Wear Behavior of Colmonoy

## INTERNATIONAL CONFERENCE ON LIQUID METAL TECHNOLOGY IN ENERGY PRODUCTION

and Stellite Alloys in a Sodium Environment"

G. Whitlow: Are you concerned about high corrosion rates probably exhibited by nickel base Colmonoy alloys at 540°C?

H. Atsumo: Colmonoy alloys are used primarily in the fuel assembly wear pad. Although I do not know the exact time of exposure, it will be short duration.

G. Whitlow: For which component application are Colmonoy alloys being considered and how long will the component be exposed to high temperature sodium?

H. Atsumo: To date we believe that the optimum selection has been made, based on the results of such practical tests as irradiation.

K. Phillips: As an extension to Whitlow's question, since sodium has a marked effect on nickel corrosion, what is the expected sodium velocity in the vicinity of the assembly pad?

H. Atsumo: Depending on the design of the reactor core, it will be less than 1 m/sec.

R. Johnson: Since Colmonoy alloys are being considered for fuel assembly wear pad applications, what irradiation effects are to be expected, and is the transmutation of boron to helium of concern to you?

H. Atsumo: We recently performed tests to evaluate transformation of boron and are planning irradiation tests.

W. Wilson: To what do you attribute the decrease in static friction coefficient, which Colmonoy alloys experience with increasing sodium temperature?

H. Atsumo: Decrease in the static friction coefficient depends on the state of Colmonoy alloy sliding surface, which is hard after testing because of the presence of sodium-oxides despite the increase in temperature.

Paper IIB-6: "Wear of Rolling Element Bearings in Sodium"

T. Galimoto: Since you correlate wear depth with applied contact load, how do you determine the specimen wear depth?

H. Atsumo: Wear depth was measured by a linear differential transformer transducer before and after testing.

Paper IIB-7: "Evaluation of Cobalt and Nickel-Base Materials for Sliding and Static Contact Applications in a Liquid Metal Fast Breeder Reactor"

D. Sandusky: Grain boundary dissolution noted in Inconel-718 has also been observed in other alloys (e.g., Incoloy-800, stabilized 300-series stainless steels exposed to sodium in the absence of cyclic loading. Are we to assume that cyclic loading could

cause grains to be dislodged from this weakened structure?

N. Hoffman: Whatever the cause of grain introduction between rubbing surfaces, the results can well be erratic friction behavior.

K. Phillips: You have obviously carried out considerable studies into the structure of Stellite 6 coatings. Have your studies included investigation into the effects of methods of application on dilution and the optimum structure/dilution for wear resistance without effecting to coating integrity?

N. Hoffman: No, we have conducted neither of the investigations you propose, although both are very important.

H. Borgstedt: Although introducing Ni and Co alloys into a sodium circuit implies the classical "dissimilar metal mass transfer" problem, you do not indicate such effects as the formation of the rich surface layers on Stellite 6 as observed by Berkey and Whitlow. Have you detected such effects with the three materials described in your paper?

N. Hoffman: Surface chemistry changes of these alloys have been observed during exposure in a  $\Delta T$  loop and friction tests after exposure in the  $\Delta T$  loop are planned. Results may serve to explain mass transfer effects on friction. Grain boundary leaching and grain fall-out are a mass transfer effect believed to have a major effect on friction. The specific phenomenon you mention, i.e., the formation of an iron rich layer on a Stellite 6 surface is one we hope to study in detail.

Paper IIB-8: "Investigation into the Self-Welding Behavior of Metallic Materials Exposed to Sodium"

R. Johnson: What correlations exist between tests where self-welded specimens are separated at the test temperature in sodium and the tests where the specimens have first been removed from sodium, cleaned and then separated at room temperature?

K. Mattes: After comparing the results from tests carried out at 700°C for the ferritic material we found an approximate relationship that may be described as:

$$\frac{F_r(R_t)}{F_h(700^\circ F)} = \frac{G_r(R_t)}{G_r(700^\circ C)}$$

where:  $F_h$  = area breakaway force

$R_t$  = ambient temperature

$G_r(R_t)$  = real ultimate tensile strength at ambient (room) temperature

$G_r(700)$  = real ultimate tensile strength at 700°C

However, this statement should be substantiated by further testing.

J. Chang: Your conclusion indicated that the time and temperature did not directly influence the breakaway

force. Within what temperature time and pressure limits is this statement correct in your experiment?

K. Mattes: We did conclude that higher the temperature the higher the area breakaway forces. However, other factors that influence this effect include time-and temperature-dependent creep effects, temperature dependent redox-processes, high-temperature strengths and the temperature-dependent recrystallization process.

J. Chang: If the breakaway force was shown to be approximately proportional to the contact pressure, then, in what pressure range is this true for a given contact area?

K. Mattes: There is a mixing up of pressure and force. In my paper, pressure is used as force where pressure = force.

J. Chang: At what oxygen level of Na do you first contact the samples after flushing impurity from the mating surfaces?

K. Mattes:  $C_O < 10 \text{ ppm}_m$  (SNR 300 specification).

J. Chang: What is surface roughness and waviness of your lapped contact areas?

K. Mattes: We measured about  $0.2 \mu\text{m}$  as average value.

T. Galioto: You had specimens in compression during testing and subsequently break them apart in tension. Does relaxation of the compressive load reduce the measured breakaway force by prematurely breaking some of the formed junctions?

K. Mattes: There are, I suppose, elastic as well as plastic deformation of the points of contact. Elastic deformations forming real areas of contact will self-weld and I agree that relaxation of the load would have the same effect on the breakaway force. However, I believe the force to be negligible.

J. Chang: Does your thin ring type specimen experience Hertzian stress rather than stress you observe on large flat on flat specimen?

K. Mattes: Pressure distribution in the ring is parabolic. The smaller the annulus width, the higher the pressure at the border zones. However, in terms of breakaway force, this effect is probably without influence since the size of the real area of contact is not influenced. I suppose that there were different thermal expansion coefficients, producing shear stresses during the cooling process.

III A-1\*

BAGGED MAINTENANCE TECHNIQUES FOR SODIUM SYSTEMS

A. Stewart (AI)

Plastic bag sodium component techniques for handling sodium-contaminated components in inert atmospheres will be described. Atmosphere requirements, bag material and construction, bag adaptor needs, and large bag handling will be discussed.

III A-2

DEVELOPMENT AND TESTING OF HIGH-PERFORMANCE FUEL PIN SIMULATORS FOR BOILING EXPERIMENTS IN LIQUID METAL FLOW

V. Casal (Karlsruhe)

There are unknown phenomena, about local and integral boiling events in the core of sodium cooled fast breeder reactors. Therefore at GfK out-of-pile boiling experiments have been performed using electrically heated dummies of fuel element bundles. The success of these tests and the amount of information derived from them depends exclusively on the successful simulation of the fuel pins by electrically heated rods as regards the essential physical properties. This report deals with the development and testing of heater rods for sodium boiling experiments in bundles including up to 91 heated pins.

To obtain relevant experimental results, heater rods have to fulfill the following principal requirements:

- The outer dimensions including the microstructure of the cladding surface must be identical to that of fuel pins.
- The heat production must be the same as in the fuel pins at nominal load but at substantially increased coolant temperature which might be encountered in the core in case of incidents.
- The heat production in the heater rods must be independent of the outer coolant temperatures, the azimuthal heat release to the outer cladding must be similar to that of the fuel pin.
- The transient behavior during coolant boiling must be similar to that of the fuel pin.
- The heater rods must be instrumented with thermocouples.

- The design must be adapted to technical requirements of large bundle tests.

The synthesis proposed between the physical and experimental requirements and the technical means is an electric fuel pin simulator with the following design:

- Cladding: stainless steel tube with the same specifications as a fuel element cladding and the dimensions adapted to the fuel pin dimensions.
- Conductor: suitably dimensioned nickel-chromium tape helix with electric resistance independent of temperature. This helix is internally supported by a ceramic having the same thermal dilatation.
- The thermal and mechanical link between the conductor and the cladding consists of a layer of densified boron nitride powder with a high thermal conductivity.

Obviously, this simulator does not allow a perfect analogy of physical properties between fuel pin and simulator to be established. The design described was chosen because priority was given to the requirement of constant heat release. Local boiling as a result of local plugging causes considerable local variations of the coolant temperature. Only in the case of temperature-independent heat production in the heater rod, which is achieved by heater rods provided with nickel-chromium conductors, the experimental results can be reasonably used for fuel element design.

On account of the low melting point of nickel-chromium (about 1400°C) the admissible conductor temperature in the heater rod must be limited to some 1250°C. With a sodium boiling temperature of 950°C the possible temperature gradient in the heater rod is reduced to 300°C as the maximum value against 1300°C in the fuel pin. This limited temperature gradient calls for an extremely high heat transfer within the heater rod, which is achieved by a boron nitride insulation of the conductor. A different azimuthal heat release at the cladding of the heater rod with local variation of coolant temperatures and a different transient behavior must be accepted as the price for complying with the principal requirement.

\*Summaries only are available for these informal sessions.

## INTERNATIONAL CONFERENCE ON LIQUID METAL TECHNOLOGY IN ENERGY PRODUCTION

These requirements were largely satisfied by appropriate selection of the heater rod design, by suitable dimensioning and, partly, by selecting adequate materials for the single heater rod components.

The heater rods developed at GfK were subjected in preliminary tests both to individual tests and bundle tests comprising seven heated rods under conditions of sodium boiling. The heater rods were able to withstand the following loads with a high operating liability:

- without sodium boiling:
  - specific surface heat density: 170 W/cm<sup>2</sup>
  - coolant temperature: 950°C
  - life-time: >10 h
  - 100 shutdowns from full load
- with sodium boiling:
  - specific surface heat density: 170 W/cm<sup>2</sup>
  - boiling temperature: 950°C
  - life-time: >1 h
  - 12 tests involving "dryout" during which the rods were disconnected at a cladding temperature of roughly 1100°C.

These results show that the heater rods developed satisfy the conditions called for by the boiling experiments which will be performed in bundles with 91 heated rods.

### III A-3

#### LMFBR, SODIUM/STEAM GENERATOR WITH AN INERT LIQUID METAL INTERFACE

J. H. McLoughlin (James Henry Consult.)

A sodium/steam generator design is described in which the secondary circuit of an LMFBR is replaced by an inert liquid metal in the annulus formed by a tube within a tube.

The concept is worked up into a duplex walled once through sodium steam generator. Design aspects, together with pros and cons of the concept are discussed in the light of LMFBR operation.

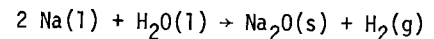
### III A-4

#### DYNAMIC RESPONSE OF THE EBR-II SECONDARY SODIUM SYSTEM TO POSTULATED LEAKS OF STEAM AND WATER INTO SODIUM\*

S. Srinivas, P. S. Chopra, C. C. Stone (ANL)

This paper presents evaluations of the dynamic response of a steam generator system to postulated leaks of steam and water into sodium. This work is part of a comprehensive fail-safe analysis of the steam generator system of the Experimental Breeder Reactor-II (EBR-II).<sup>(1)</sup>

Leaks of steam from a hole in a superheater duplex tube or water from a hole in an evaporator duplex tube into flowing sodium in the superheater or evaporator shells are postulated. To be conservative, the leaks are assumed to occur close to the steam inlet in the superheater and to the water inlet in the evaporator. The leak rate per unit area of the hole is obtained as a function of the pressure inside the duplex tube, the pressure inside the shell and the state of the fluid being discharged. The leaking steam or water is assumed to react instantaneously with sodium. The reaction, which occurs in excess sodium above 600°F, is characterized by:



Impedence of the rate of this reaction by the actual transport of reactants to the reaction site is conservatively ignored. The pressure build-up at the site of the sodium-water reaction is expressed analytically through a bubble model<sup>(2)</sup> based upon mass balance, energy-balance and water leak rates. This model is combined with the one-dimensional hydrodynamic equations<sup>(3)</sup> to compute the pressure distribution in the EBR-II secondary sodium systems.

Pressure-time histories are obtained for leaks in an EBR-II superheater and an evaporator as well as the times that would elapse before a rupture disc in the secondary sodium system would break. Instantaneous guillotine failure of a duplex tube in a superheater yields a maximum pressure in the shell of 1230 psi and similar failure of a tube in the evaporator yields a

---

\*Work performed under contract to the United States Energy Research and Development Administration



## INTERNATIONAL CONFERENCE ON LIQUID METAL TECHNOLOGY IN ENERGY PRODUCTION

maximum pressure of 1990 psi. If a non-instantaneous leak progression rate is assumed, the maximum shell pressures are reduced to 397 psi in a superheater and 492 psi in an evaporator.

Dynamic shell and piping stresses also are obtained and found to be equal to approximately one half of the yield strength of the material for the case of non-instantaneous leak progression.

### References

1. Chopra, P. S. (Editor), Failure Analysis of the EBR-II Steam Generator System - Final Report of the EBR-II Steam Generator Task Group, Volumes I, II and III, Argonne National Laboratory, May 1975.
2. Zaker, T. A. and Salmon, M. A., "Effects of Steam Tube Rupture in EBR-II Superheater," IITRI-578T076-2, September 1968.
3. Shin, Y. W., "The Method of Characteristics for Analysis of Pressure Transients Resulting from Sodium-Water Reaction in Hydraulic Networks," ANL-8049, 1973.

### III A-5

#### EVENTS FOLLOWING POSTULATED FAILURES IN THE EBR-II STEAM GENERATOR SYSTEM\*

G. C. Wolz, C. Gukeisen, P. S. Chopra (ANL)

The progression of events following three postulated spontaneous failure initiating events in the steam generator system of the Experimental Breeder Reactor - II (EBR-II) are described with the help of fault trees and accident progression diagrams. The analyses are presented for reactor operating and standby conditions since the consequences differ in the two cases.

The failure initiating events postulated are; a leak at the weld between the steam tube and the steam tube-sheet, a leak at the weld between the sodium tube and the sodium tube-sheet, and a leak that has progressed through the wall of the duplex tubes. Leaks in an evaporator and a superheater are considered individually.

---

\*Work performed under contract to the United States Energy Research and Development Administration.

The significant failure events that are considered in the analyses include; physical damage to tube sheets and steam tubes in the generator shells, damage to the sodium storage tank, damage to the intermediate heat exchanger, plugging of sodium piping, and damage to the steam system. Occurrence of each of these events would render the steam generator system, and hence the reactor, inoperable for varying durations.

The fault-tree and failure progression analyses are used with detailed analytical investigations<sup>(1)</sup> to determine realistic end states for the system following each of the postulated failure initiating events. It is shown that a duplex tube leak during plant operation would result in less severe consequences than a similar leak during plant standby. The analyses further suggest the modifications that may be made to the steam generator system and to the emergency operating procedures to assure that the end states to which the system may progress, following a postulated failure, are acceptable.

Fault-trees and accident progression diagrams also are presented for the system assuming that all the recommended modifications are implemented. These analyses demonstrate that the modified EBR-II steam generator system would be capable of continued safe and reliable operation within three months following a sodium-water reaction.

### Reference

1. Chopra, P. S. (Editor), Failure Analysis of the EBR-II Steam Generator System - Final Report of the EBR-II Steam Generator Task Group, Volumes I, II and III, Argonne National Laboratory, May 1975.

### III A-6

#### PRIMARY STEAM GENERATORS FOR THE LMFBR

J. D. Mangus (WARD)

Two concepts for primary steam generators, i.e., steam generators with such high reliability and safe design to render large sodium-water reactions an impossibility are being investigated at WARD. The first concept is based on conductive heat transport between re-entrant (bayonet) sodium and water/steam tubes. Extruded 2 1/4 Cr-1 Mo conductors are assembled to form a matrix into

which the re-entrant tubes are inserted; high conductivity thermal bonding is achieved by the use of a lead-base alloy in the annular spaces between the tubes and the extruded conductors. The second concept uses a bed of inert particles fluidized by helium to transport heat from a bank of sodium tubes to banks of water/steam tubes. At the present time both concepts appear to be technically feasible but require additional evaluation of costs, maintenance, availability, licensability, safety, and plant systems effects in order to select the preferred concept for further development.

## III B-1

## INVESTIGATION OF EMBRITTEMENT BY LIQUID-METALS

M. Nicholas (UKAEA-AERE)

A programme on liquid metal embrittlement has been in progress at Harwell for about a year with investigations of the relationship between experimentally determined wettability and reported embrittlement data for zinc and of the fracture of aluminum single crystals in the presence of gallium. Wetting data obtained for bismuth, cadmium, indium, lead, mercury and sodium show that reduction in interfacial energies achieved by the embrittling metals is greater than that by the non-embrittling metals and that the relative embrittling efficiencies of gallium and mercury predicted from these measurements agree well with the results of Westwood and Kamdar. Fracture studies of aluminum single crystals wetted by gallium have shown failure to occur by slow,  $10^{-1}$  propagation of cleavage crack that was initiated after a plastic deformation of 10-20 percent. No tendency to cleave along a particular plane was noted, and the cracks could be arrested by removing the stress.

## III B-2

## SOME OBSERVATIONS ON THE SODIUM-SODIUM HYDROXIDE SYSTEM

F. A. Cafasso, K. M. Myles and A. K. Fischer (ANL)

Experiments have been done to determine (a) the transformation temperature and equilibrium hydrogen pressure for the reaction  $\text{Na}_2\text{O}_{(s)} + \text{NaH}_{(s)} \rightleftharpoons \text{Na}_{(l)} + \text{NaOH}_{(l)}$  and (b) the kinetics of decomposition of sodium hydroxide in solution in liquid sodium at 500°C.

The  $\text{Na}_2\text{O}_{(s)} + \text{NaH}_{(s)} \rightleftharpoons \text{NaOH}_{(l)} + \text{Na}_{(l)}$  reaction was studied by X-ray and tensimetric methods. Capsules, loaded with sodium - NaOH mixtures and subjected to various heat treatments under controlled and monitored hydrogen pressures, were quenched and the products formed determined by X-ray diffraction. On the basis of the observed products and the observed hydrogen pressure plateaus, it was concluded that the transition temperature was  $412 \pm 2^\circ\text{C}$  and the equilibrium hydrogen pressure for this reaction was  $180 \pm 10$  Torr.

The kinetics of the decomposition of sodium hydroxide dissolved in sodium at 500°C was studied by means of an isotope-exchange technique in which NaOD was used as a stand-in for NaOH. Data obtained from mass

spectrometric monitoring of the  $\text{D}_2$  evolved upon heating Na-NaOH mixtures combined with the measurement of residual NaOD by an alcoholysis exchange technique provided information on the rate of decomposition of NaOD. The decomposition reaction was found to be first order in  $\text{OD}^-$  and to have a half-time of about 150 minutes.

## III B-3

## CORROSION MODEL FOR IRON-BASE ALLOYS IN SODIUM

G. Scibona (CNEN)

Any corrosion model dealing with the corrosion behavior of iron base alloys has to account for several experimentally observed phenomena, namely, (1) the dependence of the corrosion rate on oxygen concentration, sodium velocity, downstream position, temperature, and geometry of the test section (2) the independence from the differential temperature of the loop (3) the difference in oxygen dependence of the corrosion rate of AISI 316 with respect to iron. A model for a flat surface in contact with a laminar liquid sodium layer is developed. The model is based on the steady state coupling of interfacial chemical reactions and of diffusive processes at the solid and liquid boundary layers. By using the shell mass balance approach the model is adapted to describe the corrosion rate in loop experiments. The corrosion rate equation accounts fairly well for the observed corrosion experimental phenomena. It is also shown that most of the literature corrosion rate equations are particular cases of a more general equation. The conclusion is reached that unless the chemistry of the system is better defined there is no chance to further exploit the model.

## III B-4

PLASMA AND DETONATION GUN APPLIED COATINGS -  
DESIGN ALTERNATIVES TO REDUCE FRICTION AND WEAR

T. A. Wolfla, Richard K. Dagley (UCC)

Plasma and detonation gun coatings offer increased flexibility of design. In particular, friction and wear properties not obtainable in the substrate alloy can be achieved through the use of a broad spectrum of materials which can be deposited as coatings. A review of the processes and materials is presented and illustrated through the use of a filmed processing sequence, which highlights current reactor applications.

III B-5

SMALL SODIUM LEAK BEHAVIOR IN LOW MOISTURE,  
LOW OXYGEN, NITROGEN ATMOSPHERES

W. L. Matheys, G. R. Taylor (WARD)

Flow and corrosion characteristics of small sodium leaks, from several grams per hour to about one hundred grams per hour, into low oxygen, ( $\sim 1$  v/o) and low moisture (1,300 to 6,000 ppm (vol)) have been investigated in a series of glove box tests. Results of these experiments will be presented and the behavior illustrated by motion pictures.

# INTERNATIONAL CONFERENCE ON LIQUID METAL TECHNOLOGY IN ENERGY PRODUCTION

## MATERIALS ENGINEERING ISSUES, LMFBR STEAM GENERATORS

C.N. Spalaris

K.D. Challenger

R.A. Day

D. Dutina

P.J. Ring

General Electric Company  
San Jose, CA

Fast Breeder Reactor Department

### ABSTRACT

Selection of 2-1/4 Cr-1 Mo as the reference construction material for LMFBR steam generators assumed a balance between its known intrinsic properties and our ability to accommodate certain of its deficiencies through design allowance. A comprehensive development program was undertaken to define base data needed, confirm assumptions made relative to desired performance, minimize defects by optimization of melting, fabrication and heat treatment processes, and prepare specifications for purchasing reactor components.

Results obtained from the development programs, now in their third year, indicate that risks from certain assumptions made originally are minimal. To date, forging stock produced by the VAR (Vacuum Arc Remelt) process in large quantities was found to be well within the specified chemistry and microcleanliness standards. Fracture toughness tests show that the reference heat treatments provide a stable microstructure with excellent resistance to brittle fracture for VAR (Vacuum Arc Remelt) or ESR (Electroslag Remelt) produced stock.

Decarburization kinetics of 2-1/4 Cr-1 Mo base and weld metal in sodium at 950°F show that recommended values for design basis still hold after exposures of 7,000 to 10,000 hours. A weld design has been selected for the transition welds which join austenitic and ferritic steel piping. The weld geometry selected minimizes thermal stress in the joint. Defect-free transition welds have been made.

Some important assumptions made in upgrading 2-1/4 Cr-1 Mo material and process specifications, to reflect current state of the art, have been favorably resolved. Potential risks have been minimized by better understanding of the material properties through the cooperation between the scientific community and industry. The program envisaged for resolving remaining concerns is now in full swing, and considered timely for the LMFBR Clinch River Project.

### INTRODUCTION

In the early studies leading to the selection of 2-1/4 Cr-1 Mo as a steam generator reference alloy, it was concluded that the intrinsic advantages (e.g., resistance to stress corrosion cracking) outweighed its deficiencies. Further, the deficiencies were better understood and more amenable to metallurgical control by melting practice, composition, specifications and fabrication procedures than the major austenitic steel deficiency, namely stress corrosion cracking. Having selected 2-1/4 Cr-1 Mo, based on the preceding rationale, it follows now that the material must be characterized, optimized and its disadvantages minimized. An excellent example of this is obtained by considering the impact of melting practice and composition control on weld performance, in particular tube to tubesheet welds. To optimize weld reliability, it was necessary to:

1. Minimize stresses in the weld region (a function of steam generator and weld design),
2. Eliminate potential embrittlement (controlled by material composition and microstructure),
3. Produce consistent top quality welds by minimizing weld defects such as porosity, lack of fusion, etc. (a function of weld design, weld process and material composition).

Having optimized the steam generator and weld design as far as possible within other constraints, the remaining two requirements could be satisfied by close control of material composition, purity, heat treatment, and welding practices.

#### Minimizing Potential Embrittlement

Four embrittlement phenomena are recognized: temper embrittlement, creep embrittlement, stress relief embrittlement, and "500°F" embrittlement.<sup>(1,2)</sup> The extent of embrittlement of 2-1/4 Cr-1 Mo is largely a function of alloy content, impurity element levels and material strength, with impurity elements (P, Sb, Sn, As) in particular phosphorus,

Session IV A - Steam Generator  
Chairman: G. W. Meyers (AI)

INTERNATIONAL CONFERENCE ON LIQUID METAL TECHNOLOGY IN ENERGY PRODUCTION

having the greatest contribution.<sup>(3)</sup> The higher the impurity element content and higher the material strength, the greater the possibility of embrittlement.

Stress relief embrittlement, in addition to requiring control of impurity element levels, is also a function of welding speed, welding current and heating rate to the stress relief temperature; however, post weld heat treatment at temperatures greater than 1200°F (649°C) has been shown to prevent this condition.<sup>(4)</sup>

From a consideration of the embrittlement phenomena, it is apparent that control of impurity elements to low levels by using high purity air-melt ingots and remelt techniques such as the Vacuum Arc Remelting (VAR) or Electroslag Remelting (ESR) processes, together with selection of heat treatment procedures to maintain material strength levels below 85 ksi, should do much to alleviate this problem.

To reduce the potential for tube defects and weld porosity, the steel must have a low inclusion content. This requirement again dictates the use of remelted steel for the critical sodium/water boundary.

Even though the reference alloy has been used in the U.S. in large quantities, nearly all industrial experience is with air melted grades. It was necessary to devise specifications acceptable both to ourselves and the steel industry and obtain VAR and ESR material with rigid quality and compositional control in quantities never before attempted. A test program was initiated to determine if the property values of the consumable remelt material varied appreciably from those of air melt material used to establish ASME Code criteria. An appreciable amount of data on both VAR and ESR material are now available, and selected results are given in Figures 1, 2, 3, 4, and Table I. Yield strength (0.2% offset) ultimate tensile strength, total elongation and reduction in area values for VAR material are shown in Figures 1 and 2 as a function of test temperature. For comparison purposes, upper and lower tolerance values taken from the Nuclear Systems Materials Handbook (NSMH) and expected minimum yield stress values from ASME Code Case 1592 have been superimposed on the plots. In general, the strength property values tend to lie

towards the lower, rather than the upper, region of the data band. This could be due to the remelt process but is more probably due to the imposition of a 1340°F (727°F) post weld heat treatment after normalizing and tempering or annealing. The 2-1/4 Cr-1 Mo data base used in the ASME Code Case 1592 was not given a post weld heat treatment. Additional tests are being performed to further investigate this situation.

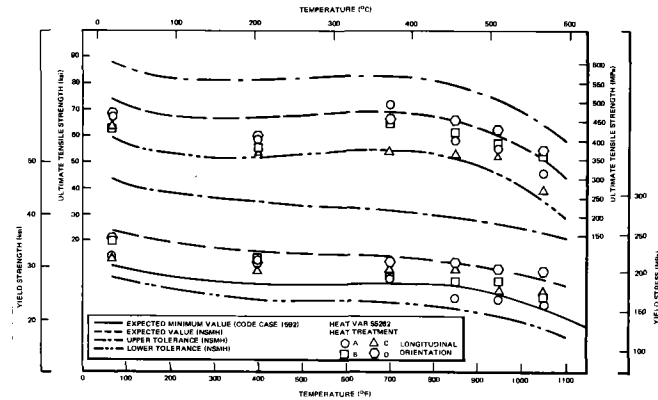


Figure 1. High Temperature 0.2% Yield Stress And Ultimate Tensile Stress Values For VAR 2-1/4 Cr-1 Mo Steel

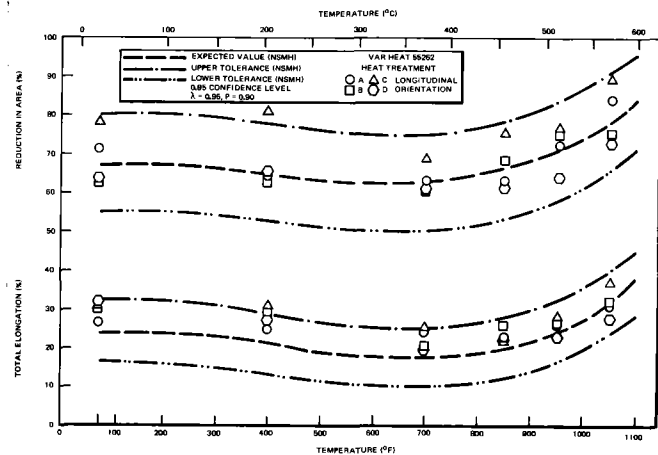


Figure 2. High Temperature Total Elongation And Reduction In Area Values For VAR 2-1/4 Cr-1 Mo Steel

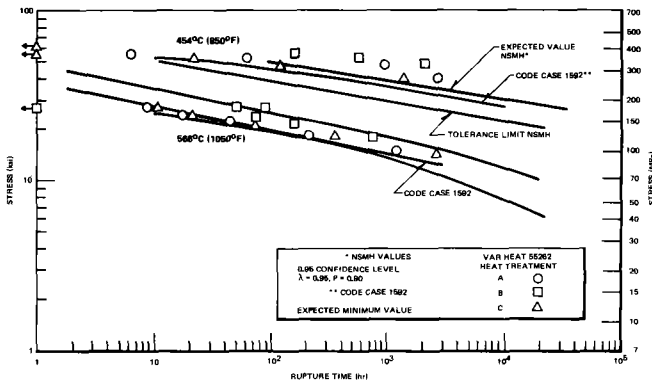


Figure 3. Stress Rupture Values For VAR 2-1/4 Cr-1 Mo Steel At 454°C And 566°C

material for the reference isothermal anneal with post weld heat treatment. Figure 4 shows the data for VAR material after full anneal and post weld heat treatment, the heat treatment designated for the tube sheets.

TABLE I  
CHARPY V-NOTCH RESULTS FOR 2 1/4 Cr - 1 Mo STEEL  
Heat VAR 55262, Transverse Orientation  
Isothermal Anneal with Post Weld Heat Treatment

CVN J (ft.-lb.)	Temp. °C (°F)	Lateral Expansion µm (mils)	Shear Fracture (%) Observation
4.2 (3.1)	-17.8 (0)	0 (0)	#1 #2 #3 Avg
5.2 (3.8)	-6.67 (20)	76 (3)	2 5 4 4
14.9 (11.0)	15.6 (60)	356 (14)	2 4 4 3
12.8 (9.5)	18.3 (65)	305 (12)	12 15 5 11
15.2 (11.2)	21.1 (70)	279 (11)	8 10 5 8
90.8 (67.0)	23.9 (75)	1520 (60)	10 14 5 10
76.7 (56.6)	37.8 (100)	1380 (55)	30 20 10 20
116.6 (86.0)	65.6 (150)	1910 (75)	35 25 15 25
137.8 (101.6)	98.9 (210)	1980 (78)	65 65 60 63
139.6 (103.0)	176.7 (350)	1930 (76)	85 80 75 80
			100 99 98 99

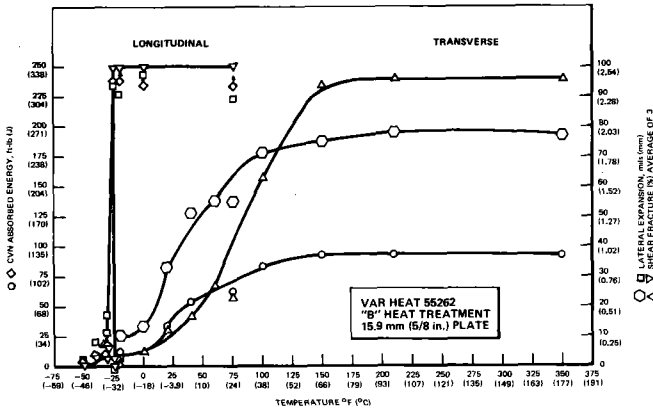


Figure 4. Longitudinal And Transverse Charpy Impact Values For Fully Annealed 2-1/4 Cr-1 Mo Steel

The full anneal plus post weld heat treatment gave the best assurance of ductile fracture based on the temperature at which the Code impact requirements [67.8J (50 ft.-lb.) and 889 mm (0.035 inches)] were met. Nil ductility transition temperatures (RTNDT, Section NB2300, ASME Code) for the VAR steel ranged from -3.9°C to -28.9°C (25 to -20°F), in the worst orientation (transverse).

Stress to rupture/time plots for VAR material are shown in Figure 3. Comparisons show that in all cases, the data fall within the tolerance limits of the NSMH and above the minimum values established by the ASME Code case 1592-7.

Fracture toughness data (Charpy impact and J Integral) have been generated on both VAR and ESR material for several heat treatments; fully annealed, isothermally annealed, both with and without post weld heat treatment, and normalized and tempered.

Results are tabulated (Table I) for VAR

In summary, to minimize the possibility of failures, a material was selected which may have problems, but which are reasonably well understood and amenable to correction. Desired chemistry and microcleanliness have been obtained in large size heats. Heat treatments were selected to produce a stable structure with low tensile strength to reduce the risk of embrittlement and obtain stable long-term elevated temperature behavior. To achieve this, it is possible that a price may have to be paid. Other property values, particularly short-term strength, may be reduced compared to more conventional material. Early results from the remelt material characterization studies, however, indicate acceptable strength property values and very satisfactory ductility and toughness levels.

## Carbon Transport

In a LMFBR secondary system, carbon will be transported from the 2-1/4 Cr-1 Mo to the austenitic stainless steels. One of the major concerns with the use of 2-1/4 Cr-1 Mo for LMFBR steam generators is its susceptibility to decarburization and attendant reduction in strength. Extensive analysis of the problem<sup>(5)</sup> revealed that the kinetics of decarburization would be sufficiently slow to allow its use for the CRBR steam generator tubing; 510C (950F) maximum operating temperature. Figure 5 presents all published decarburization data for 2-1/4 Cr-1 Mo along with the derived design correlation from Reference 5. Recent decarburization data from tests on-going at General Electric are also shown. The effect of heat treatment (annealed, A, 924C [1695F] furnace cooled to room temperature [RT] plus post weld heat treated, PWHT, at 732C [1305F] for 1 hour; and normalized, and tempered [N&T] 924C [1695F] air cooled to RT and PWHT) has been studied in titanium gettered static sodium pots. Although both heat treatments decarburize at rates lower than the design correlation; N&T decarburizes more slowly consistent with other published data.<sup>(6,7)</sup> The same effect of heat treatment (microstructure) has been observed in both VAR and ESR. In order to confirm the validity of the design correlation for the CRBR, a mockup of the Intermediate Heat Transport System, IHTS, of the CRBR has been constructed. The specific design details of this loop are presented in another paper at this conference (J.L. Krankota and K.D. Challenger, "Carbon Transport in a Model of the CRBR Secondary System"). In all but one case, the decarburization rates fall below the design correlation. The decarburization rate of a steel, with what is termed as "unstable" microstructure (15% bainite, 85% polygonal ferrite), exceeded the design correlation, Figure 5. A slight difference in the decarburization rate of VAR vs. ESR 2-1/4 Cr-1 Mo has been observed; however, no conclusion should be drawn until longer time data are available.

The static sodium pot tests have shown that the decarburization rate decreases with increasing time; after 4100 hours of Na exposure,  $12 \times 10^{-9}$  gmC/cm<sup>2</sup>-sec<sup>1/2</sup>, slowed to  $9.4 \times 10^{-9}$  after 10,000 hours, probably due to thermal aging.

In summary, it appears that the design correlation developed by Krankota and Armijo<sup>(5)</sup> satisfactorily

predicts the decarburization of 2-1/4 Cr-1 Mo; however, as longer time data become available, it appears that decarburization slows with time. Therefore, the correlation, although not precise, is conservative.

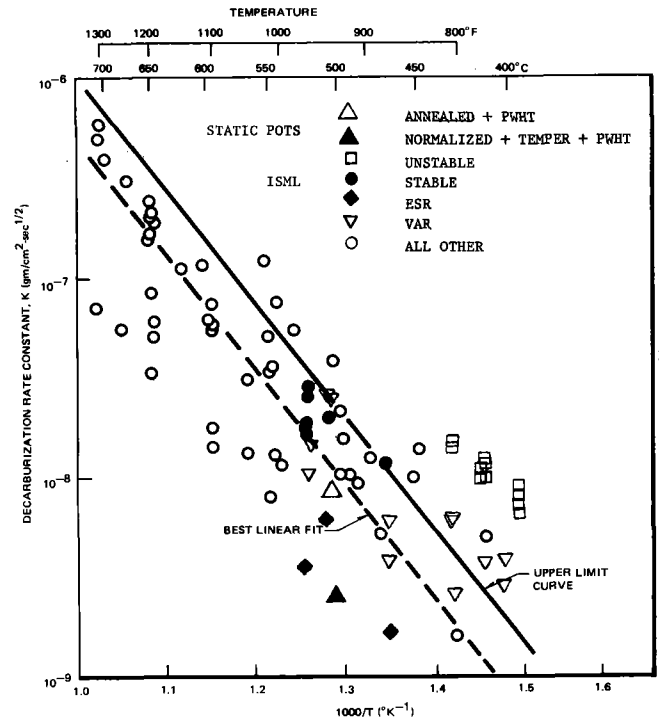


Figure 5. Decarburization Rate Constants For 2-1/4 Cr-1 Mo In Sodium: Data From ISML Compared With All Other Investigations (Run B-2)

## Corrosion

It is recognized that corrosion under heat transfer can accelerate the corrosion over that of the isothermal case.<sup>(8)</sup> Experiments designed to measure the corrosion rate of 2-1/4 Cr-1 Mo under conditions simulating the most severe environment for CRBR superheaters are in progress. The program, a cooperative GE/ORNL/Southern Nuclear Engineering effort, will verify the adequacy of the corrosion allowance specified for the CRBR. The experimental details have been described elsewhere.<sup>(8)</sup> In summary, superheated steam from the Bartow Plant of the Florida Power Corporation is passed over the outside of the electrically heated test section. Heat is transferred to the steam at a rate of about 126,000 W/m<sup>2</sup> (40,000 BTU/hr-ft<sup>2</sup>) heating the steam from 468C (875F) to 499C (930F). The temperature of the tube wall surface in contact with the steam varies linearly along the length of the heat transfer test specimen from 510C (950F) to 538C (1000F). The results of this first experiment are shown in Figure 6. Spalling of the scale was observed for the heat transfer,



but not for the isothermal specimens.

A second experiment using prototypic steels (VAR and ESR) has been initiated with slightly modified test conditions (mean tube wall temperature in contact with the steam 500C [932F] instead of the previous 524C [925F]) in order to more closely simulate the CRBR superheater environment.

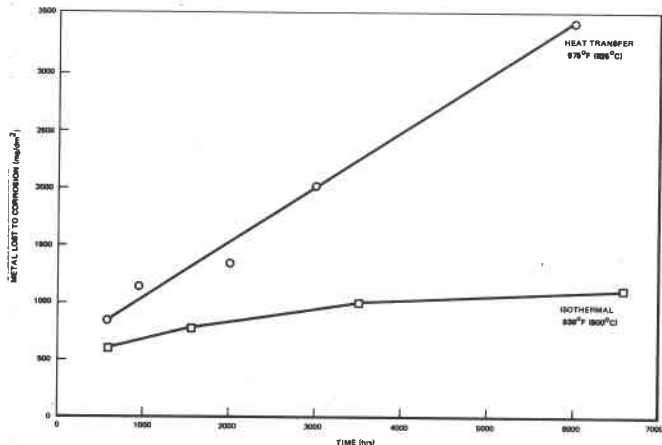
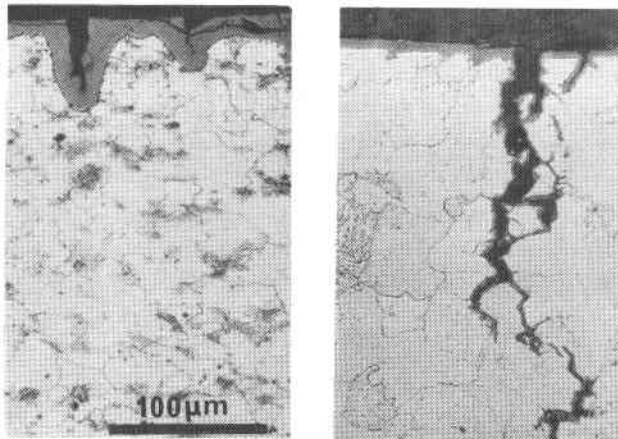


Figure 6. Heat Transfer Corrosion Results

The CRBR steam generating system design contains a steam drum and evaporators that operate with a 2:1 recirculation ratio. This results in a zone of departure from nucleate boiling, DNB, in the evaporator with attendant thermal cycles and potential for impurity concentration (dry-out). Numerous experiments are in progress in the U.S.A to investigate the effects of DNB.<sup>(9)</sup> An experiment to evaluate corrosion in the CRBR evaporators is planned, capable of measuring the corrosion rates in the nucleate and film boiling regions and assess the relative change in corrosion rate due to DNB.

An extensive evaluation of the caustic stress corrosion cracking (SCC) susceptibility of 2-1/4 Cr-1 Mo base metal and weldments has been performed.<sup>(10)</sup> Tests have been carried out in the temperature range of 316C (600F) to 482C (900F) representing the operational range of the CRBR evaporators and superheaters. Aqueous stress corrosion tests at 316C with both constant load and constant extension rates (tested to fracture) have been completed in 1, 5, and 10% NaOH. Polarization curves were determined to identify any possible regions of SCC susceptibility and straining electrode experiments were then performed with applied potentials ranging from -0.1 to +0.4 volts. No SCC was observed under any of these conditions. Metallographic examination

revealed that the general corrosion rate for 2-1/4 Cr-1 Mo under these conditions was sufficiently rapid that any crack formed during testing was blunted by oxide growth, Figure 7a. The temperature limit for resistance to caustic SCC appears to be around 232C (450F); Figure 7b illustrates the SCC observed for 2-1/4 Cr-1 Mo tested with constant extension to failure at 232C in 10% NaOH.



a. 316C (600F)

b. 232C (450F)

Figure 7. Stress Corrosion Cracking in 2 $\frac{1}{4}$ Cr-1Mo

Numerous experiments were also performed in Na saturated superheated steam at 482C (900F) with stresses up to 276 MPa (40 Ksi); steam condensate for the experiment contained 5 to 10 ppm NaOH.<sup>(10)</sup> No incidence of SCC was observed, however, many samples failed by creep rupture assisted by the very general high corrosion rate.

In summary, 2-1/4 Cr-1 Mo has been found resistant to caustic stress corrosion cracking for the operating temperature range of the CRBR steam generating systems; while the potential for cracking at lower temperatures has been confirmed.

#### Mechanical Properties

Mechanical property tests necessary to develop the design correlations needed for the high temperature design of ASME Section III, Class 1 components are being performed by ORNL<sup>(11)</sup> and GE.<sup>(9)</sup> Practically all the correlations required for design and analysis have been completed and submitted to, or issued in, the Nuclear Systems Materials Handbook, NSMH.

Testing to verify the design allowables used for 2-1/4 Cr-1 Mo in a decarburizing environment are underway. The approximate 9% reduction in allowable

stresses recommended for design to compensate for the loss in strength due to decarburization is based on the assumption that the mechanical properties are not a strong function of carbon content above 0.04%C. The total loss of carbon for a 210,000 hour exposure has been calculated using the previously discussed design correlation and for the geometry of the CRBR steam generator tubing, this amounts to 300 ppm carbon. The attendant degradation in strength is then calculated on this basis of a 300 ppm bulk loss of carbon. Both short and long-term tests in sodium at 510C (950F) are underway to verify that the bulk carbon approach satisfactorily describes the mechanical behavior of a tube containing a carbon gradient and undergoing continuous decarburization. Only very preliminary creep rupture data are available and even though a reduction in rupture life has been observed, Figure 8, the strength has remained above the ASME minimum requirements.

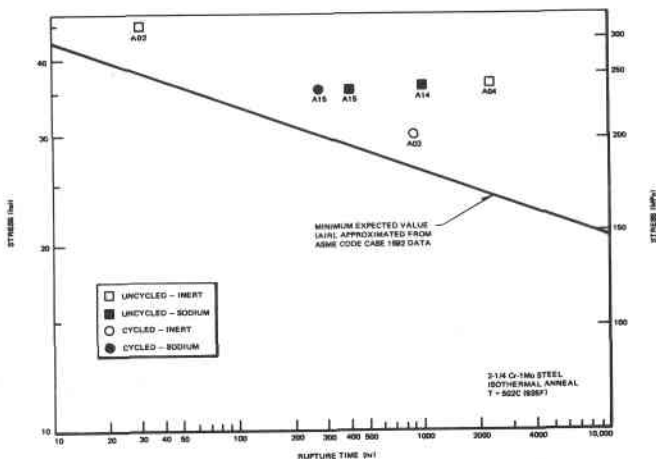


Figure 8. Stress Rupture Data For Isothermal Annealed 2-1/4 Cr-1 Mo Steel Tubular Creep Specimens

Fracture toughness testing of 2-1/4 Cr-1 Mo to supplement Appendix G of the ASME Code has begun. The maximum reference stress intensity,  $K_{IR}$ , in Appendix G was developed for light water reactor pressure vessel steels. Elastic-plastic (J-integral) testing of compact tension samples from both air melted and VAR 89mm (3.5 in.) thick plate has been completed at room temperature, Figure 9. Provided the criteria set forth in Appendix G are followed, safe material's performance can be expected. Additional testing of weldments and base metal samples given embrittling thermal treatments are planned.

The temperature fluctuations associated with the DNB previously discussed may be as large as 65C (149F).

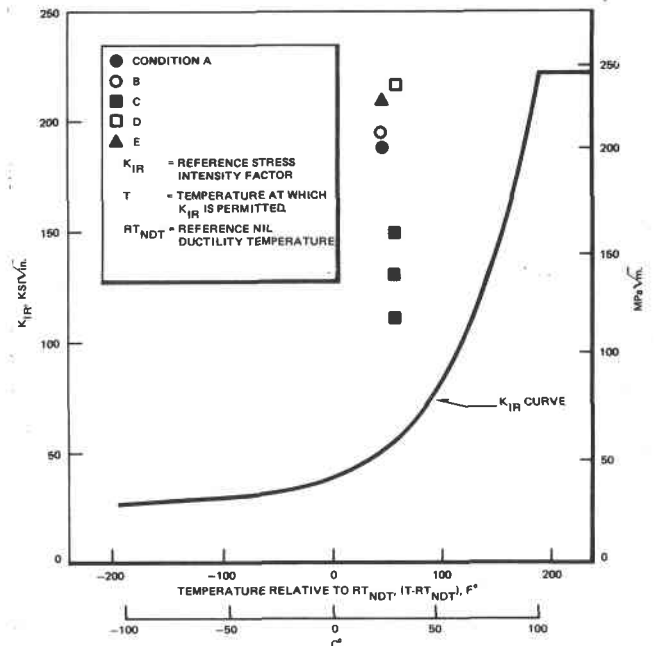


Figure 9. Comparison of Fracture Toughness Data With ASME Code Section III  $K_{IR}$  Curve

The thermal stresses associated with this frequent (1-3 cycles/second) temperature change combined with the potential for impurity concentration has caused concern with the fatigue strength of 2-1/4 Cr-1 Mo. Corrosion fatigue tests of 2-1/4 Cr-1 Mo designed to simulate the CRBR evaporator conditions are planned in autoclaves with both normal and off-chemistry water.

Transition Welds

In the Intermediate Heat Transport piping system, connections must be made between type 316 stainless and 2-1/4 Cr-1 Mo at diameters up to 26 inches (66 cm). To arrive at a weld geometry with low thermal stress, a weld process development must proceed concurrently with weld geometry stress analysis. A trimetal joint 2-1/4 Cr-1 Mo/Incoloy 800/316 with a 30° included angle was determined as optimum. Weld qualification and procedures must conform to the ASME Code and be performed by fabricators who possess the "N" stamp. Weld procedures have been developed, using a gas tungsten arc - "Hot wire" technique (preheated filler metal) with magnetic arc oscillation, parameters are closely controlled to give minimum weld metal dilution. Defect-free transition welds have been made.

Water Chemistry

Conservative choices in water treatment practices and the related plant equipment are

## INTERNATIONAL CONFERENCE ON LIQUID METAL TECHNOLOGY IN ENERGY PRODUCTION

required because of the high heat fluxes of the LMFBR concept and the acceptance of departure from nucleate boiling (liquid film dry-out) in the evaporators - both being outside of conventional power plant water chemistry experience.

The required water conditions can be achieved by the use of volatile chemistry (ammonia and hydrazine), full flow demineralization (with a requirement for low sodium, 1 ppb max.) and a 10 percent blowdown capability. The resulting water purity specifications are shown in Table II. These conditions approach once-through quality despite concentration of impurities in the drum. The sodium specification was demonstrated to be within today's state of the art by testing carried out in a fossil fired plant in conjunction with the utility, Central Power and Light, and the boiler manufacturer, Babcock and Wilcox (see Table III).

TABLE II

CRBRP WATER PURITY SPECIFICATIONS

	<u>Feedwater</u>	<u>Recirculating Water</u>
pH	8.6 to 9.1	8.5 to 9.0
Conductivity	0.3 micro mho/cm	2.0 micro mho/cm
Residual Hydrazine	5 ppb	5 ppb
Dissolved Oxygen	7 ppb	7 ppb
Sodium	1 ppb	6 ppb
Total Dissolved Solids	--	300 ppb
Total Solids	50 ppb	--

TABLE III

FEEDWATER SODIUM ION CONCENTRATION

(Central Power and Light - Nueces Bay Plant)

<u>Na Concentration</u>	<u>Time</u>
<.4 ppb ( $\mu\text{g}/\text{kg}$ )	168 hrs.
>.4; <.8 ppb	216 hrs.
>.8; <1.0 ppb	48 hrs.
>1.0 ppb	6 hrs.

TOTAL 438 hrs.

Participation with the architect engineer in the preparation of condenser specifications was carried out to insure highest integrity compatible with reasonable costs. The condenser tube material selected is 90-10 copper nickel except in the de-aerator section where the 70-30 alloy was substituted to minimize attack by oxygen/ammonia. Similarly, technical analysis was prepared to justify the use of stainless steel heaters in the feedwater train instead of copper alloys or carbon steel.

Experimental programs addressing the uncertainties in the design are in progress. Specifically, the potential damage effects ascribed to DNB operation, viz., exfoliation, cyclic thermal fatigue, and accelerated corrosion are being studied in single tube sodium heated systems both at General Electric and Westinghouse. In addition to design verification, the programs provide an examination of the adequacy of current analytical instrumentation, to monitor the adherence to, or warn of departure from, water purity specifications. Future programs will extend this investigation since high instrumental capability is clearly a critical need in determining whether the practices and materials selected can actually maintain the desired chemistry.

An additional area of investigation, currently beginning, is the examination of the effects of fouling on corrosion and thermal hydraulics and the means for reducing these effects.

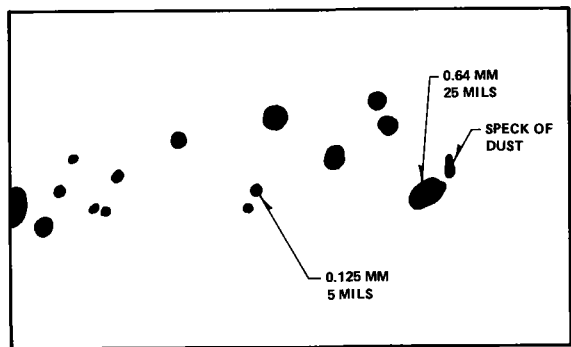
Non-Destructive Testing

Tube-to-tubesheet welds are the only welds in the sodium-water boundary and, consequently, must be free of defects including in-line porosity that might lead to potential leak paths. Experience with steam generators operated by General Electric has shown that porosity with diameters as small as 0.125 millimeters can be significant if aligned. The methods of nondestructive testing selected must detect weld porosity of 0.125 millimeters, microcracking and weld flaws such as undercutting. In-service inspection must detect cracking, tube wall thinning, small leaks, and metal loss through corrosion. The methods selected for inspection of tube-to-tubesheet welds are rod anode microfocus X-ray, visual, helium leak testing, and liquid penetrant testing of outer weld surface. Because the rod anode X-ray machine is a significant departure from commercial practice in the United States, Oak Ridge National Laboratory (ORNL) was asked to establish the feasibility of this method. A developmental machine (150KVp) was obtained from Holland in mid-1975 and has performed satisfactorily in every way. Production rates established by Dutch steam generator manufacturers averaged 20 radiographs per hour for one thousand welds in two separate manufacturing facilities. The successful use of the rod-anode on reference design welds is shown in Figure 10 where the X-ray machine was shown to have four times higher resolution of porosity than

## INTERNATIONAL CONFERENCE ON LIQUID METAL TECHNOLOGY IN ENERGY PRODUCTION

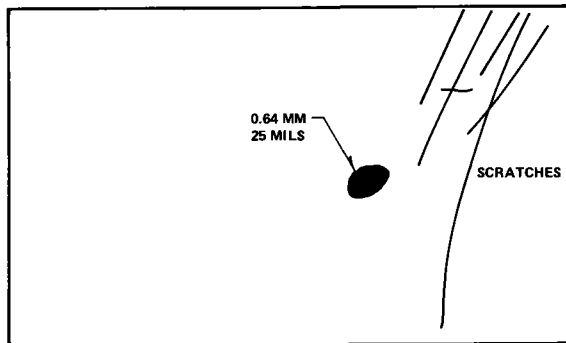
the best competitive isotopic source, Ytterbium 169. Acceptance criteria will exclude all porosity larger than 0.38 mm and smaller "clusters" of pores that could lead to leaks.

Ultrasonic examination is the only method available for in-service volumetric inspection of the tube/tubesheet weld, with sensitivity dependent on the surface contour of the weld (inner and outer surface weld crowns).



ROD ANODE X-RAY

15X



YTTERBIUM 169

15X

FIGURE 10 COMPARISON OF RADIOGRAPHIC METHODS, IDENTICAL TUBE/TUBESHEET SPECIMEN, 2-1/4 CR - 1 MO

It is required that steam generator tubing be free of flaws larger than three percent of the tube wall thickness (0.084mm) with a probability of 95 percent at 95 percent confidence. Statistical monitoring methods adopted from LMFBR fuel cladding are used to maintain this assurance using precision-machined calibration standards. Three calibration standards were fabricated, each with 12 notches (electric discharge) of 2, 3 and 5% of wall thickness, located on outer and inner surface at transverse and longitudinal orientations.

Even though the ultrasonic requirements specified for tubing are restrictive; commercial vendors agreed to try to meet them. Short, two meter lengths

of tubing have been manufactured to this requirement, but full length tubing (22 meters) has not.

In-service inspection of the steam generator is needed to locate small leaks, tube wear, corrosion and cracking before the defects grow into unacceptable proportions. No existing method possesses the required combination of speed, sensitivity and reliability. Ultrasonic wall thickness measurements have been made successfully on a single tube steam generator, General Electric's Departure from Nucleate Boiling (DNB) Test. Flaw detection has been demonstrated in the laboratory but has not been applied to an operating system. Inspection time is currently very long, two or three hours per tube, and considerable effort is needed to shorten this time. Water is used to couple the ultrasonic energy in the tube wall and special water formulations must be used to prevent pitting corrosion. Eddy current inspections are capable of very rapid speeds, five to ten minutes per tube, sensitivity has been low but ORNL is working on improving the method.

### Concerns Still To Be Resolved

Production of large quantities of tubing with successful heat treatment and desired dimensional control has yet to be demonstrated. Complete confirmation of decarburization kinetics for 2-1/4 Cr-1 Mo is absolutely essential as this knowledge is the building block for setting a design basis. Decarburization kinetics must be synchronized with mechanical properties base-line data, now being rapidly compiled.

A major effort is being directed towards the production of high quality minimum defect tube-to-tubesheet welds using ESR tubing and VAR tubesheet with high reliability and minimum rework.

Achievement of correct water chemistry control in steam generators, especially in view of DNB, is still to be realized. Fabrication details of the steam generator modules are just now being recognized, especially the application of NDT inspection techniques to qualify the units. In-service inspection details have yet to be defined, especially those necessary for determining weld integrity. Finally, a reliable leak detection scheme necessary to provide protection from Na/H<sub>2</sub>O reaction must be demonstrated.

# INTERNATIONAL CONFERENCE ON LIQUID METAL TECHNOLOGY IN ENERGY PRODUCTION

## REFERENCES

- (1) R.A. Swift, "A Review of the Embrittlement of 2-1/4 Cr-1 Mo Steel", RDR 69-23, Lukens Steel Company, Coatesville, Pennsylvania, December 1969.
- (2) L.G. Emmer, C.D. Clauser, and J.R. Low, "Critical Literature Review of Embrittlement in 2-1/4 Cr-1 Mo Steel", WRC Bulletin No. 183, Welding Research Council, New York, New York, May 1973.
- (3) R. Bruscatto, "Temper Embrittlement and Creep Embrittlement of 2-1/4 Cr-1 Mo Shielded Metal-Arc Weld Deposits", Welding Research Supplement, April 1970, pp. 148-s to 156-s.
- (4) R.A. Swift and H.C. Rogers, "Embrittlement of 2-1/4 Cr-1 Mo Steel Weld Metal by Postweld Heat Treatment", Welding Research Supplement, April 1973, pp. 145-s to 153-s.
- (5) J.L. Krankota and J.S. Armijo, *Met. Trans.* (1974), 3, 2515.
- (6) K. Matsumoto, et al, "Carbon Transfer Behavior of Materials for LMFBR Steam Generators", Int. Conf. on Materials for Nuclear Steam Generators, Gatlinburg, Tennessee, September 9-12, 1975.
- (7) K. Natesan, et al, "Compatibility of Fe-2-1/4 Cr-1 Mo Steel in Sodium Environments, *ibid.*
- (8) J. DeVan, "CRBR Environmental Effects - General Waterside Corrosion", *ibid.*
- (9) J.C. Whipple and C.N. Spalaris, "Design of the CRBRP Steam Generators", *ibid.*
- (10) M.E. Indig, "Environmental Corrosion Effect on CRBR Materials in the Steam Generator Circuit", *ibid.*
- (11) C.R. Brinkman, et al, "Mechanical and Physical Properties of 2-1/4 Cr-1 Mo Steel in Support of CRBRP", *ibid.*

## ACKNOWLEDGMENT

*This work was performed under contract with the Energy Research and Development Administration, Contract AT(04-3)-893 Tasks 10 and 18.*

# INTERNATIONAL CONFERENCE ON LIQUID METAL TECHNOLOGY IN ENERGY PRODUCTION

## STUDIES ON SOME PROBLEMS OF LEAKS IN SODIUM-WATER STEAM GENERATOR

F.A. Kozlov

G.P. Sergeev

A.R. Sednev

V.M. Makarov

The Institute of Physics and  
Power Engineering  
Obninsk, USSR

### ABSTRACT

The paper contains data on wastage of steam generators structural materials and high-nickel alloys in the zone of water leakage into sodium as well as investigation results for self-enlargement of water leaks into sodium through defects in these materials.

It is shown that the rate of material damage in the zone of sodium-water reaction and in the channel with water leaking-out decreases with increasing nickel content in steels and strongly depends on sodium temperature.

The paper presents experimentally obtained dependences of leakage self-enlargement rates on sodium temperature and leakage size for 1X2M, X18H10T and X20H40E steels.

It has been found out that heated water leakage (containing sodium hydroxide) into air through 1X2M steel results in leakage self-enlargement with the rate compared to the case of water leakage into sodium.

The paper gives the design of a special probe and measurement results of distribution in sodium flow of water-sodium reaction products (containing oxygen) near the place of water leakage.

### INTRODUCTION

When studying phenomena connected with water leakage into sodium in sodium-water steam generators considerable attention in different countries, the USSR in their number, was paid to structural materials beha-

viour under water leakage. Till recently the studies of this type have been aimed at elucidation of the influence of water or vapor original leakage in a steam generator on the tubes adjacent with the place of leakage.

With this purpose a great number of experiments were carried out on samples-targets of materials already used in steam generators or of possible alternates. The experiments made it possible to find main parameters determining the rate of material wastage in the region of water leakage into sodium and to obtain correlations for calculations.

For the recent years the efforts of investigators were aimed at studying evolution, or self-enlargement, of water leakage into sodium as a result of initial defect size change causing the leakage due to damage of the material immediately in the failed channel.

Interest to these studies is not accidental. The experiment<sup>1-3</sup> have shown that even such small water leaks into sodium as  $10^{-3}$  g.sec<sup>-1</sup> at pipe wall thickness of 2-3 mm comparatively quickly can develop into the leakages, the value of which is more than two orders greater of the initial value.

After this in the steam generator arises the danger of rapid fracture of the neighbouring pipe and appearance of secondary leakages.

Characteristic of the leakage self-enlargement process is sudden sharp increase of leakage size when material damage zone, gradually propagating from the leaking channel orifice through the wall, reaches the

inner surface of the failed pipe.

Up to this moment no considerable increase of leakage occurs. The total amount of water leaking into the circuit by the time of sharp leakage increase can make only some tens of grams. If the leakage in the steam generator from the moment of appearance till its ceasing as a result of steam generator switching-off on the emergency signal formed by the systems of leakage control does not cause serious damages in the steam generator, the emergency safety systems may be considered efficient.

To formulate the requirements to such systems, using concentration means of leak detection, it is necessary to know minimum water quantity that may penetrate into the circuit due to appearance of a leak before reaching maximum-permissible damage of the tube adjacent with the leak (not causing a leak in it) and the time during which this quantity gets into the circuit.

The data can be obtained on the basis of studying leak self-enlargement process and behaviour of targets nearby the leaks.

The paper includes some results of such studies carried out in the USSR for 1X2M, X18H10T, OX12H2M, X20H40T and Sanikro-31 steels, presents more details on experiments performed for investigation of small leak self-enlargement.

#### I. STRUCTURAL MATERIAL WASTAGE RESISTANCE IN THE NEIGHBOURHOOD OF WATER LEAKAGE INTO SODIUM

Investigation results of 1X2M, X18H10T, OX12H2M and Sanikro-31 steels damage in the zone of sodium-water vapour reaction were given in <sup>4</sup>. The experiments were performed with static sodium. Sodium temperature was 500°C, vapour was fed at the temperature of 315°C and pressure of 100 bars through the nozzle of 0.31 mm diameter with flow rates of  $1 \pm 11 \text{ g} \cdot \text{sec}^{-1}$ . The tubes with inert gas

pressure of 96 bars were used as targets. Wastage rate was determined as a ratio of target wall thickness to the time of its penetrating damage. The experiments showed that the resistance of Sanikro-31 was 2.5 times higher than that of X18H10T steel, 3.5 times higher than that of OX12H2M and 6 times higher than the resistance of 1X2M steel. Damage in the zone of sodium-water vapour reaction occurred locally. Damage form can change from toroidal to round hollow with increasing the distance from the target to the nozzle.

Peculiar was the presence of damage rate maximum at distances from the leak position equal to about 25 diameters of the nozzle, that corresponded to 0.143; 0.081 and 0.054  $\text{mm} \cdot \text{sec}^{-1}$  for steels 1X2M, OX12H2M and X18H10T, respectively. According to the data of <sup>4</sup> vapour leakage into sodium is dangerous at distances to 160 diameters of the nozzle. Sodium temperature decrease from 600 to 360°C led to a double reduction of the jet penetrating capacity. It was stated also <sup>5</sup> that at water jet leak and not steam into sodium in the reaction zone material damage is not of explicitly local character. Therefore, such a leak from the viewpoint of penetrating failure of the neighbouring tube wall is less dangerous than the steam leak.

The processes of wastage for the BN-350 plant conditions were studied at water leakage into sodium in the zone of the tube heat transferring surface <sup>6</sup>. The experiments were performed with the 19-tube model of steam generator evaporator reproducing structural and hydraulic characteristics of evaporator. Sodium flow had the rate of  $0.56 \text{ m} \cdot \text{sec}^{-1}$  and the temperature -270°C.

In the experiments water leakages were simulated at the pressure of 50 bars and temperature of 250°C through the wall of one tube in the model. Three tests were performed with leakage values of  $2.78 \cdot 10^{-3}$ ;

$3.75 \cdot 10^{-1}$ ;  $7.36 \cdot 10^{-1}$  g. sec<sup>-1</sup> with flow duration of 0.83; 0.2 and 0.67 hr, respectively.

After each test the zone of reaction products effect on the tube had the form of a dark spot. No other changes in the first test were found. In the second and third tests tube surface in front of the place where water leaked-out had a hollow. Corrosion rate found on the basis of the data obtained during the experiments ( $W_k$ , mm·sec<sup>-1</sup>) of 1X2M steel proved to be comparatively small and was defined by the expression:

$$W_k = 0.38 \text{ g } 10^{-3},$$

where  $g$  is the value of leakage in g. sec<sup>-1</sup>.

The results similar to those mentioned above were obtained by foreign authors <sup>3,7,8,9</sup>.

We studied the behaviour of steels 1X2M, X18H10T and X20H40B in the vicinity of water non-jet small leak ( $1.39 \cdot 10^{-2}$  g. sec<sup>-1</sup>) into sodium.

Water was supplied under low pressure ( $\sim 1.2$  bar) through the nozzle of 2 mm diameter in the wall of sodium piping.

The rate of sodium flow was 1 m. sec<sup>-1</sup>, temperature - 400°C. Water flow rate was adjusted with a regulating valve on the line of water supply to the nozzle. Water temperature in the place of leakage coincided practically with sodium temperature, therefore superheated water vapour penetrated into sodium.

The samples of the materials investigated had the form of rectangular plates  $15 \times 8$  mm<sup>2</sup> of 0.3 and 0.4 mm thickness, correspondingly, for steels X18H10T and X20H40B and  $12 \times 8$  mm<sup>2</sup> of 0.5 mm thickness for 1X2M steel. Sample position relative to the place of leakage was characterized by coordinates  $L$  and  $\delta$  counted from the leakage place correspondingly in the direction of sodium flowing in the test section and over the diameter drawn from the nozzle center.

The sample plane was normal to the diameter.

Water leak duration for each test was 72 min. The experimental results are given in table I as samples weight losses related to their areas and time of the experiment. In the tests marked with asterisks wastage was observed through all the sample thickness.

From the data in the table it follows that the reaction zone at non-jet leakage is carried away with sodium flow in its direction and is then disposed near the leaking-out tube. Owing to this, considerable wastage is observed of 1X2M steel samples placed at the wall ( $\delta = 1$ ; 3 mm) up to maximum distances from the leakage place ( $L = 20$  mm).

The experiments carried out have shown considerable wastage resistance of steels X20H40B and X18H10T in comparison with 1X2M steel at small non-jet water leak into sodium. The corrosion rate of samples made of 1X2M steel for similar experimental conditions proved to be about 50 and 100 times higher as compared to X18H10T and X20H40B steels, respectively.

## 2. SELF-ENLARGEMENT OF WATER SMALL LEAKS INTO SODIUM

The experiments were performed on sodium rigs with circulation at sodium temperatures of 300 and 450°C. For simulation of leaks in tube wall a special section was used-leak simulator, Fig. 1.

Annular surface of valve contact (4) and seat (5) was 2+3 mm deep.

Initial water flow rate was determined by the value of regulated gap between the valve and the seat or by dimensions of the mark on the valve surface contacting with the seat of the leak simulator. Water at room temperature was supplied into the simulator under the pressure of 50±140bars.



Damage Rates of 1X2M, X18H10T and X20H40B Steels in the Tests  
with a Continuous Small Water Leak into Sodium

Test No	Sample material	L, mm	mm	$W_k \cdot 10^3$ mg. cm <sup>-2</sup> . sec <sup>-1</sup>
1*	1X2M	0	1	59
2*	1X2M	0	3	390
3	1X2M	0	8	1.4
4*	1X2M	10	1	460
5	1X2M	10	3	100
6	1X2M	10	8	32
7	1X2M	10	12	3.6
8*	1X2M	20	1	250
9*	1X2M	20	3	330
10*	1X2M	20	8	62
11	1X2M	20	12	0.7
12	X20H40B	0	1	0.58
13	X20H40B	0	3	0
14	X20H40B	10	1	0.39
15	X20H40B	10	3	0.58
16	X20H40B	20	1	0
17	X18H10T	0	1	4.8
18	X18H10T	0	3	5.8
19	X18H10T	10	1	9.6
20	X18H10T	10	3	3.1
21	X18H10T	20	1	3.3
22	X18H10T	20	3	1.5
23	X18H10T	20	3	1.5

During the test correction of water flow rate with the leak simulator was not done. The test was begun by opening the valve in the line connecting the leak simulator with the system of water flow supply and control. Sodium velocity in the leak simulator was within the limits of  $1 \div 3$  m sec<sup>-1</sup>. At a sharp increase of water leakage as a result of its self-enlargement up to the values at which continuous operation of the rig is impossible ( $\sim 1$  g sec<sup>-1</sup>) the test was stopped by sealing-off the leak simulator from the system of water supply. In some cases for checking a possibility of "self-healing" of the defect, through which water leaked-out, in some time (from minutes to tens of hours) after stopping the test the leak simulator was again connected with the system of water supply. But reliable "self-healing" of defects was not observed. In all the cases the leakage resumed. Sometimes it appeared not at once but after a certain period of time not exceeding one hour.

After completing the test the simulator was dismantled and its examination was carried out.

The appearance of the water leak-out channel in simulators of 1X2M, X18H10T and X20H40B steels after testing is shown in Fig. 2. It is characteristic that a damage of the water-into-sodium leak-out channel is accompanied by wastage of material from the channel-orifice side, by the resulting increase of its cross-section and by progressive development of the damage zone over the total channel length (wall thickness). As a result a through channel of a considerably larger cross section than the original defect is formed. As the material damage zone reaches the inner wall surface the leak value sharply increases. In this case the water flow during about ten seconds can increase by more than a hundred times. As was shown by experiments, in the process of small leaks self-enlargement the change of their values is possible due to a strong effect of impurities and corrosion products

present in water upon the hydraulic characteristics of the leak-out channel.

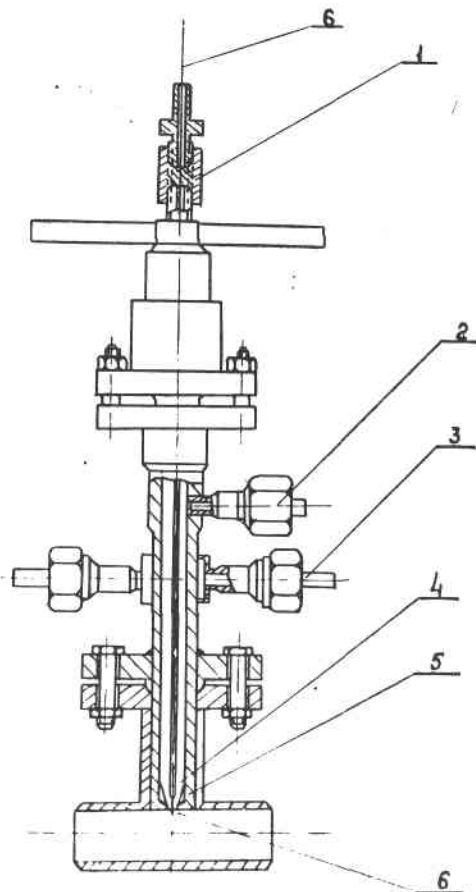
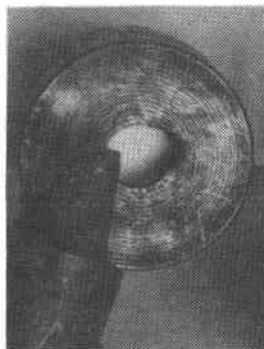
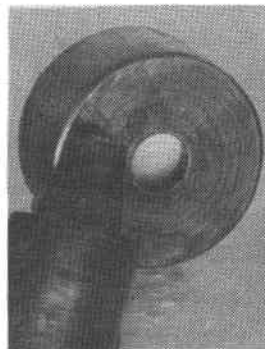


Fig. 1. Leak simulator.  
 1-thermocouple seal assembly  
 2-water supply pipe connection  
 3-cooling water lines  
 4-valve  
 5-seat  
 6-thermocouple.



a



b



c

Fig. 2. Leak simulators after tests 2 x magnification  
 a-1X2M,  $t_{Na} = 300^{\circ}\text{C}$ , leak value of  $4.7 \cdot 10^{-3} \text{ g. sec}^{-1}$ , water quantity = 397 g.  
 b-X18H10T,  $t_{Na} = 300^{\circ}\text{C}$ , leak value is  $2.5 \cdot 10^{-3} \text{ g. sec}^{-1}$ , water quantity = 516 g.  
 c-X20H40B,  $t_{Na} = 300^{\circ}\text{C}$ , leak value is  $5 \cdot 10^{-3} \text{ sec}^{-1}$ , water quantity = 2980 g.

Damage rates for 1X2M, X18H10T and X20H40B steels calculated from the results of tests on leak simulators are shown in Fig. 3 as a function of the mean water leak value.

The rate of material damage in the water leak-out channel ( $w$ ) was determined as the ratio of the damage zone penetration depth ( $\delta$ , mm) to the time during which water was leaking into sodium ( $\tau$ , sec.). The average leak value was calculated by the equation  $G = \frac{m}{\tau}$ , where  $m$  is the amount of water supplied into the loop during the test, (g).

The data in Fig. 3 in a least-squares treatment are approximated by the following equations:

$$\text{for 1X2M } \lg W = 4.703 + 1.134 \lg G - \frac{3857}{T};$$

$$\text{for X18H10T } \lg W = 2.494 + 0.807 \lg G - \frac{3001}{T};$$

$$\text{for X20H40B } \lg W = 4.121 + 1.1196 \lg G - \frac{3851}{T};$$

The experiments performed have shown that the penetration rate of the material damage zone from the water-into-sodium leak-out channel orifice into the wall depth and, therefore, the time of self-en-

largement of a small leak into a large one depend strongly on a sodium temperature. So, for a sodium temperature of 300°C the rate of material damage for 1X2M, X18H10T and X20H40B steels decreases by more than an order of magnitude compared to a temperature of 450°C. The mean leak value and the type of structural material also produce a considerable effect upon the time of self-enlargement of small water-into-sodium leaks. With the increase of nickel content in a material the resistance to water-into-sodium leak self-enlargement increases. It can be supposed that the use of nickel-based materials would considerably increase the time needed for the development of a small leak into a large one.

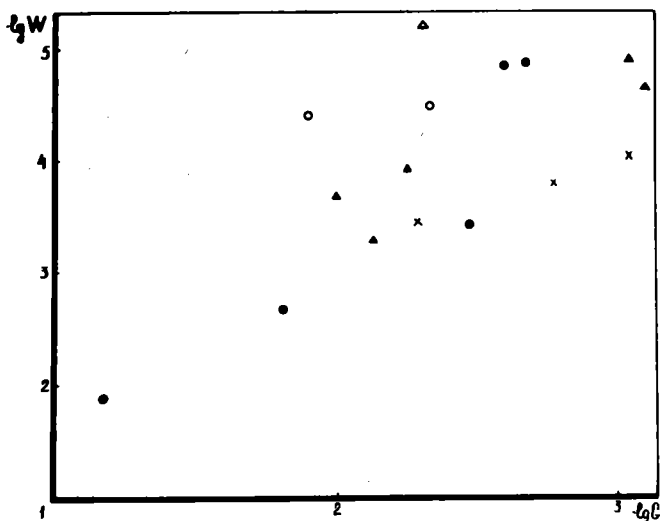


Fig. 3. The rate of damage of 1X2M, X18H10T and X20H40B steels from the results of tests on leak simulators.

● -1X2M  
 × -X18H10T  
 ▲ -X20H40B  
 ○ -1X2M  
 ⊗ -X18H10T  
 △ -X20H40B  
 $t_{Na} = 450^{\circ}C$        $t_{Na} = 300^{\circ}C$

The mechanism of material wastage in a zone of water-sodium interaction is usually related to the effect of increased local temperatures and high-speed reaction products promoting intensive corrosion due to their high chemical activity and erosion ability. For these reasons a relatively small decrease of sodium temperature ( $\sim 150^{\circ}C$ )

compared to the high-temperature level in the reaction zone should not result in a strong decrease of the material damage rate which was observed in the experiments described above. Special tests in air with water, heated up to 350°C and containing  $\sim 5$  wt.% sodium hydroxide, leaking out through a defect in 1X2M steel have shown that in this case the rate of material damage (times of small-leak self-enlargement) is of the same order as at water leak into sodium (Table II).

At the same time, leakage of 350°C water containing no sodium hydroxide does not result in corrosion effects. The increase of water alkali concentration in the leak-out channel at small leaks appears to be due to diffusion processes and water flow-rate fluctuations causing sodium penetration into the leak-out channel.

### 3. MEASUREMENT OF SODIUM-WATER REACTION PRODUCT DISTRIBUTION OVER THE SODIUM FLOW CROSS SECTION NEAR THE LEAK

For this purpose a special probe <sup>10</sup> shown in Fig. 4 was used.

It consists of the sampling tube (1) passing through the orifice in the cap of the case (2) and the gas-tight seal (3) in the upper part of the gas cavity filled with inert gas through the tube (4).

To control the sodium level the electric contact level indicator (5) was mounted. The sampling tube is displaced along the radius in any direction with the use of the mechanism (6) consisting of a screw pair connected with the tube by a bearing. The indicators (7) serve for measuring the radial displacement of the sampling tube. The accuracy of measuring the axial and radial coordinates of the sampling-tube end is  $\sim 1$  mm. A flexible spiral tube (8) is connected with the sampling one and allows it to displace in axial and radial

Conditions and Results of Tests with Heated  
Alkali Water Leaking-out into Air

Conditions	NaOH concentration in water		
	5 wt. %	5 wt. %	4 wt. %
Test N°	1	2	3
Water temperature, °C	350	350	350
Mean leak value in a test, g.sec <sup>-1</sup>	$5.3 \cdot 10^{-2}$	$4.2 \cdot 10^{-3}$	$3.9 \cdot 10^2$
Time of leak, hr	1.25	1.5	1.75
Water pressure, bar	48	50	45
Leak simulator wall thickness, mm	2	2	2
Leak value after self-enlargement, g.sec <sup>-1</sup>	>1	>1	>1
Material damage rate, mm sec <sup>-1</sup>	$4.45 \cdot 10^{-4}$	$3.7 \cdot 10^{-4}$	$3.17 \cdot 10^4$

directions within the tube of  $\varnothing 50 \times 3$  equipped with the water inlet assembly. At sampling in the water-into-sodium leakage zone the sampling tube (1) is displaced in the axial direction by a required value, then by rotating the mechanism (6) about the tube axis the direction of its movement along the radius is chosen, and the end of the sampling tube is positioned at the required point. Sodium, through the sampling tube (1) and the flexible spiral tube (8), can be supplied into the sample containers of the sampling device.

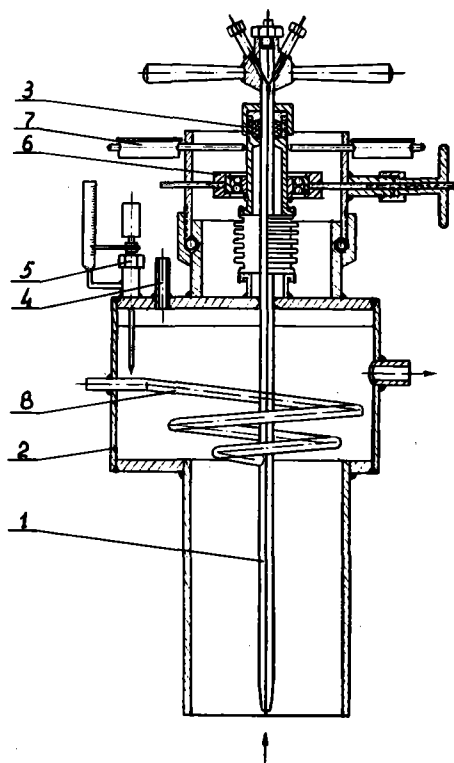


Fig. 4. Sample probe for parameters investigation in the water-into-sodium leakage zone.

The sample probe was mounted vertically on the by-pass line of the sodium loop. At sodium moving from the bottom upwards at a flow rate of 800 l/hr sampling was carried out at different points over a sodium flow cross section located at a distance of 5 mm from the point of water leakage for water leakage values of  $2.8 \cdot 10^{-2}$ ,  $3.9 \cdot 10^{-2}$  and  $9.7 \cdot 10^{-2}$  g.sec<sup>-1</sup>.

Analysis for oxygen content of the samples taken from the points of this cross section with coordinates of 2, 11, 22 and 42 mm (counted from the leakage point along the diameter of the outer probe tube up to the line being parallel to the axis of this tube and passing through the centre of the sampling tube inlet cross section) showed substantial non-uniformity of the oxygen-containing product distribution. Concentration of these products near the tube wall proved to be higher than in the centre. This is an indication of a possibility of local supersaturation in sodium flow and of reaction-product precipitation at surfaces near the leakage point.

The results of the analysis are presented in Fig. 5 as the dependence of the ratio of the oxygen concentration at the given point to that at the sampling point nearest

to the leakage point, on the sampling point coordinate. Determination of oxygen content in samples was carried out by the distillation method (the distillation temperature of 450°C).

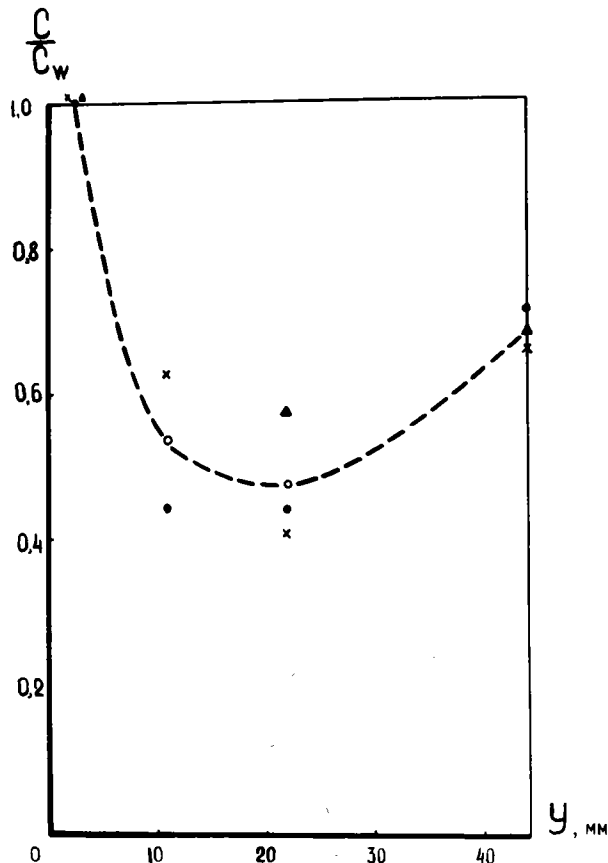


Fig. 5. Oxygen-containing product distribution in sodium flow close to the water leakage point.

- x - water flow rate of  $2.8 \cdot 10^{-2}$  g·sec.<sup>-1</sup>
- - water flow rate of  $3.9 \cdot 10^{-2}$  g·sec.<sup>-1</sup>
- ▲ - water flow rate of  $9.7 \cdot 10^{-2}$  g·sec.<sup>-1</sup>

#### CONCLUSIONS

1. The time of self-enlargement of small water-into-sodium leaks through defects in 1X2M, X18H10T and X20H40E steels strongly depends on a sodium temperature and, to a less degree, on a steel type. The decrease of a sodium temperature from 450° to 300°C results in the increase of the time of evolution of a small leak into a large one by more than an order of magnitude.

2. The resistance of the materials investigated to damage in the sodium-water reaction zone and immediately in the water-into-sodium leak-out channel increases with nickel content in steels.

3. Leakage of water heated up to 350°C into air through a defect in Type 1X2M steel does not cause its damage in the leak-out channel, but the presence of sodium hydroxide (~5 wt. %) in water leads to corrosion effects comparable to 1X2M damage at water-into-sodium leaks.

4. At small leaks the distribution of oxygen-containing products from the sodium-water reaction in the flow cross section of sodium moving from the bottom upwards near the water leak-out point may be substantially non-uniform (concentration near the wall being higher than in the centre).

#### REFERENCES

1. Lecocq P., Lannou L., Masson J. Surveillance de l'étanchéité sodium-eau du générateurs de vapeur chauffés au sodium par dosage de l'hydrogène. Proceed. of a Symposium Prague, 22-26 January (1973), IAEA-SM-168/E-7.
2. Kozlov F.A., Sergeev G.P., Makarov V.M., Sednev A.R., Bergunker V.D., Alexandrov V.V., Sobolev E.N., Gubanov V.M., Khaletskii E.E. Water leak evolution into sodium through defects in a tube wall and in joints of tube fixing in tube plates. Proceed. of Amer.-Sov. seminar on fast reactor sodium-cooled steam generators development. Vol. I, Los Angeles, USA, December 2-4, 1974.
3. Green D.A. Sodium-water wastage and reactions program performed by General Electric in support of the U.S. AEC LMFBR steam generator development. Study group Meeting on steam generators for LMFBR'S Held in Bensberg, FRG, 14-17 October 1974, Summary Report.
4. Mazanov A.S., Kulpin B.V., Petukhov V.P., Ledovskikh N.M. Experimental investiga-

## INTERNATIONAL CONFERENCE ON LIQUID METAL TECHNOLOGY IN ENERGY PRODUCTION

- tions of different steel resistances in the sodium-steam reaction zone. Study group Meeting on Steam Generators for LMFBR's Held in Bensberg, FRG, 14-17 October 1974, Summary Report.
5. Kulpin B.V., Mazanov A.S. Analytical and experimental studies of sodium-water reacting jet. Specialist's Meeting on sodium-water reactions. 18-21 May, 1971, Melekess, USSR, Summary Report.
  6. Poplavsky V.M., Borisov V.V., Bagdasarov U.E., Bogdanovich P.N., Bergunker V.D., Efimov I.A., Zotov V.V., Sobolev E.N., Testov I.N., Titov V.F., Timosh B.S., Khaletskii E.E. An experimental study of material damage processes in the small water-into-sodium leak zone as applied to BN-350 and BN-600 plant steam generator conditions. Paper presented at the COMECON symposium, 1-8 October, 1973, Obninsk, USSR.
  7. Chamberlain H.V., Choleman T.H., Kovacic, Sharidy A.A. Wastage of steam generator materials by sodium-water reactions, ANL-7520, Part I. Proceed. of the International conference on sodium technology and LFR Design, Argonne, November (1968).
  8. Lions N., Lacroix A., Schwab B., Lafon A., Trimouille. Exposé fait a la réunion des spécialistes sur la réaction sodium-eau. Specialist's Meeting on sodium-water reactions. 18-21 May, 1971, Melekess, USSR, Summary Report.
  9. Dumm K. Small water/steam leaks in sodium heated steam generators: evaluation of the reaction zone-effects on 2 1/4 Cr1Mo structural material. Study group Meeting on steam generators for LMFBR's Held in Bensberg, FRG, 14-17 October, 1974. Summary Report.
  10. Kozlov F.A., Sergeev G.P., Simakov A.I., Makarov V.M. Device for liquid metal and alloy sampling author's certificate N° 446793. Published on Oct. 5, 1974. Bulletin N° 38.

# INTERNATIONAL CONFERENCE ON LIQUID METAL TECHNOLOGY IN ENERGY PRODUCTION

## QUALIFICATION OF ALLOY 800 FOR SODIUM HEATED STEAM GENERATORS

J. M. Duke \*

C. E. Sessions\*\*

W. E. Ray †

Nuclear Energy Systems  
Westinghouse Electric Corporation

### ABSTRACT

A reference specification of Alloy 800 for use in LMFBR steam generators is defined considering water-side corrosion, weldability and mechanical properties. Additional mechanical test data is being generated to support ASME Code acceptance. Candidate weld filler metals were assessed for use in subsequent weld process development. Progress on resolving technical concerns related to the role of tertiary creep identified the impact of test conditions and gamma prime strengthening in determining the creep behavior of Alloy 800.

### INTRODUCTION

It has been well documented that Alloy 800 has significant mechanical property advantages over candidate alloys for LMFBR steam generator application.<sup>1,2/</sup> The alloy is readily weldable and has excellent overall fabricability.<sup>1,3/</sup> Excellent corrosion performance in fossil power plant steam service has been demonstrated<sup>4/</sup> and the alloy is achieving a good record in PWR and HTGR steam generator service.<sup>5,6/</sup> The selection<sup>1,2,6/</sup> of Alloy 800 for use in the French LMFBR (Super-Phoenix), its consideration as a potential backup to 2-1/4 Cr-1 Mo steel for the American LMFBR (Clinch River) and its use in the THTR and HTGR points to the wide acceptance of the material for steam generator service.

Alloy 800 was selected initially by Westinghouse in 1963 as the prime material for commercial LMFBR steam generator (1000 MWe) application for steam conditions of 1050°F and 2400 psig.<sup>2/</sup> Essentially the alloy was chosen over the austenitics because of its superior resistance to chloride cracking and in preference to the ferritic steel 2½ Cr-1 Mo because of its strength advantage and resistance to sodium-water wastage damage.

Major reasons for development of an advanced austenitic alloy like Alloy 800 for commercial LMFBR steam generators are as follows: (1) elevated temperature nuclear designs are currently based upon our

extensive experience and understanding of Types 304 and 316 stainless steels which are similar to Alloy 800, (2) Alloy 800 is superior to Type 304 and 316 stainless steel in several important areas including resistance to certain types of stress corrosion, fatigue crack growth rates, tensile properties and creep resistance, and (3) the development of a superior austenitic steel provides an alternative material in the event that the uncertainties regarding the reference ferritic material are not favorably resolved, and if additional unforeseen problems arise. The maintenance of high strength up to 538°C provides for advanced designs operating at higher temperatures than presently considered.

The USA program plan on advanced materials for LMFBR steam generator was presented earlier.<sup>7/</sup> The current paper reviews the progress made toward qualification of Alloy 800.

### Specification of Alloy 800

Early work indicated<sup>1/</sup> that a refinement in the specification of Alloy 800 was warranted. Therefore, a literature review was undertaken last year to identify a reference composition and heat treatment to focus subsequent developmental activities.<sup>8/</sup> The selection was based upon the consideration of the behavior of Alloy 800 in three areas of primary interest to steam generator designers: (1) mechanical properties (creep and tensile) at temperatures up to 593°C, (2) compatibility in off-normal water/steam environments, and (3) base metal weldability. Independent literature reviews were conducted in each of the three areas to conclude the best composition and heat treatment.

As a result, the reference material was established as a fine grained, low carbon version of Alloy 800.<sup>8/</sup> However, a coarse grain, high carbon version (Alloy 800H) was identified as a backup to the reference because of an inherent risk in obtaining the required ASME Code approval. The French<sup>6/</sup> have chosen a fine grain, intermediate carbon specification and the English<sup>1/</sup> suggest using a low carbon, coarse grained variety of Alloy 800 -- all for the same application (FBR steam generators). Although similar

\* Principal Investigator, Tampa Division

\*\* Senior Metallurgical Engineer, Tampa Division

† Manager, Materials and Processes, Advanced Reactors Division

in some aspects, the differences are not readily explainable.

#### Weld Development

Welding development of Alloy 800 has been conducted within Westinghouse during the last 10 years.<sup>3,8,9/</sup> Early evaluation of the behavior of various tube-to-tubesheet joint designs demonstrated that either butt welded or conventional front face fillet welds of Alloy 800 to Inconel 82 overlay cladding were compatible in contaminated sodium at temperature up to 538°C (1000°F). No insurmountable problems were encountered in producing sound defect-free, tube-to-tubesheet welds when using Inconel 82 filler metal or weld overlay. However, some difficulty has been reported in the literature involving hot cracking in autogenous welds.<sup>1/</sup> Since an autogenous root weld may be preferred in certain areas, weldability (defined here as the resistance to hot cracking in fused metal) was considered to assure a minimum of production weld problems in areas where filler metal dilution could be low. The weldability was measured using a number of techniques including the cast pin tear test, Varest, and hot ductility measurements on fourteen heats. Four of the heats exhibited lower weldability in one or more of the test techniques. As a result of an extensive analysis of the chemical composition of the heats involved, higher ratios of (Al+Ti)/(C+Si) together with control of copper, cobalt, phosphorous and sulfur were found to correlate with improved weldability.<sup>8/</sup> This relation of the (Al+Ti)/(C+Si) ratio to hot cracking was further substantiated by an electron beam weldability test performed at HAPD-INCO.

Besides the weldability of the base material, an assessment of candidate filler metals was undertaken.<sup>9/</sup> Several potential processes were included: SMAW with a covered electrode (Incoloy 188), MIG with the most severe spray-arc transfer, submerged arc welding and TIG using Incoloy 88. Minor problems were traced to oxide on the weld wire and the use of an improper weld flux for the submerged arc process. Specimens of the experimental welds were used to measure the coefficient of thermal expansion, tensile properties and metallography. The study concluded that Inconel 82 and 182 are satisfactory for use at temperatures of 482°C and below. Above 482°C, the filler metals Incoloy 88 and 188 are preferable, provided adequate creep ductility can be demonstrated. The experimental welds made indicate that no major problems would be encountered in identifying acceptable commercial weld processes.

#### Corrosion Studies

The literature indicates that Alloy 800 possesses good corrosion behavior in environments expected in LMFBR steam systems. Its overall performance in chloride and caustic environments, as well as superheated steam, is adequately documented. The majority of the literature was developed to demonstrate the excellent stress corrosion properties of Alloy 800 compared to other austenitic materials. Only limited data are available which systematically evaluates the effect of slight modification (i.e., composition, microstructure and heat treatment) on its stress corrosion performance.

The conclusions drawn<sup>8/</sup> from the review of effect of alloy composition reflect one of four possible choices: (1) high concentration preferable, (2) low concentration preferable, (3) no effect, or (4) insufficient data to establish an effect. The possible conclusions about optimum grain size reflect two possibilities: (1) small grains are preferable, or (2) large grains are preferable which are related to heat treatment either (1) anneal at 982°C minimum or (2) solution treated at 1149°C minimum, respectively. Although disagreement exists in the literature, Table I presents the relationships of the important properties to the parameters of the specification as established in the review.

Table I. Effects of Composition of Alloy 800 on Corrosion Resistance

<u>Type of Corrosion</u>	<u>Carbon</u>	<u>Titanium</u>	<u>Ti/C</u>	<u>Grain Size</u>
General IGA	L	H	H	F
Caustic - aqueous	NE	NE	NE	C
Caustic - steam	NE	NE	I	I
Chloride - SCC	L	H	H	I
Steam	L	I	I	F

Note: L, H, F, C, NE and I correspond to low, high, fine, coarse, no effect and insufficient data, respectively.

The low temperature, acidic, intergranular corrosion tests have generally not been found to correlate with high temperature service performance.<sup>4,10,11/</sup> This lack of correlation has been found directly for aqueous tests in the region of 316°C (600°F) to 350°C (662°F) in chloride<sup>13,15/</sup> and caustic media.<sup>12,14/</sup> No direct evidence has been presented for high temperature superheated steam service but the lack of effect of carbon and titanium variations<sup>1/</sup> and sensitization<sup>13/</sup> indicates a similar lack of correlation. For high temperature service the results from Huey



## INTERNATIONAL CONFERENCE ON LIQUID METAL TECHNOLOGY IN ENERGY PRODUCTION

and Strauss type tests should be used cautiously. The areas where such tests may have some relevance are the environments encountered during manufacture, construction and lay-up of the plant. However, there is little experience available in this area.<sup>1,4/</sup>

The high temperature 350°C (662°F) aqueous stress corrosion tests that have been assessed alloy composition<sup>1/</sup> have not indicated any differences in the performance of alloys with carbon in the range of 0.015 to 0.055% C and Ti/C ratios of 4.1 to 14.2. Results from exposure to high temperature in 3% and 10% NaOH solutions have indicated that the larger grained material is more resistant to cracking.<sup>13,15/</sup> At lower concentrations cracking was not experienced in either material. The results are largely qualitative and more quantitative data in the form of threshold stresses are necessary.

Tests in high temperature superheated steam<sup>1,13/</sup> have not shown any effect of carbon content, Ti/C ratio or sensitization. The literature data do not suggest a specific composition for superheater applications and there is no information on grain size effects in applicable environments. For Alloy 800 use in an evaporator, the literature does not suggest a specific composition but the larger grain sized material does offer better resistance to caustic cracking in aqueous solutions. This data should not be applied to superheater applications since there are instances of reversal of relative performance of materials on changing the environment from aqueous to steam.<sup>13/</sup>

The caustic exposure test results show a slightly better resistance for a sensitized structure and for a coarse grain size. Both sensitization and large grains would lead to enhanced grain boundary attack in acid solutions that should be indicative of potential attack during manufacture and wet lay-up, for example. It would appear that carbon content is relatively unimportant in affecting stress corrosion, but it has a large influence on the degree of potential sensitization. Thus, our overall recommended specification for Alloy 800 (e.g., fine grain size, low carbon and high Ti/C ratio) reflects our consideration of the possible attack of a sensitized structure rather than a slight potential improvement in resistance to stress corrosion cracking.

In a system constructed of alloys with reasonably similar compositions, for instance Type 304 stainless steel and Alloy 800, sodium corrosion and mass transfer

proceeds as a result of temperature gradients that exist within the system. Material is dissolved in high temperature regions and subsequently deposited in cold leg areas. Hence, most of the Alloy 800 used in steam generator components of an LMFBR would lie in deposition regions of the system. This is, however, not the case for the hottest end of the evaporator which would still be in a corrosion or material-removal zone; hence, sodium corrosion is still an effect whose magnitude must be considered in determining wastage allowances. Various sodium corrosion tests on Alloy 800 have been conducted within Westinghouse for time periods up to 13,000 hours. Testing conditions have been reasonably severe when compared to anticipated operating levels in the intermediate circuit of an LMFBR. For instance, maximum test temperatures have ranged from 593 to 718°C (1100 to 1325°F) and the oxygen impurity level in the sodium has been as high as 25 ppm. This was done partially to accelerate sodium corrosion effects to permit early identification of potential problems and also because it was considered that the impurity level of the sodium in the intermediate circuit could be somewhat higher than the primary circuit. The results of these tests were encouraging and showed that while corrosion rates for Alloy 800 were 2-3 times those observed in Types 304 or 316 stainless steel, the rates were still acceptably low and wall thinning would not be a major problem. For instance, at 718°C in sodium with less than 2 ppm oxygen impurity, the corrosion rate of Alloy 800 was approximately 1 mil per year. Rates for Types 304 and 316 stainless steel under equivalent conditions are in the range of 0.5 mils per year. When the present results are extrapolated down to maximum anticipated steam generator conditions, a total wastage allowance of less than 2 mils is obtained for Alloy 800 over an expected life of 30 years. The present tests have also indicated that there is no rapid selective, grain-boundary attack of the Alloy 800 even under the most severe testing conditions. Other tests have also been conducted to determine the stability of carbon in Alloy 800. Minimum carbon levels in the range of 300-400 ppm have been observed in these tests under highly decarburizing conditions.

### Mechanical Properties

The mechanical behavior of Alloy 800 has received considerable emphasis in the USA and in Europe.<sup>1/</sup> Presently, the ASME Code includes annealed and solution treated material but only Alloy 800H is approved for Class 1 nuclear power plant components operating at

## INTERNATIONAL CONFERENCE ON LIQUID METAL TECHNOLOGY IN ENERGY PRODUCTION

elevated temperature. Our work has addressed the selection of the specification relative to mechanical properties and the development of information required to obtain ASME Code approval of the annealed material for use in nuclear power plant components operating above 427°C (800°F).

Conclusions in Table II are based on mechanical properties reported in the literature<sup>1/</sup> and on an analysis of a HAPD data package on annealed material.<sup>4/</sup> Room temperature tensile properties were found to be independent of chemistry. At 538°C both the tensile and yield strengths increased with titanium and carbon but decreased with an increase in the Ti/C ratio. This well defined relationship between chemistry and strength was not as evident at 593°C.

Table II. Effect of Composition of Alloy 800 on the Mechanical Properties

Tensile Properties At 538°C	Carbon	Titanium	Ti/C	Grain Size
Yield Strength	H	H	H	F
Tensile Strength	H	H	H	F
Elongation	L	L	L	C
Creep Properties at 593°C				
Rupture Life	L	NE	H	C
Time to Tertiary Creep	L	NE	I	C
Minimum Creep Rate	L	H	H	C
Reduction of Area	H	L	I	I
Elongation	H	L	I	F

Note: L, H, F, C, NE and I correspond to low, high, fine, coarse, no effect and insufficient data, respectively.

Effect of alloy composition on the creep behavior was found to be different for annealed and solution treated material. Short term creep results<sup>4/</sup> of thirteen heats of annealed Alloy 800 tested at 593°C and 241 MPa showed that increasing the carbon content increases the creep rate. A regression analysis of this data indicated aluminum, titanium and carbon to be the primary chemical variables controlling the creep behavior. This conclusion on the role of carbon is contrary to that of Egnell<sup>1/</sup> who concluded that in solution treated material at 700°C (1292°F), an 18% increase in the rupture strength accompanied an increase in the carbon from 0.04 to 0.10%. This could be explained by a fundamentally different role of carbon depending upon whether it is in or out of solid solution and by gamma prime strengthening that is dominant at temperatures below 593°C. Thus, both conclusions could be correct.

The question concerning the effect of composition on creep ductility cannot be answered currently

because of the limited data. The Europeans are considering modified compositions which would have a lower tendency to form gamma prime during service.<sup>1/</sup> In our recommended specification the aluminum and titanium are limited to 0.45% each. This would theoretically limit by 25% the maximum amount of Ni<sub>3</sub>(Al,Ti) which could form based upon existing ASTM specifications. However, with a low carbon content some references indicate enhanced precipitation of gamma prime and thus greater loss in creep ductility.<sup>1,17/</sup> More data are obviously needed at 593°C and below to establish long term creep ductility of the recommended specification.

From solely a strength consideration, Figure 1 indicates that the time independent allowables govern the design stress up to near 538°C (1000°F). Since grain size primarily controls these tensile properties, the fine grained annealed material offers substantial advantage at this temperature. Results of creep tests at 538 and 482°C indicate that creep resistance of the two grades at constant chemistry and stress are nearly equivalent.

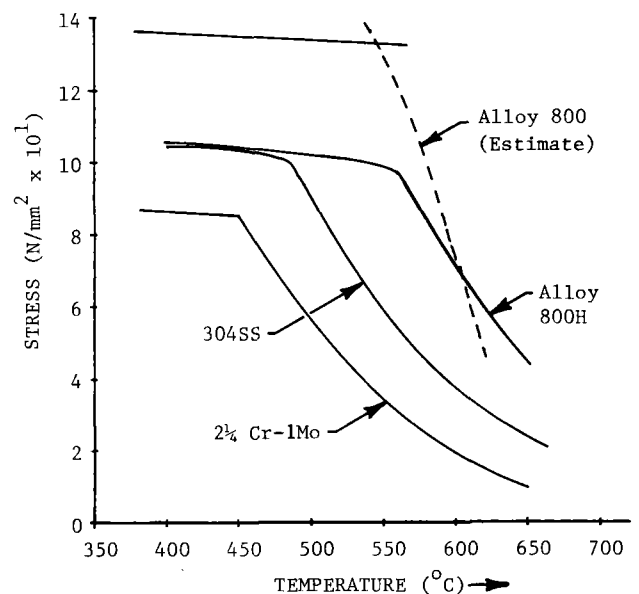


Fig. 1. Comparison of ASME B&PV Section III Allowable Stress Intensity,  $S_{mt}$ , for Various Alloys at  $3 \times 10^5$  Hours

Work on obtaining ASME Code acceptance of the fine grained annealed grade for use above 427°C (800°F) involves generation of data and resolution of technical concerns regarding the role of tertiary creep. Creep testing is being carried out at 538° and 593°C due to an inability to extrapolate results obtained at higher temperatures and because of the

## INTERNATIONAL CONFERENCE ON LIQUID METAL TECHNOLOGY IN ENERGY PRODUCTION

general lack of data in this temperature regime.<sup>1/</sup> Thirty specimens from four heats of annealed Alloy 800 have been tested. Two heats are within our selected specification range and two heats have higher carbon content. Two of the heats are from bar stock, one heat is from plate and one heat is tubing. The total testing time accumulated to date is approximately 75,000 hours; however, the maximum duration of any single test is 8,100 hours. The tests being conducted are of two types: (1) those designed to rupture, and (2) those designed to strain 1% in  $10^3$ ,  $10^4$  or  $3 \times 10^4$  hours. Fifteen tests have also compared the creep behavior to 5,000 hours of the two grades of Alloy 800. The data accumulated indicate no significant differences in rupture time or creep rate for annealed and solution treated material of the same heat. Thus, any advantages of a coarse grain size on creep resistance at  $538^\circ\text{C}$  is not apparent from existing WTD data.

A study of the role of tertiary creep is included in this program because of earlier indications that the present ASME criterion would severely reduce the design allowables and due to unresolved technical concerns regarding the appropriateness of the criterion. As presented earlier,<sup>2/</sup> the study would address three areas: (1) metallurgical implications, (2) correlation with failure in multiaxial stress conditions, and (3) effect on design analysis. The metallurgical aspects are considered since annealed Alloy 800 is observed to deviate from the minimum creep rate at a small fraction of the time to rupture under certain loading conditions. Correlations of the conditions of the creep test (stress and temperature) to the onset of tertiary creep for 108 test resulted in two conclusions. Early onset of tertiary creep (deviation from the minimum creep rate) occurs when (1) the stress is low such that the strain on loading is less than 0.4 percent, and (2) the test temperature is above that at which gamma prime  $|\text{Ni}_3(\text{Al,Ti})|$  strengthening has been reported.<sup>1/</sup> These conclusions are consistent with phenomenological explanations for the various types of creep curves observed,<sup>18/</sup> and explain the inability to extrapolate results obtained at higher temperature to the regime of interest.<sup>2/</sup> In no case could the early onset of tertiary creep be related to the fracture process or found to be indicative of unacceptable metallurgical instability.

The correlation of the onset of tertiary creep observed in a uniaxial test to failure in multiaxial

stress conditions was to be resolved by experimental results and a review of the literature. The experimental effort consisted of testing to failure four tubular creep rupture specimens and four flat plate specimens under different biaxial stress conditions corresponding to early tertiary creep in uniaxial test. The annealed Alloy 800 tubular creep sample and a representative instrumented flat plate specimen intended for creep testing are shown in Figures 2 and 3, respectively.

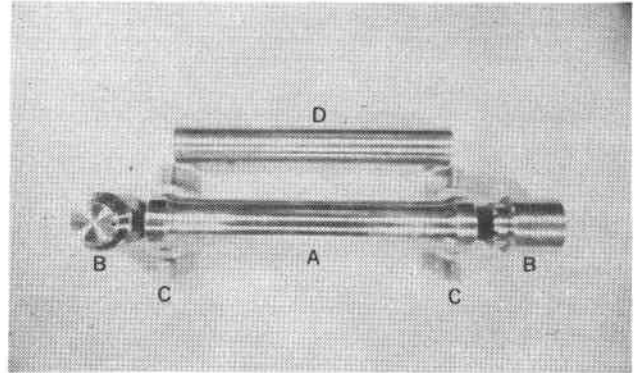


Fig. 2. Sample Tubular Creep Rupture Specimen of Annealed Alloy 800 Prior to Welding End Caps and Final Machining (1.25 mm wall x 39 mm dia.).

A. Specimen Body, B. End Plugs, C. Extensometer Tabs, D. Volumetric Reduction Bar

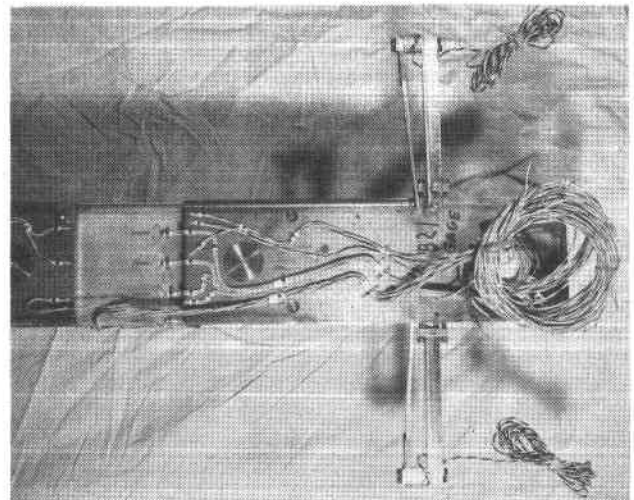


Fig. 3. Instrumented Biaxially Stressed, Uniaxially Loaded Flat Plate Specimen of Basic Specimen Configuration (6.25 mm thickness x 50 mm wide x variable gage lengths)

## INTERNATIONAL CONFERENCE ON LIQUID METAL TECHNOLOGY IN ENERGY PRODUCTION

The results of the tests would then be compared to those obtained in uniaxial specimens from the same material. The tests have not been initiated due to funding limitations. The literature survey resulted in the location of only one report relating failure in pressurized capsules to the initiation of tertiary creep in uniaxial creep tests.<sup>19/</sup> The test specimens consisted of thin walled specimens of Type 316 stainless steel with large grain size such that an average of less than four grains existed through the wall. Failure was interpreted as loss of pressure (leaking). Under these conditions, early failure would be expected, and the results are not considered applicable to fine grained material (i.e., approximately ten grains through the wall, as would be employed in prototypic components).

Tertiary creep is considered to be significant in design analysis in causing accelerating concentration of strain and increasing error in predicted behavior. This effect would be countered by stress redistribution. A mathematical model of tertiary creep (strain softening) was developed for analytic studies to quantify the effect of stress redistribution. Simultaneously the literature is being reviewed and interpreted to support elimination or modification of the present criterion. A recent paper<sup>20/</sup> on this topic is presently being reviewed.

### Conclusions

A program to qualify Alloy 800 for use in LMFBR steam generators was initiated in 1975. A literature review resulted in specification of a fine grained material with low carbon level that differs from that selected by European suppliers of LMFBR steam generators. This could reflect both a difference in selection of criteria and/or differences in the available data base for the selection. Consequently, an international cooperative effort is recommended to resolve this critical area. Additional data are needed and tests have been started to establish the impact of the low carbon level on the ASME Code design allowables and to quantify the effect of carbon level on caustic stress corrosion cracking.

The program plan included a significant effort to resolve the design criterion based on the initiation of tertiary creep. Due to subsequent funding constraints, only the assessment of the metallurgical implication of tertiary creep was accomplished. This work identified the cause of the problem in extrap-

lating higher temperature data to the temperature range of interest as related to strengthening by the gamma prime precipitation. In addition, the type of creep curve was shown to be dependent on the stress level in that plastic strain on loading results in the classical creep curve.

Development of fabrication and weld technology focused on an assessment of candidate filler materials. This work considered the acceptability of Inconel 82 and 182 and the problems which might be encountered with Incoloy 88 and 188. The results show that Inconel 82 and 182 are acceptable for use in sodium heated steam generators below 482°C (900°F) and are preferred based on the extensive experience with these materials. Above 482°C the developmental filler metals Incoloy 88 and 188 show definite advantage by the better match in chemistry and physical properties with Alloy 800 provided adequate creep ductility can be demonstrated. The welding development activities are particularly encouraging and no major problems are anticipated in subsequent process development for commercial application in LMFBR steam generators. A significant amount of work remains, however, in the preparation of prototypic welds for mechanical testing and exposure to anticipated environments.

The level of effort in this program is related to its selection for use in a future LMFBR steam generator. However, a prime requirement for its selection is the approval of design allowables by the ASME Boiler & Pressure Vessel Code for use in nuclear power plant components operating above 427°C (804°F). Therefore, our immediate future activities will continue to address this area with subsequent activities aimed at quantifying environmental effects and the development of fabrication technology.

### References

1. S. F. Pugh (Editor), A Status Review of Alloy 800, Proceedings of a BNES Conference at University of Reading UK on Sept. 25-26, 1974 (1975).
2. W. E. Ray, S. Schrock, S. Shiels, and K. C. Thomas, "Selection of the steam tubing material for the Westinghouse LMFBR demonstration plant," Nuclear Technology 11, pp. 222-231 (June 1971).
3. R. G. Hobson and E. Eilbeck, "LMFBR steam generator development and testing," IAEA-SM-130/63 Sodium-Cooled Fast Reactor Engineering (March 23-27, 1970).
4. Huntington Alloy - International Nickel Company Data Package, "Incoloy Alloy 800 data for use in design of gas cooled and liquid metal fast reactor" (January 17, 1975).

## INTERNATIONAL CONFERENCE ON LIQUID METAL TECHNOLOGY IN ENERGY PRODUCTION

5. F. A. Mazandarany and P. L. Rittenhouse, "Effect of service environment on the behavior of high temperature gas cooled reactor steam generator structural materials, Nuclear Technology, 28, pp. 406-423 (March 1976).
6. M. Julien, "Alloy 800 for LMFBR steam generators," International Conference for Nuclear Steam Generators, Gatlinburg, Tenn. (Sept. 9-12, 1975).
7. P. Patriarca, S. D. Harkness, J. M. Duke and L. R. Cooper, "US advanced materials program for steam generators," Nuclear Technology, V28, No.3, pp. 516-536 (March 1976).
8. Alloy 800 Development For Advanced LMFBR Steam Generators, Steam Generator Materials Technology Program Quarterly Progress Report For Period Ending June 30, 1975, ORNL-TM-5027, pp. 117-182 (October 1975).
9. Alloy 800 Development For Advanced LMFBR Steam Generators, Liquid Metal Fast Breeder Reactor Materials Development Program Quarterly Progress Report for Period Ending December 31, 1975, ORNL-TM-5131, pp. 97-159.
10. I.L.W. Wilson and R. G. Aspden, Paper G22 presented at International Conference on Stress Corrosion Cracking and Hydrogen Embrittlement of Iron Base Alloys, Ferminy, France (June 12-26, 1973).
11. J. C. Carlen and U. Blom, "Influence of analysis, heat treatment and structure on susceptibility to intergranular stress corrosion cracking of nickel-chromium-iron alloys (Alloy 800 and Alloy 600), paper presented Nucllex 72 Basel, Switzerland (Oct. 16-21, 1972).
12. U. Blom and M. Tynell, Corrosion (1975).
13. M. E. Indig, Environmental corrosion effects on CRBRP materials in the steam generator circuit; International Conference on Materials for Nuclear Steam Generators, Gatlinburg, Tenn. (Sept. 9-12, 1975).
14. G. J. Theus, "Caustic stress corrosion cracking of inconel 600, incoloy 800, and type 304 stainless steel," Nuclear Technology 28, pp. 383-397 (March 1976).
15. I.L.W. Wilson and R. C. Aspden, The influence of specimen type and metallurgical structure on the caustic SCC of some stainless steels, NACE paper, Toronto (April 1975).
16. D. Van Rooyen, "Review of the stress corrosion cracking of inconel 600," Corrosion, 31, No. 9, pp. 327-337 (September 1975).
17. L. Egnell and N. G. Persson, "Creep-rupture ductility of Alloy 800," paper presented 18<sup>ème</sup> Colloque de Métallurgie - Saclay (June 23-25, 1975).
18. J. E. Bird, A. K. Mukherjee and J. E. Dorn, "Correlation between high-temperature creep behavior and structure," Quantitative Relation Between Properties and Microstructure, Israel University Press, Jerusalem (1969).
19. G. H. Rowe, J. R. Stewart and K. N. Burgess, "Capped end, thin-wall tube creep-rupture behavior for type 316 stainless steel," Trans. Am. Soc. Mech. Engrs., Series D, pp. 71-86 (1963).
20. D. O. Hayhurst, C. J. Morrison and F. A. Leckie, "The effect of stress concentrations on the creep-rupture of tension panels," Paper No. 75-APM-R, Journal of Appl. Mech. (September 1975).

# INTERNATIONAL CONFERENCE ON LIQUID METAL TECHNOLOGY IN ENERGY PRODUCTION

## CALCULATION OF WASTAGE BY SMALL WATER LEAKS IN SODIUM HEATED STEAM GENERATORS

K Tregonning \*

United Kingdom Atomic Energy Authority, Dounreay Experimental Reactor Establishment  
Caithness, Scotland

(\*Now of Nuclear Installations Inspectorate, London)

### ABSTRACT

On the basis of mechanistic arguments it is suggested that the temperature of the wasting surface would provide a single physically meaningful parameter with which to correlate wastage data. A lumped parameter model is developed which predicts reaction temperature as a function of the major variables in the small water leak situation (Leak rate, tube spacing, sodium temperature).

The calculated temperatures explain much of the observed behaviour of wastage rate with these variables and compare well with the limited temperature data available. Wastage rates are correlated with predicted temperature on a total activation energy basis. The results are encouraging and a first conservative method for the calculation of wastage by small water leaks in sodium-heated steam generators is produced.

### INTRODUCTION

The problems associated with possible tube failure incidents in sodium heated steam generators have been widely discussed. For smaller leaks the problems concern primarily material wastage - both on adjacent tubes and at the leak site itself. One essential piece of information required is the relationship between wastage of a tube adjacent to a leak and water injection rate, for a particular geometry. The calculation of wastage rates has posed severe problems for some time. Various approaches have been tried from the purely empirical to the mechanistic. The purely empirical approach in which wastage is plotted directly against the major variables (leak rate, tube spacing, sodium temperature) is difficult to justify because of the sheer volume of experimental work that is required. However the mechanistic approach has not been particularly successful simply because the level of understanding of the wastage process has been insufficient to sustain a sensible mathematical description.

Recent developments have suggested an approach to the calculation of wastage based on an improved understanding of the characteristics of the sodium-water reaction jet. The work of Bell et al (1) and later Kennedy and Collier (2), on submerged jet structure has contributed significantly to this concept of the wastage process. This work showed that droplets are entrained at the interface of a submerged gas jet (Figure 1).

These droplets are carried in the gas stream and impinge on a target placed in the path of the jet to form a film which flows radially outwards under the shearing action of the wall jet immediately above it. The necessary ingredients for material wastage are evident. In the sodium-water reaction

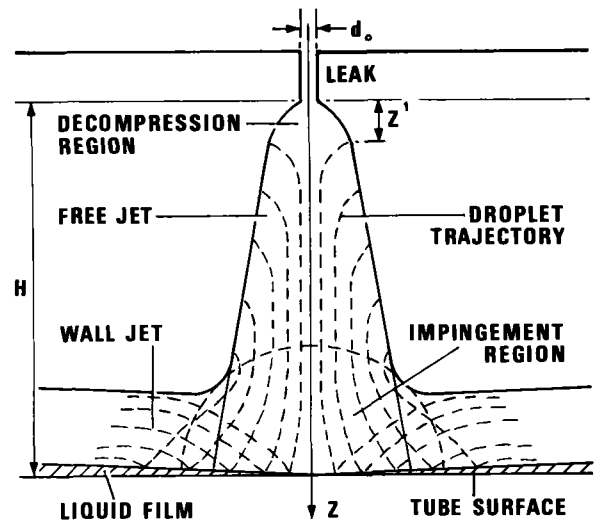


Fig. 1. Schematic of jet structure.

jet situation the droplets and film would consist of sodium and corrosive reaction products at a higher temperature than the surrounding sodium. The situation thus has both a corrosive and an erosive potential.

In order to validate this concept of the wastage process some experiments were devised by the author in which nitrogen jets submerged in hot sodium hydroxide melts were directed at stainless steel target plates (3). The resulting wastage confirmed the idea. The wastage rates were about the correct magnitude and the wastage profiles were similar to those produced by sodium-water reaction jets.

The characteristics of the wastage profiles could also be identified in terms of jet structure concepts and this together with the fact that static corrosion tests produced negligible wastage suggested that the corrosive influence may not be particularly important. However this was demonstrably not the case. Further experiments were done in which the caustic melt was replaced by cold water and the stainless steel plates by lead plates. One would expect severe erosion of the lead plates if corrosion were not an important consideration. In the event the erosion produced was negligible; clearly both the erosive and corrosive capabilities of the entrained fluid were necessary interactive components of the wastage process.

The conclusion reached was that corrosion allows erosion to proceed by presenting a continuously weakened surface structure. Further studies of the interaction are desirable but in the absence of a deeper understanding a

method of calculation is feasible. Whatever the details of the interaction and under what conditions physical or chemical limitation prevails both components will be strong functions of temperature. This is supported to some extent in reference 3. The temperature of the wasting surface would provide a single physically meaningful parameter with which to correlate wastage. A calculation method to predict this parameter as a function of the major variables could thus provide the basis for the calculation of wastage rates.

CALCULATION OF TEMPERATURE

The assumptions used in the calculation of the temperature of the wasting surface are:

- a. The dominant reaction site is the surfaces of entrained droplets.
- b. The dominant reaction is the monoxide producing reaction.
- c. The reaction rate is limited by gas-phase mass transfer.
- d. Quasi steady state mass transfer.
- e. The temperature of the wasting surface is the jet temperature at the appropriate axial station.

The model is one dimensional and the temperature is a radially integrated mean temperature.

These assumptions cannot be rigorously justified because sufficient data is not available, but it can be shown that the assumptions are reasonable.

Reaction Site

The first assumption is justified simply on the basis that the surface area presented by the droplets is orders of magnitude higher than that presented by either the jet envelope or the target film. It can be shown from the data of Kennedy and Collier (2) that the area presented by the drops in a one second interval is of the order of 10<sup>4</sup> cm<sup>2</sup> for a tube leak which is a fraction of a millimetre in diameter and which is separated from its adjacent tube by 10 mm.

Dominating Reaction and Reaction Rate

It is generally accepted that the reaction kinetics of the sodium water reaction are so rapid that in most situations the rate is limited by the transport properties of the chemical species involved. Assumptions b. and c. are consistent in that gas phase limited reaction would lead to an excess of sodium at the reaction site and therefore encourage the monoxide reaction which requires two moles of sodium per mole of water/steam, rather than the hydroxide reaction which requires only one mole per mole. Gas phase mass transfer can be calculated, but although liquid phase mass transfer can be calculated with some confidence for the sodium - sodium hydroxide system it is difficult to do the calculation for the sodium - sodium monoxide system. The problem is essentially that of determining the state of the monoxide in a transient situation and hence of assigning a value to the diffusion coefficient. The only other consistent pair of assumptions would be the dominance of the hydroxide reaction together with liquid phase limited reaction rate. The justification of assumptions b. and c. consists of demonstrating that transport of hydroxide in the liquid phase is unlikely to limit the reaction rate.

For the gas phase, convective mass transfer must be considered and transient behaviour is difficult to formulate. For steady state problems mass transfer is often written in terms of the Sherwood number Sh, ie for drops of radius a:

$$\dot{N}_s = 2 \pi a Dg Sh \left[ \bar{C} - (C_s)_a \right] \text{ (where } C = m_s/Qg \text{)}$$

The approach of Vi-D-Dang and Ruckenstein to this problem is to derive an unsteady time dependent Sherwood number (4). This approach leads to a very complex expression, but for small times the Sherwood number is fairly accurately given by the asymptotic approximation,

$$Sh = \left( \frac{1}{\pi \tau'} \right)^{\frac{1}{2}} (1 - \cos \theta_s)$$

where  $\theta_s$  is the boundary layer separation angle and  $\tau'$  is the dimensionless age of the drop.  $\theta_s$  is between 0 and  $\pi$  radians.  $\tau'$  is given by

$$\tau' = \frac{\tau Dg}{a^2}$$

where  $\tau$  is the droplet age.

The Sherwood number approaches the steady state value when the product of the Peclet number Pe and the dimensionless droplet age is approximately 1.

$$\text{Now } Pe = \frac{a u_{\infty}}{Dg} \therefore \tau \gg \frac{a}{u_{\infty}} \text{ for steady state}$$

The equations for mass transfer of steam are thus:

$$\dot{N}_s = 2 \sqrt{\frac{\pi a^4 Dg}{\tau}} (\bar{C} - (C_s)_a), \tau < \frac{a}{u_{\infty}} \quad (1)$$

$$\text{and } \dot{N}_s = 2 \sqrt{\pi a^3 u_{\infty} Dg} (\bar{C} - (C_s)_a), \tau \gg \frac{a}{u_{\infty}} \quad (2)$$

Again, if the reaction is limited by gas phase transport  $(C_s)_a$  is zero. If liquid phase mass transfer limits the reaction then  $(C_s)_a$  will be determined by the liquid phase.

The diffusion coefficient for a binary gas mixture can be written

$$Dg = \frac{K T^{1.5}}{P}$$

for steam/hydrogen this is

$$Dg = \frac{2.23 \times 10^{-4} T_{Dg}^{1.5}}{P} \text{ cm}^2 \text{ s}^{-1} \text{ for } ^\circ\text{K and bar} \quad (3)$$

$$\text{where } T_{Dg} = \frac{18 [\bar{C} - (C_s)_a] [h_o - h_{sat} + \xi_s T_{sat}] + [2\beta_s - \bar{C} - (C_s)_a] \xi_h T_R}{18 [\bar{C} + (C_s)_a] \xi_s + [2\beta_s - \bar{C} - (C_s)_a] \xi_h} \quad (4)$$

for  $T_{Dg} > T_{SAT}$

and  $T_{Dg} = T_{SAT}$  for  $T_{Dg} \leq T_{SAT}$

To calculate mass transfer rates within the entrained droplets the technique employed is similar to that used to calculate transient heat conduction in fuel particles resulting from fuel-coolant interactions in fast reactor core incidents (5). The resulting equations to determine sodium concentration  $C_{Na}$  and the hydroxide penetration thickness  $\delta = a(1-\epsilon)$  are,

when  $0 < \epsilon \leq 1$

$$\frac{d\epsilon}{dt} = \frac{12D_1}{a^2(3\epsilon^3 - \epsilon^2 - \epsilon - 1)} - \frac{(3 - \epsilon - \epsilon^2 - \epsilon^3)}{(C_{Na} - C_{Na}^o)(1 + 2\epsilon + 3\epsilon^2)} \cdot \frac{d(C_{Na})_a}{dt} \quad (5)$$

$$\frac{d(C_{Na}^o)}{dt} = 0 \quad (6)$$

when  $\epsilon \ll 0$

$$\frac{d\epsilon}{dt} = 0 \quad (7)$$

$$\frac{d(C_{Na}^o)}{dt} = \frac{12D_1}{a^2} [(C_{Na})_a - (C_{Na}^o)] - \frac{3 d(C_{Na})_a}{dt} \quad (8)$$

$$\text{and, } \dot{N}_{Na} = \frac{4\pi a D_1 (C_{Na}^o - (C_{Na})_a)}{1 - \epsilon} \text{ for } 0 < \epsilon \leq 1 \quad (9)$$

$$\dot{N}_{Na} = 4\pi a D_1 (C_{Na}^o - (C_{Na})_a) \text{ for } \epsilon \leq 0 \quad (10)$$

Because the kinetics of the sodium-water reaction are so rapid the sodium concentration at the droplet surface will approach zero if reaction is limited by liquid phase transport i.e.,

$$(C_{Na})_a = \frac{d(C_{Na})_a}{dt} = 0$$

If the reaction is limited by gas-phase transport then  $(C_{Na})_a$  will be determined by mass-transfer in the gas phase.

A mean diffusion coefficient for the liquid phase is obtained by assuming the following relationship

$$D_1 = \frac{n^{\frac{1}{3}} kT}{\mu_{Na}^x \mu_{OH}^{1-x}}$$

where x is mole fraction of sodium in the diffusion layer. The cube root of molecular density is relatively insensitive to x and T (maximum variation 0.308 → 0.355) and can be taken as constant. This is not true of viscosity.

The standard Golden and Tokar preferred correlation (6) is used for sodium viscosity. Hydroxide viscosity is obtained by fitting the limited data available (7) to Eyring's liquid viscosity relationship. The final expression for  $D_1$  is:

$$D_1 = \frac{5.1 \times 10^{-6} T_{D_1}^{1+0.5x}}{\exp \left[ \frac{3.826x - 2007.2x + 2515.3}{T_{D_1}} \right]} \quad (11)$$

Using simple heat and mass balances x and  $T_{D_1}$  are obtainable in terms of sodium concentration.

Figure 2 is a plot of reaction rate per unit area determined by liquid phase transport against mole fraction of sodium remaining in the droplet for a 250μ diameter droplet. Superimposed on this curve are the quasi-steady state gas phase limited reaction rate per unit area, and a reaction rate per unit area value obtained assuming a droplet age of 10<sup>-7</sup> s. It is clear from this curve that once the droplet has travelled a few droplet radii from its point of inception reaction rate will be limited by gas-phase transport at sodium fractions down to 20%. Even for path lengths equal to a small fraction

of a droplet radius ( $\tau = 10^{-7}$ s) half the droplet must be reacted before liquid phase transport starts to limit the reaction rate.

125μm is about the mean "large drop radius" for small submerged two-phase jets (1, 2) but a range of droplet sizes can exist. The sodium mole fraction below which liquid phase transport becomes important was calculated for several droplet radii. For small droplets ( $a \approx 10 \mu\text{m}$ ) the value is about 10%; for larger droplets this value has risen to only 30%. Assumptions b and c are therefore reasonable particularly when one considers that the presence of hydrogen would lead to even lower values of gas phase mass transfer rates.

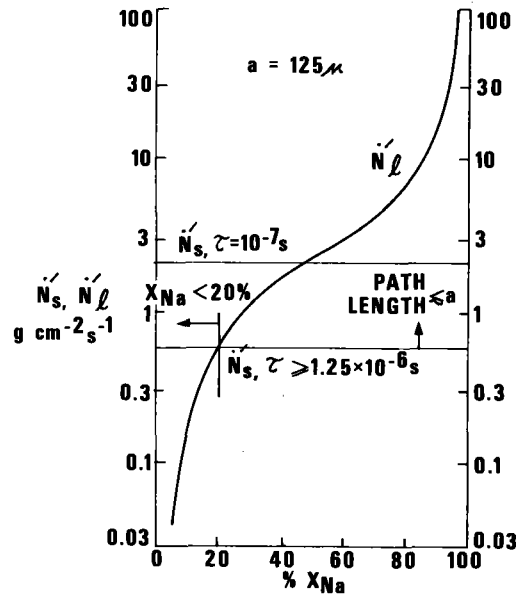


Fig. 2. Comparison of liquid phase mass transfer, as a function of mass fraction of sodium in the drop, with gas phase mass transfer.

Q. S. S. Calculation

The fourth assumption is substantiated retrospectively using the developed model. Figure 3 compares jet temperatures calculated with and without the initial transient reaction included. Clearly the transient calculation makes little difference and the simpler approach is adequate.

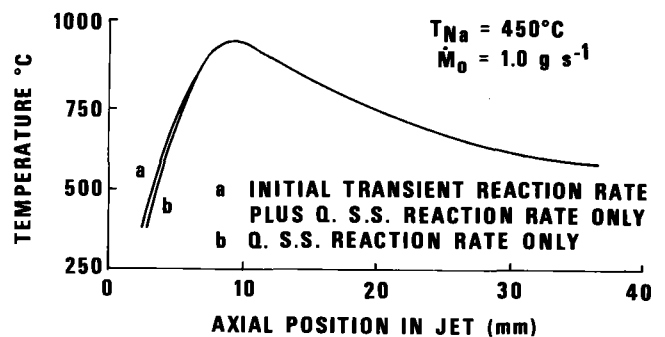


Fig. 3. Effect of initial unsteady reaction rate on jet temperature.



Heat Transfer Through the Tube Wall

Justification of the fifth assumption is obtained by demonstrating that the heat flux through the wall of the target tube is a small fraction of the heat flux in the jet. The heat flux in the jet and jet temperature are obtained from the developed model. Approximating to a plane geometry, heat flux through the tube wall is:

$$q \approx \lambda(T_{OD} - T_{ID}) / \epsilon$$

Maximum flux is obtained when the outer surface temperature  $T_{OD}$  is equated to jet temperature and the inner surface temperature is equated to the steam temperature:

$$q_{max} \approx \lambda (T_j - T_s) / \epsilon$$

Heat flux in the jet is:

$$q = [(\dot{m}_{c_2} \xi_{O_2} + \dot{m}_H \xi_H) T_R + \dot{m}_{Na} \xi_{Na} T_o + \dot{m}_S h] / A(z)$$

Thus, defining  $\psi$  as:

$$\psi = q_{max} / q$$

the criterion for validation of the fifth assumption is

$$\psi < 1$$

It should be pointed out that, although this is a steady-state treatment, the thermal time constant for, say, a PFR evaporator tube wall is a fraction of a second. Tube wastage is concerned with periods of seconds or greater.

Figure 4 shows  $\psi$  plotted against axial position in the jet for two leak rates. Clearly, the criteria for validation of the fifth assumption are satisfied.

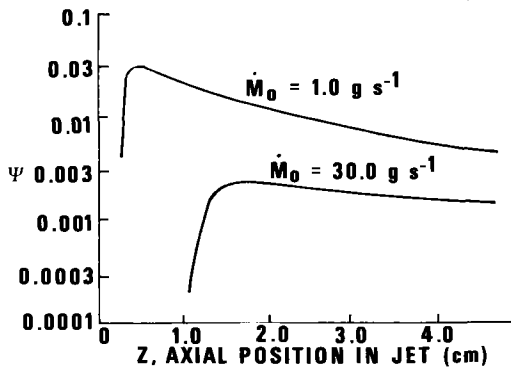


Fig. 4. Maximum heat flux through the tube wall divided by heat flux in the jet versus axial position in the jet.

The Temperature Model

The model of the sodium-water reaction jet as subsequently developed can be divided conveniently into three separate but interactive parts; jet hydraulics, jet composition and jet temperatures. Jet composition depends on reaction rates which in turn depend on jet hydraulics. Jet temperatures follow from thermodynamic data and jet composition. Target temperature is of course the parameter of interest for predicting wastage rates, but it has been shown that the

assumption that target temperature is equal to jet temperature at the relevant axial station in the jet is reasonable.

**Jet Hydraulics:** The important parameters required for calculation of jet composition are the velocities and mass flow rates in the two phases. The method for velocity calculation is the same as that reported in a previous paper (3). The resulting equations are:

$$\bar{U}_g(z) = \frac{\bar{U}_g(z') \cdot A(z')}{\alpha A(z)} \tag{12}$$

$$\bar{U}_1(z) = \frac{J - Qg \bar{U}_g(z) / A(z)}{Q_1(z) \sqrt{1 - \alpha^2}} \tag{13}$$

$$\alpha = \frac{Qg \bar{U}_1(z)}{Qg \bar{U}_1(z) + Q_1(z) \bar{U}_g(z)} \tag{14}$$

$$A(z) = \left( \sqrt{\left[ \frac{\dot{m}_o}{\pi \rho_g \bar{U}_g(z)} \right]} + \left[ z - 1.4 \sqrt{\left[ \frac{\dot{m}_o}{\pi \rho_g \bar{U}_g(z)} \right]} \right] \tan \frac{\theta}{2} \right)^2 \tag{15}$$

$$\frac{dQ_1}{dz} = 0.517 + 3.768 d_o P_o^{0.5} \tag{16}$$

**Jet Composition:** Let us first consider the rate of consumption of steam due to reaction of entrained droplets. Because of the initial short duration transient reactions the jet requires to be divided into a number of zones so that droplets entrained at different axial stations in the jet can be considered. Reaction rate for a droplet entrained in the  $i$ th zone is therefore taken from equations 1 and 2.

$$\left. \begin{aligned} (\dot{m}'_s)_i &= 2 \left( \frac{\pi a^4 Dg}{\tau_i} \right)^{0.5} \bar{C}, \quad \tau_i < \frac{a}{U_\infty} \\ (\dot{m}'_s)_i &= 2 \left( \pi a^3 U_\infty Dg \right)^{0.5} \bar{C}, \quad \tau_i \gg \frac{a}{U_\infty} \end{aligned} \right\} \tag{17}$$

where  $\tau_i$  is given by

$$\left. \begin{aligned} \frac{d\tau}{dz} &= 0 \quad \text{for } z - z' < (i-1) \Delta z \\ \frac{d\tau}{dz} &= \frac{1}{\bar{u}_1} \quad \text{for } z - z' \geq (i-1) \Delta z \end{aligned} \right\} \tag{18}$$

$$\text{Also required is } \bar{C} = \dot{m}_s / Qg \tag{19}$$

If we define a mean drop such that:

$$\text{(Mass of water consumed by mean drop in one second at } z) = \bar{m}'_s$$

$$\text{Then: (Mass of water consumed by mean drop at } z) = \int_0^z \frac{\bar{m}'_s}{\bar{u}_1} dz$$

and

(Mass of water consumed between 0 and  $Z$  per second is:

$$\frac{3Q_1}{4\pi a^3} \int_0^Z \frac{\bar{m}'_s}{\bar{u}_1} dz$$

If we define  $\Omega$ :

$$\Omega = \int_0^Z \frac{\bar{m}'_s}{\bar{u}_1} dz$$

Then total mass of water consumed between 0 and  $Z$  per

second is:

$$\frac{3 Q_1 \Omega}{4 \pi a^3}$$

and the mass flow rate of steam/water at Z is given by:

$$\dot{m}_s(Z) = \dot{m}_o - \frac{3 Q_1 \Omega}{4 \pi a^3} \quad (20)$$

where  $\Omega$  is obtained from:

$$\frac{d\Omega}{dZ} = \frac{1}{ju_1} \sum_{i=1}^j (\dot{m}_s')_i \quad (21)$$

The quasi steady state (QSS) approach allows equations 17, 18, 19 and 21 to be replaced by:

$$\frac{d\Omega}{dZ} = \frac{2 (\pi a^3 u_{\infty} D_g)^{0.5} \dot{m}_s}{u_1 Q_g} \quad (22)$$

Equation 20 together with the following three equations describes the jet composition, ie

$$\dot{m}_H(Z) = \alpha_1 (\dot{m}_o - \dot{m}_s(Z)) \quad (23)$$

$$\dot{m}_{Na}(Z) = \alpha_2 Q_1 - \alpha_2 (\dot{m}_o - \dot{m}_s(Z)) \quad (24)$$

$$\dot{m}_{O_2}(Z) = \alpha_3 (\dot{m}_o - \dot{m}_s(Z)) \quad (25)$$

Jet Temperature: A heat balance for all components gives:

$$(\dot{m}_{O_2} \xi_{O_2} + \dot{m}_H \xi_H) T_R + \dot{m}_{Na} \xi_{Na} T_o + \dot{m}_s h = (\dot{m}_H \xi_H + \dot{m}_{Na} \xi_{Na} + \dot{m}_{O_2} \xi_{O_2}) T_J + \dot{m}_s [h_{sat} + \xi_s (T_J - T_{sat})]$$

$$ie T_J = \frac{(\dot{m}_H \xi_H + \dot{m}_{O_2} \xi_{O_2}) T_R + \dot{m}_{Na} \xi_{Na} T_o + \dot{m}_s (h - h_{sat} + \xi_s T_{sat})}{\dot{m}_H \xi_H + \dot{m}_{Na} \xi_{Na} + \dot{m}_{O_2} \xi_{O_2} + \dot{m}_s \xi_s}$$

Variation of Jet Temperature with the Major Variable

Jet temperature was calculated as a function of tube spacing leak rate, sodium temperature and sodium velocity, (see Figures 5, 6 and 7). The main features of the reacting jet are well illustrated by Figure 5. Temperature increases moving out into the jet as an increasing proportion of the entrained sodium is converted to the oxide. The temperature reaches a maximum as the steam is completely replaced by hydrogen, sodium continues to be entrained with no further reaction and the mean temperature of the jet thereafter decreases.

Figure 6 is a plot of calculated temperature, at a tube immediately adjacent to a leaking tube in the PFR evaporator, against leak rate. The most striking feature of Figure 6 is the fact that temperature exhibits a maximum as the leak rate increases for a given tube spacing. This feature is also characteristic of plots of wastage rate against leak rate (Figures 8, 9) and is encouraging for two reasons. Firstly it generates confidence in the concepts employed in the model. Secondly it implies that the tube temperature may be the

overriding factor in determining wastage and therefore suggests that a sensible correlation of wastage data could be based on temperature.

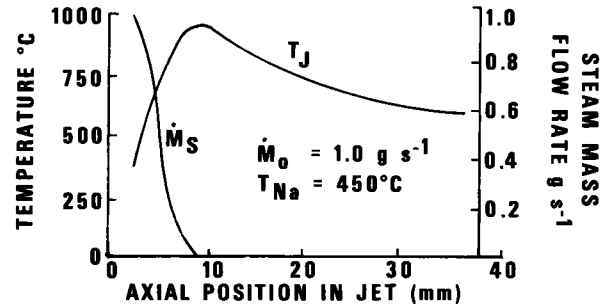


Fig. 5. Mass flow rate of steam and jet temperature versus axial position in the jet.

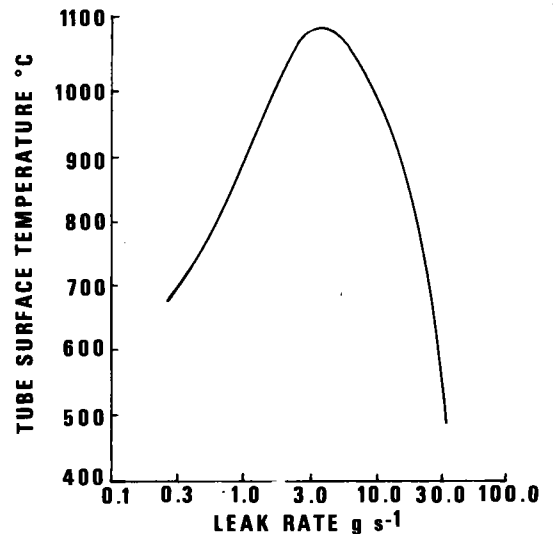


Fig. 6. Calculated tube surface temperature versus leak rate for a PFR Evaporator adjacent tube leak (Z = 12.5 mm).

The characteristic behaviour of temperature with varying leak rate can be easily explained in terms of the model. As leak rate increases the spacing at which maximum temperature occurs increases. This is because the ratio of entrained flow to injected flow decreases and the steam therefore takes longer to be depleted. Thus, at a particular tube spacing, as leak rate increases the spacing at which maximum temperature occurs passes through the chosen spacing value. On either side of this point the temperature is lower.

One immediately obvious effect of raising or lowering sodium temperature would be to increase or decrease jet temperature. This is illustrated at Figure 7 where jet temperature versus tube spacing is plotted for two different sodium temperatures. If jet temperature is the predominant factor in determining wastage rates then one would expect wastage to be a strong function of sodium temperature. This is shown to be the case by some Japanese data (9) and further supports the contention that calculation of wastage could be based on the calculation of jet temperature.

Sodium flow perpendicular to the jet axis would tend to

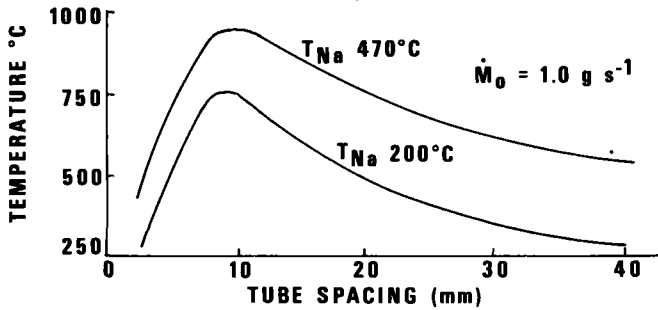


Fig. 7. Effect of sodium temperature on tube surface.

deflect the jet in the direction of flow. One might expect this to affect tube surface temperature by increasing the effective tube spacing. Calculations were done using assumptions which would result in the maximum jet deflection (ie perpendicular component of jet velocity equal to sodium velocity). Deflection only becomes significant well out in the jet where the temperature gradient is small, hence the effect on tube surface temperature at normal tube spacing is small.

Comparison with Published Data

Published temperature data for small water leaks in sodium are very limited and insufficient to test the model effectively. The most comprehensive temperature data are those given by Chamberlain et al (8). These data are for various tube spacings but only one leak rate is considered and one set of initial conditions. The data are compared with temperatures predicted by the model in Figure 8 which shows measured and predicted temperature versus tube spacing.

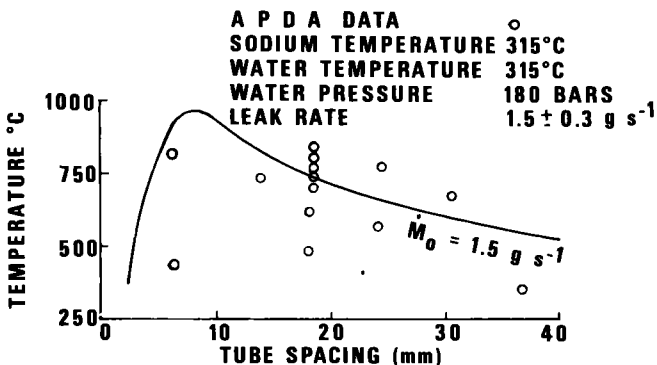


Fig. 8. Calculated and measured temperatures at different tube spacings.

Reference 9 presents temperatures measured at different radial positions in the jet for one injection. The model is one dimensional and temperature is constant across the jet. Figure 9 compares predicted and measured temperatures. This could not be considered a rigorous validation of the model. Nevertheless in the absence of data from experiments specifically designed to test the model the author felt that it would be a worth while exercise to correlate wastage data with predicted temperatures.

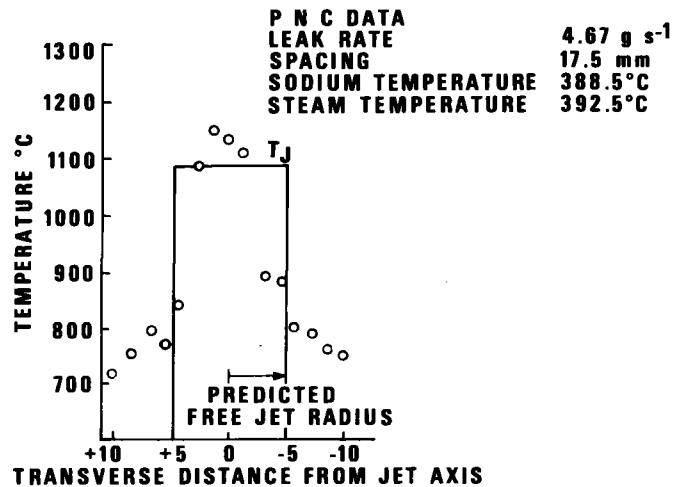


Fig. 9. Comparison of predicted and measured temperature (PNC Data)

CORRELATION OF WASTAGE RATES WITH CALCULATED TEMPERATURES

The corrosion-erosion interaction itself is likely to be temperature dependant and the way in which physical or chemical effects limit wastage rate may vary with temperature. However both the corrosion reaction kinetics and certain aspects of deformation phenomena (eg dislocation mobilities) can be described on the basis of activation energies. A reasonable approach therefore would be to ascertain whether penetration rate could be described in terms of a total activation energy, ie by the relationship

$$\dot{P} = A e^{-B/T_j}$$

If this were a reasonable description, then plotting log (penetration rate) against reciprocal jet temperature would yield a straight line of negative slope.

Figure 10 shows just such a plot using Japanese data for stainless steel and  $2\frac{1}{4}$  Cr/Mo (9). There were two main reasons for singling out the Japanese data. Firstly they are the most self-consistent data to be produced in such quantity. Secondly they all pertain to superheated steam jets, the initial hydraulics and mass transfer assumption are therefore more likely to be correct.

The evidence of Figure 10 is very encouraging for several reasons,

- The activation energy approach is supported.
- The degree of scatter of the data points is small compared with previous attempts to plot wastage data.
- The degree of scatter is sufficiently small that separate straight lines can be clearly resolved for the two materials, leading to a constant relative resistance factor of about 4.

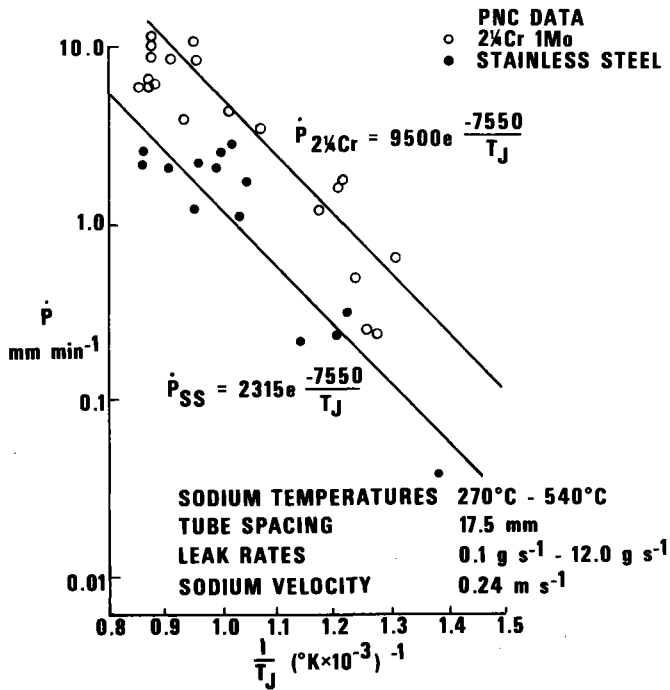


Fig. 10. Log penetration rate (PNC Data) versus reciprocal jet temperature for  $2\frac{1}{4}$  Cr 1 Mo and stainless steel.

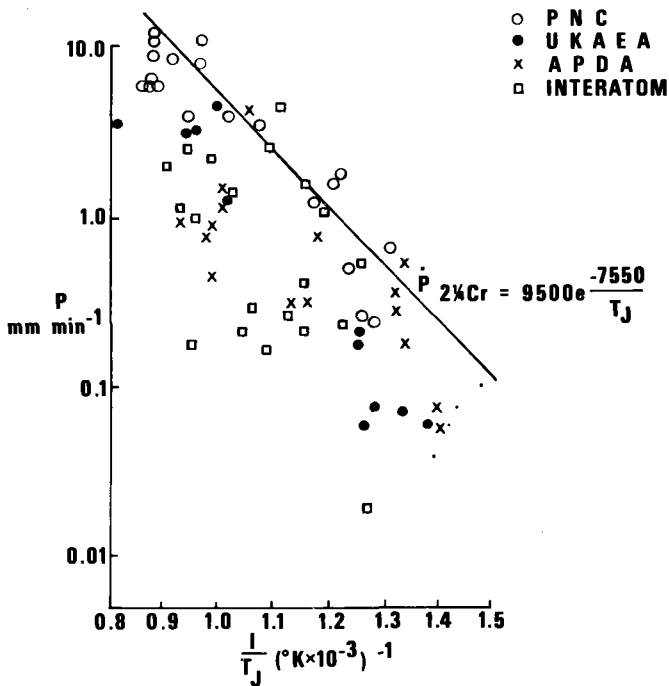


Fig. 11. Log penetration rate (world data) versus reciprocal jet temperature for  $2\frac{1}{4}$  Cr 1 Mo.

Figure 11 is a plot of world wastage data for  $2\frac{1}{4}$  Cr/Mo including the Japanese data and data from the SWLR. The picture presented by Figure 11 is rather less encouraging than that presented by Figure 10. The scatter of data is

significantly larger. It should be pointed out straight away that the range of sodium velocities and waterside conditions is larger and this may be contributory. However it should also be pointed out that much of the scatter can be attributed to inconsistencies within a given set of data, ie widely varying penetration rates were obtained for almost identical experimental conditions indicating that experimental control may not have been adequate.

It is interesting to note that all of these data are contained within or lie below the Japanese data, supporting the contention that much of the scatter may be attributable to departure from 'ideality' in experimental conditions (eg circular orifice, normal impingement). Until the limitations of the temperature model can be fully investigated in terms of temperature data the relative importance of the different factors affecting the scatter will not be resolved. However a conservative calculation method is provided by the line drawn through the Japanese data together with the temperature model.

CONCLUSIONS

Mechanistic studies have led to the conclusion that a calculation method for wastage could be based on calculation of the temperature of the wasting surface, and have provided much of the information necessary to do the calculations.

A method for calculating these temperatures has been developed which explains many observable characteristics of behaviour of penetration rate with varying conditions in the steam generator. More temperature data than presently exists are required for proper validation of the model.

Wastage data have been correlated with predicted temperature on a total activation energy basis. The results are encouraging and provide the basis for a first conservative calculation method for penetration rate.

Because a mechanistic approach has been used there is scope for further improvement of this method.

NOMENCLATURE

- a Droplet radius
- A Cross-sectional area of jet or constant
- B Constant
- C Concentration
- D Diffusion coefficient
- g Acceleration due to gravity
- h Water enthalpy
- j Number of zones in jet length Z
- J Efflux momentum
- K Constant
- k Boltzmann's constant or constant in number distribution of radii
- $\dot{m}$  Mass flow rate
- $\dot{m}'$  Reaction rate on a single drop
- $\eta$  Molecular density
- N Mass transfer rate
- N' Mass transfer rate per unit area
- P Pressure
- $\dot{P}$  Penetration rate
- Pe Peclet number
- q Heat flux

## INTERNATIONAL CONFERENCE ON LIQUID METAL TECHNOLOGY IN ENERGY PRODUCTION

Q	Volume flow rate
R	Adiabatic reaction temperature
Sh	Sherwood number
t	Time
T	Temperature
u	Velocity
x	Mole or mass fraction
Z	Displacement along jet axis
$\alpha$	Void fraction
$\alpha_1$	Mass of hydrogen generated per unit mass of water reacted
$\alpha_2$	Mass of sodium reacted per unit mass of water reacted
$\alpha_3$	Mass of monoxide generated per unit mass of water reacted
$\delta$	Thickness of liquid phase diffusion layer
$\epsilon$	Dimensionless thickness of liquid phase diffusion layer
$\theta$	Jet divergency angle or boundary layer separation angle
$\lambda$	Thermal conductivity of tube
$\mu$	Viscosity
$\xi$	Specific heat
$\rho$	Density
$\tau$	Droplet age
$\tau'$	Dimensionless droplet age
$\chi$	Mass fraction
$\Omega$	Mass of water reacted on a mean drop at Z

6. GOLDEN G H and TOKAR J V  
"Thermophysical properties of sodium."  
ANL-7323, 1967
7. MELLOR J W  
A comprehensive treatise on inorganic and theoretical chemistry  
Longman, London. 1952. Vol 2, Chapter XX
8. CHAMBERLAIN H V and others  
"Studies of material wastage resulting from reactions of water in sodium."  
APDA-254 1970
9. HIROMICHI N E I and others  
"Wastage of steam generator tubes during small leak of steam into sodium."  
PNC Publication 1974

### SUBSCRIPTS

a	At radius a
g	Gas phase
H	Refers to hydrogen
i	Refers to droplet entrained in ith zone
l	Liquid phase
max	Maximum
Na	Refers to Sodium
o	Initial
O2	Refers to sodium monoxide
s	Refers to steam
sat	Saturation

### REFERENCES

1. BELL R, and others  
"The structure of a submerged impinging gas jet"  
J. Br. Nucl Energy Soc., 1972, 11 No.2 183-193
2. KENNEDY T D A and COLLIER J G  
"The structure of an impinging gas jet submerged in a liquid".  
Chem E Symp-Multiphase Flow, Strathclyde  
April 1974, Paper 83.
3. TREGONNING K and others  
"Studies of a mechanism for material wastage by sodium-water reaction jets."  
J. Br. Nucl. Energy Soc., 1975, 14 Jan, No.1 77-82
4. VI DUONG DANG and RUCKENSTEIN E  
"High Reynolds numbers unsteady convective mass transfer from fluid spheres."  
International Journal of Heat and Mass Transfer, Vol. 16, No. 7, 1973, pp 1371-1385.
5. CHO D H and others  
"Rate-limited model of molten fuel/coolant interactions: model development and preliminary calculations."  
ANL-7919, 1972

# INTERNATIONAL CONFERENCE ON LIQUID METAL TECHNOLOGY IN ENERGY PRODUCTION

## SMALL LEAK SHUTDOWN, LOCATION AND BEHAVIOR IN LMFBR STEAM GENERATORS

D. W. Sandusky

General Electric Company  
San Jose, California

### ABSTRACT

This paper summarizes an experimental study of small leaks tested under LMFBR steam generator conditions. Defected tubes were exposed to flowing sodium and steam. The observed behavior of the defected tubes is reported along with test results of shutdown methods. Leak location methods were investigated. Methods were identified to open plugged defects for helium leak testing and detect plugged leaks by non-destructive testing.

### INTRODUCTION

Steam generators often have small leaks in the metal boundary between steam and the heat source. These leaks arise from fabrication defects, accelerated corrosion, stress corrosion cracking, fatigue, etc. In fossil-fired power stations and light water reactors, these leaks represent a problem of low to moderate concern from the standpoint of cross contamination between two different systems (steam and heat source). However, for sodium-heated steam generators, leaks are one of the major design/materials/operation problems for Liquid Metal Fast Breeder Reactors (LMFBR's).

Through-wall defects in the steam generator tubing or tube-to-tubesheet welds will allow the injection of high pressure steam or water into sodium. If the leak is very large ( $>0.05$  gm/sec  $H_2O$ ), it has been observed that it can form a jet which may rapidly penetrate adjacent tubes<sup>(1,2)</sup>. For a leak smaller than  $0.05$  gm/sec, damage to adjacent tubes does not occur, but there will be self-wastage of the leaking tube. It has been observed in this test program and others that small leaks in steam generator tubing grow to become large leaks<sup>(3,4,5)</sup>. It is desirable to shut down the steam system and locate a leak while it remains small rather than allow it to grow. Failure to terminate operation of the system while the leak is small can result in damage to adjacent tubes and generation of large amounts of corrosive reaction products.

It is desirable to keep a leak open on shutdown to facilitate location by helium leak testing. Tests

were oriented to shutdown techniques that increased the probability of a leak remaining open. It is also considered important to use a shutdown technique that avoids intrusion of sodium on the steam side of the system. The KNK reactor suffered significant sodium intrusion on the steam side of the plant because of difficulties with the shutdown procedure<sup>(6)</sup>.

If it is assumed in the worst case that the system is shut down and the leak plugs, then methods other than helium testing must be used to locate the leak. Therefore tests were performed to identify potential methods to (1) open plugged leaks, (2) locate plugged leaks (NDE techniques).

### EXPERIMENTAL TECHNIQUE

The principal system used for these small leak tests was Loop 9 located at GE, San Jose, California. Loop 9 was originally used to study high temperature sodium corrosion of LMFBR fuel cladding materials. For the small leak tests, the loop was modified considerably. The modifications included installation of a test pot in a bypass line, construction of a high pressure water loop, and addition of a high capacity cold trap to remove sodium/water reaction products. The capacity of the main loop and cold trap combined is approximately 246 l (65 gallons) of sodium. During testing, the full sodium flow (19 l/min; 5 gal/min) is routed through the cold trap. The leaks are monitored by two diffusion tube hydrogen meters. The test pot is capable of exposing three tubular specimens simultaneously to flowing sodium and steam. The steam pressure is generated by a mechanical pump and controlled by back-pressure regulators.

Leak specimens were fabricated from  $2\frac{1}{2}Cr-1Mo$  steam generator tubing. A  $100 \mu m$  (0.004 in.) hole was first drilled through the tube wall. The tube was then swaged to reduce the diameter. In the process, the through-wall hole was deformed to a slit shape, thereby reducing the leak rate. Leak rate was determined at room temperature by measuring the flow rate of argon exiting the defected tube when the internal pressure was 10.5 MPa (1525 psig). This flow rate was compared to a curve that related the mass flow rate of steam at  $496^\circ C$  ( $925^\circ F$ ) to room temperature argon.

During sodium testing, the leak rate was measured with the hydrogen meters. Since the sodium was completely purified on each circuit of the loop, the leak rate could be determined directly from the deviation of the hydrogen meters above the background level.

### EXPERIMENTAL RESULTS

NOTE: Unless otherwise stated, the test conditions were flowing sodium at 496°C (925°F), flowing steam at 10.5 MPa (1525 psig).

**Leak Behavior:** When the test program was initiated, it was not known whether leaks smaller than  $5 \times 10^{-2}$  gm/sec  $H_2O$  would self-plug or remain open or if self-damage would occur. In the first test of three specimens, all of the above occurred. Two leaks self-plugged with sodium/water reaction products shortly after initiation of the test. The initial leak rate of the other specimen was larger than the other two ( $2 \times 10^{-2}$  gm/sec vs.  $7 \times 10^{-3}$  gm/sec). It remained open for the duration of the test (1.75 hours). The test was terminated by a rapid increase in leak rate over a period of approximately 25 seconds. Post test examination showed a large hole in the tube wall (Figure 1). The hole was roughly circular, tapering from about 3.8 mm (0.15 in.) diameter at the sodium side of the tube wall to 1.3 mm (0.05 in.) at the steam side. The final leak rate was estimated to be 14 gm/sec (0.03 lb/sec). In subsequent tests, it was repeatedly observed that an open leak smaller than  $5 \times 10^{-2}$  gm/sec suffers rapid self-wastage of the base metal surrounding the defect.

Leaks smaller than about  $2 \times 10^{-2}$  gm/sec showed a strong tendency to self-plug. However, in several instances, leaks that were plugged reopened. The reopened leaks suffered self-wastage and grew in size. An exposure history of one such specimen is shown in Figure 2. Other plugged leaks were observed to open and replug spontaneously during continued exposure.

The mechanism by which plugged leaks reopen was not conclusively identified in these tests. However, there were some observations that were significant. Figure 3 compares a leak that reopened (the specimen from Figure 2) to a companion specimen that remained plugged. The plugged specimen shows considerable enlargement of the leak path near the steam side of the tube wall. Similar enlargement was observed in varying degrees in every specimen examined metallographically.

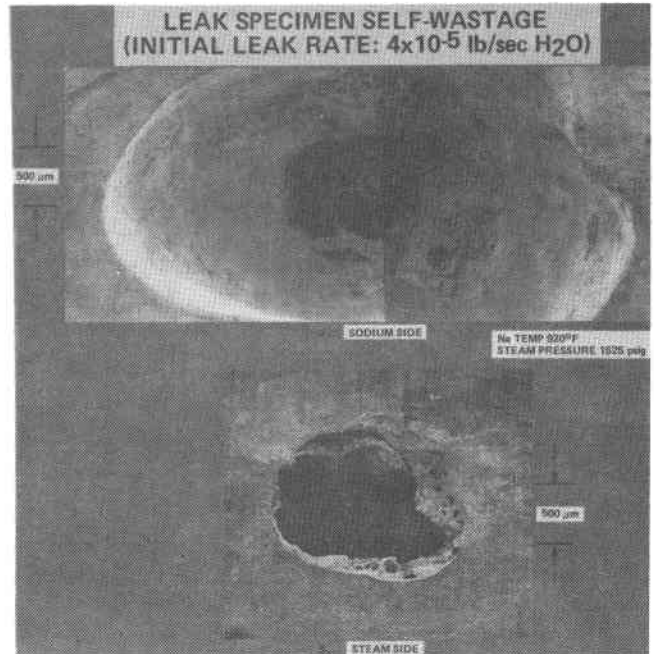


Figure 1.

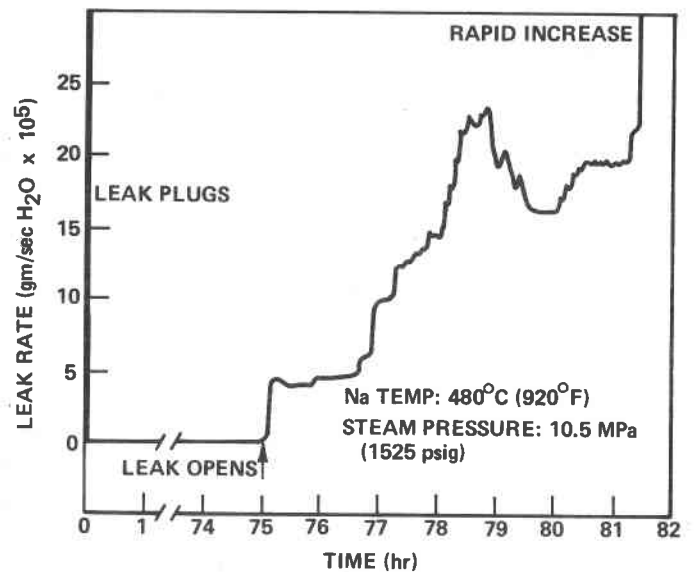


Figure 2. Exposure History of a Self-Plugged Leak

Since the enlargement of the cross-section of a plugged leak suggests a corrosive process, this region was examined for chemical species. The area immediately around the steam side of the leak was characterized by excessive oxidation of the base metal. Application of moistened pH paper to this region resulted in a pH range of 12.0 to 12.5. The region around the steam side of a leak was examined in a scanning electron microscope. Dispersive x-ray analysis showed sodium to be a major constituent of the layer around the leak site. Microprobe analysis of a

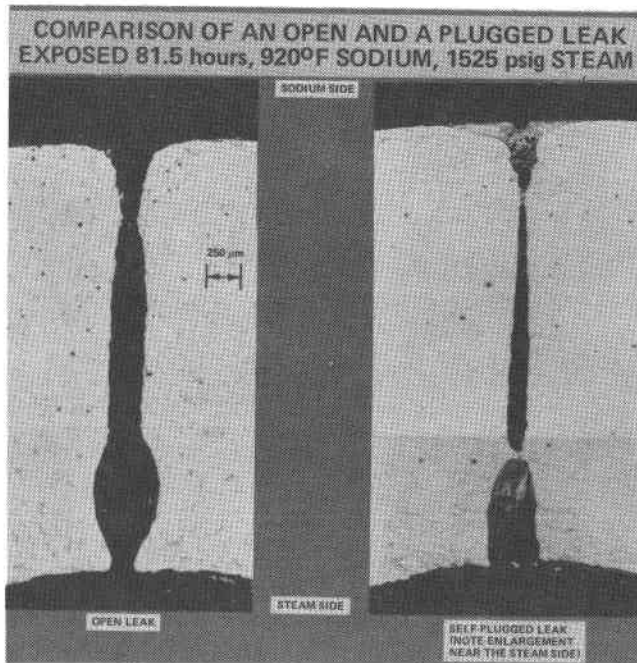


Figure 3.

cross-section of a plugged leak also indicated that sodium was present in the oxide plug. A special specimen was used to allow sampling of the plug material in an inert atmosphere. Low angle x-ray scattering performed on this material indicated that NaOH was a major constituent.

**Small Leak Shutdown:** During the early part of the scoping tests, it was observed that bulk sodium entered some leak specimens by capillary action and plugged the steam lines. The inert gas purge pressure before and after the test was 483 kPa (70 psig) above the sodium side pressure. Use of a 6.9 MPa (1000 psig) purge apparently eliminated the problem because bulk sodium intrusion in the steam lines was not observed in subsequent tests.

Based on the observations made in the scoping phase of the leak behavior study, tests were run to evaluate various means to shut down a leaking tube such that the leak remained open. A defected tube was placed in the test rig and the sodium system and steam system started. When the presence of the leak was indicated by the hydrogen meters, the selected shutdown sequence was initiated. This eventually resulted in sodium being drained from the test vessel and the specimen being cooled to near room temperature. The specimen was then removed from the vessel in an inert atmosphere and helium leak checked. The leak checking was performed by evacuating the inside of the specimen and flooding the outside of the tube with helium.

The tests in this series proved difficult to perform because initiation of the shutdown sequence required that a leak be open. It was found that leaks in the size range of interest ( $5 \times 10^{-3}$  to  $5 \times 10^{-2}$  gm/sec) were very difficult to keep open during start-up of the steam system. Some leaks plugged in the presence of sodium or sodium vapor only.

The first shutdown tests were performed to determine if replacing the high pressure steam with high pressure inert gas would keep the leak open. After initiation of the test, steam flow was maintained for 30 minutes, then terminated. As the steam pressure was lowered to 6.9 MPa (1000 psig), argon flow was initiated. The sodium was cooled to 316°C (600°F) and drained. After cooling to room temperature, a helium leak check showed the leak was open at a low level ( $\sim 5 \times 10^{-8}$  std cc He/sec). This specimen was reinserted in the loop and the test repeated. The leak again was open at start-up, but at a much reduced rate compared to the first test (as indicated by the hydrogen meter). Duplication of the shutdown procedure again produced an open leak (confirmed by helium leak check).

While replacement of steam with high pressure inert gas proved successful, this method would impose a considerable thermal transient on the steam generator. To minimize the thermal transient, it is necessary to cool the sodium before replacing the steam with inert gas. A test series was run to determine if leaks would stay open under these conditions. As soon as the presence of a leak was confirmed, the steam pressure was reduced to 10 MPa (1450 psig). In the first test, the system was cooled at 55°C (100°F) per hour to 316°C (600°F). Sodium was then drained and the steam replaced with argon at 1 MPa (140 psig). This produced a 0.83 MPa (120 psig)  $\Delta P$  between the inside and outside of the tube. The system was then cooled to ambient. The leak remained open in this case. Another sequence was used to simulate cooling the sodium to 204°C (400°F) before draining. Continuing steam flow until draining at 204°C was not feasible in the Loop 9 test system because the small sodium volume could be saturated with sodium/water reaction products. As a compromise, the system was cooled at 110°C (200°F) per hour to 316°C (600°F) and the steam replaced with 1.7 MPa (250 psig) argon\*. Cooling was continued and the sodium drained at 204°C (400°F). This procedure also produced open leaks.

\*The saturation pressure of steam at 204°C.



## INTERNATIONAL CONFERENCE ON LIQUID METAL TECHNOLOGY IN ENERGY PRODUCTION

Aside from the fact that leaks remained open, there was another significant observation made in these tests. The time required to shut down the system was in some cases over three hours. However, the self-wastage of the specimens showed removal of less than one-half the tube wall thickness. This indicates that the self-damage rate was reduced by lowering the temperature as soon as the leak was detected.

Opening Plugged Leaks: It was evident from the shutdown tests that even under well controlled conditions, small leaks would self-plug. It was therefore considered important to evaluate methods to reopen self-plugged leaks so they could be located by helium leak checking.

Preliminary tests on a single plugged leak in an inert atmosphere showed that thermal cycling and pressure cycling did not dislodge or crack the plug sufficiently to allow detection by helium mass spectrometer. A further test was run in sodium with high pressure steam in the leak specimen. Repeated cycling from 427°C (800°F) to 316°C (600°F) failed to unplug the leak.

It was also considered possible that given time, sodium would dissolve the sodium/water reaction product plug. In one case a  $\text{Fe}_3\text{O}_4$  plug was exposed to sodium and inert gas for 100 hours. Metallographic examination showed sodium dissolution of the plug to be minimal. In another test a self-plugged leak was soaked in sodium at 496°C (925°F) for 100 hours. There was no evidence of the leak unplugging.

Citric acid is commonly used to clean ferritic steam generators<sup>(7)</sup>. One leak that plugged during shutdown testing was swabbed with a dilute citric acid solution on the sodium side of the tube. The leak immediately opened. This led to exposing the steam side of plugged leaks to determine if citric acid would dissolve the plug. Specimens were placed in an oven at 77 to 82°C (170 to 180°F); 5 or 10% citric acid solutions were circulated through the specimen. In six out of six tests, plugged leaks were reopened by this method. The time required to unplug the leaks ranged from 45 minutes to 88 hours. Qualitatively, it took the 5% acid solution longer to open the leaks than the 10% solution.

Leak Detection: It was assumed (based on test results) that some leaks will plug upon shutdown of an LMFBR steam generator. Therefore, methods were investigated to locate a plugged (passive defect). These

investigations centered on conventional nondestructive examination techniques. For comparative purposes a single plugged leak was examined by several methods. First, the specimen was examined by x-radiography. This revealed that after sodium/steam exposure, the defect cross-section was larger near the tube surfaces than at mid-wall. Neutron radiography was much less successful at locating the defect. Even though the location was known, the defect was only faintly visible. Ultrasonic examination of the defected tube from the outside wall clearly identified the location of the plugged leak. Similar examination by pulsed eddy current testing also clearly indicated the presence of the defect.

Aside from the screening tests performed on a single plugged leak, one other location technique was attempted. Residual Krypton-85 adsorbed on the inner tube surface was used to produce an auto-radiograph map of irregularities. Although this method did show the presence of plugged leaks in the two specimens tested, the oxide layer caused many spurious indications. The plugged leaks would not have been definitely identified had not the exact locations been known.

### DISCUSSION OF RESULTS

With respect to small leak self-damage, it appears that the mechanisms were somewhat different depending on the leak being open or plugged. For open leaks, the general observation has been that the leak remains constant for some period of time followed by a rapid increase in leak rate<sup>(3,4)</sup>.

The time to sudden enlargement appears to be related to the initial leak rate. A plot of  $\log$  leak rate versus  $\log$  time to sudden enlargement is in fact found to be linear (see Figure 4). There is some scatter in the data which may be attributed to variations between the different experiments in tube wall thickness, steam pressure, and leak geometry.

Although the data are still sparse, they suggest that leak geometry is a significant variable. In Figure 5 the French results along the bottom line were all leaks produced by fatigue cracking. The one French data point along the upper line was a leak resulting from a bad weld. This defect would be likely to have a pin-hole geometry. The observations of Greene and this work resulted from leaks produced by drilling and swaging. This results in elliptic holes rather than linear cracks produced by fatigue. The available data then fall into two categories: linear cracks and pin-

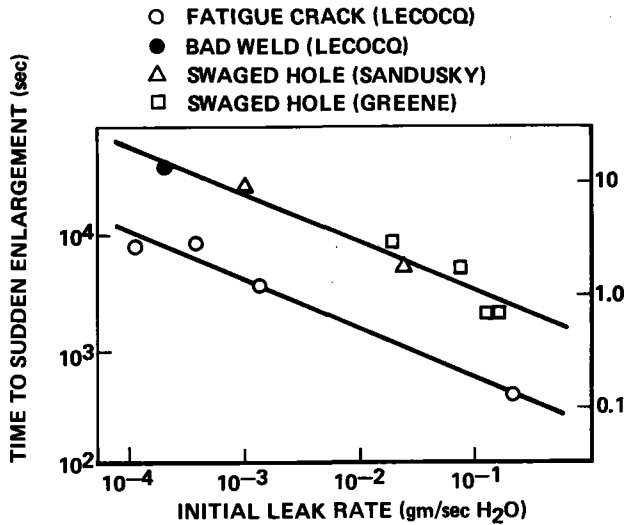


Figure 4. Self-Enlargement VS. Exposure Time

holes/elliptic holes. The linear cracks appear to reach the stage of sudden enlargement sooner.

The size of leaks after sudden enlargement was not fully determined because the tests were terminated as soon as the leak rate increased, to protect the equipment. Based on the cross-sectional area of defects after testing, it is estimated that the leak rates increased at least three orders of magnitude.

The cause of leak enlargement in 2½Cr-1Mo can be explained in terms of hot caustic corrosion of the metal surrounding the defect. The sodium/water reaction at the steam exit of the leak produces local high caustic concentrations which at the superheater temperature (~900°F), rapidly attack the steel. The metal surface temperature is probably higher than ambient because of the heat generated by the sodium/water reaction. Newman, et.al.<sup>(8)</sup> have studied this phenomenon by impinging a sodium vapor jet on a steel surface in a water vapor atmosphere. They concluded that the wastage observed could be accounted for by hydroxide corrosion plus the action of the jet removing reaction products and loose grains of base metal. An analogous situation probably occurs during self-wastage of a leaking tube.

The phenomenon of a sudden rapid increase in leak rate is explained schematically in Figure 5. This representation is inferred from metallographic examination of specimens in this test program. The leak removes metal near the sodium side of the tube in the form of a roughly circular pit. Once formed, the pit advances through the tube wall at a relatively constant rate. Since the high-pressure steam is in

choked flow, the leak rate does not change appreciably until the pit contacts the inner tube wall. At this point, only a thin edge remains. This is rapidly removed. In a short period of time then, the leak rate increases from that governed by the cross-section of the original defect to that governed by the diameter of the pit.

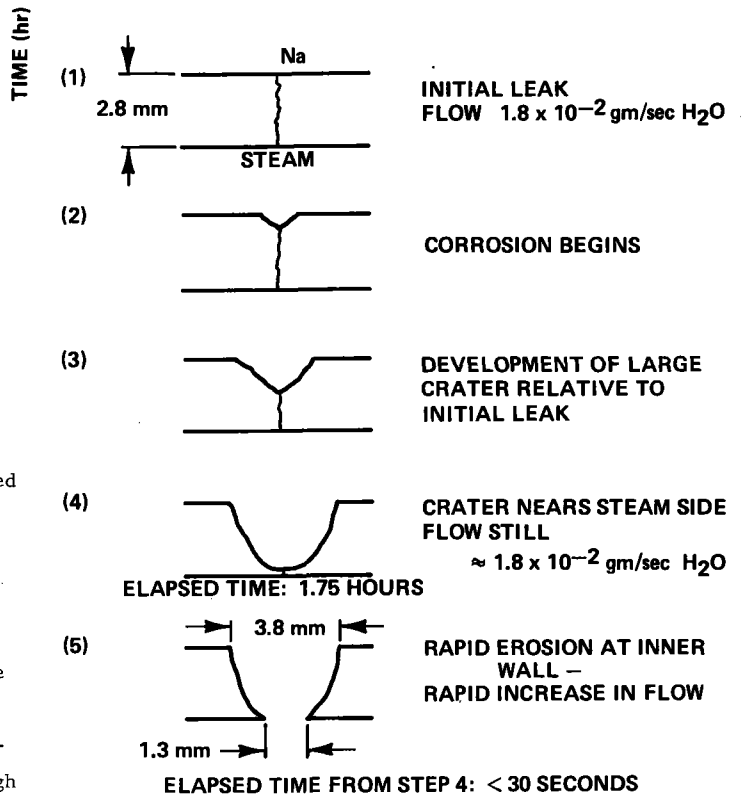


Figure 5. Large Leak Development

The mechanism by which a self-plugged leak reopens is not so evident. Even after numerous observations of small leaks in various stages of development, it is not possible to positively identify a leak-opening process. However, some observations can be noted that indicate a possible process.

Small leaks plug simply from the rapid build-up of sodium/water reaction products in and immediately around the defect. The volume of sodium/water reaction products is considerably greater than the reacting species. It can be shown by a simple calculation that  $5 \times 10^{-3}$  gm/sec leak produces enough reaction product in one second to plug its entire length many times over.

One proposed unplugging mechanism was the simple dissolution of the plug by sodium. Most of the plug constituents ( $\text{Na}_2\text{O}$ ,  $\text{NaOH}$ ,  $\text{NaH}$ ,  $\text{Fe}_3\text{O}_4$ ) are soluble in sodium. However, the length of the leak path is long compared to the cross-section such that dissolution of

## INTERNATIONAL CONFERENCE ON LIQUID METAL TECHNOLOGY IN ENERGY PRODUCTION

the plug is likely slowed to a process controlled by diffusion. Slow dissolution was shown experimentally with a plugged leak exposed to sodium and dry argon for 100 hours. Metallographic examination showed very little penetration of the plug by sodium.

Another unplugging mechanism involves sodium diffusion through the plug. It is possible that  $\text{Na}^+$  ion would be a mobile species in a  $\text{Na}_2\text{O}$  matrix. Once transported to the steam side of the leak, the sodium would form  $\text{NaOH}$  that would in turn attack the base metal surrounding the defect. The plug would be undermined by a continuous corrosion process and eventually dislodge.

There are numerous observations to support this supposition. These include repeated observations of sodium on the steam side of the defect by pH measurement, dispersive x-ray analysis, electron microprobe, and low-angle x-ray scattering. Examinations of self-plugged leaks exposed to sodium and steam by scanning electron microscopy and optical metallography have consistently shown enlargement of the leak path near the steam side of the defects. The most outstanding example of this was shown in Figure 3. The diameter of the defect after 80 hours exposure was considerably greater than that of the original drilled hole. Although these observations are not conclusive, they appear to strongly implicate some process related to corrosion accelerated by  $\text{NaOH}$ .

The greatest concern about small leaks aside from the potential to become large leaks is rapid location and repair of the defect. A commercial breeder reactor cannot afford repeated and lengthy shutdowns to find small and possibly intermittent leaks. It is therefore important to identify shutdown techniques for the system that give the highest probability the leak will be open after the unit is drained of sodium. Leak location by helium checking is then relatively straightforward. Previous experience with a leaking steam generator has shown that keeping a leak open could be a problem<sup>(9)</sup>. A striking observation in the tests under discussion was the ease with which leaks smaller than  $\sim 5 \times 10^{-2}$  gm/sec plug. In fact, the performance of shutdown tests was impaired by test leaks repeatedly plugging during startup. Special startup procedures had to be employed to produce open leaks. It is therefore concluded that most small leaks in an LMFBR steam generator will initially plug. However, there is ample evidence that plugged leaks can reopen, often in relatively short times.

One problem associated with shutdown technique is intrusion of sodium on the steam side of the system. This can result in plugged tubes and caustic contamination of components susceptible to stress corrosion cracking. In the early part of the test program, considerable quantities of sodium intruded on the steam side of specimens. It was found that this was avoided by maintaining a substantial ( $\geq 1.0$  MPa) positive pressure of steam or inert gas inside the defective tube.

The general intent of the shutdown tests was to determine if any technique would keep a small leak open during shutdown. The first tests employed high pressure inert gas ( $\sim 6.9$  MPa) as a replacement for steam. It was assumed that the steam going through an open leak would suddenly be replaced by a non-reactive gas at approximately the same pressure. The uninterrupted flow of gas would keep the passage clear of sodium and reaction products while the bulk sodium was cooled and drained from the system. Overall, this technique proved successful at keeping leaks open during shutdown. However, in a large steam generator, rapid replacement of steam by inert gas would cause the temperature of the evaporator to increase to near the superheater temperature in a short time. This imposes high thermal stresses on the unit.

The test program then concentrated on shutdown techniques that minimized the thermal transient imposed on the steam generator. This approach, in general, involved cooling the sodium at a controlled rate to a point at which removing the water would not impose a severe thermal transient. The steam in this case was replaced with inert gas at relatively low pressure, 1.0 to 1.7 MPa (145 to 250 psig). This was considered to be within the operating limits of a large steam generator.

There are conflicting demands on cooling rate of the sodium. A slow rate is desired to minimize thermal stresses and a rapid rate is desired to minimize leak damage. It was observed in these tests that, within the range of 55 to 110°C/hr., cooling rate did not affect the tendency of small leaks to plug, i.e., leaks remained open in both cases.

From the results of the leak behavior tests, it seems safe to assume that the self-damage process is directly related to corrosion. This would predict that the rate will be sensitive to temperature by the familiar log (RATE) VS.  $1/T$  relationship. Therefore,

## INTERNATIONAL CONFERENCE ON LIQUID METAL TECHNOLOGY IN ENERGY PRODUCTION

cooling the sodium should reduce the self-damage rate.

Experimentally, it was observed that the amount of tube wall penetration was greatly reduced by cooling the sodium. In the scoping tests it was observed that a leak about  $2 \times 10^{-2}$  gm/sec ( $4 \times 10^{-5}$  lb/sec) reached the point of sudden enlargement in about 1.75 hours at 482°C (900°F). In the shutdown tests, a similar leak penetrated only one third of the wall thickness in 3 hours when the sodium was cooled at 55°C/hr. (100°F/hr.). This represents at least a factor of five increase in the time available to shut down the system safely. The actual time gained by cooling cannot be accurately predicted because there is considerable scatter in the current data.

With respect to leak location, two approaches were investigated. The first was to reopen a plugged leak so that it could be found by helium leak checking. Thermal cycling and pressure cycling both proved unsuccessful at unplugging leaks. Sodium dissolution of a plug also did not appear promising. The only successful approach involved circulating a solution of dilute citric acid through the steam side of the defected tube. This method worked in six out of six tests. Citric acid solutions have been used to clean oxide scale in conventional power boilers. Adaptation of this process to leak unplugging in LMFBR steam generators appears to be feasible and further tests are planned.

The second approach to leak location is use of NDE techniques to find a plugged leak. The most promising methods investigated were ultrasonic and pulsed eddy current. The reason these methods can locate defects may be related to the self-damage to the base metal immediately around the leak site on the steam side of the tube. In these tests it was observed that significant enlargement of the leak path occurred during exposure. This may allow location of a leak that was originally smaller than the detection limit of the NDE techniques attempted.

### SUMMARY/CONCLUSIONS

The following list summarizes the principal observations and conclusions resulting from this test program.

- O Small leaks ( $< 5 \times 10^{-2}$  gm/sec) are likely to plug in-service.
- O An open leak smaller than  $5 \times 10^{-2}$  gm/sec will suffer self-damage and grow. The self-damage process is related to corrosion.

- O Small leaks that self-plug can spontaneously reopen and grow.
- O A positive pressure of inert gas in the steam system kept small leaks open during shutdown of the sodium system.
- O Reducing the sodium temperature reduces the self-damage rate of a small leak.
- O Pressure and thermal cycling do not open plugged leaks.
- O Citric acid solutions will unplug small leaks.
- O Ultrasonic inspection and pulsed eddy current appear to be the most promising methods of nondestructive examination to locate plugged leaks.

### ACKNOWLEDGMENT

*This work was performed under contract with the Energy Research and Development Administration, Contract AT(04-3)-893-10.*

### REFERENCES

1. J. A. Ford, "A Recent Evaluation of Foreign and Domestic Wastage Data from Sodium-Water Reaction Investigations", CTS-73-05, January 1973.
2. D. A. Greene, D. W. Sandusky, "Proceedings of the US/USSR Seminar on the Development of Sodium-Cooled Fast Breeder Reactor Steam Generators", Paper No. 15, Los Angeles, California, December 2-4, 1974.
3. D. W. Sandusky, "Behavior of Small Leaks in LMFBR Steam Generators", Trans. ANS, V 19, Washington, D.C., October 27-31, 1974.
4. P. Lecocq, L. Lannou, J. C. Masson, IAEA/SM168/E7, January 1973.
5. J. R. Donati, et.al., J. Nuclear Materials, v. 54, pp. 217-223, November 1974.
6. Symposium on Experience from Operating and Fueling of Nuclear Power Plants, IAEA/SM178/17, Vienna, October 8-12, 1973.
7. S. Alfano, Combustion, pp. 17-24, May 1962.
8. R. Newman, C. A. Smith, J. Nuclear Materials, 52, pp. 173-183, 1974.
9. J. S. Armijo, J. M. Scott, GEAP-10580, July 1972.

# INTERNATIONAL CONFERENCE ON LIQUID METAL TECHNOLOGY IN ENERGY PRODUCTION

## SMALL LEAK DAMAGE AND PROTECTION SYSTEMS IN STEAM GENERATORS

David A. Greene

General Electric Company  
Fast Breeder Reactor Department  
Sunnyvale, CA

### ABSTRACT

A small leak of water into sodium in a liquid metal heated steam generator can cause damage to adjacent tubes, a phenomenon termed wastage. Theories on this phenomenon range from corrosion from sodium-water reaction products to erosion by supersonic particles. An alternative approach considers the water injection to form a simple combustion process. Using this approach many aspects of over 250 wastage experiments can be explained both analytically and physically.

The U.S. has an extensive technology in the general area of acoustic surveillance. High temperature in-sodium microphones, in-vessel waveguides, and data analysis techniques have been successfully demonstrated in national development programs. This technology has been applied specifically to the development of an acoustic leak detection/location monitor for small leaks in an operating steam generator.

### 1. INTRODUCTION

The first generation of liquid metal cooled reactors, such as DFR, EBR II, FERMI, Rhapsodie, and BOR 60 have been followed by demonstration power plants. In the last few years PFR, Phenix, and BN 350 have been completed, with others still under construction in the U.S., Germany, and Japan. A pattern can be discerned in the operating history of these plants. If the steam generator operates satisfactorily, then although the reactor and balance of plant may have minor initial problems the power plant is extremely well behaved and efficient within a short time. The French demonstration plant Phenix and the US - EBR II are examples. If problems exist in the steam generator units, these cause significant economic losses in time and operating ability. Experience from FERMI, PFR, and BN 350 indicates that sodium-water reactions are the prime source of such problems. Even small water-to-sodium leaks can have catastrophic consequences in terms of lost operating capability as evidenced by PFR.

Sensitive leak detectors are installed in the steam generating systems to indicate the presence of a sodium-water reaction. When a leak is detected the plant is shut down, and the leak must be located so that repairs can be made. The main objective in performing wastage studies is to establish design criteria for small leak protection systems, and provide operating and shutdown criteria for small leak protection systems, and provide operating and shutdown criteria for steam generators following detection of a small sodium-water reaction. In order to protect against severe wastage damage, it is essential that the operator has sufficient knowledge of the phenomena and its consequences to judge the extent of damage from the behavior of leak detection monitors.

Since the phenomena of wastage were first experienced in the Enrico Fermi Atomic Power Plant (FERMI) steam generators, the U.S. steam generator development programs have recognized the importance of obtaining a quantitative understanding of wastage damage and sodium-water reaction phenomena. Atomic Power Development Associates performed many wastage experiments to provide the earliest quantitative basis of the damage rates associated with small leaks.<sup>1</sup> Since 1971 General Electric has investigated under the sponsorship of the United States Energy Research and Development Administration many aspects of wastage phenomena.<sup>2</sup> European countries have also undertaken comprehensive investigations of wastage<sup>3,4,5</sup>, together with Japan<sup>6</sup> and the USSR<sup>7,8</sup>. At the start of the General Electric program on small leak behavior, a comprehensive survey of all published data was made<sup>9,10</sup>. Umbrella type of correlations were produced from all published world data, much of which was not directly applicable to the reference design of the steam generator. The objectives in making the current investigations were: 1) to provide data for a specific design configuration, 2) to cover all operating conditions associated with the Clinch River Breeder Reactor Plant, and 3) to obtain an understanding of the phenomena so that the results could be used for future LMFBR plants.

## 2. TEST FACILITIES

The wastage tests were conducted in two sodium water reaction rigs: flowing sodium loop (SOWAT) and a static sodium pot (SOLLACE).

● SOWAT. This is a flowing sodium loop which has a 20 gpm (1.25 liters/sec) electromagnetic pump which can circulate against heads up to 20 psi. The normal operating limits are 15 psig (103 MPa), 1000°F (538°C), maximum water quantity 0.5 lb (227 gm), and injection rates up to  $\sim 10^{-3}$  lbs/sec (1.36 gm/sec). The main vessel is approximately 12 inches (30.5 cm) diameter and about 30 inches (76.2 cm) high. Within the vessel the sodium inlet pipe enters through the wall and then flows into an internally held 3 inch (7.62 cm) diameter tube. Sodium surrounds the outside of the tube, and a removable test section is placed within the tube. (Figure 1.)

● SOLLACE. This rig is a simple static sodium vessel made of carbon steel which is capable of operation up to 1000°F (538°C). The maximum cover gas pressure is a few psia and in general it operates at a few inches water-gauge. The pot is designed for sodium-water reaction experiments, with an internal hydrogen venting and burning system; and a water injection capability of up to 2 lbs (908 gm) of water, injected at rates below  $\sim 10^{-2}$  lbs/sec (4.54 gm). (Figure 2.)

● Water Flowrate (lbs/sec) - Quantities of water injected during a test are monitored by observing the rate of descent of the water in the sight glass (Figure 3). This sight glass has a scale of approximately 5 inches (127 mm) subdivided into tenths to give 50 divisions. If the sight glass was isolated from the reservoir, the quantity of water available for injection was about 1 ml/division. When the sight glass monitored the level in the reservoir, each division corresponded to about 5 ml. By timing the descent of water in the sight glass the H<sub>2</sub>O injection rate was obtained.

## 3. IMPINGEMENT WASTAGE PHENOMENA

Three distinct damage mechanisms have been observed during the course of the program. First is impingement wastage of a tube in the path of a flame. The second type is called self-wastage in which damage occurs both in the immediate vicinity of the orifice and within the orifice walls. The third type of damage is caused by recirculation or back-

wash of reaction products as a result of injecting against a concave surface, or due to injecting in a restricted geometry. This is designated as backwash-damage. Examples of the three types of damage are shown in Figure 5.

A small leak of water into sodium in a liquid metal heated steam generator can cause damage to adjacent tubes, a phenomenon termed wastage. Theories on this phenomenon range from corrosion from sodium-water reaction products to erosion by supersonic particles. An alternative approach considers the water injection to form a simple combustion process. Using this approach many aspects of over 250 wastage experiments can be explained both analytically and physically. It also permits correlation of data from different facilities, and integrates and explains experimental observations.

Turbulent flames are believed to be the cause of wastage damage. A sodium-water reaction takes place on the surface of the combustion cone; reaction products form the remainder of the "flame". This reaction is exothermic producing liquid-gas-solid reaction products with temperatures in the region of 1200°C to 1400°C. Curves shown in Figure 4 explain some of the properties of flames.<sup>11</sup> A flame is characterized by three parameters: its length  $L$ , angle  $\theta$ , and injector orifice diameter  $d_0$ . Although the "fuel" and environment are rather exotic, the sodium-water flame appears to have the same behavior and characteristics of more normal combustion materials such as hydrocarbons. A laminar flame has a length given by the ratio

$$L_D \propto d_0^2 \cdot V/D \quad (\text{Eqn. 1})$$

where  $D$  is a diffusion coefficient and  $V$  is the velocity of the fuel at the orifice. Making the assumption that for turbulent flames  $D \propto d_0 \cdot V$ , the length of a turbulent flame is:

$$L_T \propto d_0 \quad (\text{Eqn. 2})$$

This indicates that the turbulent flame length is a function of the orifice diameter, and only a weak function of the fuel velocity. It is also found that when the injected phase is a gas and the environment is a liquid, the flame angle is  $\sim 13^\circ$ . When a liquid is injected into a liquid, it forms a  $25^\circ$  flame angle.<sup>11</sup>

For the special case of water injected from an orifice under choked flow conditions it is more appropriate to use the jet diameter at which entrainment of the sodium into the jet can first occur. This is given by<sup>13</sup>

$$d = d_o (P_c/P_e)^{1/2\gamma} \quad (\text{Eqn. 3})$$

where d = diameter of the jet after expansion

$P_e$  = ambient pressure

$P_c$  = pressure inside orifice

$\gamma$  = ratio of specific heats.

A series of experiments has been made to provide visual evidence of the combustion flame nature of water injections into sodium. The earliest technique used injected water/steam parallel to a metal surface (see Figure 6), with the flame-like nature of the reaction being etched onto the metal.

Using combustion theory outlined in Figure 4 and the equations above, it is possible to predict the effect of operating parameters on impingement wastage. Two such predictions were made and experimentally verified: the effect of water-side pressure and the effect of water phase. It was assumed that the effective orifice, as defined in equation 3 above, would control the flame length. If pressures of 73 bar, 106 bar, and 143 bar are used in equation 3, the resulting effective orifice diameter changes are relatively minor ( $\pm 20\%$ ). For these tests the  $L/d_o$  is  $\sim 80$ . For this location in the flame, the change in effective diameter is predicted to have little effect. In other words, little change in penetration rates would be predicted for significant changes in water-side pressure. Tests were made and the results are shown in Figure 7, confirming the prediction.

From Figure 4 and equation 2, it would be expected that the flame length is only dependent upon orifice diameter. If the water is injected as a liquid rather than as steam, the mass flowrate is about four times higher from the same orifice. However, the angle of the flame is also double for water over that for steam, therefore, it can be hypothesized that the energy density of the flame would be similar for both liquid and gas injections from the same orifice; and hence the penetration rates would be similar. The damage area for the liquid would be twice that for the steam. Tests were made using four

different orifice diameters and the penetration rates are shown in Figure 8. The damage rates and areas were as predicted prior to the tests.

A parametric study of impingement wastage damage was made covering the following parameters:

- Target materials - 1800, austenitic (Type 304 s/s), ferritic (2-1/4Cr:1Mo)
- Water/steam injection rates - up to 0.6 g/sec
- Injector orifice geometry - up to 0.034 cm (also slits)
- Sodium temperatures - 300°C to 500°C
- Water/steam pressures - 70 to 150 bar
- Sodium flow velocity - 0 to 3 meters/sec
- Water phase - liquid, vapor
- Injector-to-target spacing - 0.3 to 3.5 cm.

Most of the results have been reported previously<sup>12</sup>. The tests were performed in the SOWAT and SOLLACE test rigs. Cooling of the target was not attempted, since it is considered to have a negligible effect on wastage rate. A computer code analysis of the heat transfer associated with reaction product impingement indicated high temperatures exist only in the immediate region of the wastage area, and cooling of the target has negligible effect on these local conditions. In the APDA tests, the effect of target cooling was also examined experimentally, and no effect of cooling was measured.<sup>1</sup>

Three materials were examined for wastage resistance, although only one (2-1/4 Chrome: 1 Moly) was investigated fully. The resistance of Type 304 stainless steel and Incoloy 800 are compared to the wastage of the ferritic steel in the table below.

Table 1. Comparative Wastage Resistance

Material	High Temp. 460°C	Low Temp. 340°C
2-1/4 CR:1Mo	1	2.5
Type 304 s/s	4	30
1800	6	100

The resistances of 1800 and 304 s/s increase dramatically at low temperature compared to high temperature. 2-1/4Cr:1Mo does not exhibit such a large temperature effect.

The French report a distinct effect of sodium velocity on penetration rate<sup>3</sup>, while GE<sup>12</sup> and the USSR<sup>8</sup> report a negligible effect. It is believed that a sodium velocity effect is negligible when the injection-to-target distance is less than  $L/d_0 = 100$ . It is possible that sodium velocity becomes important when the flame impinges on a target that is greater than  $\sim 150 L/d_0$  from the source.

#### 4. SELF-WASTAGE PHENOMENA

It is also found that water leaking into sodium causes self-enlargement of the defect, a phenomenon termed self-wastage. Tests were performed in flowing and static sodium and steam. Defects which penetrate the sodium-water barrier will eventually enlarge into much larger openings. Self-wastage appears to result from two separate causes; the first operating on plugged leaks possibly causing intermittent opening of the leak path, the second operating when a continuous flow of water passes through the leak path. Data on self-wastage were obtained for both austenitic and ferritic steels.

Accepting the hypothesis that the water injection forms a turbulent flame, and that this flame has a strong pumping action to suck sodium into the combustion region, an explanation of self-wastage can also be presented. If the flame is inadequately fed by water-steam, the phenomena of reverse flame velocity can occur, with the flame moving back into the orifice. Since the flow of water is choked by the minimum orifice diameter, and the flame characteristics are defined by this diameter, the flame will be relatively small and contained within the cavity formed. The amount of self-damage may well depend upon the temperatures reached by the reaction products, and this temperature will depend upon the thermal conductivity of the surrounding steel. Austenitic steels are poorer thermal conductors than ferritic, and the resulting higher reaction product temperature may more than compensate for the increased corrosion resistance of the austenitic. For very small orifice sizes the flow of water through the defect may not be continuous, with the leak intermittently opening and plugging. Under these circumstances, it is believed that sodium diffuses into the orifice and reacts intermittently. The resulting corrosive reaction products are essentially at the surrounding metal temperature and the rate of growth of the orifice will be more dependent upon the

corrosion characteristics.

Accepting these hypotheses, predictions of self-wastage phenomena can be made. It would be expected that stainless steel (austenitic) would self-damage at higher rates than 2-1/4Cr:1Mo steel (ferritic) at larger micro-defect sizes, but slower at very small micro-defect sizes. This is shown to be the case for the experimental data shown in Figure 9. The type of growth of micro-defects should also be different for austenitic and ferritic steels. With ferritic steels the corrosion will be relatively fast, and chambers of damage will be formed. Monitoring the choked water flowrates through the self-wasting defect, one would predict step changes in the injection rate, with relatively long periods between changes, since the reaction products are cooled by heat transfer. With austenitic steel, the orifice walls will be attacked slowly until the flame forms within the orifice, then the damage rate will increase rapidly. Monitoring the water injection rate, one would predict a long period of very low injection rates followed by a relatively smooth but rapid increase. Such characteristic injection rate phenomena have been measured with ferritic and austenitic steels.

#### 5. LEAK DETECTION

A small leak of water into sodium in a steam generator has the potential for causing significant damage to the unit, with associated economic penalties, if not detected and located within a relatively short time. Therefore, a reliable detection/location system is required. The present reference small leak protection system is based on the detection of reaction products at the outlet of each unit. A major disadvantage of this system is its dependence on transit of reaction products from within the unit to the detector, which reduces its effectiveness at low sodium flowrates and makes its effectiveness uncertain for leaks in the static regions of the unit. Experience in operating plants and test facilities indicates that reaction product detectors are also susceptible to hide-out and intermittent release of reaction products<sup>14</sup>. Experience also shows that detecting a small leak is not sufficient to reduce any economic penalties, if the leak cannot be precisely located following detection. While the reference system for leak detection continues to be the Hydrogen Diffusion Tube Detector, other systems of detection have been inves-



tigated.

The only known technique which has potential for rapid detection of a small sodium-water reaction, even in static sodium, is based on acoustic monitoring of the unit. It is also the only known technique for pinpointing the leak location. The United States has actively developed acoustic techniques for potential use in many areas of a Liquid Metal Fast Breeder Reactor. High temperature in-sodium microphones, in-vessel waveguides, and acoustic data analysis techniques have been successfully demonstrated in national development programs. This broad base technology has now been specifically applied to development of an acoustic technique to monitor steam generator units for small sodium-water reactions.

The development of an acoustic leak detection/location system requires investigation of five areas:

- a. Sodium-water reaction, acoustic signal characterization.
- b. The amplitude and character of the steam generator background noise.
- c. Hardware, instruments and transducers for data acquisition.
- d. Software for data handling.
- e. Modelling and simulation of the acoustic phenomena and structural responses of the steam generator; signal to noise ratio predications for CRBRP.

The sodium-water reaction produces an acoustic signal which does not have a unique frequency. Most of the signal power lies in the bandwidth 1 KHz to 10 KHz. The background noise measured in steam generators is also broad-band with most of the power in the range 1 KHz to 20 KHz. When water is present in the steam generator tubes the majority of the signal is produced by boiling, far exceeding the quiescent noise levels. The noise in the steam generator is a reverberent field. An impulsive noise will decay slowly. Because of the multiple reflections undergone by pressure waves from the sodium-water reaction, it tends to produce incoherent noise which adds to the background noise levels. However, a coherent signal from the source allows location by examining the spatial coherence of signals reaching transducers over a relatively short period. A mini-computer-based detection/location system has been developed, together with a simple operator interface, which has

the capability for giving almost "real-time" leak location. By the use of an appropriate algorithm multiple reflections are aborted; this algorithm is programmed into the mini computer.

#### ACKNOWLEDGMENT

John Hunsicker, William Minderler, Frank Adorno, Paul Trafford, and Raymond Madeiros from the Facilities Unit, under the direction of J. M. Scott, greatly contributed in obtaining the test data for this report. Technical contributions from C. Ulpindo, J. Gudahl, and F. Alhgren are gratefully acknowledged.

The work described in this paper was performed under US-ERDA contract.

#### REFERENCES

1. Chamberlain, et al., "Wastage of Steam Generator Materials by Sodium-Water Reaction." A.N.L., Internation Conference, Argonne, November 1968.
2. D. A. Greene, "Preliminary Results from Small Leak Tube Wastage Tests," Conf. 740401, ANS Fast Reactor Safety Meeting, Los Angeles, April 1974.
3. Lions, et al., "Study of the Effects of Small Leakage of Water into the Sodium of the Steam Generator," ANS Fast Reactor Safety Meeting, Los Angeles, Conf. 740401, April 1974.
4. K. Dumm, "Large Leak Tests in a Model of a Straight Tube Steam Generator," Specialist Meeting on Sodium-Water Reaction, Melekess, USSR, Conf. 710548, May 1971.
5. J. A. Bray, "Some Notes on Sodium-Water Reaction Work," Conf. 710548, May 1971, Melekess.
6. Nei, et al., "Wastage of Steam Generator Tubes during Small Leak of Steam into Sodium," Conf. 740401, April 1974, Los Angeles.
7. Andreev, et al., "Experimental Study of Interaction of Water with Sodium during Small Leak of Water into Sodium," Melekess, Conf. 710548, May 1971.
8. Kul'pin, et al., "Analytical and Experimental Study of Reacting Water-Sodium Flow," Melekess, Conf. 710548, May 1971.
9. J. A. Ford, "A Recent Evaluation of Foreign and Domestic Wastage Data from Sodium-Water Reaction Tests," prepared for GE by Atomic Power Development Associates, Reference CRS-73-05, January 1973.
10. D. A. Greene, "The Leakage of Water into Sodium in Steam Generators and Test Rigs," Nuclear Tech., Vol. 18, June 1973, pp. 267-276.
11. Lewis and Von Elbe, "Combustion Flames and Explosions of Gases," 2nd Edition, 1961, Academic Press.
12. D. A. Greene, "Sodium-Water Wastage and Reactions Program Performed by General Electric in Support of the U.S. AEC LMFBR Steam Generator Development," IAEA Study Group, "Steam Generators for LMFBR's", Interatom, Bensburg, October 14-17, 1974.

13. T. D. A. Kennedy and J. Collier, "The Structure of an Impinging Gas Jet Submerged in a Liquid", International Symposium of Multiphase Flow Systems, 1974.
14. Smit, C. C., "Experience on Detection of Leakages in LMFBF Steam Generators", Paper KS. Study Group Meeting on Steam Generators for LMFBF's, IAEA, Bensburg, October 1974.

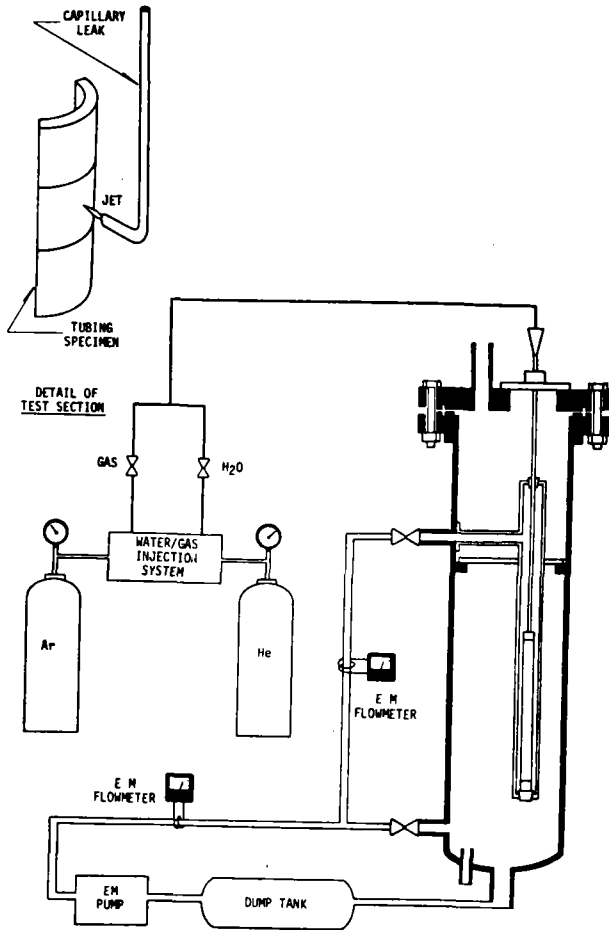


Figure 1. Small Leak Wastage Facility (SOWAT)

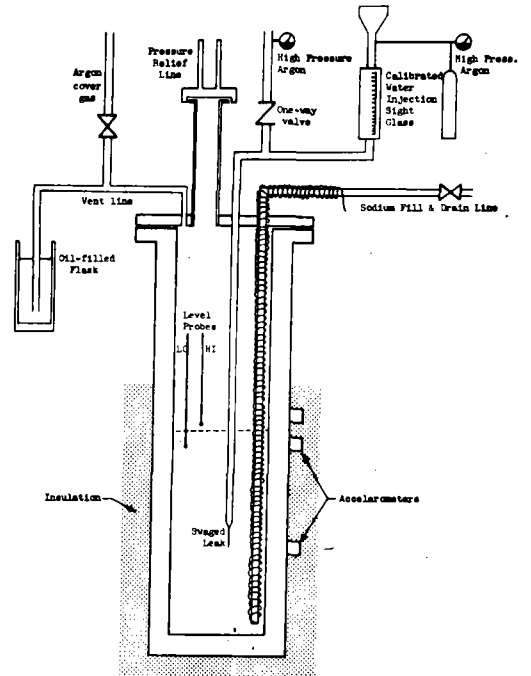


Figure 2. SOLLACE II Rig

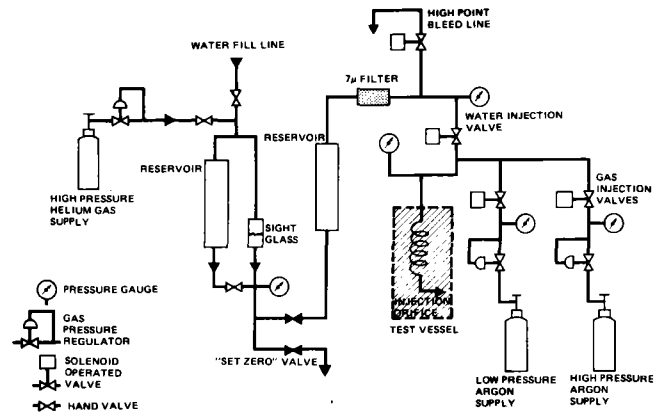


Figure 3. Water Injection System

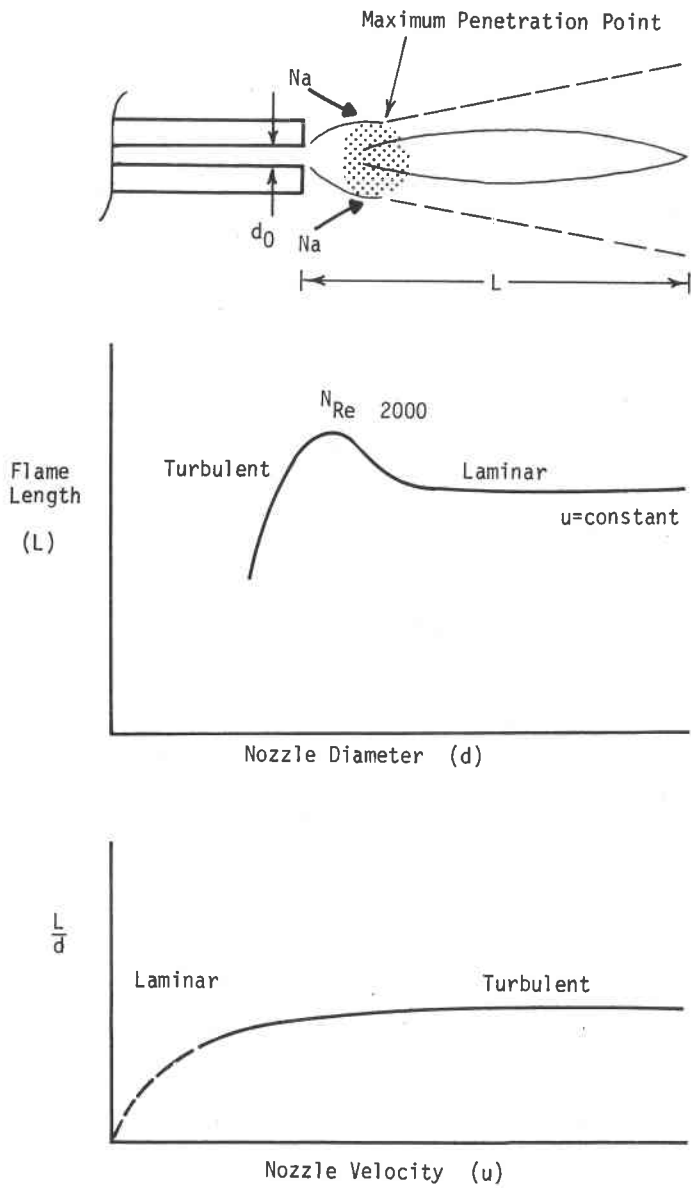
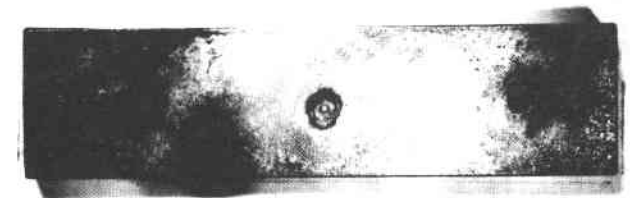
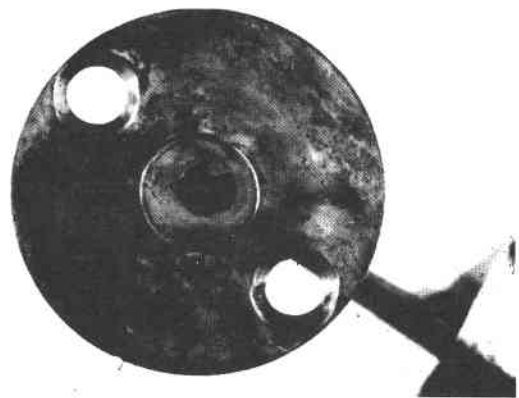


Figure 4. Fundamental Properties of Flame



CRATER WASTAGE

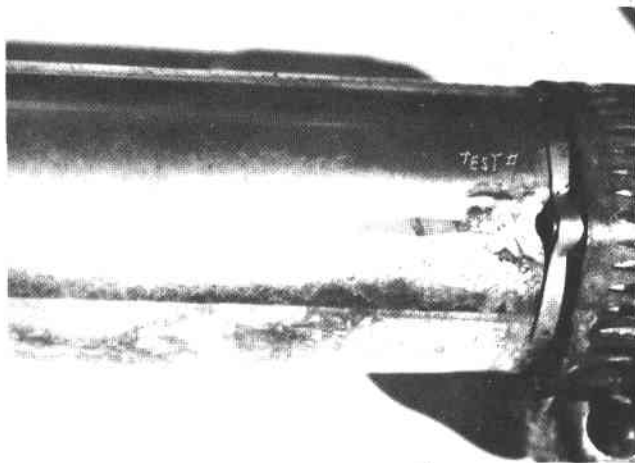


TIP WASTAGE

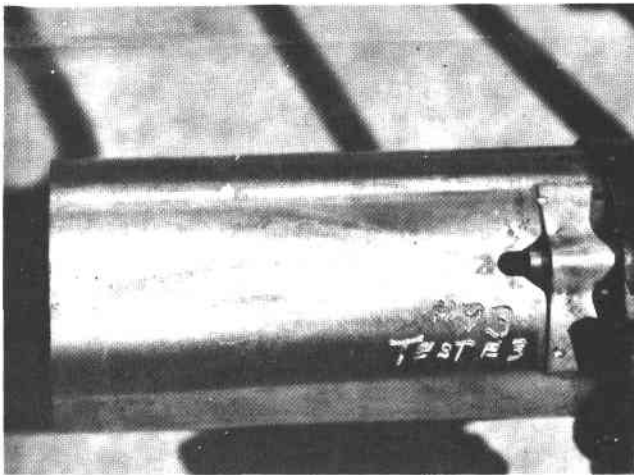


BACKWASH WASTAGE

Figure 5. Types of Damages



-a-



-b-

Figure 6. Photographs Showing Flamelike Structure Of Reacting Water Jets

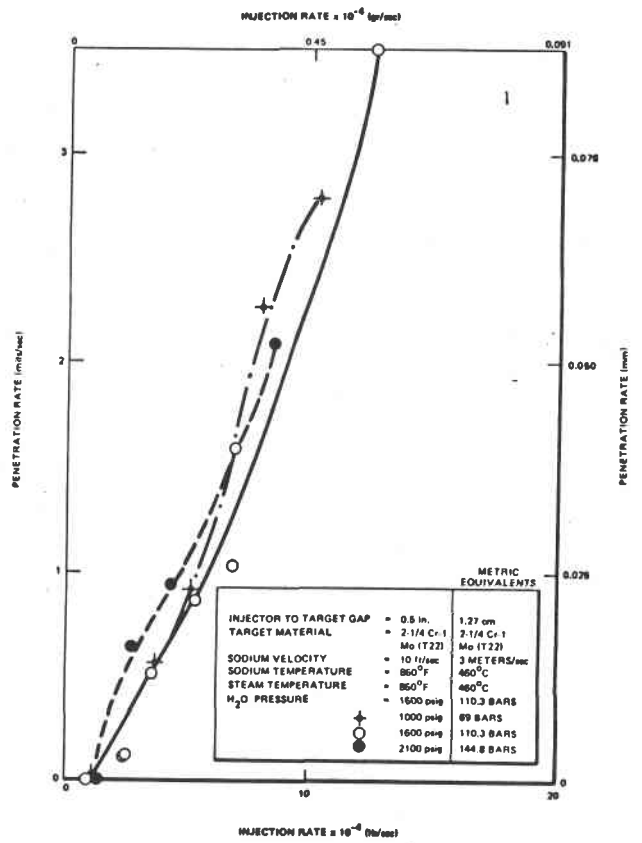


Figure 7. Effect of Water Pressure On Injection Rate

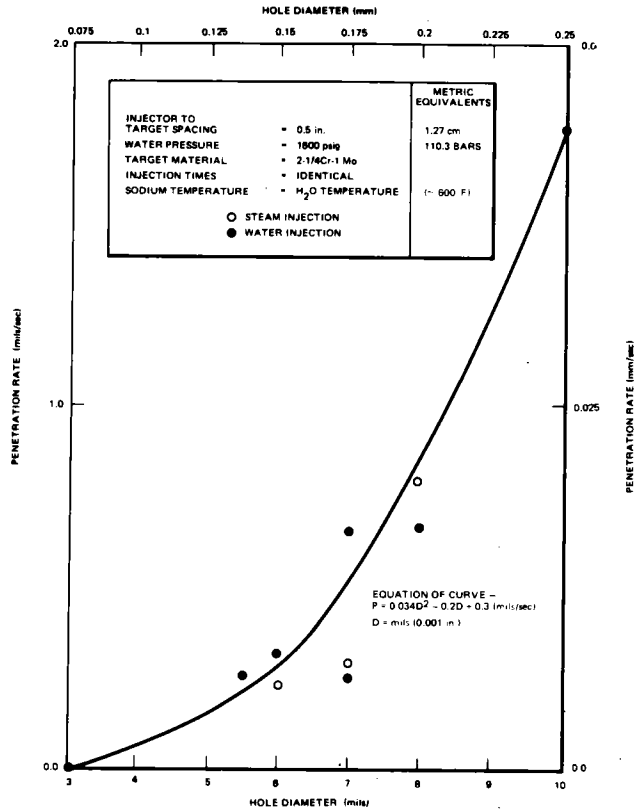


Figure 8. Effect of Water Phase on Penetration Rate of Target

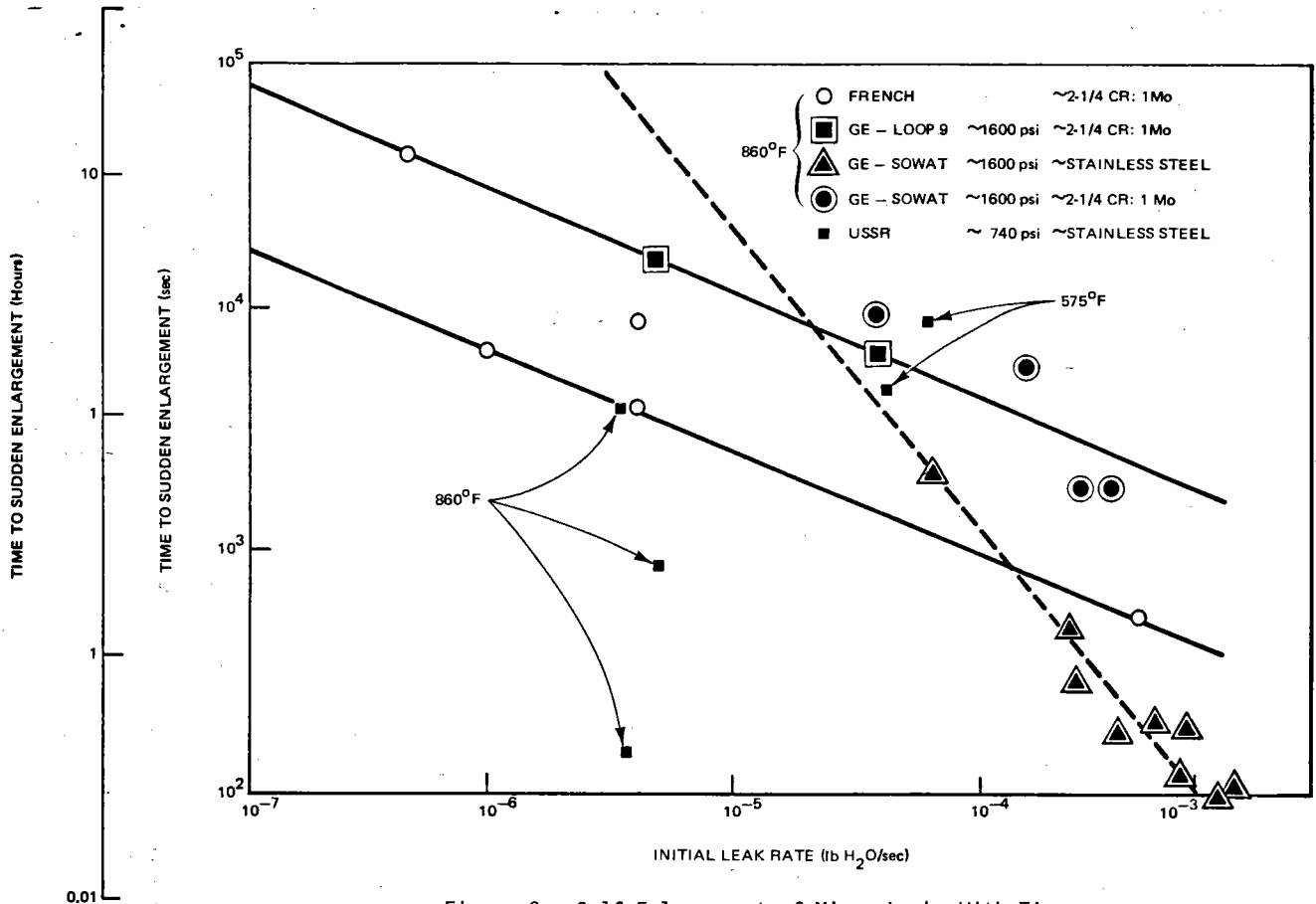


Figure 9. Self-Enlargement of Micro-Leaks With Time

# INTERNATIONAL CONFERENCE ON LIQUID METAL TECHNOLOGY IN ENERGY PRODUCTION

## LARGE SCALE SODIUM-WATER REACTION TESTS FOR MONJU STEAM GENERATORS

Minoru Sato,

Hiroshi Hiroi,

Masao Hori

Power Reactor and Nuclear Fuel Development Corp.

Tokyo, Japan

### ABSTRACT

To demonstrate the safe design of the steam generator system of the prototype fast reactor Monju against the postulated large leak sodium-water reaction, a large scale test facility SWAT-3 was constructed. SWAT-3 is a 1/2.5 scale model of the Monju secondary loop on the basis of the iso-velocity modeling. Two tests have been conducted in SWAT-3 since its construction. In this paper, the test items using SWAT-3 are discussed, and the description of the facility and the test results are presented.

The tests were performed for two water-injection rates; 6.7 kg/sec and 14.2 kg/sec. The following results briefly summarize the tests:

- (1) No structural damage to the facilities' components were found.
- (2) Performance of the pressure relief system was demonstrated.
- (3) No secondary heat transfer tube rupture occurred.
- (4) Much knowledge for sodium handling were obtained; in particular, the post-test drain and post-accident clean-up procedures were established.

### INTRODUCTION

The study to establish the safety of the steam generator design for the prototype fast reactor Monju against the potential large scale sodium-water reaction accident has been carried out at PNC since 1970. The SWAT-1 (Sodium-Water Reaction Test)<sup>(1)</sup> rig first used is a 1/8 scale of the Monju SG. The extrapolation of the test results from this small scale experiment to the prototypic condition was difficult due to the complexity of the phenomena and the potential size effect.

Therefore, the construction of a large scale mock-up test facility SWAT-3 was initiated in 1973 at PNC O-arai Engineering Center, completed the construction in 1975 and water injection tests have been conducted since then. This paper presents specific test objectives, the description of the facility, and some results of the past two tests.

### PURPOSE OF THE TESTS

The hypothetical water leak considered for the safe design of Monju SG is the instantaneous full rupture of one heat transfer tube. Moreover, owing to the sodium-water reaction caused by this primary leak, the heat transfer tubes adjacent to the reaction region may be damaged and secondary tube failures may take place. These additional leaks resulting from the secondary tube failures are estimated to be a simultaneous double-ended rupture of three heat transfer tubes. Hence, the guillotine rupture of four heat transfer tubes is adopted as the design basis leak for the Monju SG design and safety analysis.

The objectives of the tests are:

- (1) To determine the extent of the secondary tube failures caused by the initial one tube rupture.

- (2) To establish the overall system integrity of the SG vessel, intermediate heat exchanger (IHX), other components and piping of the secondary loop during the design basis leak accident.

For these purposes, the SWAT-3 facility was designed to obtain the following data:

- (1) Pressure and temperature data in the troubled SG.
- (2) Data describing the performance and reliability of the pressure relief system.
- (3) Secondary tube failure data
- (4) Structural deformation and damage of the troubled SG wall.
- (5) Pressure wave propagation through the secondary loop, particularly to the IHX
- (6) Demonstrate post-accident clean-up and recovery procedures

Although actual size tests are desirable, Monju SG is too large (Monju SG is the so called unit type and a typical size is 3 m dia. x 13 m height for which the sodium inventory is about 50 ton) to carry out the tests due to the cost considerations and technical difficulties in handling the large size components contaminated by sodium and reaction products. Therefore, a scaled down model was chosen in which the shell size of the model SG is 1/2.5 of the Monju SG. This ratio is the mid value between 1/8 of SWAT-1 rig and 1 of the actual SG, and is considered a suitable size to apply directly or to extrapolate analytically the test results to the actual system.

To obtain data for secondary failures, the size and the material of the heat transfer tubes and tube supports are kept the same as the prototype design since the damages on tubes adjacent to the initially failed tube are mainly affected by local phenomena. Water injection capacity provided is the same as the leak rate from one tube double-ended rupture. This is to say that the test results (namely the pressures, temperatures, performance of the relief line, etc.) of SWAT-3 are actual proof of one tube rupture accident.

To convert the water injection rate of the scale model to the leak rate of the actual SG, the method of the iso-velocity modeling, that is used for modeling liquid accelerated phenomena such as the under-water explosion, is applied<sup>(2)</sup>. According to the iso-velocity modeling,

scale ratio actual to model is	1:1/n
time ratio is	1:1/n
ratio for water injection rate is	1:1/n <sup>2</sup>
pressure ratio	1:1

Therefore, when the water injected in SWAT-3, (the 1/2.5 scale model) is the same as the leak rate in the actual one tube rupture, the pressures in SWAT-3 will reach the pressure levels expected in the actual SG as results of the rupture of  $(2.5)^2 = 6.25$  tubes. The SWAT-3 scale is thus big enough to predict the pressure behaviours for four tubes double-ended rupture that is assumed as the design basis leak in the safety analysis of the Monju SG.

FACILITY

The sodium test circuit simulating the secondary cooling system is consisted of an evaporator (1.3 m dia. x 6.35 m height), a superheater (0.8 m dia. x 4 m height), an intermediate heat exchanger (8 inch dia. x 4.5 m height), and the piping circuit (8 inch dia. x 22.5 m long, and 2 inch dia. x 25.5 m long) (See Fig.-1). Water/steam is injected in the evaporator in the quiescent sodium. Further, a sodium pumping circuit to heat up the sodium to the test condition with a pump and an electric heater, and a cold trap circuit to purify the test circuit sodium are installed, but these circuits are valved off from the sodium test circuit prior to water/steam injection.

The drain tank separates the reaction products from sodium. After the water injection, the reaction products and sodium are drained into the drain tank, and separated there from each other by the density difference causing deposits of the reaction products on the tank wall by the temperature decrease. Then the separated pure sodium in the drain tank is reused.

The pressure relief system is consisted of the relief line and the reaction products tank. The relief line is a Y shape lay out, where the three ends of the Y are connected to the evaporator, the superheater, and the reaction products tank respectively. The relief line from the evaporator is of a 12 inch dia. line 14.5 m long that includes four bends and a 5 m long vertical piping. The relief line from the superheater to the three line junction point is a 8 inch dia. line 12 m long. The rupture disks installed in the relief line are the reverse buckling type with cutting knives, and the bursting pressures are 3 kg/cm<sup>2</sup>. The reaction products tank includes a cyclone separator, an impingement type mist separator, and a vent line including a rupture disk (reverse buckling type with bursting pressure of 1.5 kg/cm<sup>2</sup>). A spring type check valve is installed on top of the

reaction products tank.

The water injection system is consisted of the water injection line and an electrically heated water tank designed to attain sub-cooled and saturated water conditions up to 150 kg/cm<sup>2</sup>G, and superheated steam up to 150 kg/cm<sup>2</sup>G, 500°C. As the trigger valve in the water injection line is opened, water in the water tank begins to flow through the line, break two rupture disks (one is installed after the trigger valve and the other is installed in front of the water injection hole) and then discharges into the sodium. As the trigger valve is closed, the water injection is terminated. Prior to the water injection, the injection line is evacuated to avoid injection of the gas remaining in the line.

The evaporator which is the reaction vessel simulating the troubled SG is somewhat modified for easy handling (See Fig.-2). The pressure relief lines are connected to the top of the evaporator and superheater in case of run-1 and run-2 tests. The piping diameter between the evaporator and the reaction products tank is expanded from the 1/2.5 scaling to 12 inch for an increased safety of the facility. The design pressure of the sodium test circuit

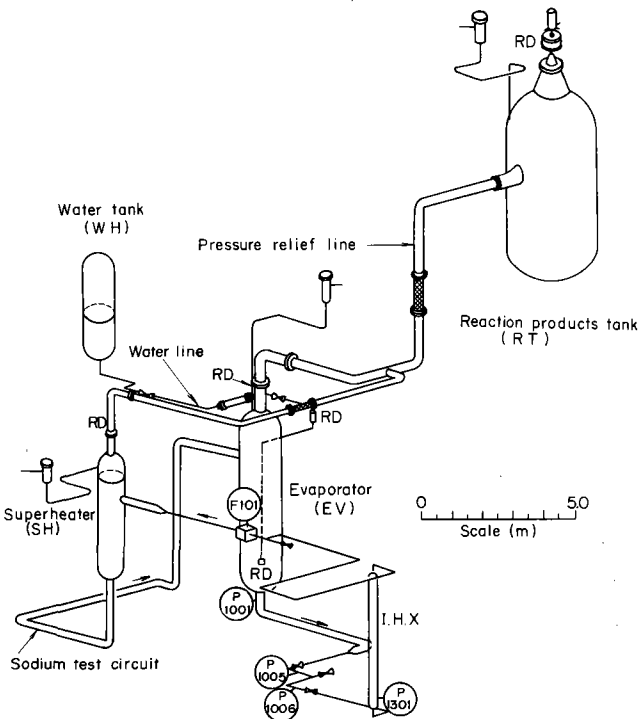


Fig. 1 Components, piping layout, and instrumentations of SWAT-3

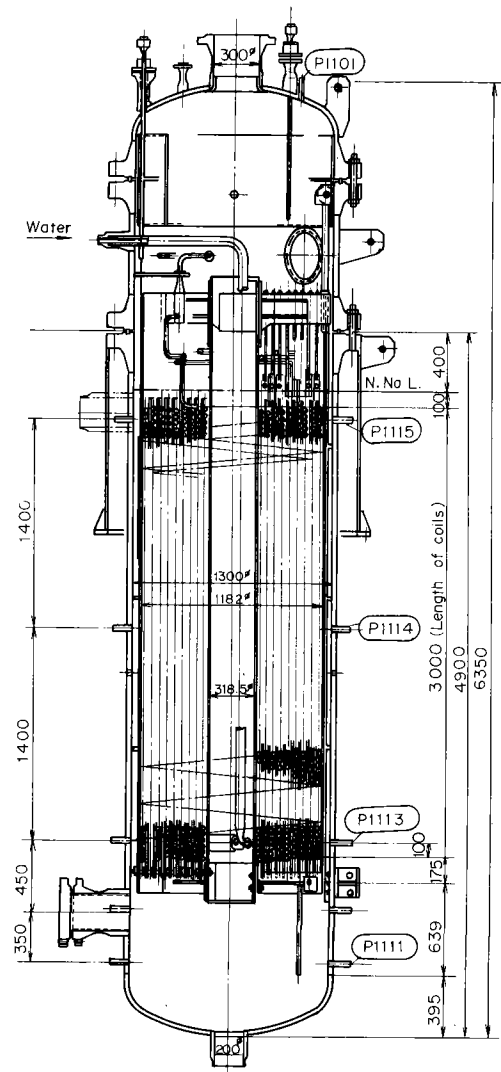


Fig. 2 Evaporator (Reaction Vessel).

is 20 kg/cm<sup>2</sup> instead of 10 kg/cm<sup>2</sup> of Monju SG. This choice was made to avoid the potential damage on the vessel and the piping resulting from repeated loading by the initial spike pressures exceeding the design pressure of Monju SG. The material of the evaporator chosen is SUS-304 stainless steel instead of the 2-1/2 Cr-1 Mo steel of the Monju SG, as needs were realized for consideration of the corrosion damage by the reaction products.

The internals of the evaporator consist of a center-pipe, helical coiled heat transfer tubes, and a shroud. The downcomer structure was omitted because the water injection points were located inside the helical coils in the two tests. To obtain the data for secondary tube failures, the heat transfer tubes used are made of the same material (STBA-24), of the same diameter and wall thickness (25.4 mm dia. x 3.2 mm<sup>t</sup>), of the same pitches of the tube bundle (vertical/horizontal = 40 mm/45 mm), and of the same structure of the tube supports as the Monju SG. But only nine layers of helical coils are installed because of the limited space resulted by the scaled down vessel diameter. The inner five of the nine layers are pressurized by gas to provide the simulated pressure condition in these tubes.

The water injection hole, in the case of run-1, is consisted of a nozzle to control the water injection rate and a rupture disk installed outside of the nozzle to initiate the leak (See Fig.-3). The water line runs through the center pipe, and the injection point is located in the annular region of the helical coils with a radially outward injection direction.

In the case of run-2, one of the fifth layer tubes is chosen as the water line. A total of eight water injection holes are provided around the tube (See Fig.-3). This design of water injection is considered to simulate a single tube double-ended rupture, and water belows out radially around the tube. The rupture sleeve is installed around these holes, and the water injection rate is restricted by the friction of the water/steam line and the two phase critical flow condition.

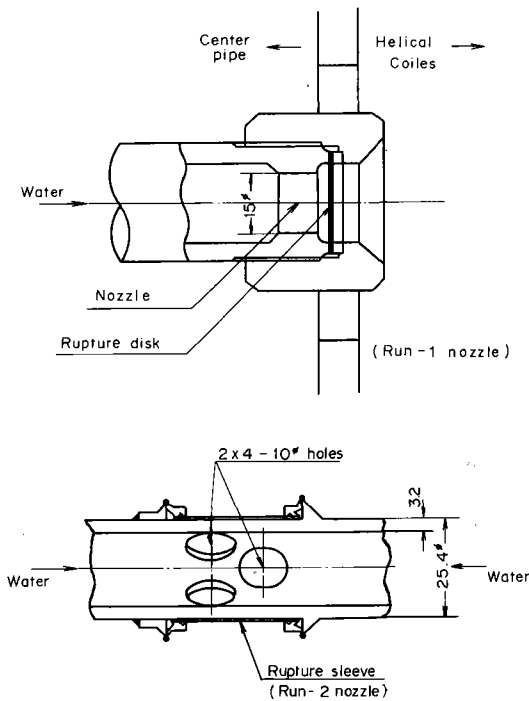


Fig. 3 Injection nozzle.

TEST RESULTS

CONDITIONS OF THE EXPERIMENTS

Two test runs have been completed. In the case of run-1, the water tank condition was a saturated water, while in the case of run-2, a subcooled water condition was selected because of the increased water injection rate.

Two counteracting considerations were given in the selection of sodium temperature: the possible boiling in the water line as result of heat transfer from high temperature sodium if a high sodium temperature is chosen on one hand, and the possible sodium solidification in the sodium drain line if a low sodium temperature is chosen on the other hand. The water and sodium temperatures selected in these tests are approximately the same as those at the middle and the lower parts of the helical coils in the Monju evaporator.

Other conditions chosen were the same as those of the Monju SG. The test conditions used are shown in Table-1.

Table - 1 Test Conditions

	Unit	Run 1	Run 2
Water pressure	kg/cm <sup>2</sup> G	153	153
Water temperature	°C	343	259
Diameter of injection nozzle	mm	15 φ	10 φ × 8
Duration of injection	sec	7.6	9.9
Injection rate	kg/sec	6.7	14.2 ~ 9.7
Total quantity of injection	kg	61.2	122
Sodium temperature	°C	378	320
Cover gas pressure	kg/cm <sup>2</sup> G	0.5	0.5
Burst pressure of rupture disk	EV, SH	3.0(515°C)	3.0(515°C)
	RT	1.5(150°C)	1.5(150°C)
Temp. of relief line	°C	255	250
Temp. of RT	°C	361	333
Temp. of drain line	°C	370	320
Temp. of drain tank	°C	291	294

DESCRIPTION OF THE PHENOMENA

Following the trigger valve opening in the water line, the sodium-water reaction was initiated as shown in Fig.-4.

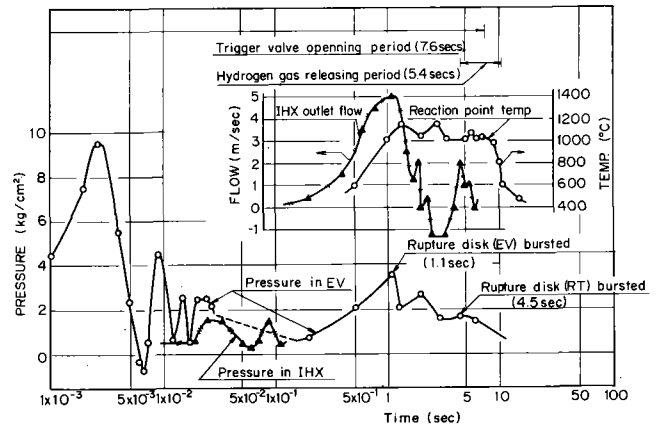


Fig. 4 Time history of run-1 test.



The initial spike pressures were observed immediately after the water injection. The duration of the spike pressures were very short, and the pressures diminished after the time that was needed to propagate the pressures from the reaction point and return the rarefaction waves from the free surface of sodium.

This spike pressure was propagated into the secondary loop circuit, and reached IHX after a certain elapsed time.

After the initial spike pressure diminished, the quasistatic pressure increase takes place in the evaporator due to the hydrogen gas build up. The quasistatic pressure increased in a simple form until it reached the burst pressure of the rupture disk in the relief line of the evaporator. Then, as the rupture disk burst, the argon gas in the cover gas area, the hydrogen gas, and sodium were flown out together through the relief line into the reaction products tank. In the case of run-1 where the water injection rate was small, the pressure in the evaporator attenuated immediately as the rupture disk burst. In contrast to this, in the case of a large water injection rate (run-2), the pressure sustained in a high level until the termination of water injection even after the rupture disk burst.

As the evaporator pressure increased, the sodium flow to the superheater from the evaporator took place through the secondary circuit, followed by the pressure increase in the superheater. In the run-1, the rupture disk in the relief line of the superheater did not burst; therefore, a reversed sodium flow was observed (from the superheater to the evaporator). In the run-2, the rupture disk of the superheater burst, and the sodium reverse flow to the evaporator did not occur.

The pressure in the reaction products tank increased due to the hydrogen gas build up and reached the burst pressure of the rupture disk at the vent stack of the reaction products tank. Then the rupture disk burst, the check valve in the vent stack opened, and the hydrogen gas in the reaction products tank was released into the open atmosphere.

During these stages, the water injection into the evaporator was still continuing, reacted with remaining sodium in the evaporator, and as a result, the high temperature reaction zone resided around the injection point, sometimes quite stationary.

As the trigger valve closed, the water/steam remaining in the water line was finally discharged into the sodium; subsequently, the pressure in the secondary circuit decreased, the hydrogen gas release stopped, and the sodium-water reaction test then was completed.

WATER INJECTION RATE

A turbine type flowmeter that was installed in the water line at some distance upstream of the water injection point (run-1; 9.2 m, run-2; 13.5 m one end, 46.5 m the other end) showed that an extremely large volumetric flow occurred immediately after the trigger valve opened, and this flow transient gradually decreased to the stationary flow rate.

Since the transient state continued for about 1 second at the place of the flow meter installed, the true water injection rate at the injection point was not known during this transient period.

INITIAL PRESSURE SPIKE

As shown the run-1 in Fig-5, the shape of the initial spike pressure obtained in the two tests was simple, exhibiting no high fre-

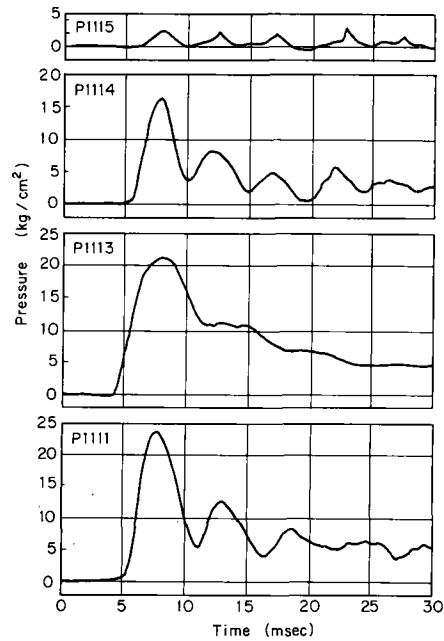


Fig. 5 Initial spike pressure in EV (run-2).

quency oscillations. Furthermore, no negative pressures were observed. It is assumed that the peak pressure value and duration of the spike pressure obey the iso-velocity modeling; SWAT-3 pressure data are plotted against the parameter combination  $q/D^2$  ( $q$ ; injection rate,  $D$ ; diameter of the vessel,  $L$ ; length between reaction point and sodium free surface) together with the SWAT-1 ( $D = 0.4$  m dia,  $L = 1.15$  m long) data as shown in Fig-6. It is seen that the peak values

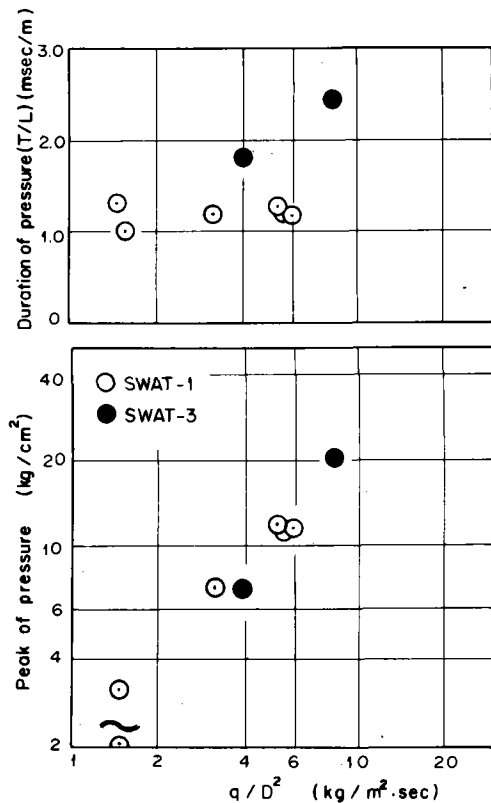


Fig. 6 Comparison of initial spike pressure.

of both facilities are in good agreement. The duration of the spike pressure depends on the geometry of the vessel rather than the injection rate, and thus, data seem to be almost constant with the parameter combination  $q/D^2$ .

The response of wall strain of the evaporator agreed quantitatively with the one calculated statically from sodium pressures measured by the pressure sensors mounted on shell inner surface.

PRESSURE PROPAGATION TO IHX

The secondary circuit between the evaporator and the IHX consisted of eight bends, two valves, two reducers (8 inch to 2 inch and 2 inch to 8 inch), and the piping (8 inch dia. x 5.2 m long and 2 inch dia. x 8.3 m long). The supports of this piping are made moveable to avoid the thermal stress such as the slide supports and the spring hangers of ordinary sodium loops. Furthermore, there are some places where gas bubbles can be held, for example, in the bonnet of the valve.

In run-1, the pressures propagated into the IHX was considerably decayed and deformed in the secondary circuit. But, in Run-2, the pressures in the IHX were not so strongly deformed as those of run-1. A clear explanation has not been obtained as yet as to the exact pressure decay mechanism, but it is conceived that the difference in the bubble distribution in the secondary circuit in the two cases is the main cause for the difference in the IHX pressure measurements.

No negative pressures were observed in both of the tests.

The duration of the oscillatory pressure waves propagating into the IHX was about 0.2 seconds; subsequent to this, the pressure in the IHX increased monotonically following the pressure in the evaporator.

A comparison of the pressure-time histories between the run-1 test and the SWAC-5H computer code is shown in Fig-7. The computer code calculation was made using the pressure-time history obtained by the experiment at the outlet pipe from the evaporator as an input to the code. The method of the numerical calculation

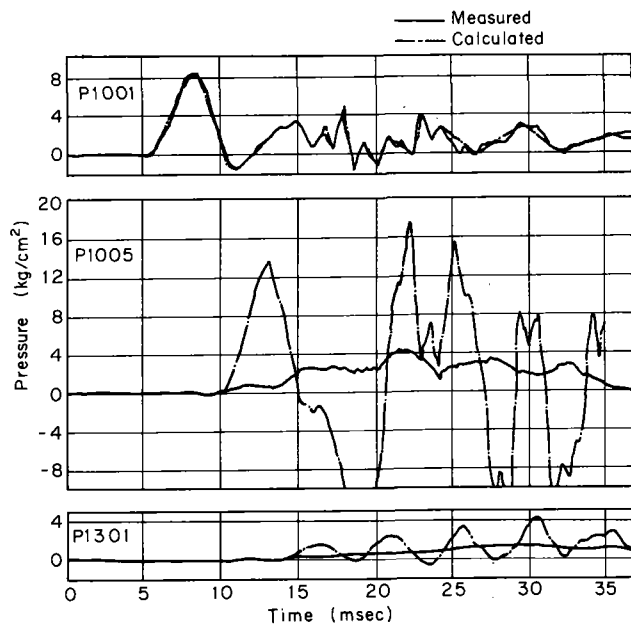


Fig. 7 Pressure propagation to IHX (run-1)

used in this code is the superposition method neglecting such effects as the pipe movement, column separation, or cavitation. As shown Fig-7, the result of the calculation in the IHX is oscillatory and exhibits negative pressures. On the other hand, the test result seems to show averaged values of the pressures calculated.

QUASISTATIC PRESSURE INCREASE

The initial stage of the quasistatic pressure increase, the sodium levelmeter readings, and the thermocouple measurements installed in the cover gas region of the evaporator showed that the sodium levels were raised first in the center pipe region and the region between vessel wall and the shroud. And next, the sodium in the annular region of the helical coils were risen.

TEMPERATURES IN SODIUM

The temperature field in the evaporator is divided into three regions; the unreacted water region, the reaction region, and the sodium region.

In the unreacted water region a low temperature of about 120°C was observed due to the adiabatic expansion of water injected into sodium (See Fig-8). In run-1, due to the smaller water injection rate, the unreacted water region was of a spindle like shape (~ 200 mm dia.), and was quite stable. In run-2, due to the large water injection rate, this region was a spherical shape (~ 430 mm dia.) periodically expanding and shrinking.

In the reaction region (this region surrounding the unreacted water region), the temperatures showed a wide variation ranging from the initial sodium temperature to the maximum temperature.

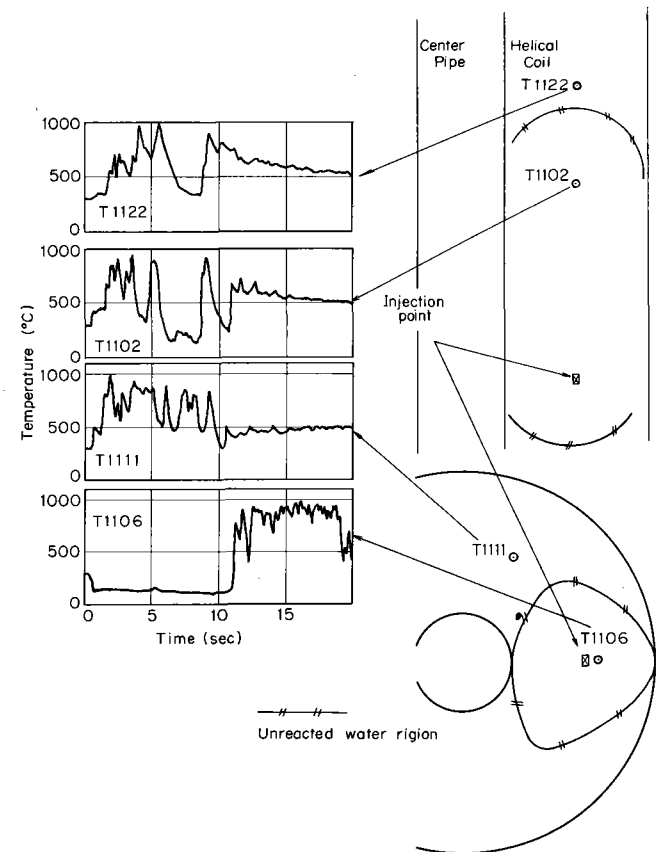


Fig. 8 Temperature in sodium (run-2)

## INTERNATIONAL CONFERENCE ON LIQUID METAL TECHNOLOGY IN ENERGY PRODUCTION

The maximum sodium temperature recorded was 1100°C. In the run-1, there was a position where the maximum temperature sustained for the entire injection duration. In run-2, temperature readings of the reaction region was unstable and oscillated between the high and low valves.

In the sodium region (this region surrounding the reaction region), far from the water injection point, the temperatures essentially showed the initial temperature of sodium.

### SECONDARY TUBE FAILURE

The helical coil heat transfer tubes of the inner five layers were pressurized to 126 kg/cm<sup>2</sup>G in run-1 and to 136 kg/cm<sup>2</sup>G in run-2 by nitrogen gas; however, no rupture was experienced by either one or by any combined effects of the high internal pressures, the high reaction temperatures, and the wastage phenomenon.

After the run-1 test, the internal structure of the evaporator was disassembled and inspected; but no distortion of the coil or no severe wastage was observed.

Since the internals of the run-2 test is under the disassembling stage, the inspection results are not available.

### HYDROGEN GAS RELEASE

In both the tests, the hydrogen gas was ignited soon after the gas released from the reaction products tank. The reason for not having observed a violent explosive burning was considered due to the low concentration of hydrogen in the released gas; a large volume of argon gas is also released from the reaction products tank during the initial stage of the gas release. An electrically heated igniter was installed on top of the stack to set the gas ignited, and its surface was heated to over 700°C.

A quantitative measurement of the sodium mist carried by the released gas was not made; but, from the visual observation, that is, the colors of the gas and the flame, and the circumstantial evidence exacted around the stack after the gas release, we concluded that little sodium mist was carried by the released gas, and the mist separator was functioning satisfactorily.

### DRAIN AND DECONTAMINATION

In the case of run-1, the drain of the reaction products and remaining sodium was carried out from 1.5 hours after the water injection under the temperature condition of the drain line at 370°C.

In the case of run-2, drain lines were heated up to 320°C; but the drain line (2 inch dia.) was choked in the middle of the evaporator draining. Subsequently another line (2 inch dia.) was used to drain the sodium, but this line was also choked. About 700 liters of sodium and reaction products were remaining in the evaporator.

Hence, a temporary drain line was installed at the bottom of the evaporator, after the choked drain line was cut and removed, to remelt and drain the remaining content of the vessel.

The decontamination of the reaction products in the vessel was carried out by a steam cleaning procedure without removing the vessel.

### CONCLUSIONS

The large scale sodium-water reaction test facility SWAT-3 was constructed in a 1/2.5 scaled down size from Monju SG system, and two tests have been performed, from which the following results were obtained:

- (1) The water injection rates and total water injected were 6.7 kg/sec and 61.2 kg, and 14.2 kg/sec. to 9.7 kg/sec. and 122 kg.
- (2) No damage to the facilities' structural components, or no phenomenon leading to the failure of the integrity of the facilities was observed.
- (3) The performance of the pressure relief system was demonstrated.
- (4) No secondary tube rupture occurred in the two tests.
- (5) The hydrogen gas was ignited and burned immediately after the gas release.

The quantities of sodium mist carried by the released gas were insignificant.

- (6) The disposal of the reaction products and the remaining sodium was safely performed.

Additional tests to establish the overall safety of the Monju SG system are presently under way and the final results will be reported at the completion of the series of the planned tests.

### ACKNOWLEDGEMENTS

This paper includes data obtained from SWAT-1 tests performed under the direction of Mr. N. Tanaka.

The authors are greatly indebted to Messrs. T. Saito, K. Sato, Y. Ouchi and other members of SWAT test group for their contributions to this work.

### REFERENCE

- (1) Hori, M. et. al. "Sodium-water reaction studies for Monju steam generators" IAEA Study Group Meeting on Steam Generators for Liquid Metal Fast Breeder Reactors. Bensberg, W. Germany, Oct. 1974.
- (2) Friedland, A. J. et. al. "Gas-water simulation studies of sodium-water reaction" APDA 226, Sept. 1968.

# INTERNATIONAL CONFERENCE ON LIQUID METAL TECHNOLOGY IN ENERGY PRODUCTION

## FAIL-SAFETY OF THE EBR-II STEAM-GENERATOR SYSTEM\*

P. S. Chopra, C. C. Stone, E. Hutter, W. K. Barney, and R. G. Staker

Argonne National Laboratory  
Argonne, Illinois 60439

### ABSTRACT

Fail-safe analyses of the EBR-II steam-generator system show that a postulated non-instantaneous leak of water or steam into sodium, through a duplex tube or a tubesheet, at credible leak rates will not structurally damage the evaporators and superheaters. However, contamination of the system and possible shell wastage by sodium-water reaction products may render the system inoperable for a period exceeding six months. This period would be shortened to three months if the system were modified by adding a remotely operated water dump system, a steam vent system, a secondary sodium superheater relief line, and a tubesheet leak-detection system.

### INTRODUCTION

The steam-generator system of Experimental Breeder Reactor No. 2 (EBR-II) has operated successfully for more than 10 years. Meanwhile, failures of steam-generators in several foreign and domestic LMFBR plants and tests installations have been reported<sup>(1)</sup>. These failed units and the systems in which they operated differ significantly from the unique EBR-II design, which uses double-tube, double-tubesheet evaporators and superheaters. However, in the light of available foreign and domestic service experience and with increasing emphasis on safety and reliability, and to assure the continued high availability of the reactor, the EBR-II Project conducted a comprehensive evaluation of the response of the EBR-II steam-generator system to postulated failure events. This evaluation resulted in recommendations of preventive and protective actions, including modifications to the system, which would assure that credible failure events would not lead to reactor downtimes in excess of three months. This paper summarizes the analysis made of the fail-safety of the system and throws light upon some significant questions facing designers of steam-generator systems for liquid-metal fast breeder reactors (LMFBRs).

The analysis was conducted within the two established structural-integrity concepts of safe-life and fail-safety<sup>(2)</sup>. Limited elevations of safe-life were conducted to define credible failure-initiating events for use in subsequent detailed analyses of fail-safety. The evaluations of safe-life and the operating philosophy for EBR-II led to the establishment of the following ground rules for conducting the fail-safe analysis of the steam-generator system.

1. Three credible failure-initiating events are postulated: A spontaneous leak in the steam tubesheet, a spontaneous leak in the sodium tubesheet, and a spontaneous through-the-wall crack in the duplex tube. All three events are postulated for evaporators and superheaters during both reactor operating and standby conditions, since the consequences differ for the two conditions.

2. The end states to which failure may be permitted to propagate are limited such that: (a) there shall be no injury to personnel, (b) there shall be no damage to the intermediate heat exchanger (IHX); and (c) the damage to the components of the steam-generator system can be repaired within three months.

3. The reactor should be capable of continued safe and reliable operation within three months after the failure.

Following these ground rules, evaluations and analyses of fail-safety were conducted to obtain the information required to construct fault trees and accident-progression diagrams for the steam-generator system. Significant analyses and evaluations are summarized in the subsequent sections of this paper.

### HYPOTHESIZED LEAK RATES AND SODIUM-WATER REACTION RATES

#### Leak Rates

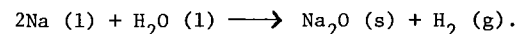
Stress and fracture-mechanics analyses of the duplex tubes demonstrate that instantaneous critical fracture, rupture, or shear of the tube is incredible<sup>(3)</sup>. In the unlikely event that an inherent flaw propagates, it is expected to cause a pinhole leak due to subcritical crack propagation and advance micro-cracking<sup>(4)</sup>; however, additional work is required to confirm this hypothesis.

The tubesheets were not analyzed, and it is assumed that leaks in them would be similar to pinholes. Furthermore, the consequences of a leak in a tubesheet are significantly milder than those of a leak in the duplex tube.

It is hypothesized that the thermal, erosive, and corrosive effects of a sodium-water reaction will enlarge a pinhole in a duplex tube by self-wastage and adjacent-tube wastage<sup>(5,6)</sup>. The leak progression described by the dotted lines (Curve A) in Fig. 1 were based upon the mechanism of wastage, using data given in Ref. (6). The leak progression rates shown by curves B and C envelop conservatively the expected leak-progression rates in an EBR-II superheater and an evaporator, respectively. These rates were used in subsequent calculations of pressures in the secondary sodium network. For the same leak diameter, the discharge rates are higher in an evaporator because the water or steam density is higher.

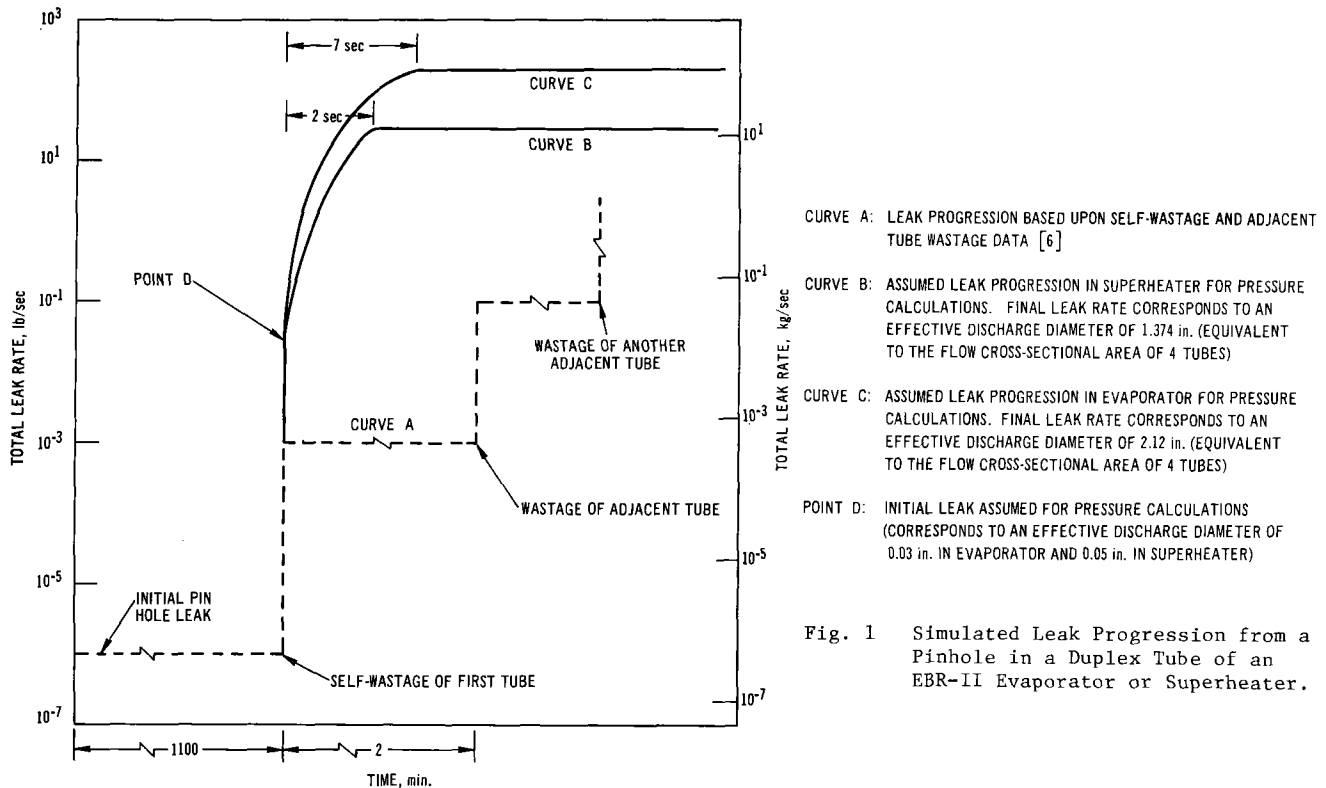
#### Sodium-Water Reaction Rates

Leak rates for steam and water were used to determine sodium-water reaction rates in a superheater and an evaporator. The reaction used as a basis was



The rate of this reaction, which occurs above 316°C (600°F), in excess sodium is limited by the transport of reactants to the reaction site. The hydrogen produced, which reacts only slowly with sodium, may separate the reactants and impede the reaction. Such impedance is conservatively ignored in this investigation.

\* Work supported by the U.S. Energy Research and Development Administration.



For very small leaks, the pressure in the sodium system can rise only after the sodium is saturated with hydrogen. Based on the stoichiometry and the solubility of hydrogen in sodium, it was determined that approximately 1,000 hrs would be required to reach saturation at a constant leak rate of  $0.454 \times 10^{-6}$  kg/sec ( $10^{-6}$  pounds of water/sec). Wastage data show that at this leak rate the duplex tube would self-waste in 17 hr, well before the sodium system pressure rises. Thus small leaks that are not critical by themselves would, as a result of a sodium-water reaction, enlarge to large leaks and thus lead to increasing system pressure. Such leaks are characteristically different, in their progression as well as in their effects, from those resulting from instantaneous rupture of a tube, as is shown later.

#### ANALYSIS OF THE SECONDARY SODIUM NETWORK

The pressure buildup at the site of the sodium-water reaction was expressed analytically through a bubble model based upon mass balance, energy balance, and water leak rates. This model was combined with the one-dimensional hydrodynamic equations to compute the pressure distribution in the sodium system<sup>(7,8)</sup>.

The secondary-sodium system was represented by the network model shown in Fig. 2. Based on the simulated leak progression rates given by curves B and C in Fig. 1, network pressures were computed for a leak in a superheater and in an evaporator from up to four failed duplex tubes. The resultant pressure-time history for a leak in a superheater is shown in Fig. 3. Significant results obtained by the simulated leak progression model are summarized in Table 1. Maximum shell and piping pressures are below 2.76 MPa (400 psi) for failure in a superheater and below 3.58 MPa (520 psi) for failure in an evaporator. In both cases the

maximum pressure in the IHX is below 1.03 MPa (150 psi). By contrast, maximum shell pressures due to an instantaneous guillotine failure of a single duplex tube in a superheater were computed to be as high as 13.72 MPa (1990 psi). For comparison, results obtained by the guillotine model also are shown in Table 1.

Figure 4 shows the influence of an instantaneously initiated leak in a superheater, which remains of constant size, on the maximum pressures experienced within the system and on the time at which a rupture disk would open. It is seen that an instantaneous leak from a hole with a diameter of 0.648 cm (0.255 in.) yields a maximum shell pressure of 2.74 MPa (397 psi). This is equal to the maximum shell pressure obtained due to a much larger leak that has grown gradually from a diameter of 0.127 cm (0.05 in.) to a diameter of 3.49 cm (1.374 in.) - a leak area equivalent to the cross-sectional area of four duplex tubes. The results suggest that even if only a fraction of a second elapses between leak initiation and the occurrence of a large leak (equivalent to that from one or more tubes), the resulting system pressures would be significantly less than those resulting from an instantaneous large leak. Thus it appears that the assumption of an instantaneous guillotine failure results in unrealistically high predictions of system pressures.

Analyses also were conducted for the EBR-II secondary system with an additional rupture disk installed between the superheaters and the IHX as shown in Fig. 2. The addition of this disk did not reduce the maximum pressure in a superheater shell resulting from a guillotine failure of a single duplex tube in the superheater. However, the pressure at the IHX was reduced from 6.76 MPa (980 psi) to 0.76 MPa (110 psi), suggesting the value of such an installation

## INTERNATIONAL CONFERENCE ON LIQUID METAL TECHNOLOGY IN ENERGY PRODUCTION

in preventing failure of the IHX. The influence of installing rupture disks on the superheater and evaporator shells and other sodium network investigations are reported in Ref. (8).

The dynamic stresses in the secondary-sodium piping and the superheater and evaporator shells based upon the pressures resulting from the simulated leak rates shown in Fig. 1 were found to be less than approximately half the yield strength of the 2 1/4 Cr-1 Mo material. This indicated that dynamic structural failure in the sodium network was not a likely event based upon the assumed leak progression rates.

### RESPONSE OF THE STEAM-GENERATOR SYSTEM

The consequences of the three postulated failure initiating events on the existing steam-generator system were analyzed with system fault trees and accident-progression diagrams along with the detailed analytical investigations described in the previous section. Reactor operating and standby conditions were both considered since the consequences differ in the two cases. During plant standby, the steam header is isolated, the steam drum contains 76.2 cm (30 in.) of water, and the pressurized vent valve is available for use. During plant operation, the steam

header is pressurized, the steam drum contains 45.7 cm (18 in.) of water, and the main condenser cooling system and main cooling tower are in operation. Progression of a sodium-water reaction in each case leads to the emergency procedure outlined in the accident-progression diagram shown in Fig. 5.

The fault trees and accident progression diagrams constructed yielded six significant failure events or transitional states of the system, each of which would render the system inoperable<sup>(9)</sup>. Due to limited space, the detailed trees and diagrams are not presented, but the significant results are summarized in Tables II and III. The fault trees were not evaluated quantitatively to obtain probabilities of occurrence of various events or system reliability due to the absence of adequate experience with such systems.

Table II defines the six significant failure events, and gives the principal causes for these events and the recommended actions to mitigate the consequence of them. It is seen that early leak detection and rapid separation of sodium and water are key elements of a fail-safe steam-generator system. The table suggests the modifications that may be made to the system and to the emergency procedures to assure that the end states to which the system may

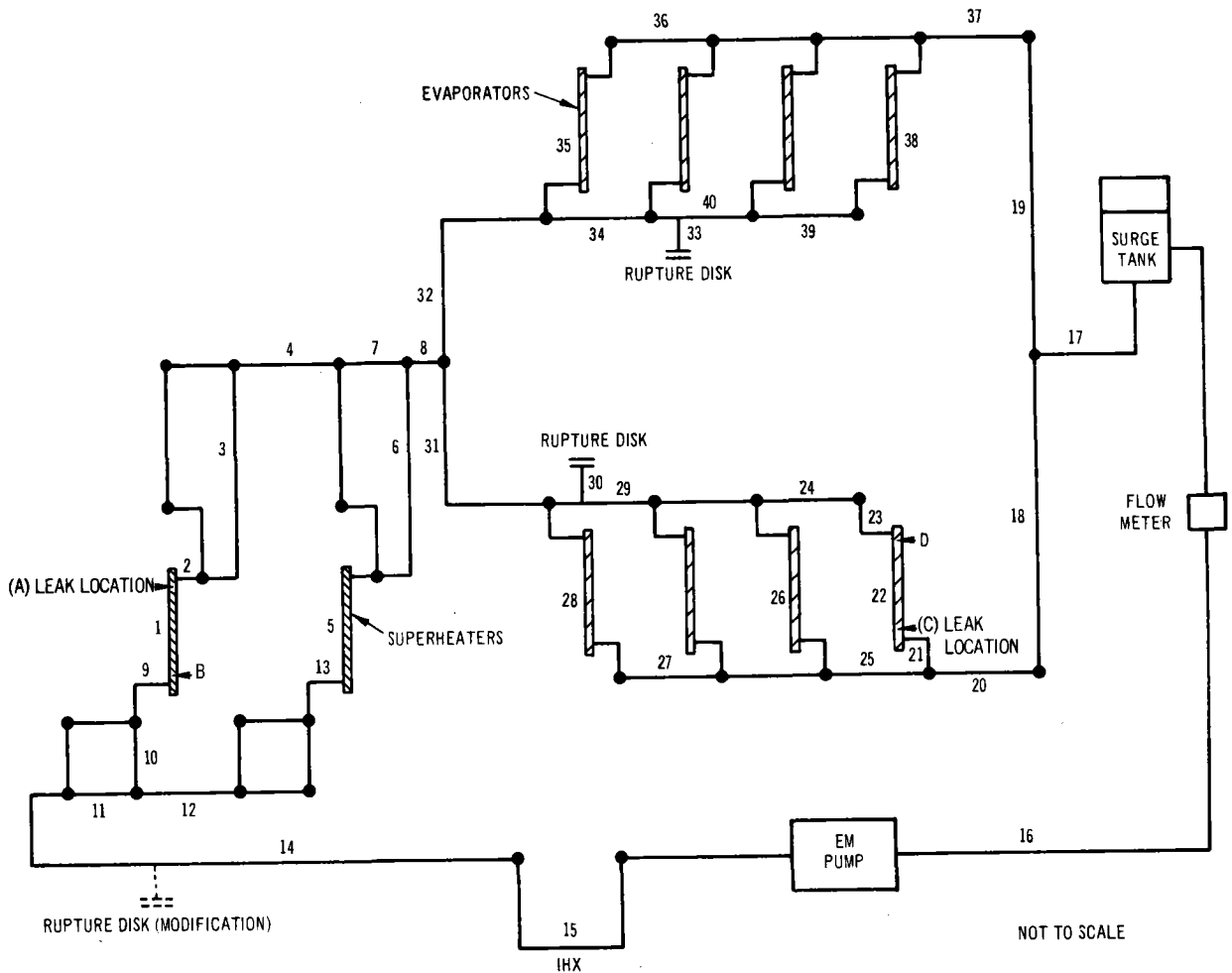


Fig. 2 Network Model used for Calculating Pressures in the EBR-II Secondary Sodium.

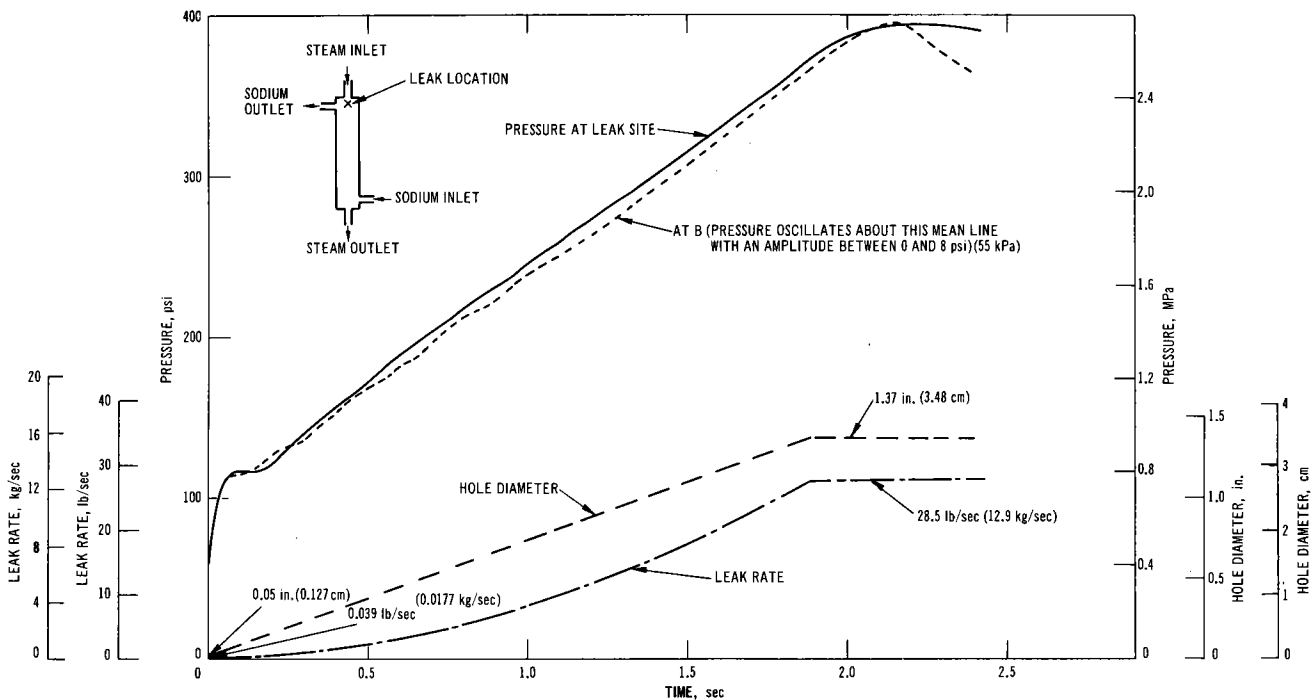


Fig. 3 Calculated Pressures in an EBR-II Superheater Shell due to the Progression of a Non-instantaneous Leak in the Superheater.

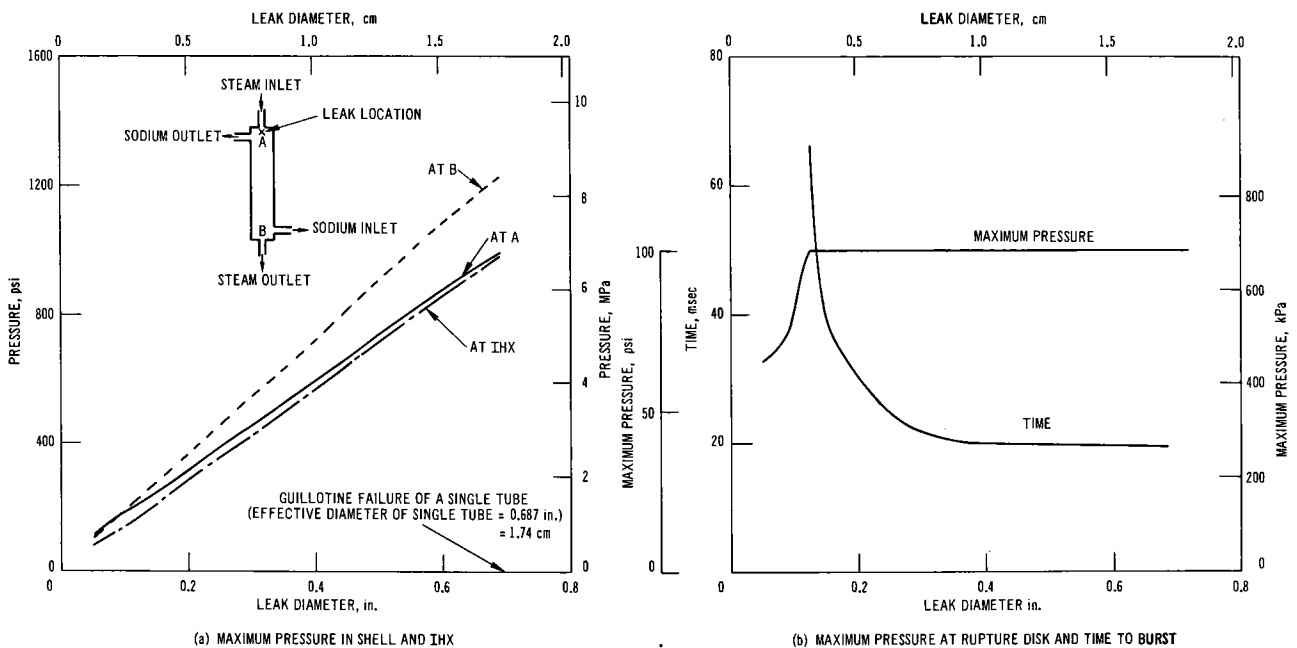


Fig. 4 Calculated Maximum Pressures in an EBR-II Superheater, the Intermediate Heat Exchanger (IHX) and at the Rupture Disk, and the Time Required to Burst a Disk, as a Function of the Size of a Constant Leak in the Superheater.

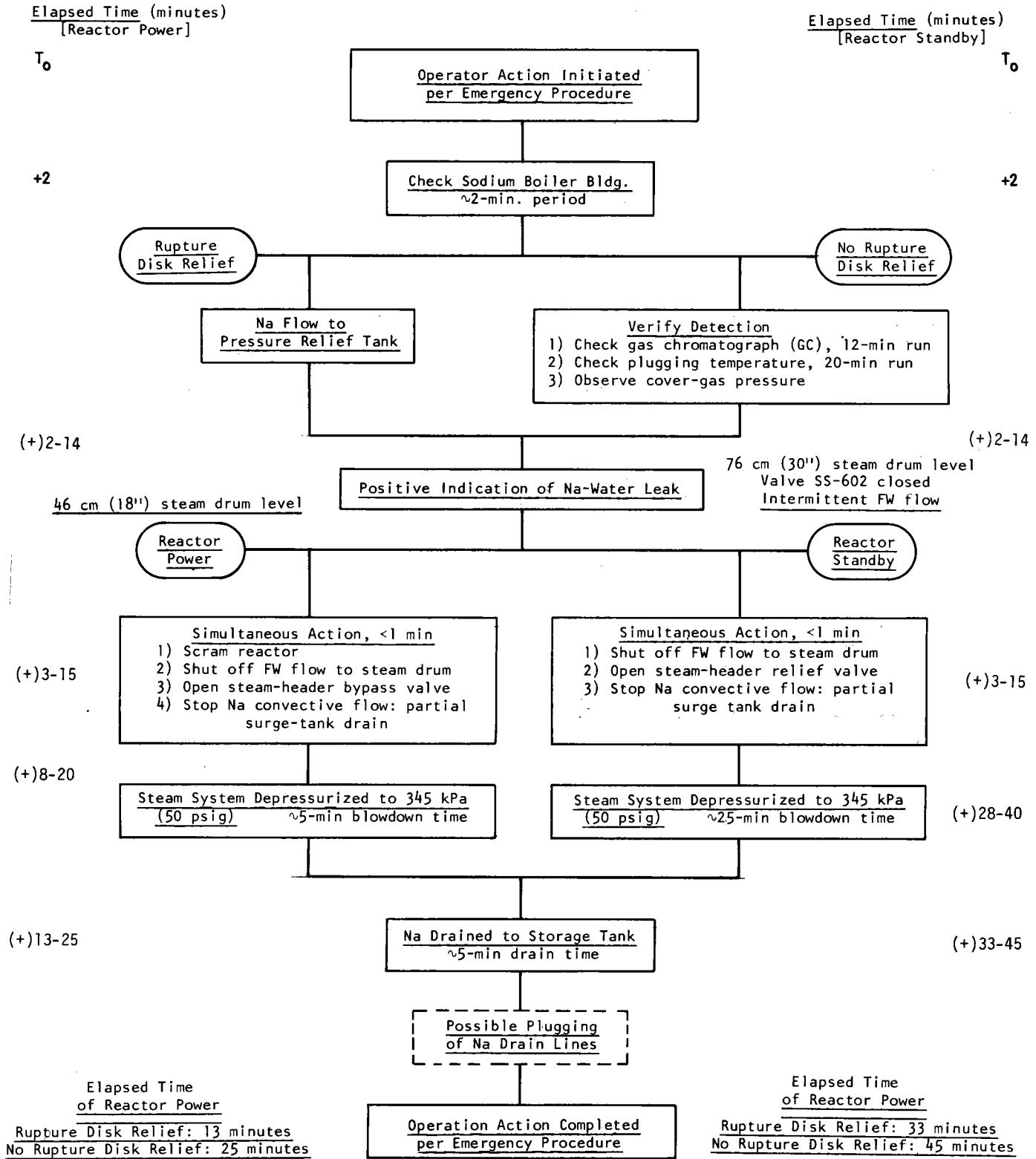


Fig. 5 Events Following a Sodium-Water Reaction in the EBR-II Steam-Generator System.



# INTERNATIONAL CONFERENCE ON LIQUID METAL TECHNOLOGY IN ENERGY PRODUCTION

TABLE I. Maximum Shell and Piping Pressures Following a Sodium-Water Reaction in an EBR-II Superheater or Evaporator.

	Failure in Superheater		Failure in Evaporator	
<u>Noninstantaneous Leak Progression (up to four duplex tubes failed)</u>				
Max pressure in shell near leak location, MPa (psi)	2.71	(393)	3.56	(517)
Max pressure in shell remote from leak location, MPa (psi)	2.74	(397)	3.39	(492)
Max pressure in IHX, MPa (psi)	0.92	(133)	0.57	(83)
<u>Guillotine Failure of a Single Duplex Tube</u>				
Max pressure in shell near leak location, MPa (psi)	6.82	(990)	11.17	(1620)
Max pressure in shell remote from leak location, MPa (psi)	8.48	(1230)	13.72	(1990)
Max pressure in IHX, MPa (psi)	6.76	(980)	0.62	(90)

TABLE II. Postulated Failures in the EBR-II Steam-Generator System, Their Causes, Corrective Measures and Recommended Actions.

Failure Event	Primary Causes	Corrective Measures	Recommended EBR-II Actions
(i) Physical damage to tubesheets and steam tubes in the tubesheet plenum	Sodium fire in the tubesheet plenum due to a leak of sodium into the plenum.	Early detection of sodium leaks in the tubesheet plenum followed by rapid dump of sodium.	Installation of on-line tubesheet-leak-detection system.
(ii) Physical damage to duplex tubes	Tube wastage due to sodium-water reaction resulting from a leak in a duplex tube.	Early detection of duplex-tube leaks and rapid separation of sodium and water.	Installation of HMLDs, rapid water and steam dump and nitrogen purge system and modified emergency procedures.
(iii) Physical damage to steam-generator shell	Shell wastage due to sodium-water reaction resulting from a leak in a duplex tube.	Installation of shell liners. <sup>a</sup> Early detection of duplex leaks and rapid separation of sodium and water.	Installation of HMLDs, rapid water and steam dump and nitrogen purge system and modified emergency procedures.
(iv) Physical damage to the steam system	Sodium fire and explosive forces due to sodium-water reaction resulting from a leak in a duplex tube. Corrosive contamination.	Early detection of duplex-tube leaks and rapid separation of sodium and water.	Installation of HMLDs, rapid water and steam dump and nitrogen purge system and modified emergency procedures.
(v) Damage to the IHX	Presence of corrosive reaction products in the stainless steel IHX by pumped circulation or by a large pressure pulse following a sodium-water reaction.	Early detection of duplex-tube leaks and rapid separation of sodium and water. Provision of a rupture disk and reaction-products relief line between superheaters and IHX.	Installation of HMLDs, rapid water and steam dump and nitrogen purge system and modified emergency procedures. Installation of a rupture disk between superheaters and IHX and a reaction-products relief line.
(vi) Plugging of sodium lines	Prolonged presence of reaction products in the sodium lines.	Early detection of duplex-tube leaks and rapid separation of sodium and water to limit the quantity of reaction products.	Installation of HMLDs, rapid water and steam dump and nitrogen purge system and modified emergency procedures.

<sup>a</sup> Not practical for an operating steam-generator.

**INTERNATIONAL CONFERENCE ON LIQUID METAL TECHNOLOGY IN ENERGY PRODUCTION**

TABLE III. Response of the Present and Modified EBR-II Steam-Generator System to Postulated Failures.

Failure Initiating Event	Response of Existing System	End State of Existing System	Response of Modified System	End State of Modified System
Failure of a duplex tube in an evaporator or a superheater	<p>During Plant Standby approximately 30 to 45 min are required to complete all steps of emergency procedure 3-8.</p> <p>During Power Operation approximately 15 to 25 min are required to complete EP 3-8. Evaporators would be half full of water, steam-drum pressure would be 345 kPa (<math>\sim 50</math> psig), temperatures of evaporators and superheaters would be <math>149^{\circ}\text{C}</math> (<math>\sim 300^{\circ}\text{F}</math>). All sodium-system heaters would be deenergized and sodium drained to the storage tank.<sup>a,b</sup></p>	<p>Water would remain in the evaporators and could continue to leak into the sodium side of the system.<sup>b</sup> The drain valves leak when closed, so water leaking from the failed duplex tube could drain to the storage tank, resulting in continued sodium-water reaction with possible plugging of the drain-tank outlet lines and corrosion of the stainless steel tank. Failure of a duplex tube could produce massive reaction-product contamination and corrosion of the stainless steel IHX and piping.</p>	<p>Leaks, in the range of <math>1.36 \times 10^{-6}</math> to <math>1.82 \times 10^{-6}</math> kg/sec (<math>3 \times 10^{-6}</math> to <math>&lt; 4 \times 10^{-4}</math> lbs/sec) would be detected by HMLD <math>\sim 15</math> to 20 min before adjacent-tube wastage. Leak rates <math>1.36 \times 10^{-6}</math> kg/sec (<math>&lt; 3 \times 10^{-6}</math> lbs/sec) would not cause HMLD alarm prior to self-wastage. If these leaks enlarged gradually, they may be detected <math>\sim 15</math> to 20 min prior to adjacent-tube wastage. Leak rates <math>1.82 \times 10^{-6}</math> kg/sec (<math>&gt; 4 \times 10^{-4}</math> lbs/sec) would cause adjacent-tube wastage in 1 to 90 min depending on whether the leak is in a superheater or evaporator and the plant at power or standby. An HMLD alarm would occur in <math>\sim 5</math> min unless the automatic rupture disk bursts. Simultaneous, emergency action would permit depressurization and drainage of water and Na in <math>\sim 5</math> min with disk relief and in <math>\sim 15</math> min after alarm.</p>	<p>The system would be depressurized, drained of water, and isolated from the power plant. The failed steam-generator module would be drained of Na, depressurized and drained of water, and contaminated with Na-water reaction products. The secondary Na system would be drained of Na &amp; contaminated with Na-water reaction products. No structural damage and minimal contamination of the IHX.</p>
Failure of a water tube sheet or tube in an evaporator or a superheater	<p>Steam would enter the tube-sheet plenum. If the leak were small, long-term galvanic corrosion could occur inside the tubesheet plenum. A large leak could expel steam through the tube-sheet inspection ports and might cause personnel injury.</p>	<p>Periodic visual inspection by operators would permit the prevention of long-term galvanic corrosion.</p>	<p>Same as for existing system.</p>	<p>Same as for existing system.</p>
Failure of a sodium tubesheet in an evaporator or a superheater	<p>Sodium would enter the tube-sheet plenum, and a sodium fire would occur and could damage the sodium and water tubesheets and the steam tubes between the tubesheets. Na could be expelled through the tubesheet inspection ports. Eventual detection would be either visual or by an alarm from smoke detectors resulting in emergency actions. One of four actions: push the "Fire" or the "Emergency" button, scram the reactor, drain the Na to the storage tank, or activate the sodium fire extinguishing system.</p>	<p>The steam-generator unit could be severely damaged, with possible damage to other components and a fire in the sodium boiler building.</p>	<p>The proposed leak-detector system for tube-sheet plenum will provide early detection of a spontaneous leak in the Na tube-sheet to tube-to-tubesheet weld. Corresponding operator action would still be initiated as for the existing system.</p>	<p>The advantage of early detection is to allow earlier drainage of Na to the storage tank and thereby reduce the possibility of physical damage to the tube-sheets and the steam tubes between the tube-sheets by a Na fire within the tubesheet plenum.</p>

<sup>a</sup> If the leak is sufficiently large, and timely detection and corrective action is not taken, the drain and vent lines may plug, thereby precluding the draining of Na after a leak is detected.

<sup>b</sup> Approximately 13.6 kg (30 lb) of Na remains in each evaporator and superheater after the Na system is drained.

## INTERNATIONAL CONFERENCE ON LIQUID METAL TECHNOLOGY IN ENERGY PRODUCTION

progress following a postulated failure are acceptable. In particular, protection of the IHX and other stainless steel components can be assured by judicious location of rupture disks and reaction-products relief lines. It is seen also that a duplex-tube leak during plant operation would result in less severe consequences than a similar leak during plant standby. This is due to possible earlier detection and additional steam-venting capability through the condensers during plant operation.

Table III compares the response of the steam-generator system, with and without the corrective modifications shown in Table II, to the three failure-initiating events studied. As expected, the modified system has a significantly higher degree of fail-safety. However, since it is hypothesized that a sodium-water reaction would occur, limited damage to a steam-generator cannot be precluded, even in the modified system.

To meet the objective of continued safe and reliable operation of the steam-generator system within three months following a sodium-water reaction, several contingency plans have also been implemented. These plans include design, analyses and material procurement for bypassing the superheater or blocking of two evaporators in the system in the event of damage to either unit, and establishment of procedures for repair and cleanup of individual components and the system. In addition, nondestructive testing and general surveillance of the system are continuing.

### DISCUSSION AND CONCLUSIONS

The analyses of fail-safety presented here for the EBR-II steam-generator system were accomplished by a synergism of various elements of steam-generator system design, analysis, operation, modification, and repair. The system, designed to provide safe-life operation, has performed successfully for more than 10 years. However, to assure the continued total availability of the system, it was considered desirable to make changes to the system and its operating emergency procedures as suggested by the current fail-safe analyses.

Our experience has shown that it is considerably easier to design a fail-safe system initially rather than to modify a similar existing safe-life system to assure fail-safety. For example, it is relatively simple to include, in a new design, protective liners for steam-generator shells, whereas it is impractical to retrofit liners. In order that fail-safe design may not become an unacceptable economic burden, an optimum degree of safe-life must be built into the system. Such safe-life is provided to the EBR-II system by the unique duplex concept. The duplex design not only lowers the probability of occurrence of a sodium-water reaction by providing a double barrier between the two reactants, but also minimizes the consequences of such a reaction by retarding the crack propagation rates through the duplex walls. This, along with the analyses conducted, provides the necessary confidence that instantaneous large leaks of steam or water into sodium are not credible for EBR-II steam-generators. Once this confidence is established for other LMFBR steam-generators, designers can divert their attention from economically prohibitive concepts aimed at withstanding large sodium-water reactions and can instead focus upon designing the system to respond rapidly to small and moderate reactions.

With this philosophy, the important fail-safe elements of the EBR-II steam-generator system become

common to other existing and planned sodium-to-water steam-generator systems. The present analyses demonstrate that the key fail-safe elements of such systems are: early detection; rapid separation of reactants; provision of rupture disks and relief lines; and procedures for cleanup and repair.

### ACKNOWLEDGEMENTS

The authors appreciate the contributions made by members of a special EBR-II Steam-Generator Task Group who collectively completed the various investigations described in this paper.

### REFERENCES

1. Anon., Proc. of the US/USSR Seminar on the Development of Sodium-Cooled Fast Breeder Reactor Steam Generators, Vol. 1, Los Angeles, Dec. 1974.
2. P.S. Chopra, Ed., *Fatigue and Fail-Safe Training Manuals*, Concepts and Terminology, Vol. 1, Boeing Document D6-30681-1, Seattle, Dec. 1970.
3. T.S. Wu and P.S. Chopra, *Fracture Mechanics Analysis of EBR-II Steam Generator Duplex Tubing*, Trans. ANS 1975 Winter Mtg., San Francisco, Nov. 1975 (p. 225).
4. F.A. McClintock and G.R. Irwin, *Plasticity Aspects of Fracture Mechanics*, Fracture Toughness Testing and its Application, ASTM STP 381, April 1965 (pp. 84-128).
5. A.S. Mazanov, B.V. Kulpin, V.P. Petukhov and N.M. Ledovskikh, *Investigation of Failure in Various Steels Caused by a Sodium-Steam Reaction Jet*, Proc. US/USSR Seminar on the Development of Fast Breeder Reactor Steam Generators, Los Angeles, Dec. 1974.
6. D.A. Green and D.W. Sandusky, *Small Leak Damage and Behavior Test Results*, Proc. US/USSR Seminar on the Development of Fast Breeder Reactor Steam Generators, Los Angeles, Dec. 1974.
7. Y.W. Shin, *The Method of Characteristics for Analysis of Pressure Transients Resulting from Sodium-Water Reaction in Hydraulic Networks*, ANL-8049, (1973).
8. S. Srinivas and P.S. Chopra, *Analysis of EBR-II Secondary Sodium Network for Pressure Pulses due to Leaks of Steam or Water into Sodium*, communicated for publication in Nuclear Eng. & Des., April 1976.
9. G.C. Wolz, C. Gukeisen and P.S. Chopra, *Events Following Postulated Failures in the EBR-II Steam Generator System*, to be presented at 1976 ANS Summer Mtg., Toronto, June 1976.

# INTERNATIONAL CONFERENCE ON LIQUID METAL TECHNOLOGY IN ENERGY PRODUCTION

## SODIUM AND STEAM LEAK SIMULATION STUDIES FOR FLUIDIZED BED STEAM GENERATORS

A.R. Keeton, W.G. Vaux, P.K. Lee, and R.E. Witkowski  
Westinghouse Research Laboratories  
Pittsburgh, Pennsylvania 15235

### ABSTRACT

An experimental program was conducted designed to study the effects of sodium or steam leaking into an operating fluidized bed of metal or ceramic particles at 680 to 800°K. This effort was part of the early development studies for a fluidized-bed steam generator concept using helium as the fluidizing gas. Test results indicated that steam and small sodium leaks had no effect on the quality of fluidization, heat transfer coefficient, temperature distribution, or fluidizing gas pressure drop across the bed. Large sodium leaks, however, immediately upset the operation of the fluidized bed. Both steam and sodium leaks were detected positively and rapidly at an early stage of a leak by instruments specifically selected to accomplish this.

### INTRODUCTION

A fluidized bed steam generator (FBSG) has been under development at Westinghouse as an alternate steam generator for liquid metal fast breeder reactors (LMFBRs). This steam generator concept allows heat to be transferred from sodium piping to steam piping through a fluidized bed of particles in an inert gas environment. This scheme enhances both the reliability and safety of the component by making sodium-water reactions very unlikely. Fluidized bed steam generator concepts and a preliminary design for a fluidized-bed steam generator for the LMFBR have been previously reported<sup>(1,2)</sup>. A schematic for the basic system is shown in Figure 1.

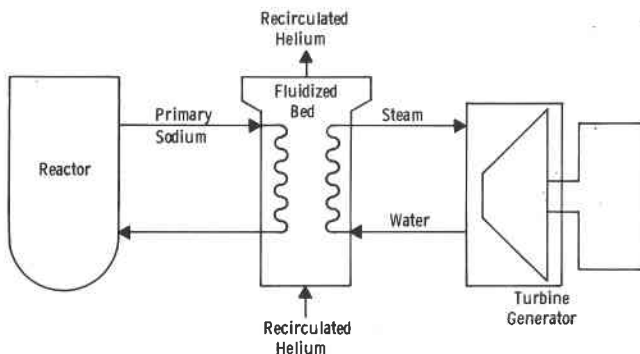


Fig. 1 - Fluidized bed steam generator

Among the important factors which must be evaluated for this steam generator approach are the effects of sodium and/or steam leaks into the fluidized bed and the ability to achieve early detection of a leak. These factors must be understood in order to establish design criteria and operating procedures.

An experimental test program was conceived to investigate the effects of sodium, steam, and water leaking into an operating fluidized bed of sufficient size to provide meaningful engineering data. Two candidate bed materials, magnesia and nickel powders, were selected for use in the study. Helium was the fluidizing gas selected, and fourteen simulated leak tests were conducted. These ranged from low-volume

steam and sodium tests, simulating small cracks or pin-hole leaks, to massive leaks that simulated the complete failure of a heat exchanger tube. This paper describes the test equipment, the test procedure, and the results of the study.

### TEST APPARATUS

#### Test Equipment

The fluidized bed test apparatus consisted of a cylindrical, stainless steel vessel approximately 0.36 m in diameter and 0.61 m high (Figure 2). Either

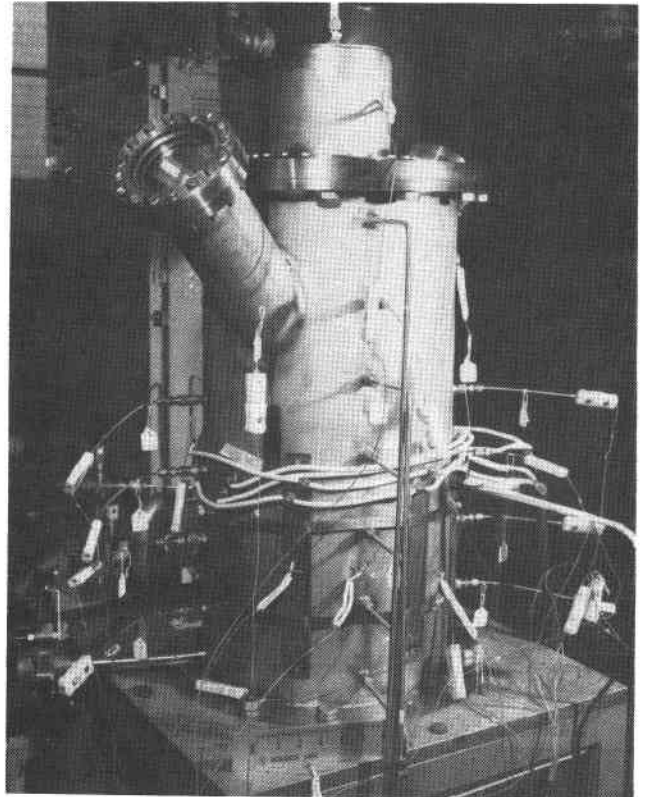


Fig. 2. Fluidized bed leak test apparatus (without insulation).

magnesia or nickel powder filled the bed to a height of 0.41 m and was prevented from sifting into the gas inlet plenum by a layer of 400 mesh screen covering the gas distributor plate. Pressure and temperature sensors were located at various axial and radial positions around the bed. Two sight ports, 180° apart, allowed direct illuminated viewing of the top of the bed.

The bed was heated externally through the vessel with electrical resistance heaters (shown in Figure 2) and also by preheating the incoming helium gas. An injection nozzle for simulating the leaks, consisting of a series of small diameter holes in a tube, was placed at the approximate center of the bed. An immersion heater with appropriate temperature sensors was located within the bed for monitoring heat transfer coefficients. Figure 3 schematically represents the fluidized-bed test system. The sodium injection

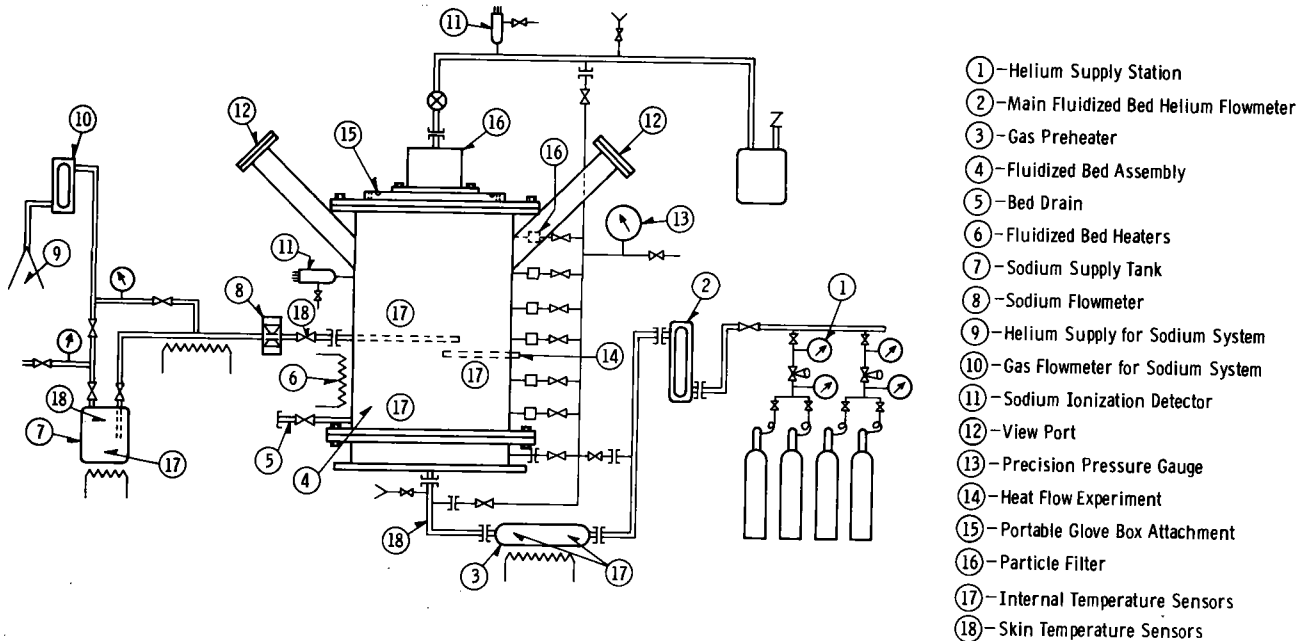


Fig. 3 - Fluidized bed system for sodium & steam leak experiment

and monitoring system is shown attached to the bed. When steam or water was being injected, the sodium system was disconnected, and the steam/water system, including a flowrate meter, was connected. A sintered-metal filter located at the top of the bed prevented loss of bed power through carryover with the effluent gas.

Two Westinghouse Sodium Ionization Detectors (3,4) (SIDs) were used to monitor sodium leaks. One of these was located immediately above the fluidized bed and the other was placed downstream from the main gas filter. A steam leak detector was located in the pressure-sensing manifold, so that any pressure port could be monitored for moisture. A Panametrics™ Model 1000 Hygrometer was used for this purpose.

Selection of Fluidized Bed Particles

Fluidized bed candidate particles are generally selected by their size, density, flow behavior, mixing rate, heat capacity, and thermal conductivity. For this particular application in a sodium-heated steam generator, in addition to these general requirements, acceptable particles should also be reasonably inert and compatible with sodium and steam at the operating temperatures, so that the bed system can continue near-optimum behavior in case of a small and tolerable leak in either tube bundle of the steam generator system.

An extensive literature review was made of a number of particle candidates according to their physical and chemical properties. From this review it was concluded that particulates of iron, nickel, stainless steel, aluminum oxide, magnesium oxide, and certain nickel alloys were the potential candidates for the fluidized-bed steam generator. Further screening of these candidate particles was based on the results of our compatibility tests.

Rapid screening compatibility tests for the above-mentioned particulates, except nickel alloys, were carried out in a static nickel capsule with

saturated sodium vapor at 873°K and with steam pressure of 1.013-1.419 MPa at 773°K. Post examinations of these tested particles were made by sieving (for caking and agglomeration, a result of wetting) and by optical and scanning electron microscopy or x-ray diffraction analysis (for surface reactions). Results indicate that only particles of nickel, aluminum oxide (fused), and magnesium oxide (heavy-duty) showed no caking and no reaction with either sodium vapor or steam under the severe testing conditions. Iron and stainless steel particulates showed no interaction with sodium vapor, but were severely oxidized by steam, and are not good candidates. Therefore, for this program, nickel and (fused) magnesium oxide were selected as the bed materials.

TEST PROCEDURE

The overall objectives of the test program were to provide design and operating criteria and to identify potential problems associated with leaks in a fluidized bed steam generator. Specific objectives were: (1) to determine the effects of sodium or steam leaking into operating fluidized beds of two candidate materials -- nickel and fused magnesia, and (2) to investigate detection of the leaks.

Tests were conducted by injecting predetermined amounts of sodium, steam, or water into the operating bed. Pertinent data were recorded before, during, and after injection. Upon completion of a test, the bed was cooled to room temperature, and samples of bed particles from selected locations were analyzed for physical and chemical changes.

A typical test began by filling the bed with the selected material. Nickel powder was charged to the bed in the as-received condition. Since 30% by weight of the magnesia consisted of particles smaller than 44 microns, magnesia powder was added to the bed and the fines were blown from the powder before tests began. The bed was fluidized by flowing helium up through the distributor plate at the bottom of the vessel. Pressure distribution throughout the bed was

recorded over a gas velocity range from 4 to 21 cm/s. Figure 4 shows pressure profiles in a bed of nickel powder for various gas flow velocities. The data on sloped portions of the curves correlate well with

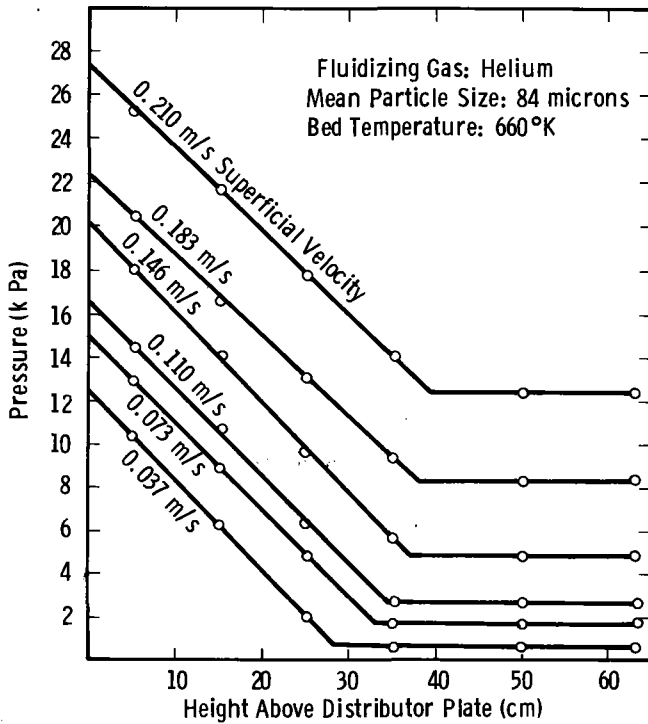


Fig. 4 - Variation of pressure with height above distributor plate in the bed of fluidized nickel

straight lines and give precise values of the pressure at the grid when extrapolated to zero bed depth. The knees of the curve indicate expanded bed depth at various gas velocities.

The bed was heated until temperatures reached steady state at selected temperatures between 680 and 800°K, with the bed fluidized. After recording several replicate data sets covering bed pressures, temperatures, flowrates, cartridge heater power, and leak detector signals, either sodium or steam was injected into the bed to simulate the start of a leak. During and immediately after injection, several more sets of data, including visual observations, were recorded. After cooling, a portable glove box was attached to the top of the bed housing. The bed interior was inspected and the particles were sampled for agglomeration and analysis.

TEST RESULTS

Bed Effects: Simulated Steam Leaks

Four low-level steam leak tests of 0.126 g/s (1 lb/hr) were conducted with fluidized beds of nickel and magnesia. Figure 5 shows the results of one of these tests, which was typical of all. Pressure drop across the bed was very constant with a confidence interval of  $16.91 \pm 0.09$  kPa for all observations. The heat transfer coefficient  $h$  was not significantly altered during the steam leak tests, although there was some variation due to the measuring technique. The increase in heat transfer coefficient and distributor plate  $\Delta P$  was caused by an increase of fluidizing gas flow velocity from 0.049 to 0.067 m/s.

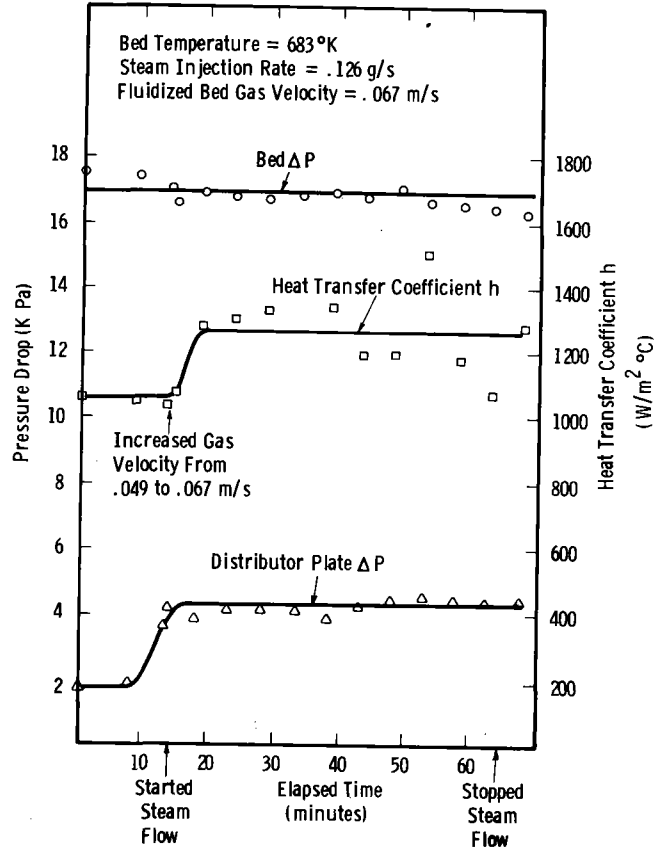


Fig. 5 - Results from simulated small steam leak into fluidized nickel

Four high-level steam leak tests were conducted to simulate massive leaks into beds of nickel and magnesia. In three of these, steam was injected at a rate of 0.756 g/s (6 lb/hr), while in the fourth steam and water were injected at 1.89 g/s (15 lb/hr). Figure 6 shows the results of this fourth test, which was the most severe of the high-level steam leak tests. Inlet water was only partially vaporized to simulate release of water and steam during a tube failure. Liquid water appeared at the bed surface from time to time during the test and evaporated quietly without popping. Although there was considerable scatter in the data, the trends indicated no change in heat transfer coefficient or pressure drops because of the simulated massive steam leak. The heat transfer coefficient averaged  $2157 \text{ W/m}^2\text{°C}$  before and during water/steam injection. The increase, compared with the previous test (Figure 5), is attributed to the increased gas flow velocity. Inspection of the bed though the sight glass showed no evidence of agglomerates.

Magnesia and nickel fluidized well at all temperatures up to 811°K. Nickel powder, in the absence of steam, tended to agglomerate weakly above 711°K, if fines were not removed. Removal of fines reduced this tendency.

Results of these tests indicate that neither low-level nor massive steam leaks affected the heat transfer, gas distribution, or quality of fluidization. Water and steam leaks did not cause particle agglomeration; nor did they cause chemical change or surface character change as revealed by x-ray diffraction and scanning electron microscope (SEM) examination.

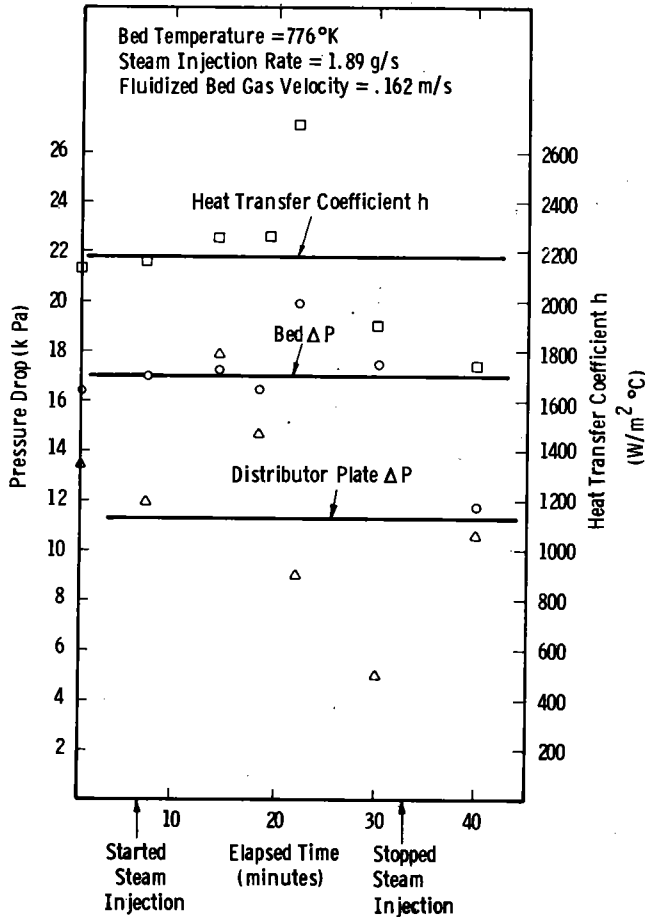


Fig. 6 - Results from simulated massive steam leak into fluidized nickel

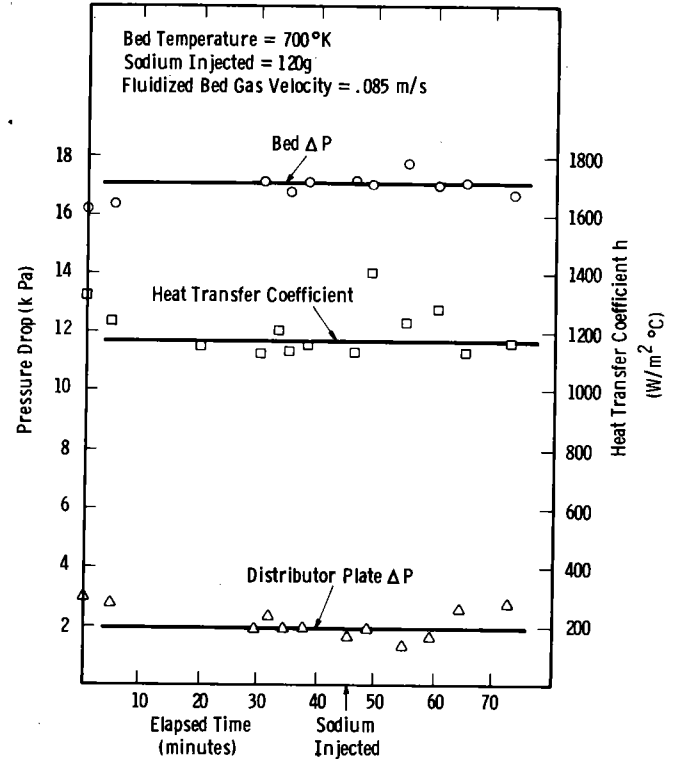


Fig. 7 - Results from simulated small sodium leak into fluidized nickel

Figure 8 shows results of injecting 1.81 kg of sodium into 0.405 m<sup>3</sup> of magnesia (0.043 g Na/g MgO = ~ 4 wt %). This represents a sodium release per unit volume approximately ten times greater than projected for a

Bed Effects: Simulated Sodium Leaks

Sodium leaks of 12 g, 36 g, and 120 g were used during separate tests to investigate the effect of low-level sodium leaks into fluidized beds of nickel and magnesia. These tests represent a small sodium leak from a sodium tube. Results of a typical test are shown in Figure 7, in which the amount of sodium released, 120 g, represents a leak of 2977 g/m<sup>3</sup>, or 0.00066 g Na/g Ni.

Upon addition of the sodium, no visible change in fluidization was immediately evident. No liquid sodium rose to the surface of the bed. Occasional lumps, 6 to 25 mm in diameter, with the appearance of dry nickel, were seen surfacing shortly after sodium injection.

When the cooled bed was opened, nickel powder, agglomerated with sodium, was found in rock-hard balls (typically < 25 mm in diameter; 0.5 to 1.5% Na), soft agglomerates (0.15 to 0.4% Na), and loose powder (0.09 to 0.12% Na). These observations suggest that a small amount of hot sodium injected into a nickel bed is quickly coated with powder before it can adhere to internal metal surfaces. The data show that the nickel, although wetted with sodium, remained granular and fluidized adequately to maintain a high heat-transfer coefficient.

In three tests, massive leaks of sodium were released into beds of nickel and magnesia. For example,

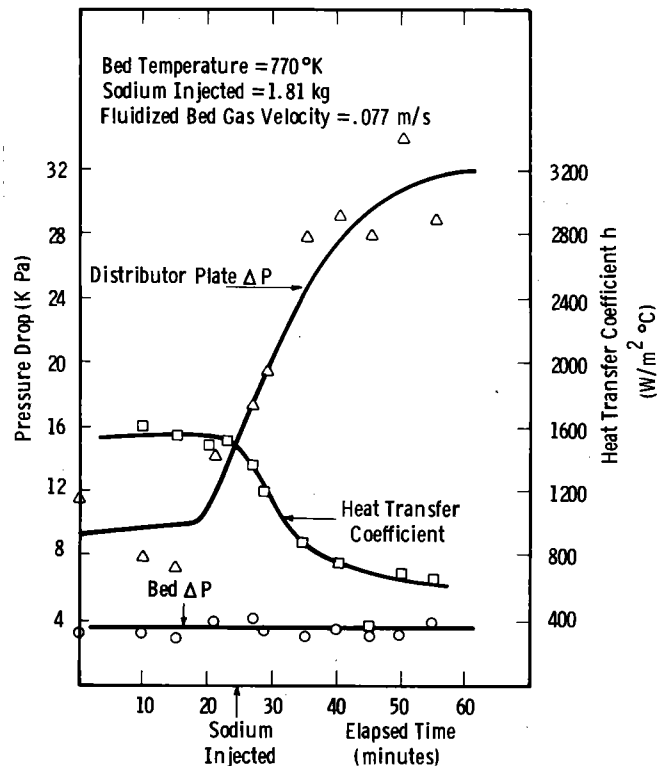


Fig. 8 - Results from simulated massive sodium leak into fluidized magnesia

large-component design. The bed surface was not visible in this test because sodium vapor condensed on the sight port window.

Pressure drop across the fluidized bed remained quite constant, showing that the bed remained fluidized without channeling or becoming rigid. However, the pressure drop across the distributor plate increased from 11.2 to 29.2 kPa, probably from fouling by sodium.

The heat-transfer coefficient  $h$  was quite constant at  $1493 \text{ W/m}^2\text{C}$  in the sodium-free bed; after the large sodium injection, the heat-transfer coefficient decreased erratically to  $681 \text{ W/m}^2\text{C}$  over a 30-minute interval.

Upon disassembling the bed, sodium was found distributed quite uniformly throughout the bed. The cold bed was solidified and contained between 2.9 and 6.2 weight percent sodium. Large hard lumps at the bottom of the bed contained 13.1 weight percent sodium. Seventy percent of the distributor plate holes were plugged.

Results of these tests indicate that small sodium leaks ( $\sim 0.07 \text{ wt } \%$ ) did not affect the fluidized bed operation, although small agglomerates were formed. Large sodium leaks ( $\sim 4 \text{ wt } \%$ ), however, immediately upset operation of the fluidized bed, fouling the distributor plate and lowering heat transfer properties. Sieve analysis, x-ray diffraction and SEM examination of both nickel and magnesia powders showed no substantial change in particle size, composition or surface characteristics because of the sodium tests.

#### Leak Detection

A critical consideration for the FBSG concept is the ability to detect system leaks and thereby prevent sodium-water reactions, which can potentially occur if sequential or concurrent sodium and water/steam leaks happen within a fluidized bed. A simple and reliable leak detection system is essential to alert plant personnel to the onset of either a sodium or water leak, long before a problem situation develops.

If a leak is present on the water/steam-side of a FBSG, the species added to the bed system is water vapor or superheated steam. Alternatively, if a leak is present on the sodium side, sodium may reach the fluidized bed in three possible states; liquid, vapor, and/or aerosol. At temperatures of  $723\text{--}823^\circ\text{K}$ , and under a continuous stream of high purity fluidizing gas, sodium transported within the fluidized bed will be in the vapor state. Because the purity of the gaseous helium within the steam generator may vary during a given time interval, leaking sodium may behave differently at various times. If the helium contains significant quantities of water vapor or oxygen, the sodium will either hydrolyze or oxidize and sodium aerosol, a mixture of sodium-containing compounds, will be formed<sup>(5)</sup>. Consequently, a suitable sodium leak detector for the FBSG should be responsive to both sodium vapor and sodium aerosols.

A Sodium Ionization Detector (SID), currently being developed jointly by the Westinghouse Research Laboratories and the Nuclear Instrumentation and Control Department under contract with ERDA, was selected as the sodium vapor/aerosol detector.<sup>(3,4)</sup> The SID takes advantage of the low ionization potential of sodium ( $IP_{\text{Na}} = 5.12 \text{ v}$ ) relative to helium or impurities that may be present. Sodium vapor is thermally ionized on a hot filament and detected as a

current that is proportional to the number of positive sodium ions reaching a collector plate. Sodium vapor concentrations have been detected as low as  $3 \times 10^{-12} \text{ g Na/cm}^3$ . Studies have also shown that the presence of oxygen (or air) and water vapor in the inert carrier gas affect the sensitivity and response of the detector by less than 10%. Thus, if either  $\text{Na}_2\text{O}$  or  $\text{NaOH}$  reach the SID they will also be detected, yielding a response similar to that of sodium; the compounds will first be dissociated by the hot filament and then the sodium will be ionized.

An instrument manufactured by Panametrics, Incorporated, was selected as the water vapor detector for this study<sup>(6,7)</sup>. This instrument employs a probe-type detector which may be located remotely from the measurement instrumentation. The dynamic detection range of the instrument is 20,000 ppm (v) to about 0.001 ppm (v) water vapor. In a related study, experimental measurements have demonstrated that positive leak detection was achieved for holes in steam generator tubing ranging from  $< 0.1$  to  $0.5 \text{ mm}$  in diameter<sup>(8)</sup>.

Positive detection of both steam and sodium leaks was demonstrated in the test apparatus. Steam leaks were detected in less than 15 seconds by the Panametrics™ Hygrometer, even though the sensor was located three meters from the bed. Sodium leaks were also detected rapidly by both the bed SID and the downstream SID. However, there was a time delay of several seconds to several minutes at the downstream sensor. Figure 9 shows the response time and signal magnitude of the two SIDs when 1.81 kg of sodium was injected into fluidized nickel at  $700^\circ\text{K}$ .

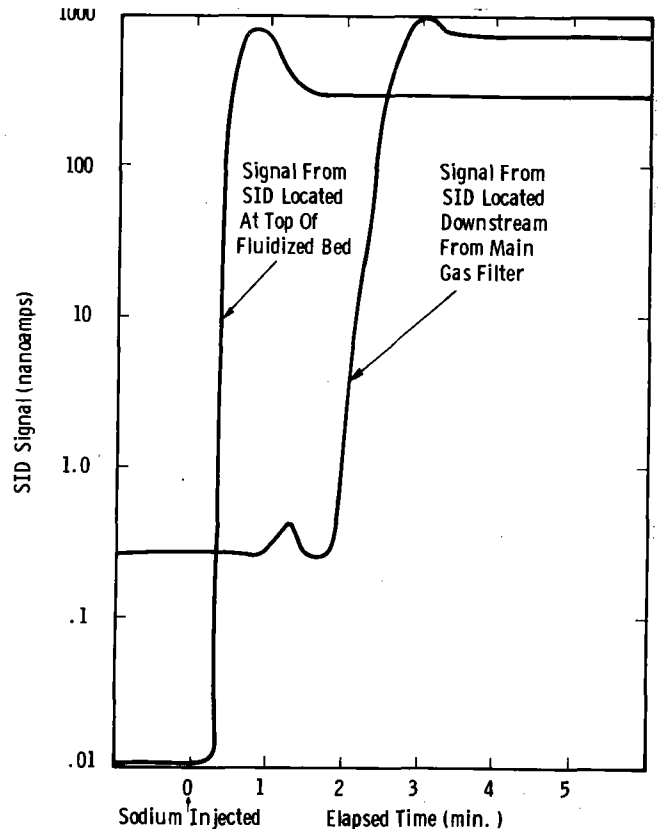


Fig. 9 — Signal generated by sodium ionization detectors (SID) from injection of 1.81 kg sodium into fluidized nickel



## INTERNATIONAL CONFERENCE ON LIQUID METAL TECHNOLOGY IN ENERGY PRODUCTION

Physical location of the SIDs was found to be important to their operation. In initial tests, when the bed sensor was located at the end of a well-filtered line, there was little response to low-level sodium leaks. Relocating the sensor to the top plate of the bed without a filter caused a decisive and rapid response to occur upon injection of sodium. Thus, both steam and sodium leaks were detected rapidly in the fluidized bed test apparatus.

### ACKNOWLEDGMENTS

The Westinghouse Advanced Reactors Division is directing the development of alternative steam generator concepts for the LMFBR. Work on the FBSG concept has been partially funded by the Energy Research and Development Administration since September 1974.

The Authors wish to express their appreciation to Drs. R. A. Newby, and M. H. Cooper for their participation and contributions to the test program, and to A. W. Fellers and A. F. Berringer for their work in obtaining the experimental data.

### REFERENCES

1. Keairns, D. L., Newby, R. A., and Archer, D. H. "Fluidized Bed Steam Generator Concepts for the LMFBR", Proceedings International Fluidization Conference, Engineering Foundation Conference held at Asilomar Conference Grounds, California, June 1975.
2. Keairns, D. L., Newby, R. A., Cooper, M. H., Adkins, C. R., and Bieberbach, G. "Conceptual Design of a Fluidized Bed Steam Generator for the LMFBR", Proceedings 10th Intersociety Energy Conversion Engineering Conference, University of Delaware, August 17-22, 1975.
3. Reed, W. H., Bauerle, J. E., Berkey, E. "A Thermal Ionization-Type Leak Detector for Sodium Vapor and Aerosol", Transactions of the American Nuclear Society, Philadelphia, Pennsylvania, June 23-27, 1974.
4. Reed, W. H., Bauerle, J. E., Berkey, E. "Development of a Sodium Ionization Detector for Sodium-to-Gas Leaks", presented at the ANS International Conference on Liquid Metal Technology in Energy Production, Champion, Pennsylvania, May 3-6, 1976.
5. Davis, K. A. "Sodium Leakage Detection, State-of-the-Art Study", Liquid Metal Engineering Center Memo 69-35, Canoga Park, CA (February 1970).
6. "The Newest Moisture Minder - Model 2000", Technical Bulletin, Panametrics, Inc., 221 Crescent Street, Waltham, MA.
7. "Expanded Scale Option, Model 2000 Hygrometer PN2000-132", Hygrometer Technical Bulletin H-2002, Panametrics, Inc., 221 Crescent Street, Waltham, MA, November, 1973.
8. Lohmeier, A., "February Progress Report on Duplex Tube Third Fluid Leak Detection Steam Generator Development", Westinghouse Contract AT(04-3)-962 under GE Contract AT(04-3)-893, Task 10 LMFBR Steam Generator Development Program, March 22, 1974.

# INTERNATIONAL CONFERENCE ON LIQUID METAL TECHNOLOGY IN ENERGY PRODUCTION

## DISCUSSION

Paper IVA-2: "Investigation of Sodium-Water Reactions at Steam Generator Leaks"

N. Lions: Did you record the water flow rate versus time during self-enlargement tests and did you observe differences between various steels tested?

F. Kozlov: When the nickel content in steel was high, the time for self-enlargement increased.

Paper IVA-5: "Small Leak Shutdown Location and Behavior in LMFBR Steam Generators"

G. Wolz: What are your reasons for not draining Na either during or after steam depressurization since, by separating the reactants immediately, reaction effects are reduced?

D. Sandusky: Such a procedure would be implemented only for very small leaks, those immediately above the detection limit. Our intent was to minimize thermal stresses inherent in rapid removal of steam or sodium for the system. CRBRP allows a finite number of such transients in the life of the plant. Imposition of rapid transients was not considered desirable in the event of these very small leaks.

G. Wolz: Your philosophy apparently requires cooling Na to reduce reaction rates. Yet, while you retain Na in the steam generator because of stress considerations, is it possible that continued reaction during cooldown is more adverse to the generator?

D. Sandusky: The reduced self-damage rate was a fortuitous outcome of cooling the sodium at 110°C/hr (maximum) to minimize thermal stresses. Notice that the leaks in question do not cause impingement wastage of adjacent steam generator tubes and do not generate appreciable amounts of reaction products. Since the leaking tube will be plugged in any case, further damage during a controlled shutdown is not significant if the leak rate remains constant.

Paper IVA-7: "Small Leak Damage and Protection Systems in Steam Generators"

N. Hoffman: Robertson has theorized two temperature-sensitive competitive processes for target wastage but presented as rate vs.  $1/T$  curve with only one slope. You suggest only one process for target wastage, but indicate that one slope illustrating rate vs. time is insufficient to explain the data. Do you consider your data and Robertson's complementary or contradictory?

D. Greene: Data not presented in this report indicate that two competing processes are causing damage. One is corrosion probably present at all temperatures; the other is erosion probably only present within the immediate vicinity of the combustion cone and possibly not present at all sodium temperatures. Data presented on the effect of temperature of 2-1/4 Cr-1Mo, stainless steel, and Inconel 800 indicate a strong effect of tem-

perature on the difference in wastage rates; and a variation that is not constant with temperature. This finding is inconsistent with the prediction proposed by Robertson. It is not inconsistent with the concept that erosion particle formation is dependent sodium temperature, and erosion is associated with the combustion cone.

Paper IVA-9: "Fail-Safety of the EBR-II Steam Generator System"

C. Spalaris: Was your conclusion "double ended or guillotine failures are not likely to occur," based on an analysis of double wall generator tube design or single wall designs?

P. Chopra: The fracture mechanics and stress analyses results presented were based upon EBR-II's duplex tubes. However, credit was not taken for the interface between the two tubes. This interface, if properly designed, could act as a crack retarder or arrestor. Thus, the analyses could be applied directly to single tubes with appropriate changes to account for tube geometry, temperature and internal steam or water pressure.

C. Spalaris: How is conclusive proof that such failures are never possibly achieved?

P. Chopra: To prove that guillotine failures are not possible as an initiating mechanism in any steam generator, it is necessary to check the tube for shear failure or tensile rupture failure caused by axial forces and internal pressure and for failure resulting from flow induced vibration (a problem with the Fermi steam generators not present in EBR-II steam generators). Finally, fracture mechanics analyses must be performed to compute subcritical crack growth rates in the tube from hypothesized "maximum-credible" flaws under the existing steady state and transient loading conditions. Material crack growth data are required in these analyses. If possible, such analyses should be substantiated by periodic nondestructive examinations or periodic inspections in an operational unit.

J. Bauerle: Would you comment on your statement that leak detection, in the EBR-II system is presently not rapid enough to provide safe-shut down in a leak situation?

P. Chopra: My statement referred to the existing leak detection capability, without the hydrogen meters; namely, the gas chromatograph and pressure rise in the surge tank on failure of a rupture disc. When all the hydrogen meters are installed as Gerry Wolz and I described, leaks could be very rapidly detected, provided that they are within the range of detection. As you may know, hydrogen meters cannot detect very small leaks, and if a leak is very large, excessive wastage may occur before they can alarm.

Even if our leak detection capability were as rapid as is technically feasible today, subsequent shutdown of the system would not assure the absence of severe damage to the system. To fully utilize the early leak detection provided by the hydrogen meters, the EBR-II system has to be modified by the addition of the steam drum vent and the evaporation drain systems as discussed.

## RADIOACTIVE CORROSION PRODUCT TRANSPORT AND CONTROL

By  
W. F. Brehm

Hanford Engineering Development Laboratory  
Operated by Westinghouse Hanford Company  
Richland, Washington 99352

## ABSTRACT

Buildup of radioactive species in primary system piping and components of LMFBR's will occur due to transport of radioactive materials from the reactor core to external piping and components. This buildup will give rise to gamma radiation fields strong enough to cause difficulty in maintenance and repair operations. The strength of the radiation fields will depend strongly on the reactor operating temperature and the effectiveness of control measures applied.

Sodium-cooled reactors with core outlet temperatures of about 500-550°C have experienced significant amounts of radioactive corrosion product transport. It is predicted that reactor operations with core outlets near 600°C and with the long fuel cycles necessary for maximum breeding gain will produce radiation fields of over 1R/hr adjacent to some primary heat transport system equipment. Experience on existing reactors has shown that maintenance is cumbersome, expensive, and time consuming under such conditions.

Experimental studies have shown that no one control method against corrosion product transport will be sufficient to completely solve the problem. Reducing the oxygen level of sodium by reducing the cold trap temperature to 115°C is only partially effective. The control concepts now under investigation are (1) coolant purity control, (2) reduced temperature, (3) trapping, (4) additives, (5) improved fuel cladding, and (6) decontamination. Reduced temperature is the best short-term control method, but trapping, use of improved fuel cladding, and decontamination are promising control techniques now being studied. Development of successful control methods reduces downtime for maintenance and repairs and permits longer fuel cycles at high temperatures. These considerations increase breeding gain, steam cycle efficiency, and plant factor while reducing plant capital cost.

## INTRODUCTION

In a Liquid Metal Fast Breeder Reactor the cladding and in-vessel structural materials become radioactive from the neutron flux. Buildup of radioactive species in the primary circuit external to the core occurs due to corrosion of the activated material and transport of the radionuclides to the primary components (e.g. pumps, heat exchangers, valves, and sodium purification system). The deposition of these species gives rise to gamma-radiation fields strong enough to cause difficulties in maintenance and repair operations. This process is shown schematically in Figure 1. The corrosion product transport (or "crud transport" problem as it is called in water reactor technology) is well known, and considerable maintenance experience has been gained on both water- and sodium-cooled reactors. However, these repairs have required large amounts of manpower and resulted in long plant shutdowns, neither of which is economically favorable.

This paper reviews the past experience in operating plants and experimental facilities. The estimated magnitude and proposed methods of solution of the corrosion product transport problem in the U.S.A. are presented and the most recent experimental results and the future plans are discussed.

The most important points discussed are as follows:

1. Calculations made for reactor plants operating with long fuel cycles and at high (600°C) core outlet temperatures predict radiation levels above 1 Roentgen per hour (1 R/hr) adjacent to the primary system piping<sup>(1,2,3)</sup> after decay of the  $^{24}\text{Na}$ .
2. Even in present-day reactors with lower outlet temperatures and shorter fuel cycles, substantial corrosion product transport to produce radiation levels of about 100 mR/hr is being observed. Extrapolation of calculations to the existing reactor situations results in reasonable agreement.
3. Reactor experience and test loop data show that both the release of irradiated material and its distribution within the circuit are nonuniform. The most abundant nuclide is  $^{54}\text{Mn}$ .  $^{60}\text{Co}$  and  $^{58}\text{Co}$  are also produced but are not released at as high a rate as  $^{54}\text{Mn}$ .

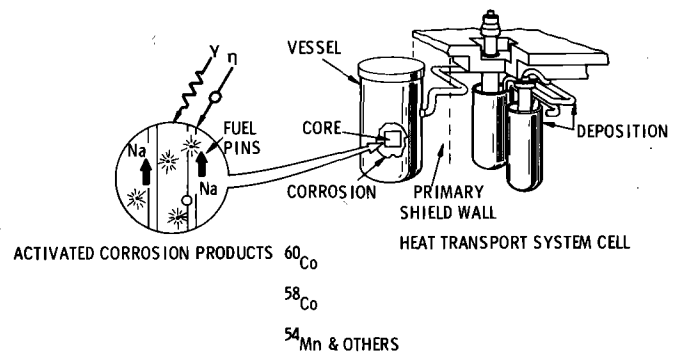


FIGURE 1: Activated Corrosion Product Transport

nor are they transported through the circuit to the same degree. A major fraction of the deposited corrosion product activity is adherent to the deposition site and is not removed by sodium draining or sodium removal processes.

INTERNATIONAL CONFERENCE ON LIQUID METAL TECHNOLOGY IN ENERGY PRODUCTION

4. No one control method will be sufficient to solve the problem, a combination of methods is required.

Topics under active investigation are the effect of oxygen and temperature on nuclide release, development of traps, use of improved fuel cladding alloys, and methods for removing deposited activity (decontamination). Trapping and decontamination show promising early results. Reduction of the oxygen level of the sodium to that level corresponding to a 115°C cold trap temperature is only partially effective at reducing <sup>54</sup>Mn and <sup>60</sup>Co release.

Radionuclide Sources

Information about the radionuclides of interest is shown in Table 1. The most prevalent nuclides seen in reactors are <sup>54</sup>Mn and <sup>60</sup>Co; the others have been observed in smaller quantities. It can be seen from Table 1 that little can be done to eliminate <sup>54</sup>Mn while some control over <sup>60</sup>Co formation is possible by restricting the Co content of fuel cladding and ducts to 0.05% and by restricting the use of cobalt-base bearing and hardfacing materials especially in the epithermal neutron flux just above the fuel zone.

Control of fission products released from breached fuel cladding, and the control of tritium, is beyond the scope of this report. It should be noted, however, that some of the control methods developed for corrosion products may also be effective against fission products.

REACTOR OPERATING EXPERIENCE

The specific experience at various sodium-cooled reactors is shown below:

DFR (U.K.)

Repair of a leak in a radiation field equal to that predicted for high-temperature LMFBR operation required several hundred people and several months' downtime for repair<sup>(4)</sup>.

BR-5 (USSR)

Fission products, <sup>54</sup>Mn, and <sup>60</sup>Co were observed on the piping. Treatment of the piping with acid etches was necessary to remove all the deposited radioactivity<sup>(5,6)</sup>.

BOR-60 (USSR)

Radiation levels of up to 100 mR/hr adjacent to primary system piping was observed after three years' operation. The core outlet temperature varied between 510° and 550°C. The <sup>60</sup>Co and <sup>54</sup>Mn radioactivity was spread throughout the circuit, with greater nuclide deposition in the cold leg<sup>(7)</sup>.

KNK (Germany)

Radiation levels of 100 mR/hr near the heat exchangers after 146 days full power operation were measured. Core outlet temperature is 550°C. The radiation level was reduced only

TABLE 1. Corrosion Product Radionuclides

Nuclide	Formation reaction(s)	Half-life, Days	Gamma-ray energy, MeV	Comments
<sup>54</sup> Mn	<sup>54</sup> Fe(n,p) <sup>+</sup> <sup>55</sup> Mn(n,2n)	313	0.84	The most prevalent nuclide. Eliminating all the others still leaves a significant problem.
<sup>60</sup> Co	<sup>59</sup> Co(n,γ) <sup>+</sup> <sup>60</sup> Ni(n,p)	1913	1.17,1.33	Source is Co impurity in nickel and Co-base wear pads, bearings, and hardfacing materials.
<sup>58</sup> Co	<sup>58</sup> Ni(n,p) <sup>+</sup> <sup>59</sup> Co(n,2n)	71	0.81	Use of a ferritic steel for fuel cladding eliminates most <sup>58</sup> Co.
<sup>59</sup> Fe	<sup>58</sup> Fe(n,γ) <sup>+</sup> <sup>59</sup> Co(n,p)	45	1.10,1.29	
<sup>182</sup> Ta	<sup>181</sup> Ta(n,γ)	115	1.12,1.22	Source concentration increases if Nb-bearing steel is used in the neutron flux.
<sup>65</sup> Zn	<sup>64</sup> Zn(n,γ)	243	1.11	Source is Zn in sodium or from contamination by ZnCrO <sub>3</sub> rust-proofing paint.
<sup>110m</sup> Ag	<sup>109</sup> Ag(n,γ)	253	0.65,0.76,1.47	Suspected source is Ag impurity in nickel. This nuclide has not been observed in significant quantities in the U.S.
<sup>51</sup> Cr	<sup>50</sup> Cr(n,γ) <sup>+</sup> <sup>52</sup> Cr(n,2n) <sup>54</sup> Fe(n,γ)	28	0.32	Although substantial, low gamma energy makes <sup>51</sup> Cr transport inconsequential.

<sup>+</sup>Dominant Reaction

## INTERNATIONAL CONFERENCE ON LIQUID METAL TECHNOLOGY IN ENERGY PRODUCTION

~ 15% by draining the sodium.  $^{54}\text{Mn}$ ,  $^{60}\text{Co}$ ,  $^{65}\text{Zn}$ , and  $^{110\text{m}}\text{Ag}$  were the principal nuclides.  $^{54}\text{Mn}$  showed a tendency to preferentially deposit on a nickel-rich surface in the hot leg but not the cold leg<sup>(8)</sup>. It is noteworthy that considerable  $^{182}\text{Ta}$  was produced in the KNK core but only small amounts were detected in the piping.

### RAPSODIE (France)

Radioactive  $^{54}\text{Mn}$  was observed throughout the piping system, particularly in the cold leg. Little  $^{60}\text{Co}$  was observed. Radiation levels up to 200 mR/hr were observed on the pump and piping (core outlet 540°C). Water washing, alcohol washing, and a relatively mild nitric-phosphoric acid treatment were all ineffective at removing deposited radioactivity; the acid etch was somewhat more effective than the other treatments<sup>(9,10)</sup>.

### EBR-II (U.S.A.)

Deposited  $^{54}\text{Mn}$  and  $^{60}\text{Co}$  were observed on the pump and heat exchanger and in the cold trap. Examination of 316 SS fuel cladding from a high-temperature fuel test showed substantial preferential corrosion of  $^{54}\text{Mn}$  and preferential retention of  $^{58}\text{Co}$  and  $^{60}\text{Co}$  at 650°C, but hardly at all at 510°C<sup>(11,12)</sup>.

The observed radiation levels in the plants mentioned above are in reasonable agreement (by a factor of 3) with those predicted using the techniques of References 1 and 13. A significant result is that the contribution of "nuclear corrosion" (recoil ejection plus fast neutron sputtering) has been shown to be unimportant, in apparent disagreement with the hypotheses of Anno and Walowit<sup>(14)</sup>. It can be shown, using the techniques of References 1 and 13, that a uniform removal rate of 25 $\mu\text{m}$  per year by fast neutron sputtering would lead to primary system radiation levels well in excess of 10 R/hr, contrary to actual observations in operating reactors.

### EXPERIMENTAL PROGRAMS

Well before the operational data on the reactors became available, investigators in the USA, Germany, Japan, and the U.K. began nuclide release and deposition studies in small test loop systems. The need for mass transport data in addition to that generated from the more conventional corrosion studies of steel in sodium arises for two reasons: (1) it can be shown that an average material corrosion rate of 5 to 10 $\mu\text{m}$  per year for fuel cladding (completely satisfactory from a wall thinning standpoint) will give rise to intolerable radiation levels near the primary system components, and (2) the problem nuclides (Mn and Co) are present as only minor constituents of the cladding alloys. Existing corrosion theories do not treat minor alloying element behavior in any detail.

Most corrosion/deposition studies<sup>(11,15,16,17,18,19,20)</sup> investigated the release and deposition of  $^{60}\text{Co}$ ,  $^{54}\text{Mn}$ ,  $^{59}\text{Fe}$ ,  $^{51}\text{Cr}$ , and  $^{58}\text{Co}$  at temperatures between 550 and 600°C. (The study of Reference 15 had a source temperature of 700°C.) Oxygen level in sodium was controlled by cold-trapping and measured by a variety of methods; cold trap temperatures were in the range of 115°-160°C. (Reference 19 reported work using a cold trap temperature of 200°C.) In general, the studies agreed with reactor observations and with each other; the most important similarities and differences were as follows:

1.  $^{54}\text{Mn}$  was the most abundant nuclide reduced from irradiated stainless steel;  $^{51}\text{Cr}$ ,  $^{59}\text{Fe}$ ,  $^{60}\text{Co}$ , and  $^{58}\text{Co}$  were released in proportionately lesser amounts. However, the high concentrations, long half life, and high-energy gamma radiation of  $^{60}\text{Co}$  make it a more important problem than  $^{51}\text{Cr}$ ,  $^{58}\text{Co}$ , or  $^{59}\text{Fe}$ , which have been seen only in small amounts in actual reactor observations.
2. For the most part,  $^{54}\text{Mn}$  was transported throughout the test circuits and deposited more heavily in the lower temperature portion of the loops.  $^{60}\text{Co}$  and  $^{51}\text{Cr}$  showed preferential deposition in loop hot legs.  $^{54}\text{Mn}$  deposited in loop hot legs in the first few hundred hours of loop operation gradually migrated to lower temperature regions.
3. The loop cold traps were more or less ineffective at removing radioactivity at rates more than proportional to the cold trap fractional flow. They did, however, act as irreversible sinks for whatever Co and Mn deposited in them. The concentration of  $^{54}\text{Mn}$  in cold traps was apparently dependent on how much  $^{54}\text{Mn}$  had deposited upstream of the cold trap branch line. This suggests that the cold trap branch line should come from a reactor hot leg or above the core; to be most effective as a radionuclide sink.
4. Reducing the oxygen level by reducing cold trap temperature resulted in an apparent reduction in the  $^{60}\text{Co}$  source rate but only a small decrease in  $^{54}\text{Mn}$  source. Quantitative determination of source rates<sup>(11,21)</sup> showed  $^{54}\text{Mn}$  to be preferentially released and  $^{60}\text{Co}$  to be preferentially retained from irradiated 316 SS specimens.
5. At all locations in the test loop, deposition was enhanced at regions of increased fluid turbulence where the hydrodynamic boundary layer thickness is reduced. This effect is shown schematically in Figure 2; actual deposition data are given in Figure 3 (Figures 2 and 3 are taken from Reference 15). The significance of these data is that increased nuclide deposition should be expected on pumps, valves, and any other location where additional turbulence is introduced. Unfortunately these regions are where maintenance problems are expected to occur. On the other hand, this information can be used to aid in the design of "nuclide traps" which enhance deposition of the nuclides and prevent their spread into the reactor primary system.
6. Radioactive material was firmly deposited on the test system piping at temperatures above 400°C; sodium removal processes such as draining, or water, steam, or alcohol rinse removed very little activity. Use of acid solutions was necessary to remove deposited activity as described in References 6, 9, 10, and 20. Significant penetration of activity over 10 $\mu\text{m}$  into the pipe wall has been observed even at 400°C. Under certain conditions, deposits build up to a limiting thickness and then are sheared off<sup>(20)</sup>. This phenomenon could have practical implications for removing deposits from an intermediate heat exchanger in a pot-type reactor.

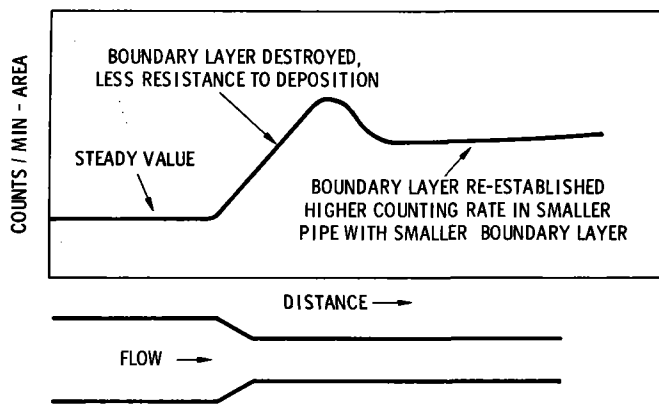


FIGURE 2. Schematic Representation of Nuclide Deposition Near Flow Perturbations.

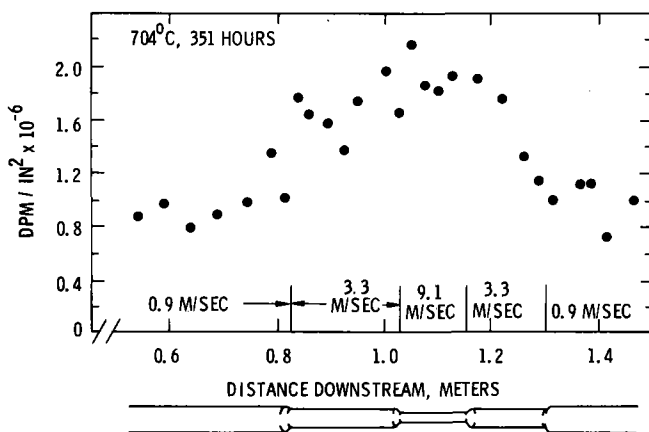


FIGURE 3. Counting Rate of <sup>54</sup>Mn in Velocity Change Sections.

- There was not good agreement between test loop data and reactor operating experience in the case of <sup>60</sup>Co deposition patterns, with proportionately more <sup>60</sup>Co being reported in reactor cold legs and cold traps than in the test loops; also, examination of fuel pins at the top of an EBR-II fuel assembly (0.5 m above the fuel zone) showed no preferential deposition of <sup>58</sup>Co or <sup>60</sup>Co on the fuel pin surface.

The Radioactivity Control Technology program has been underway in the U.S. since 1966. Reduction of the primary system radionuclide burden is necessary since calculations<sup>(1,13)</sup> have shown that radiation levels may exceed 1 R/hr in the primary heat transport cells of the Fast Flux Test Facility (Figure 4). [NOTE: The lower curves depicting 527° and 482°C core outlets are extrapolated from the upper experimental curve depicting a 593°C core outlet]. The extrapolation is by no means certain, since substantial discrepancies are reported among various investigators on the temperature dependencies of metal-sodium reactions<sup>(16,22,23)</sup>. In addition, the release of <sup>54</sup>Mn is determined by at least two separate rate-controlling steps; diffusion to the surface of the metal and release into the sodium. The nuclide release in the 450-600°C range is critical since the extrapolated radiation levels are close to the 200 mR/hr value above which "hands-on" contact maintenance becomes impractical for large jobs.

The various release and deposition control concepts can be visualized by considering the contributions to a radiation level,  $L$ , at a point  $P$  in the primary equipment cell.

$$L_P = \sum_i C_i \times R_i \times F_{i,P} \times D_{i,P} \times T_i$$

Where  $R_i$  = the release rate of nuclide  $i$  from the corroding material,

$C_i$  = the concentration of nuclide  $i$  in the corroding material,

$F_i$  = the fraction of nuclide  $i$  that contributes to the radiation level at point  $P$ ,

$D_i$  = the shielding factor for nuclide  $i$  at point  $P$ , and

$T_i$  = the time buildup factor arising from simultaneous irradiation and corrosion with fuel cycling.

The actual calculations are described in further detail in Reference 1; earlier calculations are given in References 10 and 13. The most practical methods of control are (1) reduce  $R$  by restricting the plant operating temperature, (2) reduce  $C$  by restricting Co content of in-core materials (some of the advanced fuel cladding candidate materials have less Fe and more Ni than 316 SS; thus reducing the <sup>54</sup>Mn potential), and (3) reduce  $F$  at maintenance locations by trapping the nuclides elsewhere (raising  $F$  inside the reactor vessel for example). The factor  $D$  can be

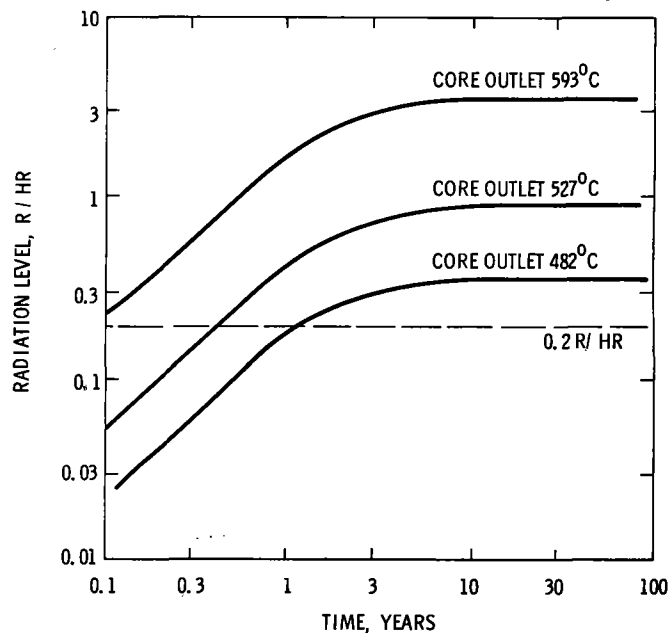


FIGURE 4. FFTF Activated Corrosion Product Radiation Levels as Function of Time and Core Outlet Temperature.

reduced by selective shielding in areas of high  $F$ , but total primary system shielding is impractical. Tooling the reactor plants for complete remote maintenance procedures is, at the present, not a proven technology, and would undoubtedly be expensive. Development of control measures is a much more cost-effective approach.

# INTERNATIONAL CONFERENCE ON LIQUID METAL TECHNOLOGY IN ENERGY PRODUCTION

It is interesting to note that in the Fast Flux Test Facility primary loop, the piping circuit labyrinth causes the radiation level  $L$  at points in the cell to be insensitive to various assumed distribution patterns ( $F_p$ )<sup>(13)</sup>. In other words, any nuclides transported outside of the reactor vessel will contribute to the radiation level  $L$ . This fact, in turn, means that nuclide traps should be located inside the reactor vessel (or inside the vessel shield wall). The distribution factor becomes important, however, in the event that components have to be removed from the cell for repairs. It is also important to realize that changing to a pot-type reactor concept (PFR or PHENIX) does not alleviate the nuclide transport problem since some components will have to be withdrawn from the primary tank for repair, or are already externally located (e.g. purification system lines).

The nuclide concentration  $C$  can be reduced by reducing neutron flux or fuel irradiation cycle time; both these actions are directly in conflict with the goal of reduced doubling time for fuel production.

## UNITED STATES EXPERIMENTAL PROGRAM

The present experimental program in the USA concentrates on several control techniques:

1. Coolant Purity Control. The idea is to reduce  $R$  by reducing the oxygen level of the sodium. Most of the experimental work to date has been directed to this effort<sup>(11)</sup>.
2. Effect of Reduced Temperature. The reduction in the release rate  $R$  as a function of temperature needs to be better determined, especially in the light of the present trend toward lower reactor operating temperatures. [Use of a ferritic alloy fuel cladding, an attractive proposition if core outlet temperatures are restricted to 540°C., will essentially eliminate the <sup>58</sup>Co and most of the <sup>60</sup>Co, but unfortunately not the <sup>54</sup>Mn, which represents over 80% of the problem.]
3. Traps. Work has begun on the development of devices which provide an irreversible deposition sink at a location away from maintenance areas. Early results are promising.

4. Additives. The idea is to find an additive to the sodium that will inhibit nuclide release and/or retard deposition on surfaces. Little progress has been made, the concept does not appear promising, and the effort is now inactive.
5. Improved Fuel Cladding. The LMFBR Alloy Development program is geared toward development of materials with better strength, ductility, swelling resistance, corrosion resistance, and a reduced potential for radionuclide transport in comparison to the present 316 SS reference material.
6. Decontamination. The goal of this task is to develop a chemical method that will remove deposited radioactivity to an acceptable level and leave the remaining material in such a condition that it can be requalified for reinsertion into the reactor for further service. Even though chemical decontamination is a major decision for a large components, a development program performed now ensures that techniques will be available when needed.

Most work to date has concentrated on the effect of reduced oxygen levels on the nuclide release rate. It has been shown that reducing oxygen level by reducing cold trap temperature from 154°C to 115°C is apparently effective against <sup>60</sup>Co transport from irradiated 316 SS but unfortunately reduced the <sup>54</sup>Mn release by only 30%<sup>(11)</sup>. The test temperature in the 6000 hour tests was 604°C and the sodium velocity at the specimens was 6.7 meters/sec; both values represent average conditions at the top of the fuel stack in the Fast Flux Test Facility at its rated operating conditions. (The extra 11° above average core outlet corrects for the film  $\Delta T$  between the fuel pin surface and the center of the coolant channel.)

A third 6000-hour test has recently been completed with an oxygen level below 0.01 ppm using a hot trap (Zr foil at 700°C) for sodium purification. A complete data analysis has not yet been completed; however, preliminary specimen weight-loss measurements and examination of a specimen removed after 3000 hours show that a further decrease in weight loss or nuclide release at low oxygen levels does not occur. In fact, the weight loss and nuclide release were greater than that at the 115°C cold trap conditions, as seen in Figures 5, 6, and 7.

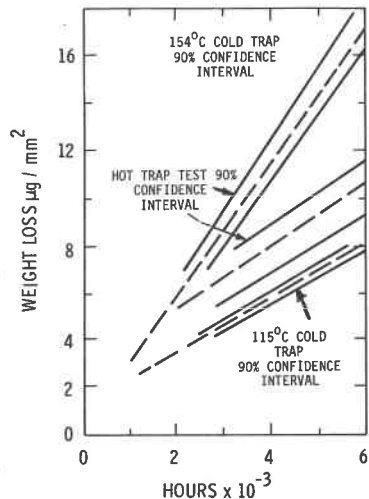


FIGURE 5. Weight Loss Data

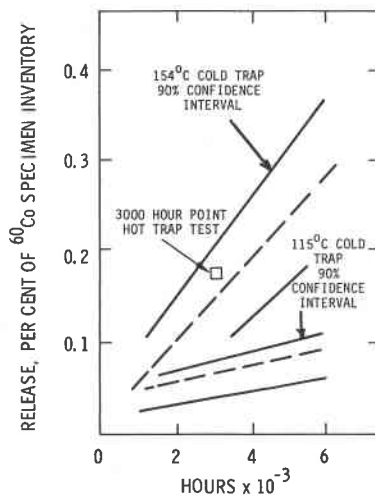


FIGURE 6. <sup>54</sup>Mn Release

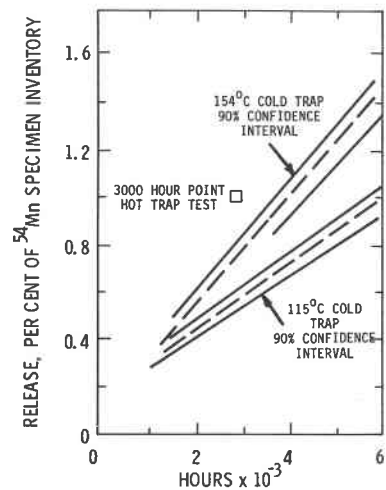


FIGURE 7. <sup>60</sup>Co Release

During this experimental investigation, consistent values of electrolyte oxygen meter voltage with cold trap temperature were obtained. With the cold trap operating at 115°C, exposing a vanadium wire for 4 hours at 750°C always produced the same amount of oxygen in vanadium as measured by vacuum-fusion analysis--540 ppm oxygen in V, which is equivalent to 0.5 ppm O in Na according to Reference 24. The oxygen level corresponding to 154°C cold trap temperature is 2.5 ppm. The oxygen level during the hot trap run was also measured continuously by electrolytic oxygen meters and verified by vanadium wire equilibration(21,24).

The deposition trends during the 21,000 hours of testing in the sodium facility (Source Term Control Loop #1 or STCL-1) were in good agreement with previous test loop observations(15-21). Figure 8 shows the deposition pattern in the heat exchangers in STCL-1. The first heat exchanger was replaced after 15,000 hours; the second heat exchanger was in place for 6000 hours during the hot trap run.

Enhanced deposition was noted in one of the flow control valves in the STCL-1 cold leg as shown in Figures 9 and 10. It can be seen that there are two abrupt changes in flow direction, which add turbulence even when the valve is fully open. Figure 10 shows the comparison between the valve and the adjacent upstream cold leg pipe. The valve was replaced after 6000 hours' operation; note the rapid <sup>54</sup>Mn buildup in the new valve. Examination of the old valve showed that some of the deposits were not so adherent as those in the piping.

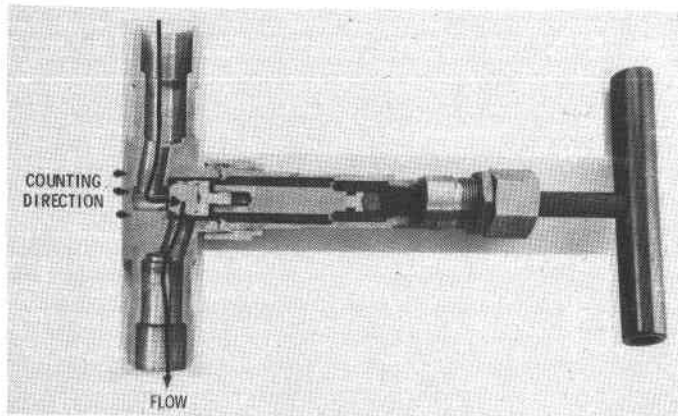


FIGURE 9. Counting Direction in STCL-1 Valve

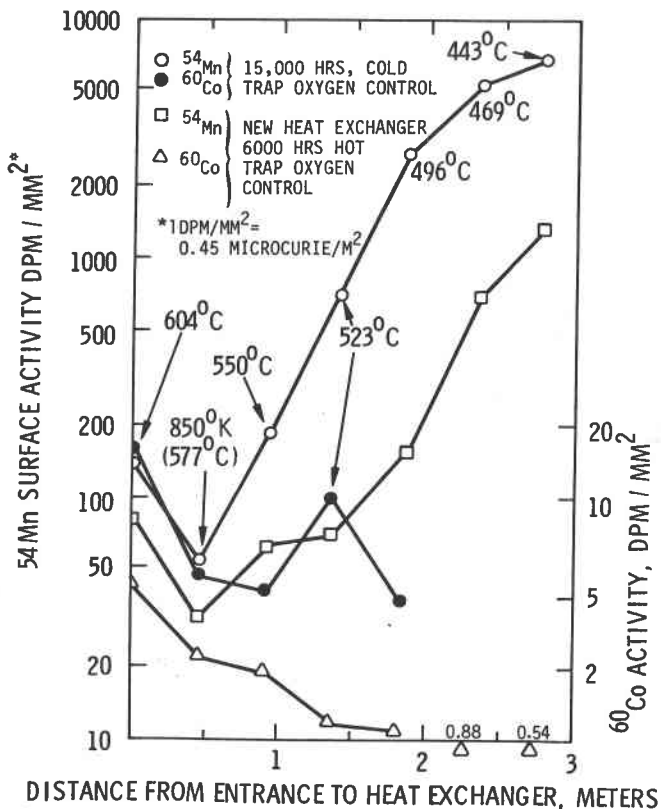


FIGURE 8. Radionuclide Deposition Patterns

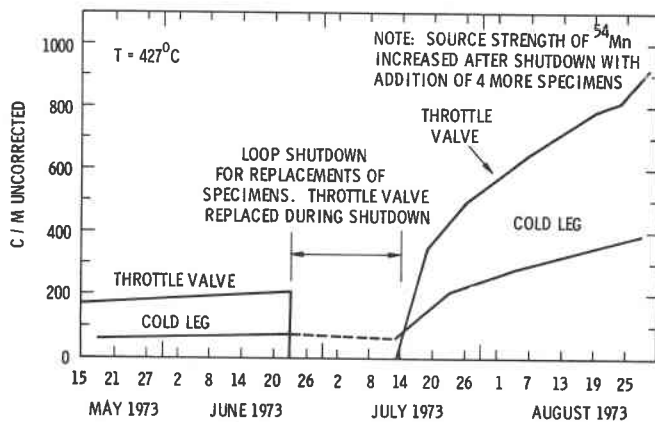


FIGURE 10. Buildup of <sup>54</sup>Mn in STCL-1 Throttle Valve and Cold Leg.

U.S. Program Conclusions and Recommendations

The conclusions and recommendations from this work are (1) operating a reactor with cold trap temperature of 115°C will reduce the radionuclide burden, but additional control measures are required; (2) the use of a hot trap to reduce nuclide release to achieve an extremely low oxygen level is not effective; and (3) radionuclide deposits are generally adherent to the pipe. The possibility of non-adherent deposits exists but is not well defined.

The complete detail of this work (except the hot-trap test corrosion results) is given in References 11 and 21. The sub-surface composition profiles of specimens used in this study agreed well with those obtained on 316 SS cladding exposed in EBR-II as part of a fuels performance study(11,12). The test loop, STCL-1, is being dismantled to provide specimens for the decontamination program.

Progress in other phases of the program is limited as yet; the status is as discussed below:

Effect of Reduced Temperature. A test is underway with irradiated 316 SS specimens at a source temperature of 538°C to determine release rates at lower temperatures. Data after 6000 hours will be available in early 1977. This test also has a



## INTERNATIONAL CONFERENCE ON LIQUID METAL TECHNOLOGY IN ENERGY PRODUCTION

"nuclide trap" in the piping. It is important to note that nuclide deposits may be less adherent and/or penetrating at lower temperatures of operation.

**Trapping.** Traps have been effective for 6000 hours at 604°C and a trap test at 538°C is underway. A trap test program has been defined which includes testing of a trap in EBR-II.

**Additives.** This program is inactive at present. Today's knowledge of sodium chemistry is still too limited to define a good corrosion inhibitor. The failure of the hot-trap test to reduce the nuclide release rate at extremely low oxygen levels means that the "soluble getter" concept of adding Ca, Ba, or Li to the sodium to remove oxygen is no longer a viable concept for corrosion inhibition.

**Improved Cladding.** Measurement of nuclide release from the advanced fuel cladding candidates is scheduled to begin in late 1977. The sodium corrosion considerations in advanced alloy cladding development are described in another paper at this meeting<sup>(25)</sup>.

**Decontamination.** As mentioned, the STCL-1 loop has been cut apart to provide specimens for the decontamination program. In addition, some primary piping from the Sodium Reactor Experiment plant (SRE) will become available this year. Work has begun on evaluating various decontamination solutions, mostly weak acids. This work is being accompanied by a study of electrochemical reactions at the corroding surface in the decontamination solution.

A combination of these methods will be required to attain control over corrosion product transport. Achieving successful control methods will permit longer LMFBR fuel cycles at higher temperatures, thus increasing the breeding gain, and steam-cycle economy. The ability to perform maintenance operations in a timely fashion without complete remote operation will result in lower capital costs and a higher plant factor.

**Acknowledgements.** The author is pleased to acknowledge all personnel that contributed to the design and operation of the experimental facilities<sup>(11,21,26)</sup>, and to R. J. Cash and J. M. Atwood for supervision of the program. The author also thanks W. L. Kuhn, J. C. McGuire, and R. P. Colburn for helpful discussions. This work was sponsored by the United States Energy Research and Development Administration under contract E(45-1)-2170.

### REFERENCES

1. W.L. Kuhn, "A Computational Technique for Estimating Corrosion Product Release in an LMFBR", HEDL-SA-1077, May 1976. International Conference on Liquid Metal Technology in Energy Production, Champion, PA, May 1976.
2. A. Merkel and G. Menken, "Estimation of the Radiation Levels Near the Components in the SNR-300 Primary System Induced by Deposition of Corrosion Products". Proceedings of BNES International Conference on Liquid Alkali Metals, Nottingham, U.K. Published by Thomas Telford Co., London, 1973, pp 301-305.
3. T. Yanagisawa et al., "Design Considerations of Fission and Corrosion Products in Primary System of MONJU. Paper #11 at IAEA Specialists' Meeting on Fission and Corrosion Products in Primary Systems of LMFBR's, Dimitrovgrad, USSR, September 1975.
4. R. R. Mathews, "Location and Repair of a Leak in the Dounreay Fast Reactor Primary Circuit", *J. British Nuclear Energy Society*, July 1969.
5. A.E. Leypunski et al., "Study of the 5-year Operation of the BR-5 Reactor". Paper #312 at 3rd Geneva Conference on Peaceful Uses of Atomic Energy, 1964.
6. I.A. Efimov et al., "BR-5 Primary Circuit Decontamination". Paper #17 at IAEA Specialists' Meeting, Dimitrovgrad, USSR, September 1975.
7. V.D. Kizin et al., "Studies of Radioactivity Buildup and Distribution in the BOR-60 Circuit". Paper #15 at IAEA Specialists' Meeting, Dimitrovgrad, USSR, September 1975.
8. H.H. Stamm, K.C. Stade, "Corrosion Product Behavior in the Primary Circuit of the KNK Nuclear Reactor Facility". Paper #5 at IAEA Specialists' Meeting, Dimitrovgrad, USSR, September 1975.
9. R. deFremont, "Decontamination Experience on RAPSODIE" presented at IAEA Specialists' Meeting on Fission and Corrosion Products in Primary Systems of LMFBR's, Bensberg, Germany, September 1971; in USERDA Report CONF-710959.
10. L. Costa et al., "Corrosion and Activity in the Primary Circuit of a Sodium Reactor-Code CORONA". Paper #3 at IAEA Specialists' Meeting, Dimitrovgrad, USSR, September 1975.
11. W.F. Brehm, "Effect of Oxygen in Sodium Upon Radio-nuclide Release from Austenitic Stainless Steel", HEDL-SA-985. Paper #19 at IAEA Specialists' Meeting, Dimitrovgrad, USSR, September 1975.
12. J. R. Humphreys et al., "Problem Considerations in the U.S. Radioactivity Control Technology Program". Paper #20 at IAEA Specialists' Meeting, Dimitrovgrad, USSR, September 1975.
13. T.J. Kabele et al., "Activated Corrosion Product Transport Radiation Levels Near FFTF Reactor and Closed Loop Primary System Components", USERDA Report HEDL-TME-72-71, May 1972.
14. J.N. Anno and J.A. Walowit, "Analysis of Corrosion of Stainless Steel in a Sodium and High Radiation Environment", *Nuclear Technology* vol. 10, pp 67-75 (January 1971)
15. W.F. Brehm et al., "Radioactive Material Transport in Flowing Sodium Systems", in *Corrosion by Liquid Metals*, Plenum Press, New York (1970) pp 97-111.
16. P. Roy et al., in USERDA Report GEAP-10394 (1971).

## INTERNATIONAL CONFERENCE ON LIQUID METAL TECHNOLOGY IN ENERGY PRODUCTION

17. R.P. Colburn, "Transport of Activated Corrosion Products in Sodium Loops", Trans. ANS, vol. 17, p 165 (1973).
18. G. Menken and H. Reichel, "Corrosion and Deposition Behavior of  $^{60}\text{Co}$  and  $^{54}\text{Mn}$  in the SNR Mockup Loop". Paper #6 at IAEA Specialists' Meeting, Dimitrovgrad, USSR, September 1975.
19. N. Sekiguchi et al., "Behavior of Corrosion Products from Irradiated Stainless Steel in Flowing Sodium". Paper #8 at IAEA Specialists' Meeting, Dimitrovgrad, USSR, September 1975.
20. K.T. Claxton and J.G. Collier, "Effects of Corrosion Product Transport in Fast Reactors", at BNES Conference, Nottingham, 1973, pp 289-300.
21. W.F. Brehm et al., "Techniques for Studying Corrosion and Deposition of Radioactive Materials in Sodium Loops"; HEDL-SA-986. Paper #18 at IAEA Specialists' Meeting, Dimitrovgrad, USSR, September 1975.
22. A.W. Thorley and C. Tyzack, "Corrosion and Mass Transport of Steel and Nickel Alloys in Sodium Systems", BNES Nottingham Conference 1973, pp 257-274.
23. C. Bagnall and D.C. Jacobs, "Relationships for Corrosion of Type 316 Stainless Steel in Sodium", USERDA Report WARD-NA-3045-23, May 1975.
24. D.L. Smith and R.H. Lee, "Characterization of the Vanadium Wire Equilibration Method for Measurement of Oxygen Activity in Liquid Sodium", USERDA Report ANL-7891, January 1972.
25. W.F. Brehm, "Sodium Corrosion Considerations in Alloy Development", HEDL-SA-1009, International Conference on Liquid Metal Technology in Energy Production, Champion, PA, May 1976.
26. L.E. Chulos, "Operational Techniques Employed for the Liquid Sodium Source Term Control Loops", HEDL-SA-1078, International Conference on Liquid Metal Technology in Energy Production, Champion, PA, May 1976.

H.H. Stamm

Institut für Radiochemie  
Kernforschungszentrum Karlsruhe  
Federal Republic of Germany

ABSTRACT

Determination of radionuclides in KNK primary sodium yielded different results when ceramic crucibles instead of nickel crucibles were used for sodium sampling. It was shown that adsorption of some radionuclides on nickel crucibles was the reason for this effect. Small cylinders and metal coupons were introduced into the KNK primary sodium sampling station for radionuclide deposition studies. These deposition samples, made of different types of stainless steel, nickel, tantalum, titanium, and molybdenum, were exposed to the contaminated, flowing primary coolant for times up to 24 hours. Gamma spectrometric measurements indicated a strong adsorption of  $^{65}\text{Zn}$  on all nickel samples; the activities of  $^{51}\text{Cr}$ ,  $^{54}\text{Mn}$ ,  $^{60}\text{Co}$ , and at low temperatures (473 K) even of  $^{110\text{m}}\text{Ag}$  were higher on nickel samples than on any other material exposed to the primary sodium. These results were confirmed for the adsorption of radionuclides on crucibles of various metals. Consequently, stainless steel crucibles will be used for sampling primary sodium in order to determine radionuclides at KNK-II.

INTRODUCTION

KNK is a sodium-cooled, experimental nuclear power station of GfK<sup>+</sup>, situated on the site of the Nuclear Research Center, Karlsruhe/Germany. The plant was operated by KBG<sup>++</sup> until September 1974 with a thermal core as "KNK-I" (1); it is now being converted into "KNK-II" with a fast core (2). The contamination of the primary coolant with radionuclides originating from neutron activation of metallic impurities in the sodium was evaluated in advance by activation analysis of KNK sodium (3). After shut-down of KNK-I the experience from plant operation with reference to chemistry was summarized (4), and a survey of radionuclide built-up and behavior in the primary system was given (5,6).

<sup>+</sup> Gesellschaft für Kernforschung, Karlsruhe

<sup>++</sup> Kernkraftwerk-Betriebsgesellschaft, Leopoldshafen

EXPERIMENTALSampling

In order to determine various impurities in the primary coolant of the reactor, samples are taken from the flowing sodium by means of an overflow sampling device in a special bypass of the main coolant circuit (Fig.1). Up to seven crucibles (20 mm high, 20 mm diameter) may be introduced with an appropriate holder into a closable steel tube, which is then mounted vertical in the sampling cell. Trace heating keeps the

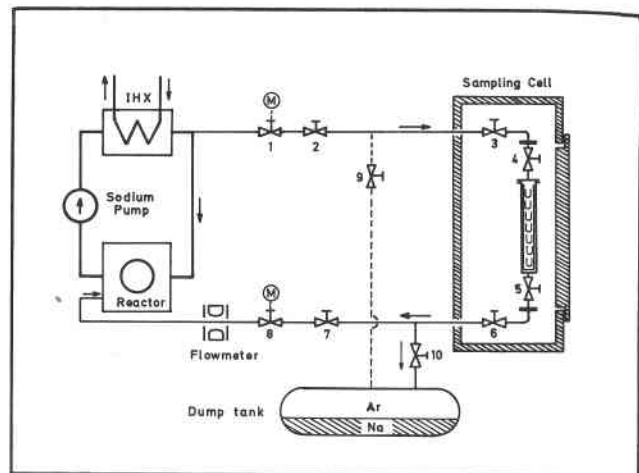


Fig. 1. KNK Primary Sodium Sampling Station

valves and piping of the station at temperatures above 473 K. By opening valves 1 to 8, sodium flows from the cold leg of the primary circuit (after leaving the intermediate heat exchanger, IHX, nominally at 634 K at full power operation) to the sampling station, and back to the reactor tank. After a suitable flushing time the valves 1, 2, 7, and 8 are closed, and valves 9 and 10 are opened. All the sodium from the station (except the samples in the crucibles) flows down into the dump tank, and the station is filled with cover gas from the (dashed) argon line.

After decay of  $^{24}\text{Na}$  to a safe level, valves 3 to 6 are closed, and the trace heating is disconnected. The

sampling tube is taken from the station, and transported into an argon-filled glovebox in the laboratory. The central flange, and valves 3 and 4 are opened and the crucibles are removed from the holder. Nickel crucibles were commonly used for the determination of oxygen by the vacuum distillation method (7), crucibles made of ceramic material (sintered  $Al_2O_3$ ) for carbon determination. In addition crucibles made of quartz, stainless steel, and molybdenum were used during the KNK-I experimental program.

Typical Na content of 7 Ni crucibles (one sampling):

1.	3.971 g	
2.	3.947 g	Average value $\bar{m} = 4.006$ g Na
3.	4.004 g	Standard deviation $s = 0.105$
4.	4.047 g	Relative standard deviation 2.6 %
5.	4.015 g	
6.	3.858 g	
7.	4.201 g	

Deposition Samples

The only possibility to introduce deposition samples into KNK primary sodium during reactor operation is the sodium sampling station.

Small cylinders and metal coupons as shown in Fig. 2 were mounted into the crucible holder of the station, and exposed to the flowing primary coolant as described above. The removed samples were cleaned with methanol, and sometimes in addition with distilled water prior to activity measurements.

Size of deposition samples:

- Cylinders: a) 20 mm o.d. x 1 mm wall pipe sections  
20 mm long, surface  $25.1 \text{ cm}^2$   
b) 20 mm o.d. x 1 mm wall pipe sections  
30 mm long, surface  $37.0 \text{ cm}^2$   
Coupons: c) 20 mm x 17 mm x 1 mm; surface  $7.60 \text{ cm}^2$   
d) 30 mm x 17 mm x 1 mm; surface  $10.6 \text{ cm}^2$ .

Surface Pretreatment

- a) As delivered: Surface degreased with acetone  
b) Electropolished: 150 ml  $H_2SO_4$ , 430 ml  $H_3PO_4$ ,  
420 ml  $H_2O$ ; 300 K ( $27^\circ C$ ) at  $>5 \cdot 10^{-2} \text{ A/cm}^2$   
c) Pickled:  
Ni: 250 ml  $CH_3COOH$ , 150 ml  $HNO_3$ , 50 ml  $H_2SO_4$ ,  
50 ml  $H_3PO_4$ ; 8-10 seconds at 363 K ( $90^\circ C$ ).  
Stainless steel: 75 ml  $HNO_3$ , 25 ml  $H_2F_2$ , 500 ml  
 $H_2O$ ; 5 minutes at room temperature.  
Mo: 2M HCl at 353 K ( $80^\circ C$ ).

Measurements

After it was demonstrated that certain losses of radioactive species may occur during vacuum distillation of sodium (8), gamma emitting radionuclides were assayed directly by gamma spectrometry by gamma spectrometry in undecomposed sodium samples, and enclosed in gastight plastic containers. Measurements were carried out on a lithium-drifted germanium detector used in conjunction with a 1024 channel pulse height analyzer (Nuclear Data Model 2200), data output was accomplished by a Hewlett-Packard plotter, a Teletype ASR33 machine, and by a fast Tally paper tape puncher. Activities were calculated from characteristic peak areas by means of a suitable computer program. The gamma activity of the samples was measured several times. The identification of the gamma rays in the observed spectra was based on the energies, relative intensities, and half-lives of the peaks. All the spectra have been taken at a count rate for which the analyzer dead time was less than 20 %. The activities in the following tables are given as disintegration rates ( $10^2 \text{ s}^{-1}$ ); they are calculated back to the time at the end of sampling.

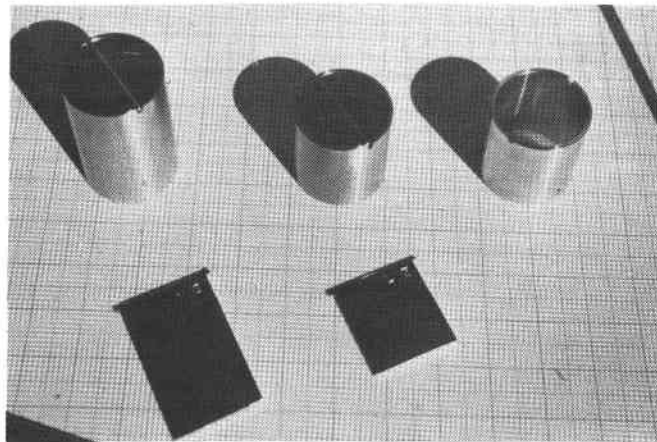


Fig. 2. KNK Deposition Samples

RESULTS

Table I shows activity concentrations of radionuclides in four sodium samples, taken on January 29, 1973, in nickel crucibles. It is obvious that the sodium isotopes  $^{24}Na$  and  $^{22}Na$  are always distributed homogeneously in metallic sodium, and that variations of the specific activities of these radioactive sodium isotopes indicate simply and solely the precision of the balance in the glovebox. If the activity concentra-

INTERNATIONAL CONFERENCE ON LIQUID METAL TECHNOLOGY IN ENERGY PRODUCTION

tions of the other radionuclides in Table I are compared, there are nuclides with relatively even distribution, and others with rather different concentrations from one crucible to the next one.

TABLE I. Radionuclides in KNK Sodium, Samples Taken in Ni Crucibles

Crucible	Activity ( $10^2 \text{s}^{-1} \text{g}^{-1} \text{Na}$ )			
	1	3	5	7
Na Content	2.574 g	3.566 g	3.042 g	2.612 g
$^{24}\text{Na}$	$3.7 \times 10^7$	$3.7 \times 10^7$	$3.9 \times 10^7$	$3.7 \times 10^7$
$^{22}\text{Na}$	7.8	7.8	8.2	7.9
$^{54}\text{Mn}$	4.8	2.9	3.0	4.3
$^{60}\text{Co}$	...	0.3	0.3	0.2
$^{65}\text{Zn}$	79	59	85	89
$^{110\text{m}}\text{Ag}$	3.0	3.0	3.3	3.0
$^{124}\text{Sb}$	0.4	0.5	0.5	0.4
$^{182}\text{Ta}$	0.5	0.4	0.4	0.5

If ceramic crucibles were used for sampling sodium in addition to nickel crucibles, variations in the activity concentrations of  $^{65}\text{Zn}$ ,  $^{54}\text{Mn}$ , and  $^{182}\text{Ta}$  seemed remarkably increased (Table II).

TABLE II. Radionuclides in KNK Sodium, Samples Taken in Ni- and  $\text{Al}_2\text{O}_3$ -Crucibles

Sampling R. Power	Jan. '74 31 MW <sub>th</sub>		Aug. '74 48 MW <sub>th</sub>	
	$\text{Al}_2\text{O}_3$	Ni	$\text{Al}_2\text{O}_3$	Ni
Na Content	1.07 g	3.68 g	2.61 g	3.24 g
	Activity ( $10^2 \text{s}^{-1} \text{g}^{-1} \text{Na}$ )			
$^{22}\text{Na}$	36	35	97	98
$^{54}\text{Mn}$	2.6	14	7.6	103
$^{65}\text{Zn}$	20	135	64	742
$^{110\text{m}}\text{Ag}$	16	16	52	52
$^{124}\text{Sb}$	0.6	0.5	0.8	0.9
$^{182}\text{Ta}$	4.5	0.8	4.0	5.5
$^{136}\text{Cs}$	3.2	2.1	4.0	4.1
$^{140}\text{Ba}$	-	-	0.7	0.8

It was, therefore, soon suspected that the material of the sampling vessels might have an influence on the results of the analysis. Dissolution of the sodium in methanol, and measurement of residual gamma activities on the crucibles verified the assumption that the apparent differences of the radionuclide content in crucibles of various materials were caused by sorption effects at the walls of the sampling ves-

sels as they were described by Davies and Drummond from NaK sampling at DFR<sup>(9)</sup>. Table III shows residual activities on five Ni crucibles (sampling on May 15, 1973) after vacuum distillation of the metallic sodium at 633 K (360°C), and dissolving the residue with water for acidimetric titration on NaOH. No  $^{22}\text{Na}$  or  $^{24}\text{Na}$  was left, the variations of the other radionuclides were in the same order of magnitude as in metallic sodium (Table I).

TABLE III. Radionuclides on Ni Crucibles (Na Distilled off, Crucibles Washed with Water)

Position	$10^2 \text{s}^{-1}$				
	1	2	3	4	5
$^{65}\text{Zn}$	530	470	510	510	350
$^{110\text{m}}\text{Ag}$	46	43	53	45	52
$^{54}\text{Mn}$	34	30	29	27	27
$^{182}\text{Ta}$	3.9	3.9	4.0	3.3	3.4
$^{124}\text{Sb}$	1.2	1.2	1.0	0.9	1.0
$^{60}\text{Co}$	-	0.11	0.14	0.13	0.13

Adsorbed activities on Ni,  $\text{Al}_2\text{O}_3$ , and quartz sampling vessels (sampling on Oct. 14, 1973) after dissolution of Na in methanol, and after washing the crucibles with distilled water are shown in Table IV.

TABLE IV. Radionuclides Adsorbed on Crucibles Made of Ni, Sintered Corundum, and Quartz at 493 K (Na dissolved in methanol, crucibles washed with water)

Position Material	3	4	5	6	7
	Ni	$\text{Al}_2\text{O}_3$	Ni	$\text{Al}_2\text{O}_3$	$\text{SiO}_2$
	$10^2 \text{s}^{-1}$				
$^{65}\text{Zn}$	104	1.0	71	0.6	1.1
$^{110\text{m}}\text{Ag}$	37	2.3	39	2.2	0.2
$^{54}\text{Mn}$	1.4	-	0.8	-	-
$^{182}\text{Ta}$	-	1.6	-	1.5	0.6

The differences in the adsorbed activities of  $^{65}\text{Zn}$  were two orders of magnitude between nickel and ceramic crucibles, whereas  $^{182}\text{Ta}$  was not detectable on Ni crucibles.

Separated dissolution of radioactive species from crucible walls by carrier containing 7M  $\text{HNO}_3$  indicated

**INTERNATIONAL CONFERENCE ON LIQUID METAL TECHNOLOGY IN ENERGY PRODUCTION**

that about the same amounts of activities had been adsorbed at the inner wall and at the outer surface of nickel crucibles. The external wall of a sampling vessel was contacted by flowing sodium in the course of flushing only (usually 4 hours), while the interior contained liquid sodium for the much longer cooling time (12 days). Equal activities on both sides of a crucible are therefore implying that the sorption processes take place at a relatively high rate, and that equilibrium is already attained during the regular period of flushing. This was confirmed, when besides ordinary sampling vessels a crucible with a hole in the bottom was exposed to the flowing sodium for four hours. When measured, the bottomless crucible showed about the same activities of <sup>54</sup>Mn and <sup>65</sup>Zn as the previous crucible containing 3.48 g Na; in fact, the activity of <sup>65</sup>Zn was higher on the walls of the empty vessel than in the sodium-filled crucible (Table V).

TABLE V. Radionuclides in a sodium-filled and on a bottomless Ni crucible

Position	6	7
	Na content 3.48 g	Bottomless crucible without Na
Nuclide	$10^2 \text{ s}^{-1}$	
<sup>54</sup> Mn	28	23
<sup>60</sup> Co	0.29	0.28
<sup>65</sup> Zn	1160	1930
<sup>110m</sup> Ag	49	4.0
<sup>124</sup> Sb	0.75	--
<sup>182</sup> Ta	4.1	3.1

On the other hand no measurable amount of <sup>124</sup>Sb, and only a small amount of <sup>110m</sup>Ag were found on the bottomless crucible.

Removal of Radionuclides by Water

After vacuum distillation the sampling crucibles are treated with demineralized water; adhering sodium has to be removed from deposition samples by methanol and/or water prior to gamma spectrometric measurements of the adsorbed activities. In order to check if radionuclides are removed from the specimens by that kind of treatment, nickel crucibles are brought into contact with water a second time.

Table VI shows that radionuclides are removed by cold and hot water, even if all sodium residues were removed in a previous operation. That means that sodium removal has to be performed in exactly the same manner, if the experimental results are to be compared.

TABLE VI. Removal of Deposited Activities from Ni Crucibles by Water

Treatment with water	1 h	48 h	1 h
at	293 K	293 K	373 K
% activity removed			
<sup>54</sup> Mn	35	47	35
<sup>65</sup> Zn	5	21	8
<sup>110m</sup> Ag	4	0.3	1

Experiments with Deposition Samples

Because it is easier to interpret results obtained with specimens of a simple geometry like coupons and cylinders, crucibles were sometimes replaced by deposition samples as shown in Fig. 2 during the following sampling operations.

a) The first experiment, which introduced two stainless steel cylinders and one nickel cylinder in addition to four stainless steel crucibles, confirmed the result obtained with the bottomless crucible. The activity of <sup>65</sup>Zn was higher on stainless steel cylinders than in stainless steel crucibles (Table VII). Furthermore, it was demonstrated that the adsorption of <sup>65</sup>Zn on nickel cylinders may be higher by a factor of  $10^2$  as compared to stainless steel tube sections.

TABLE VII. Radionuclides on Crucibles and Cylinders (Flushing 4.33 h at 493 K and 1 m<sup>3</sup>/h)

Pos.	Mat.		Activity ( $10^2 \text{ s}^{-1}$ )			
			<sup>54</sup> Mn	<sup>65</sup> Zn	<sup>110m</sup> Ag	<sup>182</sup> Ta
1	ss	3.62 g Na	3.6	-	50	4.8
2	ss	4.12 g Na	3.5	1.09	60	4.5
3	ss	3.89 g Na	3.1	1.14	54	4.5
4	ss	2.78 g Na	2.7	1.08	34	4.6
5	ss	Cylinder	0.5	3.5	0.7	1.2
6	ss	Cylinder	0.5	2.3	0.9	1.6
7	Ni	Cylinder	2.7	275	1.3	0.8

INTERNATIONAL CONFERENCE ON LIQUID METAL TECHNOLOGY IN ENERGY PRODUCTION

b) Coupons made of a Nb-stabilized ferritic steel (6770), an austenitic steel (4961), and of nickel were set into the primary coolant for 4.3 hours at 493 K (220°C). All these materials are used in KNK (see Table VIII). Again, Ni had adsorbed nearly a factor of  $10^2$  more  $^{65}\text{Zn}$  than stainless steel, the activity of this nuclide on ferritic steel was higher by a factor of 10.  $^{54}\text{Mn}$  and  $^{60}\text{Co}$  followed the same order Ni > ferritic steel > austenitic steel, only the activity of  $^{182}\text{Ta}$  was higher on stainless steel than on the other materials (Table IX).

TABLE VIII. Deposition Sample Materials

Designation	Type	Use in KNK
6770	Nb stabilized ferritic steel	Primary system piping
4961	Nb stabilized austenitic steel	KNK-I fuel cladding
4981	Nb stabilized austenitic steel	KNK-II fuel cladding
4541	Ti stabilized austenitic steel	Crucible holder
Ni		Sampling crucibles

TABLE IX. Radionuclides on Test Coupons Deposited from Flowing KNK Primary Sodium at 493 K

	Nb stabilized Ferritic Steel	Austenitic Stainless Steel	Ni
	Activity ( $10^2 \text{ s}^{-1}$ )		
$^{65}\text{Zn}$	15	1.5	105
$^{54}\text{Mn}$	0.7	0.3	1.1
$^{110\text{m}}\text{Ag}$	0.5	0.3	0.2
$^{182}\text{Ta}$	0.5	1.5	0.4
$^{60}\text{Co}$	0.02	0.01	0.04

c) Seven cylinders (made from nickel, and from three different types of steel) were exposed to the primary KNK sodium for 11.6 hours at  $2.3 \text{ m}^3/\text{h}$  and 578 K (305°C). The deposited activities of  $^{51}\text{Cr}$ ,  $^{54}\text{Mn}$  and  $^{60}\text{Co}$  on the removed samples showed a steady slope for all steel specimens from cylinder 1 to cylinder 7, the activities on the Ni cylinder, however, interrupted this continuity (Fig. 3).  $^{65}\text{Zn}$  was measured with a high activity ( $1.6 \times 10^5 \text{ s}^{-1}$ ) on the Ni sample, two orders of magnitude less on the ferritic steel

( $1.2 \times 10^3 \text{ s}^{-1}$ ), and was not detectable on the austenitic steels.  $^{182}\text{Ta}$  decreased steadily from the first to the last specimen (Fig. 3).  $^{110\text{m}}\text{Ag}$  and  $^{124}\text{Sb}$  were not adsorbed in measurable activities from sodium at this temperature.

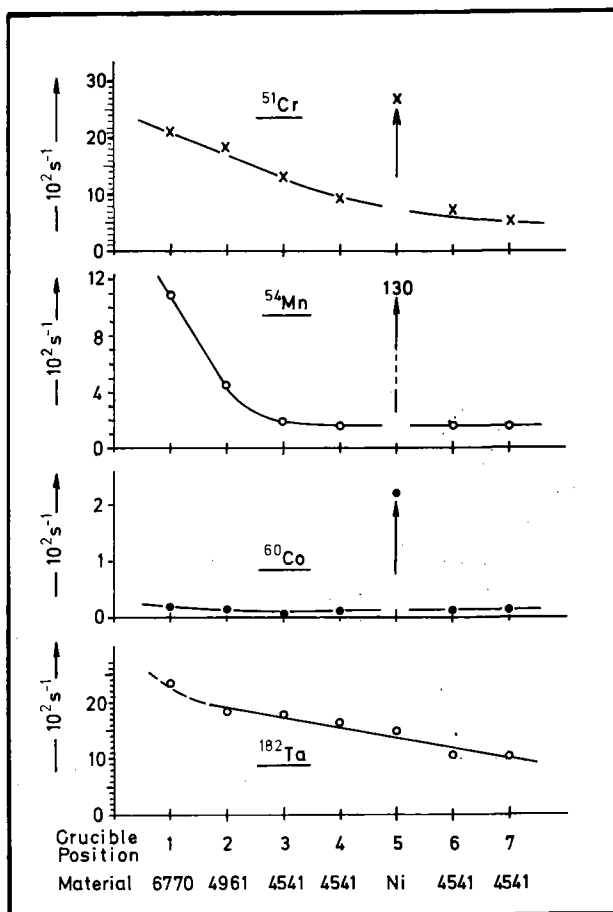


Fig. 3. Radionuclides Deposited on Metal Cylinders from Flowing KNK Primary Na at 578 K

d) Seven coupons had been mounted into the cylinders described above. In addition to the steel types already mentioned in Fig. 3, another Nb-stabilized austenite (4988), and an unstabilized steel (AISI 316ss) were used. Activity measurements confirmed the results obtained with the cylinder samples. Gamma spectra before and after removal of adhering sodium with water proved that the tendency of adsorption (Ni>steel) is not changed, even if substantial activities of  $^{51}\text{Cr}$ ,  $^{54}\text{Mn}$  and  $^{65}\text{Zn}$  are washed off.

e) Metal coupons made of Mo, Ta, Ti, and Ni (all surfaces as delivered) were mounted into seven stainless steel cylinders (4541), and exposed to the flowing sodium for 24 hours at 618 K (345°C) and  $2 \text{ m}^3/\text{h}$ . During

## INTERNATIONAL CONFERENCE ON LIQUID METAL TECHNOLOGY IN ENERGY PRODUCTION

that time (June 1974) the reactor was operated at a thermal power of 53 MW, and small amounts of  $^{140}\text{Ba}/^{140}\text{La}$  were measurable in the primary coolant ( $2.3$  to  $3.8 \times 10^2 \text{ s}^{-1}$ ). Table X shows the deposited activities of four radionuclides, in addition  $^{183}\text{Ta}$  was found at a rather constant ratio to  $^{182}\text{Ta}$ . Again the deposited activities of  $^{54}\text{Mn}$  and  $^{65}\text{Zn}$  were higher by a factor of ten or more on Ni coupons than on any other metal specimen. On the contrary,  $^{140}\text{Ba}/^{140}\text{La}$ ,  $^{182}\text{Ta}$  and  $^{183}\text{Ta}$  were deposited on all introduced metal tabs up to the same amount.  $^{110m}\text{Ag}$  and  $^{124}\text{Sb}$  were not detectable on any sample, although the activity concentration of  $^{110m}\text{Ag}$  was of the same level as the concentrations of  $^{65}\text{Zn}$  and  $^{54}\text{Mn}$  at that time.

On the stainless steel cylinders the deposited activity of  $^{140}\text{Ba}$  was second to  $^{54}\text{Mn}$ , it was even higher than the activity of  $^{65}\text{Zn}$  per square centimeter of sample surface.

TABLE X. Radionuclides on Metal Coupons Deposited from Flowing Primary Sodium at 618 K

Sodium Flow Direction	Activity ( $10^2 \text{ s}^{-1} \text{ cm}^{-2}$ )				
	Material	$^{54}\text{Mn}$	$^{65}\text{Zn}$	$^{182}\text{Ta}$	$^{140}\text{Ba}/^{140}\text{La}$
↓	Mo	7	7	1.2	0.9
	Ta	2	7	1.2	0.5
	Ti	1	1	1.3	0.8
	Ni	69	300	0.8	0.7
	Mo	6	9	1.5	0.7
	Ta	2	17	0.8	0.2
	Ti	1	2	1.2	0.7

f) Nickel coupons of different surface treatment (as delivered, electropolished, and pickled) were exposed 24 hours to primary sodium at 493 K ( $220^\circ\text{C}$ ) and  $0.5 \text{ m}^3/\text{h}$ . The results (Table XI) indicated that electropolishing and pickling may reduce the adsorption

TABLE XI. Sorption of Radionuclides on Ni Coupons (Different Surface Pretreatment) at 493 K

Deposited Nuclide	$^{54}\text{Mn}$	$^{65}\text{Zn}$	$^{110m}\text{Ag}$
Surface Treatment	$\text{s}^{-1} \text{ cm}^{-2}$		
As delivered	4.2	172	13
Electropolished	3.6	42	2.2
Pickled	2.4	41	5.9

of radionuclides on nickel surfaces up to a certain

amount. The surface treatment effect is small, however, compared to the material effect (see Table X, and Fig. 3).

### Experiments with Crucibles

During the following sampling operations crucibles of two different materials (Ni, steel; Ni,  $\text{Al}_2\text{O}_3$ ; Ni, Mo) were placed into the crucible holder alternately. The Na contents were used by the KNK chemistry laboratory for the determination of oxygen ( $^{10}$ ), the activities on the empty crucibles were counted therefore after dissolution of sodium oxide in water.

g) Sampling with Ni and stainless steel crucibles at 493 K ( $220^\circ\text{C}$ ) and  $1 \text{ m}^3/\text{h}$  (flushing time 5 h; 24 hours after reactor shut down) resulted in the expected differences of the deposited  $^{65}\text{Zn}$  activities; however,  $^{54}\text{Mn}$  was found in same amounts on both types of sampling vessels. Surprisingly, no  $^{140}\text{Ba}/^{140}\text{La}$  was detectable.

h) Sampling with Ni and stainless steel crucibles at 573 K ( $300^\circ\text{C}$ ) and  $1.5 \text{ m}^3/\text{h}$  (flushing time 5.2 h; reactor at  $27.5 \text{ MW}_{\text{th}}$ ) yielded the expected differences in the deposited activities of  $^{65}\text{Zn}$  and  $^{54}\text{Mn}$  (Table XII),  $^{140}\text{Ba}/^{140}\text{La}$  was present again.

TABLE XII. Radionuclides Adsorbed on Ni and Stainless Steel Crucibles (Na dist. off) at 573 K

Pos.	Mat.	$^{54}\text{Mn}$	$^{65}\text{Zn}$	$^{124}\text{Sb}$	$^{140}\text{Ba}$
		$10^2 \text{ s}^{-1}$			
1	Ni	190	380	2.5	0.7
2	ss	69	6	2.7	1.3
3	Ni	160	660	3.3	0.7
4	ss	56	9	2.0	0.8
5	Ni	130	760	3.0	0.6
6	ss	74	6	3.3	1.1
7	Ni	140	570	2.5	0.9

i) Sampling with Ni and  $\text{Al}_2\text{O}_3$  crucibles at 608 K ( $335^\circ\text{C}$ ) and  $2 \text{ m}^3/\text{h}$  (flushing time 6 h; reactor at  $48 \text{ MW}_{\text{th}}$ ) confirmed earlier results with crucibles at lower temperatures (see Table IV): Very high activities of  $^{54}\text{Mn}$  and  $^{65}\text{Zn}$  on Ni crucibles as compared



# INTERNATIONAL CONFERENCE ON LIQUID METAL TECHNOLOGY IN ENERGY PRODUCTION

to ceramic vessels.

k) Sampling with Ni and Mo crucibles at 573 K (300°C) and 2 m<sup>3</sup>/h (flushing time 4.25 h; 48 h after reactor shutdown) yielded the results in Table XIII: <sup>54</sup>Mn higher by a factor of about ten on Ni than on Mo vessels; <sup>65</sup>Zn on Ni crucibles main activity, and not detectable on Mo crucibles. Other radionuclides showed no significant variations; <sup>140</sup>Ba was not detectable two days after reactor shutdown.

TABLE XIII. Radionuclides Adsorbed on Ni and Mo Crucibles at 573 K (Na distilled off)

Pos.	Mat.	<sup>54</sup> Mn	<sup>60</sup> Co	<sup>65</sup> Zn	<sup>182</sup> Ta
		10 <sup>2</sup> s <sup>-1</sup>			
1	Ni	92	0.3	520	2.2
2	Mo	10	0.2	-	2.5
3	Ni	80	0.5	410	2.8
4	Mo	9	0.3	-	2.4
5	Ni	76	0.8	410	4.5
6	Mo	12	0.3	-	4.1
7	Ni	82	0.5	200	-

### DISCUSSION

On the contrary to the results obtained at DFR, a significant difference of the deposition behavior of radionuclides on Ni and stainless steel from KNK sodium was observed. Two possible reasons for this discrepancy are:

- At KNK main activities are activation products; two of them - <sup>65</sup>Zn and <sup>54</sup>Mn - are responsible for the difference of the total gamma activities on Ni and on stainless steel specimens. At DFR main activities are fission products; the activity of <sup>54</sup>Mn was negligible and <sup>65</sup>Zn was never reported.

- Sampling temperature at DFR was about 523 K. Regular sampling temperature at KNK was about 600 K; if the samples were taken at lower temperatures, the differences of adsorbed activities between Ni surfaces and other materials decreased.

<sup>54</sup>Mn was strongly adsorbed on Ni surfaces at higher temperatures (about 600 K); it is easily removed by flushing crucibles or deposition samples with water. <sup>65</sup>Zn showed a selective deposition on Ni surfaces at all temperatures covered by the experiments (473 K to 618 K); it was removable to a certain extent by water.

<sup>110m</sup>Ag was deposited on material specimens only at low temperatures; in that case the activity on Ni surfaces was higher than on any other material. <sup>110m</sup>Ag was hardly removable by treatment with water.

No adsorption of <sup>124</sup>Sb was observed.

<sup>182</sup>Ta was deposited on Ni surfaces to the same amount as on other metal surfaces. No special effects were observed for <sup>182</sup>Ta on Ta coupons; that means that <sup>182</sup>Ta was in a chemical state which allowed no isotopic exchange with metallic Ta surfaces.

It was concluded that nickel crucibles are not suitable for Na sampling, if radionuclides are to be measured in primary sodium. At KNK-II stainless steel crucibles will be used for radionuclide determination.

### REFERENCES

- 1) Tebbert, H., Bruder Müller, G., Harde, R., Stöhr, K.W. "Die Kompakte Natriumgekühlte Kernreaktoranlage" At.Strom 13, 117 - 129 (1967)
- 2) Andrae, H., Marth, W. "Das Projekt KNK-II" Atomwirtsch., Atomtech. 18, 93 - 95 (1973)
- 3) Stamm, H.H., Clauss, H., Nolte, K. "Aktivierungsanalytische Bestimmung von metallischen Verunreinigungen in KNK-Primärnatrium" Z.Anal.Chem. 266, 337 - 340 (1973)
- 4) Haubold, W., Stade, K.Ch., Stamm, H.H. "Chemie in natriumgekühlten Kernkraftwerken" VGB-Kraftwerkstech. 55, 94 - 104 (1975)
- 5) Stamm, H.H. "Radionuklide im KNK-Primärsystem" Reaktortagung Nürnberg 1975, Compacts pp. 730 - 733
- 6) Stamm, H.H., Stade, K.Ch., "Corrosion product behaviour in the primary circuit of the KNK nuclear reactor facility" IAEA specialists meeting on fission and corrosion product behaviour in primary circuits of LMFBR's, Dimitrovgrad/USSR, 1975
- 7) Borgstedt, H.U., Perić, Z., Wittig, G. "Anlage zur Natriumdestillation für analytische Zwecke NADESTAN 4" Report KFK 1941 (1974)
- 8) Stamm, H.H. "Die Bestimmung von Radionukliden im Primärkreislauf natrium-gekühlter Kernreaktoren" Workshop über moderne analytische Methoden 1973 Report Jül-Conf-11 (Bd. 1), 1974
- 9) Davies, R.A., Drummond, J. "Behaviour of radioactive impurities in DFR liquid metal coolant" J.Brit.Nucl.Energy Soc. 12, 427 - 435 (1973)
- 10) Stade, K.Ch., unpublished

# INTERNATIONAL CONFERENCE ON LIQUID METAL TECHNOLOGY IN ENERGY PRODUCTION

## THE ON-LINE SEPARATION OF RADIOIODINE IN HIGHLY RADIOACTIVE EBR-II SODIUM

R. Villarreal C. C. Miles

Argonne National Laboratory  
Argonne-West Idaho Falls, Idaho 83401

### ABSTRACT

Radioiodine in molten sodium cooled to  $\sim 100\text{--}130^\circ\text{C}$  ( $373\text{--}403^\circ\text{K}$ ) will quantitatively segregate to the walls of a stainless steel vessel and remain after the sodium is drained off. This segregation phenomenon is the basis for the rapid and quantitative separation of I-131 from highly radioactive sodium for subsequent determination by radiochemical techniques. This paper reports the results of experiments conducted to determine the segregation and redistribution of I-131, and certain other nuclides, in molten sodium in the temperature range of  $100\text{--}370^\circ\text{C}$  ( $373\text{--}643^\circ\text{K}$ ). The success of these experiments led to the system proposed for the on-line separation of radioiodine from highly radioactive EBR-II sodium. Radioiodines determined within 2-4 hours after sampling will greatly aid in the characterization of fuel-cladding failures in LMFBRs.

Iodine is a low-boiling point fission product which is released to the sodium coolant of a fast-breeder reactor when fuel is exposed to the sodium coolant. The quantity and rate of radioiodine release from the fuel to the sodium coolant may be indicative of the extent or absence of sodium-fuel contact. The rapid determination of radioiodine, namely I-131, immediately following a fuel cladding breach in EBR-II has not been feasible because of problems involved in sampling, transferring, and working with sodium samples containing  $\sim 2.5$  millicuries of Na-24 per gram of sample. The dissolution of the highly radioactive sodium and subsequent separation of radioiodine must be performed either in a remote facility or the Na-24 ( $t_{1/2} = 15\text{h}$ ) allowed to decay for several days before the sample can be handled in a cold laboratory.

A new method is outlined for the on-line separation and subsequent determination of radioiodine in the highly radioactive sodium coolant of EBR-II and other similar LMFBRs. The method is based on the segregation of iodine in molten sodium and is rapid, simple, and may be upgradeable to the on-line determination of radioiodine. The lengthy dissolution of radioactive sodium samples and exposure of analytical personnel to Na-24 radiation is eliminated.

The segregation of many nuclides to the walls of

sample vessels has been recognized for many years; however, several of the nuclides that segregate to the sodium-vessel interface are partitioned when the sodium is drained off at  $100\text{--}130^\circ\text{C}$ <sup>1,2,3</sup>. Iodine that has segregated to a vessel surface remains on the surface when the sodium is drained off, even after the surface is washed with new sodium at a temperature of  $100\text{--}130^\circ\text{C}$ . This characteristic of iodine led to the analytical application of the segregation technique for the separation and subsequent determination of I-131 in EBR-II sodium.

A series of EBR-II sodium samples taken at  $370^\circ\text{C}$  in stainless steel tubes were allowed to cool to the solid state and then stored until the Na-24 activity had decayed to  $\sim 100$  mR/hr. The tubes were then heated to  $\sim 98^\circ\text{C}$  in an argon atmosphere glove box and the sodium drained from the tube. The tube was then washed with water and the I-131 was separated and radiochemically determined. Ninety-five percent of the I-131 in the original sodium was recovered from the walls of the tube. After several confirming experiments, the design and construction of a segregated-iodine sodium-sampler (SISS) for on-line testing in EBR-II was initiated. The SISS is a 125-cc stainless steel tube designed to remain on line while the highly radioactive molten sodium is cooled and forced out of the tube with argon after segregation has occurred. This returns most of the Na-24 to the coolant system and eliminates the need for several days decay before handling. The decontamination factor for Na-24 obtained by draining the SISS is  $\sim 150$  and the I-131 recovered radiochemically is 90-95% with a total analyses time of  $\sim 4$  hours from time of sampling. Other radioiodines qualitatively identified in the SISS were I-132 (2.3h), I-133 (2h), I-135 (6.7h), and a trace of I-134 (53 min).

The recovery of I-131 from a radioactive sodium sample taken in a stainless steel tube, cooled, drained, and washed with nonradioactive sodium at  $100\text{--}130^\circ\text{C}$ , was  $\sim 94\%$ . The decontamination factor for Na-24 in a tube after a single nonradioactive sodium wash is  $>5600$ . Other nuclides followed qualitatively in this experiment were Cs-137, Cs-134, Na-22, Sn-In-113m, Sn-117m, Mn-54, Ag-110m, and Au-198. Also, an experiment was conducted to determine which

## INTERNATIONAL CONFERENCE ON LIQUID METAL TECHNOLOGY IN ENERGY PRODUCTION

of the above nuclides that segregate are redistributed into molten sodium at 370°C, the operating temperature of EBR-II sodium. The segregation and redistribution characteristics of some of the nuclides studied are given in Table I.

Table I  
Segregation and Redistribution of Some Nuclides

Nuclide	Segregates in Na @ 100-130°C	Redistributed in Na Wash @ 100-130°C	Redistributed in Na @ 370°C
I-131	yes	no	yes
Cs-137	yes	partially	mostly
Sn-117m	no	-	-
Mn-54	yes	no	no
Ag-110m	no	-	-
Au-198	no	-	-
Sb-125	yes	no	partially

The analytical application of the segregation technique for separating radioiodine from highly radioactive sodium and the elimination of residual Na-24 activity with a nonradioactive sodium wash followed by direct counting of the segregated radioiodine with a Ge(Li) detector system is a proposed method for the on-line determination of radioiodine in EBR-II. A sketch of the SISS proposed for EBR-II is shown in Figure 1. EBR-II sodium coolant would normally flow through the SISS at 370°C where segregation does not occur. When a sample is desired, the system is valved off and the radioiodine in the sodium quantitatively segregates to the walls of the SISS upon cooling the sodium to ~100-130°C. The cooled sodium is then forced out of the SISS into the primary sodium tank with pressurized argon. A measured volume of nonradioactive sodium at ~100-130°C is fed into the SISS to exchange with the residual radioactive sodium and is likewise forced out with pressurized argon. The radioiodine will remain on the walls of the SISS while Na-24 and some of the other residual nuclides are removed with the non-radioactive sodium wash.

The segregation vessel may now be removed and the radioiodine may be determined by directly counting the SISS vessel. If direct counting of the radioiodine on the vessel is not feasible, the SISS, now cleaned of Na-24, may be removed to the laboratory for the separation and radiochemical determination of radioiodine and possibly other nuclides of like behavior.

The rapid determination of all the radioiodines with half lives in the range of 53 minutes to 8 days with the proposed system will provide a new tool for the characterization of fuel-cladding failures. The rate of release and the ratio of the released fission-product radioiodines with different half lives is information which may be helpful in differentiating fuel-cladding failures in which the fuel has direct contact with the sodium coolant from failures where there is no direct sodium-fuel communication.

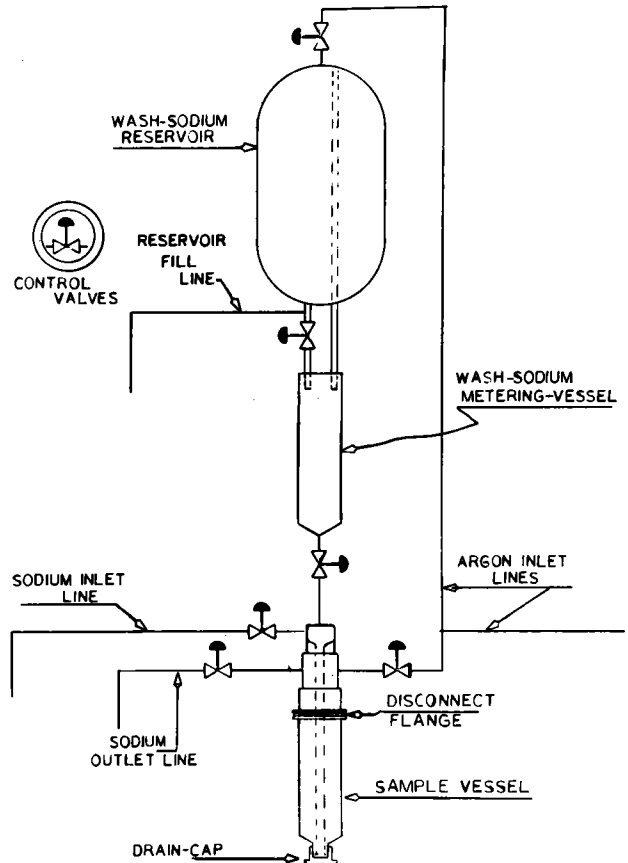


Fig. 1. Segregated-iodine sodium sampler

### REFERENCES

1. Segregation of Radiocesium in Samples of Primary Sodium, Reactor Development Program Progress Report, June 1967, Argonne National Laboratory Report ANL-7349, pp. 37-39.
2. Studies of Cesium Segregation, *ibid.*, Nov 1967, p. 73.
3. C. C. Miles, Experiments on the Absorption of I-131 by 304 Stainless Steel Surfaces in Sodium, Argonne National Laboratory, unpublished letter (1971).

# INTERNATIONAL CONFERENCE ON LIQUID METAL TECHNOLOGY IN ENERGY PRODUCTION

## A COMPUTATIONAL TECHNIQUE FOR ESTIMATING CORROSION PRODUCT RELEASE IN AN LMFBR

By

W. L. Kuhn

### ABSTRACT

A model is developed to predict the release of activated corrosion products in an LMFBR. Model parameters are obtained from literature correlations and from fitting the model to release rates observed in experimental sodium loops. The model is simplified to consider only two cases: release controlled by corrosion only or controlled by simultaneous corrosion and diffusion only. The release rates, radionuclide inventories, and resulting radiation fields near primary system components are predicted for the Fast Flux Test Facility as a function of operating temperature, oxygen concentration in the sodium, and time of operation. Saturation inventories are reported for  $^{54}\text{Mn}$ ,  $^{60}\text{Co}$ ,  $^{58}\text{Co}$ ,  $^{51}\text{Cr}$ , and  $^{59}\text{Fe}$ . The resulting radiation fields are due mainly to  $^{54}\text{Mn}$ , and are found to reach the 5 R/hr range for operation at a core outlet temperature of 593°C.

### INTRODUCTION

During the operation of an LMFBR, sodium circulating through the core acquires various radionuclides released from activated fuel cladding. The most important isotopes are  $^{54}\text{Mn}$ ,  $^{60}\text{Co}$ ,  $^{58}\text{Co}$ ,  $^{51}\text{Cr}$ , and  $^{59}\text{Fe}$ . The radionuclides are released both by wastage of the activated cladding due to sodium corrosion and by solid-state diffusion of nuclides out of the cladding into the circulating sodium. The released radionuclides circulate with the sodium and tend to deposit in the piping and components of a "loop" type LMFBR. The deposited radionuclides can cause appreciable radiation fields near key components which greatly complicate maintenance procedures.

Work is currently in progress at HEDL to improve our previous estimate<sup>(1)</sup> of the magnitude and distribution of the radiation fields near the FFTF Heat Transport System, which includes the primary sodium piping, pump, and intermediate heat exchanger. Our goal is to characterize the radionuclide release and distribution in order to evaluate potential control measures, to predict decontamination factors required to allow "hands-on" maintenance of key components, and to estimate the radiation fields so that appropriate maintenance procedures can be developed.

This paper summarizes the computational techniques being used to estimate the inventories of radionuclides released to an LMFBR as a function of time, temperature, and oxygen concentration in the sodium. A full discussion of the computations will be published elsewhere.

### RADIONUCLIDE RELEASE MODEL

The inventory of a given radionuclide released from an LMFBR core obeys

$$\frac{dI}{dt} = \oint_A F(t) dA - \lambda I,$$

where  $I$  [Ci] is the inventory,  $t$  [sec] is time,  $F$  [Ci/m<sup>2</sup>-sec] is the radionuclide mass flux (i.e., the release rate per unit area) from an element of the core cladding surface,  $\lambda$  [sec<sup>-1</sup>] is the decay constant, and  $F$  is integrated over the cladding area  $A$  [m<sup>2</sup>] of the core. Since  $I = 0$  at  $t = 0$ ,

$$I = e^{-\lambda t} \oint_A P(t) dA, \text{ and } P(t) = \int_0^t e^{\lambda t} F(t) dt.$$

The integration over the core surface area is required since the temperature, neutron flux, and sodium velocity, which influence the radionuclide release rate, vary throughout the core. The mass flux is obtained from a release model.

We have developed a radionuclide release model applicable either to release from cladding undergoing simultaneous activation or from activated cladding specimens in HEDL experimental sodium loops. Model parameters needed to predict LMFBR radionuclide inventories can thus be evaluated by fitting the model to the analysis of experimentally determined release rates from activated cladding.

The model comprises two principal parts: an expression for the release rate from the cladding surface which depends on the radionuclide concentration at the cladding surface, and a partial differential equation describing the changing radionuclide concentration profile in the cladding near the surface.

The partial differential equation is written relative to a coordinate system moving inward with the corroding surface. The resulting unsteady-state diffusion equation written for a given radionuclide is

$$\frac{\partial c}{\partial t} - u \frac{\partial c}{\partial x} = D \frac{\partial^2 c}{\partial x^2} - \lambda c + R,$$

where  $c$  [Ci/m<sup>3</sup>] is the radionuclide concentration in the cladding,  $u$  [m/sec] is the surface corrosion rate,  $x$  [m] is the depth from the surface into the cladding,  $D$  [m<sup>2</sup>/sec] is the diffusivity of the radionuclide in the cladding,  $\lambda$  [sec<sup>-1</sup>] is the radionuclide decay constant, and  $R$  [Ci/m<sup>3</sup>-sec] is the activation rate. We assume that  $u$ ,  $D$ , and  $R$  are constant with  $x$  and  $t$ . This assumption can be relaxed to obtain a more sophisticated and flexible model, but this requires the evaluation of additional adjustable parameters.

Three expressions for the mass flux from the cladding to the sodium are proposed and equated to obtain the surface boundary condition. The expressions are

$$\begin{aligned} \left[ D \frac{\partial c}{\partial x} + u c \right]_{x=0} &= k_o c(x=0) - k_i c_L(x=0) \\ &= k_L [c_L(x=0) - c_B], \end{aligned}$$

where the first part describes the mass flux in the cladding to the cladding surface, the second part describes that across the cladding-sodium interface, and the last part describes that in the sodium from the surface to the bulk flowing sodium. The terms  $k_o$  and  $k_i$  are "outward" and "inward" kinetic constants [m/sec];  $c_L$  [Ci/m<sup>3</sup>] is the radionuclide concentration in the sodium,  $k_L$  [m/sec] is a liquid phase mass transfer coefficient, and  $c_B$  [Ci/m<sup>3</sup>] is the mixed average or "bulk" radionuclide concentration in the flowing sodium. These expressions are combined to eliminate  $c_L$  ( $x=0$ ), to obtain the surface boundary condition:

$$D \frac{\partial c}{\partial x} \Big|_{x=0} = (k-u) c(x=0) - \kappa k c_B, \text{ where}$$

$$k = \frac{k_o k_L}{k_i + k_L} \text{ and } \kappa = \frac{k_i}{k_o}$$

The other  $x$ -boundary condition is  $c \rightarrow$  finite as  $x \rightarrow \infty$ , with the initial condition that  $c = c_o$  at  $t = 0$  for all  $x$ . The partial differential equation and associated boundary conditions are easily solved by Laplace transforms to obtain the concentration profile in the cladding and thence the functions  $F(t)$  and  $P(t)$ .

To date we have used only two special forms of the radionuclide release: those for  $k \rightarrow \infty$  and for  $k = u$ . The former corresponds to a zero surface concentration in the cladding and the latter to "stoichiometric" release, for which the radionuclide is released in proportion to its concentration deep in the cladding. We have assumed  $c_B$  is negligible in all cases. The resulting forms of  $P(t)$  for release from activating cladding are equations 1A and 1b.

$$\text{For } k = u, P'(t) = \frac{Ru}{\lambda} \left( \frac{e^{\lambda t_1}}{\lambda} - t \right), \quad (1a)$$

and for

$$k \rightarrow \infty, P'(t) = \frac{R}{\lambda} \left\{ \frac{u}{2\lambda} \left[ e^{\lambda t} - 1 + \sqrt{1 + \frac{4D\lambda}{u^2}} e^{\lambda t} \operatorname{erf} \sqrt{\lambda t + \frac{u^2 t}{4D}} \right] \right. \\ \left. - \frac{ut}{2} - \left( \frac{D}{u} + \frac{ut}{2} + \frac{u}{2\lambda} \right) \operatorname{erf} \sqrt{\frac{u^2 t}{4D}} - \sqrt{\frac{Dt}{\pi}} e^{\frac{u^2 t}{4D}} \right\} \quad (1b)$$

These primed expressions refer to the release of radionuclides if  $R$  is constant (uninterrupted reactor power) during the residence of a fuel assembly in the core.

The evaluation of  $P(t)$  for an LMFBR is complicated by the periodic replacement of fuel assemblies and by power fluctuation during the in-core residence of a subassembly caused by the typically staggered refueling schedule. Fuel replacement causes the release from a given location in the core to be a periodic function of period  $t_c$ , the fuel cycle. For a given core location,  $P(t)$  can be replaced by a sum of products involving decay factors which are multiples of  $\lambda t_c$  and in which  $P(t)$  is evaluated for time periods no greater than  $t_c$ . For times between  $N$  and  $(N + 1)$  fuel cycles, the result is:

$$P(t) = P(t_c) + e^{\lambda t_c} P(t_c) + e^{2\lambda t_c} P(t_c) + \dots \\ + e^{N\lambda t_c} P(t - Nt_c), \quad Nt_c < t < (N + 1)t_c$$

During a given subassembly's residence in the core, the reactor power, and hence  $R$ , will drop to zero periodically as other core locations are refueled. Thus, the fuel cycle is divided into successive periods  $t_1$  at full power and periods  $t_2$  at zero power. During full power operation activation, decay, corrosion, and diffusion occur, but during zero power periods only decay occurs (i.e.,  $R = u = D = 0$ ). Over a fuel cycle,  $P(t)$  can be evaluated in terms of  $P'(t)$  by a superposition technique involving displacements in the time variable.

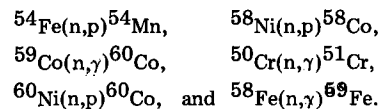
The result of this kind of calculation is

$$P(t_c) = P[n(t_1 + t_2)] \\ = P'(nt_1) + e^{\lambda t_1} (e^{\lambda t_2} - 1) P'[(n-1)t_1] \\ + e^{2\lambda t_1} e^{\lambda t_2} (e^{\lambda t_2} - 1) P'[(n-2)t_1] + \dots \\ + e^{\lambda(n-1)t_1} e^{(n-2)\lambda t_2} (e^{\lambda t_2} - 1) P'(t_1),$$

where  $1/n$  is the fraction of the core refueled at once. These relations can be further refined to account for the different ages of subassemblies in the core at any one time.

ESTIMATED PARAMETERS FOR THE FFTF

The activation rate  $R$  for the nuclides of interest is obtained as a function of position in the core from three-dimensional neutron transport calculations. The important reactions are the following:



## INTERNATIONAL CONFERENCE ON LIQUID METAL TECHNOLOGY IN ENERGY PRODUCTION

The corrosion rate  $u$  and the diffusivity  $D$  are found from literature correlations in combination with experimental observations of activated cladding corrosion tests conducted in HEDL sodium loops.

The HEDL corrosion tests have been conducted at 604°C and at oxygen concentrations of 0.5 and 2.5 ppm. From cladding specimen weight-change data and from radionuclide concentration profiles obtained by sectioning the specimens, the corrosion rate and apparent diffusivity are found at the experimental conditions. Since both  $u$  and  $D$  are strong functions of temperature and the temperature varies significantly across an LMFBR core, our experimental results must be supplemented by literature correlations for the temperature dependence of  $u$  and  $D$ .

Bagnall and Jacobs<sup>(2)</sup> have reported a correlation for the corrosion rate of type 316 stainless steel in sodium as a function of temperature and sodium oxygen concentration which is independent of sodium velocity for velocities greater than about 3 m/sec. Since recent HEDL corrosion tests<sup>(3)</sup> have shown that the corrosion rate becomes independent of sodium oxygen concentration below 0.5 ppm and is not linear in the concentration below 2.5 ppm, we have adopted the correlation's temperature dependence but not the oxygen dependence. After incorporating our corrosion rates at 0.5 and 2.5 ppm oxygen and doubling the predicted corrosion rate to account for large axial temperature gradients present in an LMFBR core<sup>(2)</sup>, we obtain

$$u = \exp(14.665-18120/T) \text{ mm/yr at 0.5 ppm oxygen}$$

and

$$u = \exp(15.574-18120/T) \text{ mm/yr at 2.5 ppm oxygen,}$$

where  $T$  is the temperature [ $^{\circ}$ K].

Smith and Hales<sup>(4)</sup> report a correlation for the diffusivity of manganese in 316 stainless steel. Extrapolated to our experimental temperature (604°C), the correlation predicts a diffusivity which is an order of magnitude below the apparent diffusivity obtained from an analysis of  $^{54}\text{Mn}$  concentration profiles in the cladding specimens using our model and the experimentally measured corrosion rate. The discrepancy is probably due to the relatively simple model used in our analysis; e.g., behavior such as the corrosion roughening of the specimen surface, the partial or complete formation of a ferrite phase, and a time-varying corrosion rate are not accommodated by the model. Nevertheless, the apparent diffusivity obtained using our model is the best choice when applying the same model to predict radionuclide release in an LMFBR. Combining our observations with the reported temperature dependence, we obtain

$$D = \exp(6.719-31253/T) \text{ mm}^2/\text{sec.}$$

In principle, an analysis of the experimental radionuclide concentration profiles or release rates will yield values of the parameter  $k$  for the various nuclides; however, as stated above we have so far considered only the cases  $k \rightarrow \infty$  and  $k = u$ .

The first case is applied to the release of  $^{54}\text{Mn}$  and  $^{51}\text{Cr}$ , which exhibit small surface concentrations after corrosion in sodium occurs. The second case of stoichiometric release is applied to the release of  $^{59}\text{Fe}$ ,  $^{60}\text{Co}$ , and  $^{58}\text{Co}$  along with a multiplicative correction factor. The correction factors are based on concentration profiles found in activated stainless steel specimens exposed to sodium in HEDL sodium loops and in EBR-II, and account for the non-stoichiometric release of such radionuclides as  $^{60}\text{Co}$  and  $^{58}\text{Co}$ .

Corrections are also made for the surface depletion or enhancement of precursor isotopes, such as  $^{50}\text{Cr}$  or  $^{58}\text{Ni}$ . The overall correction factors adopted for the important activation reactions are

Reaction	$k/u$	Correction
$^{54}\text{Fe}(n,p)^{54}\text{Mn}$	$\infty$	1
$^{50}\text{Cr}(n,\gamma)^{51}\text{Cr}$	$\infty$	0.5
$^{59}\text{Co}(n,\gamma)^{60}\text{Co}$	1	0.45
$^{58}\text{Ni}(n,p)^{58}\text{Co}$	1	0.13
$^{60}\text{Ni}(n,p)^{60}\text{Co}$	1	0.13
$^{58}\text{Fe}(n,\gamma)^{59}\text{Fe}$	1	1

### RESULTS FOR FFTF RADIONUCLIDE INVENTORIES

Expected radionuclide inventories for the FFTF have been calculated for three operating conditions, as follows:

Condition	Core Inlet Temp ( $^{\circ}$ C/ $^{\circ}$ F)	Core Outlet Temp ( $^{\circ}$ C/ $^{\circ}$ F)	Oxygen (ppm)
A	427/800	593/1100	0.5
B	427/800	593/1100	2.5
C	316/600	482/900	0.5

Case A is the rated FFTF operating condition; the other cases explore the effect of temperature and oxygen concentration. The FFTF core will be refueled by thirds. All calculations are for  $t_1 = 100$  days and  $t_2 = 32$  days, corresponding to a fuel cycle of  $t_c = 396$  days.

The saturation inventories for the three operating conditions are as follows:

	A	B	C
$^{54}\text{Mn}$	638 Ci	799 Ci	32 Ci
$^{60}\text{Co}$	32	81	1.4
$^{68}\text{Co}$	42	103	1.5
$^{51}\text{Cr}$	208	236	12
$^{59}\text{Fe}$	4.8	12	0.2

Only the first three radionuclides contribute significantly to the radiation fields exterior to the reactor piping and components. Typical radiation levels within the FFTF Heat Transport System cells are shown in Figure 1 as a function of time for the three operating conditions.

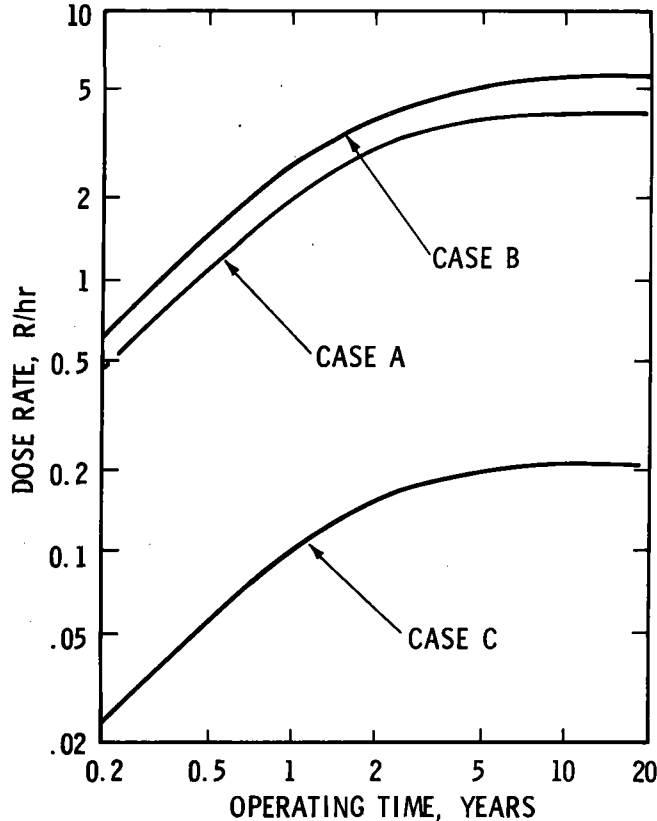


FIGURE 1. Typical expected dose rates in the FFTF Heat Transport System cells.

#### DISCUSSION

From the above it is clear that the oxygen concentration has only a slight effect on the radiation levels. This is because the release of the most important radionuclide,  $^{54}\text{Mn}$ , is mostly diffusion controlled, which has been verified by HEDL corrosion experiments<sup>(5)</sup>. The diffusive release becomes dominant at small times, causing the inventories to increase as  $t^{3/2}$  instead of  $t^2$  as for "stoichiometric" release.

The effect of changing the reactor operating temperature is very large because of the large temperature dependence predicted by the correlations for  $u$  and  $D$ . The release of activated corrosion products at  $538^\circ\text{C}$  will be determined by sodium loop tests to be conducted at HEDL over the next two years. The results will improve our knowledge of the temperature dependence of the radionuclide release rates over the temperature range of interest here.

#### REFERENCES

1. T.J. Kabele, W.F. Brehm, and D.R. Marr, "Activated Corrosion Product Radiation Levels Near FFTF Reactor and Closed Loop Primary System Components", HEDL-TME-72-71, May 15, 1972.
2. C. Bagnalls and D.C. Jacobs, "Relationships for Corrosion of Type 316 Stainless Steel in Liquid Sodium", WARD-NA-3045-23, May 1975.
3. W.F. Brehm, "Radioactive Corrosion Product Control and Transport", International Conference on Liquid Metal Technology in Energy Production, May 3-6, 1976, Champion, PA, HEDL-SA-1008.
4. A.F. Smith and R. Hales, "Diffusion of Manganese in Type 316 Austenitic Stainless Steel", U.K. Paper RD/B/N2756, November 1973.
5. HEDL Quarterly Technical Report, January-February-March 1975, HEDL-TME-75-3.

FISSION PRODUCT MEASUREMENTS IN THE INPILE FISSION  
PRODUCT LOOP

N.Mitsutsuka, Y.Gohshi, H.Shimajima (Toshiba) and  
H.Feuerstein (GfK Karlsruhe)

The behavior of fission gases in a circulating sodium system was investigated. The release rates to the covergas were strongly influenced by the sodium temperature. For the system I-135 /Xe-135 m, Xe-135 the release behavior of the xenon isotopes followed exactly the adsorption of iodine within the loop. The behavior of nuclides formed during irradiation is more complex and could not be explained completely. Two kinds of half lives for the degassing process were found. Degassing half lives in the range of 17 to 32 minutes are explained by diffusion through the sodium-covergas interface. Another kind of degassing half life, ranging from 80 to over 200 minutes must be explained by some special features of the system.

## INTRODUCTION

The release of fission gases to the cover gas of a reactor is an indicator for cladding failures. By measuring nuclides of different half life, information about the type of failure is obtained. The knowledge of the transport behavior of the fission gases from the source within the core to the covergas system is therefore very important. Furthermore to predict the amount and distribution of fission gases remaining in the primary sodium loop and to calculate contamination and radiation levels of the covergas system, detailed information about the fission gas behavior is needed.

In the case of a cladding failure, fission gases will be released into the sodium and transported to the covergas. This transport is usually delayed. The delay is expressed in the form of a degassing

probability  $\lambda_d$  or a corresponding degassing half life  $HL_d$ .  $\lambda_d$  ( $HL_d$ ) has for each system a specific value. To describe degassing, often the release fraction or the release to birth ratio, R/B, is used. This is the number of atoms of the nuclide, released per second to the covergas, divided by the production rate of the same nuclide. Even if this production rate is not known, relative release fractions are useful. Because of the degassing delay, the release fraction is a function of the nuclide half life.

Degassing half lives and release fractions were determined over a wide range of parameters.

## EXPERIMENTS

The Fission Product Loop was used for the investigations. A detailed description is given by reference <sup>(1)</sup>. Fig. 1 shows a flow diagram of the loop. Actually the loop consists of two parts. Only one part was used for investigating the fission gas behavior. In the inpile plug, 150 grams of UO<sub>2</sub>- spheres, each 2 mm diameter, were irradiated in the Toshiba Training Reactor. Under the conditions of the experiments, fission products were released from the fuel by recoil. Circulating high purity sodium (less than 5 ppm Na<sub>2</sub>O) transported them to the expansion tank, where the sodium was in contact with the covergas. Released fission gases were transported



During and shortly after the irradiation, the following nuclides were measured:

Kr : 85m, 87, 88 and 89

Xe : 135m, 135, 137 and 138, and

furthermore, the daughter nuclides Rb-89 and Cs-138. After the irradiation, Xe-135m and Xe-135, produced by the decay of I-135, could be used for measurements for a longer period of time. The sodium temperature was varied from 160 to 400°C, the sodium flow rate from 0,5 to 5 l/m. The cover gas flow rate was also changed.

RESULTS

1. The cover gas flow rate had no effect on the release rates of the fission gases.

2. Fig. 2 shows the effect of the sodium temperature (isothermal system) on the release fraction of Kr-89 and Xe-138 during irradiation. All other nuclides show the same behavior if corrected by build up functions.

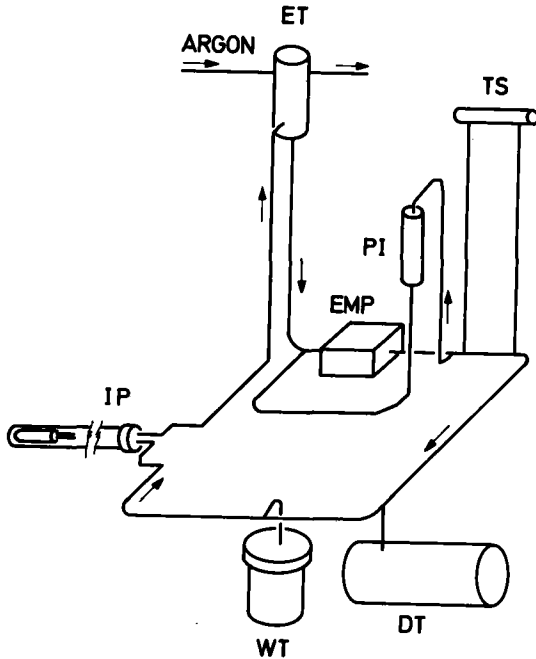


Fig.1: Fission Product Loop, Part I.

- IP : Inpile Plug
- ET : Expansion Tank
- EMP: Sodium Pump
- PI : Plugging Indicator
- TS : Test Section
- DT : Dump Tank
- WT : Waste Tank

out of the expansion tank by a stream of fresh argon and measured with a Ge(Li)-detector, connected to a multichannel analyzer.

Depending on the sodium flow rate, the transport time for fission products from the fuel to the expansion tank was 4 to 40 seconds and the sodium circulation time 22 to 220 seconds.

In most of the experiments the loop was operated as a nearly isothermal system. The plugging indicator was used only before the irradiation. In some experiments, parts of the loop were cooled to a lower temperature than the average loop temperature.

In the experiments, the reactor always operated 4 hours at full power. Release fractions and degassing half lives were determined during and after the irradiation.

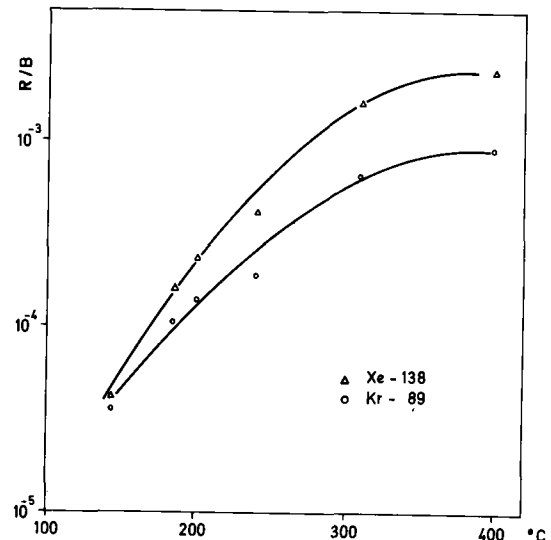


Fig.2: Effect of Sodium Temperature on the Release Fraction

Increasing the temperature from 150 to 400°C always increased the release fractions of Xe isotopes by a factor of 50, and those for Kr isotopes by a factor of 20. If only a part of the loop was cooled, the change of the release fractions was smaller. Then the strongest effect was obtained with a cooled inpile plug.

Fig.3 shows the effect of the sodium flow rate on the release fractions for three nuclides. Lower flow rates always gave smaller release fractions, the effect was smaller at higher temperatures.

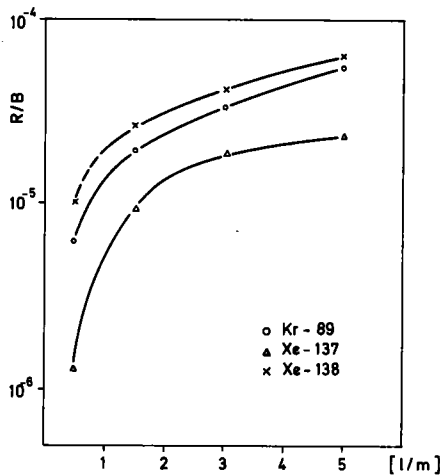


Fig.3: Effect of Sodium Flow Rate on the Release Fraction. Sodium Temperature 260°C.

An example for the function

$$\log(R/B) = f(\log(\lambda_i)) \quad (1)$$

for a sodium temperature of 390°C and a sodium flow rate of 3 l/m is shown in Fig.4. At all conditions the shape of this function was the same.

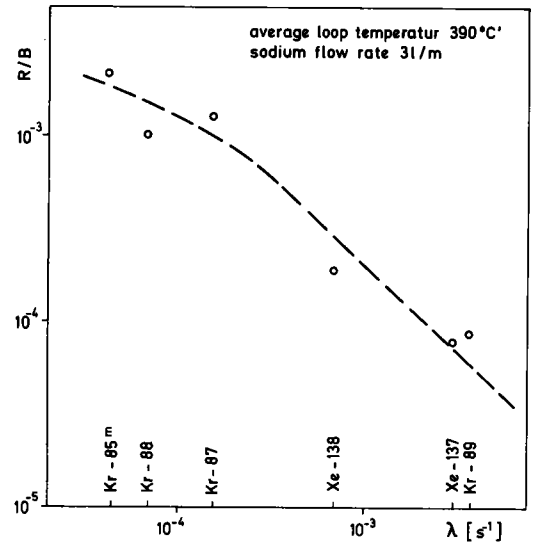


Fig.4: Effect of the Decay Constants on the Release Fractions.

3. Measurements after irradiation confirmed the findings as given under 1. and 2. The release fractions always increased with increasing sodium temperature and flow rate. The measurements of Xe-135m and Xe-135 were especially useful for the investigation of the transport and release behavior of fission gases.

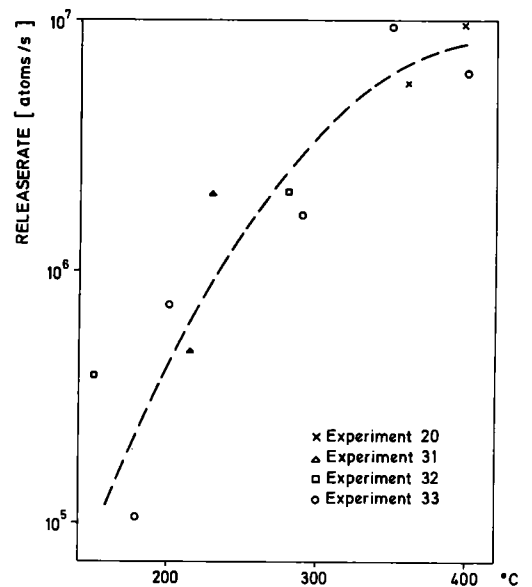


Fig.5: Effect of Sodium Temperature on the Release Rate of Xe-135.

Fig.5 shows the release rate of Xe-135 as a function of the sodium temperature. The equivalent function for Xe-135m was somewhat steeper, indicating a smaller release rate than for Xe-135 at lower temperatures.

4. Several methods were used to determine the half life of degassing. After the reactor start the release rates for fission gases increased, after reactor shut down, they decreased with time. Both processes were influenced by the degassing half life and were used to determine this.

The ratios of the release rates of nuclides with different half lives have also been used to determine HLD. During irradiation best results were obtained for the release rates of Kr-89, Xe-137 and Xe-138, relative to the Kr-88 release rate. After irradiation the ratio of the release rates of Xe-135m to Xe-135 was used.

5. Two kinds of degassing half lives were found.

- a) Calculations from the release rates after reactor shut down, as well as from function (1), gave values between 80 and longer than 200 minutes. These HLD's depend on the half life of the investigated nuclide; longer nuclide half lives gave longer HLD's.
- b) Calculations from the increasing release rates after the start of the reactor, as well as from release rate ratios, gave independent from the nuclide half life values from 17 to 32 minutes, dependent from the sodium temperature (Fig. 6).
- c) Both degassing half lives could be obtained for some nuclides from the release rates after reactor shut down in a few experiments.

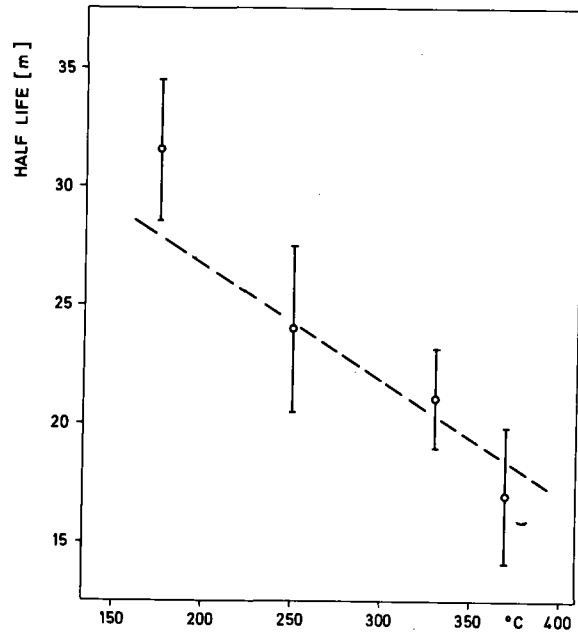


Fig.6: Effect of Sodium Temperature on the Degassing Half life

DISCUSSION

1. With the assumption that a simple degassing model is valid, the release rate for a nuclide i is given by

$$R_i = P_i \cdot \frac{\lambda_d}{\lambda_d + \lambda_i} \cdot (1 - e^{-(\lambda_d + \lambda_i) \cdot t}) \quad (2)$$

Here,  $P_i$  is the production rate. The release fraction at equilibrium from function (2) is given as (2)

$$R_i/P_i = \frac{\lambda_d}{\lambda_d + \lambda_i} \quad (3)$$

This function for a degassing half life of 140 minutes is shown in Fig. 4. As can be seen, 140 minutes was a good assumption.

2. With function (2) or (3), relative release fractions of the nuclides can be explained. While for all loop conditions the same shape as in Fig. 4 was found, the absolute values of the release fraction depend very strongly on the sodium temperature and flow rate. This points to a source term which is dependent on the loop conditions.

3. After the irradiation, especially at higher temperatures, I-135 is homogeneously distributed within the loop sodium. So the production of Xe-135m and Xe-135 takes place throughout the loop. The strong influence of the sodium temperature on the release rates of these nuclides could be explained by the iodine behavior.

4. At lower temperatures iodine was adsorbed on the stainless steel walls. Using the temperature dependence of the iodine adsorption and loop parameters such as surface, temperature and sodium volume, the fraction of the total iodine dissolved in sodium was calculated for each average loop temperature. This fraction -relative values- is shown in Fig. 5 as dashed line. The release rate of Xe-135 follows exactly the fraction of iodine dissolved in sodium. In other words, xenon produced by the decay of adsorbed iodine, was not transported to the covergas. (There is still a possibility that this xenon is also transported to the gas phase, however with a much longer degassing half life than the one found. This could not be investigated).

For Xe-135m the steeper function could be explained by the temperature dependence of the degassing half life.

That the iodine adsorption was responsible for the smaller release rates at lower temperatures could also be proved by lowering the temperature of a part of the loop, usually the test section, while keeping the temperature of all other parts of the loop higher. In such a case, the fraction of iodine dissolved in sodium, was higher, and the effect of the test section temperature on the release rates was smaller, as found in the experiments.

5. The results discussed under point 4 are in agreement with observations at sodium cooled reactors. Operating a cold trap in such a system reduces the concentration of Xe-133 and Xe-135 in the cover gas, because the iodine precursor nuclides are partly

removed from the circulating sodium. How much the fission gas level is reduced depends on the specific design of the system. Leipunskij, et al (3) reported for the reactor BR-5 a factor of 3 for Xe-133 and a factor of 2 for Xe-135, whereas Brunson (2) reported for the EBR-II a reduction of only 10 %.

6. During irradiation, fission products are released from the fuel to the sodium by recoil. Some of the fission gas atoms are formed directly (independent yield), some by the decay of their bromine or iodine precursors. The adsorption of the precursors, however, is not sufficient to explain the observed results. For the xenon release, the temperature dependence is not so strong as discussed under point 4, indicating a stronger loss of xenon atoms at higher or an additional source for xenon atoms at lower temperature. However, it can be seen clearly from Fig. 2, that the influence of the sodium temperature on the release rates of xenon is larger than on the release rates of krypton. This behavior is caused by stronger absorption of the iodine precursors (for xenon) than of the bromine precursors (for krypton).

7. In order to explain the measured degassing half lives, the two kinds of half lives have to be discussed separately.

The shorter ones -17 to 32 minutes- can be explained by diffusion through the liquid sodium-covergas interface. Kessie (4) and Chellew et al (5) developed for a degassing bubbler a model for the diffusion controlled process. Even if the Fission Product Loop is quite different from a bubbler, a similar temperature dependence of the degassing should be obtained. From the model, the half life of degassing is directly proportional to  $1/\sqrt{D}$ , with  $D$  ( $\text{cm}^2\text{s}^{-1}$ ) the diffusion constant of the considered gas in sodium. By using  $D$ -values as given by Kessie (4), the relative temperature dependence for the degassing half life was calculated. The function is included in Fig. 6. Except

## INTERNATIONAL CONFERENCE ON LIQUID METAL TECHNOLOGY IN ENERGY PRODUCTION

for the lowest temperature the measured data fit this function within the error limits. This confirms that these degassing half lives are connected with the release from the sodium to the covergas.

8. The longer degassing half lives must be explained on a different basis. As discussed in point 6, one must assume an other effect besides precursor adsorption to explain the observed temperature dependence of the release rates during irradiation. Even at a sodium temperature of 400°C, a large part of the fission gases was trapped within the sodium loop. Any change of loop parameters was followed by a strong burst of fission gases, similar to such an effect for Ne-23, observed at the EBR-II (2). The release of fission gases from these "traps" to the flowing sodium will be delayed by the measured longer half lives for the degassing. However a simple model is not sufficient for explanation, because the observed degassing half life was dependent on the nuclide half life. These "traps" were at or near the fuel area, as could be seen by changing the temperature of only a part of the loop. The strongest effect was observed with a cooled inpile plug. What the nature of these "traps" is or what the meaning of such a "trap" model will be, is not yet understood. Because of the strong sodium flow rate influence on the release rates - stronger than found for the release of Xe-135 and Xe-135m - it is assumed that not all the produced fission products were transported out of the fuel column.

9. In discussing the two kinds of degassing half life, it must be mentioned that also two different degassing half lives must be expected from the theory. Degassing half lives as calculated by Kessie (4) and Chellew et al (5) are derived from a simple diffusion controlled model at the sodium-cover gas interface. However, degassing half lives as given for reactors contain all possible delay processes in a complicated system, including the production. While

the observed shorter half lives of degassing are clearly connected to the first type, the longer ones probably must be explained on the basis of some special features of the Fission Product Loop.

10. For the EBR-II also, two half lives of degassing have been reported (2). For measurements after the start up of the reactor and after shut down, 2.7 hours were measured, whereas from function (3) 7.7 hours were calculated. Even if Brunson (2) explains these two half lives by having used an excessively simple model ( $\lambda_d$ ) for a complicated system, there could be some connection to the findings in the experiments reported here.

### SUMMARY and CONCLUSIONS

Using the Fission Product Loop, the behavior of fission gases was investigated. The release fractions were very strongly dependent on the sodium temperature. For the Xe-135 and Xe-135m release this could be explained by the observation, that xenon atoms produced by the decay of adsorbed iodine, will not be transported to the cover gas. This is in agreement with observations at sodium cooled reactors. In future experiments it will be investigated if the xenon atoms are fixed at the site where the iodine is adsorbed and if rare gas adsorption, which is discussed sometimes in the literature, is possible. Further studies are needed to explain the effects during irradiation.

Two kinds of degassing half lives were found. One, depending on the sodium temperature, could be explained as a diffusion controlled process at the sodium-cover gas interface. The degassing half life ranged here from 17 minutes at 380°C up to 32 minutes at 180°C. The other degassing half lives from 80 to longer than 200 minutes were depended on the half life of the nuclides and must be explained by some special features of the experimental system.

## REFERENCES

- 1 Fujii, I., Ohno, M., Takehara, K., Okano, H., Miyazawa, T., Ishizaka, T., Yokozawa, A., Kamei, H., Mitsutsuka, N., Hada, M. and Nagamine, T., "Development of Sodium Inpile Loop", J. Brit. Nucl. Energy Society, 13, 403 (1974)
- 2 Brunson, G.S., "Monitoring fission gas in EBR-II by high resolution gamma spectrometry", Nucl. Technology 25, 553 (1975)
- 3 Leipunskij, A.I., Kazachovskij, O.D. and Ovechkin, D.M., "Results of eight years of operation of the BR-5 reactor", AEC-tr-6976 (1969)
- 4 Kessie, R.W., "Inert gas-sodium contactors", p.44 at ANL-7817 (1971)
- 5 Chellew, N.R., Miller, W.E., Kessie, R.W., McPheeters, C.C. and Nelson, P.A., "A method for detecting fuel cladding penetration in LMFBR's by monitoring the sodium coolant for I-135", Nucl. Technology 21, 125 (1974)

# INTERNATIONAL CONFERENCE ON LIQUID METAL TECHNOLOGY IN ENERGY PRODUCTION

## FISSION PRODUCT DEPOSITION IN A STAINLESS STEEL SODIUM SYSTEM

N. Mitsutsuka      Y. Gohshi      H. Shimojima  
Tokyo Shibaura Electric Co., Ltd.  
Kawasaki, Japan

H. Feuerstein  
Gesellschaft für Kernforschung  
Karlsruhe, Germany

### ABSTRACT

Deposition of longer half lived fission products in a stainless steel inpile sodium loop was investigated. A strong down stream effect was found on inlet and outlet pipes to the uranium dioxide fuel. Deposition of iodine and tellurium was strongly affected by the loop temperature, showing higher deposition at lower loop temperature. Cold trapping of the fission product containing sodium was also investigated, using the attached cold trap loop. Iodine and cesium were found to deposit reversibly to the cold trap and distribution coefficient  $K(\text{cm})$  were obtained as  $\log K = (3.08 \pm 0.17) - (0.0112 \pm 0.0006) \times T(^{\circ}\text{C})$  and  $\log K = -(4.55 \pm 0.29) + (1830 \pm 140) \times 1/T(^{\circ}\text{K})$ , respectively.

### INTRODUCTION

The release and transport of fission products in a stainless steel sodium system is especially important in the study of radioactive contamination of a LMFBR primary system. Deposition of long half lived fission products causes a serious problem in maintenance. Several papers giving information on fission products deposition and transport were published, but the parameters which affect the fission products deposition are scarcely understood<sup>2)</sup>. In order to obtain data on the fission product behavior, a small sodium inpile loop, Fission Product Loop (FPL), has been installed at the Toshiba Training Reactor (TTR).

This paper describes the results of fission product deposition measurements, which were performed using the FPL. Depositions of longer half lived fission product around inpile loop pipings were measured. Cold trapping of the fission product containing sodium was also performed and deposition characteristics of several fission products during cold trapping were investigated.

### EXPERIMENTAL

#### Fission Product Loop (FPL)

Figure 1 shows an FPL flow diagram and Table 1 summarizes the major specifications. FPL details have been reported by Fujii et al<sup>(1)</sup>. The FPL consists of two independent stainless steel sodium loops. One is for inpile experiments, with natural uranium dioxide fuel in it, and the other is for sodium purification experiments, with a cold trap. There is a test section in the inpile loop which allows setting up a temperature gradient around the 70 cm pipe by an air blower. These loops were connected to the sodium dump tank.

Table 1. Fission product loop design data

Sodium inventory	4.8 kg
UO <sub>2</sub> inventory	150 g (natural uranium)
Pressure	-1 to 4 kg/cm <sup>2</sup> gauge
Main pipe	13.8 mm o.d., 2.2 mm thick
Cover gas	Argon
Main structural material	AISI 304
Temperature	~ 500°C
Sodium flow rate	~ 5 l/min

#### Fission Products Cold Trapping

Cold trapping experiments were usually performed in connection with inpile loop experiments, such as fission gas measurements reported in the previous paper. Prior to each experiment, an inpile loop experiment with four-hour irradiation at full reactor power was accomplished and fission products containing sodium were drained into the dump tank. Cold trapping was started with six days cooling time after irradiation, in order to reduce Na-24 radioactivity. The cold trap is a conventional cylindrical type with stainless steel wire mesh at a density of 0.35 grams per cm<sup>3</sup> in it. Dump tank sodium was recirculated through a heat exchanger to the cold trap. Oxygen concentration in the cold trap loop,

including the dump tank, was about 80 ppm. At first, the cold trap was flushed with sodium at a sodium temperature near 400°C and then the temperature was decreased and increased stepwise. Temperature equilibrium of the loop was usually established within one hour and the duration time of each temperature step was four to six hours. Ge(Li) detectors with lead shields were positioned at the dump tank and the cold trap. Gamma ray spectra at these positions were measured with a 4096 channel pulse height analyzer.

#### Test Section Measurements

After four days of cooling from four hours irradiation without sodium, purified sodium (less than 5 ppm oxygen) was filled in the inpile loop. The fuel was flushed for two hours with sodium at a temperature of 400°C and then the test section was cooled to a lowest temperature of 140°C. Around the test section, eight positions, including inlet and outlet pipe and valves, were measured, using a Ge(Li) detector from the outside of the containment. Measurements were also performed after draining the sodium. Same measurements were repeated at a test section temperature of about 400°C.

#### Inpile Loop Pipe Measurements

After performing many experiments, inpile loop pipe measurements were performed with 40 days cooling time. Various positions of the inpile loop pipes were measured by positioning a Ge(Li) detector inside of the containment, directly connected to the pipes. Background gamma rays inside of the containment were sufficiently low that only a simple shielding was used for the measurements.

### RESULTS

#### Fission Products Detected in Irradiated Sodium

Gamma ray spectrum at the dump tank was measured with six day cooling time after four hour irradiation under sodium convection. Major radioactivities were found to be I-131 and Te-132/I-132. Some long half lived nuclides, for example, Cs-137 and Ce-144, were also detected. However, Mo-99, Ce-143 and Nd-147, which were expected to show

high counting rate at this cooling time, were not detected in the dump tank sodium. Ba-140/La-140 also showed extremely low counting rate, compared with that of I-131 and Te-132. The long lived nuclides have been accumulated during the previous operations. Among the long lived nuclides, Cs-137 showed extremely high count rate in the dump tank sodium, in spite of its long half life.

#### Fission Products Cold Trapping Behavior

Figure 2 shows typical cold trapping behavior of several fission products at the dump tank. With increase and decrease of the counting rate at the dump tank, most corresponding decrease and increase values were measured at the cold trap. I-131 was fairly temperature sensitive and deposited on the cold trap at lower temperatures. I-131 deposition was reversible to the cold trap temperature with negligible hysteresis. Some parts of Te-132/I-132 and Cs-137 were also removed by the cold trap in reversible manner. The count rate change of these nuclides was fairly quick and equilibrium seemed to be established within three hours after changing the cold trap temperature. On the other hand, other nuclides, such as Zr-95, Nb-95, Ru-103 and Ba-140/La-140, showed no marked change during cold trapping. These nuclides do not show marked change with filling and draining the cold trap sodium and seemed not to be dissolved in sodium but deposit on the inner surface of the dump tank. Cs-137 is in radioactive equilibrium with its decay product Ba-137m and is determined by Ba-137m counting. Special care should be taken in the Cs-137 determination under flowing sodium. At higher cold trap temperatures, Ba-137m count rate was strongly affected by sodium flow rate, showing lower counting rate at higher sodium flow rates. On the other hand, it remained almost constant at lower cold trap temperature. Another Cs-137 cold trapping experiment was performed, measuring the dump tank after standing about 30 minutes in a stopped sodium flow, in order to establish radioactive equilibrium at each cold trap temperature. The results were almost the same as those shown in Fig. 2, which were measured under a sodium convection of 0.7 l / min flow rate.



Cold Trap Deposits

In order to investigate fission product deposition at the cold trap, a sodium draining test was undertaken. Two Ge(Li) detectors were set up at the dump tank and the cold trap and gamma ray spectra of fission products and Na-24 were measured before and after the sodium draining. From the change of the counting rate before and after the sodium draining, distribution coefficient  $K(\text{cm})$  was determined for I-131, Cs-137 and Te-132.  $K$  is defined as:

$$K = \frac{\text{fission product weight/surface unit area}}{\text{fission product weight/liquid sodium unit volume}} \quad (1)$$

Equation (1) is modified to evaluate present experimental data, as follows:

$$K = \frac{\text{FP count rate at surface}}{\text{FP count rate in sodium}} \cdot \frac{1}{\text{cold trap surface to volume ratio}} \quad (2)$$

Figure 3 shows the obtained  $K(\text{cm})$  value of I-131, Cs-137 and Te-132 against reciprocal cold trap temperature. By least square fitting, the following equation was obtained for I-131 and Cs-137.

$$\text{I-131} : \log K(\text{cm}) = -(5.61 \pm 0.32) + (2.95 \pm 0.15) \times 10^3 \times 1/T(^{\circ}\text{K}) \quad (3)$$

$$\text{Cs-137} : \log K(\text{cm}) = -(4.55 \pm 0.29) + (1.83 \pm 0.14) \times 10^3 \times 1/T(^{\circ}\text{K}) \quad (4)$$

Deposition around the Test Section

Figure 4 shows the radioactivity deposition of Nb-95 and I-131 on test section pipes against the cumulative inner surface together with pipe temperature after sodium drain. Two valve positions and one corner of the pipe were also measured. All other positions were pipes with 9.8 mm inner diameter. Deposition of I-131 was very temperature sensitive and more than two orders of difference in radioactivity deposition was found with 155°C temperature difference around the pipe. Deposition of Nb-95 showed no temperature effects. Deposited Nb-95 was almost the same at a temperature of 140°C and 400°C, and distributed around the pipe nearly homogeneously, except at two valve positions. Valves showed a more marked effect on the deposition of Nb-95, compared with temperature effects increas-

ing the deposition more than a factor of five.

Deposition around the Inpile Loop Pipe

Figure 5 shows radioactivity deposition against the cumulative inner surface of the inpile loop pipe. The inpile loop had been operated under nearly isothermal conditions, except for a few test section measurements. The latest operation of the loop was 40 days before the measurements. Detected nuclides were Zr-95, Nb-95, Ru-103, La-140 (Ba-140), Ce-141 and Ce-144. I-131 and Te-132/I-132 were considered to have been decayed out. Cs-137 was not detected on the pipe, whereas it was found in drained sodium. All the nuclides show strong down stream effect of more than one order of difference between the inlet and outlet to the uranium dioxide fuel.

DISCUSSIONGeneral Considerations

The results of the FP deposition experiments indicate two types of deposition; one is temperature sensitive deposition, such as iodine, cesium and tellurium, and the other is something like structure sensitive deposition, such as Zr-95, Nb-95, Ru-103, Ba-140/La-140, Ce-141 and Ce-144. Release fractions to the dump tank sodium of second group nuclides were extremely low. Irradiations of the fuel without sodium convection, due to routine reactor operation, make the estimation of relative radioactivity of these nuclides much more complicated. However, release fraction of the second group fission products should be at least one order lower, compared with that of I-131 and Cs-137. Residual fractions are considered to remain in the inpile loop as pipe deposits, as is shown in Fig. 5. Recently, Erdman et al. reviewed radionuclide behavior in LMFBRs<sup>2)</sup>. The results obtained here are consistent with previously published literatures.

Distribution Coefficient  $K(\text{cm})$ 

Concentration of the fission products in FPL sodium was far lower than their solubilities. The temperature sensitive depositions observed in the cold trap and test section experiments are considered due to adsorption on the stainless steel surface.

In the present experiments, I-131  $K$  values

were calculated using the cold trap measurement data. K values of I-131 can also be estimated using test section measurement data. In a forced convection sodium system, concentration of a nuclide can be assumed as constant. Hence, depositions of a nuclide at different temperature positions are directly proportionate to the K function and, in logarithmic treatment, deposition of a nuclide should have the same slope as log K against temperature:

$$A_i = K(T_i) \cdot S_i \cdot C \quad (5)$$

where  $A_i$  is the amount of deposited nuclide at region  $i$ ,  $t_i$  is the temperature of region  $i$ ,  $S_i$  is adsorption area of region  $i$  and  $C$  is the concentration of the nuclide in sodium. In logarithmic expression:

$$\log A_i = \log K(T_i) + \log S_i \cdot C \quad (6)$$

where, in measuring the same detector and same geometry,  $S_i$  can be assumed constant. Figure 6 shows the I-131 deposition at different temperature positions against reciprocal temperature. As is shown in the figure,  $\log A_i$  shows the same slope as is obtained from the cold trap experiments. This result indicates that iodine K values, which were obtained from the cold trap experiments, are also valid for the description of iodine deposition around the test section, in spite of large structural differences.

Several K values have been reported for iodine and cesium in stainless steel sodium system<sup>(3)-(5)</sup>. A K function of iodine adsorption on stainless steel surface from liquid sodium was reported by Allan<sup>(3)</sup>. Allan's K function was fitted against centigrade temperature. Present data on I-131 K value is also better fitted against centigrade temperature and is obtained as follows:

$$\log K(\text{cm}) = (3.08 \pm 0.17) - (0.0112 \pm 0.0006) \times T(^{\circ}\text{C}) \quad (7)$$

Equation 7 shows good consistency with Allan's K function.

Several K functions have been reported for cesium. Surface deactivation effect, after exposing high temperature sodium, was also reported<sup>(6)-(8)</sup>. The FPL cold trap had never been heated

up higher than 420°C. The obtained K function of cesium is similar to that of deactivated surface reported by Guon<sup>(8)</sup>.

The K-function of tellurium in the stainless steel sodium system has not yet been reported. High deposition tendency of tellurium in NaK system was reported by Davies<sup>(9)</sup>. K value obtained here also shows high deposition tendency, however, it seems to saturate at lower than about 250°C.

#### Oxygen Effect on Fission Product Deposition

From the cold trapping experiments, the conclusion that oxygen concentration does not have a large effect on the deposition of iodine and cesium can be derived. Oxygen concentration in the cold trap loop sodium is also changed with the cold trap temperature. Total oxygen concentration within the loop was about 80 ppm. It begins to precipitate at a cold trap temperature of 280°C and more than 90% of oxygen plates out at a cold trap temperature of 200°C. However, no marked change in K was observed in this temperature region on iodine and cesium deposition. Iodine deposition showed almost the same slope against temperature at the cold trap and at the test section, which contains less than 5 ppm oxygen. In spite of high oxygen concentration, K function of iodine and cesium shows good agreement with published data, which were determined with lower oxygen concentration. Therefore oxygen, at least 80 ppm doesn't affect the iodine and cesium deposition process. However, tellurium deposition seems to begin saturation at a temperature at which oxygen begins to precipitate. Oxygen seems to have some effects on the tellurium deposition.

#### Structure Sensitive Deposits

Deposition of Zr-95, Nb-95, Ru-103, La-140 (Ba-140), Ce-141 and Ce-144 was found more sensitive to the loop structure than to the loop temperature. A strong down stream effect shows a high deposition tendency of these nuclides. Strong effect of valves was also found, which are considered due to sodium flow turbulence.

These effects have already been found in some reactor systems and are now confirmed to occur in a

## INTERNATIONAL CONFERENCE ON LIQUID METAL TECHNOLOGY IN ENERGY PRODUCTION

small sodium loop. It seems difficult to treat the deposition of these nuclides quantitatively. However, a small inpile loop will be helpful to better understanding of these depositions.

### CONCLUSION

Several fission product deposition measurements were performed at the Toshiba Fission Product Loop (FPL). The following conclusions are derived.

- (1) I-131, Te-132/I-132 and Cs-137 deposit to the cold trap and cooled test section in a temperature sensitive manner, with negligible hysteresis.
- (2) Other nuclides, Zr-95, Nb-95, Ru-103, La-140 (Ba-140), Ce-141 and Ce-144 show extremely low release fraction (less than 1/10 compared to I-131 and Cs-137) to the FPL sodium. These nuclides are found to have deposited to the inpile loop pipe with strong down stream effect.
- (3) Oxygen impurity does not seem to effect the deposition of iodine and cesium, whereas it does seem to have some effect on the tellurium deposition.

### REFERENCES

- (1) Fujii, I., et al.; "Development of a sodium inpile loop"; J. Brit. Nucl. Energy Soc.; 13; PP. 403-406; (1974).
- (2) Erdman, C. A., Kelly, J. L., Reynolds, A. B.; "Radionuclide behavior during normal operation of liquid-metal-cooled fast breeder reactors. Part 2: transport"; Nucl. Safety; 16; PP. 318-336; (1975).
- (3) Allan, C. G.,; Liquid Alkali Metals; Brit. Nucl. Energy Soc.; London; 1973, PP. 159-164.
- (4) Colburn, R. P.; Nature of Cs and I deposits in sodium systems; Trans. Am. Nucl. Soc.; 14; PP. 626-627; (1974).
- (5) Cooper, M. H., Grundy, B. R., Taylor, G. R.; "Behavior of iodine in sodium systems"; Trans. Am. Nucl. Soc.; 15; PP. 232-233; (1972)
- (6) Evans, H. E., Watson, W. R.; Liquid Alkali Metals; Brit. Nucl. Energy Soc.; London; 1973 PP. 153-158.

- (7) Cooper, M. H., Taylor, G. R.; "Measurement of cesium sorption isotherms in liquid sodium", Nucl. Technology; 12; 83-92; (1971).
- (8) Guon, J.; Deposition of cesium and barium in a sodium-stainless steel system; AI-AEC-12952; 1970.
- (9) Davies, R. A., Drummond, J.; "Behavior of radioactive impurities in DFR liquid metal coolant"; J. Brit. Nucl. Energy Soc.; 14; PP. 427-435; (1974).

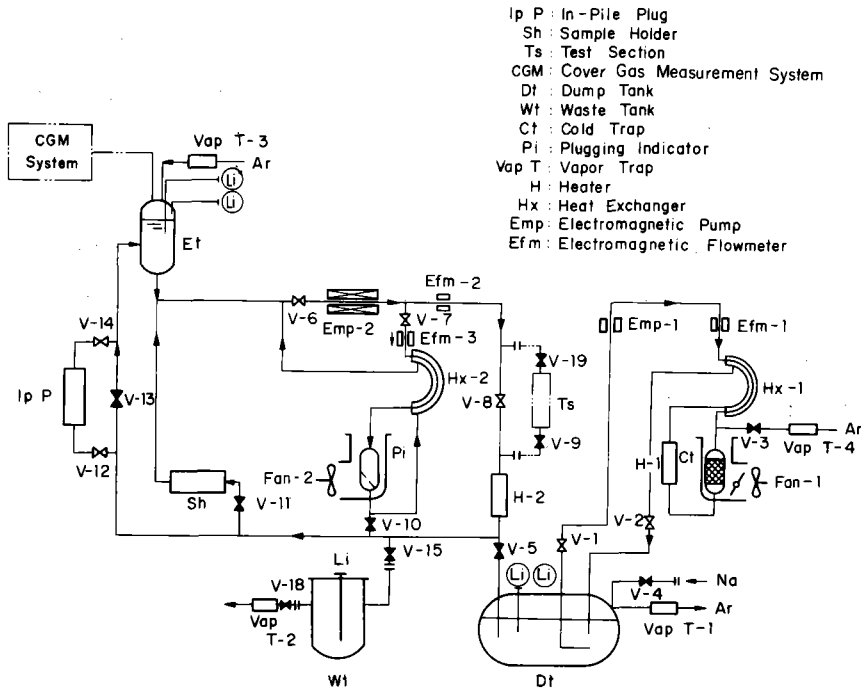


Fig. 1. Fission Product Loop flow diagram.

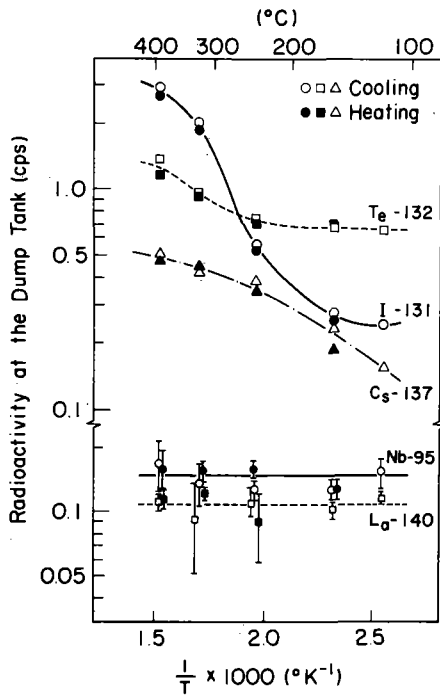


Fig. 2. Fission product radioactivity at the dump tank at different cold trap temperatures.

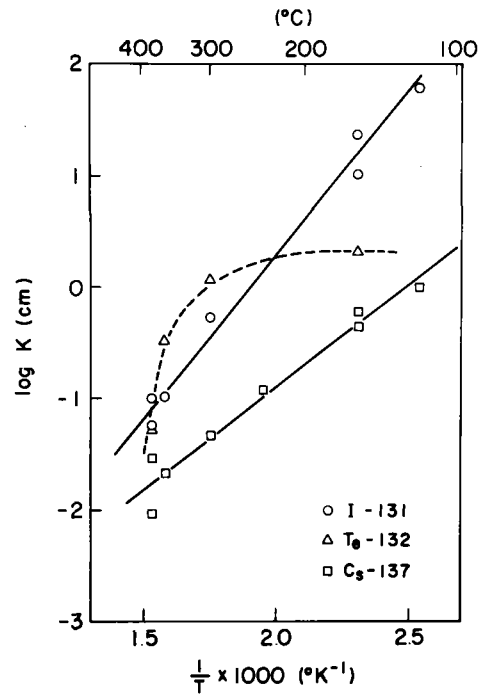


Fig. 3. Fission product distribution coefficient vs reciprocal temperature.

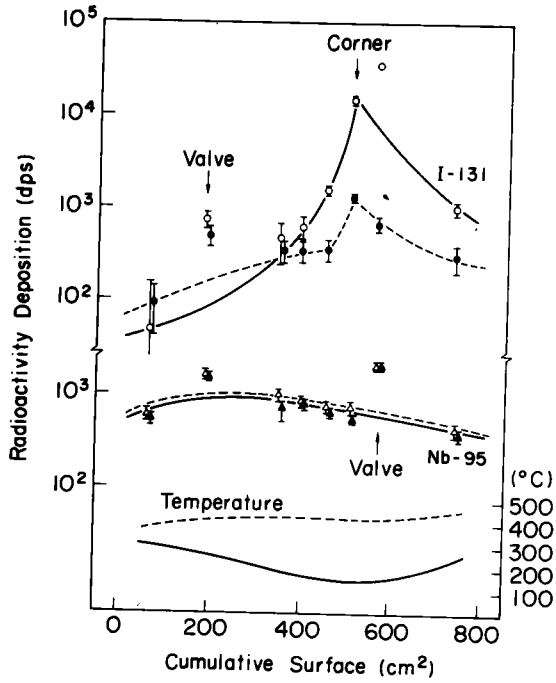


Fig. 4. Fission product deposition around the test section.

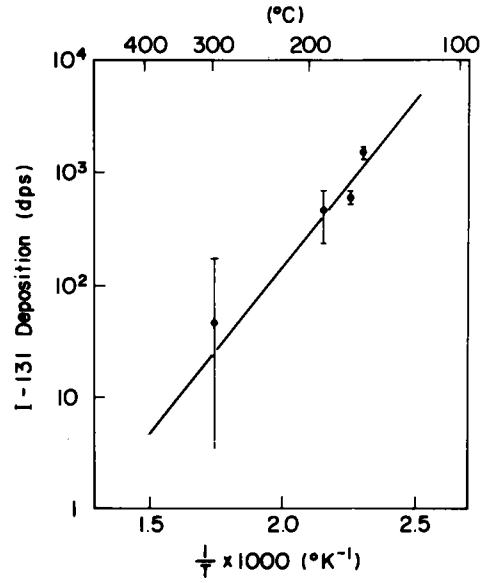


Fig. 6. I-131 deposition at the test section vs reciprocal pipe temperature.

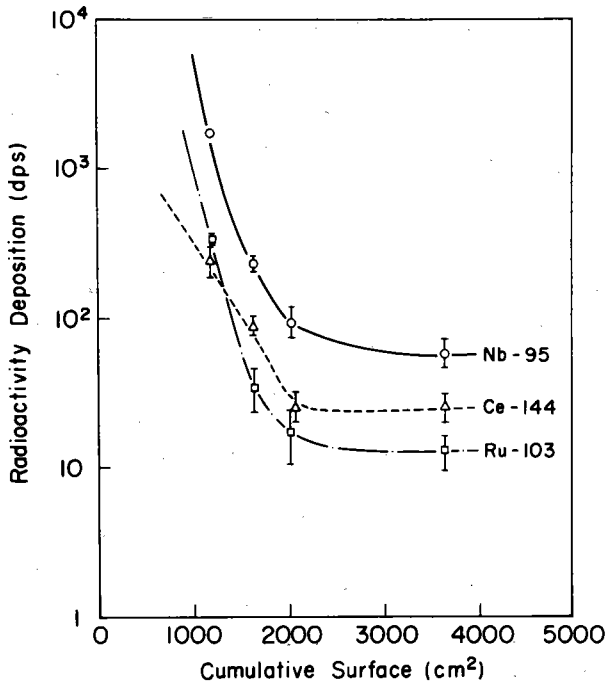


Fig. 5. Fission product deposition around the inpile loop.

# INTERNATIONAL CONFERENCE ON LIQUID METAL TECHNOLOGY IN ENERGY PRODUCTION

## CONTROL OF TRITIUM IN LMFB SODIUM BY COLD TRAPPING

C. C. McPheeters and D. Raue

### ABSTRACT

Control of tritium in the sodium coolant of LMFBs is important for achieving as low as practicable release of radioactivity. Cold-trapping has been shown to be an effective method for controlling hydrogen in sodium and should be effective for controlling tritium as well. Two mechanisms for removal of tritium from sodium have been studied: (1) coprecipitation of hydrogen and tritium from solution in sodium in a cold trap and (2) isotopic exchange of tritium in sodium with hydrogen in solid NaH in a cold trap.

Mathematical models have been developed to describe the two mechanisms and experimental runs have been made to determine their relative effectiveness. These experiments, together with the models, have indicated that the coprecipitation mechanism is, as expected, much more effective in removing tritium from sodium than the isotopic exchange mechanism. The model was used to calculate tritium levels in the EBR-II primary system, and agreement with measured levels was achieved within a factor of three.

The isotopic exchange mechanism by itself cannot be expected to adequately control tritium in LMFBs. Hydrogen sources such as corrosion in the steam generators will be important factors in controlling the tritium level.

### INTRODUCTION

One of the objectives of the Clinch River Breeder Reactor Plant (CRBRP) and future LMFBs is to achieve as low as practicable radioactivity releases to the environment. One of the most difficult radioactive isotopes to contain in the LMFB is tritium ( $^3\text{H}$ ) because, as an isotope of hydrogen, it diffuses readily through structural materials at the LMFB temperatures. Cold-trapping the sodium coolant is an effective method for removing hydrogen from sodium, and it is expected that the method should be effective in retaining tritium and preventing its release. The purpose of this paper is to present the results of studies with sodium cold traps and their effectiveness for removing tritium from sodium under various operating conditions.

Tritium is produced in the reactor core by three primary mechanisms: 1) three-particle fission of the fuel, 2) activation of boron in the  $\text{B}_4\text{C}$  control rods, and 3) activation of boron and lithium impurities in the fuel, sodium coolant, and structural materials. One fission in every 200-300 results in a third particle. These third particles are either alpha-particles or tritons; the alpha-particles being favored roughly ten to one over the tritons. The fission yield of tritium<sup>1</sup> from LMFB fuel is expected to be of the order of 25 to 50 kd/s-Je (2 to  $4 \times 10^4$  Ci/1000 MWe-yr). Tritium production from the  $\text{B}_4\text{C}$  control rods is expected to be approximately 76 kd/s-Je ( $6.5 \times 10^4$  Ci/1000 MWe-yr), whereas the combined production of the impurity sources should be less than 2 kd/s-Je ( $2 \times 10^3$  Ci/1000 MWe-yr).<sup>2</sup> Essentially all of the tritium generated in the fuel and from impurity sources is expected to be released to the coolant sodium,<sup>3,4</sup> whereas as little as 20 percent of that

born in the control rods may be released.<sup>5,6</sup> Thus, the total tritium source, released into the sodium coolant is expected to be 40 to 90 kd/s-Je ( $3.5$  to  $7.5 \times 10^4$  Ci/1000 MWe-yr). To keep the release as low as practicable, the cold traps will be required to remove at least 90 percent of this tritium burden.

### MECHANISMS OF COLD-TRAP OPERATION

At least two mechanisms are available for control of tritium in sodium: 1) coprecipitation with hydrogen and 2) isotopic exchange with hydrogen in solid NaH. The coprecipitation mechanism is simple precipitation from a solution of hydrogen isotopes in sodium. Tritium should be precipitated with hydrogen in the same ratio as they exist in solution. The isotopic exchange mechanism consists of exchanging tritium in solution with hydrogen in the cold-trap deposit. The driving force for this exchange is proportional to the difference between the tritium specific activities in solution and in the solid deposit.

A simple cold-trap model was developed to describe the behavior of tritium and the operation of the two mechanisms described above. The model for the coprecipitation mechanism is quite simple in that it is assumed that tritium precipitates with hydrogen in the same ratio as the tritium/hydrogen ratio in solution. In a finite system with no significant hydrogen or tritium sources, the tritium would be removed by the cold trap along with the hydrogen, and the tritium specific activity,  $C_T$ , would decline according to the relationship

$$C_T = C_H \frac{C_{TO}}{C_{HO}} \quad (1)$$

where  $C_{TO}$  = the initial tritium specific activity, d/s-kg,

$C_H$  = the hydrogen concentration at any time, mg/kg, and

$C_{HO}$  = the initial hydrogen concentration, mg/kg.

The tritium/hydrogen ratio in solution would remain constant throughout the cold-trapping run.

The hydrogen concentration,  $C_H$ , changes during a cold-trapping run according to the equation

$$C_H = (C_{HO} - C_e) e^{-\frac{E_H W}{M} t} + C_e \quad (2)$$

where  $C_e$  = the equilibrium hydrogen concentration based on the minimum cold-trap temperature, mg/kg,

$E_H$  = efficiency expressed as the fraction of hydrogen removed by the cold trap in a single pass,

$W$  = the sodium flow rate through the cold trap, kg/s

$M$  = sodium mass in the system, kg, and

$t$  = elapsed time from the beginning of the cold trap run, s.

The decline of tritium specific activity in a closed sodium system with no significant hydrogen or tritium sources during a cold-trapping run can be described by combining equations 1 and 2.

INTERNATIONAL CONFERENCE ON LIQUID METAL TECHNOLOGY IN ENERGY PRODUCTION

$$C_T = (C_{T0} - \frac{C_{T0} C_e}{C_{H0}}) e^{-\frac{E_{HM} W}{C_{H0}}} + \frac{C_{T0} C_e}{C_{H0}} \quad (3)$$

The model describing the isotopic exchange mechanism is more complex than the coprecipitation model. This complexity arises from the experimentally-determined fact that the isotopic exchange mechanism is so ineffective that hydrogen from even small sources in the system becomes important in coprecipitating with tritium. This model consists of two parts, and includes a coprecipitation term and an isotopic exchange term. The tritium mass balance in the system is expressed as follows:

$$M \frac{dC_T}{dt} = S_T - R_C - R_I \quad (4)$$

where  $S_T$  = the tritium source term, d/s<sup>2</sup>, (zero in these experiments),  
 $R_C$  = the coprecipitation removal term, d/s<sup>2</sup>, and  
 $R_I$  = the isotopic exchange removal term, d/s<sup>2</sup>.

If the tritium source term were not zero, it could be carried through the integration as a constant. This source term is used in models that describe the behavior of tritium in LMFBRS; however, during the cold-trapping experiments, the tritium source was zero.

The coprecipitation removal term was assumed to be the same as that described by the differential of equation 3. In describing the isotopic exchange term,  $R_I$ , it was assumed that the driving force for isotopic exchange is simply the difference between the tritium specific activity in solution and the specific activity that would be in equilibrium with the solid deposit.

$$R_I = kA [C_T(ave) - C_{Te}] \quad (5)$$

where  $k$  = the tritium mass transfer coefficient, kg/m<sup>2</sup>-s,  
 $A$  = precipitation surface area, m<sup>2</sup>  
 $C_T(ave)$  = the average tritium specific activity in solution in the cold trap, d/s-kg.  
 $C_{Te}$  = the equilibrium tritium specific activity based on the composition of the solid cold-trap deposit, d/s-kg.

If the isotopic exchange mechanism were solid-state-diffusion limited, the differences in specific activities above would occur in the solid deposit, and the mass-transfer coefficient would be independent of sodium flow rate.

$R_I$  may be rewritten as

$$R_I = \alpha kA (C_{Tout} - C_{Te}) \quad (6)$$

where  $\alpha = \frac{C_T(ave) - C_{Te}}{C_{Tout} - C_{Te}}$

and  $C_{Tout}$  = the specific activity of tritium in the cold trap effluent, d/s-kg. The constant,  $\alpha$ , is used simply to relate the driving force to measurable quantities. Previous cold-trapping studies<sup>7</sup> have shown this constant to be in the range of 0.5 to 0.8.

From mass balance,  $R_I$  may also be written

$$R_I = W (C_T - C_{Tout}) \quad (7)$$

Combining equations 4, 6, and 7, and integrating we obtain the equation that describes the combined isotopic exchange and coprecipitation mechanisms:

$$C_T = [C_{T0} - \frac{E_T}{D} C_{Te}] e^{-\frac{W}{M} Dt} + \frac{E_T}{D} C_{Te} \quad (8)$$

where  $D = [E_H(1 - \frac{C_e}{C_H}) + E_T]$ , and

$E_T = \frac{\alpha k A}{W + \alpha k A}$  = efficiency of the cold trap for removing tritium by isotopic exchange, fractional.

The ratio,  $C_e/C_H$ , depends upon the hydrogen source term; the larger the hydrogen source, the smaller the ratio. The term,  $D$ , is the sum of the tritium removal efficiencies of the two mechanisms. The term,  $\frac{E_T}{D} C_{Te}$ , is the final tritium concentration at  $t \rightarrow \infty$ . If there were no hydrogen source,  $D$  would reduce to  $E_T$  and the final tritium specific activity would be  $C_{Te}$ ; however, with a hydrogen source, the final tritium specific activity is lower than  $C_{Te}$ . In the case where both tritium and hydrogen sources exist, the final tritium level may be either above or below  $C_{Te}$ , depending upon the relative magnitudes of the sources. The efficiencies were experimentally determined using the final tritium concentration,  $\frac{E_T}{D} C_{Te}$ , and equation 8; it was not necessary to determine  $C_{Te}$  experimentally.

EXPERIMENTAL

The cold-trapping experiments were conducted with the Apparatus for Monitoring and Purifying Sodium (AMPS). The AMPS is a .378 m<sup>3</sup> (100-gallon), forced convection sodium system capable of operation at 650°C (1200°F) and 340 kPa (50 psig) pressure. It is equipped with two cold traps: one for impurity control and one for experimental work. Impurity monitoring instrumentation, which includes an in-sodium hydrogen meter, a cover-gas hydrogen meter, an oxygen meter, two tritium meters and a multi-purpose sodium sampler are part of the AMPS system. Each of the hydrogen meters<sup>8,9</sup> consists of a nickel membrane inserted in the sodium (or in the cover gas) with a vacuum system attached to the nickel membrane. The vacuum system is capable of measuring either hydrogen flux (as an ion-pump current) or hydrogen pressure (with an ion gauge). The hydrogen pressure in the vacuum system reaches equilibrium quickly and can be interpreted as being in equilibrium with the hydrogen in the sodium.

The oxygen meter is an electrochemical cell,<sup>10,11</sup> the voltage of which is related to the oxygen activity of the sodium. The cell uses a solid ThO<sub>2</sub>-15 wt % Y<sub>2</sub>O<sub>3</sub> electrolyte tube and an air reference electrode. This type of cell has been used extensively in sodium systems with good results.

The tritium meters<sup>12</sup> are similar to the hydrogen meters in that they use nickel membranes to allow the tritium to diffuse through from the sodium. They differ in that an argon-1% hydrogen sweep gas is used to carry the tritium from the membrane to a counting chamber where the tritium activity is constantly monitored.

The multi-purpose sampler<sup>13</sup> was used both to take sodium samples for tritium analyses and to equilibrate scandium tabs and vanadium wires. The scandium tabs and vanadium wires were analyzed for hydrogen and oxygen content respectively, and these analyses were correlated with hydrogen and oxygen

## INTERNATIONAL CONFERENCE ON LIQUID METAL TECHNOLOGY IN ENERGY PRODUCTION

activities in sodium using previously determined distribution coefficients. The results of these analyses were compared with the hydrogen, oxygen and tritium meter readings for calibration purposes.

One of the tritium meters was used as a tritium-injection device to add tritium to the sodium. Argon containing 200 vppm hydrogen and tritium with an activity of  $10 \times 10^{10}$  d/s-m<sup>3</sup> was passed through the membrane region at a very low flow rate. The tritium entered the sodium quantitatively, so that the amount added could be accurately determined by integrating the gas flow.

The cold-trap used in these experiments was of an integral economizer-crystallizer design with the economizer located in the upper half of a vertical pipe 168 mm O.D. x 7.1 mm wall thickness, [6-in. schedule 40 (NPS)] and the crystallizer region in the lower half. Sodium flowed into the top of the cold trap, downward through the economizer into the annulus of the crystallizer region. The crystallizer was packed with stainless-steel wire mesh and was air-cooled on the outer surface. The sodium continued up the center section of the crystallizer, through the economizer, and out the top of the cold trap. Temperature control was maintained by varying the input to heaters on the external surface of the cold trap while the air coolant flow was maintained constant. The volume of the crystallizer region was 9300 cm<sup>3</sup> (2.46 gallons).

The hydrogen source term for the AMPS was experimentally determined at two separate times. The primary sources of hydrogen were thought to be the two tritium meters and corrosion of the piping by atmospheric moisture. During all the runs, except run 1-15-76, both tritium meters were in operation using a sweep-gas composition of argon + 5 percent hydrogen. For run 1-15-76, one of the tritium meters was shut down and the other meter was operated with a sweep-gas composition of argon + 1 percent hydrogen. The hydrogen source was measured before this change and was found to be 140 ng/s. Following the change, the source dropped to 8.6 ng/s. The sources were measured over periods of three weeks and one week, respectively. The day-to-day variations in the source are not known.

The coprecipitation runs were initiated with high (above equilibrium) hydrogen and tritium concentrations. The cold-trap flow was started with a low cold-trap temperature, and the hydrogen and tritium concentrations were carefully monitored as the cold trap removed them from the system.

The isotopic exchange runs were conducted differently. Both hydrogen and tritium were cold-trapped to a low level initially and the cold trap was isolated from the system. Tritium was injected to increase the tritium/hydrogen ratio, and the hydrogen concentration was carefully measured. The cold trap was then started up at the hydrogen saturation temperature to avoid any transfer of hydrogen into or out of the cold trap. The tritium specific activity was then measured as it declined, and the hydrogen concentration was measured periodically to be assured that it was remaining constant.

### RESULTS

#### Tritium Injections

A total of five coprecipitation and five isotopic

exchange cold-trapping runs were completed. Tritium injections were made prior to each isotopic exchange run to increase the tritium/hydrogen ratio at the beginning of each run. The results of the tritium injections are summarized in Table I. The injections resulted in excellent recovery of the tritium, *i.e.*, the tritium concentrations observed with the tritium meter were, in all cases, within 27 percent of the quantities added. This discrepancy is thought to be an accumulation of uncertainties in gas flowmeter readings and statistical counting variations. The tritium measurement error is thought to be less than the injection error because the flowmeters were operating very near the lower end of their range. Uncertainties in reading flow rates could easily reach 20 percent. The data appear to have a negative error bias that could also be attributed to a bias in the flowmeter at the lower end of the scale.

Table I. Tritium Injections into AMPS Sodium

No.	Tritium (kd/s-kg)			Meas. (%)	Diff. (%)
	Inj.	Init.	Total		
1	10.1	2.52	12.6	14.5	+15
2	11.8	2.48	14.3	14.2	-.8
3	23.6	2.78	26.4	26.1	-1.1
4	23.6	1.96	25.5	18.7	-26.8
5	23.6	21.5	45.1	38.8	-13.8

#### Coprecipitation Runs

The first assumption in the coprecipitation model is that tritium and hydrogen are precipitated in the same ratio as they exist in solution. This assumption leads to the conclusion that the tritium/hydrogen ratio should remain constant during a coprecipitation run. The tritium/hydrogen ratio was determined as a function of time during each of the five coprecipitation runs. Some variation was observed in the ratios, and the limits of these variations are shown in Table II. Also shown are the hydrogen removal efficiencies determined with the use of equation 2, and the uncertainties associated with the counting statistics for the different tritium activity levels of the various runs.

Table II. Variations of Tritium/Hydrogen Ratios During Coprecipitation Runs

Run No.	Residence Time, (s)	H Removal		T/H Ratio (kd/s-mg)	Final T Conc. (kd/s-kg)
		Efficiency (percent)	Ratio		
6-18-75	150	40	15 + 31%	1.29 + 11%	
7-17-75	588	100	4.8 + 23%	.78 + 12%	
7-30-75	588	100	28 + 33%	1.89 + 10%	
9-10-75	264	63	30 + 4%	25.9 + 4%	
9-25-75	192	67	17 + 6%	10.0 + 6%	

The tritium/hydrogen ratio remained constant within statistical counting variations for the last two runs; however, larger variations were observed during three earlier runs. These first three runs were conducted at such low tritium levels that the variations in tritium/hydrogen ratio, although larger than the statistical counting variations, are not considered to be significant.

The hydrogen and tritium reductions during run 9-10-75 are shown in Fig. 1. The data points are the concentration and specific activity readings, whereas the curves represent equations 2 and 3 plotted with a hydrogen removal efficiency of 30 percent. As can be



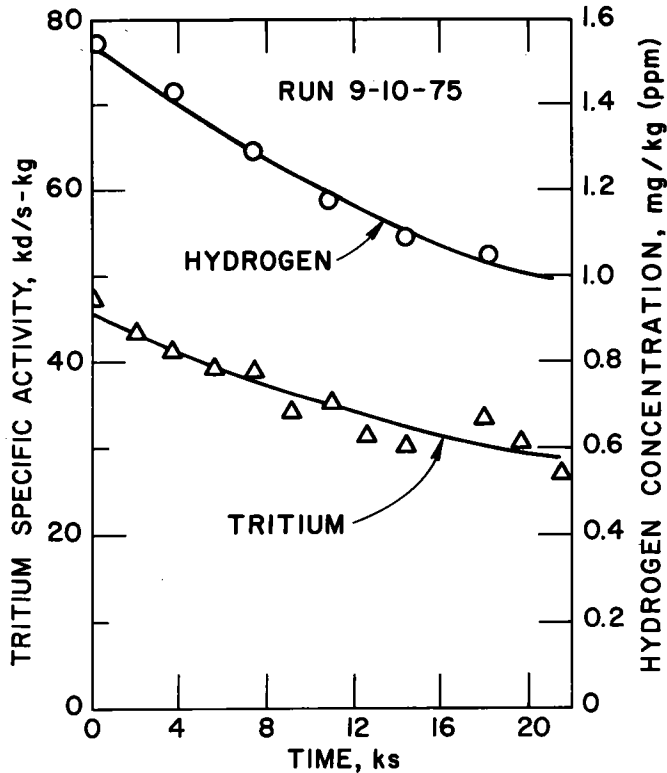


Fig. 1. Tritium and hydrogen removal by the cold trap during run number 9-10-75.

seen from this figure, the coprecipitation model expresses the tritium and hydrogen reductions very well.

#### Isotopic Exchange Runs

The isotopic exchange model (equation 8) was used to analyze each of the five runs of this type. One of these runs (run 1-15-76) is shown in Fig. 2 where the tritium specific activity and hydrogen concentration are shown as a function of elapsed time following the startup of the cold trap. Equation 8 is plotted using a tritium removal efficiency of 22 percent. The fit of the model with the tritium specific activity data is fair, but not as good as desired. The tritium level drops more rapidly in the first 50 ks of the run than the model predicts; also the decline continues more rapidly than the model predicts after 400 ks of elapsed time. Some slight variations in the hydrogen source term during these runs could cause these deviations from the predicted behavior.

#### Summary of Coprecipitation and Isotopic Exchange Runs

Equations 3 and 8 were used to determine the cold-trapping efficiencies of all the runs conducted in this study. Efficiencies were chosen that resulted in the best fit with the experimental data. The results of this analysis are shown in Table III where the sodium residence times in the cold trap, the sodium flow rate and the resulting tritium removal efficiencies are listed for each run.

The data in Table III are shown graphically in Fig. 3, where cold-trap efficiencies are plotted *vs.* sodium residence times. In general, efficiencies

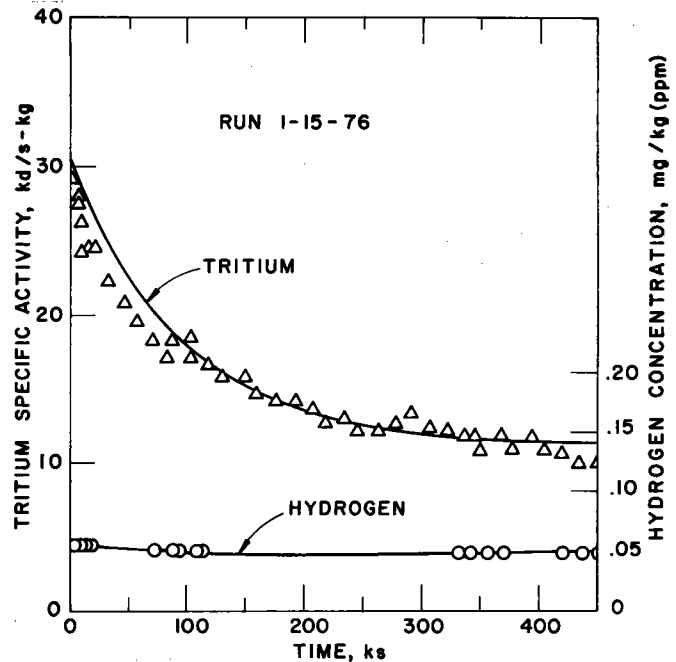


Fig. 2. Tritium removal by the cold trap during run number 1-15-75.

Table III. Cold-Trapping Efficiencies for All Runs

Run No.	Sodium Flow Rate (cm <sup>3</sup> /s)	Sodium Residence Time (s)	Tritium Removal Efficiency (Percent)
<u>Coprecipitation Runs</u>			
6-18-75	62	150	40
7-17-75	16	580	100
7-30-75	16	580	100
9-10-75	35	270	63
9-25-75	47	200	67
<u>Isotopic Exchange Runs</u>			
11-6-75	32	290	7.0
11-11-75	32	290	7.5
11-19-75	60	160	2.4
12-8-75	17	550	30
1-15-76	16	580	22

increase with increasing residence times, as expected. The effectiveness of the isotopic exchange mechanism is much lower than that for the coprecipitation mechanism; however, the efficiencies increase with residence time in both cases.

#### DISCUSSION AND CONCLUSIONS

The specific cold trap used in this study has demonstrated impurity removal characteristics similar to some cold traps of similar design that have been tested in the past.<sup>14</sup> Hydrogen removal efficiencies tend to increase with increasing sodium residence times up to 300 to 600 s. Tritium removal efficiencies were found to increase similarly in the coprecipitation experiments.

The data obtained in this work are applicable to a specific cold trap and sodium system, and caution should be used in applying the numbers to systems that are significantly different. Large variations in cold trap efficiencies from system to system are not expected; however, the scaling factors are not well understood and are the subject of continuing work.

The general conclusions are considered to be valid for most cold-trap systems; however, the uncertainties in the efficiencies applied to other systems are not known.

To assess the applicability of the mathematical model developed in this work, a modified version of equation 8 was compared with tritium data from the EBR-II primary sodium system. It was necessary to modify equation 8 to include the tritium source term and an overall system-boundary permeation term. The modified equation is:

$$C_T = (C_{TO} - \frac{E_T}{D} C_{Te} - \frac{S_T}{DW}) e^{-\frac{D}{M} t} + \frac{E_T}{D} C_{Te} + \frac{S_T}{DW} \quad (9)$$

where D is redefined as  $[E_H(1 - \frac{C_e}{C_H}) + E_T + \frac{P}{W}]$ , and P =

an overall permeation constant, kg/s. In the calculations, Kumar's<sup>15</sup> values for the permeation constant, 0.032 kg/s, and tritium source term, 288 kd/s<sup>2</sup>, were used. The "equilibrium" tritium concentration for C<sub>Te</sub> (if no hydrogen source were present, C<sub>Te</sub> would be the final tritium concentration) was determined using the following reasoning: The rate of hydrogen deposition in the cold trap was calculated from the hydrogen concentration in the EBR-II system, the equilibrium concentration based on the cold-trap temperature, and the cold-trap flow. The rate of deposition was calculated to be 19 µg/s. The rate of tritium transfer to the cold trap was calculated using Kumar's source term and the permeation constant. This transfer rate was 231 kd/s<sup>2</sup>. The ratio of these rates should be equal to the tritium/hydrogen ratio in the cold-trap deposit. This tritium/hydrogen ratio is 12.3 Md/s-mgH. The equilibrium hydrogen concentration is known based on the cold trap temperature, and the equilibrium tritium concentration should be in the same ratio as that in the solid deposit, i.e., C<sub>Te</sub> = C<sub>e</sub> × 12.3 Md/s-mgH so that C<sub>Te</sub> was calculated to be 737 kd/s-kg.

The hydrogen and tritium removal efficiencies were taken directly from the data in Fig. 3 so that

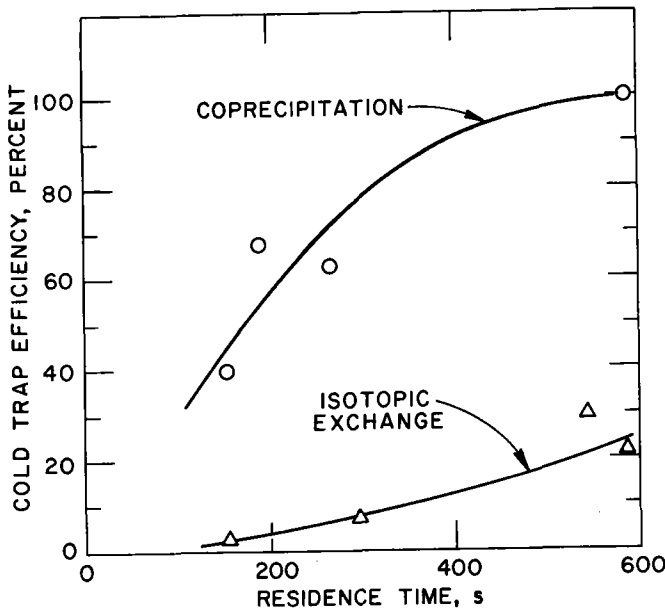


Fig. 3. Cold-trapping efficiencies for coprecipitation and isotopic exchange experiments.

$E_H = 1$  and  $E_T = 0.3$ . Figure 4 is a plot of equation 9 showing the predicted rise of the tritium specific activity in the EBR-II primary system from an initial value of zero to equilibrium at ~1000 kd/s-kg (27nCi/g) after one month of operation. Also shown in figure 4 are data from three reactor-startup periods over the last three years. In general, the predicted specific activity is within a factor of three of the observed values, and the activities appear to rise to equilibrium in approximately one month of operation. (The vertical bar represents the range of equilibrium values that have been observed in EBR-II primary sodium in recent years). Considering the uncertainties in some of the values used in this analysis (source term, permeation data, and correlation between AMPS cold trap and the EBR-II cold trap), the agreement appears to be fairly good. Additional tritium data from EBR-II, along with improved permeation data and additional AMPS cold-trapping data, should be helpful in improving the LMFBR tritium behavior model.

Several additional conclusions may be drawn from the results of this study with the AMPS system:

- A. The isotopic exchange mechanism is much less effective than the coprecipitation mechanism for removing tritium from sodium. The data produced in this study indicate that for any given sodium flow rate, the isotopic exchange mechanism is only 10 to 20 percent as effective as the coprecipitation mechanism.
- B. The isotopic exchange mechanism by itself was not considered a candidate mechanism for controlling tritium in future LMFBRs. This work has confirmed the previous thinking and has allowed order-of-magnitude prediction of expected efficiencies of the mechanism. At typical LMFBR cold-trap residence times (approximately 5 min.) the tritium removal efficiency with no hydrogen source will be less than 10 percent. Normal hydrogen sources in the system will increase the overall tritium removal efficiency; the extent of removal will depend on

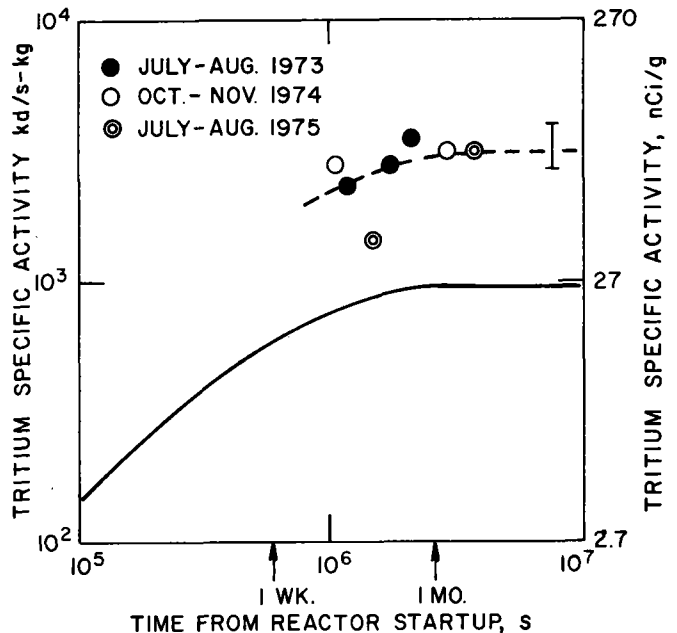


Fig. 4. Tritium specific activities observed in EBR-II primary sodium compared with the activities predicted by the mathematical model.

## INTERNATIONAL CONFERENCE ON LIQUID METAL TECHNOLOGY IN ENERGY PRODUCTION

the magnitude of the hydrogen source.

- C. Models designed to describe the behavior of tritium in LMFBRs should account for hydrogen sources, including corrosion in the steam generators and permeation through the IHX from the secondary to the primary system. These hydrogen sources may constitute the primary mechanism for removal of tritium with the primary and secondary cold traps.
- D. The equations developed in this work are useful in determining the respective hydrogen and tritium removal efficiencies of a cold trap. The equations also allow separate determinations of the coprecipitation efficiency and the isotopic exchange efficiency. Additional work is needed (and is planned) to describe the hydrogen and tritium mass-transfer coefficients and the composition and location of the impurity deposits. This work will allow development of a more sophisticated model for tritium cold-trapping.

11. B. R. Grundy, E. Berkey, E. T. Weber, and W. A. Ross, "Performance of the Improved Electrochemical Oxygen Meter Using High Purity Electrolytes," *Trans. Amer. Nucl. Soc.* 14(1), 186 (1971).
12. R. Kumar, A. F. Panek, D. J. Raue, and P. A. Nelson, "Continuous Monitors for Tritium in Sodium Coolant and Cover Gas of an LMFBR," AEC Report ANL-8079 (March 1974).
13. V. M. Kolba, J. T. Holmes, S. B. Skladzien, M. A. Slawicki, E. C. Filewicz, and P. A. Nelson, "Multipurpose Sodium Sampler for LMFBRs: Design and Operation," USAEC Report ANL-8031 (February 1974).
14. I. L. Gray, R. L. Neal and B. G. Voorhees, "Control of Oxygen in Sodium Heat Transfer Systems," *Liquid Metal Technol.*, Part I. 53, (1957).
15. R. Kumar, "Tritium Transport in an LMFBR," AEC Report ANL-8089 (August 1974).

### REFERENCES

1. M. J. Fluss, N. D. Dudgey, and R. L. Makewicki, "Tritium and Alpha-Particle Yields in Fast and Thermal Neutron Fission of  $^{235}\text{U}$ ," *Phys. Rev. C*, 6 (December 1972).
2. L. E. Trevorrow, B. J. Kullen, R. L. Jarry, and M. J. Steindler, "Tritium and Noble-Gas Fission Products in the Nuclear Fuel Cycle," AEC Report ANL-8102 (October 1974).
3. J. H. Goode and V. C. A. Vaughen, "ORNL Experiments on the Behavior of Tritium During Head-End Processing of Irradiated Reactor Fuels," AEC Report ORNL-TM-2792 (February 1970).
4. G. P. Wozadlo, B. F. Rubin and P. Roy, "Tritium Analysis of Mixed Oxide Fuel Rods Irradiated in a Fast Flux," AEC Report GEAP-13864 (August 1972).
5. C. C. Miles, S. Werder, and E. R. Ebersole, "Tritium Retention in EBR-II Irradiated Boron Carbide," AEC Report ANL-8107 (June 1974).
6. J. A. Basmajian, Neutron Absorber Technology Staff, Hanford Engineering Development Laboratory, Richland, Washington, private communication (November 1975).
7. C. C. McPheeters, "Mass Transfer of Oxygen in Sodium Cold Traps," AEC Report LA-3936 (June 1968).
8. D. R. Vissers, J. T. Holmes, C. C. McPheeters, L. G. Bartholme, V. M. Kolba, P. A. Nelson and L. Burris, "Hydrogen-Meter Leak Detector for LMFBR Steam Generators," USAEC Report ANL-8047 (October 1973).
9. D. R. Vissers, J. T. Holmes, L. G. Bartholme, P. A. Nelson, "Hydrogen Activity Meter for Liquid Sodium and its Application to Hydrogen Solubility Measurement," *Nucl. Technol.* 21(3), 235 (March 1974).
10. B. Minuskin and M. Kolodney, "Development of a Continuous Electrochemical Meter for Oxygen in Sodium," USAEC Report UNC-5131 (1967).

# INTERNATIONAL CONFERENCE ON LIQUID METAL TECHNOLOGY IN ENERGY PRODUCTION

## RADIOCHEMICAL MEASUREMENT OF MASS TRANSPORT IN SODIUM

M. H. Cooper  
Westinghouse Electric Corporation  
Advanced Reactors Division  
Madison, Pennsylvania 15663

S. H. Chiang  
Chemical/Petroleum Engineering Dept.  
University of Pittsburgh  
Pittsburgh, Pennsylvania 15261

### ABSTRACT

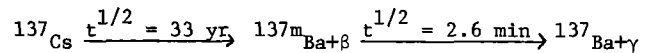
Mass transport between rotating, concentric cylinders in molten sodium has been investigated using a unique radiochemical method. Long-lived (33 year) cesium-137, dissolved in the sodium, decays radioactively emitting a beta to barium-137m, which decays with a short half-life (2.6 minutes) emitting a gamma. Cesium is weakly adsorbed and remains in solution, while the barium is strongly adsorbed on the stainless steel surfaces. Hence, by measuring the barium-137m activity on movable stainless steel surfaces, one can calculate the mass transport to that surface. Mass transfer coefficients in sodium measured by this method are in agreement with published heat transfer correlations when the effect of the volumetric mass source is taken into account. Hence, heat transfer correlations can be confidently utilized by analogy in estimating mass transfer in liquid-metal systems.

### INTRODUCTION

Mass transport processes in the sodium coolant of Liquid Metal Fast Breeder Reactors (LMFBRs) are significant in determining rates of corrosion and deposition of radioactive nuclides from the fuel cladding, deposition and cold trapping of fission products from defect or failed fuel, carbon and nitrogen redistribution in the containment materials, and removal of impurities by cold trapping or hot trapping. Convective mass transfer in liquid-metals has not been extensively investigated. McPheeters<sup>(1)</sup> inferred the mass transfer rate of sodium oxide from its rate of precipitation in a cold trap. Issacs<sup>(2)</sup> found that the rate of oxygen removal from sodium at 600°C by rotating uranium cylinders was proportional to the square root of the circumferential velocity of the rotating cylinder. Cooper and Taylor<sup>(3)</sup> measured the rate of transport of  $^{137m}\text{Ba}$  from  $^{137}\text{Cs}$  dissolved in sodium in the piping of a forced-convection sodium loop. The purpose of the experiments reported in this paper was an investigation of mass transport of a low concentration solute in a dynamic sodium system.

### PRINCIPLE OF THE METHOD

In the present investigation, transport of  $^{137m}\text{Ba}$  in sodium to concentric, rotating, stainless steel cylinders was measured using a unique radiochemical technique. The principle of this method is based on a radioactive decay chain in which the daughter nuclide decays with a very short half-life compared to the parent:



In the sodium- $^{137}\text{Cs}$  system, the radioactive daughter  $^{137m}\text{Ba}$  is strongly adsorbed by stainless steel surfaces, whereas the  $^{137}\text{Cs}$  is weakly adsorbed and remains in solution. Hence,  $^{137}\text{Cs}$  in this system behaves as a volumetric source for  $^{137m}\text{Ba}$  while the latter is transported to the surfaces. By measuring the  $^{137m}\text{Ba}$  radioactivity on the surface of removable cylindrical specimens, one can readily calculate the rate of mass transport to the surface.

At steady-state, the mass transfer flux of  $^{137m}\text{Ba}$  to the specimen surface must be equal to its radioactive decay rate at the surface, which may be expressed as:

$$N = \lambda_1 B_s \quad (1)$$

The term  $\lambda_1 B_s$  represents the number of disintegrations per unit time per unit surface area of the specimen at the time the specimen is removed from the crucible into the counting section. This term may be determined by counting the  $^{137m}\text{Ba}$  preferentially removed from the solution by adsorption on the surfaces. The steady-state mass balance for  $^{137m}\text{Ba}$  is then:

$$\lambda_2 \Sigma_2 - \lambda_1 \Sigma_1 - \Sigma_a = 0$$

or

$$\Sigma_1 = \frac{(\lambda_2 \Sigma_2 - \Sigma_a)}{\lambda_1} \quad (2)$$

The mole fraction of  $^{137m}\text{Ba}$  can be calculated from Equation (2):

$$X_1 = \frac{\Sigma_1}{\Sigma_t} \approx \frac{\Sigma_1}{\Sigma_{\text{Na}}} \quad (3)$$

## INTERNATIONAL CONFERENCE ON LIQUID METAL TECHNOLOGY IN ENERGY PRODUCTION

The mass transfer coefficient can then be calculated based on the measured mass transfer flux (Equation 1) and the concentration of  $^{137}\text{mBa}$ :

$$k = N/X_1 \quad (4)$$

In Equation (4), the liquid phase concentration of  $^{137}\text{mBa}$  in the vicinity of the specimen surface is assumed to be negligible because the barium is strongly adsorbed (instantaneously and irreversibly) on stainless steel surfaces.

### EQUIPMENT AND PROCEDURE

The experiment apparatus, shown in Figure 1, consists of five major components: (1) containment vessel, (2) crucible, (3) cylindrical specimen, (4) electric stirrer, and (5) gamma counting system.

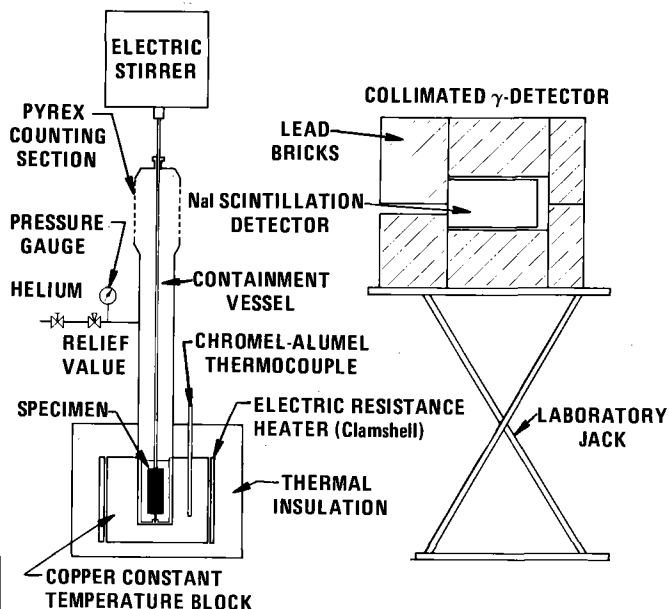


Fig. 1. Equipment Arrangement

The containment vessel was made of 2.5 cm-diameter stainless steel tubing with a 5cm-long "Pyrex" counting window connected with a vacuum coupling. A Veeco vacuum seal was provided at the top of the containment vessel to provide a dynamic seal for the rotating specimen shaft to contain the helium cover gas in the containment vessel.

Liquid sodium with radioactive tracer was contained in a stainless steel crucible, which was tightly fitted within the containment vessel. A cylindrical specimen

1.27 cm or 0.95 cm diameter, was installed concentrically with respect to the crucible and fitted with a shaft passing through the vacuum seal on the containment vessel. The shaft was connected to an electric stirrer capable of rotating the specimen from a speed of 4 to 6000 r.p.m.

Heat was supplied to the lower end of the containment vessel by a 600-watt resistance heater mounted outside a copper block. Temperature of the system was controlled within  $\pm 2^\circ\text{C}$  of the desired setting by a Wheelco Temperature Controller.

Radioactivity on the specimen was measured by the gamma counting system consisting of a 2.5 cm NaI crystal and a multi-channel gamma spectrometer. The gamma counting system was calibrated against a standard of known activity with similar geometry to the specimens.

The procedure consisted of rotating the specimen for at least ten minutes to ensure that equilibrium had been established and then withdrawing the specimen into the counting section, while simultaneously starting a timer. Gamma activity counts were then made for 30 second periods at two-minute intervals until the  $^{137}\text{mBa}$  had decayed (about 20 minutes). The gamma activities could then be separated into that contributed by  $^{137}\text{Cs}$  in the adherent sodium film and the  $^{137}\text{mBa}$  and could be extrapolated to the time of withdrawal.

### RESULTS AND DISCUSSION

The experimental results are correlated as the ratio of Sherwood number (transport term) to the Schmidt number (physical property term) raised to the one-fourth power versus Taylor number (analogous is to Reynolds number) in Figure 2. The mass transfer data yield the following empirical equation for Taylor numbers less than 5,000:

$$N_{\text{Sh}}/(N_{\text{Sc}})^{1/4} = (3.04 \pm 0.001) N_{\text{Ta}}^{(0.247 \pm 0.057)} \quad (5)$$

Also, shown in the same figure is the heat transfer correlation for cylindrical flow reported by Tachibana and Fukui<sup>(4)</sup>.

$$N_{\text{Nj}}/(N_{\text{Pr}})^{1/4} = (0.21) N_{\text{Ta}}^{(0.50)} \quad (6)$$

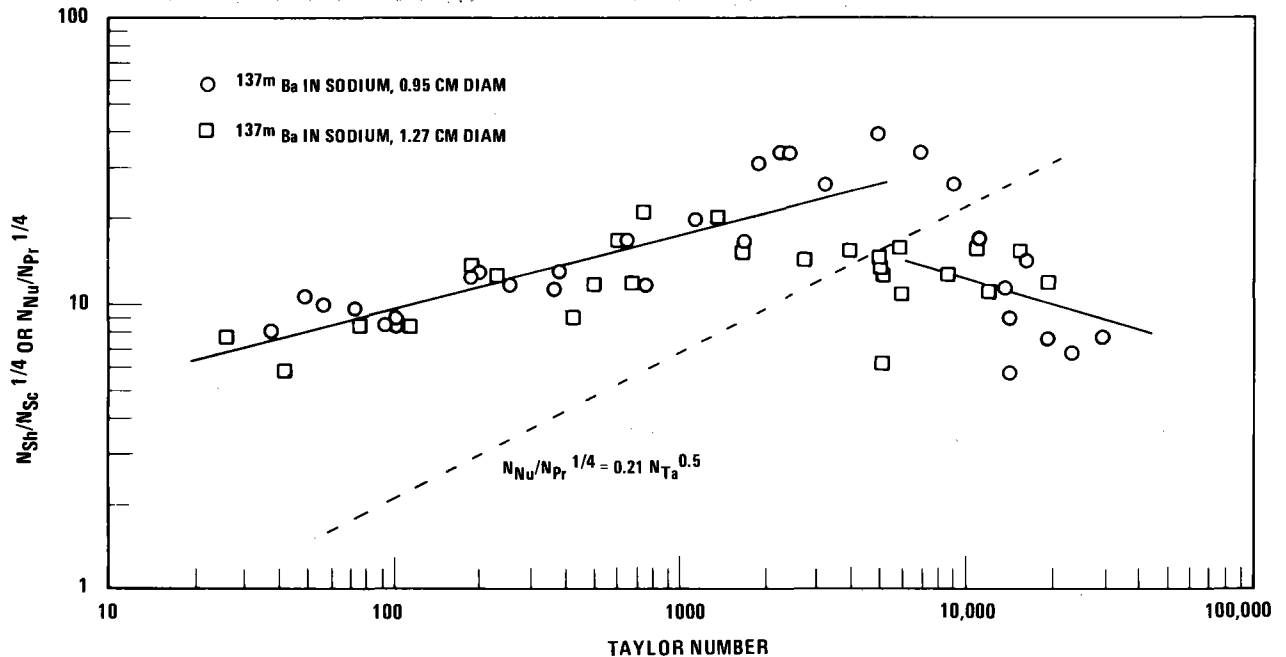


Fig. 2. Comparison of Mass and Heat Transfer Coefficient for Cylindrical Flow

Two major differences are apparent between the mass transfer and heat transport correlations illustrated in Figure 2 and Equations (5) and (6):

- (1) At low Taylor numbers ( $N_{Ta} < 30$ ), the mass transfer data, in terms of  $N_{Sh}/(N_{Sc})^{1/4}$  are almost one order of magnitude higher than the corresponding heat transfer results, expressed in the form of  $N_{Nu}/(N_{Pr})^{1/4}$ .
- (2) As the Taylor number rises, the present mass transfer correlation increases at a much slower rate, indicated by the smaller exponent,  $\sim 0.25$ , as compared to the heat transfer correlation, which shows a  $1/2$ -power dependency on the Taylor number. At Taylor numbers near 5,000, the two correlations approach each other to give numerical agreement within experimental uncertainty.

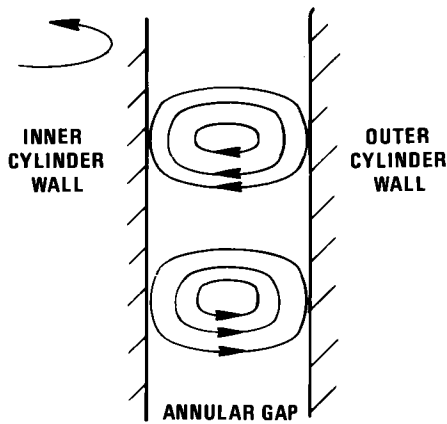
The first difference results from the volumetric source of  $^{137m}\text{Ba}$  in the mass transfer experiment, compared to heat transfer from a heated outer cylindrical (planar source) to a cooled inner cylinder. At low Taylor numbers ( $N_{Ta} < 30$ ), mass and heat transfer are governed by molecular diffusion and conduction, respectively. The rate of transport for a system with a volumetric source is about five times greater than that with a planar source, as shown by the solution for this case, which is similar to that for annular viscous flow derived in Bird, Steward, and Lightfoot<sup>(5)</sup>. Thus, the

observed difference is in accordance with the results expected for a volumetric diffusion source compared with a planar source.

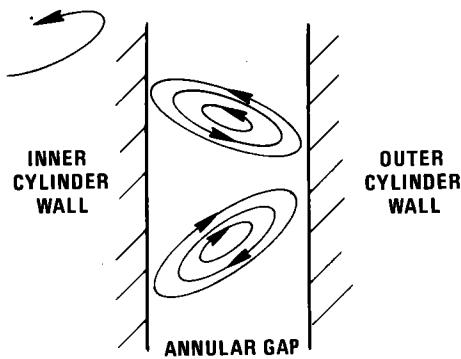
The second difference can be explained by considering the effect of vortex formation in the annulus above the critical Taylor number of 30. In the heat transfer experiment, heat is transported from the heated surface to the cooled surface by the vortex flow. In contrast, the  $^{137m}\text{Ba}$ , which is produced volumetrically, is transported and deposited on both the inner and outer cylinders. Hence, the effect of Taylor number of the rate of  $^{137m}\text{Ba}$  transport to the inner cylinder alone will be less than that of the simple heat transfer case with one heated wall and one cooled wall. If the contribution from the volume source is subtracted from the mass transfer data, the two correlations agree within experimental error for Taylor numbers less than 5,000.

At Taylor numbers greater than 5,000, the mass transfer correlation shows a sharp decrease while the heat transfer correlation continues to rise at the same rate. The reduction in mass transfer to the inner cylinder is caused by the onset of turbulence at this Taylor number. The altered circulation pattern illustrated in Figure 3 and random motion of turbulent eddies enhances the transport of  $^{137m}\text{Ba}$  to the outer cylinder, thus reducing the transport to the inner cylinder. Since the total production rate of  $^{137m}\text{Ba}$  is fixed by the quantity of  $^{137}\text{Cs}$ , the enhanced transport to the outer cylinder

(four times the surface area of the inner cylinder), has the effect of reducing the effective  $^{137}\text{mBa}$  concentration and shifting the maximum concentration away from the inner cylinder.



(a) TAYLOR VORTICES IN LAMINAR PLUS VORTICES FLOW REGIME



(b) TAYLOR VORTICES IN TURBULENT PLUS VORTICES FLOW REGIME

Fig. 3. Schematic Streamlines for Flow Between Concentric Cylinder with Inner Cylinder Rotating

According to mass transfer analogy theory, the mass transfer factor,  $j_D$ , is equal to  $1/2 f$  (friction factor) at equivalent hydrodynamic conditions. To demonstrate this equivalence, the logarithms of  $j_D$  and  $1/2 f$  are compared graphically as functions of the logarithm of the Taylor number in Figure 4.

The friction factor in cylindrical flow is calculated from correlations developed by Bjorklund and Kays<sup>(6)</sup> and confirmed to be valid beyond the transition to turbulent flow by Gandhi and Estrin.<sup>(7)</sup> The friction factor for cylindrical flow in both the Taylor vortices regime and the turbulent regime can be shown to be given by

Equation (7) obtained by rearranging the Bjorklund and Kays correlations:

$$f = \frac{0.76 \left(\frac{d}{a}\right)^{3/2} N_{Ta}^{-0.478}}{1 - \left(\frac{1}{1+d/a}\right)^2} \quad (7)$$

The mass transfer factors agree closely with  $1/2f$  until the turbulent regime is reached at a Taylor number of about 5,000. Then, the mass transfer factor decreases more steeply than the friction factor for the reasons discussed previously. The closer agreement between the mass transfer factor measured with this method and friction factor result from the similarity between the volumetric mass source and the volumetric viscous forces resulting from fluid flow.

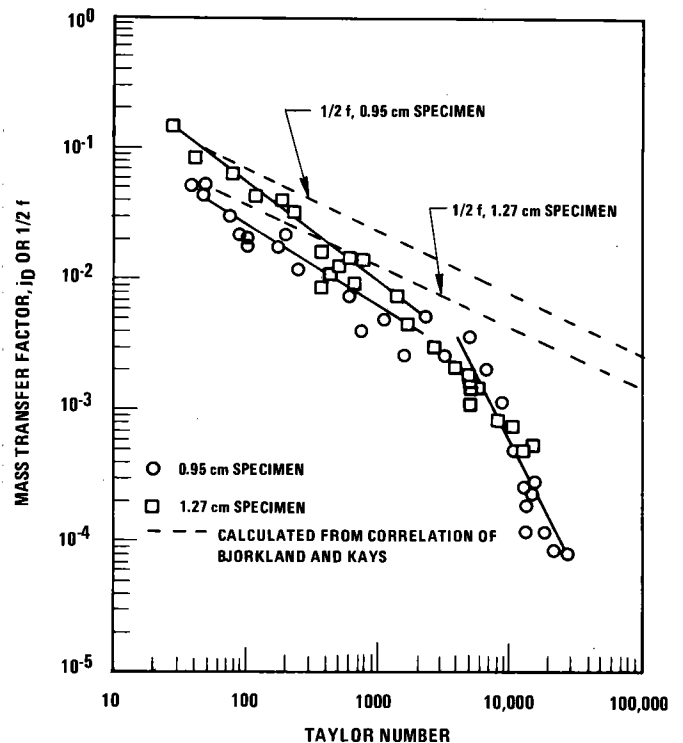


Fig. 4. Comparison of Mass Transport Factor With Friction Factor as a Function of Taylor Number

# INTERNATIONAL CONFERENCE ON LIQUID METAL TECHNOLOGY IN ENERGY PRODUCTION

## CONCLUSIONS

The following conclusions are reached from this investigation:

- (1) A unique radiochemical method using  $^{137}\text{Cs}$  and its daughter  $^{137\text{m}}\text{Ba}$  has been successfully applied to the measurement of convective mass transfer in liquid sodium between concentric cylinders.
- (2) The mass transport correlation is in agreement with a previously published heat transfer correlation for similar hydrodynamic conditions, when the effect of the volumetric mass source is taken into account.
- (3) The mass transport correlation agrees closely with the friction factor correlation, since the frictional fluid flow losses are analogous to the volumetric solute source in the mass transfer experiments.
- (4) Heat transfer or fluid friction correlations can thus be confidently utilized by analogy in estimating mass transfer at low solute concentration in liquid-metal systems.
- (5) In the laminar flow regime, a correction must be applied to heat transport correlations to account for the "volume source effect" when the analogy is used for the transport of a nuclide produced uniformly in the bulk liquid.

## ACKNOWLEDGEMENTS

The authors wish to thank the Shell Oil Company and the University of Pittsburgh for the support of this work. The assistance of Dr. G. R. Taylor of the Advanced Reactors Division, Westinghouse, in supplying the cesium tracer and his helpful consultations are also appreciated.

## NOTATION

- a - radius of specimen (inner cylinder), cm  
 $B_s$  - surface concentration of  $^{137\text{m}}\text{Ba}$ , atoms/cm<sup>2</sup>  
 c - heat capacity, cal/gm - °C  
 d - thickness of annulus between cylinders, cm  
 D - binary diffusion coefficient, cm<sup>2</sup>/sec  
 f - friction factor (dimensionless)

- h - heat transfer coefficient, cal/cm<sup>2</sup>-sec-°C  
 k - mass transfer coefficient, gm-mole/cm<sup>2</sup>-sec-mol fract.  
 K - thermal conductivity, cal/cm<sup>2</sup>-sec-°C  
 $N$  -  $^{137\text{m}}\text{Ba}$  flux, atoms/cm<sup>2</sup>-sec  
 $N_{Nu}$  - Nusselt number =  $\frac{hd}{K}$   
 $N_{Pr}$  - Prandtl number =  $\frac{\mu}{ck}$   
 $N_{Sc}$  - Schmidt number =  $\frac{\mu}{\rho D}$   
 $N_{Sh}$  - Sherwood number =  $\frac{k}{\rho_m} (2:d)/D$   
 $N_{Ta}$  - Taylor number =  $(\omega ad\rho/\mu) (d/a)^{1/2}$   
 X - mole fraction

## Greek Symbols

- $\mu$  - absolute viscosity, gm/cm-sec  
 $\rho$  - density, gm/cm<sup>3</sup>  
 $\omega$  - angular velocity, radians/sec  
 $\lambda$  - decay constant, sec<sup>-1</sup>  
 $\Sigma$  - number of atoms

## Subscripts

- 1 -  $^{137}\text{Cs}$   
 2 -  $^{137\text{m}}\text{Ba}$   
 a - adsorbed on surfaces  
 Na - sodium  
 t - total  
 s - surface  
 m - molar



# INTERNATIONAL CONFERENCE ON LIQUID METAL TECHNOLOGY IN ENERGY PRODUCTION

## REFERENCES

1. McPheeters, C. C., Mass Transfer of Oxygen in Sodium Cold Traps, LA-3936, 1968, Los Alamos Scientific Laboratory.
2. Issacs, H. S., BNL-50193(T-543), pp. 27-30, 1969, Brookhaven National Laboratory.
3. Cooper, M. H. and Taylor, G. R., Trans. Am. Nucl. Soc., 1970, 13, 579.
4. Tachibana, F. and Fukui, S., Bull. J.S.M.E., 1964, 7, 385.
5. R.B. Bird, W.E. Stewart, and E.N. Lightfoot, "Transport Phenomena," John Wiley Co., N.Y., N.Y. 1960,p.53.
6. I. S. Bjorklund and W. M. Kays, "Heat Transfer Between Concentric Rotating Cylinders," Journ. Heat Transfer, Vol. 81 (Aug., 1959), pp. 175-185.
7. R. Gandhi and J. Estrin, "Turbulent Momentum Transfer in Two-Phase Cylindrical Couette Flow," AIChE Journ., Vol. 17 (March, 1971), pp. 349-352.

## DISCUSSION

Paper IVB-2: "Sorpton of Radionuclides on Sodium Sampling Vessels"

C. Allan: Could greater sorption on nickel than steel be due to its oxide film that is more readily reduced? This property will facilitate sorption (for instance due to intermetallic compound formation between Ni and Ag or Zn).

H. Stamm: I agree that only the increased  $^{110m}\text{Ag}$  deposition at lower temperatures could be explained by simple solubility effects. Selective deposition of  $^{65}\text{Zn}$ ,  $^{54}\text{Mn}$  (at higher temperatures), and of  $^{110m}\text{Ag}$  (again at lower temperatures) on Ni surfaces indicates that chemistry (such as increased reduction of NiO on Ni\*) is responsible for the described effect.

\* as compared to oxides on a stainless steel surface

C. Allan: Have you studied kinetics of sorption, which should differentiate between phase partition and particle deposition by using different sodium exposure times?

H. Stamm: We hope to perform such kinetic experiments although, as I mentioned, the sampling station is the only possibility to introduce deposition samples into the KNK primary sodium during reactor operation. Because of the operators' steady demand for sodium samples for the analytical survey of the primary system, experimental time was limited.

W. Kuhn: In what temperature range did sorption occur?

H. Stamm: Experiments were performed in the temperature range of 200° to 350°C.

Paper IVB-3: "The On-Line Separation of Radioiodine in Highly Radioactive EBR-II Sodium"

K. Claxton: In Table 1 does the observation that  $^{137}\text{Cs}$  is partially redistributed in the sodium wash at 100 to 130°C and mostly redistributed in sodium at 370°C reflect the change in partition coefficient with temperature or could it imply that sodium at 370°C might be an effective decontaminant for this important fission product?

R. Villarreal: Although 100% of the  $^{137}\text{Cs}$  segregated to the walls of the stainless steel tube, about 1/3 of the  $^{137}\text{Cs}$  activity is drained with or remains with the originally drained sodium. Also, about 1/3 of the  $^{137}\text{Cs}$  activity is washed or redistributed into the 100 to 130°C sodium and about 30% remains on the walls of the tube. About 10% of the  $^{137}\text{Cs}$  activity remains on the walls of the stainless steel tube even after washing with water.

K. Claxton: What are the implications of no redistribution of  $^{54}\text{Mn}$  on questions of diffusion of this species into the underlying base metal?

R. Villarreal:  $^{54}\text{Mn}$  was not washed off or redistributed from the surface once it had segregated to the surface.

We have observed  $^{54}\text{Mn}$  on reactor hardware and the EBR-II cold trap but, as other speakers have asserted, the mechanism is not known.

N. Krasnoyarov: Have you determined carbon content in sodium since it has influence on redistribution of cesium and iodine between sodium and surfaces?

R. Villarreal: Total carbon content of the sodium is about 1 ppm, and active carbon content of EBR-II sodium is about 0.1 ppm.

Paper IVB-4: "A Computational Technique for Estimating Corrosion Product Release in an LMFBR"

K. Claxton: Does the essentially oxygen-independent  $^{54}\text{Mn}$  release observed result from an enhanced solid state diffusion coefficient caused by the fact that nickel release is oxygen-independent and hence the surface condition (i.e., ferritic layer formation) is being established continuously?

W. Kuhn: That conclusion is not valid since, first the effect of ferrite layer formation has not been considered and, second, the enhanced release of  $^{54}\text{Mn}$  is caused by diffusion in the austenite phase. Presumably the diffusivity in a ferrite phase would be still greater. The slight sensitivity of the predicted  $^{54}\text{Mn}$  release to the oxygen concentration is due to the greater importance of the oxygen-independent diffusion release relative to oxygen-dependent corrosion release.

H. Feuerstein: Are you currently evaluating a source term for fission products to provide for a failed fuel accident case?

W. Kuhn: We have an ongoing experimental program to study the transport of fission products and fuel. To date, our modeling effort has considered only activated corrosion products.

Paper IVB-5: "Fission Product Measurements in the Inpile Fission Product Loop"

N. Krasnoyarov: Have your tests proven that no effect occurs when argon was captured into sodium from the gas plenum?

H. Feuerstein: Model experiments with water and methyl-alcohol were conducted to investigate the mixing behavior of the liquid and gas phase in the tank. Only at very high flow rates of the liquid phase was cover gas absorbed from the liquid. We have not tested such high flow rates at FPL.

H. Kottowski: Since the fraction of fission gas release is measured in the gas blanket, in what form are fission products transported?

H. Feuerstein: Fission products are completely dissolved in sodium and diffuse through an interface-boundary layer to the cover gas.

## INTERNATIONAL CONFERENCE ON LIQUID METAL TECHNOLOGY IN ENERGY PRODUCTION

H. Kottowski: Have you determined Na saturation conditions for the fission products measured?

H. Feuerstein: We are many orders of magnitude away from achieving saturation. Saturation concentration of rare gases have been measured in a special system by H. Shimojima, Toshiba.

B. Y. So: How was the fission source rate determined?

H. Feuerstein: Total fission rate was determined by calculating the following expression: measured neutron flux  $\times$  number of atoms  $\times$  cross section.

B. Y. So: How was the recoil surface area determined?

H. Feuerstein: Recoil area was first calculated using the geometrical surface of our fuel. Because some change in release rates has occurred during the last 3 years, all data in the paper depend on the total fission rate. Therefore, we do not know the current recoil area.

B. Y. So: Is there a stagnant sodium layer at the argon/sodium interface at the flow rates considered in your study?

H. Feuerstein: No, model experiments showed a strong stirring effect on the sodium-cover gas interface at all investigated liquid flow rates.

Paper IVB-6: "Fission Product Deposition in a Stainless Steel-Sodium System"

C. Allan: Did you measure total Te content of the sodium? We have also determined K values for tellurium in sodium-steel capsule experiments, observing reversible partition in the range from 150 to 750°C,  $4 \times 10^{-3}$  - 400 ppm with  $\Delta H_{\text{desorption}} \sim 40$  k J/mole Te. K values up to  $10 \text{ cm}^{-1}$  are observed for I-131. I would assume that your K vs  $1/T^\circ\text{K}$  but becomes constant at  $T < 250^\circ\text{C}$  because the surface has scavenged Te at higher temperatures.

Y. Gohshi: We did not measure the tellurium content although we suspect that it is very low because neutron flux is rather low and fuel amounts to only about 150 gr. Flattening is presumed to be caused by oxide precipitation covering the surface of the CT less than 250°C.

N. Krasnoyarov: Are you sure that the same sodium type (from the same plant) will be used for Joyo and Monju reactors? Impurity content may change the behavior of some fission product very strongly; as it happened in our BR-5 reactor.

Y. Gohshi: Since the FPL research program utilizes a basic approach, we will not apply our data directly to the actual reactor system, such as Joyo or Monju. However, it may be possible to utilize our FPL results in obtaining basic input data for the evaluation of fission product behavior in an actual reactor system. Because FPL is very small and the addition of various impurities is a simple process, we are planning to investigate their effects or fission product behavior.

N. Krasnoyarov: What was carbon content during experimentation?

Y. Gohshi: Carbon content was not determined.

Paper IVB-7: "Control of Tritium in LMFBR Sodium Systems by Cold Trapping"

W. Kuhn: You noted a discrepancy by a factor of 3 between predicted and observed tritium levels in EBR-II. Do you attribute the discrepancy primarily to uncertainties in source terms for hydrogen and tritium, or to uncertainties in the model you described?

C. McPheeters: The discrepancy is primarily attributable to the uncertainty in tritium and hydrogen source terms in EBR-II; although our model is not completely developed and now utilizes some uncertain assumptions. Neither the tritium nor the hydrogen sources is well known in EBR-II, and the hydrogen source is variable as a function of the number of fuel-handling operations that are performed.

W. Kuhn: If a significant ingress of hydrogen from the sweep gas in the tritium meter occurred, did it affect the isotopic exchange measurements?

C. McPheeters: Ingress of hydrogen from the tritium meter sweep gas was carefully measured and its effect on the isotopic exchange runs integrated in the mass balance equations. Reported isotopic exchange removal efficiencies were calculated independent of the hydrogen source.

B. Grundy: In your graph of efficiencies versus residence time in the cold trap, were curves through the data points achieved by any form of regression analysis?

C. McPheeters: No, these curves were drawn by a visual best fit.

P. Roy: How do you estimate or calculate the hydrogen source in the secondary system caused by the water-side corrosion of the ferritic steam generator?

C. McPheeters: In our modeling of the EBR-II tritium level, the hydrogen source from the secondary system was negligible, relative to other sources. Although this situation should also prevail in the CRBR, there are discrepancies between hydrogen sources measured in the U.S. and Europe. This uncertainty in hydrogen sources may present a problem to our final development of the tritium behavior model. The hydrogen source to be used in our calculations has not been determined.

Paper IVB-8: "Radiochemical Measurement of Mass Transport in Sodium"

W. Kuhn: Were you able to verify that the cesium did not segregate to the surface?

S. Chiang: The count due to adsorbed cesium was measured and subtracted from the total count. Thus, the reported data were properly corrected for cesium segregation to the surface.

INTERNATIONAL CONFERENCE ON LIQUID METAL TECHNOLOGY IN ENERGY PRODUCTION

C. Miles: Did you remove the cylinder from sodium before or after it stopped spinning at the experimental set point?

S. Chiang: We remove the cylinder from the sodium immediately after the rotation is stopped.

C. Miles: Do you expect other isotopes (than  $^{137}\text{Cs}$ ) to behave differently?

S. Chiang: No, we do not expect other isotopes (than  $^{137}\text{Cs}$ ) to behave differently so far as mass transfer is concerned.

MATERIAL EFFECTS IN LMFBR SODIUM SYSTEMS

W. Dietz E.D. Grosser H. Lorenz  
 INTERATOM  
 Bensberg/FRG

ABSTRACT

Within the scope of this paper environmental effects on materials for heat exchanging equipments for LMFBR systems as irradiation, corrosion and operational conditions are discussed. Relevant consequences on the design of fuel cladding, intermediate heat exchanger, and steam generator are outlined.

INTRODUCTION

The operating conditions of commercial LMFBR's can result in material performance problems. Corrosion, radiation damage, temperature requirements, plastic deformation, and the superposition of these effects, have been defined as important limiting factors for the design of components. A detailed knowledge of the various parameters which can influence the behavior of materials under LMFBR conditions, is therefore necessary. The objective of this paper is to identify the influence of the sodium environment on the most important properties of materials which are used for the construction of heat transfer components. This paper considers the fuel cladding, the IHX, and the steam generator to be the major heat exchange units to be evaluated.

FUEL PIN CLADDING

It is generally accepted that the combination of operating conditions and materials effects (Fig.1) results in a reduced burn up capability of fuel pin cladding in a fast breeder reactor environment. In the following, sodium corrosion phenomena related to some other material effects under LMFBR-operating conditions will be evaluated with regard to mechanical properties.

Materials

Various types of materials have been

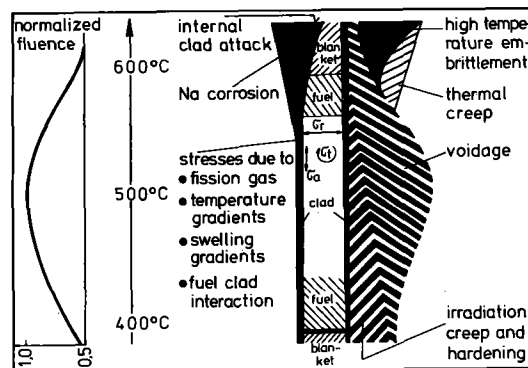


Fig.1: Material Effects and Phenomena Affecting Clad Behavior (schematic) (Ref.H.Böhm)

considered as potential fuel pin cladding within the frame work of the international LMFBR-programs (Tab.1).

Table 1: Nominal Chemical Composition of Potential Cladding Materials for LMFBR-Projects

Element	SNR-300			PFR <sup>1)</sup> /FFTF <sup>1)</sup> Phenix <sup>1)</sup>			EBR 2 304 <sup>2)</sup>
	14970 <sup>1)</sup>	14981 <sup>1)</sup>	14988 <sup>1)</sup>	321 <sup>2)</sup>	316 <sup>2)</sup>	318 <sup>2)</sup>	
B	0.005	<0.001	<0.001	—	—	0.003	—
C	0.1	0.06	0.06	0.07	0.07	0.08	0.07
Cr	15	16	16	18	17	16.5	18
Mn	1.7	1.3	1.3	<2	<2	1	2
Mo	1.2	1.8	1.3	—	2.5	1.5	—
N	<0.02	<0.02	0.1	—	—	—	—
Ni	15	16	13	12	11	11.5	11
P	0.02	0.02	<0.02	<0.03	<0.03	—	0.04
S	0.02	0.02	0.02	<0.03	<0.03	—	0.03
Si	0.4	0.4	0.4	<0.75	—	0.4	—
Ti	0.4	—	—	0.35	—	—	—
V	—	—	0.7	—	—	—	—
Nb	—	0.8	0.8	—	—	1	—

1) German DIN 17007 2) American AISI-stand. 3) Reference AISI 316

The French, United States, British and Japan prototypic LMFBR's use the unstabilized AISI 316 as reference cladding material, the DEBE-NELUX-prototype SNR 300 will have a Ti-stabilized X 10 CrNiMoTiB 1515 (1.4970). These materials are used generally in the cold worked condition. The main difference between these types of materials is the stability of the austenitic structure, the precipitation behavior, and the carbon activity in the austenitic matrix.

Sodium Corrosion Phenomena

Sodium corrosion effects related to mechanical properties may be divided into two groups (Tab.2):

- surface effects
- bulk material effects

The data in Tab.2 are values from the literature<sup>1,2</sup> for a clad temperature of 700°C, which is considered as a hot spot temperature in fuel pin cladding.

Table 2: Sodium Corrosion Phenomena-Design Consideration

	Type	Depth for 10 <sup>4</sup> h [μm]	Design consideration
Surface	Metall loss	20	Live fraction rule accelerated creep
	Ferritic layer	10	—
	Surface hole	10	—
	Grain bound. grooving.	10	—
	Grain bound. ferrite	40	—
Bulk	Decarburization *	> 100	AISI 304 / AISI 316 ΔC <sub>γ</sub> /10 <sup>4</sup> h ~ 30%
	Carburization *	> 100	—
	Nitrogen loss *	> 100	—
	Boron loss	> 100	—
* depend upon loop chemistry			
T=700°C; V <sub>Na</sub> = 3-10m; 0-10 ppm			

The various types of austenitic ss shall not differ significantly in the type and depth of penetration in the surface<sup>1,2</sup>. The bulk material effects depend upon sodium chemistry (e. g. carbon activity) and type of steel (stabilized, unstabilized, nitrogen and boron content). For most of the fuel pin claddings of the prototypic LMFBFR's the sodium affected zone (metal loss, selective corrosion in the surface region) is about 10 % of the nominal wall thickness of the tubes (SNR 300: 0,38 mm). At first the influence of this effect on short and long time mechanical behavior will be discussed.

Mechanical Properties

Tensile Properties

The 0.2 % proof strength at room temperature has been measured on pressurized tubes after 5000 and 10000 hours exposure in sodium at 600 and 700°C (experimental sodium condition Ref.2). For material 1.4970 (14 % CW, 800°C/2 h) a  $\sigma_{0.2}$ -decrease after 10<sup>4</sup>h in sodium was observed (Fig.2), but the magnitude of

this decrease can be attributed to the recovery of the cold worked structure. Data from annealing experiments of the same heat in Fig.2 determine the shape of the curve. The same trend was observed for the other heats of 1.4970 in the same metallurgical condition and also for material 1.4981 in the cold worked condition (14 %). Solution annealed samples (600, 700°C) and cold worked samples at 600°C and 10<sup>4</sup> hours are within the scatter band of the tubes in the as-received condition.

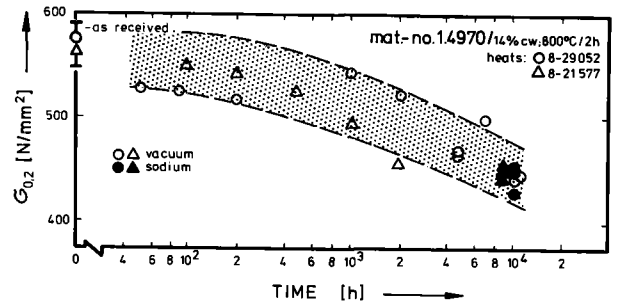


Fig.2: Yield-strength  $\sigma_{0.2}$  at 25°C after Exposure in Vacuum and Sodium at 700°C for ss-tubing 1.4970

High temperature (700°C) burst tests have been performed to determine the effect of sodium exposure (3000 h/700°C) and various cleaning procedures on the mechanical properties<sup>3</sup>. Grain boundary ferrite of about 30 μm did not change the burst properties (strength, ductility) of the tubes. At present there is no experimental evidence that sodium effects near the surface have a significant influence on the short time mechanical properties of the material. However there is some uncertainty in this conclusion, because the corroded samples investigated carburized to some extent<sup>2</sup>. Furthermore some effects (strength reduction) due to cleaning procedures cannot be excluded<sup>3</sup>. Tensile tests on material samples from compatibility tests with fuel have shown that a corrosion depth of 10 % of the bulk material can significantly influence the mechanical properties ( $\sigma_{0.2}$ ,  $\sigma_{UTS}$ ,  $\epsilon_R$ )<sup>4</sup>.

Short time tensile behavior is of interest for the fuel pin designer during normal reactor power changes and for off-normal conditions. Regarding sodium corrosion effects, at present only metal loss is considered as a damage factor whereas for fuel corrosion wall-thickness reduction and grain boundary penetration are both considered. In Fig.3 sodium corrosion data (normalized to one year exposure) are compared with internal clad corrosion data from various SNR fuel pin irradiation experiments. The sodium corrosion data from various loops are analyzed on a statistical basis for metal loss from samples (max. values) in the location of max. temperature<sup>5</sup>. The internal clad corrosion data represent average values observed on pins from DFR and Rapsodie irradiation with O/M-ratio from 1.96 - 2.00<sup>6</sup>. The corrosion depth is including homogeneous and grain boundary attack.

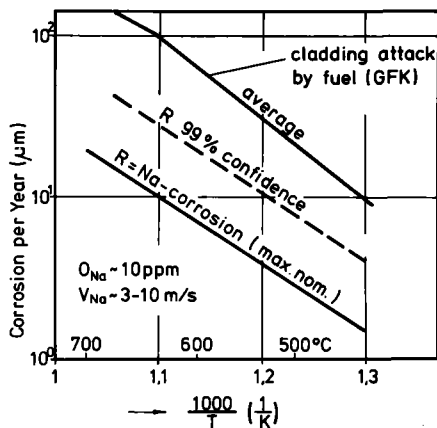


Fig.3: Corrosion of Austenitic Stainless Steels by Fuel and Sodium

The ductility of sodium exposed tubes (burst tests after 3000 h / 700°C<sup>3</sup>) has not been influenced significantly, comparing the data with as-received tubing. For comparison high temperature irradiation to  $\phi \cdot t \sim 10^{22} \text{ n/cm}^2$  will reduce the rupture ductility to 10-30 % of the as-received condition, depending upon the cold work of the material.

### Creep / Creep-Rupture Behavior

Fission gas pressure will be the main reason for creep damage at the hot part of the fuel pin cladding for steady state operating condition. Some experimental work was performed in static and dynamic anisothermal sodium loop systems, using thinwalled cladding tubes of various types of material<sup>7,8,9</sup>. Drastic effects of sodium have been observed for AISI 304 ss on the creep rupture strength ( $\sigma_R$ ) at 1300°F (~700°C) for tests up to  $\sim 10^4$  hrs<sup>9</sup>. The decrease of 30-40 % in the rupture strength  $\sigma_R/10^4$  h could be attributed to the loss of carbon and, to some small extent, to a reduced ductility (50 % relative) in sodium compared with control samples. In general smaller reduction was observed for AISI 316ss (20-25 % decrease  $\sigma_R/10^4$  hrs). At a lower temperature of 620°C no sodium effect was observed.

Within the DEBENELUX-LMFBR-Program creep tests have been performed on stabilized ss-cladding at 600 and 700°C<sup>10,2,11</sup>. For the material X 8 CrNiMoVNB 1613 (1.4988) during 5000 hrs exposure at 700°C a reduction in creep rupture strength  $\sigma_R$  of about 10 % was observed, probably due to a loss in nitrogen content<sup>10</sup>. The rupture ductility was not changed by more than a max. of 30 % (relative). The same material (tube lot) was investigated in another sodium loop, but no change in the creep resistance was observed<sup>2</sup>. For the SNR-reference cladding material X 10 CrNiMoTiB 515 (1.4970) no significant change in creep resistance was observed, although an extensive boron loss in this type of steel was measured<sup>2,10,11</sup>. The influence of environmental condition on creep properties of material 1.4988 is shown in Fig.4 for a temperature of 600°C. Similar results were observed at 700°C. At 600°C the results of pressurized capsules in dynamic sodium follow the curve of pressurized tubes in air, no sodium effect on the 1 % strain limit is obvious<sup>2</sup>. On the same heat of material (tubing lot) creep and creep rupture tests, have been performed with internally pressurized sections from fuel pins (ir-

radiation temperature  $T > 550^{\circ}\text{C}$ ) and with samples from high temperature irradiation ( $T \sim 600^{\circ}\text{C}$ ) in the BR-2<sup>12</sup>. Mainly due to high temperature embrittlement phenomena (grain boundary weakening by He from  $(n, \alpha)$ -reactions) the ductility loss ( $\sim 70-90\%$ ) reduces the creep rupture strength ( $G_R$ ) by  $\sim 25\%$  compared to the 1%-strain limit.

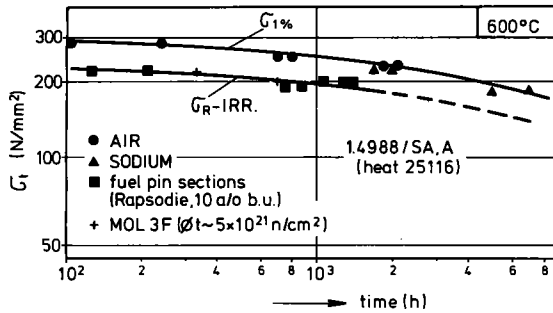


Fig.4; Long Time Properties of 1,4988 Tubing at 600°C in Sodium and in Irradiated Condition

It is therefore concluded that other environmental effects (irradiation, corrosion by fuel) cause more severe material damage than sodium corrosion. Concerning creep behavior, the design of the SNR 300 fuel pin cladding at the present does not consider an influence of sodium corrosion, except the wall thickness reduction (s. Tab.2). Further experimental work must support these design assumptions. For future R+D-work the interrelation between bulk corrosion effects e.g. carburization and mechanical properties degradation or structural changes due to neutron irradiation should be considered.

INTERMEDIATE HEAT EXCHANGER

The intermediate heat exchanger as the most important component of the secondary sodium loop has only safety functions in mode of operation of the power station. The IHX separates radioactive and inactive sodium, protects the primary loop in the case of a sodium/water-reaction in the steam generator and prevents the tertiary loop in case of a hypothetical Bethe Tait accident.

The main engineering duty is to optimize the safety function of the IHX in relation to a minimum in heat loss. This engineering incentive resulted in basically similar constructions. This is shown in Table 3, where some characteristic design details are given.

Table 3: Design Characteristics of LMFBR-IHX

	PFR	Phenix	SNR 300	FFTF	CRBRP
Reactor power	600	563	765	400	975
IHX power	100	94	85	133	325
Prim. Inlet/Sec. Outlet-Temp.	560/400	560/400	546/377	566/414	535/388
Tubes/IHX	1808	2280	846	1540	2778
Tube dimensions	19.0x1.0	14.0x1.0	21.0x1.4	22.2x1.2	22.2x1.14
Tube assembly	circular	circular	hexagonal	circular	circular
Strain compensat.	yes	no	no	yes	yes
Isolation *	Na	gas	gas	Na	Na
Spacers	6	6	9	7	20/2
Material	321	316	304	304	304
Tube plate weld construction					

\* between bayonet tube and primary sodium

In principle the IHX is composed of a tube bundle of thin walled tubes with one larger central tube fixed to two tube-plates by welding and surrounded by shells. The secondary sodium system is operated at a higher system pressure than the primary loop. This is aimed at preventing an activated primary sodium inleakage into the secondary system.

With concern to the specific sodium impacts on the material properties and on the mechanical conditions, resp., three different problem areas exist:

- long-time interaction between the IHX-tube material and sodium resulting in surface structures modified in composition
- transport of activated corrosion products in the primary loop and relevant questions on distribution and deposition behavior
- consequences of the thermophysical properties of sodium on the mechanical material loading.



Corrosion

Regarding the parameter sodium corrosion, the temperature for the IHX tubing is about 150°C lower than that for the fuel cladding, but the design time is more than one magnitude higher as compared to the cladding tube. With regard to the safety function of the IHX, being a containment border of the primary system the design has to be conservative. The intermediate heat exchanger represents the heat sink for the primary loop and the heat source for the secondary system. For both sides the different kinds of corrosion, i.e. abrasive corrosion, selective corrosion and interstitial element transfer have to be evaluated in the design process.

The corrosion allowances which were used in the SNR 300 design are given in Table 4. These data were defined in accordance with the competent technical supervision authority.

Table 4: Reference Conditions and Corrosion Data for SNR 300 Intermediate Heat Exchanger

Reference Data	Loop		Design Data
	Primary	Secondary	
Oxygen content (ppm)	10 ± 3		10
Sodium velocity (m sec <sup>-1</sup> )	1.4	2.1	
Temperature (°C)	546	520	555/535
Design time (h)	200,000		2.0 × 10 <sup>5</sup>
Statistical significance			2
Ferrite layer (µm)	20	20	40
Corrosion rate (µm/a)	2.7	2.8	31/35
Corrosion allowance (µm)	90	99	189

In addition to this, by an official request the actual corrosion conditions of the heat transfer systems are monitored by an in-sodium coupon surveillance programme.

The primary and secondary heat transfer loops are both bimetallic systems. In the primary system the stabilized clad material is inserted in the region of increasing as well as maximum temperature. Structural material components as hot leg piping, vessel etc. as well as the heat consuming IHX make use of unstabilized austenitic steel.

As compared to the conditions of the primary system the unstabilized IHX material represents the heat producing area; corrosion phenomena are governed by the interaction of this unstabilized austenitic material and ferritic stabilized 2.25 Cr - 1 Mo steel as steam generator material. For both circuits thermodynamical calculations have shown that carbon transfer can be kept in tolerable limits.

Deposition of Corrosion Products

The transport and deposition of corrosion products in a sodium loop could result in two important engineering consequences:

- deposition of corrosion products on the heat exchanging surfaces which could reduce the heat transfer characteristics,
- deposition of activated corrosion products in loop sections where the accessibility may be influenced seriously because these regions are not specially shielded.

Table 5 lists data from the literature and from tests at INTERATOM on the deposition of corrosion products in the cooling areas of sodium systems which impedes heat transfer<sup>13</sup>.

Table 5: Normalized Deposition versus Loop Temperature

TEMPERATURE (°C)	DEPOSIT (µm/a)					REF.
	RANGE	MAX. DEP.	MIN.	AV.	MAX. (µm/22.8a)	
650 - 550	(565)	2.2	24.5	-	560	WARD*
650 - 480	593	-	1.4	5.5	125	GE
~ 550	-	-	-	-	~40	UK
600 - 350	530/400	-	0.2	3	68	PNC
600 - 380	500	-	-	1.1	25	IA*

\* calculated from mg/cm<sup>2</sup>h by  $\delta = 7.85 \text{ g/cm}^3$

This table gives the temperature range of the cooling section and, as far as documented, the temperature of maximum deposit. The data is illustrated in Fig. 5.

Table 6: Relative Deposition of Co 60 and Mn 54 in SNR 300 Loop Components

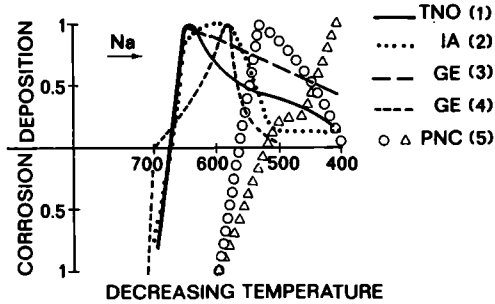


Fig.5: Normalized Depositions versus Temperature in Sodium Loops

The deposition rates arising from these different investigations differ by about a factor of 20 thus providing deposit data between 25 and 70  $\mu\text{m}$  in 22.8 years time. Ray<sup>14</sup> has reported on experimental determinations of a marked heat transfer degradation in sodium/sodium heat exchangers due to the deposition of corrosion products. These results show that in order to overcome a decrease of heat transfer performance as a result of deposition of corrosion products an allowance in heat transfer areas should be taken into account.

Long time experiments were performed at INTERATOM in order to evaluate the engineering consequences of deposition behavior of activated corrosion products<sup>15</sup>. For these tests, a mock-up loop was used, which represents the SNR 300 primary system situation as heat exchanging surfaces, heat flux, temperature gradients etc. in a scaled and optimized manner. The following results have been obtained from a longtime test of 6430 hours. The average cold-trap temperature was held at 140°C (105-164°C). The distribution of deposits of the most important isotopes Mn 54 and Co 60 is given in Table 6.

Component	Co 60	Mn 54
	(% of total deposition)	
IHX	15	75
Reactor vessel	64	17
Hot piping	19	0.5
Cold piping	0.5	6
Cleaning bypass	1.5	1.5

The most predominant part of corrosion products have been deposited in the reactor vessel (17 % Mn, 64 % Co) and the intermediate heat exchanger (75 % Mn, 15 % Co) that means in the shielded regions of the primary loop.

Influence of Sodium on Mechanical Behavior of Austenitic Stainless Steels

Sodium systems are subjected to thermal gradients which result in a cyclic loading of components. Current high temperature design rules take these sodium specific conditions into account by asking for a design against fatigue failure. The current high temperature design rules are based on material data which in general have been developed from mechanical testing in air, i.e. the design codes do not reflect environmental conditions which might have an influence on the integrity of components. To provide the reliable design and hence operation of a component, therefore, means that input data for the design have to be examined whether or not they are influenced by the working coolant of a plant. Moreover, those material characteristics which are used for safety considerations as part of the licensing procedure (crack-propagation e.g.) have to be rechecked.

Data obtained so far from strain-controlled fatigue testing in sodium lead as compared to tests in air to the following preliminary conclusions:

- reactor grade quality sodium does not diminish the fatigue life
- the AISI 304 ss and 316 ss do not show a comparable impact of sodium on the fatigue life

Combinations of creep and fatigue have not been investigated extensively. Uniaxial creep testing in sodium has revealed in some instances a reduced stress-to-rupture time, which could be correlated to a sodium influence in the tertiary regions<sup>16</sup> (Fig. 6). Results of the impact of sodium on the secondary creep rate are contradictory; creep rate increases, reductions as well as unchanged behavior have been observed. Effects of sodium on the combined creep-fatigue interaction are considered only to occur when the above-mentioned effects are confirmed.

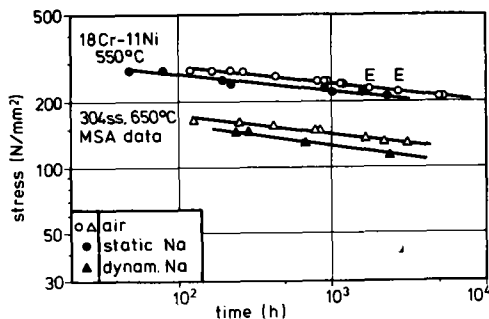


Fig.6: Rupture Strength in Sodium and Air

## STEAMGENERATORS

### Material Selection for Steam Generator Tubes

Steam generators, as the third type of heat exchangers discussed in this paper, represent the transition units from the secondary sodium system to the conventional tertiary water/steam system. As compared to the austenitic materials commonly used for cladding tubes and IHX piping the materials considered for use in steam generators include nonstabilized and stabilized ferritic alloys as 2.25 Cr-1Mo, 9 Cr - 1 Mo, 12 Cr - 1 Mo, Incoloy

800 and other austenitic steels. Table 7 shows, for comparison, the tubing materials used in steam generators of various LMFBR projects<sup>17</sup>: Among these alloys, ferritic alloys of the type 2.25 Cr - 1 Mo are predominantly employed in the evaporator units; superheaters also use austenitic-steels.

Design characteristics of the steam-generators are listed in Table 7. Sodium inlet temperatures in the superheaters are mainly between 502°C (CRBRP) and 550°C (Phenix), the lowest one, 450°C, being the Russian BN-350. The tube dimensions range between 32 and 16mm OD with wall thicknesses between 4 and 2 mm. The design time commonly is 200000 hrs to 230000 hrs, respectively. As illustrated in Table 7, the high alloy materials are exclusively applied to superheater units. Exceptions to this selection show the LMFBR projects in the USA, Russia and in the DEBENELUX where alloys of a 2.25 Cr - 1 Mo type are used. Due to the differences in the design temperatures and on the interstitial mass transfer, the SNR 300 uses a modified stabilized 2.25 Cr - 1 Mo - Ni - Nb steel which completely avoids any interstitial element loss. With concern to the French Phenix reactor the simultaneous application of the stabilized and non-stabilized 2.25 Cr - 1 Mo steel in the evaporator units expresses the different opinions with regard to the temperatures where interstitial element transfer is expected to occur. The incentive for considering alloys as alternate materials for other than those presently selected for steam generator duties is mainly based on the interest of having materials with higher strength, but nevertheless unchanged resistance to stress corrosion cracking on the water side or decarburization in sodium.

Under strong consideration for application in the superheater of the British CFR is the 9 % Cr - 1 Mo steel. A recent publication in the USA states that interest on potential alternate alloys for steam generators is concentrated on the high-strength ferritic alloys with 9 or 12 % Cr and on Incoloy 800<sup>17</sup>. The French interest on materials for the steam

INTERNATIONAL CONFERENCE ON LIQUID METAL TECHNOLOGY IN ENERGY PRODUCTION

Table 7: Steam Generator Tubing (Materials and Design Data)

	UK PFR	France PHENIX	Germany SNR-300	Russia BN-350	Japan MONJU	US CRBRP
Sodium Inlet Temp. (°C)	532	550	520	450	515	502
Superheat Steam Temp. (°C)	513	513	500	435	485	482
Superheat Steam Pressure (MPa)	15.9	16.6	16.6	5.07	13.4	10.0
Evaporator Mat. [Dimension (mm)]	2.25 Cr 1 Mo-Nb	2.25 Cr 1 Mo <sup>a</sup> (28 x 4)	2.25 Cr 1 Mo-Nb (17,2 x 2)	2.25 Cr 1 Mo	2.25 Cr 1 Mo (15,9 x 2,3)	2.25 Cr 1 Mo (15,9 x 2,8)
Superheater Mat. [Dimension (mm)]	316 ss	321 ss (31,8x3,6)	2.25 Cr 1 Mo-Nb (17,2x2,9)	2.25 Cr 1 Mo	ss <sup>b</sup> (15,9 x 2,9)	2.25 Cr 1 Mo (15,9 x 2,8)
Reheater Mat.	316 ss	321 ss			ss <sup>b</sup>	

<sup>a</sup>12 of 36 modules 2.25 Cr - 1 Mo-Nb    <sup>b</sup>Type 304, 316, or 321 ss    <sup>c</sup>straight tube type

generators of the Superphenix is focussed in the moment on Incoloy 800, with some indications that this kind of material could also be expected to be applied to the steam generators of the post-Superphenix plant<sup>18</sup>.

This part of the paper will give a review on some aspects of corrosion and mechanical properties of ferritic alloys on a 2.25 Cr - 1 Mo base and with 12 % Cr, respectively, in the sodium heated steam generators. Interstitial element loss of alloys on a 2.25 Cr - 1Mo base will not be treated within the scope of this paper since within the SNR-project this type of steel has been modified by addition of columbium to overcome interstitial element transfer difficulties.

Corrosion in Steam Generators

Referring to the environmental conditions steam generator tubes are subjected to two categories of corrosion; metal/sodium reactions and metal/water-steam interactions.

Sodium Corrosion

The sodium/metal interactions result in a general corrosion, parameters of which are temperature, sodium velocity, oxygen content

of the sodium, etc. A compilation of corrosion rates for ferritic steels on a 2.25 Cr - 1 Mo base, compared to rates of austenitic stainless steels is provided in Figure 7. From this evaluation results a corrosion rate of 110 μm (2σ-limit; 97 % confidence limit) for the design conditions (200000 hrs at 528°C).

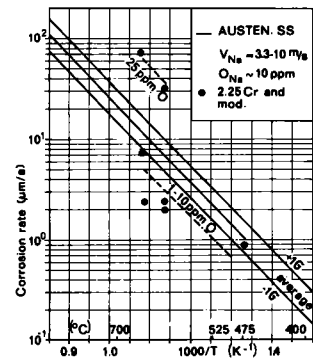


Fig. 7: Corrosion Rate of Ferritic and Austenitic Steels in Sodium

With regard to the location of the steam generator in the secondary sodium system and the negative temperature gradient in this component this value is rather conservative.

Beside the metal loss by sodium corrosion, a deposition of corrosion products occurs at lower temperatures due to supersaturation pro-

cesses. For temperature conditions which are relevant for a secondary sodium system the corrosion deposit thickness on the tube surface has been linearly extrapolated to values between 25 and 70  $\mu\text{m}$  for 200000 hrs<sup>13</sup>. Additional corrosion allowances which take into account selectively formed diffusion layers on the tube surfaces need not to be regarded since the ferritic materials tend to be alloyed by the mass transfer of chromium and nickel from the austenitic alloys used in the IHX.

### Water and Steam Corrosion

Corrosion allowances for the evaporator of the steam generator do not need very extensive discussion. The water side corrosion allowance for the 2.25 Cr - 1 Mo type of steel at a temperature of 357°C is about 25 - 35  $\mu\text{m}$  for 200000 hrs service time<sup>19</sup>. Necessary presumptions for this value are that the corrosion occurs uniformly under proper water chemistry conditions and that during standby periods the magnetite layer is shielded against pitting corrosion. A pressure drop due to formation of rippled magnetite layer has been observed when water velocities exceed a limiting range of 1.6 to 2.9 m/sec. The water velocities in the steam generators for SNR 300 are at the lower edge of this range and are therefore believed not likely to cause trouble. Even, if under heat transfer conditions the corrosion would increase by a factor of 2 the resulting corrosion allowance of 70  $\mu\text{m}$  would not give any trouble<sup>20</sup>.

An evaluation of corrosion data for the 2.25 Cr - 1 Mo ferritic alloy in superheated steam is given in Figure 8<sup>13</sup>.

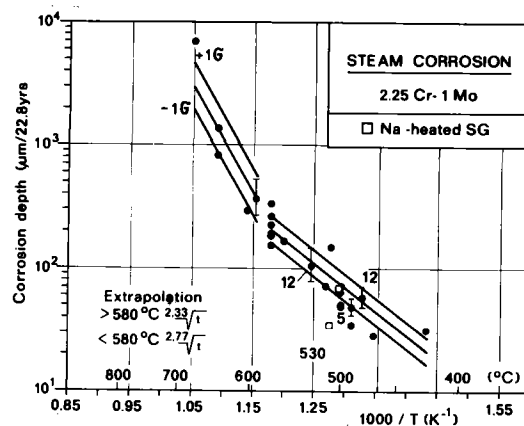


Fig.8: Results of Regression Analysis for Uniform Corrosion

The regression analysis of the data below 580°C showed that the exponent in the parabolic law describing the magnetite formation is about 2.8. The metal loss ( $d$ ) for 200000 hrs given by the equation

$$\ln d = 9.152 - \frac{9,113}{T} \pm 0.26 (\pm 16\%)$$

for  $T < 853$  K, reaches a mean value of 110  $\mu\text{m}$ . Results from post-operational examinations of sodium heated steam generators as indicated in Figure 8 do agree with the data of fossil heated components<sup>21,22</sup>. Also, the hydrogen production rate in a large scale steam generator test confirmed that the magnetite layer did not spall off even under fast cyclic power changes<sup>23</sup>. Under these conditions the hydrogen production rate a few minutes after power variations reached a value of  $\sim 3$  mg  $\text{H}_2/\text{h}$  equivalent to  $\sim 100$   $\mu\text{g}$   $\text{H}_2/\text{m}^2$  h; this corresponds to an average metal loss of 2.3  $\mu\text{m}/\text{a}$  of the steam generator tube..

### Corrosion During Sodium-Water Reactions

The corrosion behavior of the steam generator materials in the case of a sodium-water / steam reaction has been studied systematically by K.Dumm<sup>24</sup>. The extrapolation of these data is given in paper<sup>25</sup>. The operation of the KNK-Reactor has shown that it is possible to continue the operation of a repaired steam generator which had a sodium water reaction<sup>26</sup>. Referring to the work of D.A.Greene

the development of a secondary leak during the sodium water reaction depends more on the type and diameter of the primary leak than on the wastage rate of the ferritic steam generator material<sup>27</sup>.

Mechanical Properties of Ferritic Alloys for Steam Generator Purposes

The environmental effects that the steam generator tubes are subjected to result not only in corrosion phenomena such as abrasive corrosion or depositing of corrosion products, but also could affect the mechanical properties of steam generator materials. The environmental impact could consist of two main phenomena; i.e. changes of mechanical properties due to interstitial element transfer, or changes due to the physical presence of sodium as a medium with low oxygen partial pressure. Interstitial element changes are not considered here, because the 2.25 Cr - 1 Mo steel of the SNR 300 project has been stabilized by addition of columbium, and ferritic alloys like those with 9 or 12 % Cr do not suffer interstitial element loss because of their high chromium contents.

The influence of sodium on the time dependant stress behavior of 2.25 Cr - 1 Mo stabilized and of 12 % Cr - 1 Mo steel has been investigated under uniaxial conditions. With concern to the 12 % Cr-alloy, specimens were uniaxially creep tested in static sodium at 560°C up to about 9000 hrs; parallel tests were conducted in air<sup>16</sup>. The experimental results show that sodium did not influence the

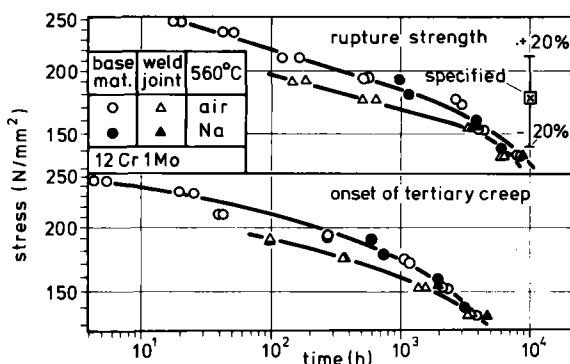


Fig.9: Rupture Strength and Onset of Tertiary Creep

creep and stress rupture of both base material and welded joints (Figure 9). A more detailed evaluation of the creep curves obtained from continuous measurements did not reveal significant changes in ductility nor in secondary creep rate (Figure 10).

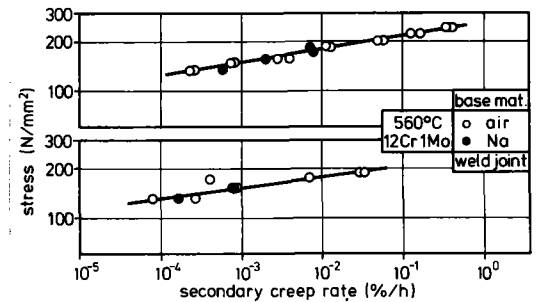


Fig.10: Stress Versus Secondary Creep Rate

The onset of the tertiary creep regime remains unaffected. Post-sodium exposure examinations of the creep specimens after 3900 hrs and 6000 hrs test time did indicate only a small carbon pick-up at the surfaces which did not exceed a penetration depth of about 40 μm. Scanning electron microscopy of the fracture surfaces of specimens creep tested in air and sodium showed no differences which could be attributed to the environment.

Stress-to-rupture data in sodium, obtained so far from uniaxial tests of 2.25 Cr - 1 Mo modified alloy, showed a behavior which corresponds to that of the 12 % Cr-alloy.

ACKNOWLEDGEMENT

The authors wish to acknowledge the efforts of all those people who in their various spheres have contributed to this paper.

REFERENCES

- 1 BNES-Conference, Liquid Alkali Metals, Nottingham University, April 4-6, 1973
- 2 H. Borgstedt, this conference
- 3 F. Casteels, G. Menken, M. Soenen, ibid. 1, page 251
- 4 O. Götzmann, P. Hofmann, J. Nucl. Mat. 59 (1976) p. 192-198

## INTERNATIONAL CONFERENCE ON LIQUID METAL TECHNOLOGY IN ENERGY PRODUCTION

- 5 G. Menken, INTERATOM,  
private communication
- 6 O. Götzmann, P. Hofmann, F. Thümmeler,  
J. Nucl. Mat. 52 (1974) 33
- 7 W.T. Lee,  
USAEC-Report AI-AEC-19694 (1968)
- 8 D.F. Atkins et al.,  
USAEC-Report AI-AEC-12976 (1970)
- 9 G.P. Wozadlo et al.,  
USAEC-Report GEAP-10394 (1971)
- 10 H. Borgstedt, W. Dietz,  
KFK 1932 (Juli 1974)
- 11 H. Tas et al.,  
this conference
- 12 H. Schäfer et al.,  
BNES/KTG-Conference, Karlsruhe, Dez. 1974
- 13 E.D. Grosser, G. Menken,  
IAEA-SGM on Steam Generators for LMFBRs,  
Bensberg/FRG, Oct. 14-17, 1974
- 14 W.E. Ray et al.,  
Nucl. Techn., Vol. 16, Oct. 72, p. 249/62
- 15 INTERATOM, unpublished experimental  
results
- 16 E. te Heesen, E.D. Grosser,  
Int. Conf. Materials for Nuclear Steam  
Generators, Gatlinburg, Sept. 9-12, 1975,  
paper F. 3
- 17 P. Patriarca, *ibid.* <sup>16</sup>, paper F. 2
- 18 M.G. Robin, *ibid.* <sup>16</sup>, paper F. 2
- 19 H. Koehle, R. Richter,  
Energie 24, 1972, p. 4/9
- 20 C. Tyzack, A. Chitty, *ibid.* <sup>13</sup>
- 21 I.P. Page et al.,  
IPCG Conference, Miami Beach/Florida,  
Sept. 8-12, 1974
- 22 E.D. Grosser, INTERATOM,  
unpublished data
- 23 E. Büscher, *ibid.* <sup>13</sup>
- 24 K. Dumm, *ibid.* <sup>13</sup>
- 25 H. Mausbeck,  
this conference
- 26 H. Lorenz, G. Herberg,  
ENS-Conference, Paris, April 21-25, 1975,  
Session B 2 - 16
- 27 D.A. Greene, *ibid.* <sup>13</sup>

# INTERNATIONAL CONFERENCE ON LIQUID METAL TECHNOLOGY IN ENERGY PRODUCTION

## THE EFFECT OF LIQUID SODIUM THERMOCHEMICAL REACTIONS WITH STAINLESS STEELS ON MECHANICAL RESPONSE

Ganesan Subbaraman

Virginia Polytechnic Institute and State University  
Blacksburg, Virginia

Kenneth L. Reifsnider

Virginia Polytechnic Institute and State University  
Blacksburg, Virginia

### ABSTRACT

An analytical approach is presented to study the elastic response of an LMFBR fuel clad subject to strong property degradation in liquid sodium environment and internal poison pressure, at the gas plenum section of the fuel pin. The nature and analysis of the thermochemical reactions and the available experimental data are briefly reviewed. Property variations in the radial direction due to these in-service reactions are represented by a generalized, continuous function,  $f(r)$ , which is introduced into the constitutive equations of stress equilibrium. By introducing an adjustable constant  $A$  into a specific form of  $f(r)$ , various severities in the variation of the elastic parameters through the thickness of the clad are accommodated and particular analytical solutions are obtained for the displacement. Closed form solutions which are available for particular values of  $A$ , are used as validity checks in computing the more general solutions. The stress-strain responses including the deviatoric stresses used in creep analyses are presented for several cases. The merits of the analytical formulation of the problem and the need to include similar approaches in fuel performance calculations are stated.

### INTRODUCTION

The mechanical behavior of the stainless steel alloys (S.S. 316) used in LMFBR fuel clads is an important parameter that influences fuel performance calculations. Due to large in-service and burn-up requirements compared to light water reactors imposed on the LMFBR fuel pins, the complexity of the thermochemical reactions with flowing sodium, and the fast neutron flux, more detailed study of the property degradation of the clad alloys has been necessitated. Moreover, the structure and mechanical properties of stainless steels are sensitive to impurity contents such as carbon, which is a mobile element in the LMFBR thermochemical environment. Thus, while neutron economy for the efficient operation of the reactor imposes limits on the clad thickness and the amount of stainless steel in the core, severe property variations and increased poison pressures set the limits based on which the integrity of the fuel-pin and the safe operation of the reactor for prolonged period of time can be guaranteed. It is, therefore, imperative that fuel performance codes must include realistic calculations of the mechanical response of the clad based on in-service property variations. The objectives of this paper are: 1) to briefly review and examine the processes and reactions responsible for the property changes, 2) to provide a simple, two dimensional, analytical representation of the through-the-thickness variation of the parameters, 3) to perform a design-base type of elastic stress analysis that would include provisions for change of the elastic parameters and 4) to evaluate the responses due to these variations.

The variables involved in the thermochemical and metallurgical interactions that cause the property degradation of the LMFBR clad have been studied by several investigators(1-4). Such investigations include the thermodynamics and kinetics of the carburization and decarburization behavior of the clad under

controlled carbon conditions, exposure times and temperatures in sodium(5-7), and mechanical property measurements under such conditions(2,4). The carburization and decarburization effects in the radial direction have been explained in terms of diffusion mechanisms and the axial composition variations have been accounted for by the influence of axial temperature variation on the carbon distribution between sodium and steel (8). The carbon pickup in the clad appears to be orders of magnitude higher compared to the original composition (up to 1 wt %) in some cases, and even if in the ideal reactor systems such drastic changes are not likely, exposure to new surfaces and long range effects might introduce significant carbon pickup in the steel. This introduces microstructural changes in the clad influencing the mechanical and corrosion behavior.

Thermal effects on the properties have been better understood than chemical effects because thermal effects are not unique to the LMFBR system. The influence of temperature on the plastic deformation and creep behavior of stainless steel under normal conditions and in sodium systems has been studied (9,2,4), and variations introduced by impurity content changes have also been included (9). Elastic constants in stainless steels have been found to vary up to 20% between room temperature and 755° K (~900° F), which is purely a temperature effect (10). An investigation of the synergistic influence of impurity and temperature changes on the variation of the elastic constants has not been attempted (11) although strong grounds exist to believe that such variations occur, based on the above arguments.

It must also be noted that the synergistic effects must include radiation induced property variations and these need to be included in the Reactor Research Development Standards. Analytical and numerical (12-14) methods for assessing the fuel performance have, so far, considered the clad as a single region with no property variations through-the-thickness.

The objective of this effort is to introduce elastic property variations through the thickness of the clad and study the response of the material under such variations. A previous analysis (15) investigated the introduction of radial property variations limited by the thickness of the clad. Here, such a restriction is removed by modifying the function specifying the property variations. The approach is limited to elastic property variations only and these are introduced at the gas plenum section of the clad in two dimensions, for the sake of analytical simplicity.

The most general property function that should be introduced into the constitutive equations of stress equilibrium in the study of the elastic response of the clad to thermochemical interactions would include all the spatial and time coordinates and such implicit variables as impurity composition and temperature. The function directly reflects the property change at a coordinate point. Evidently, if one were to construct this function on the basis of experimental data it would be a polynomial, discretized in time and varying with respect to the



spatial coordinates. Since the greatest property changes are thought to occur through the thickness of the clad, we limit the function to vary with respect to  $r$ , the radial direction in the polar coordinate system, assuming polar symmetry in the  $\theta$  direction. In studies involving hot spots, etc., the function could be generalized to accommodate asymmetric variations of properties.

In order to permit an analytical solution to the stress equilibrium equations, and to qualitatively demonstrate the influence of strong property variations on the response of the clad, the function,  $f(r)$ , chosen here is a simple relation that would modify the elastic parameters through the thickness of the clad. The function is normalized such that the inner surface of the clad at the interior radius will always correspond to the original material. The adjustable constant,  $A$ , is introduced to vary the severity of the property degradation. The calculations are made for an extreme internal poison pressure of  $6.8794 \times 10^7$  Pa. (1000 psi) and an outside coolant pressure of  $5.1711 \times 10^6$  Pa. (75 psi), which prescribe the boundary conditions for the particular solutions.

FORMULATION OF THE EQUATIONS

The general equations of stress equilibrium in two dimensional polar coordinates for the stresses  $\sigma_{ij}$  are written as

$$\frac{\partial \sigma_{rr}}{\partial r} + \frac{1}{r} \frac{\partial \sigma_{r\theta}}{\partial \theta} + \frac{\sigma_{rr} - \sigma_{\theta\theta}}{r} = 0 \tag{1}$$

$$\frac{1}{r} \frac{\partial \sigma_{\theta\theta}}{\partial \theta} + \frac{\partial \sigma_{r\theta}}{\partial r} + 2 \frac{\sigma_{r\theta}}{r} = 0 \tag{2}$$

$$\frac{\partial \sigma_{zz}}{\partial z} = 0 \tag{3}$$

for the case of plane strain (16). The  $\sigma_{ij}$ 's are stresses specified in coordinates  $r$  and  $\theta$  and are related to the strains,  $e_{ij}$  by the tensor relation

$$\sigma_{ij} = \lambda \delta_{ij} e_{kk} + 2\mu e_{ij} \tag{4}$$

where  $\delta_{ij}$  is the Kronecker delta,  $e_{kk}$  in the first strain invariant and  $\lambda, \mu$  are the Lamé constants. Further, in plane polar coordinates, the strains are expressed in terms of the displacements,  $u$ , as follows

$$e_{rr} = \frac{\partial u_r}{\partial r} \tag{5}$$

$$e_{\theta\theta} = \frac{1}{r} \frac{\partial u_\theta}{\partial r} + \frac{u_r}{r} \tag{6}$$

$$e_{r\theta} = \frac{1}{2r} \left( \frac{\partial u_r}{\partial \theta} - u_\theta + r \frac{\partial u_\theta}{\partial r} \right) \tag{7}$$

We make the following assumptions:  $u_\theta = 0, \frac{\partial u_r}{\partial \theta} = 0$  so that  $e_{r\theta}, \sigma_{r\theta} = 0$ . These allow us to rewrite eqs. (5) and (6) as

$$e_{rr} = \frac{du}{dr} \tag{8}$$

$$e_{\theta\theta} = \frac{u}{r} \tag{9}$$

with  $u = u_r$ . Substituting eqs. (8) and (9) into eq. (4), we obtain,

$$\sigma_{rr} = \lambda \left[ \frac{du}{dr} + \frac{u}{r} \right] + 2\mu \frac{du}{dr} \tag{10}$$

$$\sigma_{\theta\theta} = \lambda \left[ \frac{du}{dr} + \frac{u}{r} \right] + 2\mu \frac{u}{r} \tag{11}$$

$$\sigma_{zz} = \lambda \left[ \frac{du}{dr} + \frac{u}{r} \right] \tag{12}$$

At this point we introduce variations in  $\lambda$  and  $\mu$  (and therefore in  $E$ , the elastic modulus) in the radial direction, as stated in the previous section.

$$\lambda = \lambda_0 f(r) \tag{13}$$

$$\mu = \mu_0 f(r) \tag{14}$$

$$E = E_0 f(r) \tag{15}$$

where  $\lambda_0, \mu_0$  and  $E_0$  are the constants applicable to the original, undegraded material, and  $f(r)$  is a normalized continuous function of  $r$ . Invoking the same assumptions of plane-strain and cylindrical symmetry used in obtaining eqs. (8) and (9), and substituting eqs. (13) and (14) in eqs. (10) and (11) and back into eq. (1), we obtain the following equation for  $u$  (15).

$$\frac{d^2 u}{dr^2} + \frac{1}{r} \frac{du}{dr} - \frac{u}{r^2} + \frac{f'(r)}{f(r)} \left[ \frac{du}{dr} + \frac{\xi u}{r} \right] = 0 \tag{16}$$

where  $f'(r) = \frac{df(r)}{dr}$  and  $\xi = \frac{\lambda_0}{\lambda_0 + 2\mu_0} = \text{constant}$

Eq. (16) can be solved for any variations in  $\lambda$  and  $\mu$  as long as the derivative of  $f(r)$  exists.

In order to find useful solutions, specific forms of  $f(r)$  need to be introduced into eq. (16). The following expression is chosen so as to allow strong variations in  $E$ .

$$f(r) = \frac{(a-A)}{(r-A)} \tag{17}$$

where  $r$  is the radius of the clad at which property variations are considered,  $a$  is the internal radius of the clad and  $A$  is an adjustable constant with the dimensions of  $r$ . A plot of  $f(r)$  with respect to  $r$  for several values of  $A$  is shown in Fig. 1.

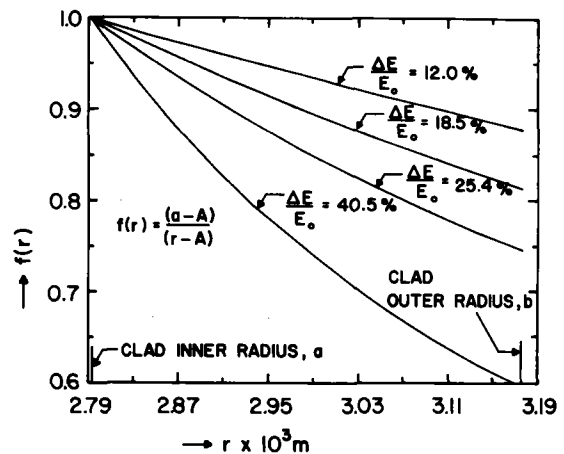


Fig. 1 Plot of function  $f(r)$ , eq. (17), illustrating varying severities in elastic modulus.

Introducing eq. (17) into eq. (16) we obtain,

$$\frac{d^2u}{dr^2} + \frac{1}{r} \frac{du}{dr} - \frac{u}{r^2} + \frac{1}{(A-r)} \left[ \frac{du}{dr} + \frac{\epsilon u}{r} \right] = 0, \quad a \leq r \leq b \quad (18)$$

where b corresponds to the external radius of the clad. For convenience of obtaining the solution, we non-dimensionalize the variables by setting  $y = \frac{u}{a}$ ,  $x = \frac{r}{a}$  and  $A_0 = \frac{A}{a}$  and rewrite eq. (18) as

$$x^2(A_0 - x) \frac{d^2y}{dx^2} + A_0 x \frac{dy}{dx} + (xk - A_0)y = 0, \quad 1 \leq x \leq R_b \quad (19)$$

where  $k = 1 + \frac{\lambda_0}{\lambda_0 + 2\mu_0}$  and  $R_b = b/a$ .

General Solutions: Power series solutions to eq. (19) around some ordinary point,  $R$ , can be obtained as shown below. By judiciously choosing  $A_0 \neq x$  the singularity of the equation at  $x = A_0$  is avoided.

The singularity at  $x = 0$  occurs at a point that is not of physical interest. However, both the singularities are regular in nature and a general solution around the singularities can be obtained (17) which will be convergent within a radius of  $|x - A_0|$ . It is observed here that as values of  $A$  are changed in order to introduce greater severities in property variations, the singularity at  $A_0$  moves towards  $R$ , the ordinary point around which we offer the solution; however, the solutions converge to desired accuracies without any difficulty in the current calculations.

We choose to obtain the complete solution to eq. (19) by expanding around  $R$ , written as

$$y = \sum_{m=0}^{\infty} C_m Z^m \quad (20)$$

where  $Z = (x-R)$  is the transformed independent variable and  $C_m$  are the coefficients of the power series. Eq. (19), when written in terms of  $Z$  and evaluated through Eq. (20) reduces to

$$\sum_{m=2}^{\infty} \{ (C_m m(m-1)) [-Z^{(m+1)} + (A_0 - 3R)Z^m + (2RA_0 - 3R^2)Z^{(m-1)} + (A_0 R^2 - R^3)Z^{(m-2)}] \} + \sum_{m=1}^{\infty} C_m [A_0 Z^m + RA_0 Z^{(m-1)}] + \sum_{m=0}^{\infty} (C_m [kZ^{(m+1)} + (Rk - A_0)Z^m]) = 0 \quad (21)$$

Expansion and rearrangement of terms in eq. (21) results in

$$\begin{aligned} & -[2C_2 Z^3 + 3 \cdot 2C_3 Z^4 \dots + (S-1)(S-2)C_{S-1} Z^S + \dots] + \\ & (A_0 - 3R)[2C_2 Z^2 + 3 \cdot 2C_3 Z^3 + 4 \cdot 3 C_4 Z^4 \dots + S(S-1)C_S Z^S + \dots] + \\ & (2RA_0 - 3R^2)[2C_2 Z + 3 \cdot 2 C_3 Z^2 + 4 \cdot 3 C_4 Z^3 + 5 \cdot 4C_5 Z^4 \dots + (s+1) \\ & (C_{s+1} Z^S + \dots) + \\ & A_0 [C_1 Z + 2C_2 Z^2 + 3C_3 Z^3 + 4C_4 Z^4 \dots + SC_S Z^S + \dots] + \\ & RA_0 [C_1 + 2C_2 Z + 3C_3 Z^2 + 4C_4 Z^3 + 5C_5 Z^4 \dots + (s+1)C_{s+1} Z^S + \dots] + \end{aligned}$$

$$\begin{aligned} & k[C_0 Z + C_1 Z^2 + C_2 Z^3 + C_3 Z^4 \dots + C_{s-1} Z^S + \dots] + \\ & (Rk - A_0)[C_0 + C_1 Z + C_2 Z^2 + C_3 Z^3 + C_4 Z^4 \dots + C_S Z^S + \dots] = 0 \quad (22) \end{aligned}$$

By equating coefficients of the terms with powers  $s = 0$ , and  $s$ , the following two relations are obtained from eq. (22).

$$(A_0 R^2 - R^3)2C_2 + RA_0 C_1 + (Rk - A_0)C_0 = 0 \quad (23)$$

and

$$\begin{aligned} & (A_0 R^2 - R^3)(s+2)(s+1)C_{s+2} + [s(s+1)(2RA_0 - 3R^2) + (s+1) \\ & RA_0]C_{s+1} + [s(s-1)(A_0 - 3R) + SA_0 + (Rk - A_0)]C_s + \\ & [k - (s-1)(s-2)]C_{s-1} = 0 \quad (24) \end{aligned}$$

Eq. (24) constitutes the principal recursion relation for obtaining the complete series solution, eq. (20). Two separate series  $y_1$  and  $y_2$  with two arbitrary constants  $\hat{C}_1$  and  $\hat{C}_2$  are obtained by setting (a)  $C_0 = 0$  and  $C_1 = 1$  in Eq. (23), obtaining  $C_2$  from the same equations and obtaining  $C_s$ ,  $S > 3$  from eq. (24) and (b)  $C_0 = 1$ ,  $C_1 = 0$  in eq. (23) proceeding as in (a). Thus the general solution to eq. (19) is

$$y = \hat{C}_1 y_1 + \hat{C}_2 y_2 \quad (25)$$

Analytical Procedure and Particular Solutions: The two series  $y_1$  and  $y_2$  are obtained by setting up the four-point recursion relation, eq. (24), and the initial relation, eq. (23) on a digital computer, for desired values of  $x$  and  $A_0$ . The convergence is set

on the term  $C_s Z^S$  and  $SC_S Z^{S-1}$  (the derivative of the last term in eq. (20)), whichever is larger. Subsequently, the convergence is checked by substituting the solution back into the differential equation (eq. (18) or eq. (19)) and obtaining the residues.

In order to obtain the constants  $\hat{C}_1$  and  $\hat{C}_2$  of the complete solution, eq. (25) we proceed by evaluating the two boundary conditions

$$\sigma_{rr} \Big|_a = \left\{ \lambda \left[ \frac{du}{dr} + \frac{u}{r} \right] + 2\mu \frac{du}{dr} \right\}_a = -p_1 \quad (26)$$

$$\sigma_{rr} \Big|_b = \left\{ \lambda \left[ \frac{du}{dr} + \frac{u}{r} \right] + 2\mu \frac{du}{dr} \right\}_b = -p_2 \quad (27)$$

where  $p_1$  and  $p_2$  correspond to the internal poison pressure at the inner radius, and the coolant pressure incident on the outer radius of the clad.

Once the series  $y_1$  and  $y_2$  are obtained, these values and their derivatives are re-dimensionalized to  $u$  and  $du/dr$  so that eqs. (26) and (27) can be evaluated providing two simultaneous equations in  $\hat{C}_1$  and  $\hat{C}_2$  which can be readily solved for  $\hat{C}_1$  and  $\hat{C}_2$ . One then proceeds to evaluate the stresses and strains with known numerical values of  $u$  and  $du/dr$  using eqs. (8) - (12).

Closed-form Solutions: Validity checks on solutions

eq. (25), are performed by utilizing the fact that closed-form solutions are available for eq. (18) for specific values of A. Such closed form solutions have been presented for A = 0 and |A| >> r (15). If we set A = 0, eq. (18) becomes

$$\frac{d^2 u}{dr^2} - (1+\xi) \frac{u}{r^2} = 0 \quad (28)$$

for which the following general solution is obtained by the method of Cauchy,

$$u = C_1 r^{m_1} + C_2 r^{m_2} \quad (29)$$

where  $m_{1,2} = \frac{1 \pm \sqrt{1+4(1+\xi)}}{2}$ , and  $C_1$  and  $C_2$  are

arbitrary constants different from those in eq. (20). When |A| >> r, f(r) can be treated as a constant and eq. (16) becomes

$$\frac{d^2 u}{dr^2} + \frac{1}{r} \frac{du}{dr} - \frac{u}{r^2} = 0 \quad (30)$$

for which the solution is

$$u = c_1 r + \frac{c_2}{r} \quad (31)$$

where  $C_1$  and  $C_2$  are the new arbitrary constants.

The validity check is performed by letting A = 0 and |A| >> r in solving for the coefficients in eq. (20) on the computer and comparing the results with those obtained by using eqs (29) and (31) for the same cases. It has been found that there is excellent agreement between the two solutions, thus establishing a necessary condition for the accuracy of the more general cases.

The ordinary point, R, chosen to obtain the expansion, eq. (20), does not influence the accuracy of the solutions, although more terms are required to obtain convergence of solutions, the farther one sets R away from the physical region of interest. In the calculations that are shown, the mid point, (a+b)/2.0 was chosen for expansion of the series. Also, as values of  $A_0$  were increased toward 1.0, (the internal boundary, ref. eq. (19)), more terms were required to meet the convergence criteria. All calculations were carried out in double precision and no more than 17 terms were required to attain the desired accuracy.

DISCUSSION OF RESULTS

Typical LMFBR (1000 MW(e)) clad parameters, property values (12) and pressures (12,18) were used in evaluating the responses using the solutions, eqs. (25), (29), and (31). The internal radius of the clad, a, was chosen to be  $2.794 \times 10^{-3}m$  (0.1100 in.), with a thickness of  $3.81 \times 10^{-4}m$  (15 mils). By choosing the values of  $A_0$ , (eq. (19)) to be 0.0, 0.6, and 0.8, percentage variations of 12.0, 25.42 and 40.54, respectively, in the elastic modulus were obtained. Intermediate and higher values of  $A_0$  will result in corresponding degrees of variation in E,  $\lambda$  and  $\mu$ . No attempt is made here to justify variations in E up to 40 percent or more in the LMFBR system. It is merely stated that the model is not limited to small variations. Hence the conclusions drawn are based on such projected variations in E,

acknowledging the fact that data do not exist to confirm or deny these variations.

Figures 2-5 show the variations of the principal stresses,  $\sigma_{rr}$ ,  $\sigma_{\theta\theta}$  and the corresponding strains  $e_{rr}$  and  $e_{\theta\theta}$  within the clad for the variations in E stated above. The 'original material' variations shown in the plots correspond to solutions obtained through eq. (31) or eq. (25) with |A| >> r. (A =  $3.0 \times 10^6$  was chosen; this satisfies the condition that  $f'(r)/f(r) \leq 0.01 u_{min}$  causing the last term in eq. (16) to become insignificant). The 'bimaterial' variations relate to the case where the clad is considered to be made of two materials, without any through-the-thickness property variations or geometric discontinuities; the interior half consists of the original material, while the exterior half consists of the alloy degraded in bulk by setting  $f(r) = a/r, r=b$ . (The solutions were obtained through eq. (31), with appropriate boundary conditions.) More discussion of these solutions has been presented earlier (15).

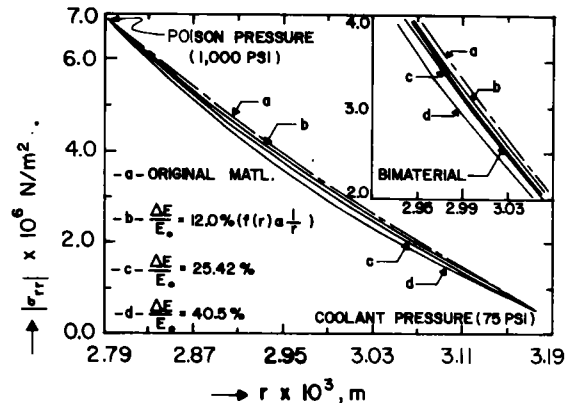


Fig. 2 Through-the-thickness variations of the radial stresses,  $\sigma_{rr}$ . (Insert shows variations in the case of bimaterial.)

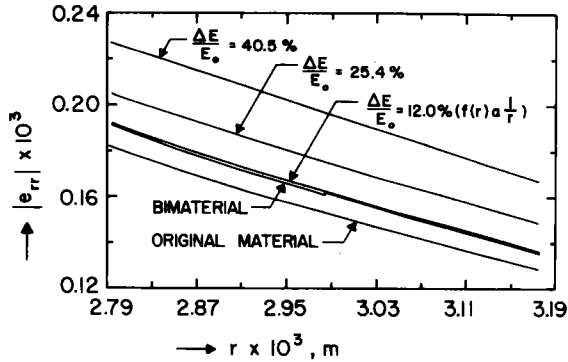


Fig. 3 Through-the-thickness variations of the radial strain,  $e_{rr}$ .

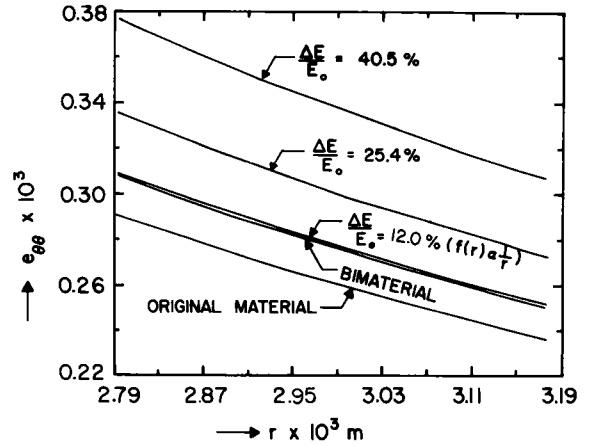


Fig. 5 Through-the-thickness variations of the tangential strains,  $e_{\theta\theta}$ .

Comparison of the stresses and the corresponding strains for the same degradation on these plots shows that the degraded materials undergo larger strains at any given point in the clad. Note that the range of radial stresses remains the same, as stipulated by the boundary conditions, eqs. (26) and (27); a similar restriction applies to the radial strains also. However, the tangential stresses  $\sigma_{\theta\theta}$ , vary by as much as 50% between the inner and outer radius for the 40.52 percent degraded alloy as opposed to 6.4 percent for the original material.

Sensitivity of the  $\sigma_{\theta\theta}$  response is also exemplified in the case of the bimaterial where there is a sharp change of  $\sigma_{\theta\theta}$  values at the interface of the two materials. This is a result of the introduction of an abrupt bulk change of 12% in stiffness at the interface. If the clad were to be considered in terms of two materials (of course, without any geometric discontinuities) one half as a carburized case and the other as the original material, and if the elastic modulus of the two materials were to be different by this amount, such sharp changes in  $\sigma_{\theta\theta}$  can be predicted to operate within the clad. Such cases of carburization and abrupt material property changes can be visualized in certain ranges of operating temperatures and impurity concentrations (4).

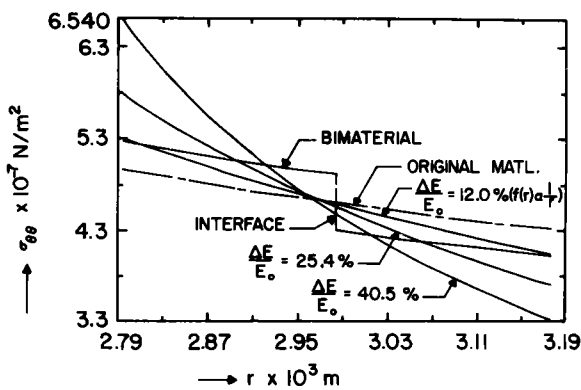


Fig. 4 Through-the-thickness variations of the tangential stresses,  $\sigma_{\theta\theta}$ .

The rather large variations in  $\sigma_{\theta\theta}$  induced by the stiffness degradation are of special importance. That stress component is the largest in the pressurized tube and controls failure. Design against failure and evaluation of possible failure conditions is based, for the most part, on the  $\sigma_{\theta\theta}$  or  $e_{\theta\theta}$  values. The variations in those quantities predicted by the present analysis for situations which are apparently at least within the realm of possibility are quite large enough to be of considerable concern to design codes in general and safety considerations in particular.

Fig. 6 illustrates effects of bulk degradation on the displacement behavior of the clad. Bulk degradation is taken to mean that the whole clad has new values of elastic modulus decreased by a given percentage (25.42% in the figure); solutions were obtained, once again, by using eq. (31). Although, conservative estimates of the response can be obtained by treating the material to be bulk degraded, realistic data show that property gradients do exist corresponding to thermal and chemical gradients (18) which justify the introduction of through-the-thickness variations as opposed to consideration of bulk changes.

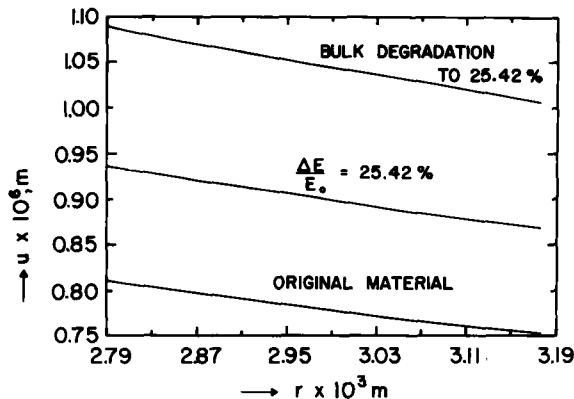


Fig. 6 Comparison of displacements in the case of bulk degraded material and material degraded through-the-thickness by same amount.

Figures (7) and (8) are plots of deviatoric stresses,  $s_{rr}$  and  $s_{zz}$  with respect to the radius. These parameters are employed in calculating creep responses by elastic analysis using simplified analytical models (12). The values of  $\sigma_{zz}$  are calculated using eq. (12) and  $S_{jj}$  is calculated using the equation

$$s_{jj} = \sigma_{jj} - \frac{1}{3} \sum_{i=r,\theta,z} \sigma_{ii}$$

For the original materials, values of  $S_{rr}$  are found to change (Fig. 7) whereas values of  $S_{zz}$  remain constant with respect to  $r$  in the plane strain analysis; however, with gradients in  $E$ , the deviatoric stresses  $S_{zz}$  become strongly dependent on  $r$ . Further influence on these values can be expected if we remove the plane strain restrictions, and also allow property variations commensurate with thermochemical effects in the axial direction (8). Creep analyses based on such property variations should include the marked influence on these deviatoric stresses.

In conclusion, through the thickness variation of elastic stiffness parameters can be accommodated through the formulations provided above. The method applies to a two dimensional case only, and an

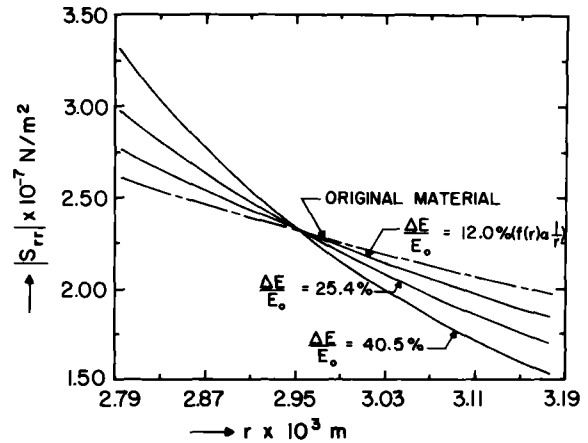


Fig. 7 Variations of the radial deviatoric stresses,  $s_{rr}$ .

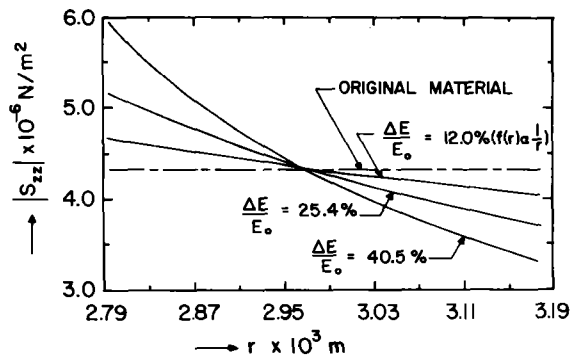


Fig. 8 Variations of the axial deviatoric stresses,  $s_{zz}$ .

a priori assumption that elastic parameters in the radial direction are influenced by thermochemical interaction in the sodium-stainless steel system has been made. The analysis is analytical in nature and variations in the moduli are not restricted by the dimensions or other mathematical constraints. The method suggests an approach to incorporate in-service property variations into performance codes. Variations in properties in studies such as those pertaining to hot spots can be admitted into the formulation by appropriate choice of the function,  $f$ , and efforts of this nature are being made. The formulation is sufficiently general to be used in other cases involving property variations introduced in

## INTERNATIONAL CONFERENCE ON LIQUID METAL TECHNOLOGY IN ENERGY PRODUCTION

fabrication such as in composites, or in service such as the LMBFR clad.

### REFERENCES

1. P. Murray, "Fast Breeder Fuel," Reactor Technology, 15-1: 16-58 (1972).
2. C. N. Spalaris and E. L. Zebroski, "Consideration of Stabilized Stainless steel alloys for LMFBR fuel cladding," Proceedings of Conference on Fast Reactor Fuel Element Technology (American Nuclear Society): 89-100 (1971)
3. K. Natesan, T. F. Kassner, and Che-Yu Li, "Effect of Sodium on Mechanical Properties and Friction-Wear Behavior of LMFBR materials," Reactor Technology, 15-4: 244-277 (1972-73).
4. L. H. Kirschler and R. C. Andrews, "Effect of High Temperature Sodium on the Mechanical Properties of Candidate Alloys for the LMFBR program," International Conference on Sodium Technology and Large Fast Reactor Design, Argonne National Laboratory, Illinois, Report 7520: 41-54 (1968).
5. K. Natesan and T. F. Kassner, "Thermodynamic and kinetic aspects of Carbon Transport in Sodium-Steel Systems," Journal of Nuclear Materials, 37-2: 223-235 (1970).
6. K. Natesan and T. F. Kassner, "Monitoring and Measurement of Carbon Activity in Sodium Systems," Nuclear Technology, 19: 46-57, (1973).
7. S. A. Shields, C. Bagnall, and S. L. Schrock, "Carbon Equilibrium Relationships for Austenitic Stainless Steels in a Sodium Environment," Nuclear Technology, 23: 273-283 (1974).
8. R. B. Snyder, K. Natesan, and T. F. Kassner, "Kinetics of the Carburization-Decarburization Process of Austenitic Stainless Steels in Sodium," Journal of Nuclear Materials, 50: 259-274 (1974).
9. J. K. Y. Hum and N. J. Grant, "Austenite Stability and Creep-Rupture Properties of 18-8 Stainless Steels," Trans. ASM 45: 105-133 (1953).
10. "Mechanical and Physical Properties of Austenitic Chromium-Nickel Stainless Steels at Ambient Temperatures," Chromium-Nickel Stainless-Steel Data, The International Nickel Company, New York, 1963, Page 30.
11. K. Natesan, Argonne National Laboratory, Private Communication, 1976.
12. D. E. Lamkin and R. L. Brehm, "Analytical Stress Analysis Solution for a Simplified Model of a Reactor Fuel Element," Nuclear Technology, 27: 273-285 (1975).
13. M. C. Billone and V. Z. Jankins, "Benchmark Testing of the Structural Analysis in the LIFE-II Fast Reactor Fuel-Element Code," Nuclear Science Abstracts, 31-1: 244 (1974).
14. M. C. Billone, J. Rest, and R. B. Peoppel, "UNCLE-A Computer Code to Predict the Performance of Advanced Fuel in Breeder Reactors," Trans. American Nuclear Society, Argonne, Illinois, 19-1-482: p. 96 (1974).
15. G. Subbaraman and K. L. Reifsnider, "Mechanical Response of a Fuel Clad with Radial Property Variations," Proceedings, 12th Annual Meeting of the Society of Engineering Science, Austin, Texas, pp. 1235-1243 (1975).
16. W. F. Hughes and E. W. Gaylord, Basic Equations of Engineering Science, McGraw-Hill, Inc., New York, 1964 (pp. 69)
17. E. L. Ince, "Ordinary Differential Equations," Dover Publications, Inc. New York, 1956, pp. 158-185.
18. J. B. Van Erp, T. C. Chawla, R. E. Wilson and H. K. Fauske, "Pin to Pin Failure Propagation in LMFBR Fuel Subassemblies," Nuclear Safety, 16-3, 291 (1975).

# INTERNATIONAL CONFERENCE ON LIQUID METAL TECHNOLOGY IN ENERGY PRODUCTION

## THE INFLUENCE OF SODIUM CORROSION ON THE MECHANICAL PROPERTIES OF FUEL ELEMENT CLADDING

H.U. Borgstedt      G. Frees

Kernforschungszentrum Karlsruhe, Institut für Material- und Festkörperforschung

Fed. Rep. of Germany

### ABSTRACT

The creep and corrosion behaviour of cladding tubes of austenitic stainless steels has been tested in a test series up to 10,000 hours. The test temperature has been 873 resp. 973K, the flow velocity 5 m/s. The purity of the sodium has been varied within the range 3.5 to 9 w-ppm oxygen.

The weight losses depend linearly on the oxygen content of the sodium, the temperature dependence follows an ARRHENIUS law. Metallurgical and analytical examinations show that more than a third of the wall thickness suffers changes of composition and micro structure at 973K. The observed phenomena are ferritic surface layers, grain boundary ferritization, carburization, increases of hardness, and finally weak carburization.

In spite of the changes due to the sodium corrosion the largest part of the specimens does not show losses of creep strength. However, cold worked specimens of 1616CrNiMoNb creep with accelerated rates. The examinations lead to the conclusions that changes in micro structure may have caused the loss of creep strength of this material.

### INTRODUCTION

The corrosion of fuel element cladding materials for LMFBR's by liquid sodium causes changes of their chemical composition and micro structure. The corrosion phenomena may influence the high-temperature creep strength of the austenitic stainless steels serving as fuel element clads. Among the compositional changes the selective leaching of interstitial elements from the steels is of high importance. The elements carbon, nitrogen and boron are of particular importance for the high-temperature strength of these materials.

The decarburization of stainless steels can be prevented by the use of stabilized materials<sup>1</sup>. However, corrosion tests of stabilized stainless steels with contents of nitrogen or boron have demonstrated that both elements can be removed selectively by liquid sodium at temperatures above 873K<sup>2,3</sup>. The loss

of one of these elements can cause the decrease of strength of the materials as has been shown in a preceding test<sup>4</sup>. The aim of our test series is to define the loss of material and the corrosion phenomena and their influence on the mechanical properties of the cladding materials.

### EXPERIMENTAL METHODS

#### Sodium circuit for corrosion tests

The new constructed test rig is similar to a loop described earlier<sup>5</sup>. It contains three parallel test sections with 973K as the maximum temperature. At this temperature a flow velocity up to 12 m/s can be reached. The test sections are constructed of the stabilized stainless steel No. 1.4981 (one of the specimen materials), the main loop consists of the steel type AISI 316.

A continuously operated cold trap and devices for purity controls are placed in two by-pass lines. The oxygen content is measured by electrochemical cells and out-of line sodium distillation analysis. Carbon is calculated from the analysis of equilibration tabs of 18-9 CrNi steel exposed at 973K for 120 - 200 hours.

The cover gas is analysed to control the contents of H<sub>2</sub>, N<sub>2</sub>, and CH<sub>4</sub>. Additionally, a mass spectrometer can detect traces of He escaping from a cracked inside pressurized specimen.

The tube specimens of 6 mm diameter are centered in four parallel channels of 10 mm diameter. Each of the channels contains five specimens in series, the three test sections have the capacity to expose 60 specimens.

#### Parameters of the test series

The Table I gives a survey on the parameters of the sodium exposure of the specimens. The three materials are exposed at two temperatures and under different tangential stresses. The Table II describes the temperature and stress field of the programme. The composition of the three materials is listed in Table III. The different batches do not show remarkable differences in their chemical compositions. The material

no. 1.4981 is tested in solution annealed and cold worked conditions, the steel no. 1.4970 has got an annealing, two hours aging at 800°C and about 5 - 10 % cold working, and the third material the same conditioning, but only one hour aging.

Table I: Parameters of the 10.000 h Corrosion and Creep Test.

Temperatures	test section I	873 ± 5K
	test section II	973 ± 5
	test section III	973 ± 5
	cold leg	593 ± 20
	cold trap	443 - 473
Flow velocity	test sections	5 ± 0.5 m/s
	R <sub>e</sub>	10 <sup>5</sup>
Oxygen Concentration		3.5 - 9 w-ppm
Carbon Concentration		<1 w-ppm
Carbon Activity		5 · 10 <sup>-3</sup>

Table II: Field of Temperatures and Stresses

Material no.	Temperature K	Range of Stresses N/mm <sup>2</sup>
1.4970	873	180 - 270
	973	70 - 120
1.4981	873	140 - 240
	973	35 - 80
1.4988	873	180 - 220
	973	35 - 70

Table III: Chemical Compositions of the Materials

Element/Material	1.4970	1.4981	1.4988
C w-%	0.11	0.054	0.067
Si w-%	0.3	0.3	0.4
Mn w-%	1.40	0.98	1.27
P w-%	0.005	0.005	0.005
S w-%	0.01	0.01	0.01
Cr w-%	15.13	16.59	16.00
Ni w-%	14.97	16.59	12.89
Mo w-%	1.14	1.73	1.28
Ti w-%	0.48	-	-
Nb w-%	-	0.85	0.78
V w-%	-	-	0.72
B w-ppm	29	3	2
N w-%	-	0.025	0.079

Evaluation of effects

The losses of material are measured by the aid of

a microbalance. Metallographic methods are applied to demonstrate the structural effects. New etching procedures are used to develop the optical differences between ferritic and austenitic parts of the steels<sup>6</sup>. Cross sections and surfaces are examined using the scanning electron microscope. We measure the selective leaching of substitutional elements and carbon by application of GDOS and other analytical methods<sup>7</sup>. The growth of diameter due to the creep of the tubes is controlled by inductive probes, which are contacting the tubes in a helical trace during interruptions of the test. Parallel control tests are performed in vacuum capsules.

EXPERIMENTAL RESULTS

Losses of material

The losses of material as determined by weighing are different in the different parts of the test series as is demonstrated by Fig. 1. The analysis of these differences shows that the weight loss rate con-

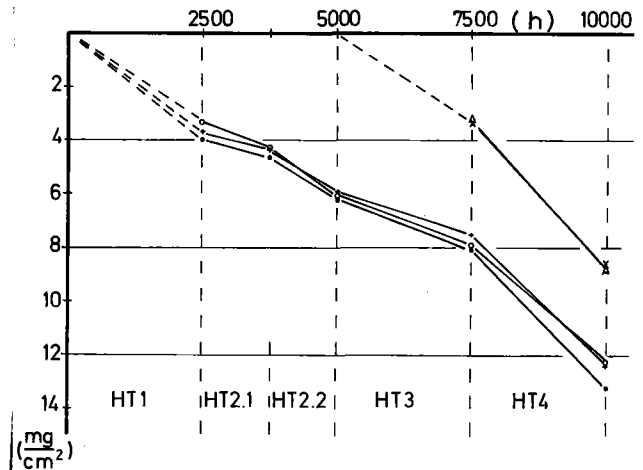


Fig. 1: Weight losses at 973K as a function of the time.

stant depends on the oxygen content of the sodium as is drawn in Fig. 2. The rate constant k is a nearly linear function of c<sub>O</sub> within the range 3.5 to 9 w-ppm oxygen in sodium, which is measured by electrochemical cells and distillation analysis.

The temperature dependence of the weight loss rate constant k corresponds to equation (1).

$$\log_{10} k = 4.438 - 3.376 \cdot 10^{-3} \frac{1}{T} \quad (1)$$

(k in mg · cm<sup>-2</sup> · h<sup>-1</sup> and T in K)

The energy of activation of the weight loss cau-



sing reaction is 15.4 kcal/mole, somewhat lower than reported in the literature<sup>8</sup>.

Effects on structure and morphology

We have seen by the application of metallographic methods that all the three materials are influenced in their micro structure in layers of 20 to 120 microns depending on the temperature of the sodium exposure. Ferritic surface layers do not exceed 2 microns after 10,000 hrs. at 873K and 8 microns after the same time at 973K. The next layer shows ferritic grain boundary

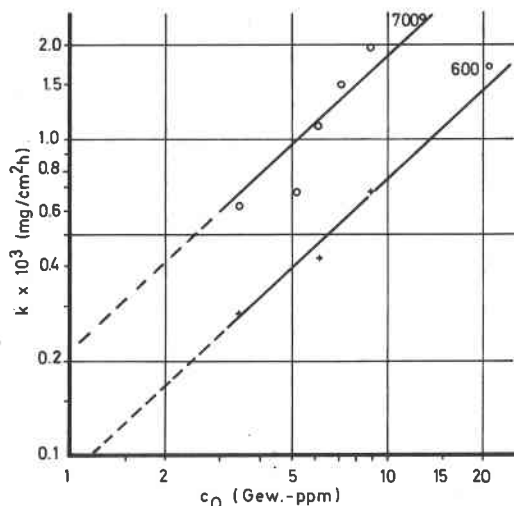


Fig. 2: Dependence of weight loss rate constant on the oxygen concentration of the sodium.

areas and austenitic grains with precipitated carbides. The maximum carbide precipitation is located at the end of the zone of grain boundary ferritization. The micro hardness reaches its maximum value in the same area. The zone of carbide precipitation is followed by the unaffected or weakly influenced center of the tube wall, in which sigma phases are precipitated in the steels with Nb as the stabilizing element.

The Fig. 3 compares the effects of corrosion, which are typical for the two temperatures of 873 and 973K. In some of the specimens exposed at 973K the surface areas contain holes of 5 to 10 microns diameter and up to 25 microns depth. Among more than 100 specimens we have not observed any formation of holes exceeding the area of grain boundary ferritization. The formation of such intergranular cavities, which are reported in the literature, does not seem to be a characteristic phenomenon of corrosion of stabilized austenitic steels<sup>1</sup>. The morphology of the surfaces is changed in a specific manner. The grain

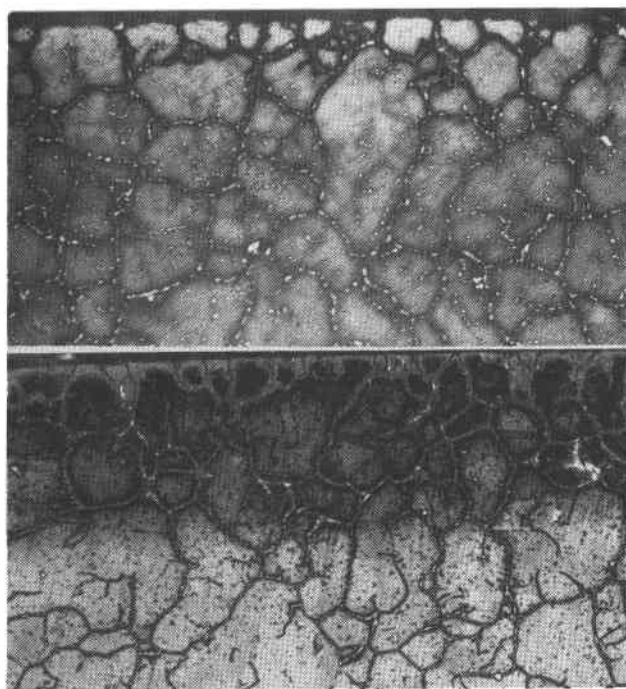


Fig. 3: Effects of sodium corrosion on the micro structure of the steel no. 1,4981 at 873K and 973K (10,000 hrs.)

boundaries are somewhat grooved and at grain corners we can see the holes crossing the surfaces. Some coral like looking particles are on the corroded surfaces, larger in size and number after exposure at 973K. The typical morphology of the corroded surface is shown in Fig. 4.

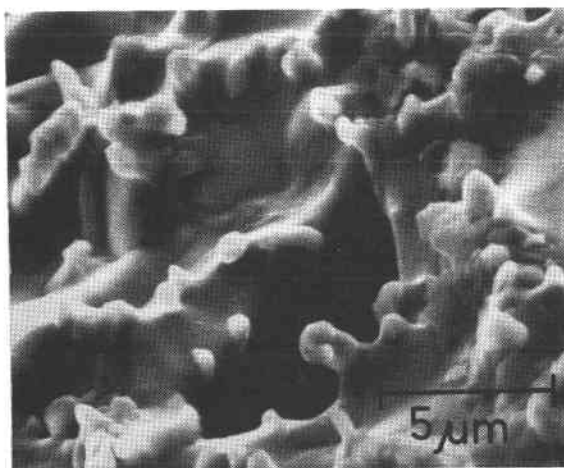


Fig. 4: Typical morphology of the surface of a steel specimen exposed at 973K for 10,000 hrs.

Effects on the steel composition

The effects of sodium on the chemical composition of the surface layers of the cladding tubes are ana-

lyzed and the results are described in detail in an other paper<sup>7</sup>. The formation of the ferritic surface layer is due to the selective leaching of Cr, Ni, and Mn, these elements are further leached out of the ferritic grain boundaries. Mo is located at the coral like looking particles. Carbon is leached out of the surface ferrite layer, its content is raising in the zone of ferritic grain boundaries reaching a maximum value beneath the ferrite containing region (see Fig. 5). The maximum value of carburization depends on the temperature. At 873K the values reach the range of 0.5 to 0.8 w-%, at 973K only of 0.2. However, at the higher temperature the raise of carbon can be measured up to the center of the cladding tubes, at 873K only up to about 50 microns. The two materials containing B or N are partially losing these interstitial components,

changes of interstitial elements.

Table IV: Results of determinations of C and B

Material	uncorroded		10,000 hrs. 973K		10,000 hrs. 873K	
	% C	ppm B	% C	ppm B	% C	ppm B
1.4970	0.09	85	0.15	10	0.21	53
1.4981	0.06	-	0.16	-	0.17	-
1.4988	0.08	-	0.09	-	0.18	-

Effects on creep rates

The creep curves of the two materials 1.4970 and 1.4988 exposed at 873K are nearly identical in the two environments sodium and vacuum. The creep rates are very small and a sodium influence cannot be observed. However, the specimens of the steel 1.4981 show an accelerated creep rate in the cold worked state even at the lower exposure temperature. The creep curves measured at 973K are also nearly the same in both environments for the steels 1.4970 and 1.4988. Fig. 6 gives an example for two pairs of specimens exposed under the same tangential stresses in sodium and in vacuo, steel no. 1.4970. However, cold worked specimens of the steel 1.4981 are creeping much faster in sodium than in vacuo as is shown by the upper part of Fig. 6 for two pairs of specimens of this material.

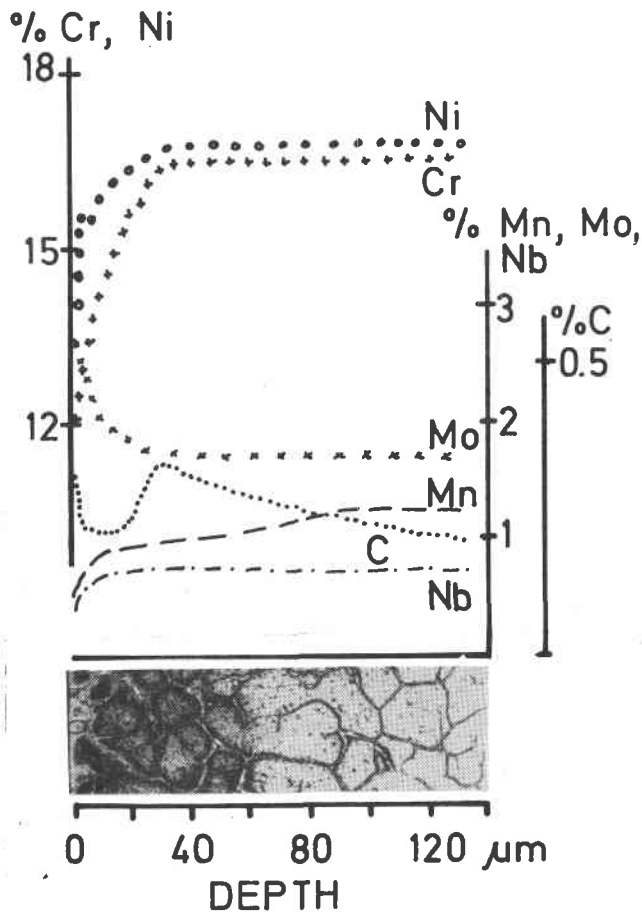


Fig. 5: Relation of structural effects on the clad material to changes in the chemical composition.

but to a lower degree than expected from results obtained earlier<sup>2,4</sup>. The Table IV gives a survey on the

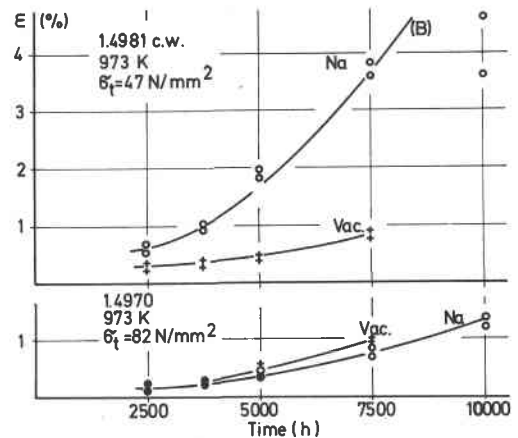


Fig. 6: Creep curves of pairs of specimens strained by the same levels of stress at 973K in Na and in vacuo.

The Fig. 7 summarizes the results of the comparison of creep deformations of specimens of the three steels in sodium and in vacuo. The tangential stresses are fitted as a function of the time up to 1 % strain of the diameter. All the results gained for the two steels no. 1.4970 and 1.4988 at 973K in the two envi-

ronments are situated within a more or less narrow band of scatter, the steel 1.4970 has one band for each of the individual batches. The same character of the results we find with the steel 1.4981 in the annealed condition. However, the same material in a 10 to 15 % cold worked condition gives a contradictory result. The time to 1 % strain is only 20 % of the 1 % strain limit measured in vacuo indicating a faster creep due to the action of the sodium.

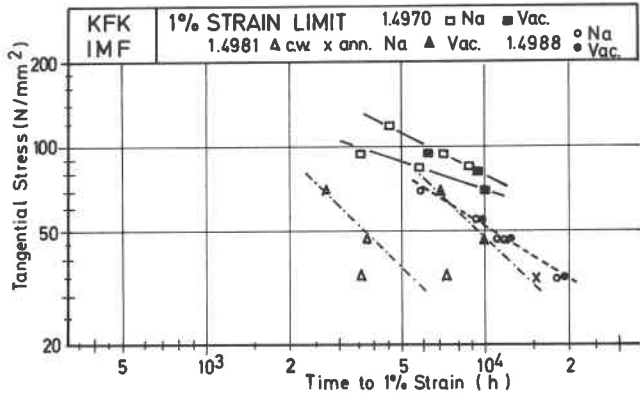


Fig. 7: 1 % Strain limit lines for the three steels at 975K, comparison of the values measured in Na and in vacuo.

Two of the specimens are stresses at very high tangential stresses at 973K. These tubes show a different rupture behaviour. They reach higher values of strain (~ 3 % in less than 2500 h), at which the matrix material gets a large number of crack germs in the dimensions of a grain diameter. The most of these cracks do not reach the surface of the tubes. The surface ferrite layers close the cracks. Only the main crack, which leads to the rupture, is crossing this layer. Fig. 9 shows a cross section of the crack germs under the ferrite layer.

DISCUSSION

The examination of the corrosion effects on the cladding tubes has shown that considerable parts of the tube walls are influenced by the corrosion reactions in micro structure and composition. The effects of corrosion and mass transfer are schematically summarized in Fig. 10.

The major changes of structure and composition are in the range of 6.6 % of the wall thickness at 873K and 24 % at 973K. If we assume that these corroded layers do not contribute to the strength of the tube walls the stress on the remaining unchanged part of them should be raised by 7 % at 873K and 30 % at

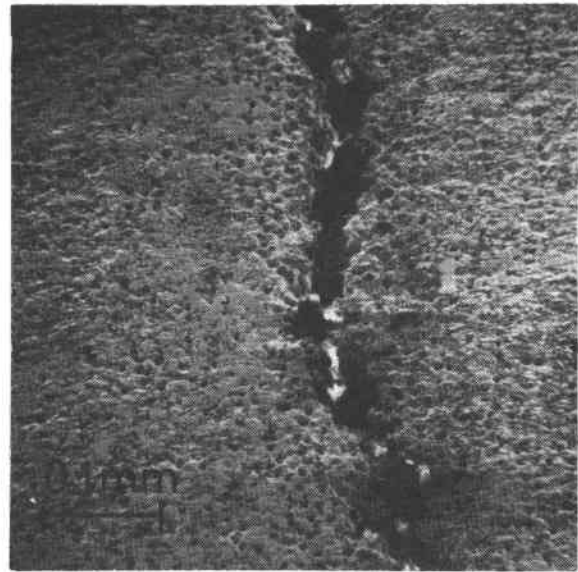


Fig. 8: SEM surface micrograph of the crack of a specimen of 1.4970 exposed at 973K.

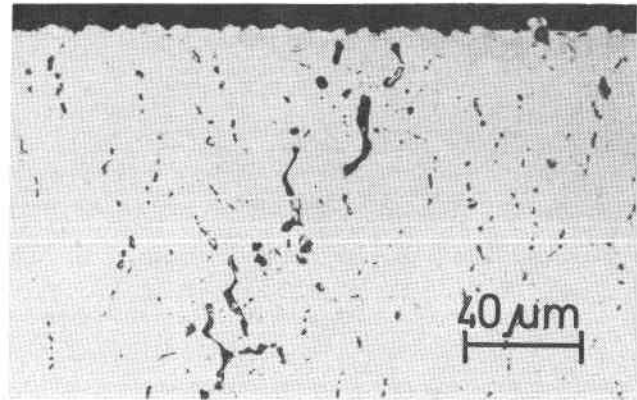


Fig. 9: Cross section of the crack area of a specimen of 1.4981 stressed with about 200 N/mm<sup>2</sup> at 973K.

973K. These increased stresses should cause increased creep rates, which should be higher than the creep rates of control tests in vacuo. This is mostly not the case. The strength of the tubes does not show differences in the two environments in spite of the fact that there are losses of thickness, formation of surface and grain boundary ferrite, pitting, and the loss of interstitial elements like B or N. However, the content of carbon is increased due to the sodium exposure. Therefore, we conclude that mainly the carburization causes an increase of the strength and compensates all the other corrosion effects including the selective leaching of interstitials in respect to their influence upon the creep behaviour.

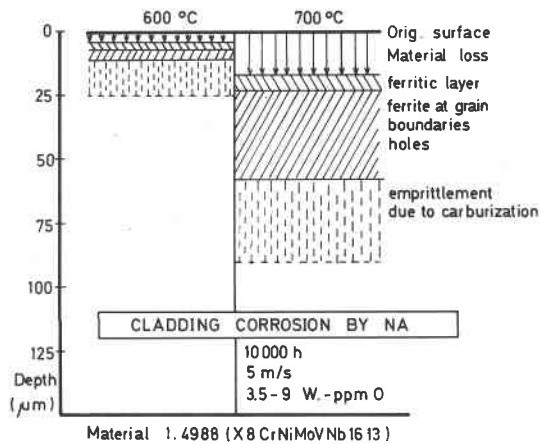


Fig. 10: Corrosion phenomena on the tube wall due to the exposure to sodium of the 10,000 hours corrosion and creep test.

However, it has been shown that carburization increases the hardness of the materials. Additionally to the strengthening of the cladding tubes we have to expect an effect of embrittlement due to the carburization. From our results we can conclude, that up to 10,000 h of sodium exposure the strengthening influences the cladding materials more than the growing brittle. The kinetics of the carburization of the stabilized steels indicate that the effects are growing very slowly after long periods of contact to sodium. Most probably the beneficial effect of the carburization of this type of steels can be predicted to last for limited times longer than 10,000 hours.

The examination of the surrounding of cracks of cladding tubes show some evidence for an acceleration of corrosion phenomena in this part of the materials. In these areas the strain rate should be much higher during the period of crack growth. The formation of large numbers of holes close to the crack in the strongly deformed materials may have a feedback to the nucleation and growth of the cracks. The sodium induced pitting may accelerate the tertiary creep, the state before the failure of the tubes.

The different behaviour of the cold worked tubes of 1.4981 may be discussed under the assumption that a strengthening due to a carburization should be necessary to prevent a higher stress on the remaining uncorroded part of the tube wall. This material does not lose B or N, the carburization has nearly the same extent as in the solution annealed condition. Therefore, one should assume that the cold working

of the steel must have influenced the carbide precipitation. The precipitated carbides do not seem to have the same strengthening effect as in the solution annealed condition.

The carbides prefer to precipitate on the sliding planes in the cold worked condition. The precipitates appear to be larger than those originated in specimens in other states of metallurgical conditioning. This is the only observation of structural differences between the materials showing different influence of sodium on the creep rate. We cannot interpret the appearance of a larger number of larger surface holes in the cold worked steel 1.4981 as another micro structural phenomenon, which may cause accelerated creep. As discussed above, the formation of such holes may be induced by the reaction of sodium with the steel creeping at faster rates than that of the other specimens.

The corrosion phenomena caused by the action of the liquid sodium may interfere with irradiation induced effects. Swelling of the cladding and embrittlement due to irradiation can be changed by the micro structural and compositional effects of sodium corrosion and mass transfer. The irradiation effects are examined with materials of the original composition<sup>9</sup>. In that state they have a micro structure, in which carbides precipitate as compounds of carbon and the stabilizing elements (Nb, Ti). Since the higher carbon contents in the diffusion layers of the corroded steels should give rise for the formation of Cr carbides of the  $M_{23}C_6$  type or even compounds with still higher C contents, it may be that there will be interference between sodium corrosion and irradiation. Additionally, the irradiation may cause higher diffusion rates of carbon and other elements in the clads. Therefore, the thickness of diffusion layers may be enlarged due to the irradiation. The question is still open. Examinations of experimental fuel elements can help to find the answers.

#### CONCLUSION

1. Up to 973K the stabilized cladding alloys do not suffer losses of carbon as does AISI 316, but a moderate carburization.
2. The selected cladding alloy 1.4970 has not shown any influence of sodium corrosion upon the creep strength at 873 and 973K up to 10,000 h.
3. The steel 1.4981 in cold worked condition creeps five times faster in sodium than in vacuo. The

## INTERNATIONAL CONFERENCE ON LIQUID METAL TECHNOLOGY IN ENERGY PRODUCTION

effects may be due to a different manner of carbide precipitation in this material.

4. The formation of surface layers up to nearly a quarter of the tube wall thickness does not lead to reduced strength. Carburization may compensate a possible effect.
5. Creep at large rates as during the tertiary phase seems to increase the surface pitting, and this may accelerate the crack formation.
6. The corrosion effects in the surface near zone may interfere with irradiation induced effects. This must be examined during the inspections of experimental fuel elements.

### ACKNOWLEDGEMENTS

We are glad to express our thanks to INTERATOM, Bensberg, for providing us with the major part of the specimens, Mr. Dietz and Mr. Weinert of the same corporation for some contributions to the experimental work. Additionally, we are indebted to Mrs. Dr. Schneider, Mrs. Kammerichs, Miss Perić, Mr. Drechsler, Mr. Schlindwein and Mr. Wittig for their contributions to the test programme.

### REFERENCES

1. D.W. Sandusky, J.S. Armijo, W.J. Wagner, J. Nucl. Mat. 46 (1973) 225.
2. N. Wieling, Proc. Intern. Meeting on Fast Reactor Fuel and Fuel Elements, Karlsruhe 1970, p. 589.
3. H.U. Borgstedt, E.D. Grosser, "Liquid Alkali Metals", BNES, London 1973, p. 275.
4. H.U. Borgstedt, W. Dietz, Reprot KFK 1932 (1974).
5. H.U. Borgstedt, G. Drechsler, G. Frees, "Alkali Metal Coolants", IAEA, Vienna 1967, p. 119.
6. E. Beraha, Prakt. Metall. 5 (1968) 443.
7. Helga Schneider, this conference.
8. A.W. Thorley, C. Tyzack, "Liquid Alkali Metals" BNES, London 1973, p. 257.
9. H. Böhm, W. Dienst, K. Kummerer, Report KFK 1999 (1974), parts VII and VIII.

# INTERNATIONAL CONFERENCE ON LIQUID METAL TECHNOLOGY IN ENERGY PRODUCTION

## EFFECT OF SODIUM ON THE CREEP-RUPTURE BEHAVIOR OF TYPE 304 STAINLESS STEEL

K. Natesan, O. K. Chopra, and T. F. Kassner

Materials Science Division  
ARGONNE NATIONAL LABORATORY  
Argonne, Illinois 60439

### ABSTRACT

Uniaxial creep-rupture data have been obtained for Type 304 stainless steel in the solution-annealed condition and after exposure to a flowing sodium environment at temperatures of 700, 650, and 600°C. The specimens were exposed to sodium for time periods between 120 and 5012 h to produce carbon penetration depths of  $\sim 0.010$ , 0.020, and 0.038 cm in the steel. The results showed that, as the depth of carbon penetration and the average carbon concentration in the steel increase, the rupture life increases and the minimum creep rate decreases. Creep correlations that relate rupture life, minimum creep rate, and time-to-tertiary creep have been developed for the steel in both the solution-annealed and sodium-exposed conditions. Isochronous stress-creep strain curves and results on the calculations of the stress levels for 1 percent creep strain and long-term rupture life are also presented.

### INTRODUCTION

The austenitic stainless steels used for the fuel cladding, in-core structural components, piping, valves, and intermediate heat exchanger in Liquid-metal Fast-breeder Reactors (LMFBRs) are subjected to a flowing sodium environment at elevated temperatures, which can result in compositional and microstructural changes as well as time dependent (creep) deformation in the materials. In the case of out-of-core components that have a design life of 20 to 30 y, the influence of the sodium environment, namely the time- and temperature-dependent migration of carbon and nitrogen, on the mechanical behavior of the materials must be considered.<sup>(1)</sup>

Nonmetallic elements such as carbon and nitrogen migrate in sodium heat-transport systems as a result of chemical activity differences. Transfer of these elements occurs in monometallic austenitic stainless steel systems with temperature gradients as well as in systems where combinations of materials of different composition are used. The ASME Boiler and Pressure Vessel Code Case 1592 for elevated-temperature nuclear-component design<sup>(2)</sup> requires consideration

of mechanical-property changes that arise from compositional variations in the materials, due to the sodium environment during the service life of a component. Extensive research is being conducted at Argonne National Laboratory to establish quantitatively the influence of the sodium environment on the tensile, creep-rupture, and low-cycle fatigue behavior of austenitic stainless steels.

Limited data are available for the creep-rupture properties of austenitic stainless steels under carburizing conditions in liquid sodium. The creep-rupture strength of Type 304 stainless steel in flowing sodium at 650°C was reported<sup>(3)</sup> to be the same as that in helium; however, the carburization in these experiments was confined to a 50- to 75- $\mu\text{m}$  surface region of the 0.15-cm-thick specimens for exposure times of  $\leq 1000$  h. If thinner specimens or longer exposure times were used, the alloys would have carburized throughout their entire cross section, and significant property changes, when compared with the tests in helium, would have been observed. Furthermore, in these experiments the carbon concentrations in the sodium were considerably higher than can reasonably be expected<sup>(4)</sup> in reactor heat-transport systems. Figure 1 shows the regions of carburization and decarburization for austenitic stainless steels with a nominal carbon concentration of 0.06 wt%. Presently, the carbon concentration in the primary sodium of the U.S. Experimental Breeder Reactor II (EBR-II) is in the range of 0.16-0.19 ppm.<sup>(5)</sup> Under such conditions, the stainless steels with an initial carbon content of 0.06 wt% would almost be in thermodynamic equilibrium with a carbon concentration in sodium of  $\sim 0.17$  ppm at  $\sim 625^\circ\text{C}$ , and would carburize at temperatures below 625°C, and would decarburize above 625°C. The extent to which the steels can undergo carburization or decarburization upon exposure to a sodium environment can be calculated from the carbon activity-concentration relationships developed as a function of temperature for these steels<sup>(6)</sup> and the carbon solubility values in sodium.<sup>(7)</sup> Figure 2 shows the equilibrium carbon concentration values for Type 304 stainless steel calculated as a function of carbon concentration in sodium at various temperatures. The predictions based upon

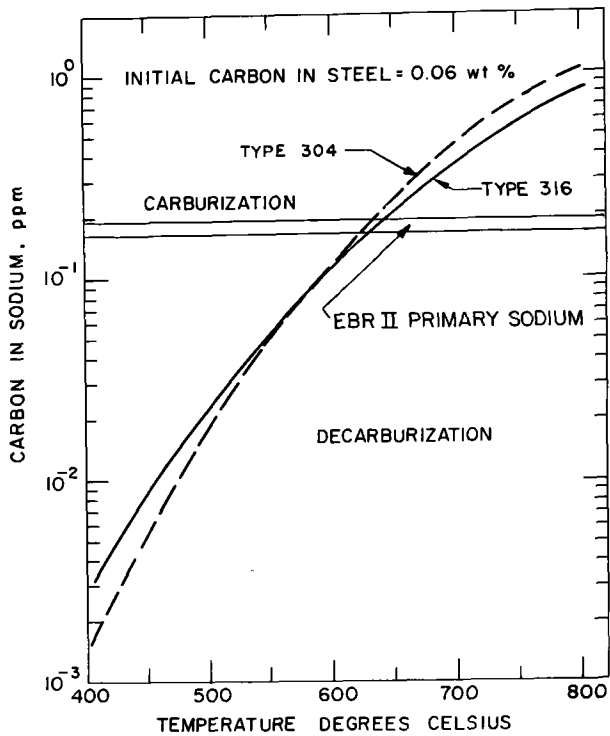


Fig. 1. Carburization-Decarburization Behavior of Austenitic Stainless Steels in a Sodium Environment.

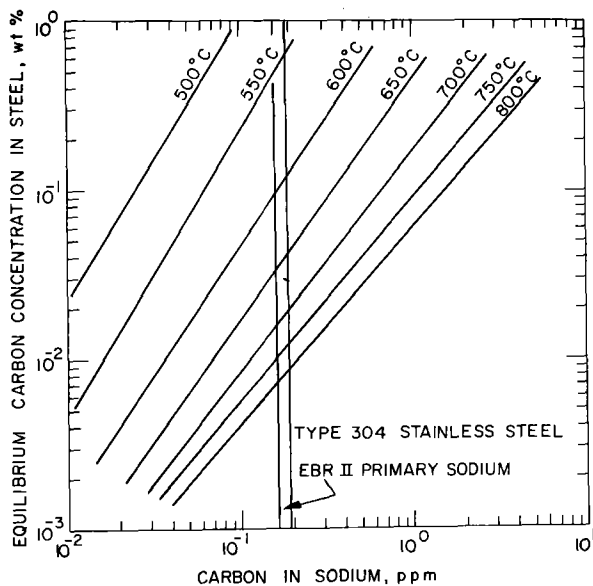


Fig. 2. Equilibrium Carbon Concentration in Type 304 Stainless Steel as a Function of Carbon in Sodium and Temperature.

these curves are that the steel in contact with primary sodium in EBR-II would carburize to  $\sim 0.60$  wt% carbon at  $550^\circ\text{C}$  and decarburize to  $\sim 0.04$  and  $\sim 0.02$  wt% at  $650$  and  $700^\circ\text{C}$ , respectively. The sodium-exposure time required for the steel to attain these equilibrium carbon concentrations depends upon the diffusion

coefficient for carbon in the steel and the thermal-mechanical history that influences the microstructure of the material. A mathematical analysis has been developed<sup>(4)</sup> to obtain carbon concentration-distance profiles as a function of time, temperature, and carbon concentration in sodium. Because of the relatively low operating temperatures and the large thickness of the materials in structural components, carbon concentration profiles rather than a uniform equilibrium carbon distribution will result in the steels during the service life of the reactor. Thus, it is essential to obtain mechanical-property data on materials with specific carbon penetration depths and to correlate the property changes with the penetration depth and surface carbon concentration in the material. In the present paper, data are presented on the effect of carburization on the creep behavior of Type 304 stainless steel for temperatures between  $600$  and  $700^\circ\text{C}$ .

EXPERIMENTAL PROCEDURE

The Type 304 stainless steel, identified as heat 9T2796, that is used extensively in breeder-reactor research programs, had the following chemical composition (in wt%): 0.046 C; 0.038 N; 17.7 Cr; 9.3 Ni; 1.17 Mn; 0.47 Si; 0.33 Mo; 0.20 Cu; 0.012 S; and 0.026 P. The steel was cold rolled to 0.0375-cm-thick flat stock, solution annealed for 30 min in argon at  $1025^\circ\text{C}$ , and water quenched. The grain size of the material was  $\sim 25$   $\mu\text{m}$ . Uniaxial creep-rupture specimens were fabricated with a gauge length of 2.22 cm and a width of 0.559 cm. The creep tests were conducted on conventional constant-load creep-rupture machines in an argon environment at temperatures of  $600$ ,  $650$ , and  $700^\circ\text{C}$  over a stress range of 55 to 243 MPa (8 to 35 ksi). The creep strain in the specimens was measured by a linear-variable-differential transducer, in which displacements of  $5 \times 10^{-4}$  cm could be accurately determined.

A schematic diagram of the sodium loop used for the exposure of creep specimens, to achieve the desired depths of carbon penetration, is shown in Fig. 3. The loop, which was constructed of nickel, consists of four specimen-exposure vessels, a carbon trap for controlling carbon concentration in sodium, purification system, diffusion-type carbon meter, hydrogen meter, and electrochemical oxygen meters. The volume of sodium in the loop was  $\sim 100$  liters, and the sodium flow rate was  $\sim 1.0$  liter/min. The specimen-exposure vessels were connected in series and operated at  $700$ ,

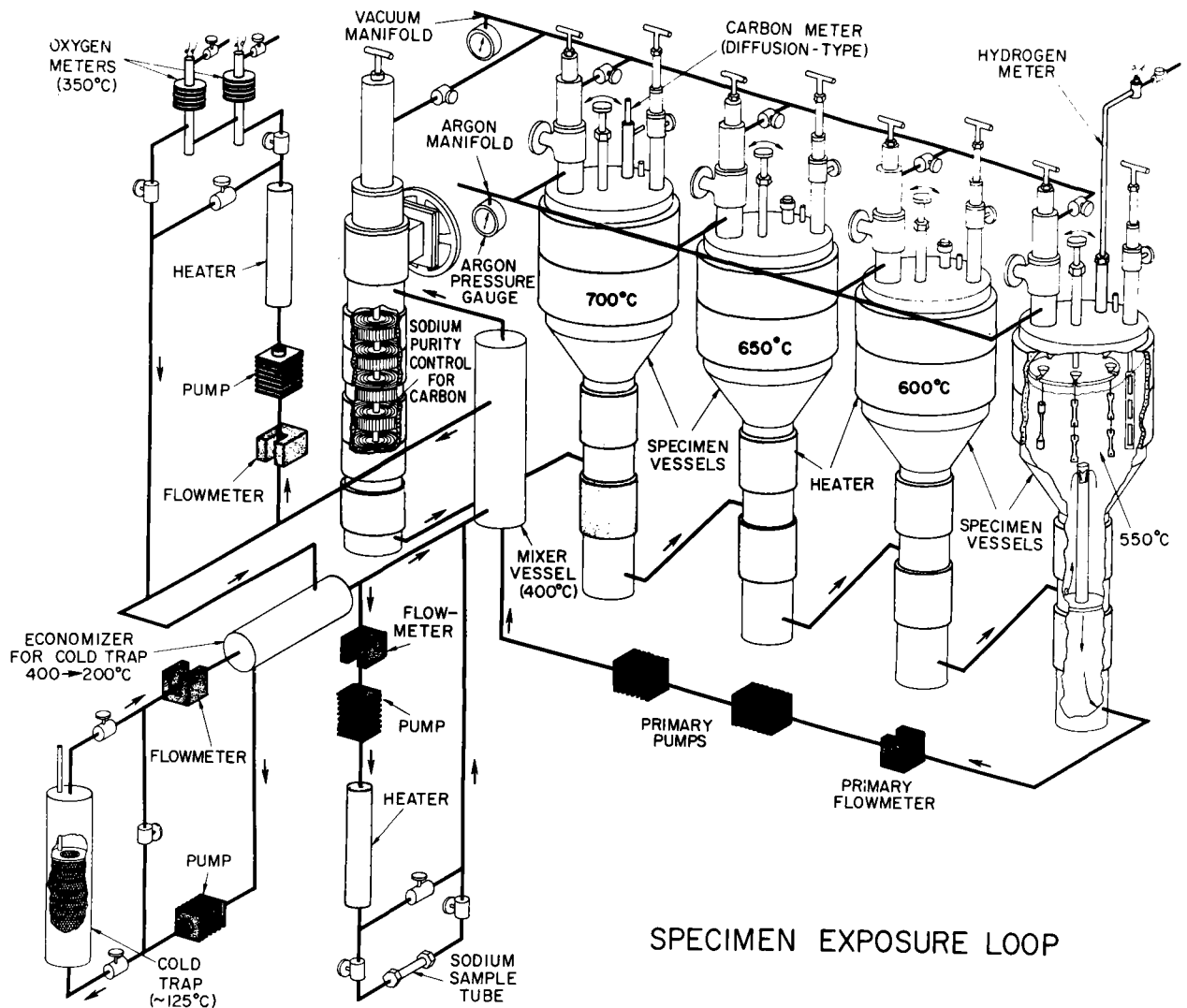


Fig. 3. Schematic of the Sodium Loop Used for Exposure of Mechanical Test Specimens.

650, 600, and 550°C. The sodium flowed successively from the highest to the lowest temperature and subsequently through the carbon trap prior to reentering the 700°C vessel. The electrochemical oxygen meters, with Cu/Cu<sub>2</sub>O and Na/Na<sub>2</sub>O reference electrodes and ThO<sub>2</sub>-15 wt% Y<sub>2</sub>O<sub>3</sub> solid electrolyte tubes, were used to monitor the oxygen concentration in sodium. The oxygen concentration in sodium was <1 ppm for all experiments. The carbon concentration in sodium was established by equilibrating a high-purity Fe-18 wt%Cr-8 wt%Ni alloy in sodium and using the reported<sup>(8)</sup> data on the distribution of carbon between this alloy and sodium. The carbon concentration in sodium was in the range 0.4-0.8 ppm for all experiments.

Creep specimens were exposed to flowing sodium at temperatures of 600, 650, and 700°C for times between 120 and 5012 h to produce carbon penetration depths of

~0.01, 0.02, and 0.0375 cm, which were calculated from the mathematical analysis in Ref 4. The specimens were subsequently used in creep-rupture tests in an argon environment to obtain the creep curves and creep-rupture times.

#### RESULTS AND DISCUSSION

A schematic of a creep curve that is obtained from a constant-load creep test is shown in Fig. 4. Strain values  $\epsilon_1$  and  $\epsilon_2$  and times  $t_1$  and  $t_2$  were determined, respectively, from the beginning and end of the secondary creep stage. At rupture, elongation  $\epsilon_r$  and rupture time  $t_r$  were determined. The minimum creep rate  $\dot{\epsilon}_m$ , that is, the slope of the linear portion between  $t_1$  and  $t_2$ , was also obtained from the creep-rupture curve. The values for these creep parameters are tabulated elsewhere<sup>(9)</sup> for specimens tested in the solution-



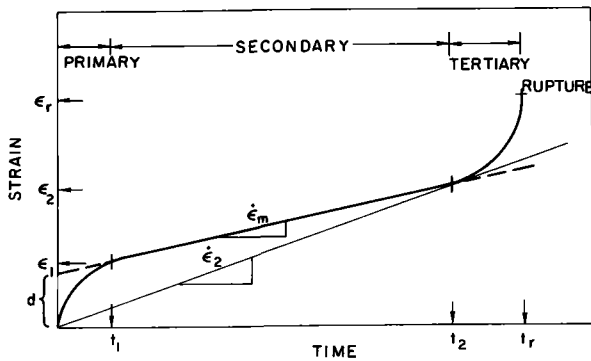


Fig. 4. Schematic of a Creep Curve from a Constant-load Creep Test.

annealed condition and after exposure to a flowing sodium environment. Figure 5 shows the variations in rupture life and minimum creep rate with applied stress at 700, 650, and 600°C for specimens in both the annealed and sodium-exposed conditions. The surface carbon concentrations in the mechanical test specimens were determined from combustion analyses of 50- $\mu\text{m}$ -thick foils of the same material equilibrated in sodium during the specimen-exposure period. The values obtained were  $\sim 0.05$  wt% at 700°C, 0.25 wt% at 650°C, and 0.30 wt% at 600°C. The average carbon concentrations in the sodium-exposed specimens ranged from 0.043-0.046 wt% at 700°C, 0.078-0.195 wt% at 650°C, and 0.145-0.25 wt% at 600°C where the larger values correspond to longer exposure times. In general, the creep data show that, for the range of carburization attained in the present investigation, the exposure of the stainless steel to the sodium environment results in an increase in rupture life and a decrease in minimum creep rate when compared with the results for material in the solution-annealed condition. The carbon concentration in sodium is such that Type 304 stainless steel with an initial carbon content of 0.046 wt% is almost in thermodynamic equilibrium with the carbon in sodium at 700°C. As a result, the creep behavior of specimens that were exposed to sodium at 700°C was essentially the same as that of specimens tested in solution-annealed condition. At sodium-exposure temperatures of 650 and 600°C, the steel carburizes; the amount depends on the time of exposure. The creep tests results at these temperatures clearly show the beneficial effect of carburization in the stress range of our investigation.

The microstructures of the sodium-exposed specimens (in the axial direction) before and after creep testing showed that the specimens with larger rupture

strain have grains elongated significantly in the axial direction. It was observed that in Type 304 stainless steel the carbide particles preferentially precipitate at the grain boundaries and that the size of the particles in the specimen with longer sodium exposure is larger, which indicates growth of these particles with time. The precipitate morphology in these specimens should inhibit grain-boundary sliding and migration during the testing period. The respective contributions of grain elongation and relative grain movements to the deformation, that were determined in these specimens by evaluating the change in shape of internal grains and computing the intragranular deformation, showed negligible contribution of grain-boundary sliding to the creep strain in the stainless steel.<sup>(10)</sup> Examination of the fracture surfaces of annealed and sodium-exposed specimens creep tested at different stress levels showed that the fractures are dimpled, which is indicative of a ductile mode, and can be associated with the growth of internal voids or holes.<sup>(10)</sup>

#### CREEP-RUPTURE CORRELATIONS

To understand creep-rupture behavior more fully, various correlations between rupture life and other quantities determined from the creep curves were attempted. Relationships between rupture life  $t_r$  and minimum creep rate  $\dot{\epsilon}_m$  or time for onset of tertiary creep  $t_2$  are useful if they describe the creep behavior of the material over a wide range of temperatures and applied stresses. Furthermore, such relationships, if developed, can be used to evaluate the necessary creep quantities from standard stress-rupture tests. Current elevated-temperature design rules<sup>(2)</sup> require not only a knowledge of rupture behavior but also information on the time to the onset of tertiary creep and time to reach a specified strain. Tertiary creep is generally indicative of material cracking and void formation, and therefore is metallurgically related to material damage. Also, tertiary creep results in material instability, since an increase in strain rate occurs with an increase in strain and strain concentrations induced by creep are accelerated. As a result, a correlation between the rupture life and the time-to-tertiary creep will be useful to establish the onset of instability in design studies.

The variation of  $t_r$  as a function of  $\dot{\epsilon}_m$  can be written as

$$t_r = C(\dot{\epsilon}_m)^{-\alpha} \quad (1)$$

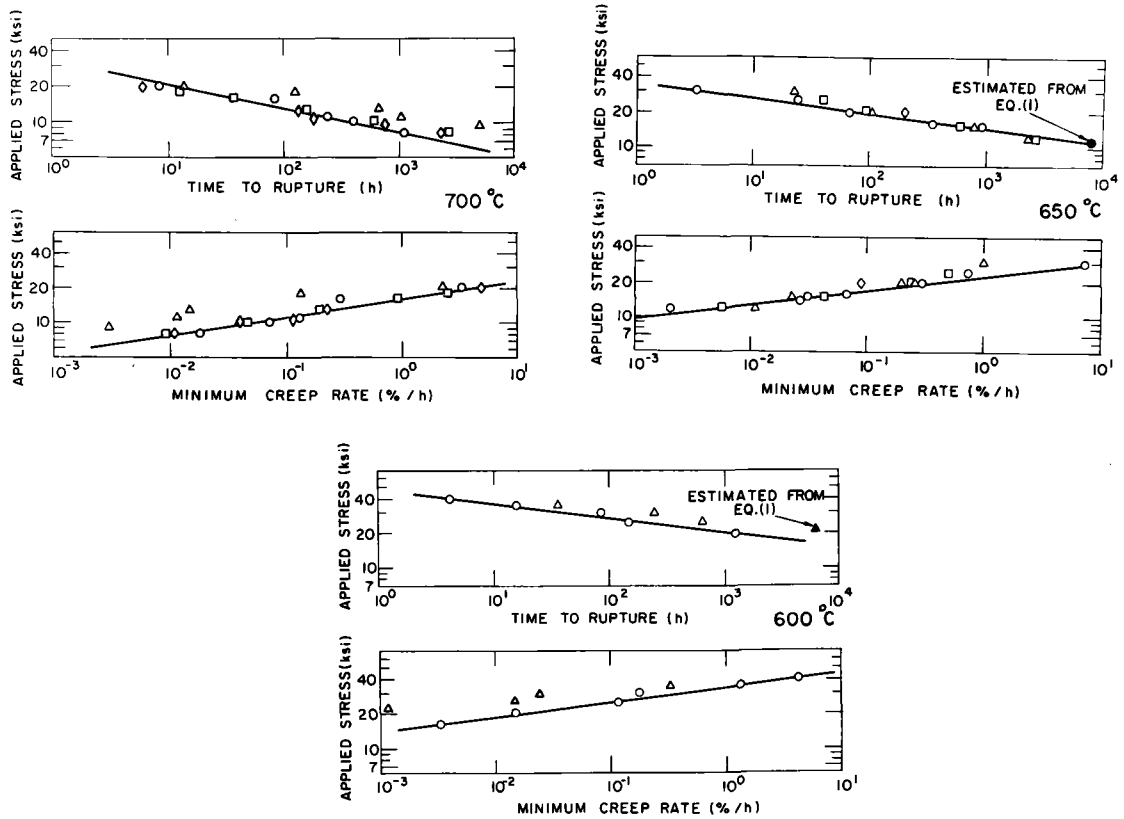


Fig. 5. Variation of Time to Rupture and Minimum Creep Rate with Applied Stress at 700, 650, and 600°C. Solution annealed:  $\circ$ , Carburization depths:  $\Delta$  = 100  $\mu\text{m}$ ,  $\square$  = 200  $\mu\text{m}$ , and  $\diamond$  = 375  $\mu\text{m}$ . Conversion factor: 1 ksi = 6.894 MPa.

where C and  $\alpha$  are constants. Figure 6 shows a plot of  $\ln t_r$  versus  $\ln \dot{\epsilon}_m$  for specimens tested in the solution-annealed condition and after exposure to flowing sodium

rate decreases as the amount of carburization increases. The evaluations of constants C and  $\alpha$ , for different sets of data in Fig. 6, are given in Table I. The correlations developed here are used to estimate the rupture lives of specimens for tests terminated prior to fracture. The calculated values, i.e., the solid symbols in Fig. 5, are in excellent agreement with extrapolations based on data obtained at the higher stresses.

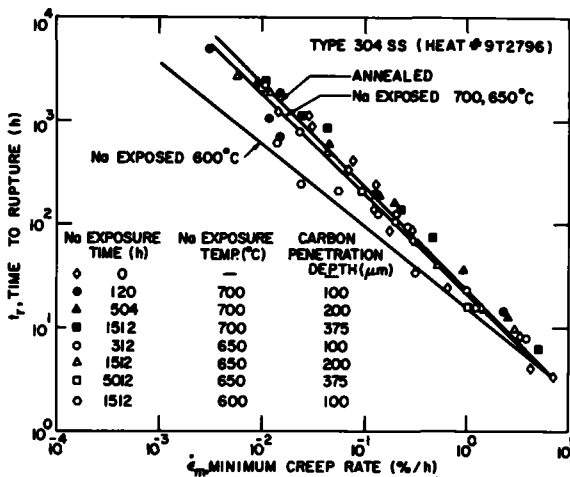


Fig. 6. A Plot of Rupture Life versus Minimum Creep Rate for Specimens in Solution-annealed and Sodium-exposed Conditions.

at 700, 650, and 600°C. In general, the results indicate that, for a given rupture time, the minimum creep

The time for the onset of tertiary creep can be correlated with rupture life by the expression

$$t_2 = B (t_r)^\beta \quad (2)$$

where B and  $\beta$  are constants. Figure 7 shows a plot of  $\ln t_2$  versus  $\ln t_r$  for specimens tested in the solution-annealed condition and after exposure to flowing sodium at 700, 650, and 600°C. The constants B and  $\beta$ , evaluated for different sets of data, are given in Table I. The results show that the time to initiation of tertiary creep is a fixed fraction of the time to rupture for the annealed and carburized conditions in the temperature range 600-700°C. The rate of coalescence of voids and growth of cracks during tertiary creep should

INTERNATIONAL CONFERENCE ON LIQUID METAL TECHNOLOGY IN ENERGY PRODUCTION

Table I. Creep Correlations

$t_r = C \left( \dot{\epsilon}_m \right)^{-\alpha}$			
Treatment	$\alpha$	$C$	
Solution Annealed	0.99	22.16	
Na Exposed at 650 and 700°C	0.95	22.45	
Na Exposed at 600°C	0.79	17.90	

$t_2 = B \left( t_r \right)^\beta$			
Treatment	$\beta$	$B$	
Solution Annealed	1.025	0.558	
Na Exposed (All Temperatures)	1.061	0.475	
All Data	1.05	0.501	

$\dot{\epsilon}_2 = D \left( \dot{\epsilon}_m \right)^\gamma$			
Treatment	$\gamma$	$D$	
Solution Annealed	0.987	1.072	
Na Exposed at 650 and 700°C	0.972	1.079	
Na Exposed at 600°C	0.918	1.075	

$\dot{\epsilon}_m = A(\sigma)^n$			
Treatment	Temperature, °C	$n$	$A$
Solution Annealed	700	5.60	$1.53 \times 10^{-7}$
Solution Annealed	650	5.90	$5.33 \times 10^{-9}$
Solution Annealed	600	6.40	$7.31 \times 10^{-11}$
Na Exposed	700	6.23	$2.74 \times 10^{-8}$
Na Exposed	650	6.48	$5.26 \times 10^{-10}$
Na Exposed	600	10.71	$9.22 \times 10^{-18}$

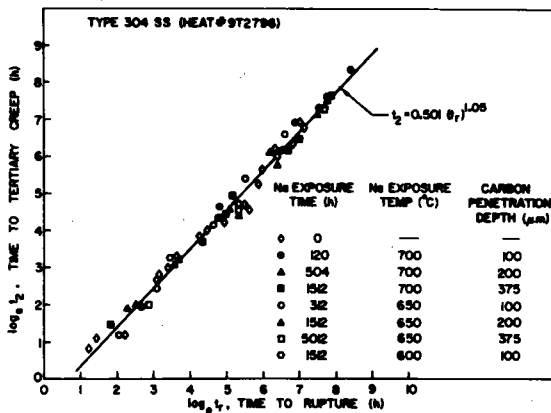


Fig. 7. A Plot of Rupture Life versus Time-to-tertiary Creep for Specimens in Solution-annealed and Sodium-exposed Conditions.

be related to quantity B in Eq. (2). Since  $\beta$  is almost unity,  $B = t_2/t_r$ . From the values of B reported in Table I for specimens in the solution-annealed condition and after exposure to sodium, it can be concluded that the void coalescence rates in the carburized specimens are slower than in the annealed specimens.

The time to a specified strain limit (currently

set at 1 percent total inelastic membrane strain) has been analyzed by the use of isochronous stress-strain curves.<sup>(11)</sup> This involves analysis of individual strain-time curves from constant-load constant-temperature tests and development of analytical formalisms to describe the strain-time behavior. In the present paper, the experimental strain-time curves were analyzed in terms of the creep equation developed by Booker.<sup>(12)</sup> The equation is a single rational polynomial and is written as

$$\epsilon = \frac{dpt}{1 + pt} + \dot{\epsilon}_m t \quad (3)$$

where  $\epsilon$  is the creep strain, d the intercept strain,  $\dot{\epsilon}_m$  the minimum creep rate, and t the time. The parameter p is related to the curvature of the primary portion of the curve. The intercept d was evaluated by the expression

$$d = \epsilon_2 - \dot{\epsilon}_m t_2 \quad (4)$$

where  $\epsilon_2$  and  $t_2$  are strain and time that correspond to the onset of tertiary. The parameter p was assigned a value of  $49/t_2$  since this value resulted in a good agreement between the experimental strain-time data for Type 304 stainless steel (heat 9T2796) and Booker's analysis.<sup>(12)</sup> Analytical expressions that relate the minimum creep rate  $\dot{\epsilon}_m$  and applied stress  $\sigma$  were also developed for temperatures of 700, 650, and 600°C from the creep data generated in this program on specimens in both the annealed and sodium-exposed conditions. The expression can be written as

$$\dot{\epsilon}_m = A(\sigma)^n \quad (5)$$

where A and n are constants, the values of which are also given in Table I.

The correlations given in Table I were used in Eq. (3) to compute the strain-time curves and a comparison of the experimental data with the calculated values for specimens in annealed and sodium-exposed conditions was attempted. Figure 8 shows that the calculated values are in good agreement with the experimental data generated on solution-annealed and sodium-exposed specimens at 600 and 650°C. Generally the agreement was good in the temperature range 600-700°C and stress range of 8 to 35 ksi. Figure 9 shows the isochronous stress-creep strain curves that were generated at temperatures of 700, 650, and 600°C for annealed and sodium-exposed conditions. The results show that the carburization of the steel in the sodium environment in the range of our investigation enhances the creep-rupture properties of the material. The

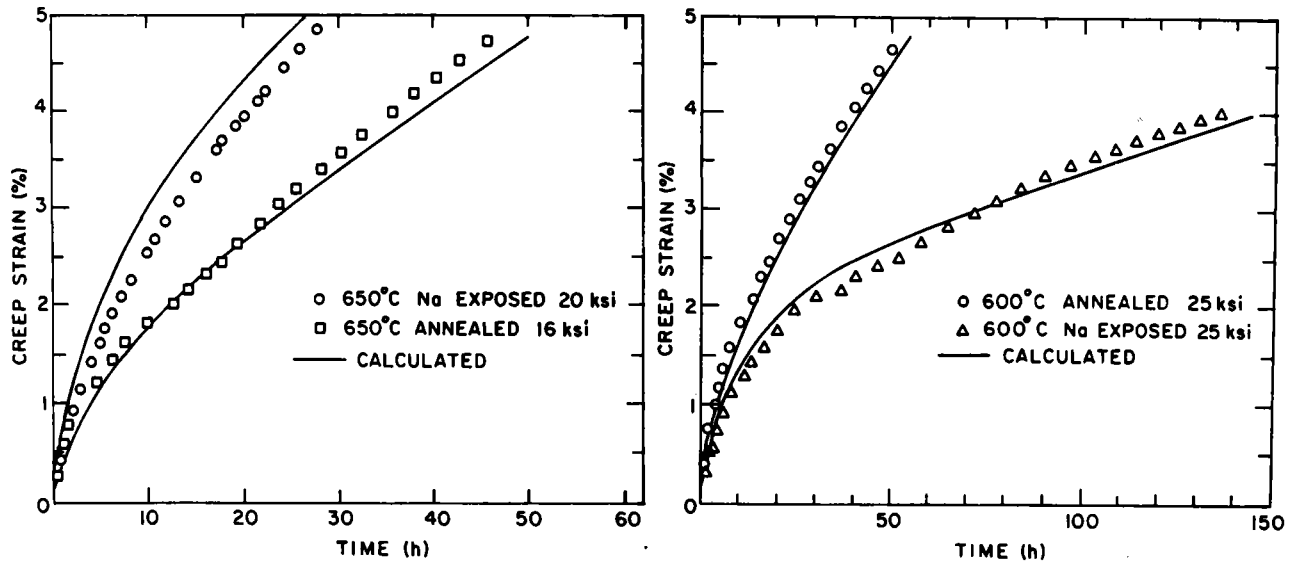


Fig. 8. A Comparison of Experimental Creep Strain-Time Curves with the Calculated Values.

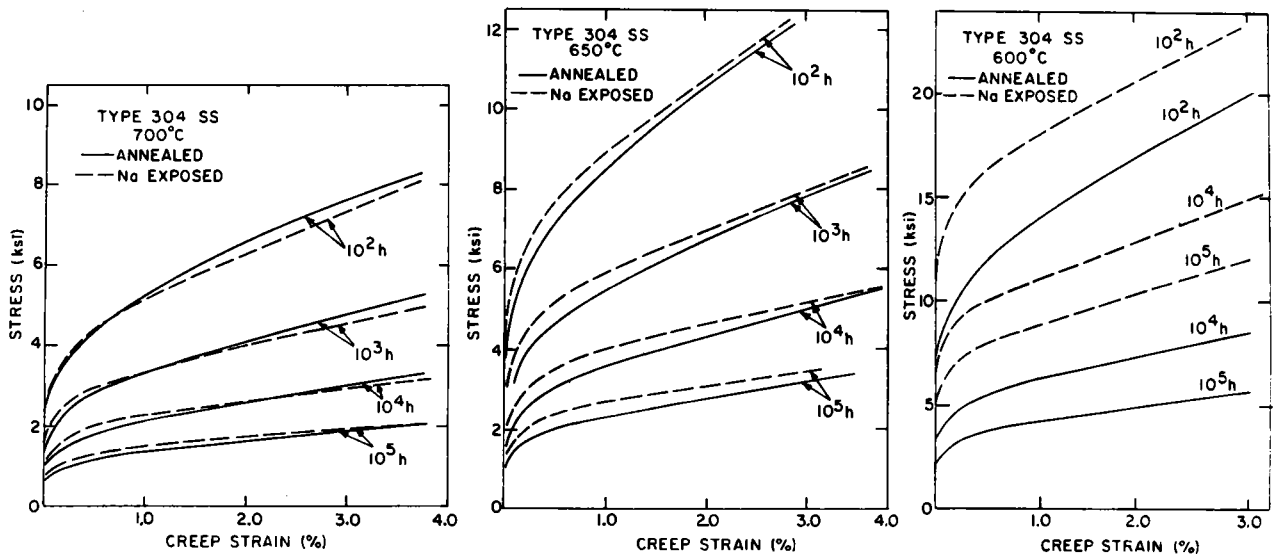


Fig. 9. Isochronous Stress-Creep Strain Curves for Specimens in Solution-annealed and Sodium-exposed Conditions. Conversion factor: 1 ksi = 6.894 MPa.

beneficial effect is more pronounced at 600°C where the material has undergone a larger degree of carburization than at 650 and 700°C.

Figure 10 shows the stress levels calculated for 1 percent strain limit in a specified time as a function of temperature for the steel in the solution-annealed and sodium-exposed conditions. Figure 11 shows the stress levels calculated for  $10^4$  and  $10^5$  h rupture strengths as a function of temperature.

SUMMARY

Uniaxial creep-rupture data have been obtained for Type 304 stainless steel in the solution-annealed

and sodium-exposed conditions in the temperature range 600-700°C. The creep behavior of the steel carburized in sodium containing 0.4-0.8 ppm carbon, which represents an upper level for the carbon concentration in the sodium of an LMFBR heat-transport system, indicates that an increase in rupture life and a decrease in minimum creep rate will occur in this temperature range. Creep correlations have been developed which aid in the evaluation of creep quantities, such as minimum creep rate and time-to-tertiary creep, from standard stress-rupture tests. Isochronous stress-creep strain curves were generated for the steel in both the solution-annealed and sodium-exposed

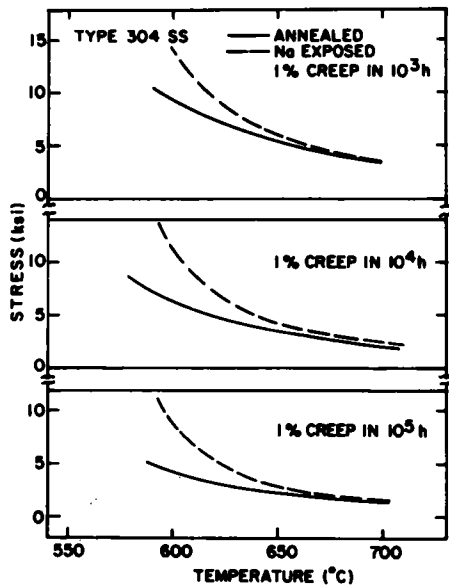


Fig. 10. A Plot of Stress Values to Produce 1 Percent Creep Strain as a Function of Temperature for Solution-annealed and Sodium-exposed Conditions. Conversion factor: 1 ksi = 6.894 MPa.

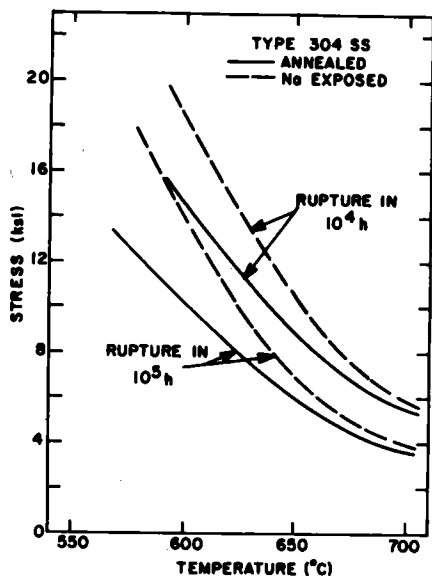


Fig. 11. A Plot of Stress Values for  $10^4$  and  $10^5$  h Rupture Strengths as a Function of Temperature for Solution-annealed and Sodium-exposed Conditions. Conversion factor: 1 ksi = 6.894 MPa.

conditions, with the use of a single polynomial creep equation. Results on the calculations of the stress levels for 1 percent creep strain and for long-term rupture life are also presented.

#### ACKNOWLEDGMENTS

The authors gratefully acknowledge the assistance of D. L. Rink and R. W. Bunce during the sodium-

exposure and creep test program. S. Mihailovich assisted in the carbon analyses of specimens. This work was supported by the U. S. Energy Research and Development Administration.

#### REFERENCES

1. K. Natesan, T. F. Kassner, and Che-Yu Li, "Effect of sodium on the mechanical properties and friction-wear behavior of LMFBR material," *Reactor Technol.* 15, 244 (1972-73).
2. Interpretations of the ASME Boiler and Pressure Vessel Code, Case 1592, American Society of Mechanical Engineers (1974).
3. R. C. Andrews, USAEC Report MSAR-64-81, MSA Research Corporation (1964).
4. R. B. Snyder, K. Natesan, and T. F. Kassner, "Kinetics of the carburization-decarburization process of austenitic stainless steels in sodium," *J. Nucl. Mater.* 50, 259 (1974).
5. *Reactor Development Program Progress Report, July-August 1975*, Argonne National Laboratory, ANL-RDP-42, p. 1.10.
6. K. Natesan, "Carbon activities in Types 304 and 316 stainless steel," Argonne National Laboratory, to be published.
7. B. Longson and A. W. Thorley, "Solubility of carbon in sodium," *J. Appl. Chem.* 20, 372 (1970).
8. K. Natesan and T. F. Kassner, "Monitoring and measurement of carbon activity in sodium systems," *Nucl. Technol.* 19, 46 (1973).
9. *Mechanical Properties Test Data for Structural Materials Quarterly Report for Period Ending January 31, 1976*, Oak Ridge National Laboratory Report, in press.
10. K. Natesan, O. K. Chopra, and T. F. Kassner, "Effect of sodium environment on the creep-rupture behavior of austenitic stainless steel," to be published in the *Proceedings of the 5th International Symposium on Heat-resistant Metal Materials*, Vsetin, Czechoslovakia, September 1976.
11. L. D. Blackburn, J. C. Tobin, and R. A. Moen, "Materials creep behavior and elevated temperature design," *Nucl. Technol.* 16, 278 (1972).
12. M. K. Booker, Oak Ridge National Laboratory, private communication.

# INTERNATIONAL CONFERENCE ON LIQUID METAL TECHNOLOGY IN ENERGY PRODUCTION

## INFLUENCE OF DYNAMIC SODIUM ON THE CREEP PROPERTIES OF STABILIZED AUSTENITIC STEELS

H.Tas\*

F.Casteels\*

M.Schirra\*\*

\* Studiecentrum voor Kernenergie,  
S.C.K./C.E.N., Mol, Belgium

\*\* Kernforschungszentrum, KFK Karlsruhe,  
Federal Republic of Germany

### ABSTRACT

Uniaxial creep tests on X8CrNiMo V Nb 1613 (DIN 1.4988) and X10NiCrMoTiB 1515 (DIN 1.4970) tubes have been carried out at 700°C both in dynamic sodium and in vacuum at different stress levels in order to establish the influence of a well-defined sodium quality on the secondary creep rate, the onset of tertiary creep, the time-to-rupture and the fracture mechanism for these stabilized austenitic steels. Mechanisms which can be responsible for changes of creep properties are diffusion-controlled processes such as preferential leaching of substitutional elements and loss or pick-up of interstitial elements; furthermore, physico-chemical processes such as general corrosion, grain boundary grooving, surface pitting and crack promoting processes. The observed structural and chemical changes have been evaluated and cannot be responsible for variations of the creep parameters. The dynamic sodium environment promotes intergranular cracking in the DIN 1.4988 steel, whereas in the DIN 1.4970 steel rapid local corrosion in deformation bands causes the growth of an irregular branched fracture path from the sodium exposed surface. However, the main creep parameters of both steels are not significantly influenced by the presence of flowing sodium.

### INTRODUCTION

A high creep strength is one of the necessary requirements for a candidate cladding tube material for fast reactors. During reactor operation the mechanical resistance is affected by neutron irradiation induced embrittlement and swelling and by corrosion phenomena at the inner and outer sides of the tube. The influence of exposure to dynamic sodium on the creep properties of unstabilized AISI 300 type stainless steels is well documented in literature (1)(2)(4). Under decarburizing conditions a loss of creep strength is generally observed which can mainly be attributed to a decrease of the carbon content to values as low as 100 ppm (3). Much less information is available about the influence of dynamic sodium on the creep properties of stabilized austenitic steels such as DIN 1.4970 and DIN 1.4988, which are candidate cladding materials for SNR 300 (5). Since these steels are alloyed with respectively boron and nitrogen, particular attention should also be given to the migration of these interstitials and its effect on the high-temperature creep strength.

A number of uniaxial creep tests both in vacuum and in dynamic sodium have therefore been carried out, allowing the determination of the influence of sodium exposure on secondary creep rate, onset of tertiary creep, time-to-rupture and fracture mechanism. These results have been correlated with chemical and metallographical analyses of the sodium creep specimens, specimens treated during the same time and at the same temperature in an inert gas atmosphere and in dynamic sodium, and as-received specimens.

### EXPERIMENTAL TECHNIQUES

Uniaxial creep tests on DIN 1.4970 and DIN 1.4988 tubes have been carried out on two test apparatus mounted in parallel on the high-temperature test section (700°C) of the Na<sub>2</sub> loop at Mol. Identical unstressed specimens were exposed immediately upstream of the creep specimens. In order to differentiate between thermal and corrosion effects unstressed tube specimens have been submitted to equivalent thermal treatments under vacuum both in steel and quartz capsules.

Creep tests on the same material but under vacuum ( $1.40 \cdot 10^{-5}$  torr) have been carried out at KFK. The stresses at which tests have been performed both in vacuum and in sodium are given in table I.

The tube dimensions were 40 x 6 x 0.38 mm. Chemical compositions and metallurgical conditions are given in table II.

The maximum duration of the sodium experiments reached 3250 h, the sodium velocity was 4.5 m/s and the oxygen content 5 ppm. The total carbon content determined by combustion was found to be 3 ppm (6).

### EXPERIMENTAL RESULTS

Effects, which may be responsible for a different creep behaviour under dynamic sodium, such as loss of wall thickness, ferritization, intermetallic compound formation, cavity formation, transport of interstitial and substitutional elements and crack promoting factors have been investigated.

Microstructural changes: the formation of continuous and grain boundary ferrite can be revealed by inter-ferrometric techniques after evaporation of a thin ZnSe film (7) on the polished section. As illustrated in fig. 1 and table III, no influence of stress on the depth of the ferrite layers has been noticed. The continuous ferrite layer is more irregular in the unstressed DIN 1.4988 steel. The network of intergranular ferrite is more developed in the DIN 1.4988. In the as-received condition, the DIN 1.4970 steel contains precipitates of the TiC, TiN, Ti(C,N) and M<sub>23</sub>(C,B)<sub>6</sub> type. No metallographic changes of this microstructure could be observed after heat treatments lasting up to 3250 h. A similar heat treatment of the DIN 1.4988 steel results in the precipitation of a sigma phase. Initially a blue-grey (Nb,V)(C,N) is present together with carbides of the M<sub>23</sub>C<sub>6</sub> type.

The grain size of the bulk material is not influenced by strain, temperature or sodium exposure. A precipitate depleted zone extends to the maximum depth where grain boundary ferrite is present. Intergranular cavities are present up to a depth of about 15 microns in the stressed and unstressed sodium exposed samples (fig. 1).

**Microprobe analysis** : the variation in concentration of metallic elements in the steels due to sodium exposure has been measured. Main bulk and surface concentrations are given in table IV. A selective loss of Cr, Ni, Mn and Si is found, whereas Ti and Mo concentrations remain roughly unaffected. At the surface nickel and chromium concentrations decreased by 2 to 6 wt.%. This change of composition cannot cause a transformation to ferrite at the test temperature but renders the austenite unstable, consequently martensite is formed during cooling down of the loop. This has been demonstrated recently (8) by high-temperature X-ray diffraction measurements up to 700°C on various austenitic steels, after a 4000 h sodium exposure at 700°C. The surface ferrite was found to nucleate during cooling from 700°C at temperatures lower than 200°C.

**Microhardness** : Vickers microhardness measurements have been carried out both on sodium exposed and vacuum creep specimens in the necking zone and in the zone of homogeneous deformation.

All values remained within the scatter band of the as-received material except for the measurements in the necking zone where a decrease occurred indicating a strain weakening. This effect is more pronounced in the sodium exposed specimens as compared with the vacuum creep specimens.

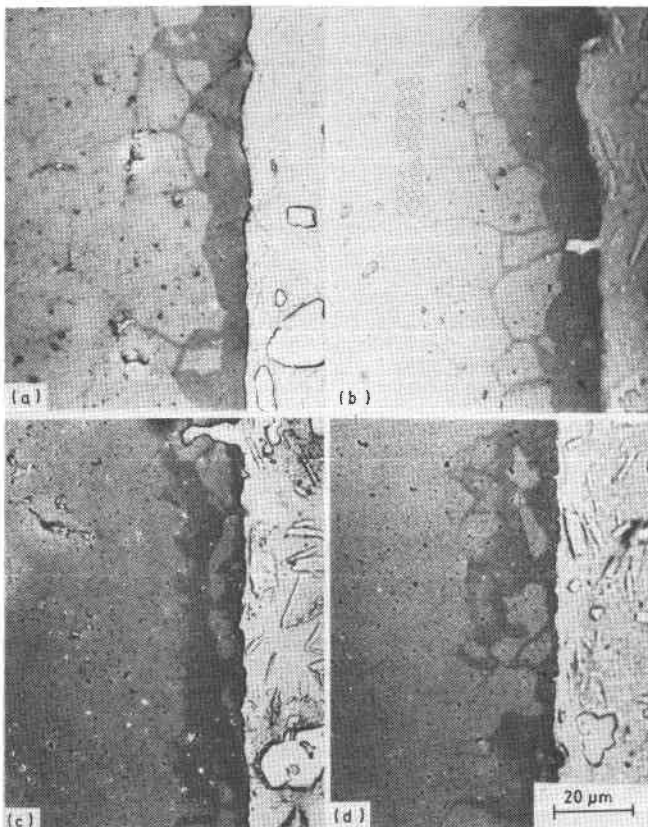


**Fig.1.**  
 (a) : DIN 1.4988 ; 100 N/mm<sup>2</sup>, 3250 h at 700°C  
 (b) : DIN 1.4988 ; unstressed, 3250 h at 700°C  
 (c) : DIN 1.4970 ; 130 N/mm<sup>2</sup>, 3000 h at 700°C  
 (d) : DIN 1.4970 ; unstressed, 3000 h at 700°C  
 Ferrite formation in sodium

**Surface morphology and fracture** : Microscan analysis of the corroded and the as-received surface revealed a change in its morphology. During the corrosion test the mechanically perturbed layer is removed and a preferential attack at the grain boundaries occurs. Small pores, with or without particles in them, develop at isolated places during sodium exposure (fig.2 and fig.3). The holes correspond with the intergranular cavities visible on the cross-sections presented in fig.1. Close to the fracture these holes combine to form cracks parallel to the main fracture. Many small bright Mo-rich corrosion products are present especially on the 1.4988 corroded surface. The fracture mode of the two steels is influenced in a different way by sodium exposure.

In vacuum the DIN 1.4970 fractures by a ductile transgranular mechanism after strong local necking and relatively small uniform elongation (fig.4). In sodium cracks nucleate in deformation bands (fig.5 g, h) causing the growth of many parallel cracks (sodium could be detected by microprobe analysis in several of these crack tips) ; at the inner side of the tube, which was not in contact with sodium, deformation proceeds leading to necking and finally rupture (fig.4).

This results in a fracture surface consisting of two halves with a completely different appearance (fig.5c) : from the outer side an irregular branched fracture path has been followed (fig.5d), whereas from the inner side a characteristic ductile shear fracture with dimples has developed (fig.5e), similar to the fracture appearance of the vacuum creep specimens (fig.5 a, b).

In vacuum the DIN 1.4988 steel fractures by a ductile partly intergranular shear type mechanism after a more pronounced uniform elongation and without appreciable necking. In the fractured zone many intergranular cracks develop. In sodium intergranular cracking is promoted resulting in a smaller

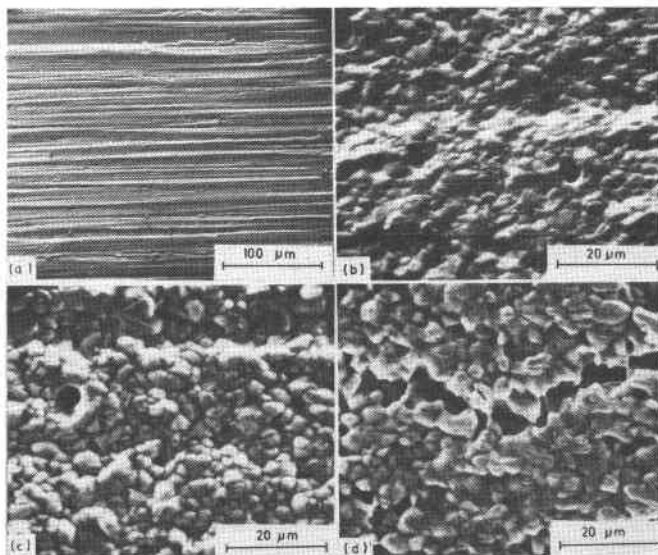


**Fig.2.**  
 DIN 1.4970 : Surface appearance  
 (a) : as-received condition  
 (b) : unstressed ; 3000 h at 700°C in sodium  
 (c) : 110 N/mm<sup>2</sup> ; 3000 h at 700°C in sodium without  
 rupture  
 (d) : 130 N/mm<sup>2</sup> ; rupture after 2843 h in sodium

total elongation at fracture. A larger fraction of the sodium fracture surface is of the intergranular type (fig.6b) as compared with the vacuum fracture surface, where a larger portion of transgranular void coalescence type fracture is present.

Chemical profiles : the occurrence of carbon loss or pick-up in sodium could not be deduced from wet chemically determined carbon concentration-penetration

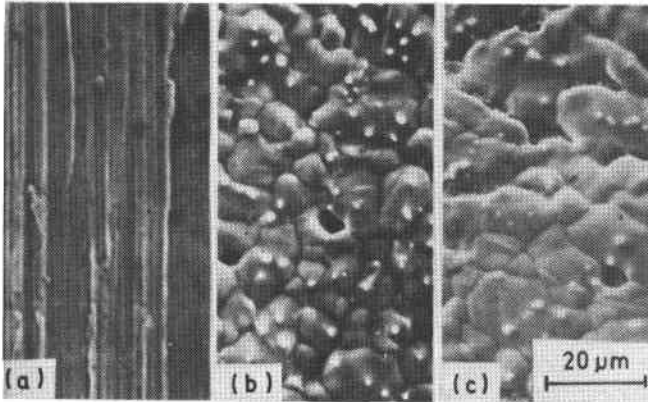


Fig.3.

DIN 1.4988 : Surface appearance

- (a) : as-received condition
- (b) : unstressed ; 3000 h at 700°C in sodium
- (c) : 100 N/mm<sup>2</sup> ; rupture after 3250 h in sodium

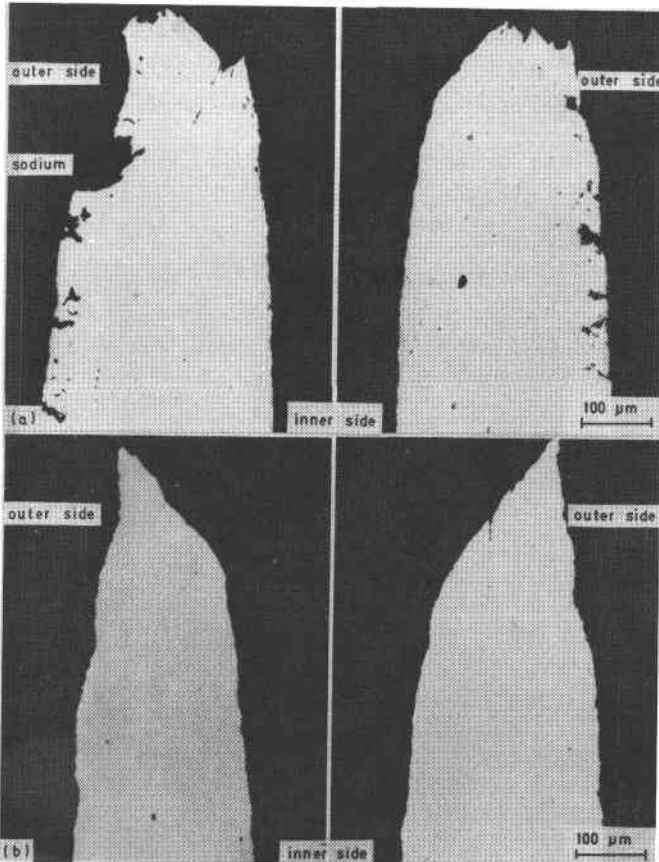


Fig.4.

DIN 1.4970

- (a) 220 N/mm<sup>2</sup> ; rupture after 137 h in sodium
- (b) 220 N/mm<sup>2</sup> ; rupture after 90 h in vacuum

profiles. This neutral behaviour was confirmed by profiles obtained by R.S.V. analyses (9).

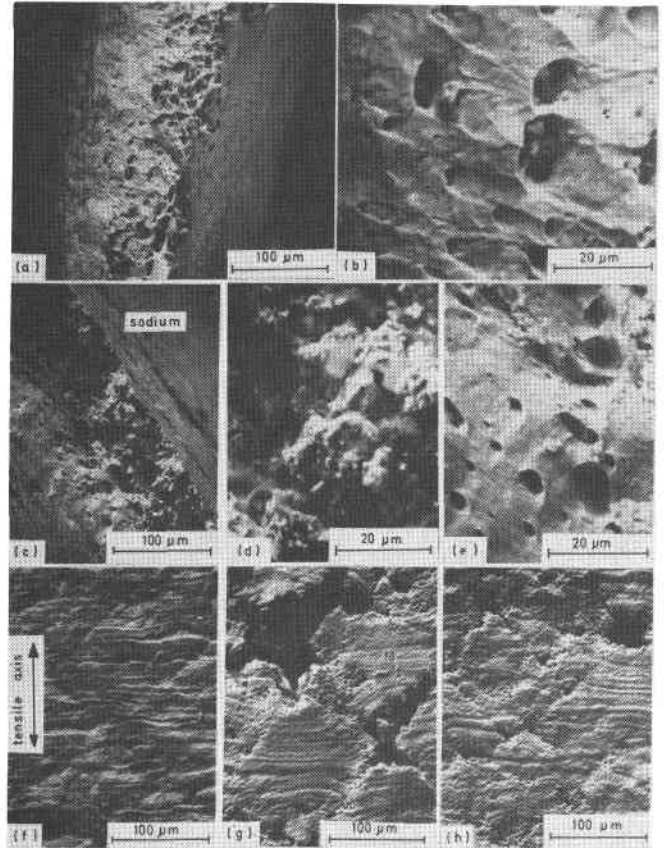


Fig.5.

DIN 1.4970 : Fracture appearance and rapid corrosion in glide bands

- (a)(b) : 200 N/mm<sup>2</sup> ; rupture after 344 h in vacuum ; ductile fracture type
- (c)(d)(e) : 220 N/mm<sup>2</sup> ; rupture after 137 h in sodium mixed fracture
- (d) : detail of sodium-induced fracture area
- (e) : detail of ductile fracture area
- (f) : 260 N/mm<sup>2</sup> ; rupture after 20 h in vacuum : formation of glide bands
- (g),(h) : 200 N/mm<sup>2</sup> ; rupture after 63h in sodium : rapid corrosion in glide bands
- (g) : 1 mm from fracture edge
- (h) : 10 mm from fracture edge

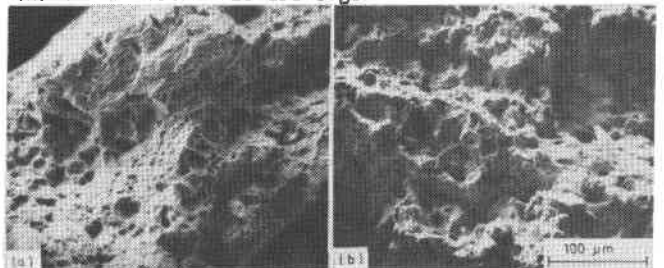


Fig.6.

DIN 1.4988 : Fracture appearance

- (a) 140 N/mm<sup>2</sup> ; rupture after 629 h in vacuum
- (b) 100 N/mm<sup>2</sup> ; rupture after 3250 h in sodium



As illustrated in fig.7a the nitrogen concentration profiles of the DIN 1.4988 steel reveal a loss of nitrogen in the sodium creep specimens. The loss is more pronounced under applied stress. The calculated nitrogen penetration coefficients as a function of applied stress are presented in table V.

From the available boron profiles, as illustrated in fig.7b, it may be concluded that a heat treatment in a steel capsule gives rise to practically the same boron loss as the one provoked by an exposure to dynamic sodium; the presence of stress does not produce a measurable change of these profiles. However, the atmosphere present in the vacuum creep apparatus does not cause a preferential boron loss (fig.7b). In sodium the boron concentration at a depth of 250 microns drops from 35 ppm (as-received material) to a surface concentration less than 5 ppm. The calculated boron penetration coefficients are presented in table V.

**Mechanical tests :** when the values of secondary creep rate, rupture time and total elongation at fracture for the creep tests carried out in sodium are compared with those obtained for creep tests carried out in vacuum, the following conclusions may be drawn :

1. no significant change of time-to-rupture is evident for the two steels tested (fig.8a) ;
2. the secondary creep rate is not affected for the DIN 1.4988 steel whereas a slight increase is noticed for the DIN 1.4970 steel (fig.9) ;

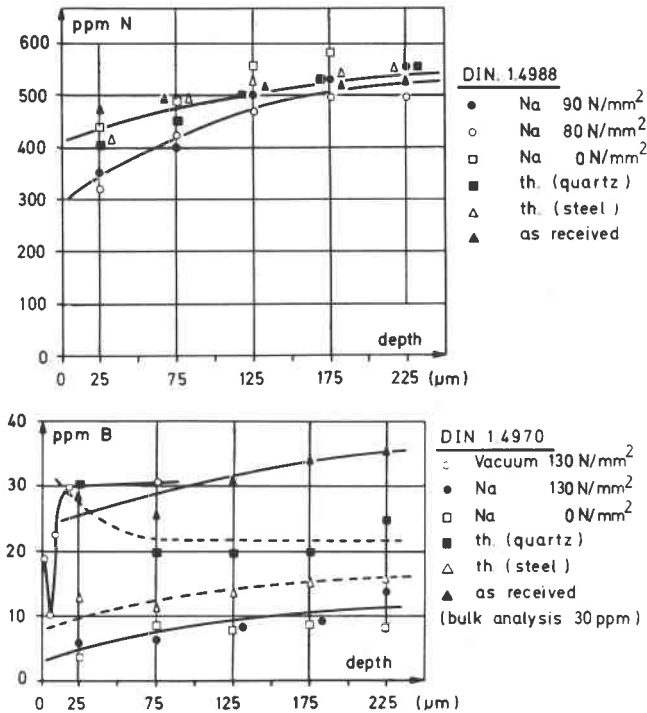


Fig.7. Boron and nitrogen profiles

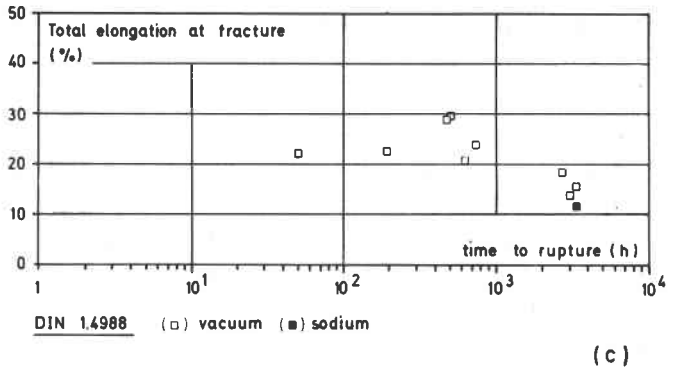
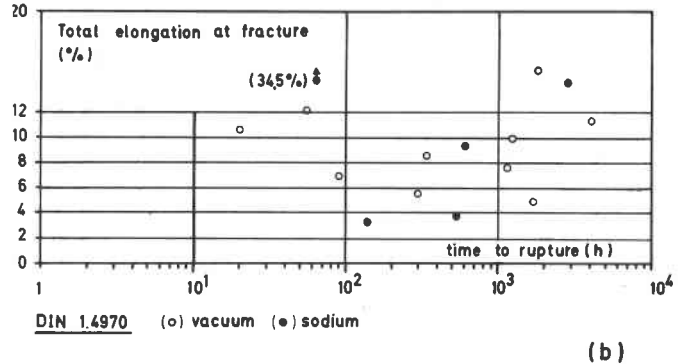
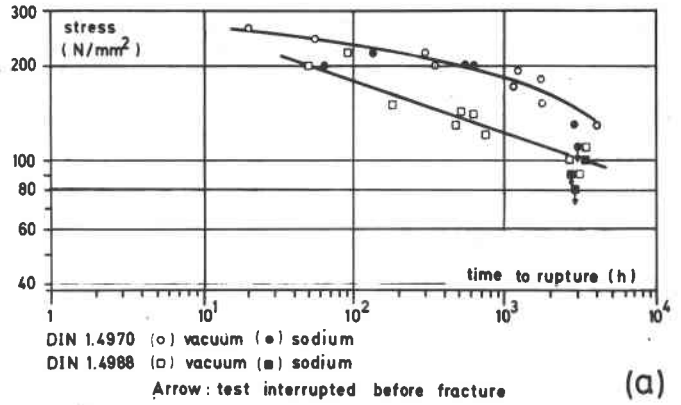


Fig.8. Time-to-rupture and total elongation values

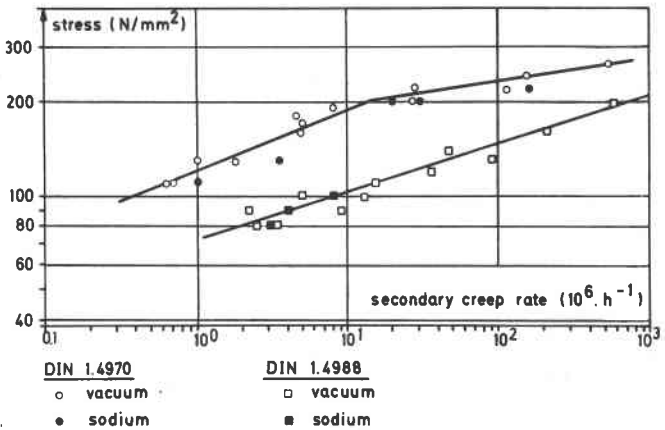


Fig.9. Secondary creep rate values.

## INTERNATIONAL CONFERENCE ON LIQUID METAL TECHNOLOGY IN ENERGY PRODUCTION

3. the total elongation at fracture decreases for the DIN 1.4988 steel whereas for the DIN 1.4970 steel, depending on the extent of the well-developed necking zone obtained in sodium, the elongations varied between 3 and 35% (fig.8b, 8c) ;
4. no influence of sodium exposure on the onset of tertiary creep and the ternary creep rate could be demonstrated.

### DISCUSSION AND CONCLUSIONS

Mechanisms which can be responsible for changes of creep properties are diffusion-controlled processes (3, 4), such as preferential leaching of substitutional elements causing microstructural changes, and physico-chemical processes such as general corrosion, grain boundary grooving, surface pitting, wedging-induced crack formation, reduction in surface energy and adsorption-induced reduction in cohesion (10)(11)(12) (13). The observed penetration depths of the continuous and intergranular ferritic zones are in agreement with published values after sodium corrosion tests carried out under similar conditions (14). The compositional change in these ferritic zones, as measured by microprobe analysis, cannot have led to the formation of a stable ferrite at the sodium exposure temperature but has rendered the austenite unstable causing a martensitic transformation during cooling down of the specimen. This has been confirmed by high-temperature X-ray analysis (8).

A sigma phase depleted zone extends to a depth corresponding with the intergranular ferrite. The bulk microstructural changes are to be attributed solely to the thermal effect.

The observed neutral behaviour of carbon in the DIN 1.4970 steel, despite the relatively high carbon potential of the sodium, is due to its hypo-stabilization.

The DIN 1.4988 loses nitrogen to a depth of about 200 microns. The observed surface concentrations are comparable with the surface concentrations reported in the literature (15)(16)(17). The presence of an applied stress has no influence on the overall nitrogen penetration coefficient.

A marked loss of boron across the whole section occurs in the sodium exposed DIN 1.4970 specimens. Although no such pronounced boron loss takes place in the vacuum creep specimens, no important difference in creep behaviour is to be expected, since it has been shown that boron has only little effect on the creep properties of titanium stabilized austenitic steels (18).

It follows that the effect of nitrogen and boron transport on the creep properties of both steels is limited.

All values of secondary creep rate, time-to-rupture and tertiary creep rate obtained in dynamic sodium lie in the scatter band of the corresponding creep parameters obtained in vacuum.

This means that the above-mentioned diffusion controlled phenomena do not have a measurable effect on these creep parameters. However, physico-chemical processes influence the fracture mechanism and cause the development of corrosion channels thereby changing

the total elongation at fracture.

The intergranular failure mode of the DIN 1.4988 steel is promoted by the presence of sodium resulting in a smaller total elongation at fracture.

On the inner side of the DIN 1.4970 sodium creep specimens the failure mode is of the same transgranular shear type as for the vacuum creep specimens. At the outer side many cracks develop in the glide bands resulting in a branched irregular fracture path. These cracks grow by the coalescence of pores of which high numbers develop in the glide bands. A limited number of these pores is also present in unstressed specimens at some triple points.

This rapid local corrosion can be triggered off by a critical lowering of the surface energy in certain areas through the presence or formation of a high density of point and line defects. Other possible mechanisms are accelerated corrosion along secondary phase particles as described by Sandusky et al (13) or a wedging mechanism through the reaction of sodium and its impurities with secondary phases causing volume changes and local stresses (12).

Summarizing, it can be concluded that the main creep parameters of the DIN 1.4970 and DIN 1.4988 steels are not significantly influenced by a dynamic sodium environment. Hence, the choice of the DIN 1.4970 as casing material for SNR 300, which has been based on many different criteria, can also meet the requirements for compatibility with the coolant under stress.

### REFERENCES

- (1) Lee W.T.  
Biaxial stress-rupture properties of austenitic stainless steels in static sodium  
AI-AEC-12694 (1968)
- (2) Atkins D.F.  
Stress-rupture behaviour of types 304 and 316 stainless steel cladding in high-temperature static sodium  
AI-AEC-12976 (1970)
- (3) Wozadlo G.P. ; Wagner W.J.  
Effects of sodium exposure on the corrosion and strength of stainless steels. Summary report : Sodium mass transfer program GEAP-10394 (1971)
- (4) Natesan K., Chopra O.K.  
Influence of sodium environment on the uniaxial creep-rupture behaviour of AISI type 304 stainless steel.  
Transactions American Nuclear Society 21 (156-157)(1974)
- (5) Borgstedt H.U. and Dietz W.  
Korrosions- und mechanisches Langzeitverhalten von Hüllrohren in Natrium von 700°C  
KFK 1932 (July 1974)
- (6) Lievens F., Soenen M.  
Sodium characterisation during the starting period of a sodium loop.  
This conference
- (7) Pepperhoff W.,  
Quantitative Auflichtmikroskopie mit Hilfe aufgedampfter Interferenzschichten  
Archiv Eisenhüttenwesen 36 (941-950)(1965)

**INTERNATIONAL CONFERENCE ON LIQUID METAL TECHNOLOGY IN ENERGY PRODUCTION**

- |   |   |
|---|---|
| (8) Tas H.<br>Unpublished results   | (14) Borgstedt H.U.<br>Arbeiten zur Brennelement-Entwicklung für den schnellen Brutreaktor SNR-300<br>Böhm H., Dienst W., Kummerer K.,<br>KFK 1999 (1974)(173-190)  |
| (9) Schneider H.<br>Investigations of changes in the surface layer composition of materials exposed to sodium by glow discharge optical and Auger electron spectroscopy<br>This conference.                 | (15) Borgstedt H.U. ; Grosser E.D.<br><u>Liquid Alkali Metals</u><br>The British Nuclear Energy Society<br>London (1973)(275-282)   |
| (10) Böhm H., Schneider H.<br>Über das Zeitstand- und Kriechverhalten von austenitischen Cr-Ni Stählen in Gegenwart von Natrium<br>Journal of Nuclear Materials <u>24</u> (188-197)(1967)                   | (16) Casteels F., Fevery M.J., Menken G., Soenen M., Cools A., Diels P.<br>Corrosion d'aciers ferritiques et austénitiques dans le sodium.<br>Influence des méthodes de nettoyage<br>5 <sup>th</sup> European Congress of Corrosion<br>Paris 24-28 september 1973 |
| (11) Kamdar M.H.<br>Progress in Materials Science <u>15</u> (287- ) (1973)  | (17) Fevery M.J.<br><u>Effects of environment on material properties in nuclear systems</u><br>The British Nuclear Society<br>London (1972)(149-153)  |
| (12) Klueh R.L.<br><u>Corrosion by Liquid Metals</u><br>Draley J.E., Weeks J.R.<br>Plenum Press, New York (1970)(177-197)   | (18) Schirra M.<br>Unpublished results  |
| (13) Sandusky D.W., Armijo J.S., Wagner W.J.<br>Influence of long-term sodium exposure on the composition and microstructure of austenitic alloys<br>Journal of Nuclear Materials <u>46</u> (1973)(225-243) |   |

Table I  
Survey of creep tests

Stress ( N/mm <sup>2</sup> )	80	90	100	110	120	130	140	150	160	170	180	190	200	220	240	260
DIN 1.4988	time-to-rupture vacuum	5230*	2977*	2693	3058	737	473	629	498	191			51			
	time-to-rupture sodium	5406*	3324	5061*												
DIN 1.4970	time-to-rupture vacuum	2843*	3000*	3250												
	time-to-rupture sodium				4426*		4071			1806	1155	1728	1261	344	90	56
				5136*			5481*							304		20
				3000*			2843							63	137	
													605			
													527			

\* Interrupted before fracture

Table II  
Alloy composition (original and control analyses)

	Melt No.	Cr	Ni	Mo	Mn	Si	Ti	Nb	V	C	B	N
DIN 1.4970 1100°C, 5 min 13% c.w. ; 2 h at 800°C	78419	15.02	14.91	1.18	1.51	.43	.40	-	.01	.11	.0046	.009
		15.02	14.03	1.19	1.36	.40	.41	-	.01	.11	.0030	.014
DIN 1.4988 1100°C 7% c.w. ; 1 h at 800°C	70095	16.02	12.74	1.34	1.30	.39	.01	.78	.76	.057	.0014	.071
		15.92	12.95	1.36	1.18	.50	-	.85	.72	.065	-	-

**INTERNATIONAL CONFERENCE ON LIQUID METAL TECHNOLOGY IN ENERGY PRODUCTION**

Table III  
Depth of continuous (I) and intergranular (II) ferrite

Steel	DIN 1.4970			DIN 1.4988			
	0	110	130	0	80	90	100
Load (N/mm <sup>2</sup> )							
Ferrite layer I (μm)	18	20	18	14	12	12	14
Ferrite layer II (μm) (total depth)	28	30	30	40	45	50	30
Exposure time (h)	2843	3000	2843	3250	2843	3000	3250

Table IV  
Concentration gradients measured by microprobe analysis (wt.%)

		Ni	Cr	Fe	Mn	Mo	Si	Ti	Nb	V	average penetration depth
DIN 1.4970 130 N/mm <sup>2</sup> sodium	bulk	15.30	13.68	67.61	1.32	1.17	0.53	0.40	-	-	20 μm
	surface	12.89	11.41	73.56	0.43	1.28	0.00	0.43	-	-	
DIN 1.4970 110 N/mm <sup>2</sup>	bulk	15.49	13.92	67.21	1.37	1.13	0.53	0.32	-	-	25 μm
	surface	9.59	9.04	79.52	0.21	0.98	0.00	0.66	-	-	
DIN 1.4988 100 N/mm <sup>2</sup>	bulk	13.27	15.30	67.34	1.33	1.26	0.42	-	0.42	0.67	20 μm
	surface	9.81	10.51	77.43	0.57	1.57	0.05	-	0.03	0.04	

Table V  
Nitrogen and boron penetration coefficients

Steel diffusing element	Condition	Penetration coefficient (cm <sup>2</sup> /s)	
1.4988 nitrogen	unstressed (Na)	0.451	10 <sup>-11</sup>
	stressed (88N/mm <sup>2</sup> ) (Na)	0.378	10 <sup>-11</sup>
	stressed (90N/mm <sup>2</sup> ) (Na)	0.583	10 <sup>-11</sup>
1.4970 boron	unstressed (Na)	0.150	10 <sup>-11</sup>
	stressed (130N/mm <sup>2</sup> ) (Na)	0.211	10 <sup>-10</sup>
	treated in steel capsules (vacuum)	0.256	10 <sup>-10</sup>

## LOW CYCLE FATIGUE TESTING IN FLOWING SODIUM AT ELEVATED TEMPERATURES

P. N. Flagella and J. R. Kahrs  
Westinghouse Electric Corporation  
P. O. Box 158  
Madison, Pa. 15663

## ABSTRACT

This paper describes equipment developed to obtain low cycle strain-controlled fatigue data in flowing sodium at elevated temperatures. Operation and interaction of the major components of the system are discussed, including the calibration technique using remote strain measurement and control. Confirmation of in-air results using the special technique are demonstrated, with data presented for Type 316 stainless steel tested in high purity flowing sodium at 593°C. The fatigue life of the material in sodium is essentially the same as that obtained in air for a  $\Delta\epsilon_t = 1\%$ . On the other hand, sodium pre-exposure at 650°C for 5000 hours increased the fatigue life in-sodium by a factor of two, and sodium pre-exposure at 718°C for 5000 hours increased the fatigue life in-sodium by a factor of three.

## INTRODUCTION

Liquid Metal Fast Breeder Reactors (LMFBR) will have numerous structural components submerged in sodium at elevated temperatures for long periods of time. It has been shown that the environment can have a significant effect on the elevated temperature fatigue life of some materials<sup>(1-3)</sup>. In these cases, the data have been obtained from tests in vacuum or argon and the results compared to data obtained in air. The reduced fatigue life resulting from specimens tested in air is attributed to a "wedging" effect caused by oxides formed at the crack tip, producing increased crack-growth rates.

In the case of a sodium environment, a redistribution of carbon can take place in a stainless steel - sodium heat transport system as a result of chemical activity differences<sup>(4)</sup>. This effect is important since the mechanical properties of austenitic stainless steels are significantly altered by variations in the carbon content<sup>(5,6)</sup>. The problem is further complicated by the development of carbon gradients in the stainless steels during the lifetime of the structural components contacting the sodium. Mechanical properties of the materials can also be affected by microstructural and compositional changes resulting from the extended time in the high temperature sodium.

The present investigations are being performed to determine the effects of a flowing sodium environment on the low-cycle fatigue behavior of various materials to assist in the design of reactor components. Presented here is a technique developed to obtain low-cycle fatigue data for materials in flowing sodium. In addition, results of tests on Type 316 stainless steel at 593°C are presented.

## EQUIPMENT AND EXPERIMENTAL PROCEDURE

The facility for performing low-cycle fatigue tests in flowing sodium involves two MTS closed-loop servo-hydraulic fatigue machines, each with its own environmental test chamber, and one sodium loop which provides the dynamic test conditions. A schematic diagram of the system is shown in Figure 1 and an overall photograph of the facility is shown in Figure 2. Testing is performed in one chamber while disassembly and assembly of specimens is accomplished in the other.

## Sodium Loop

The sodium loop was constructed from 1.27 cm OD x 0.13 cm wall Type 304 stainless steel tubing and is capable of continuously recirculating an inventory of approximately 10 kg of sodium to temperatures of 750°C. All tubing, chambers, tanks, and valves are wrapped with trace heaters to preheat the system before filling with sodium, and insulated to minimize heat loss during operation. Starting at the variac controlled electro-magnetic (EM) pump, which is located in the "cold-leg" of the main loop system, the sodium flows to the 5 kW main heater. Power to the heater is automatically controlled by a thermocouple located at the outlet of the heater to give the desired sodium temperature for testing. Actual test specimen temperature is based on two thermocouples located in the sodium just ahead of the specimen. Sodium leaving the heater enters one of the test chambers and is channeled through tubing to a shroud around the test specimen. The shroud allows for a controlled sodium velocity to be maintained over the surface of the specimen. All tests are performed with the velocity maintained at  $\sim 1.0$  meters per second. After leaving the shroud, the sodium discharges to the main volume of the test chamber. The sodium level in the chamber is maintained above the specimen fixture to insure a uniform temperature over the length of the test specimen. Resistance heaters and insulation are also used

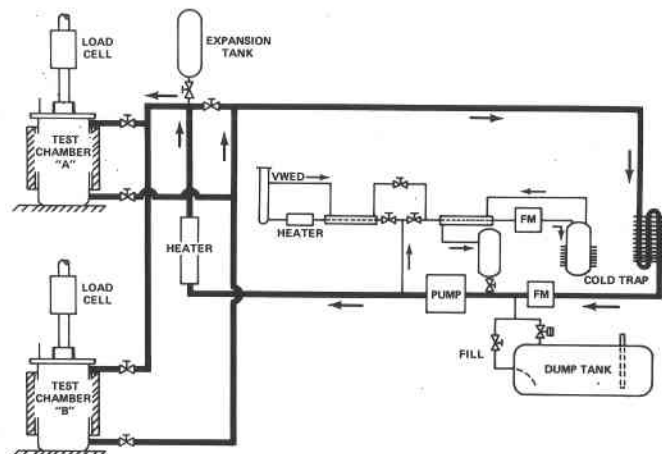


Figure 1. Schematic of facility for fatigue testing in sodium

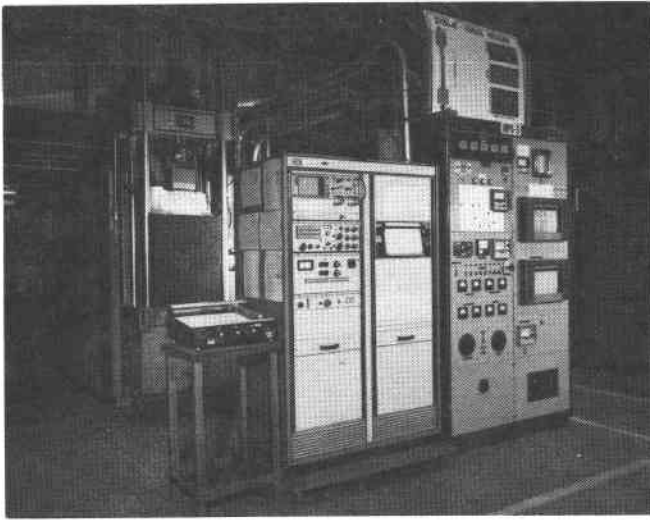


Figure 2. Facility for fatigue testing in sodium showing control panels, test stand, and the sodium loop enclosure located behind the MTS machine

on the outside of the vessel to compensate for heat loss from the sodium pool in the chamber. A flowing argon ( $\sim 0.03 \text{ m}^3/\text{h}$ ) pressure of 0.1 MPa gauge is maintained above the sodium pool. Leaving the test chamber, the sodium travels to the finned tube air cooled heat exchanger where heat is removed to provide the desired  $55^\circ\text{C}$  temperature differential for the main loop. The sodium then passes through the flow meter and back to the EM pump.

A side loop, also shown in Figure 1, is used to continuously cold trap the main loop sodium. Approximately 10% of the main loop flow is circulated through the cold trap with the trap maintained between  $145$  and  $150^\circ\text{C}$  by an air blower operated by a temperature controller. The actual oxygen content in the sodium is determined by use of the vanadium wire equilibration device (VWED) at frequent intervals. Vanadium wires, 0.05 cm in diameter, are exposed to the sodium at  $750^\circ\text{C}$  for four hours and then chemically analyzed to determine the oxygen concentration in the sodium. The  $145$  to  $150^\circ\text{C}$  cold trap temperature yields the desired 1.5 to 2.0 parts per million oxygen value. Carbon concentration in the sodium is also determined using the VWED, with 0.08 mm foil of Type 18-8 stainless steel being used in place of vanadium wires. The foil is exposed to the loop sodium at  $700^\circ\text{C}$  for 72 hours and then chemically analyzed for equilibrated carbon in the foil. This carbon value identifies the carbon activity for the sodium which is then converted to the carbon concentration for the sodium. The value obtained for the loop sodium is nominally 0.10 ppm carbon.

#### Test Chamber and Fixture

An MTS closed-loop servohydraulic testing machine fitted with the test chamber shown in Figure 3 is being utilized for the fatigue testing program. The test chamber is rigidly bolted to the fixed lower platen of the load frame, with the sodium exit-line being the only breach of containment in the lower part of the chamber. Access to the chamber is from the top, and the MTS load frame was

specially ordered with the actuator mounted on the movable upper crosshead for this reason.

Transmission of load to the specimen test section is accomplished through the test fixture assembly, which provides for specimen gripping and for alignment with the direction of actuator movement. The test fixture assembly includes the tapered bushing fittings used for tightly clamping the button-head ends of the specimen assembly. It includes the triangular arrangement of three guide rods to discourage buckling, and it also includes the pull-bar shaft which actually transmits the load into the test chamber from the actuator drive rod. The test chamber penetration for the pull-bar shaft is sealed with a 0.25 mm thick low-load flexible stainless steel bellows. The lower end of the bellows is welded to the chamber cover and the upper end is sealed to the pull-bar by compression of a replaceable metal O-ring.

The test chamber is completely assembled prior to mating the actuator drive shaft to the pull-bar shaft. The first step in the assembly process is the preparation of the specimen, schematically shown in Figure 4, which is mated with an adapter to produce a specimen assembly compatible with the test fixture gripping technique. A solid union between specimen and adapter is achieved by using a fillet weld (TIG) around the diameter of the joint. The specimen assembly is then carefully tightened into the upper plate of the test fixture, maintaining concentric alignment with the pull-bar shaft. The flow shroud is then placed over the specimen test section, and the lower half of the test fixture slipped onto the assembly and the grips carefully tightened. The resulting test fixture assembly is then bolted to the

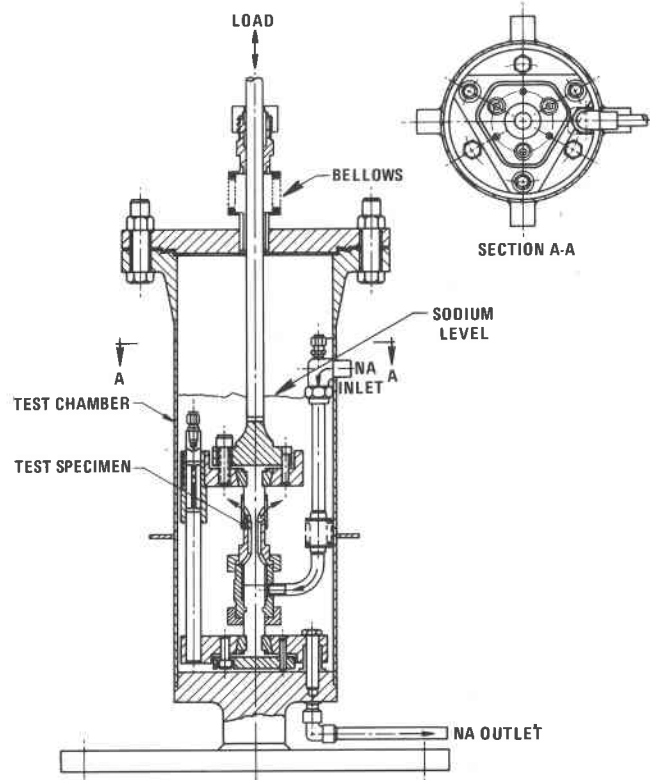


Figure 3. Test chamber design for fatigue testing in flowing sodium

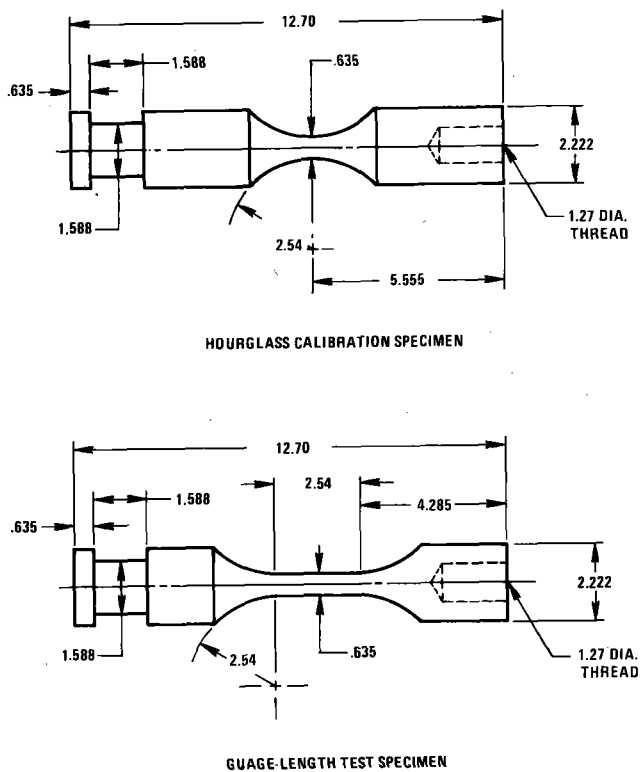


Figure 4. Calibration and test specimen configurations for fatigue testing in sodium (dimensions in centimeters)

bottom of the test chamber, the inlet sodium line to the flow shrouding connected, and the chamber sealed by fitting the lid down over the pull-bar shaft. The load frame crosshead is lowered and the actuator drive shaft coupled to the pull-bar shaft, always maintaining zero load on the sample.

The test chamber is then filled with sodium from the sodium loop and operations necessary to achieve proper test conditions carried out. After filling and flowing through the chamber at approximately 425°C, cold-trapping of the sodium is performed for ~ 24 hours to remove any impurities that may have entered the system during assembly of the fixture and test chamber. The sodium system is then adjusted to the desired test conditions of specimen temperature, sodium velocity, and loop ΔT, and then allowed to come to thermal equilibrium overnight. During all the pretest operation of the system, the MTS machine is in the load-control mode maintaining a zero load on the test specimen. Immediately prior to initiating a test, the machine is transferred to the strain-limit stroke control mode.

Measurement and Control

The important specimen parameters measured during tests are stress, strain, and number of strain cycles completed. Cycles are automatically counted and load continuously monitored using a 455 kg load cell mounted between the actuator drive shaft and the pull-bar shaft. Due to the test environment of liquid sodium at 593°C, the strain is indirectly determined through the combination of an LVDT (Linear Variable Differential Transformer) measurement and predetermined calibration data.

The calibration data are based on the behavior of the system at test conditions using an hourglass "zero gauge" calibration specimen in place of an actual test specimen. (See Figure 4).

During testing, the LVDT, mounted on top of the actuator, measures the total actuator stroke which includes the strain of all components subjected to loading including the test section itself. The test section strain must, however, be isolated from the total stroke to make the measurement useful. The following general equation can be written describing the system:

$$S = D + \epsilon$$

where:  
 S = total stroke  
 D = load train deflection  
 ε = test section strain

Since total stroke is the LVDT measurement, load train deflection must be determined as a function of load to make use of the above equation. This is accomplished using the hourglass calibration specimen, a "zero gauge" specimen, in place of the normal gauge length specimen. This assembly is set up exactly like a normal test assembly in sodium at the temperature of interest, to determine the load/stroke behavior of the "system minus gauge length" (load train deflection). The load train deflection versus load function has been found to remain constant from test to test as long as the environmental conditions are not changed. This is due to the nearly elastic nature of all strains outside the test section of the sample. The function not only remains constant, but also very nearly linear, an observation that is put to use by the MTS control electronics to provide for constant strain amplitude control. The functional relationship of load train deflection to load can be written in the form of the equation:

$$D = CL \tag{2}$$

where:  
 L = load  
 C = a constant

This equation, when combined with equation (1) above, gives the following:

$$\epsilon = S - CL \tag{3}$$

The MTS electronics provide a direct readout of test section strain by continuously solving this last equation. Inputs of total stroke from the LVDT and load from the load cell are combined with the value of "C", determined from earlier zero gauge calibration specimen testing, to produce the actual strain signal for the gauge section.

The strain signal produced by the method described above is used to control the limits of actuator travel and maintain constant strain amplitude during tests. The strain signal controls the limits of stroke, but actuator movement is in the stroke control mode for all other portions of the cycle. The stroke is controlled to produce a triangular wave form with zero mean strain, and the frequency adjusted to yield and average strain rate of  $4 \times 10^{-3} \text{ sec}^{-1}$ . The test section strain waveform itself deviates from a true triangular shape due to the non-linear stress/strain behavior of the material, as would be expected with the large plastic strains imposed.

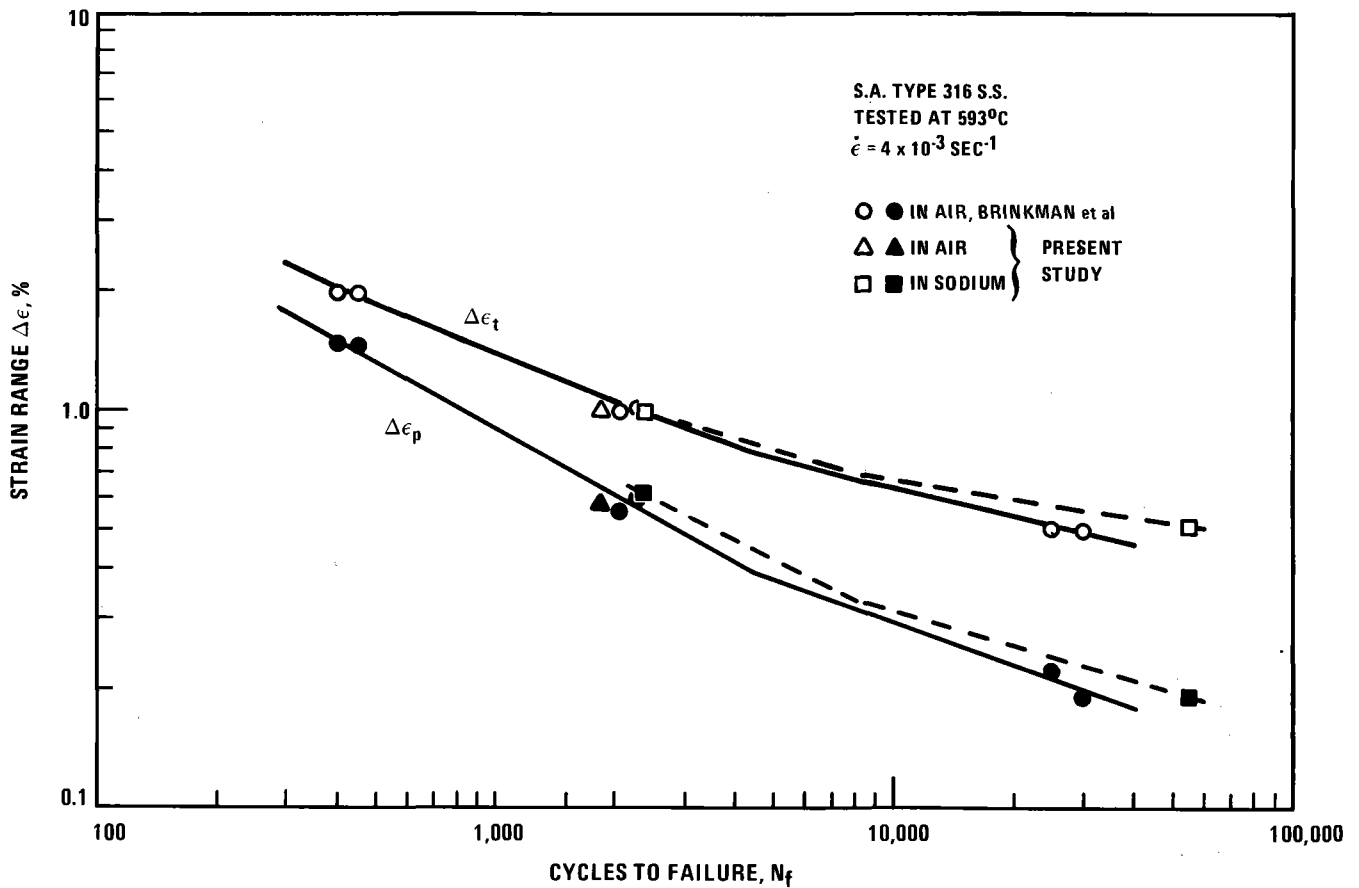


Figure 5. Comparison of low cycle fatigue results for S.A. Type 316 S.S. tested at 593°C in-air and in sodium

Although results are not presented, creep/fatigue interaction tests were also run with the control waveform modified to provide for hold-time in tension only. Here again, constant strain limit control was used, with control reverting back to the actuator total stroke once the preset limits were reached. This allowed for some amount of stress relaxation due to creep during the tensile hold times, with both being constantly monitored through the load and test section strain signals.

Verification of the testing technique comes primarily from correlation of results with those of published reports. Because of the scarcity of published in-sodium fatigue test results, an in-air test was conducted using the technique developed for the in-sodium testing. The air environment was established by sealing the test section of a specimen assembly inside a stainless steel bellows fitted with stainless steel tubing to provide a constant flow of fresh air. The test chamber was filled with sodium to the normal level for testing and the temperature brought to 593°C. The entire specimen assembly including the bellows was, therefore, immersed in an isothermal pool of sodium at the test temperature and the test conducted in the usual manner. Air flow to the bellows was maintained at a very low rate and the internal bellows pressure adjusted to be slightly less than the cover gas pressure of the test chamber.

FATIGUE RESULTS FOR TYPE 316 SS

Initial low cycle fatigue results, obtained from the system described above, involved solution annealed Type 316 stainless steel rod material. The 2.54 cm diameter material was cut in 15 cm long pieces, solution annealed at 1060°C for one half hour and then rapidly cooled. Test specimens were then machined into the configuration shown in Figure 4. Chemical composition of the material is given in Table 1.

Table 1  
Composition of Type 316 Stainless Steel from Heat 53835

Element	Concentration wt%	Element	Concentration wt%
Cr	17.5	Cu	0.21
Ni	12.1	Co	0.12
Mo	2.29	C	0.065
Mn	1.50	P	0.032
Si	0.33	S	0.024



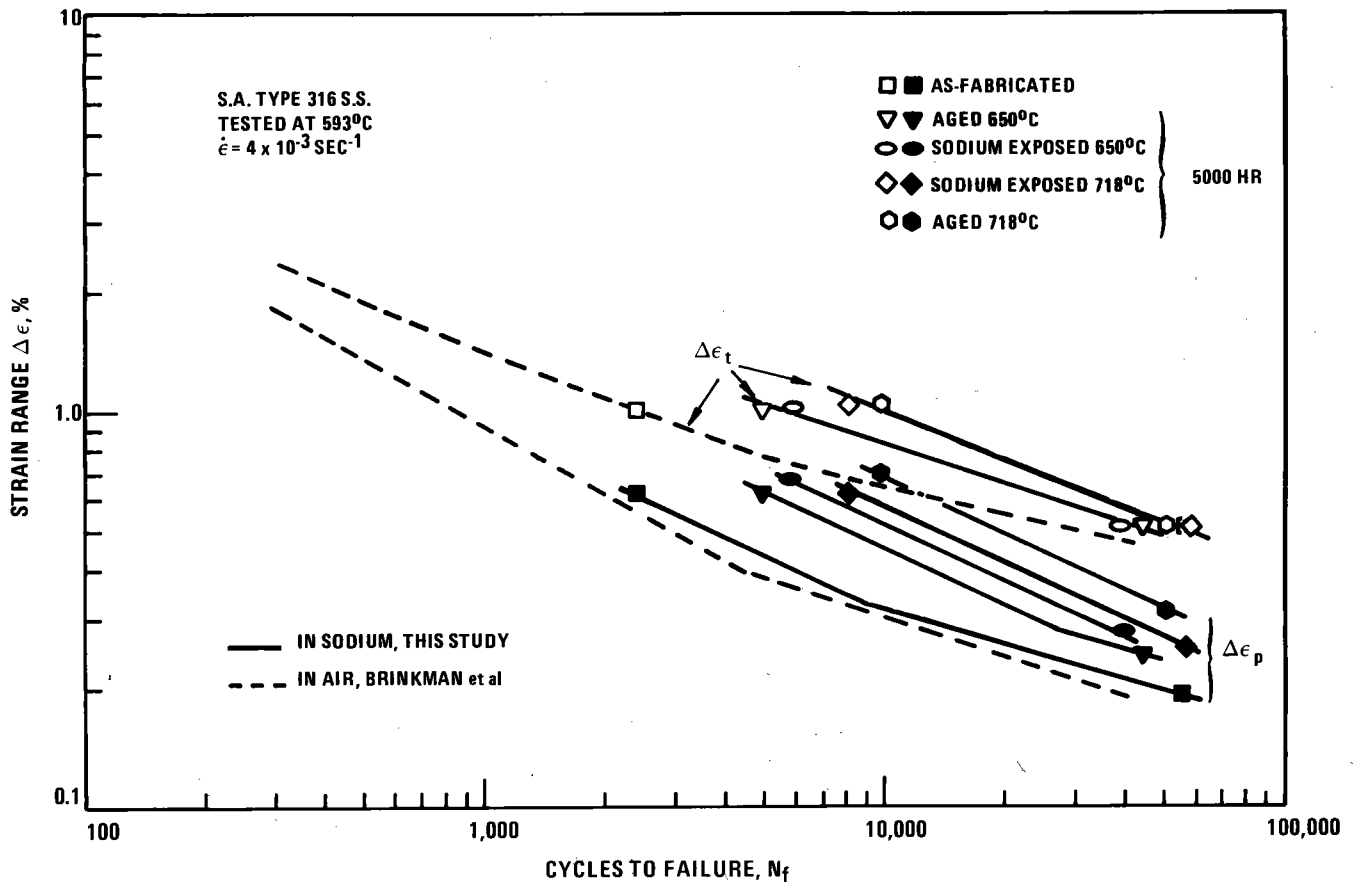


Figure 6. Fatigue results for S.A. Type 316 S.S. obtained in-sodium for aged and sodium exposed material

Some specimens were tested in the "as-fabricated" condition, and others tested after receiving one of four different pre-treatments, all performed for 5,000 hours. The first pre-treatment involved argon aging at 650°C and the second, argon aging at 718°C. The third and fourth pre-treatments involved sodium exposure in a loop at 650 and 718°C respectively. With a number of specimens located in the "hot-legs" of the exposure loop, the "cold-leg" was maintained at 550°C, with a controlled sodium velocity of 1.0 meter per second past the test specimen gauge section. The loop sodium was continuously cold trapped, and the oxygen concentration measured to be between 5 and 10 ppm based on the amalgamation technique. Carbon concentration in the sodium was determined to be 0.1 ppm based on the exposure of Type 18-8 stainless steel foil to the sodium.

Low cycle fatigue tests were performed at 593°C sodium for the Type 316 stainless steel specimens in the various conditions described above. Figure 5 compares the results of two specimens in the as-fabricated condition tested in sodium, to data reported in the literature obtained in air at 593°C<sup>(7)</sup>. The slope changes for the plastic strain range curves was assumed to occur at the transition fatigue life ( $N_T$ ). The 1% total strain range test indicates no difference in the fatigue life between tests in air or sodium. This is probably due to the relatively short test time (~ 2.5 hours) for the strain range and strain rate involved. To

insure that the results were not biased by the fact that material from different heats are being compared, a test specimen from heat 53835 was also tested in air at a total strain range of 1%, using loop sodium as the heat source as described earlier. The fatigue life obtained in air is in good agreement with the results of Brinkman et al obtained in air as well as the in-sodium result. The in-sodium test for as-fabricated material at a total strain range of 0.5% indicates a possible increase in fatigue life by a factor of two when compared to the in-air results. The in-air tests involve approximately 19 hours for failure, indicating that the fatigue life in air at 593°C is decreased when compared to tests in sodium as the time of testing increases. This appears reasonable since the oxidation effect on the fatigue life of Type 316 stainless steel at 593°C in air should increase as the time at temperature increases.

Figure 6 presents the low cycle fatigue results for the aged and sodium-exposed Type 316 stainless steel (Heat 53835) tested in 593°C sodium at total strain ranges of 1% and 0.5%. Also shown in the figure are the data for the as-fabricated specimens tested in sodium and the in-air curves representing the data of Brinkman et al. The results show that at a total strain range of 1%, pre-treatment at 650°C (in argon or sodium) for 5,000 hours increases the fatigue life by a factor of two, and pre-treatment at 718°C (in argon or sodium) increases the fatigue life by a factor of four. Apparently this is mainly the result of microstructural

changes in the material due to aging. Creep-Rupture tests of the same material at 593°C, presently in progress, show a significant increase in minimum creep rate and elongation at rupture for the pre-treated material. The decrease in strength and increase in ductility apparently contribute to the increase in low cycle fatigue life at the higher strain ranges. Results of the fatigue tests in sodium at a total strain range of 0.5% are not as clear since all the data are within plus and minus 20% of the average fatigue life, including the as-fabricated specimen. A significant difference is shown in the plastic strain range values for the different pre-treatments and their consistent correlation with the values obtained for the 1% strain range tests. The plastic strain range curves are essentially parallel and have a slope of approximately -0.5, consistent with the Coffin-Manson Equation and exponent. The plastic strain range curves also indicate that the transition fatigue life,  $N_T$ , (intersection of the plastic and elastic strain range curves) occurs at increasingly higher cycles as the pre-treatment temperature increases (for 5,000 hours). This increase is not as great for the sodium exposed material as it is for the argon aged material, indicating a possible degradation at the higher temperature in sodium.

#### SUMMARY

A technique developed to obtain low-cycle fatigue data at elevated temperatures in a flowing sodium environment with controlled purity is described. The system components, interaction, and operation are described, along with the calibration, measurement and control technique for constant strain amplitude testing.

The fatigue life for solution annealed Type 316 stainless steel at 593°C in sodium (containing 2 ppm oxygen and 0.1 ppm carbon) is essentially the same as that obtained in air when tested at the same conditions of  $\Delta\epsilon_t = 1\%$  and  $\dot{\epsilon} = 4 \times 10^{-3} \text{ sec}^{-1}$ . At a total strain range of 0.5% the fatigue life in sodium is approximately a factor of two greater. The greater time-at-temperature for the tests at lower strain ranges apparently decreases the fatigue life in air, due to increased oxidation.

The fatigue life of solution annealed Type 316 stainless steel at 593°C in sodium is increased at a strain range of 1% by thermal aging or pre-exposure to sodium for 5,000 hours. Pre-treatment at 650°C enhances the fatigue life by a factor of two, and pre-treatments at 718°C increases the fatigue life by a factor of four. At a total strain range of 0.5%, the fatigue life for all pre-treatments tested in sodium are within  $\pm 20\%$  of the average, including the as-fabricated material.

#### ACKNOWLEDGEMENTS

The authors wish to thank S. L. Schrock for his helpful comments and review of the manuscript and R. A. O'Shell for his assistance in constructing the equipment and performing the tests.

The work was sponsored by the U. S. Energy Research and Development Administration.

#### REFERENCES

1. Coffin, L. F., "Fatigue at High Temperature," *Fatigue at Elevated Temperatures*, ASTM-STP-520, American Society for Testing and Materials, 1973, pp. 5-34.
2. Gall, M., and Leverant, G. R., "Mechanisms of High-Temperature Fatigue," *Fatigue at Elevated Temperatures*, ASTM-STP-520, American Society for Testing and Materials, 1973, pp. 37-66.
3. Soloman, H. D., and Coffin, L. F., "Effects of Frequency and Environment on Fatigue Crack Growth of A286 at 1100°F," *Fatigue at Elevated Temperatures*, ASTM-STP-520, American Society for Testing and Materials, 1973, pp. 112-122.
4. Snyder, R. B., Natesan, K., and Kassner, T. F., "Kinetics of the Carburization-Decarburization Process of Austenitic Stainless Steels in Sodium," *J. Nucl. Mater.* Vol. 50, 1974, pp. 259-274.
5. Goodell, P. D., Cullan, T. M., Freeman, J. W., "The Influence of Nitrogen and Certain Other Elements on the Creep-Rupture Properties of Wholly Austenitic Type 304 Steel," *Trans. ASME, J. Basic Eng.*, 1967, pp. 517-524.
6. Charnock, W., et al, "Effect of High Carbon Activity Sodium Upon the Mechanical Properties of AISI 316 Stainless Steel," *The Metals Society, Physical Metallurgy of Reactor Fuel Elements*, 1975, pp. 37-46.
7. Brinkman, C. R., Korth, G. E., and Hobbins, R. R., "Estimates of Creep-Fatigue Interaction in Irradiated and Unirradiated Austenitic Stainless Steel," *Nucl. Tech.* Vol. 16, 1972, pp. 297-307.

# INTERNATIONAL CONFERENCE ON LIQUID METAL TECHNOLOGY IN ENERGY PRODUCTION

## INFLUENCE OF SODIUM ON THE LOW-CYCLE FATIGUE BEHAVIOR OF TYPES 304 AND 316 STAINLESS STEEL

by

D. L. Smith, G. J. Zeman, K. Natesan, and T. F. Kassner

Materials Science Division  
ARGONNE NATIONAL LABORATORY  
Argonne, Illinois 60439

### ABSTRACT

Fatigue tests in sodium were conducted to investigate the influence of a high-temperature sodium environment on the low-cycle fatigue behavior of Types 304 and 316 stainless steel. The effects of testing in a sodium environment as well as long-term sodium exposure were investigated. The fatigue tests were conducted at 600 and 700°C in sodium of controlled purity, viz., ~1 ppm oxygen and 0.4 ppm carbon, at a strain rate of  $4 \times 10^{-3} \text{ s}^{-1}$ . The fatigue life of annealed Type 316 stainless steel is substantially greater in sodium than when tested in air; however, the fatigue life of annealed Type 304 stainless steel is altered much less when tested in sodium. A 1512-h preexposure to sodium had no significant effect on the fatigue life of Type 316 stainless steel tested in sodium. However, a similar exposure substantially increased the fatigue life of Type 304 stainless steel in sodium.

### INTRODUCTION

The austenitic stainless steels are of interest as containment and structural materials in the Liquid-Metal Fast-Breeder Reactor (LMFBR). For these applications, much of the stainless steel in contact with sodium at elevated temperatures will be subjected to a variety of stress conditions that can limit its performance. Although extensive fatigue data in support of the LMFBR program have been obtained in air at room and elevated temperatures<sup>(1-4)</sup>, little data exist for the effects of the sodium environment on the fatigue behavior of austenitic stainless steels.

It has been shown that the testing environment can have a significant effect on the elevated-temperature fatigue life and fatigue-crack propagation rate of certain materials<sup>(5-10)</sup>. Typically these data have been obtained from tests in air, argon, or vacuum, and the enhanced crack-growth rates of specimens tested in oxidizing environments have been attributed to "wedging" caused by oxides that formed at the crack tip. The oxygen potential in reactor sodium is much lower than the oxygen potentials of other typical test

environments and no oxides will form on stainless steel in sodium. Therefore, enhanced crack-growth rates caused by an oxide "wedging" effect are not expected for stainless steel tested in a sodium environment. However, carbon is known to migrate in stainless steel-sodium heat-transport systems as a result of chemical activity gradients produced by both temperature and compositional differences. Data in the literature indicate that the mechanical properties of austenitic stainless steels are strongly dependent on the carbon concentration<sup>(11-14)</sup>. The problem is further complicated since, under most conditions, carbon concentration gradients will be established in the stainless steel during the lifetime of the components. Crack initiation and propagation in the material may be influenced by the sodium environment as well as the carburization and thermal aging that occur during long-term exposure of the steels.

The purpose of the present investigation is to determine the effects of a high-temperature sodium environment on the low-cycle fatigue behavior of AISI Types 304 and 316 stainless steel under conditions pertinent to LMFBR applications. Data obtained at one strain rate under slightly carburizing conditions are presented.

### EXPERIMENTAL PROCEDURE

The facilities for fatigue testing in sodium (FFTS), which consist of 20-kip MTS closed-loop servo-controlled hydraulically-actuated fatigue machines with associated sodium loops, have been described previously<sup>(15)</sup>. The recirculating sodium loops provide a well-characterized sodium environment for fatigue testing at temperatures to 750°C. The specimens are inserted into the fatigue fixture, which is then lowered into the sodium test vessel at the selected temperature. The sodium is continuously circulated during this period to maintain the desired sodium purity.

The specimen stress is determined by a fatigue-rated load cell attached to the actuator. Since direct measurement of the specimen strain in the sodium en-

INTERNATIONAL CONFERENCE ON LIQUID METAL TECHNOLOGY IN ENERGY PRODUCTION

RESULTS AND DISCUSSION

vironment was not considered feasible, the tests were conducted in a stroke-control mode by means of a standard resistive-type extensometer located on the upper portion of the fixture in an ambient temperature region. The extensometer measures the sum of the elongation in the fixture, the specimen gauge section, and the transition region of the specimen. Hourglass specimens with identical geometry, except for the gauge section, were used as a reference to determine the amount of elongation in the fixture and the transition region of the specimens as a function of load at each test temperature. The measured displacement obtained with an hourglass specimen was subtracted from the measured displacement of a test specimen under identical loading conditions to determine the strain in the gauge section of the test specimens. The fatigue tests were conducted at a strain rate of  $4 \times 10^{-3} \text{ s}^{-1}$  with a fully-reversed triangular waveform and a zero mean strain.

The compositions of the Types 304 and 316 stainless steel, identified as heats 9T2796 and V87210, are given in Table I. The fatigue test specimens with a 0.508-cm-dia by 1.27-cm-gauge length were fabricated from 1.6-cm-dia rods that had been solution annealed for 30 min in argon at 1025°C and water quenched. These samples are referred to hereafter as the annealed condition. A number of these specimens have been exposed to recirculating sodium at temperatures of 600 and 700°C for periods of 1512 and 5012 h in a sodium exposure loop, which has been described previously<sup>(14)</sup>. The oxygen concentration in sodium during these exposures was 1.0 ppm and the carbon concentration in sodium was maintained at 0.4 ppm. The carbon concentrations in the two steels were not altered significantly by the exposures at 700°C since the initial carbon levels were almost in equilibrium with sodium containing ~0.4 ppm carbon. After the 1512-h exposure at 600°C, the carbon profile in the Types 304 and 316 stainless steel varied from 0.3 and 0.4 wt%, respectively, at the surface to the initial concentration in the steels at a depth of 0.01 cm. The 5012-h exposures at 600°C produced a profile depth of 0.02 cm.

The low-cycle fatigue data on Types 316 and 304 stainless steel in sodium are listed in Tables II and III. Values for the total strain range  $\Delta\epsilon_t$ , plastic

Table II. Low-Cycle Fatigue Data on Type 316 Stainless Steel Obtained in a Sodium Environment.

Specimen No.	Matl. Condition*	Temp., °C	$\Delta\epsilon_t$ (%)	$\Delta\epsilon_p$ (%)	$\Delta\sigma_{\frac{1}{2}N_f}$ (MPa)	$N_f$ Cycles	$t_f$ min
C-67	1	600	1.65	1.11	686	1,017	172
C-74	1	"	1.50	0.91	676	1,874	248
C-57	1	"	1.10	0.63	599	7,738	648
C-59	1	"	1.10	0.60	599	6,411	538
C-52	1	"	1.08	0.61	601	8,232	699
C-54	1	"	1.08	0.59	602	7,826	665
C-55	1	"	1.06	0.60	605	6,878	579
C-56	1	"	0.77	0.37	512	26,917	1561
C-63	1	"	0.76	0.36	509	27,115	1571
C-72	1	"	0.69	0.31	471	57,170	2927
C-34	2	"	1.61	1.17	579	1,279	168
C-33	2	"	1.16	0.76	546	4,843	408
C-35	2	"	1.11	0.69	523	6,087	510
C-36	2	"	0.88	0.52	464	17,603	1021
C-37	2	"	0.81	0.44	436	36,250	2102
C-38	2	"	0.75	0.38	422	43,247	2212
C-71	1	700	1.36	0.94	464	1,835	237
C-69	1	"	0.94	0.59	437	5,777	482
C-68	1	"	0.81	0.46	424	13,690	911
C-73	1	"	0.77	0.40	398	23,065	1363
C-25	4	"	1.42	1.09	459	1,353	175
C-27	4	"	0.89	0.62	420	7,122	556
C-26	4	"	0.72	0.43	398	19,898	994
C-30	4	"	0.70	0.46	418	12,166	727

\*Conditions: (1) Solution annealed, (2) 1512 h in 600°C sodium, and (4) 1512 h in 700°C.

strain range  $\Delta\epsilon_p$ , cyclic stress range at half the fatigue life  $\Delta\sigma_{\frac{1}{2}N_f}$ , fatigue life  $N_f$ , and time to failure  $t_f$  are listed for the materials in the annealed and sodium exposed (~1500 and ~5000 h at 600°C and ~1500 h at 700°C) conditions. The relationship between total and plastic strain range and the fatigue life of annealed Types 316 and 304 stainless steels in sodium at 600°C is shown in Figs. 1 and 2, respectively. The dashed curves in both figures represent comparative data obtained in air for the two steels<sup>(2,3,16)</sup>. For Type 316 stainless steel at 600°C, the ratio of fatigue life in sodium to that in air increases by factors of

Table I. Compositions of Austenitic Stainless Steels

Material	Heat	Concentration, wt%											
		C	N	P	S	Cr	Ni	Mn	Si	Mo	Ti	Cu	Co
Type 304	9T2796	0.046	0.038	0.026	0.012	17.7	9.3	1.17	0.47	0.33	0.03	0.02	0.10
Type 316	V87210	0.058	0.007	0.026	0.011	16.7	13.9	1.43	0.46	2.84	0.04	0.06	0.03

INTERNATIONAL CONFERENCE ON LIQUID METAL TECHNOLOGY IN ENERGY PRODUCTION

Table III. Low-Cycle Fatigue Data on Type 304 Stainless Steel Obtained in a Sodium Environment.

Specimen No.	Matl. Condition*	Temp., °C	$\Delta\epsilon_t$ (%)	$\Delta\epsilon_p$ (%)	$\Delta\sigma_{1/2N_f}$ (MPa)	$N_f$ Cycles	$t_f$ min
A-61	1	600	1.86	1.43	602	418	71
A-93	1	"	1.48	1.02	597	624	85
A-65	1	"	1.38	0.83	495	1,275	109
A-63	1	"	1.33	0.82	515	1,152	98
A-96	1	"	1.05	0.59	544	1,975	202
A-71	1	"	0.95	0.56	481	1,950	123
A-92	1	"	0.82	0.49	497	4,293	363
A-91	1	"	0.80	0.43	468	7,066	605
A-77	1	"	0.72	0.44	513	2,563	220
A-73	1	"	0.70	0.38	433	5,856	349
A-70	1	"	0.52	0.23	353	30,628	1306
A-104	1	"	0.46	0.15	407	25,783	1320
A-10	2	"	1.67	1.19	595	545	74
A-14	2	"	1.36	0.93	535	2,402	246
A-08	2	"	1.24	0.73	471	3,649	312
A-09	2	"	1.01	0.55	460	8,015	678
A-15	2	"	0.69	0.38	411	31,036	1422
A-80	3	"	1.48	0.99	517	996	118
A-79	3	"	1.28	0.85	505	1,441	120
A-84	3	"	1.02	0.60	477	4,819	403
A-81	3	"	0.85	0.47	454	7,644	522
A-83	3	"	0.55	0.23	392	31,309	1555
A-74	1	700	1.72	1.34	463	368	47
A-106	1	"	1.02	0.68	430	1,321	136
A-105	1	"	0.91	0.52	406	2,024	171
A-97	1	"	0.52	0.24	377	13,282	773
A-68	4	"	1.16	0.81	410	1,303	119
A-61	4	"	0.99	0.62	379	3,463	343
A-85	4	"	0.65	0.36	384	6,533	380
A-87	4	"	0.53	0.24	355	21,123	1054

\*Conditions: (1) Solution annealed, (2) 1512 h in 600°C sodium, (3) 5012 h in 600°C sodium, and (4) 1512 h in 700°C sodium.

2 to 6 as the total strain range decreases from 1.5 to 0.7%, which indicates the environmental effect is more pronounced at the longer lifetimes. These observations are in qualitative agreement with elevated temperature crack-growth behavior of stainless steel in sodium and air<sup>(10)</sup>. However, the fatigue life of annealed Type 304 stainless steel in sodium at 600°C is essentially the same as that in air for total strain ranges from 0.5 to 1.0% and somewhat less than that in air at higher strain ranges (Fig. 2). Although no explanation for the difference in the environmental effect on the two steels can be given at this time, the microstructure and fracture surfaces are being analyzed in an attempt to rationalize this behavior.

Figures 3 and 4 show the effect of temperature on the fatigue life of the two steels tested in sodium. The fatigue life at 600°C is ~50% greater than that at 700°C for both materials, which is similar to the temperature dependence in an air environment.

The effect of long-term sodium exposure on the

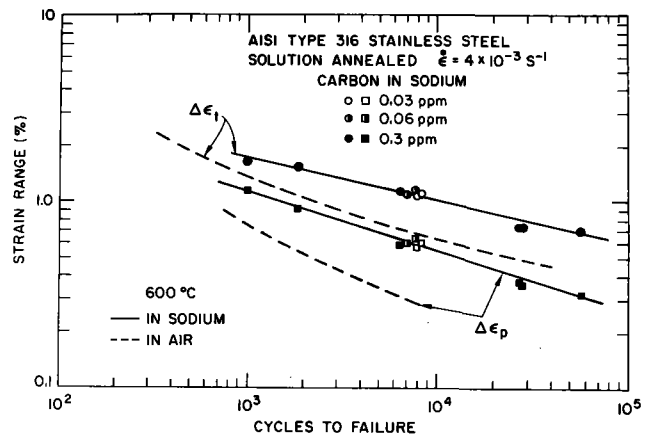


Fig. 1. Plot of Total and Plastic Strain Ranges Versus Cycles to Failure for Type 316 Stainless Steel Tested in Sodium and Air at 600°C.

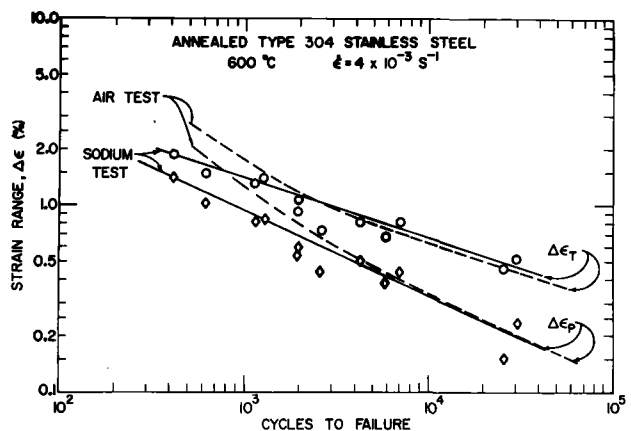


Fig. 2. Plot of Total and Plastic Strain Ranges Versus Cycles to Failure for Type 304 Stainless Steel Tested in Sodium and Air at 600°C.

fatigue life of the two steels is shown in Figs. 5 through 8. The fatigue life of Type 316 stainless steel, in Figs. 5 and 7, was not altered significantly by the 1512-h exposure at either 600 or 700°C for the strain ranges investigated. Since the 700°C exposure did not result in carburization or decarburization of the material, the specimens were essentially subjected to thermal aging. Cheng et al.<sup>(1)</sup> reported that aging of Type 316 stainless steel had little effect on fatigue life in air at 650°C, which may explain the results in Fig. 6. Carburization of the surface of the steel during the 600°C sodium exposure did not influence the life significantly; however, small increases in the plastic strain were observed for the preexposed specimens.

In contrast to the results for Type 316 stainless steel, preexposure to sodium increased the fatigue life

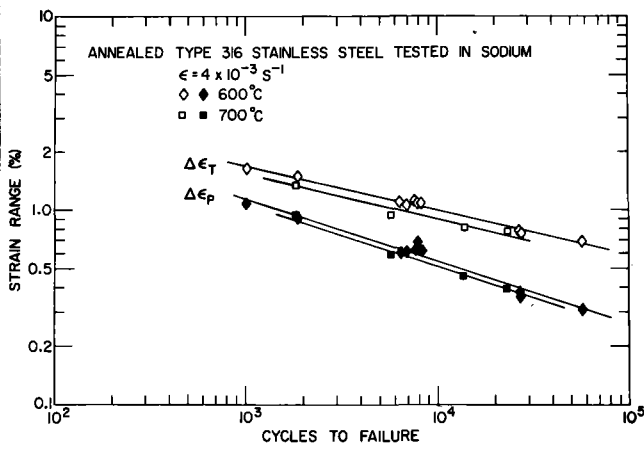


Fig. 3. Fatigue Data Obtained on Annealed Type 316 Stainless Steel Tested in Sodium at 600 and 700°C.

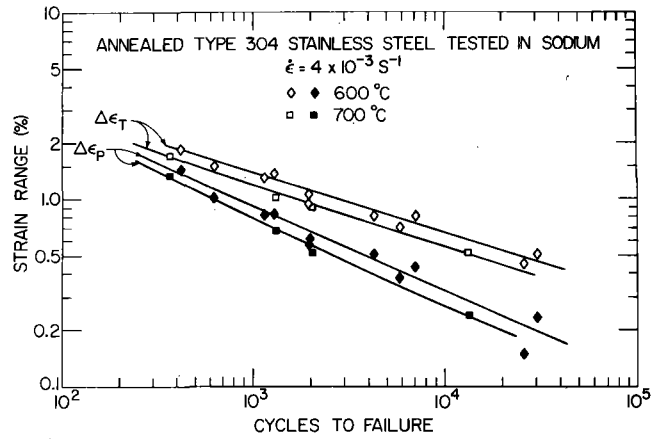


Fig. 4. Fatigue Data Obtained on Annealed Type 304 Stainless Steel Tested in Sodium at 600 and 700°C.

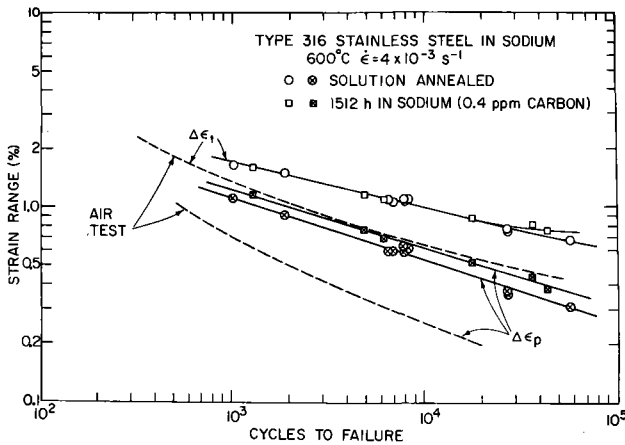


Fig. 5. Fatigue Data Obtained in Sodium at 600°C on Type 316 Stainless Steel in the Annealed and Sodium-exposed Conditions.

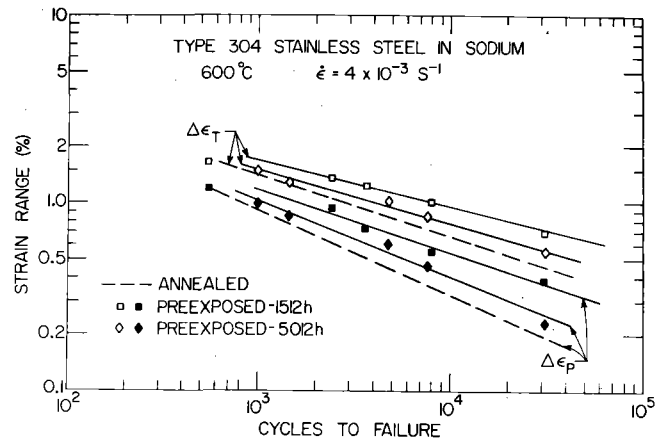


Fig. 6. Fatigue Data Obtained in Sodium at 600°C on Type 304 Stainless Steel in the Annealed and Sodium-exposed Conditions.

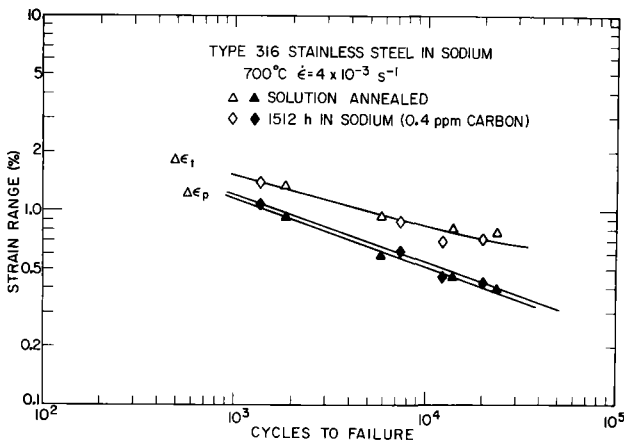


Fig. 7. Fatigue Data Obtained in Sodium at 700°C on Type 316 Stainless Steel in the Annealed and Sodium-exposed Conditions.

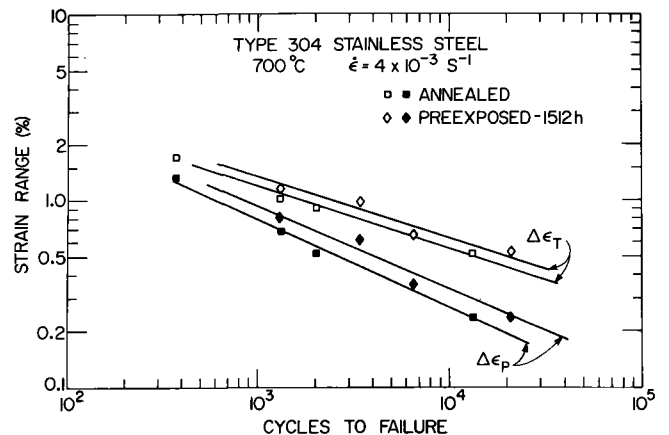


Fig. 8. Fatigue Data Obtained in Sodium at 700°C on Type 304 Stainless Steel in the Annealed and Sodium-exposed Conditions.

of Type 304 stainless steel at both 600 and 700°C (Figs. 6 and 8, respectively). As in the previous case, the 700°C exposure was primarily an aging process since the carbon concentration in the material remained constant. The modest increase in lifetime produced by exposure at 700°C, i.e., 30 to 50%, is in agreement with the effect of aging reported for Type 304 stainless steel<sup>(1,2)</sup>. The 1512-h sodium exposure at 600°C increased the fatigue life of Type 304 stainless steel by factors of 2 and 4 for total strain ranges of 1.4 and 0.7%, respectively. This increase is substantially greater than the 50% increase in fatigue lifetime for aged material tested in air<sup>(1,2)</sup>. Therefore, much of the increase can be attributed to the surface carburization of the material. The Type 304 stainless steel was also exposed to sodium for 5012 h at 600°C before testing in sodium. As indicated in Fig. 7, the fatigue lifetime decreases with an increase in the exposure time. This may be related to the greater depth of carburization that occurred during the longer exposure.

The cyclic stress-strain response of the two steels is shown in Figs. 9 and 10. The cyclic stresses for the annealed materials in sodium at 600°C are in agreement with the stresses obtained in air tests at the same temperature. In contrast to the data of Weeks et al.<sup>(2)</sup> for Type 316 stainless steel aged for 1000 h at 565°C and tested in air at this temperature, considerable softening of the Type 316 stainless steel occurred during the 1512-h exposure to sodium. At 700°C the stresses in preexposed Type 316 stainless

steel were only slightly lower than in the annealed material. Apparently substantial aging occurs at 700°C during exposure to sodium for the thermal equilibration period just before fatigue testing. This conclusion is also supported by the much lower strain-hardening exponent for the annealed material, i.e., 0.15 at 700°C in comparison with a value of 0.31 at 600°C. Sodium-exposed Type 304 stainless steel exhibited less softening than Type 316 stainless steel at 600°C, and only a slight reduction in the cyclic stress occurred in both materials after the 1512-h sodium exposure at 700°C.

SUMMARY

Types 304 and 316 stainless steel exhibit different low-cycle fatigue behavior in a sodium environment. At a total strain range of ~1% and a strain rate of  $4 \times 10^{-3} \text{ s}^{-1}$ , the fatigue life of annealed Type 316 stainless steel at 600°C was a factor of four greater in sodium than in air. Under similar conditions the fatigue life of annealed Type 304 stainless steel tested in sodium did not differ significantly from the reported lifetime in air. The fatigue lifetimes in sodium for both steels at 600°C were ~50% greater than their respective lifetimes at 700°C; similar to results obtained in an air environment. The fatigue lifetime of Type 316 SS tested in sodium was not influenced significantly by a 1512-h exposure to sodium at either temperature; however, a substantial increase in fatigue life of Type 304 stainless steel was produced by a 1512-h exposure to sodium at 600°C. A modest increase in fatigue life of Type 304 stainless steel resulted from

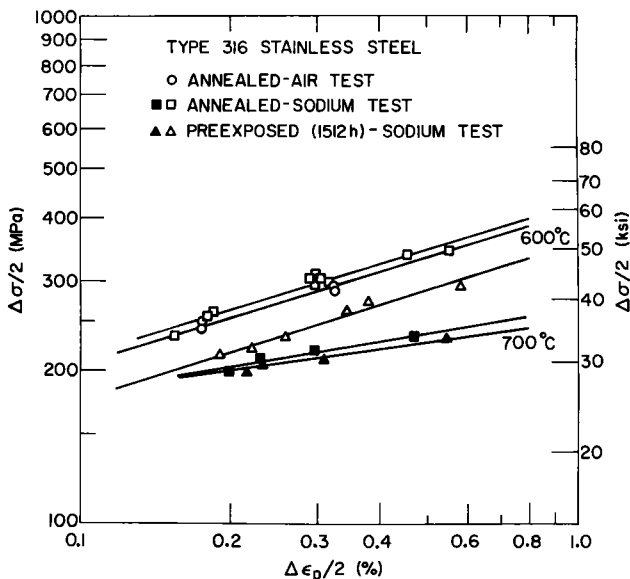


Fig. 9. Cyclic Stress-strain Response for Type 316 Stainless Steel Tested in Sodium at 600 and 700°C in the Annealed and Sodium-exposed Conditions.

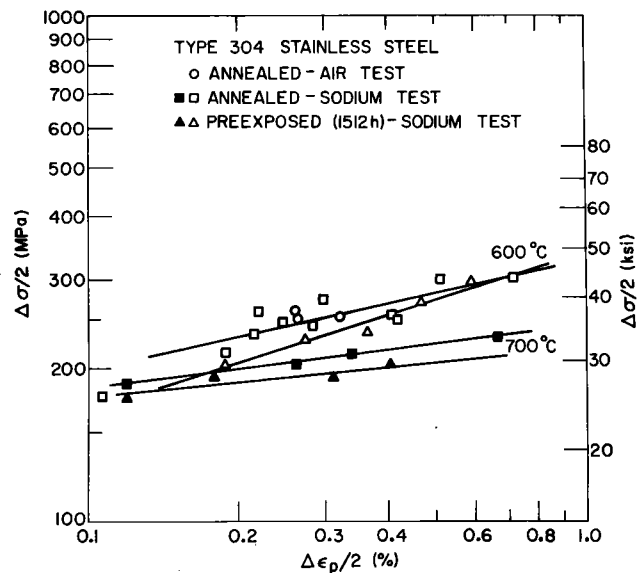


Fig. 10. Cyclic Stress-strain Response for Type 304 Stainless Steel Tested in Sodium at 600 and 700°C in the Annealed and Sodium-exposed Conditions.

## INTERNATIONAL CONFERENCE ON LIQUID METAL TECHNOLOGY IN ENERGY PRODUCTION

the 700°C exposure. Lower cyclic stresses were observed for both steels after the 600°C sodium exposure. The 700°C sodium exposure had almost no effect on the cyclic stress response. An increase in the exposure time of Type 304 stainless steel to sodium from ~1500 to 5000 h at 600°C reduced fatigue life.

### REFERENCES

1. C. F. Cheng, et al., "Low-cycle fatigue behavior of Types 304 and 316 stainless steel at LMFBR operating temperatures," Fatigue at Elevated Temperatures, ASTM-STP-520, American Society for Testing and Materials, 355 (1973).
2. R. W. Weeks, D. R. Diercks, and C. F. Cheng, "ANL low-cycle fatigue studies -- program, results, and analysis," Argonne National Laboratory, ANL-8009, (1973).
3. C. R. Brinkman, G. E. Korth, and R. R. Hobbins, "Estimates of creep-fatigue interaction in irradiated and unirradiated austenitic stainless steel," Nucl. Tech. 16, 297 (1972).
4. J. T. Berling and T. Slot, "Effect of temperature and strain rate on low-cycle fatigue resistance of AISI 304, 316, and 348 stainless steel," Fatigue at High Temperatures, ASTM-STP-459, American Society for Testing and Materials, 3 (1969).
5. M. Gall and G. R. Leverant, "Mechanisms of high-temperature fatigue," Fatigue at Elevated Temperatures, ASTM-STP-520, American Society for Testing and Materials, 37 (1973).
6. H. D. Soloman and L. F. Coffin, "Effects of frequency and environment on fatigue crack growth of A286 at 1100°F," Fatigue at Elevated Temperatures, ASTM-STP-520, American Society for Testing and Materials, 112 (1973).
7. L. F. Coffin, "Fatigue at high temperature," Fatigue at Elevated Temperatures, ASTM-STP-520, American Society for Testing and Materials, 5 (1973).
8. H. H. Smith, P. Shahinian, and M. R. Achter, "Fatigue crack growth rates in Type 316 stainless steel at elevated temperatures as a function of oxygen pressure," Trans. TMS-AIME 245, 947 (1969).
9. L. A. James and R. L. Knecht, "Fatigue-crack propagation behavior of Type 304 stainless steel in a liquid sodium environment," Met. Trans. 6, 109 (1975).
10. L. A. James, "Fatigue-crack propagation in austenitic stainless steels," to be published Atomic Energy Review 14, No. 1, (1976).
11. L. H. Kirschler, R. H. Hiltz, and S. J. Rodgers, "Effect of high temperature sodium on the mechanical properties of candidate alloys for the LMFBR program," MSA Research Corporation Report, MSAR-70-76, (1970).
12. A. Thorley, B. Longson, and J. Prescott, "Effects of exposure to sodium on the mechanical properties and structure of some ferritic, austenitic, and high nickel alloys," British TRG-Report-1909(c), Technical Research Group, (1969).
13. A. Thorley and C. Tyzack, "The carburization of stainless steels in sodium containing carbon impurities and its effect on mechanical properties," Effects of Environment on Material Properties in Nuclear Systems, Conference Proceedings, Brit. Nucl. Energy Soc., London (1971).
14. K. Natesan, et al., "Influence of sodium environment on the tensile behavior of austenitic stainless steels," ASME Symp. on Structural Materials for Service at Elevated Temperatures in Nuclear Power Generation, MPC-1, pp. 302-315 (1975).
15. D. L. Smith, et al., "Effects of sodium on the low-cycle fatigue behavior of austenitic stainless steel," ASME Symp. on Structural Materials for Service at Elevated Temperatures in Nuclear Power Generation, MPC-1, pp. 290-301 (1975).
16. C. R. Brinkman and G. E. Korth, "Heat-to-heat variations in the fatigue and creep-fatigue behavior of AISI Type 304 stainless steel at 593°C," J. Nucl. Mater. 48, 293 (1973).



# INTERNATIONAL CONFERENCE ON LIQUID METAL TECHNOLOGY IN ENERGY PRODUCTION

## DISCUSSION

Paper VA-1: "Materials Effects in LMFBR Sodium Systems"

K. Natesan: I understand that your testing program is based primarily on materials in an annealed condition. Have you made property determinations on specimens that have been exposed to sodium long enough to see microstructural and compositional changes?

H. Lorenz: Normally, solution annealed 304 stainless steel or ferritic alloys in the as received condition have been tested. Changes in microstructure during long-term tests have been observed.

P. Wu: Can you comment on the preferential deposition of  $^{54}\text{Mn}$  in the IHX and the preferential deposition of  $^{60}\text{Co}$  in the reactor vessel region?

H. Lorenz: To date, we have no special idea concerning the different deposition behavior of both isotopes. The interpretation of the test results is in progress.

J. Krankota: Were steam corrosion rates measured on 2-1/4 Cr-1 Mo under heat transfer?

H. Lorenz: The stabilized type 2-1/4 Cr-1 Mo steel was used as steam generator material in our 5-MW test facility. However, special investigations concerning heat transfer influence on corrosion behavior have not been performed at Interatom.

W. Brehm: How serious is a swelling gradient in the cladding, compared to the other stress sources? Certain elements that affect swelling, such as silicon, will be leached preferentially by the sodium from the outer 20 $\mu\text{m}$  of cladding, creating a Si gradient and a possible swelling gradient.

H. Lorenz: I have not observed the effect you describe, and instead attribute swelling gradients to variations in diametral walls with different heat flux.

Paper VA-2: "The Effect of Liquid Sodium Thermo-Chemical Reactions with Stainless Steels on Mechanical Response"

C. Brinkman: Can you experimentally verify your model?

G. Subbaraman: The model requires no "verification" because we are treating a system of mathematically linear equations that have unique solutions. However, we do need experimental values of the elastic constants through-the-thickness to obtain the actual stress distributions. Further, the model forms a simple basis from which we can develop problems, including variations in other directions such as  $\theta$  and  $Z$ . In such cases, the equations will be solved numerically and analytical, and closed form solutions can be used as validity checks. The expression for  $f(r)$  can be expanded binomially and truncated to a polynomial. If elastic parameter variations are supplied as a polynomial, the model is sufficient to describe the response behavior accurately.

Paper VA-3: "The Influence of Sodium Corrosion on the

Mechanical Properties of Fuel Element Cladding Tubes"

T. Galloto: How was the reported material loss of 17 $\mu\text{m}$  determined for one material investigated at 600°C?

H. Borgstedt: The individual specimen that lost 17 $\mu\text{m}$  of wall thickness was exposed at 700°C. Wall thickness losses have been calculated from weight losses without corrections for elemental leaching. Calculated results have been used to evaluate the exact diameter growth of the pressurized tubes.

K. Schaller: Why did you choose test conditions that were more severe than expected reactor conditions for your experiments?

H. Borgstedt: The choice of 700°C was made as the closest approximation to the hot spot temperature of the clad. Oxygen content for SNR 3 or as specified to < 10 ppm; our range of 3.5 to 9 ppm corresponds to that limit.

Paper VA-4: "Effect of Sodium on the Creep Rupture Behavior of Type 304 Stainless Steel"

J. Krankota: At what %C does increase in strength caused by increasing carbon become detrimental in terms of strain limitations that may become as low as present allowable strain limits, 1-5%?

K. Natesan: We have not determined the carbon level at which the strain values will be less than the allowable design values for austenitic stainless steels. However, we don't anticipate carbon concentrations in reactor sodium to exceed 0.5 ppm; under these conditions, stainless steels would not carbonize sufficiently to reduce the strain values below 15 to 20%.

I. Levy: What differences in resultant mechanical properties would you expect from your testing after exposure in sodium rather than conducting the testing in sodium?

K. Natesan: Failure under creep loading occurs by formation and subsequent coalescence of cavities in the bulk of the specimen and will be controlled primarily by the material properties rather than the test environment. Furthermore, the creep behavior of austenitic stainless steels is essentially the same in sodium, helium and argon. Therefore, our program objective is to evaluate creep properties of the steels as affected by sodium exposure prior to creep testing.

G. Subbaraman: In calculating the composition profiles using your diffusion model for the interstitial elements, do you use bulk diffusion rates or different rates through the lattice and the grain boundaries for the low temperature cases?

K. Natesan: Tracer diffusion coefficients for carbon were employed for all calculations. No enhanced grain boundary diffusion of carbon in the temperature range 600 to 700°C was observed throughout investigation. Tests are presently being conducted at lower temper-

## INTERNATIONAL CONFERENCE ON LIQUID METAL TECHNOLOGY IN ENERGY PRODUCTION

atures, and specimens from these will be examined by metallography.

R. Pape: Were the effects of possible carbon transport via the argon atmosphere during the creep tests considered in your analysis?

K. Natesan: Negligible carbon transport resulted during creep testing in a purified argon environment under static conditions. Carbon analyses on the sodium-exposed specimens were conducted before and after creep testing and showed no significant variation.

P. Flagella: How was the ductility affected by the carburization, and did the change occur primarily in the third stage of creep?

K. Natesan: Carburization affected minimal change in the total creep ductility. In both the solution-annealed and sodium-exposed specimens, almost half the total elongation occurs in the tertiary stage of the creep process.

P. Flagella: Since carburization of the surface will affect the strength and ductility of the material in proportion to the cross-sectional area, what size were the samples tested?

K. Natesan: Specimen thickness for the data in this paper is 375  $\mu\text{m}$  (15 mils).

Paper VA-5: "Influence of Dynamic Sodium on the Creep Properties of Stabilized Austenitic Steels"

H. Borgstedt: Considering both your results and those presented earlier, interference of corrosion and creep is apparent. Would you therefore conclude that the 1-hour sodium creep test would yield more realistic results than the creep test conducted after sodium exposure?

F. Casteels: Testing materials in dynamic sodium is advantageous to creep testing sodium-corroded specimens under vacuum in that some creep parameters and the fracture mode can be influenced by the combined effect of stress and sodium environment. This conclusion was experimentally proven by the obvious influence of sodium on the crack nucleation and growth on slide bands. Transferring corroded specimens from the sodium loop to the testing facility can cause damage to the creep specimens through interaction of the residual sodium with ferrite or martensite phase in the subsurface layer of the specimen.

Paper VA-6: "Low Cycle Fatigue Testing in Flowing Sodium at Elevated Temperatures"

R. Pape: What are the typical time durations of the tests you describe?

J. Kahrs: Time duration of each test can be calculated from the strain rate, strain range and cycles to failure data, and in this case ranged from approximately 2.5 to 40 hours.

H. Borgstedt: What is the flow velocity at the surface of the specimens?

J. Kahrs: Average flow velocity past the specimen gauge length is approximately 1 m/s, calculated from the measurement of mass flow rate and the area of the flow channel for the length of specimen gauge.

I. Levy: Was the carbon content of sodium in the specimen preexposure the same as the test loop carbon content?

J. Kahrs: Yes, carbon content of sodium in the pre-exposure loop was measured to be essentially the same as that in the test loop (0.1 ppm carbon). The value for both systems was determined from exposure of Fe-18 Cr - 8 Ni foil to the sodium at 700°C for 72 hours, followed by analysis.

K. Natesan: How was the carbon concentration of 0.1 ppm measured?

J. Kahrs: Carbon concentration in the sodium was measured by exposing 18-8 stainless steel foils to the sodium flow and analyzing them for carbon content. Exposure was set at 700°C for 72 hours in the Vanadium Wire Equilibration Device of the sodium loop.

K. Natesan: Have you analyzed the preexposed fatigue specimens (exposed at 650°C and 700°C sodium) to evaluate the carbon gradients?

J. Kahrs: These analyses have not yet been performed.

B. Vegter: In your opinion, does the comparison of your results with Brinkman's show no apparent effect of sodium on low cycle fatigue?

J. Kahrs: Analysis of as-fabricated material reveals no effect of a liquid sodium environment at a total strain range of 1.0 percent. At the lower strain range of 0.5 percent, fatigue life appears to increase by a factor of two. Comparison of plastic strain range data for specimens pretreated at 718°C, indicates a decrease in fatigue life for the sodium-exposed material.

Paper VA-7: "Influence of Sodium on the Low-Cycle Fatigue Behavior of Types 304 and 316 Stainless Steel"

R. Pape: Have crack propagation rates been predicted from well-known effects of sodium exposure on mechanical properties at plain surfaces? Such an evaluation might show that, if diffusion of alloying elements in steel is significant, exposure times utilized in analysis of crack propagation in sodium are insufficient for the manifestation of these effects. Thus, the behavior might be expected to be similar to that in inert environments in short-term tests.

D. Smith: Exposure times during fatigue testing at a strain rate of  $4 \times 10^{-3} \text{ s}^{-1}$  are brief relative to those for significant diffusion of alloying elements in steel. However, the preexposures to sodium provide some insight into long-term diffusion effects and microstructural changes occurring in steel during reactor operation. Additional fatigue tests with hold times and tests at

## INTERNATIONAL CONFERENCE ON LIQUID METAL TECHNOLOGY IN ENERGY PRODUCTION

much lower strain rates are being conducted in sodium to differentiate between creep-fatigue interaction and environmental effects.

P. Flagella: Although high temperature low cycle fatigue design curves for 304 and 316 stainless steel in air are the same, you cite differences in fatigue life after testing both at the same conditions in sodium. Do you know the reason for the difference?

D. Smith: Currently, fracture surface and microstructural examinations of test specimens are being conducted in an attempt to explain the differing results of 304 and 316 stainless steel under testing in sodium.

C. Brinkman: What have been your observations concerning the mode of crack propagation?

D. Smith: For the conditions investigated to date, the mode of failure has been transgranular. A photomicrograph showing a surface crack typical of those observed is given in Reference 15 of this paper.

# INTERNATIONAL CONFERENCE ON LIQUID METAL TECHNOLOGY IN ENERGY PRODUCTION

## CORROSION, TRANSPORT AND DEPOSITION OF STAINLESS STEEL IN LIQUID SODIUM

B.H. Kolster

Metaalinstituut TNO  
Apeldoorn  
The Netherlands

L. Bos

### ABSTRACT

With a nonisothermal multi purpose sodium loop system experiments have been carried out to reveal the influence of oxygen level, flow velocity, temperature and downstream position on corrosion of and deposition on stainless steel AISI 316 specimens. The exposed specimens have been characterised by means of weight change and metallographic appearance. A different mechanism of Cr-transport can be distinguished at low and high oxygen concentration. The activation energy for the steady state corrosion at low oxygen level is 40 kcal/mol. With Reynolds no. in excess of 50,000 no influence of flow velocity on corrosion has been observed. The same holds for deposition in a nonisothermal circuit, but not under isothermal conditions, for which an explanation is given. Magnetic measurements revealed that downstream effects are mainly caused by ferritisation.

### INTRODUCTION

An important objective with regard to sodium corrosion and mass transport of steel is the accurate determination of their dependence on the relevant parameters and the understanding the mechanisms underlying these relationships. In the literature the available evidence is rather diverse. In particular with respect to the main parameters, oxygen level of the sodium, temperature, sodium flow velocity and downstream effect, experimental results and interpretations are not always in agreement, probably because of the different circuit parameters. Realizing that the TNO loop system suffers the same problem we have one definite advantage. That is, for each experiment not only corrosion but deposition has been studied extensively, in our opinion an important combination of data in view of a better understanding of the mass transport mechanism. The influence of downstream position and temperature on corrosion and deposition has been investigated for each run separately. The influence of oxygen level at the same flow velocity of about 6 m/s has been determined at 6 different oxygen levels. The most accurate values of the oxygen concentration have been determined by a thorough evaluation of all the data available. With regard to the sodium flow velocity care has been taken to keep all conditions identical, except the flow velocity.

The results published till now mainly concerned the metallographic examinations of the exposed specimens (1, 2, 3). This paper deals with the weight change and some metallographic results not yet published, resulting in a tentative explanation for the corrosion behaviour of stainless steel and for the mass transport of steel elements, in particular Fe and Cr.

### EXPERIMENTAL

#### Preparation and handling of specimens

The exposed material is an AISI 316 type with specified composition: Fe/0,055 wt.% C/17.0 wt.% Cr/11.2 wt.% Ni/2.78 wt.% Mo/0.42 wt.% Si/1.56 wt.% Mn. The required specimens of 33.33 x 9.8 x (1.95-2.00)mm have been prepared by the following procedure: sawing - annealing at 1050°C and subsequent quenching - milling - grinding - coding - scouring (600 Emery paper) and po-

lishing (6 µm diamant and 1 µm alumina, respectively). Prior to inserting the specimens into the specimenholders they were cleaned and weighed. After exposure and dumping the sodium, the remaining sodium was distilled off for 6 hours at 450°C. Subsequently the specimens were dismantled carefully from the specimenholders and flushed with demineralized water until no alkalinity could be observed. They were weighed and examined metallographically after drying.

#### Loop system and specimenholder

A schematic diagram of the basic loop system is given in fig. 1. For some experiments specimenholder 8 at 700°C, downstream to specimenholder 3 has been withdrawn. The loop system is constructed from an AISI 316 steel and contains about 60 l of sodium. For one experiment an additional specimenholder at 480°C, heated zone, has been used.

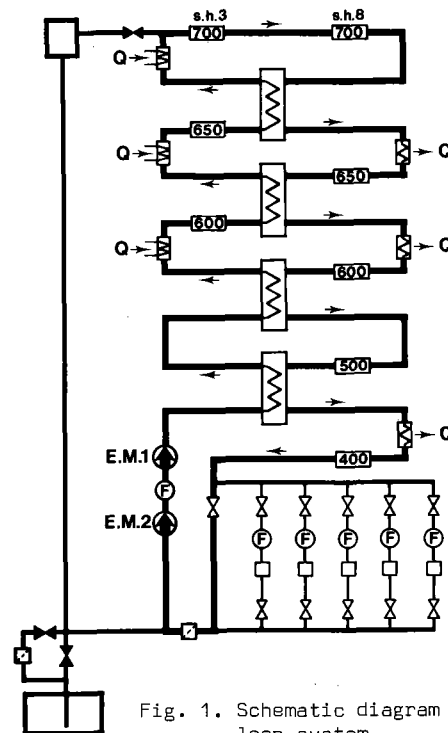


Fig. 1. Schematic diagram of the basic loop system.

In the heated zone (left side of fig. 1) the sodium is heated from 400°C up to 700°C, passing the indicated specimenholders at 600, 650 and 700°C consecutively. In the cooled zone (right side of fig. 1) the sodium is cooled down from 700°C to 400°C passing the indicated specimenholders at 650, 600, 500 and 400°C. Heating and cooling of the sodium is achieved by heaters and coolers in addition to the heat exchangers (fig. 1).

The auxiliary equipment of the loop system, represented as bypass systems in fig. 1, serves various purposes. One bypass is used as a cold trap in order to establish the required oxygen level. Another bypass contains the plugging meter, indicating the presence of contaminants in the sodium. Sodium sampling for oxygen measurements was also accomplished in one of the bypass-

ses, initially by means of a sampling device, followed by off-line distillation. Afterwards the in-line distillation technique (ILDA) was developed, which proved to function very satisfactorily. Both techniques are described in detail<sup>(4, 5)</sup>. After sodium distillation, the residue is diluted and analysed titrimetrically.

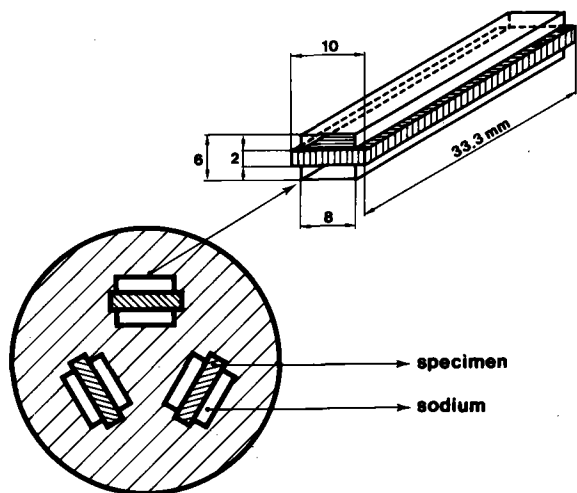


Fig. 2. Cross section of a specimenholder and sketch of a slot.

Each specimenholder consists of three parallel and identical slots containing the specimens (fig. 2). The sodium is flowing over a width of 8 mm on both sides of the flat specimens. The total exposed length of the specimens measures 300 mm. As specimens of 33.33 mm were usually exposed, 9 of these could be situated downstream to each other.

Metallography

The experimental technique used for the examination of exposed specimens are the following:

- optical microscopy,
- X-ray diffraction,
- transmission electron microscopy and diffraction,
- scanning electron microscopy,
- electron microprobe analysis.

The optical microscope was used mainly for examining sectioned specimens, cross sections as well as taper sections, the latter showing a tenfold broadened corrosion and deposition zone. In order to distinguish austenite and ferrite optical etching by means of a ZnSe evaporated interference layer was applied.

X-ray diffraction was used mainly to identify deposition products, either in the form of powder (Guinier camera) or as present on the specimens (diffractometer).

Electron microscopy and electron diffraction were used to identify particles at the surface of the exposed specimens. Usually the particles were collected on extraction replicas. Scanning electron microscopy was used mainly for studying the topography of the exposed specimen surface. Additional electron micro-analysis was performed in most electron microscopy studies.

The electron microprobe was used for semi-quantitative line profile analysis of taper sections. In ad-

dition, quantitative point analysis was carried out on the taper section as well as on the surface of the unprepared specimens, the latter providing information on the surface composition of the exposed specimens.

Exposure conditions

The series of 7 experiments can be subdivided into two groups; 6 experiments, designated as run 2-3, 2-4, 2-5, 2-6, 2-7 and 2-9, where only the oxygen level was varied and one experiment, run 2-11, with varying flow velocity. For the first series the temperature levels mentioned before and a flow velocity of about 6 m/s for each run have been maintained. The accurate values for flow velocity at the various temperatures and the corresponding Re numbers are given in table I.

Table I: Sodium velocity and Re number for the specimenholders.

Temperature of specimenholder(°C)	Sodium velocity in m/s	Re number
400	6	59.200
500	6.2	69.400
600	6.4	78.000
650	6.5	81.900
700	6.6	86.000

The exposure time for each run was different and is given in table II. In this table also the number of slots available for AISI 316 specimens with 33.33 mm length are given for each run and for each temperature. As far as the oxygen level, given in table II, is concerned a few remarks should be made. In particular as for run 2-3, 2-4 and 2-5 they do not correspond with the values given previously, e.g.<sup>(1)</sup>. The reason for this is a thorough evaluation of the exposure conditions.

Starting with run 2-6 both off-line as well as in-line distillation has been used systematically for determining Ocontent, resulting in values of 2-4 and 1 ppm respectively. According to the cold trap temperature and Eichelbergers solubility curve the oxygen level should be 0.7 ppm, which is better in agreement with the ILDA measurements (the hot trap used at 670°C for 4% of the main flow is considered as a minor factor). For run 2-5 the newly developed ILDA technique has been used as an incidental check. The 8 measurements carried out resulted in an oxygen level of 3-4 ppm. At that time no attention has been paid to these incidental observations, instead the systematically determined data from off-line distillation has been averaged to 7 ppm O. Now having noticed the agreement between ILDA and cold trap values for run 2-6, the same evaluation has been carried out for run 2-5, giving an oxygen level of 3 ppm from cold trap values. As the cold trap, unlike the ILDA, has been used all through the exposure, the average value of 3 ppm O determined from the cold trap temperature should be considered as the most realistic one for run 2-5. For run 2-3 and 2-4 off-line distillation values for the oxygen level in addition to cold trap temperatures have been recorded, the average of the first being taken as the oxygen level<sup>(1)</sup>. From the above mentioned it is justified to consider the average cold trap temperature and to calculate with Eichelbergers saturation curve the oxygen level for run 2-3 and 2-4. This results in the more reliable data of 35 and 21 ppm respectively, instead of the values considered till now, that is 22 and 15 ppm O respectively<sup>(1)</sup>. In conclusion, we state that for our experiments the most reliable data are obtained by ILDA measurements and if these are not available by

INTERNATIONAL CONFERENCE ON LIQUID METAL TECHNOLOGY IN ENERGY PRODUCTION

Table II: Exposure conditions for the runs with different oxygen level.

Run no.	Exposure time (hr)	Oxygen level (ppm O)	Cold trap	Hot trap	480°C†* (S.H.9)	600°C† (S.H.1) 650°C† (S.H.2) 700°C† (S.H.3)	700°C† (S.H.8)	650°C†* (S.H.4) 600°C† (S.H.5) 500°C† (S.H.6) 400°C† (S.H.7)
2/3	2493	35	+	-	-	2	-	2
2/4	3034	21	+	-	-	3	3	3
2/5	4198	3	+	-	-	3	3	3
2/6	4949	1	+	+	3	3	-	3
2/7	3090	1.5	+	-	-	1	1	1
2/9	3649	8	-	-	-	2	1	1

\*†: heated zone  
+†: cooled zone

means of the cold trap temperature and Eichelbergers solubility curve. For run 2-7 and run 2-9 we therefore used the ILDA figures. It is interesting to note here that run 2-9 has been carried out without a cold trap, so the measured value of 8 ppm is some kind of an "equilibrium" value.

Run 2-11 concerned specimenholders at 650°C, heated and cooled zone, and a specimenholder at the top temperature of 700°C. Behind the three slots of each specimenholder a constriction was fixed, giving rise to flow velocities of about 3, 6 and 9 m/s (the exact figures will be given later). The main objective of this set-up is that the conditions for all slots, except the flow velocity, are identical, so a reliable comparison of the results may be possible. An average oxygen level of 5 ppm (ILDA measurements) and an exposure time of 3999 hours apply for this run.

RESULTS

Weight change

The weight change of each specimen divided by the exposure time has been considered as the corrosion or deposition rate. In fact this is correct if the weight change should be proportional to time. From what follows this is not the case during the first period of exposure, the incubation period. Not knowing the extent of this period the above mentioned way of calculation has been applied, resulting in corrosion or deposition rates expressed as mg/cm<sup>2</sup>yr. These figures at all temperatures have been plotted as a function of downstream position or oxygen level. The first variable is expressed as the distance to the entrance of the slot (L) over the hydraulic diameter (D<sub>h</sub>). The results are qualitatively comparable for all oxygen levels and therefore only one example is shown (fig. 3). Each corrosion or deposition rate given in fig. 3 represents the average value of the specimens at identical L/D<sub>h</sub> values in the 3 parallel slots. Obviously an influence of downstream position on corrosion as well as on deposition is present, the effect being more pronounced for higher exposure temperature. Further a pronounced influence on the first specimens is present, probably due to hydrodynamic instability. In order to avoid this entrance effect the average corrosion or deposition rate for each specimenholder has been determined for all available specimens, except the first three ones from each slot. The results are given in table III and plotted in fig. 4.

In general fig. 4 reveals 2 oxygen dependent regions: above 8 ppm O a strongly oxygen dependent corrosion and deposition behaviour and below 8 ppm O a slight oxygen influence on corrosion and deposition. The temperature influence on deposition rate is

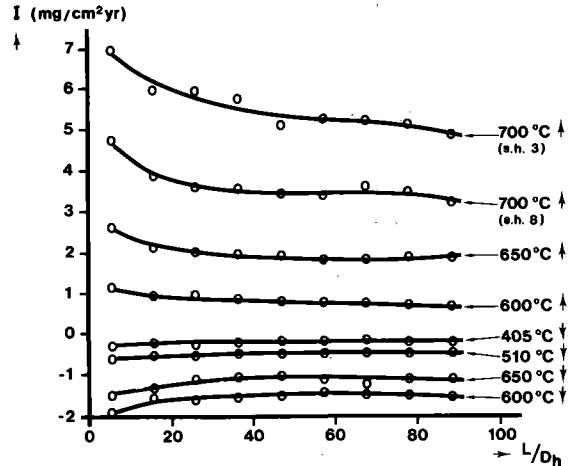


Fig. 3. Corrosion and deposition rate as a function of downstream position at various exposure temperatures and at 8 ppm O.

consistent, that is an increasing rate at higher temperature for all oxygen levels considered. An increasing corrosion rate with increasing temperature only holds for the lower oxygen levels (≤ 8 ppm) but certainly not for high oxygen level (fig. 4), as at 21 ppm

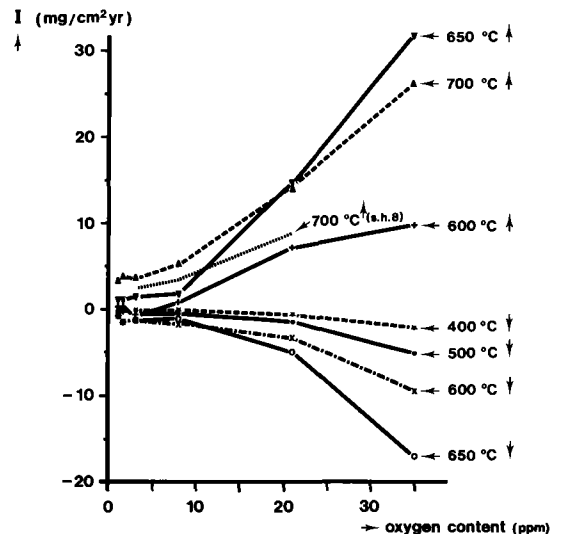


Fig. 4. Corrosion and deposition rate as a function of oxygen level at various exposure temperatures.

INTERNATIONAL CONFERENCE ON LIQUID METAL TECHNOLOGY IN ENERGY PRODUCTION

Table III: Average corrosion rate in the heated zone (†) and average deposition rate in the cooled zone (‡), in mg/cm<sup>2</sup>yr.

Temp. (°C)	Run 2-3 <sup>1)</sup> 35 ppm O	Run 2-4 <sup>2)</sup> 21 ppm O	Run 2-5 <sup>2)</sup> 3 ppm O	Run 2-6 <sup>2)</sup> 1 ppm O	Run 2-7 <sup>3)</sup> 1.5 ppm O	Run 2-9 <sup>4)</sup> 8 ppm O
480†	-	-	-	0.17	-	-
600†	9.61	7.10	- 0.46	0.19	0.29	0.75
650†	31.73	14.33	1.53	1.23	1.19	1.87
700†	25.97	14.19	3.59	3.34	3.81	5.22
(S.H.3)						
700†	-	8.83	2.36	-	-	3.44
(S.H.8)						
650‡	- 17.12	- 4.97	- 1.21	- 0.82	- 1.48	- 1.13
600‡	- 9.56	- 3.39	- 1.16	- 0.86	- 1.49	- 1.53
500‡	- 5.42	- 1.54	- 0.28	- 0.09	- 0.28	- 0.50
400‡	- 2.18	- 0.58	+ 0.05	- 0.09	- 0.23	- 0.20

- 1) Average from 2 x 6 specimens in each specimenholder, except for 700°C†: 2 x 3 specimens.
- 2) Average from 3 x 6 specimens in each specimenholder.
- 3) Average from 1 x 6 specimens in each specimenholder.
- 4) Average from 2 x 6 specimens in specimenholders 1-3 and from 1 x 6 specimens in specimenholders 4-8 (cf. table II).

0 no difference in corrosion rate between 650°C and 700°C can be observed, whereas at 35 ppm O corrosion is even faster at 650°C compared to 700°C.

An effect of sodium velocity on corrosion and deposition rate for run 2-11 turned out to be not obvious. As the downstream effect is quite different for each flow velocity the average values are less representative. For that reason the corrosion and deposition values for all AISI 316 specimens are given as a function of their downstream position (fig. 5).

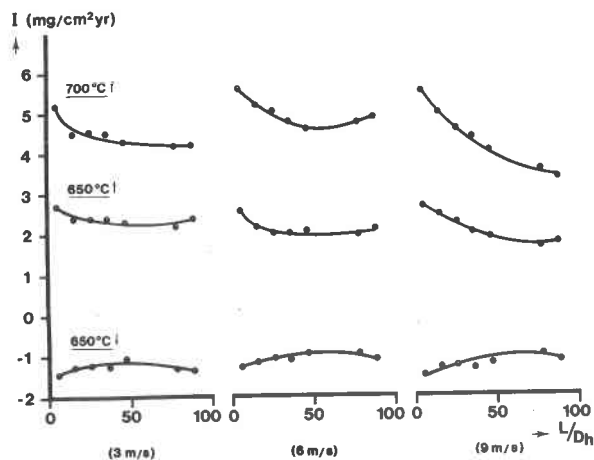


Fig. 5. Corrosion and deposition as a function of downstream position at various exposure temperatures and sodium flow velocities, and at 5 ppm O.

The plots in fig. 5 show that the influence of sodium velocity on corrosion and deposition can be neglected.

In particular the velocity independent deposition rate should be emphasized, as it is contradictory to the experimental evidence obtained previously, that is to say, results obtained in an isothermal loop system at about 580°C. As the circuit referred to is actually a pump test facility no precautions were taken to control the oxygen level during exposure. As far as oxygen was measured values between 2 and 50 ppm have been de-

termined. A bypass of this system contained 10 parallel specimenholders. By means of constrictions behind the specimenholders the sodium velocity along the specimens was kept at 5 different values between 6 and 26 m/sec. The exposed specimens consisted of pure Ni, for which the average weight gain, as a function of sodium velocity is given in fig. 6. By means of chemical analysis the main AISI 316 elements, Fe and Cr, have been determined in the deposition products. The amount of iron as a function of sodium velocity is given as well in fig. 6. It turns out that the deposition rate for iron and chrome is proportional to  $v^{0.7-0.9}$ . So, the deposition rate for iron and chrome is more or less completely governed by hydrodynamics, contradictory to the results obtained with run 2-11.

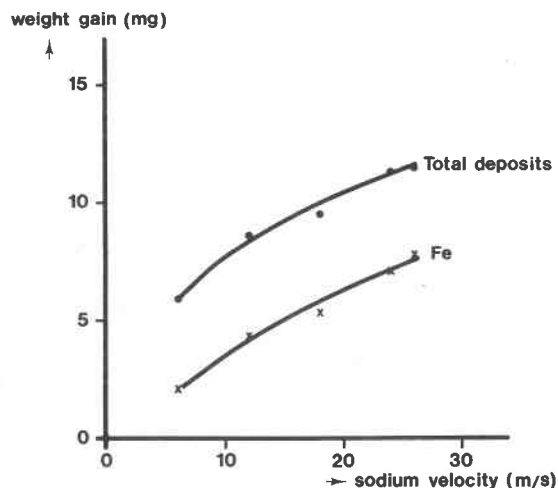


Fig. 6. Weight gain of Ni specimens as a function of sodium flow velocity and under isothermal conditions (580°C).

Metallographic investigations

As most results of the metallographic investigations have been published<sup>(1, 2, 3)</sup>, the main features will be summarized as far as they are important in view of the discussion, hence only the highest temperatures will be considered. As far as additional

information is available this will be reported as well. The latter only holds for runs 2-3, 2-4, 2-5, 2-6, 2-7 and 2-9, as the specimens from run 2-11 have not yet been examined. With regard to the different mass transport processes at low and high oxygen levels it is appropriate to distinguish the corrosion and deposition features as well.

Table IV: Microscopically determined average thickness of the ferritic layer formed in the heated zone.

Number of run	Oxygen concentration (ppm O)	Temperature (°C)	Thickness of layer (µm)
2/6	1	650	5
		700	8
2/7	1.5	650	5
		700	8
2/5	3	650	4
		700	5
2/9	8	650	1.5
		700	4

At low oxygen levels ( $\leq 8$  ppm) a ferritic layer is formed at the surface of the heated zone specimens. As this phenomenon is dependent on the well-known leaching of alloying elements such as Ni, Cr, Mn and Si, the thickness of the ferritic layer is dependent on temperature and oxygen level (table IV). Such a dependence does not appear for the concentrations of alloying elements, being 6-8 and 1.5-2 wt.% for Cr and Ni, respectively, in all specimens<sup>(1, 3)</sup>.

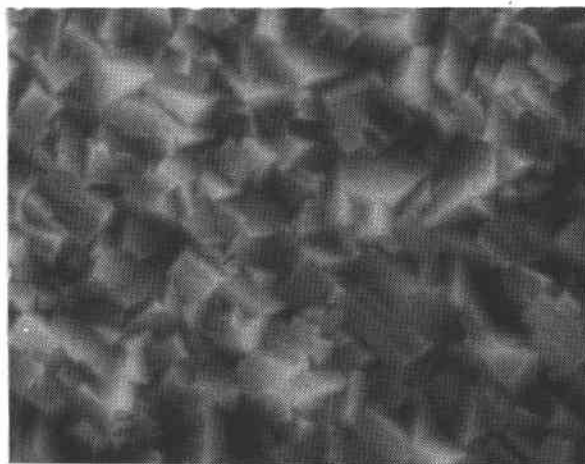


Fig. 7. SEM image of carbides deposited at 650°C and 1.5 ppm O (V = 7.500 x).

In the cooled zone the presence of a carbide layer has already been reported for the low oxygen runs of  $\leq 8$  ppm O<sup>(1)</sup>. A detailed examination of the carbide layer reveals the crystalline morphology of the  $M_{23}C_6$  particles (fig. 7). A further investigation has shown that the thickness of the carbide layer depends on the oxygen level in the sodium (table V).

Further investigations with regard to the deposition products have revealed that apart from the carbide layer metallic particles are present as well. In particular the SEM images of the surface show these particles (fig. 8), suggesting that they are situated

Table V: Microscopically determined thickness of the deposited carbide layer in the cooled zone at 650°C.

Number of run	Oxygen concentration (ppm O)	Layer thickness (µm)
2/6	1	3.7
2/7	1.5	3
2/5	3	1
2/9	8	0.8

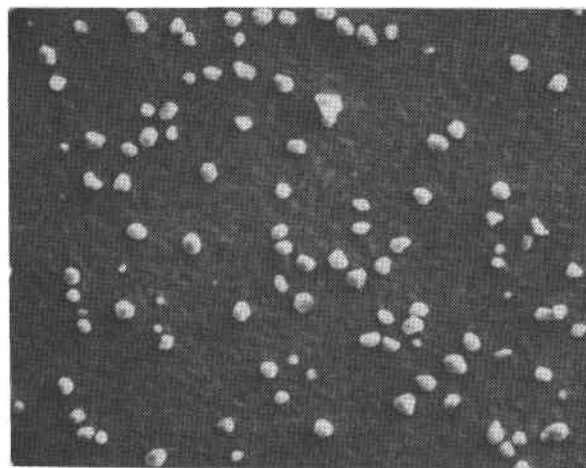


Fig. 8. SEM image of carbides and metallic particles deposited at 650°C and 8 ppm O (V = 750 x).

more or less on top of the carbide layer. As a matter of fact this could be proved by taper and cross sections (see e.g. fig. 9). By examining the surface of specimens from all low oxygen runs only run 2-7 did not show these metallic particles. A final electron microscopical and microprobe analysis revealed that the particles are more or less comparable with AISI 316 steel, both with regard to their crystallographic structure as well as with respect to their composition.

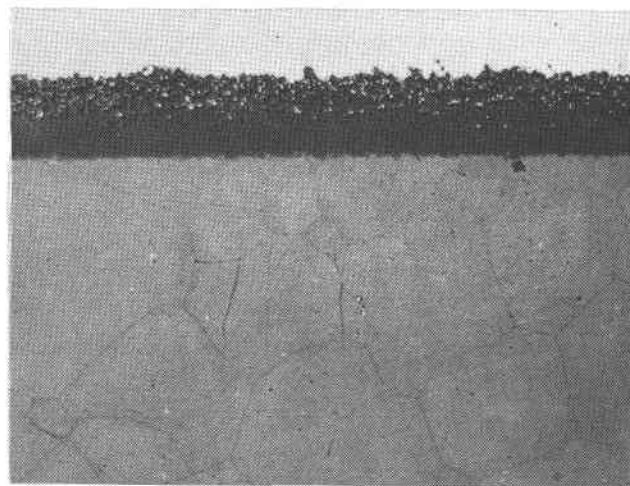


Fig. 9. Optical micrograph of taper sectioned and optical etched deposition specimen exposed at 650°C and 1 ppm O (V = 310 x).

At high oxygen levels ( $\geq 21$  ppm) leaching of alloying elements also has occurred for the heated zone specimens, but to such an extent (the surface concentration of Cr and Ni is 13-14% and 7-9% respectively) that



no ferritisation has occurred.

At the cooled zone the appearance of the specimens at oxygen levels  $\geq 21$  ppm is different as well. Instead of a carbide layer and metallic particles the deposition products consist of a metallic layer with  $\text{NaCrO}_2$  crystals<sup>(1)</sup>.

#### DISCUSSION

Having summarized the weight change and change in metallographic appearance due to sodium exposure, the remaining question is whether the exact influence of oxygen level, temperature, downstream position and sodium velocity can be evaluated and if so, whether the relationship of the corrosion and deposition rate with these variables can be understood. In the following these problems will be discussed for each parameter separately.

#### Effect of oxygen level

With respect to the influence of the oxygen level a distinction can be made between low oxygen level ( $\leq 8$  ppm) and high oxygen level ( $\geq 21$  ppm). As no experiments with oxygen levels between 8 and 21 ppm have been carried out with our circuit, a more exact indication of the point of inflexion cannot be given. The above mentioned distinction is obvious for the metallographic appearance of heated and cooled zone specimens as well as for the corrosion rate, the latter showing a strong influence of high oxygen concentrations and an almost negligible oxygen influence at low level (fig. 4). In particular the latter result is surprising, as the metallographic appearance shows a definite influence of the oxygen level on the ferritisation (cf. table IV), indicating a remarkable influence on the corrosion behaviour. In fact table IV reflects that with decreasing oxygen level the ratio in corrosion rate of the alloying elements, in particular Ni, to Fe is increased, resulting in a thicker ferritic layer<sup>(1)</sup>. This is in agreement with the experimental evidence of an oxygen independent and oxygen dependent corrosion for Ni and Fe respectively<sup>(6, 7)</sup>. Thus, in view of the dependence of the metallographic features on oxygen level it is conceivable to expect a more pronounced oxygen dependent corrosion rate than the one observed in fig. 4 for  $\leq 8$  ppm O.

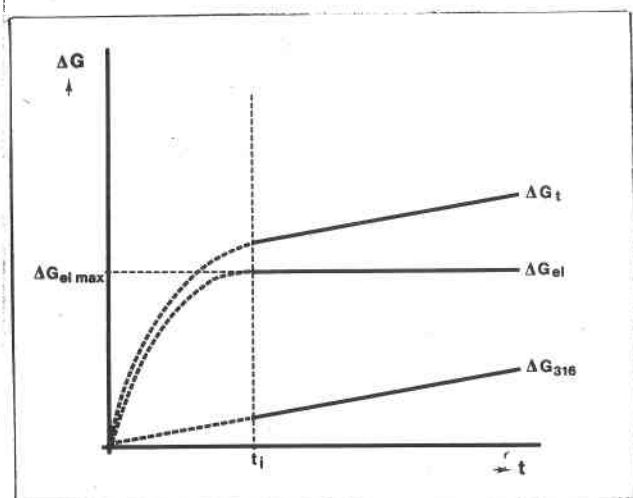


Fig. 10. Total weight loss,  $\Delta G_t$ , loss of alloying elements during the incubation time,  $\Delta G_{el}$ , and steady state weight loss,  $\Delta G_{316}$ , as a function of time.

However, one should realize that the corrosion rates in fig. 4 are determined from the weight changes observed after the total exposure time. During that time the weight loss can be considered to be a consequence of two processes. One process is the formation of the ferritic region up to the maximum value possible under the conditions of temperature, oxygen level and sodium velocity. During this process the corrosion rate gradually decreases as the ferritic layer, as diffusion barrier, increases. As soon as the diffusion rate of the alloying elements through the ferritic layer equals the rate of dissolution of the alloying elements (except for Mo with the composition of AISI 316), the second, steady state corrosion process is the relevant one. Schematically the two different corrosion processes are illustrated in fig. 10. After the incubation time  $t_i$  has been reached the rate of preferential leaching  $\frac{d(\Delta G_{el})}{dt} = 0$ , whereas the steady state corrosion rate,  $\frac{d(\Delta G_{316})}{dt}$ , is constant. The total weight loss,  $\Delta G_t$ , is

the one measured and used to calculate the corrosion rate I in table III. The true dependence of the processes at  $t < t_i$  is not known. For the steady state corrosion it has been assumed that it is not influenced by the leaching process. Nevertheless, the uncertainty at  $t < t_i$  for all processes is represented by dotted lines in fig. 10.

It will be understood that the interesting oxygen dependent corrosion rate value from a mechanism point of view is  $\frac{d(\Delta G_{316})}{dt}$ , the reliable data of which will be obtained for  $t > t_i$ , the calculated figure being more accurate for larger  $t/t_i$  (cf. fig. 10). Taking  $t > t_i$  as a criterium for the calculation of the steady state corrosion rate, the question is for which runs this criterium holds. The answer can be found by considering the cooled zone specimens. It should be recalled that the deposition products consist of a Cr rich carbide layer, on top of which are metallic particles. It is conceivable that the Cr rich carbide layer has been formed at  $t < t_i$ , that is during the preferential leaching of Cr, whereas the metallic particles are precipitated during the steady state process ( $t > t_i$ ) characterized by dissolution of steel with approximate AISI 316 composition.

This implies a possible correlation between ferrite layer thickness and carbide layer thickness, as indeed can be concluded from tables IV and V. On the other hand it means that the corrosion process (viz. in the heated zone) takes place under steady state conditions if the deposition product (viz. in the cooled zone) contains metallic particles. Applying this argument for the runs under consideration it is clear that for run 2-7  $t < t_i$ , in other words preferential leaching is still not completed after about 3100 hr for AISI 316 at 700°C and 1.5 ppm oxygen. For runs 2-5, 2-6 and 2-9 the incubation time has been passed.

In order to calculate the steady state corrosion rate for the last mentioned runs, the value for  $\Delta G_{el,max}$  (cf. fig. 10) has been determined from the

ferritic layer thickness and the decrease in concentration of the alloying elements in the ferrite compared to the austenitic base material. The figures are given in table VI (for the sake of interest run 2-7 has been considered as well). Now, from the measured weight loss  $\Delta G_t$  and from:

$$\Delta G_{316} = \Delta G_t - \Delta G_{el,max}$$

Table VI: Steady state corrosion rate at 700°C.

Number of run	$\Delta G_{el,max}$ (mg/cm <sup>2</sup> )	$\Delta G_t$ (mg/cm <sup>2</sup> )	$\Delta G_{316}$ (mg/cm <sup>2</sup> )	$I_{316}$ (mg/cm <sup>2</sup> yr)
2/5	1.00	1.72	0.72	1.5
2/6	1.61	1.89	0.28	0.5
2/7	1.61*	1.34	< 0	
2/9	0.80	2.18	1.38	3.3
2/3				26.0
2/4				14.2

\*  $\Delta G_{el}$

the steady state corrosion rate  $I_{316}$  has been calculated (table VI). Since at  $\geq 21$  ppm O the leaching is not pronounced, the observed overall corrosion rate for run 2-3 and 2-4 has been considered as the steady state corrosion rate. It should be noticed that for run 2-7  $\Delta G_{316} < 0$ , resulting from the small difference between  $\Delta G_t$  and  $\Delta G_{el}$  in combination with the not accurate estimation of the ferritic layer thickness.

The resulting values for  $I_{316}$  show a more pronounced oxygen dependence than the ones from table III. For comparison both values are represented in fig. 11. Calculation of the most accurate slope at low oxygen level gives  $0.91 \pm 0.22$ . In other words the corrosion rate of AISI 316 is almost linearly proportional to oxygen concentration. This means that the oxygen dependence for the corrosion rate of Fe must be linear as well, in agreement with the model proposed previously (4, 8).

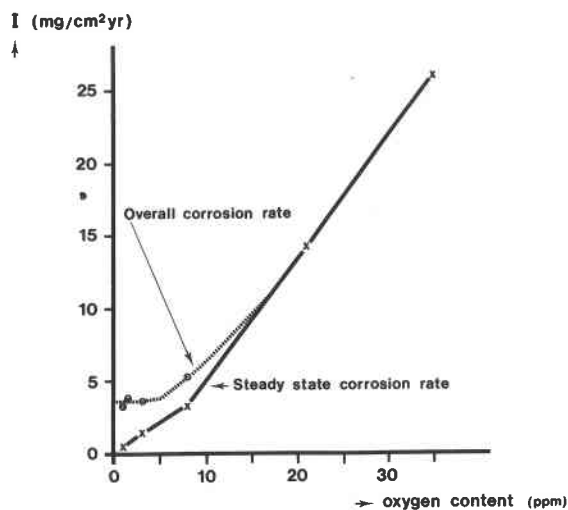


Fig. 11. Steady state and overall corrosion rate as a function of oxygen level at 700°C.

With respect to Cr no conclusive evidence is available. If Cr dissolves in sodium without interaction with oxygen the expected order for AISI 316 would be about 0.67 (the influence of Mn, Mo and Si has been neglected). However, if a first order reaction between Cr and O should be taken into account the anticipated order for steel would be 0.84. This value is in better agreement with the experimental value, however, the arguments may not be regarded as decisive evidence.

The same calculation for  $I_{316}$  has been performed for the 650°C specimens. The results are summarized in table VII. As for run 2-7 at 700°C, for three runs the 650°C specimens have conceivably not yet reached the

Table VII: Steady state corrosion rate at 650°C.

Number of run	$\Delta G_{el}$ (mg/cm <sup>2</sup> )	$\Delta G_t$ (mg/cm <sup>2</sup> )	$\Delta G_{316}$ (mg/cm <sup>2</sup> )	$I_{316}$ (mg/cm <sup>2</sup> yr)
2/5	0.75	0.73	< 0	
2/6	0.93	0.70	< 0	
2/7	0.93	0.42	< 0	
2/9	0.28	0.78	0.50	1.2
2/3				31.7
2/4				14.3

steady state situation. That is to say, at 1 ppm O and 650°C steady state corrosion has not yet been reached after about 5.000 hrs. At the higher oxygen level of 8 ppm the incubation time is less than 3.600 hrs.

At high oxygen level ( $\geq 21$  ppm O) the determination of the reaction order with respect to oxygen at 700°C, is not possible as the corrosion is strongly influenced by the upstream corrosion at 650°C (cf. fig. 4). For 650°C the influence of the upstream specimens at 600°C is less and thus the order calculated (about 1.5) for this temperature is more reliable. Anyway an order exceeding one is conceivable for high oxygen level.

From a practical point of view the existence of the extended incubation time is interesting. As the canning materials will be changed regularly an important part of their residence time leaching takes place. As during this time the deposits consist of carbides this may be regarded as the main deposition product under practical conditions. It is interesting to notice that the stable carbides at the surface do not cause carbon diffusion into the austenitic steel (fig. 12).

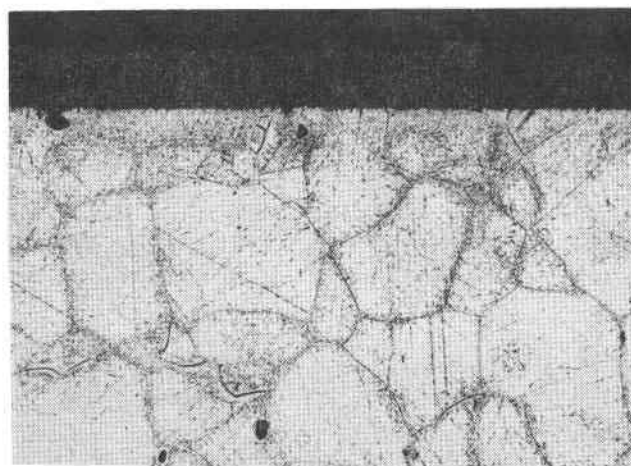


Fig. 12. Optical micrograph of taper sectioned deposition specimen exposed at 650°C and 1 ppm O, after oxalic acid etching on carbides.

(V = 190 x)

Effect of downstream position

The effect of saturation of sodium with corrosion products is clear from the downstream effects (decreasing weight loss with increasing  $L/D_h$ ) found for all series of corrosion specimens (e.g. fig. 3). This effect also appears from the two separated specimenholders at 700°C (fig. 3). The nature of the corrosion products responsible for the downstream effect has been proposed by Isaacs et al. to be Ni and Cr (9). Whether the influence of Ni and Cr is a poisoning effect (9) or merely a saturation effect, the consequence will be that leach-

ing of Ni and Cr will be diminished and thus the ferritic layer thickness as well. In order to check this the layer thickness has been measured by means of magnetic saturation induction. Although this has not resulted yet in quantitative values the relative amounts of ferrite present in the specimens can be expressed as a magnetic signal. The series of signals have been compared with the weight loss values, from which a strong correspondence can be detected. As an example fig. 13 shows the results for run 2-6.

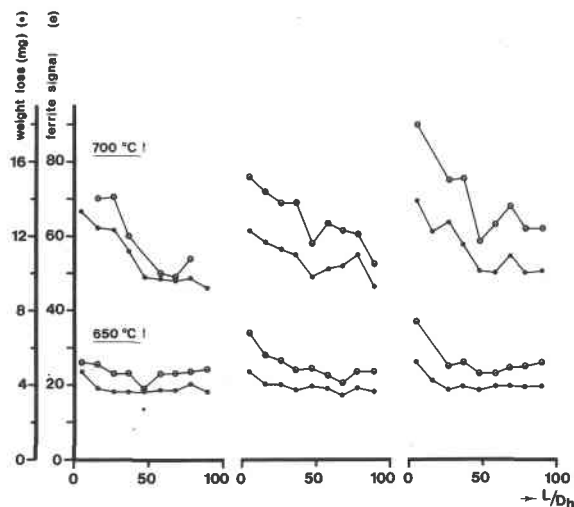


Fig. 13. Correlation between weight loss and amount of ferrite formed in AISI 316 specimens at 650°/700°C and 1 ppm O.

So, indeed it may be stated that the downstream effect is caused by diminishing leaching of Ni and Cr, because their concentration in Na increases with downstream position. However, it is not clear whether the downstream effect is identical with a decreasing ferritic layer thickness, as is suggested by fig. 13. If so, this means that the effect is caused during the incubation period and, consequently, that no influence of downstream position on the steady state corrosion is present. This is an interesting conclusion and therefore further study with regard to quantifying the amount of ferrite will be carried out.

Considering fig. 5 it seems that the downstream effect is more pronounced at higher sodium velocity. This result is in contradiction with what might be expected. That is to say, for higher flow velocity the saturation of corrosion products is less and so should be the downstream effect, as can be expressed quantitatively<sup>(8)</sup>. This discrepancy needs further study, among others by means of quantitative ferrite measurements.

#### Effect of temperature

The main objective of the study of the temperature dependent corrosion rate is the evaluation of the activation energy for the corrosion process. From our investigations it follows that the temperature dependent corrosion rate is ambiguous. Because the specimen holders at different temperatures are situated downstream to each other, at high oxygen levels the consumption of oxygen and probably the saturation of sodium with corrosion products, such as  $\text{NaCrO}_2$ , even results in lower or comparable corrosion rates at 700°C compared to 650°C (cf. table III). So, under conditions of high oxygen level it is impossible to determine the activa-

tion energy from our experimental results. At low oxygen level the situation is quite different. Now the 700°C corrosion rate no doubt exceeds those at 650°C (table III). According to the model proposed for the corrosion of  $\text{Fe}^{(1)}$  and represented in fig. 14 this can be explained: at higher temperature the amount of active oxygen ions is raised, a process that governs the corrosion of iron and which is independent on the upstream phenomena.

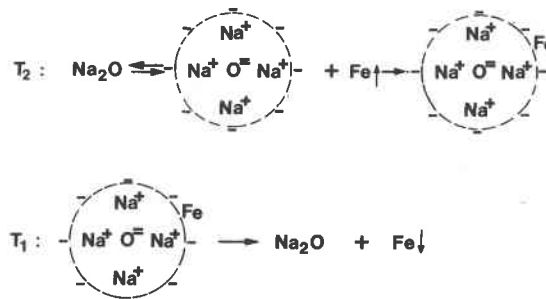


Fig. 14. Model for the transport of Fe from a temperature  $T_2$  to a lower temperature  $T_1$ , as proposed previously<sup>(1)</sup>.

So, at low oxygen levels ( $\leq 8$  ppm O) it seems possible to start from the experimental figures and calculate the activation energy. For the runs under consideration this results in values between 19 and 42 kcal/mol. Although these values lie within the range of activation energies from Thorley and Tyzack: 18 kcal/mol<sup>(7)</sup>, General Electric: 26 kcal/mol<sup>(10)</sup> and Weeks and Isaacs: 50 kcal/mol<sup>(11)</sup> they cannot be realistic ones because at low oxygen levels one must take into account that the corrosion rates measured are the accumulated values resulting from two processes. It is conceivable that the activation energy for the leaching process is quite different than the one for the steady state process. As the contribution of the two processes to the total weight loss depends on the total exposure time in relation to the incubation time all possible values of activation energy, lying in between activation energies for the leaching process and steady state process, may be found. The significant process is the steady state process, for which the activation energy can be calculated if the steady state corrosion rate as a function of temperature is known. In our case this is only true for run 2-9 (cf. table VI and VII). From the values at 650 and 700°C an activation energy of 40 kcal/mol has been calculated. This value agrees fairly well with the activation energy of 36 kcal/mol determined by Bagnall and Jacobs<sup>(12)</sup> from all available literature data.

#### Effect of flow velocity

From run 2-11 it is clear that the corrosion rate is not influenced by sodium velocity in excess of about 3 m/s (fig. 5). Expressed in Re numbers this means that at least for  $\text{Re} > 50.000$  the corrosion rate is not influenced by hydrodynamics. This value is lower than  $\text{Re} = 70.000$ , the inflexion point observed by Thorley<sup>(7)</sup> at 650°C and 20-30 ppm O. However, Thorley stated that the inflexion point shifts to lower number with lower oxygen level, so the results of Thorley and ours are not necessarily in contradiction. But Thorley's explanation for the velocity independent corrosion behaviour does not hold for our experiments. This

could be deduced from a comparison of the calculated laminar diffusion layer thickness,  $\delta_m$ , and the peak to valley height (R) of the surface in the flow direction, measured by means of the Talysurf. The values given in table VIII obviously prove that the surface roughness is very small compared to the laminar layer.

Table VIII: The velocity dependent laminar diffusion layer ( $\delta_m$ ) and peak to valley height (R) for AISI 316 specimens.

T (°C)	V (m/s)	Re no.	$\delta_m$ ( $\mu\text{m}$ )	R ( $\mu\text{m}$ )
650†	4.0	52,200	11.7	1.1
	6.5	84,900	7.9	1.0
	9.7	126,700	5.8	1.0
700†	3.9	53,100	11.9	2.4
	6.8	92,600	7.6	2.4
	9.8	133,400	5.7	2.6
650‡	3.8	49,600	12.2	0.6
	6.4	83,600	8.0	0.8
	10.0	126,700	5.6	1.0

For the calculation of  $\delta_m$  the following empirical formula has been used:

$$\delta_m = 37 D_h \cdot \text{Re}^{-0,8} \text{Sc}^{-0,33}$$

The value of Sc ( $= \frac{v}{D}$ ) has been calculated with the Stokes-Einstein relation for the diffusion coefficient:

$$D = \frac{RT}{6N\pi\eta r}$$

The atomic radius r has been taken for iron as 0,69 Å. However, actually one should take the radius of the O-Na-Fe complex, proposed in the model for iron corrosion (fig. 14), which is not known. But it is possible to estimate the value of this radius in order to satisfy the condition that the surface roughness is about the same as the laminar layer thickness. For the most favourable situation (table VIII: 700°C, 9.8 m/s) the radius should be 8 times the radius of iron, which seems very unlikely. So, from our experimental results it must be concluded that at low oxygen level and at Re numbers at least 50.000 the corrosion rate is governed by the surface reaction between O and Fe, because its resistance is much higher than the one for diffusion in sodium.

For the deposition again it must be concluded that the independence of flow velocity is not caused by the roughness of the surface (table VIII). That is to say, the deposition is governed by the surface reaction. A most disturbing conclusion, as for the isothermal run mentioned before the deposition rate of the main steel elements, Fe and Cr, is completely governed by hydrodynamics at Re numbers between 35.000 (6 m/s) and 150.000 (26 m/s).

For a tentative explanation of this discrepancy it should be realized that the results imply that for the nonisothermal run 2-11 the resistance of the surface reaction exceeds the resistance for diffusion, whereas the reverse holds for the isothermal run. Let us consider now the first case and recall the mechanism of deposition proposed previously (fig. 14). That is to say, by lowering the temperature from  $T_2$  to  $T_1$  the Na-O cluster transforms to a Na<sub>2</sub>O molecule, thus releasing Fe, which, being supersaturated, will diffuse to the surface and subsequently will be deposited. Thus, it is the iron which actually determines the rate of the processes. This is probably not the case for the isothermal run. Here no decrease in temperature takes place, so the iron in the sodium must be considered as present in the complex. The driving force for deposi-

tion is the substrate material Ni in an otherwise all stainless steel system. The diffusing species is therefore the O-Na-Fe complex, which subsequently reacts at the surface, releasing Fe.

Considering the two cases it is not possible to predict in which case the surface reaction has the highest resistance. However, this is very well possible for the diffusion step. The resistance for the larger complex is no doubt higher. So, at least for this process it can be understood that under isothermal conditions the diffusion step governs the corrosion rate up to higher Re numbers.

The foregoing explanation holds for iron, whereas in run 2-11 most of the deposits consist of Cr-carbides. Once again the question arises whether Cr is transported in sodium as a Cr-C complex. We think it is not, as in the above mentioned isothermal run Cr was deposited as such. And as the amount of Cr deposited was very small compared to the amount of iron the gettering action for carbon is very small, unlike the nonisothermal experiments, where the high Cr-concentration in the deposits probably in combination with the supersaturation of C with decreasing temperature, causes the formation of Cr-carbides. However, even if this view is correct, the question remains how Cr is transported in sodium. Because of the conclusions drawn from the oxygen influence of corrosion rate we think that at the low oxygen levels under consideration Cr corrodes according to a first order reaction with oxygen. Probably it forms a similar complex as iron does (cf. fig. 14). In that case it explains the difference in deposition rate under isothermal or nonisothermal conditions.

#### CONCLUSIONS

- The main conclusions from the experimental results with respect to corrosion and mass transport of AISI 316 in flowing sodium can be summarized as follows:
- Two oxygen concentration regions can be pointed out where corrosion and mass transport is different.
  - At oxygen levels  $\leq 8$  ppm transport of Fe and Cr in sodium takes place as a complex with O and Na. The deposition product consist of the metal itself. If the concentration of Cr in the deposits is high enough it may form carbides with C from the sodium (see below). At an oxygen level  $\geq 21$  ppm, but not to high level, Fe is still transported as a complex, whereas Cr is transported and deposited as NaCrO<sub>2</sub>. At very high oxygen level probably also Fe forms NaFeO<sub>2</sub>, so the behaviour of Fe and Cr is in principle identical.
  - At low oxygen level ( $\leq 8$  ppm) the incubation period, where leaching of alloying elements takes place, increases considerably with decreasing oxygen level (e.g. 7 months at 1 ppm O). During this period the deposition product contains very much Cr, which forms carbides with C from the sodium. During the steady state corrosion the metallic deposits have a composition roughly corresponding with those of AISI 316.
  - In general putting the corrosion rate of AISI 316 proportional to  $c_0^n$  with  $c_0$  as the oxygen concentration, it can be stated that n is almost 1 for the steady state corrosion at low oxygen level ( $\leq 8$  ppm), whereas n is  $> 1$  for higher oxygen levels.
  - The activation energy for corrosion has been determined for the steady state corrosion at low oxygen level at 40 kcal/mol. In view of the large incubation times the variety of activation energies given in literature can be understood. It may be expected that the experimentally determined values for the

## INTERNATIONAL CONFERENCE ON LIQUID METAL TECHNOLOGY IN ENERGY PRODUCTION

- activation energies are better in agreement if they are referred to the steady state corrosion process only.
- The downstream effect is mainly, if not completely caused by a decreasing ferritisation with downstream position, consequent on an increasing concentration of Ni and Cr in sodium and thus a decreasing leaching of these elements from the steel.
  - Neither corrosion nor deposition under nonisothermal conditions is influenced by hydrodynamics at  $Re$  no.  $> 50.000$ . In both cases this is not caused by the surface roughness but rather depends on the fact that the resistance of the surface reaction is in excess of the resistance of the diffusion process in the laminar diffusion layer.
  - Under isothermal conditions deposition is completely governed by hydrodynamics at least up to  $Re = 150.000$ . This can be tentatively explained by the difference of species diffusing through the laminar sublayer. Under nonisothermal conditions this is supposed to be the metal atom or ion (Fe, Cr), under isothermal conditions it may be a larger complex, giving rise to a higher resistance to diffusion.
9. H.S. Isaacs, A.J. Romano, C.J. Klamut and J.R. Weeks: "A model for the downstream effect in the corrosion of steels by liquid sodium". Proc. Symp. Chem. Aspects of Corrosion and Mass Transfer in Liquid Sodium, Detroit, pp. 223-231 (1971)
10. E.L. Zebroski, R.S. Young, F.A. Comprelli and D. Dutina: "Effects of mass transfer, and of changes in properties, on austenitic steels in flowing sodium". Proc. Symp. on Alkali Metal Coolants, Vienna, pp. 195-211 (1966)
11. J.R. Weeks and H.S. Isaacs: "A general model for the corrosion of steels in high velocity sodium". Proc. Symp. Chem. Aspects of Corrosion and Mass Transfer in Liquid Sodium, Detroit, pp. 207-222 (1971)
12. C. Bagnall and D.C. Jacobs: "Relationships for corrosion of type 316 stainless steel in liquid sodium". Ward - Na - 304 5-23 (1975)

### Acknowledgements

This work was sponsored by the Group Nuclear Energy TNO as part of the Dutch contribution to the joint De-BelLux SNR-300 development programme. For the metallographic work described, the authors are much indebted to J. v.d. Veer and Ir. N. Drost for their optical microscopical and SEM work, respectively. The assistance of Ir. P.L.F. Rademakers and C.J.M. de Bruyn is gratefully acknowledged.

### REFERENCES

1. B.H. Kolster: "Mechanism of Fe and Cr transport by liquid sodium in nonisothermal loop systems". J. of Nucl. Mat. 55, pp. 155-168 (1975)
2. H.B. Zeedijk, J. Jansen and B.H. Kolster: "Identification of the corrosion products on liquid sodium exposed stainless steel specimens by electron microscopy". Beitr. elektronenmikroskop. Direktabb. Oberfl. 6, pp. 87-102 (1973)
3. A.P. von Rosenstiel, D.J. Gras, T. Krisch and B.H. Kolster: "Electron microprobe analysis of sodium exposed stainless steel specimens". Beitr. elektronenmikroskop. Direktabb. Oberfl. 6, pp. 103-132 (1973)
4. L. Bos: "In-line distillation units and sampling device for the analysis of liquid sodium for a loop system". Proc. Int. Conf. on Liquid Alkali Metals, Nottingham, pp. 53-58 (1973)
5. J.F.M. Rohde, M. Hissink and L. Bos: "Equipment for sampling sodium". J. Nucl. Energy 24, pp. 503-508 (1970)
6. A.W. Thorley and C. Tyzack: "Corrosion behaviour of steels and nickel alloys in high-temperature sodium". Proc. Symp. on Alkali Metal Coolants, Vienna pp. 97-118 (1966)
7. A.W. Thorley and C. Tyzack: "Corrosion and mass transport of steel and nickel alloys in sodium systems". Proc. Int. Conf. on Liquid Alkali Metals, Nottingham, pp. 257-273 (1973)
8. B.H. Kolster and A.J. Bogers: "An expression for monometallic corrosion rate in liquid sodium". Proc. Symp. Chem. Aspects of Corrosion and Mass Transfer in Liquid Sodium, Detroit, pp. 253-264 (1971)

IN-REACTOR CORROSION BEHAVIOR OF STAINLESS STEEL  
IN HIGH TEMPERATURE SODIUM

J. W. Weber

Westinghouse-Hanford Company  
Richland, Washington

## ABSTRACT

Sodium-cladding chemical interaction has been studied on fuel pins clad with 20% cold worked type 316 stainless steel and irradiated in the EBR-II at temperatures up to 705°C and for exposures to 5300 hours. The measured corrosion rate of the cladding surface immediately above the top of the fuel column was 12.5  $\mu\text{m}$  per year at 690°C. The loss of Ni at 700°C resulted in the formation of a ferrite layer approximately 5  $\mu\text{m}$  thick. A zone depleted in Ni and Cr extends into the austenite from the ferrite-austenite interface an additional distance of approximately 15  $\mu\text{m}$ . No large changes in volumetric average carbon or nitrogen were observed. The results suggest a slight increase in carbon during the first 2300 hours followed by a slow decrease for longer exposure times. A 25-30% decrease in bulk nitrogen was observed in cladding with an initial nitrogen content of 225 ppm. Cladding with a lower initial nitrogen content of 63 ppm showed essentially no change. Fuel pin cladding corrosion behavior agrees well with that predicted using out-of-reactor Na loop data, thus providing confidence that out-of-reactor corrosion data can be reliably used in predicting in-reactor fuel cladding performance.

## INTRODUCTION

This paper describes the sodium corrosion loss, ferrite formation, interstitial element changes, and the metallographic characterization of the cladding on fuel pins irradiated in the EBR-II at cladding surface temperatures ranging from 370°C to 705°C for times up to 5300 hours.

One of the objectives of the FFTF/LMFBR Fuel Development Program<sup>(1)</sup> has been to investigate the corrosion behavior of fuel pins in flowing sodium in the EBR-II at a variety of temperatures and to a range of exposure times. Although several types of austenitic stainless steels are included in the program the composition of primary interest for cladding has been 316 with 20% cold work.

The initial fuel pin design allowances for the Fast Flux Test Facility (FFTF) for cladding thickness decrease from Sodium-Cladding Chemical Interaction (SCCI) were necessarily very conservative since only small amounts of out-of-reactor sodium loop data were available. Since then, extensive testing programs have been conducted and the results presented in recent conferences<sup>(2,3,4)</sup> and reports<sup>(5,6)</sup> show that these allowances are conservative. However, it is essential that in-reactor verification of these data be obtained at least at selected operating conditions. The trend in the design of fuel pins for Liquid Metal Fast Breeder Reactors (LMFBR's) is to use thinner cladding; thus, there are strong incentives to make the allowances for SCCI as realistic as possible to avoid excess stainless steel in the core.

## DESCRIPTION OF TESTS

The fuel pins were irradiated in 37-pin EBR-II subassemblies using special sodium bypass hardware. The fuel pins, containing 34.3 cm of 25 w/o PuO<sub>2</sub> - 75 w/o UO<sub>2</sub> mixed-oxide sintered pellets, were clad with 20% cold-worked type 316 stainless steel tubing 87.6 cm long by 0.584 cm outside diameter by 0.038 cm thick. The chemical composition for the cladding used in these tests is given in Table I. A gas plenum approximately 39.8 cm long is located above the fuel column. Each

HEAT NUMBER	ELEMENT - WT %						
	Cr	Ni	Mo	Mn	Si	C	N
87210	16.49	13.68	2.43	1.47	0.46	0.054	0.005
88229	16.71	13.84	2.32	1.66	0.48	0.052	0.021

HEDL 7603-268.10

Table I. Chemical Composition of Stainless Steel  
Cladding for P-23 Series Fuel Pins

fuel pin is wrapped with 0.14 cm diameter 20% cold-worked type 316 stainless steel wire on a 30.5 cm spiral pitch. The 37 pins are contained in a hexagonal duct 4.70 cm across the inside flat.

The fuel pins operate at nominal peak linear powers of 394 W/cm giving a cladding heat flux of  $1.61 \times 10^6$  W/m<sup>2</sup>. Sodium enters the subassembly at the bottom at 371°C flowing through the bundle at a nominal  $3.53 \times 10^{-3}$  m<sup>3</sup>/s and exiting at the top of the pins at temperatures ranging from 595°C in the outer flow channels to 675°C in the inner flow channels. Coolant velocity for the pins was 2.1 m/s.

There are some conditions in these tests resulting in part from physical constraint placed on the experiment by the EBR-II, that are not completely prototypic for the FFTF. One is the low velocity of sodium, 2.5 m/s, compared to the 7 to 8 m/s. Another is the short fuel column length that imposes a much higher dT/dL on these tests than in an LMFBR, 960 C°/m vs 360 C°/m. Also missing is the capability to directly measure corrosion losses in the cladding along the heat generating fuel column.

The pins discussed in this paper came from two subassemblies, HEDL-P-23A and HEDL-P-23B, essentially identical in design and operating at approximately the same nominal conditions as described above. The objectives of these tests included the evaluation of performance at a series of exposure times ranging from 1000 hours to more than 10,000 hours. Selected pins have been removed from the subassembly at various times and replaced with fresh unirradiated pins. Exposure times for which SCCI data are available are 1152, 2256, 4608 and 5328 hours. Additional pins exposed for 10,000 hours have been removed from the reactor and are now being examined.

# INTERNATIONAL CONFERENCE ON LIQUID METAL TECHNOLOGY IN ENERGY PRODUCTION

The selected pins were visually examined, photographed and measurements made of the cladding outside diameter and other fuel pin performance characteristics. Each pin was then cut at several locations along the length to obtain samples for metallographic examinations, and chemical analysis of the cladding.

The sodium in EBR-II is periodically analyzed for metallic and non-metallic elements, including oxygen and carbon<sup>(7)</sup>. Oxygen content is reported as being approximately 1 ppm using the vanadium wire equilibrium device, and the sodium plugging temperatures as 107°C. Carbon in the sodium ranged from .16 to .19 ppm.

## RESULTS

This section will describe the results and techniques used for measurements and characterization of sodium corrosion, ferrite formation, carbide dissolution or depletion and interstitial element changes.

### Sodium Corrosion

Measurements of sodium corrosion loss from cladding have been obtained on nine irradiated fuel pins shown in Table II for three exposure times, 1152, 2256 and 4608 hours.

The customary techniques for measuring corrosion in test samples by weight changes or dimensional changes are severely restricted in an irradiated fuel pin. Weight changes are the combined effects of corrosion/erosion of cladding and wire wrap over a continually changing temperature gradient and the possible deposition of foreign materials. Cladding thickness in the fueled region and into the 1.27 cm long UO<sub>2</sub> insulator is affected not only by the outside surface sodium corrosion but by the inside surface fuel cladding chemical interaction (FCCI). Therefore, data on sodium corrosion could only be obtained on that part of the cladding in the plenum above the fuel-column insulator region.

Cladding thickness was measured on 225X photomicrographs of transverse cross sections from several axial locations along the fuel column and in the plenum. The photomicrographs were taken at every 45 or 22-1/2° around the circumference of the cladding. For each set of photomicrographs on a given cross section a US National Bureau of Standards grid was photographed to establish the magnification settings of the metallograph. Five measurements were made on each photograph and averaged. An average cross section thickness was calculated from the measurements on the 8 or 16 photomicrographs and the results plotted as a function of axial location along the fuel pin. An estimate of the precision of the individual section averages is ± 1 μm as determined by comparing thickness measured on the same section as-polished and as-etched.

Since cladding fabrication tolerances allowed variations of 25 μm in thickness, it was necessary to use the thickness of the irradiated pin cladding itself as a reference. Measurements showed that cladding thickness at the top of the cladding and 5 to 7 cm below the fuel column agreed to within 1 μm of one another. Since data were not available at the bottom of all fuel pins, it was decided to use the thickness at extreme top of the pin as the reference.

The measure of thickness reduction shown in Table II was obtained by comparing thickness at the reference point against the thickness at a position 2.54 cm above the top of the fuel column. If there was no section taken at 2.54 cm an interpolation line was drawn between the reference and the next section

PIN NUMBER	OUTSIDE SURFACE TEMP. °C	CLADDING THICKNESS DECREASE ( μ m)	EXPOSURE TIME (HOURS)	CORROSION RATE ( μ mpy)
23A-60D	688	0.76	1152	5.8
23A-26	692	1.52	2256	5.9
-31	674	2.54	2256	9.9
-32	661	1.78	2256	6.9
23B-49C	697	2.29	2256	8.9
-50C	697	2.54	2256	9.9
-62D	694	2.03	2256	7.9
23A-21	667	4.06	4608	7.7
-25	692	6.60	4608	12.6

HEDL 7603-268.11

Table II. Corrosion Rate of Cladding

below 2.54 cm. When the lower section was in the fuel or insulator region the cladding thickness was measured so as to present the minimum effect of internal FCCI. Thus, the values presented in Table II are maximum reductions expected.

Corrosion rates were calculated for each pin using the Equivalent Full Power Days (EFPD) of the EBR-II as the exposure time.

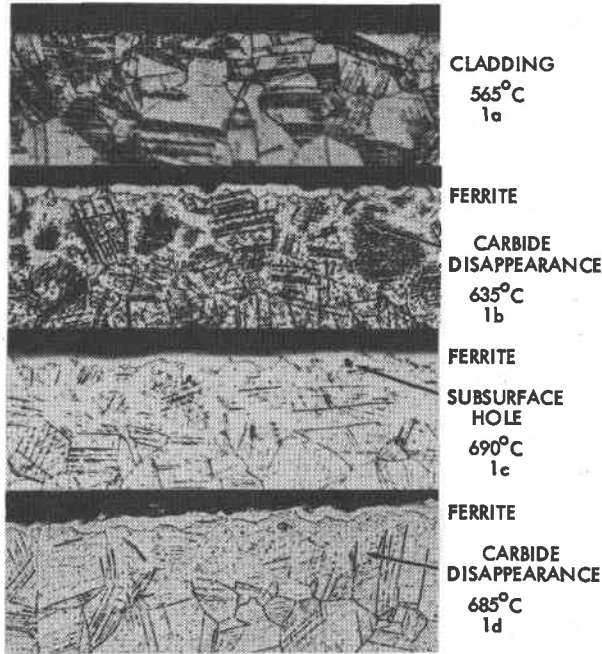
Temperatures of the cladding outside surface at 2.54 cm above the fuel, Table II, are time averaged over the exposure time. Temperature variations of the cladding outside surface over the entire irradiation period were 15°C maximum.

### Ferrite Formation and Carbide Depletion

The formation of ferrite and the disappearance of carbides along grain boundaries of the austenite were observed on the cladding outside surface of all fuel pins in the upper portion of the fuel column and the plenum. Cross sections of cladding were etched with a 2% chromic acid solution and photographed at 750X at up to 32 equally spaced intervals around the cladding.

Typical metallography of the outside cladding surface is shown in Figure 1 for pin P-23B-35B irradiated for 5328 hours. These photomicrographs show the ferrite layers, subsurface holes and the disappearance of carbides in and alongside austenite grain boundaries as a function of axial position and temperature. The ferrite was visible at very few locations on the surface of P-23B-35B at 565°C, Figure 1a. The disappearance of carbides along austenite grain boundaries was first evident at 635°C, Figure 1b. The thickness of the ferrite and depth of carbide disappearance was a maximum at the top of the fuel column, Figure 1c. Numerous subsurface and surface-connected holes were noted in the ferrite, generally at the ferrite-austenite interface. These holes were found only at the higher temperatures near the top of the fuel, Figure 1c, with very few in the downstream plenum region. Ferrite formation and carbide disappearance were noted at the minimum exposure examined, 1152 hours on pin P-23A-62F, at a temperature of 637°C, but neither were visible at 548°C.

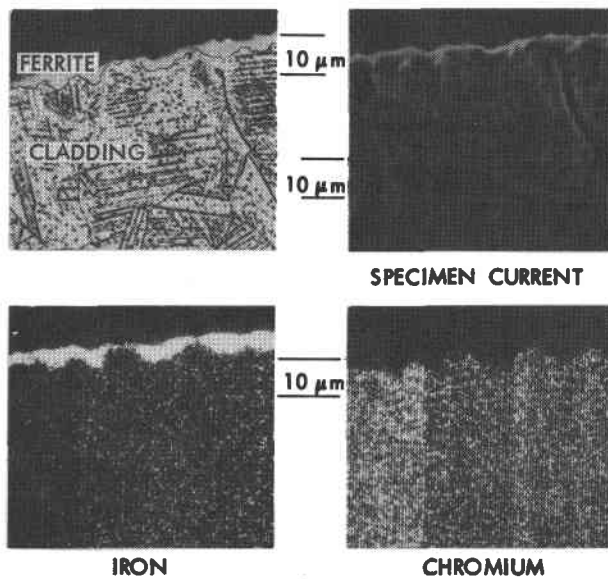




HEDL 7603-268.6

Figure 1: As etched irradiated P-23B-35B showing ferrite layer on outside and carbide disappearance along austenite grain boundaries after 5328 hours exposure in sodium at 2 m/s.

Typical electron microprobe analysis results are shown in Figure 2 for P-23A-25 near the top of the fuel column. The

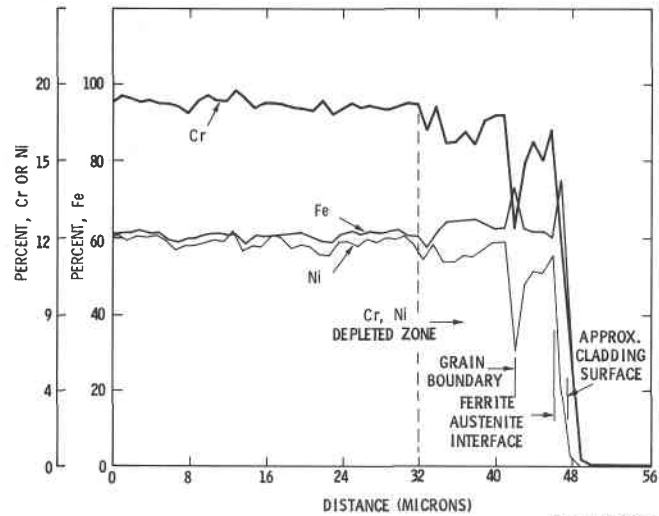


HEDL 7603-268.1

Figure 2: Electron microprobe analysis of irradiated cladding ferrite layer after 4608 hours exposure at 690°C.

thickness of the ferrite layer, approximately 4 μm, in the etched photomicrograph, corresponds very closely to the depth of the enhanced Fe layer. The depletion of Ni which caused the austenite-to-ferrite transformation closely duplicated the depletion of Cr shown on the rate meter scan.

To determine the composition along some of the grain boundaries where carbides disappeared, electron microprobe step scan analysis was made at 1 μm intervals across the ferrite layer and an austenite grain boundary located approximately 6 μm from the cladding outside surface near the top of the fuel column of P-23B-2A, Figure 3. The ferrite layer was 2 μm thick.



HEDL 7603-268.7

Figure 3: Electron microprobe step scan analysis perpendicular to surface exposure time 5328 hours at 700°C

The minimum Cr and Ni content shown in Figure 3 was 11% and 7.3%, respectively, in the grain boundary and 14% and 12.4% at the ferrite-austenite interface. The general depletion of Cr and Ni in the austenite extended from the ferrite-austenite interface to a depth of 16 μm.

Measurements were made on each of the 750X photomicrographs and an average and maximum thickness of ferrite and depth of carbide disappearance was calculated. For each cross section the average thickness of ferrite and depth of carbide disappearance was plotted. In the plenum region the cladding temperature decreases gradually by 15°C and is therefore considered to be of constant temperature. From these data plots the average thickness of ferrite and depth of carbide disappearance were determined at 2.5, 10.2, 20.3, 30.5 and 35.6 cm above the top of the fuel column in the plenum, and at five temperature regions of the cladding outside surface along the fuel column, 705/675, 675/650, 650/620, 620/595 and 595/565°C. Tables III and IV show the results for the ferrite measurements and depth of carbide disappearance, respectively, from eleven pins that can be grouped into three lengths of exposure time. Several pins had no data available at the lower temperature end of the fuel columns. Averaging the ferrite thickness and depth of carbide disappearance at each axial position for each of the three exposure periods indicate that the ferrite thickness and depth of carbide disappearance increases with increasing temperature along the fuel column and



# INTERNATIONAL CONFERENCE ON LIQUID METAL TECHNOLOGY IN ENERGY PRODUCTION

decreases with increasing distance downstream along the plenum from the top of the fuel column.

PIN NUMBER	EXPOSURE TIME-HRS	FUEL COLUMN					PLENUM REGION				
		CLADDING SURFACE TEMP. °C					DISTANCE ABOVE TOP OF FUEL - cm				
		565	595	620	650	675	2.5	10.2	20.3	30.5	35.6
23A-62F	1152	0.51	0.76	1.27	1.52	1.65	1.78	1.65	1.40	1.27	1.27
23A-26	2256	0	0.25	-	-	-	-	-	-	-	-
-63G	2352	0	0	0.38	1.27	1.91	2.29	2.29	2.16	1.40	1.27
23B-49C	2256	0	0	0.38	1.27	1.91	2.29	2.29	2.16	1.40	1.27
-50C	2256	-	-	1.45	2.03	3.05	3.30	3.30	2.29	2.03	1.78
-62D	2256	-	-	0.76	1.02	1.27	1.27	1.27	0.51	0.82	1.27
AVERAGE		0	0.12	0.91	1.46	2.06	2.29	2.35	1.59	1.40	1.40
23A-21	4608	1.02	1.78	2.79	3.56	4.32	4.32	3.81	3.18	2.54	2.16
-25	4608	-	-	-	3.81	3.81	3.81	3.56	3.30	3.05	2.79
23B-2A	5328	0.51	1.27	2.03	2.79	5.08	5.84	5.33	4.83	3.81	3.43
-14A	5328	-	-	-	-	3.56	3.05	2.54	2.03	1.79	-
-35B	5328	-	1.27	2.54	3.43	3.81	3.81	3.56	3.05	2.79	2.54
AVERAGE		0.76	1.44	2.45	3.40	4.25	4.27	3.86	3.38	2.84	2.54

HEDL 7603-268.8

Table III. Ferrite Layer Thickness -  $\mu\text{m}$

PIN NUMBER	EXPOSURE TIME-HRS	FUEL COLUMN					PLENUM REGION				
		CLADDING SURFACE TEMP. °C					DISTANCE ABOVE TOP OF FUEL - cm				
		565	595	620	650	675	2.5	10.2	20.3	30.5	35.6
23A-62F	1152	0	0	0	2.54	7.62	7.11	6.10	6.10	6.35	7.11
23A-26	2256	-	-	1.02	-	-	-	-	-	-	-
-63G	2352	-	-	-	-	7.87	7.87	5.33	5.84	6.06	6.10
23B-49C	2256	0	0	1.27	3.30	7.87	8.13	7.42	6.60	6.64	9.91
-50C	2256	-	-	8.64	10.16	15.24	16.26	15.24	13.46	12.45	11.43
-62D	2256	-	-	5.08	5.33	5.33	5.33	4.32	1.52	2.03	2.79
AVERAGE		0	0.51	5.00	6.26	9.98	9.59	8.13	6.86	7.50	7.56
23A-21	4608	0	2.54	8.13	14.48	14.73	14.22	11.94	10.67	9.14	7.11
-25	4608	-	-	-	11.43	13.72	13.72	13.21	12.45	11.94	11.68
23B-2A	5328	0	0	5.08	11.43	12.70	12.95	14.22	12.95	11.68	-
-14A	5328	-	-	-	-	13.21	11.43	9.14	7.42	6.86	-
-35B	5328	-	-	10.16	13.21	17.78	15.24	12.95	12.45	12.70	12.70
AVERAGE		0	1.27	9.14	11.05	14.42	13.82	12.50	11.79	10.87	9.84

HEDL 7603-268.9

Table IV. Depth of Austenite Grain Boundary Carbide Disappearance -  $\mu\text{m}$

### Carbon and Nitrogen Analysis

Chemical analyses for bulk carbon and nitrogen were performed on 6.4 cm long cylindrical sections of cladding at several axial locations on 11 pins from the P-23A and P-23B series. From one to four sections were analyzed for each axial position and the results averaged. Tables V and VI show the carbon and nitrogen analyses for each pin and unirradiated control specimens grouped by cladding heat number and length of exposure. The unirradiated control sections of cladding were processed in the hot cells and analyzed along with the irradiated sections to provide a check for contamination. The average carbon and nitrogen for each of the two cladding heats was determined from the unirradiated control section analyses.

Changes in the carbon and nitrogen from the data in Tables V and VI are plotted in Figures 4 and 5 as a function of cladding temperatures over the fueled region and as a function of distance downstream from the top of the fuel column.

Some trends are indicated:

- Those pins, Figure 4, with cladding from heat 88229, with an initial carbon content of 490 ppm, showed carbon increases of 80 to 180 ppm after approximately 2300 hours exposure, whereas pins with cladding from heat 87210 having a higher initial carbon content of 550 ppm showed slightly lower carbon increases, from 0 to 60 ppm, for the same exposure time.
- Pins from both cladding heats showed a decreased carbon content after approximately 5000 hours as compared to the carbon at 2300 hours.

HEAT NO.	CLADDING PIN NUMBER	SURFACE TEMP. °C	DISTANCE ABOVE BOTTOM OF FUEL cm	NUMBER OF SAMPLES	AVERAGE CARBON ppm	CARBON CHANGE ppm	
HEAT NO. 87210							
EXPOSURE TIME: 1192 HOURS							
23A-60D	370	-6.3		3	588	33	
	690	35.5		2	565	10	
	685	47.5		2	569	14	
	675	71.1		2	544	-10	
	EXPOSURE TIME: 2256 HOURS						
23B-49C	440	6.9		2	606	51	
	565	19.2		2	599	44	
	23B-50C	370	-11.2		3	572	17
		455	8.1		4	528	-27
		565	19.6		3	572	17
23B-50C	650	27.6		3	582	27	
	695	36.2		3	607	52	
	690	55.1		2	564	9	
	685	69.8		3	561	6	
	EXPOSURE TIME: 2352 HOURS						
23A-63G	370	-4.2		4	557	2	
	695	34.8		3	633	78	
	685	57.1		2	602	47	
	675	73.9		3	587	32	
	EXPOSURE TIME: 5328 HOURS						
23B-2A	370	-11.2		3	477	-78	
	455	7.4		3	526	-29	
	570	19.6		3	548	-7	
	645	27.4		3	608	53	
	690	38.1		3	515	-40	
23B-14A	680	56.1		3	548	-7	
	680	69.6		3	521	-34	
	370	-11.4		3	540	-15	
	565	18.5		3	510	-45	
	695	38.6		3	507	-48	
23B-35B	690	55.9		3	483	-72	
	370	-10.9		3	543	-12	
	HEAT NO. 88229						
EXPOSURE TIME: 2256 HOURS							
23A-26	370	-8.9		1	640	150	
	550	19.1		2	679	189	
	690	35.6		1	675	185	
	680	66.5		1	647	157	
	675	84.6		1	733	243	
23A-31	370	-8.9		1	570	80	
	590	22.8		2	585	95	
	665	57.6		1	635	145	
EXPOSURE TIME: 4608 HOURS							
23A-21	370	-7.1		3	528	38	
	450	8.1		2	570	80	
	665	36.1		3	532	42	
	660	56.4		3	540	50	
	655	74.8		3	554	64	
23A-25	370	-7.7		3	475	-15	
	455	8.6		2	533	43	
	565	19.8		3	553	63	
	690	35.9		3	528	38	
	685	56.9		3	486	-4	
680	75.0		3	469	-21		

HEDL 7603-268.13

Table V. Carbon Analysis of Irradiated Cladding

- For the group of pins at 2300 hours exposure, the carbon increase is higher at the top of the fuel column than at the bottom. In the plenum the carbon increase drops in going downstream.
- At the highest exposure time, approximately 5000 hours for heat 88229 pins, the carbon increase is a maximum in the lower half of the fuel column then tends to drop in going to the top of the fuel and on downstream over the plenum. For heat 87210 pins the results are confused.
- Pins with cladding from heat 87210 with an initial nitrogen content of 63 ppm showed no significant changes in nitrogen up to 2300 hours exposure, Figure 5. After approximately 5000 hours exposure there was a slight decrease over the fueled region with a greater decrease going downstream over the plenum.

INTERNATIONAL CONFERENCE ON LIQUID METAL TECHNOLOGY IN ENERGY PRODUCTION

6) For pins with cladding from heat 88229 with an initial nitrogen content of 225 ppm the trends were confused at the lower exposure time of 2300 hours although one pin 23A-26 showed a marked decrease which was larger at the top of the fuel column than at the bottom.

7) At the longer exposure time of 5000 hours the pins from heat 88229 also showed a marked decrease in nitrogen at the top of the fuel column. Over the plenum the trend reversed for both exposure times, that is, the decrease was smaller at the top of the plenum than upstream at the top of the fuel.

PIN NUMBER	CLADDING SURFACE TEMP. °C	DISTANCE ABOVE BOTTOM OF FUEL cm	NUMBER OF SAMPLES	AVERAGE NITROGEN ppm	NITROGEN CHANGE ppm
HEAT NO. 87210				63 ± 5	
EXPOSURE TIME: 1192 HOURS					
23A-60D	370	-5.6	1	63	0
	685	35.3	1	71	8
	675	71.1	1	61	-2
EXPOSURE TIME: 2256 HOURS					
23A-49C	450	7.6	3	69	6
23A-50C	370	-10.2	3	73	10
	575	20.3	3	63	0
	655	28.4	3	61	-2
	695	37.3	3	74	11
	690	57.2	3	60	-3
	685	68.6	3	69	6
EXPOSURE TIME: 2352 HOURS					
23A-63G	370	-5.1	3	65	2
	695	37.1	3	55	-8
	685	64.8	3	71	8
	675	74.9	3	68	5
EXPOSURE TIME: 5328 HOURS					
23B-2A	370	-9.4	3	49	-14
	470	9.4	3	55	-8
	590	21.3	3	57	-6
	655	28.9	3	47	-16
	690	39.6	3	50	-13
	685	57.9	3	47	-16
	680	67.6	3	42	-21
23B-14A	370	10.2	3	60	-3
	570	19.3	2	62	-1
	690	39.4	3	58	-5
	685	57.2	3	35	-28
23B-35B	370	-10.2	3	55	-8
HEAT NO. 88229				225 ± 27	
EXPOSURE TIME: 2256 HOURS					
23A-26	370	-8.6	1	184	-41
	690	34.6	1	152	-73
	680	67.1	1	162	-63
	675	84.8	1	151	-74
23A-31	370	-8.9	1	218	-7
	590	23.9	1	218	-7
	665	57.2	1	293	68
EXPOSURE TIME: 4608 HOURS					
23A-21	370	-6.4	2	200	-25
	665	36.3	1	158	-67
	660	56.9	2	186	-39
	655	74.4	2	194	-31
23A-25	370	-7.6	1	234	9
	605	23.9	2	228	3
	690	36.3	2	182	-43
	680	73.4	2	232	7

HEDL 7603-268.12

Table VI. Nitrogen Analysis of Irradiated Cladding

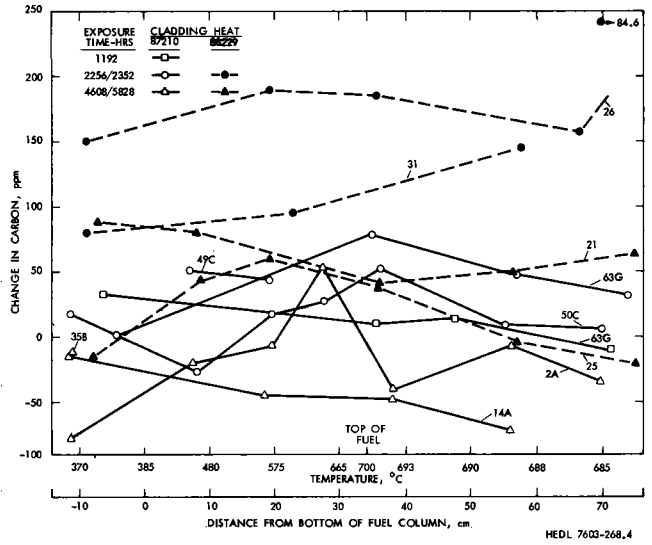


Figure 4: Changes in carbon content of cladding irradiated in EBR-II

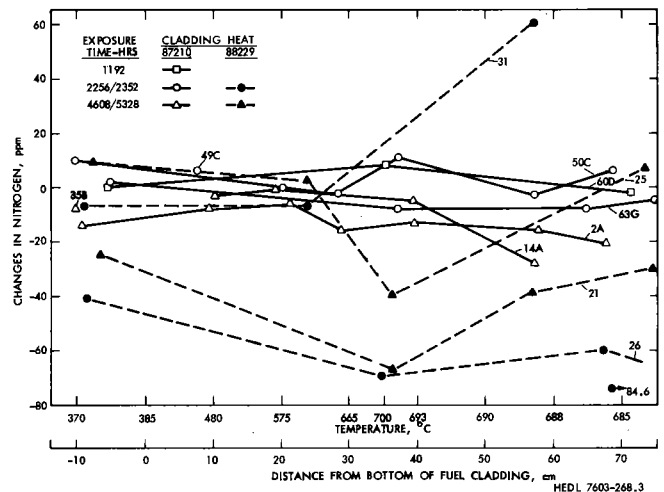


Figure 5: Changes in nitrogen content of cladding irradiated in EBR-II

DISCUSSION

Sodium Corrosion

The sodium corrosion rates presented in Table II and shown plotted in Figure 6 as a function of temperature, are believed to represent the maximums to be expected on a fuel pin cladding immediately above the heat generating surface at a cladding temperature from 670°C to 700°C in sodium flowing at 2.1 m/s. Although the averages of corrosion rates at the three exposure times suggests an increasing corrosion rate with time the accuracy of the measurements and small amount of data available do not warrant such a conclusion. Other studies on the effect of time on sodium corrosion rates have shown an initially high rate of corrosion that approaches a steady state rate after less than 300 hours<sup>(5)</sup>. Data at longer irradiation exposure times which will be available by the end of 1976 are required.

In the sodium velocity range for these irradiation experi-

ments (2.1 m/s) out-of-reactor sodium corrosion results have shown a velocity dependence<sup>(5)</sup>. An extensive review of low velocity out-of-reactor data was made and relationships developed to describe the data for velocities less than 3 m/s<sup>(6)</sup>. In Figure 6 a curve for this relationship at a sodium velocity of 2.1 m/s and oxygen content of 1 ppm is plotted for comparison of the HEDL in-reactor rates. Most of the HEDL irradiation test data at the longer exposures times lie at corrosion rates approximately twice that of the unirradiated test rates. However, as pointed out in Reference 6, a large axial temperature gradient, as exists in these irradiation tests, is expected to result in a doubling of the corrosion rate in the heat generating zone and a continuation of the higher corrosion rate for some distance downstream. The measurements of cladding thickness as a function of axial position showed that reduction of thickness decreased rapidly going downstream from the point 2.54 cm above the top of the fuel, where corrosion rates were estimated. These results suggest that within 15 cm downstream the corrosion rate has reduced by a factor of 10.

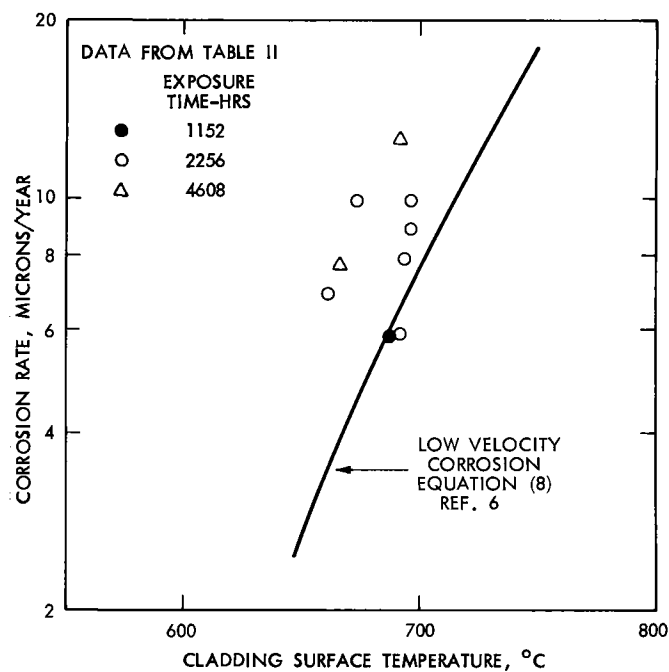


Figure 6. Corrosion rate of type 316-20% cold worked fuel pin cladding irradiated in EBR-II

Ferrite Formation and Carbide Disappearance

The observations of ferrite formation in these irradiation experiments is typical of those reported from out-of-reactor corrosion studies. Ferrite is being formed by the depletion of austenite-stabilizing elements Ni and perhaps Mn, C, and N into the sodium. Cr is also being leached out of the cladding by the sodium and the result is an Fe-enhanced layer on the cladding surface, Figure 2. From the quantitative step scans in Figure 3 for cladding exposed for 5300 hours the surface composition appears to be from 1 to 4% Ni and from 4 to 10% Cr which is in agreement with other reported cladding surface compositions<sup>(8,9)</sup>.

The quantitative measurements of Cr and Ni in the austenite matrix at the ferrite to austenite interface, Figure 3, show that compositional changes are occurring up to 15 to 20 μm deep into the austenite. However, along grain boundaries the changes are larger, the Cr and Ni decreasing from 16.5 and 13.7% nominal to 11 and 7.3%, respectively at 6 μm from the cladding surface. At the same distance in from the surface, the matrix composition is 14.5% Cr and 13.5% Ni. It is not certain if the disappearance of carbides from austenite grain boundaries near the ferrite interface are the result of very local carbon losses to the sodium, or if the decreasing Cr content of the grain boundaries is leading to a resolution of the carbides as suggested in Reference 10. However, bulk carbon losses, if any, are not large (see section on Carbon and Nitrogen Analysis).

The measurements of ferrite thickness and depth of carbide disappearance shown in Tables III and IV have been plotted in Figure 7 to show the depth and thickness as functions of axial position in the plenum and temperature in the fueled region.

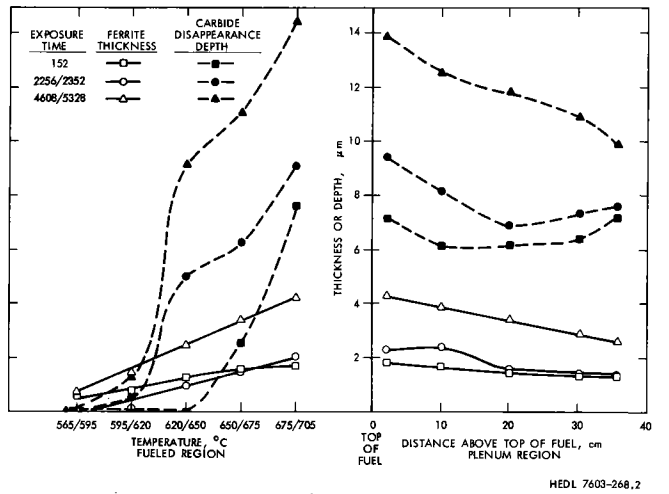


Figure 7. Thickness of ferrite layer and depth of carbide disappearance in austenite grain boundaries in fuel pin cladding irradiated in EBR-II

In the fueled region the ferrite thickness appears to be linear with temperature for the two longer exposure periods, and to be increasing with time beyond 2300 hours exposure. At 625 to 700°C the rates are approximately equal for 2300 and 5000 hours, 7.5 μmpy, while at 1100 hours the rate is approximately twice that, 13.1 μmpy, indicating an initial high rate of formation followed by a rapid slowing down to an equilibrium rate of 7.5 μmpy. The maximum thickness of 4.3 μm is consistent with results reported in Reference 8, 6 μm at 718°C after 5500 hours.

Over the plenum region the thickness of ferrite decreases with distance downstream from the top of the fuel and, after 5000 hours appears to be linearly dependent with distance. As in the fuel column region, the formation rate for 2300 hours and 5000 hours are approximately equal at the top of the fuel column while the rate after 1100 hours exposure was twice as high.

The depth of carbide disappearance in the austenite grain boundaries, plotted in Figure 7, increases more rapidly with temperatures in the fueled region than does the ferrite thickness.

Both the 2300 and 5000 hour exposure show an inflection at approximately 620 to 650°C. At 675 to 705°C the rate is 34.8  $\mu\text{m}$ py at 2300 hours and 25.3  $\mu\text{m}$ py at 5000 hours.

The depth of carbide disappearances are believed to correlate at least qualitatively with the depth of Cr and Ni depletion into the austenite. After approximately 5000 hours at 675-705°C the metallographic results show the total depth of carbide disappearance from the cladding surface is 19  $\mu\text{m}$ , approximately 4  $\mu\text{m}$  through the ferrite layer and approximately 15  $\mu\text{m}$  through the austenite. The electron microprobe result shows a similar depth for the Cr, Ni depleted zone, approximately 16  $\mu\text{m}$  from the ferrite austenite interface. These irradiation test results show shallower depleted zone than reported in out-of-reactor tests, 44  $\mu\text{m}$  at 718 C after 5500 hours<sup>(8)</sup>. This work by Whitlow, et al.<sup>(8)</sup> on the equilibrium thickness of depleted layers as a function of temperatures and corrosion rates would indicate that the depth of Cr and Ni depletion will continue to increase on further exposure.

#### Carbon and Nitrogen Analysis

Discussions and analysis of the behavior of interstitial elements carbon and nitrogen in austenitic stainless steels exposed to flowing sodium have shown the processes leading to increases or decreases in carbon or nitrogen to be extremely complex relationships to temperature, interstitial element contents of the sodium and cladding and length of exposure<sup>(11,12,13)</sup>. Snyder, et al.<sup>(12)</sup> proposed that carburization and decarburization could take place in EBR-II irradiated fuel pins with maximum cladding outside surface temperatures in the range of the P-23A and P-23B fuel pins. The maximum carburization would occur between one half and two thirds the way up the fuel column. Near the top of the fuel column and into the plenum either decarburization or carburization could occur depending upon the carbon content of the sodium and the irradiation temperatures. Except for one of the highest exposures pins from heat 87210, P-23B-14A, all of the HEDL fuel pins showed some apparent carburization, the maximum generally occurring near the top of the fuel column (Figure 4). The trend towards a lower amount of carburization with increased exposure as shown in the HEDL pins is not in agreement with the results postulated by Snyder, et al.<sup>(12)</sup> where some increase in carburization was expected with longer exposures.

Nitrogen loss from 316 stainless steel has been reported<sup>(13)</sup> in flowing sodium after 3300 hours at 690°C. Other studies have shown nitrogen losses to have a very steep temperature dependence, going from an initial 1000 ppm at 600°C to 400 ppm at 700°C<sup>(14)</sup>. Analysis of irradiated cladding from a Mol 7A experiment<sup>(14)</sup> showed no change in nitrogen, however, the cladding temperature was approximately 600°C where no changes would be expected. The behavior of the bulk nitrogen content of the HEDL irradiated fuel pin cladding is in general agreement with these findings; however, the changes are not so severe as would be predicted at 700°C. The higher nitrogen cladding heat 88229 tends to show more nitrogen decrease than the low nitrogen heat 87210. Also the nitrogen decrease is greatest (except pin P-23A-31) at the temperature from 600 to 700°C. There is apparently a downstream effect as illustrated by pins P-23A-21, -25 and -26, which reduces the nitrogen loss.

#### SUMMARY AND CONCLUSIONS

- These irradiation test results have shown corrosion rates in-reactor in flowing sodium with a heat generating source that are approximately those predicted from unirradiated out-of-reactor loop tests.

- Mass transfer of substitutional Cr and Ni was found to occur in these irradiated pins with essentially identical results to that out-of-reactor. After 5000 hours exposure the formation of a measurable ferrite layer begins as low as 560°C and reaches an average thickness of slightly less than 5  $\mu\text{m}$  at a temperature of 700°C. Extending into the austenite from the ferrite interface a distance of approximately 15  $\mu\text{m}$  is a zone depleted in Cr and Ni.

- Large changes in carbon and nitrogen were not observed. Slight carburization was noted at lower exposure times but decreased carbon content was observed at exposure times exceeding 5300 hours. Loss of nitrogen appears to occur with the longer exposures, but this is dependent upon the initial level of nitrogen in the cladding, being greater at 225 ppm than at 63 ppm.

The sodium corrosion effects observed on these irradiated fuel pins have provided an initial comparison of the in-reactor behavior with the out-of-reactor sodium loop test data on 316 type stainless steel cladding. In general, these comparisons look good. For exposure times up to 5000 hours there are no significant deviations from the expected performance predicted from out-of-reactor loop tests.

#### REFERENCES

1. J.E. Hanson and W.E. Roake, "FTR driver fuel development program status," in Proceedings at the Conference on Fast Reactor Fuel Elements Technology, American Nuclear Society, Hinsdale, Ill, 1971, (pp 497-515).
2. J.E. Draley and J.R. Weeks, Corrosion by Liquid Metals, Plenum Press, New York, 1970.
3. S.A. Jansson, Chemical Aspects of Corrosion and Mass Transfer in Liquid Sodium, The Metallurgical Society of the AIME, New York, 1973.
4. Liquid Alkali Metals, Proceedings of the International Conference on Liquid Metals, Nottingham University, April 1973, sponsored by the British Nuclear Energy Society.
5. J.R. Weeks and H.S. Isaacs, "Corrosion and deposition of steels and nickel-base alloys in liquid sodium," in Advances in Corrosion Science and Technology, Vol 3, Plenum Press, New York, 1973, (pp 1-66).
6. C. Bagnall and D.C. Jacobs, Relationships for Corrosion of Type 316 Stainless Steel in Liquid Sodium, WARD-NA-3045-23, May 1975.
7. Reactor Development Program Progress Report, Series, ANL-RDP-1 through ANL-RDP-37, January 1972 through February 1975, Argonne National Laboratory.
8. G.A. Whitlow, J.C. Cwynar, and S.L. Schrock, "Sodium corrosion behavior of alloys for fast reactor applications,"

## INTERNATIONAL CONFERENCE ON LIQUID METAL TECHNOLOGY IN ENERGY PRODUCTION

in Chemical Aspects of Corrosion and Mass Transfers,  
AIME, New York, 1973 (pp 1-63).

9. C.A. Thorley and C. Tyzack, "Corrosion and mass transport of steel and Ni alloys in sodium system," in Liquid Alkali Metals, BNES, 1973 (pp 257-264).
10. B. Weiss and R. Stickler, "Phase instabilities during high temperature exposure of 316 austenitic stainless steel," Metallurgical Transactions, Vol 3, pp 851-966 (1972).
11. S.A. Shiels, C. Bagnall and S.L. Schrock, "Carbon equilibrium relationships for austenitic stainless steels in a sodium environment," Nuclear Technology, Vol 23, pp 273-283 (1974).
12. R.B. Snyder, K. Natesan, and T.F. Kassner, "Kinetics of the carburization decarburization process of austenitic stainless steel in sodium," Journal of Nuclear Materials, Vol 50, pp 259-274 (1974).
13. S.A. Shiels, C. Bagnall, and S.L. Schrock, "Interstitial mass transfer in sodium systems," in Chemical Aspects of Corrosion and Mass Transfer in Liquid Sodium, AIME, New York, 1973 (pp 157-176).
14. H.U. Borgstedt and E.D. Grosser, "Interstitial element movement of austenitic steels in sodium," in Liquid Alkali Metals, BNES, 1973 (pp 276-282).

## THE INFLUENCE OF LMFBR FUEL PIN TEMPERATURE PROFILES ON CORROSION RATE

S. A. Shiels, C. Bagnall, S. L. Schrock, S. J. Orbon

Westinghouse Electric Corporation  
Advanced Reactors Division  
Madison, Pennsylvania 15663

## ABSTRACT

This paper describes the sodium corrosion behavior of 20% cold worked Type 316 stainless steel fuel pin cladding under a simulated reactor thermal environment. A temperature gradient, typical of a fuel pin was generated in a 0.9 m long heater section by direct resistance heating. Specimens were located in an isothermal test section immediately downstream of the heater.

A comparison of the measured corrosion rates with available data showed an enhancement factor of between 1.5 and 2 which was attributed to the severe axial temperature gradient through the heater. Differences in structure and surface chemistry were also noted.

The observed increase in corrosion rate is considered to be particularly important in estimating radioactive corrosion product release rates. Application of these data will lead to higher estimates for the radiation levels at downstream locations such as the primary pump and IHX and may, therefore influence the planned maintenance procedures for these components.

## INTRODUCTION

In a sodium cooled reactor, the fuel pin, fabricated from 20% cold worked Type 316 stainless steel tubing, will experience the most severe corrosive environment. In some designs, not only will the pin experience surface temperatures up to 738°C, but also heat fluxes up to nearly 1600 kW/m<sup>2</sup>. This high heat flux gives rise to a steep radial temperature profile through the sodium and also introduces a large axial temperature gradient of about 340°C/m.

The corrosion rate of the fuel cladding will be strongly influenced by these factors, in conjunction with the geometry and sodium mass flow prevailing in the reactor core.

Most corrosion testing in the past has been performed under low axial temperature gradient (dT/dL) conditions. The sodium was usually heated with regenerative heat exchangers and external radiant heaters. Typical temperature gradients achieved in this manner were about 40°C/m. These available data have been summarized and statistically evaluated by Bagnall and Jacobs<sup>(1)</sup>. They derived two equations, one for velocities below 3 m/s and one for velocities above 3 m/s, which give the corrosion rate of Type 316 stainless steel as a function of temperature, oxygen level and velocity. The equations are currently in use in the USA. They do not, however, take into account the effect of heat flux and the resultant temperature gradient or the effect of the mass flow rate (G) to exposed surface area (A) ratio.

The lack of data generated under high heat flux is due principally to the experimental difficulties involved. Past attempts at reproducing fuel pin conditions in the laboratory were somewhat inconclusive.<sup>(2,3)</sup> It appeared that the resulting enhanced corrosion rates were due to a temperature difference between the specimen wall and the bulk sodium and not to the heat flux per se. In another study, an enhancement of a factor to two to three was observed when the corrosion rates of Type 316 stainless steel specimens were compared under both high and low dT/dL conditions in the same system.<sup>(4)</sup>

The current work attempted to simulate the thermal environment of the fuel cladding. Specimens were located at the immediate outlet of a high dT/dL heater section and were exposed to sodium at the fuel cladding hot spot temperature (~740°C). The temperature gradient through the heater reproduced the wall temperature gradient along the hottest fuel pins and the G/A ratio in the heater section approximated that of a fuel assembly sub-channel, thus eliminating the uncertainties of temperature profile and geometry effects.

The work was performed at Westinghouse Advanced Reactors Division (WARD) as part of an ERDA funded program on Sodium Component Materials Compatibility.

## The Test Facility

The high heat flux work was carried out in the Interstitial Transfer Facility (ITF). The facility, shown in Figure 1, was designed as a small scale simulation of a reactor primary system specifically for interstitial transfer studies. A report of this work is covered elsewhere in these proceedings. Three test legs, the primary heater/isothermal leg, the bypass leg and the secondary heater leg, represent the reactor core. Sodium flow from the three sections mixes in the surge tank and then exits through a fourth test leg, representative of the Intermediate Heat Exchanger (IHX). Oxygen levels are controlled by a cold trap, installed in a separately pumped bypass leg, and are measured by the vanadium wire technique. The Vanadium Wire Equilibration Module (VWED) is installed in a second bypass line also with its own pump.

The test section of interest in this work is the primary heater/isothermal leg. The required axial temperature gradient is achieved by direct resistance heating; the current is passed directly through the sodium in the heater section, via electrodes which are an integral part of the containment tubing. The axial temperature profile is thus obtained without the severe radial temperature gradient and high wall temperatures experienced with radiant heaters.

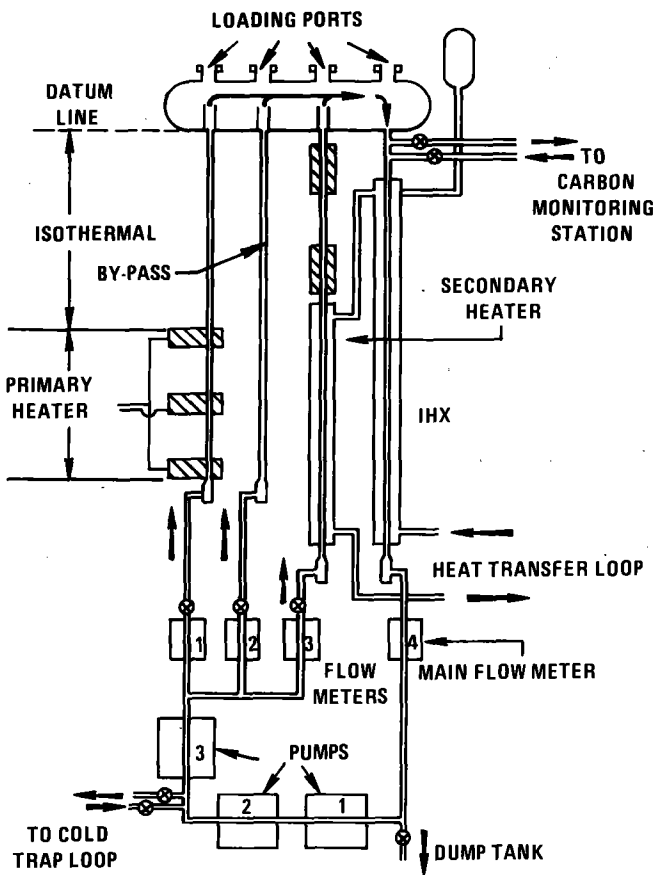


Figure 1. ITF main loop schematic

The heater section consists of three heavy stainless steel electrodes with a 94 mm (0.370 in.) dia. flow path, connected by two length of 127 mm (0.5 in) O.D. x 2.65 mm (0.065 in.) wall Type 316 stainless steel tubing. The all welded test section has an overall length of 0.91 m (3.0 ft.). Power is supplied to the electrodes from a step-down transformer via 150 mm x 50 mm copper bus bars and flexible copper cables. The two outer electrodes are kept at the same potential to insure that the current only passes through the heater section. The required axial temperature gradient is achieved with a power input of about 7.5 VAC and 7500 A. The heating rate obtained is the equivalent to ~ 1580 kW/m<sup>2</sup> (500,000 Btu/hr/ft<sup>2</sup>).

Test specimens are located in the 1.22 m (4 ft) long isothermal test section immediately above the heater. The first specimen experiences the sodium exiting the heater at the maximum corrosion potential and is therefore representative of a reactor hot spot location.

The Specimens

Two types of specimens were exposed in the isothermal section.

- 20% Cold Worked Type 316 stainless steel fuel pin cladding, 5.84 mm O.D. x 0.38 mm wall (0.230 in x 0.025 in) 25.4 mm (1 in) long, located at the most upstream and downstream locations.

- Type 316 stainless steel foils, 0.076 mm (0.003 in) thick, approximately 9 mm wide and up to 150 mm long.

The 25.4 mm cladding samples were held on a mandrel, which was designed to prevent flow on the I.D. surface. Foil samples were wired onto a central support rod held in position by means of spring fingers. Foils were also exposed in the heater section. Chemical compositions of the specimen materials are given in Table I.

Table I  
Specimen Chemical Composition (w/o)

Material	C	N	Cr	Mn	Ni	Mo	Ti	Si
T 316(L) Foil*	0.02	0.05	16.7	1.5	13.1	2.5	0.01	0.4
T 316 Foil**	0.07	0.09	18.5	1.5	13.8	2.6	0.02	0.3
T 316 20% CW Cladding (*)(**)	0.05	0.03	17.0	1.5	13.6	2.3	0.01	0.5

\*Run 4

\*\*Runs 5 and 6

Experimental Procedure

Specimens were carefully cleaned and vacuum dried prior to initial weighing. The sample train was assembled by screwing the specimen mandrels and intermediate support rods together. The total assembly was then installed in the primary heater/isothermal test section. Test conditions for each run are given in Table II. Oxygen levels were monitored periodically using the vanadium wire equilibration technique.

After exposure, specimens were cleaned, vacuum dried and re-weighed. Metallographic, scanning electron microscopy and electron microprobe studies were performed on selected samples.

Table II  
Loop Operating Conditions for ITF

		ITF-4	ITF-5	ITF-6
Main Htr. Flow Rate	(l/s)	7.9x10 <sup>-2</sup>	9.5x10 <sup>-2</sup>	9.1x10 <sup>-2</sup>
	(gpm)	1.25	1.5	1.45
Main Htr. Inlet	(°C)	435	447	443
	(°F)	815	837	830
Main Htr. Outlet	(°C)	738	738	738
	(°F)	1360	1360	1360
Cold Trap	(°C)	121	115	115
	(°F)	250	240	240
Run Duration	(h)	1500	2136	(2477)*
Mean O <sub>2</sub>	(ppm)	0.82	0.87	1.01

\*Selected specimens accumulated a total exposure of 2477 hours.

EXPERIMENTAL RESULTS

Corrosion Data

The corrosion data from three runs, Nos. 4, 5 and 6 are given in Table III. The downstream position, L/D, was measured from the exit of the heater section with L being the linear distance from the reference point and D being the hydraulic diameter which is given by:

$$\frac{4 \times \text{cross sectional area of flow}}{\text{wetted perimeter}} \quad (1)$$

This is equal to  $0.356 \times 10^{-2}$  m for the cladding and  $0.480 \times 10^{-2}$  m for the foil.

Table III  
ITF Corrosion Data

Specimen Number	Distance From Leg Inlet (m)	L/D (From Htr. Exit)	R/φ (μm/y/ppm O <sub>2</sub> )
4A7 (c)*	0.956	6.0	33.0
4A8	1.411	101.9	17.3
4A9	1.511	127.0	18.3
4A10	1.600	145.8	22.3
4A13	2.057	237.7	13.6
4A14 (c)	2.101	257.8	16.7
5A4	0.622	H**	1.3
5A5	0.762	H	9.3
5A7 (c)	0.940	6.0	30.4
5A8i	1.448	109.7	14.9
5A8ii	1.524	129.5	17.2
5A12	1.943	191.7	13.4
5A14 (c)	2.121	244.8	16.9
6A20	0.165	H	-0.03
6A21	0.320	H	0.4
6A22	0.409	H	3.4
6A26 (c)	0.942	3.6	22.4
6A8 (c)	1.323	110.0	21.1
6A27	1.501	137.0	14.0
6A28	1.631	166.0	13.6
6A29	1.814	195.0	12.6
6A30	1.885	214.0	13.0
6A32 (c)	2.121	251.7	14.0

Note: \*(c) denotes cladding sample; all others are foils.

\*\* H denotes specimen located in the heater, prior to isothermal zone.

Figure 2 shows the foil data for two of the runs as a function of position. The corrosion values, normalized to 1 ppm oxygen are compared with the values predicted using the low velocity equation from reference 1:

$$R/\phi_{(VWED)} = (2.9728 \times 10^8 + 2.9133 \times 10^8 V) \times \text{Exp}(-18120/T_K) \quad (2)$$

where R = corrosion rate in μm/y  
φ = oxygen level in ppm (VWED)  
V = sodium velocity in m/s

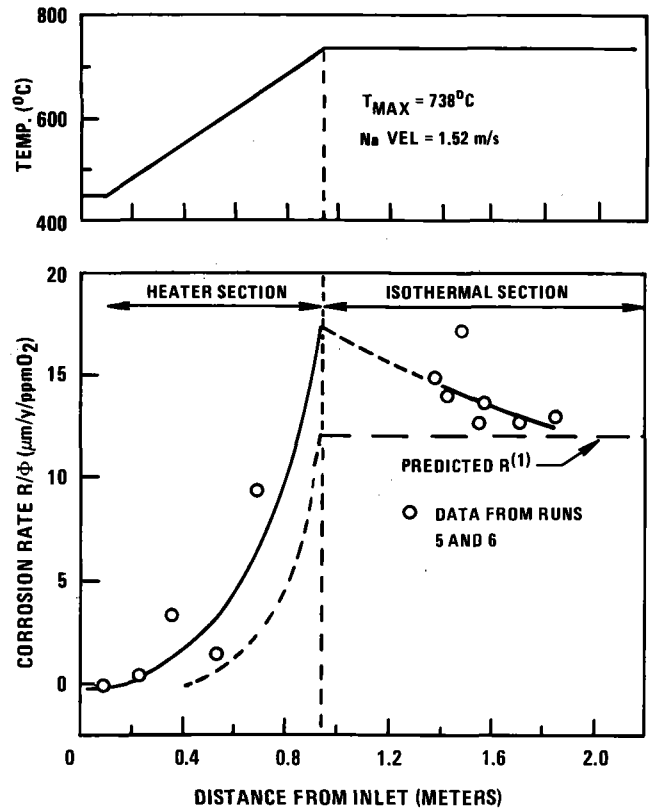


Figure 2. Effect of high dT/dL on the corrosion behavior of Type 316 stainless steel

Values from the isothermal region showed a definite downstream effect. In all cases the measured corrosion rate was higher than predicted. Extrapolation back to the heater exit region gave a maximum corrosion rate of 17.5 μm/y, compared with the value predicted by Equation (2) of 12.2 μm/y. Corrosion rates in the heater section itself were also substantially higher. Note that some deposition occurred at the heater inlet, (Sample 6A20, Table III). The crossover from deposition to corrosion was estimated to occur at about 485°C, about 0.2 meters from the test leg inlet or 0.1 meter into the heater section.

The normalized corrosion rates for the 20% cold worked cladding are plotted as a function of L/D in Figure 3 along with the foil data from runs 4, 5, and 6. The zero L/D position is taken as the outlet of the heater section. All data are from the isothermal section only.



Extrapolated values at  $L/D = 0$  are  $29 \mu\text{m}/\text{y}$  for the cladding at  $\sim 2\text{m}/\text{sec}$  and  $17.5 \mu\text{m}/\text{y}$  for the foils at  $\sim 1.5 \text{m}/\text{sec}$ . These compare with predicted values of  $16 \mu\text{m}/\text{y}$  and  $12.2 \mu\text{m}/\text{y}$ . A definite downstream effect is apparent for both the cladding and the foils; the slopes are different, however. The corrosion rates remain above the predicted values until at least the 240  $L/D$  position.

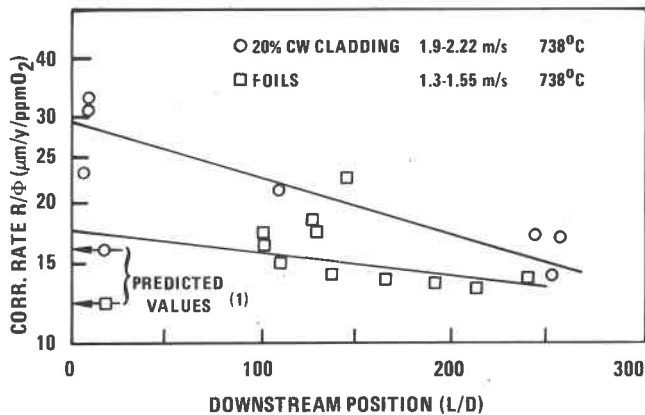


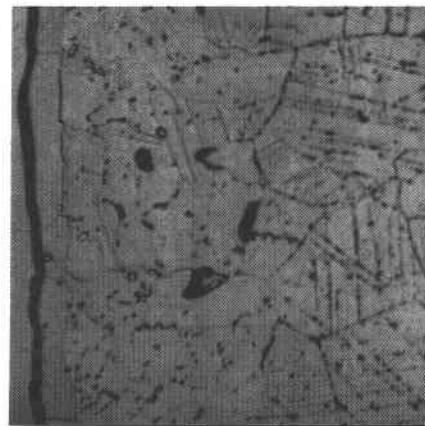
Figure 3. Corrosion rate of Type 316 stainless steel as a function of position downstream from high  $dT/dL$  heater

#### Metallography - Cladding Specimens

The most notable structural change to the cladding material exposed in the isothermal region was the formation of a ferritic surface layer  $\sim 7.5 \mu\text{m}$  thick at  $L/D = 0$ . Photomicrographs taken from cross sections at the sodium exposed O.D. of ITF-4 specimens are shown in Figure 4. Depletion of alloy constituents after this exposure period has not reached an equilibrium condition, but the loss of austenitizing elements (Ni, Mn, C) has clearly been enhanced in Specimen 4A7 to the point at which a transformation of the original austenite has occurred. It appears that at a downstream position of  $L/D = 260$  (Specimen 4A14) there has been a much smaller net loss of these elements, and the alloy surface has remained austenitic.

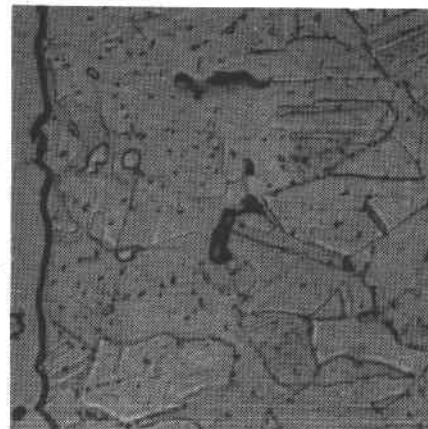
Evidence for a depleted zone, however, does exist in both specimens. The density of carbide precipitate shows a marked decrease within 25 - 50  $\mu\text{m}$  of the O.D. This does not necessarily reflect the extent of a gradient for any one element, but indicates some alloy change and the depth to which carbide dissolution, at this exposure period, is kinetically favored.

Samples 4A7 and 4A14 have been given a second etch with a solution of 1 percent chromic acid in water to distinguish the stable second phase sigma particles in the structure. The sigma is attacked and appears black. It will be noted that many medium-sized particles, beneath the ferritic in Figure 4a, but even visible on the surface in Figure 4b, remain unattacked, by the etchant, suggesting that they are of different composition. This is not the case in midwall regions where all the intermetallic particles appear to be sigma. These differences again point to the composition gradient which exists at the sodium-exposed surface of the cladding.



a) #4A7,  $L/D = 0$

10  $\mu\text{m}$



b) #4A14,  $L/D = 260$

10  $\mu\text{m}$

Figure 4. Microstructure of OD surface of 20% CW Type 316 stainless steel cladding after 1500 h Na exposure at  $738^\circ\text{C}$

#### Scanning Electron Microscopy

The metallographic observations made on run No. ITF-4 cladding samples were supported with evidence obtained from the Scanning Electron Microscope (SEM). Figure 5a shows the topographical appearance of unexposed material, and the X-ray analysis of the matrix depicts a typical distribution of molybdenum, chromium, iron, and nickel for Type 316 stainless steel. Figure 5b illustrates the appearance of the cladding immediately above the primary heater, at the start of the isothermal section. Exposure for 1500 hours at  $738^\circ\text{C}$  has resulted in the formation of an uneven iron-rich ferritic surface containing small amounts of molybdenum and chromium, with nickel markedly absent. The downstream specimen, however, revealed an undulating surface with many small, rounded, corrosion resistant particles (Figure 5c). Analysis of the matrix showed that it was close in composition to the unexposed material, although the iron; chromium and iron; nickel ratios were somewhat higher. The particles, on the other hand, contained a high concentration of molybdenum and no nickel. This finding strongly suggests that the etch-resistant phase observed in metallographic cross-sections was indeed not sigma ( $\text{Fe}/\text{Cr}$ ), but another intermetallic such as Laves phase, ( $\text{Fe}_2\text{Mo}$ ).

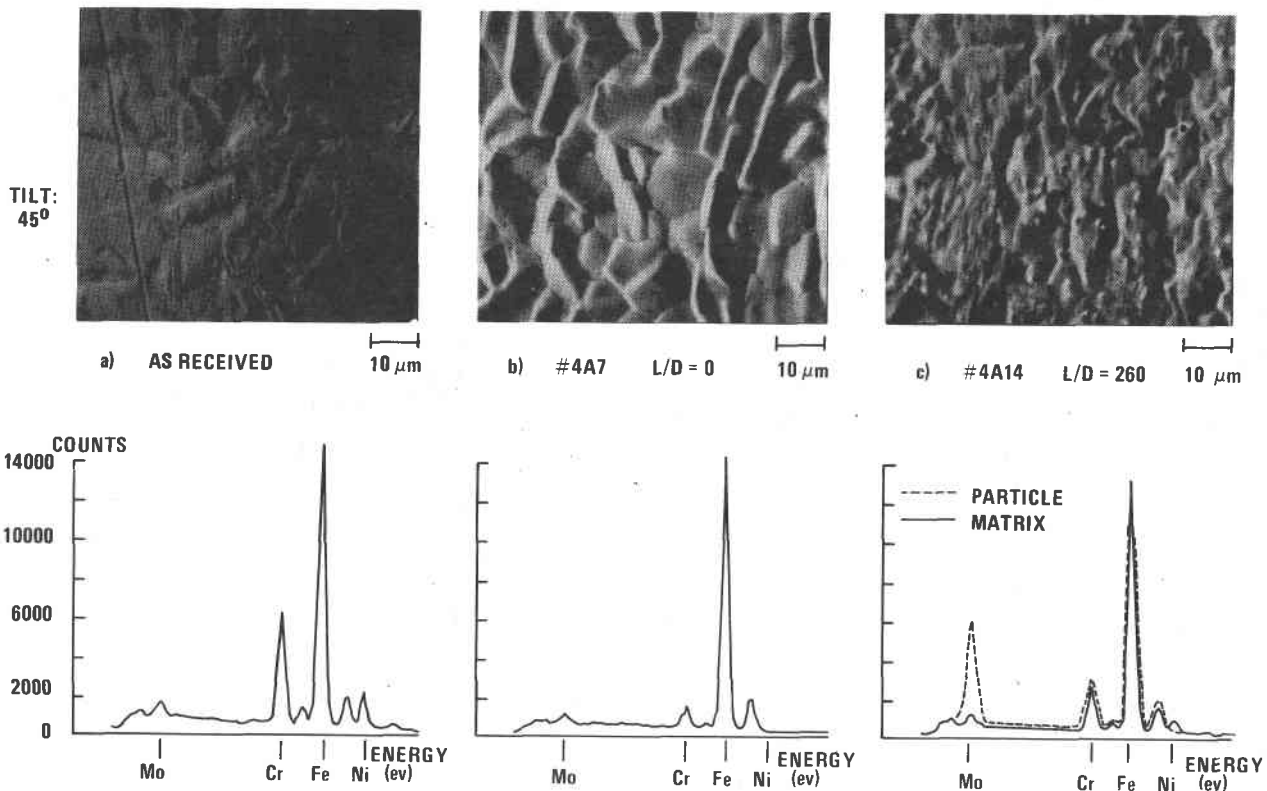


Figure 5. Surface features of 20% CW Type 316 stainless steel cladding before and after 1500 h Na exposure at 738°C

The foregoing observations, made on specimens which were subjected to high temperature flowing sodium in which the  $dT/dL$  was also high, showed significant departure from earlier data obtained in forced convection systems incorporating a low heating rate. Berkey and Whitlow<sup>(5)</sup> found topographical structures similar to the downstream specimen shown in Figure 5c, on Type 316 stainless steel tubular samples exposed at a zero downstream location for 5500 hours and 10,000 hours at 718°C. It appears that in a high  $dT/dL$  environment at low  $L/D$  positions, the "Fe/Mo" particles either do not remain stable in the ferrite layer or they are dissolved as they become exposed to the sodium. Metallographic evidence would support the former theory, since considerable intermetallic precipitate similar to the Laves phase was observed in the depleted zone beneath the ferritic surface. Further, in the earlier work the Fe/Mo particles were found in conjunction with ferrite, whereas in this study they were absent, suggesting that differences in ferrite composition can influence their stability. Evidence of such compositional differences was found in the electron microprobe studies; these are described below.

#### Electron Probe Microanalysis

The chemical composition profiles at the sodium exposed surface of cladding samples were examined from each experiment. Data for the 2000 hour run (ITF-5) are shown in Figure 6. At  $L/D = 0$  the original basic 17 Cr - 13 Ni - 69 Fe alloy has been depleted over a 40  $\mu\text{m}$  depth resulting in a composition at the surface of about 3 Cr - 3 Ni - 92 Fe.

A comparison of these results, with the earlier work<sup>(5)</sup> again demonstrates the magnitude of the change produced by this high  $dT/dL$  environment. The earlier data, obtained at 718°C under moderate heat input conditions of about 158  $\text{kW}/\text{m}^2$  showed the development of an equilibrium surface condition after 5,500 hours with the composition basically at 6 Cr - 2 Ni - 90 Fe. With an order of magnitude increase in heat input in the ITF, the depletion of major alloying elements raised the surface iron content to this same level in one third of the exposure period.

While this comparison does serve to illustrate the marked effects the reactor core will have on element depletion in the base alloy, particularly with regard to chromium, the degree of change in this example may be enhanced somewhat by the 15-20°C temperature differential between the two experiments.

Further observations, as illustrated in Figure 6, were the near-total depletion of manganese at  $L/D = 0$  and the marked downstream effect for nickel. The surface concentration of the latter element at  $L/D = 260$  was noted to be in excess of 11%, while chromium remained low at 5-6% in this location. The erratic profile for molybdenum was indicative of compound formation. Conclusions of the X-ray microprobe work from the three runs may be summarized as follows:

- At a fuel pin hot spot temperature of 738°C, surface concentrations of both chromium and nickel will be at or below 3 w/o after 2000 hours exposure.

- Chromium depletion will remain high throughout the upper blanket regions of the fuel pin. Nickel loss, will be confined to a relatively small upstream area of the blanket region.
- Molybdenum enhancement at the surface will occur at all locations; this element appears more resistant than all the other constituents of Type 316 SS to sodium corrosion. The formation of Fe/Mo compounds at the surface appears to be dependent on the prevailing surface composition.
- Manganese concentration at the surface will be close to zero at the hot spot temperature.
- The depth of depletion for the major alloy elements will extend at least  $10\ \mu\text{m}$  from the sodium exposed surface. A ferrite layer at least  $5\ \mu\text{m}$  thick will form in the upper regions of the core and for some distance into the isothermal region.

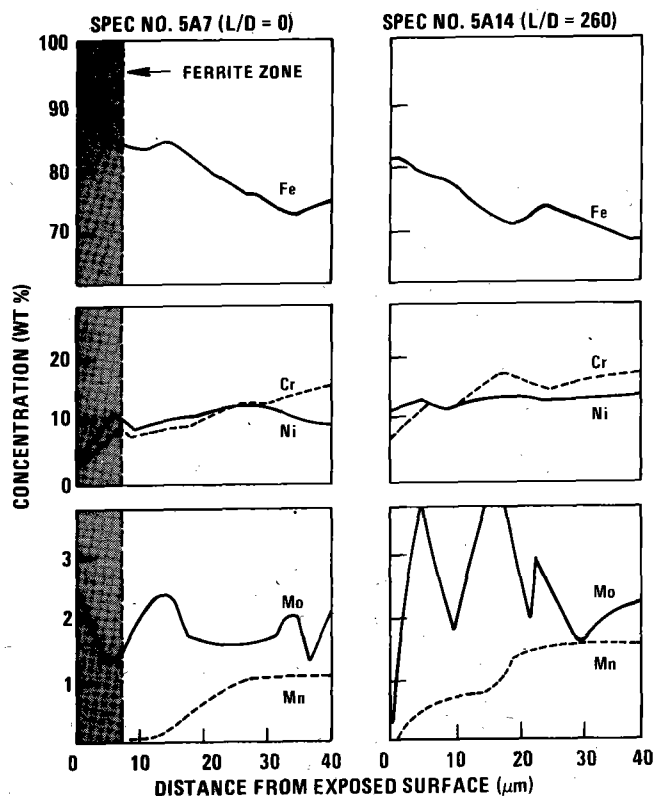


Figure 6. Major element profiles in Type 316 stainless steel cladding samples exposed at  $738^\circ\text{C}$  for 2136 h

#### DISCUSSION

Results from the present tests have shown that the rate at which the sodium is heated influences the corrosion behavior of materials in both the region in which the heating takes place and immediately downstream of that region. Differences in surface morphology and chemical composition were also noted when compared to earlier experiments conducted under relatively low rates of heat input conditions.

Corrosion rates are conventionally thought to depend on a mass transfer coefficient,  $k$ , and the chemical activity difference between the corroding surface and the bulk fluid for each corroding element or species, i.e.,  $(A_m^s - A_m^{Na})$ , where  $A_m^s$  is the activity of an element in the corroding material at the sodium interface and  $A_m^{Na}$  is the activity of that element in the bulk sodium. This activity difference may be termed the "corrosion potential" of the system.

By analogy to heat transfer theory, the coefficient,  $k$ , is dependent on the Reynolds' number  $DV\rho/\mu$ , the Schmidt number,  $\mu/d\rho$ , and the diffusivity of the corroding material in the fluid. None of these parameters should exhibit a strong dependency on heating rates. It is concluded, therefore, that the present observations are caused by an increase in the corrosion potential for the various corroding species, with this increase either caused by an increase in  $A_m^s$  or a decrease in  $A_m^{Na}$ . However, as described previously, since the surface concentration (or activity) of the most easily corroded elements (Cr, Ni, Mn) in the present tests, is equivalent to or lower than those observed in previous, low  $dT/dL$ , experiments,  $A_m^s$  is not higher but, in fact may be somewhat lower. The explanation for the present observations, therefore, must be that the activity of a particular element or chemical species in the sodium,  $A_m^{Na}$ , is lower, at any temperature level, under high  $dT/dL$  conditions that it is under low  $dT/dL$  conditions. A qualitative explanation for this is that the sodium is being heated so rapidly that it has no opportunity to become saturated with corrosion products, in spite of the fact that the corrosion rate in upstream positions is also 1.5 - 2.0 times the normal rate. The heating rate and, hence, the departure from saturation, is so large that it overcomes this compensating effect of a high upstream corrosion rate.

The observed chemical and surface structural changes reflect the higher prevailing corrosion rates. The ferritic layer is well established after 1500 hours and the absence of the corrosion resistant Fe/Mo nodules, which have been noted on Type 316 stainless steel in all previous sodium corrosion studies, is suggestive of a surface chemistry condition not previously observed.

The element in Type 316 SS most influenced by downstream position is nickel which increases from a value of 3% at  $L/D = 0$ , to a value of 11% at  $L/D = 260$ . In contrast, chromium, although reduced to the same level at  $L/D = 0$ , recovers to only about 6% at the downstream location. If the present corrosion rates, obtained at a sodium velocity of  $\sim 2\text{m/s}$ , are extrapolated via equation (2) to typical reactor flow conditions (7-8 m/s), a maximum corrosion rate of  $39\ \mu\text{m/y}$  (1.5 mils/y) is obtained. Sufficient conservatism is built into cladding wastage allowances to compensate for this increased corrosion rate over the projected lifetime of a fuel pin. A more important aspect of the factor of 2 increase in corrosion is the impact on radioactive mass transport calculations. The larger corrosion product release rates will presumably lead to a factor of two increase in the mass of deposits at any particular location within the primary system. This, in turn, will lead to higher estimates of radiation levels and thus will influence maintenance and repair procedures.

# INTERNATIONAL CONFERENCE ON LIQUID METAL TECHNOLOGY IN ENERGY PRODUCTION

## CONCLUSION

The measurement of the corrosion rate of 20% CW Type 316 stainless steel cladding in the high dT/dL environment of ITF has demonstrated an enhancement over previously predicted rates by a factor of 1.5 - 2.0. In terms of the reactor, this will not lead to impairment of the structural integrity of the fuel cladding, but will undoubtedly result in higher radiation levels in deposition regions such as the pump and the IHX.

The examination of specimens exposed for periods up to 2500 h revealed many features that have been observed in earlier studies. The most significant changes were largely due to a difference in the ferrite surface composition, rendering it unfavorable for the formation of Fe/Mo compounds.

Consideration of the mechanisms involved in the corrosion process suggests that under high dT/dL conditions, the sodium temperature is raised so rapidly that it has no time to saturate; the result is a high corrosion potential, and an increase in corrosion rate for a considerable distance downstream.

## REFERENCES

1. C. Bagnall, D. C. Jacobs, "Relationships for Corrosion of Type 316 Stainless Steel in Liquid Sodium," WARD-NA-3045-23, May 1975.
2. J. Hopfenfeld, "Corrosion of Type 316 Stainless Steel with Surface Heat Flux in 1200°F Flowing Sodium," in *Corrosion by Liquid Metals*, pp. 33-39, Plenum Press, New York, 1970.
3. S. J. Wachtel, A. J. Romano, and C. J. Klamut, "High-Flux Induction Heater for Sodium Corrosion Testing," *Trans. Amer. Nucl. Soc.* 12, pp. 125-126 (1969). (See also NBL-50205 (S-72), 1969, pp. 98-99.
4. G. A. Whitlow, J. C. Cwynar, R. L. Miller, and S. L. Schrock, "Sodium Corrosion Behavior of Alloys for Fast Reactor Applications," in *Chemical Aspects of Corrosion and Mass Transfer in Liquid Sodium*, pp. 1-63, The Metallurgical Society of the American Institute of Mining, Metallurgical and Petroleum Engineers, Inc., New York, 1973.
5. E. Berkey, G. A. Whitlow, "Microstructural and Compositional Changes in Sodium-Exposed Stainless Steel by Scanning Electron Microscopy," *ibid.*

**INTERNATIONAL CONFERENCE ON LIQUID METAL TECHNOLOGY IN ENERGY PRODUCTION**  
**THE CORROSION OF STEELS IN LIQUID SODIUM**

C.F. Clement  
 Atomic Energy Research Establishment,  
 Harwell, Oxon

P. Hawtin  
 Atomic Energy Research Establishment,  
 Harwell, Oxon

**ABSTRACT**

Proposed expressions for the corrosion and deposition rates and other relevant data are examined theoretically using models which treat both particle and molecular transport and the coupling between particle and molecular concentrations. It is difficult to reconcile some properties of the observed rates, including sodium velocity dependence, with currently accepted best values for the equilibrium iron concentration in sodium. To overcome this difficulty we propose a new model which contains two iron solubilities, one with and one without association with oxygen, which can also explain some existing anomalies in solubility measurements. The models also give a qualitative understanding of some properties of particles in circuits including the observed size distribution.

**1. INTRODUCTION**

The corrosion of steels by liquid sodium and the subsequent deposition of the corrosion products around the primary circuit are of major significance to the design of liquid metal cooled fast reactors. As such they have been the subject of intensive experimentation over the past decade leading to the production of large amounts of data on the rates of corrosion of steels in liquid sodium and the corresponding rates of deposition of the corrosion products.

A recent comprehensive review of the subject has been made by Weeks and Isaacs<sup>(1)</sup> who also develop a model of the corrosion process. In this paper we examine their proposed corrosion rate together with empirical rates obtained by workers at General Electric (see for example ref. 2) in the light of mathematical models of mass transport in liquid circuits produced by one of us.<sup>(3)</sup> We confine our remarks to the molecular transport of iron in a steady state corrosion situation and also treat the transport of particles. Extended and more detailed accounts of the work presented here are available as reports.<sup>(4,5)</sup>

**2. DEVELOPMENT OF A PHYSICAL MODEL**

Figure 1 shows in schematic form the way in which molecular corrosion and particle entrainment interact under flow conditions. We can consider two parallel paths. In the first molecular corrosion occurs in the hot zone dissolving iron (say) into the sodium. The dissolved molecules are transported around the circuit in the sodium and may thus become deposited at the walls at a point where the concentration driving forces are reversed. Similarly particles present on the wall can be entrained in the sodium flow, transported around the circuit and be redeposited elsewhere. The two mechanisms are coupled via the growth or dissolution of the particles at the expense of the molecular iron concentration.

The experimental evidence cited by Weeks and Isaacs<sup>(1)</sup> does not support the hypothesis that particles are eroded from already corroded steel and we conclude that the major source of particles in the circuit is erosion of deposited materials.

Conventional understanding of chemical reaction engineering kinetics allows us to make the following general statements:

- (i) If the deposition of dissolved corrosion products at the wall is controlled by a diffusion mechanism the molecular concentration profile must be of the form shown in Figure 2(i).
- (ii) If the corrosion rate is controlled by the rate of diffusion of the products away from the reacting surface the profile is qualitatively the mirror image of that illustrated in Figure 2(i).

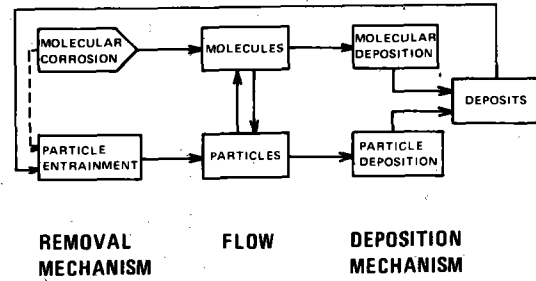


Figure 1. Flow Diagram Illustrating Deposit Formation

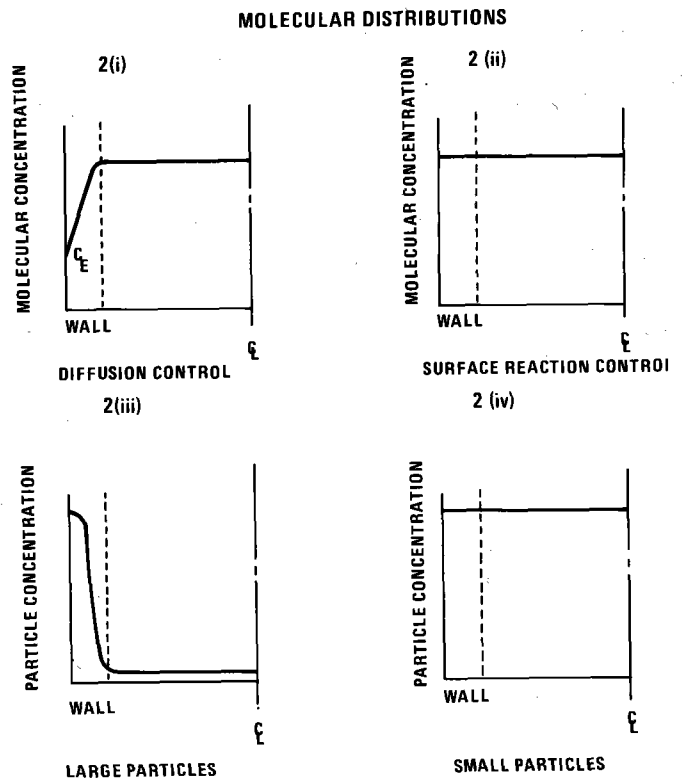


Figure 2. Distribution Of Molecules And Particles Across A Tube

- (iii) If the corrosion or deposition is controlled by the surface chemical reaction rate the profile has the form shown in Figure 2(ii).
- (iv) In view of the temperature differences around the circuit it is reasonable to assume that different mechanisms will be important at different points in the circuit.
- (v) Similar generalisations apply to particles but if they are large their rate of transfer to the wall is greater than that from it with a marked concentration enhancement in the boundary as shown in Figure 2(iii).

(vi) For small particles the deposition rate will be determined by the 'sticking probability' which is a measure of the efficiency with which a surface retains a particle when the particle actually strikes it.

In the succeeding sections we use currently available theoretical treatments to quantify the various mechanisms and also to highlight continuing areas of ignorance.

The basic data required to construct an adequate steel corrosion model in liquid sodium are equilibrium concentrations, surface reaction rates, molecular diffusivities and any relevant chemical reaction rates, particularly those involving oxygen. Unfortunately the experimental emphasis hitherto has been to perform dynamic corrosion experiments rather than the detailed experiments necessary to yield such information. We summarise here the available data for iron corrosion collected by Weeks and Isaacs.<sup>(1)</sup>

Crucial to our discussion is the solubility of Fe in Na and we initially use the formula of Singer et al<sup>(6)</sup> as adopted by Weeks and Isaacs which is equivalent to:

$$C_E(T) = 0.1445 \exp(-9924/T) \quad \dots (1)$$

There is conflicting evidence on this solubility, particularly as to whether it is oxygen dependent, and we return to the subject in section 5.

For oxygen, which is generally well below its equilibrium concentration in almost all circuits, we use an expression based on figures quoted by Weeks and Isaacs<sup>(1)</sup>:

$$C_{E_{Ox}} = 1.9 \cdot 10^6 \exp(-5560/T) \quad \dots (2)$$

There appears to be no information on the diffusivities of Fe, Ni and Cr in liquid Na<sup>(1)</sup>. Epstein<sup>(7)</sup> however has shown that a number of metals diffuse more slowly than Na itself in liquid sodium ( $13 \times 10^{-5} \text{ cm}^2/\text{s}$  at  $300^\circ\text{C}$ )<sup>(8)</sup>. In the absence of reliable direct data we assume that the diffusivities lie within a factor 10 of  $10^{-5} \text{ cm}^2/\text{s}$ .

The scanty evidence on reactions at surfaces is summarised by Weeks and Isaacs<sup>(1)</sup>. It is almost certain that the iron dissolution reaction rate depends on the oxygen concentration because of the observed dependence on the latter of empirical corrosion rates.

### 3. MASS TRANSPORT IN A LOOP

In this section we summarise the theoretical work of Clement<sup>(3)</sup> on molecular mass transport in liquid circuits which is relevant to the subsequent discussion.

#### (a) Corrosion Rate and Transport Equations

A bulk concentration  $C_B$ , as illustrated in Fig. 2(i) can be introduced for the Reynolds numbers characteristic of turbulent flow since in sodium the Schmidt number (Sc) satisfies the criterion:

$$Sc = \frac{\eta}{D_f \rho} \gg 1 \quad \dots (3)$$

Then, in terms of the surface reaction rate,  $k_D$ , and the mass transfer coefficient between the surface and bulk fluid,  $k_B$ , the steady state net corrosion rate is:

$$R_c = \rho k (C_E - C_B) \quad \dots (4)$$

where 
$$k = \frac{k_B k_D}{k_B + k_D} \quad \dots (5)$$

The basic transport equation for a circular pipe, diameter D, in which the fluid flows at a mean velocity, u, is:

$$\frac{dC_B}{dz} = \frac{4k}{uD} (C_E - C_B) = \frac{4R_c}{\rho u D} \quad \dots (6)$$

For the continuity of  $C_B$  round a circuit with constant fluid density,  $\rho$ , we have:

$$\int kD (C_E - C_B) dz = 0 \quad \dots (7)$$

With  $k_B$ ,  $k_D$  and  $C_E$  as functions of z, principally through their dependence on T(z), equations (6) and (7) determine  $C_B(z)$  and hence  $R_c(z)$ .

#### (b) Mass Transfer Coefficients

The surface reaction rate,  $k_D$ , is expected to be a strong function of T but independent of u. In a constant temperature region at a distance  $L/D > 60$  from a tube entrance the heat transfer analogy<sup>(9)</sup> gives:

$$\frac{k_B D}{D_f} = 0.023 Re^{0.8} Sc^{0.4} \quad \dots (8)$$

for  $10^4 \leq Re \leq 1.2 \times 10^5$ ,  $0.7 \leq Sc \leq 120$ .

For the same Re but  $Sc \rightarrow \infty$  the following correlation is suggested<sup>(3)</sup>:

$$k_B = 8.6 \times 10^{-3} u Re^{-0.1} Sc^{-0.67} \quad \dots (9)$$

In a rising or falling temperature region where  $k_B \ll k_D$  and is therefore rate controlling a different correlation is necessary since the boundary condition  $C_s(z) \approx C_E(T(z))$  at the wall is varying rapidly. For this condition Clement<sup>(3)</sup> suggests, based on the work of Hanna<sup>(10)</sup>, the use of the correlation

$$\frac{k_B(z)D}{D_f} = 0.729 (DZ)^{1/3} A^{1/3} Sc^{1/3} Re^{(2-a)/3} \quad \dots (10)$$

where A and a are evaluated from the friction factor equation

$$f = A Re^{-a} \quad \dots (11)$$

Sc and Re have their mainstream values and

$$Z = \frac{1}{C_E - C_B} \frac{d}{dz} (C_E - C_B) \quad \dots (12)$$

The correlation is only valid if temperature variations in the fluid properties  $D_f$  and  $\eta$  can be neglected and the distance from the entry z lies in the region  $zZ \geq 0.5$ .

#### (c) Isothermal Legs. The Approach to Saturation

The well-known solution of equation (6) is:

$$C_B(z) = C_E - (C_E - C_0) \exp(-\alpha z) \quad \dots (13)$$

where  $\alpha = 4k/(uD)$  and  $C_0$  is the entrance concentration.

The corrosion rate follows from equation (4) and for small  $z=L$  such that  $\alpha L \ll 1$  is:

$$R_c = R_0 [1 - \lambda L/D] \quad \dots (14)$$

where 
$$R_0 = \rho k (C_E - C_0), \quad \lambda = 4k/u \quad \dots (15)$$

We notice that we can check whether an observed L/D dependence arises from an approach to saturation even when k is unknown by forming the ratio

$$\frac{R_0}{\lambda} = \frac{\rho u (C_E - C_0)}{4} \quad \dots (16)$$

This ratio is strictly proportional to u and, if conditions are such that  $C_E \gg C_0$ , can be evaluated and compared to observation where  $C_E$  is known.

(d) Rising Temperature Regions

Where  $k_D \gg k_B$  and  $C_E \gg C_B$  away from the entrance to a rising temperature region, it was shown<sup>(3)</sup> that use of correlations (9) and (10) gives a ratio of the corrosion rate to that in a constant temperature region at the same temperature of

$$\frac{R_C(T \text{ rising})}{R_C(T \text{ const.})} = 30 \frac{(DZ)^{1/3}}{Re^{0.3}} \dots (17)$$

For typical values of the parameters this ratio is less than one so that the theoretical correlation (10) predicts a smaller corrosion rate than that for the same temperature in a constant temperature region.

4. PROPOSED CORROSION RATE EQUATIONS AND THEIR DEPENDENCE ON CIRCUIT VARIABLES

Two empirical corrosion rate equations have been derived<sup>(1,2)</sup>. They arise from markedly different approaches to the problem. The heuristic model derived at General Electric uses a statistical approach to attempt to fit empirical data obtained from various loops with a formula whose parameters take account of changes in the variables  $u$ ,  $C_{Ox}$ ,  $T$ ,  $L$ ,  $D$  and  $\Delta T$ , where the symbols have the meanings assigned to them in the nomenclature section. For 316 stainless steel the rates are:

$$R_1 \text{ corrosion} = 7.03 \cdot 10^{-8} u^{0.884} C_{Ox}^{1.156} \exp\{-13,240/T - 0.00676 L/D\} \dots (18)$$

$$R_1 \text{ deposition} = 2.49 \cdot 10^{-2} C_{Ox}^{0.94} \exp\{-17,790/T - 0.0684 \Delta T + 55.3 \Delta T/T - 0.0032 L/D\}, \dots (19)$$

where we have changed the original units to:  $u$ , cm/s;  $T$ , °K;  $C_{Ox}$ , ppm; and rates, g/cm<sup>2</sup>s..

Weeks and Isaacs<sup>(1)</sup> on the other hand, have constructed a corrosion model based on a surface reaction mechanism and have fitted the parameters of the model using experimental data. In the same units their corrosion rate for 316 SS is

$$R_2 \text{ corrosion} = 3.48 \cdot 10^{-6} C_{Ox}^{1.3} T \exp\{-18,050/T [1 - c(\frac{L}{D})^2]\}, \dots (20)$$

where we have substituted for  $C_{E_{Ox}}$  using equation (2) in their original expression.

Figure 3 compares the predicted corrosion rates from equations (8) and (10). The results are plotted in the  $(u, T)$  plane for  $C_{Ox} = 10$  ppm at  $L/D = 0$ . The position of the line  $R_1 = R_2$  changes only slowly with  $C_{Ox}$ . It is readily apparent from this curve that as  $u$  increases  $R_1$  increases more rapidly than  $R_2$  and that as  $T$  increases the converse is true.

In the absence of any additional information it would be reasonable to hypothesise (see Figure 2) that the picture represents two competing mechanisms of surface reaction- and boundary layer- limited corrosion. Consequently we would expect to see the smaller of the two rates. Thus  $R_1$  with its  $u$  dependence would be valid for small  $u$  or large  $T$  and  $R_2$  would be valid for small  $T$  or large  $u$ . An attempt has been made using the data of Thorley and Tyzack<sup>(11)</sup> at 650°C to obtain a corrosion rate of the form given by equations (4) and (5) which combine the two mechanisms. The attempt was not successful probably because of the assumptions made that  $k_B$  and  $C_E$  are both independent of  $C_{Ox}$ .

We now examine the dependence of the corrosion rate on the following circuit variables: the geometry and in particular the maximum  $L/D$  values, temperature, the maximum-minimum temperature difference ( $\Delta T$ ), the oxygen concentration,  $C_{Ox}$ , and the sodium velocity  $u$ .

(a) Geometry and the Mean Iron Concentration

Experimental observation shows that corrosion rates in the hot sections of the circuit are independent of  $\Delta T$  and are quantitatively of a

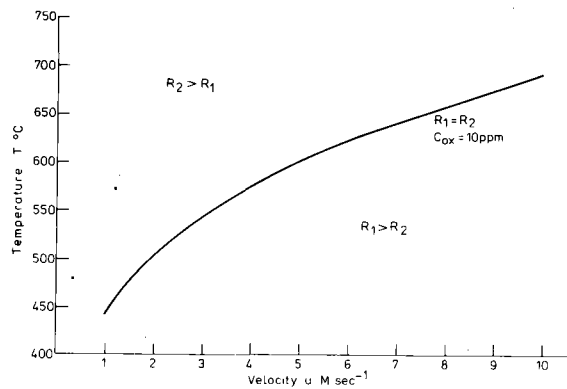


FIG. 3 COMPARISON BETWEEN THE GE CORROSION RATE,  $R_1$ , AND THE WEEKS-ISAACS CORROSION RATE,  $R_2$ , FOR  $C_{Ox} = 10$  ppm.

similar magnitude, excluding the  $L/D$  dependence in the isothermal section, whether the point is in the isothermal section or in a rising temperature region.<sup>(1,12)</sup> More specifically, the rates are independent of the  $T_{max}$  variation in  $\Delta T$ .

In the surface reaction controlled regime (i.e. where  $k_B \gg k_D$ ) the form of equation (4) where  $C_B$  is a function of position  $z$  shows that this can only happen if

$$C_E \gg C_B \dots (21)$$

From the result (17) it is not logical to conclude that this is the case if  $k_B \ll k_D$ . However, corrosion is observed to take place as soon as the temperature begins to rise<sup>(12)</sup> which means that  $C_B \approx C_E$  near the beginning of a rising temperature region. If we accept the solubility (1) it is easy to verify that the numerical smallness of the corrosion rates given by equations (18) and (20) imply that, unless hot sections are extremely long, the mean concentration is near  $C_E(T_{min})$ , and equation (21) holds over most of the hot regions in the circuit.

Using the solutions given in section 3(c) two model circuits have been considered by Clement:<sup>(3)</sup>

- (i) Short hot leg and long cold leg
- (ii) Short hot and cold legs.

A long leg is such that  $C_B \rightarrow C_E$  at the end of it and a short leg's length satisfies  $\lambda L/D \ll 1$ . In both cases the deposition rate generally depends on  $L$  and  $D$  in the hot section. The empirical deposition rate (19) only depends on the overall circuit through  $\Delta T$  and cannot guarantee a mass balance for the circuit. It cannot therefore be used for extrapolation to different geometries. The corrosion rates (18) and (20) in the appropriate kinetic control regimes should be applicable to different geometries provided that the cold leg  $L/D$  values are not much smaller, or the hot leg  $L/D$  values are not much bigger, than in the laboratory circuits. If these conditions are violated  $C_B$  will be larger in the hot regions and thus corrosion rates should be reduced.

(b) The  $L/D$  Dependence

This is possibly the most interesting dependence of the corrosion rate. Weeks and Isaacs conclude that it does not arise from an approach to saturation<sup>(1)</sup>, contrary to the apparent GE assumption and the PFR model assumption of Tanner<sup>(13)</sup>. We reinforce this conclusion using the argument developed in section 3(c). We have concluded that  $C_E \gg C_O$  at the entrance to an isothermal section so that the right hand side of equation (16) can be calculated from the solubility (1). Calculated values of

$R_o/\lambda$  are compared to experimental values<sup>(14)</sup> in Table 1. The expected  $u$  dependence does not appear and the theoretical values are 3-4 orders of magnitude too large. The data of Table 1 at 3 ft/s could represent an approach to saturation with

$$C_E (700^\circ\text{C}) \approx 6 \cdot 10^{-9} \dots (22)$$

This value compares with  $C_E (700^\circ\text{C}) = 5.4 \cdot 10^{-6}$  obtained from equation (1). Recent work of Thompson<sup>(15)</sup> in which the solubility of iron in oxygen-free sodium was measured, has tended to confirm the results of Singer et al<sup>(6)</sup>.

TABLE 1

L/D dependence observed for the corrosion of type 316 stainless steel in Na flow at 705°C and <10 ppm oxygen (Roy and Gebhardt<sup>(14)</sup>). The theoretical values are those expected for an approach to saturation.

$u$ ft/s	$R_o / \lambda$ mils/yr	$\lambda^*$	$\frac{R_o}{\lambda}$ Observed# gm/cm <sup>2</sup> s	$\frac{R_o}{\lambda}$ Theory
3	0.2	$7.5 \cdot 10^{-4}$	$1.1 \cdot 10^{-7}$	$4.1 \cdot 10^{-4}$
6	0.3	$1 \cdot 10^{-7}$	$1.2 \cdot 10^{-7}$	$8.1 \cdot 10^{-4}$
16	0.66	$1.7 \cdot 10^{-3}$	$1.6 \cdot 10^{-7}$	$2.2 \cdot 10^{-3}$
28	0.72	$1.5 \cdot 10^{-3}$	$2.0 \cdot 10^{-7}$	$2.8 \cdot 10^{-3}$

$\lambda$  Measured at L/D = 200.

\* Observed slope taken from the corrosion rates at L/D = 200 and 600.

# Calculated assuming a dissolution of the 65% iron content of the stainless steel.

On the basis that the L/D dependence does not arise from an approach to saturation there is no theoretical justification for the empirical exponential L/D form used in correlations (18) and (19).

The hypothesis of Weeks and Isaacs<sup>(1)</sup> that the L/D dependence arises from the poisoning of iron corrosion sites by Ni and Cr lacks a quantitative basis which would explain the small observed  $u$  dependence in  $R_o/\lambda$ .

(c) The  $u$  Dependence

An empirical value of  $k_B$  can be obtained from equations (18), (1), and (4):

$$k_B = 4.1 \cdot 10^{-7} u^{0.884} C_{Ox}^{1.156} \exp(-3316/T) \text{ cm/s} \dots (23)$$

This may be compared to a theoretical value from the correlation (9) (the correlation (8) gives numerical values differing by less than 30%):

$$k_B = 0.41 D^{-0.1} u^{0.9} D_f^{2/3} \exp\left(\frac{-451}{T}\right) \text{ cm/s} \dots (24)$$

with units  $D$  cm,  $u$  cm/s,  $D_f$  cm<sup>2</sup>/s, and where we have used for the viscosity of sodium<sup>(16)</sup>

$$\eta = 8,516 \cdot 10^{-4} \exp\left(\frac{796.2}{T}\right) \dots (25)$$

Although the observed  $u$  dependence is very close to that expected theoretically, the implied oxygen dependence of  $D_f$  is unexpected and its magnitude is far too small compared to the expected figure of  $\approx 10^{-5}$  cm<sup>2</sup>/s. For example, with  $C_{Ox} = 10$  ppm,  $T = 700^\circ\text{C}$  and  $D^{-0.1} = 1$  we get a value of  $6.5 \cdot 10^{-10}$  cm<sup>2</sup>/s.

The only simple explanation for this discrepancy is that  $C_E$  given by (1) is incorrect. In the above example the value which would make the theoretical and empirical values of  $k_B$  agree when  $D_f = 10^{-5}$  cm<sup>2</sup>/s is

$$C_E (700^\circ\text{C}) \approx 8.7 \cdot 10^{-9} \dots (26)$$

The magnitude of this estimate is similar to that given by equation (22) so that a smaller  $C_E$  would explain both the observed  $u$  dependence and part of the L/D dependence.

(d) The T Dependence

A numerically accurate activation energy form of  $k_D$  can be obtained from equations (1) and (20):

$$k_D = 4.5 \cdot 10^{-2} C_{Ox}^{1.3} \exp(-9000/T) \text{ cm/s} \dots (27)$$

It is important to note that  $k_D$  has a stronger temperature dependence than  $k_B$  given by (23). This implies that for low  $T$  the surface reaction rate is the limiting rate which fits in with the lack of  $u$  dependence in the deposition rate (19). Neglecting the  $\Delta T$  dependent terms of (19), which almost cancel out, we obtain a corresponding surface reaction rate proportional to  $\exp(-7900/T)$  which is not dissimilar to that in (27).

5. A QUALITATIVE EXPLANATION OF THE DATA FOR IRON CORROSION IN LIQUID SODIUM

We have seen that majority of measurements of iron solubility in sodium appear to be incompatible with the small corrosion rates observed in loops and the appearance of  $u$ -dependence in the rates.

Most workers find that  $C_E$  is independent of  $C_{Ox}$  at low values of  $C_{Ox}$  but that  $C_E$  increases with  $C_{Ox}$  for  $C_{Ox}/C_{Ox}(\text{sat}) > 0.1$ <sup>(1)</sup>. On the other hand, one experiment<sup>(17)</sup> finds that  $C_E$  is dependent on  $C_{Ox}$  down to very small values of  $C_{Ox}$ . The results of this experiment are illustrated diagrammatically in Fig. 4, which is an adaptation of Fig. 3 in reference 7. The values of  $C_E$  measured by Fleitman and Isaacs<sup>(17)</sup> are up to a factor  $10^3$  smaller than those considered normal.<sup>(1)</sup>

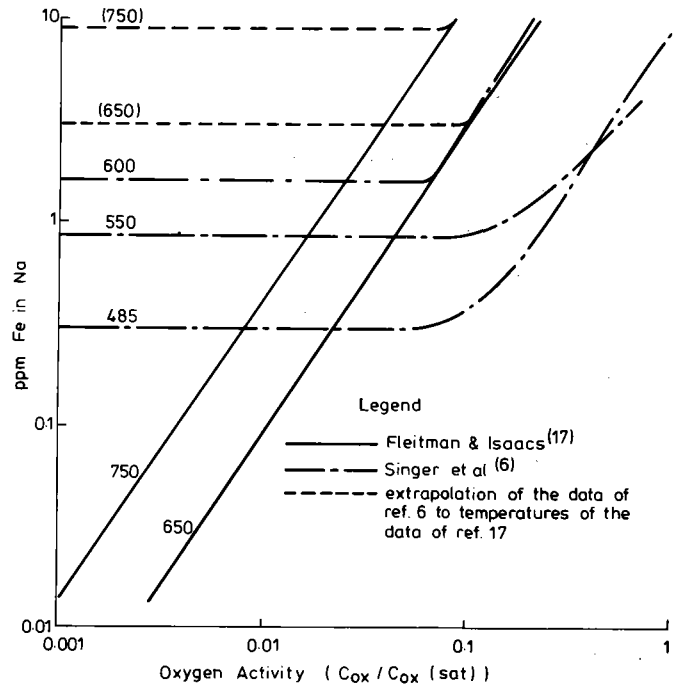


FIG. 4. EFFECT OF THE OXYGEN ACTIVITY OF LIQUID Na ON THE APPARENT SOLUBILITY OF Fe IN Na (TAKEN FROM REF. 1.)

We seek to explain these results together with the "anomalous" corrosion rate data by hypothesising that there are two effective solubilities of iron in liquid sodium. The first,  $C_{E1}(T)$ , is independent of  $C_{Ox}$  and is associated with a relatively slow surface reaction rate,  $k_{D1}(T)$ . The second,  $C_{E2}(C_{Ox}, T)$ , is that of some iron-oxygen compound and is associated with a fast surface reaction rate,  $k_{D2}(C_{Ox}, T)$ . There could also be a transfer between the two modes in solution which, if it exists, must be characterised by a slow reaction rate.



The total corrosion rate thus becomes

$$R_c = k_{D1} \rho (C_{E1} - C_{S1}) + k_{D2} \rho (C_{E2} - C_{S2}) \quad \dots (28)$$

Now from Fig. 4, it follows that at low oxygen activities (the usual case in sodium circuits)  $C_{E1} \gg C_{E2}$ . Since  $k_{D1} \ll k_{D2}$  (by hypothesis) it is entirely possible that the two terms in equation (28) are of comparable magnitude. From equations (1), (22) and (26) estimates at 700°C are

$$C_{E1} \approx 5 \cdot 10^{-6}, \quad C_{E2} \approx 6 \cdot 9 \cdot 10^{-9} \quad \dots (29)$$

The value of  $k_D$  given by equation (27) was obtained using the solubility (1). Because of its oxygen dependence we expect it to be associated with  $C_{E2}$  rather than  $C_{E1}$  so that its new value at 700°C and  $C_{Ox} = 10$  ppm is

$$k_{D2} \approx 6 \cdot 10^{-2} \text{ cm/s} \quad \dots (30)$$

This compares with the original value of  $8.6 \cdot 10^{-5}$  cm/s given by (27) and is comparable with boundary layer mass transfer coefficients given by equations (8) and (9) which, with  $D_f = 10^{-5}$  cm<sup>2</sup>/s,  $u = 10$  ft/s = 305 cm/s, and  $D = 1$  cm giving  $Sc = 250$ , are about the same, viz

$$k_B \approx 2.1 \cdot 10^{-2} \text{ cm/s} \quad \dots (31)$$

In order not to dominate the observed corrosion,  $k_{D1}$  must be at least a factor  $10^3$  smaller than  $k_{D2}$  so that

$$k_{D1} \lesssim 6 \cdot 10^{-5} \text{ cm/s} \quad \dots (32)$$

With these postulated values of  $k_D$  and  $D_f = 10^{-5}$  cm<sup>2</sup>/s we now see what would happen in the isothermal solubility experiments discussed in chapter 2 of reference 3. For a cavity with a volume to area ratio of  $\ell$  the timescale for equilibrium to be reached is given by the longer of

$$t_s = \frac{\ell}{k_D}, \quad t_D = \frac{4}{\pi^2} \frac{\ell^2}{D_f} \quad \dots (33)$$

where the diffusion timescale actually depends on the geometry of the cavity so that the factor  $4/\pi^2$  could be replaced by another constant of order unity.

With  $\ell$  in cm,  $D_f = 10^{-5}$  cm<sup>2</sup>/s and  $k_D$  given by equations (30) and (32) the relevant times are

$$t_{s1} \approx 4.6 \ell \text{ h}, \quad t_{s2} = 48 \ell \text{ s}, \quad t_D = 11 \ell^2 \text{ h} \quad \dots (34)$$

Most of the timescales of existing experiments are reported to be long<sup>(1)</sup> which would indicate that diffusion was the dominant delaying mechanism for saturation. However, in one of the experiments<sup>(18)</sup> which reported very low values of  $C_E$  the time allowed was only 4 hours, which would fit in with a number close to  $C_{E2}$  being observed. To remove the dominance of  $t_D$  without going to very small values of  $\ell$  the sodium could be stirred. Our hypothesis would then imply that  $C_{E2}$  is reached exponentially in a short time,  $t_{s2}$ , followed by a different exponential dependence to reach  $C_{E1}$  in a long time,  $t_{s1}$ .

If, as may well be the case, there is transfer between the two modes in solution, the analysis would be more complicated but we would still expect two timescales, one long and one short, to appear.

The implications of this model for corrosion in loops are profound. The iron concentration,  $C_{S1}$ , could build up over a long timescale to be of the same order of magnitude as  $C_{E1}$ . We know that the iron density in particles is an order of magnitude greater than  $C_{E1}$ . However, if we have an efficient condensation, deposition or breakup mechanism for the Fe - Ox species in the cold areas of the loop,  $C_{S2}$  will be reduced to its equilibrium value. Corrosion will then take place as soon as the temperature starts to rise from the second term in equation (28). It is possible, and indeed likely from the observed oxygen dependence of the corrosion, that the first term in equation (28) is relatively small over most of the circuit.

Now the important feature of this argument is that  $C_{E2} \ll C_{E1}$ ;

this being the case the major difficulty associated with arguments concerning rapid changes in  $C$  around the circuit, namely that the corrosion necessarily is too large (see section 4(b)), becomes invalid. Our hypothesis suggests in part how a variation around the circuit in  $C_2$  (the concentration of the iron/oxygen complex) could lead to an L/D effect due to saturation in the sodium of this complex. The hypothesis also explains how two widely different solubilities might be observed and why the observed corrosion rate is so low when one solubility value is large.

We believe that the present hypothesis is sufficiently plausible that it should be subjected to formal experimental test.

## 6. PARTICLES IN SODIUM CIRCUITS

Weeks and Isaacs<sup>(1)</sup> have summarised the existing experimental data which we discuss using the particle-molecule transport model developed in section 6 of reference 3. A typical particle concentration is 20 ppm Fe as  $1 \mu\text{m}$  diameter particles ( $3.77 \cdot 10^6$  particles/cm<sup>3</sup>) and corresponds to an iron density of  $1.55 \cdot 10^{-5}$  g/cm<sup>3</sup> which is about an order of magnitude greater than the equilibrium molecular density from eq. (1). Experiments carried out at GE<sup>(19)</sup> suggest that there are no particles present of  $10 \mu\text{m}$  diameter or larger and at  $T = 600^\circ\text{C}$  the typical diameter is  $2\text{-}3 \mu\text{m}$ .

### (a) The Mass Transport of Particles

The areas of deposition and size distribution of particles can be understood from simple considerations. The particle diffusivity is

$$D_p = \frac{K_B T}{6\pi\eta R} = \frac{8.6 \cdot 10^{-11} T}{R} \exp\left(\frac{-796.2}{T}\right) \text{ cm}^2/\text{s} \quad \dots (35)$$

where  $R$  is the particle radius in  $\mu\text{m}$  and  $\eta$  is the viscosity of sodium.

For  $R = \frac{1}{2} \mu\text{m}$  and  $T = 700^\circ\text{C}$  we have

$$D_p = 7.4 \cdot 10^{-8} \text{ cm}^2, \quad Sc = 3.3 \cdot 10^4 \quad \dots (36)$$

At such small diffusivities the particle concentration is uniform inside the flow and, for small particles that move with the flow, the correlation (9) gives a particle mass transfer coefficient for  $Re = 1.2 \cdot 10^5$  and  $u = 10$  ft/s.

$$k_{Bp} = 7.9 \cdot 10^{-4} \text{ cm/s} \quad \dots (37)$$

This coefficient refers to the particle number density whose change between the bulk fluid and wall is related to the mass corrosion (or deposition) rate  $R_{cp}$  by<sup>(3)</sup>,

$$(n_B - n_s) = R_{cp} \left/ \left[ \frac{4\pi}{3} R^3 \rho_m k_{Bp} \right] \right. \quad \dots (38)$$

At  $700^\circ\text{C}$   $R_{cp}$  is less than  $R_c$  given by (18) or (20) and, with the particle material density  $\rho_m = 7.3$  g/cm<sup>3</sup>,  $R = \frac{1}{2} \mu\text{m}$  and  $n_B = 3.77 \cdot 10^6$ , we obtain

$$(n_s - n_B) / n_B \leq 10^{-2} \quad \dots (39)$$

We reach the important conclusion that the particle density is uniform throughout the flow, at least in places with regular geometry. The removal of particles from the wall and deposition on the wall is governed by wall properties such as 'sticking probabilities', and is independent of flow properties. This provides an explanation for the deposition of particles in regions of the circuit with irregular geometry.

To understand the size distribution we assume that particles of a size smaller than the smallest eddy size,  $\lambda_0$ , do move with the flow whereas larger particles are rapidly ejected by the mechanism of Hutchinson et al<sup>(20)</sup> (see also the discussion in reference 3, section 6).

For smooth tube flow with  $D = 1$  cm,  $Re = 1.2 \cdot 10^5$  (21)

$$\lambda_0 = 4.11 D Re^{-0.675} \approx 15 \mu m \quad \dots (40)$$

Particles about this size may well be ejected whereas those about an order of magnitude smaller should be unaffected by eddies and would be expected to be very persistent.

The variation of parameters in (40) suggest that the areas of a circuit likely to be affected by ejected marginally-sized particles will have small D, large u and small  $\eta$ . Actually  $\eta$  does not vary greatly with T so that places like pumps, grids and meshes are the most likely to receive deposits.

**(b) The Particle – Molecular Concentration Interaction**

The hypothesis that the L/D effect arises from dissolution from particles has been examined by Wachtel et al<sup>(22)</sup> in a crude model. Their conclusion is that the observed L/D effect does not arise from the dissolution of the iron content of the particles.

One of us<sup>(3)</sup> has suggested that the rate of change of the bulk concentration as a function of distance z along a tube is

$$\frac{dc_B}{dz} = \frac{4(C_E - C_B)}{u} \left[ \frac{k}{D} + \pi k_D \int \frac{R^2}{1 + \delta} n_B(R, z) dR \right], \quad \dots (41)$$

where  $n_B(R, z)$  is the particle density at size R and position z,

$$\delta = k_D R / D_f. \quad \dots (42)$$

The particles are assumed to have the same surface reaction rate,  $k_D$ , as the walls and the two terms in (41) arise from the contribution of the walls and the particles to the concentration change. If we take  $k_D$  from (27) and a reasonable value of  $10^{-5} \text{ cm}^2/\text{s}$  for  $D_f$ , then  $\delta \ll 1$  for micron size particles so that their dissolution is surface-reaction controlled. To estimate the relative magnitude of the two terms we take  $k = k_D$  and  $n_B = 4 \cdot 10^6 \delta$  ( $R = 1 \mu m$ ) so that, with D in cm.,

$$\pi k_D \int \frac{R^2}{1 + \delta} n_B(R, z) dR / \frac{k}{D} \approx 0.13 D, \quad \dots (43)$$

For a narrow tube with  $D \approx 1 \text{ cm}$  the influence of the particles is negligible compared to the walls but in a large tank with  $D \approx 1 \text{ m}$  the particle dissolution would dominate the concentration change.

With  $\delta \ll 1$  we have<sup>(3)</sup>

$$\dot{R} = u \frac{dR}{dz} = \frac{k_D \rho}{\rho_m} (C_E - C_B(z)) \approx - \frac{Du}{4} \frac{\rho}{\rho_m} \frac{dC_B}{dz}, \quad \dots (44)$$

using equation (41) with neglect of the second term.

With  $\rho = 0.78 \text{ g/cm}^3$ ,  $\rho_m = 7.8 \text{ g/cm}$ ,  $D = 1 \text{ cm}$  and a maximum value of  $C_B - C_{B_i}$  of about  $10^{-6}$  we would only have a radius change of

$$R(z) - R_i \approx 2.5 \cdot 10^{-8} \text{ cm} \quad \dots (45)$$

Thus unless a circuit has large tanks with long particle residence times size changes round the circuit are expected to be extremely small. We conclude that particles originate from the walls, principally from deposits although possibly from erosion from grain boundaries. Residence times will be extremely long since their 'sticking probabilities' must be very small and there is a very small chance of their being ejected by the mechanism of Hutchinson et al<sup>(30)</sup> because of their small growth. The time taken to reach an 'equilibrium' concentration must be extremely long but there is no direct experimental evidence on this point.

**(c) The Effect of Very Small Particles**

We have seen that the observed micron-sized particles do not affect the iron concentration greatly in a relatively narrow tube. The possibility remains that there could be a large number of very small iron particles in the circuit. Their presence need not be in contradiction to the observed total iron concentration as their total mass is proportional to

$\int n_B(R) R^3 dR$  whereas their concentration effect (see equation (41)) is proportional to  $\int n_B(R) R^2 dR$ . The question whether they could be responsible for the observed u-dependence and L/D-dependence of the wall corrosion rate has been investigated on the basis of equation (41).<sup>(4)</sup>

The conclusion is that it is impossible to explain the observed u- and L/D-dependence of  $R_C$  from the iron dissolution of tiny particles. The latter conclusion agrees with that of Wachtel et al<sup>(22)</sup>.

**7. CONCLUSIONS**

The corrosion of iron by liquid sodium appears to be kinetically limited under some conditions and limited to boundary layer transmission under others. This competition cannot be reconciled with a reasonable value for the iron diffusivity in sodium and the iron solubility of Singer et al<sup>(6)</sup>. Our hypothesis of two iron solubilities in sodium would qualitatively explain the competition and possibly some of the L/D effects observed, and could reconcile the widely different values measured in iron solubility experiments. More of these static experiments, with particular emphasis on equilibrium timescales, are needed to test the hypothesis.

Some of the observed properties of particles in sodium circuits have been qualitatively explained but, since their removal from and deposition on the walls appears to be governed by 'sticking probabilities', further understanding is likely to be gained by experiment rather than by theory.

**REFERENCES**

- (1) J.R. Weeks and H.S. Isaacs, *Advances in Corrosion Science and Engineering* 3, 1 (1972).
- (2) R.W. Lockhart and R.C. Blair, GEAP-4881 (1967).
- (3) C.F. Clement, AERE T.P. 606 (1975).
- (4) C.F. Clement and P. Hawtin, AERE - R 8037 (1975).
- (5) C.F. Clement and P. Hawtin, AERE - R 8195 (1976).
- (6) R.M. Singer, A.H. Fleitman, J.R. Weeks and H.S. Isaacs, *Corrosion by Liquid Metals*, ed. J.E. Draley and J.R. Weeks. Plenum Press, New York (1970) p.561.
- (7) L.F. Epstein, *Liquid Metals Technology, Chemical Engineering Progress Symposium Series* 53 No. 20 (1957) p.67.
- (8) R.E. Meyer and N.H. Nachtreib, *J. Chem. Phys.* 23, 1851 (1955).
- (9) W.H. McAdams, *Heat Transmission* (3rd Ed.) McGraw-Hill, New York (1954).
- (10) O.T. Hanna, *Chem. Eng. Sci.* 29, 149 (1974).
- (11) A.W. Thorley and C. Tyzack, *Alkali Metal Coolants*, IAEA, Vienna (1970) p.97.
- (12) A.W. Thorley and C. Tyzack, *Liquid Alkali Metals*, Brit. Nuc. En. Soc. London (1973).
- (13) M.C. Tanner, unpublished work (1967).
- (14) P. Roy and M. Gebhardt, GEAP-13548 (1967).
- (15) R. Thompson, private communication (1975).
- (16) E.L. Dunning, ANL 6246 (1960).
- (17) A.H. Fleitman and H.S. Isaacs, unpublished work reported in ref. 1.
- (18) A.D. Bogard, NRL 4131 (1953).

# INTERNATIONAL CONFERENCE ON LIQUID METAL TECHNOLOGY IN ENERGY PRODUCTION

(19) G.W. Wozadlo, W.J. Wagner and J.S. Amijo, GEAP-13539-13 (1970).	<b>Suffices</b>	
(20) P. Hutchinson, G.R. Hewitt and A.E. Dukler, Chem. Eng. Sci. <u>26</u> , 419 (1971).	B	pertaining to bulk of fluid
(21) C.F. Clement, AERE TP 605 (1975).	E	pertaining to equilibrium
(22) S.J. Wachtel, A.J. Romano, C.J. Klamut, H.S. Isaacs, J.R. Weeks and D.H. Gurinsky, AIME Symposium, Chemical Aspect of Corrosion and Mass Transfer in Liquid Sodium, ed. S.A. Jansson, Detroit (1971) p.232.	P S i,o	pertaining to particles pertaining to surface pertaining to initial values

## NOMENCLATURE

A,a	friction factor constants
C	molecular iron concentration
$C_{Ox}$	oxygen concentration
D	tube diameter
$D_f$	molecular diffusivity
$D_p$	particle diffusivity
f	friction factor
$k, k_B, k_D$	total, boundary layer and surface mass transfer coefficients
$K_B$	Boltzmann constant
$\ell$	volume to area ratio
L	downstream distance
n	particle number density
R	particle radius
$R_c, R_1, R_2$	corrosion rates
T	temperature
$\Delta T$	temperature difference for loop
$t_s, t_D$	equilibrium times
u	mean fluid speed
Z	rising temperature region constant
z	distance along tube
$\delta$	particle parameter
$\epsilon$	empirical constant
$\lambda$	coefficient of L/D
$\lambda_0$	smallest eddy size
$\eta$	fluid viscosity
$\rho$	density
$\rho_m$	particle material density
Re	Reynolds number
Sc	Schmidt number

# INTERNATIONAL CONFERENCE ON LIQUID METAL TECHNOLOGY IN ENERGY PRODUCTION

THERMODYNAMIC AND DIFFUSION STUDIES ON CORROSION OF AUSTENITIC STAINLESS STEEL IN LIQUID SODIUM

H.R. Konvicka

K.L. Komarek

I.E. Schreinlechner

Institute for Inorganic Chemistry  
University of Vienna  
Vienna, Austria

Department of Metallurgy  
Österreichische Studiengesellschaft  
für Atomenergie Ges.m.b.H.  
Vienna, Austria

## ABSTRACT

Critical oxygen concentrations for formation of double oxides of sodium and steel constituents at the sodium-steel interface are derived. Under loop conditions only chromite can be formed. Stainless steel samples were investigated after 2600 hours exposure time to sodium at 730° C by means of a scanning electron microscope with an energy dispersive X-Ray analyzer (EDAX), X-Ray-diffraction and metallography. Results are used to propose a diffusion model of steel corrosion. The downstream effect and velocity dependence of corrosion are explained as functions of grain boundary diffusion and iron corrosion.

## INTRODUCTION

Corrosion of austenitic stainless steel in flowing liquid sodium is a very complex problem since chemical reactions, diffusion and hydrodynamic phenomena are involved. In order to study the long time behavior of construction materials and the parameters governing corrosion rates liquid alkali metal test facilities are operated in a joint research program between OSGAE (Österreichische Studiengesellschaft für Atomenergie Ges.m.b.H.) and VEW (Vereinigte Edelstahlwerke A.G., former Gebr. Boehler A.G.). Detailed information about the loop system was given by Matyas<sup>(1)</sup>.

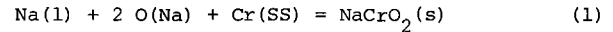
Since it is a wellknown fact that nonmetallic impurities in sodium play an important role in corrosion, the possibility of double oxide formation of sodium and iron, chromium or nickel was estimated by thermodynamic calculations. These calculations together with an analysis of diffusion results were used to interpret the corrosion experiments.

## DOUBLE OXIDE FORMATION AT THE SODIUM STEEL INTERFACE

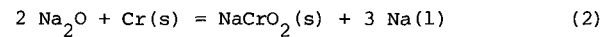
### Thermodynamic Calculations

Chromium; Sodium chromite is the only stable

chromium-oxygen-sodium compound in contact with liquid sodium at the temperatures used in coolant technology. Higher chromium oxides will be reduced. The formation of NaCrO<sub>2</sub> can be written as:



The standard Gibbs free energy for the reaction



was evaluated by Gross et al. as a function of temperature<sup>(2)</sup>:

$$\Delta G^\circ(\text{NaCrO}_2) = -8300 - 19,6 T \quad (\text{cal/mol NaCrO}_2) \quad (3)$$

This may be applied to eq. (1), if sodium is saturated with oxygen. Assuming the activities of chromite and sodium equal to 1, the equilibrium constant for reaction (1) is only a function of chromium and oxygen activity. Using the relationship

$$\Delta G^\circ = -RT \ln K \quad (4)$$

eq. (5) is derived:

$$\Delta G^\circ(\text{NaCrO}_2) = 2RT \ln a_{\text{O}} + RT \ln a_{\text{Cr}} \quad (5)$$

Applying Henry's Law to small oxygen concentrations in sodium,

$$a = c/s \quad (6)$$

eq. (5) may be rewritten:

$$\ln c_{\text{O}} = \frac{\Delta G^\circ(\text{NaCrO}_2)}{2 RT} + \ln s_{\text{O}} - \frac{\ln a_{\text{Cr}}}{2} \quad (\text{ppm}) \quad (7)$$

The solubility of oxygen in sodium was given by Noden<sup>(3)</sup>:

$$\log^{10} s_{\text{O}} = 6,2571 - 2444,5/T \quad (\text{ppm}) \quad (8)$$

With eqs. (3) and (8) eq. (7) can be evaluated numerically to yield the critical oxygen concentration for chromite formation as a function of chromium activity and temperature (Fig. 1).

oxygen concentration  $c_O$ , ppm

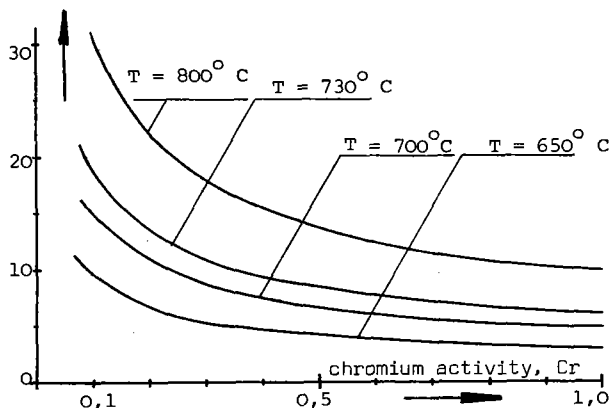


Fig. 1 Isotherms indicating equilibrium conditions for chromite formation

Data on chromium activity in the ternary system Fe-Cr-Ni are used to give a relationship between chromium activity and chromium and nickel content of the steel (Fig. 2) for  $T = 730^\circ\text{C}$  by extrapolation<sup>(4)</sup>. Interpolation for various chromium contents was done by a computer program.

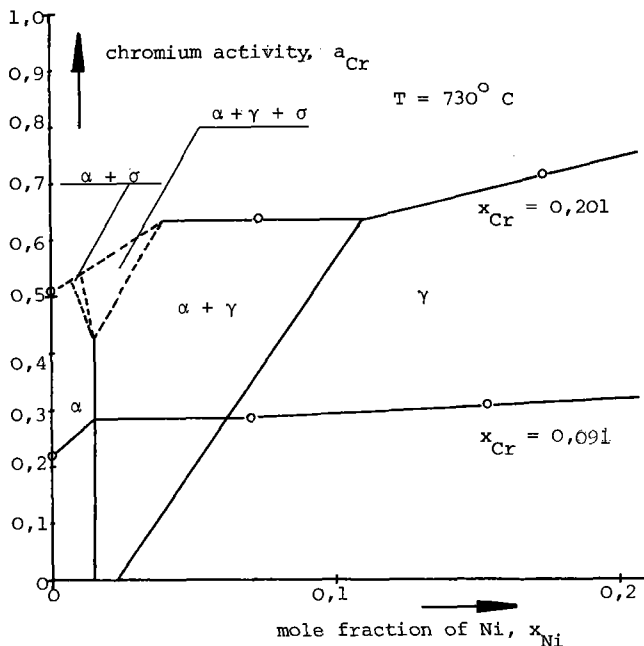
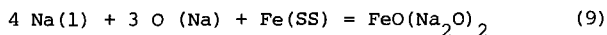


Fig. 2 Dependence of chromium activity on nickel and chromium content of steel, isothermal section at  $T = 730^\circ\text{C}$

Iron; With data obtained by Gross one can derive critical oxygen concentrations for formation of the double oxide



as described above<sup>(5)</sup>. Results indicate that under the usual conditions in liquid sodium systems ferrite is not formed. However, oxygen may play another role in iron corrosion, as for example is discussed in a model proposed by Kolster<sup>(6)</sup>.

Nickel; Referring to Gross formation of  $\text{Na}_2\text{NiO}_2$  is not possible under loop conditions<sup>(5)</sup>.

Discussion

As can be seen from the foregoing thermodynamic calculations, only the formation of sodium chromite can effect the corrosion process. A summary of the influence of oxygen content in sodium on the corrosion rates of stainless steel is given by Kolster<sup>(7)</sup>. Results indicate that below a threshold value of 7-8 ppm oxygen corrosion rates are more or less independent of oxygen content. At higher oxygen levels a relationship between a linear and a square dependence of corrosion rates with the oxygen content holds. Later experimental results confirmed the deposition of  $\text{NaCrO}_2$  at oxygen levels above 15 ppm<sup>(6)</sup>.

In order to prove eq. (7) critical oxygen concentrations were calculated with the data for the experiments described above. Results cover a range from 4 to 7 ppm depending on chromium and nickel content of the stainless steel and on temperature. This seems to be in good agreement with the experiments, if the errors introduced due to uncertainty in estimating the chromium activity, in the oxygen solubility limit and in  $\Delta G^\circ(\text{NaCrO}_2)$  are taken into account.

Furthermore, it seems to be important to point out that the oxygen solubility is not affected by the carbon content of liquid sodium up to about 500 ppm O<sup>(8)</sup>.

DIFFUSION MODEL

Simplified Hypothesis

At the sodium-steel interface at least four zones showing divergent diffusion properties have to be taken into account:

# INTERNATIONAL CONFERENCE ON LIQUID METAL TECHNOLOGY IN ENERGY PRODUCTION

Sodium, turbulent flow	no diffusion
sodium, laminar sublayer	$D_{lam}$
stainless steel, ferritized zone	$D_{\alpha}$
stainless steel, austenite matrix	$D_{\gamma}$

If one assumes as a first crude approach corrosion to be a simple diffusion process of chromium and nickel out of an iron matrix, the smallest diffusion coefficient of those considered above would be rate determining. Diffusion coefficients in a laminar sublayer can be estimated<sup>(9)</sup>. Results lie in the range of about  $10^{-5}$  cm<sup>2</sup>/sec. This is very high compared to diffusion coefficients in austenite, which are about  $10^{-14}$  to  $10^{-15}$  cm<sup>2</sup>/sec at temperatures around 700° C for chromium and nickel. Since in a turbulent flow no diffusion occurs and diffusion coefficients in ferrite are known to be 1 to 2 orders higher than in austenite, diffusion out of the austenite matrix into liquid sodium should govern the leaching process.

Therefore, one can use the solution of the diffusion equation for the following boundary conditions:

$$\begin{aligned} c(x,0) &= c_o & 0 < x < \infty \\ c(0,t) &= c_s & t > 0 \end{aligned} \quad (10)$$

$$c(x,t) = c_s + (c_o - c_s) \operatorname{erf}(x/2 \sqrt{Dt}) \quad (11)$$

The total mass lost after time  $t$  is given by eq. (12):

$$M(t) = (c_o - c_s) \sqrt{4Dt/\pi} \text{ (g/cm}^2\text{)}. \quad (12)$$

Using a diagram  $\bar{M}(t)$  vs.  $\sqrt{t}$ , where

$$\bar{M}(t) = M(t) \cdot \sqrt{\pi/2} (c_o - c_s), \quad (13)$$

should yield a straight line the slope giving  $\sqrt{D}$ . To have an experimental prove of the hypothesis the weight loss of samples after certain intervals and the surface concentrations of chromium and nickel have to be determined.

## Experimental Data

Corrosion Run; The test run parameters were as follows<sup>(10)</sup>:

temperature (test section):	730° C
sodium velocities:	0,3 and 4 m/sec
cold trap equilibrium temperature:	180° C
total exposure time:	2637 h

The weight loss data of stainless steel samples made of W.Nr. 1.4981. (Boehler Turbotherm<sup>+</sup> 1616M, X8CrNiMo1616) have been determined after 126, 342, 738, 1577 and 2637 hours total exposure time, respectively (Table I.)<sup>(11)</sup>. A chemical analysis of stainless steel is given in Table II.

Table I. Weight loss data of investigated samples, mg/sample surface (= 10,7 cm<sup>2</sup>).

sample	total exposure time, hours				
	126	342	738	1577	2637
1	3,4	5,5	10,2	17,9	28,2
2	2,3	3,4	7,0	11,9	16,7
3	1,7	2,9	5,6	10,4	15,5
4	0,7	1,1	2,8	5,8	9,1

Table II: Chemical analysis of SS 1.4981. (wt%).

C	Cr	Fe	Mo	Mn	Nb	Ni	Si
0,062	15,88	bal	1,94	1,39	0,94	16,68	0,45

EDAX Analysis; Surface concentrations of chromium and nickel and their concentration vs. depth profiles were measured by means of a scanning electron microscope combined with an EDAX. An oblique grinding technique was used. Samples investigated had been exposed to sodium at different downstream positions and sodium velocities (Table III.).

Table III: Downstream and velocity parameters of investigated samples.

sample	L/D	$v_{Na}$ (m/sec)
1	30	4
2	600	4
3	2	0,3
4	30	0,3

## Diffusion Data available in Literature

A review of the scanty data available in literature on diffusion coefficients of steel constituents in Fe-Cr-Ni systems was given by Demel<sup>(12)</sup>. Chromium diffusion coefficients in 1.4981. can be estimated to be  $1,7 \cdot 10^{-14}$  cm<sup>2</sup>/sec at 730° C from data on 18Cr-8Ni and 16Cr-11Ni steel. For nickel diffusion coefficients, only data for 20Cr-25Ni exist. Extrapolation yields  $1 \cdot 10^{-14}$  cm<sup>2</sup>/sec at 730° C.

## Results

### Estimation of Diffusion Coefficients from Profiles

Chromium and nickel profiles of samples 1 and 2 show no ferritic surface layer as indicated in 3 and 4 by

the point of inflection (Fig. 3). Comparison with calculated profiles (D as discussed above,  $c_s$  from profiles, using eq. (11)) indicates rather good agreement of the slope of the curves with the theoretical diffusion coefficient as far as a depth of 5 to 10  $\mu$ . Then deviations observed are due to grain boundary diffusion yielding ferritic grain boundaries, especially at samples 1 and 3, which were positioned at low L/D ratios. In summary, one can say that there is little difference in volume diffusion coefficients for chromium and nickel from literature and experiment.

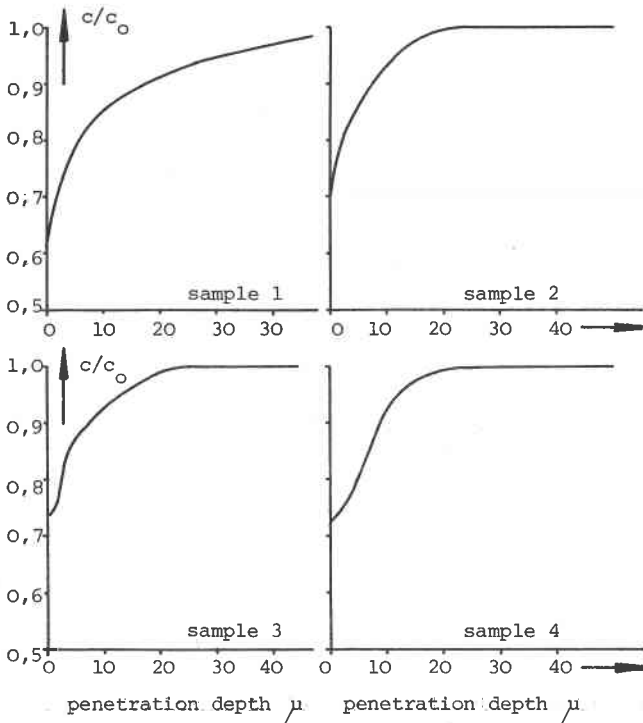


Fig. 3 EDAX-profiles of Cr (Ni-profiles differ only slightly)

Evaluation of mean transport coefficients from  $\bar{M}(t)$  vs.  $\sqrt{t}$  diagram; From the results above one can assume a mean transport coefficient  $\bar{D}_t$  for chromium and nickel in the order of  $1,5 \cdot 10^{-14} \text{ cm}^2/\text{sec}$ .

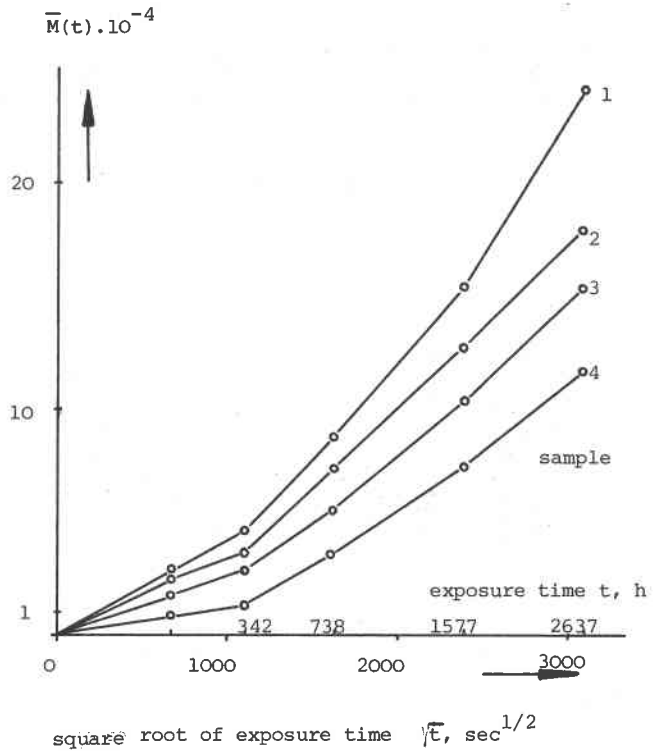


Fig. 4  $\bar{M}(t)$  v.s.  $\sqrt{t}$  diagram

In Fig. 4., linear relationships between  $\bar{M}(t)$  and  $\sqrt{t}$  hold only up to 300 hours total exposure time. Mean transport coefficients evaluated from these slopes cover a range from  $1,7 \cdot 10^{-14}$  to  $1,9 \cdot 10^{-13} \text{ cm}^2/\text{sec}$ . The higher values obtained at low L/D ratios and high velocity may be due to a higher portion of grain boundary diffusion. Sample 4 shows the best agreement with literature diffusion data.

Analyzing the experimental curves above 300 hours much more chromium and nickel depletion than due to volume diffusion is observed. This may be explained as follows:

1. Grain boundary diffusion yields broad ferritic grain boundaries (up to 1  $\mu$ ) representing preferred paths of transport for chromium and nickel out of the austenite matrix, since  $D_\alpha > D_\gamma$  (Fig. 5.).

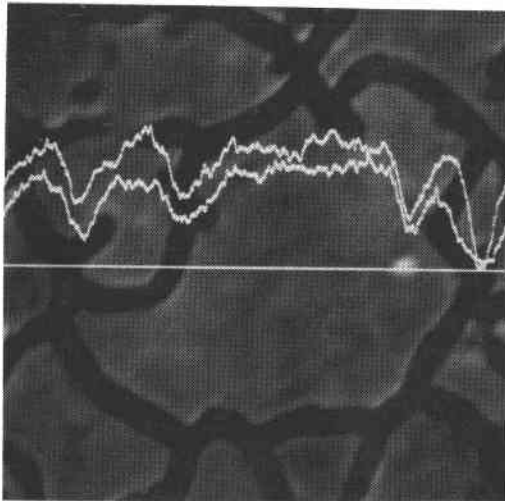


Fig. 5 Electron microprobe traces of chromium and nickel along ferritic grain boundaries (magnification 1200).

2. Iron corrosion cannot be neglected any longer as done in the first approximation.

Iron Corrosion: Since, as far as the accuracy of EDAX is concerned, mass lost due to grain boundary diffusion is included in profile measurements, weight losses calculated from measured profiles should be in the order of the observed ones, if our simplified hypothesis holds. This is not observed. The difference deminishes with larger L/D ratios and lower velocity.

If one subtracts the calculated data from total weight loss, one can assume to get corrosion rates due to bulk corrosion only. This means, stoichiometric amount of these weights corresponds to mass lost due to iron corrosion. In order to estimate the time dependence of iron corrosion, an ideal diffusion behavior of (Cr + Ni) according to eq. (12) is assumed. Results are represented in Fig. 6 and Table IV. It is a striking fact that the slope of iron corrosion rates are rather parallel indicating that the predominant factor in corrosion is grain boundary diffusion.

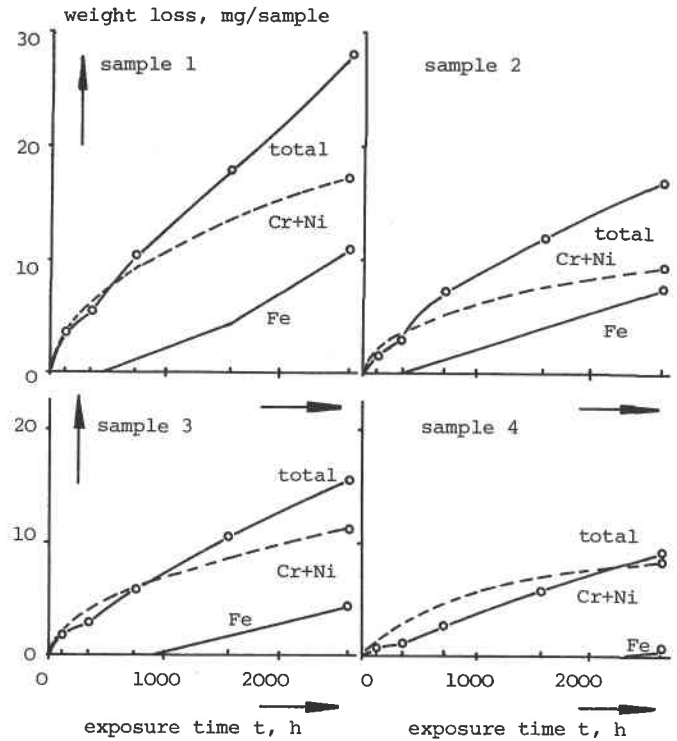


Fig. 6 Calculated iron weight loss of corrosion samples.

Table IV. Measured and calculated data of investigated samples

	1	2	3	4
penetration depth, $\mu$	50	40	45	25
ferrite, wt%	30	30	50	20
surface concentration, Cr, wt%	10,0	11,0	11,7	11,9
surface concentration, Ni, wt%	10,3	11,6	12,0	12,5
iron weight loss, calculated, mg (after 2637 hg)	10,9	7,6	4,5	0,6
(Cr+Ni)/Fe weight loss ratio	2,5	2,2	3,4	11,4

X-Ray Measurements, Metallography: X-Ray diffraction analysis of sample surfaces show that the amount of ferrite of high velocity test pile samples 1 and 2 do not differ appreciably. In low velocity sodium, the amount of ferrite decreases with the downstream position. Since one can assume that all of the ferrite is measured - at least to a depth of  $30 \mu$  - this is in good agreement with the results discussed above: the (Cr+Ni)/Fe weight loss ratios calculated for samples 1 and 2 and their penetration depths obtained by metallography are about equal. (Cr+Ni)/Fe ratios of sample 3 is higher than of 1 and 2, but the penetration depth does not differ significantly. Therefore, a



higher amount of ferrite is measured. In sample 4 most of the weight loss is due to chromium and nickel depletion. One would therefore expect a high amount of ferrite. This is not the case since the affected zone is only about half in thickness as compared to samples 1, 2 and 3 (Table IV.).

#### Discussion

All the data including the thermodynamic calculations should be used to decide about the real oxygen content of sodium in our corrosion experiment.

From thermodynamics, our experiment - cold trap equilibrium temperature 180° C corresponding to 7 ppm oxygen at 730° C - was exactly in the range of equilibrium conditions. Since nickel leaching tends to decrease the chromium activity, the equilibrium concentration of oxygen for chromite formation should be increased according to Fig. 2.

The weight loss of samples in this experiment was about 15 % higher than that of a previous one using samples of same material and heat treatment and same test parameters except the oxygen level, which was kept at 3,5 ppm.

From diffusion measurements, one obtains relatively high surface concentrations of chromium and nickel. No marked ferritic layer could be found. Compared with Kolster's data this should indicate that the oxygen level was above critical conditions<sup>(6)</sup>.

Chemical analysis shows that the oxygen content of liquid sodium was not constant with time. Values as low as 8 and as high as 17 ppm were obtained<sup>(10)</sup>.

From all these data no clear picture emerges. Apparently the samples were exposed to oxygen contents lying below and above the critical concentration, so that corrosion was caused by a combined process of chromite formation and of diffusion without chemical reactions.

#### CONCLUSIONS

1. Thermodynamic calculations give an explanation of the oxygen threshold value in corrosion rates due to chromite formation.

2. Analysis of diffusion data indicates that significant amounts of the total weight loss are due to grain boundary diffusion and iron corrosion. These results make it necessary to modify our hypothesis.

3. Grain boundary diffusion may be the predominant factor causing the downstream effect and velocity dependence of corrosion rates.

#### ACKNOWLEDGEMENTS

The authors wish to thank Mr. P.A.R. Scholze for his assistance in measuring the EDAX-profiles.

#### REFERENCES

- (1) Matyas E., Rajakovics G., Schwarz N.: "Problems of a sodium loop designed to operate at temperatures up to 800° C", Proceedings of the IAEA-Symposium on Alkali Metal Coolants, Vienna 1967, pp. 367 - 378.
- (2) Gross P., Wilson G.L., Gutteridge W.A.: "Composition and heat of combination of a double oxide of chromium and sodium", Journ.Chem.Soc. (A), pp. 1908-1913, (1970)
- (3) Noden J.D.: "A general equation for the solubility of oxygen in liquid sodium-addendum", Journ.Brit.Nucl.En.Soc., 12, pp. 329-331, (1973)
- (4) Mazandarany F.N., Pehlke R.D.: "Thermodynamic properties of solid alloys of chromium with nickel and iron", Met.Trans., 4, pp. 2067-2076, (1973)
- (5) Gross P., Wilson G.L.: "Composition and heat of combination of a double oxide of iron and sodium", Journ.Chem.Soc. (A), pp. 1913-1916, (1970)
- (6) Kolster B.H.: "Mechanism of Fe and Cr transport by liquid sodium in non-isothermal loop systems", Journ.Nucl.Mat., 55, pp. 155-168, (1975)
- (7) Kolster B.H.: "Einfluß der Sauerstoffkonzentration auf die Korrosion von austenitischen Stählen", TNO-Report, M 73/05/718, (1973)
- (8) Ainsley R., Hartlib L.P., Holroyd P.M., Long G.: "The solubility of carbon in sodium", Journ.Nucl.Mat., 52, pp. 255-276, (1974)

## INTERNATIONAL CONFERENCE ON LIQUID METAL TECHNOLOGY IN ENERGY PRODUCTION

- (9) Schwarz N.: "Laminare Randschichten, die Ähnlichkeitsbeziehungen zwischen Wärmeübergang und Stoffaustausch und deren Anwendbarkeit auf Flüssigmetallkorrosion",  
SGAE-Report, No. 2174, (1973)
- (10) Schwarz N.: "Versuchsbericht Korrosionsversuch 1.10, Teil I",  
SGAE-Report, No. 2488, (1975)
- (11) Schwarz N.: "Versuchsbericht Korrosionsversuch 1.10, Teil II",  
SGAE-Report, No. 2489, (1975)
- (12) Demel O.: "Basic studies of diffusion in HTR-metals, part I, review of literature",  
SGAE-Report, No. 2185, (1973)

# INTERNATIONAL CONFERENCE ON LIQUID METAL TECHNOLOGY IN ENERGY PRODUCTION

## SOLUBILITY OF OXYGEN IN LIQUID SODIUM EFFECT ON INTERPRETATION OF CORROSION DATA

K. T. Claxton  
Atomic Energy Research Establishment,  
Harwell, Oxon

### ABSTRACT

No solubility correlation relating the equilibrium oxygen concentration with the sodium saturation temperature has yet been derived which has gained general acceptance. A statistical analysis of all the available data which directly or indirectly may be taken as representing a measurement of solubility has been made. The results indicate that a real and seemingly permanent difference is apparent between the assumed equilibrium levels of oxygen measured at different saturation temperatures as reported by UK and US workers.

Data analysis procedures producing sub-sets of culled data which are then used to derive a compromise solubility function are considered less than adequate. It is considered preferable and more realistic to distinguish data sub-sets by the analytical technique employed.

The established vacuum distillation method is shown to yield results differing amongst themselves by up to a factor of four at cold trap temperatures of relevance to fast reactor operation.

The vanadium wire and electrochemical cell techniques are shown to give the lowest solubility values.

Appropriate factors relating UK oxygen levels to values derived from alternative methods are presented.

The divergent positions prevailing for oxygen-in-sodium analysis can lead to apparent anomalies when comparisons of corrosion rates from different sources have to be made. It is shown that this situation is, in part, apparently resolved by effecting comparisons at the equivalent cold trap temperature instead of the equivalent oxygen level. It is recognised that the approach presumes equilibrium of the oxygen in the sodium with the cold trap and reference is made to alternative 'sinks' for oxygen. It is demonstrated, by comparison of a number of recommended and observed corrosion rates from US and European sources, that, in spite of the above and other qualifications, the approach is reasonable.

### 1. INTRODUCTION

In order to assess sodium corrosion and deposition data emanating from different laboratories and to use this information to predict events in a fast reactor circuit, it is clearly necessary to be in a position to compare 'like-with-like.' Measurement of sodium temperature, velocity and various geometrical parameters would seem relatively unambiguous. The determination of the oxygen concentration, however, is unique in seemingly being very dependent on the measurement technique employed.

In the UKAEA there has been general acceptance of the oxygen measurements made by the vacuum distillation method over the past fifteen years. The experimental position in this area has remained essentially unchanged and no major discrepancies have been reported. Measured oxygen levels at given circuit conditions show a high degree of reproducibility. Over the same period of time the position elsewhere, particularly in the US, appears to have altered appreciably.

The statement 'reactor grade sodium' was generally interpreted, until relatively recently, as indicating an oxygen content in the range 5-10 ppm. Whilst in the UK this would still appear to be the practice, the current US view places an increasing emphasis on "quoted" oxygen levels, of 1 ppm and less. This position would also seem to be held by the Interatom laboratories. (26)

In this paper, an attempt is made to clarify the situation on "quoted" oxygen levels for a given circuit condition by recognising, amongst other things, the intrinsic difference in oxygen levels as measured and interpreted by UK and US workers.

### 2. SOLUBILITY OF OXYGEN IN LIQUID SODIUM

Relevant to any anomalies surrounding reported oxygen levels, is an awareness of the discrepancies arising from experimental determinations of the oxygen solubility. In twenty years no solubility correlation has been derived which receives international acceptance. This effect is illustrated in Figures 1 and 2 and in Table 1. These represent an analysis of data (1-18) which directly or indirectly can be assumed to represent a measurement of the solubility.

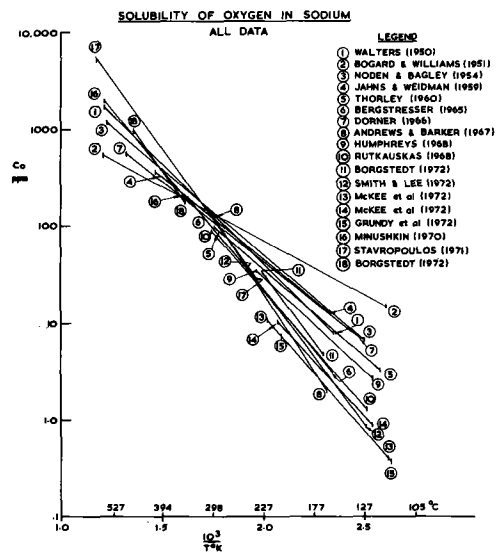


FIG. 1

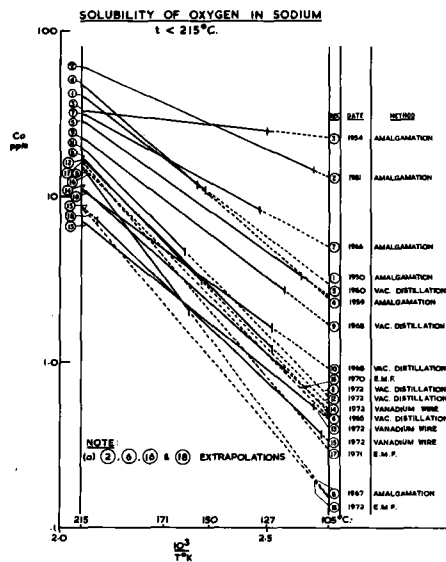


FIG. 2

## INTERNATIONAL CONFERENCE ON LIQUID METAL TECHNOLOGY IN ENERGY PRODUCTION

A "direct" solubility measurement is one in which the declared intention of the investigator has been to measure solubility. As a consequence of this approach due regard has been paid to establishing the proper circuit conditions including equilibrium with the cold trap. An "indirect" solubility measurement is where an author has reported oxygen levels in a circuit under conditions where equilibrium with the cold trap and around the circuit might have been expected to exist.

Figures 1 and 2 and Table 1 amply demonstrate the large variation of oxygen concentrations measured at a given cold trap temperature. For cold trapping conditions relevant to fast reactors (110–160°C) a spread of more than an order of magnitude is apparent. If data from the vacuum distillation method only are considered, it can be seen from Table 1 that at a cold trap temperature of 110°C assumed equilibrium oxygen levels range from 0.4 to 2.8 ppm with an average value of 1.3 ppm ± 80%, i.e. one standard deviation. Equally interesting, however, are the extrapolated oxygen solubilities at much higher temperatures. Table 1 shows derived oxygen levels at 650°C, a temperature of interest to coolant-fuel chemical interaction studies. Again considering only the vacuum distillation data, oxygen levels extend from 1547 to 8552 ppm about a mean of 4114 ppm ± 60%.

Since the first appearance of the UK data in 1960 all subsequent analyses have, with one exception, yielded progressively lower solubilities. Comparison of the results from all the methods published from as recently as 1972 reveals a factor of two difference at a saturation temperature of 105°C.

The results presented in Figures 1 and 2 and Table 1 were obtained by analysing the different data sets in the conventional manner, viz:

$$\log_{10} C_o \text{ (ppm)} = A + \frac{B}{T} \text{ (}^\circ\text{K)} \quad \dots(1)$$

- C<sub>o</sub> – oxygen concentration
- T – absolute temperature
- A, B – derived constants

Implicit in the least squares analysis is the assumption that the errors at any value of  $\frac{1}{T}$  are distributed normally on the logarithm of C<sub>o</sub>. Unity weighting has been assigned to each data point used which seems the most appropriate with the limited data available.

Included in Table 1 are the derived values for ΔH, the so-called differential heat of solution, given by

$$\Delta H = 2.303RB \quad \dots(2)$$

R = gas constant (= 1.987 cal/deg. mole)

The more precise data would seem to be those of Humphreys<sup>(9)</sup>, Thorley<sup>(5)</sup>, Grundy<sup>(15)</sup> and Jahns and Weidmann<sup>(4)</sup>. Of these only one, Grundy<sup>(15)</sup>, yields values for C<sub>o</sub> as low as those currently being quoted in America and elsewhere. No account has been taken of any bias in the data. Thus, although a particular sub-set of data points might show a small random scatter the experimental technique might be such as to impose a larger systematic error on the measured C<sub>o</sub> values. The extent of any bias, is not easily deduced from the published reports of different pieces of work. Whether it is correct, statistically, to correlate the data in the form of equation (1) is not considered in this report.

Several reviews have been carried out over the last fifteen years to try to evaluate the solubility of oxygen in liquid sodium. Most of these have applied selection and rejection criteria to obtain a sub-set of culled data points. These data have provided a best fit of the form of equation (1) which is then presented as the recommended solubility equation.

The nature of the criteria adopted and the fact that statistically, little appears to be gained, make the procedure of culling data points of questionable value.

As an example, the reviews of Eichelberger<sup>(23)</sup> (1968) and Noden<sup>(24)</sup> (1972) are considered. The results are given in Table 2 with the results of correlating all the data considered by the respective reviewers from which they produced their culled data. Unpublished overall correlations derived by the author in 1965 and 1974 are also given in the Table. These serve to illustrate the significant reduction in the average level of oxygen concentrations being analysed at any given saturation temperature over the last decade. The different correlations referred to above are plotted in the conventional manner in Figure 3.

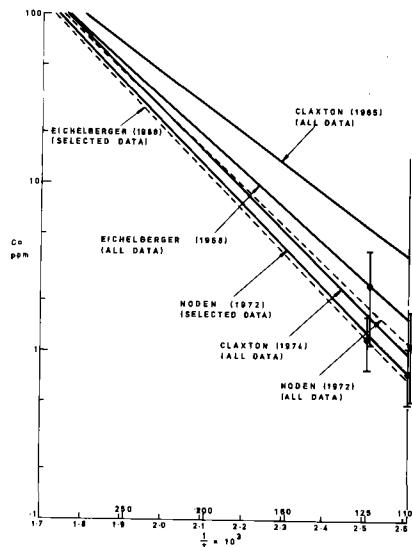


FIG. 3 C<sub>o</sub> (ppm) vs  $\frac{1}{T} \times 10^3$  SOLUBILITIES FROM DIFFERENT REVIEWS

With regard to the separate correlations in Table 2 the derived C<sub>o</sub> values presented at different temperatures show that the culled values are lower than the respective equivalent figures obtained when correlating all the data. With the errors on the culled data correlations, as shown in Figure 3, the differences are less significant than may be at first apparent. It is therefore considered that culling procedures for oxygen-in-sodium solubility data are less than ideal. At best they provide a compromise between widely divergent results and, at worst, may distort the true situation towards, in this context, lower oxygen solubilities. It would seem preferable to recognise that different techniques lead to differing apparent oxygen solubilities. This effect is brought out in Figure 4 which shows the overall correlations obtained by least squares analysis of sub-sets of data categorized by the method of analysis employed. The vacuum distillation correlations shown represent derivations with and without the UK data and the UK data by itself. The results are further summarised in Table 3.

Figure 4 shows that much lower results are obtained, particularly at the lower temperatures, with the vanadium wire and electrochemical cell techniques relative to the vacuum distillation method. With the relatively low correlation coefficient for the amalgamation-with-mercury correlation, even allowing for the large error, it does not seem possible that these data can be reconciled with the other sets of results. Figure 4 also indicates the difference between the UK line and the other vacuum distillation results.

Some of the methods cited suffer from being somewhat indirect and require for the development of the solubility function, the use of other functions which are not precisely known. An example, is the electrochemical cell (EMF) method<sup>(16–18)</sup>. Although somewhat indirect the three equations derived from this subset do show good internal consistency.

The vanadium wire method, has been used exclusively in America for solubility measurements and routine oxygen monitoring. It is not accepted in the UK over the oxygen range reported and a recent assessment<sup>(27)</sup> has served to question the assumed equilibrium partitioning of oxygen in solution in liquid sodium and solid vanadium. A recent evaluation at GE<sup>(28)</sup>

also refers to the uncertainty in the attainment of equilibrium. Although controversy exists, the method is finding application in American laboratories and reported derivations do show reasonable consistency.

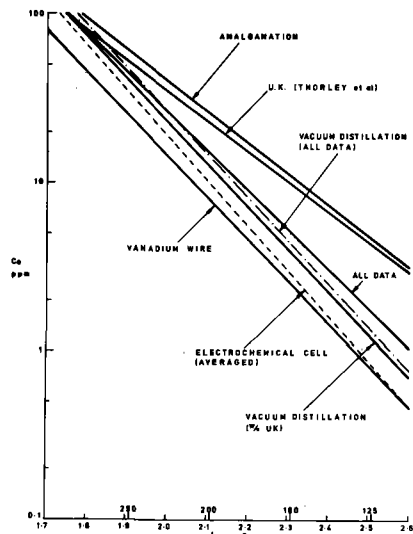


FIG. 4. OVERALL CORRELATIONS FOR DIFFERENT TECHNIQUES OF ANALYSIS

The implicit assumption is made in solubility experiments, of equilibrium of the oxygen in solution with the lowest temperature (notionally the cold trap) of the circuit. A competing "sink" for oxygen in the circuit such as the formation of sodium chromite ( $\text{NaCrO}_2$ ) could compromise this assumption. The extent of this reaction in non-isothermal systems is dependent on many factors. These include the maximum temperature of the circuit, the residence time in different temperature regions, the dissolved oxygen content, the activity of chromium in the stainless steel, etc. Doubts over the functions used in the thermodynamic arguments deployed make a quantitative assessment difficult.

In techniques in which all the oxygen is assumed to exist as sodium monoxide any oxygen present as sodium chromite would be undervalued by a factor of four. Whilst not relevant to the amalgamation-with-mercury results which seem too high, it could be relevant to vacuum distillation data. Reported chromium levels seem too low, however, to make a significant contribution to the overall error in the analysis.

As a general point the 'Na<sub>2</sub>O - only' assumption in the analysis of the vacuum distillation residue can lead to oxygen concentrations too high or too low depending on the composition of any other species present in the sodium (carbonate, chloride, carbide etc.).

Other factors influencing the solubility determination include adequate instrumentation of the cold trap to accurately determine the true minimum sodium temperature. It is also necessary to have a sufficient oxygen inventory in the system to ensure equilibrium at all cold trap temperatures. This requirement has been found, not surprisingly, to be more difficult to satisfy at high cold trap temperatures (~ 250°C) than at temperatures of more relevance to reactor operation (< 160°C).

The vacuum distillation method, although well established, still shows a number of inconsistencies. Figure 5 shows the result of analysing the data over different discrete temperature ranges. The Rutkauskas data shows a significant decrease in the heat of solution as the temperature decreases. Recently identical tests<sup>(19)</sup> at the JEN laboratories have indicated solubilities at low cold trap temperatures substantially higher than the Rutkauskas data. Figure 6 presents these data as measured oxygen level (vs) time at different cold trap temperatures and indicates the apparently better agreement with the UK solubilities.

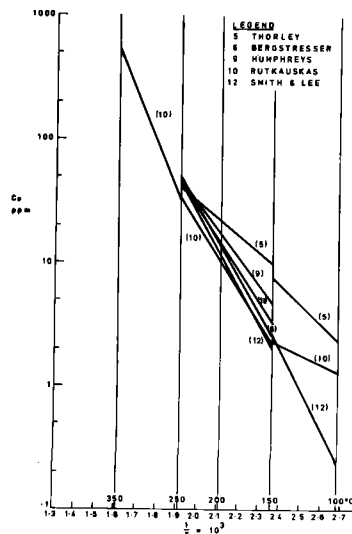


FIG. 5.  $C_p$  (vs)  $\frac{1}{T}$  FOR VACUUM DISTILLATION METHOD FOR DIFFERENT TEMPERATURE RANGES

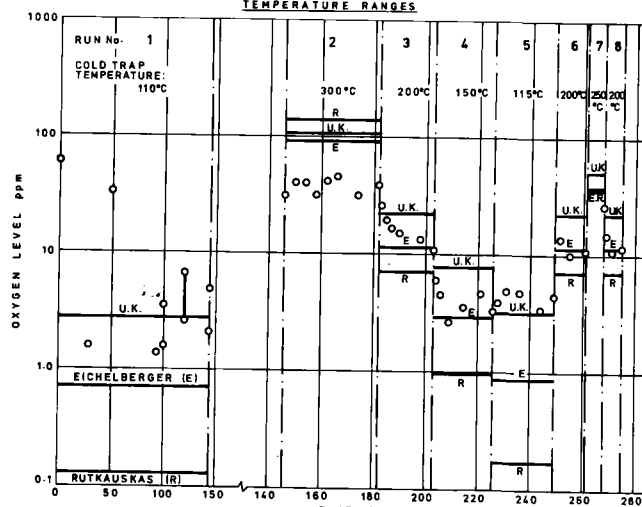


FIG. 6. OXYGEN LEVEL (vs) TIME AT DIFFERENT COLD TRAP TEMPERATURES FOR VACUUM DISTILLATION BY INDUCTION HEATING (JEN)

A completely definitive judgement on the most reliable solubility correlation cannot be made. The difference between the UK data and the various representations of data by technique as shown in Fig. 4 is unlikely to alter. The usually held philosophy in analytical work that, as techniques 'improve' lower levels of detection will prevail and have greater validity is not necessarily applicable for oxygen-in-sodium analysis.

Moreover, even if some judgement were possible the situation would still remain of oxygen levels being quoted in a number of cases which are significantly lower than those which the UK technique is capable of yielding. Recognition and acceptance of this difference would, for the moment, seem the only realistic approach.

### 3. RELATIONSHIP BETWEEN OXYGEN LEVELS DERIVED BY UK AND US WORKERS

The different positions in oxygen analysis apparent from the previous section have been related by determining the ratio of the UK solubility to that derived from considering (1) all the vanadium wire data and (2) all the vacuum distillation data (w/o UK). These ratios are plotted against saturation temperature in Figure 7 and show that over a saturation temperature range of interest to a fast reactor namely 160°C (PFR) to 110°C (PHENIX), the ratio changes from 4.3 to 6.2 in the UK to vanadium wire comparison.

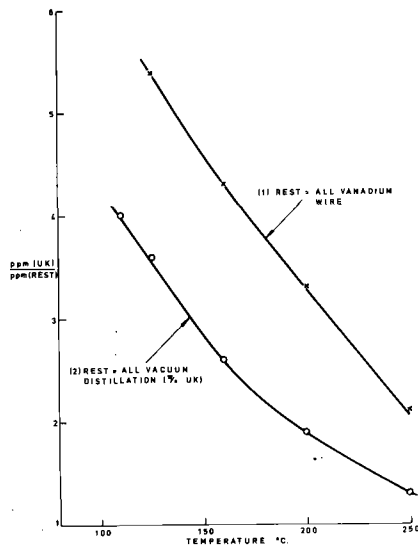


FIG. 7. RATIO OF O-IN-NA FOR U.K. TO (1) VANADIUM WIRE & (2) VACUUM DISTILLATION (% UK)

This is a purely empirical result. It does, however, appear to be one way of reconciling the widely disparate positions on oxygen analysis. The divergent oxygen levels arising from even well-established techniques of analysis such as vacuum distillation make it difficult to imagine that this procedure is any less reliable than comparing events at equivalent measured oxygen levels.

Cold trap temperature as a measure of the oxygen condition of a sodium system therefore seems a reasonable alternative. Some support for this can be cited and it will be seen that this approach can provide the means for making a plausible comparison of corrosion data.

4. COMPARISON OF CORROSION DATA

Consideration is given first to the GE PA.15 programme. Phase I of this work culminated in the development of an empirical relationship<sup>(29)</sup> for the corrosion rate of stainless steels in liquid sodium as a function of the major test variables. This is presented below for the steady state situation as equation (3).

$$\log_{10} S = 3.397 + 0.884 \log_{10} V + 1.156 \log_{10} C_o - \frac{26300}{2.303 RT} - 2.94 \times 10^{-3} \left(\frac{L}{D}\right) \dots(3)$$

- S = corrosion rate (mils/yr)
- V = velocity (ft/sec)
- C<sub>o</sub> = oxygen concentration (ppm)
- T = temperature (°K)
- R = gas constant (1.987 cal/deg mole)
- $\left(\frac{L}{D}\right) = \frac{\text{Distance downstream in isothermal section}}{\text{Tube diameter}}$

This equation applied up to a maximum sodium temperature of 650°C (1200°F), over a velocity range of 7–21 ft/sec, and oxygen concentrations of 12 to 50 ppm, these latter figures being based on observed plugging temperatures of 152°C (305°F) and 232°C (450°F).

In Phase II of the programme the maximum temperature was extended to 704°C (1300°F). A new relationship was derived<sup>(29)</sup> which is presented below in equation (4) for the steady state situation.

$$\log_{10} S = 4.137 + 0.435 \log_{10} V + 1.156 \log_{10} C_o - \frac{26300}{2.303 RT} - 4.16 \times 10^{-4} \left(\frac{L}{D}\right)_1 - 0.122 \log_{10} \left(\frac{L}{D}\right)_2 \dots(4)$$

where

$$\left(\frac{L}{D}\right)_1 = \frac{\text{Distance downstream in isothermal section}}{\text{Tube diameter}}$$

$$\left(\frac{L}{D}\right)_2 = \frac{\text{Distance downstream in isoveloccity section}}{\text{Tube diameter}}$$

All other units are as in equation (3).

The large bank of UK data has been correlated by Thorley<sup>(22)</sup> for use at a velocity of 25 ft/sec (Reynolds number 10<sup>5</sup>) and at a position 4 ins from the isothermal corrosion section inlet. This relationship is presented below in equation (5).

$$\log_{10} S = 2.44 + 1.5 \log_{10} C_o - \frac{18000}{2.303 RT} \dots(5)$$

Units as in equation (3).

A comparison has been made of corrosion rates predicted by this correlation with the corresponding values from the two GE equations. The results are presented graphically in Figure 8(a).

The conditions chosen for the GE equations are as follows.

Velocity. A figure of 25 ft/sec was used to agree with the UK condition applicable in equation (5).

Oxygen concentration. For both equations a figure of 12 ppm was chosen as reported to apply by GE for a plugging temperature of 152°C.

Downstream effects. The UK data corresponds to an '(L/D)' figure of 25. This has been used for all the Phase I and II downstream terms.

Equation (5) can be evaluated two ways either the oxygen concentration as estimated by GE (12 ppm) can be used or the UK relationship between plugging temperature and oxygen concentration can be used to estimate the oxygen concentration. Both these approaches have been used and the results are plotted in Figure 8(a). These plots show that better agreement is obtained over most of the temperature range between the UK and GE predictions at equivalent cold trap temperature rather than equivalent oxygen level.

A further relationship was presented by GE in 1971, viz:

$$\log_{10} S = 4.15 - \frac{18300}{2.303 RT} \dots(6)$$

The symbols have the same meaning and units as in equation (3).

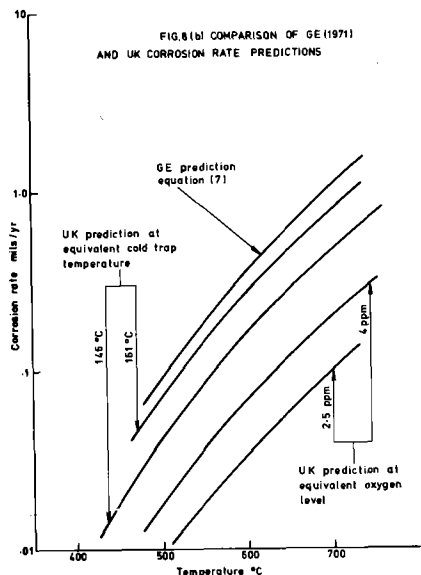
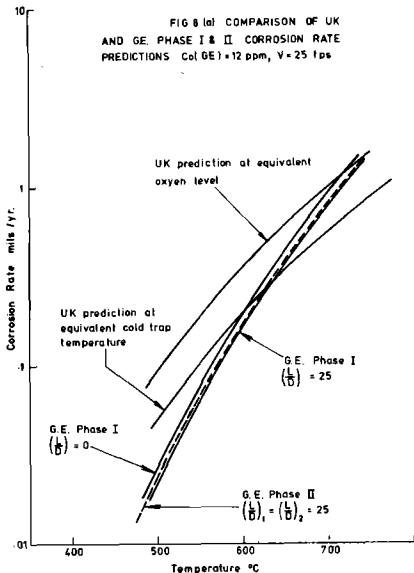
This equation was said to apply over a velocity range of 15 to 28 ft/sec and at an oxygen level of "approximately 4 ppm" and "2.5 ± 1.5 ppm". One of these figures must presumably be in error.

The predicted corrosion rates from equation (6) are represented graphically by the upper line in Figure 8(b). The lower two lines in this plot represent the corresponding UK predictions based on equation (5) at the same oxygen levels quoted by GE. A significant difference can be seen between the GE and UK predictions in spite of the reported extensive use made by GE of UK corrosion data in deriving equation (6).

As noted above however implicit in the respective corrosion rate equations are the oxygen solubility measurements made by the two sets of workers. Since these are clearly different it is instructive to compare the predictions on the basis of equivalent cold trap temperatures. Accordingly in Figure 8(b) the UK predictions are presented on the basis of equivalent cold trap temperatures. In making this calculation it was assumed that the GE oxygen levels quoted were based on the Eichelberger solubility scale. From this assumption it is possible to deduce a plugging temperature and hence via the UK oxygen concentration/plugging temperature relationship an equivalent oxygen concentration for use in equation (5). It is apparent from Figure 8(b) that closer agreement is again obtained between the two predictions based upon cold trap temperature rather than oxygen concentration.

# INTERNATIONAL CONFERENCE ON LIQUID METAL TECHNOLOGY IN ENERGY PRODUCTION

Since the GE workers quote two oxygen concentrations (4 and 2.5 ppm) there are two corresponding cold trap temperatures (161°C and 146°C). Closest agreement is observed between the two predictions when the UK prediction is evaluated with an oxygen concentration based upon the higher assumed cold trap temperature (161°C) corresponding, on the GE scale, to an oxygen concentration of 4 ppm.



This situation can be attributed to the differing means employed during the long GE programme for establishing the oxygen concentration of liquid sodium. Initially, the oxygen level was deduced from plugging temperatures interpreted using at first the Salmon-Cashman solubility curve. Later developments included checking the plugging meter derivations with analysis by amalgamation-with-mercury and vacuum distillation techniques. In recent years use has been made of 'lower-level' oxygen solubility relationships as typified by Eichelberger's equation. The oxygen level quoted with equation (6) is an example of the latter situation.

Whilst at no time has any major difference been suggested as existing between UK and GE corrosion results, changes in the oxygen scales against which the data are compared can obviously prove misleading. As low oxygen levels are now quoted repeatedly in the ERDA programme, some clarification seems appropriate.

Westinghouse<sup>(20)</sup> have also reported corrosion rates at 20 ft/sec and at different oxygen levels. Data were presented at a cold trap temperature of 135°C with the oxygen level, as determined by a flow-through-sampler technique, being specified as 'less than 10 ppm'. It has been stated that these data are essentially in agreement with the UK results. Figure 9 shows a comparison of these results based on equivalent cold trap temperature which supports this statement reasonably well.

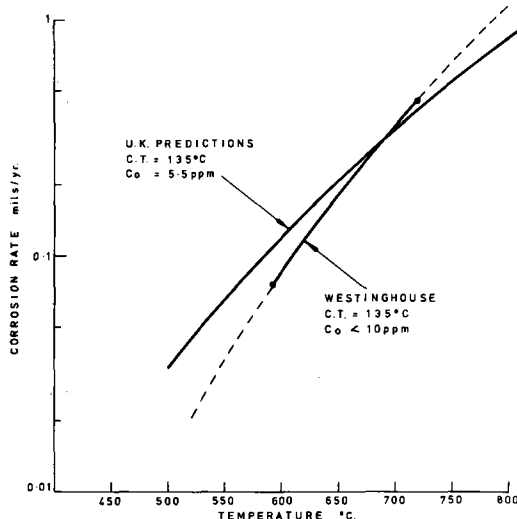


FIG. 9. COMPARISON OF U.K.A.E.A. & WESTINGHOUSE CORROSION DATA AT EQUIVALENT COLD TRAP TEMPERATURES

A further comparison of corrosion rates is possible by considering reported Interatom recommendations<sup>(26)</sup>.

The following relationship was proposed:

$$\log_{10} S = 2.954 - \frac{17000}{2.303 RT} \quad \dots(7)$$

Units as in equation (3)

This function was said to apply at velocities in excess of about 10 ft/sec and at an oxygen level of 1 ppm stated to be equivalent to a saturation temperature of 120°C on the Eichelberger oxygen scale. A comparison of the predictions from equations (5) and (7) at equivalent oxygen levels and cold trap temperatures is shown in Figure 10.

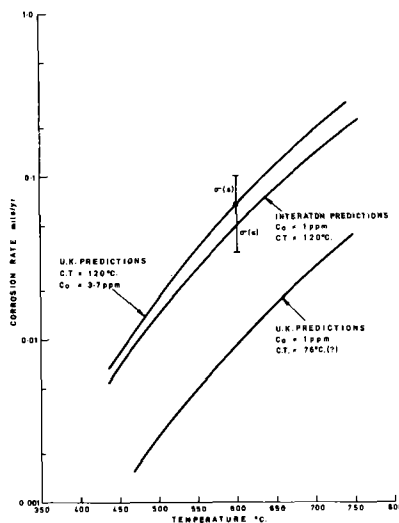


FIG. 10. COMPARISON OF U.K.A.E.A. & INTERATOM CORROSION RATE PREDICTIONS AT EQUIVALENT OXYGEN LEVELS & COLD TRAP TEMPERATURES

# INTERNATIONAL CONFERENCE ON LIQUID METAL TECHNOLOGY IN ENERGY PRODUCTION

As before, better agreement obtains at equivalent cold trap temperature.

Weeks (BNL) (21) has derived a corrosion rate relationship in which oxygen activity instead of oxygen concentration is employed. This is shown below in equation (8).

$$S = \frac{7.93 \times 10^{11} T}{x_{Fe}} \left\{ \left( \frac{C_o}{C_{sat}} \right)^{2x_{Fe}} \exp \left( \frac{-50300}{RT} \right) \right\} \left[ 1 - \epsilon \left( \frac{L}{D} \right)^2 \right] \quad (8)$$

where

$x_{Fe}$  = mole fraction of Fe in steel

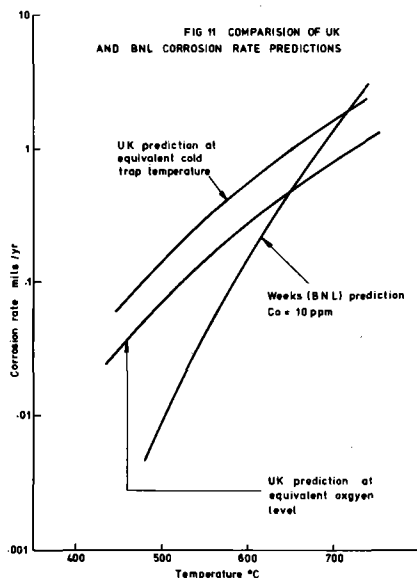
$C_{sat}$  = saturation oxygen concentration at T

$\epsilon$  = downstream factor.

For  $x_{Fe} = 0.65$  and  $\left( \frac{L}{D} \right) =$  equation (8) becomes:

$$\log_{10} S = 12.08 + 1.3 \log_{10} \left( \frac{C_o}{C_{sat}} \right) + \log_{10} T - \frac{50300}{2.303 RT} \quad (9)$$

Figure 11 shows a comparison between the BNL predictions using equation (9) with  $C_o = 10$  ppm and UK predictions at the equivalent oxygen level and cold trap temperature, the latter figure being derived from unpublished BNL solubility data. The different downstream values prevailing for equations (5) and (9) introduce an insignificant error, based on the values for  $\epsilon$  reported by Weeks.



Although showing good agreement at 650°C the BNL predictions diverge significantly from the UK values below this temperature. This difference is such as to make the question of better agreement at equivalent oxygen level or cold trap temperature of little relevance.

## 5. CONCLUSIONS

No attempt is made in this paper to decide on the relative merits of the various corrosion rate correlations considered. It would however appear that:

(i) there is a significant systematic difference in the oxygen levels in sodium as determined by the different analytical techniques used by the various groups of workers;

(ii) this difference is reflected in the corrosion rate equations proposed by these various groups;

(iii) this difficulty can be largely overcome by assuming that the cold trap or plugging temperature is an accurate representation of the actual oxygen concentration and using this temperature to estimate an appropriate "oxygen concentration" for use in the particular corrosion rate equation;

(iv) in the high velocity regime the closer agreement between UK data and the various published corrosion rate predictions is obtained with the original GE relationship.

## REFERENCES

1. WALTERS, S. L. (1950). 'Effect of Adding Oxygen to Sodium Flowing in a Stainless Steel System'. Report N.P. 1955 (MSA-TR-V1).
2. BOGARD, A. D. and WILLIAMS, D. D. (1951) 'Solubility of Sodium Monoxide and of Sodium Hydroxide in Metallic Sodium,' Report NRL-38
3. NODEN, J. D. and BAGLEY, K. Q. (1954) 'Solubility of Oxygen in Sodium and NaK Alloy'. UKAEA Report R and DB(c) - TN - 80.
4. JAHNS, W. and WEIDMANN, C. (1959). 'Determination of Low Oxygen Concentrations in Sodium'. Nukleonik 1, p. 189.
5. THORLEY, A. W. (1961). To be published.
6. BERGSTRESSER, K. S. et al. (1965). 'Determination of Trace Amounts of Oxygen Added to Metallic Sodium.' LA-3343.
7. DORNER, S. and BEISSWENGER, H. (1968). 'Solubility of Oxygen in Liquid Sodium.' J. of N. Mat. 28, p. 297-302.
8. ANDREWS, R. C. and BARKER, K. R. (1967). MSAR - 67 - 207, p.8.
9. HUMPHREYS, J. R. (1968). ANL - 7460, p. 31. ANL - 7518, p. 30
10. RUTKAUSKAS, V. J. (1968). 'Determination of Solubility of Oxygen in Sodium by Vacuum Distillation.' LA - 3879.
11. BORGSTEDT, H. U. et al. (1972). 'Löslichkeit des Sauerstoffs in Natrium bei 150 bis 230°C'. Atomwirtschaft, Mary, p. 157.
12. SMITH, D. L. and LEE, R. H. 'Characterization of the Vanadium-Wire Equilibration Method for Measurement of Oxygen Activity in Liquid Sodium' ANL-7891 (1972).
13. McKEE, J. M. et al. (1972). 'Calibration Stability of Oxygen Meters for LMFBR Sodium Systems.' Private draft copy, Table 1.
14. McKEE, J. M. et al. (1972). 'Calibration Stability of Oxygen Meters for LMFBR Sodium Systems.' Private draft copy, Table 2.
15. GRUNDY, B. R. et al. (1972). 'Characterisation of On-Line Metal Oxygen Meters.' WARD - 3045 T1 - 4.
16. MINUSHKIN, B. and KISSEL, G. (1969). 'Solubility and Reactions of Oxygen in Sodium.' Met. Soc. AIME - Philadelphia. Session V, Paper 2. p. 515.
17. STAVROPOULOS, G. and CAFASSO, F. A. (1971). 'Oxygen in Liquid Sodium: Thermodynamics and Electrochemical Determination.' Trans. A.N.S. 14 (2), p. 621.
18. BORGSTEDT, H. U. et al. (1972). 'Measurement of Oxygen Saturation Concentrations in Sodium by EMF Determination,' Atomwirtschaft, 17, July p. 361. or C.E. Translation 6073.
19. de la TORRE, M. (1974). JEN. Private Communication.



## INTERNATIONAL CONFERENCE ON LIQUID METAL TECHNOLOGY IN ENERGY PRODUCTION

20. WHITLOW, G. A. et al (1971) 'Sodium Corrosion Behaviour of Alloys for Fast Reactor Applications' Proceedings of Symposium on Chemical Aspects of Corrosion and Mass Transfer in Liquid Sodium. Met. Soc. AIME Detroit p. 1.
21. WEEKS, J. R. and ISAACS, H. S. 'General Model for the Corrosion of Steels in High Velocity Sodium' p. 207 Ref. 20.
22. THORLEY, A. W. and TYZACK, C. (1972) 'Corrosion and Mass Transport of Steel and Nickel Alloys in Sodium Systems.' Proceedings of Int. Conf. on Liquid Alkali Metals, BNES, Nottingham p. 257.
23. EICHELBERGER, R. L. (1968) 'Solubility of Oxygen in Liquid Sodium: A Recommended Expression.' AI - AEC - 12685.
24. NODEN, J. D. (1972). 'A General Equation for the Solubility of Oxygen in Liquid Sodium.' CEGB/RD/B/R2146, and (1972) 'An Addendum'. CEGB/RD/B/N2500.
25. WOZALDO, G. P., et al. (1971) 'Calculated Radioactivity of the FFTF Primary Sodium System due to Mass Transfer.' GEAP - 13671.
26. MERKEL, A. and MENKEN, G. (1972) 'Estimation of Radiation Levels near Components of the SNR - 300 Primary System Induced by Deposition of Active Corrosion Products' p. 301 Ref. 22.
27. HOOPER, A. J. and TREVILLION, E. A. (1973). 'Oxygen Analysis of Sodium by Equilibration with Vanadium: An Assessment. J. of N. Mat. 48. p. 216-222.
28. ADAMSON, M. G. (1974) Oxygen Thresholds for the Sodium-Fuel Reaction; An Evaluation of Experimental and Theoretical Results. GEAP - 12519.
29. WOZALD, G. P. and SPALARIS, C. N. (1969) 'Corrosion of Stainless Steels and Deposition of Particulates in Flowing Sodium Systems' GEAP - 13544.

**TABLE 1**  
**Analysis of Data for Solubility of Oxygen in Liquid Sodium**

Reference No./ Name	Method of Analysis	N	A	B	ΔH cal mole <sup>-1</sup>	Co (ppm) at			σ (Co) %	σ (log Co)	Correlation coefficient R
						110 °C	160 °C	650 °C			
1. Walters	Amalgamation (D)	25	5.71	-2043	9349 ± 466	2.4	9.8	3137	43	.185	-.97
2. Bogard and Williams	Amalgamation (D)	10	4.08	-1120	5125 ± 491	14	31	735	32	.137	-.97
3. Noden and Bagley	Amalgamation (D)	46	5.25	-1777	8132 ± 632	4.1	14	2112	54	.235	-.89
4. Jahns and Weidmann	Amalgamation (I)	27	5.05	-1691	7738 ± 279	4.3	14	1652	18	.078	-.98
5. Thorley	Vac distillation (D)	7	5.13	-1791	8196 ± 415	2.8	9.8	1547	14	.062	-.99
6. Bergstresser	Vac distillation (I)	22	6.39	-2517	11518 ± 419	.7	3.8	4603	29	.125	-.99
7. Dorner	Amalgamation (D)	30	4.94	-1653	7564 ± 441	4.2	13	1410	37	.162	-.96
8. Andrews and Barker	Amalgamation (I)	19	7.40	-3053	13971 ± 836	.3	2.2	12368	34	.148	-.97
9. Humphreys	Vac distillation (D)	19	5.30	-1918	8778 ± 330	2.0	7.4	1667	12	.050	-.99
10. Rutkauskas	Vac distillation (D)	52	6.12	-2395	10960 ± 328	.7	3.9	3351	28	.123	-.98
11. Borgstedt	Vac distillation (I)	10	6.39	-2487	11381 ± 1186	.8	4.4	4961	21	.089	-.96
12. Smith and Lee	Vac distillation (D)	51	6.97	-2804	12831 ± 432	.4	3.1	8552	23	.102	-.97
13. McKee	Vanadium wire (I)	10	5.75	-2348	10745 ± 679	.4	2.1	1607	24	.104	-.98
14. McKee	Vanadium wire (I)	9	5.68	-2261	10346 ± 813	.6	2.9	1700	22	.094	-.98
15. Grundy	Vanadium wire (I)	10	5.79	-2362	10809 ± 574	.4	2.2	1702	18	.079	-.99
16. Minushkin	Electrochem cell (I)	-	6.46	-2600	11898	.5	2.9	4396	-	-	-
17. Stavropoulos	Electrochem cell (I)	-	7.11	-2877	13165	.4	2.9	9840	-	-	-
18. Borgstedt	Electrochem cell (D)	-	6.429	-2606	11925	.4	2.6	4033	-	-	-

D - Direct measurement

I - Indirect measurement

**INTERNATIONAL CONFERENCE ON LIQUID METAL TECHNOLOGY IN ENERGY PRODUCTION**

**TABLE 2**

Summary of Correlations from Data Considered in Different Reviews

Reference	N	A	B	$\Delta H$ Kcal mole <sup>-1</sup>	Co (ppm) at			$\sigma$ (Co) %	$\sigma$ (log C <sub>0</sub> )	Correlation coefficient R
					110 °C	160 °C	650 °C			
(1) Claxton (1965)	88	5.21	-1777	8.13 ± .37	3.7	12.8	1926	59	.255	-
(2) Eichelberger <sup>(23)</sup> (1968)	-	-	-	-	-	-	-	-	-	-
(a) Selected data	107	6.239	-2447	11.20 ± .17	0.7	3.9	3871	34	.148	-.99
(b) Rejected data	111	4.71	-1518	6.94 ± .29	5.6	16.1	1162	40	.173	-.92
(c) All data	218	5.765	-2130	9.75 ± .23	1.6	7.0	2866	57	.299	-.94
(3) Noden <sup>(24)</sup> (1972)	-	-	-	-	-	-	-	-	-	-
(a) Selected data	268	6.2571	-2444.5	11.20 ± .14	0.75	4.1	4061	35	.154	-.98
(b) Rejected data	50	4.90	-1592	7.29 ± .71	5.5	16.7	1497	49	.212	-.83
(c) All data	318	5.9805	-2268.2	10.38 ± .20	1.1	5.5	3335	55	.240	-.94
(4) Claxton (1974)	347	6.16	-2372	10.86 ± .20	0.9	4.8	3892	58	.252	-.95

**TABLE 3**

Summary of Overall Solubility Correlations for Data Grouped by Method

Reference	N	A	B	$\Delta H$ Kcal mole <sup>-1</sup>	Co (ppm) at			$\sigma$ (Co) %	$\sigma$ (log C <sub>0</sub> )	Correlation coefficient R
					110 °C	160 °C	650 °C			
(1) All data	347	6.16	-2372	10.86 ± .20	0.9	4.8	3892	58	.252	-.95
(2) Amalgamation (all data)	157	5.33	-1859	8.51 ± .28	3.0	10.9	2070	55	.237	-.92
(3) Vacuum distillation (all data)	161	6.27	-2449	11.21 ± .25	0.75	4.1	4137	34	.148	-.96
(4) Vanadium wire (all data)	29	5.80	-2354	10.77 ± .44	0.45	2.3	1777	24	.105	-.98
(5) Electrochemical cell	-	6.46	-2600	11.89	0.5	2.9	4396	-	-	-
	-	7.11	-2877	13.17	0.4	2.9	9840	-	-	-
	-	6.429	-2606	11.93	0.4	2.6	4033	-	-	-
(6) Vacuum distillation (W/O UK)	154	6.39	-2516	11.51 ± .22	0.7	3.8	4614	30	.129	-.97
(7) Vacuum distillation (UK data)	7	5.13	-1791	8.20 ± .42	2.8	9.8	1547	14	.002	-.99

# INTERNATIONAL CONFERENCE ON LIQUID METAL TECHNOLOGY IN ENERGY PRODUCTION

## DISCUSSION

Paper VB-1: "Corrosion, Transport, and Deposition of Stainless Steel in Liquid Sodium"

H. Issacs: Have you studied the velocity effect on corrosion rates at high oxygen concentrations?

B. Kolster: No, the study I referred to concerned an oxygen level of 5 ppm, i.e., the low oxygen level range.

L. Epstein: How did you measure oxygen levels?

B. Kolster: Oxygen levels were measured by means of in-line distillation and subsequent chemical analysis.

A. Thorley: Did you measure corrosion rates at various increments of time or are the corrosion rates quoted for one time period? If as it appears they are for one time period only, how do you know you have reached a steady-state composition in your various temperature positions? This is important in evaluating the activation energy for the corrosion process. For example, if the lower temperature specimens had not reached a steady-state composition then the activation energy could be in error.

B. Kolster: The answers to your questions are all in the paper. Because of lack of time, I could not present it here, however the weight change measurements reflects the value for one time period, in other words for one point of the  $\Delta G_t$  curve as Fig. 10. From a mechanistic point of view the value of one point on the  $\Delta G_{316}$  curve is required. We determined this value by subtracting  $\Delta G_{e1}$  from  $\Delta G_t$  (see Fig. 10),  $\Delta G_{e1}$  being calculated from the thickness of the ferrite layer and the decrease in concentration of the alloying elements Cr, Ni, Mn and Si. However, as I pointed out in the paper, the most reliable results for this procedure will be obtained if the process is under steady-state conditions, that is if the exposure time exceeds the incubation time  $t_1$  (Fig. 10). As a criterion for this requirement we used the appearance of metallic particles in the cooled zone. From the explanation for their appearance, as I pointed out, it can only be concluded however that at least the 700°C heated zone specimens reached steady-state corrosion, the situations for 650°C not being clear. This problem can be solved by the proper calculation, for which I must refer again to the paper. I just will mention the conclusion we reached. From the four runs carried out at low oxygen level ( $\leq 8$  ppm) three reached an activation energy of 40 k cal/mole.

J. Weeks: Do your measurements represent the total weight change divided by the total exposure time or is it not also necessary to know the steady state rate and often, the incubation period for formulation of meaningful kinetic data?

B. Kolster: Essential to my paper is the recommendation to refer the influence of temperature, oxygen level, etc. to the steady state corrosion, as this is the relevant process from a mechanism point of view. As I pointed out, for our experimental results the steady state corrosion rate is proportional to  $[O]^{0.91}$  and the activation energy for steady state corrosion is about 40 k cal/mole.

J. Weeks: If all specimens were downstream from the heater, is the rate at zero downstream position from the available results estimated?

B. Kolster: The corrosion rate at 700°C and at high oxygen levels is definitely influenced by the corrosion upstream from the specimen holder including the heater. Because of this and because of the hydrodynamic entrance effect we chose not to try to calculate the zero downstream effect. Instead, we used the average weight change of 18 specimens, from each specimen holder, the remaining number of specimens by neglecting the first three specimens of each set.

Paper VB-2: "The In-Reactor Corrosion Behavior of Stainless Steel Cladding in High Temperature Sodium"

J. Weeks: How did the measured ferrite thickness differ in the fueled and unfueled part of the pins?

J. Weber: Figure 7 revealed little difference in averaged ferrite thickness at the top of the fuel and immediately downstream. However individual fuel pins did in some cases show a significantly thicker ferrite layer at the top of the fuel.

C. Bagnall: Comment on difference between "Heat Flux" and " $dT/dL$ " - there is an effect on corrosion rate of the latter. How thick was the ferrite layer at 565°C?

J. Weber: Although Table III indicates that the average ferrite thickness was zero, actual data showed a very discontinuous or intermittent layer of ferrite.

P. Roy: Have you observed any effect of heat flux on the corrosion rate?

J. Weber: Fuel pins have a heat flux that produces a  $dT/dL$  condition in the heat generating zones. Thus, experimentation is presently insufficient to determine whether the higher corrosion rate relative to out of reactor is a heat flux effect or the  $dT/dL$  effect.

G. Whitlow: Have you observed any signs of surface corrosion effects such as selective grain removal during studies on the clad surface?

J. Weber: Although not included in this paper, SEM examination of cladding of the extensive downstream end of the fuel pin was conducted. No grain removal was observed. Holes of the size seen on transverse metallography specimen as penetrations into the ferrite were noted at grain boundary triple points. These holes are much smaller than the grain sizes.

D. Sandusky: In concurrence, I would add that our experimentation indicated pitting in the ferrite layer to be dissolution at grain boundary triple points and not fall-out of whole grains.

J. Weber: These observations prior to the pin examination is acknowledged.

## INTERNATIONAL CONFERENCE ON LIQUID METAL TECHNOLOGY IN ENERGY PRODUCTION

- A. Thorley: Are the values you report metal temperatures or sodium temperatures?
- J. Weber: I have referred to temperatures recorded for the cladding outside surface.
- Paper VB-3: "The Influence of LMFBR Fuel Pin Temperature Profiles on Corrosion Rates"
- B. Kolster: Is a thicker ferrite layer associated with a radial heat flux compared with no heat flux, assuming all other conditions to be identical?
- S. Shiels: The effect of radial heat flux and therefore radial temperature gradient on the thickness of the depleted zone is uncertain. In terms of kinetics, more rapid loss of constituent elements may indicate variation in the diffusion coefficient  $D$  with temperature. In thermodynamic terms, a reverse result can be postulated. The driving force for the migration of a species between positions A & B is given by the chemical potential difference  $\mu_A - \mu_B$  which is  $RT_A \ln A_A - RT_B \ln A_B$  for an isothermal situation and reduces to the concentration difference  $C_A - C_B$ . With a temperature gradient, however, the situation is more complex. If the solubility of the species obeys Henry's Law, the activity  $A$  will be an inverse function of the solubility and will actually decrease with increasing temperature, assuming constant concentration. Migration could therefore occur at a higher level on the temperature gradient. Finally, I would suggest that the 'state of the art' is such that it would be very difficult if not impossible to show a conclusive effect.
- J. Weeks: Were the enhanced corrosion rates you measured based on total weight change over total time, or on steady state rates?
- S. Shiels: Rates were obtained by dividing total weight change by total time and were not steady state values. At the high corrosion rates obtained for these conditions, greater than  $25 \mu\text{m}/\text{yr}$ , equilibrium should not occur until about 10,000 hours have elapsed. Since this time interval represents a significant portion of the fuel pin life, these data are considered to be representative.
- J. Weeks: In what L/D range were the data used to derive the Bagnall/Jacobs corrosion equations?
- C. Bagnall: Wherever possible, data used in the development of corrosion equations were restricted to isothermal regions in the range  $L/D = 0$  to 50.
- W. Apblett: What is the effect of the imposed electrical field on observed corrosion rates?
- S. Shiels: Although electric field effects were not considered extensively, those manifested as potential differences can cause problems in aqueous environments where corrosion is galvanic. In this case however, a potential difference between the specimens and the associated sodium cannot be maintained because of the high electric conductivity of the sodium, and 2) corrosion in sodium is not galvanic.
- Paper VB-5: "Thermodynamic and Diffusion Studies on Corrosion of Austenitic Stainless Steel in Liquid Sodium"
- B. Kolster: Can you comment on the assumption that depletion of Cr and Ni occurs because the diffusion rate is slower than the surface reaction rate in view of your statement that depletion occurs because it is the slowest process?
- H. Konvicka: During the starting period of corrosion, the measured total weight loss is primarily due to the selective leaching process, documented by well known diffusion equations. Therefore, diffusion is the dominating effect at this time. For longer corrosion times, diffusion will be subordinated by weight loss caused by iron corrosion and therefore, diffusion does not represent a limiting factor.
- P. Hawtin: Can you correlate the assumption that velocity effect is associated with the liquid phase and your statement that the velocity effect is due to diffusion along the grain boundaries in the solid phase?
- H. Konvicka: The connection of both ideas may be given by grain boundary grooving. Since the grain boundary diffusion coefficient is a function of grooving angle and the width of the grain boundary, a change in these parameters may achieve a change in diffusion coefficient.
- P. Wu: Is the statement that  $(\text{Na}_2\text{O})_2 \text{FeO}$  will not form in a sodium/stainless steel with oxygen content less than 2000 ppm based on experimental results or literature values?
- H. Konvicka: My statement is based on  $\Delta h$  values given by Fross in the literature.
- P. Wu: Is the flow rate effect on Cr diffusion normalized on oxygen concentration for all tests?
- H. Konvicka: Oxygen level in our corrosion experiment was 7 ppm in the high velocity test pile as well as in the low velocity test pile.
- P. Wu: What is the reference state in defining the Cr activity in your thermodynamic studies, and is the formation of  $\text{NaCrO}_2$  taken into consideration in your diffusion studies?
- H. Konvicka: Reference state is pure chromium of unit activity and does not consider chromite formation.
- W. Kuhn: Did your reminder of the importance of grain boundary diffusion refer to grain boundary diffusion through a single austenite phase or enhanced diffusion in a second ferrite phase forming along grain boundaries?
- H. Konvicka: I referred to enhanced diffusion along ferritic grain boundaries formed in the austenite matrix.
- Paper VB-6: "Solubility of Oxygen in Liquid Sodium:

## INTERNATIONAL CONFERENCE ON LIQUID METAL TECHNOLOGY IN ENERGY PRODUCTION

### Effect on Interpretation of Corrosion Data"

D. Sandusky: What are the cause(s) of the observed difference in oxygen concentration as measured by distillation and vanadium wire?

K. Claxton: Two points can perhaps be concluded. The presence of other species such as chlorides and carbides in the residue remaining after vacuum distillation can lead to oxygen concentrations derived from the  $\text{Na}_2\text{O}$ -only assumption that could be too high. The possibility of equilibrium not having been attained in the partitioning of oxygen between sodium and vanadium can lead to under-estimates of the oxygen level. Both points will result in the difference between the two techniques becoming even more exaggerated.

A. Thorley: I think the point should be made vis-a-vis vanadium wire vs distillation that the vanadium wire technique was calibrated against the distillation technique.

K. Claxton: This point is well taken. It is to be noted that the partition coefficient for the Na-O-V system from theory and experiment do not seem to agree to better than about a factor of 2. As I said in my presentation, however, the adoption of standard operating procedures for the vanadium wire technique is the most sensible means of allowing the method to give an acceptable indication of the oxygen condition of the sodium. I must moreover reiterate an earlier point, namely that my paper is not concerned with settling any issues such as vanadium wire versus vacuum distillation. It is more concerned with recognizing the differences that do prevail and accommodating them.

W. Brehm: Does a corrosion rate of 0.06 mils/yr at 600°C, 115°C cold trap (US value of 0.5 ppm oxygen) fit the UK correlation?

K. Claxton: As an estimate, a cold trap temperature of 115°C on the UK scale corresponds to an oxygen level of about 3 ppm. Assuming that your question relates to a velocity of 25 ft/sec, then the predicted UK corrosion rate would be approximately 0.018 mil/yr, a factor of 3 greater than the figure you quote. With margin of error from  $\pm 30$  to 50%, this difference is clearly less significant than it initially appears. The UK prediction at your US oxygen level of 0.5 ppm is less than .005 mil/yr.

# INTERNATIONAL CONFERENCE ON LIQUID METAL TECHNOLOGY IN ENERGY PRODUCTION

## COMPATIBILITY OF STRUCTURAL MATERIALS WITH BOILING POTASSIUM\*

J. H. DeVan

Oak Ridge National Laboratory  
Oak Ridge, Tennessee 37830

### ABSTRACT

The suitability of iron-, nickel-, and cobalt-base alloys for use as structural materials in boiling-potassium systems is examined with particular attention to corrosion and mass transfer. Corrosion results for high-temperature sodium and potassium loops are summarized and related to the corrosion requirements of a boiling-potassium Rankine-cycle system. This analysis indicates that, in a recirculating boiler with an efficient vapor separator, mass transfer effects will be counter to those in an all-liquid system. Solution will be restricted to the cooler zones and deposition to the hottest zone (i.e., the boiler) as potassium is distilled off and dissolved material is left behind. This hypothesis is evaluated against the data available for boiling-potassium systems, and the results observed are consistent with the hypothesis. Mass transfer rates are notably lower than in all-liquid systems, and in the absence of contamination effects recirculating boilers have shown negligible corrosion.

### INTRODUCTION

This report surveys the information available on the compatibility of austenitic stainless steels, nickel-base alloys, and cobalt-base alloys with potassium under boiling and condensing conditions. The purpose is to appraise the corrosion and mass transfer behavior of these metals in Rankine-cycle, boiling-potassium systems.

A substantial background of information on the corrosion problems associated with the use of alkali metals at high temperatures (greater than 750°C) has been derived from development programs for high-temperature liquid-cooled nuclear reactors. These studies have shown that the alkali metals sodium and potassium afford very similar corrosion properties with respect to most structural metals. Thus, although this review is aimed specifically at potassium, sodium and NaK data have been incorporated where

pertinent to give a broader background for interpreting and detailing the potassium compatibility picture.

This report begins with a review of the classes of structural materials that have been considered for vessel and piping applications in boiling-potassium systems. The various classes are compared in terms of their general compatibility characteristics and development potential. Next attention is directed to the corrosion mechanisms operative in liquid-metal systems and to the corrosion experience at temperatures above 750°C. The last portion of the report analyzes the corrosion properties of boiling-potassium systems. It considers the corrosion mechanisms in recirculating and once-through boilers and relates the analysis to the corrosion data that have been acquired from boiling-loop systems at Oak Ridge National Laboratory.

### POTASSIUM AS A WORKING FLUID

The two principal ways of increasing the thermal efficiency of thermodynamic cycles were indicated by Carnot over a century ago — increase the peak temperature in the cycle or find ways to make the actual cycle more closely approach the ideal Carnot cycle. In either case allowances must be made for the practical limitations imposed by materials, capital cost, and reliability considerations.

The potassium-vapor topping cycle was first proposed in 1958 for use with high-temperature (~800°C) fission reactors and more recently was shown to be remarkably well suited for use with fusion reactors.<sup>1,2,3</sup> By superimposing this high-temperature Rankine cycle (760°C or more turbine inlet temperature) on a conventional 540°C steam Rankine cycle, the overall thermal efficiency of the combined cycle can be increased to the 50 to 60% range. Further, over 200,000 hr of boiling-potassium system operation was obtained in the 1960s under various space power plant development programs. This experience has demonstrated the use of potassium in stainless steel

\*Research sponsored by the Energy Research and Development Administration under contract with the Union Carbide Corporation.

## INTERNATIONAL CONFERENCE ON LIQUID METAL TECHNOLOGY IN ENERGY PRODUCTION

recirculating boilers at temperatures up to 870°C and in refractory-metal boilers at temperatures up to 1300°C.<sup>4,5,6</sup>

It was thought initially that combustion gas-side corrosion would restrict the operating temperature of a potassium-vapor cycle to much less than 800°C, and hence it would not be suited for use with fossil-fuel fired systems. However, it became evident in 1970 that antipollution regulations were forcing the use of low-sulfur fuels and that with such fuels the corrosion problem should be greatly alleviated. Further, the impending fuel supply crisis coupled with increasing fuel costs provides a greater incentive to obtain the marked improvement in thermal efficiency promised by the potassium-vapor topping cycle. The potential of the potassium topping cycle for fossil-fuel energy production will ultimately be decided by developments currently under way in coal conversion and coal combustion technologies.

### MATERIALS SELECTION

The selection of structural materials for the containment of boiling potassium has been based on a combination of the following factors:

1. suitable mechanical properties at operating conditions,
2. compatibility with potassium at elevated temperatures,
3. resistance to environmental deterioration (air or vacuum), and
4. ease of fabrication.

Materials finding application under these selection criteria divide into three classes: austenitic stainless steels, nickel- or cobalt-base superalloys, and refractory metals. The relative strength properties afforded by these alloys for boiling-potassium service are compared in Fig. 1. The comparison is based on the ratio of allowable stress for 1% creep in 10,000 hr to the potassium vapor pressure. Since the forces acting on the boiler and piping walls are largely governed by the vapor pressure, this ratio indicates the relative section thicknesses required for a given safety factor at each temperature. Note that the temperature dependence of creep strength and vapor pressure causes their ratio to fall off very rapidly as temperature increases. The mechanical properties of stainless steels impose a practical temperature limit of about 840°C for extended operation. The cobalt-base

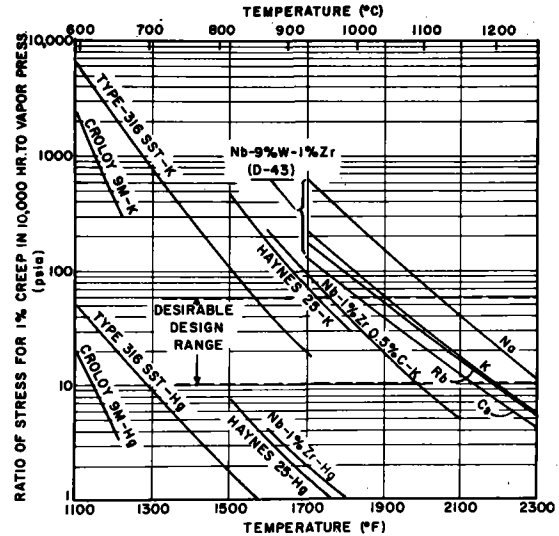


Fig. 1. Effects of Temperature on the Ratio of the Allowable Stress to the Vapor Pressure in the Boiler for Typical Combinations of Materials for Rankine-Cycle Systems.

Haynes alloy No. 188 shows promise for service to 900°C and refractory metals appear useful at temperatures above 1000°C.

### Austenitic Stainless Steels

The austenitic stainless steels have found extensive application in alkali-metal cooled heat transfer systems operating between 300 and 700°C. As a class, these alloys offer special advantages in terms of cost, ease of testing, and ease of fabrication.

The corrosion rates measured for these materials in sodium, NaK, and potassium are indicated in Fig. 2.<sup>7-12</sup> The rates below 800°C fall generally within the range 0.2 to 2 mg cm<sup>-2</sup> month<sup>-1</sup>, which is equivalent to the uniform removal of 0.1- to 1.0-mil thickness of material per year. However, sufficient intergranular penetration may occur above 750°C to affect the strength of thin cross sections. Moreover, the weight losses plotted in Fig. 2 reflect preferential removal of chromium, nickel, and carbon, which, while minor in terms of material lost, materially affect the mechanical properties of these steels.

Although the operating conditions of the various loop tests plotted in Fig. 2 are not directly comparable, there is some indication that the mass transfer rates for potassium are slightly lower than for sodium. The corrosion properties of sodium and potassium were directly compared by United Nuclear Corporation<sup>13</sup> using identical type 316 stainless steel thermal-convection loops operating at 860°C. Corrosion rates were lower

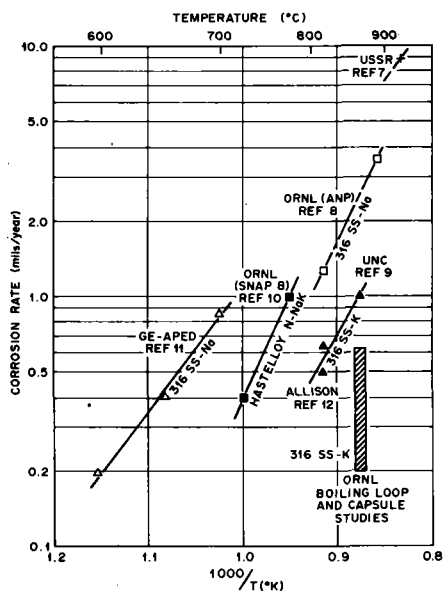


Fig. 2. Relative Corrosion Rates of Stainless Steels in Sodium and Potassium.

in the potassium loop than in the sodium loop throughout the 5000-hr test exposures; however, the compositional changes effected in the stainless steel were quite similar for both coolants.

#### Nickel- and Cobalt-Base Alloys

The mechanical properties of certain nickel- and cobalt-base alloys permit a 50 to 100°C increase in the operating temperature of a boiling-potassium system over the maximum temperature level practicable with austenitic stainless steels. Since these "super-alloys" derive their strength from age-hardening reactions, they impose potential fabrication and operational difficulties. Notwithstanding, these materials have drawn some interest both for cladding and vessel applications in potassium systems.

Principal sources of corrosion data on nickel-base alloys include the Aircraft Nuclear Propulsion Program,<sup>8</sup> the SNAP-8 development program,<sup>10</sup> and Russian work.<sup>9</sup> These studies have shown that nickel-base alloys are generally more susceptible to temperature-gradient mass transfer in sodium and NaK than are the iron-base alloys. Although their corrosion rates increase more rapidly with temperature, the resultant attack tends to be quite uniform without serious pitting or intergranular fissuring. Hence, flow restrictions stemming from the growth of mass transfer deposits are a more troublesome problem than reductions in tube wall thickness.

The available corrosion data on nickel-base alloys relate almost entirely to nonboiling systems. As explained in the next section, corrosion requirements of boiling and nonboiling systems differ significantly. Thus, the mass transfer tendencies that nickel-base alloys show in polythermal all-liquid loops do not *a priori* carry over to a two-phase boiling system. It is also significant that nickel-base alloys are much less affected by oxide contamination in sodium than are iron-base alloys.<sup>8,10</sup> Hence, nickel-base systems permit a much greater latitude in purity control than do stainless steels, particularly above 700°C.

The corrosion properties of cobalt-base alloys in either sodium or potassium are not well documented at present. Theoretical considerations indicate that cobalt should resist dissolutive attack by these liquid metals to at least the same degree as iron and better than nickel. In two loop experiments of Haynes alloy No. 25 conducted with boiling potassium,<sup>14</sup> corrosion rates at 870°C were equivalent to those of type 316 stainless steel at similar temperatures. Furthermore, weight losses of Haynes alloy No. 25 at a 980°C boiling-condensing temperature were not significantly higher than at 870°C. Thus cobalt-base alloys show considerable promise for boiling potassium service above 800°C.

#### Refractory Metals

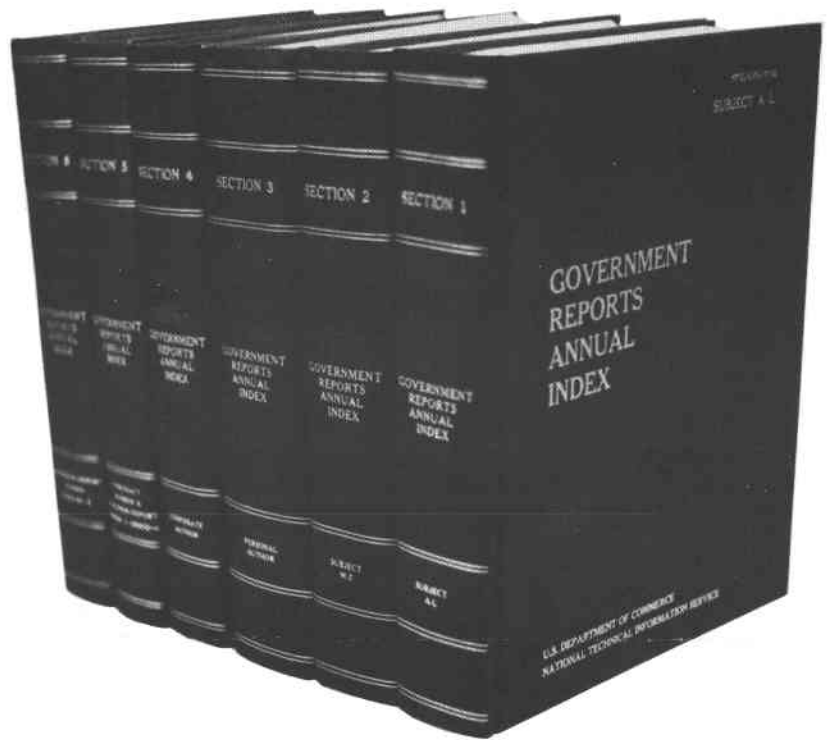
Refractory metals (Groups VA and VIA) are more resistant to dissolutive attack by alkali metals than conventional metals, and their strength is retained to the temperature region above 1100°C, where conventional alloys cease to be useful engineering materials. The primary disadvantage of refractory metals for vessel and piping applications lies in their susceptibility to air oxidation. The presence of oxygen in alkali metals is also quite deleterious to most of the refractory metals.

Although considerable progress has been made in the development and testing of refractory metals for boiling potassium service,<sup>15</sup> the present capability for the production, fabrication, and oxidation protection of these materials does not permit the short-term exploitation of these materials in large, earth-based power systems. For this reason, we shall omit further consideration of refractory metals in this paper.



**Just Released . . .**

# **The New Government Reports Annual Index**



**This cumulative Annual Index  
guides you to more than 70,000 Government R&D  
reports made available by NTIS in 1980.**

When time means money . . . and you need to find the latest developments in your field . . . the new Government Reports Annual Index can solve both problems . . . and more. You get a single reference source for every Government report announced by NTIS in the past year . . . from more than 350 Federal agencies. Convenient and compact, the Annual Index is an important tool for quickly locating reports of the latest developments in your field . . . to aid you in online searches . . . and help you keep up with the competition. This attractive, six-volume, hard bound set lets you search five convenient ways. The set includes indexes by:

- *Subject (two volumes), over 2,200 pages.*
- *Personal author, over 1,100 pages.*
- *Corporate author, approx. 1,000 pages.*
- *Contract number, over 200 pages.*
- *Accession number, approx. 2,500 pages.*

The Annual Index is your key to the entire 1980 NTIS information collection . . . an important source you will use over and over again.

**Update Your NTIS Reference Library**  
**ORDER /**  
**NOW /** *Order: NTIS/ANNI-80*  
*Price: \$375 (foreign price on request)*

**NTIS** National Technical Information Service  
U.S. DEPARTMENT OF COMMERCE  
Springfield, VA 22161

YES! Please send me the 1980 Annual Index.

Charge to my NTIS Deposit Account,  
No. \_\_\_\_\_

CHARGE TO MY

American Express

VISA

MasterCard

Acct. No. \_\_\_\_\_

Exp. Date \_\_\_\_\_

Enclosed is a  
check or money  
order for \$ \_\_\_\_\_

Name \_\_\_\_\_

Occupation \_\_\_\_\_

Address \_\_\_\_\_

City, State, ZIP: \_\_\_\_\_

Signature \_\_\_\_\_  
(Required to Validate Order)

# INTERNATIONAL CONFERENCE ON LIQUID METAL TECHNOLOGY IN ENERGY PRODUCTION

## CORROSION MECHANISMS

The corrosion properties of liquid alkali metals have been under systematic investigation since 1946. Manly<sup>16</sup> noted the corrosion processes in liquid metals to be of two principal types:

1. simple solution leading to general surface removal, grain boundary attack, or preferential leaching of alloying constituents;
2. chemical attack involving impurities in the liquid metal and in or on the container wall.

As a further consequence of either of these corrosion processes, elements of the container metal may undergo continual transport from one part of a dynamic system to another. Two factors contributing to this mass transfer are (a) solubility differences resulting from temperature gradients in the system and (b) chemical activity differences resulting from dissimilar metals in the system. Since equilibrium solubilities in liquid metals nearly always change with temperature, temperature-gradient mass transfer is an inevitable effect in any high-temperature, liquid-metal, thermal- or forced-convection system. Dissimilar-metal mass transfer, on the other hand, can be minimized through the selection of system materials that are not prone to interalloying.

### Solubility Studies

In general, the solubilities in alkali metals of elements making up our useful high-temperature structural alloys are relatively low. Theoretical predictions by Strauss et al.<sup>17</sup> and measurements in lithium by Leavenworth and Cleary<sup>18</sup> suggest that both solubility and the temperature coefficient of solubility depend strongly on the disparity in the atomic radii of solvent and solute atoms. Since the size factor is large between alkali metals and the container metals of interest, their mutual solubility should be small. The Hildebrand model,<sup>19</sup> which considers the available free volume in a liquid, affords another approach to solubility predictions. Using the Hildebrand formula, Swisher<sup>20</sup> calculated the solubilities of iron, nickel, and cobalt in potassium and compared them with experimental values. His results are shown in Table I and indicate poor agreement between the calculated and experimental results; however, the Hildebrand model does not take into account any complex bonding that may occur between solute and solvent and, more importantly, any bonding arising from the presence of impurity elements.

Table I. Experimental and Theoretical Solubility and Heats of Solution of Iron, Nickel, and Cobalt in Potassium at 1000 K (727°C). (Ref. 20)

Solute	Experimental Solubility <sup>a</sup> (ppm)	Experimental Heat of Solution (kcal/mole)	Hildebrand Model Solubility <sup>a</sup> (ppm)	Hildebrand Model Heat of Solution (kcal/mole)
Iron	75.0	28.2	10 <sup>-8</sup>	64.3
Nickel	4.6	13.9	10 <sup>-10</sup>	71.6
Cobalt	<5.0		10 <sup>-10</sup>	73.1

<sup>a</sup>Atomic parts per million.

A long-term interest in iron-base alloys for alkali-metal heat transfer circuits has stimulated a number of independent investigations of the solubility of iron in sodium and potassium. Figure 3 compares solubility data for iron in sodium<sup>21,22</sup> with those for iron in potassium.<sup>20,23,24</sup> (The data are plotted logarithmically vs reciprocal temperature and have been fitted to linear functions.) Two of the curves for potassium have similar slopes but are shifted by an order of magnitude. To account for this discrepancy, Swisher<sup>20</sup> noted that his observed solubility of iron in potassium varied by two orders of magnitude depending on the metal selected for his sampling cup and attributed the higher iron concentrations in his experiments compared to those of McKisson and Eichelberger<sup>23</sup> to oxide impurities in the potassium.

There is obvious difficulty in applying the available solubility data for potassium to a worthwhile corrosion rate analysis. Besides the difficulty in selecting an appropriate solubility curve for the pure metals, there is the question of the solubilities of

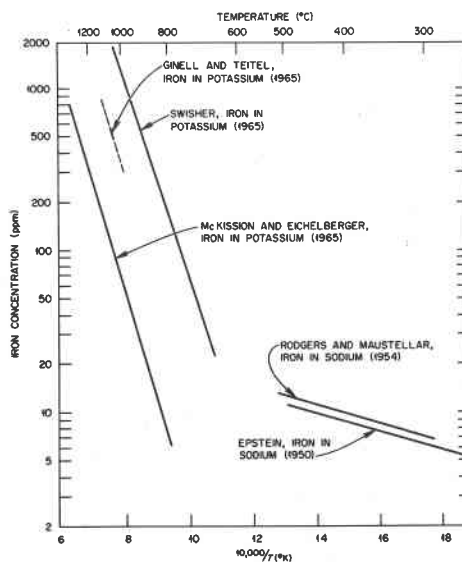


Fig. 3. Solubility of Iron in Sodium and Potassium.

the constituents of an alloy relative to the solubilities of the pure metals. Also data are not available on solution rate constants, which are essential to predicting mass transfer rates. As will be discussed, the oxygen impurities in a boiling potassium circuit tend to concentrate in the boiler. Thus if the higher solubility values in Fig. 3 are associated with oxygen impurities in the potassium, iron solubilities of the magnitude found by Swisher<sup>20</sup> will more typically apply to the boiler region of any iron-base alloy system, while the data of McKisson and Eichelberger<sup>23</sup> should be more applicable to the condenser and condensate return areas.

#### Corrosion and Mass Transfer in Boiling Systems

It is important to recognize that the obvious physical differences between boiling and nonboiling systems carry over into basic differences in corrosion patterns between the two systems. In nonboiling systems, there is continuous, interconnected liquid flow throughout the heat transfer circuit. Consequently the gain or loss of solute at any one point in the system is felt to some degree by all other points in the circuit. The addition or removal of heat from the system, since it affects the liquid metal temperature, has a direct influence on the equilibrium solute concentration and solution rate constant. The degree of undersaturation and the solution rate constant generally became maximized at the heater outlet, and the maximum corrosion rate is normally encountered at that point.

The situation in a boiling liquid metal circuit is quite different. First, solute does not flow continuously around the circuit, since, unlike the liquid metal, the vapor-filled regions present a high-resistance path to solute mass transfer. Accordingly, concentration changes occurring in the boiler are not directly transmitted downstream from the boiler. Furthermore, the major temperature drop in the boiling system occurs in the vapor phase where there is little attendant solute deposition. Secondly, heat added to potassium at its boiling point produces no discernible change in liquid temperature and, therefore, does not alter either the equilibrium concentration of the solute or the solution rate in this region. In fact, heating the boiler liquid fractionates it into pure vapor and impure liquid, concentrating the impurities and causing *supersaturation* rather than undersaturation. Thirdly, because change of state reactions

have high latent heats, the mass flow rate required to transport energy at a given rate tends to be considerably less in a boiling system than in a forced-convection circuit. Thus in boiling systems the liquid velocities are correspondingly lower.

To illustrate how corrosion effects relate to the operating characteristics of boiling potassium systems, consider the simplified block diagram of the Rankine thermodynamic cycle shown in Fig. 4. Assume the boiler to operate in the recirculating mode delivering a low quality (10–20%) vapor-liquid mixture to a vapor separator above the boiler. At the vapor separator, the vapor fraction is extracted from the boiler circuit. The liquid fraction is directed into the jet pump, mixed with the condensate return, and sent back to the boiler.

Vapor separators conventionally yield vapor qualities in excess of 99%. Given this separation, the vapor effluent from the boiler circuit carries with it a negligible fraction of liquid and, as will be argued, negligible solute. The condensate return to the boiler, on the other hand, is completely liquid and is exposed to stainless steel piping in a temperature range where dissolution can occur. The probability is high that more solute will enter the boiler than will leave.

Since the boiler circuit is nearly isothermal, it should quickly saturate with soluble stainless steel constituents, and conversion of liquid to vapor in the boiler would result in local supersaturation. The degree of supersaturation is equivalent to that achieved by evaporating 10–20% of the liquid less any

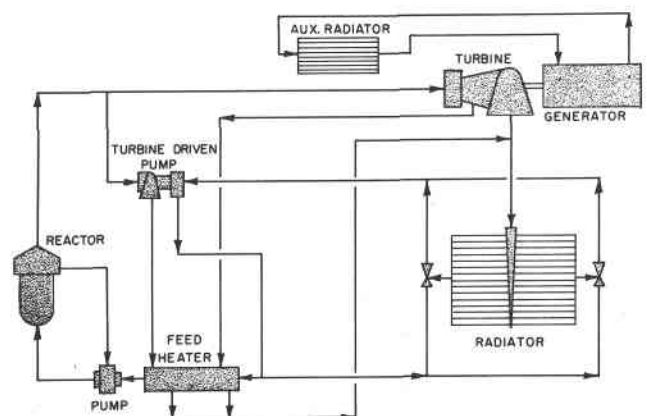


Fig. 4. Schematic Diagram of Rankine-Cycle, Boiling-Potassium Power Plant.

## INTERNATIONAL CONFERENCE ON LIQUID METAL TECHNOLOGY IN ENERGY PRODUCTION

"dust" suspended in the vapor. Thus although it is the region of maximum temperature, the boiler in Fig. 3 is potentially a region of deposition rather than dissolution.

The same forces acting to build up solute in the boiler also build up impurities in this region. For this reason, oxygen contamination introduced anywhere in the system will eventually migrate to the boiler, and contaminant effects will be felt principally in this region.

The assumption that vapor leaving the boiler carries little or no solute follows from the fact that the vapor pressures of known corrosion products are many orders of magnitude less than the equilibrium vapor pressure of potassium at 840°C. Furthermore, any solute present as "dust" in vapor leaving the boiler would be trapped by the vapor separator. By like token, the potassium vapor should be relatively free of corrosion-inducing impurities. Thus in vapor regions, corrosion either by direct solution or chemical attack should be minimal, and corrosion processes should be principally those associated with sublimation.

Because of its low overall solute content, the vapor fraction from the boiler will afford a large driving force for dissolution after condensation. However, in the Rankine cycle this vapor first passes through a turbine before reaching the condenser. The work done by the turbine reduces the vapor temperature from 840°C to ~550°C. At the latter temperature, dissolution occurs slowly, as verified in the operation of sodium-cooled reactor plants. Note that the temperature drop in the Rankine circuit is taken in the vapor phase. Thus, in contrast to the all-liquid circuit, solute deposition is not an inherent feature of the heat removal process in the Rankine cycle.

Once we have converted vapor to condensate, we are confronted with a strong driving force for dissolution. How we handle this condensate is extremely important in determining the degree of maximum corrosion in our cycle, which in turn controls the magnitude of supersaturation in the boiler. The circuit time and relative surface area between the condenser and boiler afford the potassium little opportunity to gain solute, so that the degree of undersaturation of potassium will increase steeply with temperature. Thus the maximum dissolution rate can be expected at

the outlet of the feed heater and in the line leading to the boiler recirculation pump.

In our reference system, which recirculates a relatively high percentage of the boiler effluent, it is possible to "jet" subcooled condensate into the boiler and thereby avoid extensive preheating. It is also possible to take part of the recirculating boiler liquid (equivalent in flow to the condensate return) and jet it into the condensate to cut down the degree of undersaturation in the preheater. Without recirculation, i.e., in a once-through boiler, there is no practical way to avoid significant undersaturation of the boiler feed, and relatively high corrosion rates prevail until significant fractionation to vapor has occurred. Evaporation to dryness releases all of the dissolved solids as a dust suspended in the vapor. Thus, at comparable vapor temperatures, the once-through boiler imposes a much greater corrosion problem than a recirculating boiler and could require a dust trap to avoid turbine blade deposits.

### Corrosion Experience with Boiling Potassium Systems

Various "bench-scale" corrosion devices have been used to study the compatibility of structural metals in boiling potassium. These have included refluxing potassium capsules,<sup>25</sup> boiling-potassium natural-circulation loops,<sup>14</sup> and boiling-potassium forced-circulation loops containing simulated turbine nozzles and blades.<sup>26</sup> However, as discussed above, the corrosion behavior of boiling systems is intimately tied to the degree of liquid recirculation within the boiler, and in this respect these laboratory boiling experiments are usually not representative of power boiler conditions. Nevertheless, the range of corrosion rates shown in Fig. 2 for "bench-scale" stainless steel-boiling potassium systems, have been encouragingly low.

Of more interest are corrosion results obtained from small Rankine-cycle engineering loops operated at Oak Ridge National Laboratory during the 1960s.<sup>5,27,28</sup> These loops incorporated a recirculating boiler heated by a cluster of 7 or 91 bayonet-type heaters (Fire-rods). Other major components included a vapor separator, a turbine-driven pump, a condenser-radiator, and boiler and condenser jet pumps. All components were fabricated of type 316 stainless steel except for the turbine rotor assembly, which was TZM alloy, and the turbine bearings, which were a cobalt-bonded tungsten carbide cermet. Table II lists the test runs

INTERNATIONAL CONFERENCE ON LIQUID METAL TECHNOLOGY IN ENERGY PRODUCTION

Table II. Tests with Seven-Rod Boiler System (SPS-1)

Test Run	Firerod Bundle	Time at Temperature (hr)	Boiler Temperature (°C)	Power (kw/rod)	Components Examined After Run
1	1	145	700-815	~1.9	a, b, c, d
6	5	356	740-790	2.0-3.0	d
7	5	690	790-815	2.2-2.5	a, d
8	6	433	790-840	2.0-5.0	a, b, d
9	7	1521	680-830	1-4.25	a, b
10	8	1170	790-830	1-4.25	a, b, c, e

<sup>a</sup>Firerods.

<sup>b</sup>Boiler jet pump.

<sup>c</sup>Condenser jet pump.

<sup>d</sup>Pump turbine (housing, blades, bearings, pump impeller).

<sup>e</sup>Condenser tube.

completed with one of two seven-rod boiler systems together with the components examined after each run.

The metallographic appearance of the Firerod cladding from the three bundles that exceeded 1000 hr is compared in Fig. 5. Except for carbon migration, none of these Firerods evidenced any measurable corrosive attack. Chemical analyses of the cladding revealed a small carbon increase at the base of the heater and a small carbon loss at the top of the heater. However, these small carbon changes were not manifested by any detectable differences in the distribution of carbide precipitate along the Firerods.

In contrast to these results, the Firerods from test runs 1 and 8 were intergranularly attacked, as shown in Fig. 6. The first of these test runs was terminated after 145 hr by a "burnout" failure of one of the Firerods and the second was terminated after 433 hr by a heater short in the condensate return line. The attack was a direct result of abnormally high oxygen levels that accompanied the failures.

The boiler feed jet pump was visually inspected following test runs 1, 8, 9, and 10. After runs 1 and 8, which incurred oxygen contamination, mass transfer deposits were found at the top of the nozzle that had injected condensate into the pump and at the pump exit throat leading back to the boiler. Despite considerably longer operating periods, the boiler jet pumps examined after runs 9 (1521 hr) and 10 (1170 hr) showed no evidence of deposits.

A type 316 stainless steel condenser tube was also examined after having completed ten test runs totaling about 4500 hr exposure at 540 to 650°C. Cross-section sampling at various points along the

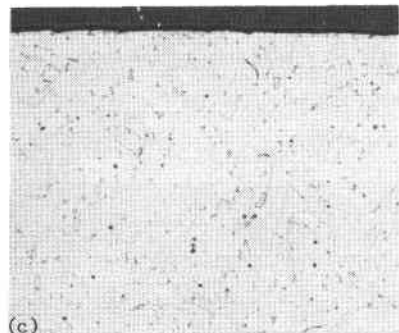
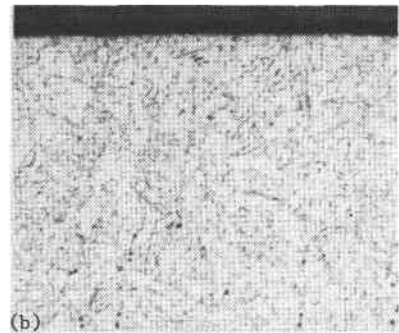
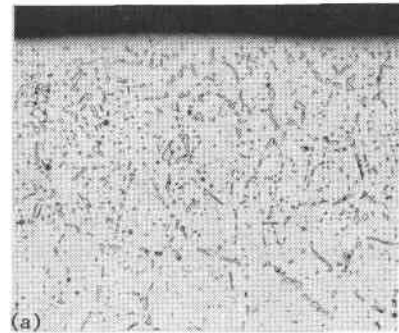


Fig. 5. Photomicrographs of Type 316 Stainless Steel Firerod Cladding After Exposure to Boiling Potassium Seven-Rod Boiler System. (a) 1046 hr at 2-3 kw/rod. (b) 1521 hr at 1-4 kw/rod. (c) 1170 hr at 2-4 kw/rod. 100x.

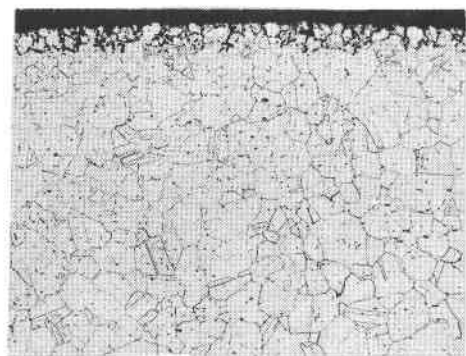


Fig. 6. Photomicrograph of Type 316 Stainless Steel Firerod Cladding, Showing Intergranular Corrosion that Occurred During Test Runs 1 as a Consequence of Oxide Contamination of the Potassium. 100x.

## INTERNATIONAL CONFERENCE ON LIQUID METAL TECHNOLOGY IN ENERGY PRODUCTION

tube showed a slight carbon loss at all points. The maximum corrosion, 0.5-mil grain boundary penetration, occurred near the midpoint of the condenser tube.

### CONCLUSIONS

1. The corrosion resistance of 300-series stainless steels appears adequate for service in potassium recirculating-boiling systems to 840°C, which is the temperature limit set by mechanical property considerations. Nickel- and cobalt-base alloys could, on the basis of high-temperature strength, increase this limiting temperature to 900°C.

2. Forced-circulation loop tests of nickel-base alloys in sodium show higher mass transfer rates above 700°C than comparable austenitic stainless steel loops. However, corrosion rates of the nickel-base alloys appear less affected by oxygen contamination in the liquid metal.

3. Few data are available on the behavior of cobalt-base alloys in sodium or potassium. The maximum corrosion rate of Haynes alloy No. 25 in a boiling-potassium loop at 870°C approximated that of a similar type 316 stainless steel loop. The corrosion rate of Haynes alloy No. 25 in a boiling potassium at 980°C was not substantially higher than at 870°C.

4. The Rankine-cycle, boiling-potassium circuit is characterized by three basically different corrosion zones: (1) the recirculating boiler, (2) the condenser and condensate return lines, and (3) the vapor lines connecting to and including the turbine. In the first of these zones, the potassium tends to remain saturated to supersaturated with solute at all points. Hence this first zone is characterized by deposition rather than corrosion. In contrast, the second corrosion zone, which carries condensate, tends to be highly undersaturated and will be the principal region of dissolutive attack in the system. The third zone, since it is kept virtually free of liquid, will be the least important from a corrosion or deposition standpoint.

5. The degree to which corrosion occurs in a potassium Rankine-cycle power conversion system is strongly affected by the liquid recirculation. At high recirculation ratios, the subcooling introduced by the condensate return is relatively small, and the boiler circuit becomes effectively isothermal. Under such conditions, corrosion is controlled by the amount of solute carried in by the condensate return relative to that carried out by saturated vapor. Operating

experience at an 80% recirculation rate indicates that the degree of supersaturation in the boiler liquid is not sufficient to cause significant solute deposition.

6. Since the major temperature drop in the Rankine cycle is taken in the vapor phase, the drop does not entail significant solute deposition. The extent of dissolutive corrosion in the cycle depends on the temperature attained by the condensate during its return to the boiler. At high boiler recirculation ratios, it is possible to return the condensate at temperatures well below the boiling temperature.

### REFERENCES

1. W. R. Chambers, A. P. Fraas, and M. N. Ozisik, *A Potassium-Steam Binary Vapor Cycle for Nuclear Power Plants*, ORNL-3584, Oak Ridge National Laboratory (May 1964).
2. A. P. Fraas, "A Potassium-Steam Binary Vapor Cycle for a Molten-Salt Reactor Power Unit," *Trans. ASME* 88(1): 355-366 (1966).
3. A. P. Fraas and D. J. Rose, "Fusion Reactors as Means of Meeting Total Energy Requirements," ASME Paper 69/WA-Ener-1, American Society for Mechanical Engineers (November 1969).
4. W. F. Zimmerman, *Two-Stage Potassium Turbine: IV Materials Support of Performance and Endurance Tests*, NASA CR-925, National Aeronautics and Space Administration (February 1968).
5. H. C. Young and A. G. Grindell, *Summary of Design and Test Experience With Cesium and Potassium Components and Systems for Space Power Plants*, ORNL-TM-1833, Oak Ridge National Laboratory (June 1967).
6. W. O. Harms and A. P. Litman, "Compatibility of Materials With Alkali Metals for Space Nuclear Power Systems," *Nucl. Appl.* 5(3): 156-172 (1968).
7. B. A. Nevzorov et al., "Corrosion Resistance of Constructional Materials in Alkali Metals," A/CONF.28/P/343, USSR, paper presented at the Third United Nations International Conference on the Peaceful Uses of Atomic Energy, Geneva, Switzerland, August 31-September 9, 1964.
8. J. H. DeVan, "Corrosion of Iron- and Nickel-Base Alloys in High Temperature Sodium and NaK," *Alkali Metal Coolants*, International Atomic Energy Agency, Vienna, 1967, pp. 643-661.

## INTERNATIONAL CONFERENCE ON LIQUID METAL TECHNOLOGY IN ENERGY PRODUCTION

9. N. Hyman, S. Kostman, and J. McKee, *MCR Liquid Metal Technology Summary Report*, GMAD 3078-32, Vol. II, General Motors Allison Division, May 3, 1965, pp. 4-69-4-73.
10. H. W. Savage et al., *SNAP-8 Corrosion Program Summary Report*, ORNL-3898, Oak Ridge National Laboratory (December 1965).
11. R. W. Lockhart and R. S. Young, G.E.-APED Mass Transfer Program, *Proceedings of Sodium Components Development Program Information Meeting*, Chicago, Illinois, June 16-17, 1965, CONF-650620, USAEC Division of Technical Information Extension, p. 23.
12. R. Fox and N. Tumey, *MCR Liquid Metal Technology Summary Report*, GMAD 3078-32, Vol. I, General Motors Allison Division, May 3, 1965, pp. 4-43.
13. United Nuclear Corporation Development Division, *Proceedings of NASA-AEC Liquid-Metals Corrosion Meeting*, NASA SP-41, Vol. I, National Aeronautics and Space Administration, Washington, D. C., 1964, pp. 213-215.
14. D. H. Jansen and E. E. Hoffman, *Type 316 Stainless Steel, Inconel, and Haynes Alloy No. 25 Natural-Circulation Boiling-Potassium Corrosion Test Loop*, ORNL-3790, Oak Ridge National Laboratory (June 1965).
15. J. H. DeVan et al., "Lithium and Potassium Corrosion Studies with Refractory Metals," *Alkali Metal Coolants*, International Atomic Energy Agency, Vienna, 1967, pp. 675-695.
16. W. D. Manly, "Fundamentals of Liquid-Metal Corrosion," *Corrosion* 12(7): 336-342 (1956).
17. S. W. Strauss, J. L. White, and B. F. Brown, "The Atomic Size Effect and Alloying Behavior in Liquid Metals," *Acta Metall.* 6(9): 604-606 (1958).
18. H. W. Leavenworth and R. E. Cleary, "The Solubility of Ni, Cr, Fe, Ti, and Mo in Lithium," *Acta Metall.* 9(5): 519-520 (1961).
19. J. H. Hildebrand and R. L. Scott, *The Solubility of Nonelectrolytes*, Reinhold Publishing Corp., New York, 1955, pp. 27, 270.
20. J. H. Swisher, *The Solubility of Iron, Nickel, and Cobalt in Liquid Potassium and the Effect of Oxygen Gettering Agents on Iron Solubility*, NASA-TN-2734, Lewis Research Center (March 1965).
21. C. B. Jackson, *Liquid Metals Handbook Sodium (NaK) Supplement*, U.S. Government Printing Office, Washington, D. C., 1955, p. 15.
22. S. J. Rodgers, L. W. Mausteller, and E. F. Batutis, *Iron and Nickel Concentrations in Sodium*, NAS Tech. Rep. 27, Mine Safety Appliances Company, Callery, Pa., June 30, 1954.
23. R. L. McKisson and R. L. Eichelberger, *Solubility Studies of Ultra Pure Transition Elements in Ultra Pure Alkali Metals, Seventh Quarterly Report*, NASA-CR-54097, AI-65-93, Atomics International, June 1965.
24. W. S. Ginell and R. J. Teitel, "Solubility of Transition Metals in Molten Potassium," *AEC-NASA Liquid Metals Information Meeting*, Gatlinburg, Tennessee, April 21-22, 1965, CONF-650411, USAEC Division of Technical Information Extension.
25. J. R. DiStefano and J. H. DeVan, "Refluxing Capsule Experiments with Refractory Metals and Boiling Alkali Metals," *Nucl. Appl. Technol.* 8(1): 29-44 (1970).
26. L. C. Fuller and R. E. MacPherson, *Design and Operation of Stainless Steel Forced-Circulation Boiling-Potassium Corrosion-Testing Loops*, ORNL-TM-2595, Oak Ridge National Laboratory (December 1969).
27. M. M. Yarosh and P. A. Gnad, *The Intermediate Potassium System - A Rankine-Cycle Test Facility*, ORNL-4025, Oak Ridge National Laboratory (October 1968).
28. J. H. DeVan, *Compatibility of Structural Materials with Boiling Potassium*, ORNL-TM-1361, Oak Ridge National Laboratory (April 1966) pp. 46-58.

# INTERNATIONAL CONFERENCE ON LIQUID METAL TECHNOLOGY IN ENERGY PRODUCTION

## APPLICATION OF BOILING LIQUID METALS IN INDUSTRIAL PROCESSES

H.M.Kottowski, C. Savatteri, M. Mol, P. Fiebelmann  
Euratom, Joint Research Center  
Ispra Establishment  
Heat Transfer and Fluid Flow Division

### INTRODUCTION

The question whether the investigations on the boiling behaviour of liquid metals may contribute to the solution of the current technical problems may be profitably discussed with the aid of some practical examples for application:

The actual built and planned liquid metal cooled reactors provide for safety reasons between the reactor cooling circuit and the steam generation system a second liquid metal intermediate circuit.

The successful development of coated particle fuel and of special graphites for the structural components of VHTR-cores has opened up the possibility of an economical nuclear heat source to provide temperatures in excess of 1000°C as "process heat application". In order to exploit this temperature potential the heat has to be transferred to the appropriate chemical processes and there is little doubt that the only practical way of achieving this on a large scale is by the use of intermediate heat exchanger systems.

The aim of this paper is to exhibit a technological possibility, both to substitute the secondary circuit of the sodium cooled reactors and to transfer the heat from the VHTR to the chemical process plant which satisfies the safety requirements and demonstrates technological advantages.

There is experimental evidence that boiling liquid metals can be applied as heat carrier and that steady state boiling at forced convection, even in a once-through channel, can be established at hydrodynamic stable conditions. We find already boiling liquid metals as heat carrier in heat pipes and special space application. Its application in industrial plants, however, has not yet been taken into account, except the mercury steam electricity plant of the G.E. about 40 years ago. In case of using a nuclear reactor as heat source for which, because of safety or technological reasons a three circuit system is required, a unit of a liquid metal boiling and condensing system could couple the reactor with the steam generation system or with the chemical process.

### MODE OF OPERATION

The reactor cooling system is essentially specified by the reactor type, and the process circuit by the nature of the process, e.g. electrical power; heat for chemical processes. The main requirements on the intermediate circuit, especially in case of the application of a nuclear reactor in a chemical process plant and high operation temperature can be identified being the following:

- high heat transport capacity
- high operation temperature
- low operation pressure
- small inventory of the heat transfer agent
- reliable operation:

These requirements are well met by a closed liquid metal boiling and condensation system, which consists of three main components, (Fig. 1):

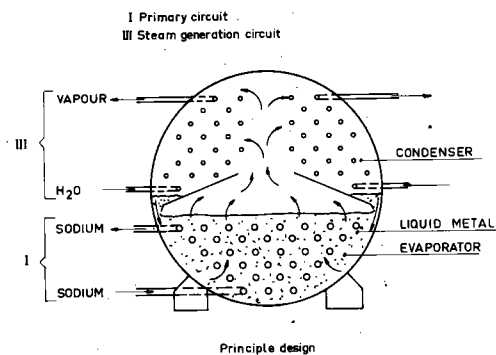


Fig. 1 HORIZONTAL E-C HEAT EXCHANGER (compact design)

- The evaporator, which is the heat exchanger of the primary reactor circuit (eg. LMFBR)
- The liquid metal as heat carrier
- The condenser, which is identical e.g. with the "chemical reactor" for H<sub>2</sub>-production, gasification of carbon or the steam generation system for electricity generation.

The heat will be transported as latent heat by the vapour. The driving force of the process is the thermohydraulic unequilibrium between the heat source and the heat sink. The maximum heat transported, depends on the pressure-temperature condition of the system.



POTENTIAL OF ALKALI METALS VAPOUR TO TRANSFER HEAT AND ITS RANGE OF APPLICATION

The liquid metals offer a wide range of operation temperature and pressure at which a boiling-condensation system could work in an optimal way. The heat transfer capacity depends on the thermodynamic conditions which determine the vapour flow from the evaporator to the condenser. The vapour flow rate is limited by the sonic velocity in the free cross section the vapour is conducted. Assuming the sonic velocity being the restricting factor the heat transfer capacity for various alkali metals is shown in Fig. 2.

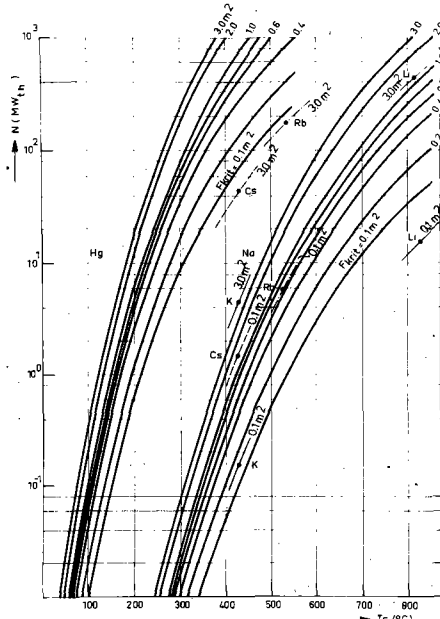


Fig 2 HEAT TRANSFER CAPACITY OF ALKALI-METAL VAPOUR

The selection of the appropriate working agent depends on the heat power to be transferred, the operation temperature, and the vapour pressure which influences significantly the design. Fig. 2 shows e.g. the maximum heat transfer capacity of Hg and Na employed in a heat transfer unit. The heat transfer capacity is plotted vs. the operation temperature and the free vapour flow cross section. The range of heat transfer capacity of Rb, Cs, K and Li is indicated (from left to right) for a vapour flow cross section of 3  $m^2$  and 0,1  $m^2$  respectively. A survey of the heat transfer capacity of various liquid metals appropriate as working agents, is given in Fig. 3. The operation conditions chosen (operation temperature and as a consequence of it the vapour pressure in the heat exchanger) are arbitrary. Taking for example Hg as heat transfer agent and a heat transfer unit design with a duct of free cross section for the vapour flow between the evaporator and condenser of 0,1  $m^2$  the heat transfer capacity limit due to the sonic velocity would be

of about 48 MW. For sodium as working agent, respectively, the operation temperature would be 780 $^{\circ}C$ .

Working agent	Operation temperat. ( $^{\circ}C$ )	Vapour pressure in the exch. (bar)	max. heat transfer capacity (MW)	
			0.1 $m^2$	3.0 $m^2$
Hg	400	2.14	~48	-
Cs	400	0.026	~0.9	~30
Rb	400	0.022	~0.4	~40
K	600	0.197	~4	~100
Na	600	0.036	~3	~100
Li	800	0.004	~12	~400

Fig 3 HEAT TRANSFER CAPACITY OF ALKALIMETALS IN LARGE UNITS AND ITS OPERATION CONDITIONS

As far as the design of the heat transfer unit is concerned the restricting factor will not be the internal heat transfer cycle (evaporation and condensation and heat transfer by latent heat) but the size of the heat exchanger on the primary (evaporator) and secondary side (condenser). A survey of the operation conditions of various liquid metals could be employed is shown in Fig. 4. The lower operation temperature limit is only realistic for laboratory scale application. On the other hand the list demonstrates that at operation temperatures exceeding even 1000 $^{\circ}C$  the heat transfer unit can be designed for atmospheric or only slight overpressure.

LIQUID METALS	TEMPERATURE RANGE ( $^{\circ}C$ )	OPERATION PRESSURE RANGE (bar)
Hg	150 - 600	$3.74 \cdot 10^{-3}$ - 22.8
Cs	300 - 850	$2.92 \cdot 10^{-3}$ - 4.54
Rb	300 - 850	$1.49 \cdot 10^{-3}$ - 4.26
K	450 - 1000	$16.7 \cdot 10^{-3}$ - 7.06
Na	450 - 1000	$1.88 \cdot 10^{-3}$ - 2.80
Li	550 - 1400	$0.716 \cdot 10^{-3}$ - 1.53

Fig. 4 PROPOSED OPERATION RANGE OF LIQUID METALS IN E-C-HEATEXCHANGERS OF 10  $KW_{th}$  - 1000  $MW_{th}$

DESIGN LIMITS OF A EVAPORATION - CONDENSATION SYSTEM

The operation point is determined by the system pressure where the evaporation and condensation occurs. That means that the vapour temperature in the heat transfer unit is determined by the lowest temperature of the primary cooling circuit of the reactor (Fig.5). For example, for a liquid metal cooled power station the temperature of the coolant behind the primary heat exchanger

is in the range of 350 to 450°C. As a consequence, the operation temperature of an evaporation-condensation unit has to be near 400°C. In case of a steam generation system for electricity generation the required steam temperature is not reached, even if the inlet temperature into the primary heat exchanger is of about 500 to 600°C. In order to obtain the required steam temperature a cascade arrangement of heat exchangers coupled to the primary circuit operating at different system pressures is necessary.

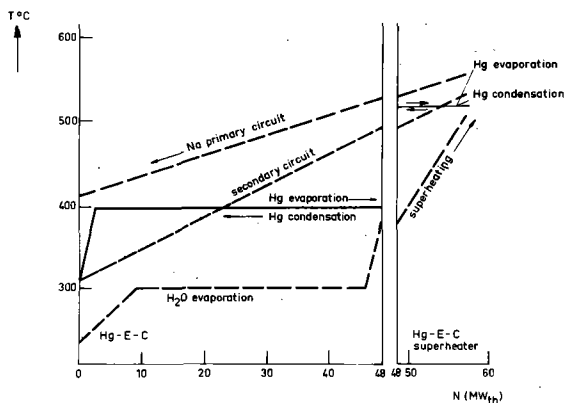


Fig 5 50 MW TEST REACTOR INTERMEDIATE CIRCUIT SUBSTITUTE BY E-C-UNIT

Fig. 5 shows an example of a reactor circuit of 50 KW power coupled to a steam generator. The sodium enters the primary heat exchanger at 580°C and leaves it at 410°C. Water is supplied to the secondary heat exchanger at 230°C where vapour of 500°C is produced. Fig. 5 shows (a) the classical solution of a three cycle system, Na-primary circuit, Na secondary circuit, steam generation circuit (dotted lines), and (b) the substitution of the secondary circuit by a E-C (Evaporation-Condensation) unit working with mercury. Supposing the same operation conditions as for the system with the secondary sodium circuit, the system requires a cascade arrangement of two E-C-Units working at different temperatures levels.

An example of a heat transfer unit of 80 MW is given in Table 1. The working agent chosen is again mercury. Due to the design requirements the total heat capacity of 80 MW for the generation of 118.7 t/h steam of 510°C and 80 bars has to be supplied to a cascade system consisting of a steam generator of 67,9 MW and a steam superheater of 12,1 MW (Fig. 6).

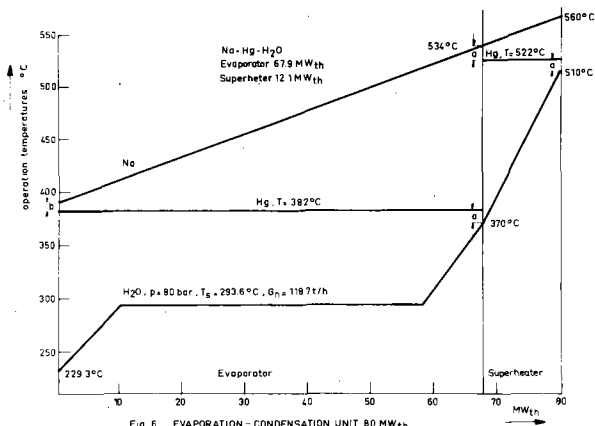


Fig 6 EVAPORATION-CONDENSATION UNIT 80 MWth

The example in question represents only an estimation of a design lay out. The heat transfer surfaces for the condenser and evaporator have been assumed equal at equivalent pressure temperature conditions. For the calculation of the heat transfer of evaporating and condensing mercury extremely pessimistic heat transfer data have been admitted. A reduction of the heat transfer surface and as a consequence a more compact design seems possible.

It has to be pointed out that mercury has been chosen because of the low temperature range in question. Employing sodium for example as working agent in the steam superheater, the cross section for the sodium vapour flow has to be at least 2 m<sup>2</sup> to avoid sonic vapour velocity, which otherwise, would not be a design limiting factor.

TABLE 1

DESIGN REQUIREMENT:

Heat transfer capacity:	N = 80 MW
Na-inlet temp.steam superheater:	T <sub>E</sub> = 560°C
Na-outlet temp. steam superheater:	T <sub>A</sub> = 390°C
Vapour temp.outlet steam superheater:	T <sub>D</sub> = 510°C
Steam pressure:	P <sub>D</sub> = 80 bar
Steam generation:	G = 118,7 t/h
Water inlet temperature:	T <sub>W</sub> = 229,3°C

CASCADE UNITS:

<u>Steam generator:</u>	N = 67.9 MW
tubes (AFNOR-Z3CN 18-10):	∅ 30 x 2 mm
Number of tubes of 6m length:	n. = 670
Cross section of Hg-vapour flow:	F > 0,19 m <sup>2</sup>
Evaporation temper.of Hg:	T <sub>Hg</sub> = 382°C
Hg-system pressure:	P <sub>Hg</sub> = 1,56 bar

## INTERNATIONAL CONFERENCE ON LIQUID METAL TECHNOLOGY IN ENERGY PRODUCTION

Na-inlet temp. steam generator:	$T_{Na\ in} = 534^{\circ}C$
Na-outlet temp. steam gener.:	$T_{Na\ out} = 390^{\circ}C$
Water inlet temperature:	$T_w = 229,3^{\circ}C$
Steam outlet temperature:	$T_{D\ out} = 370^{\circ}C$
<u>Steam superheater:</u>	$N = 12,1\ MW$
Tubes (AFNOR-Z3CN 18-10):	$\varnothing = 30 \times 2\ mm$
Number of tubes of 3.92 m length:	$n = 350$
Cross section of Hg-vapour flow:	$F = 0,05\ m^2$
Evaporation pressure of Hg:	$T_{Hg} = 522^{\circ}C$
Hg-system pressure:	$P_{Hg} = 10,8\ bar$
Na-inlet temp. steam superheater:	$T_{Na\ in} = 560^{\circ}C$
Na-outlet temp. steam superheater:	$T_{Na\ out} = 534^{\circ}C$
Steam temp. inlet:	$T_{D\ in} = 370^{\circ}C$
Steam temp. outlet:	$T_{D\ out} = 510^{\circ}C$

The temperature-power diagram determined by these design data is shown in Fig. 6.

### SUMMARY

A heat transfer system basing on the transfer of latent heat of vaporization of alkali metals becomes of interest when heat has to be made available at high temperature. For example, the heat transfer capacity of sodium in a heat transfer unit with a sodium vapour flow cross section of  $0,1\ m^2$  is increasing of an order of magnitude when changing the operation temperature from  $650^{\circ}C$  to  $880^{\circ}C$ , whereas the system pressure does not exceed 1 bar.

The use of boiling and condensing alkali metal heat transfer systems in industrial scale application seems feasible. Four main advantages can be quoted:

- Heat available on the heat sink at constant temperature
- No pumps. The vapour is flowing due to thermodynamic forces
- Low pressure
- Small heat transfer agent inventory

As disadvantage can be quoted: operation reliability problems due to corrosion, incompatibility of the alkali metals with chemical products when applied in process heat plants.

Safety measures e.g. for fast reactor power plants will not require more expenditure as already done for the LMFBR. A different nature of safety problem will rise in case of using mercury. The retention of mercury inside the confinement will become the more important safety objective.

The theoretical and experimental knowledge on the thermodynamic and hydraulic of combined boiling and condensing metal heat transfer systems are not yet adequate. Basic investigations are needed especially on:

- Boiling heat transfer and boiling pattern on the outside of a bundle structure
- Condensation heat transfer and condensation pattern on the outside of a bundle structure
- Vapour velocity and vapour flow in restricted geometries
- Hydrodynamic stability of a combined evaporation-condensation system
- Thermo-hydraulic behaviour of the system on power variation
- Influence of partial inert gas pressure on the thermodynamic behaviour and efficiency of the system.

These are questions to be solved positively before metal evaporation-condensation heat transfer systems can be employed in industrial plants. We did not weight the importance of the factors quoted here. It is possible that one or several of them will become of minor importance.

# INTERNATIONAL CONFERENCE ON LIQUID METAL TECHNOLOGY IN ENERGY PRODUCTION

## THE ROLE OF ALKALI METALS IN ENERGY CONSERVATION

G.E.Rajakovics

Vereinigte Edelmetallwerke  
Aktiengesellschaft (VEW)  
Kapfenberg/Seibersdorf  
Austria

N. Schwarz

Österreichische Studiengesellschaft  
für Atomenergie Ges.m.b.H. (SGAE)  
Seibersdorf  
Austria

### ABSTRACT

The improvement of thermal power station efficiency becomes imperative with regard to energy conservation. Thermal power station efficiency can only be improved essentially by improving thermal efficiency of the energy conversion process since the efficiencies of all other steps of power generation are already very high. Thermal efficiency depends on the Carnot efficiency given by the temperature range of the energy conversion process as well as on the degree of deviation of the chosen reversible energy conversion process from this Carnot cycle. Therefore, thermal efficiency can be improved by raising the top temperature as well as by adjusting the actual reversible process to the Carnot cycle. This cannot be realized solely with the conventional steam process, and the only approach to better efficiency lies in combining conventional steam with topping cycles. From the thermodynamic point of view, Rankine cycles are superior to Brayton cycles for topping purposes. The realization of such topping Rankine cycles in the high-temperature field is only possible with alkali metals as working fluids. In the past central power stations with alkali metal topping cycles were unfeasible since no adequate technology had yet been developed. Now, progress in alkali metal technology makes it practicable. Alkali metal topping cycles with well known materials will allow top temperatures of about  $800^{\circ}\text{C}$  to  $900^{\circ}\text{C}$  and yield about 50% overall power station efficiency. The "Treble Rankine Cycle Process (T.R.C.P.)", which further uses a diphenyl process between potassium and water process, will even achieve 56%! T.R.C.P. has the best efficiency of all processes practicable in this temperature field. Further special de-

velopment work will be required for such large - scale power stations, nevertheless, this work will have to be done with respect to the absolutely necessary energy conservation.

### INTRODUCTION

The improvement of thermal efficiency of technical plants has always been a special task of engineers. The larger expenditure mostly required for obtaining higher efficiency has always to be in an economic relationship to the possible profit in order to realize the intended improvement. The marginal conditions essential in judging the profitability of efficiency improvement have changed lately: The rapidly increasing cost of fuel and environmental protection in future large - scale power plants, especially relating to heat rejection, have been causing a substantial change of the critical point for profitability of intended efficiency improvement.

Cost for heat rejection are extremely influenced by the efficiency of the power plant. The ratio of net power to rejected heat in a power plant highly increases with rising efficiency, especially at efficiency values beyond 50 % (Fig. 1). This means that raising of power plant efficiency from 38 % to e.g. 55 % reduces the specific cost of heat rejection to half.

### WAYS AND MEANS TO IMPROVE EFFICIENCY

Only an improvement of thermal efficiency can raise the efficiency of a power plant since all other types of efficiency responsible for the overall efficiency of a power plant are already very high. The thermal efficiency is influenced by the Carnot effi-

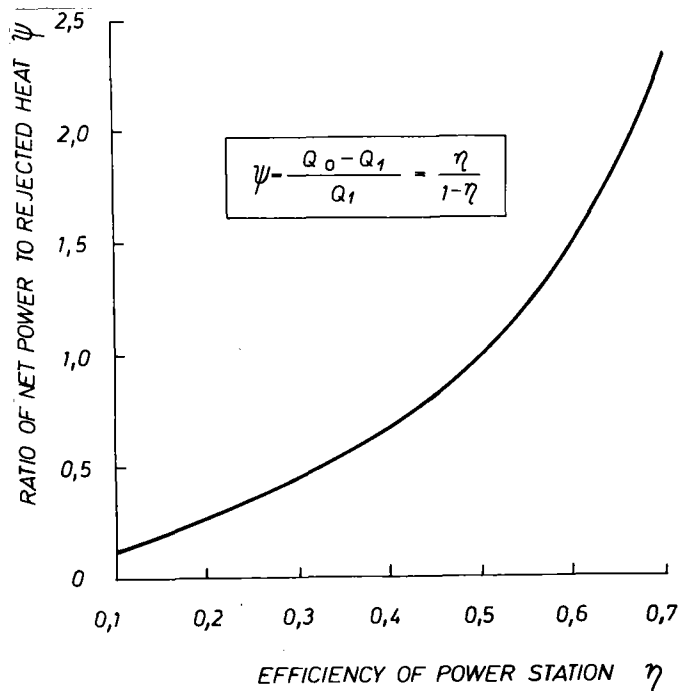


Fig. 1. Ratio of net power to rejected heat of a power station as function of the efficiency

ciency, determined by the top and bottom process temperatures, as well as by the deviation of the actual reversible process from the Carnot process. Therefore, there exist two principle possibilities for increasing the thermal efficiency:

Raising the top temperature and, thereby, the Carnot efficiency,

and adapting the actual process to the Carnot conditions.

In theory, lowering the bottom temperature would be possible as well, however due to the fact that the bottom temperature is limited by the ambient temperature, this is no practicable way. In the usual steam process neither can the top temperature be raised sufficiently nor can this process be adapted satisfactorily to the Carnot conditions. The top temperature of steam processes is limited due to great technological problems and, therefore, to highly rising cost in the range beyond  $550^{\circ}\text{C}$ . Furthermore, the steam process will deviate more and more from Carnot conditions with rising top temperatures. Therefore, the efficiency of thermal power plants, using solely the steam process, is limited

to about 38%.

For achieving higher efficiency, the steam process must be replaced by or combined with other energy conversion processes.

With respect to efficiency improvement a great number of processes had been suggested, such as the Ericson process, the Feher process, or the Stirling process. Some of them, theoretically, have the same efficiency as the Carnot process, but none of them has become important. This is due to the fact that such processes can be realized with a substantial loss of efficiency only or with uneconomic expenditure compared to the relatively small possible efficiency gain. In order to replace the steam process, only gas turbines and, to a certain extent, diesel engines have reached importance for thermal power plants, however, the efficiency of power plants with gas turbines in general is lower than that of usual steam power plants. The only way to improve significantly the efficiency of large-scale power plants seems to be a combination of the steam process with topping processes.

The topping process may be a gas turbine process as well as a steam process using another working fluid. Gas turbine processes have been used in a large number of power stations for efficiency improvement. On the other hand, the Rankine cycle was applied for topping purpose only in the seven US power plants using mercury as working fluid. Today, none of them is still in operation. Consequently, one is led to conclude that for topping purposes the Brayton process has more advantages than the Rankine cycle, however, this is a completely wrong conclusion. As will have to be demonstrated below, the opposite is true with regard to topping purposes: The Rankine cycle is superior to the Brayton process.

#### "QUALITY NUMBER" OF PROCESSES

In Fig. 2 the Brayton process as well as the Rankine cycle are working within a temperature range relevant for topping processes.

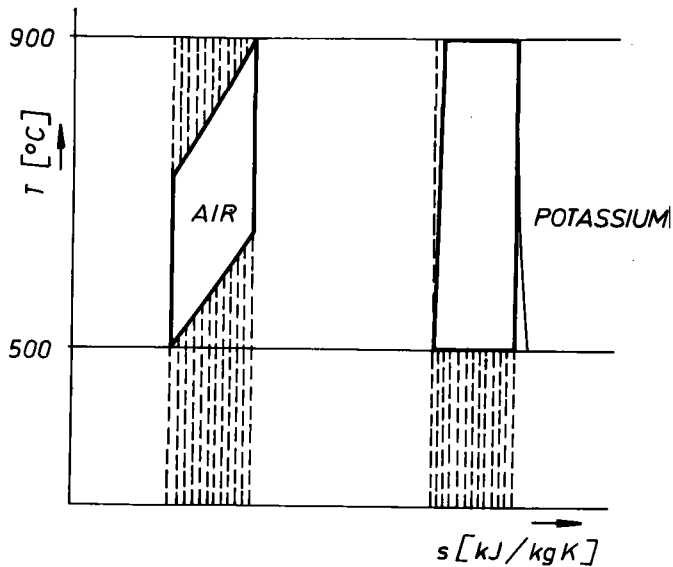


Fig. 2. Comparison of Brayton- and Rankine cycle as topping processes

Both processes are working between the same top and bottom temperatures so that the Carnot efficiency of the two processes is the same. Nevertheless, the two processes yield greatly differing thermal efficiencies due to the fact that the Brayton process deviates much more from Carnot conditions than the Rankine cycle. The ratio of thermal efficiency to Carnot efficiency will be further referred to as "Quality Number" of the process. In the example shown in Fig. 2, the quality number of the Rankine cycle reaches 94% compared to that of the gas turbine cycle being 68%. In this case, therefore, the Rankine cycle produces nearly 40% more power than the Brayton cycle.

In comparing possible topping processes, naturally the bottom process will have to be considered too, since it is the effect of the total process that is of final interest. For studying these problems, the quality number is a useful characteristic, too.

The quality number of a total process depends on the quality numbers of the individual processes as well as on their Carnot efficiencies. Under certain circumstances, the quality number of the total process may be higher than that of all individual processes or at least of one of them.

The topping process should have a high quality number not only influencing positively the quality number of the total process but also reducing, at equal marginal conditions, the dimensions of the components of the bottoming process.

The quality number of the topping process is of significant influence on the profitability of a power plant. This is due to the fact that in the high-temperature field the technological problems and, therefore, the investment cost grow considerably with increasing top temperatures of the topping process. It may be assumed that the investment cost are primarily determined by the top temperature of the topping process even though the cost are also influenced by the pressure present at such a temperature, as well as by marginal conditions specific of the chosen process. Due to the fact that at a given top temperature power generation depends directly on the quality number of the process, the topping process with the higher quality number should, consequently, be more economical than a topping process with a lower quality number.

#### COMPARISON OF QUALITY NUMBERS

The example shown in Fig. 2 has already demonstrated the better quality number of Rankine cycles compared to that of Brayton cycles. In fact, in general the quality number of Rankine cycles is better than that of Brayton cycles. Thus, generally speaking, the Rankine cycle applied as topping cycle in the high-temperature range should be more economical than the Brayton cycle used for this purpose.

FOR THESE REASONS, FOR TOPPING PROCESSES RANKINE CYCLES ARE ACTUALLY SUPERIOR TO BRAYTON CYCLES.

#### TOPPING RANKINE PROCESSES

The natural question arises why up to now the Rankine cycle has only been of limited importance for topping purposes. The reason

is that the Emmet process, using mercury as working fluid, can operate with top temperatures up to about 500°C only. Therefore, modern power plants using high-temperature superheated live steam will have the same high efficiency as power plants applying the Emmet process, but with less technological expenditure. The operation of topping Rankine processes in the high-temperature range, which is necessary for reaching higher efficiency, depends directly on the use of a suitable working fluid. Alkali metals, in particular cesium or potassium, are exclusively useable for this purpose. Therefore, alkali metals are of significant importance for future energy conservation by high-efficiency power plants using topping Rankine processes.

In the past, the use of an alkali-metal Rankine process for electricity generation in a power plant was unthinkable since the whole technology required for its realization was missing. On the other hand, the development of air craft jet propulsion generated the technology of gas turbines so that for the use of the Brayton cycle as topping process in power plants only relatively little development work has been necessary. In the last few years, the technological scene has totally changed.

Alkali metal technology has been developed using huge financial funds with regard to fast breeder reactors as well as to space projects. Therefore, the development of a power plant using an alkali metal topping process seems to be an appropriate task resulting in thermodynamic advantages of the Rankine cycle becoming effective for topping purposes in future.

#### THE DOUBLE RANKINE CYCLE PROCESS

The problems of combining a supercritical steam cycle with a potassium Rankine cycle as a topping process have been investigated intensively in the USA during the last few years (1)(2)(3)(4). The so-developed process further applies a flue-gas Brayton cycle using the heat of the flue gas exhausted by the pot-

assium evaporator. Heat rejected from this Brayton cycle is further used for preheating the feed water of the steam process.

Though this combined process is a process of very high quality, it has some disadvantages. The external preheating of the feed water by flue gas causes a lower quality number of the supercritical steam process than usual and, therewith, a reduction of the plant efficiency. Furthermore, the heat transfer from the isothermally condensing potassium to the supercritical steam includes a relatively high exergy loss. This has a negative influence upon the possible plant efficiency, too. Finally, the direct coupling of the supercritical steam system, operating at a pressure of some hundred bar, to the potassium vapor system at a temperature of about 500 - 600°C involves a considerable risk. In case of a defect in the heat exchanger at least the low pressure part of the potassium vapor turbine might be destroyed mechanically by the sudden pressure increase followed by the subsequent chemical reaction of potassium and water.

#### THE TREBLE RANKINE CYCLE PROCESS (T.R.C.P.)

The above-mentioned problems may be solved by the use of a third, intermediate, Rankine cycle. For this cycle diphenyl, a relatively stable organic medium, appears to be the optimum working fluid. The so-formed T.R.C.P. was presented on the 9<sup>th</sup>. I.E.C.E.C. in San Francisco in 1974<sup>(5)(6)</sup>. Fig. 3 shows the main flow scheme of such a fossil fuelled power plant with T.R.C.P., the main data thereof being presented in Table I. All individual processes of this T. R. C. P. are operating almost totally under wet-steam conditions so that heat absorption and heat rejection of each individual process take place nearly isothermally. Thus, the individual processes come very close to Carnot conditions. The quality number of the potassium process reaches 96 %, that of the diphenyl process 86 %, and that of the steam process 91 %. In order to obtain a proper

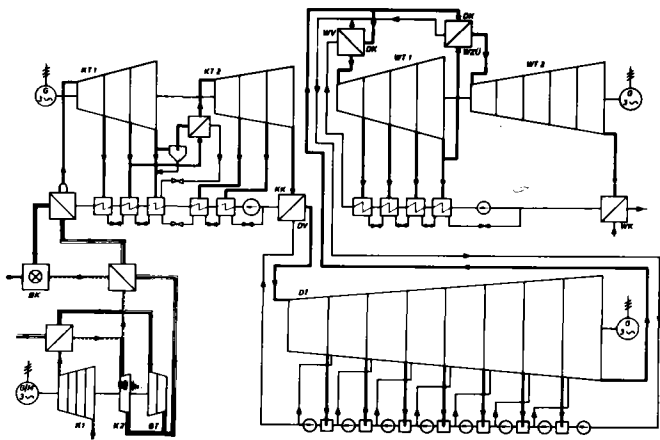


Fig. 3. Scheme of fossil-fueled power plant with T.R.C.P.

- BK ..... uncooled combustion chamber
- G ..... alternator
- GT ..... flue gas turbine
- DK/WV ... diphenyl condenser/steam generator
- DK/WZU .. diphenyl condenser/steam reheater
- DT ..... diphenyl vapor turbine
- K1, K2 .. compressors
- KK/DV ... potassium condenser/diphenyl evaporator
- KT ..... potassium vapor turbine
- WK ..... steam condenser
- WT ..... steam turbine

efficiency of the total process, not only the quality numbers of individual processes are of interest but also the problem of coupling these processes will have to be taken into consideration. Due to the fact that heat absorption and heat rejection of the individual processes are taking place by evaporation and condensation and nearly isothermally under excellent heat transfer conditions, only small temperature differences

are required for economic heat transfer between the individual processes. Therefore, the quality number of the total T. R. C. P. reaches 97 % even exceeding the values of the individual processes. The thermal efficiency of the T. R. C. P. differs from that of the ideal Carnot process by 3 % only! Therein lies the virtue of the T.R.C.P. Energy conversion processes of modern steam power plants usually have maximum quality numbers of about 80 % and all attempts to improve their efficiency (e.g. raising Carnot efficiency by an increase of steam temperatures, employment of a gas-turbine topping process) lead to a reduction of the quality number. Contrary thereto, the effect of T. R. C. P. lies not only in an increase of the Carnot efficiency but simultaneously in a substantial increase of the quality number of the total process close to the value 1.

DUE TO ITS HIGH QUALITY NUMBER, THE T. R. C. P. IS REGARDED AS THE BEST OF ALL REALIZABLE ENERGY CONVERSION PROCESSES WITH A HIGH EFFICIENCY.

Even though it appears to be a certainty that all problems concerning the realization of high - efficiency power plants with the T. R. C. P. can be solved with reasonable expenditure, extensive R & D - work will be required. The central problems will arise in the field of alkali metall technology regarding high-temperature application and the development of large-scale components, e.g. a potassium vapor turbine. Thus, further development of alkali metal technology will be of extreme importance for the construction of high-efficiency power plants, and therewith, for an economic and environment - protecting energy supply in future.

REFERENCES

- (1) Fraas, A.P.: Conceptual design of a fusion power plant to meet the total energy requirements of an urban complex. B.N.E.S. Nuclear Fusion Reactor Conference at Culham Laboratory, Sept. 1969.

System	Working data of process		Efficiency	Net power of turbine
	upper	lower		
Potassium	890°C/3 bar	477°C/0,027 bar	29,1%	291 MW
Diphenyl	455°C/20,9 bar	287°C/2,0 bar	16,9%	119,5 MW
Water	270°C/55 bar (RH 270°C/8,9 bar)	33°C/0,051 bar	33,6%	198,1 MW
T. R. C. P.			60,9%	608,6 MW
Flue gas	1800°C/3,1 bar (642°C/2,75 bar)	140°C/1 bar (500°C/1,1 bar)	92,5%	6,7 MW
Central power station			56,5%	615,3 MW

Table I. Main data of fossil-fueled 600 MWe central power station with T.R.C.P.



## INTERNATIONAL CONFERENCE ON LIQUID METAL TECHNOLOGY IN ENERGY PRODUCTION

- (2) Fraas, A.P.: A potassium - steam binary vapor cycle for better fuel economy and reduced thermal pollution. ASME-Winter Annual Meeting, Washington, 71-WA/Ener-9. December 1971.
- (3) Wilson, A.J.: Space power spinoff can add + 10 points of efficiency to fossil-fuelled power plants. 7<sup>th</sup> IECEC, No. 729050 (1972).
- (4) Fraas, A.P.: A fluidized bed coal combustion system coupled to a potassium vapor cycle. Annual Meeting of the AIChE, New York, 1972.
- (5) Rajakovics, G.E.: Extrem hohe Kraftwerkswirkungsgrade durch Dreifach-Dampfprozeß. ÖZE 27, H.4, S.102-106. (1974).
- (6) Rajakovics, G.E.: Energy conversion process with about 60% efficiency for central power stations. 9<sup>th</sup> IECEC, No. 749152 (1974).

# INTERNATIONAL CONFERENCE ON LIQUID METAL TECHNOLOGY IN ENERGY PRODUCTION

## SOLUTION BEHAVIOR OF HYDROGEN ISOTOPES AND OTHER NON-METALLIC ELEMENTS IN LIQUID LITHIUM\*

V. A. Maroni, W. F. Calaway,  
E. Veleckis, and R. M. Yonco

Argonne National Laboratory  
Argonne, Illinois 60439

### ABSTRACT

Results of experimental studies to measure selected thermodynamic properties for systems of lithium with non-metallic elements are reported. Investigations of the Li-H, Li-D, and Li-T systems have led to the elucidation of the dilute solution behavior and the H/D/T isotope effects. In the case of the Li-H and Li-D systems, the principal features of the respective phase diagrams have been delineated. The solubility of Li-D in liquid lithium has been measured down to 200°C. The solubility of Li<sub>3</sub>N in liquid lithium and the thermal decomposition of Li<sub>3</sub>N have also been studied. From these data, the free energy of formation of Li<sub>3</sub>N and the Sieverts' constant for dissolution of nitrogen in lithium have been determined. Based on studies of the distribution of non-metallic elements between liquid lithium and selected molten salts, it appears that molten salt extraction offers promise as a means of removing these impurity elements (e.g., H, D, T, O, N, C) from liquid lithium.

### INTRODUCTION

Liquid lithium is considered to be a leading candidate for the role of blanket material and primary coolant in D-T-fueled fusion power reactors. The selection of lithium stems mainly from the utility of the <sup>6</sup>Li(n,α)T and <sup>7</sup>Li(n,n'α)T nuclear reactions in breeding tritium and from the fact that liquid lithium is an excellent heat transfer medium. It is likely that, in addition to the bred tritium, a large liquid lithium system, operated as a fusion-reactor blanket, will contain significant quantities of protium, deuterium, oxygen, nitrogen, carbon, and other impurities. The successful development of efficient recovery methods and sensitive monitoring equipment for the hydrogen isotopes and other non-metallic elements in the blanket region requires exact knowledge of their solution behavior in liquid lithium. To this end, a program was initiated at ANL in the late 1960's to measure phase relationships and thermodynamic properties of solutions of non-metallic elements in liquid

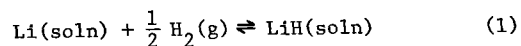
lithium. The intention of this paper is to present an up-to-date summary of the results obtained during the course of the ANL program in the context of their importance to liquid lithium technology for fusion reactors. The systems for which experimental results have been obtained are: Li-H, Li-D, Li-T, Li-N, and Li-LiX-LiX (where LiX is a lithium-containing alkali halide eutectic salt). Because all the details of experimental apparatus and procedures used in these studies have been adequately described in previous publications,<sup>(1-7)</sup> only the important features of the data analyses and the conclusions drawn from them are presented in this paper. Also, emphasis will be placed on the more recent unpublished results.

### RESULTS AND DISCUSSION

#### Isothermal Studies of the Li-H and Li-D Systems

An experimental study of the Li-H and Li-D systems has been undertaken at ANL to obtain reliable pressure-composition-temperature data that are amenable to the derivation of useful thermodynamic quantities for these systems. The experimental data were obtained by a tensimetric method using a modified Sieverts' apparatus. The equilibrium hydrogen pressure over lithium-lithium hydride mixtures, sealed in iron capsules, was measured as a function of temperature and composition. The apparatus and experimental procedures are described in detail elsewhere.<sup>(1)</sup>

Pressure-composition isotherms obtained for the Li-H and Li-D systems are shown in Fig. 1. The general features of each family of isothermal curves are analogous--there are two terminal solutions separated by an extensive two-liquid region (miscibility gap). The data in Fig. 1 were used to calculate activity coefficients for Li and LiH (or LiD) in each of the homogeneous terminal solutions as follows. The reaction between hydrogen gas and liquid lithium is assumed to result in a solution of hydride (H<sup>-</sup>, D<sup>-</sup>, or T<sup>-</sup>) in lithium according to Eq. (1).



The equilibrium constant,  $K_{\text{eq}}$ , for this reaction is given by

\*Work performed under the auspices of the U. S. Energy Research and Development Administration.

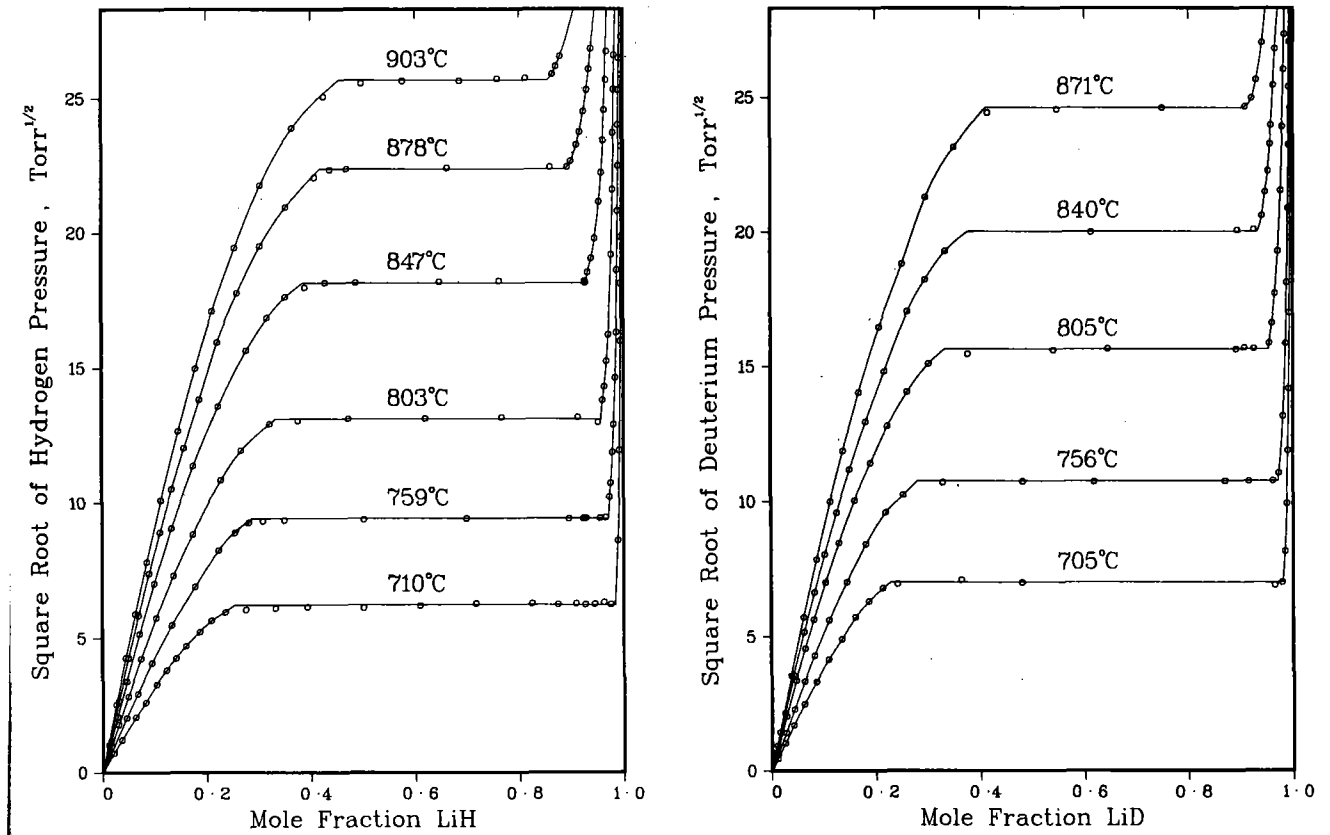


Fig. 1. Projections of Isothermal Data for the Systems Li-H and Li-D

$$K_{\text{eq}} = \frac{N_2 \gamma_2}{N_1 \gamma_1 P_{\text{H}_2}^{1/2}} \quad (2)$$

where  $N_1$  and  $N_2$  are the mole fractions of Li and LiH, respectively;  $\gamma_1$  and  $\gamma_2$  are the corresponding activity coefficients; and  $P_{\text{H}_2}$  is the equilibrium hydrogen pressure. Equation (2) can be written in the form

$$\ln \left( P_{\text{H}_2}^{1/2} \frac{N_1}{N_2} \right) = -\ln K_{\text{eq}} + \ln \frac{\gamma_2}{\gamma_1} \quad (3)$$

In accord with the Margules-type treatment of binary solutions,<sup>(1)</sup> the activity coefficients may be represented by power series in  $N_1$  and  $N_2$ . When these series are truncated at their cubic terms, the activity coefficients are consistently given by

$$\ln \gamma_1 = \alpha N_2^2 + \beta N_2^3 \quad (4)$$

and

$$\ln \gamma_2 = \left( \alpha + \frac{3}{2} \beta \right) N_1^2 - \beta N_1^3 \quad (5)$$

Substitution of Eqs. (4) and (5) into Eq. (3) gives

$$\ln \left( P_{\text{H}_2}^{1/2} \frac{N_1}{N_2} \right) = -\ln K_{\text{eq}} + \alpha(1-2N_2) + \frac{1}{2} \beta(1-3N_2^2) \quad (6)$$

The data in Fig. 1 have been refined<sup>(1,2)</sup> to give values for the parameters  $\alpha$  and  $\beta$  which allow calculation of the activity coefficients. Equations derived from these activity coefficients for (1) the equilib-

rium constants,  $K_{\text{eq}}$ ; (2) the standard free energies of formation,  $\Delta G_f^\circ$ , of LiH (and LiD); and (3) the Sieverts' Law parameters,  $K_s = N_2/P^{1/2}$  are given in Table I.

Accurate knowledge of the thermodynamic properties of the Li-H and Li-D systems has also permitted estimates of the corresponding properties of the Li-T system. An approximate relationship for the Sieverts' Law parameter for tritium solutions in lithium was obtained from the Li-H and Li-D data using the procedure described in a previous ANL report.<sup>(7)</sup> This relationship, given by Eq. (7), is probably reliable to within  $\pm 20\%$ .

$$\ln K_{s,T_2} (\text{mole fraction } T^- / \text{atm}^{1/2}) = -6.0 + 5,400 T^{-1} \quad (7)$$

Precise knowledge of  $\Delta G_f^\circ$  is important in determining the stabilities of lithium hydrides *vis-à-vis* those of the hydrides of other structural and impurity elements in the blanket of a fusion reactor. The Sieverts' Law parameter provides an important relationship between hydrogen ( $\text{H}_2$ ,  $\text{D}_2$ , or  $\text{T}_2$ ) pressure and hydride ( $\text{H}^-$ ,  $\text{D}^-$ , or  $\text{T}^-$ ) concentration for dilute solutions in lithium. This relationship is likely to be useful in the conception and development of recovery systems and monitoring equipment for hydrogen isotopes

**Table I.** Relationships for Selected Properties of the Systems Li-H, Li-D, and Li-N

System	Property <sup>a</sup> vs. Kelvin Temperature (T)
Li-H	$\ln K_{eq} (\text{atm}^{-1/2}) = -6.78 + 8,328 T^{-1}$
	$\Delta G_f^\circ (\text{kcal/mole}) = -16.6 + 13.5 \times 10^{-3} T$
	$\ln K_s (\text{mol fract./atm}^{1/2}) = -6.50 + 6,182 T^{-1}$
Li-D	$\ln K_{eq} (\text{atm}^{-1/2}) = -6.65 + 8,013 T^{-1}$
	$\Delta G_f^\circ (\text{kcal/mole}) = -15.9 + 13.2 \times 10^{-3} T$
	$\ln K_s (\text{mol fract./atm}^{1/2}) = -6.17 + 5,634 T^{-1}$
Li-N	$\ln S (\text{mole \% Li}_3\text{N}) = 7.65 - 4851 T^{-1}$
	$\ln K_{eq} (\text{atm}^{-1/2}) = -16.7 + 19,670 T^{-1}$
	$\Delta G_f^\circ (\text{kcal/mole}) = -39.1 + 33.2 \times 10^{-3} T$
	$\ln K_s (\text{mol fract./atm}^{1/2}) = -13.8 + 14,590 T^{-1}$

<sup>a</sup> $K_{eq}$  = Equilibrium Constant       $\Delta G_f^\circ$  = Standard Free Energy of Formation  
 S = Solubility                               $K_s$  = Sieverts' Constant

in a liquid-lithium blanket. The results of our studies of the Li-LiH and Li-LiD systems appear to be in good agreement with comparable data measured at other laboratories. (8-11)

#### Plateau Pressure Studies of the Li-H, Li-D, and Li-T Systems

Isotope effects resulting from the interaction of liquid lithium with hydrogen isotopes have been studied by measuring the equilibrium pressures of H<sub>2</sub>, D<sub>2</sub>, or T<sub>2</sub> over their solutions in lithium. The measurements were carried out within the two-phase fields of the respective phase diagrams. In these fields the decomposition pressures do not vary with composition, thus permitting more precise measurements.

Although a separate series of experiments was made for each system, the same lithium sample and identical procedures were employed. Briefly, the procedure was as follows. Approximately 35 mg of lithium was sealed in a small iron capsule having sufficiently thin walls to permit rapid permeation of gaseous hydrogen isotopes. The encapsulated lithium was reacted with ~40 std. cm<sup>3</sup> of gas (H<sub>2</sub>, D<sub>2</sub>, T<sub>2</sub>) to produce an ~60 mol % LiH, LiD, or LiT solution. Equilibrium decomposition pressures were then determined in 25-degree intervals between 600 and 850°C. The results are shown in Fig. 2 where the logarithms of plateau pressures ( $P_{H_2}$ ,  $P_{D_2}$ , and  $P_{T_2}$ ) are plotted against 1/T. The "as-received" tritium contained 9.0 mol % total H<sub>2</sub> and 1.6 mol % total D<sub>2</sub>. The values of  $P_{T_2}$  shown in Fig. 2 were corrected for these impurities and thus correspond to pure tritium. Each plot in Fig. 2 has two

linear branches, the crossing point of which represents the monotectic temperature for the corresponding system (694°C for Li-H, 690°C for LiD, and 688°C for Li-T).

As is seen from Fig. 2, for a given temperature, the plateau pressures tend to increase with increasing isotopic mass. This is expected<sup>(12)</sup> since, in the progression from hydride to tritide, the heats of formation increase, while the entropies of formation decrease (*cf.* Table I). The observed isotope effects are listed in Table II for several representative temperatures. At lower temperature, the values are close to the corresponding square root of mass ratios ( $\sqrt{2}$  for D/H and  $\sqrt{3}$  for T/H). Towards the higher temperatures, however, the effects tend to decrease, probably due to the differences in the temperature coefficients of the partition functions for the isotopic species involved.

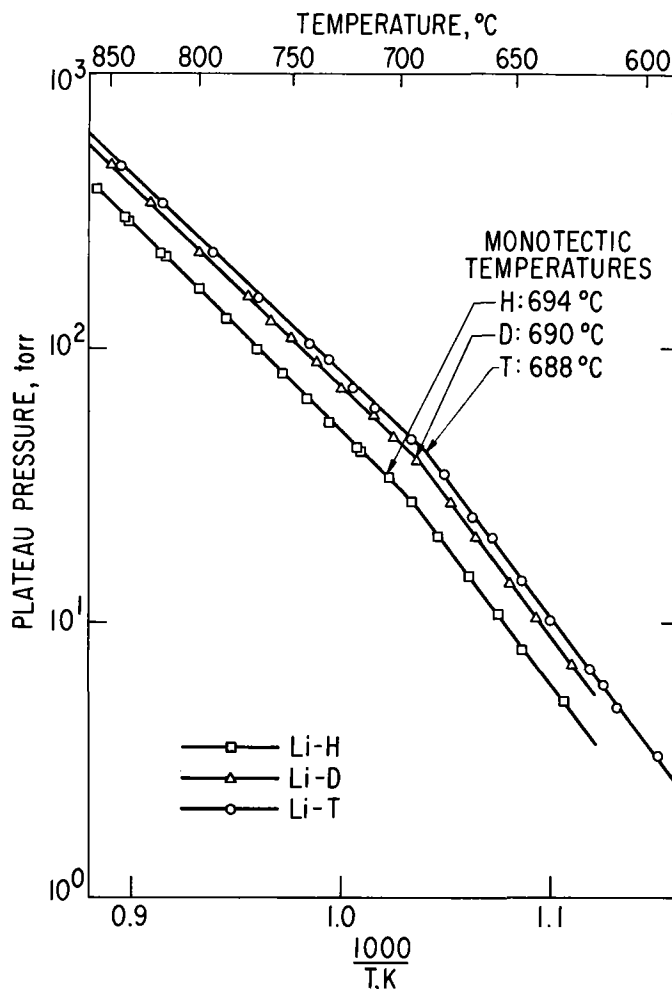


Fig. 2. Decomposition Pressure of Hydrogen, Deuterium, and Tritium over Their Solutions in Lithium Within the Two-Phase Fields

Table II. Temperature Dependence of D/H and T/H Isotope Effects

Temperature (°C)	$P_{D_2}/P_{H_2}$ (±0.03)	$P_{T_2}/P_{H_2}$ (±0.03)
600	1.46	1.75
650	1.48	1.73
700	1.45	1.65
750	1.42	1.57
800	1.38	1.51
850	1.35	1.45

Solubility of Lithium Deuteride in Liquid Lithium

The liquidus lines of the systems Li-H and Li-D are only partially known. Between the monotectic temperature (694°C for Li-H and 690°C for Li-D) and the critical solution temperature (~1000°), the lines may be determined from Fig. 1. Below the monotectic, however, essentially no data were available until recently, when a study<sup>(11)</sup> on the solubility of hydrogen in liquid lithium, using an electric resistance method, was published by the University of Nottingham. Concurrently, we initiated an investigation to measure the solubility of LiD in liquid lithium between 220 and 500°C by a direct sampling method. Twenty-four equilibrated melt samples were taken from saturated solutions of LiD in lithium. Details of the sampling technique have been presented elsewhere.<sup>(4)</sup> Briefly, ~250 g of purified lithium was placed in a large Armco iron container. A 5.5 mol % solution of LiD in lithium was prepared *in situ* by additions of measured volumes of deuterium gas to molten lithium. Samples of the melt were taken by lowering pre-evacuated, fritted sample tubes into the melt and then pressurizing the melt with helium. The deuterium content of the samples was determined by sealing the filled sample tubes in Armco iron capsules, heating them to 840°C, collecting the thermally decomposed deuterium with a Toepler pump, and measuring the volume of the evolved gas. The composition of the gas was then determined by a mass-spectrometric analysis.

Solubility data are shown in Fig. 3 on a reciprocal-absolute temperature *vs* log solubility plot. Owing to the progressively increasing deviations from ideality towards the more dilute solutions, the data do not fall on a straight line. A smooth liquidus line connecting the eutectic and monotectic temperatures was generated in the following manner. Consider a solution having a composition that corresponds to the liquidus curve at the monotectic temperature (21.5 mol % LiD). At this point,  $a_{LiD} \approx 1$  and the monotectic temperature

may be looked upon as the freezing point of pure LiD ("solvent"). As more Li ("solute") is added to this solution, it will undergo a freezing point lowering, as shown in Fig. 3 by the descending branch of the solubility curve. Activity of the solvent,  $a_{LiD}$ , is related to the freezing point lowering,  $\theta$ , by the equation<sup>(13)</sup>

$$\ln a_{LiD} = -\frac{\Delta H_f}{R} \frac{\theta}{T T_f} + \frac{\Delta a}{R} \left\{ \frac{\theta}{T} + \ln \left[ 1 - \frac{\theta}{T_f} \right] \right\} + \frac{\Delta b}{R} \frac{\theta^2}{2T} \quad (8)$$

where  $T_f$  is the monotectic temperature,  $\Delta H_f$  approximates the latent heat of fusion of LiD,  $\theta = (T_f - T)$  is the freezing point lowering, and  $\Delta Cp = \Delta a + \Delta b T = 11.90 - 0.0132 T$  (JANAF values for LiH) is the difference between the heat capacities of liquid and solid LiD.

Since  $a_{LiD} = N_{LiD} \gamma_{LiD}$ , the activities can be calculated for each experimental temperature from the  $N_{LiD}$ 's and from the activity coefficients that were extrapolated from equations previously derived<sup>(2)</sup> for higher temperatures in the same phase field. Equation (8) was then used to calculate  $\Delta H_f$  by the method of least squares. Its value, 6.35 kcal/mol, actually corresponds to the sum of the heat of fusion of pure LiD (JANAF value: 5.40 kcal/mol) and the differential heat of solution of LiD at the monotectic point. Any point on the liquidus line in Fig. 3 can then be evaluated from Eq. (8) by substituting into it an appropriate value of  $\gamma_{LiD}$ . The same treatment was applied to the electrical resistance data for the Li-H system.<sup>(11)</sup> The results (shown in Fig. 3) are in good agreement with our Li-D data--the hydrogen solubilities being somewhat higher, as expected, due to H/D isotope effects.

Extrapolation of the LiD solubility curve to the melting point of lithium (180.5°C) gives a eutectic composition of ~0.028 mol % LiD. This high value appears to rule out hydrogen isotope separation from lithium based on cold-trapping methods. The freezing point depression, calculated from the eutectic composition and the latent heat of fusion of lithium (754.3 kcal/mol), was found to be 0.15°C. This gives 180.35°C for the eutectic temperature.

Studies of the Li-N System

In previous reports,<sup>(2,7)</sup> we discussed the shortcomings of published physicochemical data on the Li-N, Li-O, and Li-C binary systems. As part of a comprehensive program to measure the thermodynamic properties and phase relationships in these systems, the solubility of Li<sub>3</sub>N in lithium and the thermal decomposition of Li<sub>3</sub>N have been studied.

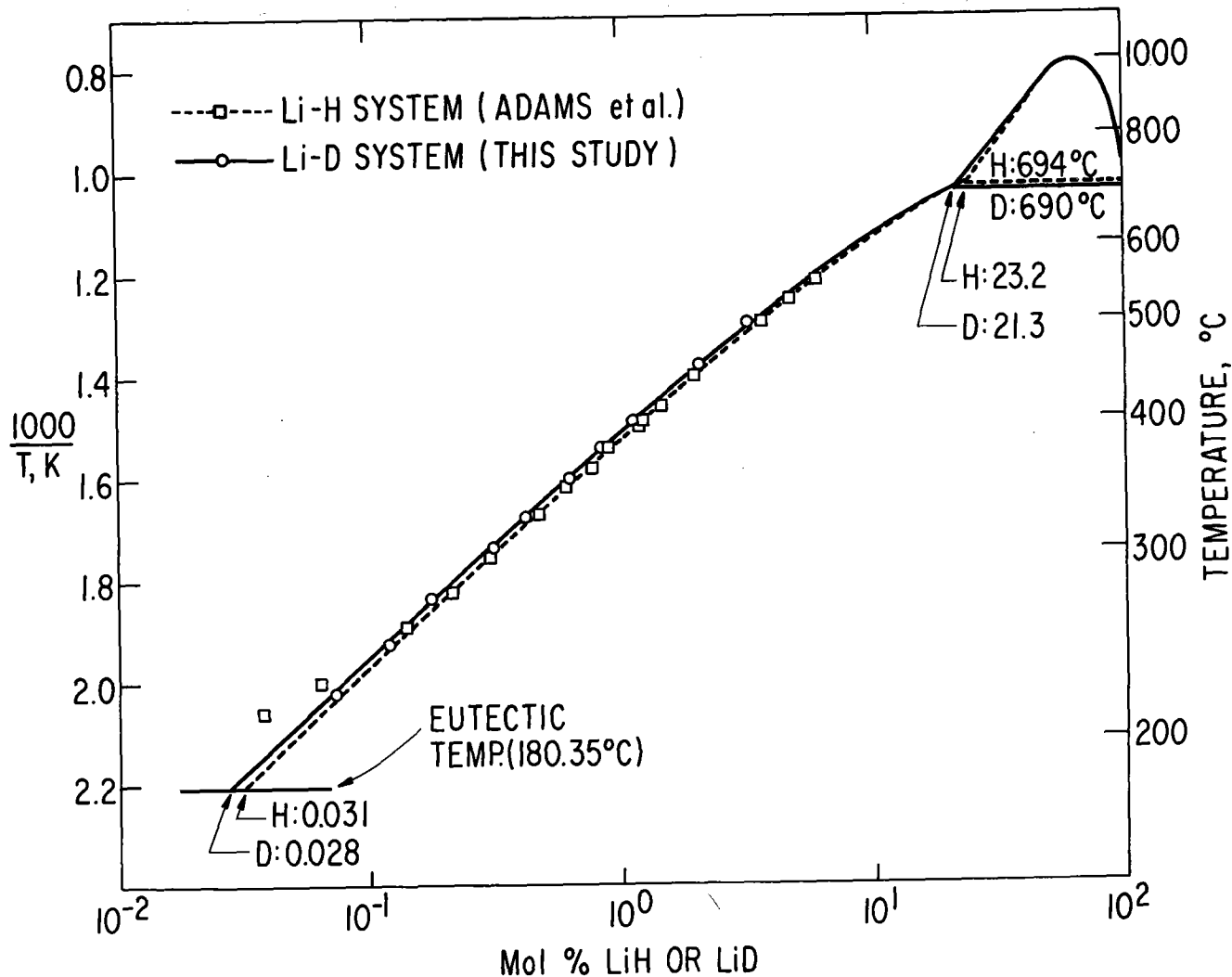


Fig. 3. Reciprocal Kelvin Temperature vs Log Composition Diagram for the Li-H and Li-D Systems

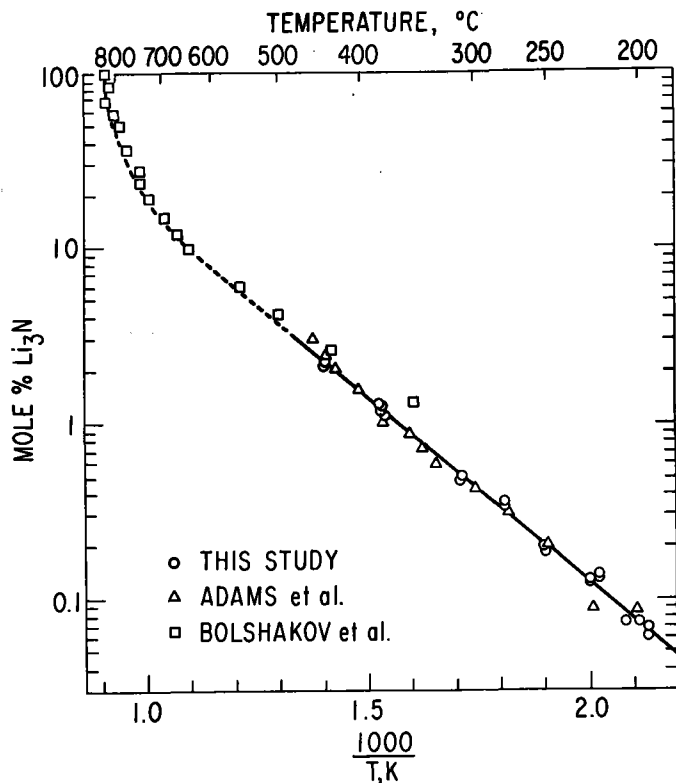
$\text{Li}_3\text{N}$  was prepared by direct reaction at room temperature of lithium metal and nitrogen gas at 8 atm pressure. The product had an oxygen content of  $\sim 0.2$  weight percent and a Li/N mole ratio of 3.01. The solubility of  $\text{Li}_3\text{N}$  in liquid lithium was measured<sup>(4)</sup> by taking filtered samples of saturated solutions at temperatures ranging from 195° to 441°C. The logarithm of mol %  $\text{Li}_3\text{N}$  is plotted against  $1/T$  in Fig. 4. Least squares analysis of 22 points representing saturated solutions of  $\text{Li}_3\text{N}$  in liquid lithium gives the expression

$$\ln S = 7.651 - 4852 T^{-1} \quad (9)$$

where  $S$  is in mol %  $\text{Li}_3\text{N}$  and  $T$  is the Kelvin temperature. The relative partial molal heat of solution of solid  $\text{Li}_3\text{N}$  is calculated to be  $\bar{H}_{\text{Li}_3\text{N}}(\text{soln}) - \bar{H}_{\text{Li}_3\text{N}}^\circ(\text{s}) = 9.6 \pm 0.3 \text{ kcal/mol}$ . The 95% confidence error in  $S$  is 4%.

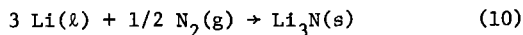
The previously published thermal analysis data of Bolshakov *et al.*<sup>(14)</sup> are also shown in Fig. 4. Their results in the 1-10 mol %  $\text{Li}_3\text{N}$  region seem to be in error, probably due to undercooling effects resulting from the steep solubility curve in this region. At  $\sim 10$  mol %  $\text{Li}_3\text{N}$ , our extrapolated solubility line appears to join smoothly with the thermal analysis data. Also included in Fig. 4 are some recently reported results of Adams *et al.*,<sup>(11)</sup> obtained by resistometric methods. Their data in the 200 to 500°C range are in excellent agreement with our results.

The decomposition pressure of  $\text{Li}_3\text{N}$  was measured by heating granular  $\text{Li}_3\text{N}$  to a selected temperature, measuring the equilibrium pressure, and analyzing the gas phase for nitrogen. Nitrogen partial pressures,  $P_{\text{N}_2}$ , measured between 660° and 778°C are given in Table III. The melting point of  $\text{Li}_3\text{N}$  was estimated from a cooling curve obtained for molten  $\text{Li}_3\text{N}$ . The


 Fig. 4. Solubility of  $\text{Li}_3\text{N}$  in Liquid Lithium

observed value of  $813 \pm 1^\circ\text{C}$  agrees well with the literature value<sup>(14)</sup> of  $815^\circ\text{C}$ .

The combined solubility and thermal decomposition data have been used to derive selected thermodynamic properties for the Li-N system, as detailed in Ref. 4. Expressions giving the equilibrium constant for the reaction



the Sieverts' constant for dilute solutions of nitrogen in liquid lithium, and the free energy of formation of  $\text{Li}_3\text{N}$  are listed in Table I. The standard entropy and enthalpy of formation of  $\text{Li}_3\text{N}$  at 1000 K disagree with values listed in the JANAF Tables but are in good agreement with recent calorimetric values obtained at ANL,<sup>(15,16)</sup> *i.e.*,  $\Delta H_f^\circ(\text{kcal/mole}) = -39.1$  (this work),  $= -40.01$  (ANL<sup>(15)</sup>),  $= -47.96$  (JANAF) and  $\Delta S_f^\circ(\text{e.u.}) = -33.2$  (this work),  $= -32.55$  (ANL<sup>(16)</sup>),  $= -38.50$  (JANAF).

Recently, Smith and Natesan<sup>(17)</sup> published an assessment of the consequences to lithium/refractory alloy compatibility due to the presence of non-metallic elements (*i.e.*, O, N, and C) in liquid lithium. The principal conclusion of this assessment, based largely on correlations involving the relative stabilities of the binary metal-non-metal compounds and their solu-

Table III. Decomposition Pressures of Solid  $\text{Li}_3\text{N}$ , Solubilities and Activity Coefficients at the Liquidus Line, Equilibrium Constants, and Sieverts' Constants for the Li- $\text{Li}_3\text{N}$  System

Temp. (°C)	$P_{\text{N}_2}$ (Torr)	$N_{\text{Li}_3\text{N}}$	$\gamma_{\text{Li}}$	$K_{\text{eq}}^{-1/2}$ (atm <sup>-1/2</sup> )	$K_s^a$
660.6	0.239	0.120	1.025	76.8	6.29
681.2	0.648	0.139	1.032	48.8	4.42
701.4	1.79	0.169	1.047	31.3	3.20
720.2	4.23	0.195	1.062	21.4	2.38
739.2	9.90	0.236	1.091	15.1	1.86
758.3	24.8	0.285	1.132	10.4	1.40
772.3	53.0	0.360	1.216	8.03	1.18
777.8	68.1	0.380	1.242	7.32	1.10

<sup>a</sup>Sieverts' constant,  $K_s = N_{\text{Li}_3\text{N}} \sqrt{P}$ , in units of mole fraction per atm<sup>1/2</sup> (dilute solution limit).

bilities in liquid lithium, was that in the case of vanadium and vanadium base alloys serious materials integrity problems can result from ppm levels of dissolved C and/or N. In light of our new data for the Li-N system, the results presented in Ref. 17 for nitride-abetted interactions can be updated. Figure 5 shows the revised free-energy-of-formation curve for  $\text{Li}_3\text{N}$  in comparison with the free energy curves for Nb, Zr, and Mo, together with their prominent alloying elements Ti, Zr, and Cr. The new solubility data reaffirm the contention of Smith and Natesan that the use of a cold trap to control nitrogen levels in liquid lithium would be largely ineffective--the solubility of nitrogen in lithium at the melting point of lithium is  $\sim 1000$  ppm.

These revised data for nitrogen related interactions in lithium/refractory alloy systems have little impact on the general conclusions in Ref. 17. The minimum nitrogen concentrations in lithium that must be reached before the corresponding container-material nitride will begin to precipitate from the metal lattice are from one to two orders of magnitude lower than those indicated in Fig. 4 of Ref. 17. Revised limits on these concentrations are given in Table IV for the temperatures 500 and  $800^\circ\text{C}$ . The calculated values are omitted in cases where they (1) exceed the saturation solubility of nitrogen in liquid lithium or (2) are below a reasonably maintainable limit for nitrogen in lithium which for the purposes of this assessment was set at the conservatively low level of  $< 10^{-5}$  wppm.

Although the results presented above and in Ref. 17 are geared toward lithium/refractory alloy

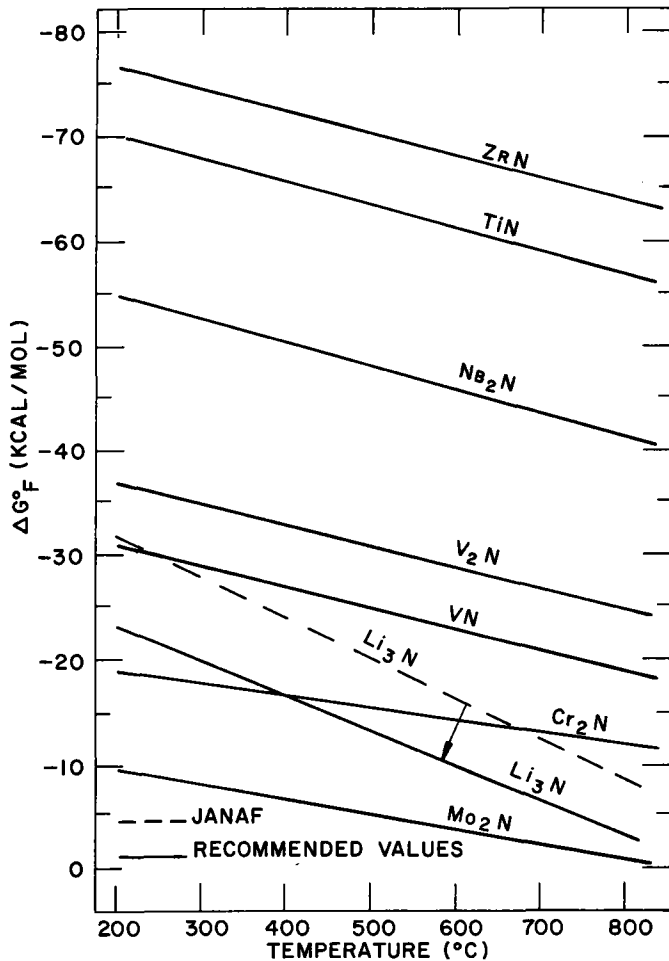


Fig. 5. Standard Free Energies of Formation of Selected Metal Nitrides (This Work and Reference 17)

Table IV. Nitrogen Concentration in Lithium (in ppm by weight) Required to Precipitate the Corresponding Metal Nitride

Material	500°C		800°C	
	Ref. 17	Revised	Ref. 17	Revised
Mo	(a)	(a)	(a)	(a)
Cr	(a)	2.7 E+4 <sup>c</sup>	3.3 E+4	1.1 E+3
V	3.5 E+1	8.9 E-1	6.1 E+1	1.9 E+1
Nb	5.5 E-4	1.4 E-5	2.8 E-2	9.1 E-3
Ti	(b)	(b)	2.1 E-5	(b)
Zr	(b)	(b)	(b)	(b)

<sup>a</sup>Exceeds the saturation solubility of nitrogen in lithium at the indicated temperature.

<sup>b</sup>Lower than any reasonably maintainable limits for nitrogen in liquid lithium (*i.e.*,  $<10^{-5}$  ppm).

<sup>c</sup>The notation E±N denotes  $\times 10^{\pm N}$ .

#### Purification of Lithium by Molten Salt Extraction

The capability of maintaining non-metallic element concentrations (particularly tritium) in liquid lithium at levels that are  $\leq 1$  ppm appears to be essential to the implementation of liquid lithium as a fusion reactor blanket material.<sup>(5-7)</sup> Studies<sup>(5)</sup> conducted in our laboratory during the past several years have shown that it may be possible to achieve very low tritium levels in liquid lithium blankets by using molten salt extraction as a processing method. Typical volumetric distribution coefficients (tritium content per unit volume in the salt/tritium content per unit volume in lithium) were found to be:  $\sim 4$  for the LiF-LiCl eutectic at 600°C,  $\sim 3$  for LiCl-KCl eutectic at 550°C, and  $\sim 1$  for LiBr-RbBr eutectic at 500°C. These results, in combination with considerations of (1) mutual solubilities between salt and metal, (2) phase separation, (3) blanket neutronics, (4) corrosion, (5) fabrication, and (6) recovery of tritium from the salt phase, indicate that molten-salt extraction of tritium from liquid-lithium fusion-reactor blankets should be feasible.<sup>(5)</sup> The most immediate aspect of the molten-salt-extraction concept in need of verification (following the studies reported in Ref. 5) is the process for removing tritium (present as LiT) from the molten salt after it has been contacted with and separated from the lithium. Experiments are currently in progress to evaluate (1) gas sparging techniques using HCl, DCl, Cl<sub>2</sub>, and other related chemicals that would react with LiT to evolve molecular tritium or a tritium halide and (2) electrochemical techniques employing either a hydrogen-permeable metal electrode or a porous-valve electrode

interactions, some comments on what they indicate with respect to lithium/stainless steel interactions can also be made. Nickel and iron are not known to form stable binary nitrides; hence, the free-energies of formation of their nitrides are assumed to be, at best, considerably more positive than those of molybdenum nitride at all temperatures of interest (*i.e.*, 200 to 1000°C) and, for the sake of this discussion, the interactions of Fe and Ni with nitrogen contaminated lithium are ignored. The data in Fig. 5 show that the crossover point in the relative stability of Cr<sub>2</sub>N and Li<sub>3</sub>N is near 400°C; therefore, at and above 400°C the chromium in stainless steel will begin to pick up appreciable quantities of nitrogen, but Cr<sub>2</sub>N will not exist as a separate phase as long as the nitrogen level in the lithium is maintained well below 10<sup>4</sup> ppm (*cf.* Table IV). The only perceptible consequence of this nitridation of the chromium will be increased chromium mass transport, to the extent that the Cr<sub>2</sub>N is at all soluble in liquid lithium.



MOLTEN SALT-LiCl/KCl EUTECTIC  
SALT TEMPERATURE -500°C  
QUANTITY OF SALT-1,000g (18 moles)

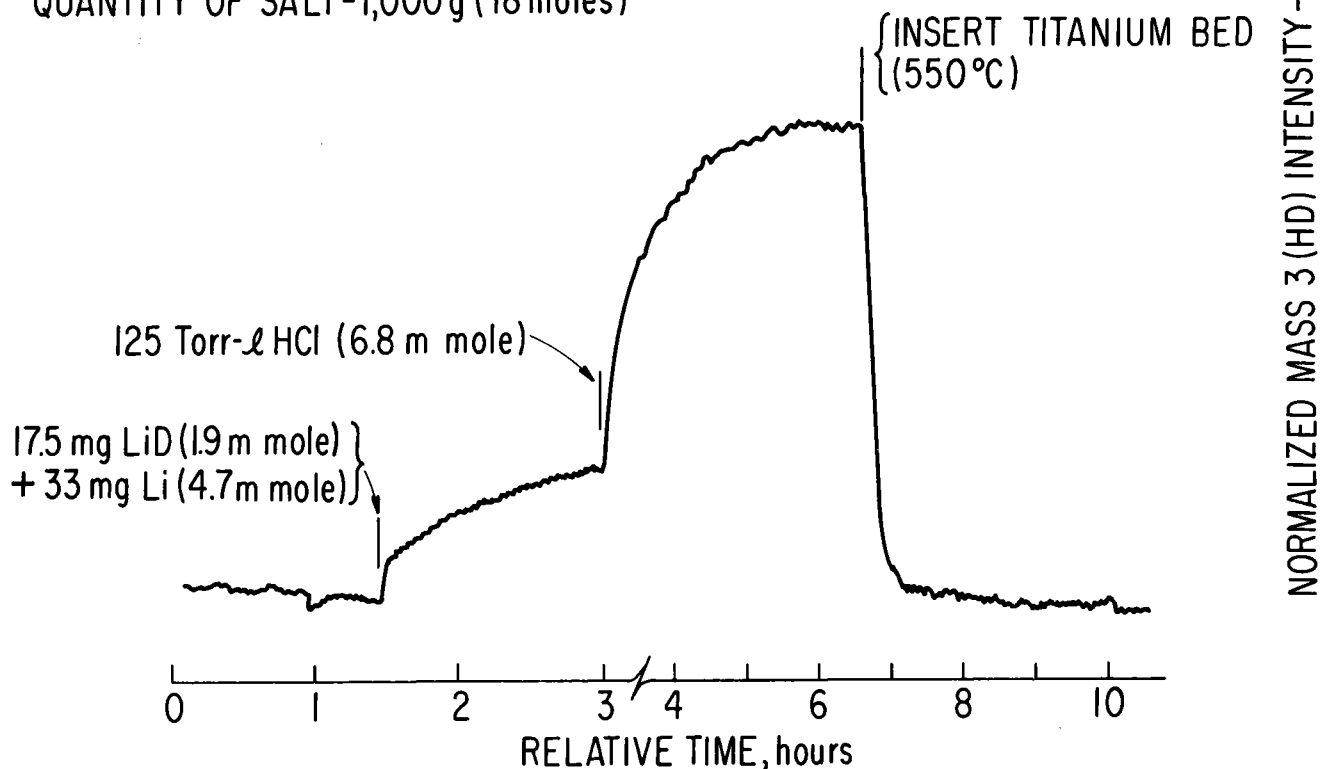


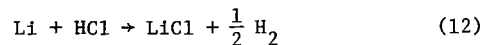
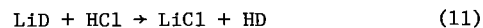
Fig. 6. Results of a Typical Gas Sparging Experiment to Evolve Deuterium from a Solution of LiD in LiCl-KCl Eutectic

that would permit simultaneous evolution and trapping of molecular tritium. (Details of both techniques are given in Ref. 5.) Initial results of the gas sparging studies, carried out using LiD as a substitute for LiT, are summarized below.

The apparatus consists of a stainless steel gas handling system connected to a furnace well containing a stirred pot filled with molten LiCl-KCl eutectic (m.p.  $\sim 350^\circ\text{C}$ ). Argon gas at  $\sim 1$  atm pressure is circulated in a closed loop through a porous graphite bubbler (immersed in the molten salt) and then past a controlled leak valve which is coupled to a quadrupole mass spectrometer. The gas line is also equipped with (1) a titanium getter bed (operated at  $550^\circ\text{C}$ ) which is used to clean up the argon sweep gas prior to and following experiments and (2) a gas metering section which permits addition of controlled quantities of the sparge gas or hydrogen (for calibration purposes) to the sweep gas.

In a typical experiment, a known quantity of a LiD-Li mixture is equilibrated with the molten salt.

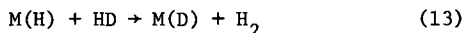
(The lithium metal is included with the LiD in anticipation of the fact that in the molten salt extraction process itself some dissolved lithium would return to the salt processor with the LiT after the contacting and separating stages.) An equimolar quantity of HCl is then added to the sweep gas producing the reactions



The LiD titration reaction (Eq. 11) is followed by monitoring the HD (mass 3) signal from the mass spectrometer. Figure 6 shows the results of an experiment wherein 17.5 mg of LiD and 33 mg of Li were added to 1.0 kg of salt and sparged with 125 torr-liters of HCl.

The initial increase in HD immediately after addition of the LiD-Li mixture is presumably due to (1) LiD reacting with impurities in the system and (2) equilibration of the Li-LiD mixture in the molten salt environment. Two probable impurity reactions are with the carbon from the graphite bubbler and residual HCl from previous titrations. Subsequent to the addition of the HCl, the mass 3 signal increases sharply as a

result of the titration reactions. After insertion of the titanium bed, the HD signal drops rapidly showing that the evolved hydrogen isotopes can be readily gettered from the argon stream in a form that would be suitable for recycle to an isotope separation system. Based on a calibration of the mass-spectrometer signal using H<sub>2</sub>, the overall recovery of the deuterium as HD is ~80% for a typical run. Additional deuterium may be present in other forms (e.g., D<sub>2</sub>, C<sub>2</sub>D<sub>2</sub>) due to the impurity reactions. It is also likely that some of the deuterium is lost due to the exchange reactions



where M(H) and M(D) represent H or D dissolved in the furnace well and salt pot.

The principal significance of the results in Fig. 6 is that the amount of LiD added to the salt corresponds to only 6 wppm of tritium in the salt, yet extraction of the deuterium appears to be complete and a sizable fraction is actually recovered. Assuming that the salt is contacted with an equal volume of lithium, taking account of the density differences between liquid lithium and LiCl-KCl eutectic (~1:3), and applying an effective volumetric distribution coefficient of 3, it turns out that the corresponding weight fraction of tritium in the lithium leaving the contactor/separator stage would also be ~6 wppm. Recovery limits for tritium in the molten salt using the sparging method illustrated in Fig. 6 appear to be limited only by the effects of having to introduce substantial amounts of the sparge gas in order to titrate out all of the dissolved lithium metal. In essence, the tritium level in the molten salt returning to the contactor/separator stages can be reduced to less than 1 wppm and, in principle, the tritium level in the corresponding lithium circuit can also be maintained at or below 1 wppm. The actual tritium level in the lithium will depend on the fraction of the blanket inventory processed per unit time, which in turn will be determined largely by cyclic turn-around times in the contactor/separator and in the salt clean-up stage.

#### ACKNOWLEDGMENTS

The authors wish to acknowledge the assistance of W. R. Wilkes and H. S. Carden of Mound Laboratory in obtaining isotopic analyses of the "as-received" tritium sample. The studies of lithium-non-metallic element systems were supported by ERDA's Division of Physical Research and the salt extraction studies were supported by the Systems Engineering Branch of ERDA's Division of Controlled Thermonuclear Research.

#### REFERENCES

1. E. Veleckis, E. H. Van Deventer and M. Blander, "The Lithium-Lithium Hydride System," *J. Phys. Chem.* **78**, 1933-1940 (1974).
2. M. Blander *et al.*, *Chemical Engineering Division Physical Inorganic Chemistry Annual Report: July 1973-June 1974*, Argonne National Laboratory Report ANL-8123 (November, 1974).
3. V. A. Maroni *et al.*, *Chemical Engineering Division Liquid Metals Chemistry and Tritium Control Technology Annual Report: July 1974-June 1975*, Argonne National Laboratory Report ANL-75-50 (September, 1975).
4. R. M. Yonco, E. Veleckis and V. A. Maroni, "Solubility of Nitrogen in Liquid Lithium and Thermal Decomposition of Solid Li<sub>3</sub>N," *J. Nucl. Mater.* **57**, 317-324 (1975).
5. V. A. Maroni, R. D. Wolson and G. E. Staahl, "Some Preliminary Considerations of a Molten Salt Extraction Process to Remove Tritium from Liquid Lithium Fusion Reactor Blankets," *Nucl. Technol.* **25**, 83-91 (1975).
6. E. Veleckis and V. A. Maroni, "Thermodynamic Properties of Solutions of Hydrogen Isotopes in Metals and Alloys of Interest to Fusion Reactor Technology," *Proceedings of the International Conference on Radiation Effects and Tritium Technology for Fusion Reactors*, October 1-3, 1975, Gatlinburg, Tennessee (in press).
7. V. A. Maroni, E. J. Cairns and F. A. Cafasso, *A Review of the Chemical, Physical, and Thermal Properties of Lithium that are Related to Its Use in Fusion Reactors*, Argonne National Laboratory Report ANL-8001 (March, 1973).
8. F. J. Smith and J. F. Land, "The Hydrogen Isotope-Lithium Systems," *Transactions of the American Nuclear Society Annual Meeting: June 1975*, p. 167 (June, 1975).
9. D. H. J. Goodall and G. M. McCracken, "An Experimental Study of Hydrogen in Liquid Lithium," *Proceedings of the 7th Symposium on Fusion Technology*, Grenoble, 1972, p. 151.
10. H. R. Ihle and C. H. Wu, "Thermodynamic Study of the System Lithium-Hydrogen Utilizing Mass Spectrometric Knudsen Effusion Method," *J. Inorg. Nucl. Chem.* **36**, 2167-2170 (1974).
11. P. F. Adams, M. G. Down, P. Hubberstey and R. J. Pulham, "Solubilities and Solution and Solvation Enthalpies for Nitrogen and Hydrogen in Liquid Lithium," *J. Less-Common Met.* **42**, 325-334 (1975).
12. G. G. Libowitz, *The Solid-State Chemistry of Binary Metal Hydrides*, W. A. Benjamin, Inc., New York, N. Y., 1965 (p. 57).
13. See, for example, G. N. Lewis and M. Randall, *Thermodynamics*, 2nd Edition, McGraw-Hill Book Co., New York, N. Y., 1961 (p. 404).
14. K. A. Bolshakov, P. I. Federov, and L. A. Stepina, "Diagram of Fusibility of the System Lithium-Lithium Nitride," *Izvest. Vysshikh Ucheb. Zavedenii, Tsvetnaya Met.* **2**, 52-53 (1959).
15. P. A. G. O'Hare and G. K. Johnson, "Lithium Nitride (Li<sub>3</sub>N): Standard Enthalpy of Formation by Solution Calorimetry," *J. Chem. Thermod.* **7**, 13-20 (1975).
16. D. W. Osborne and H. E. Flotow, Argonne National Laboratory, personal communication.
17. D. L. Smith and K. Natesan, "Influence of Non-Metallic Impurity Elements on the Compatibility of Liquid Lithium with Potential CTR Containment Materials," *Nucl. Technol.* **22**, 392-404 (1974).

## THE CORROSION OF FERROUS ALLOYS IN NITROGEN CONTAMINATED LIQUID LITHIUM

D. L. Olson and W. L. Bradley  
 Department of Metallurgical Engineering  
 Colorado School of Mines  
 Golden, Colorado 80401

ABSTRACT

Liquid lithium penetration of 304L stainless steel and Armco iron grain boundaries has been studied. The penetration kinetics for the 304L stainless steel was found to be diffusion controlled. The measured temperature dependent delay time has been associated with the initial formation of the corrosion product at the grain boundary. Nitrogen in the stainless steel or the liquid lithium has been found to accelerate the rate of attack without changing the apparent activation energy. Grain boundary grooving of Armco iron in liquid lithium indicates that the controlling mass transport is also through a corrosion product present as a surface film. Stresses as small as 12 MPa have been found to give rise to a fifty-fold increase in the rate of penetration of Armco iron by liquid lithium.

INTRODUCTION

The corrosion behavior of 304L stainless steel and Armco iron in nitrogen contaminated liquid lithium has been investigated with static isothermal experiments intended to obtain a mechanistic interpretation of the corrosion process. With a model for the rate controlling corrosion process, it is anticipated that the necessary modifications of the liquid lithium or the ferrous container alloys can be determined so that the corrosion process can be further hindered. The liquid lithium corrosion model being developed must explain the observed grain boundary penetration, weight loss and grain boundary grooving results reported in this paper.

STAINLESS STEEL IN LIQUID LITHIUM

Penetration and weight loss kinetics were determined for unstressed 304L stainless steel as functions of both temperature and nitrogen concentration. All tests were conducted under inert protective atmosphere of 99.5% pure argon. A low oxygen level was accomplished by bubbling the incoming argon through a liquid sodium-potassium alloy and then maintained by stirring another flask of liquid sodium-potassium open to the glove-box atmosphere at room temperature.

Test specimens from an annealed 304L stainless steel sheet with an initial grain size of 0.0449 mm were immersed in liquid lithium (99.9% purity) con-

tained in a 304L stainless steel crucible to eliminate dissimilar metal effects. The liquid lithium was brought slowly to the test temperature and then maintained there for six hours to allow quasi-equilibrium to be established before introduction of the test specimen. After removal from the liquid lithium, the stainless steel specimens were cleaned by immersion in water followed by an ultrasonic cleaning in methanol. At least two specimens were examined for each test condition to establish reproducibility. The grain boundary penetration of the various specimens was measured metallographically. Ferric chloride, chromic acid, and oxalic acid etches were all investigated to eliminate the possibility that the observed penetration traces were only artifacts of the special etching technique used. All penetration measurements were taken perpendicular to the edge of the nitrated sample and represent a 10 reading average. The weight change measurements were made after cleaning. A more detailed account of the experimental procedures used in this work has been published elsewhere (1-4).

LIQUID LITHIUM PENETRATION

The results of measurements of the grain boundary penetration by liquid lithium as a function of time at various temperatures are presented in Figures 1 and 2. The penetration,  $X$ , as a function of time,  $t$ , can

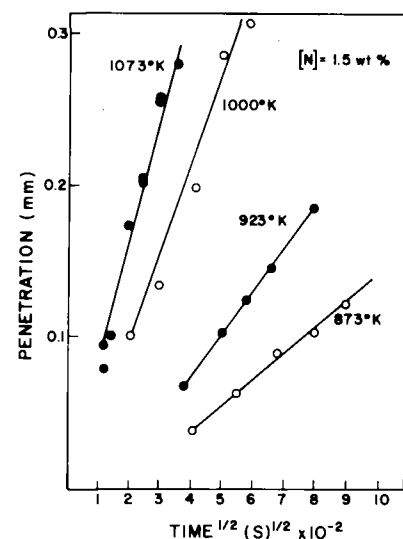


Fig. 1. The grain boundary penetration of 304L stainless steel versus the square root of time for temperatures below 1073°K.

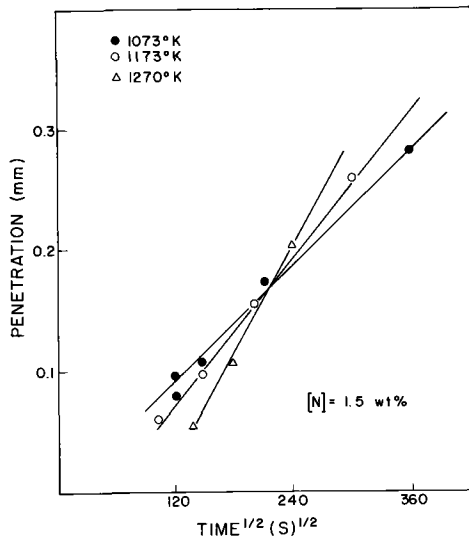


Fig. 2. The grain boundary penetration of 304L stainless steel versus the square root of time for the temperatures above 1073°K.

be described by an equation of the form

$$X = (Kt)^{1/2} \quad (1)$$

where  $K$  is a temperature dependent penetration rate coefficient. This  $t^{1/2}$  dependence for grain boundary penetration suggests that the rate controlling process involves diffusion of species through a constant chemical potential difference, but with a diffusion distance that is increasing with time.

It is probable that the temperature dependence of  $K$  is associated with some thermally activated process described by an Arrhenius rate expression of the form

$$K = K_0 e^{-Q/RT} \quad (2)$$

Determining the penetration rate coefficient from Figures 1 and 2 and plotting these coefficients as a function of temperature as shown in Figure 3 allows the determination of " $Q$ ", the apparent activation energy barrier for the rate limiting mechanisms. Below 1073°K, the apparent activation energy for grain boundary penetration is approximately 130 kJ/mole (31 kcal/mole). Above 1073°K the apparent activation energy changes to 71 kJ/mole (17 kcal/mole) indicating a change in the rate controlling step for this corrosion process.

If one extrapolates the " $X$ " versus " $t^{1/2}$ " plots of Figures 1 and 2, they are found to intersect  $X=0$  at times greater than zero, indicating the penetration may only proceed after some initial incubation period, or delay time. It should also be noted that the delay time is temperature dependent. The delay time when plotted as a function of temperature (Figure 4) has the frequently observed c-shape. This is

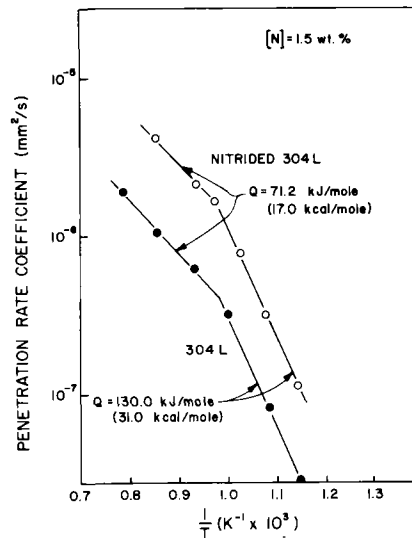


Fig. 3. The temperature dependence of the grain boundary penetration rate coefficients for the 304L and nitrided 304L stainless steel.

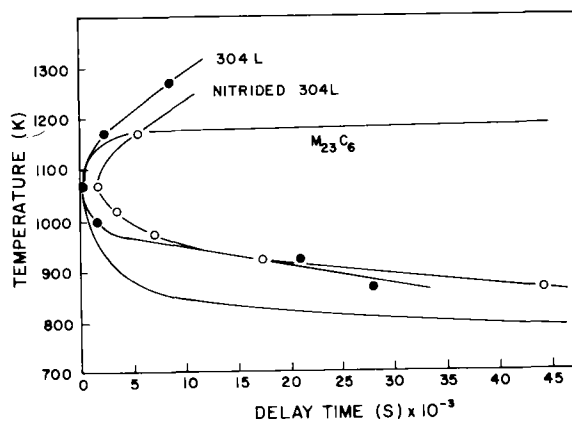


Fig. 4. The delay time for the grain boundary penetration in 304L and nitrided 304L stainless steel as a function of temperature is compared to the time to nucleate a metal carbide in 316L stainless steel.

usually attributed to a small thermodynamic driving force at higher temperatures and sluggish mass transport kinetics at lower temperatures. This shape is very similar to that found for typical nucleation rate versus temperature curves. If a corrosion product is assumed to be formed in the penetrated grain boundaries, the nucleation kinetics for this corrosion product could explain the observed delay time.

#### THE EFFECT OF NITROGEN ON LIQUID LITHIUM PENETRATION

Nitrogen has been reported to accelerate the corrosion of stainless steel by liquid lithium (5). Therefore, it was decided to investigate nitrogen in the stainless steel (via nitriding) as well as the role of nitrogen in the liquid lithium on grain boundary penetration and weight loss in stainless steel

attacked by liquid lithium.

The initial part of this investigation involved experimental determination of the effect of nitrogen in the stainless steel on the rate of grain boundary penetration by liquid lithium. The nitriding of the stainless steel was achieved by annealing in an ammonia atmosphere until saturation occurred (approximately 0.21 wt percent nitrogen). The penetration was found to have a parabolic time dependence in the temperature range of 873<sup>o</sup>K to 1273<sup>o</sup>K as was previously observed with the unnitrided samples. The logarithm of grain boundary penetration rate coefficients,  $K$ , were determined and plotted as a function of the inverse of temperatures to determine the apparent activation energy. These results are presented in Figure 3 along with similar results for unnitrided 304L stainless steel for comparison.

The grain boundary penetration rate for the nitrated stainless steel was definitely higher for all temperatures, but the shape of the Arrhenius plot remained the same. There was also the change in apparent mechanism at approximately 1073<sup>o</sup>K. The similarity of the apparent activation energies for nitrated and unnitrided stainless steel strongly suggests that the migration of atomic nitrogen along the grain boundaries is not the rate controlling mechanism though the availability of nitrogen at the corrosion interface is seen to accelerate the penetration rate. It would seem that " $K_0$ " in equation (2) is a function of nitrogen concentration, but not " $Q$ ".

A delay time was also observed for the grain boundary penetration in the nitrated stainless steel. Figure 4 shows the delay time for both conditions as a function of temperature. Both of these curves have the typical c-shape of a nucleation temperature-time plot. The minimum in both of these delay time curves apparently occurs at approximately 1073<sup>o</sup>K.

In Figure 4 the temperature-delay time curves have reasonable agreement with the reported (6) nucleation time for metal carbide ( $M_{23}C_6$ ) in 316 stainless steel. The shift for longer delay times for the penetration of the nitrated stainless steel could possibly be explained by the metal carbide nucleation at the grain boundaries. The excessive nitrogen saturation in the stainless steel could be hindering the carbon migration in stainless steel, thus delaying the carbide nucleation.

In order to investigate the effect of nitrogen concentration in the liquid lithium on its corrosion of 304L stainless steel, a preliminary experimental

program was undertaken to determine how to vary, control and measure the nitrogen concentration in the test liquid lithium. The results of this work have been published elsewhere (2,3) and may be summarized as follows. First, a technique for the measurement of lithium nitride in the liquid lithium was developed using a modified Kjeldahl distillation technique. Second, it was determined that the exposure of the system to sufficient nitrogen to allow lithium nitride saturation as evidenced by a lithium nitride crust on top of the liquid gave a relatively constant composition of nitrogen (in the form of lithium nitride) over a temperature range of 873<sup>o</sup>K to 1073<sup>o</sup>K, as seen in Figure 5. It is believed that the leveling off of the nitrogen concentration in the non-titanium gettered liquid lithium above 773<sup>o</sup>K is due to the increasing effectiveness of chromium from the stainless steel system as a nitrogen getter. Third, titanium additions to the liquid lithium were made to provide a lower nitrogen level in the lithium, since titanium nitride is more thermodynamically stable than lithium nitride. The nitrogen concentration as a function of temperature for the titanium gettered liquid lithium is also seen in Figure 5. Note that the nitrogen concentration of the titanium gettered liquid lithium is an order of magnitude smaller than the ungettered lithium. The break in the nitrogen concentration of titanium gettered liquid lithium is possibly related to the dissociation of lithium nitride at 1088<sup>o</sup>K (7), which would affect the equilibrium conditions.

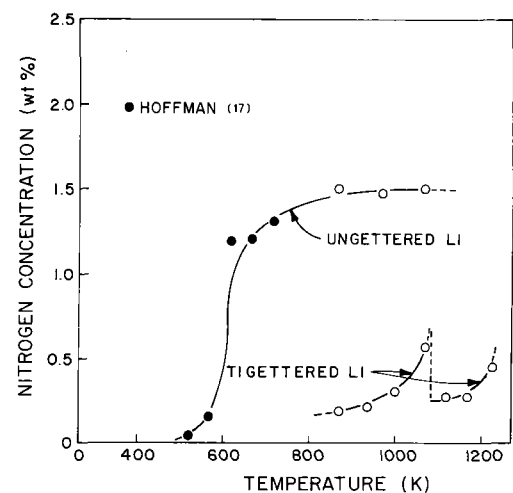


Fig. 5. Nitrogen concentration of the test liquid lithium as a function of temperature.

The grain boundary penetration of 304L stainless steel at 1073<sup>o</sup>K in ungettered and titanium gettered liquid lithium is seen in Figure 6. Nitrogen is clearly seen to accelerate the penetration rate. The

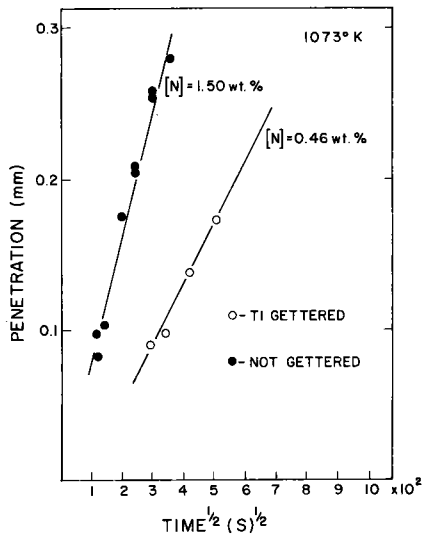


Fig. 6. Penetration versus the square root of time for ungettered and titanium gettered liquid lithium at 1073°K.

temperature dependence for the grain boundary penetration rate coefficient for 304L stainless steel in titanium gettered liquid lithium can be seen in Figure 7.

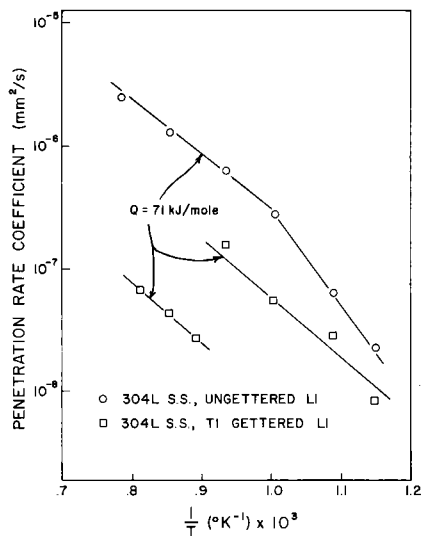


Fig. 7. The temperature dependence of the penetration rate coefficients for 304L stainless steel in ungettered and gettered liquid lithium.

Notice the discontinuity in the rate coefficients at 1123°K and that the apparent activation energy has the same value of 71 kJ/mole (17 kcal/mole) at the lower temperature as has been reported for all the high temperature results.

Typical results of the weight loss behavior of 304L stainless steel in liquid lithium for two nitrogen concentrations at 1073°K are shown in Figure 8. A duplex weight loss behavior was observed in the higher nitrogen concentrated liquid lithium. The

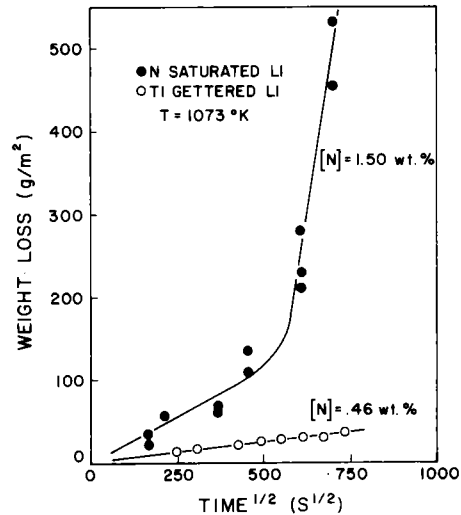


Fig. 8. Weight loss as a function of square root of time for 304L stainless steel for various nitrogen concentrations of the liquid lithium.

observed increase in the rate of weight loss is due to a more highly localized attack which causes a breaking up and degradation of the surface. The duplex nature of weight loss was not observed in any of the tests run in titanium gettered liquid lithium. This secondary weight loss behavior may appear in the titanium gettered liquid lithium at much longer test times.

The initial weight loss,  $w$ , was also found to follow a parabolic time dependence:

$$w = \frac{\text{weight loss}}{\text{surface area}} = (k't)^{1/2} \quad (3)$$

where  $k'$  is the weight loss rate coefficient. An Arrhenius plot of the experimental weight loss rate coefficient is shown in Figure 9. Since the rate of attack is dependent on the nitrogen concentration, different curves are plotted for the various nitrogen concentrations using ungettered and titanium gettered liquid lithium. The similar slopes for the three curves indicate (as with the earlier results on nitrated stainless steel) that nitrogen availability accelerates the attack but does not change the apparent activation energy. The weight loss coefficients as a function of nitrogen concentration and temperature were found to be given by:

$$k' = 53.3[N]^{2.5} \exp(-71[\text{kJ/mole}]/RT) \text{ gm}^2/\text{m}^4\text{-S} \quad 873^\circ\text{K} \leq T \leq 1073^\circ\text{K} \quad (4)$$

and

$$k' = 82.2[N]^{2.5} \exp(-71[\text{kJ/mole}]/RT) \text{ gm}^2/\text{m}^4\text{-S} \quad 1123^\circ\text{K} \leq T \leq 1273^\circ\text{K} \quad (5)$$

where  $N$  is nitrogen concentration in liquid lithium measured in weight percent. Equations (4) and (5) are both required in order to describe the weight loss

behavior above and below the discontinuity in the nitrogen concentration seen in Figure 5.

#### ARMCO IRON IN LIQUID LITHIUM

The liquid lithium corrosion behavior of pure iron, which has a low corrosion rate compared to other ferrous alloys, must be determined if the influence of alloy additions on this corrosion behavior is to be understood. The morphological relaxation of iron grain boundary grooves in nitrogen contaminated liquid lithium was used to determine the mass transport mechanism associated with the iron-liquid lithium interface.

The width of the grain boundary groove was determined as a function of time and temperature. The experimental details have been published elsewhere (10). The mean value of the exponent of the power law time dependence obtained for each of the test temperatures was determined to be 0.32 which is in good agreement with the predicted value of 0.33 for volume diffusion (8). Another technique for determining the mechanism of grain boundary grooving is by analyzing the individual thermal groove profiles (9). Both ridge height and ridge depth were measured for a number of groove profiles and the results obtained had a mean ratio ( $h/d$ ) of 0.143, which is very close to the expected value of 0.149 for volume diffusion.

The grain boundary grooving rate coefficients,  $K$ , for the various temperatures can be obtained as the slope of the plots of width versus  $(\text{time})^{1/3}$ . The expression for the volume diffusion coefficient,  $D_v$ , can be related to the measured rate coefficient,  $K$  (8). This expression is:

$$D_v = \frac{K^3 kT}{125 \gamma_{s1} C_0 \Omega^2} \quad (6)$$

where  $\gamma_{s1}$  is solid-liquid interfacial tension,  $C_0$  is the concentration of the diffusing atoms,  $\Omega$  is the atomic volume, and  $kT$  has the usual significance. A value of  $2.00 \text{ J/m}^2$  was obtained for interfacial tension,  $\gamma_{s1}$ , by measurements of the dihedral angle of the thermal groove. The diffusion coefficients can be calculated for two of the three possible volume diffusion paths; diffusion through the liquid lithium and diffusion through the alpha-iron. Where the diffusion path is assumed to be through the solid alpha-iron, the resulting activation energy obtained was approximately  $133 \text{ kJ/mole}$  ( $31.9 \text{ kcal/mole}$ ) which is not in agreement with the reported value of  $240 \text{ kJ/mole}$  ( $57.3 \text{ kcal/mole}$ ) (11) for self-diffusion of iron in iron. In addition to this disagreement in activa-

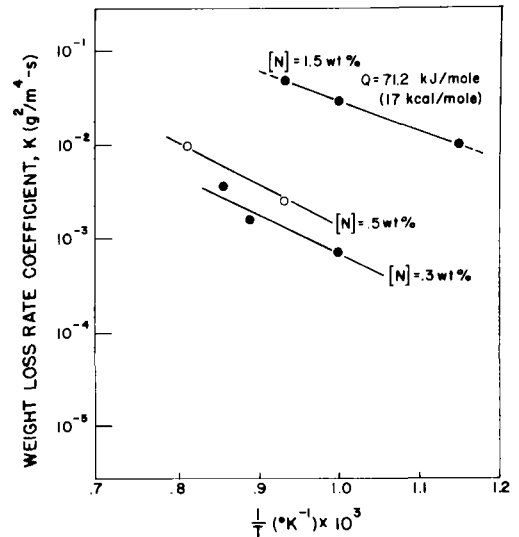


Fig. 9. The temperature dependence for the weight loss rate coefficients for various nitrogen concentrations of the liquid lithium.

tion energies, the magnitude of the calculated diffusion coefficients are not consistent with the diffusion coefficients for self-diffusion in iron for this temperature range. Assuming the diffusion path is through the liquid lithium, the reported values for the activation energy and the magnitudes of liquid diffusion coefficients are also not consistent with the calculated values ( $75 \text{ kJ/mole}$ ) obtained from this investigation. These results strongly suggest, by the process of elimination of the possible paths being considered, that there may exist a corrosion product film and that the rate controlling process is associated with volume diffusion in this corrosion product.

For thermal grooving of pure iron in nitrogen contaminated liquid lithium, there are three major diffusing species (Fe, Li, and N). The value of the concentration of diffusing atoms,  $C_0$ , is unknown. However, by assuming that the corrosion product has a definite stoichiometry,  $C_0$  can be treated as a constant. With the measured rate coefficients,  $K$ , established,  $\log K^3 T$  versus  $1/T$  was plotted as illustrated in Figure 10. The resulting activation energy was found to be  $134 \text{ kJ/mole}$  ( $32 \text{ kcal/mole}$ ).

This activation energy is identical to values obtained for the grain boundary penetration of 304L stainless steel (1) and for nitrided 304L stainless steel (4). In the penetration experiments the lithium would be expected to be the diffusing species, whereas in this grain boundary grooving investigation the migration of iron from the groove is measured. For all of these processes to be governed by the same rate

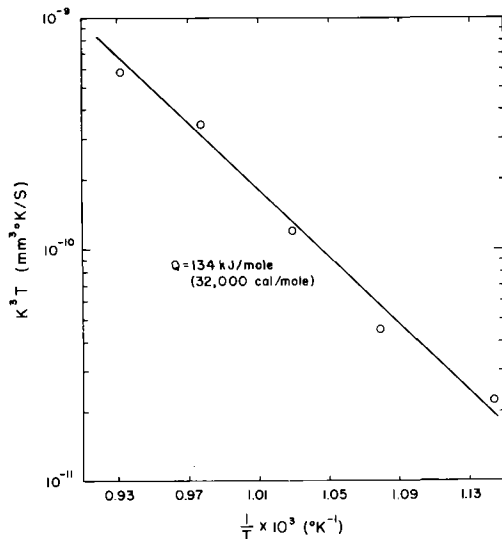


Fig. 10. The determination of the apparent activation energy for the rate controlling volume diffusion process for the grain boundary grooving of iron in liquid lithium.

controlling step, a more complex mass transport process must be operating. It is possible for a coupled diffusion process to be rate controlling. This process would involve migration of ions in the corrosion product. The ionic migration will be controlled by the concentration gradients and maintenance of charge neutrality.

The liquid-solid and grain boundary interfacial energies may be thought of as giving rise to tension per unit length along triple points. Force equilibrium requires that

$$2\gamma_{ls} \cos\theta = \gamma_{gb} \quad (9)$$

For  $\gamma_{gb}/2\gamma_{ls} < 1$ , force equilibrium may be established, and  $\cos\theta$  measured, which was the result in this work. But if  $\gamma_{gb}/2\gamma_{ls} > 1$ , then force equilibrium could not be established, no grain boundary grooving would occur and capillarity would then be expected to be the driving force for grain boundary penetration.

#### STRESS DEPENDENCE OF LIQUID LITHIUM PENETRATION

Earlier work by other investigators (12) suggests that liquid lithium may penetrate a stressed metal much more rapidly than an unstressed one. Experiments were run to determine whether this would also be true of Armco iron. The experimental details have been published elsewhere (13).

The stress dependence of the liquid lithium penetration of the Armco iron grain boundaries is presented in Figure 11 for various times and temperatures. Replotting the data of Figure 11 in the form of "X"

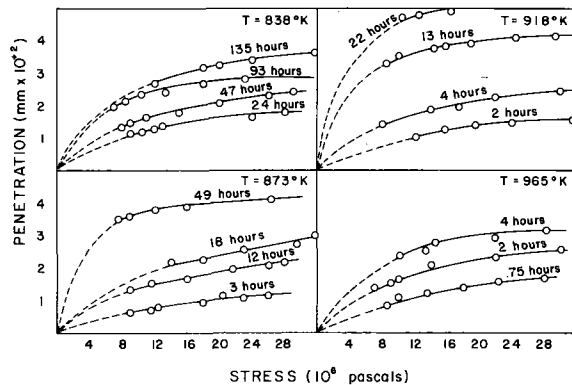


Fig. 11. Lithium penetration into pure iron as a function of applied stress on the specimen for various times and temperatures.

versus " $t^{1/3}$ " allows one to determine the penetration rate coefficients,  $K(\sigma, T)$  for various combinations of stress and temperature, as shown in Figure 12. It is worth noting that a  $t^{1/2}$  dependence is more typically observed for penetration of unstressed specimen. If one assumes that the liquid lithium penetration of the grain boundaries is a thermally activated process described by an Arrhenius expression

$$K(\sigma, T) = K_0 e^{-Q/RT} \quad (10)$$

then the apparent activation energy,  $Q$ , for a stress level can be determined as shown in Figure 13. The results for a stress level of 28 MPa (Figure 13) imply two different mechanisms are rate controlling at temperatures above and below 923°K. The lower temperature mechanism has an apparent activation energy of 311 kJ/mole (74.3 kcal/mole). A similar analysis of the results presented in Figure 12 for a stress of 12 MPa suggests an apparent activation of 284 kJ/mole (67.8 kcal/mole) which is essentially identical to the results for a stress of 28 MPa within experimental uncertainty. The stress appears to affect only the pre-exponential term " $K_0$ " in equation (2), causing it to increase with increasing stress. The liquid lithium penetration of Armco iron grain boundaries has been found to increase with increasing temperature, stress,  $\sigma$ , and time,  $t$ , and may be described as follows:

$$X = (K_0(\sigma) e^{-\frac{296 \text{ kJ/mole}}{RT}} t)^{1/3} \quad (11)$$

The measured apparent activation energies for liquid lithium penetration of Armco iron is similar to that observed for creep in Armco iron; namely, 285 kJ/mole (14). To test the hypothesis that creep is the rate controlling process, the total penetration distance was plotted as a function of the total creep strain, as seen in Figure 14. The linear relationship between penetration distances and total strains obtained for a variety of test times, temperatures, and stresses lends



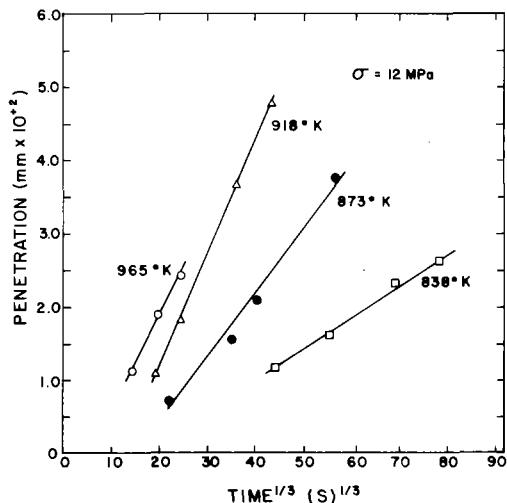


Fig. 12. Lithium penetration into pure iron vs. (time)<sup>1/3</sup> at several temperatures and for a stress of 12 MPa.

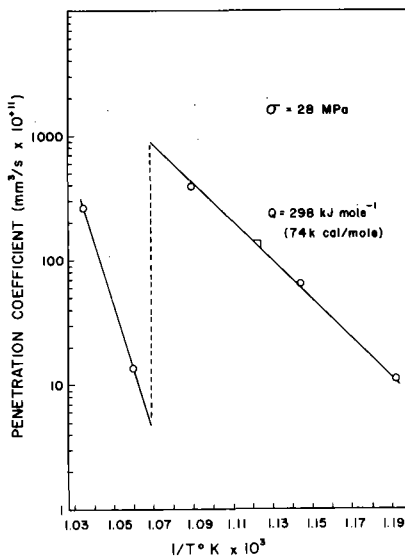


Fig. 13. Temperature dependence of the penetration rate coefficient for pure iron at a stress of 28 MPa in liquid lithium.

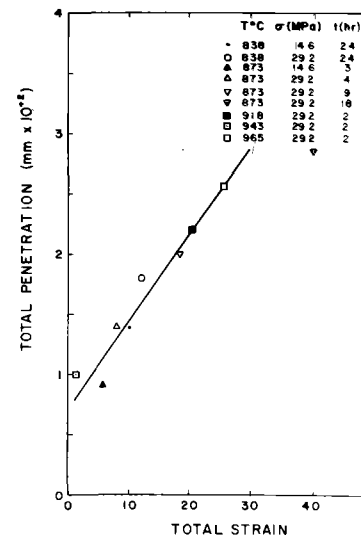


Fig. 14. Total iron penetration by the liquid lithium vs. total strain for various combinations of temperature, stress, and time.

support to the hypothesis that creep deformation is the rate limiting process in liquid lithium penetration of stressed Armco iron grain boundaries.

Parkins (15) has recently suggested that stress accelerates the corrosion rate in many systems by producing deformation which either ruptures the surface films or prevents its formation. Since most surface films offer some measure of protection to the base metal, this would result in a more rapid corrosion attack. Parkins suggests that stress and temperature are only important indirectly through their respective effects on the creep rate. The fact that the total penetration distances observed were apparently a single valued function of creep strain for various combinations of time, temperature and stress seems to support the model of Parkins. It appears that during corrosion of Armco iron by liquid lithium, a thin surface film is formed which greatly decelerates the corrosive attack. Application of even a small stress can cause creep deformation which ruptures this film and greatly accelerates the attack. Several unstressed specimens placed in the liquid lithium-containing crucible at T=9180K with a stressed specimen were found to have less than 1x10<sup>-5</sup>m of grain boundary penetration compared to approximately 5x10<sup>-4</sup>m of penetration for the stressed specimen (σ=12 MPa). Thus, it is clear that very low level stresses can produce a fifty-fold increase in the rate of grain boundary penetration of Armco iron by liquid lithium.

It has been suggested that penetration distance is a single valued function of creep strain. This would

imply that the creep strain should also be a function of "t<sup>1/3</sup>". Such a dependence is often observed during primary creep of metals. To see if such a time dependence for creep strain could be observed for creep of Armco iron in liquid lithium, several creep tests were run. The limited data taken suggested that primary creep of Armco iron in liquid lithium could be described by  $\epsilon = Ct^{.37 \pm .07}$  (12) This result is in reasonable agreement with the expected one of "t<sup>1/3</sup>".

A discontinuity in the temperature dependence of the penetration rate can be seen in Fig. 13. A change in the mechanism of corrosion of unstressed Armco iron in liquid lithium has also been found in this same temperature range by Popovich (16).

ACKNOWLEDGMENT

The authors acknowledge and appreciate support of this investigation by the Energy Research & Development Administration under contract E(11-1)-2313.

REFERENCES

1. R.A. Patterson, R.J. Schlager & D.L. Olson, Nucl. Mat. 57, 312 (1975).
2. R.J. Schlager, D.L. Olson & W.L. Bradley, Nucl. Tech. 27, 439 (1975).
3. R.J. Schlager, R.A. Patterson, D.L. Olson & W.L. Bradley, Nucl. Tech. 29, 94 (1976).
4. J.A. Reeves, Jr., D.L. Olson & W.L. Bradley, accepted for publ. in Nucl. Tech.
5. E.E. Hoffman, USAEC Rept. ORNL-2024 (1960).
6. B. Weiss and R. Strickler, Met. Trans. 3, 851 (1972).
7. R.P. Elliot, ed., Constitution of Binary Alloys, McGraw-Hill, N.Y., p. 582 (1965).
8. W.W. Mullins, Metal Surfaces, ASM, p. 17 (1962).
9. B.C. Allen, Trans. Met. Soc. AIME 236, 915 (1966).
10. L.B. Whitefield, M.S. Thesis (T-1727), Colo. Sch. Mines (1975); submitted for publication.
11. D. Graham & D. Tomlin, Phil. Mag. 8, 1581 (1963).
12. V.V. Popovich, Fiz. Khim. Mekh. Mat. 5, 444 (1969).
13. W. Jordan, W.L. Bradley & D.L. Olson, to be published in Nucl. Tech.
14. J.E. Dorn, Creep and Recovery, ASM, 255 (1955).
15. R.N. Parkins, Corrosion 29, 251 (1973).
16. V.V. Popovich, Fiz. Khim. Mekh. Mat. 6, 282 (1970).
17. E.E. Hoffman, USAEC Rept. ORNL-2894 (1960).

SHIPPED FROM NTIS  
MAY 11 1981